

DOCUMENT RESUME

ED 306 099

SE 050 495

AUTHOR Clark, John W., Ed.; And Others
 TITLE Proceedings of the World Congress on Medical Physics and Biomedical Engineering (San Antonio, Texas, August 6-12, 1988).
 INSTITUTION Alliance for Engineering in Medicine and Biology, Washington, DC.
 PUB DATE 88
 NOTE 445p.; Contains small and light print which may not reproduce well.
 PUB TYPE Collected Works - Conference Proceedings (021)
 JOURNAL CIT Physics in Medicine & Biology; v33 suppl 1 1988

EDRS PRICE MF01/PC18 Plus Postage.
 DESCRIPTORS *Biological Sciences; Biomechanics; Biomedical Equipment; Biomedicine; *Biophysics; *Engineering Technology; Global Approach; Human Factors Engineering; *Medicine; Physics; Research Problems; *Science and Society; *Scientific and Technical Information; Technology

ABSTRACT

This document contains the proceedings of a joint meeting of the International Federation for Medical and Biological Engineering and the International Organization for Medical Physics. Participants from over 50 countries were in attendance. The theme of the program, "Challenges for the Year 2000," was a reminder of the challenges which confront the world community; specifically, better, more widely distributed, and less expensive health care, and a continuing concern for the well being of humanity and of the earth. The proceedings contain abstracts from over 200 papers, speeches, and sessions, and is organized into medical physics and biomedical engineering sections. (CW)

 * Reproductions supplied by EDRS are the best that can be made *
 * from the original document. *

U.S. DEPARTMENT OF EDUCATION
Office of Educational Research and Improvement
EDUCATIONAL RESOURCES INFORMATION
CENTER (ERIC)

- This document has been reproduced as received from the person or organization originating it.
- Minor changes have been made to improve reproduction quality.
- Points of view or opinions stated in this document do not necessarily represent official ERIC position or policy.

"PERMISSION TO REPRODUCE THIS MATERIAL HAS BEEN GRANTED BY

Patricia Horner

TO THE EDUCATIONAL RESOURCES INFORMATION CENTER (ERIC)."

Proceedings of the World Congress on Medical Physics and Biomedical Engineering

1983, Vol. 1, 2, 3, 4, 5, 6, 7, 8, 9, 10, 11, 12, 13, 14, 15, 16, 17, 18, 19, 20, 21, 22, 23, 24, 25, 26, 27, 28, 29, 30, 31, 32, 33, 34, 35, 36, 37, 38, 39, 40, 41, 42, 43, 44, 45, 46, 47, 48, 49, 50, 51, 52, 53, 54, 55, 56, 57, 58, 59, 60, 61, 62, 63, 64, 65, 66, 67, 68, 69, 70, 71, 72, 73, 74, 75, 76, 77, 78, 79, 80, 81, 82, 83, 84, 85, 86, 87, 88, 89, 90, 91, 92, 93, 94, 95, 96, 97, 98, 99, 100, 101, 102, 103, 104, 105, 106, 107, 108, 109, 110, 111, 112, 113, 114, 115, 116, 117, 118, 119, 120, 121, 122, 123, 124, 125, 126, 127, 128, 129, 130, 131, 132, 133, 134, 135, 136, 137, 138, 139, 140, 141, 142, 143, 144, 145, 146, 147, 148, 149, 150, 151, 152, 153, 154, 155, 156, 157, 158, 159, 160, 161, 162, 163, 164, 165, 166, 167, 168, 169, 170, 171, 172, 173, 174, 175, 176, 177, 178, 179, 180, 181, 182, 183, 184, 185, 186, 187, 188, 189, 190, 191, 192, 193, 194, 195, 196, 197, 198, 199, 200, 201, 202, 203, 204, 205, 206, 207, 208, 209, 210, 211, 212, 213, 214, 215, 216, 217, 218, 219, 220, 221, 222, 223, 224, 225, 226, 227, 228, 229, 230, 231, 232, 233, 234, 235, 236, 237, 238, 239, 240, 241, 242, 243, 244, 245, 246, 247, 248, 249, 250, 251, 252, 253, 254, 255, 256, 257, 258, 259, 260, 261, 262, 263, 264, 265, 266, 267, 268, 269, 270, 271, 272, 273, 274, 275, 276, 277, 278, 279, 280, 281, 282, 283, 284, 285, 286, 287, 288, 289, 290, 291, 292, 293, 294, 295, 296, 297, 298, 299, 300, 301, 302, 303, 304, 305, 306, 307, 308, 309, 310, 311, 312, 313, 314, 315, 316, 317, 318, 319, 320, 321, 322, 323, 324, 325, 326, 327, 328, 329, 330, 331, 332, 333, 334, 335, 336, 337, 338, 339, 340, 341, 342, 343, 344, 345, 346, 347, 348, 349, 350, 351, 352, 353, 354, 355, 356, 357, 358, 359, 360, 361, 362, 363, 364, 365, 366, 367, 368, 369, 370, 371, 372, 373, 374, 375, 376, 377, 378, 379, 380, 381, 382, 383, 384, 385, 386, 387, 388, 389, 390, 391, 392, 393, 394, 395, 396, 397, 398, 399, 400, 401, 402, 403, 404, 405, 406, 407, 408, 409, 410, 411, 412, 413, 414, 415, 416, 417, 418, 419, 420, 421, 422, 423, 424, 425, 426, 427, 428, 429, 430, 431, 432, 433, 434, 435, 436, 437, 438, 439, 440, 441, 442, 443, 444, 445, 446, 447, 448, 449, 450, 451, 452, 453, 454, 455, 456, 457, 458, 459, 460, 461, 462, 463, 464, 465, 466, 467, 468, 469, 470, 471, 472, 473, 474, 475, 476, 477, 478, 479, 480, 481, 482, 483, 484, 485, 486, 487, 488, 489, 490, 491, 492, 493, 494, 495, 496, 497, 498, 499, 500, 501, 502, 503, 504, 505, 506, 507, 508, 509, 510, 511, 512, 513, 514, 515, 516, 517, 518, 519, 520, 521, 522, 523, 524, 525, 526, 527, 528, 529, 530, 531, 532, 533, 534, 535, 536, 537, 538, 539, 540, 541, 542, 543, 544, 545, 546, 547, 548, 549, 550, 551, 552, 553, 554, 555, 556, 557, 558, 559, 560, 561, 562, 563, 564, 565, 566, 567, 568, 569, 570, 571, 572, 573, 574, 575, 576, 577, 578, 579, 580, 581, 582, 583, 584, 585, 586, 587, 588, 589, 590, 591, 592, 593, 594, 595, 596, 597, 598, 599, 600, 601, 602, 603, 604, 605, 606, 607, 608, 609, 610, 611, 612, 613, 614, 615, 616, 617, 618, 619, 620, 621, 622, 623, 624, 625, 626, 627, 628, 629, 630, 631, 632, 633, 634, 635, 636, 637, 638, 639, 640, 641, 642, 643, 644, 645, 646, 647, 648, 649, 650, 651, 652, 653, 654, 655, 656, 657, 658, 659, 660, 661, 662, 663, 664, 665, 666, 667, 668, 669, 670, 671, 672, 673, 674, 675, 676, 677, 678, 679, 680, 681, 682, 683, 684, 685, 686, 687, 688, 689, 690, 691, 692, 693, 694, 695, 696, 697, 698, 699, 700, 701, 702, 703, 704, 705, 706, 707, 708, 709, 710, 711, 712, 713, 714, 715, 716, 717, 718, 719, 720, 721, 722, 723, 724, 725, 726, 727, 728, 729, 730, 731, 732, 733, 734, 735, 736, 737, 738, 739, 740, 741, 742, 743, 744, 745, 746, 747, 748, 749, 750, 751, 752, 753, 754, 755, 756, 757, 758, 759, 760, 761, 762, 763, 764, 765, 766, 767, 768, 769, 770, 771, 772, 773, 774, 775, 776, 777, 778, 779, 780, 781, 782, 783, 784, 785, 786, 787, 788, 789, 790, 791, 792, 793, 794, 795, 796, 797, 798, 799, 800, 801, 802, 803, 804, 805, 806, 807, 808, 809, 810, 811, 812, 813, 814, 815, 816, 817, 818, 819, 820, 821, 822, 823, 824, 825, 826, 827, 828, 829, 830, 831, 832, 833, 834, 835, 836, 837, 838, 839, 840, 841, 842, 843, 844, 845, 846, 847, 848, 849, 850, 851, 852, 853, 854, 855, 856, 857, 858, 859, 860, 861, 862, 863, 864, 865, 866, 867, 868, 869, 870, 871, 872, 873, 874, 875, 876, 877, 878, 879, 880, 881, 882, 883, 884, 885, 886, 887, 888, 889, 890, 891, 892, 893, 894, 895, 896, 897, 898, 899, 900, 901, 902, 903, 904, 905, 906, 907, 908, 909, 910, 911, 912, 913, 914, 915, 916, 917, 918, 919, 920, 921, 922, 923, 924, 925, 926, 927, 928, 929, 930, 931, 932, 933, 934, 935, 936, 937, 938, 939, 940, 941, 942, 943, 944, 945, 946, 947, 948, 949, 950, 951, 952, 953, 954, 955, 956, 957, 958, 959, 960, 961, 962, 963, 964, 965, 966, 967, 968, 969, 970, 971, 972, 973, 974, 975, 976, 977, 978, 979, 980, 981, 982, 983, 984, 985, 986, 987, 988, 989, 990, 991, 992, 993, 994, 995, 996, 997, 998, 999, 1000

15th International Conference on
Medical and Biological Engineering

8th International Conference on
Mechanics in Medicine and Biology

30th Annual Meeting of the American Association
of Physicians in Medicine

4th Annual Conference on Engineering
in Medicine and Biology

34th Annual Meeting of the Division of
Medical and Biological Physics
Canadian Association of Physicists

10th Annual Meeting of the
Canadian Conference of Physicists in Medicine

10th Annual Meeting of the
Canadian Conference of Physicists in Medicine

10th Annual Meeting of the
Canadian Conference of Physicists in Medicine

10th Annual Meeting of the
Canadian Conference of Physicists in Medicine

10th Annual Meeting of the
Canadian Conference of Physicists in Medicine

10th Annual Meeting of the
Canadian Conference of Physicists in Medicine

10th Annual Meeting of the
Canadian Conference of Physicists in Medicine

PHYSICS IN MEDICINE AND BIOLOGY

Published by IOP Publishing Ltd (the publishing division of The Institute of Physics) for The Institute of Physical Sciences in Medicine

Editor: S.C. Lillicrap, Wessex Regional Health Authority, Royal United Hospital, Combe Park, Bath BA1 3NG, UK

Publishing Offices:

IOP Publishing Ltd, 7 Great Western Way, Bristol BS1 6HE, UK, Telephone: 0272 292151, Telex: 449907 STONEBG

U.S.A., Canada, and Mexico:

American Institute of Physics, Dept N/M, 335 East 45th Street, New York, NY 10017, U.S.A., Telephone: 516/349-7800, Telex: 960983

Japan: Maruzen Company, Ltd, 3-10 Nihonbashi 2-Chome, Chuo-Ku, Tokyo 103, Japan, Telephone: 272 7211, Telex: J26516 MARUZEN

1988 Subscription Rates:

UK 205.00, North America US\$360.00, Single issue price UK 17.25, US\$30.00. Details of special rates for members of the societies listed below are available on request from the Marketing Department, IOP Publishing Ltd

To receive your free sample copy and further information please contact:

Journals Marketing Manager, IOP Publishing Ltd, Techno House, Redcliffe Way, Bristol BS1 6NX, UK

An official journal of the:

Hospital Physicists' Association, Medical and Biological Physics Division Canadian Association of Physicists, Deutsche Gesellschaft für Medizinische Physik, European Federation of Organizations for Medical Physics, Japanese Association of Radiological Physicists, and the International Organization for Medical Physics. Published in association with the American Association of Physicists in Medicine and the American Institute of Physics.

Authorization to photocopy items for internal or personal use, or the internal or personal use of specific clients, is granted by IOP Publishing Ltd for libraries and other users registered with the Copyright Clearance Center (CCC), Transactional Reporting Service, provided that the base fee of \$2.50 per copy is paid directly to CCC, 21 Congress Street, Salem, MA 01970, U.S.A. This authorization does not extend to other kinds of copying such as copying for general distribution, for advertising or promotional purposes, for creating new collective works, or for resale. Payment is additionally required for copying of articles published prior to 1978.

Physics in Medicine & Biology

VOLUME 33

SUPPLEMENT I

1988

Proceedings of the World Congress on Medical Physics and Biomedical Engineering

AUGUST 6-12, 1988

SAN ANTONIO, TEXAS

15th International Conference on
Medical and Biological Engineering

8th International Conference on
Medical Physics

6th International Conference on
Mechanics in Medicine and Biology

30th Annual Meeting of the American Association
of Physicists in Medicine

41st Annual Conference on Engineering
in Medicine and Biology

34th Annual Meeting of the Division of
Medical and Biological Physics
Canadian Association of Physicists

10th Annual Meeting of the
Canadian College of Physicists in Medicine



Editors: John W. Clark
Alfred R. Smith

Patricia I. Horner
Kathleen Strum

Supplement published with the co-operation of the
International Union for Physical and Engineering Sciences in Medicine

Journal of the International Organization for Medical Physics

*Proceedings of the
World Congress on Medical Physics and Biomedical Engineering
August 7-12, 1988, San Antonio, Texas*

15th International Conference on Medical and Biological Engineering
8th International Conference on Medical Physics
6th International Conference on Mechanics in Medicine and Biology
30th Annual Meeting of the American Association of Physicists in Medicine
41st Annual Conference on Engineering in Medicine and Biology
34th Annual Meeting of the Division of Medical and Biological Physics,
Canadian Association of Physicists
10th Annual Meeting of the Canadian College of Physicists in Medicine

Volume 30
ISSN 0589-1019
LC 61-24788

Copyright © 1988
Alliance for Engineering in Medicine and Biology

All rights reserved. This book or any part thereof may not be reproduced in any form without the permission of the publisher.

Publisher: Alliance for Engineering in Medicine and Biology for the Organizing Committee of the World Congress on Medical Physics and Biomedical Engineering

Printed in the United States of America
Dependable Printing Company, Inc.

Foreword

We welcome participants from fifty nations of the world to the 1988 World Congress on Medical Physics and Biomedical Engineering. This Congress is a joint meeting of the International Federation for Medical and Biological Engineering (IFMBE) and the International Organization for Medical Physics (IOMP), which are joined together in the International Union of Physical and Engineering Sciences in Medicine. It is the first time this joint meeting has been held in the United States, although the IFMBE has had previous international conferences here in 1961 and 1969. The host organizations from the United States are the Alliance for Engineering in Medicine and Biology (AEMB) and the American Association of Physicists in Medicine (AAPM). Meeting with the World Congress is the International Conference on Mechanics in Medicine and Biology. We welcome their participation as well as the participation of the Canadian Association of Physicists and the Canadian College of Physicists in Medicine. Although the AEMB involves 20 constituent societies, the Biomedical Engineering Society and the IEEE/Engineering in Medicine and Biology Society have been particularly active in organizing scientific sessions. In addition to the scientific program, there is a large commercial exhibits program, and we appreciate the participation of these exhibitors and the support they have provided for the World Congress. We are particularly appreciative of the efforts of the staff of the AAPM and AEMB and for the volunteer help from members of both organizations. The tireless attention of Dr. David Kopf, Secretary General of the Congress, to innumerable details deserves special praise and thanks; the meeting would not have been as valuable without him. We also are appreciative of the support provided by our own institutions.

Co-Presidents

Gary D. Fullerton, Ph.D.
University of Texas Health
Sciences Center at San Antonio

Robert M. Nerem, Ph.D.
Georgia Institute of Technology

August 1988

Greetings!

The Alliance for Engineering in Medicine and Biology and the American Association of Physicists in Medicine welcome you to San Antonio, to the United States, and to the 1988 World Congress on Medical Physics and Biomedical Engineering. We anticipate that this will be the largest meeting of its kind ever held and we are pleased to have the support of a very large number of exhibitors. A diverse scientific and educational program is planned which we trust will provide a forum for the exchange of information and experiences. An excellent social program is also planned by our experienced Texas hosts. We hope that this meeting will be fruitful and your stay enjoyable. We are happy to have you as our guest!

Gary T. Barnes, Ph.D
President, AAPM

Arthur T. Jonnson, Ph.D
President, AEMB

Preface

We welcome you to the 1988 World Congress on Medical Physics and Biomedical Engineering. The process of developing the scientific program has been exciting and rewarding for us and we hope that the week of the Congress is equally as exciting and rewarding for you.

The 1988 World Congress presents a record-breaking program with respect to the numbers, excellence and diversity of scientific papers, symposia, short courses and exhibits. Over 1950 abstracts were submitted to the scientific program committee from 43 countries. From outside the USA and Canada, there were excellent responses from Austria, Brazil, China, France, West Germany, India, Italy, Japan, The Netherlands, Spain, Sweden, and the United Kingdom. We would like to especially thank the participants in the scientific program and the vendors exhibiting products at this meeting.

The theme of the Congress, **Challenges for the Year 2000**, is a reminder of the challenges, many of a global nature, which confront us. These problems will only be successfully addressed through the efforts of our world community and a recognition of our universal responsibilities toward better, more widely distributed and less expensive health care, and a continuing concern for the well being of each other and for our mother earth.

Alfred R. Smith, Ph.D
Co-Chairman for
Medical Physics

John W. Clark, Ph.D
Co-Chairman for
Biomedical Engineering

Acknowledgments

As these proceedings go to press, all signs point to a very successful World Congress on Medical Physics and Biomedical Engineering. I received over 1900 inquiries about the Congress from individuals representing 54 countries. Submission of over 1700 regular abstracts and several hundred works-in-progress further demonstrated this great interest. More than 80 commercial exhibitors subscribed to over 180 commercial exhibit booths. The success of this Congress must be credited to the efforts of a large number of dedicated individuals. I am extremely grateful to my committee chairmen for their untold contributions. They are: Larry Donovan, Nancy Fullerton, Dennis Gilstad, Bill Hyman, and Al Zermeno. I am also indebted to Elaine Osterman and to Pat Horner and their staffs, in particular Trish Irmen and Susan Leone, for their guidance and tireless efforts. Finally, I gratefully acknowledge the invaluable secretarial support of Barbara Rowe and the understanding, encouragement and support of my wife Claire.

David T. Kopp, Ph.D.
Secretary General

International Union of Physical and Engineering Sciences in Medicine

President:
Øivind Lorentsen
Norway

Vice-President:
Alexander Kaul
Federal Republic of Germany

Past President:
John Mallard
United Kingdom

Secretary-General:
John A. Hopps
Canada

Vice Secretary-General:
Robert Clarke
Canada

Members of the Council:
Nandor Richter
Hungary

John R. Cunningham
Canada

Orest Z. Roy
Canada

Lawrence H. Lanzl
United States of America

Robert Nerem
United States of America

Brian Stedeford
United Kingdom

International Organization for Medical Physics

President:
Lawrence H. Lanzl
United States of America

Vice-President:
John R. Cunningham
Canada

Past President:
Alexander Kaul
Federal Republic of Germany

Secretary-General:
Brian Stedeford
United Kingdom

Past Secretary-General:
Rune Walstam
Sweden

Affiliate Organizations:

Australia
Australasian College of Physical
Scientists in Medicine

Greece
Greek Association of
Medical Physicists

Norway
Norwegian Society for
Medical Physicists

Austria
Osterreichische Gesellschaft fur
Medizinische Physik

Hong Kong
Hong Kong Association of
Medical Physics

People's Republic of China
The Chinese Society of
Medical Physics

Belgium
Societe Belge des Physiciens
des Hopitaux

Hungary
Medical Physics Section,
Hungarian Biophysical Society

Philippines
Philippine Organization
of Medical Physicists

Brazil
Associcao Brasileira de
Fisicos em Medicina

India
Association of Medical Physicists
of India

Poland
Polskie Towarzystwo Fizyki Medycznej

Canada
Division of Medical and Biological
Physics, Canadian Association
of Physicists

Ireland
Insh Hospital Physicists' Association

South Africa
South African Association of
Physicists in Medicine and Biology

Columbia
Sociedad Colombiana de Fisica
Medica y Radioprotection

Israel
Israel Society for Medical Physics

Spain
Sociedad Espanola de Fisica Medica

Denmark
Danish Association for
Medical Physics

Italy
Associazione Italiana di
Fisica Biomedica

Sri Lanka
Sri Lanka Medical Physicists'
Association

Federal Republic of Germany
Deutsche Gesellschaft fur
Medizinische Physik e.V.

Japan
Japanese Association of
Medical Physics

Sweden
Swedish Association of Physicists
in Medicine

Finland
Finnish Society for Medical
Physics and Medical Engineering

Mexico
Asocion de Fisicos de
Hospitales, AC

Switzerland
Societe Suisse de Radiobiologie
et Radiophysique

France
Societe Francaise des
Physiciens d'Hopital

The Netherlands
Nederlandse Vereniging voor
Klinische Fysica

Thailand
Medical Physics Club of Thailand

German Democratic Republic
Sektion Medizinische Physik in der
Gesellschaft fur Mathematische und
Physikalische Biologie der DDR

New Zealand
New Zealand Branch,
Australasian College of
Physical Scientists in Medicine

United Kingdom
UK National Committee for Medical
Physics, incorporating British
Institute of Radiology and
Hospital Physicists' Association

Nigeria
Nigerian Association of
Medical Physicists

United States of America
American Association of Physicists
in Medicine

International Federation for Medical and Biological Engineering

President:
Nandor Richter
Hungary

Vice-President:
Robert Nerem
United States of America

Past-President:
Øivind Lorentsen
Norway

Secretary-General:
Orest Z. Roy
Canada

Treasurer:
Uwe Faust
Federal Republic of Germany

Members of the Administrative Council:

Marcello Bracale
Italy

Richard L.G. Kirsner
Australia

Gunter Rau
Federal Republic
of Germany

Astrid Gautier-Levine
United States of America

Rudolph Millner
German Democratic
Republic

Niilo Saranummi
Finland

Fumihiko Kajiya
Japan

Jan Persson
Sweden

Affiliate Organizations:

Argentina
Sociedad Argentina de
Bioingenieria

German Democratic Republic
Gesellschaft für Bio-Medizinische
Technik der Deutschen
Demokratischen Republik

The Netherlands
Vereniging voor Biofysica

Australia
Australian Federation for
Medical and Biological
Engineering

Federal Republic of Germany
Deutsche Gesellschaft für
Biomedizinische Technik E.K.

Norway
Norsk Forening for
Bio-Medisinsk Teknikk

Austria
Osterreichische Gesellschaft
für Biomedizinische Technik

Finland
Laaketteellisen Fysiikan ja
Tekniikan Yhdistys R.Y.

Poland
Polish Federation of
Engineering Associations/NOT

Belgium
Belgian Society for Medical
and Biological Engineering
and Computing

France
Societe des Electriciens des
Electroniciens et des
Radioelectriciens (S.E.E.)

South Africa
Biomedical Engineering Society
of South Africa

Brazil
Sociedade Brasileira de
Engenharia Biomedica

Greece
Greek Society for
Biomedical Engineering

Korea
South Korean Society of Medical
and Biological Engineering

Bulgaria
Bulgarian National Society
of Biomedical Physics
and Engineering

Hungary
Meresteknikai es Automatizalasi
Tudomanyos Egyesulet

Spain
Agrupacion Espanola de
Bioingenier

Canada
Canadian Medical & Biological
Engineering Society

Israel
Israel Society for Medical
and Biological Engineering

Sweden
Svenska Foreningen for
Medicinsk Fysik och Teknisk

China
Chinese Society of Biomedical
Engineering

Italy
Associazione Italiana di
Ingegneria Medica e Biologica

United Kingdom
Biological Engineering Society

Cuba
Sociedad Cubana de
Bioingenieria

Japan
Japan Society of Medical
Electronics and Biological Engineering

United States of America
Alliance for Engineering
in Medicine and Biology

Denmark
Dansk Medikoteknisk Selskab

Mexico
Sociedad Mexicana de
Ingenieria Biomedica

Yugoslavia
Yugoslav Society for Medical
& Biological Engineering

World Congress on Medical Physics and Biomedical Engineering

Executive Committee

Gary D. Fullerton, Ph.D.
Co-President, Medical Physics
University of Texas HSC-SA
San Antonio, Texas

Alfred R. Smith, Ph.D.
Co-Chair, Scientific Program, Medical Physics
Hospital of the University of Pennsylvania
Philadelphia, Pennsylvania

David T. Kopp, Ph.D.
Secretary General
University of Texas HSC-SA
San Antonio, Texas

Robert M. Nerem, Ph.D.
Co-President, Biomedical Engineering
Georgia Institute of Technology
Atlanta, Georgia

John W. Clark, Ph.D.
Co-Chair, Scientific Program, Biomedical Engineering
Rice University
Houston, Texas

Jack L. Lancaster, Ph.D.
Treasurer
University of Texas HSC-SA
San Antonio, Texas

Participating Organizations

International Union of Physical and Engineering Sciences in Medicine
International Organization for Medical Physics
International Federation for Medical and Biological Engineering
International Conference on Mechanics in Medicine and Biology
American Association of Physicists in Medicine
Alliance for Engineering in Medicine and Biology
Canadian Association of Physicists
Canadian College of Physicists in Medicine

International Advisory Committee

Arabinda Bose, Ph.D.
Cancer Centre & Welfare Home
Calcutta, India

Jean Chavaudra, Ph.D.
Institut Gustave-Roussy
Villejuif, France

Carlos Eduardo de Almeida, Ph.D.
Inst de Radioprotecao e Dosimetria
Rio de Janeiro, Brasil

Tapani Jauhainen, M.D.
Helsinki University Central Hospital
Helsinki, Finland

Robert M. Kenedi, Ph.D.
University of Strathclyde
Glasgow, Scotland

George Kossof, D.Sc.Eng.
Ultrasonics Institute
Sydney, Australia

John Mallard, Ph.D.
University of Aberdeen
Aberdeen, Scotland

Anna Benini Mori, Ph.D.
IAEA
Vienna, Austria

Victor M. Tovar Munoz, Ph.D.
Inst Nac de Investigaciones Nucleares
Salazar, Mexico

Bertil R. R. Persson, Ph.D.
Lund University Hospital
Lund, Sweden

Ervin B. Podgorsak, Ph.D.
McGill University/Montreal Gen Hospital
Montreal, Canada

Masao Saito, Ph.D.
University of Tokyo
Tokyo, Japan

Max Schaldach, Ph.D.
Friedrich Alexander Universitat
Erlangen, West Germany

Samuel Sideman, Ph.D.
Technion-Israel Institute of Technology
Haifa, Israel

Max E. Valentinuzzi, Ph.D.
Universidad Nacional de Tucuman
San Miguel de Tucuman, Argentina

Lojze Vodovnik, Ph.D.
Edvard Kardelj University
Ljubljana, Yugoslavia

Walter Zingg, M.D.
University of Toronto
Toronto, Canada

Organizing Committee

Al Zermeno, Ph.D.
Co-Chair, Scientific Exhibits/Posters
M. D. Anderson Hospital

Kenneth Vanek, Ph.D.
Chair, Commercial Exhibits
Wilford Hall Medical Center

Dennis L. Watts, M.S.
Chair, Hotel Liaison
Brooke Army Medical Center

Lary Donovan, M.A.
Chair, Social Program
Brooks Air Force Base

Dennis Gilstad, M.D.
Chair, Publicity/Advertising
Southwest Research Institute

Arthur Sherwood, Ph.D.
Co-Chair, Scientific Exhibits/Posters
Baylor College of Medicine

William Hyman, Ph.D.
Chair, Audiovisual Aids
Texas A&M University

Donald Johnson, M.S.
Chair, Convention Center Liaison
Moncrief Radiation Center

Nancy Fullerton
Chair, Companions' Program
San Antonio, Texas

Jack S. Krohmer, Ph.D.
Chair, Registration/Information
J. S. Krohmer Ph.D., Inc.

American Association of Physicists in Medicine

Elaine P. Osterman
Executive Officer

Trish Immen
Assistant Executive Officer

Alliance for Engineering in Medicine and Biology

Patricia I. Homer
Executive Director

Scientific Program Committee

Medical Physics

Lowell L. Anderson
Jerry J. Battista
Peter J. Biggs
Bengt E. Bjärngård
Peter H. Bloch
John R. Cameron
Paul L. Carson
James C. H. Chu
Robert L. Chu
Laurence Clarke
David Cohen
J. Michael Collier
Jake Van Dyk
Aaron Fenster

James M. Galvin
Jan Van de Geijn
Jean St. Germain
John C. Gore
James R. Halama
R. Mark Henkelman
Kenneth R. Hogstrom
Philip F. Judy
Faiz M. Khan
Gerald J. Kutcher
Paul P. Lin
Mark T. Madsen
Seong K. Mun
Bhudatt R. Paliwal

Dennis L. Parker
Michael S. Patterson
Nagalingam Suntharalingam
Goran K. Svensson
Norman Tepley
Lynn J. Verhey
Jeffrey F. Williamson
Joe P. Windham
Michael L. Wood
Kenneth A. Wright
Martin J. Yaffe
James A. Zagzebski
Sandra R. Zink

Biomedical Engineering

Kazuhiko Atsumi
James B. Fassingthwaight
Susan Blanchard
Colin G. Caro
Dudley S. Childress
Yadin Davi
William J. Dorson, Jr.
Morton H. Friedman
Monique Frize
Donald P. Giddens
Craig J. Hartley
Robert M. Hochmuth
Michael Y. Jaffrin

Roger D. Kamm
Fumihiko Kajiya
Hiroshi Kanai
Richard I. Kitney
Periklis Y. Ktonas
Jacques Lefevre
Dieter W. Liepsch
Marko S. Markov
Michael R. Neuman
Timothy J. Pedley
Robert Plonsey
Aleksander S. Popel
John M. Radovich

Helmut Reul
Peter Rolfe
Subrata Saha
Gerald M. Saidel
Louis C. Sheppard
Samuel Sideman
Dick W. Slaaf
Willis A. Tacker, Jr.
Raymond P. Vito
Dean C. Winter
Takami Yamaguchi
Ajit P. Yoganathan
Yoji Yoshida

Table of Contents

SECTION I. PLENARY SESSION SCIENTIFIC PAPERS		xvii
P1.	Space Medicine and Biology: Challenges for the Year 2000	xix
P3.	Medical Physics and Bioengineering in Latin America: Challenges for the Year 2000	xx
P4.	Medical Imaging: Challenges for the Year 2000	xx
P5.	Artificial Organs: Challenges for the Year 2000	xxi
 SECTION II. MEDICAL PHYSICS SCIENTIFIC PAPERS		 1
MPSC.	Medical Physics Short Courses	3
MPS1.	Young Investigators Symposium	7
MPS2.	Artificial Intelligence: Promises and Reality	9
MPS3.	Issues in Ultrasound Standards and Safety	10
MP1.	Therapy: Treatment Planning 1	12
MP2.	Quantitative Imaging	14
MP3.	Medical Lasers	15
MP4.	Nuclear Medicine	19
MP5.	Photon Calculation	21
MP6.	General Medical Physics Posters 1	23
MP7.	Radiation Protection	30
MP8.	Biomagnetism 1	32
MP9.	Digital Imaging 1	34
MP10.	Therapy Posters: Hyperthermia, Q.A., Beam Modifiers, Accelerators	36
MP11.	Therapy: Dosimetry 1	43
MP12.	Radiation Therapy Imaging	45
MP13.	Therapy Posters: Hyperthermia, Q.A., Beam Modifiers, Accelerators	47
MP14.	Therapy: Electron Dosimetry	56
MP15.	Therapy: Brachytherapy 1	58
MP16.	Biomagnetism 2	60
MP17.	Nuclear Medicine Posters: Magnetic Resonance Spectroscopy and General	62
MP18.	General Diagnostic Posters	70
MP19.	Therapy: Heavy Particles	73
MP20.	Ultrasound	75
MP21.	General Radiation Therapy	78
MP22.	Magnetic Resonance: Spectroscopy	80
MP23.	Imaging Posters: CT, Therapy Imaging, General	82
MP24.	Therapy: Treatment Planning 2	90
MP25.	Magnetic Resonance: Imaging	92
MP26.	Therapy Posters: Dosimeters and Detectors	94
MP27.	Diagnostic: General Imaging	99
MP28.	Nuclear Medicine: Spect and Pet	102
MP29.	Diagnostic: Computerized Tomography	104
MP30.	Therapy: Electron Calculations	106
MP31.	Imaging Posters: MRI, Spect, Digital, PET	108

MP32.	Therapy Posters: Dosimetry for Photons, Electrons, Perturbations	118
MP33.	Therapy Posters: Brachytherapy 2	125
MP34.	Therapy Posters: Particles, Calculations, Computer Applications	131
MP35.	Therapy: Dosimetry 2	141
MP36.	General Medical Physics Posters 2	143
MP37.	Digital Imaging 2	149
MP38.	Therapy: Brachytherapy 3	151

SECTION III. BIOMEDICAL ENGINEERING PAPERS 157

BE1A.	Electrophysiology 1: Simulation Methodologies in Biomedicine-- Fundamentals of Excitable Membranes	157
BE1B.	Electrophysiology 2: Electrophysiology of Skeletal Muscle	158
BE1C.	Electrophysiology 3: Electrophysiology of the Peripheral Nervous System	159
BE1D.	Electrophysiology 4: Cardiac Electrophysiology . . .	160
BE1E.	Electrophysiology 5: Functional Neuromuscular Stimulation	161
BE1F.	Electrophysiology 6: Brain Motor Control Assessment .	162
BE1G.	Electrophysiology 7: Cardiac Potential Mapping . . .	163
BE1H.	Electrophysiology 8: EEG Modeling	164
BE1I.	Electrophysiology 9: Electrical Fields for Defibrillation	165
BE1J.	Electrophysiology 10: Models in Automated EEG Analysis	166
BE1K.	Electrophysiology 11: Cardiac Arrhythmias	167
BE1L.	Electrophysiology 12: Clinical Applications of Automated EEG Analysis	168
BE1M.	Electrophysiology 13: Inverse Solutions in Electrocardiography	169
BE1O.	Electrophysiology 15: The Next Exciting Use of High Intensity Magnetic Field-- Tissue Stimulation for Clinical Monitoring	170
BE1P.	Electrophysiology 16: Clinical Aspects of Cardiac Electrophysiology	171
BE1Q.	Electrophysiology 17: Studies in Fibrillation and Defibrillation	172
BE1R.	Electrophysiology 18: Quantitative Techniques for Evoked Potential Analysis	173
BE2A.	Control of Drug Delivery 1: Modeling and Simulation-- The Effects of Drugs on Physiological Variables . . .	175
BE2B.	Control of Drug Delivery 2: Research in Auto- matic and Adaptive Control, Programmed Infusion and Controlled Release of Therapeutic Agents	176
BE2C.	Control of Drug Delivery 3: Clinical Trials and Implementation of Strategies for Controlled Drug Administration	177
BE3A.	Cardiac Mechanics 1	178
BE3B.	Cardiac Mechanics 2	179

BE3C.	Intramyocardial Flow 1	180
BE3D.	Intramyocardial Flow 2	181
BE3E.	Measurements of Cardiac Performance 1	182
BE3F.	Measurements of Cardiac Performance 2	183
CETA.	Past, Present, and Future of Biomedical Engineering; Management and Maintenance of Healthcare Equipment	183
CETC.	Clinical Engineering: Role Qualification and Performance	184
BE4A.	Clinical Engineering: Education and Career	184
BE4B.	Clinical Engineering 2: Standards and Regulations	186
BE4C.	Clinical Engineering 3: Medical Lasers	188
BE4D.	Clinical Engineering 4: Cardiopulmonary Parameters, Measurements and Techniques	190
BE4E.	Clinical Engineering 5: Ethical Issues in Health Care Technology	191
BE4F.	Clinical Engineering 6: Technology Assessment	193
BE4G.	Clinical Engineering 7: Practice and Programs	196
BE4H.	Clinical Engineering 8: Clinical Engineering Finance	197
BE4I.	Clinical Engineering 9: Computers and Networks	199
BE4J.	Clinical Engineering 10: Physiological Measurements and Instrumentation	201
BE4K.	Clinical Engineering 12	203
BE5A.	Orthopedics 1: Bone Remodeling-- Mechanical and Metabolic Factors	205
BE5B.	Orthopedics 2: Bone Mechanics	206
BE5C.	Orthopedics 3: Bone Tissue	207
BE5D.	Orthopedics 4: Orthopedic Implants	208
BE5E.	Orthopedics 5: Spine Biomechanics	210
BE5F.	Orthopedics 6: Joint Mechanics and Dynamic Effects	212
BE6A.	Respiration 1: Stability Analysis of Respiration--Apneas and Periodic Breathing	213
BE6B.	Respiration 2: Respiration in Sleep--Advanced Methodologies	215
BE6C.	Respiration 3: Gas Exchange in the Respiratory System	216
BE6D.	Respiration 4: Modeling of the Respiratory System: Analysis and Identification	217
BE6E.	Respiration 5: Mechanical Ventilation	218
BE6F.	Respiration 6: Models of Mechanically-Assisted Ventilation	219
BE6G.	Respiration 7: Lung Parenchymal Tissue Mechanics	220
BE6H.	Respiration 8: Chest Wall Mechanics	221
BE6I.	Respiration 9: Respiratory Fluid Mechanics	223
BE6J.	Respiration 10: Mechanical Models of the Pulmonary Circulation	224
BE6K.	Respiration 11: Aerosol Deposition in the Lungs	225
BE7A.	Biological Systems Modeling 1: Interaction Between Artificial Intelligence and Simulation	226
BE7B.	Biological Systems Modeling 2: Simulation Methodology in Biomedicine	227
BE7C.	Biological Systems Modeling 3: Fractals and Chaos in Physiology and Medicine-- of Molecules, Surfaces, and Reactions	229

BE7D.	Biological Systems Modeling 4: Fractals and Chaos in Physiology and Medicine-- On Organs and Organisms	229
BE7E.	Biological Systems Modeling 5: Modeling Aspects of Cardiac Electrophysiology	230
BE7F.	Biological Systems Modeling 6: Modeling and Signal Processing in Electrocardiography	232
BE7G.	Biological Systems Modeling 7: Methods for Modeling in the Time Domain 1	233
BE7H.	Biological Systems Modeling 8: Methods for Modeling in the Time Domain 2	235
BE8A.	Advances in Artificial Organs 1	236
BE8B.	Advances in Artificial Organs 2	237
BE8C.	Artificial Organs 3: Advances in Artificial Organs	238
BE8D.	Artificial Heart Valves 1	239
BE8E.	Artificial Heart Valves 2	240
BE8F.	Artificial Heart Valves 3	242
BE8G.	Mass Transport in Artificial Organs	243
BE8H.	International Aspects of Medical Device Regulation	244
BE8I.	Artificial Heart 1: Blood Pump Monitoring and Control of the Artificial Heart	245
BE8J.	Artificial Heart 2: Energy Converters and Energy Sources	246
BE8K.	Cardiovascular Assist Devices	247
BE9A.	Atherosclerosis 1	248
BE9B.	Atherosclerosis 2	249
BE9C.	Atherosclerosis 3	251
BE9D.	Atherosclerosis 4	252
BE9E.	Atherosclerosis 5	253
BE9F.	Atherosclerosis 6	254
BE10A.	Heart Rate Variability 1	255
BE10B.	Heart Rate Variability 2	257
BE10C.	Heart Rate Variability 3	258
BE11A.	Flow in Collapsible Tubes 1	259
BE11B.	Flow in Collapsible Tubes 2	261
BE12A.	Poster Session 1: Flow in Collapsible Tubes	262
BE12B.	Poster Session 2: Cardiovascular Mechanics 1	263
BE12C.	Poster Session 3: Renal Systems/Hemodialysis	268
BE12D.	Poster Session 4: Clinical Engineering 1-- Administrative Aspects/Equipment and Maintenance	270
BE12E.	Poster Session 5: Clinical Engineering 2-- Computer-Based Analysis Systems	274
BE12F.	Poster Session 6: Artificial Heart Valves	277
BE12G.	Poster Session 7: Microcirculation	280
BE12H.	Poster Session 8: Cardiovascular Mechanics 2	285
BE12I.	Poster Session 9: Ultrasound in Medicine	291
BE12J.	Poster Session 10: Cardiac Electrophysiology	292
BE12K.	Poster Session 11: Clinical Engineering 3-- Indirect Cardiac Assessment Techniques	295
BE12L.	Poster Session 12: Orthopedics	299
BE12M.	Poster Session 13: Respiratory System	302
BE12N.	Poster Session 14: Mass Transfer	305
BE12O.	Poster Session 15: Bioheat Transfer	307
BE12P.	Poster Session 16: Biomedical Engineering: General	309



BE12Q.	Poster Session 17: Clinical Engineering: General . . .	316
BE12P.	Poster Session 18: Cardiac Potential Mapping	325
BE12S.	Poster Session 19: Electroencephalography	327
BE12T.	Poster Session 20: Expert and Decision Support Systems	330
BE12J.	Poster Session 21: Sound Production and Audition . . .	331
BE12V.	Poster Session 22: Medical Imaging	333
BE12W.	Poster Session 23: Biomedical Applications of Spectral Analysis and Signal Processing	335
BE12X.	Poster Session 24: Stereometrics and Special Surgical Techniques	337
BE12Y.	Poster Session 25: Nerve and Muscle Electrophysiology	339
BE12Z.	Poster Session 26: Traditional Chinese Medical Science	341
BE12ZZ.	Poster Session 27: Cellular Bioprocessing	342
BE13A.	Soft Tissue Mechanics 1	344
BE13B.	Soft Tissue Mechanics 2	345
BE13C.	Soft Tissue Mechanics 3	346
BE14A.	Rheology	347
BE14B.	Microcirculation: Mechanics of the Vascular Wall 1 . .	349
BE14C.	Microcirculation: Mechanics of the Vascular Wall 2 . .	350
BE14D.	Microcirculation 3	350
BE14E.	Cellular Biomechanics 1	352
BE14F.	Cellular Biomechanics 2	353
BE14G.	Cellular Biomechanics 3	354
BE15A.	Ultrasound in Medicine: Cardiac Doppler Methods . . .	356
BE15B.	Ultrasound in Medicine 2: Doppler Velocity and Flow Measurements	357
BE15C.	Ultrasound in Medicine 3: Doppler Signal Processing	358
BE15D.	Ultrasound in Medicine 4: Intravascular and Intraoperative Techniques	360
BE15E.	Ultrasound in Medicine 5: Improvements in Imaging	361
BE15F.	Ultrasound in Medicine 6: Pressure and Tissue Property Measurements	363
BE16A.	Auditory System Research	364
BE16B.	Vision 1: Eye Movements/Glaucoma	365
BE16C.	Vision 2: Normal and Abnormal Visual Function	367
BE17.	Analysis and Control of Movement	369
BE18A.	Hemodynamics 1	370
BE18B.	Hemodynamics 2	372
BE18C.	Hemodynamics 3	373
BE18D.	Hemodynamics 4	374
BE18E.	Hemodynamics 5	376
BE18F.	Hemodynamics 6	377
BE18G.	Hemodynamics 7	379
BE19.	Biomedical Signal Processing	380
BE20A.	Impedance Methods 1: Acquisition of Physiological Data Using Electrical Impedance . . .	382
BE20B.	Impedance Methods 2: Cardiac Measurements Using Electrical Impedance	383

BE21A.	Rehabilitation Engineering 1: Control of Muscles Through Electrical Stimulation-- Techniques and Systems	385
BE21B.	Rehabilitation Engineering 2: Stimulation of Biological Tissue: Electrodes and Methods	386
BE21C.	Rehabilitation Engineering 3: Ambulation Systems for Persons with Disabilities-- Orthoses and Protheses	387
BE21D.	Rehabilitation Engineering 4: Integration of Disabled Persons with their Environment	389
BE21E.	Rehabilitation Engineering 5: Rehabilitation Technology and Functional Restoration	390
BE22A.	Image Analysis 1	391
BE22B.	Image Analysis 2	393
BE23A.	Acupuncture and Related Electrostimulation Techniques 1: Acupuncture-- A Tutorial Overview	394
BE23B.	Acupuncture and Related Electrostimulation Techniques 2: Relationship Between Tens and Acupuncture	395
BE23C.	Acupuncture and Related Electrostimulation Techniques 3: Tens and Acupuncture-- Controversial Twins	397
BE23D.	Acupuncture and Related Electrostimulation Techniques 4: Low Current Transcranial Stimulation	398
BE23E.	Acupuncture and Related Electrostimulation Techniques 5: Legal and Regulatory Issues	399
BE24A.	Biosensor Research 1: Microelectronics- Based Sensor Systems	400
BE24B.	Biosensor Research 2: Oxygen and Glucose Sensors	401
BE24C.	Biosensor Research 3: Optically-Based Sensors	403
BE24D.	Biosensor Research 4: Pressure Sensors and Measurements	404
BE24E.	Biosensor Research 5: Biotelemetry	405
BE25.	The Influence of Electromagnetic Fields on Living Tissues	406
BE26A.	Bioheat Transfer 1	407
BE26B.	Bioheat Transfer 2	409

Section I

Plenary Sessions

P1.1

Medical Research and the Future of Manned Space Flight, C. L. Huntoon, Space and Life Sciences Directorate, NASA/Johnson Space Center, Mail Code SA, Houston, Texas 77058, United States.

One of the most complex challenges to medical science in the twentieth century is to make human habitation possible in space and on other planets. Over a 30-year period, the physiologic response of humans to space flight has been investigated during short flights, flights of more than 300 days, flights to the Moon. Most of the systems of the body are affected in some way by conditions of space flight, but research has given us hope that the most serious problems can be circumvented. Space medicine and technology have advanced to the point where continuous human habitation of low Earth orbit is becoming a reality and a manned mission to Mars is being discussed. In this session we are going to hear about medical findings from long- and short-term space flights, as well as what it is like to live and work in microgravity and some of the experiments planned for future flights.

P1.3

Science Operations in Space, Bonnie J. Dunbar, Mission Specialist Astronaut, NASA-Lyndon B. Johnson Space Center, Houston, TX 77058.

Throughout the course of human exploration in space, astronauts have been an integral part of scientific experimentation. During the Apollo and Skylab programs, astronaut crews conducted scientific investigations both as initiators and as extensions to ground-based principal investigators. Experiments were conducted in a variety of disciplines: human physiology, astrophysics, fluid physics, botany, biology, and materials science. The advent of the Space Shuttle program and Spacelab flights has brought more sophisticated experiments, increased demand of experiment and crew time, and the need to optimize the human element with automation. Lessons learned with respect to experiment protocol, hardware design, operations, and "in flight" maintenance will be discussed. Recommendations for the development of the Space Station experiments will also be reviewed.

P1.2

The German D-Spacelab Missions: Opportunities for International Life Sciences Research in Space, Karl.E. Klein, DFVLR Institute for Aerospace Medicine, D-5000 Köln, FRG

To utilize the opportunity "microgravity" is offering for studies of basic phenomena in fluid physics, material sciences, biology and medicine, the Federal Republic of Germany has initiated a series of microgravity missions with Spacelab. The first one, Spacelab Mission D-1, orbited the earth between 30 October - 6 November 1985. It had three European Scientists on board, specially trained to operate a payload compiled from proposals of seven European countries and the USA. For the first time, science crew training, experiment integration and payload operation control occurred outside of the USA, i.e. in Germany.

From a total of 75 experiments one third was devoted to studies in the life sciences with the main objectives being cell functioning, developmental processes, gravity perception, cardiovascular adaptation and cognitive behaviour. Most of the results were of high scientific interest, some even unexpected. Among others, they have

- shown evidence, that - against a long-standing opinion - gravity effects unicellular systems (like bacteria),
- indicated a synergistic negative effect of microgravity and cosmic radiation on the development of an insect, and
- produced data appropriate to strongly question hypothesis on human vestibular organ responses, valid since many years.

The second mission in this series, the German Spacelab Mission D-2, originally planned to fly in 1988 now is scheduled for 1991. Again, the payload will be microgravity oriented and will contain experiments from many countries, including Japan and the USA. The Life Sciences are represented with three payload elements, including a human physiology research device "ANTHRORACK", and a "BIOTEX" for biotechnology studies.

P1.4

Status of Japanese Spacelab (SL-J) Experiments
Chiaki Mukai, National Space Development Agency of Japan, 2-4-1 Hamamatsu-cho, Minato-ku Tokyo 105 Japan

The SLJ mission is the first step of Japanese full-scale space experiments that utilize the characteristics of the space environment. Thirty-four experiments (22 on material processing and 12 on life science) from Japan and several from the U.S. are scheduled to be performed aboard space shuttle/spacelab in 1991.

Material processing experiments will produce new materials in the fields of compound semiconductors and metal-based composites. These experiments will develop space and earth-based processing technology and investigate physical phenomena such as Marangoni convection and gas evaporation.

Life science related experiments are dedicated to fields of biotechnology (free flow electrophoresis, crystal growth of enzyme, cell culture) and biological adaptation to space environment (vestibular function, perceptual-motor function, visual stability, calcium metabolism, endocrinology, radiation biology, circadian rhythm).

SLJ mission status including ground-based control data and hardware for these experiments, especially those focused in the life science field, will be discussed.

P3.1

PROBLEMS CONCERNING THE DEVELOPMENT OF MEDICAL PHYSICS IN LATIN AMERICA, Carlos E. de Almeida, SSDL/Rio de Janeiro-Brazil.

In the last decades medical physics in Latin America have improved considerably, nevertheless it is common understanding that there is still a long way to go in order to reach a desirable level of quality. With the advent of linear accelerators the demand for physicists in radiotherapy have increased but unfortunately in diagnostic radiology and nuclear medicine it has been quite stationary regardless to the fact that sophisticated technology has been introduced i.e. CT, SPECT, NMR and ULTRASOUND. The creation of the SSDL in several countries has been very positive in establishing traceability to the measurements as well as to serve as support for training. The absence of formal training centers with the support of International Organizations contribute to the increase lack of appropriate education. Several physicists sent abroad for training have either not returned or changed jobs or position in their own organization due to lack of scientific motivation or salary. Regional projects i.e. Arcal/IAEA must be explored in order to stimulate the exchange of experiences well as the Nuclear Information Centers to minimize the difficulties in accessing current scientific papers. The Latin America situation still deserves more coordinated efforts in the areas of training. QA programs, research and a better recognition by the national authorities of the important role played by medical physics to society.

P4.1

Expanding the Extraction of Diagnostic Information from the Body, Gary D. Fullerton and Jack L. Lancaster, Radiology Department, University of Texas HSCSA, San Antonio, TX, USA

Positron emission tomography (PET), nuclear magnetic resonance imaging (MRI), and other computer imaging techniques dramatically expand the range of diagnostic information. In spite of this many physicians and scientists remain unaware of the broader range of physical parameters available to provide anatomical and physiological images of a patient. X-rays were limited to images of density variation with small overlays of atomic number information. MRI images proton density modulated by T1 and T2 parameters determined by motional characteristic of biomolecules and associated water. But it can also be used to create contrast related to flow. Both PET and MR can be used to image the biodistribution of isotopically enriched metabolites. We now have the possibility of imaging *in vivo* physiological processes. The location and point of effect of labeled drugs can be followed directly. Thus modern medical imaging has not only application as a provider of anatomical pictures but also as a means of following complex biochemical processes. Such applications, however, demand an understanding of human biochemistry and organ pathologies that pushes the limits of present understanding. Full diagnostic and therapeutic use of these new imaging devices presents a scientific challenge of great import for the year 2000.

P3.2

MEDICAL PHYSICS AND BIOMEDICAL ENGINEERING IN ARGENTINA: CHALLENGES FOR THE YEAR 2000. Max E. Valentinuzzi, Bioingenieria, Universidad Nacional de Tucumán, (UNT), cc 28, suc 2, (4000) Tucumán, Argentina.

Adequate health care on a widespread basis poses a major problem in Argentina. It faces large geographical distances, poor communication and telecommunication systems, and serious insufficiency of economic resources. The current situation of our health care system (without considering a few advanced and well equipped centers, usually located in big cities) can be labeled as distressing and of serious concern, specially if children health, prevention of diseases, early diagnosis and emergencies, taking into account regional pathologies, are considered as priorities. This setting brings us to evaluating a possible high-tech high-cost oriented health care system versus a low-tech low-cost one. The first will benefit in all probability a medium to high income minority group in a relatively narrow band of pathologies, making believe that the system is among one of the best systems on an international scale. The second, instead, will probably benefit a low income majority in a wide spectrum of diseases.

P4.2

Manipulating Tissue Parameters and Diagnostic Data to Yield Increased Diagnostic Information, William R. Hendee, Vice President for Science and Technology, American Medical Association, Chicago, IL, USA

Improved diagnostic capabilities of modern imaging methods depends to a large extent on the possibility of influencing contrast properties of the body by new receptor specific pharmaceutical or contrast agents. These materials provide agents to manipulate diagnostic data to reveal subtle details of the patients response. This presentation will project this topic into the future to look at ways to combine information, match images to observer characteristics, and use "smart" devices and other computer-level techniques as an aid to the diagnostic process. It will also look at our current understanding of how we detect and process visual data, and how we need to improve that understanding to accommodate new techniques such as 3D displays, computer visualized images, and other diagnostic aids.

P5.1

Clinical Readiness and the Artificial Heart
John T. Watson, National Institutes of Health,
National Heart, Lung, and Blood Institute,
Bethesda, MD, USA

Clinical Readiness and the Artificial Heart

Total mortality from cardiovascular disease continues to decline while the incidence and prevalence of end-stage heart disease continues to increase. Congestive heart failure is now the nation's number one listed Diagnosis Related Group. Presently, biologic or mechanical replacement of cardiac function are the only treatment options for end-stage heart disease. Cardiac transplantation is eminently successful, but its application is limited by donor availability to several hundred procedures per year. It is estimated that additionally 17,000 to 35,000 patients per year below age 70 would benefit from an effective, safe, fully implantable mechanical circulatory support device.

The research, development and reliability testing of electrically powered implantable ventricular assist devices is nearing completion. Powered by electro-chemical batteries, these systems are now being tested for patient safety in laboratory and animal tests. These systems represent a new frontier for technological complexity and reliability never before required for an implanted cardiovascular device. Further, these systems require automatic control that must meet the daily circulatory requirements of the implant recipient for a period of two years of uninterrupted function. The next immediate goal is systems that operate effectively for five years and eventually for ten years or longer. The quality of life and longevity of current cardiac transplant recipients will provide the benchmarks for implantable mechanical circulatory support devices to emulate in the future.

The ongoing Device Readiness Testing Program is designed to provide laboratory reliability and animal test data that will demonstrate that an implantable VAS is ready for clinical evaluation in human patients. Twelve systems are undergoing two year bench testing on a rock-loop. Success is being measured by an 80% reliability at a 70% confidence level. For a sample size of 12 this represents zero or one system failure. A failure being defined as a degradation of cardiac output to less than 4 L/min for over 60 seconds. VAS performance will be validated in animals during acute studies of transient behavior and twenty-five months of chronic investigations.

Having convincingly shown that the VAS works effectively in the laboratory and safely in animals, a clinical evaluation will be initiated in patients with end-stage heart disease and for whom there is no alternate therapy. The program will have a VAS production center and probably two clinical centers performing 20 implants per center.

Section II

Medical Physics Scientific Papers

MPSC1.

Artificial Intelligence and Expert Systems in Medicine. J.A. Siegel, Temple University Hospital, Philadelphia, PA 19140

Since the development of digital computers, there has been a growing interest in the creation of "intelligent" computers. Machines that use complex information in intelligent ways are said to exhibit artificial intelligence (AI). AI is a branch of computer science concerned with the study of: 1) methods for knowledge representation and 2) techniques for searching that knowledge in order to derive intelligent conclusions. Its major areas of application include natural language processing, robotics, machine vision, and expert systems. An expert system is a rule-based computer algorithm, consisting of a knowledge base and an inference engine, designed to emulate the decision-making behavior of an expert in a specific field or domain. Several expert systems responsible for the birth of AI in medicine (AIM) have been developed. Some of these have been so popular that their frameworks or shells (a shell is essentially the expert system without its knowledge base) are now commercially available. These shells are currently being used to develop many new expert systems in medicine. This course will include: 1) a historical perspective of AI, 2) the fundamentals of expert systems, 3) the languages of AI, and 4) the use of AIM.

MPSC3.

Hyperthermia Dosimetry
L.H. Gerig, Ontario Cancer Foundation
Ottawa, Ontario, Canada K1H 8L6

Clinical hyperthermia for cancer therapy is the process of elevating tumor bearing tissues to a temperature in the range 42° -> 45° for a specified time. The clinical importance of hyperthermia as an effective synergistic adjuvant to cancer radiation therapy or chemotherapy is becoming clear. Without adequate thermal mapping, hyperthermia will never realize its full potential. This short course will describe various techniques for temperature measurement and the problems associated with the techniques. A detailed analysis of the clinical use of invasive thermometry will be given. The course will discuss the factors which influence the temperature reported by an invasive thermometry system and will describe how problems of measurement error can be overcome.

MPSC2.

Medical Laser Concepts and Applications
Daniel R. Doiron, Ph.D., Laserguide, Inc.
Santa Barbara, CA 93117

The first and still the largest area of application is in ophthalmology, but other areas of application are increasing and expanding rapidly. The use of carbon dioxide lasers for vaporization of tissue is standardly used in various surgical specialties. The high power Nd:YAG and argon lasers are finding significant applications in endoscopy because of their deliverability using small optical fibers. These lasers are primarily used for coagulation, but since the introduction of contact delivery systems they are now being used for vaporization and cutting. New lasers and medical applications for them are beginning to take advantage of the lasers potential of producing very short pulses with extremely high peak powers. Applications such as laser lithotripsy and angioplasty are examples of these new applications. In addition, the monochromatic and possible tuneability of the lasers is now being used in areas such as Photodynamic Therapy and the treatment of birth marks and tattoos. A description of the various lasers, their characteristics and applications, will be presented.

MPSC4.

Quantitative Techniques Utilizing Computerized Radiologic Imaging Instrumentation.
Stephen R. Thomas, Department of Radiology,
University of Cincinnati, Cincinnati, OH 45267

Along with the capability for implementation of well recognized functions (e.g. image reconstruction, display manipulation, digital archiving, etc.), computerization of radiologic imaging modalities has offered the promise of providing quantitative information. Three principal categories for quantitation are: (a) spatial, (b) temporal, and (c) feature characterization. Frequently, the defined parameters of interest cross category boundaries and incorporate multiple facets. This course will review the theoretical objectives, procedural methodology, limitations and practical clinical utility for various quantitative imaging techniques including: 1.) X-ray CT: xenon enhanced cerebral blood flow, bone mineral densitometry; 2) SPECT: regional quantitation of absolute radioactivity, spatial distribution; 3) PET: tracer kinetic models applied to physiologic, biochemical and hemodynamic processes (e.g. cerebral blood flow or volume, metabolism, oxygen extraction ratios, receptor density, neurostimulated foci); 4) ultrasound: tissue characterization through back scatter analysis, doppler quantitation of flow velocity; and, 5) magnetic resonance imaging: tissue differentiation through calculated relaxation parameters (T1, T2), spectroscopic analysis of metabolic components.

Medical Physics Scientific Papers

MPSC5.

Requirements in radioimmunotherapy.
S-E Strand, Radiation Physics Department, Lund University, S-221 85 Lund, Sweden

The limiting factor in radioimmunotherapy is the absorbed dose to normal tissues. Therapy, using radiolabelled monoclonal antibodies, requires a proper dose calculation, involving the radiobiological effects on tumor and normal tissues. The dosimetric considerations must involve the tumor geometry i.e. large tumors, small tumors, micrometastases or circulating cancer cells.

Very few published papers on the possibilities for radioimmunotherapy, however, have been focused on the dosimetry, coupled to radiobiological considerations. The aim of this course is to review the most important parameters necessary to take into consideration in radioimmunotherapy.

The review will include such parameters as different monoclonal antibodies, selection of therapeutic radionuclides, antigen expression on tumor cells, biokinetics *in vivo*, compartment analysis, absorbed dose calculations, dose planning, dose rate, radiation biology, etc.

MPSC7.

Imaging Applications in Radiotherapy.
R. Mark Henkelman, Department of
Medical Biophysics, University of
Toronto, Toronto, Canada M4X 1K9

Medical Imaging is in the midst of dramatic technological development. Sectional techniques such as ultrasound, computed tomography, magnetic resonance now provide detailed three dimensional tumour and anatomical definition.

What is the impact of this change for radiotherapy? Improvements in imaging impact all aspects of oncological management: screening, diagnosis, staging, response, follow-up, relapse and restaging. For radiotherapy planning, developments in imaging present the challenges of more precise three dimensional planning. But even more important is the prospect of moving beyond geographic definition into the use of imaging for tumour characterization.

MPSC6.

Biomagnetism: Principles and Applications in the Study of the Human Brain. Gian Luca Romani, Istituto di Fisica Medica, Università di Chieti, and Istituto di Elettronica dello Stato Solido - CNR, Via Ceneto Romano 42, 00156 Roma, ITALY

The investigation of the physiology and pathology of the human brain by neuromagnetic measurements is providing impressive results and is raising increasing interest from the clinical world. The state of the art of instrumentation permits to detect the spatial distribution of magnetic fields over the scalp by means of 'multichannel' systems featuring a few adjacent magnetic sensors. Each of these measuring units consists of a superconducting magnetometer, namely a (dc) SQUID, and a superconducting detection coil. This kind of instrumentation is only partially satisfying, in that a sequential positioning of the sensors over adjacent regions of the scalp is required to detect the whole field distribution associated to a specific source, with significant limitations to the measurement itself. Nevertheless, important findings are being collected in the study of the organization of cerebral primary areas as well as in that of some diseases, like focal epilepsy. Several projects are being carried on in different countries to develop large multichannel systems, with as many as 100 adjacent sensors, which in the near future will permit to detect magnetic activity over the whole scalp and, with the use of adequate, devoted computers and of appropriate modeling of neural activity, will provide real time functional imaging.

MPSC8.

Safety Considerations for Medical
Linear Accelerator, J.A. Purdy,
Washington University School of
Medicine, St. Louis, MO, USA.

Recent past events involving medical linear accelerators which resulted in overexposures to radiotherapy patients have prompted the radiation therapy community to re-evaluate the safety aspects of these systems. Multimodality treatment units are of particular concern as are those units which utilize computer technology in their control systems. This refresher course will review safety matters pertaining to medical linear accelerator acceptance testing, periodic quality assurance testing, operator training and incident reporting. Particular attention will be directed to tests of the operation of the entire interlock and computer systems.

MPSC9.

Monte Carlo Simulation of Electron-Photon Transport and Applications to Radiation Dosimetry

D.W.O. Rogers* and Alex F. Bielajew, Ionizing Radiation Standards, Division of Physics, NRCC, Ottawa, Canada K1A 0R6

The course begins with a very brief introduction to the Monte Carlo simulation of electron and photon transport followed by a description of the current state-of-the-art. This will draw heavily on the International School held last year at the Ettore Majorana Centre in Erice, Sicily, on the subject of "Monte Carlo Transport of Electrons and Photons below 50 MeV" (proceedings published by Plenum Press, 1988, edited by W.R. Nelson *et al.*). Special emphasis will be given to contrasting the two major general purpose code systems, ETRAN(ITS) and EGS, and to discussing recent extensions and corrections to these systems. The course finishes with several examples of radiation dosimetry applications which will demonstrate the degree of sophistication and accuracy which is possible with today's software and hardware technology.

MPSC11.

Update on Heavy Particle Therapy. Borje Larsson, Department of Radiation Sciences, Box 535, S-751 Uppsala, Sweden

Medium-energy ion accelerators are engaged in radiotherapy with "heavy particles", i.e. protons, or heavier ions, neutrons or negative pions. Thousands of patients with deep-seated tumors or vascular malformations have now been treated, and the prospects for further developments seem to be significant. The aim of this course is to confront the participants with the radiological characteristics of the various members of the family of heavy particles.

The major part will be devoted to physical and biophysical aspects on the various forms of heavy particle therapy: interaction of the particles with living matter, dosimetry, dose planning, and radiobiology. The accelerator technology will also be briefly reviewed and problems concerned with the introduction of new radiotherapeutic modalities in clinical practice will be discussed.

To facilitate the understanding of the role of radiotherapy in the treatment of cancer disease, today and tomorrow, some relevant themes in the evolution of competing or supplementary modalities will also be touched upon.

MPSC10.

Computer Management Systems in Clinical Facilities
Don P. Ragan, Wayne State University
Detroit, Michigan

Clinical Management Systems have moved from curiosity to necessity. Physicists and engineers need to take an active part in departmental and institutional information systems since these systems are used to measure productivity and profitability and are often the basis for management decision making. Not only can these systems provide motivation for improved staffing but they can offer substantial quality assurance tools. This course will review the characteristics of departmental information systems. Also considered will be acquisition of systems including administrative justification. Computer requirements, interfacing to hospital information systems, cost of operation in terms of personnel, time and money and cost benefit will be reviewed. Popular systems in radiology and radiation oncology will be discussed. Limitations and future prospects will be presented.

MPSC12.

An Introduction to Photodynamic Therapy
M.S. Patterson, Ontario Cancer Foundation
Hamilton, Ontario, Canada, L8V 1C3

Photodynamic therapy (PDT) is a method of treating localized malignancies in which cell-killing is due to chemical reactions initiated by the interaction of light with a photosensitizing drug. The principle has been known for close to a century but clinical use has grown only recently due mainly to the advent of selective photosensitizers, laser light sources, and fiber optics. About a hundred groups around the world are now involved in PDT and, as this number increases, medical physicists are being called on to support these clinical efforts.

This course will be aimed at such physicists and will stress the "nuts and bolts" required for clinical applications. After a brief discussion of the photophysics of PDT, the principles and peculiarities of different light sources will be discussed. This will be followed by a description of various irradiation methods (e.g. intraluminal, interstitial) and the technology required to achieve them. The important topic of light dosimetry will be discussed from the standpoint of clinical measurement and the uncertainties involved. Finally, several areas of research in PDT will be indicated which would benefit from the participation of medical physicists.

Medical Physics Scientific Papers

MPSC13.

Time Dose Relationships in Radiotherapy. D. Herbert, University of South Alabama, Dept. of Radiology, Mobile, AL. and C. Orton, Harper Hospital and Wayne State University, Dept. of Radiation Oncology, Detroit, MI.

The course consists of two parts. The first part provides a perspective on the principal clinical dose-time models. In this part the background, development and clinical uses of each of these models are examined and compared. Models of the responses of normal tissues and tumours to brachytherapy and teletherapy regimens are considered. A brief introduction to the deficiencies of these models will be presented. The second part of the course provides a resumé of modern statistical methods for the construction, criticism, validation, discrimination and deployment of models of dose-response. Regression Diagnostics for identification of observations that are not well explained by the model or that may dominate some important aspects of the fit - or both - are introduced. Bayesian regression methods for combining a priori and sample information on the model parameters are considered. Resampling (jackknife) methods of model validation and estimation of ratios of parameters are examined. Examples of the use of each of these methods on data taken from the literature are provided.

MPSC15.

Radiology Image Management Network.
Samuel J. Dwyer III and Larry T. Cook
University of Kansas Medical Center, Kansas City,
KS 66103

Radiology image management networks are designed to acquire, display and manipulate, archive and generate hardcopy recordings of digitally formatted image data. These networks are combinations of Local Area Networks and microcomputer systems. Image management networks are currently required to acquire 1 GByte of image data per day and future requirements will be 50 GBytes per day. Display workstations are required to display and manipulate 15 GBytes of image data per day. Archiving requirements exceed 10 TeraBytes. The experience of implementing Radiology image management networks is limited. Only a few departments have operational networks in portions of the clinical facility. The benefits of these networks include faster patient throughput and increased referral physician response.

MPSC14.

Recent Advances in MRI and MRS
John C. Gore
Yale University School of Medicine
New Haven, CT 06510 U.S.A.

In this presentation the performance and potential roles of several advances in NMR techniques will be described. Whole body MRI currently provides excellent images with good soft tissue contrast. Recent trends have emphasized faster scanning methods to reduce motion artifacts and provide dynamic information. Extremely fast images can be made using echo planar techniques that can image the human body in 1/40 second. These and other schemes can be used to quantify blood flow. In vivo spectroscopy with good spatial localization can now be achieved to detect protonated or phosphorylated metabolites in humans, and these methods are being evaluated at fields up to 4.0T with promising results. NMR images of small samples at high field can be made with resolution of under 10 μ m so that microscopic imaging is also a developing area. The technological advances needed to further such endeavours will be addressed.

MPSC16.

Recent Advances in Ultrasound Imaging
F.S. Foster, Ontario Cancer Institute
500 Sherbourne St., Toronto, Ontario, Canada
M4X 1K9

Ultrasound imaging plays an important role in the detection and management of a wide range of human diseases. Although ultrasound has been used predominantly in obstetrics, abdominal imaging and dynamic imaging of the heart, the advent of new technologies and scanning approaches has opened up a number of promising areas of specialization in diagnostic imaging. Among these techniques, neo-natal imaging, intra-operative ultrasound, peripheral vascular imaging, realtime blood flow mapping, tissue characterization and breast imaging are important examples. The purpose of this course is to examine the physics behind the newest innovations in medical ultrasound imaging and to explore potential future developments in this rapidly expanding field. Topics include: 1) electronic beamforming with phased linear and annular arrays; 2) effects of beamforming parameters on image quality; 3) the physics and applications of realtime two dimensional Doppler blood flow mapping and 4) progress in tissue characterization and studies on the interaction of ultrasound with tissue.

MPS1.1

Fast Neutron Dosimetry Using Positron Emission Tomography, J. Kleck*, J. Smathers, L. Myers, M. Mandelkern and W. Digby, University of California, Los Angeles U.S.A.

The UCLA Neutron Therapy Facility uses a p(46) Be neutron beam for cancer therapy treatment. Patients undergoing treatment were measured for neutron induced radioactivity with an Intrinsic Germanium gamma spectrometry system. The principal isotopes produced were identified as C-11 and O-15. Carbon-11 and O-15 decay by positron emission with half-lives of 20.3 min. and 122 sec., respectively. The radionuclides were determined to be predominantly from C-12(n,2n)C-11 and O-16(n,2n)O-15 reactions. Measurements performed on similarly irradiated acrylic phantoms also indicated the presence of C-11 and O-15 radionuclides.

The patients were imaged on the V.A. Wadsworth Positron Emission Tomography (PET) scanner. The resulting images displayed the activation left in the beam paths. Visual inspection of the PET images revealed marked contrast between tissues of differing elemental composition, due primarily to carbon concentration variations. Thus, acrylic phantoms were employed to image activation distributions without the irregularities caused by variations in tissue carbon concentration. The resulting activation distributions characterize the high energy component of the neutron kerma. This research is supported by NCI contract CM 97315.

MPS1.3

Energy Response of LiF TLD-100 to High Energy Photon Beams, R. C. Robinson* and T. H. Kirby, Radiation Physics Dept., University of Texas System Cancer Center

Lithium fluoride thermoluminescent dosimeters (LiF-TLD) have been used for a number of years in the measurement of absorbed dose from high energy photon beams used in radiation therapy. To convert from TLD response to dose requires a number of correction factors, including: A dose linearity correction factor, a factor to account for the fading of the TLD, and a factor to account for the variance of TLD response with energy.

This paper presents a definition of TLD energy response and measurements of that response for a range of therapeutic energies (Co-60 to 18 MV). The resultant energy response curve is compared to theoretical values which are predicted by various cavity theories (Bragg-Gray, Spencer-Attix, and Burlin). The practical benefit of this paper is to present well defined energy correction factors in the clinical radiation therapy energy range for both water and acrylic mediums.

This work supported by Grant Number CA 10953, awarded by the National Institute of Health, DHHS.

MPS1.2

RADIONUCLIDE DISTRIBUTION AND DOSIMETRY IN SOFT TUMOR TISSUE: IMPLICATIONS TO RADIOIMMUNOTHERAPY, R.W. Howell, D.V. Rao, University of Medicine & Dentistry of New Jersey, Newark, NJ; and K.S.R. Sastry, University of Massachusetts, Amherst, MA.

Current methods for estimating the absorbed dose from radionuclides localized in solid tumors assume the activity is uniformly distributed. The growing evidence that tumor uptake of radiolabeled monoclonal antibodies is highly nonuniform requires new methods of calculating the tumor dose. We have developed a spherical tumor model, in which the radial dependence of the tumor dose is examined as a function of tumor size, activity distribution within the tumor, and radiation type and energy. Tumors of diameters 0.1 cm and 1.0 cm, containing spherically symmetric activity distributions depending linearly and exponentially on the radial position, are considered. Dose rate profiles are calculated for the beta-emitters P-32, Cu-67, Y-90, Ag-111, I-131, and Re-188, and for the conversion electron emitter Pt-193m. Our results show that high energy beta-emitters (e.g. Y-90) are effective for large tumors ($d \geq 1$ cm), medium energy emitters (e.g. Cu-67) for smaller ones ($d \approx 0.1$ cm), and low energy emitters (Pt-193m) for very small tumors.

Work is supported by USPHS Grant No. CA-32877.

MPS1.4

Quantitative Magnetic Resonance Imaging of Diffusion
D Chien*, R B Buxton, K K Kwong, T J Brady, B R Rosen. Massachusetts General Hospital, Boston.

In magnetic resonance, the random translational motion of water causes attenuation of the spin echo signal when magnetic field gradients are applied. This change in signal intensity allows the calculation of the diffusion coefficient D.

We have implemented diffusion imaging on a 0.6 Tesla whole body imager and have tested the precision of the technique in phantoms. MR imaging of diffusion was performed in 18 normal volunteers to study the accuracy and reproducibility of the quantitation in vivo, and to determine the mobility of water in normal grey matter and white matter in the human brain. D was calculated on a pixel by pixel basis to generate diffusion maps of the brain. The measured D is 1.10 ± 0.11 cm²/s for grey matter and 0.81 ± 0.13 cm²/s for white matter (measured at a diffusion time of 114 msec). In contrast to unrestricted diffusion, the presence of barriers in tissue causes D to vary with diffusion time. This is demonstrated in the carrot, and in the human brain, showing the effects of restriction on the measured D.

MPS1.5

A Generalized Method for Constant Feature Suppression in Digital Angiography, DA Reimann*, JP Windham, Henry Ford Hospital, Detroit, Michigan 48202.

A method is presented which insures that the sum of the weighting arguments of any temporal linear filter is zero, while preserving the significant aspects of the filter. By insuring that this sum is zero, constant features as well as noise which has an expected value of zero is suppressed in the final image. A new sequence is formed by subtracting the average image from each image in the original sequence. This new sequence is used to define the signature vectors of features that are to be enhanced and/or suppressed. These signatures are used in the filter definition to create a new linear filter which is then applied to the original sequence. A mathematical derivation of the convolution of these two operations shows that the sum of the weighting arguments of the new filter is zero. The method is applied to the classical matched filter and the eigenimage filter. A comparison is made between the technical characteristics of the modified and the original filters. This method is illustrated on a cardiac study and a simulated sequence.

MPS1.7

NMR Spectrometry of Radiation-Induced Lung Damage

C.H. Newcomb and J. Van Dyk

Ontario Cancer Institute, Toronto, ONT. M4X 1K9

There are indications that Magnetic Resonance Imaging (MRI) may be sensitive to early physiological changes associated with radiation-induced lung damage. In MR images, much of the observed contrast is the result of different T1 and T2 relaxation times between various tissues. It is the changes of relaxation times associated with radiation which will determine the potential usefulness of MRI for imaging lung damage.

Magnetic Resonance Spectrometry has been used in an in vitro study of Sprague-Dawley rat lungs. The T1 and T2 relaxation times have been determined for lung tissue as a function of time after irradiation. Single component fits have been made to the relaxation data which compare favourably with those determined from imaging data. In addition, multiple and continuous fits have also been determined.

Significant changes have been observed at times which correspond to those times of known physiological change.

The results have confirmed the potential role for MRI to image lung damage and provided the necessary data to optimize imaging parameters.

MPS1.6

STEREOTAXIC LOCALIZATION OF TARGETS IN THE BODY
Philip L. Pepmiller*, Robert L. Siddon, and Norman Barth, Department of Radiation Therapy, Joint Center for Radiation Therapy, 50 Binney Street, Boston, MA, 02115

We have developed a generalized method for stereotaxic localization of targets in the body. The method relies on a two film reconstruction technique which places no constraints on source, target, localizer apparatus, or film locations. The target and certain parts of the localizer apparatus must appear on both films. The method has been implemented through the construction of two pieces of localizer apparatus, one utilizes a large rectangular box into which the patient is placed, the other uses a smaller "U" shaped apparatus which is placed adjacent to the patient. Relative positions of objects can be determined to within 1mm. This procedure is useful for determining relative positions of objects such as radioactive implants and hyperthermia thermometers

MPS1.8

Verification of a 3-D Electron Pencil Beam Algorithm for Irregular Field Dose Calculations, Harunor Rashid*, Hanne M.

Kooy, Roger K. Rice and Lee Chin, Joint Center for Radiation Therapy, Harvard Medical School, Boston, MA 02115, USA.

We have implemented a 3D non-coplanar electron pencil beam algorithm based on the Hogstrom gaussian pencil beam model. We present measurements of doses and output factors in water and special phantoms for a variety of irregular fields. The electron fields consist of stationary beams and rotational arcs. Arcs include rotations performed over field cutouts fixed relative to the patient anatomy, providing the ability to shape the dose distribution during the rotation. Measurements are compared with calculated doses and output factors using our algorithm. The effect of heterogeneities present in the volume is considered in the calculations. Results show good agreement between measured and calculated dose distributions and output factors. The effects of heterogeneities and field shape on the output factor will be discussed.

MPS1.9

Computer Algorithms for Scatter Rejection with Multiple Fore Scanning Slits, C. Nayak* and D. Plenkovich, Department of Radiology, Tulane Medical Center, New Orleans, LA, USA

A highly efficient method for rejection of scattered x-ray radiation and veiling glare has been developed. Multiple fore slits are scanned across the x-ray beam. For each position of the slit assembly an image is detected with an image intensifier-TV camera system, digitized using a frame grabber and stored on disk of a MicroVAX II computer. The resultant image is reconstructed from a series of slit images using an appropriate computer algorithm. The peak-detection algorithm keeps in each pixel the highest value recorded during the scan. An advantage of this algorithm is that it does not demand precise control of the slit motion. However, it requires overlap of the slits increasing radiation dose to the patient. An alternative method for image reconstruction is to threshold each of slit images by cutting off the component due to x-ray scatter and veiling glare. The resultant image is obtained by summation of thresholded images. This algorithm utilizes all primary radiation, but requires very precise control of the slit motion. Neither algorithm requires any synchronization of slit scanning and video camera readout.

MPS2.2

EXPERT SYSTEMS IN MEDICINE: REALISTIC EXPECTATIONS
Lawrence E. Widman, Dept Med, UTHSC, San Antonio, TX
Expert systems are large computer programs which incorporate a well-defined, narrow, but deep knowledge of some field of human expertise. When well constructed, they mimic excellently the behavior of a human expert in diagnostic and therapeutic tasks. They differ from conventional programs in their capacity for symbolic reasoning and their explicit expert knowledge database.

This overview talk is intended for listeners new to the field of expert or knowledge-based systems. It will review the basic principles of this technology, the advantages and disadvantages of the most commonly used methods for representation and application of symbolic knowledge, and examples of successful expert systems developed in medical fields. Building on this introduction, the short- and medium-range potential of this technology in medical applications will be discussed.

MPS1.10

A Ray Tracing Method for Calculating the Speed of Sound in Layered Media Using Reflected Ultrasound, G. R. Lockwood*, F. S. Foster and J. W. Hunt, Department of Medical Biophysics, University of Toronto, Toronto, Ontario, Canada.

The speed of sound in a tissue could in many cases provide diagnostically useful information about the state of the tissue. Some success has been achieved calculating the speed of sound from reflected signals for a single layered or parallel layered media, but no satisfactory methods have been developed for *in vivo* measurements of the speed of sound in non-parallel layered media. The signal received from a reflected ultrasound pulse contains information about the distribution of the speed of sound along its path. Although the depth of the reflector is usually not known, the average speed of sound along the path can be calculated using triangulation provided that the source and receiver are separated. By scanning the source, a model of the speed of sound at the surface can be created. Ray tracing through this model allows the calculation of the speed of sound for subsequent layers. A computer simulation in which images of the speed of sound are reconstructed from data generated by ray tracing through two models is presented. Ideas on how this method could be implemented are also suggested.

MPS2.3

Knowledge Based Systems for Oncology
Niilo Saranummi, Simo Hyodynmaa, Pentti Kolari, Jukka Rantanen (#) and Antti Ojala (*) Medical Engineering Laboratory, Technical Research Centre of Finland, Information Processing Laboratory, Technical Research Centre of Finland *Oncology Clinic, Tampere University Central Hospital

Decision support is required in clinical medicine both in making the diagnosis, planning and prescribing therapy and in managing the patient during therapy. It can be provided with knowledge based on systems that are integrated with patient data. In oncology e.g. with the patient database, diagnostic image database and clinical register. In addition, a decision support system must cooperate with the user when giving advice and suggestions not compete with him. Data input required from the users must also be minimized.

Our solution to these requirements, CARTES, builds on the results of the Nordic Computer Aided Radiotherapy programme (CART), where a data set standard and a network concept was developed to facilitate the exchange of data between radiotherapy modules. The CARTES workstation acts as one module in the CART network and comprises three knowledge based modules integrated with each other and the clinical register and protocol database. These modules support therapy selection, protocol design and outcome analysis. A prototype has been built of the 1st module. Its domain is therapy selection for the unoperable non-small cell lung carcinoma. This was done in Xerox-1186 AI workstation using Loops and InterLisp. Presently we are working with the outcome analysis module and the clinical register.

Medical Physics Scientific Papers

MPS2.4

The Role of Virtual World Systems in Medical Imaging in the 21st Century.
Prof. Henry Fuchs, University of North Carolina at Chapel Hill

Inspired by Ivan Sutherland's 1965 vision of an "ultimate display", many groups are developing real-time 3D graphics systems with tiny head-mounted displays whose images are continuously modified to account for head position so that the user feels as if he is moving inside the simulated environment. These advanced systems allow immediate comprehension of the data and direct hand manipulation of the simulated objects. Medical imaging may be the greatest beneficiary of such systems which allow viewing of complex 3D anatomical data together with direct editing, such as the elimination of obscuring regions, "erasing" them by hand, and allow easier understanding of the spatial relationship between multiple objects. In radiation oncology, the user may view patient anatomy together with treatment beam sources, and isodose contours. The systems may provide direct manipulation of design parameters such as location and orientation of radiation sources and blocks. The realization of such systems presents daunting technical challenges. The system's three components, a real-time computer image generation system, a small head-mounted display unit, and a real-time head tracking system, each challenge the state of the art in engineering and computer science. Recent developments about each will be discussed.

MPS3.1

Acoustic Output Levels and Performance Standards for Modern Ultrasound Instruments,
J. Zagzebski*, University of Wisconsin-Madison, Madison, WI, 53706, USA.

The purpose of this symposium is to discuss and elucidate current issues regarding safety, performance and standards in diagnostic ultrasound. This background should be relevant to the practicing medical physicist and bioengineer in evaluating the several standards which are extant and to be released in the near future.

One of the difficulties facing the user when making decisions regarding the choice of ultrasound instruments for specific applications is that of obtaining data on the acoustic output and quantitative performance levels of these devices. One user organization, the American Institute of Ultrasound in Medicine, has accumulated acoustic output data through a manufacturer's commendation process; and these cumulative data will be summarized.

This presentation will also outline a standard being developed for measuring imaging performance of pulse echo scanners.

MPS2.5

The Diagnostic Radiology Workstation in the Year 2000 Henry A. Swett, Dept Diagnostic Imaging, Yale Univ Sch Med, New Haven, CT
Evolving techniques in artificial intelligence, picture archiving and communication systems, and medical information management systems are converging in a way that will lead to a powerful intelligent radiologic workstation. By the turn of the century, radiologists will no longer sit in front of x-ray view boxes and they will no longer be limited to making diagnoses of entities that they have seen before. Instead, they will view images on an intelligent radiologic workstation. This workstation will not only display and manipulate images, but it will provide highly specific information that will enable the radiologist to function with a much higher and broader level of expertise than previously possible. This information will include selected and annotated excerpts from patients electronic medical record, artificial intelligence decision support and analysis tools, and automatic retrieval of pertinent selections from the medical literature.

MPS3.2

Technical Factors and Clinical Uses of Pulsed Doppler for Studying the Fetus,
P. Burns*, Department of Radiology, Thomas Jefferson University Hospital, Philadelphia, PA, USA.

Pulsed Doppler instruments are receiving considerable attention at the present time, both in regards to the rapid technological developments and their expanding clinical uses. However, these devices currently produce the highest time average acoustic output levels among diagnostic ultrasonic instruments, with time average intensities in some systems exceeding 1-2 W/cm². The purpose of this presentation is to review recent technical developments of pulsed Doppler devices and report on new uses of these devices for studying the fetus. Tradeoffs between pulsed Doppler performance and acoustic output levels will also be addressed.

MPS3.3

Problems in Characterizing Acoustic Emissions From Diagnostic Instruments: The Manufacturer's Perspective, J. Abbott*, Diasonics, Inc., Milpitas, CA, 95035, USA.

The multiplicity of operating modes and sophisticated electronic control of beam focusing patterns in modern ultrasound instruments presents a major challenge when measuring acoustic output levels of ultrasound instruments as well as when reporting data to the user. Important features of a new standard, being developed by the American Institute of Ultrasound in Medicine and the National Electrical Manufacturers Association, for specifying acoustic output levels of diagnostic ultrasound equipment will be described. The standard requires measurements and intensity calculations in water, but also allows calculation of "derated" intensity values assuming a uniform sound beam attenuation path. The merits of both reporting systems will be addressed.

MPS3.4

Concerns With Acoustic Exposures: Alternative Safety Proposals for Medical Ultrasound Equipment, P. Carson*, University of Michigan Hospital, Department of Radiology, Ann Arbor, MI, 48109-0030, USA.

The concept of "derated intensity" was adopted to allow meaningful comparisons between acoustic output levels produced by modern ultrasound instruments, which usually utilize high frequency transducers, and levels of older, lower frequency systems.

The adequacy of "derating models" will be discussed and an alternative, which may be particularly relevant for fetal exposures, will be presented. This presentation will also address the topic of thermal mechanisms for specifying potentially hazardous exposures for diagnostic ultrasound. In addition, an ultrasound power control feature for diagnostic instruments will be recommended.

MPS3.5

Possibility of Cavitation Induced Bioeffects from Medical Ultrasound and Shock Wave Devices, B. Fowlkes*, University of Mississippi, Department of Physics, University, MS, 38677, USA.

One of the mechanisms by which the large pressure amplitudes associated with diagnostic ultrasound pulses could induce a biological effect is through cavitation. Recent experimental and theoretical data for cavitation thresholds for diagnostic ultrasound will be presented.

MPS3.6

Second WFUMB Symposium on Safety and Standardization of Ultrasound in Obstetrics, G. Kossoff*, Ultrasonics Institute, Sydney, NSW 2000, Australia.

An overview of the ultrasound safety issues, particularly as seen from the ultrasound community outside the United States will be presented. These issues will be discussed in greater detail at a World Federation of Ultrasound in Medicine and Biology (WFUMB) meeting on Ultrasound Safety and Standards, scheduled for October 22-23, 1988, in Washington, D.C. The goals and anticipated outcome of this meeting will be discussed.

MP1.1

A Quality Assurance Protocol For The Testing Of Treatment Planning Systems, U.F. Rosenow*, M.K. Islam, G. Mitev, S. Rajaratnam, O. Cintron, T. Urrutia, Albert Einstein College Of Medicine and Montefiore Medical Center, Bronx, NY 10467

Quality Assurance of treatment planning systems is structured in three different levels of performance: (1) initial system tests, aimed at a most comprehensive test of total system performance; (2) constancy checks which are to be done at regular intervals and comprise of a subset of the initial system checks; (3) intermediate system tests, which are performed following any hardware, software or data base modifications. These consist of any number of checks from constancy check up to the full set of initial system tests depending on the nature of the modification.

For reasons of practicability the set of test cases has to be rather limited. It consists of various single beams in a water phantom including oblique incidence, wedges, blocks and simple inhomogeneities where comparisons between calculations and measurements can be made. Further included are opposing and matching beams, and a selection of patient plans. The latter are mainly used for constancy checks. Results obtained with the quality assurance protocol with different versions of a treatment planning system will be presented.

MP1.3

Constraints in 3-D Treatment Planning System Design, B.A. Fraass*, D.L. McShan, and W.A. Roberts, University of Michigan Medical Center, Ann Arbor, MI 48109.

A number of groups have reported on various features and uses of their 3-D treatment planning systems. Although design philosophy and aims have a large impact on each of these systems, the way in which various design constraints are handled is often of crucial importance. We describe a number of basic constraints and design considerations for 3-D planning systems and the various ways in which those issues have been addressed during the four years of development of the 3-D planning system U-MPlan. In a general 3-D system, a three-way trade-off decision must often be made between interactivity, disk space and access speeds, and computer resource usage. A second basic type of constraint is that imposed by system hardware (which can be solved, or at least changed, by purchase of new equipment) and more difficult limits caused by operating system software design. A number of these limits have been reached during the development of our software, including limits on disk space, real and virtual memory, CPU usage, and multiple user environments. Major design changes, operating system reconfiguration, and new hardware have all been used to address the various limits.

MP1.2

A Comparison of Treatment Techniques for Prostatic Cancer Irradiation. M. Sontag*, R. Whittington and E. Cheng. Radiation Oncology, University of Pennsylvania 3400 Spruce St., Philadelphia, PA. 19104

An analysis has been made of 30 treatment plans for 5 patients to determine the optimal treatment technique for prostatic cancer irradiation. 15 MV x-rays were used. Techniques examined included 4 field box, bi-lateral 110° arcs, 300° anterior arc and 360° rotation, each without and with blocks. Simulation of blocked arc treatments with multi-leaf collimation were also performed. CT scans were taken at 1 cm intervals throughout the irradiated volume and plans were generated using a 3-D radiation therapy treatment planning system. Isodose distributions, dose-volume histograms and dose statistics were made available to the physician for treatment plan evaluation. Each plan was optimized to maximize target dose homogeneity for a minimum target dose of 70 Gy. Target volume size varied from 87 to 163 cm³. No correlation among target volume, bladder and rectal volume was found. Analysis of the dose to the femoral heads, bladder, and rectum indicates that a clinically acceptable femoral head dose is obtained regardless of the treatment approach. All blocked beam techniques result in a clinically significant reduction of the bladder and rectal dose, particularly for smaller target volumes. The best results were obtained with the 4 field box and bi-lateral 110° arc techniques, each having comparable bladder and rectal doses. An error analysis indicated that both blocked and unblocked bi-lateral arc techniques is somewhat more forgiving of patient set-up uncertainty and motion than the blocked 4 field box technique.

MP1.4

Dynamic Wedge Field Techniques through Computer Controlled Collimator Motion and Dose Rate, Dennis D. Leavitt*, Melissa Martin+, and John H. Moeller, Univ. of Utah, Salt Lake City, Utah 84132, and St. Joseph Hospital+, Orange, CA 92667

Clinical treatment planning situations arise which require different wedge angles within segments of a single field. Solutions to these cases can be attained through dynamic wedge field generation

Dynamic wedge field generation is achieved by 1) specifying the desired dose at a series of points in the plane of the wedge, under the constraint that the points may be at different depths but must be on different fanlines (cannot specify dose at more than one depth on same fanline); 2) calculating the dose contribution to each point due to collimator-defined asymmetric strip fields having one contiguous edge while increasing in width across the field; 3) determining optimized field weights for each field, while accounting for the dependence of output factor of each strip field on width and radial distance.

Calculation and measurement of dynamic wedge fields and verification by film dosimetry are reported for the Varian Clinac 1800 and Clinac 2100-C.

MP1.5

OSCAR - An objective approach to treatment plan evaluation, S. Shalev*, D. Viggars, P. Therrien, P. Hahn, Manitoba Cancer Treatment and Research Foundation, Winnipeg, Canada R3E 0V9.

An objective approach to treatment planning is described in which a planned dose distribution is evaluated in terms of prescribed limits of acceptability, and any discrepancies (referred to as "regions of regret") are displayed in the form of a parametric image in which colors are used to represent different types and degrees of regret. The program OSCAR (Objective Scoring with Coloured Areas of Regret) is used in conjunction with the AECL Theraplan treatment planning system to display images of regret in addition to conventional isodose plots, and is used for the comparison of alternative plans in terms of adequate target coverage and minimal irradiation of sensitive organs. Quantitative score functions are derived for target coverage and over-irradiation of normal tissues, which provide a clear indication of the acceptability of the dose distribution in each organ. Required tumor dose levels and organ-specific tolerance doses are prepared in advance by the clinician for each site. The method is objective and reproducible, and provides clear documentation of the selection process. Examples are shown for selection of one from several rival plans for treatment of the prostate, esophagus and lung.

MP1.7

Dose Surface Display for Three Dimensional Treatment Planning, J.A. Purdy*, J.W. Wong, W.B. Harms, B. Emami, R.E. Drzymala, and J.W. Matthews, Washington University School of Medicine, St. Louis, MO, USA.

The evaluation of the volumetric three dimensional (3D) dose distribution has proven to be a difficult and time consuming task in 3D treatment planning. We have developed code for our prototype 3D treatment planning system which allows the generation of user specified isodose surfaces. Surfaces are represented as cross-hatched contours, and allow one to view target volumes and/or internal structures which are enclosed or protruding from the isodose surface. While dose surface display for 3D treatment planning is not new, its implementation on a real time display system is. Dose surface display in combination with high speed interactivity has proven to be an extremely effective tool in plan evaluation. Examples will be shown demonstrating dose surface displays versus multi-planar 2D isodose distribution displays as a more effective way of evaluating 3D treatment plans. (Supported in part by NCI CM-47696)

MP1.6

Evaluation of Three-Dimensional Photon Treatment Planning of the Intact Breast, J. Chu†, L. Solin, M. Sontag, L. Brewster, E. Cheng, K. Doppke, R. Drzymala, M. Hunt, R. Kuske, J. Manolis, B. McCormick, J. Munzenrider, Univ. of PA & FCCC, Phila., PA, Mem. Sloan-Kettering Cancer Center, NY, NY, Mass. Gen. Hosp., Boston, MA, Mallinckrodt Inst. of Radiology, Wash. Univ., St. Louis, MO

Early breast cancer can be effectively treated with lumpectomy followed by radiation therapy. Uniform dose distribution within the target volume is difficult to achieve due to the significant breast contour variations and the large dose perturbations produced by the lung tissues inside the irradiated volume. Two intact breast patients have been extensively planned and 39 three-dimensional treatment plans were evaluated as part of a multi-institutional treatment planning project sponsored by NCI. Dose distributions, dose volume histograms, and dose statistics were used to quantify the dose to the target volume and eight normal tissues. The physical parameters studied include: effect of contour variation, effect of tissue inhomogeneity correction, effect of photon energy, effect of dose modifiers, and the use of field shaping blocks. Our preliminary data indicate that the dose heterogeneity can be as much as 23% within the treated volume and it is important to consider the entire irradiated volume when evaluating treatment plans for intact breasts.

MP1.8

THE EVALUATION OF A NEW 3-D SCATTER CORRECTION ALGORITHM WITH ALREADY EXISTING METHODS. A. T. Redpath* and D. I. Thwaites, Dept. of Medical Physics, Western General Hospital, Edinburgh, Scotland.

A number of methods have been developed to correct for the presence of inhomogeneous structures when calculating absorbed dose distributions for radiotherapy. The two algorithms that take into account changes in the scattered component of absorbed dose are the power law tissue air ratio method and the equivalent tissue air ratio method (ETAR). Both algorithms have been implemented on a treatment planning system running on a SUN 3/180 microprocessor. A new algorithm based on the principles of ETAR has been developed and has also been implemented on the treatment planning system.

All three algorithms have been assessed in a variety of situations designed to simulate those occurring in radiotherapy practice, and their performance compared to experimental results.

MP1.9

Horizontal Tangential Technique and Dose Calculating Methods for Breast Irradiation, Yi-min Hu*, Chun-ii Zhang, Zheng-gong Luan, and Shin Zhang, Radiation Oncology Dept., Cancer Institute (Hospital), Chinese Academy of Medical Sciences, Beijing, China.

A horizontal tangential three-field technique has been developed to solve effectively the technical problems and difficulties encountered by the conventional three-field technique used to treat breast cancer by radiation. A mathematical model is built up for Cobalt-60 and 8 MV X-ray. And from this model, one can easily choose a proper wedge filter (as tissue compensator) for individual shape of target volume for a better dose distribution with an uniformity of less than 10%. By using a gravity-oriented trapezoid tangential field block especially designed, a proper matching of the fields between tangential and supraclavicular ones can be obtained. A special treatment couch for the tangential fields and a water level buried-in slide-pointer is made to improve the accuracy of localization and the repetition of setting up of patients.

MP2.1

AN ANALYSIS OF LEFT VENTRICULAR STRUCTURE BASED ON REGIONAL WALL THICKNESS AND CURVATURE BY GATED CT, G. Tomonaga*, K. Iga, T. Tamamura, H. Gen, T. Matsumura, K. Hori, Tenri Hospital, Tenri, Nara 632, Japan

Many cardiologists have assumed that wall stress remains within normal range in compensated hypertrophic or normally growing hearts. To investigate this hypothesis, we attempted to measure regional wall thickness and curvature of the left ventricle in 6 normal and 3 hypertensive subjects using ECG-gated computed tomography. The longitudinal image of the left ventricle was reconstructed at end-diastole. From the tracings of outer and inner edges of the ventricular wall, mid-wall line (MWL) was determined by measuring wall thickness. Meridional radius (R_m) was measured sequentially by fitting circles on MWL. Minimum distance from each point on MWL to longitudinal axis was measured as circumferential radius (R_c). Mean value of the two reciprocals $[(1/R_m + 1/R_c)/2]$ was defined as mean mid-wall curvature. The relationship between regional wall thickness and curvature showed hyperbolic correlation in every patients, that was statistically significant ($p < 0.01$ in 8 cases, $p < 0.05$ in 1 case). This result suggested that the product of the regional wall thickness and curvature is constant. Accordingly, regional wall stress may be constant throughout the left ventricle.

MP2.2

RELIABILITY OF T_1 AND T_2 AS QUANTITATIVE PARAMETERS WITHIN LONG TERM CLINICAL RESEARCH PROTOCOLS, R.C.Samaratunga*, S.R.Thomas, Dept. of Radiology and W.Ball, Childrens Hospital Medical Center, University of Cincinnati, Cincinnati, OH 45267-0579

The recognized potential value of reproducible quantitative NMR parameters such as calculated T_1 and T_2 includes their practical clinical utility as indicators of tissue changes secondary to disease or in relationship to treatment protocols. Investigations of white matter abnormalities in pediatric brains following bone marrow transplant are being conducted with the objective of defining progressive or regressive neuroresponse on MRI. A major component of this study involves establishing and maintaining a clinical calibration standard for long term monitoring of (apparent) tissue T_1 and T_2 . Preliminary data acquired over a period of two months on a 1.5 Tesla GE Signa unit utilizing a compartmental plexiglass phantom with different concentrations of $CrCl_3$ (0.1 to 1.0 mM) indicate: a) Long term reproducibility of 8% to 15%, b) T_1 and T_2 position dependence of 8% and 25%. A newly designed phantom consisting of a matrix of sealed glass vials (of sterilized $CrCl_3$ solutions) in a loading medium is being used to evaluate: a) Long term reproducibility, b) Optimum pulse protocol and c) Measurement precision in conjunction with periodic verification of phantom T_1 and T_2 stability using spectroscopic measurements. Temperature dependence of the calibration standard is also monitored.

36

MP2.3

A Comparison of Selective Cancellation Excitation Methods for Flow Measurement by NMR,
Eduardo Benitez-Read,* Arvind Caprihan, and Eiichi Fukushima, Lovelace Medical Foundation, 2425 Ridgecrest Drive SE, Albuquerque, NM, USA.

NMR flow measurements in the presence of an abundance of stationary spins require that the signal from the static spins be suppressed. Cancellation excitation either drives the static spins to equilibrium or inverts the magnetization to obtain the signal only from the moving spins, while the subtractive methods are based on subtraction of two data sets, in which the signals from the static spins are the same while the signal from the moving spins is different. The cancellation excitation methods have an advantage over subtractive methods in that the dynamic range of the A/D converter is more adequately utilized.

The method to be analyzed consists of a pair of selective rf pulses with opposite phases and appropriate slice selection gradients. Other variations of the pulse sequence include the use of one or more π pulses for reducing the sensitivity to B_0 and rf inhomogeneities, phase cycling the rf pulses, and alternating the polarity of gradient pulses. These variations will be compared for their sensitivity to instrument imperfections (B_0 and rf inhomogeneities, and eddy current effects), flow characteristics (mean velocity, and laminar or plug flow), and pulse sequence parameters (the ratio of repetition time T_R to T_1 , slice width, pulse angle, and frequency offset).

MP2.4

X-ray Spectroscopic Imaging, JM Boone*, JA Seibert[†] and GS Shaber, Departments of Radiology, Thomas Jefferson University, Philadelphia, PA and [†]University of California-Davis, Sacramento, CA

Dual energy image pairs are conventionally used to render bone or tissue subtracted images. X-ray Spectroscopic Imaging (XSI) is a technique in which the spectral properties of the transmitted x-ray beam are overlaid using subtle color mapping, onto the original (raw) grey scale radiograph. Dual energy images are acquired, and are numerically processed to generate the relative hardening index (RHI) image, which is a parametric map qualitatively related to the relative beam hardness. The RHI image is colored and overlaid on the raw grey scale image. Therefore, the transmitted x-ray spectral properties are essentially displayed using the visible spectrum. XSI can be used to discriminate between calcified and non-calcified nodules, and thus could be clinically useful in mammography, chest and abdominal radiology. A brief theoretical introduction, computer simulation results, and spectroscopic images will be presented.

MP2.6

In Vivo Flow Measurement by NMR Imaging. M.A. Smith*, M. Tarnawski, D.J. West, G.M. Taylor, V.T. Ayton, R.G. Gosling and M.N. Maisey. Division of Radiological Sciences, United Medical and Dental Schools of Guy's and St. Thomas's Hospitals, Guy's Hospital, London.

In vivo flow measurements have been performed using a 1.5T MR system (Philips Gyroscan) with a flow adjusted gradient (FLAG) pulse sequence. The technique utilizes gradient echoes and pairs of bipolar gradient pulses to encode velocity information in the phase of the NMR signal. Two types of flow images can be acquired: MR angiograms of thick (150mm) sections to demonstrate the presence of flow and MR phase maps of thin sections (5mm-10mm) to give quantitative measurements of velocity. Calibration was performed using a rotating flow phantom with a maximum velocity at the edge of 4m/s. The accuracy of velocity measurements was 5.6%. The maximum velocity detected through the section was 2.6m/s and within the section was >4m/s. Results will be presented of flow measurements in the aorta, head and legs in 30 normal subjects. MR angiograms of the leg have also been performed and compared with X-ray angiography in 15 patients.

MP2.5

New Approach to Quantifying Cerebral Blood Flow Measurements by the Xenon/CT Technique
Abund O. Wist*, Panos P. Fatouros, Richard L. Keenan, and P.R.S. Kishore
Medical College of Virginia, Richmond, VA

With the recently developed Xe/CT method for measuring cerebral blood flow, high resolution blood flow maps are possible which contain a large amount of information not readily accessible. By using pattern recognition techniques we are producing composite images combining anatomical and hemodynamic data. Specifically, information from the partition coefficient ("lambda") maps is combined with blood flow distribution in composite maps indicating normal, ischemic or hyperemic areas. Further by drawing isoflow lines into these maps the physician can determine quickly the actual blood flow at a given point. To speed up the calculation of the blood flow maps (for each pixel a two parametric non-linear regression analysis has to be carried out), we developed a new high speed algorithm which can solve the appropriate equations by about a magnitude faster. We have incorporated several other improvements designed to improve the accuracy and readability of the information presented. The high diagnostic capability of this method will be demonstrated with a series of blood flow maps obtained from recent head injury patients.

MP2.7

Individual and local lung density variations observed by computed tomography in rodent lungs after irradiation
E. El-Khatib*, S. Lehnert†
KFHS&RC, Riyadh 11211, Saudi Arabia
†McGill University, Montreal, Canada

Lung toxicity is recognized as a major limiting factor in radiotherapy of the thorax region. The factors associated with radiation damage to lung are expected to produce an increase in the density of lung. Densitometry using computed tomography (CT) is a non-invasive method to measure tissue densities in-vivo and has been used to monitor radiation damage to lung. Measuring an average lung density, however, is not a sensitive index of radiation damage since radiation pneumonitis is a focal disease where areas of increased density are adjacent to areas of decreased density. In the present study, the average lung density was measured repeatedly in rats irradiated with various single doses to the thorax. In addition, the density of small elements along the outer parenchyma of the lung was recorded. Abnormal regional densities and density gradients were observed at lower doses and earlier times than changes in average lung density. Moreover, areas of very low density were observed close to denser areas. The regional density analysis thus proved to be a more sensitive index of radiation damage to the lung.

MP2.8

A Method of Quantifying and Correcting for the Effects of Scatter, Veiling Glare and Beam Hardening in Quantitative Arteriographic Imaging. I.A. Cunningham* and A. Fenster, Victoria Hospital and Imaging Research Laboratories, Robarts Research Inst, Univ of Western Ontario, CANADA.

Obtaining quantitative estimates of arterial lumen narrowings (stenoses) from image data is made difficult by the effects of scatter, veiling glare, beam hardening and image noise. We describe a method of quantifying the influence each of these effects has on the accuracy of stenosis severity measurements from a direct measure of the system modulation transfer function (MTF). The MTF is obtained for a particular set of conditions using an edge technique, which produces an accurate measure of the low frequency drop, both with and without a phantom to produce scatter. The effective attenuation coefficient of the iodine contrast media, as would be estimated from attenuation measurements using image data, is modeled theoretically as a function of beam path-length through the iodine. This model is verified experimentally, and is used to determine the relative importance of scatter, glare and beam hardening in determining stenosis severity for a range of conditions. It is shown this approach can be used to correct image data for these effects with images of iodinated step wedge phantoms.

MP3.1

Holographic Display of X-ray Absorption in Medical Specimens. M. J. Flynn*, J. Roebuck, L. Lacey, R. Block, Henry Ford Hospital and Holo-source, Inc., Detroit, Michigan.

A method based on radiographic measurements has been developed to depict the interior structures of a specimen with a white light hologram. The method has been applied to display the complex topography of blood vessels within the brain. Specimens are placed in a cylindrical chamber and rotated in .5 degree increments. Digital radiographs (1024^2) with water equalization are obtained at each angular position. Each radiograph is recorded with 2x magnification using a .3 millimeter focal spot to achieve a resolution of 5lp/mm. The digital radiographs are computer processed to remove nonuniformities and enhance structures of interest. A total of 120 radiographs covering a 60 degree angular field of view are transferred to a high-resolution, black/white cine film. The sequence of cine views is reprojected through an image enlarger onto a master plate using an argon laser mounted on an interferometrically stable optical bench. The hologram is produced from a single laser projection of the master plate onto a second photographic plate. Stereoscopic perception of the specimen in different orientations is achieved when the holographic plate is viewed using a white light point source.

MP2.9

Sensitivities for Elemental Imaging in Computerised X-ray Tomography, K.J. McCarthy and J. Fryar National Institute for Higher Education, Dublin, Ireland*

There are two basic ways to determine analyte concentration by using monochromatic X-ray beams in computerised tomography. The first method is to scan the matrix, add the analyte and scan again. The second method is to scan at two or more energies which straddle an absorption edge of the analyte. The resulting reconstructions show the analyte concentration. The sensitivities of both methods have been theoretically analysed for the situation where the analyte is homogeneously mixed with a cylindrical matrix. For the first scan method, it is shown that the maximum sensitivity occurs for a matrix diameter of 2.5 mean free paths. The sensitivity at any other diameter can be readily determined by using a universal curve of relative sensitivity versus thickness in mean free paths. Sensitivities are shown to be approximately 100 times better than when the analyte is added to the equivalent of one voxel. In the second experimental method it is shown that the same universal curve as for the first method also applies to the determination of the sensitivity at any diameter when that at one diameter is known. The theoretical predictions are compared with experimental measurements.

MP3.2

RELATION BETWEEN REFLECTANCE IMAGE AND LESION FORMATION ON SIMULATED EYE MODEL

Y. Yang*, A.J. Welch, H.G. Rylander III, W.S. Weinberg
University of Texas at Austin

One of the goals of our laser robotics work at UT Austin is to control the size of a lesion using reflectance feedback for ophthalmic treatment. A simulated eye model has been created that is composed of three layers. A thin absorptive layer to simulate the pigment epithelium is placed between two thick transparent layers containing protein. The pigmented layer is heated by Argon laser irradiation and a video camera with a 32×32 pixel array operating at 420 frames per second records the reflectance images (in real time) owing to coagulation of the protein. Simultaneously cross section temperatures of some lesions are recorded with a thermal camera. Different protein and absorptive materials are chosen to indicate the effects of absorption and coagulation rate constants. Formed lesions are examined under a microscope and the extent of damage is compared to predictions with a computer model.

This work was supported in part by the Free Electron Laser Biomedical/Materials Science Program: ONR Contract number N00014-86-K-0875.

MP3.3

Comparative Analysis of Laser Ablation of Plaque Using Direct Laser Irradiation and a Metal Contact Probe

GL LeCarpentier*, S Rastegar*, AJ Welch,
SA Prahll, and H Hussein**

Biomedical Engineering Program,
University of Texas at Austin
*Bioengineering Program, Texas A&M University
**Trimedyne Inc., Santa Ana, CA

The purpose of this research was to establish the theoretical temperature distribution and ablation characteristics in atherosclerotic plaque resulting from both direct Argon laser irradiation and the application of a metal contact probe. The plaque was assumed to be a single-layered homogeneous medium, and the laser light distribution within the tissue was calculated using a delta-Eddington approximation. One dimensional temperature distributions and ablation depths were calculated using an immobilized finite element method. Thermal and optical properties of the tissue were assumed to remain constant. Ablation front positions and temperature profiles at times prior to ablation, at the onset of ablation, and during the ablation process were calculated for both modalities. Additionally, ablation velocities were calculated as a function of both tissue water content and heat flux transmitted through the metal probe tip. For the typical operating conditions used, calculated values agreed qualitatively with experimental results. Temperature calculations after the onset of ablation indicated high sub-surface temperature rises beyond the surface ablation threshold temperature for the direct irradiation case but monotonically decreasing profiles for the metal probe. However, deeper within the tissue, calculated temperatures appeared to be higher for the probe than for direct irradiation

MP3.5

Infrared Laser Heating of Thermoluminescent Plates for the Purpose of Spatially and Dosimetrically Characterizing Radiotherapy Beams, M. Grupen* and K. Kearfott, Arizona State University, Tempe, AZ 85287-6006.

Laser heating of a Thermoluminescent (TL) plate may provide a method of extracting spatially encoded dosimetric data. Two-dimensional collocation of the digital data extracted will provide a dose distribution map or image. This information may be valuable for quality assurance of radiation-producing equipment or for obtaining beam isodose curves which are prerequisites for radiotherapy patient treatment planning. To develop and optimize a laser heating device, time variant spatial temperature distributions within the TL detector must be known. A numerical model (solved using the Alternating Direction Implicit Scheme) has been developed to determine radial and axial temperature profiles in a TL layer when a 4 Watt carbon dioxide Gaussian laser beam is used to heat a single or a series of spots. The results for LiF plates reveal heating rates on the order of 350 K/s to 2000 K/s for plates 0.5 mm to 0.1 mm thick, respectively. Laser heating of thicker TL plates becomes impractical due to the limited depth of infrared radiation penetration within the material layer. Furthermore, it is revealed that spatial resolution of such a system is a stronger function of laser beam diameter than radial conduction.

MP3.4

Radiation Safety and Quality Control Program for Medical Lasers, Suresh M. Brahmavar*, David Fleet, Cathy Miller and Marilyn Riddle. Baystate Medical Center, Inc., Springfield, MA 01199

The Radiation Safety and Quality Control (RS/QC) program for medical lasers was developed at Baystate Medical Center in compliance with DHHS/CDRH/FDA and DPH requirements. The RS/QC procedures are based on the recommendations of ANSI Z136.1, ANSI Z136.3 and AMA Council report. The RS/QC program manual includes five (5) distinct groups of procedures for use of medical lasers. The procedures include regulatory compliance, laser safety, quality control standards for approval of laser user, service and maintenance. The details included in above procedures developed for clinical lasers relate to laser environment, patient and personnel safety, electrical safety, smoke plume, fire safety, institutional safety policies, compressed gases, medical surveillance of staff, LSO responsibilities, MPE for skin/eye, nominal hazard zones, pre-op/post-op check lists, daily start-up and user log, administrative and engineering controls, educational and practical experience standards, periodic QC tests, output measurements, testing of protective devices, records and audits. The clinical lasers at Baystate Medical Center include CO₂, Argon, Nd-Yag in OR, Ob-Gyn Service, Immunology Labs and in Eye Surgery.

MP3.6

Measurement of the concentration of hematoporphyrin in different tissues by opto-acoustic spectroscopy, U. Bernini, A. Andreoni, E. Quarto, P. Russo*, A. Mancini, M. Mastrocinque, University of Naples, Naples, Italy.

Hematoporphyrin (Hp) is a known photosensitizing agent, used in the treatment of tumors by activation with lasers, since it absorbs in the red and accumulates into tumors more than into normal surrounding tissues. We measured the Hp concentration in different organs of lab mice, that received the drug 24 h in advance, without extracting it, by opto-acoustic spectroscopy. As the technique is less noisy with powders, samples of known weight were lyophilized and the signal from the powder were compared in amplitude to the signal obtained from a mixture of Hp with BaSO₄ (having a uniform absorption in the spectral range of interest). Although the absorption of Hp almost overlaps that of hemoglobin, we proved it is possible to measure the drug levels in different tissues following I.V. injection with drug doses of the order of the therapeutic dose used for phototherapy with lasers on tumor models implantable into the mice.

MP3.7

HUMAN ERYTHROCYTE'S MEMBRANE DAMAGE DUE TO LASER AND PHOTSENSITIZERS. S. Ganesan*, V. Velmurugan, V. Masilamani and G. Prasad, Dept of Physics, Anna University, Madras, India.

The use of lasers in Photo Radiation Therapy (PRT) has assumed great importance because of its specificity and its capability of regressing tumors even in internal organs. The characterisation of this PRT is still incomplete. In this connection photohemolysis of human erythrocytes are studied as a simple model system using five different lasers and three photosensitizers - Acridine Orange, Fluorescein and Rose Bengal. The percent Hemolysis (pH) in the presence of laser and sensitizer was found to be higher when compared to laser alone. The pH was found to increase towards shorter wavelengths. It was also found that the pH depends on post incubation time, indicating the photochemical nature of the damage due to delayed photo oxidation via the cross linking between biomolecules. Also, of the three sensitizers, Acridine Orange has the higher effect in photo-modification of cells.

MP3.8

Comparison of surface temperatures and damage volume in canine bladders during *in vivo* irradiation at 1.06 μm wavelength.

W.F. Cheong*, A.J. Welch, S. Thomsen*, A.C. von Eschenbach*, J.H. Torres, R. Swanson*

Biomedical Engineering, The University of Texas at Austin;
*The University of Texas System Cancer Center,
Houston, Texas.

The efficacy of cw light at 1.06 μm in creating thermal damage in *in vivo* bladder tissue were assessed based on peak mucosal and serosal temperatures, and histology of denaturation patterns. Two physical conditions were examined: (1) air-tissue-air boundaries where exposed canine bladders, suspended with minimum hemorrhaging, were irradiated; and (2) water-tissue-air interfaces in a water-filled bladder under cystoscopic irradiation. Only the serosal spatial and temporal temperatures were monitored in case 2. Thermal images were recorded with 8-12 μm and 3-5 μm thermal cameras. In cystoscopic irradiations at 7 s and 4 s using powers greater than 30 W and 40 W respectively, serosal charring and collapse of blood vessels were observed with only simultaneous intense coagulation at the mucosal surface. Subsequent correlation analyses will determine whether surface temperature can be used for prediction of the volume of thermal denaturation.

MP3.9

Tissue Effects of Neodymium-YAG Laser Irradiation of Pig Ureter, R.A. Siwek*, R. Kodama, J. Srigley and L. Klotz, Toronto-Bayview Regional Cancer Centre and Sunnybrook Medical Centre, Toronto, Canada

Neodymium-YAG laser radiation at 1060 nm produces a deep homogeneous coagulation in tissue. This is due to its low absorption and high scattering properties. The Nd-YAG laser has been successfully applied endoscopically to treat bladder neoplasms. In select patients, the treatment of well differentiated tumours in the ureter would lend themselves to laser therapy. However, the wall of the ureter is much thinner than the bladder and a reduction of laser energy would be necessary. No safe dosage guidelines have yet been established.

We report our preliminary data of Nd-YAG therapy on the normal pig ureter. This was an acute study on laparotomised pig ureter. Each ureter was opened longitudinally. Using a specially designed laser fibre holding device, the spot size was kept constant. Various doses of laser radiation were delivered. Heat measurements at the peri-adventitial surface of the ureter were measured with microthermocouples. Ureteral sections were examined histologically for the effect of the laser radiation. Our results correlating radiant exposure and tissue temperature are reported, together with heat distribution and histology.

MP3.10

Fiberoptic Neuroendoscopy and Nd-Yag Laser Interfaced to Imaging-Guided Stereotaxis-Henry Ford Hospital Det., MI
Zamorano L*, Chavantes C, Dujovny M, Malik, G, Ausman J I.

Imaging-guided stereotaxis constitute the most accurate method to approach intracranial lesions. With 3D/Multiplanar Imaging, size, shape, axis of lesions can be considered to select the best approach for diagnostic and therapeutic purposes. This information can be transposed into stereotactic space with high accuracy and reliability. Nevertheless major critics are lack of direct visualization and intraoperative monitoring, changes in intracranial coordinates after aspiration of cystic cavities or intraventricular lesions and difficulties on aspiration of high dense contents like hematoma, tumor etc. New adaptation for direct visualization of stereotaxic procedures has been designed that include: rigid and flexible endoscope with a 2mm working channel each, specially designed instrumentation and Nd-Yag laser fiber. Methodology, experimental and clinical experience will be presented. Interfacing of Imaging-guided stereotaxis with neuroendoscopy not only changes an intraoperative blind procedure into a direct visual one, but also increases the scope of use of these procedures in the management of intracranial lesions. It allows to explore ventricles, cysts, cavities extensively with minimal damage to surrounding brain tissue: drainage, biopsies, and resection of lesions under direct visual monitoring became possible.

MP4.1

MEASUREMENT OF THE COUNT RATE PERFORMANCE OF THE MULTIWIRES GAMMA CAMERA BY DECAYING SOURCE WITH 9.3 MINUTE Ta-178. R. Adams*, J.L. Lacy, M.E. Ball, and L.J. Martin, Loma Linda University, Loma Linda, CA and Baylor College of Medicine, Houston, TX.

The multiwire gamma camera has unusually good performance at high count rates. This study was designed to evaluate this property by a decaying source method. Data from a Ta-178 source in the NEMA scatter phantom were acquired in 1 minute frames. A FORTRAN program corrects the net cps values for deadtime loss by a trial deadtime (τ) and converts to their natural logarithms. A 2nd order polynomial is fitted to the data: $\ln R = A + B\tau + C\tau^2$ where R is the net corrected cps, and T is the elapsed time. τ is adjusted and data corrections and curve fittings are repeated until C approaches zero, to yield the deadtime (τ), measured half life, and the input versus observed count rate curve. The paralyzing deadtime measured 0.41 μ sec, and the half life, 9.19 minutes, only 1.4% low. The validity is also supported by close agreement between fitted and corrected cps values. The camera can be operated up to 840,000 cps with Ta-178 in first-pass studies without exceeding 50% data loss, 2-3 times greater cps than any other commercial NaI device.

MP4.3

The Use of a Restoration Filter to Improve the Quantification of I-131 Scintigraphs, M.T. Madsen, Thomas Jefferson University, Philadelphia PA.

The quantification of activity from scintigraphs of I-131 labeled pharmaceuticals presents special problems because of scatter and the large amount of septal penetration associated with the collimators routinely used for this radioisotope. Because of this, the counts associated with I-131 sources are very dependent on both the location and size of the selected regions (ROIs) drawn about the source images. The efficacy of a restoration filter applied to the I-131 images to circumvent this problem was evaluated for a variety of source distributions. The restoration filter was derived from an image of an I-131 point source located on 10 cm of polystyrene. Test images with both point and disk sources of I-131 were acquired with 0, 5, 10 and 15 cm of polystyrene. The counts in two different sized concentric ROIs about the I-131 source images were compared for both the raw and restored images. The counts in the concentric ROIs varied in the raw images by 20-40% while those in the restored images varied by less than 5%. These results suggest that the application of a restoration filter to I-131 images will significantly improve the estimates of activity.

MP4.2

Scatter from Distributed Sources Within a Uniform Scattering Media. MS Rosenthal*, and LA Henry, University of Pittsburgh, Pittsburgh, PA, 15261, USA

Scattering is a major source of quantitation loss in nuclear medicine. It is also difficult to correct for. We have investigated scattering in uniform media with either distributed or multiple point sources. We performed Monte Carlo simulations of this scattering problem using a 22 cm diameter cylindrical acrylic shell phantom filled with water. The code modeled the transport of photons into a large field of view gamma camera (Tc-99m, 3/8" NaI crystal, LEAP collimator). Tested were various sizes of ring sources, as well as multiple point sources plus a combination of the two. In addition, experimental measurements were made of the same configurations as calculated by the transport code. We took into account Compton scatter, coherent scatter, diffraction, photoelectric effect, and production of lead x-rays. Statistics generated were 500 to 1000K events detected by the camera, both my calculation and experiment.

Results of this modeling demonstrate that the Monte Carlo simulations reproduce the experimental data relatively well. For the most part, the simulations agree within statistics with the experiment.

MP4.4

NUCLEAR DECAY BY INNER ATOMIC SHELL IONIZATION: BIOLOGICAL EFFECTS IN VIVO, D.V. Rao, R.W. Howell, University of Medicine & Dentistry of New Jersey, Newark, NJ; and K.S.R. Sastry, University of Massachusetts, Amherst, MA.

Most of the radionuclides used in Nuclear Medicine decay by inner atomic shell ionization processes (electron capture and/or internal conversion). The numerous low energy Auger electrons that follow the decay event result in a highly localized deposition of energy. When these Auger emitters are incorporated into mammalian cells, the biological effects may be severely underestimated by currently adopted dosimetric methods, which consider the low energy electrons as trivial.

Our experiments over the past several years have repeatedly shown that Auger cascades do cause severe biological damage in vivo. The targets in these studies are the highly radiosensitive spermatogonia in mouse testis and the primary oocytes in the mouse ovary. The biological end points are survival of spermatogonia (primary oocytes) and induction of abnormal sperm-head shapes. Our conclusions are: (1) Auger-emitters (Tl-201, In-111, Fe-55, etc.) are much more effective than their beta-emitting analogs, when injected in the same chemical form. (2) The same Auger-emitter In-111 as oxine is far more effective than as a citrate because very different subcellular distributions in the two chemical forms. Hence, subcellular distribution depending on the chemical forms of the Auger emitter is an important determinant of the effects. (3) conventional dosimetry is inadequate, and cellular dosimetry is essential to predict the effects of internal Auger emitters.

Work is supported by USPHS Grant No. CA-32877.

MP4.5

Eigenimage Filtering of Nuclear Image Sequences of the Liver. W.J. Potvin*, A.B. Abche, J.B. Farison, L.R. Low, J.P. Windham, Medical College of Ohio, Department of Radiology, Toledo, Ohio 43699 USA.

The effectiveness of the eigenimage filtering technique as applied to human liver dynamic nuclear studies has been investigated. Processing was performed on sequential digital images obtained during first transit of technetium-99m labeled sulfur colloid. Temporal signature vectors were obtained from regions of interest established on the aorta, vena cava and parenchymal liver tissue. These vectors were used to generate signature matrices corresponding to image features designated as desired or interfering. For each choice of a desired or interfering process, an associated weighting vector is used to produce a composite eigenimage in which a feature of interest is enhanced while suppressing undesired processes.

The results of this processing provide images in which features demonstrating arterial blood flow can be clearly separated from structures associated with the venous system. Applications to the liver's arterial and portal blood supplies and vascular and avascular pathological structures are presented.

MP4.7

ON THE CODED APERTURE IMAGERS WITH PASSIVE AND ACTIVE ELEMENTS, K V Ettinger, II University of Rome and J Brondo*, Scientific Innovations Inc., Wainscott NY, USA

Coded aperture systems of imaging are capable of imaging gamma rays with energies which are unsuitable for conventional multi-hole collimators. An efficient system of coded aperture imaging, using uniformly redundant arrays is described as a basic building block for assembling a scanner, a gamma camera or a tomographic imager. The principle of redundant arrays is to ensure that the obscuration of detectors from radiation sources being mapped, is such that the signals can be uniquely unscrambled. Modulation is performed by switching between two masks, one being a complement of another. The system can be implemented either with scintillation detectors (BGO or NaI) or with germanium solid state detectors. Discussion includes comparisons between circular and rectangular masks as well as incorporation of coincidence technique into the coded aperture design. It is worthwhile to note that coded aperture systems can be used to image fast neutron distribution, albeit with different detectors than for gamma rays.

MP4.6

Sensitivity and Applicability of Quality Control Indices for Gamma Cameras, A. Hughes* and P. F. Sharp, University of Aberdeen, Aberdeen, Scotland, AB9 2ZD.

Much of the work carried out on quality control of gamma cameras has concentrated on defining ways in which measurements can be made. Very little work has been done into the practical value of these indices particularly into two major problems; firstly, how sensitive the indices are both to changes in device performance and the conditions under which they are measured and, secondly, how different indices interact in determining image quality.

Studies of the sensitivity of various measures of gamma camera uniformity were carried out. It was shown that sensitivity of uniformity indices to the presence of a localised area of non-uniformity increased with count density, being most sensitive for images containing 10 000 counts/pixel. Images acquired according to the NEMA Specifications were less sensitive to changes in detector response. The uniformity indices which were the most sensitive were those calculated using all the pixels in the image contrary to the NEMA recommendations. The interaction between the spatial resolution and sensitivity of a collimator has been recognised as a problem for many years. Our work demonstrates how the perceived sharpness of an image depends upon image count density. The effectiveness of various figures of merit in combining the effects of both resolution and sensitivity will be discussed.

MP4.8

Pediatric Total Body Potassium Counter Kenneth J. Ellis*, USDA/ARS Children's Nutrition Research Center, Department of Pediatrics, Baylor College of Medicine, Houston, Texas 77030.

The direct *in vivo* measurement of total body potassium (TBK) can provide information concerning the body's lean tissue mass. Although many nutritional studies have been performed in children, few have measured lean tissue mass directly. The non-invasive nature of the TBK measurement makes it ideal for pediatric use.

Longitudinal studies in infants, however, are difficult because of changes in the counting geometry caused by the rapid growth of the infant. To overcome this restriction, we have designed a whole-body counter that is invariant to body size from the premature infant (36 cm, <2 kg) to the 3-yr-old toddler (100 cm, <17 kg). The counting system consists of eight NaI(Tl) detectors (7.6 cm x 7.6 cm x 100 cm) positioned lengthwise along the child. The cross-sectional geometry of the counter can be varied to match that of the child. The signals from the two photomultiplier tubes at each end of the 100-cm length are operated in multi-parameter mode. Custom software has been written for an ND9900 series analyzer that combines the two signals to give energy and spatial information per measurement. The average resolutions are $\pm 8.5\%$ full width half maximum at 662 keV for energy and ± 2.5 cm for position. For a 1000-sec counting time, the average error is less than $\pm 4\%$ for TBK measurements in infants.

MP4.9

Development of a Knowledge Based System for the Radionuclide Renogram, P.J.Vassilakos*, Ch.Pierrakeas, N. Pallikarakis, Dpt. of Nuclear Medicine and Dpt.of Medical Physics, University of Patras,Greece.

The Radionuclide Renogram (RR) using ^{99m}Tc-DTPA, has been established during the last decade as a basic diagnostic tool in Nephrology and Urology. Today, the efforts are oriented towards a quantitative analysis of the parameters expressed by the Renogram curve and their relation to the pathophysiology of the kidneys. Such parameters are, the time and slope to peak activity, which expresses the ability of the filtration of renal parenchyma as well as the time for half peak activity which is related to the excretory ability of the kidneys.

The analysis and processing of these parameters may lead to the development of a Knowledge Based System (KBS) for computer assisted diagnosis of renal diseases.

So far 14 such parameters have been identified as quantitative indicators for the characterization of the renogram curve using data from 240 cases from our electronic archive. According to the results obtained we can conclude that we are able to built a KBS for diagnosis of renal functional abnormalities.

MP5.2

Monte Carlo Dose Calculation in a Three-Dimensional CT Image
C. Chui* and R. Mohan
Memorial Sloan-Kettering Cancer Center
New York City, New York, U.S.A.

The Monte Carlo code EGS4 has been employed to simulate radiation transport through a three dimensional CT image to calculate dose distributions for both electrons and photons. Since dose measurements in arbitrary geometries are often difficult if not impossible, especially in regions of electronic disequilibrium, Monte Carlo simulation remains the only viable alternative to produce accurate results. In principle, all physical processes can be included in such simulations. Calculations were first performed in a water phantom and other simple heterogeneous geometries for which reliable measurements can be made to ensure the validity of this method. Calculations were then performed on Rando phantom and actual patient CT images employing arbitrarily oriented and shaped beams in 3D treatment plans. Since Monte Carlo simulations require a large amount of computing time (up to weeks on a VAX-8550), it cannot be used routinely. However, they may serve as benchmarks against which other approximate methods may be compared to estimate uncertainty distributions of those methods. We present the simulation method, results and describe some variance reduction techniques that may be used to increase the efficiency of simulations.

MP5.1

Monte Carlo calculations of tissue dose to determine stochastic and nonstochastic risks in Radiology. G. Williams*, W.J. Potvin, G. Drexler†, R.A. Brinker, Medical College of Ohio, Department of Radiology, Toledo, Ohio 43699 USA.

In certain tissues such as bone marrow and periosteum, realistic dose calculations and measurements are difficult to make. The determination of the risks of leukemia and osteosarcoma induction for children and young adults is important. Also there are many other radio-sensitive tissues in the body at risk. In diagnostic and therapeutic radiology significant doses can be deposited in such tissues. A Monte Carlo method coupled to realistic 3D CT models has been used to calculate tissue doses. The results of the method to determine doses in radiology will be given. Also the latest data from this work, published in ICRP 44 and ICRP 51, will be discussed and the work of a new ICRU Report Committee which is studying experimental and theoretical phantoms in radiology, radiotherapy and radiation safety, will be described.

†ISS, GSF, Ingolstaedter Landstrasse 1, D8042 Neuherberg, West Germany

MP5.3

Is a Strict Convolution Applicable to the Computation of Dose Distributions for Megavoltage Photon Beams? G.C. Field and J.J. Battista*, Cross Cancer Institute Edmonton, CANADA

Two kernel-based algorithms are used to produce dose distributions for Cobalt-60, and 15 MV X radiation beams incident on a water medium. We first review the convolution and superposition integrals as descendants of the general dose equation, and identify major assumptions adopted by various investigators. Dose distributions are then computed with a VAX-11/780 computer in both the real and Fourier domains and are compared with doses measured experimentally. The impact of different implementations on computational speed is measured while the effects on dose accuracy are visualized with colour maps of dose differences. We conclude with recommendations on the practical usefulness of the strict (fast) convolution and the less restrictive (slower) superposition algorithms.

MP5.4

Dose Perturbations at Interfaces in Photon Beams: the partial fluence model.

Barry L. Werner, Ph.D.* Indra J. Das, M.S.
Department of Therapeutic Radiology Box 494
University of Minnesota Hospital and Clinic
Harvard Street at East River Road Minneapolis,
MN 55455

An improved version of the partial fluence model (Med Phys 14, 585, 1987) for photon beam dose distributions at medium interfaces, is presented. The original model explains how photon beam dose distributions in soft tissue surrounded by bone depends on the beam energy, thickness of the bone, and orientation of the interfaces with respect to the beam. Although the original model predicts approximate limits between which dose perturbation can be expected to be found, these limits are not narrow enough to calculate dose perturbations for clinical treatment planning purposes. The present, improved version of the model describes how calculations of the actual dose perturbation can be made for photon beams of any energy at interfaces between materials of any composition. Dose perturbation predictions made with the improved version of model are compared with measurements made in layered phantoms consisting of polystyrene and materials of atomic number ranging from bone to lead, for photon beams ranging in energy from Co-60 to 24 MV.

MP5.6

Comparison of Algorithms for Solving Inverse Problems in Radiotherapy
Bengt K. Lind, Department of Radiation
Physics Karolinska Institute, P.O.
Box 60204 S-104 01 STOCKHOLM, SWEDEN

Radiotherapy treatment planning of today is mainly focused around what is called the forward problem in radiotherapy, i.e. calculation of the resultant dose distribution in the patient from a given treatment setup, including beam modality, energy, beam angles etc. As the goal of radiation treatment is to deliver a specific dose to a target volume, without damaging surrounding healthy tissue or organs at risk, some sort of optimization has to be done.

An alternative approach is to solve the inverse problem of radiotherapy, this has the benefit of including the optimization part in a natural way. We have developed an iterative inversion algorithm for solving the inverse problem in radiotherapy. The properties of this algorithm will be discussed, and compared with other methods.

MP5.5

Convolution Isodose Distributions of X-Ray Fields Derived from Monte Carlo Spectra. A.L. Boyer*, Y.P. Zhu, F. Pascal, L. Wang, Department of Radiation Physics, The University of Texas System Cancer Center, M.D. Anderson Hospital and Tumor Institute, Houston, Texas 77030.

Isodose distributions of unwedged and wedged x-ray fields were modeled using convolutions employing the fast Fourier transform. The distributions were calculated on a 64x16x64 array representing voxels 0.5cm x 2.0cm x 0.5cm. The convolution kernels were based on Mackie's Monte Carlo calculations. The EGS-4 Monte Carlo code was also used to simulate the production of x-rays in a Siemens linac and to transport the radiation through a complex beam modifying geometry. Wedged fields were modeled by ray-tracing through the physical wedge. 6 MV and 18 MV beam spectra were calculated as the weighted sum of 2,5 and 10 components and compared with measured distributions. Small changes in the spectra attributable to scattering from the collimators were determined by fitting to measured depth dose data. When five convolutions were used, the accuracy was on the order of 1% and the calculation time was on the order of 20 min using a VAX/750 computer. A technique was explored to reduce the number of convolutions while maintaining good accuracy.

This investigation was supported by PHS Grant CA43840 awarded by the N.C.I., DHHS.

MP5.7

Angular Distribution of Thick Target Bremsstrahlung Photons, R. Mohan*, G. Miklos, C. Chui, Memorial Sloan Kettering Cancer Center, New York, USA and A. Bielajew, National Research Council of Canada, Ottawa, Canada.

Angular distribution of bremsstrahlung photons emitted from the target of a medical linear accelerator affects the photon energy fluence and spectrum as a function of radial distance from the central ray as well as the magnitude of photon angular spread resulting from scattering from the flattening filter and the collimating system. The variation of energy fluence and spectrum with radial distance determines the magnitude of "horns". The angular spread determines the variation of output with field size and affects the sharpness of the beam boundary. Energy spectra and angular spread may be calculated by Monte Carlo simulation of treatment machine heads and the EGS Monte Carlo code has been employed widely in medical physics for this and other purposes. We have not been able to predict accurately the phenomena cited above using the default version of the EGS code. In an attempt to calculate more accurately, we have incorporated improved bremsstrahlung angular dependence in EGS and employed "parameter reduced electron-step transport algorithm" (PRESTA) of Bielajew and Rogers to calculate energy fluence and spectra and angular distribution of photons as a function radial distance from the central ray. The effect of these improvements on "horns" and output factors will be demonstrated and a comparison of results of calculations with experiments will be shown.

MP5.8

Beam Data Generator for Asymmetrically Collimated Fields, D.D. Loshek
Marshfield Clinic, Marshfield WI, USA

X-ray fields that are shifted away from the central axis by independent collimators exhibit alterations of output, beam profile and average energy. These perturbations are not well described by treatment planning systems that rely on discrete fan-line beam data. Two software modules capable of generating appropriate fan-line data for use in these systems are described. Both employ an off-axis output function and a profile generator. The profiles are generated as a product of three field-size-independent functions. These are a function describing the x-ray intensity in the absence of the collimator assembly, a function describing the scattering phenomena and a function describing the effects of the collimators. The variation in beam energy is described by an explicit correction for the variation in zero-field-size tissue-maximum-ratio as a function of off-axis distance. One module utilizes the fan-line data for a symmetric field of equal size to calculate the values of scatter-maximum-ratio while the other module uses a sector integration over the field boundaries of the scatter-maximum-ratio data. The execution time of these modules is sufficiently fast to allow in-line use in the beam definition process.

Supported in part by NCI grant 1 R01 CA40253

MP6.1

Where Does the LQ Model "Fit"?, D. Herbert,
University of South Alabama, College of Medicine,
Dept. of Radiology, 269 CSAR, Mobile, AL. 36688.

The LQ hypothesis is now regularly deployed to explain, with apodictic assurance, a wide variety of so-called stochastic radiation responses at both high and low dose. For example, mutagenesis in plants (pink mutants in *Tradescantia* 02); carcinogenesis in humans (leukemia incidence and cancer mortality at Hiroshima and Nagasaki); cell survival (bone marrow stem cell survival in the mouse and the rat); radiation "complications" of normal tissues (hind leg paresis in rats). For each of these endpoints we have compared the appropriate generalized linear model (either Poisson or Bernoulli response) of the LQ hypothesis with the cognate model of a leading rival hypothesis (eg., Target theory, NSD, etc.) on published experimental data. Our analyses include the respective regression diagnostics for both models of each set of data as well as some use of semi-Bayesian regression methods where appropriate. The paper includes discussions of - and empirical evidence for - several current heterodoxies. One conclusion is that the choices of the respective published versions of the LQ hypothesis cannot be easily defended on the basis of these data - except as, in M. V. Berry's locution, "an invocation."

MP5.9

Inclusion of Electron Multiple Scattering in Photon Dose Calculation, C.X. Yu* and J.W. Wong,
Washington University School of
Medicine, St. Louis, MO, USA.

Changes in atomic number can result in large dose changes by perturbing electron multiple scattering. To incorporate atomic number effects in inhomogeneity correction, explicit electron transport based on Ferme-Eyges theory was made for electrons generated by primary photon interactions. Monte Carlo simulations of broad photon beam incident on thin slabs of different materials were used to obtain the energy spectra of secondary electrons. The angular and spatial distributions at each energy increment were also scored to derive initial scattering parameters. Electrons were then transported layer by layer using a mini-pencil summation method. Electron losses during transport were calculated with an empirical function. Calculations are being made to predict the small inhomogeneity data. The model forms the basis of a photon dose calculation algorithm which include electron multiple scattering. (Supported by NCI grant CA-41574).

MP6.2

Hazard Analysis and Radiation Survey of UV Lamps in Operating Rooms, Suresh M. Brahmavar, Cathy Miller*, Helen Bollea and Marilyn Riddle. Baystate Medical Center, Inc., Springfield, MA 01199

The adverse effects of exposure to germicidal UV lamps (254 nm) used in destruction of bacteria in air are erythema, eye burn, skin irritation, excessive dryness and incidents of conjunctivitis. The beneficial or adverse effects depend on the product (uwsec/cm²) of time and intensity of UV exposure in operating rooms. A hazard analysis of UV lamps was undertaken to establish reasonable output levels at various locations in operating room. The intensity measurements were made at seventeen (17) different locations in two ORs for a set of seven (7) UV ceiling lamps per room. The intensity controls for inner and outer group of UV lamps were set independently to read 20 uw/cm² directly below each lamp at 6' from the floor. This results in output of 30 uw/cm² at 3' from lamp surface. The locations included are: 6 spots at a height of 6' near OR table and 4 spots on the OR table at a height of 3'. The questionable effectiveness of UV lights in OR is further complicated by the need to observe short time of exposure to avoid erythema or eye burns. Therefore, a RS/QC program for UV lamps has been established to overcome observed adverse health effects among OR staff.

MP6.3

Some Aspects of Radiation Environment for Space Radiobiology: A Selected Review, Dr. R. Datta and Dr. S. Datta*, Department of Radiology, LSUMC-S, Shreveport, Louisiana, USA.

Space radiobiology has just born as a consequence of manned missions in space. Previous missions in space involved short trips in the relatively less hazardous radiation environment of equatorial low-earth orbits. Future planned missions, however, are expected to involve increasing human activities in space, flights to Mars, extended excursions to geosynchronous and polar orbits for extended periods.

The earth's magnetic field is populated with trapped electrons, protons, and low energy heavy ions. The radiation environment in free space, however, are the geomagnetically trapped, galactic cosmic, and solar flare-associated particulate radiations. Radiobiological factors in a rather complex radiation exposure to humans in space exploration may have synergistic effect. Virtually nothing is known as to their effects on biological systems, especially at low doses for long term exposure and under microgravity conditions. Scenarios as to radiati induced-effects need to be quantified. Relevant topics such as spaceflight dosimetry, biological effects of the so-called HZE particles, interactions of dynamic spaceflight factors and radiation, and finally the necessary trade-offs of system performance to address sytems safety concerns as to radiation effects on both electronic components and population at risk are highlighted.

MP6.4

Hazards to the Earth's Ozone Environment over India B.L. Acharya*, A.A. Chougule and G.R. Agarwal, R.N.T. Medical College, Udaipur, INDIA

It is increasing concern of artificial production of nitric oxide and fluroromethanes, nitrogenous fertilizers and nuclear explosions reduce the ozone through reactions which are now fairly well understood and for which reaction rates are now available. In the present investigation suitable model for ozone and recent available reaction rates constant have been used to find out the concentration of ozone. The ozone data obtained from baloon sonde recently for various Indian stations like Trivandrum, Poona, Delhi, Ahmedabad, Mount Abu have been compared with that obtained from model calculation. It is found that the ozone layer concentration is reduced day by day and the flux of ultraviolet radiation reaching the earth have been increased. This can result in a variety of environmental consequences including possible increase in skin cancer, stoppage of tissue growth, albumin, coagulation, change in global temperature, rain fall conditions and introduction of ecological disturbances. Biological, climatic and ecological effect of ozone depletion have been discussed in detail.

MP6.5

In vitro measurements of 5-iminodaunomycin laser induced toxicity, A. Andreoni, A. Colasanti, U. Giani, A. Kisslinger, A. Mancini, M. Mastrocinque, G. Roberti, P. Russo*, University of Naples, I-80125 Naples, Italy.

In order to evaluate the effectiveness of antracyclines in tumoral phototherapy, we investigated the effects of laser light on cellular cultures of human liposarcoma incubated in a medium containing 5-iminodaunomycin. Cells were irradiated, with different light doses, at the absorbance peak of the drug (590 nm), with a cw dye laser pumped by an Argon laser. Cell viability was evaluated by measuring their uptake of [H3] thymidine. Our results show that the treatment with drug (at a given concentration) and laser light affects the cell mortality more than drug alone (at the same concentration). The results are discussed taking into account some possible interaction mechanisms between 5-iminodaunomycin and DNA

MP6.6

ROLE OF LASERS AND DIHEMATO PORPHYRINE ETHER (PHOTOFRIN-II) IN DAMAGING THE MEMBRANES OF HUMAN ERYTHROCYTES. S. Ganesan*, S.R. Manoharan, V. Masilamani and G.N.S. Prasad, Dept. of Physics, Anna University, Madras-25, INDIA.

Photoradiation therapy for local treatment of tumours utilizing hematoporphyrin derivative as photosensitizing drug is undergoing clinical trials in several countries. But the action mechanism in the killing of cells is still unclear. The present study was under taken to explore the possible role in memkrane damage of human erythrocytes due to lasers at different wavelengths and the photosensitizer, Photofrin-II. It was found that, i) the percent hemolysis increases in increasing the concentration of the drug, ii) increases with pre-incubation time, indicating the uptake of drugs by the cells, iii) depends on the post incubation time indicating the photochemical nature of the damage and complete hemolysis was found within 24 hours after irradiation and iv) the percent hemolysis purely depends on the wavelengths of laser used, indicates that, the nature of the effect was purely chemical one and not thermal one.

MP6.7

Ultrasound Irradiation of Chicken Embryos - Technique. MS Rosenthal*, JW Yip, YPL Yip, and C Capriotti, University of Pittsburgh, Pittsburgh, PA, 15261, USA

Documentation of bio-effects from non-ionizing radiation requires precise knowledge of the exposure to the animal system and as natural environment as possible. We report here an exposure system that allows good quantitation of the embryos' exposure to ultrasound irradiation.

The embryos are prepared by making two openings in the egg shell, one at the air sac, the other at the opposite end. Over the second hole a gas permeable, ultrasound transparent membrane is applied. For irradiation, the egg is placed vertically with the air sac towards the bottom in a large water bath maintained at 37°C. The embryo is positioned in the middle of the second hole. The ultrasound energy is transported from the transducer to the egg using an acoustic coupler. Below the egg is a microprobe whose output is fed into an A/D converter on board a PC/AT computer providing online monitoring of the exposure.

Results indicate that the SWR is approximately 1.1 with this configuration, and that there is 80% transmission through the egg.

MP6.9

BACTERICIDAL EFFECTS OF LASERS AND ACRIDINE ORANGE ON E-COLI: IN VITRO STUDIES, S.Ganesan*, V.Jayapal+, V.Masilamani, G.N.S.Prasad, S.P.Thiagarajan+, and D.Subramniam+, Dept. of Physics, Anna University, Madras-25 +Dept. of Medical Microbiology, Institute of Basic Medical Science, Univ. of Madras, Taramani, Madras-113, INDIA.

Laser play a vital role in orthopedics as an adjunct treatment for chronic osteomyelitis. The paper presents the study of bactericidal effect of lasers in the presence of a sensitizer Acridine Orange on E-Coli, the organism encountered in chronic osteomyelitis. The results shows that Nitrogen laser has better effect than other laser has better effect than other lasers and the killing effect enhanced in the presence of Acridine Orange. So the Bactericidal effect was essentially photochemical in nature and not a thermal one.

MP6.8

BI-PYRAMIDAL MULTIMODE RESONATORS FOR IN-VIVO ELECTROMAGNETIC SPECTROSCOPY, J Brondo, Scientific Innovations Inc., Wainscott NY, USA.

A large bi-pyramidal cavity resonator is described, intended for the measurement of thermal noise emission in a broad range of microwave frequencies from a human or animal subject placed inside the cavity. This is a more sensitive arrangement than an anechoic chamber with an antenna array and it is a matter of interest to establish not only the shape of thermal noise emission spectra but also to register any non-thermal components of emission, which have been postulated by others. The relationships between the dimensions of the source, the cavity and the wavelengths in question are such that the cavity operates as a multi-mode resonator. The bi-pyramid shape permits an introduction of pick-up couplers into the side walls with a smaller amount of perturbation than in other designs. The system can be calibrated with a white noise generator and the cavity can be also used to measure absorption by the body in the microwave region. The absorption measurements require a broadband noise generator and a spectrum analyzer. In the absence of the body, a swept frequency source is needed to measure the intrinsic response of the cavity.

MP6.10

Study of the Metabolism of Nuclear Fallout Products by means of Stable Isotopes as Tracers.

M.C.Cantonex^o, C.Cavicchioli^o, G.Gambarini^o, N.Molho^o, L.Pirola^o, Ch.Hansen*, E.Werner*
^x Dipartimento di Fisica dell'Università, Milano, Italy
^o I.N.F.N. Sezione di Milano, Milano, Italy
⁺ Istituto di Fisica del Politecnico, Milano, Italy
^{*} Ges. für Strahlen-und Umweltforschung, Frankfurt/Main, FRG

The evaluation of the dose due to the intake of radioisotopes from fallout is based on specific metabolic models. These models in some cases are quite detailed and may be supported by much experimental evidence from observation on humans. In other cases, data may be limited to a few observations on a particular group of population or on species of experimental animals.

We believe of particular significance to study the human metabolism of elements, like for instance Mo, whose radioactive isotopes are included in nuclear fallout. Considering that radioactive and stable isotopes follow the same metabolism, stable isotopes are used as tracers to prevent radiation damage. Proton Nuclear Activation technique, which allowed us to study iron metabolism by means of stable isotopes, was applied to the study of Mo metabolism. The optimization of the relevant parameters was previously tested in order to evaluate the sensitivity limits for an instrumental analysis.

MP6.11

Study of the Tannin Influence on Iron Metabolism studied by means of Stable Isotopes as Tracers.

M.C. Cantone^{xo}, G. Gambarini^o, N. Molho^{xo},
L. Pirola^{xo}, P. Sala^{xo}, Ch. Hansen^{*}, E. Werner^{*}
x Dipartimento di Fisica dell'Università,
Milano, Italy
o I.N.F.N. Sezione di Milano, Milano, Italy
+ Istituto di Fisica del Politecnico,
Milano, Italy
* Ges. für Strahlen- und Umweltforschung,
Frankfurt/Main, FRG

The possibility of studying in humans the correlation between intestinal iron absorption and the assumption of particular substances included in alimentary diet, is related to the method used for investigating the intestinal absorption itself.

By considering that it is not free of danger to carry out such a study on humans by means of radioactive tracers, we believe that a method using stable isotopes as tracers finds a good field of application.

We developed a method for the study of iron metabolism by means of stable isotopes measured by proton nuclear activation. This method was first tested on rabbits and then on humans. The present study is aimed to verify the hypothesis that tannin influences the iron intestinal absorption.

For this purpose healthy people is investigated before and after assumption of a tannin rich food.

MP6.12

PHOTON ACTIVATION ANALYSIS IN-VIVO FOR MAJOR BODY ELEMENTS, K V Ettinger, II University of Rome, Italy and U J Miola* Royal Armed Forces Hospital, Riyadh, Saudi Arabia .

Photon activation analysis has got a number of advantages in comparison with the technique of neutron activation analysis in present use. The uniformity of detection is very good and the effect of the body shape can be easily accounted for or even ignored. It is possible to measure oxygen, carbon and nitrogen using bremsstrahlung of sufficiently high energy, in order to form positron emitters which could be distinguished from each other by the differences in their half lives. One of the most common measurements in-vivo is the determination of nitrogen, which is most easily measured by photonuclear method, having the lowest formation threshold (10.6 MeV). Potentially most accurate are measurements which utilize as a source of photon fluence, X-rays produced in reverse Compton scattering of laser light from electron beams, a facility which is now becoming available in most of the synchrotron light sources. Two examples are given of the installations for photonuclear activation analysis in-vivo. The radiation dose imparted to the patient, in order to attain a result with accuracy and precision adequate for clinical use, is about 1 - 2 cGy.

MP6.13

Influence of Rotating Magnetic Field on the Activity of Alkaline Phosphatase in Inflammatory Exudate, Hu Jixiang*, Wang Mibin, Chen Dezhong, Yang Zhengong, Hunan Medical University, Changsha, Hunan, The People's Republic of China

The purpose of this experiment investigation was trying to search the mechanism of antiedema effect of rotating magnetic field (antiedema was one of the effects of magnetic field). The rat paw was immersed into hot water of 60°C for 10 seconds to induce local edema, one of the rat paw exposed to rotating magnetic field of 1000 Oe. for six hours. At this time an exudate sample of 2-4 microlitre was taken by microlitre injector. The rapid method for determining alkaline phosphatase activity in serum with thymolphthalein monophosphate as a new substrate was used.

The activity of alkaline phosphatase of the exposure group and the control was employed for statistical estimation. Significant difference (n=33, P 0.01) between two groups was noted. It indicated that the activity of alkaline phosphatase in exudate of the treated group was higher than that of the control.

MP6.14

IMPROVED DIAGNOSTIC PERFORMANCE ON THE SEVERITY OF LEFT VENTRICULAR HYPERTROPHY USING BODY SURFACE MAPPING. M. Yamaki, K. Ikeda, I Kubota, K Nakamura, K Hanashima, and S Yasui. Yamagata University School of Medicine, Yamagata, Japan

To improve the ECG diagnosis on the severity of left ventricular hypertrophy (LVH), 87 unipolar ECGs were recorded from 87 pts with LVH (34 hypertension, 23 HCM, 30 AR). The ECG changes were evaluated by two following points: 1) increasing in QRS voltage, 2) delaying local activation. We measured for each lead, a) R voltage, b) AQRS (the net area of QRS), c) VAT (ventricular activation time), and d) DI of AQRS and VAT, where $DI = (X - \text{mean}) / SD$. From those measurements, we calculated 7 ECG parameters for each patient: 1) R max, 2) AQRS max, 3) AQRS-max DI, 4) AQRS +2SD area (area size where $DI > 2$), 5) VAT max, 6) VAT-max DI, and 7) VAT +2SD area. Among these, we selected the most effective parameters for the LVH diagnosis employing a stepwise multiple regression analysis. In the hypertension and HCM group, the combination of VAT +2SD area and R max was the best for estimating the wall thickness (multiple R = 0.73). In the AR group, the AQRS max was the best for estimating LV internal dimension (r = 0.73). Developed regression equation correctly diagnosed 87% of subjects on the presence of the LVH. These were superior to the 12-lead ECG. We can improve the ECG diagnosis for LVH by ECG mapping.

MP6.15

A Simulation Study of 3D Vascular Bed Reconstruction. J. Wu* and D. L. Parker, LDS Hospital/University Utah, SLC, Utah 84143.

This paper presents a simulation study of the effects of various imaging parameters and physical image degradation sources on the accuracy and precision of 3D artery reconstruction. 3D coordinates of the vessel centerline are determined from the centerline coordinates in two views. Orientation corrected densitometric information is averaged over the entire, visible, arterial bed, to determine a densitometric conversion factor for each image. Absolute lumen cross sectional area is determined densitometrically for all vessel positions.

For the simulation study, a 3D representation of a human left coronary artery is used to generate two projection images at arbitrary orientations. The effects of beam hardening, x-ray scatter and system blurring are incorporated in the forward projection, to match the imaging physics. The resulting 3D representation is compared with the original "true" representation. In the absence of beam hardening and when the vessel is clearly seen in both views, an average error of 0.08 +/- 0.13 mm in vessel radius is obtained. While the system is moderately insensitive to scatter, beam hardening causes a large and small x-ray paths through iodine to be under- and over- estimated, respectively.

MP6.17

Microcomputer-based Nuclear Probe: an experience in Cardiac Surgery, R.M.V. Piva*, J.M.S.Pascual, J.O.C.Auler Jr., J.C.Menegueti, C.P.Melo and C.C.Robillotta, Heart Institute and Physics Institute of University of São Paulo, C.P. 8091, São Paulo - BRAZIL.

The interfacing of a scintillation detector (a 2" x 2" NaCl(Tl) crystal) with an appropriate collimator to a microcomputer can provide a simple method for beat-to-beat ventricular function evaluation. The technique, which includes an injection of Tc-99m labelling red blood cells, was previously validated with cardiac gated blood pool imaging using a conventional gamma camera system.

At the Heart Institute, the potential of this device as a bedside monitoring system has been tested in patients submitted to various cardiac surgical procedures. Ejection fraction, heart rate, systolic and diastolic intervals were measured at pre-operative period as basal parameters to be compared with the ones obtained at post-operative period mainly in high risk patients. It was noted a good correlation with clinical evolution.

The method is presented as a low cost and non-invasive alternative for continuous monitoring of cardiac function in patients submitted to cardiac surgery.

MP6.16

Study of Biomechanical Mechanism for Occupational Exposures to Vibration, J. Xie*, S. Ma, M. Xiong, and X.Liu, Hunan Medical University Changsha, Hunan, P. R. China

This paper describes the study of mechanism on secondary Raynaud's phenomenon according to biomechanical principles and methods. We finished the researches of 8 mine areas and 1067 pneumatic drillers. We made some animal experiments as well. The results follows: a). Irradiating with vibration can make micrangiums resistance to increase up to 4.5 times. b). Irradiating with vibration can cause blood vessel collapse. The collapse grade is determined by the vibrational acceleration and the stress due to the power of gripping. Usually, the effect of stress is bigger than acceleration's. c). As far as vibrational harm is concerned, in the part of high frequency, Raynaud's phenomenon is the main damage. In the part of low frequency, the whole body vibrational damage is main.

MP6.18

ATPase Enzyme Structure Extraction From Its Blurred Image, Liuda Chu, Institute Of Electronics, Academia Sinica, China

The structure of ATPase enzyme has been studied by using different methods including protein sequencing which has produced its general structure. The shape and density taken under microscope show high background noise and low resolution. Image processing algorithms have been developed and implemented for reducing noise, enhancing and detecting edges to extract contours. Gauss-Laplacian filter, histogram equalization, linear transform and non-linear statistical transform have been used. In addition geometrical transform has been combined with a digitizer to achieve rearrangement of those enzymes for comparison. It is proved practical and useful.

MP6.19

Predicting decay in radical concentration in an amino acid following heavy ion exposures. J.W. Hansen and K.J. Olsen, Risø National Laboratory, DK-4000 Roskilde, Denmark. Herlev Hospital, 2730-Herlev, Denmark.

The decay rate of the $\text{CH}_3\dot{\text{C}}\text{OOH}$ radical in the amino acid L- α -alanine depends on the deposited energy and is less than 1% per year after exposure with ^{60}Co γ -rays to doses an order of magnitude below the dose for maximum obtainable radical production, saturation dose. A decay of 13% in 2000 hours has been measured after exposures to saturation doses with fast electrons of high dose rate. Increasing decay rates of radical concentration have been measured at low average doses, single tracks, from heavy charged particles. Exposure with penetrating 16 MeV protons results in a small but significant decay, while an appreciably larger decay has been measured for stopping particles of higher average LET in the sample. We have compared measured radical decay after exposures to low average doses from heavy charged particles with an expected decay obtained from calculations on track energy density distributions and measured decay after fast electron exposures to saturation doses. We see a good agreement between experimental data and results obtained from this model.

MP6.21

T₃, T₄ & TSH levels estimation for testing the thyroid function in Adivasiarea, G.R. Agarwal, B.L. Acharya* and M. Tyagi, R.N.T. Medical College, Udaipur-313001(India)

The thyroid hormones estimation is an important investigation in assessing the different thyroid diseases. The total 1050 Cases have been considered in the present investigation. In the heart disease Cases (35) serum T₃ is found to be low. The stress generally causes a fall in serum T₃ levels in heart disease patients. In diabetes patients (.47) T₃ is found to be low in most of cases where as T₄ and TSH levels are normal in diabetes cases as well as in heart disease cases. The hormones levels estimation in malignant head and neck cases (45) show after external irradiation induces cuthyroid sick. The female cases in the age group of 16-30 years are maximum. The laboratory normal range has been given using control charts for T₃, T₄ & TSH. The results have been discussed.

MP6.20

CARDIAC OUTPUT MEASUREMENT USING DOPPLER TECHNIQUE. S. Sakthivel, S. Suresh, I. Suresh, and G. Prasad*, Dept. of Physics, Anna University, Madras-25, INDIA

Cardiac output is the most important descriptor of ventricular function in clinical use today. Doppler principle allows accurate assessment of cardiac output noninvasively. To determine cardiac output we need the heart rate and the stroke volume. The stroke volume can be calculated from the flow velocity integrated and cross sectional area. The cardiac output was calculated from the Doppler in formation measured from the apical window. The cardiac output can be measured either at mitral valve or at aortic root at pulmonary valve. In this study, the cardiac output was measured from LVOT close to aortic root. In case of pulmonary flow, it is very difficult to get the proper window. The cardiac output is seen to increase with advancing age from this study (childhood to adulthood). It reaches a plateau which adult stages and it was also found that the stroke volume and heart rate are inter-related. If the stroke volume is high, the heart rate is less and vice versa. The compensates the final output.

MP6.22

A Preliminary Experimental Study on Reflection, Transmission and Absorption of Light By Human Skin, Tang Jianming*, Fu Changyu, Third Military Medical College, Chongqing, P.R.China

It was found in this study that light irradiated on the human body is reflected not only by the superficial skin but also by the tissue layers underneath the skin. The absorption peaks of the reflectance curves for the light with the wavelength between 400-800 nm by the human body are similar to those of the transmittance curves by the human blood; and in the same range of light wavelength, the reflectance and transmittance curves of the skin or skin plus hypodermic tissues possess the similar tendency of alterations. Thus this study provides certain useful parameters for the treatment and protection against light and laser.

MP6.23

EPR and Dielectric Relaxation applied to in vitro Myogenesis: Effects of Ions, M.T. Santini*, Lab. di Fisica, ISS, Rome, Italy, A. Bonincontro, C. Cametti, Dip. di Fisica, U. di Roma, Rome, Italy, R.E. Hausman, Biology Dept., Boston U., Boston, MA and P.L. Indovina, Dip. di Fisica, U. di Napoli, Naples, Italy

Electron Paramagnetic Resonance (EPR) and dielectric relaxation (in the radiofrequency range) allow information of membrane order and the conductivity and permittivity of membranes to be obtained. We applied these two techniques to the study of membrane changes occurring during myogenic differentiation. With EPR, we have shown that membrane order varies during myogenesis and that this variation is altered by the addition of monovalent ions (Li^+ , Cs^+). An analysis using a "single-shell" model of the conductivity dispersion due to interfacial polarization (Maxwell-Wagner Effect) seen in myoblasts during development demonstrated that conductivity and permittivity of the membrane goes down abruptly during the period of known fusion. Moreover, the addition of the above-mentioned ions shifted the abrupt drop in conductivity and permittivity to later culture times, indicating that fusion had also been delayed. A possible model for the effects caused by these ions on myogenesis is suggested.

MP6.25

The Short-Range Acoustical Field Calculation and Resolution Estimate of Linear Array in Medical Ultrasonic Tomograph
R.C.Chen* and Y.Z.Jing
Shanghai Jiao Tong University, Shanghai, China

The calculation of the acoustical field radiated by a definite aperture is based on Huygens-Fresnel principle. The mathematical operation may be simplified, if Fresnel or Fraunhofer approximation is adopted. But the condition for approximation are usually unsatisfied for the most of detected regions in medical ultrasonic apparatus. In this article, the calculation is mainly accomplished by means of angular spectrum method which is suitable for all regions in acoustical field. With the application of FFT algorithm in this method, the time of the numerical calculation may be saved. In this paper, the choice of interval and amount of sampling points is discussed with an example of linear array. The result of calculation provides a basis for researching lateral resolution of linear array and for dynamic focussing segment by segment.

MP6.24

Soft X-ray Contact Micrographs of Various Biological Cells: A Test of Resolution, G. D. Guttmann* and M. R. Howells, Center for X-ray Optics, and E. L. Alpen, Life Sciences, Lawrence Berkeley Laboratory, Berkeley, CA 94720, U. S. A.

Numerous biological samples have been examined by soft x-ray contact microscopy at LBL. An effort has been made to establish a protocol for preparing biological samples for examination in the soft x-ray contact microscopy station at LBL. Development and electron microscopy examination of the exposed x-ray sensitive resists have also followed an established procedure. The images presented will test the resolution of soft x-ray contact microscopy as applied to biological samples. Typical samples being examined are premature condensed chromatin, 9L gliosarcoma cells, and vesicles made from the "brush border" of the LLC-PK (pig kidney tubule) cells. This research is supported by the U. S. Department of Energy under Contract No. DE-AC03-76-SF00098.

MP6.26

INTELLIGENCE, COGNITION AND FUZZY LOGIC
Madan M. Gupta*, Intelligent Systems Research Laboratory, College of Engineering, University of Saskatchewan, Saskatoon, S7N 0W0, Canada.

This paper is concerned with the modeling aspects of the process of human mentation and cognition using fuzzy logic for the emulation of intelligence and other associated attributes on a machine. The human mentation acts upon cognitive information. The natural sensors, eyes, ears, nose etc. acquire the fresh information from our environment on a continuous basis. This information is relayed to the cognitive processor, the brain, through sensory neurons. The cognitive processor recalls the previously stored information in the memory, (experience, knowledge-base) and converts the freshly acquired information into relative grades. Then the process of mentation does an appropriate processing yielding the phenomenon known as 'perception'. This process of mentation thus deals with the graded-uncertainty and its cognate graded-information. We call such an information as the cognitive information and model it using the notion of graded membership embedded in fuzzy logic. This notion of graded membership leads towards the natural mentation, cognition and perception phenomena. Presently our studies are directed towards the emulation of natural vision-perception phenomenon and cognitive process.

MP6.27

Meeting the Demand of Medical Physicists for the year 2000, U. Madhvanath, DRP, Bhabha Atomic Research Centre, Bombay-400 085, India.

Human resources development is required to be consciously planned if we are to effectively man the diagnostic and therapeutic facilities of populations in the emerging countries-all looking into the year 2000. The unique experiment carried out by the Bhabha Atomic Research Centre in a period of 25 years stands testimony to this development programme. Sensing the advent of cobalt-60 teletherapy machines to India in mid-fifties, six physicists of this centre were deputed to Toronto, London, Stockholm and other places of radiotherapy centres and following their return, a one year training course on Hospital Physics and Radiological Physics was started in 1961 to train 15-20 physics graduates drawn from all over the country each year and provide them to hospitals, industries and research institutions handling radiation sources. Country's demand is abundantly met. They man today 150 teletherapy facilities, 90 each of brachytherapy and nuclear medicine centres. The success of this programme rested in the generous financial support by the Government of meeting the living expenses of the candidates as it was realized that a new discipline and profession is not viable at the universities. Problems of developing countries, when advanced technologies of the West were borrowed, can only be overcome by organised training programmes of this type.

MP7.2

THE CHINESE HUMANOID PHANTOM AND ITS APPLICATIONS IN MONITORING FOR RADIATION DOSAGE IN CHINA. Lin Da-quan* and W. Da-ke, Chengdu University of Science and Technology, Sichuan, P.R.C.

The humanoid phantom has been widely used in medical radiation fields. For the first time in China since 1984, we have developed a new humanoid phantom which has successfully applied in monitoring for radiation dosages. This phantom, which is 165 cm in height and 57.5 kg in weight, is based on the average adult man of china. The thermoplastic coupled materials, which radiation equivalence is assured among 12-1250 KeV and its deviation is within $\pm 5\%$, are adopted as the tissue substitute for all parts of the phantom except the lungs. Our phantom consists of 11 parts and 20 cross sections and each section has 3x3cm rectangular hole grid and organ hole, and the TLD holes (3x20mm) are over 500. Assemble devices have been developed which provide a new ease of use in patient-like positioning. Internal nylon rods pass through holes in each section.

The type of phantom has been produced 10 sets since 1984 in China and they are the important experimental tool in radiation protection, medical diagnosis, radiotherapy, medical education and the radiation research field, etc.

MP7.1

THE RADIOLOGICAL ACCIDENT IN GOIÂNIA: AN OVERVIEW
C. E. de Alaeida*, J. J. Pozenthal and R. N. Alves
Comissão Nacional de Energia Nuclear - BRAZIL

A radiation accident involving a radiotherapy Cs-137 source, with an activity of 1375 Ci, has occurred last september in Goiânia (1.100.000 inh.). A radiotherapy source head in disuse, was removed by a group of people involved with the junkyard business. Later on, it was broker, releasing its radioactive content to the environment in the chemical form of Cesium chloride. Due to the high solubility of this compound the dispersion into the environment was favoured by the winds and rainfalls. However, the major contamination vector was indeed the people directly involved, since they have transferred parts of the source with the lead shielding to three junkyards in the city and distributed small parts of the source to members of their families. "The blue glow emitted by the compound, led them to believe that they could be facing a precious stone". As result of this, seven major radiation spots was found in the city within the same neighborhood, with radiation levels up to 110R/h at one meter, immediately evacuated and isolated. External and internal contamination was found in 244 people out of 118 220 monitored; 129 people required medical care, including some with severe internal contamination and external radiation injuries. Four people died of acute radiation effects and one had his right forearm amputated. This paper will present an overview of the accident, the scenario, the emergency procedures, the dosimetry and its environmental impact.

MP7.3

A Survey of Radiation Exposure in Diagnostic Radiology in Latin America, G.P. Hanson, World Health Organization, 1211 Geneva 27 Switzerland and G. Gómez Crespo, PAHO/WHO Consultant.

In 1984 the Pan American Health Organization arranged visits by the authors to Argentina, Brazil, Colombia, Costa Rica, Ecuador, Mexico, Netherlands Antilles and Nicaragua in order to collect information concerning the availability and utilization of radiodiagnostic services in Latin America and the Caribbean. That study included a survey of the radiation exposure received by patients during the most frequently requested x-ray examinations.

To our knowledge this survey is unique because a standard methodology was used and all the measurements were made with instruments provided and/or calibrated by a single reference dosimetry laboratory whose secondary standard calibration instruments are compared directly with a primary radiation standards laboratory, the U.S. National Bureau of Standards.

MP7.4

CT useage in Manitoba and the correspond-
ing patient doses (1977-1987). W. Huda*
and G.A. Sandison, Medical Physics, MCTRF,
100 Olivia Street, Winnipeg, Canada, R3E 0V9.

The use of CT in Manitoba has increased from an
initial rate of 4.2 patients per year per 10^3 pop-
ulation in 1978 to 18.2 patients per year per 10^3
in 1987. Values of effective dose equivalents,
 H_E 's, have been evaluated for the EMI 5005, GE 9800
and Siemens DRH CT scanners used in this province
over the 11 year period under study. Modern CT
scanners result in an H_E value of 200 mrem for
typical head examinations and H_E values in the
range 600-1,700 mrem for typical body examinations.
The per caput population effective dose equivalent
in Manitoba increased from 0.52 mrem in 1978 to
8.1 mrem in 1987.

MP7.6

Image Analyzing System to Measure Etched
Nuclear Tracks on CR-39 Detectors to Neutron
Dosimetry and LET Spectroscopy of Heavy
Charged Particles

Julius J. Aimasi*[§] and Cornelius A. Tobias
Lawrence Berkeley Laboratory
University of California, Berkeley, CA 94720

Neutron spectrometry and dosimetry are important
subjects of radiation safety at medical
accelerators. CR-39 track etch detectors are
the most sensitive low cost passive neutron
dosimeters. CR-39s are also used to three
dimensional LET spectroscopy of heavy charged
particle beams and can be used to heavy ion
radiography as well as to several other
applications. All the above-mentioned
applications of the CR-39s require a fast
and reliable image analyzing system which can
discriminate between tracks and background
spots and can count and measure a large number
of etched nuclear tracks. We are reporting
about the development of such a fully automatic
low cost and high performance system. We will
present examples of the application of our system
at different dosimetry and spectroscopy
measurements.

[§] NIH postdoctoral fellow, Present address
Siemens Medical Labs., 2404 N. Main Street
Walnut Creek, CA 94596

MP7.5

A Comparison of Several Mammography Films Using
a Contrast-Detail Imaging Phantom and a 152-ACR
Phantom. R.C. Fleischman*, L.N. Rothenberg,
Memorial Sloan-Kettering Cancer Center,
New York, NY 10021.

Reading a mammogram is one of the most diffi-
cult tasks required of a radiologist, the film/
screen system greatly influences the ability of
the radiologist to detect clinically important
information. The dose required to obtain an image
is also an extremely important characteristic
of the film.

We have compared Dupont SR-329,
Dupont SP-150, Kodak OM-1, Kodak TM and Fuji MI-NH
mammography films using a Kodak Min-R cassette
for all exposures. A 152-ACR phantom approved
for use in The American College of Radiology
Mammography Accreditation Program was
radiographed to obtain images of clinically
significant targets. A contrast-detail phantom
was also radiographed to evaluate the films.
For each type of film, three radiographs were
taken of each phantom. The radiographs were
ranked in order of the detectability of the
various targets.

The dosimetry characteristics of the films
were measured using a Radcal 10X5-3M chamber.
The film speed as well as the H&D characteristics
of the films were obtained using BR-12 phantom
material.

MP7.7

Biological Half-life of I-125 in
Japanese Thyroid : Kunihide Nishizawa,
Nagoya University, 55 Tsuruma-cho,
Showa-ku, Nagoya 466 Japan

In vivo thyroidal monitoring was
executed for 51 workers doing iodization
and for 38 workers doing radioimmunoassay
from 1984 to 1987. The monitoring
system was composed of a multichannel
pulse height analyzer(MCA) and two
NaI(Tl) scintillation detector or an
NaI(Tl) survey meter having a connector
to the MCA. The counting efficiency was
determined with an anthropomorphic neck
phantom. Contamination was detected in
17 persons doing iodization and the
measurements of the biological half-lives
were completed for 6 persons of them.
No contamination was found in the workers
doing radioimmunoassay. Biological half-
life of iodine-125 ranged from 20 to 90
days, the average being 48.3 days. These
values are considerably shorter than the
biological half-life of iodine of 120
days for reference man of ICRP.

MP7.8

Radiation Protection in the Treatment Room during Intraoperative Radiation Therapy

J. Rao Nibhanupudy*, G. King, E. Ashayeri, AL. Goldson - Howard University Hospital

During intraoperative radiation therapy in certain cases, it may become a requirement for medical personnel to be in the treatment room near the patient. In order to provide radiation protection for medical personnel during treatment, measurements were made behind lead shielding for 6 MeV, 9 MeV, 12 MeV, 15 MeV, and 18 MeV electron energies at different locations. Results are reported.

MP7.9

Estimated Doses in Tissues Resulting From Radionuclides in Dental Porcelain. P. Tortal*, Radiation Health Service Department of Health, Sta. Cruz Manila, Philippines 1003

U-238, Tl-208, K-40 and Cs-137 were found to be present in dental porcelain through a gamma spectral scan performed using high purity Geli scintillation detector coupled to an ND66 multi-channel analyzer.

Annual doses to the tongue, gums and the inner cheeks and lips were computed assuming continuous contact with the exposed tissues. Calculated doses from alpha and beta were derived from the definition of absorbed dose. Doses due to gamma were calculated using the MIRD method. The resulting dose to the tongue was estimated to be 1.57 rads per year for male and 1.50 rads per year for female. The resulting dose at the gums and the inner cheeks and lips was estimated to be 0.80 rad per year.

MP8.1

Noninvasive Functional Localization by Biomagnetic Methods, T. Katila, Laboratory of Biomedical Engineering, Helsinki University of Technology, 02150 Espoo, Finland

Various imaging methods, CT, MRI, ultrasound and radioimaging are today indispensable in clinical work. However, usually these methods do not give information on the functional level, or in practice only long time averages can be obtained.

Electric surface potential measurements can be used for noninvasive studies on the bioelectric functioning of e.g. heart, brain, eye and muscles. The time scale of these studies ranges from milliseconds to sustained phenomena.

Lately, biomagnetic measurements have often turned out to be superior to electric surface studies in functional localization of the bioelectric activity. Sources of abnormal cardiac electric activity have been localized with an accuracy of about 1 - 2 cm. In brain studies, cortical sources of evoked potentials have been localized with a reproducibility of about 2 mm and source shifts even smaller than that are detectable. For more accurate results, the source and volume conductor models as well as the measurement policy are important. An overview on the factors affecting the localization accuracy is given.

MP8.2

Methods to Improve Neuromagnetic Imaging of Brain Functionality in Evoked Response Studies. E. R. Flynn*, D. L. Arthur, C. J. Aine, J. S. George, P. A. Medvick, P. Lewis, W. Overton, G. S. Sullivan, and D. van Hulsteyn. Los Alamos National Laboratory, Los Alamos, New Mexico, USA.

Neuromagnetic images of functional neural sources may be obtained by using evoked responses from visual, auditory, and somatosensory stimuli. The weak magnetic fields are detected by an array of SQUID coupled gradiometers and neural generators deduced by solving the inverse electromagnetic problem. The results may be overlaid onto nuclear magnetic resonance anatomical images to present three-dimensional images of functional structures within the human brain. The limitations of this technique are signal-to-noise (SN) characteristics of the sensor output, localization accuracy of the sensor-head system, and parameters of the source itself. The first of these (SN) may be substantially improved by a proper magnetic shielded environment, the application of singular-value decomposition methods and the use of correlations between members of the sensor array. The second, localization of sensors with respect to landmarks on the head, may be addressed by the use of multiple sets of transmitting orthogonal dipoles in the form of a headband with the neuromagnetic sensors acting as receivers. Finally, the source problem is approached by theoretical modeling of increasingly complex source descriptions.

MP8.3

Pathological Foci in AC- and DC-Magnetoencephalogram (MEG) Compared to Electroencephalogram (EEG), J. Vieth*, P. Schueler, C. Meyer, S. Malliarou, S. v.Harsdorf, University Erlangen, D-8520 Erlangen, Fed. Rep. Germany.

MEG (1-channel D.C.-SQUID) and EEG (reference: contralateral ear or average) was recorded in 16 patients with a focal EEG- activity caused by epilepsy and/or tumor or ischemia. The recording grid was narrow (point distance: MEG 2-3 cm; EEG 2-6 cm). In 8 epileptic patients averages of spike activity were performed. The spikes of the MEG and EEG averages were selected and triggered by using a suitable EEG electrode (in case: sphenoidal electrode). In all patients with a pathological slow wave activity (delta or theta) the "relative covariance" method was used. In all cases isocontour maps were made. 3D- localizing of the focal source only was performed if the map showed a clear dipolar pattern (12 cases). The EEG never showed a dipolar pattern. The MEG did it and was able to localize the anatomically verified lesions in all these patients. The activity during the start of an epileptic seizure was similar in the AC-MEG and the AC-EEG. The directly coupled (DC) MEG recording showed a similar shift preceding the start of an epileptic fit as the DC-EEG recording via a foramen ovale electrode (STODIEK and WIESER, 1987).

MP8.5

Improvement of Biomagnetic Field Representation by Using the Current Multipole Expansion, S.N. Erné, L. Trahms and Z. Trontelj*, P.T.B., Institut Berlin, Abbestr.2-12,D-1000 Berlin 10 and* Phys.Dept. University E.Kardelj of Ljubljana, Jadranska 19, 61000-Ljubljana, Yugoslavia.

The inverse problem in bioelectricity and in bio-magnetism is usually studied due to its nonunique solution in a model approach. Already the simplest equivalent current source in a form of a current dipole brought success and allowed to localize some sources in the heart and in the brain. On the other hand, magnetic field distributions which cannot be explained by a single dipolar source are also known.

More complicated equivalent sources have to be considered: We will take into account the next higher order term in the current multipole expansion- the current quadrupole. In the present work the current sources are supposed to be active in a homogeneous half space. The analysis of the equivalent current quadrupolar term contribution to the magnetic field is presented. The attempt to localize the source of bioelectric activity from the measured biomagnetic field (MCG and MEG) will be also shown.

MP8.4

Equivalent Localization in the Brain to Somatosensory Evoked Magnetic Fields Using the ECD Technique, Y.Uchikawa*, A.Adachi,T.Hasegawa, and M.Kotani, Tokyo Denki University, Hatoyama,Saitama, 350-03 Japan.

We have performed the magnetic measurement at more than 25 different positions on the surface of the head in a nonmagnetically shielded room with a SQUID connected to a second order gradiometer with a baseline of 3.2 cm and a coil of 2.48 cm diameter. In the measurement of somatosensory evoked magnetic fields(SEFs) the electric current was applied to stimulate the median nerve of the right hand with the duration of 0.2 msec and the interval of 0.5 sec. All magnetic recordings were averaged with more than 500 samples. In order to estimate the location of current source in the brain generating the magnetic field distribution the 3-D ECD(equivalent current dipole) technique was introduced in the meaning of the best fit between experimental and theoretical distribution. Using this technique we could estimate the equivalent localization in the brain of the SEFs in latencies of around 80 msec to 150 msec. The calculated ECD was located at the Rolandic fissure of the left hemisphere of the head where is the motor region related to the finger.

MP8.6

Volume Current Effects in Magnetoencephalography, E. Ducla-Soares*, D.F. Rose and S. Sato, Neurophysiology Unit, MNB, NINCDS, National Institutes of Health, Bethesda, MD

Magnetoencephalographic data have usually been analysed in terms of Biot-Savart's Law for the magnetic field of an impressed current. This method neglects the effects of volume currents. However, for the multi-channel magnetometers now available and for numerous clinical problems like temporal lobe epilepsy, that approach is a poor approximation. We present results on the magnetic field of a current dipole implanted in the temporal zone of a skull filled with a saline agar solution. They show a 50% departure from Biot-Savart's predictions for the relative amplitude of the extrema and also a considerable difference in the position of the zero line. We interpret these results in terms of a spherical model of concentric layers and also with a homogeneous model that matches the digitized internal surface of the skull. These models, which include effects of volume currents, show considerable improvement relative to Biot-Savart's approach and are capable of localizing the implanted dipole within several millimeters.

ES

MP8.7

Traveling Source Model of ABR Electric and Magnetic Fields, S. Ueno*, T. Tanabe, K. Iramina, K. Harada, S. Wada, and S. Matsuoka, Dept. of Electronics, Kyushu University, Fukuoka, 812, Japan, and Dept. of Neurosurgery, Univ. Occupational and Environmental Health, Japan

The origins of auditory evoked brainstem responses (ABRs) have not been fully understood. In the present study we investigate a possible mechanism for ABR. A source model of ABR is proposed, which simulates, in part, ABR waveforms. It is assumed that ABR signals are generated by action potentials which propagate along auditory nerves. Pathways of auditory nerves are represented by a combination of six curved lines which involve both ipsilateral and contralateral pathways. The sources of ABR signals are modeled by a twin-dipole which travels along the curved lines. The twin-dipole consists of two oppositely oriented dipoles which are located within a distance apart from each other. The effect of the distance between two dipoles on ABR waveforms is also focused in the present study. Based upon our source model, the waveforms and spatial distributions of electric potentials and magnetic fields of ABRs are calculated. The periodic patterns in ABR waveforms are simulated well by the model. The component waves in ABR are explained by the change of dipole orientation. The spatial pattern of wave V is also simulated well by the model.

MP9.1

Digital Tomo-synthesis By Inverse Filtering, A. Iwata*, H. Matsuo, I. Horiba, H. Wei, N. Suzumura, and T. Sawada, Nagoya Inst. of Tech., Showa-ku, Nagoya, 466 JAPAN

Conventional X-ray tomographic technique with X-ray film provides a sagittal image by one scanning of measurement. Digital Tomosynthetic technique, however, can produce sagittal images at any arbitrary slice of the body. This paper proposes a new reconstructing method for digital tomo-synthesis. It utilizes a 3-dimensional convolution process with the inverse filter function, which is derived analytically from the point spread function determined by the projection geometry. Unstability of inverse filter has been eliminated considering the localization of frequency component of projectional images. By the phantom experiment, it has been shown that the proposed algorithm is able to reproduce the expected gray level corresponding with X-ray attenuation coefficients on the slice. It can also reduce the blurred images from outside of focused slice.

MP8.8

Distribution of the magnetic field associated with P-300, Z. Dunajski*, C. Massen, E.v.d. Voorden, P. Elias and C. Brunia University of Technology Eindhoven, Postbox 513, 5600 MB EINDHOVEN, the Netherlands.

The P-300 wave present in electrically measured evoked brain responses is of great interest in psychological research. Until now very limited knowledge exists about the magnetic field elicited from task relevant events and about the possibility of applying a magnetic method for investigation. Measuring possibilities and conditions of the magnetic investigation of P-300 are studied in some details. The distribution of the magnetic field around the head, evoked by auditory stimuli in the oddball paradigm is measured using a rf-SQUID with a second-order gradiometer in an unshielded environment. The frequent 1 kHz and infrequent (target) 2 kHz tonebursts were presented at 80 dB SPL with probability ratio 5:1. Reliable recordings of the magnetic P-300 wave have been obtained. The results show that magnetic measurements of P-300 provide further information about sources of underlying processes. The magnetic P-300 may be either positive or negative depending on the measuring position above the head. Its shape and latency are also position-dependent and reflect the involvement of active sources.

MP9.2

DIGITALLY ENHANCED MAMMOGRAPHY: TV SCANNED FILM VERSUS LASER ACTIVATED IMAGING PLATE
C. Kimme-Smith*, L. Bassett
L. Gormley, R. Gold

Dept. of Radiological Sciences, UCLA School of Med. Los Angeles, CA 90024

OM/Min R film-screen images of test objects containing simulated calcifications and images of breasts of 40 women (25 with pathology and 15 normal) were scanned by a Damon Mammography Enhancement System. The same test objects and breasts were also imaged with FUJI high resolution plates and laser activated by a Philips Computed Radiography (PCR) system (.100 mm pixel size). The images produced by the two methods were compared. The PCR system was found to be superior for imaging dense breasts because the H and D curve and overall film density could be manipulated, while the Damon system was found to be superior for examining the simulated micro-calcifications. The Damon system, however, was unable to compensate for improper film exposure, so that dense breast parenchyma below .45 O.D. and photon-poor on film remained noisy when enhanced. Imaging with the FUJI plates required half the exposure of the film-screen images. Out of 10 cases with calcifications, three were not well represented on the FUJI plates.

MP9.3

A Novel Digital Radiographic System Using Selenium Plates and Laser Scanning Readout, J.A.Rowlands* and D.M.Hunter, R.B.Holmes Radiological Research Laboratories, University of Toronto, Toronto, Ontario, M5S 1A8 Canada and N.Araj, Noranda Research Centre, Pointe Claire, Quebec, Canada.

A new imaging system for radiography based on charged photoconductive plates with read-out by a scanning laser beam is described. It is shown theoretically that this system should have an exceptionally good spatial resolution as well as an adequate signal-to-noise ratio (SNR). These expectations are confirmed with a prototype system designed in our laboratory which has shown a modulation transfer function of 50% at 5 lp/mm; 20% at 10 lp/mm and a SNR of 1000:1. A clinical system is being developed which will be suitable for the most demanding radiological imaging tasks currently undertaken with screen/film combinations. Because it is digital new tasks impossible with current screen/film combinations will be feasible. Evaluations of the system using the Wiener spectrum will be used to compare this method with stimuable phosphor systems.

MP9.5

Noise reduction in dual energy imaging, W. Kalender, Siemens Medical Systems, D-8520 Erlangen, West Germany

An algorithm for noise reduction in dual energy radiographic imaging using the basis material decomposition technique is presented; it is based on exploiting the negative correlation between the noise in the soft tissue image and the noise in the bone or iodine image. The algorithm will be derived by physical considerations and be demonstrated using simulated data. Typically, pixel noise is reduced by a factor of 2-5 without an increase in dose. Results of clinical studies are presented both for scanned projection digital radiography and for hybrid DSA.

MP9.4

Description of a Three-dimensional Motion Correction Algorithm for Digital Subtraction Angiography. D.R. Pickens*, J.M. Fitzpatrick, V. Mandava and J. Grefenstette, Vanderbilt Dept of Radiology, Nashville, Tennessee 37232

Patient motion which occurs between a mask image and a contrast image is often a source of artifacts in digital subtraction angiography (DSA). We have been evaluating a method for the automatic registration of selected mask and contrast sub-images prior to subtraction which is able to remove or reduce the effects of three-dimensional motion. The technique uses an eight term polynomial whose coefficients are determined automatically to stretch a mask subimage, resulting in a reduction of artifacts after subtraction. The polynomial coefficients are determined by a heuristic search method which seeks to minimize the absolute value of the difference between mask and contrast subregions. A factor, the Jacobian, is used to alter the gray level values of the mask subregion to compensate for stretching or contracting. There is improved visualization of arterial segments in subtraction images of phantoms and in clinical DSA images due to artifact reduction when compared to the results of subtraction without motion correction.

Supported in part by NIH 1-R01-HL 33951, by NSF #ECS-8608588, and the Whitaker Foundation Equipment Grant.

MP9.6

Post Imaging Contrast Enhancement in Digital Mammography, P.J. Bjorkholm* and M. Annis, American Science and Engineering, Inc., Cambridge, MA 02139, D.B. Kopans and J.M. Taveras, Massachusetts General Hospital, Boston, MA 02114

A high spatial resolution detector with good X-ray absorption characteristics over a wide energy range has been used to obtain mammograms on a number of volunteers. Because the digital images can be contrast enhanced after acquisition, the X-ray spectrum utilized in imaging is not constrained as in conventional imaging which requires a low voltage to achieve an acceptable calcium contrast. Low voltage usually results in high contrast for micro calcifications and a limited dynamic range. The new digital system, Microdose Mammography, utilizes a 70 kV_p tungsten anode spectrum. While the transmitted image has a lower intrinsic contrast for the calcifications, the contrast enhanced images are presented with nearly identical contrast for micro calcifications with excellent dynamic range. Because of the higher voltage spectrum on the peak dose to the breast is of the order of 30 times less with the Microdose system as compared to standard film screen techniques, while achieving comparable spatial resolution and superior contrast resolution.

MP9.7

Non-recursive Parametric Filtration of Medical Images for Scatter Rejection, J.A. Seibert* and J.M. Boone, University of California, Davis, California 95616

X-ray scatter is a major degradation in 2-D transmission medical images. Using a parametric technique developed in our laboratories, a scatter point spread function (PSF) distribution is measured, based upon imaging geometry, object thickness, and presence of anti-scatter devices (grids). The PSF is parameterized as a modified symmetric Gaussian function in terms of a scatter fraction and distribution width. Transformation of the PSF into the frequency domain permits inverse filtering of Fourier transformed digital images to non-arbitrarily remove the scatter component. Inverse transformation provides the scatter corrected image.

We describe methods that allow the use of such a technique in a clinical environment, based upon input variables such as field size, air gap, photon energy and patient thickness. Improved image contrast and quantitative accuracy for densitometric measurements, with minimal negative effects such as increased image noise or artifacts are obtained. Implementation as an optional processing scheme has been accomplished in the clinic on our digital angiography unit.

MP9.9

Focused collimator for scanned projection digital radiography, R. Sones, Mt. Sinai Medical Center, Cleveland, OH 44106.

The fan beam collimator typically used in scanned projection digital radiography consists of a single slit positioned roughly midway between the x-ray tube focal spot and image receptor. To produce a thin fan beam with this type of collimator, a small focal spot must be used, and focal track loading becomes a dominant system constraint. Furthermore, the slit collimator generates a fan beam whose thickness increases with distance from the slit. For most applications this divergence is undesirable.

A focused collimator design is proposed which, for given fan beam thickness, permits the use of a significantly larger focal spot and provides 2-5 times greater x-ray fluence than a slit collimator. The focused collimator consists of a set of thin, closely spaced, radio-opaque vanes oriented nearly parallel to the central plane of the fan beam, but slightly angled to focus at a point within the central ray. This geometry allows non-diverging or even converging fan beams to be generated. A mathematical model of a focused collimator is developed, and potential implementations are discussed.

MP9.8

Incorporation of Various Physical Factors in Statistical Image Reconstruction Methods, C.-T. Chen, The University of Chicago, Chicago, Illinois, U.S.A.

Recent developments in statistical theory and associated computational techniques have opened a new avenue for solving problems in image reconstruction. Mathematical models based on statistical theory can be built to incorporate every physical factor involved in image formation. Various estimation methods, e.g., maximum likelihood, Bayesian, etc., can then be employed to derive iterative algorithms for computing estimate of the original object. In principle, improved image quality can be achieved by using these statistical methods because more faithful and more complete mathematical models can be employed. In addition, since stationarity is not a necessary condition in the derivation of the formulas employed in these algorithms, some common shift-variant characteristics can be compensated for as well. Various implementation strategies have been investigated for incorporating physical factors such as photon attenuation, scattered radiation, system spatial resolution, etc., in emission computed tomography. Various mathematical models that describe these physical processes have been formulated for generation of related probability density functions. Computer simulation studies have been performed to evaluate these strategies in terms of resulting image quality and computational requirement. In general, images reconstructed by these statistical methods have superior quality at the expense of more processing time, when compared to those obtained by conventional convolution methods.

MP10.1

Total Body Irradiation with 10MV x-rays, S.N. Rustgi*, G. Popescu, J. Rodgers and J. Torrisi, Department of Radiation Medicine, Georgetown University Hospital, Washington, D.C. 20007

We are participating in a protocol using total body irradiation (TBI) for immunosuppression prior to bone marrow transplantation for adult leukemia. This paper details the dosimetric considerations of using a 10MV x-ray beam at an extended distance of 5 m. We have fabricated a patient support and a lung shielding block support system, which minimizes patient movement during AP/PA treatment and helps position the lung blocks accurately. The patient stands 30 cm behind a 1 cm thick lucite sheet to enhance the skin dose to 93% of the d_{max} dose. Nondivergent lung blocks, 1 HVL in thickness, are placed at a distance of 30 cm from the patient midline and their position checked daily by port filming. The chest wall under the lung blocks is boosted with electron beams of appropriate energy. The measured TMR values at 5 m were found to be within 2% of the values obtained at the nominal SAD of 100 cm. We have also performed *in vivo* measurements of entrance and exit doses on a number of TBI patients using a calibrated silicon diode detector. Aspects of this treatment approach and dosimetry will be presented.

MP10.2

Dosimetry of lung and bone for total body irradiation: Comparison of 18 MV to Co^{60} and 8 MV photon irradiations

Ellen El-Khatib*, Jurek Rymel, F. Mahyoub
Biomedical Physics Dept.
KFSH&RC, Riyadh 11211, Saudi Arabia

In most centers total body irradiation (TBI) is performed with either Co^{60} or X-rays of energy below 10 MV. At the King Faisal Specialist Hospital And Research Centre (KFSH&RC) an 18 MV X-ray beam is used for TBI. This higher energy beam produces a more homogenous dose distribution to the body for parallel opposed beams while giving a lower radiation dose to the lung. Lung toxicity is a limiting factor in TBI. Most of the data available on lung and bone radiation dose is for photon energies in the range 1-10 MV. In the present work radiation absorbed dose in and beyond bone and lung in tissue equivalent phantoms and also in a humanoid phantom was measured and calculated. Results were compared for 18 MV, 8 MV, and Co^{60} large field irradiations. The TBI technique and dosimetry are evaluated in terms of dose homogeneity and a comparison of bone and lung dose for various photon energy irradiations is presented.

MP10.4

Sweeping, an universal technique in Total Body Irradiation, R.G. Müller, Institut für Radiologie, Universität, D-8520 Erlangen, F.R.G.

Sweeping is a technique without the need of a special room design. The patient lies in supine and prone position on a low couch on the floor. The beam direction is along the shortest diameter, ventral to dorsal. The required accessories as moving flatness filter defined lung shielding blocks, and beam attenuation will be demonstrated. The midplane dose is calculated to 12 Gy (6 fractions, 3 days). The lung dose is reduced to 8 Gy. The underdosage of the chest wall is compensated by electron beams with matched energy and bolus material.

The maximum dose rate is reduced to 0.2 Gy/min at midplane, and the effective dose rate in the lung is about 0.07 Gy/min.

MP10.3

A Technique for Hemibody Skin Skin Irradiation, D.L. Wilson, Dept. of Radiation Oncology, University of Louisville Brown Cancer Center, Louisville, KY 40292

A new technique for electron beam skin irradiation of mycosis fungoides or Kaposi's sarcoma patients is presented. A uniform skin dose is delivered to either the upper or lower half of the body, while sparing the opposite half. The treatment is done with a Therac 20 linear accelerator. The patient lies on the floor and assumes six different orientations which correspond to the six standing positions normally used in the standard total skin technique as described by the AAPM TG 30 protocol. A 0.6 cm lucite sheet is used to lower the nominal 6 Mev beam energy to 3.9 Mev. The untreated portion of the body is blocked by lead sheets. Two adjacent fields are used to achieve beam uniformity. The separation of the fields was determined by fitting the beam to a gaussian curve and looking at the two field combination that gives the most uniform dose over one meter. Calibration factors were derived from ion chamber and TLD measurements made according to recommendations from the AAPM TG 30. All field parameters, calibration and phantom measurements are presented.

MP10.5

The design and evaluation of lung compensators for total body irradiation treatment, C. Simms*, L. Doyle and J. Conway, Department of Medical Physics and Clinical Engineering, Weston Park Hospital, Whitham Road, Sheffield, S10 2SJ., England.

A total body irradiation (TBI) technique, for patients requiring bone marrow transplant, has recently been developed to allow a fractionated regime rather than the previously employed single dose treatment. No bolusing of the patient requires the design of customized tissue compensators for dose uniformity to the body. This paper describes the methods used to provide a thorax compensator to correct for increased lung transmission and tissue obliquity. A 'beams-eye-view' facility developed for the Picker Treatment Planning System allows the precise identification of compensator shape required with respect to the patient's arm, which acts as the compensator for the posterior section of the lung. Analysis of the resulting 3D dose distribution is obtained using 'dose volume histograms'.

Measurements taken in a thorax 'Rando' phantom, using thermoluminescent dosimetry (LiF powder) will be presented.

Patient positioning and compensator alignment is discussed with regard to dose uniformity for this TBI method.

MP10.6

Hyperfractionated T.B.I.: results and dosimetric considerations after three years experience.
G.Gobbi*, C.Raymondi*, M.P.Leogrande, S.Beneventi, S.Ricci and P.Latini. Fisica Sanitaria and Radioterapia*. Policlinico Hospital - Perugia - Italy.

48 patients received hyperfractionated T.B.I. (1.2Gy 13 fractions 3 times a day, total dose 15.6 Gy). A modified ^{60}Co unit with a horizontal beam and a $190 \times 125 \text{ cm}^2$ field is used, the dose-rate being about 70 mGy/min at 226.5 cm source-midline distance. The patients lie supine for the lateral fields and on their sides for AP fields, the legs slightly bent. In the supine position a compensation bolus is applied to the neck and the arms are alternatively raised. The most uniform dose distribution is achieved with 9 AP fractions and 4 lateral fractions (inhomogeneity indexes: AP=3.2, lat.=6.9, 9 AP+4 lat.=2.6). In the treatment planning the TPR for very large fields is used taking the mean thickness of 3 transverse sections: pelvis, umbilicus and nipples. During the first 2 fractions TLD's are placed in 7 body sections and midline dose distribution is evaluated from combined entrance and exit doses, thus allowing treatment time correction. The mean ratios of measured/calculated doses are: 0.919 in AP and 0.970 in lateral irradiation.

MP10.8

Analysis of Short FSD Techniques for Total Skin Electron Irradiation. D.I. Thwaites, Medical Physics, Western General Hospital, Edinburgh, Scotland, U.K.

Total skin irradiation is the treatment of choice for certain conditions. Long fsd, high-output techniques are generally used, with multiple beams or patient rotation for uniformity. Problems arise if this cannot be achieved due to machine or room limitations, or if the patient cannot stand for the treatment time involved. Short fsd scanning or tracking has been used, but the two or four fields generally employed inevitably reduce uniformity.

Our technique uses a short fsd (~ 150 cm) and large fields added along the patient. Using a specially designed applicator, distributions added side-by-side can be made essentially flat. A four-position technique is used with energies of 2 - 4 MeV, as required. Depth doses and distributions were measured in detail in phantoms and checked on patients. They depend heavily on cross-section and number of fields. For a basic four-field approach under these conditions, distributions around a trunk section typically average 130 - 140% of given dose on equally weighted beams, with a $\pm 20\%$ variation. However the technique allows gantry angulation, to increase the effective number of fields, achieving spreads within 10%. To correct for variations with cross-section, longitudinal field edge positions can be selected and different weighting applied at each level depending on average cross-section. The technique is more complicated and time-consuming to set up than typical long fsd treatments, but its flexibility allows very acceptable distributions to be achieved in reasonable machine times.

MP10.7

The Physical Aspects of Hyperfractionated Total Body Photon and Electron Irradiation for Bone Marrow Transplantation. Azam Niroo-mand-Rad*, Michael T. Gillin. Dept. of Radiation Oncology, Medical College of Wisconsin 8700 W. Wisconsin Ave. Milwaukee, WI 53226 USA

Total body photon and electron irradiation (TBI) involves delivering an adequate immuno suppressive dose before transplantation to achieve a successful marrow graft and to eradicate the malignant cells while avoiding pneumonitis and toxicity to organs such as lung and liver. To achieve these goals a hyperfractionated regimen for TBI with partial lung and liver blocks have been adopted. Chest wall areas which have been shielded by lung blocks are boosted with electron beams. CT scans are used to select electron beam energy and to calculate lung doses. A conventional linac in a standard treatment room is utilized to deliver 18 MV X-Ray beam at a dose rate of 20 cGy/min at 350 cm treatment distance. A special chair is used to treat the patient AP/PA in an upright sitting position with the legs bent backward. The dose to lower extremities are monitored and raised to the total body dose. Following the guidelines recommended by AAPM Task Group No.29(1), the physical aspects of TBI is described. The dose distribution and the dose uniformity are presented. Details of this scheme, in-vivo and in-vitro dosimetry, boosting techniques and lung dose calculations are presented. (1) AAPM Report No. 17: The Physical Aspects of Total and Half Body Photon Irradiation (1986).

MP10.9

Energy Degradation of Low-Energy Electron Beam for Treatment of the Superficial Malignancies. W. Sewchand, M. Sarfaraz*, N. Bauto, Rad. Therapy Dept., Univ. of Maryland Hospital, Baltimore, MD 21201

Energy degradation of conventional low-energy electron beams, by deliberate placement of degraders in the path of the beams is often used in Total Skin Electron Beam (TSEB) therapy at extended Source-Surface Distance (SSD). When local areas require booster doses, it is desirable to administer it at standard SSD with a degrader that produces similar dose characteristics as TSEB. Extensive measurements were carried out to study the effect of various thicknesses of polystyrene degraders on a conventional low-energy (6MeV) electron beam at a standard (100cm) SSD for five different field sizes. The study evaluated the effect of degraders on: 1) energy and depth dose characteristics, 2) surface doses, 3) field flatness, 4) bremsstrahlung component, and 5) the output for certain monitor setting. The results were analyzed and significance of the study will be discussed.

MP10.10

Total skin electron arc technique
for disabled patients

B.J. Gerbi*, F.M. Khan, F.C. Deibel, and
T.H. Kim. University of Minnesota, Dept. of
Therapeutic Rad., Minneapolis, MN 55455.

Most of the current techniques used for total skin irradiation using electron beams presuppose that the patient is capable of maintaining a standard position for the duration of the treatment. For patients either weakened by disease or those suffering from a loss of limbs, this is often an unrealistic expectation. We will describe a technique that allows the patient to remain in a reclined position without sacrificing dose uniformity. This technique employs two, symmetric ($\pm 48^\circ$ from the vertical axis) pendulum-arc electron beams to provide a field uniformity of $\pm 5\%$ over a range of ~ 220 cm along the length of the patient. The standard six patient positions [1] are employed to provide a uniform dose to all surfaces of the patient. A description of the treatment technique along with details of the dosimetry will be given.

1. V. Page et al., Radiology 94:635 (1970).

MP10.12

*A Method for Shaping Arbitrary Fields for
Intraoperative Radiotherapy (IORT)*, P.
Biggs*, W. Shipley and C. Willett, Mass.
Genl. Hosp. Cancer Centre, Boston, Ma USA

A technique has been devised for arbitrarily shaping electron fields in IORT. This has been achieved by cutting a 15mm thick lead disc, which fits inside the base of an 8cm diam. circular cone and which is attached through a series of holes around its perimeter. The desired shape of the blocked area is determined by the therapist at surgery, using a dummy cone. After cutting the disc, the cutout is sterilized and taken to the therapy room. This lead piece is attached to the cone by one or more screws before the cone is inserted into the patient. The dosimetry for two shielding arrangements has been tested: (i) a single straight edged piece, varying in width up to 4cm and (ii) a circular cone down, varying in diameter from 7 to 4cm. These sizes represent the extreme limits of any likely blocked fields. As expected, the depth dose decreases with field size (independent of field shape) and increasing energy (up to 3mm at 9 MeV, 8mm at 15 MeV and 17mm at 23 MeV) as does the location of d_{max} , while the surface dose also increases (up by an average of 5% for (ii) and $\sim 1.5\%$ for (i)). The 'cone ratios' show an increase of $\sim 3\%$ for 9 MeV, 3-5% for 15 MeV and 4-9% for 23 MeV for (ii) and less than 3% overall for (i).

MP10.11

Modification of an Intraoperative Radiation
Therapy Applicator System, N. Samsami*, F.R.
Bagne, Medical College of Ohio, Toledo, Ohio.

Earlier studies have shown that the intraoperative radiation therapy applicator system developed at the Medical College of Ohio can produce a clinically significant dose nonuniformity across the radiation field by as much as 18%. This dose nonuniformity is caused by radiation contamination from different components of the system. We have developed a technique for eliminating this undesired dose non-uniformity. In this study, the scatter contributions from different components of the system are differentiated. Energy-specific rings are then designed which fit at the gantry end of the applicators. The materials used are aluminum, stainless steel and copper, all of which can be cold-gas sterilized. To determine the optimum thickness, a series of measurements are done using rings of varying heights and thicknesses. All data are taken in water using 6, 9, 12, 15 and 18 MeV electrons. The applicators employed are circular in cross-section with diameters ranging from 1" to 4" and have either flat, 15° , or 30° beveled end. This paper presents the results of our study and recommends the ring height, thickness and material for various electron energies and applicator sizes necessary to provide a uniform dose with less than 5% variation.

MP10.13

*A Study of the Factors Affecting the Perform-
ance and Use of Intra-Operative Radiation
Therapy Applicators*, P. Stafford*, J. Chu,
G. Hanks, Univ. of PA and Fox Chase Cancer
Center, Philadelphia, PA.

Intra-operative radiation therapy is now in routine use at many facilities, both dedicated and non-dedicated in nature. The applicator generally consists of a holder/periscope and a series of electron cones of various diameters and angulations. This paper investigates one such system (Radiation Products Design, Inc.) for the effects of: a) less than perfect alignment of the viewer-cone assembly; b) the presence of a suction tube or other surgical apparatus in the cone; c) field size setting of the photon jaws; and d) the behaviour of output factors with distance from the nominal 100 cm treatment distance. Both radial and depth profiles will be shown illustrating these effects, as well as graphs for field size and output factor behavior.

MP10.14

MRI Stereotaxis: An Indirect Method of Transposition of MRI-Generated Data into CT Multiplanar Images Zamorano L,* Dujovny M, Malik G, Mehta B - Henry Ford Hospital Det., MI

Inhomogenities and nonlinearities induced by eddy currents during the pulse sequence distort images and produces displacement of coordinates in both the X-Y plane and Z axis. Correction of geometric distortion requires special algorithms, phantom measurements, shim adjustment, etc. A methodology of indirect transposition of MRI generated data into CT Multiplanar stereotaxis is presented, which uses available software from MRI (GE Signa 1.5T) and MRI laser beam to establish the plane of placement of stereotactic frame. Axial, coronal and sagittal T1, T2 weighted images are displayed. X coordinates are selected from axial and coronal cuts. Y from axial and sagittal and Z from all three cuts. Trajectories are determined and plotted in similar ways. Areas and volumes of region of interest are determined. Stereotactic frame is placed on the predetermined region. Frame is isocentric to the CT gantry and parallel to the scanning plane. 1.5mm thickness slices of the region of interest are performed. Error factors for MRI generated data are calculated for each cartesian plane. This factors can be introduced on computer program that automatically will correct any MRI coordinates. These can be plotted on axial, coronal, sagittal and paraxial reformatted images and AP and lateral scoutviews. Methodology details will be presented.

MP10.16

A high energy photon collimator for stereotactic irradiation with a linear accelerator. D.A.Mazal, J.C.Rosenwald*, J.J.Baron. Institut Curie- 26,rue d'Ulm. 75005. Paris. France.

Small size, high energy X-ray beams from a linear accelerator are used to perform stereotactic convergent irradiations of small volumes in the brain. Additional collimators have been developed to produce small circular beams, well adapted to this technique, and to ensure the accuracy of their dimensions and positioning. The collimator design is based on the following criteria : precise beams diameters, 5 to 40 mm at isocenter, without introducing modifications on the accelerator and maintaining a unique aperture of the main collimator; adjustable direction and position, with the possibility of changing collimators without modifying these two parameters and without moving the patient; the transmission factor and the primary collimator opening (where the beam is attenuated only by the additional collimator) should be minimized, as well as the collimator weight and beam contamination, for all the energies under consideration; strong, easy to manufacture from cheap and available materials, easy to manipulate.

The modular design we have chosen gives independent functions (fastening, micrometric displacements); 10 cm lead ensure less than 1% transmission for a 5X5 cm² field, measured in the range 6 to 25 MV; a brass cylinder provides mechanical protection and allows strong and precise attachments. The distance from the collimator base to the isocenter (28 cm) ensures enough free space around the isocenter and avoids beam contamination. Total weight of the system is 14.3 kg, with 7.8 kg corresponding to the exchangeable collimator. Two removable cross hairs are used for precise centering.

MP10.15

Recurrence vs radionecrosis:an indication for 3D/ Multiplanar Imaging-guided stereotaxis. Zamorano L, Katakik D., Dujovny M., Yakar D., Malik G Henry Ford Hospital, Detroit, MI 48202

External RT has proved to be an important adjuvant in the treatment of malignant gliomas. Its effect on survival is dose-dependent. Intent to localize the field of high dose RT to the tumor area have been performed with the aim to spare damage of normal brain tissue. Between 8/83 to 1/87, 33 patients with malignant astrocytoma underwent high dose localized hyperfractionated external RT after surgery. Patients received 57.6 Gy to the tumor+edema area and a localized boost of 7.4, 14.4 or 24 Gy. In the follow-up, 16 patients died with evidence of CT/MRI increase of size of lesion. Since 7/87 11 patients have undergone multitrajectory serial stereotactic biopsies: 4 patients were "real" recurrences were treated with I-125 interstitial RT. Radiation necrosis were treated with corticoides and diuretics, obtaining partial or complete remission of symptoms and decrease or disappearance of CT lesions. Should these localized external boost after surgery and conventional external RT? Advantages would be: higher intratumoral dose, less damage of surrounding brain tissue and more favorable radiobiological conditions.

MP10.17

Some Physical Problems Associated with Combined Electron and Photon Fields in the Treatment of Mesothelioma, M. Soubra*, P. Dunscombe, D. Hodson and G. Wong, Manitoba Cancer Foundation, 100 Olivia Street, Winnipeg, Manitoba CANADA

Combined fields of electrons and photons can be used effectively to treat the pleural membrane of patients with malignant mesothelioma. Various problems may be identified in the implementation of such a treatment strategy: non-uniform dose distribution in the join-up region of the two fields; increased electron penetration into lung; increased lung dose from photon side-scatter and the effect of the ribs on both the electron and the photon fields, are among the major problems encountered. To investigate the significance of these effects a phantom simulating, under simple geometrical conditions, bone, lung and soft tissues has been constructed. Dose distributions under various simulated clinical conditions, have been measured and compared with calculated data. The significance of the effects studied for the treatment of pleural mesothelioma is discussed.

MP10.18

A Modified Technique of Neck Irradiation in Head and Neck Carcinoma: Its Effectiveness, R. Datta*, F. Ampil and S. Datta, LSU Medical Center, Dept. of Radiology, P.O. Box 33932, Shreveport, Louisiana 71130

In the treatment of head and neck carcinoma, the junctional area between the parallel opposed lateral upper neck fields and the anterior lower neck/supraclavicular neck field poses a challenging problem. The major concern involves the desire to adequately treat the entire area at risk of recurrence without exceeding 'tolerance' of the spinal cord. To overcome this difficulty, a modified technique of irradiation has been utilized at the Louisiana State University Medical Center since 1980. This report retrospectively evaluates the effectiveness of this technique in 47 patients given adjuvant post-operative external beam irradiation during 1980-1984. Actuarial four-year disease-free survival was 51 percent. Recurrent disease was not observed at the junctional blocked (and underdosed) area of irradiation in any of the treated patients. Neither was there an example of radiation-induced myelitis. We feel that this modified partial block radiotherapy technique is useful, provided evident disease is not being blocked. Description of this technique, its dosimetric aspects and its effectiveness will be highlighted.

MP10.20

Matching of Orthogonal Fields in Cranio-spinal Irradiation, M. Tatcher,* Quality Assurance Review Center, Rhode Island Hospital, Providence, RI 02903.

Patients with malignancies that require cranio-spinal irradiation (CSI) are usually treated with parallel-opposed lateral cranial fields coupled to a long posterior spinal field. To improve dose uniformity at the junction, many radiotherapy protocols specify compensation for beam divergence by rotating the cranial fields so that their inferior edges follow the projection of the superior edge of the spinal field. In this method, when the borders of the orthogonal fields are matched in the mid-sagittal plane, there is no gap at the junction of the fields on the posterior surface of the body. A review of treatment charts from institutions that participate in clinical trials involving CSI shows that some departments separate the cranial and spinal portals by up to 1-2 cm when treating by a divergence compensating technique. To study the dosimetric effects of such gaps, we have calculated dose distributions in the junction region for typical CSI treatments by cobalt and 4 MV photons. Stationary and moving junction methods were considered. The results demonstrate how the extent and magnitude of overdosage and underdosage depend on the width of the gap.

Supported by NCI Grant CA29511.

MP10.19

Radiation Therapy Techniques In Breast Cancer, J.S.B.Gunasekar, V.Dilip Kumar, S.J.Supe, J.B.Sasane Dept. of Radiation Oncology, Jaslok Hospital, Bombay 400 026, India.

In 183 breast cancer patients, various radio-therapeutic techniques were used, with the aim of prophylactic, radical and palliative measures depending upon the stage of disease. For the treatment of chest wall irradiation, tangential portals were used with open fields, breast applicator and wedges and the patients were grouped accordingly. Comparison of these techniques are done by (i) plotting of isodose distribution (done manually because of non availability of computer) of the techniques in two chest wall contours (one with chest wall alone and the other Breast and Chest wall and (ii) Observing the radiation sequelae in these groups of patients during and after the completion of treatment.

With the advent of various concepts like CRE, TDF and TSD, attempts have been made in various centres to compare the treatment plans based on isoeffect lines using these concepts. In the present study isoresponse lines using these concepts for radical treatment techniques were obtained and compared.

MP10.21

Orthovoltage Therapy with X-ray Contrast Media for Brain Tumors, K.S. Iwamoto, M. Wollin, A. Olch, J. Bellotti, A.R. Kagan, and A. Norman*, Departments of Radiation Oncology, UCLA, and Radiation Therapy, Kaiser Permanente, Los Angeles, California.

Orthovoltage x-rays have two potential advantages over conventional high energy photons for the treatment of brain tumors. One, if the tumor is first loaded with x-ray contrast media, the high photoelectric absorption in iodine makes it possible to enhance the tumor dose (Med. Phys., 10,75-78, 1983; Radiother. Oncol., 8,161-170, 1987). Two, the low exit dose spares normal brain tissue on the far side of the tumor. The disadvantage of large entrance and bone doses can be reduced by using multiple fields. We have measured the dose distributions from orthovoltage x-ray beams in phantoms and used these to construct treatment plans. The results show that multiple orthovoltage fields, when used to treat selected tumors loaded with contrast media, have potential advantages over conventional opposed field cobalt-60 gamma rays. They also indicate a potential use for this technique to boost the tumor dose after conventional therapy by treating either through the skull or through a bone flap.

MP10.22

Radiation Dose To Radiosensitive Organs In Treatment Of Medulloblastoma, F.R. Bagne*, D.G. Bronn, S. Hoke, Medical College of Ohio, Toledo, Ohio

Treatment of medulloblastoma requires irradiation of the entire cranio-spinal axis. The alternating head position technique is a method by which the entire CNS of a child is treated in a single field with the patient in the prone position. The head is turned to the opposite lateral position on alternative treatment days. A separate cast block is made for each alternating head position which excludes the face and the eyes. To determine the dose to radiosensitive organs, TL dosimetry was done on patients. It was found that with the standard Cerrobend blocking, a total dose of 3600cGy to the spine results in 44cGy to the gonads, 380cGy to the thyroid, and 648cGy to the lens. A fractionated dose above 400cGy is considered cataractogenic. To reduce the lens dose, supplementary blocks were placed directly over the proximal eye. The total lens dose was then reduced to 308cGy. Gonadal doses above 250cGy are associated with temporary sterility. Our data indicate that the gonadal dose is not a concern with this technique. The absolute threshold for hypothyroidism or secondary cancer of the thyroid has not been established. However, it is generally accepted that the thyroid dose should be kept to a minimum. Our study indicates that the thyroid dose can be further reduced by 50% by means of supplementary blocks.

MP10.24

MINIBEAMS AND THEIR APPLICATION IN CEREBRALS IRRADIATION. Maria Cristina Plazas

In the last years, the development of Computer Tomography (CT) and Nuclear Magnetic Resonance (NMR) imaging, have considerably changed the possibility to give treatment to cerebral tumors. These methods give the possibility to an early diagnosis of small lesions and to a more precise treatment of the lesion with stereotactic methods.

The therapeutic problem is to distinguish between the tumor that is surgically accessible and those that are positioned in a non accessible topography. The minibeams with high energy X-rays were proposed by different groups and the goal of this work is the dosimetry of minibeams of different diameters (5 mm to 20 mm diameters) and with energy of ^{60}Co , 6 MV, 10 MV, 18MV, 23 MV, 25 MV X-rays.

The following characteristic have been considered:

1. The dose measurement along beam axis (depth dose, TMR) with the different dosimetric methods.
2. The dose measurement off beams axis (profile, scans, isodose curves),
3. The evaluation of the different dosimetric methods: film, thermoluminescence, ionisation chamber and diodes.
4. The collimating system.
5. The problem linked to lack of lateral electronic equilibrium and the existence of a possible virtual source.
6. Monitor calibration.
7. Comparison with others methods of irradiation.

MP10.23

Reduction of Gonad dose during treatment of Testicular tumours. T.M. Kehoe and D.I. Thwaites *, Western General Hospital, Edinburgh, Scotland.

The large field treatment of testicular tumours presents the problem of reducing the dose to the remaining testicle to an acceptable level. Unfortunately an acceptable dose has never been clearly defined and in general the philosophy is to keep the dose as low as practical. We have designed a new shield to protect the testicle from scattered radiation on a 9MV linear accelerator.

The design had to allow the patient to rotate from supine to prone for parallel opposed fields. An analysis of the routes by which scattered radiation enters the testicle is presented. The majority of the patient scatter enters via the trunk. To attenuate this component the superior face of the shield is placed between the testicle and the trunk and is 1cm thick. The anterior and posterior faces of the shield need to attenuate high energy scatter from the field defining blocks and the collimators, they are 2cm thick. The lateral sides are 0.5cm thick for rigidity and the inferior face is left open. The anterior lid is mobile and lockable, and is positioned by the patient between the testicle and penis effectively trapping the testicle beneath it. This reduces the patient scatter contribution to a minimum. The shield is made of Pb and weighs 51b 10oz. TLD measurements reveal doses of 50cGy to the testicle for a course of 3000cGy to mid-line is obtainable.

MP10.25

A Mono-Isocentric Breast and Supraclavicular Irradiation Technique Using Asymmetric Beam Collimation, U.F. Rosenow, Albert Einstein College of Medicine and Montefiore Medical Center, Bronx, NY 10467

A new breast and supraclavicular irradiation technique is described which uses a single isocenter for the tangential and supraclavicular fields. The technique is especially suited for treatment machines with independently movable collimators but can also be performed using half-beam blocking on conventional machines. The advantages of the techniques are:

- accurate matching of the supraclavicular and tangential beams
- use of a well-defined set-up point
- simplified set-up
- insensitivity to day-to-day set-up variations
- coplanarity of beams, which simplifies the calculations of dose distributions

A dosimetric evaluation including the sensitivity to day-to-day set-up variations is given. Some possible methodical variations of the technique will be discussed. The optimization of the dose distribution, within the technique, to achieve a better dose homogeneity in the target volume and better lung sparing will also be addressed.

MP11.1

Energy Spectra and Angular Distributions of Electron Beams Scattered by Different Phantom Materials, L. André* and H. Neuenschwander, Dept. of Medical Radiation Physics, Inselspital, University of Berne CH-3010 Berne, Switzerland

The geometrical acceptance angle of our spectrometer is 4.2 degrees. Within this angular resolution we measure the differential fluence of electrons from medical accelerators. The energy resolution ($\Delta E/E$ with 99% valleys) depends on the width of the variable entrance slit and is generally of the order of 3%.

To obtain angular distribution, two different methods are used. For small angles we subtract the spectra measured with a small entrance slit from those measured with a large one in order to eliminate the scattered electrons. For larger angles we use an entrance slit with asymmetric blinds. We have measured the spectra of the linear accelerator SL75/20 (Philips) and the betatron A 45 (BBC) behind different slabs of water-, lung- and bone equivalent materials as well as without any absorbing material. The increase of spread in the angular and energy distribution of the spectrum and the decrease of the most probable energy with increasing thickness of phantom material will be discussed.

MP11.3

The Use of Single Field Superpositions to Design Uniform TSET Dose Distributions. D.P. Fontenla*, H. Weiss, Dept. of Medical Physics, Memorial Sloan-Kettering Cancer Center, 1275 York Avenue, New York, NY 10021

In Total Skin Electron Beam Therapy (TSET) the patient, located behind a 1 cm thick polystyrene screen, is irradiated at various angles of rotation by low energy electrons. The purpose of the procedure when exposures at each angle of rotation are weighted appropriately is to provide as near as possible a uniform surface and depth dose over the whole skin. To determine the effect of different weighting factors, on the distribution of the dose around the phantom, a humanoid phantom has been wrapped at chest height with film at various depths. Dose distributions obtained from anterior, posterior and lateral films from single angle exposures were mathematically combined in different ratios by computer. The combined distributions obtained in this way are compared with the dose distribution obtained when irradiations from multiple angles were made on a single film, by rotation of the humanoid phantom, as is done in the actual treatment. This is a report on the application and advantage of combining exposures to explore and facilitate the design of treatment.

MP11.2

The Effect of Charged-Particle Equilibrium on the Response of an Aluminum-Walled Argon/Propane Ionization Chamber. Allan F. deGuzman and R. J. Schulz, Yale University

The evaluation of the dose from neutrons in a mixed neutron/low-energy-gamma field using an argon/propane ionization chamber requires a careful analysis of energy deposition within the argon or propane from the low-energy gamma rays. Using a plane-parallel, guard-field ionization chamber (10.2 cm in diameter, 1.3 cm plate spacing), measurements made with I-125 (effective energy = 27 keV) revealed an argon/propane ratio of 15. As the charged-particle equilibrium doses to argon and propane, which are obtained at the midplane of the present chamber, are in the ratio of 36.2, there is a clear suggestion that dose buildup (in argon) and build-down (in propane) occurs near the aluminum plates. To verify this, a computer program was written which tracks the paths and energy deposition of secondary electrons in the chamber gas. The electrons are assumed to travel in straight lines with a range equal to 0.70 times the GSDA range. The computational prediction of the argon/propane ionization ratio is 39.9 which is in reasonable agreement with experiment considering assumptions necessarily included in the program.

This work supported by NCI grant CA-09259.

MP11.4

An Experimental Determination of the Penumbra for Multileaf Collimation James M. Galvin*, Alfred Smith, Hospital of the University of Pennsylvania, 3400 Spruce St., Philadelphia, PA. Ronald Moeller, Varian Radiation Division, 611 Hansen Way, Palo Alto, CA.

Multileaf collimators (MLC) offer the interesting possibility of directly shaping static treatment fields, thus eliminating the need for cerrobend blocks. This study compares the penumbra for fields shaped with MLC with the edges for standard blocks. The MLC was double-focused, following the divergence of the x-ray beam, and projected a width of 1 cm at 100 cm SAD. The dose changes rapidly in two dimensions in the penumbra region for the "stepped" MLC. We have used film to monitor this dose distribution and will present a technique which corrects for the inaccuracies usually seen when this dosimeter is used for measurements in the penumbra region. An Optronix microdensitometer with a 400 micron spot size was used to determine dose distributions perpendicular to the beam center axis. The penumbra for MLC was scalloped at the beam edge as a result of approximating the block as a step function. The measure of penumbra used was the 80 to 20% (and 90 to 10%) width of the beam profile at the edge. For the scalloped MLC edge, an "effective" penumbra was determined as the distance between the outermost peaks of the 20% line and the innermost peaks of the 80% line. Scalloping varied according to the exact shaping situation, but was most severe when the block cut diagonally across the field (the situation investigated here). The change in the penumbra width for the two field shaping techniques was determined at 5 and 10 cm depths for a 15x15 cm field and a 6 MV accelerator. For 5 cm depth, the edge increased from 5 mm to 10 mm (22 mm to 24 mm) wide when the MLC was used. For 10 cm depth, the edge increased from 8 mm to 12 mm (31 mm to 34 mm) wide.

MP11.5

PERTURBATION CORRECTION OF A CYLINDRICAL THIMBLE-TYPE CHAMBER IN A GRAPHITE PHANTOM FOR Co-60 GAMMA RAYS, C. E. de Almeida, A. M. Perroche Roux, and M. Boutillon, BIPM F - 92310 Sevres - France

The determination of absorbed dose in graphite for ⁶⁰Co Gamma rays by means of an ionization chamber located in a graphite phantom requires the knowledge of the perturbation on the photon and electron fluence made by the chamber cavity and its wall if the material or the density of the wall differs from that of the phantom. The necessary perturbation correction can be determined theoretically for a flat chamber (Boutillon 1983 and Niatel 1983). However, for a cylindrical chamber (thimble type) the theoretical calculation is difficult, due mainly to the geometry of the chamber. An experimental determination has been made of the perturbation correction to be applied to a graphite cylindrical ionization chamber. The results indicate that the magnitude of correction increases with depth and that is also closely related to the size of the cavity. This makes possible the use of such a chamber as an excellent standard of absorbed dose in graphite for ⁶⁰Co gamma rays, as well as an appropriate transfer instrument.

Boutillon, M. Phys. Med. Biol 28, 1983 pp 375-388,

Niatel, M - I. Phys. Med. Biol. 28, 1983, pp 407 - 410.

This work was undertaken at the Bureau International des Poids et Mesures during the tenure of an American Cancer Society - Eleanor Roosevelt - Fellowship awarded by the International Union Against Cancer.

MP11.7

In vivo dosimetry during external photon beam treatment using diodes, S. Heukelom, H. Lanson and B.J. Mijneer*, The Netherlands Cancer Institute, 1066 CX Amsterdam, The Netherlands

Silicon diodes are well suited for *in vivo* dosimetry if a number of characteristics, such as energy and temperature dependence of the dosimeter response, are taken into account. The energy and dose rate dependence is reflected in a depth-field size correction during external photon beam treatment. The variation in the value of this correction factor and the calibration factor was determined as a function of time and total amount of radiation received by different types of diodes. After establishing accurately these correction and calibration factors, *in vivo* dose measurements were performed, mainly during pelvic treatment. Relatively large series of measurements on the same patient showed that the average standard deviations of the entrance and exit dose determinations are about 1% and 1.5%, respectively. Slightly larger values were observed during wedged beam irradiations. Actual dose delivery to the patient was compared with stated dose values obtained from treatment planning.

MP11.6

The influence of calculation grid size on the error in dose estimation, A. Niemierko*, M. Goitein, Massachusetts General Hospital, Boston, MA 02114

The standard technique in which the dose distribution is presented as an isodose map is based on interpolation between doses calculated at a matrix of equally spaced points. We explored the question of how the grid used for the dose matrix affects the error in the interpolated value of the dose at any point and hence in the position of a calculated isodose contour. We defined the dose calculation error as a difference between the interpolated and true dose for a given point, and a position error as a distance between that point and the nearest point which has, in fact, the same dose value. We examined the problem using an analytical and measured beam profiles of Co-60, X-rays and protons. Our analysis showed that the interpolation errors are proportional to the curvature of the dose distribution, and are relatively high in either side of, but not including, the steepest part of the penumbra. Our results show how big an interpolation error one should expect for a given size of the calculation grid. The specification of dose accuracy should be cast in the form of a pair of requirements, one as dose and the other as position. At a given point, only one requirement need be satisfied. The position requirement is almost always the less demanding in clinical practice and, if accepted, permits the use of larger grid spacing than if only a dose requirement is applied. As a rule of thumb, we recommended a grid size 2.5 times the largest acceptable positioning error, when that error is in the range of from 1 to a few millimeters.

MP11.8

Experimental Evaluation of the Hogstrom Pencil Beam Algorithm in the Vicinity of Cylindrical Bones with 2D and 3D geometry. J. Antolak*, E. Mah, J.J. Battista, J.W. Scrimger Cross Cancer Institute, Edmonton, CANADA

We have studied the influence of small bone substitutes of various density and cylindrical geometry on the dose distribution for incident electron beams of 10 and 18 MeV (1). Dose distributions were measured with a scanned p-type diode and compared with 2D and 3D dose computations based on the work of Hogstrom (2). The cylindrical rods have a fixed diameter (1 cm) but variable lengths (1-10 cm), separations (1.2-5.0 cm), and compositions (CT Number of 495-2224 HU). Measurements for increasing density and length show the progressive changes in "off-axis" electron scattering. The gain in dose accuracy achieved with a 3D implementation appears significant only for the smaller higher density bones and requires a computation time of 5 min. on a VAX-11/780 processor for the central dose plane (4096 pts). The clinical implications of these results will be discussed in conclusion.

(1) Phys. Med. Biol. 32, 1073 (1987)

(2) Phys. Med. Biol. 26, 445 (1981)

MP11.9

BOSIMETRIC APPLICATIONS OF FIVE RECONSTRUCTED BREMSSTRAHLUNG SPECTRA BETWEEN 4MV AND 10MV
 A.Piermattei*,G.Arcovito,L.Azario, Catholic University, Rome,Italy - C.Bacci, G.Giacco La Sapienza University,Rome, Italy - L.Bianciardi, M.Benassi, Nat.Cancer Inst.,Rome,Italy - E.De Sapió,S.Camillo Hospital - Rone,Italy.

There is a lack of experimental bremsstrahlung x-ray spectra produced by radiation-therapy accelerators due to several difficulties. We report relative transmission data obtained by measurement along the central axis and off-axis of five photon beams generated by two 4MV, and 6,9,10 MV linear accelerators. A numerical analysis of transmission data has been applied to determine the fractional energy fluences on the central axis and off-axis of each beam. The central axis spectra have been used to find the Spencer-Attix stopping power ratios and a comparison with the data obtained by methods reported on protocols are shown. A correlation between the mean energy of the spectrum and the quality index TPR_{10}^{10} was found. The off-axis Spectra have been used to account for the softening effect on the flattening filter. Corrections of clinical computer programs using conventional zero field size TM_k were made. With these results and those in phantom measurements, off-axis quality indexes were obtained.

MP12.2

Digital Image Processing to Enhance the Detail of Anatomical Structures within a Portal Film Image Obtained with High Energy Photons. P. Bloch*, W. Powlis and L. Buhle. University of Pennsylvania School of Medicine, Department of Radiation Oncology, Philadelphia, PA.

Anatomical details seen on the portal film are viewed together with higher contrast films obtained during treatment simulation with lower diagnostic x-ray energies, to identify relevant discrepancies in beam alignment between simulation and treatment due to shielding block or patient positioning. The treatment portal image, however, has low tissue contrast, primarily due to the minimal differences in attenuation properties of high energy photons in bone and soft tissue. To improve the quality of the portal image, digital processing is used to (1) increase the display contrast between tissue types and (2) compensate for degradation in the portal image due to the finite size of the x-ray source target and the metal-screen film cassette. The portal image was digitally copied using a laser scanner microdensitometer, into 4096 grey-scale levels and 1684x2048 pixels each 200 microns². A 2D-Fourier Transform of the image was obtained, and filtered in the frequency domain. The filter function used the measured inverse MTF for both the focal spot of the high energy photon source and the metal-screen film combination. The noise power of the imaging system is also incorporated into the filter function. The method permits a rapid reconstruction of the port image that can be interactively adjusted to emphasize desired particular anatomical features.

MP12.1

First clinical experience with an ionisation chamber device for portal imaging. H. Meertens*, M. van Herk and J. Bijhold, Netherlands Cancer Institute, Amsterdam, The Netherlands

A portal imaging device based on the measurement of ionisation currents in a matrix ionisation chamber became recently available for clinical application. The field of view of the system is 32 x 32 cm or 16 x 16 cm, depending on the pixel size: 2.5 mm or 1.25 mm respectively. The noise in the image is less than 0.3% for a scantime of 2 s. During dose delivery, images can be displayed every 2 s. The quality of the images obtained with this device is sufficient for the purpose of patient set-up verification. Portal images of various tumor sites will be shown and the following clinical potentialities of the device will be discussed: a) the use of instant portal information, i.e. obtained within 10% of the fraction dose; b) the patient motion during dose delivery; c) the variation of field edges during dose deliver,.

MP12.3

A digital fluoroscopic imaging device for radiotherapy localization P. Munro*, J.A. Rawlinson, University of Toronto, Toronto, Canada M4X-1K9, and, A. Fenster, John P. Roberts Research Institute, London, Canada, N6A 5K8.

Portal films are used to ensure that the correct region of the patient is treated during radiation therapy. Unfortunately, portal films suffer from low contrast and often lack sufficient detail of the bony anatomy to determine what region of the patient has been irradiated. While the poor image quality is primarily due to the high energy x-ray beam, which reduces subject contrast, film granularity and the poor display contrast of film contribute to the image degradation. We have developed a digital fluoroscopic imaging device as an alternative to portal films. The system consists of a metal plate/phosphor screen detector, a 45° mirror, and a high quality T.V. camera. While other investigators have demonstrated systems of similar design, we have made modifications to the detector and the operation of the T.V. camera in order to improve the signal-to-noise ratio of the images. The phosphor has been bonded directly to the metal plate, the light is integrated on the target of the T.V. camera for lengthy (1-10sec) periods, and the T.V. camera is operated in a slow-scan mode. The effects of these modifications on camera performance and on image quality will be presented.

MP12.4

Contrast enhancement for on-line portal imaging, K. Leszczynsky*, S. Shalev, Manitoba Cancer Treatment and Research Foundation, Winnipeg, Canada R3E 0V9

Portal verification images (from film or on-line imaging systems) suffer from poor contrast and digital processing is used to enhance the visual perception of anatomical landmarks. Local histogram manipulation routines are widely used for this purpose, in which grey level transformations are computed for predefined neighborhoods around each pixel, and various schemes have been proposed to reduce the computational burden by interpolating between a sparse grid of such transformations. A new algorithm is proposed, Moving Histogram Equalization (MHE), which differs from the widely accepted technique of Adaptive Histogram Equalization (AHE) in that linear rather than two dimensional interpolation of transformation functions is employed. MHE is compared to AHE and other methods of contrast enhancement (global histogram modification, windowing, filtering, etc), and its advantages are demonstrated in terms of computational speed and superior image quality. The ripple artifacts commonly associated with AHE are greatly reduced by MHE, and examples are presented for the enhancement of portal images using the new algorithm.

MP12.6

Low Energy Imaging With High Energy Bremsstrahlung Beams, Duncan M. Galbraith*, Princess Margaret Hospital, Toronto, Ontario, Canada

A method is described for verification imaging with low energy (keV) photons produced by a radiotherapy accelerator in the bremsstrahlung process. These diagnostic energy x-rays are normally filtered out by thick high Z target materials. Using a beryllium target with no flattening filter and a low (4-6 MeV) operating energy, low energy photon images can be produced on film in contact with a thin high Z fluorescent screen. The screen selectively absorbs the low energy component of the broad spectrum of photon energies. The imaging performance of this beam relative to conventional diagnostic and therapeutic beams is assessed by comparing, a) measured object contrast, b) images of the RMI contrast phantom and c) images of the Alderson Rando phantom.

MP12.5

On-Line Radiotherapy Imaging Using Fiber-Optic Image Reducers, Y.A. Cheng*, J.W. Wong, W.R. Binns, J. Klarmann and J.W. Epstein, School of Medicine and Department of Physics, Washington University, St. Louis, MO, USA.

On-line digital imaging devices are being developed for radiotherapy verification. Optical imaging is one promising approach and relies on capturing the light output from an irradiated fluorescence screen with a digital camera interfaced to a small computer. There are no moving parts and the components are readily available. However, the system requires a large mirror to direct the light to the camera located some distance away from the radiation and is inconvenient. We have replaced the mirror in such an optical system with an array of optical fiber image reducers to "pipe" the image. Each reducer itself is made up of a bundle of 15 x 15 plastic fibers with an input dimension of 1.6mm x 1.6mm. The output is reduced to 1mm x 1mm within a height of 12cm. The characteristics of the reducers for image transfer are studied. Images can be acquired in the order of seconds and will be presented.

MP12.7

The Use of Storage Phosphors for Portal Imaging in Radiation Therapy: Therapists' Perception of Image Quality. D Gur*, M Deutsch, PA Clayton, MS Rosenthal, AG Bukovitz, JC Weiser. University of Pittsburgh, Pittsburgh, PA, 15261, USA

A major drawback in the interpretation of portal images in radiation therapy is their low contrast. This is due to the low differential absorption of body tissues at therapeutic energies and to a relatively large focal spot. We used an experimental storage phosphor imaging system (Eastman Kodak Co.) to produce portal images. The system consists of a storage phosphor detector, a laser scanner (12 bit), an image processing module, and a laser printer (12 bit). Ninety-three patients undergoing radiation therapy treatments had both a conventional portal image and a storage phosphor image taken. The storage phosphor image was scanned, image processed, and displayed on a laser-printed film. The conventional image and the storage phosphor images were then displayed side-by-side and were evaluated independently by three radiotherapists for information content. Each of the three radiotherapists found the storage phosphor images to be superior ($p < 0.001$) to the conventional images.

This work is supported in part by the Eastman Kodak Company.

MP12.8

Image Manipulation and Processing in Radiation Oncology, M.S. Weinhaus,* Washington University School of Medicine, St. Louis, MO, USA.

Radiation Oncologists use a variety of dissimilar imaging modalities (plane films, CT, MRI, portal films, etc.) in prescribing and verifying treatment. We have implemented digital image manipulation and processing techniques to provide the physicians with a consistent, correlated, and appropriately enhanced set of images. Consistent in that the rendered images have the same magnification factors, points of view, and similar contrasts. These consistently rendered images are examined for both spatial and temporal correlation (e.g. a similar film with a portal film with a calculated portal image [from CT or MR]; or serial portal films with one another). When appropriate, enhancement is accomplished by contrast modification, high-pass filtering, deblurring, etc. Ultimately, physicians are provided with an improved data set from which to make clinical judgments.

MP13.1

APPLICATION OF CALORIMETRY TO EVALUATION OF MICROWAVE ANTENNAE FOR INTERSTITIAL HYPERTHERMIA, D.A. Wilkinson*, T.K. Saylor, M.K. Mizicko and P.N. Shrivastava, Allegheny-Singer Research Institute, Pittsburgh, PA 15212

We have constructed a simple "adiabatic" calorimeter for the purpose of measuring total energy delivery from microwave antennae. This device has a volume of 270 c.c. and is filled with 0.9% saline. Temperatures are measured with a calibrated thermistor before and after the application of power, equilibration occurring within 2-3 seconds. Several types of antennae (BSD, Clini-Therm and Cheung) have been evaluated at different depths of insertion. Our data show that this technique is a simple, quick means of testing the usefulness of an antenna prior to hyperthermia treatment.

Supported in part by NCI contract #N01-CM-37512.

MP12.9

Digital Enhancement of Treatment Verification Films using a low cost video digitizer with a personal computer. Edward Mok*, Cancer Therapy & Research Center, San Antonio, Texas and John Feldmeier, D.O., The University of Texas Health Science Center at San Antonio.

Digital image processing can be used to improve the image quality of radiotherapy treatment portal films. However most of the existing digital enhancement systems require expensive video digitizers and computers, which prevents them from being broadly used by any treatment center. Recently low cost video digitizers with high resolution have become readily available for use with personal computers. A video digitizer manufactured by Matrox Electronic Systems Limited is used here. It can produce up to 1024 x 1024 pixels resolution with 256 gray levels, with "real time" digitizing capabilities. Software was developed to perform edge enhancement, histogram equalization, low and high frequency filtering and other methods of enhancement. The images could also be stored so that anatomical landmarks as well as field outlines can be compared with different simulation and treatment days. Examples of enhanced images are presented.

MP13.2

Development of 430MHz Microwave Heating System with Lens Applicator for the deep seated tumor treatment,

M.Kikuchi¹*, Y.Nikawa², T.Arioka³, T.Yoshida³, T.Terakawa³ and T.Matsuda⁴,

1. National Defense Medical College, Saitama, Japan.
2. National Defense Academy, Kanagawa, Japan.
3. Tokyo Keiki Co., Ltd, Tokyo Japan.
4. Tokyo Metropolitan Komagome Hospital, Japan.

For microwave hyperthermia, it is difficult to deposit electromagnetic(EM) energy deep in the tissues. In this paper, we have newly developed the lens applicator based on our previously reported lens technique which can deposit EM energy in the lossy medium with the convergent effort of radiated EM field, and the microwave heating system(HTS-100) operates at 430 MHz. This system consists of the compact high power unit (solid state type, 500W), the lens applicator, the multipoints temperature measurement unit, the cooling unit and the control unit which installes the calculations of thermal dose, abnormality detections and automatic safety stop. We have also carried out the experiments on heating both an Agar phantom and the miniature pigs to evaluate the temperature distribution and control performance. These results show that the heating depth of approximately 60mm was obtained, which implies great capability in clinical use.

MP13.3

REGIONAL HEATING APPLICATORS: CHARACTERIZATION IN PHANTOMS, A.M. Di Nallo*, L. Begnozzi, G. D'Ermo and M. Benassi, Regina Elena National Cancer Institute, Rome, Italy.

The cytotoxic effect of heating and the enhancement of the radiotherapy effectiveness combined with hyperthermia has favoured the development of technology for loco-regional treatments.

For a better choice of hyperthermic treatment technique, measurements have been carried out, in order to characterize two different units: a couple of capacitive electrodes working at 13.56 MHz (M.M.E.) and a waveguide TEM working at 27 MHz (Aeritalia). The phantoms used were built using compositions suitable to simulate tissues dielectric constant and electric conductivity at the frequencies of interest. Measurements were carried out to investigate the heating homogeneity and the possible existence of disperse fields and hot spots.

These two different heating techniques are used in our Institution for pelvic tumors treatments.

MP13.4

The Use of Double Node Microwave Antennae for Simultaneous Intraoperative Interstitial Hyperthermia (IOHT) and Intraoperative Radiation Therapy (IORT) with Electrons. G.C.King, M.Sc.*, R.Nibhanupudy, M.Sc. J.Smyles, M.D., A.L.Goldson, M.D., E.Ashayeri, M.D.

The dosimetry problems, because of the presence of double node antennae and nylon flexiguide in the radiation field are discussed. The solution will help to eliminate the use of numerous single node antennae for uniform heat distribution. It is essential to investigate these problems to insure an uniform heat and radiation distribution during the use of simultaneous Intraoperative Hyperthermia (IOHT) and Intraoperative Radiotherapy (IORT) for primary and recurrent tumors.

The findings presented are based on observations of a 915 MHz microwave field used to maintain a temperature of 44°C for 30 minutes while 6,9,12,15, or 18 MeV electron beam.

MP13.5

NEW INTRACAVITARY ANTENNA ARRAY FIXTURE, Thomas R. Canfield, Ph.D.* and Anne McCall, M.D., Loyola University of Chicago, Stritch School of Medicine, Maywood, IL and Edward Hines Jr. Hospital, Hines, IL.

A new fixture has been designed for introducing a hexagonal array of 915 Mhz coaxial microwave antennae into intracavitary space. The antennae are inserted into closed end catheters that are mounted in grooves parallel to the axis of a 1 cm diameter lucite rod. In one configuration all six antennae junctions are in a plane orthogonal to the rod. The rod has a telescoping mechanism that permits three alternating antennae junctions to be repositioned to elongate the energy deposition pattern. Normally pairs of antennae would be activated together. The device has been tested in vivo in the dog Larynx. These results and phantom data will be presented.

MP13.6

Low frequency I¹ Applicators for localized Hyperthermia, G.Banci, C.Franconi*, C.A.Tiberio and L.Raganella, II Univ. of Rome, Via O. Raimondo, 00173 - Rome, Italy

A family of 27 MHz hyperthermia applicators of innovative design have been developed, that provide almost uniform heating in pseudo axial symmetry body segments with the highest symmetry congruence. They have a potential use in regional hyperthermia that can be circumscribed with ring electrodes. Two implementations will be presented, i.e. the active ring electrode pair and the Toroidal Transformer systems, also working at 95 MHz, at which frequency axial focusing is exhibited. Results will be shown in which these devices provide localized heating at intermediate depths also in combination with inductive devices such as the Twin Dipoles and the open-mode Toroidal Transformer to form an hybrid type of applicator.

70

MP13.7

TARGETING OF CANCER CHEMOTHERAPY BY MICROWAVE IRRADIATION, Naoki NEGISHI*, Yasuhiko TOMITA, Makoto KIKUCHI, Yoshio NIKAWA¹, and Fumiaki OKADA¹, Dept. of Med. Eng., Natl. Defense Med. College, Saitama359, JAPAN., ¹ Dept. of Elec. Eng., Natl. Defense Academy, JAPAN.

In order to develop a temporal and spatial drug-administration method using physical actions, a basic research was made on the anticancer drug delivery system using microwave in the range of 430-MHz band. A physical-targeting method which achieves a localized drug-administration by selective irradiation of microwave is proposed in lieu of conventional biochemical-targeting method. When irradiated with 433-MHz microwave(MW) to the polymeric prodrug of methotrexates coupled with biodegradable poly(hydroxypropyl)-L-glutamine (PHPG), its temperature rise was higher than that of neutral PHPG. Polyelectrolytes which showed large values of the relative loss factor(ϵ'') were easy to generate heat by 433-MHz MW irradiation. When a strong polyelectrolyte(PE) was injected into the phantom simulated to muscle tissue in value of ϵ'' , it was confirmed that the PE was more heated than the phantom by external MW irradiation. A localized drug-administration induced by selective microwave irradiation, that is, a physical targeting can be expected if the macromolecular prodrug in polyelectrolyte system is utilized.

MP13.9

CLINICAL INTEREST OF RIDGED-WAVEGUIDES OPERATING AT 27 Mhz FOR DEEP HEATING. C. Marchal, P. Bey, and P. Aletti*, Dept. of Radiotherapy, Centre Alexis Vautrin, Vandoeuvre les Nancy, FRANCE.

A complete hyperthermia device named HPRL 27 has been developed in collaboration with SAIREM Ets (Lyon, France). The second generation of material is proposed for the treatment of pelvic tumors. A 27.12 Mhz generator of 1400 watts drives a bended water-filled waveguide of 150 Kg. This applicator is held by a motor-powered mechanical arm. The effective aperture of this waveguide is greater than 400 cm². The penetration depth was found about 8 cm but using a strong cooling of the skin the maximum heating can be dropped between 3 and 6 cm deep. Technical, physical and experimental results on "tissue-equivalent" phantoms and on animals are given. Our five years clinical experience on 54 tumors treated is presented.

MP13.8

RF Inductive Hyperthermia for Deep Seated Tumor, H.Ikeda, M.Fujii, K.Sakamoto, H.Kanai*, Sophia University, Chiyoda-ku Tokyo, Japan 102

When a cylindrical body is heated by a surrounded coil, temperature rise in the superficial part of the model is very large, but is very small in central part of it. We have already reported about a new coil system for induction heating. As the results, it was shown that tumors seated at anywhere in body can be heated by this new method.

Temperature rise distribution in head cross-section are calculated, when this new type coil is applied to brain. Both ultrasound heating and RF capacitive heating methods can not be applied to brain because of the skull. However, new our method be applied. Experimental results obtained from phantom experiment are discussed together with calculated results. Phantom is homogeneous cylinder made of agar solution which has almost the same electrical properties as that of human muscle.

We applied various type coils to the phantom. Frequency and power are 13.56 MHz and about 500w, respectively. After heating, temperature rise are measured by a small thermistor probe. Hot spot is observed in the central part of phantom. Experimental results agree well with calculated results. If we cool the superficial tissues, deep seated tumor can be heated well by this method. The effect of inhomogeneity and blood flow change on temperature rise distribution by this method are also discussed in this paper.

MP13.10

A Study of QA program of High Energy Therapy Machines in The Republic of China, Mann Tchao Wang* and Shiao Chyan Chang, National Yang Ming Medical College, Shih-Pai, Taipei, Taiwan, R.O.C.

High energy therapy machines are widely spreading in this country and the trend of use are rising rapidly. Since very few medical physicists on the island, there are some problems in maintenance and QA works. These may lead to potential harms to the patient, employee and general public. A task group was formed by the Atomic Energy Council to conduct a survey to review the situation and tried to find a solution. The over-all result shows that the most serious problems were the dose rate and the field size congruences but the radiation safety survey reveal to be highly satisfactory.

A postal method for monitoring the QA programs by using LiF and films was established to improve the problems. The dose rate and beam profile can be monitored by LiF powder. Cross hairs, field congruence, beam flatness and symmetry were measured by one film. The mechanical isocenter and radiation center measured by a second film. A special phantom was made to carry out the task. It was proved a highly satisfactory way to monitor the hospital in remote area.

MP13.11

AN EVALUATION OF A QUALITY ASSURANCE PROGRAM FOR MONITOR UNIT CALCULATORS, R. A. Dahl, E. C. McCullough, D. E. Mellenberg*, Mayo Clinic and Mayo Foundation, Rochester, Minnesota.

Computerized methods are frequently being used for computing monitor units or timer sets. These programs can be developed by the local institution, be "imported" from outside or be part of a commercial treatment planning package. An evaluation and quality assurance protocol for monitor unit calculators was developed to systematically compare and check results from MU calculators. The results from this testing revealed that errors in MU calculators are possible when they are tested over a wide range of field sizes (including blocked fields), SSDs and depths. Our protocol presents a minimal program to assure proper calculator accuracy and software integrity. A key element of any protocol is the designation of acceptability criteria since meeting these criteria can have medical-legal implications. Our results suggest that calculators be checked against hand calculations, and this be permanently documented. Monitor unit calculation program maintenance will be outlined in the light of liability and software corruption concerns.

MP13.13

Criteria for acceptance testing and commissioning of modern multimodality linear accelerators, Jatinder R. Palta* and N. Suntharalingam, Department of Radiation Therapy and Nuclear Medicine, Thomas Jefferson University Hospital, Philadelphia, PA 19107

The acceptance testing, commissioning and quality assurance of modern multimodality linear accelerators have become more complex. These machines offer dual photon and multiple electron energies, independent or asymmetric motion of jaws, electron and photon arc therapy and multiple segment therapy. Digital logics and microprocessors are also incorporated into accelerator control and monitoring to handle these complex functions. The 'Code of Practice for x-ray therapy linear accelerators'¹ in current use is not adequate for these accelerators. The inadequacies are in the following areas: (1) determination of radiation isocenter with independent jaws, (2) field size dependence for asymmetric fields, (3) beam flatness requirements for multiple photon beams, (4) beam calibration, (5) measurement of anomalous radiation leaks, (6) software and hardware interlock checks, and (7) acceptance and quality assurance of computer software. Criteria and methodology for acceptance testing, commissioning and quality assurance of modern accelerators are presented.

¹Med. Phys. 2, 110-121 (1975)

MP13.12

A Computerized Quality Assurance System, Väänänen A.*, Puurunen H., Kuopio University Central Hospital, SF-70210 Kuopio, Finland.

A computer aided dosimetry system is constructed for routine measurements, documentation and analysis of the results of quality assurance (QA) in radiotherapy. A multimode electronic unit, controlled by a desktop computer, consists of two precision electrometers, programmable voltage supply, a disc station for data communication and stepper motor controller for waterphantom and densitometer. Software consists of absorbed dose and dose distribution measurement programs, QA-analysis and data documentations. Using the electrometer readings and stored calibration and correction factors the absorbed dose can be calculated. The system controls the realization of the QA-programs and messages about unaccepted values. All the data of QA measurements are saved by computer where they are easily obtained. Written instructions about various measurements are not needed. Because the time-consuming analysis, documentations etc. are not needed, the system will help the dosimetrist in daily routine.

MP13.14

Experience in the Acceptance Testing and Use of a Computer Controlled Therapy Linear Accelerator, M.S. Weinhaus*, J.A. Purdy and C.O. Granda, Washington University School of Medicine, St. Louis, MO, USA.

In August, 1987, a Varian Clinac-1800 linear accelerator was retrofitted with the vendor's computer controlled console. In light of recent past events involving computer controlled therapy linear accelerators, extraordinary measures were taken to assure the safe operation of the entire interlock and computer systems. During acceptance testing, the traditional machine acceptance parameters were measured. In addition, however, each interlock was tested as close to the fault/signal source as was safe and practical. Finally, several days were spent trying to force the console computers out of their defined modes and into indeterminate or dangerous modes. Details of the successful acceptance testing and the results of one year of operation will be presented.

72

MP13.15

Longterm Variation in Beam Symmetry as a Function of Gantry Angle for a Computer-Controlled Linear Accelerator, M. Loyd*, J. Laxton and R. Lane, The University of Texas Medical Branch, Department of Radiation Therapy, Galveston, Texas 77550.

Longterm beam symmetry measurements have been performed on a Philips SL20 dual energy computer-controlled linear accelerator. Symmetry in both the radial and transverse axis of each x-ray beam was monitored for eight gantry positions. In the radial or gun-target axis of the beam, both computer look-up tables and servo systems are required to maintain x-ray beam flatness and symmetry with gantry angle. In the transverse or A-B axis only the look-up tables are used. The look-up tables record beam steering current settings used to produce a flat, symmetrical beam. These settings are recorded every 3 degrees for 366 degrees of gantry rotation. Recorded settings are used for each of the adjacent degrees of gantry angle positions as well as for the tabulated degree of gantry angle. These measurements were undertaken to evaluate the effectiveness of this beam steering system. Evaluation of the data shows that careful set-up procedures result in x-ray beams in which fluctuations in symmetry as a function of gantry angle are within $\pm 1.5\%$. However, day to day instabilities produce a total overall variation in beam symmetry which is on the order of $\pm 2.0\%$. Comparable data obtained from a Clinac 6/100 and a Clinac 4/100 linear accelerator will also be presented.

MP13.17

A Computerized Digital Video System For Contour Acquisition and Compensator Design, J.W. Andrew*, J. E. Aldrich, M. E. Hale and J. A. Berry, Cancer Treatment & Research Foundation of Nova Scotia and Dept. of Radiation Oncology, Dalhousie University, Halifax, N.S., Canada. B3H 1V7

Recent advances in computer and video technology have enabled significant advances in the field of surface topography measurement. This paper will describe a system for the design radiotherapy photon beam compensators. The system obtains contours using a fan-shaped light beam and a video camera which are mounted on a tray which fits into a radiotherapy simulator. Transverse contours are obtained from one digitized video image or, in the case of opposed fields, from two or more image frames taken at different gantry angles. Entire surfaces are measured by scanning the bed longitudinally and analyzing a number of images. Posterior surfaces are obtained by scanning a mold. A printer produces a template for making the compensator from sheet lead. The cost of the hardware needed to build the system was approximately \$10,000 (U.S.).

MP13.16

A Computerized Tissue Compensator System. H.I. Amols*, Columbia Univ., L.E. Reinstein and B.C. Baldwin, S.U.N.Y. at Stony Brook, New York, U.S.A.

A teletherapy tissue compensator system is described. Patient contours are obtained by sequential tracings with a hand held 3D magnetic sensing wand. Contours are analyzed and displayed on-line by the computer, with automatic 3D surface smoothing. Menu driven options allow for contour editing, isometric display, gantry, and collimator rotations. Compensator molds are cut into styrofoam templates via a computer controlled milling machine, with the user specifying scaling factors for compensator size. Molds can be filled with high density cerrobend alloy, or a special medium density gypsum stainless steel mixture (useful for tissue deficits of up to 5cm). Mounting insets are milled into the styrofoam template to permit accurate mounting on standard blocking trays. Patient contours can be obtained in a matter of minutes with this system, with compensator fabrication performed off line. A detailed system description, plus sample isodose profiles will be presented.

Huestis Corp., Bristol, R.I., U.S.A.

MP13.18

CT-Based Conformational Bolusing Technique for Electron Beam Therapy. F. Bagne*, L. Low, L.A. Fadell, Medical College of Ohio, Toledo, Ohio

In radiation therapy with electron beams a bolus is often used to compensate for surface irregularities or to conform the isodose distribution to the shape of the treatment volume. Because of the three dimensional nature of the problem, a clinically satisfactory bolus has not as yet been fully developed. We have developed a highly accurate patient-specific computerized bolus for this purpose. The system utilizes CT slices of the pertinent region under treatment position. Initially, the area to be treated is marked on each slice. These data along with other anatomical information are then entered into a VAX-780 computer. A computer program converts the sagittal data into bolus information in axial, or coronal planes. The number of bolus planes is determined by the thickness of the bolus slices and by the bolus material. This paper presents the design of the bolus system; describes the computer program used for the process and illustrates the steps necessary for computation and fabrication of the conformational bolus. Finally, the clinical application of the system is discussed by presenting actual cases which have utilized the system over a one-year period.

MP13.19

Dose Conformational Transmission Blocking
Technique, F.R. Bagne*, D.G. Bronn and L.A. Fadell, Medical College of Ohio, Toledo, Ohio

Standard cord blocks are generally used in lung cancer treatment after the spinal cord reaches its maximum tolerance dose. This technique has the disadvantage of providing a lower-than biologically-adequate daily dose to the mediastinal strip. Alternatively, posterior cord transmission blocks of a fixed thickness have been used to maintain a higher fractionated dose over the course of treatment. The latter technique neither corrects for the geometry of the cord nor for the patient's surface contour. This paper presents a conformational transmission blocking technique to compute the thickness of the transmission block along ray-lines and to provide a uniform fractionated dose across the entire spinal cord. Initially, a series of CT scans are taken over the region of interest. The location of the spinal cord on each slice is entered into a VAX-780 computer via a digitizer. A computer program combines the anatomical information and the measured transmission data for megavoltage photons to generate a demagnified blocking pattern. A standard block-cutter is modified to produce the necessary conformational transmission block. The final Cerrobend block is attached to the tray along with the field blocks. This paper presents examples of the results and discusses its clinical significance.

MP13.21

Comparison of Penumbra between Focussed and Straight Edged Blocks - Implications for Multileaf Collimators (MLC), P. Biggs*, J. Capalucci and M. Russell, Mass. Genl. Hosp., Boston Ma USA

The penumbra for straight edged (SE) blocks has been compared with that for the collimator jaws (focussed blocks) of a 10MV linac for square fields at three depths by measuring the distances between the 50% and the 80%, 90% and 95% doses respectively. Beam profiles were taken with a water phantom scanning system using 1.5mm diam. diodes. The results show that at a depth of 2.5cm, d_{max} , the penumbra is worse for SE blocks when field sizes exceed 15cm at the 80% and 90% dose and 20cm at 95%. At 11cm depth, this 'break even' field size remains the same for 80% whereas at 90% the penumbra differs only for fields greater than 30cm while at 95% the data overlap. The max. differences in penumbra amount to 2 and 1.5mm for the 2.5 and 11cm depths respectively. At 15cm depth the two sets of penumbra are indistinguishable. Since most clinical treatments prescribe to the 95% isodose or greater, SE and focussed blocks are equally effective except close to d_{max} . Thus the mechanical complexity of an MLC could be significantly reduced for a small sacrifice in penumbra. Further studies show that SE blocks with either a 1mm or a 0.5mm offset at mid-block height do not noticeably degrade the penumbra.

MP13.20

Comprehensive Study of Effective Attenuation Coefficient for Use in High-Energy Photon Treatment Planning, F.R. Bagne*, N. Samsami, S. Hoke, Medical College of Ohio, Toledo, Ohio

Precision radiation therapy with high megavoltage photons requires a uniform dose throughout the treatment volume. In compensating for the missing tissue, one area which has been neglected in the past is the region of buildup. Clinically, this region is of particular importance when the involved tissues, such as lymph nodes, are located within a few centimeters from the skin. We have undertaken a comprehensive study to determine the adequacy of a single effective attenuation coefficient, μ_{eff} , for a given compensating material for use in calculating the missing tissue. Measurements were made in a tissue-equivalent phantom using 10 MV photons (Varian Clinac-18). The compensating material used was polystyrene. Our results indicate that a single μ_{eff} does not provide the desired accuracy over the clinically-used range of field sizes, depths and missing-tissue thicknesses and that μ_{eff} can vary by as much as 70% over the region of buildup. This paper presents the specific variation of μ_{eff} with depth, field size and missing-tissue thickness and recommends a technique for minimizing the number of μ_{eff} values required for treatment planning purposes. Application of the results to computer-assisted tissue compensation techniques is also discussed.

MP13.22

PENUMBRA GENERATORS FOR CLINICAL ELECTRON BEAMS, R. G. Kurup*, S. Wang, and G. P. Glasgow, Loyola-Hines Radiotherapy, Loyola University Medical Center, Maywood, Illinois 60153

Clinical electron beams used in radiotherapy have narrow penumbra. This makes abutment of these fields extremely difficult. It is desirable to increase the width of the penumbra at the region of abutment of the fields. One way of achieving this is to introduce narrow, thin plastic strips or wedges along the edge where the penumbra is to be enhanced. The effect of such penumbra generators were studied. The influence of the width, thickness, and shape of such penumbra generators on the beam penumbra and their role in field matching for electron beam energies from 6 MeV to 18 MeV will be presented

14

MP13.23

Limitation of "Clear-Pb" as a filter to reduce electron contamination produced by high energy x-ray beams., S. Guru Prasad*, K. Parthasaradhi, Young Lee, Rajesh Ruperal, Rafael Garces, Evanston Hospital, Evanston, IL 60201.

The dose in the build-up region of high energy accelerator x-rays increases whenever blocking trays are used. The amount of electron contamination depends not only on the collimator and the flattening filter but also on the field size. It is also dependent on the x-ray energy. The use of electron filters are among the suggested methods to reduce this contamination. Several filter materials have been previously studied. It appears that the previous studies have not examined the field size in limiting the usefulness of the filter. We have studied "Clear-Pb" as a filter to reduce the electron contamination produced by 6 and 10 MV x-rays generated by Clinac-1800 with special emphasis on the field sizes over which it can be used. This tray material can be used up to $25 \times 25 \text{ cm}^2$ for 6 MV x-rays and up to $20 \times 20 \text{ cm}^2$ for 10 MV x-ray beam.

MP13.25

Clinac 4 Treatment Accessories Revisited

Wendell Lutz* and Jeff Williamson, Dept. of Rad. Oncology, Univ. of Arizona, Tucson, Arizona.

Because of the short 80 cm SAD of the Clinac 4 accelerator, treatments such as tangential breast and certain head and neck cases involving oblique angles coupled with the use of cerrobend blocks, wedges, and/or compensators are specially difficult to treat. We have designed a compact wedge-compensator-block holder that maximizes the distance from isocenter to the most distal accessory. Most notable is the mounting of the blocks "side-down". This removes lateral protrusions in addition to saving considerable space when the gantry is rotated from one field to another with no blocks in place. For head and neck cases a rigid, long, narrow extension was designed that attaches to the end of the couch. The head rests on this extension and is immobilized with a thermoplastic material molded to the patient's surface and attached to the extension. This extension is constructed of 0.050" thick aluminum rolled into a half-moon cross-section so that posterior and posterior oblique treatment beams are attenuated by less than 5% by the extension. Remounting the wedges, rotated 90° from their original position, proved to be more convenient both for treatments and block mounting. In addition, when blocks are used with wedges, the blocks no longer have the possibility of "falling out" of their slots at certain gantry angles.

MP13.24

Standard Thorax Compensators for AP-PA Treatments
Wendell Lutz* and Jeff Williamson, Dept. of Rad. Oncology, University of Arizona, Tucson, Arizona

Dose delivered by first course AP-PA portals to lung and esophagus tumors is generally limited by cord tolerance. Because of the long fields involved separation differences between superior and inferior borders may be as large as 14 cm. For a 6 MV photon beam this results in cord doses 13% above and 7% below the dose at midline on the central axis. We have designed a set of four, anterior field, standard 1 dimensional compensators for our 6 MV and 10 MV linacs. For over 80% of the cases, one of these compensators fits sufficiently well that cord dose inhomogeneity is limited to 3%, eliminating the need for customized compensation. The compensators, which accommodate $30 \times 30 \text{ cm}^2$ fields, are made from 0.031" thick copper sheets mounted to aluminum trays that slide into the wedge slots. Each compensator is designed to compensate a differently oriented sagittal contour each with a 41 cm radius of curvature. The contour orientations are defined by the angle a line, tangent to the contour at the central axis, makes with the horizontal plane. The angles used are 15°, 20°, 25°, and 30°. To quickly and quantitatively evaluate the fit of a standard compensator to a particular patient, transparent overlays of the lateral view of these "standard contours" are compared with a sagittal contour drawn from measured patient separations.

MP13.26

Dosimetry of Eye Shielding Block

F.J.Lin*, H.H.Chen, T.C.Chen, J.H.Hong,
Department of Radiation Oncology, Chang
Gung Memorial Hospital, 199, Tung Hwa
North Road, Taipei, Taiwan, R.O.C.

Lens is very sensitive to radiation and cataract can be induced even by relatively low dose of radiation. In treatment of head and neck tumors, shielding eye block is used frequently and variation in distance between the eye block and the eye surface can affect the dose to lens remarkably. Different divergent blocks were used to find out the optimal distance of eye blocks for Co-60, 6MV and 10MV x-rays from linear accelerators and to evaluate the dose distribution under eye block. PTW thin window parallel-plate ionization chamber was used in the measurement and all data were acquired in polystyrene solid phantom. The eye blocks have a surface area with diameter of 2 cm at the distance of irradiation. Eye block at optimal distance can reduce the dose to lens from 17% to 7% for 10MV and 6MV linear accelerator, from 14% to 8% for Co-60 comparing to block on the regular tray. The optimal distance is 0.9 cm, 1.4 cm and 6 cm for 10MV, 6MV and Co-60 respectively. When block diameter is larger than 2 cm, the dose to lens is independent of block size.

MP13.27

Commissioning the NEC Linear Accelerators
F.J.Lin*, C.S.Chen, R.H.Lan, C.P.Tu, H.H.
Chen. Department of Radiation Oncology,
Chang Gung Memorial Hospital, 199, Tung
Hwa North Road, Taipei, Taiwan, R.O.C.

Three NEC linear accelerators, two in Lin Medical Center and one in Kaohsiung Medical Center, have been installed recently installed in Chang Gung Memorial Hospital. Commissioning procedures included the acceptance test, radiation protection survey, the collection of dosimetry data, and acquisition and assimilation of patient treatment aids. When the machine installation was completed, the acceptance test were performed by the NEC engineers first and must be performed again by hospital physicists to verify the specifications and characteristics of the facilities. It included safety, mechanical, digital, optical, dosimetry and laser systems, then measurements of dosimetry data were made with thin wall parallel plate chamber in water phantom and cylindrical chamber in solid phantom. Dose calculation is by Task Group 21 method in our department. After commissioning procedure, quality assurance program were initiated and performed for all facilities. Specified commissioning procedures and quality assurance program are essential for maintaining high quality of radiation therapy.

MP13.29

Manual For the Use High Energy X-Ray Therapy
Linear Accelerator: Clinical and Physical
Aspects, E. Gaona*, V.M. Tovar, Depto. de Física,
Instituto Nal. de Cancerología-Universidad Autónoma
Metropolitana Xochimilco, San Fernando 22, 14080 México,
D.F., México.

The purpose of this manual is to present appropriate material for the physicist and radiotherapist in clinical and physical aspects, including historical summary, criteria for selection of linear accelerators for radiation therapy, acceptance and periodic test, high energy X-ray dosimetry, monitor unit calibration and monitor unit calculation in treatment planning. Furthermore other topics related to radiation therapy.

This Manual covers the basic needs of physics radiation therapy and clinical applications in teaching.

This Manual was published in Spanish by National Cancer Institute of México, including a brief summary in English.

MP13.28

In House Repair of Co-60 Teletherapy Units.
Amendment Requirements, Peter R. Almond, Ph.D.,
Brown Cancer Center, University of Louisville,
Louisville, Kentucky 40202 and Kenneth R.
Hogstrom, Ph.D. The University of Texas M.D.
Anderson Hospital, Houston, Texas 77030

In April of last year the Nuclear Regulatory Commission issued information notice number 87-18 "Unauthorized Service on Teletherapy Units by Non-Licensed Maintenance Personnel." The outcome of this notice is that only very limited service can now be done by "in-house" staff on these units. Although not a new regulation by the NRC, it does represent a stricter interpretation of the existing standard license conditions. Although the notice did not address the question of how licensees were to get their units repaired, it did state that "Licensees who desire to have these operations performed by qualified "in-house" staff members who are not authorized by the NRC or an Agreement State must request an amendment to their license." In order to test this provision, a license amendment was submitted to the appropriate authorities in Kentucky. The progress of this amendment and its content will be discussed and compared to guidelines for repair on Cobalt-60 units prepared by the staff at M.D. Anderson Hospital in Texas by request of the Texas Bureau of Radiation Control.

MP13.30

Single Board Computer Upgrade to a
Simulator Field Size Display,
J.J. Szabo & M.K. Sanford,
Saint John Regional Hospital,
Saint John, N.B., Canada.

When a Treatment Simulator was given a major overhaul rather than purchase a new one, a certain component could not be purchased because the parts were no longer manufactured. Lack of this component rendered the existing analog display system useless. This display indicates the treatment field parameters for subsequent patient radiation therapy - a vital loss. A completely new digital display system was therefore designed to replace the old analog system. This system consists of a 20 digit vacuum fluorescent digital display controlled by a central single-board computer. Features of this system include: low cost of parts, quick and easy calibration, transparent to Simulator Operator, and a self checking routine that notifies the Operator of calibration errors. In addition, the computer can be optimized in processing speed to achieve minimum response time to changing inputs while also minimizing the input sensitivity to random noise.

MP13.31

Electron Beam Energy Monitoring using a Staircase Filter, P. O'Brien*, R. McVittie, B.A. Gillies, Toronto-Bayview Regional Cancer Centre, Toronto, Ontario

The matrix dosimeter (1) is a computer driven square array of 49 ionization chambers spaced at approximately 3 cm. A polystyrene staircase filter in conjunction with the matrix dosimeter is used to monitor electron beam energy in addition to the normally monitored parameters output, flatness and symmetry. The staircase filter is constructed as a series of 25 varying thicknesses of polystyrene each of which shadows a different pair of ionization chambers. The ionization readings are divided by the readings from an unshielded exposure on a one-to-one basis to correct for field non-uniformity. Integration of the results yields a number which is independent of electron beam flatness or symmetry but directly proportional to mean beam energy. This technique can reliably detect energy shifts of less than 2% and is being used for nominal beam energies from 7 to 25 MeV. Data presented will demonstrate the software used and the precision and accuracy of the technique.

(1) MARTELL et al Int J Rad Onc Biol Phys 12, 2 pg 271, 1986

MP13.33

Production of Photoneutrons in a Lead Shield by High Energy X-Rays, P. McGinley*, K. Long and R. Kaplan, Emory Clinic, 1365 Clifton Road, Atlanta, GA 30322, USA

Lead and other high Z metals are occasionally used in place of concrete to fabricate primary barriers for medical accelerators. In this work measurements of photoneutron levels behind lead shields irradiated with high energy x-ray (20 to 45 MV) beams were made. Neutron fluence values of the order of 7×10^6 n/cm² per unit absorbed dose (Gy) of x-rays delivered to the point where the beam enters the shield were observed behind the lead barrier. By measuring the change of neutron fluence as a function of the lead thickness it was found that the majority of the photoneutrons were produced in the first 2.5 cm of the shield. It was observed that when 7.6 cm of borated polyethylene was added to the front of the lead shield no reduction of the neutron fluence behind the lead barrier was detected. Based on this work it was concluded that a radiological health hazard can be produced by the replacement of a concrete barrier with lead.

MP13.32

Photon Energy Spectra of X-ray Beams from Medical Electron Accelerators, E.J. Born, Dept. of Medical Radiation Physics, Inselspital, University of Berne, CH-3010 Berne, Switzerland

The knowledge of photon energy spectra of X-ray beams from medical accelerators is essential for certain dose calculation algorithms, for investigations of treatment machine head design, for the calculations of stopping power ratios etc.. A Monte Carlo program using the EGS4 code system has been developed, which allows the simulation of the radiation transport from the electron target through the treatment machine head to the patient surface, where particle charge, position, energy and angle of incidence are sampled. Currently, photon beams have been simulated from 8 to 45 MV produced by two different accelerators (SL75-20, Philips; Asklepitron 45, BBC). Energy, angular and spatial distributions of the photons were determined and the electron contamination of the beams was evaluated. For comparison to experimental data depth dose curves were calculated resulting from the simulated photon spectra and from the electron contamination of the beam. Problems of treatment machine head design can be investigated e.g. by keeping track of the last interaction point for each photon arriving at the patient surface. Work is in progress to use the photon energy spectra as input to a convolution algorithm for photon beam dose calculations and to experimentally determine these spectra by detecting the Compton electrons with a magnetic spectrometer.

MP13.34

Incorporation of Emerging Technologies into the Design of a Radiation Oncology Facility: Problems Encountered, J.D. Bourland*, M.A. Varia, G.W. Sherouse, P.E. Stancil, L.D. Stanley, E.L. Chaney, H.L. McMurry, J.E. Tepper. Radiation Oncology, University of North Carolina, Chapel Hill, NC 27599-7510.

We have recently specified an academic radiation oncology facility which includes 3 megavoltage treatment rooms, a combined high dose rate remote afterloading and minor procedures suite, 2 hyperthermia rooms, an isotope storage room, a simulator, a CT room (used for simulation and treatment planning), and, in anticipation of a highly computerized department, an expansive infrastructure for data communications. Merging this collection of existing and emerging technologies imposed unique demands on the design team. Special problems included optimization of a floor plan comprised of multiple diagnostic and treatment functions and design and integration of a coherent, facility-wide data communications system. Considerable effort was required to effectively communicate these varied requirements to the designers. We found careful pre-planning and early education of hospital plant engineering and the architectural firm to be essential. Our design philosophy, physical layout, data communications network, and practical suggestions for the physicist involved in the design of a treatment facility incorporating new technologies will be presented.

MP14.1

A Comparison of R_p - and R_{50} - Values with Measured Energy Spectra of Electron Beams from Medical Accelerators, L. André* and H. Neuenschwander, Dept. of Medical Radiation Physics, Inselspital, University of Berne, CH-3010 Berne, Switzerland

The most probable energy $E_{p,0}$ and the mean energy \bar{E}_0 at surface are parameters of the energy spectra of medical accelerators. In clinical routine these parameters are evaluated using R_{50} - and R_p - values from depth dose curves or depth-ionisation curves. We have measured the depth dose curves for all energies of the linear accelerator SL75-20 (Philips) as well as the depth dose and the depth-ionisation curves for all energies of the betatron Asklepitron 45 (BBC). The energy spectra are given by an integration over all angles of the electrons fluence in the beam. We have measured these energy spectra with a magnetic spectrometer. The relationship between electron energy and field strength B in the homogeneous part of the magnet include, beyond universal constants, only the product $R * B$ (R is the virtual radius of the trajectory). As long as the measurement of the magnetic field is linear we can use for all energies a constant for the virtual radius multiplied by the absolute calibration factor of the field measurement for the evaluation of the electron energy.

MP14.3

TE Scintillation Detector for High-Energy Photon and Electron Beam Dosimetry, A.S. Beddar*, P. D. Higgins and C.H. Sibata

A minimally perturbing Tissue-Equivalent Scintillation detector has been developed for high-energy beam dosimetry. The detector is composed of a miniature plastic scintillator probe (1.4 mm diameter and 3 mm long) connected to a radiation-resistant fiber optic bundle optically coupled to a 10 mm photomultiplier tube in series with a current or charge integrating instrument. The collected current or charge is directly proportional to the dose that would be deposited in the surrounding tissue. Noise levels associated with the radiation response of the selected optical fibers was minimal compared with the response of the scintillator. Radiation damage was found to be negligible and recovery rapid. The reproducibility of the detector for Co-60 was found to be better than 0.2% and its response to be dose-rate independent. The comparison of ionization chamber and scintillation detector measurements for photon and electron beams were in good agreement. Furthermore, the physical dimensions of this detector offer a high spatial resolution, especially when operating in the build-up or penumbra region.

MP14.2

The Influence of beam parameters on percentage depth dose in electron arc therapy, M. Pla, C. Pla *, and E.B. Podgorsak, Department of Radiation Oncology, McGill University, Montréal, Canada.

Rotational or arc electron beam therapy is the modality of choice in treatment of certain large superficial tumor volumes which follow curved surfaces. For a given treatment geometry an angle β can be defined which is uniquely determined by the two treatment parameters: the depth of isocenter d_i and field width w . The characteristic angle β is always smaller than the treatment arc angle. We found experimentally that electron beams with combinations of d_i and w , which give the same characteristic angle β , actually exhibit very similar radial percentage depth dose characteristics even though they may differ considerably in individual d_i and w . Moreover, there is a gradual change in the properties of radial percentage depth dose curves with an increase in angle β . For example, for a very small β the percentage depth dose distribution of the rotational beam is similar to that of the stationary beam; with an increase in β , however, the depth of dose maximum moves towards the surface, i.e., the beam becomes less penetrating, and the surface dose increases.

We will discuss the dependence of the rotational or arc electron beam percentage depth doses on the characteristic angle β and show that the β concept can be used in clinical situations to predict the shape of the percentage depth dose curve when w and d_i are known, or more importantly, it can be used to determine the appropriate w when d_i and the desired percentage depth dose characteristics are known.

MP14.4

Dosimetric Properties of an IORT Applicator System (SOFTDOC) for the Mevatron-80 Accelerator, C.E. Nelson* S.M. Rakfal, R. Cooke, ECU School of Medicine, Greenville, North Carolina.

A custom system for intraoperative electron radiation has been designed that does not require physical "docking" between the patient and the accelerator gantry structure. The system uses clear plexiglas for most key components and two accelerator mounted laser beams for coaxial alignment of the patient-cone axis with the accelerator beam axis. This provides both excellent target visualization and patient-accelerator alignment. A dosimetric study of the sensitivity of this system to slight (1-2°) non-coaxial alignment and non-standard SSD between the patient - fixed electron cone and the accelerator-fixed electron collimator has been completed for a variety of electron beam energies, primary collimator settings, and patient-fixed cones. The results indicate that within clinically acceptable dose variations (+ 10%), this system provides dose distributions which are comparable to fixed docking systems with substantial improvements in clinical set-up time and vastly improved target visualization.

MP14.5

On the Reliability of In Vivo Electron Dosimetry with Semiconductor Detectors, E. Vartiainen, T. Lahtinen*, A. Väänänen, H. Puurunen, University Central Hospital and University of Kuopio, SF-70210 Kuopio, Finland.

Direct measurements of entrance dose from clinical electron beams were tested. The detectors were commercially available semiconductor diodes for photon and electron beams. As compared with the reference geometry the response of some detectors was highly dependent on the direction of irradiation. Furthermore the detectors had a complicated field size dependence. The highest deviations were found for very small and very large field sizes. For non-standard SSD, the inverse square law correction does not hold for tested diodes. The SSD correction factors were different for various detector types and for scattered and scanned electron beams. The study suggests that accurate in vivo semiconductor dosimetry with electron beams is not possible at present without many correction factors.

MP14.7

Relative Output Factors of Irregularly Shaped Electron Fields, Brian J. McParland, Division of Radiation Physics, C.C.A.B.C., Victoria, Canada

The dose output of an electron beam is highly dependent upon the collimation system design, the beam energy and field dimensions. For irregularly shaped fields, the output is also a function of the spatial variation in fluence caused by the shielding and of the degree to which lateral electronic equilibrium is present at the central axis. A method of calculating the relative output factor of an irregular electron field has been developed and is presented. This relative output factor is derived as the product of a weighting factor (calculated from a discrete pencil beam model) and the known relative output factor of the regular field from which the irregular field is formed. The results of calculations are presented and are compared to data measured for a variety of irregular fields at various beam energies.

MP14.6

Parameterization of Total Skin Electron Beams. J.C. Dennett*, L. Antonuk, and R.K. Ten Haken, University of Michigan Medical Center, Ann Arbor, MI 48109.

The calibration of a total skin electron beam (TSEB) for a linear accelerator located in a large treatment room (up to 6 m SSD for TSEB treatments) and equipped with a high dose rate option for 6 MeV electrons (~100 cGy/min at 4.5 m SAD) has recently been completed according to the spirit of the proposed AAPM TG-30 protocol. This set of conditions coupled with the use of a 2.2 m long linear scanner allowed the measurement of TSEB treatment parameters under a variety of conditions using ionization chambers, films and TLD's. The changes in beam uniformity in air, skin dose uniformity on phantom, dose rate at d_{max} in phantom, depth of 80%, 50% and 10% dose, and level of x-ray background were parameterized as a function of SSD for combinations of 6 dual (up plus down) or single (normal incidence) fields both with and without the inclusion of a 1 cm thick lucite diffuser in front of the patient treatment plane. Ultimately, two beams were selected for clinical use (one with and one without diffuser for shallow and deeper penetration). A summary of the measurements, a parameterization of the results, and the process used to select and clinically implement those beams will be presented.

MP14.8

Electron beam dosimetry measurements on the Philips SL-25, Jatinder R. Palta*, K. Ayyangar, and N. Suntharalingam, Department of Radiation Therapy and Nuclear Medicine, Thomas Jefferson University Hospital, Philadelphia, PA 19107

Clinically useful uniform electron beams are generated on the Philips SL-25 using optimal settings of the primary collimators, a dual scattering foil system and new design applicators. The open-sided applicators are intended to properly collimate the beam while the second scattering foil serves as a flattening filter thus not requiring any wall scatter. A comprehensive set of electron dosimetry measurements for the nine available electron energies (4-22 MeV) for different size applicators was made. These measurements include the percentage depth dose, surface dose, isodose curves, field size dependence of machine output at the nominal SSD, output at extended distances, cerrobend shielding effects on depth dose, and leakage radiation from the electron applicators. The impact of this type of applicator design on irregularly shaped electron fields is described along with measurement data.

MP14.9

Isodose Shift Factors for Obliquely Incident Electron Beams, K. Ulin*, and E.S. Sternick, Tufts-New England Medical Center, Boston, MA 02111

It is well known that when electron beams are incident obliquely on the surface of a phantom, the depth dose curve measured normal to the surface is shifted toward the surface. Based on geometrical arguments alone, the depth of the nth isodose line for an electron beam incident at an angle θ should be equal to the product of $\cos \theta$ and the depth of the nth isodose line at normal incidence. This method, however, can cause significant errors in isodose placement for beams at large angles of incidence.

A table of isodose shift factors has been developed from which one may easily calculate the depth of any isodose line for beams at incident angles of 0° to 60° . The isodose shift factors are tabulated in terms of beam energy (6 MeV - 22 MeV) and isodose line (10% - 90%) and are shown to be relatively independent of beam size and incident angle for angles less than 60° . Extensive measurements have been made in a polystyrene phantom with a Capintec PS-033 parallel plate chamber. The dependence of the chamber response on the incident angle of the electron beam has been checked, and the scaling factor of the polystyrene phantom has been determined to be equal to 1.00.

MP15.2

A Convolution Method for Brachytherapy Dose Computation in Heterogeneous Geometries.

J.F. Williamson* and R.S. Baker Dept. of Rad. Oncology, Univ. of Arizona, Tucson, AZ 85724.

Currently-available brachytherapy dose computation algorithms ignore heterogeneities such as tissue-air interfaces, shielded gynecological colpostats, and tissue-composition variations in ^{125}I implants despite dose computation errors as large as 40%. To calculate dose in the presence of tissue and applicator heterogeneities, we have developed a computer code that describes scatter dose as a 3-D spatial integral which convolves primary photon fluence with a dose-spread array. The dose-spread array describes the distribution of dose due to multiple scattering about a single primary interaction site and is precomputed by our Monte Carlo code. To correct for heterogeneities, the primary fluence at each volume element is adjusted for heterogeneities traversed by the primary photons, the dose-spread array is renormalized to reflect the density and composition of the element, and the distance to the point of interest is scaled by the pathlength of the intervening medium. Convolution calculations for ^{125}I and ^{137}Cs point sources in the presence of finite phantoms, air voids and high-density regions have been compared to the corresponding Monte Carlo calculations. Our results show excellent agreement with the Monte Carlo calculations and a gain in efficiency of 50.

MP15.1

Dose Distribution Patterns of some Afterloading Devices. H.-K. Leetz* and G. Wiesen, Institut für Radiologische Physik der Universitätskliniken im Landeskrankenhaus, D-6650 Homburg, FRG.

For measurements of dose distribution patterns around the applicators of afterloading systems a very precise detector support for up to 36 TL-Dosimeters (Harshaw TLD 100 rods) was constructed. The TL-dosimeters are placed in thin polyethylen tubes which are circularly or helically arranged. Fittings for the afterloading catheter are also provided, allowing measurements in planes perpendicular and parallel to the applicator axis.

Dose distribution patterns of some commercially available afterloading systems with ^{137}Cs and ^{192}Ir sources were measured in air and in water. The experimental results are discussed in order to establish a relation between dose pattern, structure of applicator, structure of source and arrangement of sources and spacers. By comparison of dose in air and dose in water build-up factors were evaluated.

Based on the experimental results modifications of a voxel-oriented dose calculation model were studied in order to incorporate a suitable correction method. As a first approach the applicator structure, source structure and source spacer arrangement was transformed into the voxel-array. Physical properties and geometrical aspects are taken into account by an appropriate modification of the radiological path length which then can be applied to the primary component of radiation.

Results of dose measurement and dose computation are demonstrated and discussed.

MP15.3

A Dose Computation Model for Am-241 Vaginal Applicators Including Source-to-Source Shielding Effects, Chang

H. Park, Ravinder Nath* and Christopher King, Yale University School of Medicine, Dept. of Therapeutic Radiology, 333 Cedar St., New Haven, CT, 06510, U.S.A.

Recently, vaginal applicators containing encapsulated sources of Am-241 have been developed for intracavitary irradiation of gynecological cancers (1). A vaginal applicator may contain up to six sources, each source having an activity of 2, 5 or 8 Ci. Since Am-241 sources themselves present a significant amount of shielding, radiation from one source is shielded by the others. A dose computation model for the determination of dose distributions around these vaginal applicators has been developed and tested by comparing the model with dose measurements using LiF TLD in a solid water phantom. The dose computation model takes into account self-shielding and source-to-source shielding effects on both primary and scattered photons. This model has been incorporated into the Theraplan treatment planning system.

(1) R. Nath, R. Peschel, C. Park and J. Fischer, Int. J. Radiat. Oncol. Biol., 1988, in press.

80

MP15.4

Dose Homogeneity in Multiplanar Implants in the Manchester, Quimby and Paris Systems. J. . Paul*, R. F. Koch, P. C. Philip and F. R. Khan. NWCH, 800 W Central, Arlington Heights, Il 60005

Idealized volume implants consisting of three parallel planes have been analysed for dose homogeneity and overall quality for the Manchester, Quimby and Paris Systems for a set of given targets using all the applicable rules of source distribution of each system. Since there are no rigid rules for source plane spacing in the Manchester and Quimby Systems, except those conventionally followed, optimal spacing had to be determined first before comparing them with the Paris system of implants. The parameters calculated for comparison are treatment volume, total activity, integral dose expressed in terms of uniformity index, integral volume that receives a dose rate more than twice the stated value, which have a bearing on the quality of any implant. These values indicate that the Paris system of implants is as good as other systems and generally has an improved value of uniformity index, a parameter that quantifies the quality of interstitial implants.

MP15.6

The Calibration of Sr-90 Beta Eye Applicators with Radiochromic Radiation Detectors, J.A. Sayeg* and R.C. Gregory, Department of Radiation Medicine/Health Radiation Sciences, University of Kentucky, Lexington, Kentucky, 40536.

A radiochromic material which is a solid state solution of hexahydroxyethyl pararosanaline nitrile in a nylon polymer [i.e., thin foil], has been used to determine the surface dose rate and dose distribution of Sr-90 eye applicators. The detectors are rugged, easily handled, have an equivalent response to photons and electrons, and produce high resolution images. They have been found useful for this application due to the high surface dose rates [10-100 rads H₂O/second] and their low sensitivity [approximately 10⁶ rads for an optical density of 1.0]. The foils have been evaluated on a He-Ne scanning laser densitometer with a resolution of 0.3 micron. Comparison with NBS extrapolation ionization chamber measurements indicated surface dose rate agreement to within 5%. The dosimetric properties and clinical use of these sources will be discussed.

MP15.5

A Brachytherapy Programme to Sort the Seed Strands in an Ir-192 Implant, P. Biggs, Mass. Genl. Hosp. Boston, Ma USA

Recent trends in brachytherapy suggest that differential seed loading techniques, either by changing the activity of different seed strands or their duration in the implant are becoming increasingly important. Although many computer programmes exist that determine seed locations based on random seed entry, none of them sort out the individual strands, as encountered, for example, in the case of Ir-192 implants. The present programme uses an algorithm based on the interseed separation and the angle between three successive seeds to identify individual strands from the total list of seeds, thus permitting individual weighting of these strands. This programme has been successfully tested on a series of implants containing from 32 to 142 seeds and varying in complexity. The results show that for plane parallel implants, the interseed spacing is found to be 0.8-1.1cm for a nominal 1cm spacing and 96% of the measured angles are >170° and all are >160°. For implants where the strands are considerably more curved, while the interseed spacing remains the same, only 47% of the angles are >170° and 93% >160°. Moreover, based on these tests, several checks have been incorporated into the algorithm to prevent misidentification of seeds in the wrong strand.

MP15.7

3-D Correlation of CT Eye Anatomy with 125-I Plaque Dose Distributions Using Scleral Markers. R.K. Ten Haken*, D.L. McShan, A.K. Vine and A.S. Lichter, Univ. of Michigan, Ann Arbor, MI 48109.

Using our custom-designed, thin, heavy-alloy plaques, individual 125-I seeds may be localized on plane radiographs taken with those plaques in place. Previous attempts to correlate dose distributions computed from those films with eye anatomy on CT scans (obtained without the plaque due to artifacts) were made by immobilizing the patient and aligning bony landmarks on the films with matching ones on digitally reconstructed radiographs from the CT dataset. That technique has been greatly improved by suturing 4-6 small (1-1.5 mm) barium spheres to the scleral surface of the eye prior to CT. Plaque placement and film localization follow. Dose distributions from the films are now correlated with CT anatomy by minimizing differences in the relative coordinates of those markers as they appear between datasets. A RMS deviation of 1.1 mm in position (5.5% in dose) for 32 markers used in 7 patients has been achieved to date. In contrast, doses calculated to the optic nerve and center of the lens using this method differ on the average by 10-60% and 5-40%, respectively, from those computed using a standard 22 mm eye model; pointing out the importance of more accurate planning for these treatments.

MP15.8

Improvements in Directional Iodine-125 Plaques in the Treatment of Tumours of the Eye, D Shackleton*, R Sealy, C Stannard, J Hill, E Hering, J Korrubel, Depts of Medical Physics, Radiotherapy and Ophthalmology, Groote Schuur Hospital and University of Cape Town, Observatory 7925, RSA

Gold foil backed iodine-125 plaques have been used by us for 13 years to treat intra-ocular malignant melanoma and retinoblastoma. Several improvements now enhance this technique. A scribed globe permits geometrical details to be readily determined in spherical coordinates. The plaques now extend to a reference line 5mm from the limbus, increasing positioning accuracy and reducing time in theatre and radiation exposure to staff. Angled gold foil edges permit tailoring of the radiation field to the lesion, allowing a tumouricidal dose to be delivered within 1mm of the optic nerve while sparing that structure. Gold foil ridges effectively focus the radiation onto the target. These improvements lead to better geometrical precision than photon or electron or proton external beam therapy appear to offer.

MP16.1

Neuromagnetic Studies of Evoked Pain, J. Joseph*, R.T. Wakai, E. Howland, M. Backonja, C. Cleeland and J.R. Cameron, University of Wisconsin, Madison, Wisconsin.

We have measured evoked neuromagnetic fields and electric potentials using painful electrical stimulation of tooth pulp and intracutaneous tissue. Tooth pulp stimulation is ideal for these studies because it is predominantly innervated by pain fibers. In contrast, intracutaneous stimulation excites a mixture of sensory and nociceptive nerve fibers which results in a more complex subjective sensation. The strongest components of the evoked response occurs at latencies of 150 and 250 msec. These signals are used to provide an objective measure of pain sensation under various experimental conditions.

MP15.9

Dosimetry Analyses of I-125 Plaque Using Film Dosimetry, Andrew Wu* and Frank Krasin, Tufts-New England Medical Center, Boston, MA, USA

Nationwide studies of using an episcleral plaque containing I-125 radioactive seeds for treatment of choroidal melanoma have been undergone for two years now. However, comprehensive dosimetry studies are scarce and controversial. Since the changes of energy spectrum of I-125 in tissue are negligible, film dosimetry seems to be a logical choice, especially for high spatial resolution. In this paper, we first established an H&D curve with doses expressed in a unit of specific dose rate constant. This avoids absolute dose measurements. All film measurements are made and normalized to the density of dose exposed with 1 mCi at 1 cm. The isodose rate distribution of I-125 seed (model 6711) plaque with and without gold shield are compared and discussed. Also, the effects on dose distributions due to the presence of gold shield along the central axis or around the lip of the plaque are presented.

MP16.2

CARDIAC POTENTIAL AND MAGNETIC MAPS OF VT- PATIENTS, R. Merritt, G. Stroink*, M. J. Gardner and B.M. Horacek, Dalhousie University, Halifax, Canada, B3H-3J5.

High resolution body surface potential maps (BSPM) and magnetic field maps (MFM) have been obtained of 14 patients with ventricular tachycardia (VT). The potential maps are constructed from 117 leads distributed over the body surface and sampled simultaneously. The MFM are obtained by sequentially measuring the magnetic field at 56 points on a 4 cm grid in a plane parallel to and just above the anterior surface. The measurements are obtained in a shielded room.

Inspection of the bi-directional filtered Frank leads reveal late potentials in 10 of the 14 patients. The BSPM and MFM, plotted each 2 ms near the time instances that the late potentials occur, were analysed using, single current-dipole, inverse solutions. The success of this analysis will be discussed in terms of the location of such dipole and the S/N ratio in the two sets of measurements.

MP16.3

MOVING SINGLE DIPOLE FIT TO MCG AND BSPM MAPS USING A HOMOGENEOUS TORSO MODEL, C. Purcell, G. Stroink, B.M. Horacek and T.J. Montague, Dalhousie University, Halifax, Canada, B3H-3J5.

We have measured the 117 lead Body Surface Potential Maps (BSPM's) and 56 lead Magnetocardiographic (MCG) maps of a group of 10 normal male subjects (mean age 55 y.) and 15 subjects (mean age 57 y.) recorded on average 77 days following their first documented myocardial infarction (MI). The BSPM and MCG maps, plotted ~ 10 ms apart during the T wave interval, were analysed with an inverse solution for a single current dipole that uses a homogeneous torso model with a realistic outer boundary. We found that, using this model, 93% of the data content of the first 80% of the T wave magnetic maps and 98% of the data content of the electric maps during this interval can be attributed to a single dipole. A classification of abnormality in the results of the BSPM data of the MI's in terms of the values for dipole components and location are in agreement with the diagnosis based on the 12 lead ECG. The analysis of the MCG maps classified 9 of the 15 MI patients as abnormal.

MP16.5

SQUID-based Magnetic Sensor cooled by a Refrigerator, S.J. Williamson*, D.S. Buchanan, D. Paulson, and G. Klemic, Department of Physics, New York University, New York, NY, 10003, and Biomagnetic Technologies, Inc., San Diego, CA, 92121.

Neuromagnetic measurements relying on the SQUID sensor have up to now required liquid helium for cooling. To avoid this and gain flexibility in operation, a sensor incorporating a dc-SQUID and second-order gradiometer has been developed that is cooled by a two-stage refrigerator in the dewar, coupled by flexible lines to an external compressor. A Gifford-McMahon cycle provides a stage at 15 K, and a Joule-Thomson expansion chamber supported from this sustains a temperature of about 4 K for the SQUID and gradiometer. The sensor's white noise level is about $20 \mu\text{T}/\text{Hz}^{1/2}$, and residual noise introduced by the Gifford-McMahon displacer is virtually eliminated by real-time computer filtering. In application the dewar containing the sensor can be pointed in any direction, including upside down, and the intrinsic noise level is insensitive to orientation. A pair of such "CryoSQUIDS" has been installed in a magnetically shielded room, independently mounted so that they can monitor activity in widely separated areas of a subject's brain. Their performance used in conjunction with a conventional 5-sensor system will be described.

MP16.4

Measurement of the Magnetic Fields produced by the ON-OFF Response of the Human Retina, Y. Uchikawa, A. Adachi, T. Hasegawa*, N. Okuyama, and M. Kotani, Tokyo Denki University, Hatoyama, Saitama 350-03 Japan.

The MRGs have been measured in a nonmagnetically shielded room with a SQUID connected to a second order gradiometer with a baseline of 3.2 cm and a coil of 2.48 cm diameter. To induce the magnetic fields from the retina we used two kinds of light stimulations. One is by a flash (white light) and the other is by the red light of LED transmitted to the eye through optical fibers. The magnetic recordings were averaged with more than 100 samples.

It was found as followings; the amplitude between the a-wave and the b-wave was the range of 200 to 300 fT. The a-wave of the MRG did not observe as seen in the ERG when the intensity of the light was decreased. Especially we will present the magnetic recordings produced by the OFF response of the human retina which is the first measurement. The feasibility to analysis for transient response of the retina was confirmed by introducing this new approach of noninvasive biomagnetic measurement.

MP16.6

High-Resolution SQUID Magnetometers for Biomagnetic Studies, John P. Wikswo, Jr., Vanderbilt University, Nashville, TN 37235 USA

In studies of the human magnetocardiogram and magnetoencephalogram, the separation between the bioelectric source and the SQUID pickup coils is determined by both the thickness of the intervening bone and soft tissues, and by the distance between the pickup coils and the outside of the Dewar containing the SQUID. Tradeoffs between signal-to-noise ratio and resolution are optimized when the coil diameter is approximately equal to the coil-source separation, typically 1 to 2 cm. While this size of instrument may allow localization of effective dipole sources in the cortex to within 1-2 mm, detailed mapping of the sources is precluded by the severe low-pass spatial filtering from the 1-2 cm source-coil spacing and coil diameter. Intervening bone and tissue can be removed for experiments on *in vivo* and *in vitro* animal preparations, so that reducing the coil-Dewar spacing is paramount for high-resolution mapping of current sources. We present a design study and progress report on SQUID systems with 3 mm diameter pickup coils, 1-2 mm coil-sample spacing, and a potential sensitivity of $50 \text{ fT}/\sqrt{\text{Hz}}$. The decreased spacing may lead to an order of magnitude increase in signal-to-noise ratio for highly-localized sources. Such instruments should be able to detect as-yet-unobserved current distributions associated with differences between the intracellular and extracellular anisotropies of cardiac muscle.

MP16.7

Two-dimensional Inverse Problems in Biomagnetism, B.J. Roth, S. Tai and J.P. Wikswo, Jr.*, Vanderbilt University, Nashville, TN 37235

There is a scant but growing literature applying Fourier transform techniques to the biomagnetic inverse problem. We have solved the inverse problem analytically for a two-dimensional current distribution. If the normal component of the magnetic field, $B_z(x,y)$, is measured over a plane at a height z above a two-dimensional current density distribution, $J(x,y)$, then from the law of Biot and Savart J can be related uniquely to B_z by expressing both as functions of the spatial frequencies, k_x and k_y . The filter function relating $B_z(k_x, k_y)$ and $J(k_x, k_y)$ is proportional to the function, $\exp(-\sqrt{k_x^2 + k_y^2} z)$. Thus, the magnetic field provides a low-pass filtered version of the current distribution, with the amount of filtering depending on the distance z . Other field components, different gradiometer configurations, and the effects of finite pickup coil size can be included analytically. We use fast Fourier transform (FFT) algorithms to transform the magnetic field into the spatial frequency domain, filter the data with the appropriate function, and use the inverse FFT to obtain the current density distribution. The filter that represents the solution to the inverse problem is unique, but the stability of the results depend upon geometric parameters and the signal-to-noise ratio. The extension of this approach to 2-D and 3-D bidomain systems and to 3-D mono-domain systems may encounter non-uniqueness.

MP17.2

Application of Magnetic Resonance Spectroscopy to Study Preservation of the Heart for Transplantation

G. V. Forester, O. Z. Roy*, K. Butler, R. Deslauriers, and I. Smith, National Research Council of Canada, Ottawa, Ontario, Canada K1A 0R6.

A correct immunological match is an important consideration in the use of the donor hearts for cardiac transplantation. A match may be found that cannot be used when the time to remove, transport and implant the heart falls outside the preservation window of 4-5 hours. We have developed an isolated perfused pig heart model that can be placed in the horizontal bore of a 4.7 tesla Bruker magnet with Medspec spectrometer. ^31P spectroscopy has allowed us to follow high energy phosphate metabolism and intracellular pH as hearts are stored for 5 hours at 5°C and 12°C . We follow the recovery of the hearts with reperfusion at 37°C while measuring the metabolic and mechanical heart correlates. This allows us to determine optimal conditions for preservation and recovery of donor hearts, and will lead to a wider geographical harvest of suitable donor hearts.

MP17.1

Use of Magnetic Resonance Spectroscopy (MRS) to Assess Metabolic Effects of Therapeutic Ultrasound on the Heart.

O. Z. Roy*, G. V. Forester, and R. Buist, National Research Council of Canada, Ottawa, Ontario, Canada K1A 0R6.

We have established that therapeutic ultrasound applied to acutely ischemic myocardium in the reperfusion stage increased recovery. We used ^31P MRS to measure high energy phosphate compound reserves and intracellular pH while monitoring the mechanical response of Langendorf perfused working rat heart preparations. In non-protected hearts arrested for 60 minutes, ultrasound applied during reperfusion enhanced recovery. With cardioplegic arrest, hearts also recovered completely after 60 minutes of arrest with and without ultrasound, but only ultrasound improved recovery with cardioplegic arrested hearts at 85 minutes and 105 minutes. By 155 minutes of arrest, application of ultrasound produced no improvement in recovery. MRS metabolic profile indicates that recovery is preceded by an overshoot in the Phosphocreatine concentration; without the overshoot the heart does not recover. The intracellular pH returns to normal whether or not the heart recovers contractile function. These data are important in elucidating the effects of ultrasound in cardiac improvement and in helping to determine optimum conditions for reperfusion of the ischemic myocardium encountered in the clinical situation.

MP17.3

^1H NMR Characterization of Human Blood Plasma,

Ann E. Wright, University of Texas Medical Branch, Galveston, Texas 77550.

NMR characterization of human blood plasma is of great interest because of recent evidence that occult cancers may be detected by NMR measurement of the spectral peak width of lipoproteins (1). At this institution we have used a JEOL 270 MHz spectrometer to perform spectral analyses of plasma samples from both normal subjects and cancer patients using a Hahn spin-echo technique. After a TE of 80 msec, a long T2 component not normally present was discovered in samples from the cancer patients. High performance liquid chromatography (HPLC) is being used to analyze the spectral peak containing the long T2 moiety. HPLC has been shown useful for analysis of molecular species of phospholipids and promises to provide particularly novel information with respect to changes in molecular composition brought about by pathologic conditions (2). Isolated intact molecules eluted from the HPLC column are vacuum dried, resuspended in deuterium and reanalyzed on the NMR spectrometer. Preliminary evidence indicates the long T2 peak arises from a molecular species most abundant in plasma chylomicrons.

1. New Eng J of Med (1986) V.315, 22:1369-1376.
2. J Lipid Res (1986) V.27:131-139.

(Note: The NMR spectrometer was purchased with funds donated by the M.D. Anderson Foundation.)

MP17.4

Early post mortem changes of $^1\text{H-NMR}$ -relaxation times in mouse liver necropsies

E. Moser*⁺, H. Echsel[§] and J. Schuster
 Institut für Medizinische Physik and
 Institut für allgemeine and experimentelle
 Pathologie, Universität Wien, A-10 Wien,
 AUSTRIA

Systematic investigations of $^1\text{H-NMR}$ relaxation times in mouse liver, depending on temperature and time-after excision, have been done to be able to control storage and measurement conditions. Measurements have been performed with a BRUKER pc20 spectrometer. Data were fitted using a mono- and biexponential model for relaxation times. Extensive test measurements as well as computer simulations have been undertaken to check the validity of our results.

We found significant differences in normal mouse liver T_1 (depending on time-after-excision) due to sex and feeding status. Degenerative changes due to different glycogen content/decrease may responsible and time course of relaxation times (in vitro) could be used for diagnostic purpose.

+ present address: Dept. Biochemistry and Biophysics, School of Medicine, University of Pennsylvania, Philadelphia PA 19104

MP17.6

Detection of the Difference in Functions of Cerebral Hemispheres by Differential NMR, H.Kamei*, Y.Katayama and H.Yokoyama, Electrotechnical Laboratory, 1-1-4 Umezono Tsukuba, Ibaraki 305, Japan.

We developed a novel NMR technique to detect the difference in functions of human cerebral hemispheres. The method is based on the fact that the blood flow through the brain tissues varies inhomogeneously according to their levels of metabolism and functional activity, and that the inhomogeneous blood flow enhancement results in the changes of proton NMR signals gathered from region-selective detectors located at several parts of the head surface. The experiments were made on a homemade whole-body MRI system. Perception of music, response to taste and activation of visuo-sensory areas were examined on normal and right-handed volunteers. It was found that the left hemisphere played dominant roles in perception of musical rhythms, and the right hemisphere in the perception of melody. When a droplet of the extracted solution of red pepper as dropped on the left side of tongue, the right somato-sensory area (not taste-sensory) was activated. Linear relationship was observed between logarithmic illumination intensity of light spot in the right visual field and the intensity of the signal from left visuo-sensory. The results on time-resolved measurements will be reported.

MP17.5

THE ENIGMA OF RELAXOMETRY IN BIOLOGICAL SYSTEMS
 SYED FAROOQ AKBER*, Dept. of Biomedical Engineering, Worcester Polytechnic Institute, Worcester, MA

The present theories of proton magnetic resonance relaxation times fall short of explaining satisfactorily the physical and biological mechanism responsible for the dissimilarities of relaxation behavior in normal and pathological tissues. An alternate approach to understand the mechanism is needed.

It is well known that when water is degassed (dissolved oxygen removed), the relaxation time of water increases. The spin-lattice (T_1) relaxation time of protons in water completely saturated with oxygen is 1.4 ± 0.1 sec, and in water completely free of oxygen is 3.6 ± 0.2 sec at one atmospheric pressure at 20°C (1). This provides a clue that a similar process may take place in normal and pathological tissues, therefore it is hypothesized that the dissimilarities of relaxation behavior in normal and pathological tissues are most likely due to the concentration of paramagnetic molecular oxygen dissolved in cell-associated water (2,3). This paper will discuss the physical and biological mechanism of oxygen availability and oxygen consumption and its influence on proton spin-lattice (T_1) relaxation times in normal and pathological tissues.

1. G. Chiarotti et al.: Phys Rev 93:1241, 1954
2. S.F. Akber : Med Phys 14:910, 1987
3. S.F. Akber : Nuklearmedizin 28:37, 1988

MP17.7

T_1/T_2 Contrast in Fast MRI as a Function of Field Strength, S. Vinitski, R. Griffey**, B. Griffey**, J. Boone*, A. D'Amato, Thomas Jefferson Univ. Hospital, Philadelphia, PA, **Univ. of New Mexico, Albuquerque, New Mexico.

Many pathological changes are associated with increased water content which prolongs T_2 to a greater extent than T_1 . Soft tissue T_1 increases with magnetic field strength, suggesting that T_1 contrast may diminish in high field spin echo imaging. However, differences between T_1/T_2 ratios of edematous lesions and normal tissue should increase with the field strength. Using different solutions to the Bloch equations and taking into consideration differences in susceptibility of biological tissues, we calculated T_1 , T_2 and T_1/T_2 grey/white matter and grey matter/edema contrast in both fast gradient refocusing (GRASS or FISP) and spin echo imaging. Cat and rabbit brains were then imaged in vivo at 1.5 and 4.7 Tesla. Experimental results support the theoretical prediction that while grey matter/edema contrast increases moderately with field strength, the grey/white contrast in spin echo imaging is maximum at 1.2 Tesla and then gradually declines. On the contrary, both grey/white matter and grey matter/edema contrasts in gradient refocusing imaging increases drastically with field strength. Thus, the ratio T_1/T_2 may become a sensitive indicator of disease in high field fast imaging.

MP17.8

NMR STUDIES IN BONE MARROW AND TISSUES, A.Kennedy, G.N.S.Prasad*, S.V.Baskaran# and A.V.Lakshmanan,# Dept. of Physics, Anna University Madras and # Cancer Institute, Adyar, Madras-25, INDIA.

The aim of this work was to evaluate the use of Nuclear Magnetic Resonance(NMR) for discriminating the normal bone marrow and tissues from the malignant marrow and tissues. The parameters T_1 (spin-lattice relaxation) and T_2 (spin-spin relaxation) were measured for various bone marrows and tissues. There was a clear difference between T_1 values for normal marrow and malignant marrow. There is no clear demarcation between the values of T_2 obtained for different marrows. However the T_1 values for malignant marrow is considerably higher than that of the normal marrow. In general the T_1 values, for all kinds of normal marrows, varies between 1000 to 1600 m.sec and for malignant marrows the range varies from 1900 to 2500 m.sec at room temperature. The NMR parameters T_1 and T_2 were measured for various kinds of tissues also. The T_1 values for normal tissues are lesser than that of malignant tissues. Thus NMR can be used as a diagnostic tool in detecting the malignancy.

MP17.10

The Possible Discovery of a Reagent for Cancer Diagnosis by Urine NMR analyses, Yong Jin Kim*, Department of Physics, Hanyang University and Central Lab., Samil Pharm. Co., Seoul, Korea.

Urine NMR analyses show that the NMR signals corresponding to four aromatic protons very distinctively appear in normal and various diseased urine. However the results of many repeated NMR experiments on the urine indicate that the proton signals are much more frequently observed in cancer urine. A reagent made by mixing a dissolved metal with the well-known Milon indicator is used to identify them by observing the urine color reaction. Red precipitates caused by the reaction of the phenolic compound of tyrosine are formed in the urine. Like the NMR results it is found that the urine reaction frequency is particularly higher in the cancer urine. Moreover from the reaction it is observed that the cancer urine is very sensitive to the reagent in comparison with other urine.

An attempt is made to determine the reagent sensitivity and specificity of the urine collected by a random sampling for a differential diagnosis between the cancer and non-cancer urine. The results of the attempt show that its sensitivity and specificity are at least above 75 %.

MP17.9

Is a Faraday shield ever useful in MRI coils?

D. K. De* and P. R. Moran

Radiology Department
The Bowman Gray School of Medicine,
300 S. Hawthorne Road, Winston-Salem, NC 27103

We calculate the relative MR coil dielectric-losses, P_c and P_f , respectively due to the Coulomb's-law electric-field contribution (electrostatic field) and to the Faraday's-law electric-field contribution (inductive field), within a conducting subject, inside an MRI coil. We show that P_c is insignificantly smaller than P_f . This result quantitatively depends strongly upon the subject's dielectric constant and characteristic dimensions; and this therefore distinguishes MRI coil-behavior dramatically from the experience of small-sample MR spectroscopy. The relative effect of P_f cannot be eliminated by a slotted Faraday shield, since the relative strength of B1 must be maintained to keep optimum NMR signal sensitivity. Thus the real usefulness of a Faraday shield for MRI subjects cannot be to reduce subject/coil dissipation effects, e.g., MR thermal noise, and Faraday shields are otherwise highly questionable.

MP17.11

Quantitation of regional bone metabolism by dynamic bone scintigraphy and its age-dependence of skull, S. Wada*, K. Hayama, K. Maeda, The Nippon Dental University, school of Dentistry at Niigata, 1-8 Hamaura-cho Niitaga city, Niigata, Japan

Bone scintigraphy with ^{99m}Tc -phosphate compound is said to be reflected bone mineral turnover. Therefore it is expected that quantitative parameter of regional bone metabolism can be measured by quantitation of bone scintigraphy. We mathematically analyzed time activity curve of dynamic bone scintigraphy, applying compartment model analysis of tracer kinetics. Investigating to avoid the effect the main artery and soft tissue we made computer program which calculate the quantitative parameters fitting obtained solution with time activity curve of patient.

The analysis was carried out in every normal part of cranial and facial bones using image data of patients who have been performed dynamic bone scintigraphy. (63 men :34 women).

With distinction of sex and location quantitative parameters were statistically investigated with regression analysis. The age-related increase of a parameter was observed in cranial and part of facial bones in both sexes. And the tendency was more remarkable in women of over 50 years old, suggesting correspondence to the post-menopausal bone change.

83

MP17.12

Use of Concentration Instead of Activity for Absorbed Dose Estimation, E.A. Silverstein*, A.M. Zimmer, and S.M. Spies. Northwestern Memorial Hospital, Chicago, Illinois.

Absorbed doses from radionuclides are usually calculated using the MIRD formalism. In the S value formulation, the self-dose to an organ is expressed as a product of the cumulated activity and an S value, tabulated for the organ in question and the radioisotope used. In this work the advantages of using the cumulated concentration instead of the cumulated activity are presented. The absorbed dose is then expressed as a product of the concentration and a factor mS , where m is the "standard man" mass of the organ. It is shown here that mS varies only slightly for different organs and radioisotopes, being essentially constant as expected for pure beta emitters. By use of the concentration approach it is then possible to estimate doses for organs of unknown size and for activity-containing regions of non-standard shape. The use of these techniques can give more accurate dose estimates, especially in conjunction with quantitative SPECT which is well suited to measuring values of concentration.

MP17.14

In Vivo Neutron Activation Laboratory
K.J. Ellis* and R. Shypailo, USDA/ARS Children's Nutrition Research Center, Department of Pediatrics, Baylor College of Medicine, Houston, Texas 77030.

The quantitative assessment of body composition, especially protein, water, fat, and skeletal mass, can provide data that may increase our understanding of basic physiologic or pathologic mechanisms and aid in a patient's diagnosis and clinical management. Thus, a body composition laboratory has been set up at the Children's Nutrition Research Center for *in vivo* neutron activation analysis (IVNAA). The four major facilities include infant- and adult-size whole body counters, a variable geometry neutron irradiator for delayed activation analysis, and a scanning system for prompt-gamma activation analysis. The delayed activation system uses 56 Am,Be sources, 15 Ci each, which can be arranged into four irradiation geometries (small animal, infant, normal adult, and obese adult). The adult counter consists of 32 NaI detectors (10.2 cm. \times 10.2 cm \times 45.7 cm) arranged above and below the supine subject. For a 2-min activation time (<3 mSv), 1-min delay, and 15-min count, the precision for total body Ca, Na, Cl, P, and K is $<2\%$. The prompt-gamma IVNAA technique uses four collimated Am,Be sources and four 15.3 cm \times 10.2 cm NaI detectors for a single scan of the subject. These measurements require <10 min (<0.4 mSv) and have a precision of 3% for body protein and $<5\%$ for body fat.

MP17.13

A General Theory for the Transport and Exchange of Inert Diffusible Tracer in the Brain, T.Y. Lee* and I.W.T. Yeung, Radiology, St. Joseph's Hospital and Medical Biophysics, University of Western Ontario, London, Ontario, Canada N6A 4V2

Cerebral blood flow (CBF) and capillary permeability (PS) are two important neurophysiological parameters of the brain. Until now, they have to be measured in separate experiments. CBF is measured using inert diffusible tracer with the Kety model whereas PS is obtained by measuring extraction efficiency or transfer constant. We propose a new theory which treats the transport and exchange of inert diffusible tracer more exactly such that both CBF and PS are determined simultaneously in a single experiment which uses quantitative computed tomographic techniques to measure the tissue concentration of tracer noninvasively *in vivo*. It will be shown that under different simplifying approximations, the proposed general theory reduces to the Kety model, the Crone and Renkin model, and others which have been used by previous authors to determine CBF and PS separately. One application of the proposed theory will be the measurement of CBF and PS in patients using either H_2O^{15} and PET or D_2O and magnetic resonance imaging.

MP17.15

Scattering Within Uniform Media. LA Henry and MS Rosenthal*, University of Pittsburgh, Pittsburgh, PA, 15261, USA

Compton scatter along with other interactions cause image degradation and loss of quantitation in nuclear medicine studies. As a first step in characterization of scatter, we have modeled scattering within uniform scattering media via use of a Monte Carlo transport code. This code includes Compton scattering, coherent scattering, photoelectric effect, diffraction, and production of lead x-rays from the collimator.

The code models a 22 cm acrylic shell phantom irradiating a 3/8" thick NaI crystal through a LEAP collimator. Within the phantom a single source is positioned along the longitudinal axis using either air or water as the scattering media. For both experimental data and calculations, 500 to 1000K events were detected by the gamma camera. The Monte Carlo transport code was run on a DEC VAX 11/750. Both experimental measurements and calculations were performed as a function of position along the longitudinal axis of the phantom. Within statistics, the spectra produced by the Monte Carlo code reproduced that measured experimentally using Tc-99m point sources.

MP17.16

A new approach to the measurement of glomerular filtration rate and blood flow of each kidney using ^{99m}Tc -DTPA, G. IZZO* & A. MAGRINI, Fisica Medica - Università Tor Vergata, A. FAVELLA, F. FRINGUELLI & M. BANCII, Medicina Nucleare - Clinica Ars Medica, F. FRANCHI & L. AGATENZI, Ospedale S. Andrea - USL RM12, Rome, Italy

Model analysis of the early part (3 min) of the renogram was performed using a large-field computerized gamma-camera (90 x 15 + 15 x 6 s images) and ^{99m}Tc -DTPA as a tracer. The time-activity curve calculated over the left ventricle was used as an input function to a compartmental kidney and extrarenal tissue model. Fitting of the renogram by taking into account the real input enabled the glomerular filtration rate and blood flow of each kidney to be determined independently from background. 32 patients undergoing routine DTPA test were studied with the proposed approach, as well as with two classic nuclear-medicine methods (Gates and Constable methods). Compared with the creatinine clearance values, results appear to demonstrate that the proposed method is more accurate and/or simpler than the above-mentioned methods, also providing more complete clinical information.

MP17.18

Assessment of hepatic and splenic hemodynamics with a single radiotracer test, A. MAGRINI* & G. IZZO, Fisica Medica - Università Tor Vergata - Roma, A. FAVELLA, F. FRINGUELLI & M. BANCII, Medicina Nucleare - Clinica Ars Medica - Roma, L. VALERI, Ospedale S. Giacomo - Roma, S. SPOSITO, Ospedale Civile - Velletri, F. FRANCHI & L. AGATENZI, Ospedale S. Andrea - USL RM12 - Roma, Italy

The MARK method (Model Analysis of Radiocolloid Kinetics) for non-invasive study of hepato-splenic hemodynamics is described. Data collected by means of a computerized gamma-camera for 4 min after i.v. administration of ^{99m}Tc -colloids (4 mCi) were analyzed using a model formulated on a physiopathological basis. Several parameters of clinical interest were determined, namely, liver arterial and venous blood flows, intrahepatic blood flow, spleen flow, hepatic and splenic vascular spaces of distribution of the tracer, transit times, extraction efficiencies and clearances. On the basis of 4 years experience and 8,000 tests performed, it is concluded that the MARK method is sufficiently accurate, reproducible, safe and practical, and may thus be considered suitable for routine clinical use.

MP17.17

Attenuation Correction in Rectilinear High-Sensitivity Scanning, D. Gvozdanovic*, Dep. of Bio-Medical Physics & Bio-Engineering, Univ. of Aberdeen, Aberdeen, Scotland, U.K.

A transmission scanning procedure, using appropriate energy photons, was developed in conjunction with high sensitivity (10 min. scan of 0.1 MBq in w. b.) rectilinear scans in an attempt to assess the absolute quantity of the tracer in various organs and sites of the body, following long-term element turnover studies.

The transmission scan is taken with a collimated beam of the radionuclide used in the study, both this and the subsequent tracer scans have an image matrix of 16x52 pixels, anterior and posterior images being taken at the same time. By using an IBM compatible computer, the images are interpolated to a 46x126 matrix, filtered by a two-dimensional deconvolution process applying the image transfer function (15x15 pixels). A geometric mean is derived for each pixel from the anterior and posterior scans. This is corrected for attenuation using appropriate pixel in the transmission scan. Integration over selected area gives the fraction of tracer when compared with the integral of the whole image. Phantom studies gave an estimation accuracy of < 5% when clearly defined areas are involved.

MP17.19

Half-Value Layer (HVL) of Radionuclides Emitting Polyenergetic Gamma Photons, Ibrahim B. Syed*, Muzaffar Ali, and Mark H. Crosthwaite, V. A. Medical Center, Bellarmine College and University of Louisville Health Sciences Center, 800 Zorn Avenue, Louisville, Kentucky - 40202, U.S.A.

A knowledge of half-value layer (HVL) is important for shielding purposes in radiation safety and also for clinical interpretation of photon-deficient areas in images in nuclear medicine. For monoenergetic photons and for a given absorber (attenuator), HVL is calculated dividing 0.693 by μ (the linear attenuation coefficient). But in nuclear medicine, radio-pharmaceuticals are used with radionuclides having multiple principle gamma emissions. An equation is derived for calculating HVL of such radionuclides.

A computer program has been developed to determine the HVL of radionuclides which emit polyenergetic gamma photons by Newton's method and iteration.

MP17.20

Oedema of the neck after thyroid ablation with radioactive Iodine, M O Shackleton*, I D Werner, C S Slater, Depts of Medical Physics and Radiotherapy Groote Schuur Hospital and University of Cape Town, Observatory 7925, RSA

Radioactive iodine was used by us for thyroid ablation in 133 patients during 1983-1987. Only one patient developed acute oedema of the neck. This patient had had one thyroid lobe excised previously. This very rare condition appears to be reported only once by another group. The oedema developed within 48 hours of receiving 3 GBq of radioactive I-131. The patient was treated with corticosteroids and responded well to the treatment. Five days later the patient developed symptoms of vocal cord paralysis. Nuclear Medicine scans were performed on the patient to establish the location of the residual thyroid tissue. Sensitivity to I-131 had been ruled out by using appropriate tests. From dose calculations it is concluded that the oedema was caused by acute radiation effects. Further tests are being done to investigate this condition.

MP17.22

MINIMUM PREDICTED GAMMA CAMERA INTEGRAL AND DIFFERENTIAL FLOOD UNIFORMITIES J.R. Halama, and R.E Henkin, Loyola University Medical Center, Maywood, IL.

Gamma camera performance is routinely specified by computing flood field uniformity defined by the ratio $u = (MAX - MIN) / (MAX + MIN)$, where MAX and MIN are the maximum and minimum counts observed in a digitized flood image. For integral uniformity the entire image is searched, and for differential uniformity a 6 pixel range is used. Due to counting statistics, these indices do not, however, converge to zero for a perfectly uniform gamma camera response. This minimum can be predicted by determining the probability distribution of u . Based on order statistics, the joint probability distribution function for observing MAX and MIN is described as follows: $g(MAX, MIN) = n(n-1)[F(MAX) - F(MIN)]^{n-2} f(MAX) f(MIN)$ where F and f are the distribution and density functions governing each pixel value, and n is the number of pixels in the search. The distribution function for u can then be obtained by integrating $g(MAX, MIN)$ over the region defined by u . Assuming F is Gaussian, the expected value and variance of u were obtained numerically versus n and average pixel counts. Results compared favorably to computer simulations and actual gamma camera flood images. With this information, we can better ascertain the true uniformity of the gamma camera by u .

MP17.21

The Use of Electroporation for Labeling Leukocytes with ^{99m}Tc Radiopharmaceuticals, William Phillips, M.D., University of Texas Health Science Center at San Antonio, San Antonio, TX 78284-7800

Electroporation has been shown to create reversible pores in cell membranes without loss of cell viability. Leukocytes electroporated in plasma containing ^{99m}Tc -MDP demonstrated a significant increase in labeling compared to a control group of non-electroporated leukocytes. The labeling efficiencies ranged between 1.6%-5%. This new technique for radionuclide cell labeling has potential for applications in diagnostic imaging.

MP17.23

DOSIMETRY OF AUGER ELECTRON EMITTERS: IMPLICATIONS AND POTENTIAL APPLICATIONS, K.S.R. Sastry, University of Massachusetts, Amherst, MA; R.W. Howell, D.V. Rao, University of Medicine & Dentistry of NJ, Newark, NJ; A.I. Kassis, S.J. Adelstein, Harvard Medical School, Boston, MA; and C. Haydock, Mayo Foundation, Rochester, MN.

Several biomedical radionuclides (I-125, In-111, Tc-99m, etc.) are prolific emitters of low energy Auger electrons with highly subcellular ranges. Biophysical implications of such Auger emitters are not predictable by conventional dosimetry (e.g., MIRD Schema), which ignores the importance of these electrons. Our studies with mammalian cells in culture, and on experimental mouse models show that the biological effects of Auger cascade electrons may be highly disproportionate to the energy carried by them. Our results confirm the inadequacy of conventional dosimetry, and reveal several important parameters ignored hitherto. In terms of these determinants, phenomenological expressions are presented for a biophysically meaningful dosimetry of internal Auger emitters. Possible approaches to exploit the highly localized action of the low energy electrons in cancer therapy are examined with Sb-119 and Pt-193m as illustrative examples.

Work supported in part by USPHS Grant Nos. CA-32877 and CA-15523.

MP17.24

Dual-isotope Measurement of Lung Water in Dogs, R. Y. L. Chu*, P. V. Carlile, Jr., G. Basmadjian, University of Oklahoma Health Sciences Center and Veterans Administration Medical Center, Oklahoma City, Oklahoma, U.S.A. 73104.

To develop a noninvasive method for measurement of lung water, we have been studying the use of iodo-antipyrine. I-131-labeled iodo-antipyrine and Tc-99m-labeled erythrocytes were used to measure water content in lungs. These radioactive tracers were injected into 11 dogs with injured lungs. Blood samples were drawn and the animals were sacrificed. The lungs were removed, weighed and homogenized. Samples of blood and lung homogenate were assayed for I-131 and Tc-99m. Samples also were weighed before and after drying to a constant weight at 70-75°C. Extravascular lung water was determined by the dual-isotope technique and again by gravimetric analysis. The average ratio of the results from the two different methods is 1.14 ± 0.20 . The two methods were compared also by regression analysis and the correlation coefficient is 0.97 ± 0.09 . This investigation suggests the possibility of *in vivo* measurement of lung water with the equilibrium distribution of iodo-antipyrine.

This work was supported by a research grant from the Veterans Administration.

MP17.26

Brain Scanning with 99m-Techneium Glucoheptonate and quantitation of specific uptakes in tumors

R. Ravichandran*, S. Devaru, N. Anantha¹, B. S. Das², V. K. Jain³
 1) KIMIO, Bangalore. 29, 2) NIMHANS, Bangalore 29, 3) ICMAS, Delhi. 7, India.

Our earlier work has showed that combination of 2-deoxy-D-glucose (2DG) with ionising radiations is expected to improve therapeutic efficacy by inhibition of DNA and cellular repair process in cells with high glycolic activity. Clinical trials are planned in brain tumor radiotherapy with 2DG. For selection of patients and monitoring them we proposed to use 99m-Techneium glucoheptonate (TcGH) as glucose analogue in the place of positron emission tomography. The specific uptakes of TcGH were quantitated in human brain tumors using a conventional gamma camera and measured build up factors.

The specific TcGH uptakes were expressed as ratios against normal brain to account for variations. The ratios of specific TcGH uptakes correlated well with the grades of brain tumors, 4.4 ± 0.7 (n=8) for malignant, 2.4 ± 0.9 (n=6) for metastatic and 1.6 ± 0.6 (n=8) for benign tumors. Concentration of TcGH in viable parts of recurrent high grade tumor, increased ratios for TcGH against similar ratios for Tc-RBC blood pool scans suggest that the concentration of TcGH in brain tumors may be related to metabolism.

MP17.25

The Applications of Radionuclide Phase Image Analysis in Coronary and Noncoronary Disease, Zhao Huiyang* and Zhu Junren, Zhong Shan Hospital, Shanghai Medical University, Shanghai, China

This paper reported the results of 349 cases radionuclide phase image analysis, including 21 normal subjects, 169 patients with coronary disease, 4 patients with LBBB, RBBB and WPW syndrome, 101 hypertrophic, virus and dilated myocarditis. 19 cases of coronary patient were performed by coronary angiography; 27 cases were performed at rest and with stress. The results of phase image analysis at rest and with stress were analyzed.

The sensitivity was 92 %, the specificity was 28.6 %, but phase image analysis with stress was more sensitive and better than LVEF in the early diagnosis of CAD. Abnormal phase angle was visualized in noncoronary patients.

MP17.27

The $^{16}\text{O}(\alpha, pn)^{18}\text{F}$ and the $^{18}\text{O}(p, n)^{18}\text{F}$ channels as alternatives for the production of $^{18}\text{F}^-$ used in radiochemical labelling. A. Hermance M. Gysemans, N. Walravens, P. Van den Winkel, W. Vanryckeghem and L. De Vis. Vrije Universiteit Brussel, B-1090 Brussels, Belgium.

At the VUB Cyclotron ($E_{\alpha, \text{max}} = 47 \text{ MeV}$; $E_{p, \text{max}} = 45 \text{ MeV}$) two nuclear reactions are used for carrier free $^{18}\text{F}^-$ production:

- the rarely cited $^{16}\text{O}(\alpha, pn)^{18}\text{F}$ with $E_{\text{threshold}} = 25 \text{ MeV}$.
 - the now common $^{18}\text{O}(p, n)^{18}\text{F}$ on ^{18}O enriched targets
- Real competitiveness of these channels for ^{18}F labelling experiments depends on both the isotope production yield and the ultimate incorporation efficiency. Data on the following physical and chemical characteristics for both reactions will be presented
- * Excitation curves (α from 25 to 47 MeV; p from 10 to 25 MeV).
 - * Relation between the incident beam intensity and saturation yield; correlation with loss of target material.
 - * Levels of short (^{15}O) and longer lived radioisotopic contaminants (^{48}V , ^{51}Cr , ^{66}Ga , ^{67}Ga , ^{69}Ge).
 - * Labelling yields for a standard ^{18}F exchange reaction and influence of foil breakdown resulting in depassivation of the target.

MP17.28

Validity of the assumption of tracer equilibrium with native Vitamin B₁₂ pool, C.M.Pathak*, R.R.Sharma and K.C.Das, Biophysics Department, PGIMER, Chandigarh, India.

Serum Vit B₁₂ level does not reflect native Vit B₁₂ pool, since it gets altered in various pathological conditions. Total body vit B₁₂ can be estimated from specific activity measurement of a biopsy sample provided tracer equilibrates with native pool. It is generally assumed that whole body monoexponential fall of tracer reflects equilibrium state. This study critically examines the validity of this controversial assumption. Whole body kinetic parameters in rats using 57 Co-Vit B₁₂(s.c) showed monoexponential decline of tracer after about 32 days, whereas inter organ distribution of tracer did not stabilise even upto 64 days, resulting in continuous change of specific activity in organs. Thus whole body Vit B₁₂ values calculated from different organs at 64 days ranged between 3.9 µg(kidney) to 89.3 µg(muscle) with mean of 37.5 µg. Whole body turn over rate of 1.47% per day probably represents an average of wide spectrum of turnover rates in different organs. Variation of T_{1/2} bio. of tracer in various organs may be related to interconversion of Vit B₁₂ into other forms and their metabolic functions. This study shows that assumption of equilibrium between the tracer and the endogenous pool is not valid even after tracer is excreted- monoexponentially.

MP17.30

Bone Mineral Densitometry With X-Ray Sources,
D. P. Chakraborty*, M. V. Yester, and G. T. Barnes,
Dept. of Radiology, University of Alabama at
Birmingham, 619 19th Street South, Birmingham,
AL 35233

Two methods of dual photon absorptiometry utilizing an x-ray tube instead of a Gd-153 source have recently been introduced. In one method the kVp is switched at each pixel, in the other, a single kVp spectra is used, but photons in two energy windows are counted. We will present a theoretical study of the two methods for a typical patient (20 g/cm² of soft-tissue and 1 g/cm² of bone), with respect to the achievable coefficient of variance of the bone mineral count (CV) and the dose. Our study indicates that while the single kVp method is more dose efficient, the kVp switching method is not count rate limited and can therefore achieve a smaller CV. Our model is based on published x-ray spectra and attenuation coefficients and is in good agreement with data. It is of interest that a point source of Gd-153 would be even more dose efficient. However, in practice the source is distributed and of limited strength, and consequently the radionuclide method cannot achieve a CV as small as either x-ray method in similar scan times.

Supported in part by NCI Grant No. CA43615-02.

MP17.29

Internal Dose Estimation from Skin Dose Measurements using TLD in 18-FDG Positron Emission Tomography (PET). J.F.D.Chubaci* & S.Watanabe (Univ.São Paulo, C.P.20516, 01498-São Paulo, Brasil); H.Fukuda, H. Seino, Y. Ota, T.Matsuzawa, M.Ito & J. Hatazawa (Tohoku University, Japan).

A method has been developed to estimate the dose on target organs of PET patients by Thermoluminescence dosimetry. TL dosimeters were held on the skin, close to the target organs, of ten Japanese subjects with surgical tape, a few minutes before the intravenous administration of 2-(F-18)Fluoro-2-Deoxy-D-Glucose. The skin doses due to the target organs were obtained by reading out the TL dosimeters and extrapolating the values for 37.0 MBq of activity and for 658.8 minutes of exposure time, which is equal to six half lives of Fluorine-18. The internal dose, on various organs, were estimated using the organ/skin radio-nuclide concentration ratio. This ratio was calculated from printed PET matrix data for each scanned organ, by a method developed through tissue equivalent gelatine phantom studies. The largest internal dose obtained was 41.3 µGy/MBq in the bladder, then 34.5 µGy/MBq for the spleen; other values are for liver, heart, lung, brain, pancreas, kidneys and testes. The values found in the present work are in close accordance with previously reported works, showing that our method may be of great usefulness to evaluate absorbed dose with good accuracy for emission tomography.

MP17.31

Dual Photon Absorptiometry of Forearm Using Monochromatic X-Ray. M.Mori*, I.Tamegai, K.Tamura, S.Kimura, K.kawamura, S.Ninomiya, ALOKA Co.,Ltd., Tokyo, JAPAN

The newly developed dual photon absorptiometry (DPA) bone mineral content measuring instrument is reported. The instrument consists of area scanning mechanism for forearm, X-ray generator, diffraction unit, two NaI(Tl) scintillation detectors and a small computer. The collimated X-ray beam from conventional X-ray tube irradiate the diffraction gratings and a part of the diffracted ray are collimated through pinhole collimators and extracted as the monochromatic X-ray beams. The system uses two energy beams 27 and 53 keV, so works as dual photon absorptiometry. Sufficient beam intensity for absorptiometry are obtained at the conditions of 70 kV and 5mA on the X-ray tube. Basic studies on the instrument are performed including photon energy identification, beam intensity and stability, linearity of bone mineral content, long and short term precision and comparison with conventional single photon absorptiometry. Results of those studies suggest that the instrument can be use as DPA of forearm. Also the instrument eliminate the expense of frequent replacing radioisotope source and decrease scanning cost. The system is expected as the useful instrument.

81

MP17.32

Is detailed biodistribution data necessary for nuclear medicine dosimetry? W. Huda* and G.A. Sandison, Manitoba Cancer Foundation, 100 Olivia Street, Winnipeg, Canada R3E 0V9.

Using the concept of effective dose equivalent, H_E , it is shown that a knowledge of detailed biodistribution data in most organs and tissues taking up ^{99m}Tc labelled radiopharmaceuticals is unnecessary. Dosimetric precision of about $\pm 25\%$ can be readily obtained from urine excretion data alone providing there is no significant uptake within the gonads or thyroid. Special attention should only be paid to absorbed dose measurements in red bone marrow, skin, lungs, gonads and thyroid, with the greatest attention directed toward the retention and dosimetric aspects of radioactivity in the gonads and thyroid glands. An example of the calculation of H_E for ^{99m}Tc labelled d,l-HM-PAO is presented demonstrating the importance of these specific organs to radiation risk. Using biodistribution data obtained in rats, the H_E value for a 20 mCi administered activity was computed to be 880 mrem, of which 62% was due to the risk of genetic effects.

MP18.2

Simple QC Test Tools for Diagnostic Radiology, P. Mora*, Escuela de Fisica, Universidad de Costa Rica, San Jose, Costa Rica and J. Cameron & J. Knoche, Univ. of Wisconsin, Madison, WI 53706, U.S.A.

Hospitals in developing countries do not usually afford sophisticated quality control (QC) instruments and do not have the trained professionals to use them.

Over the last five years various simple QC test tools for use by radiographers have been developed, primarily at the University of Wisconsin. The total cost of the materials for a set of the test tools is about \$100 U.S. About ten hours of semi-skilled labor is needed for their construction. The QC tools measure: 1) quantitative image quality for general radiography, fluoroscopy, mammography, angiography, and tomography; 2) size of the focal spot; 3) accuracy of the timer; 4) accuracy of the set kV; 5) collimator function; 6) alignment of the grid; 7) film-screen contact; and 8) consistency of the output for standard exposure conditions. The devices were designed to be used by radiographers. A set of the test tools are being evaluated by radiographers in several major hospitals in Costa Rica following a two day course on their use. The test tools will be described and their use under field conditions will be discussed.

MP18.1

Logistic Parameters Compared with Conventional Sensitometry for Radiographic Film-Screens, C. E. Willis* (KRUG) and J. A. Bencomo (UTSCC), KRUG International, 1290 Hercules, Houston, TX 77058

Analysis of CDRH sensitometric data confirms empirical observations that the film characteristic curve is a logistic function of exposure. Data for seven commercial radiographic emulsions using four intensifying screens were normalized to obtain fractional response between fog and saturation. Saturation was determined from the graph of absorbance versus the inverse of exposure. Normalized data were transformed into logistic units (Logits) and plotted versus the log of exposure. These graphs are linear from <2% to >98% fractional absorbance, or a factor of 100 in exposure. Regression analysis was conducted to determine logistic sensitometric parameters based on the explicit statistical weights of logistic data. The logistic slope, or contrast analog, had an average of 1.95 ± 0.19 . The logistic intercept (value of exposure required to produce 50% of saturation absorbance) or speed analog varied from 11.2 to 36.3 units of relative exposure. Previous reports show contrast analog is unaffected by development conditions, however, speed analog, saturation absorbance, and fog depend on degree of development. Tabulation of logistic parameters for photographic emulsions could simplify catalogs of sensitometric data. The linear logistic representation facilitates quantitative measurements.

MP18.3

Computation of Off-Axis X-Ray Spectra, D. M. Tucker*, D. P. Chakraborty, and G. T. Barnes, Dept. of Radiology, University of Alabama at Birmingham, 619 19th Street South, Birmingham, AL 35233

Birch and Marshall's¹ method of computing x-ray spectra has been extended to include off-axis (i.e., "heel") effects. Both bremsstrahlung and characteristic spectral components are included. With knowledge of the x-ray tube anode material and angle, kV and mA waveforms, and inherent and added filtration, the model allows one to predict the primary x-ray beam intensity and photon energy distribution at any point in the radiation field. Predicted and experimental x-ray beam intensities and qualities versus off-axis angle are compared for different x-ray tube voltages, filtrations and target materials and target angles. The agreement between the two is typically within 1-2%. Also discussed are potential applications of the model in dual-energy imaging and patient dosimetry.

¹R. Birch and M. Marshall, Phys. Med. Biol. 29, 505 (1979)

Supported in part by NCI Grant No. CA43615-02.

MP18.4

Optimization of Cine Angiography Using Variable Input Exposures,
J.S. Whiting* and J.M. Pfaff,
Cedars-Sinai Medical Center,
Los Angeles, California, USA.

We performed an analysis to investigate the use of a variable camera aperture to optimize signal detection in coronary angiography. Signal/noise (S/N), contrast, image intensifier exposure and skin entrance exposure (D) were calculated for detection of a 0.5 mm cube of 370 mg/ml iodine in water thickness ranging from 14 to 28 cm and x-ray tube potentials from 50 to 120 kV. Assuming 34 kW iso-power operation, S/N reached a maximum at 95 kV for all tissue thicknesses, but varied by less than 10% from 65 kV to 120 kV, while maximum $(S/N)^2/D$ occurred between 60-70 kV. Skin exposure increased linearly and contrast decreased exponentially with increasing tube potential for fixed tissue thickness. When patient thickness drives x-ray tube potential above 85 kV skin exposure may be reduced 70% with less than 10% penalty in S/N by reducing image intensifier input exposure 50%. Film exposure can be maintained by compensatory opening of the camera aperture one f-stop. We conclude that incorporation of aperture control into automatic exposure control systems can significantly minimize patient dose and/or tube loading without diminishing image quality.

MP18.6

Reject Analysis in Diagnostic Radiology
U. Giugni, R. Gallini, S. Belletti, V. Berna
Spedali Civili, Università degli Studi,
I-25100 Brescia, Italy

Reject analysis is an important part of any Quality Assurance (QA) programme in diagnostic radiology; this analysis provides a means of early detection of changes in reject rates, determines the baseline for a QA programme and monitors the effectiveness of that programme.

To this end we collected 8061 films (2303 examinations), coming from 7 radiological depts. (2 belonging to regional hospitals, 3 to median size hospitals, 1 to a pediatric hospital, 1 to a private institution). We choose the dimension of each sample according to the annual workload of the dept.

We considered 588 spoiled radiographs, determining 17 different categories of "reason". Some categories give less than 1% of wasted films, whereas other five reach a percentage of 10% or more.

This investigation represents the starting point of a QA programme, which also involves a patient dose survey and an imaging quality assessment.

Research supported by Regione Lombardia (Italy), grant N° 482

MP18.5

Analyses of Different Diagnostic X-ray Procedures Used in Switzerland
R. Mini, Abt.f. med. Strahlenphysik,
Inselspital, CH-3010 Bern

In many countries the diagnostic X-ray procedures gives the largest man-made contribution to the population dose. It is therefore important to analyse the different medical procedures in order to see which one is the most significant with regard to the radiation risks. The individual organ doses, resulting from a specific procedure depend very much upon the radiation technique which may vary from doctor to doctor. Therefore our Department of Radiation Physics has made an extensive survey in order to assess the variability of the technical parameters used for the different diagnostic procedures. The data of 200 doctors were analysed. As expected we found that even in a small country like Switzerland there is a big variation in the used procedure techniques. This makes it difficult to establish mean dose values which could be representative for the Swiss population.

MP18.7

Complexity Contrast in Radiological Images. R. Reed, W.M. Gentles, W. Ho, V.V. Velocci,
Sunnybrook Medical Centre,
University of Toronto, Toronto, Ontario, M4N 3M5, Canada.

Radiological images can be generalized as containing structures of interest their surround and noise. The surrounding and overlaying anatomical structures have a masking effect, reducing the conspicuity of a known target in a scene. If the characteristics of the surrounding anatomical structures are varied, the target conspicuity will vary, becoming small as the target and surround become similar.

A model is presented which provides an analytical method of measuring the amount of anatomical structure or anatomical noise in a target or scene. This leads to the definition of complexity. The theory also provides a method of determining if frequency dependent image processing can improve the conspicuity of a known target in a surround of known complexity.

The model is based on two assumptions: 1) The complexity of a structure or surround is related to its spatial frequency content, and 2) a figure representing complexity is derived from a linearly-weighted function of power spectrum.

A second figure of merit named complexity contrast is introduced. It gives a measure of complexity differences between a target and its surround. It is shown that in the limit of frequency approaching zero, complexity contrast approaches the definition of optical contrast. Complexity contrast is related to a form of SNR between a target and the anatomical structure (ie noise) of the surround.

Medical Physics Scientific Papers

MP18.8

Comparison of different types of collimator design used in dental radiography - R. Badiello*, T. Bernardi and G. Passerini - C.N.R. Servizio di Sicurezza del Lavoro e Protezione Sanitaria; Università, Servizio di Fisica Sanitaria, Bologna, Italy

The continuous increase in the use of X-rays in dental practice calls for an accurate analysis of the radiation protection of both the patients and the workers. In the present communication a comparison is made of different types of collimator design used in dental X-rays apparatus (cone, cylinder, parallelepiped) in view to reduce the dose to the patient and to increase the quality of the imaging. It is well known that the open ended collimators should be preferred to those that have plastic ends because these act as a source of scattered radiation. The parallelepiped shape offers further advantage with respect the cylinder one for what concerns the radiation protection of the patient. In fact the irradiated volume is strongly reduced (by a factor two) with a consequent reduction of the absorbed energy at the same exposition. The skin dose is also reduced since the retrodiffusion factor is smaller in the case of the rectangular area. Moreover such a type of collimator contributes to a better definition of the radiological image. The results are discussed and applied to the estimate of the collective dose equivalent for oral diagnostic radiology.

MP18.10

EVALUATION OF SCREEN-FILM COMBINATIONS FOR MAMMOGRAPHY

Marlene H. McKetty, Ph.D.
Howard University Hospital

The purpose of this study was to evaluate films for use in screen-film mammography from two manufacturers and to determine if the use of a medium-speed screen, that is now available, provides images that would be acceptable to radiologists in our department. Breast imaging is difficult because extremely small structures must be visualized and because much of the tissues have similar attenuation coefficients and produce little subject contrast. As the variety of mammography films and screens increases, mammography facilities must choose carefully among them to ensure that they obtain the best image quality at low doses.

Several images were made of two mammography phantoms using different types of film and differing speed Kodak Min-R Screens. Techniques were varied to produce the highest quality images at reasonable doses. The images were evaluated by three observers for parameters such as density, contrast and visibility of test objects in the phantoms. The data to be presented show that the single emulsion films from both manufacturers were equally acceptable to the observers and that the double emulsion film was not acceptable for routine use.

MP18.9

Performance Evaluation of Gamma Cameras in the Philippines, E. Valdezco, Phil. Nuclear Research Inst., Diliman, Quezon City and A. Lobrigitto*, Radiation Health Service Sta. Cruz, 1003 Manila, Philippines

The gamma cameras in the Philippines vary in ages. This paper presents the results obtained from the quality control tests done on these cameras, adopting the International Atomic Energy Agency standards. The physical parameters measured are the intrinsic uniformity, intrinsic resolution, intrinsic linearity, count rate loss, energy resolution, maximum count rate and sensitivity. Several measurements are done for every parameter and the performance of the gamma camera is evaluated using the mean value, to determine the clinical acceptability of the camera in obtaining maximum diagnostic information. The current mean standard (CMS) is derived and the performance of the camera is compared with the CMS. It is hoped that, with this paper, minimum performance standards will be established and will be used nationwide.

MP18.11

The Scatter Point Spread Function in Diagnostic Radiology, JM Boone* and JA Seibert⁺, Departments of Radiology, Thomas Jefferson University, Philadelphia, PA and ⁺University of California-Davis, Sacramento, CA.

Monte Carlo techniques were used to evaluate the point spread function of scattered radiation in diagnostic radiology. A homogeneous model of infinite lateral extent and of various thicknesses was analyzed using an ideal detector; this simplified model adheres to the requisites of linearity and stationarity. 80, 100 and 120 kVp beam spectra were used in this study, with air gaps of 0, 2 and 4 cm. An analytical equation was derived using four physical parameters as input--object thickness, air gap and the attenuation coefficients of both primary and scattered radiation. Though the analytical derivation assumes only single scattering, reducing μ (scatter) by about 10% results in excellent correlation with the Monte Carlo results.

5/13

MP18.12

An Image Data Compression System for X-Ray Medical Image, Wen Gao* and Masao Saito, Saito Lab Inst of Med Elec University of Tokyo Japan

In PACS image data compression is one of important functions because of losses from transmission and storage of medical image. An design of medical X-ray image data compression system named ADCTVQ (Adaptive Discrete Cosine Transform Vector Quantization) is presented in this paper. ADCTVQ uses adaptive bit allocation scheme for DCT efficient matrix and vector quantization technique. By the adaptive bit allocation scheme a result of average 1dB up can be gotten and by vector quantization an effect of minimal quantization distortion can be made. Simulation results show that for X-ray chest images the ADCTVQ can give acceptable image with a compression ratio not less than 12. Consideration of the real-time requirement ADCTVQ is constructed into parallel structure.

MP19.1

OPTIMIZATION OF PROTON AND HEAVY ION THERAPY USING AN ADAPTIVE INVERSION ALGORITHM, A. Brahme*, P. Källman and B. Lind, Dept. of Radiation Physics, The Karolinska Institute, Box 60204, S-104 01 Stockholm, Sweden

To fully utilize the dose distributional advantages of pions, protons and heavy ions it is necessary to cover the target volume as well as possible by Bragg peaks and avoid irradiating surrounding organs at risk. The most general way to achieve this goal is by three-dimensional scanning of the beam so that its Bragg peak fall exclusively in the target volume.

We have recently developed a very powerful iterative inversion algorithm capable of calculating the optimal scanning pattern of the proton beam required to get the desired dose distribution in the target volume. From this point of view the present technique implies a reversal compared to conventional treatment planning, where treatment fields generally must be chosen by a trial and error-like approach to maximize tumor dose and minimize normal tissue irradiation. Typical dose plans will be presented.

MP18.13

Tissue-Equivalent Phantoms

P. Dvorak, G.R. Symonds*, G.R.J. Robertson and B.M. Keller
Bureau of Radiation and Medical Devices
Department of National Health and Welfare
Ottawa, Canada, K1A 0L2

Phantoms designed to simulate the patient in quality control tests on diagnostic X-ray equipment should ideally match the tissue in energy dependence of X-ray absorption and scattering properties, and be sufficiently light and small to be handled easily. These two requirements are difficult to meet simultaneously. A computer model to evaluate the best combinations of materials for the suitability as tissue-equivalent phantoms has been developed and solutions suitable for narrow beam measurements using an ionization chamber, TLDs, films or similar detectors have been found. A simple experimental verification of this approach has been performed with encouraging results.

MP19.2

A Test of Eragg-Gray Cavity Theory for Protons
L.J. Verhey, Dept. of Radiation Medicine,
Mass. General Hospital, Boston, MA 02114

An ideal Bragg-Gray cavity is defined as one in which all energy loss is local, the cavity is much smaller than the range of secondaries and the production of secondaries in the cavity is negligible. For a thimble ion chamber in a photon beam in charged particle equilibrium, these criteria are well satisfied. In the case of a proton beam, however, the ranges of electron secondaries are typically less than 1 mm of air and the proton interaction probability per mm of gas is very high, so Bragg-Gray cavity theory cannot be used without modification.

We have investigated the significance of this effect by comparing the responses in proton and Co-60 beams of ion chambers with a variety of geometries and dimensions, including 0.1cc, 1.0cc, and 80cc spherical chambers, and a thin-window parallel-plate chamber. The ratio of responses for the same gas in the chambers of widely different surface to volume ratio, can quantify the departure from classic Bragg-Gray theory. The ratios of proton responses with different gases in the same chamber gives us a way of investigating W values for protons which are needed for routine dosimetry. The results of these measurements and their significance for proton dosimetry will be discussed.

MP19.3

Computed microdosimetry of epithermal neutrons in selected biological materials. R.E. Wallace* and P. Bloch, Univ of Penna, Dept of Radiation Oncology, Phila., Pa.

In tissue-equivalent materials, epithermal neutrons generally impart dose via elastic nuclear collisions. These reactions produce low energy charged recoil nuclei which are characterized by their low lineal energy, typically $\sim 10 \text{keV}/\mu\text{m}$ for 1keV neutrons. At low neutron energies, reactions producing high-LET particles can occur in tissue materials. For example, the $N(np)$ reaction produces a 600keV proton with a dose average lineal energy of $85 \text{keV}/\mu\text{m}$ in muscle. For 100ev neutrons, this reaction accounts for 5.7% of KERMA while the 2.2MeV γ -rays from neutron capture and elastic recoils in hydrogen contribute nearly 94%. The high-LET $N(n,p)$ protons have higher RBE than the γ -rays or the recoils. For example, using single fraction survival curves for human kidney cells at the 1% level as a dose response archetype(1), $\sim 28\%$ of the total effective dose for neutrons below 200keV is delivered by the $N(np)$ protons. Computed microdosimetric results in brain, muscle, fat, and bone will be presented. The microdosimetry of neutron capture in boron and lithium infused tissues will be discussed. (1) Barendsen, G.W., Los Alamos Laboratory report #LA-5180C, p. 120, 1972.

MP19.5

Dosimetric Characterization of Helium Ion Beams Used in Radiotherapy at the Bevatron, J.M. Collier*, T. Renner, S. Henderson, P.L. Petti, S. Pitluck, Research Medicine and Radiation Biophysics Div., Lawrence Berkeley Lab., CA Berkeley 94720

Because of the dismantling of the 184-inch cyclotron at the Lawrence Berkeley Laboratory, the helium ion radiotherapy has been transferred to the Bevatron. Initially, the treatments are being carried out using the "Wobbler" dipole magnets to spread the beam laterally in circles up to 30 cm diameter and plastic "propellers" to spread the particle stopping region in depth. This is in the room currently used for Neon ion radiotherapy also. However, a new treatment room is being built. In this room will be placed the unique patient positioner from the cyclotron. A double scattering system will be employed to create the lateral spread. Dosimetric characterization of the beam in the first room has been done using film and ionization chamber, including a 144 element linear array chamber in which each element is 2 mm wide by 1 cm long. Results will be shown which give the slope of the spread out Bragg peak, the distal gradient (3-4 mm for 90% to 10% drop off), and lateral penumbra for different treatment situations. Supported by NCI Grant 1CA19138.

MP19.4

Investigation of Alternative Dose Calculation Algorithms for Charged-Particle Therapy. P.L. Petti, Lawrence Berkeley Lab, Berkeley, CA 94720

Dose calculations for charged-particle radiotherapy typically use ray-tracing techniques to calculate the water-equivalent pathlength along the beam direction through a matrix of CT data. Although these calculations provide accurate dose distributions in homogeneous or simple heterogeneous systems, as Urie et al.¹ have discussed, errors due to multiple scattering arise in more complex heterogeneous geometries. The purpose of this investigation is to explore the possibility of using methods similar to the "differential-pencil-beam" technique described by Mohan et al.,² which rely on pre-calculated Monte Carlo data, to calculate charged-particle dose distributions. Calculations based on such an algorithm will be compared to Monte Carlo simulations for selected heterogeneous systems. Since the distance over which adjacent particle tracks contribute to the dose at any given point is small for charged particles, such techniques may not be prohibitively time consuming. This work is supported by NCI grant 1CA19138.

¹Urie M, M Goitein, WR Holley, GTY Chen, Phys. Med. Biol., 31, 1-15, 1986

²Mohan, R, C Chui, L Lidofsky, Med. Phys. 13, 64-73, 1986

MP19.6

Optimum Thickness of Li and Be Targets for the Production of Therapy Neutrons by Protons and Deuterons of Different Energies, M.A. Chaudhri*, Austin Hospital, and University of Melbourne, Melbourne, Australia.

It was suggested by us in 1970's that, from light elements (Li, Be, etc.), protons from a modern cyclotron would produce more penetrant neutron beams for therapy than deuterons from the same machine, and that moderately thick targets would produce neutrons with higher mean energies than thick targets. In this paper we are presenting results of our calculations on neutron production from Li and Be targets and different backup materials. Cyclotrons of different sizes, and backing materials of Cu and Ta, have been considered. On the basis of our results, it has been suggested that moderately thick targets of Li and Be would not only produce more penetrant neutrons, but also enough intensity to carry out neutron therapy. Moreover, as the energy absorbed in such a target is smaller than in a thick target, the heat dissipation problems would be more easily manageable.

MP19.7

Heavy Ion Medical Accelerator in Chiba, K.Kawachi*, H.Ogawa, T.Kanai, M.Endo and Y.Hirao, National Institute of Radiological Sciences, Chiba-shi 260, JAPAN.

A project of Heavy Ion Medical Accelerator in Chiba (HIMAC) has been started since 1984 in Japan. The final design studies of the HIMAC including the buildings have been completed. The HIMAC consists of ion sources, RFQ linac, Alvarez linac, synchrotron, high energy beam transport system and irradiation facilities. The main accelerator synchrotron consists of double rings which are operated with the repetition rate of 0.5Hz, and with the phase difference of a half period each other. The maximum output energy of synchrotron is 800 MeV/u for the ions with the charge to mass ratio of 0.5.

The HIMAC has both horizontal and vertical beam delivery courses. The sophisticated irradiation facilities consist of beam spreading system, range modulating system, field shaping system, beam monitoring system and patient's positioning system. The HIMAC will be completed in 1993 and be able to provide the beams for the clinical trials.

MP19.8

Microdosimetric Measurements of a High-Energy Neutron Therapy Beam, S.H. Benedict*, J.B. Smathers, L.T. Myers, R.E. Wallace, University of California, Los Angeles U.S.A.

Microdosimetric measurements were made in a neutron therapy beam using a Rossi proportional counter with a 1.50-cm wall of A-150 T.E. plastic. Previous microdosimetric studies have been performed on neutron beams of 14 and 15 MeV; however, few studies have been performed at higher energies. The CP-45 isochronous cyclotron at the UCLA Neutron Therapy Facility generates a neutron beam with 46 MeV protons that bombard a thin Be and C target. Both the target design and collimation system are unique to the facility. The charged-particle energy loss spectra were measured and compared at various depths in phantom, in the penumbra region, and outside the beam using standard techniques. The calculation of lineal energy distributions and gamma components from the spectrums was performed using established calculational techniques. A comparison of the microdosimetric data of the neutron therapy beam properties of the UCLA facility to that of other fast neutron therapy facilities is presented. This research is supported by NCI contract CM 97315.

MP19.9

SPATIAL DISTRIBUTION OF FREE RADICALS PRODUCED BY NEUTRONS AND ESR DOSIMETRY, C. Franconi*, K.V. Ettinger, J. Hołowacz#, I.I. Università di Roma, Italy

* On leave from Politechnika Gdańska, Gdańsk, Poland

Determination of absorbed dose in ESR dosimetry is based on measurement of the concentration of free radicals in the solid used as a dosimeter, e.g. a polycrystalline amino acid. At the same time it appears possible to estimate in the same sample the spatial distribution of radicals. This estimation is based on the known dependence of the microwave power saturation effect in ESR spectrometry on the value of spin-spin relaxation constant. This relaxation constant is, in turn, a simple function of the spin density. The experimental ratios of free radical densities produced by 7.6 MeV neutrons and 1.25 MeV gamma rays are within 1.5 - 4.0. If reactor neutrons are compared with 1.25 MeV gamma rays, the ratios of radical densities are within 1.4 - 3.3. In order to obtain the absolute values of radical densities from the saturation curves it is necessary to know the intensity of microwave magnetic field in the measured sample. This is accomplished by means of perturbation technique in which a minuscule scatterer is introduced into the cavity. The ensuing shift of the cavity resonance is a measure of the field intensity.

MP20.1

Quantitative imaging of acoustic backscatter coefficients, E. Boote*, J. Zagzebski, E. Madsen, T. Hall and M. Pozniak, Univ. of Wisconsin, Madison, WI, 53706

Current clinical ultrasound scanners provide only qualitative information on acoustical properties of tissue because operator, instrument and transmission path dependencies are inadequately accounted for during image formation. We have developed a technique for producing quantitative, instrument independent images of the acoustic backscatter coefficient and are implementing this on a clinical scanner. Our imaging algorithms are derived from a previously reported method of data reduction which rigorously accounts for all experimental factors in a pulse-echo experiment, including the transducer pressure field, pulser-receiver electronics and attenuation, yielding a measure of the intrinsic scattering properties of a medium. A spatial mapping of the reduced data results in a grey scale image, where the brightness of each pixel is associated with a unique small range of backscatter coefficients.

To implement this technique on a real-time sector scanner, a high speed transient recorder and a memory buffer digitizes and stores echo rf signal for the entire image during a sweep of the transducer. The digitized data are sent to a computer for off-line analysis and image display.

Initial tests of the system produced accurate backscatter coefficient images of tissue-mimicking phantoms containing regions of varying scatter levels. Quantitative images have been formed of *in vitro* samples of canine kidney (normal and transplant rejection) and human liver as well as of abdominal organs *in vivo*.

97

MP20.2

High resolution imaging through image reconstruction of axially deconvolved B-Scans.

A. Herment, P. Péronneau*, G. Demoment
INSERM U. 256, Hôpital Broussais, Paris, France.

In ultrasound imaging, where reflection images of a same structure can often be acquired under various incidences, a method has been developed for acquisition and processing of data. It consists in :

- . Acquisition of R.F. B-Scans
- . Line by line 1D deconvolution of these scans
- . Video detection
- . Image reconstruction by a filtered back projection process.

A study on simulated data and phantoms for S/N ratio ranging from 50 to 5 dB will be discussed. As compared to 2D deconvolution, for a typical (256 x 256) image reconstructed from 16 scans of 32 lines each distributed on 120°, the process shows :

- . A gain of 10 on processing time
- . A gain of 4 on S/N ratio
- . A gain of 5 on image definition.

Works are now in progress to assess the influence of the variable propagation speed in tissues on the image quality.

MP20.4

Comparison of a Visual and A Digital Measure of Relative Echogenicity Applied to Fetal Lung and Liver, P. Carson*, M. DuPuy, C. Meyer, R. Bowerman, E. Chiang, R. Hayashi, University of Michigan, Ann Arbor, MI 48109-0553

Relative echogenicity is a key source of information in ultrasound images. An algorithm for quantitative measurement of relative echogenicity was implemented, which corrects for digitally estimated differences in attenuation coefficients of two tissues with presumably identical overlying tissues. This measure of relative echogenicity was studied on fetal lungs and livers in a sample of 172 digital images from 8 third trimester fetuses. Two independent digital data sorters agreed well with each other; the 95% confidence limits for one sorter predicting the other's next data point on individual images and on average values for a fetus were 2.8 and 1.3 dB, respectively. Corresponding predictions of either sorter's echogenicity from visual readings by our most experienced reader were within +/- 4.4 and 2.2 dB, with 95% confidence. The somewhat higher precision and expected higher objectivity of the digital measure suggests possible value in repeating the (generally negative) earlier studies of relative lung to liver echogenicity as a possible indicator of fetal lung maturity. The digital measure is a better, but not essential, method of incorporating relative echogenicity in a multiparameter study of fetal lung maturity.

MP20.3

Correlation of Ultrasonic Attenuation with Pathologic Fat and Fibrosis in Liver Disease, T. Lin, J. Ophir*, G. Potter, Department of Radiology, University of Texas Medical School, 6431 Fannin St., Houston, Texas, USA

The attenuation coefficient in two groups ($n_1 = 70$; $n_2 = 59$) of pathologically graded in vitro human liver specimens was measured over a frequency range from 1.25-8.0 MHz and fitted to a power law model. The slopes of the power law curves at 5MHz were correlated with pathological score for fat in Group I, which consisted of normal and fatty livers (no fibrosis); they were also correlated with the pathological score for fibrosis in Group II, which consisted of normal and fibrotic livers (no intracellular fat). Significant ($p < 0.002$) differences were found between the two groups. The fatty liver group exhibited approximately a $0.23 \pm 0.06 \text{ dB cm}^{-1} \text{ MHz}^{-1}$ (fat grade) $^{-1}$ behavior (mean \pm s.d.), while the fibrotic liver group exhibited approximately a $0.11 \pm 0.01 \text{ dB cm}^{-1} \text{ MHz}^{-1}$ (fibrosis grade) $^{-1}$ behavior. These results may explain some of the conflicting literature in this area, and suggest that attenuation may in principle be used for screening for liver disease, but not for differentiation between fatty and fibrotic conditions.

Supported by National Institutes of Health grants #R01 CA38515 and R01 CA44389.

MP20.5

BONE PROPERTIES AND ACOUSTO-ULTRASONIC BEHAVIOR

A. Jivas, I. Leichter*, A. Mittelman, and A. Weinrub, Racah Institute of Physics and School of Applied Sciences Hebrew University of Jerusalem, and the Jerusalem Osteoporosis Center
Samples of equal size of three groups of femoral heads were investigated: 32 from normal cadaveric bones without known bone pathology; 39 from osteoporotics (OP) (5 of them diabetic), and 7 from osteoarthritic patients (OA).
For each sample three parameters were measured: 1) The bone density (BD) in grams/cm³ was determined by the Compton scattering technique. 2) The bone mineral content (BMCv) was determined by the Norland Bone Mineral Analyzer. The results in gr/cm² were divided by the bone height to obtain the BMCv in gr/cm³. 3) The peak amplitude (PKA) of a transmitted ultrasonic pulse and the pulse duration (PD) were measured by a AET 5000 system. From these data the relaxation constant (RC) of the exponentially decaying pulse was calculated. The PKA and RC values were the same for the OA and OP bones, although the BD and BMCv values of the OA bones were significantly higher than those of the OP bones and those of the diabetic bones in particular. The PKA and RC values of the normal bones, however were significantly smaller than those for the diseased bones, although the BD and BMCv values for the normals lay between those of the OP and OA. The acousto-ultrasonic parameters for the normal males and females did not differ while the BD and BMCv values were significantly different. These results show that there is no simple relationship between the acousto-ultrasonic parameters and the BD or BMCv values. While the latter represent measures of bone mass, the former may strongly depend on the structural elements of bone.

MP20.6

Artifacts in Sonography: Physical Mechanisms. F.W. Kremkau, Center for Medical Ultrasound, Bowman Gray School of Medicine, Winston-Salem, NC

The occurrence and manifestation of approximately eighteen artifacts of acoustic origin in sonography are reviewed. Physical mechanisms involved are described. They include pulse length, pulse width, interference, reflection, refraction, side lobe, grating lobe, attenuation, focusing, reverberation, resonance, speed error, and high pulse repetition frequency. Unexplained cases are included to stimulate thought and discussion. These artifacts are manifested on images as added or missing objects and objects with incorrect brightness, location, size, or shape. Some artifacts are useful in interpretation and diagnosis (e.g., shadowing and enhancement), while some can cause confusion and error (e.g., section thickness and reverberation). A proper understanding of artifacts and how to deal with them when encountered enables sonographers and sonologists to use them in diagnosis while avoiding the pitfalls which they can cause.

MP20.8

Effects of Ultrasound Irradiation on Axonal Outgrowth in Chick Embryos at 1.1 MHz. JW Yip, MS Rosenthal*, YPL Yip, C Capriotti, BQ He, University of Pittsburgh, Pittsburgh, PA, 15261, USA

Studying the effects of ultrasound irradiation on the developing central nervous system is important but difficult because of the immense structural complexity of the vertebrate brain and spinal cord. Using the less complex chick sympathetic system as a model allows us to investigate the effects of ultrasound irradiation on one aspect of neuronal development, axonal outgrowth.

Two-day-old chick embryos (stage 15) had two openings made in their shells to allow for ultrasound irradiation *in ovo*. The embryos were irradiated pulse mode (2000 Hz) at 1.1 MHz with a pulse width of 75 μ sec. Average power was 1 W/cm². The embryos were irradiated for 5 minutes, on three consecutive days starting on the third day of incubation (stage 17). Following each irradiation, embryos were staged and returned to an incubator (37°C). One day post final irradiation, embryos were examined for the degree of sympathetic preganglionic axonal outgrowth using the marker horseradish peroxidase (HRP).

Results to date have shown no evidence of any effect on sympathetic preganglionic axonal outgrowth with this scheme following exposure of 75 embryos and 75 controls.

MP20.7

The Use Of Ultrasound to Assure Correct Placement of ¹²⁵I Eye Plaques, B. Japp*, C.J. Paviin, H.D. McGowan, D.G. Payne, E.R. Simpson, P.J. Fitzpatrick, Princess Margaret Hospital, Toronto, Ontario, Canada.

A popular brachytherapy method for treatment of choroidal melanoma uses an applicator consisting of ¹²⁵I seeds in a gold shell. The plaque edge results in a very sharp dose gradient so it is important to assure that the tumor base is within the periphery of the plaque. Ophthalmic ultrasound is used routinely for imaging of choroidal melanoma. Imaging at the time of plaque placement and post-operatively may be used to show plaque position relative to the tumor and sensitive structures. Scans of the plaque are obtained *in vitro* in order to familiarize the operator with the images and/or optimize the materials of a dummy plaque in order to get a better image of the plaque center or edge. At the time of operation, the plaque is secured over the tumour and its position is monitored with ultrasound or the dummy is positioned and scanned before exchanging it for the loaded plaque. We have used this method of assurance with 3 plaque designs over the past 7 years. Good localizations and some misplacements will be demonstrated.

MP20.9

Ultrasonic Computed Tomography used in Noninvasive Temperature Measuring Yi-hong Yang & Hong-zhang Wang *, Dept. of Precision Instrument, Shanghai Jiao Tong Univ., Shanghai, P.R. China

In the ultrasonic hyperthermia, for the noninvasive temperature measuring and monitoring a method of ultrasonic computed tomography with a ring transducer array model and a suitable algorithm have been developed. In order to get high resolution with shorter calculation time sparse scan and sparse reconstruction have been proposed for measuring the increment distribution of sound velocity and then the increment temperature distribution. Since the sound beam can be partly hindered by the bone and air cavity in human body, resulting in a loss of projection data, the method of projection space iteration and the method of truncated projection have been used to make a good reconstruction from a limited data.

The method of ultrasonic diffraction tomography and the fast convolution-back-propagation algorithm are used for image reconstruction. Also, a new approach of diffraction reconstruction algorithms from limited data is proposed.

MP21.1

Weighted Moving Beam Therapy (WMBT) for Fast Neutrons (with special consideration of the neutron specific inhomogeneity problem), K.H.Höver*, B.Hesse, W.J.Lorenz, Deutsches Krebsforschungszentrum, D-6900 Heidelberg, FRG

A significant benefit for fast neutrons as reported recently is related to high energy $P(65)+Be$ or - using monoenergetic 14 MeV d-t neutrons to sophisticated treatment techniques. For the fast neutron therapy facility KARIN at the German Cancer Research Center the WMBT-technique and the corresponding treatment planning system have been developed with the view towards optimization dose distribution.

This computer controlled treatment technique allows to match isodoses close to the target volume and helps to overcome some problems followed from the neutron specific inhomogeneity problem where energy deposition is highly depending on atomic composition of tissues.

The results of CT-based computerized radiotherapy treatment planning verified by phantom measurements will be demonstrated and discussed in the presentation.

MP21.3

Radiation Dose Estimation for Radioactive Isotopes of Lead Labeled with Antibodies, F. Hosain*, W.W. Layne and E.M. Billings, Department of Nuclear Medicine, Univ. of Connecticut Health Center, CT 06032, USA.

It has been possible to label a monoclonal antibody (B72.3) with lead-203 in our laboratories. Cyclotron produced Pb-203 (T_p of 52 h with 80% of 279 KeV photons), and Ra-224 generated Pb-212 (T_p of 10.6 h with alpha emitting daughter products) are potentially useful for diagnosis and therapy, respectively. Radiation dose estimates have been carried out for anticipated clinical application. Calculations are based on preliminary animal data obtained with the Pb-203 labeled antibody, and kinetic modeling. Information based on a kinetic model using human plasma clearance of indium-111 labeled F(ab')₂ predicted a maximum of 12% uptake of Pb-203 radioactivity in tumors of the size of kidneys (usual size of hepatomas treated) Pb-203, which reduced to 3.6% in the case of Pb-212 due to its short half-life. Further, a rapid uptake of 30% in the liver (clearing with a biological half-life of 1 day), and 5% uptake in trabecular bone without any biological clearance were taken for dosimetry. The S-absorbed dose factors were derived for 24 x 25 source-target combinations. Estimated doses were found to be 2.2, 0.25, 0.03 mGy/MBq with Pb-203 for tumor, liver and marrow compared to corresponding values of 23, 9.2, 3.6 for Pb-212 in equilibrium with daughter products.

MP21.2

NONINVASIVE THERMOMETRY: THE POTENTIAL OF MRI IN CLINICAL HYPERTHERMIA, N.A. Detorie*, D. Jenkins, M. Tkacik, Richland Memorial Hospital, U.S.C. Medical School, Columbia, South Carolina

Temperature was used as a contrast agent to alter the relaxation times of muscle tissue imaged with a 1.5 Tesla MRI system (Philips Gyroscan). Spin echo images prior to and post heating were T1-weighted: TR=800msec. and TE=30msec. These images demonstrate an expected and observable loss of MR signal with increasing temperature. Temperature sensitivity can be dramatically enhanced via image subtraction of the "prior" from "post heating" image. Furthermore, selective point temperature measurements in tissue "prior" and "post imaging" potentially provide a calibration for quantitatively assessing the temperature distribution throughout the entire imaged volume. Twelve image slices (128x128) utilizing a single MR measurement can be acquired in approximately two minutes. The subtraction images provide information which may be applicable not only to thermal modeling but also treatment planning. Our experience to date regarding heating and imaging both in vitro and in patients will be discussed.

MP21.4

The Impact of Dose Response Curves on the Accuracy in Clinical Dosimetry, P. Kartha*, L. Lanzl, S. Reddy and F. Hendrickson, Rush-Presbyterian-St. Luke's Medical Center, 1753 West Congress Parkway, Chicago, IL 60612

There is enough evidence that the dose response curve is rather steep and that the accuracy of dose is important clinically. The purpose of this paper is to present dose response curves derived from clinical data obtained when treating certain types of tumors e.g. head and neck and cancer of the cervix and their implications in the accuracy of clinical dosimetry. The discrepancies observed in physical dosimetry, dose prescription, treatment planning, clinical dosimetry and daily patient set-ups will be presented. These inaccuracies may lead to errors in delivered target absorbed dose of such magnitude that might change the probability of local control appreciably. Our experience and results in treating over 15,000 patients during the period 1971 to 1987 on the megavoltage units: Theratron 780, varian Clinac 4 and an AECL Therac 20, will be discussed. We have used dedicated computers to monitor and verify the set up parameters while treating the patients with radiation. An analysis of our data indicates that a good quality assurance program in Radiation Oncology Physics alone can prevent the errors from occurring.

100

MP21.5

Virtual Simulation in a Physical World: Some Practical Considerations, George W. Sherouse¹, J. Daniel Bourlard, Kevin L. Reynolds, Harris L. McMurry, Thomas P. Mitchell¹, Julian G. Rosenman, Edward L. Chaney, Radiation Oncology, University of North Carolina, Chapel Hill, NC 27514, and ¹Radiation Oncology, University of Florida, Gainesville, FL 32610

Clinical implementation of *virtual simulation* (the use of CT images and computer software in place of a conventional treatment simulator) requires the ability to transfer the geometry of the virtual patient and treatment unit to the clinical setting in a way which is both reproducible and efficient enough for routine use. We have separated this process into 1) repositioning of the patient with respect to the treatment couch, 2) localization of an absolute coordinate origin in the patient/couch system, and 3) absolute positioning "by the numbers" of the treatment couch, gantry, and collimator. The first problem has been addressed by use of full- or hemi-body polyurethane foam molds formed within alignment jigs, the second by use of a clinically-locatable coordinate reference, and the third with the help of three-axis coordinate scales. Our early experience with use of these repositioning and localization techniques will be presented.

MP21.7

Evaluation of the new 50 MeV race-track microtron with multi-leaf collimator for patient treatment, M. Karlsson*, H. Nyström, J. Stenberg and H. Svensson, Radiation Physics Department, University of Umeå, S-901 85 Umeå, Sweden.

Clinical electron and photon beams for patient treatment have been developed on a new type of 50 MeV race-track microtron in Umeå, Sweden. The collimating system on this unit is a new type of high resolution multi-leaf collimator. Electron beams at energies between 5 and 50 MeV can be used and the beam flattening is obtained by a computer controlled scanning system. A minimum of scattering material is introduced in the beam and the measured depth dose data will therefore be very close to what is theoretically achievable. Photon beams can be extracted at the same energies as for electrons. Also these beams are scanned and the use of very sharp flattening filters are thereby avoided. This will decrease the neutron contamination at high energies and also make the beam flattening more stable. The collimating system is a newly designed multi-leaf collimator with 64 leaves. To reduce the electron scattering in the treatment head the air has been substituted with helium gas. It is therefore possible to use the same collimating system for both electrons and photons. Except for a technical description of this new system, the presentation will include a full set of beam data, dosimetric data and some experience from the first patient treatments.

MP21.6

Dosimetry of I-131 Labeled A6H Antibody, *TK Johnson, RL Vessella, SE Mittelstadt, ML Mathisen, BW Wessels, MK Elson, FM Grund, DJ Leightner, RK Chiou, PH Lange, VA Medical Center, Minneapolis, MN.

A6H is a highly specific monoclonal antibody targeted against Renal Cell Carcinoma. In phase I-II clinical trials, 10-20 mg of antibody, labeled with 5 mCi of I-131, was administered to patients with primary and/or metastatic disease to ascertain in-vivo pharmacokinetics. A higher dose (50 mCi, 20 mg) was administered in a tumor site imaged as part of a therapeutic dose evaluation series. Dosimetry estimates were made using the MABDOS software of Johnson. Data were modeled as four compartments comprising whole body (blood), tumor, liver and spleen. The MABDOS environment allowed interactive model specification, integration of the resulting differential equations, calculation of cumulative activities, interactive definition of tumor site(s), Monte Carlo simulation of prominent photons for each source compartment, and dosimetry presentation in a tabular format by organ. Estimates of tumor dose ranged from 100 to 1300 rads, and were highly dependent on estimates of tumor mass. Extrapolations indicate that much higher doses (100 to 200 mCi I-131) might be tolerated by patients.

MP21.8

IMPLEMENTING AN IN-HOUSE QUALITY CONTROL PROGRAM AT HYPERTHERMIA FACILITIES, P. Shrivastava,¹ T. Saylor¹, D. Wilkinson¹, B. Paliwal¹, D. Beuchler², R. Steeves², ¹Hyperthermia Physics Center, Allegheny-Singer Research Institute, Pittsburgh, PA 15212-9986, and ²University of Wisconsin, Madison, WI.

A strong commitment to quality control measures is necessary at every hyperthermia facility to achieve safe, effective and reproducible treatments. Without these measures, the variability in heat distributions can be so large that the benefit of treatment may become inconsistent. The recommendations for an in-house QA program developed by the Hyperthermia Physics Center (HPC), under contract #N01-CM-37512 will be presented in this paper. These recommendations are based on the HPC experience in reviewing a number of hyperthermia facilities in the USA using a variety of equipment and participating in national cooperative hyperthermia trials. The recommendations include QA procedures and criteria for ensuring the proper operation of equipment and guidelines(1) for optimum patient setup, treatment delivery and documentation.

(1)Hyperthermia Quality Assurance Guidelines, HPC Report No. 8803 (Radiation Therapy Oncology Group, 1101 Market Street, Philadelphia, PA).

101

MP21.9

"Thyroidal Hormonal Changes During And After Head And Neck Irradiation" A.K.Shukla, D.K. Hazra, T.N. Edoliya, Y.C.Agarwal, V.K. Sachan, J.Chandra, J.K. Cancer Institute, Kanpur (India).

The functional disorders of thyroid gland induced by its incidental inclusion in the radiation field during head and neck irradiation may be encountered. The onset of thyroidal hormonal changes may be predicted to be of measurable order even during the progression of radiotherapy as well as after its completion. The present study included 29 patients undergoing irradiation of head and neck region. The serum T3, T4 and TSH levels were measured using radioimmunoassay technique and the results were statistically analysed. The changes in mean T3 levels were observed to be statistically insignificant both during and immediately after the course of radiotherapy, whereas the alterations noticed in mean T4 levels were more pronounced and found to be statistically significant at the end and one month after the course of radiotherapy. The TSH levels indicated similar changes and it was concluded that the radiation related abnormalities may be more common than speculated in the past.

MP22.2

In vitro Dosimetry by the Determination of the ATP-Decay in Devitalized L1210-Cells with the Help of ^{31}P -NMR-Spectroscopy. W. Ulmer, St. Marienkrankenhaus, Radiology, 5900 Siegen, FRG

Radiobiological dose-effect-relationships are usually determined by an observation of the colony-forming ability of clonogenic cell cultures. ^{31}P -NMR-Fourierspectroscopy provides a tool to determine the fraction S of devitalized cells in a more direct manner, because it is possible to measure the ATP-contents via the chemical shift after irradiation. Devitalized cells are not able to synthesize new ATP, and the remaining ATP must undergo hydrolytic decay processes. The experiments with L1210-mouse leukemia cells, which have been irradiated by 200 kV X-rays, show that the integral ATP-concentration represents an adequate surrogate for the survival probability, and the applicability of the linear-quadratic survival function

$$S = \exp(-\alpha D - \beta D^2)$$

has been tested by the determination of the ATP-contents via ^{31}P -NMR-spectroscopy and by the conventional method of the observation of the survival fraction.

MP22.1

In Vivo MR Spectroscopy of the Brain. M.A. Smith, D. Porter, V.T. Ayton, M. Lowry, C.J. Twelves, M.A. Richards, P.B. Garlick and M.N. Maisey. Divisions of Radiological Sciences and Clinical Oncology, United Medical and Dental Schools of Guy's and St. Thomas's Hospitals, Guy's Hospital, London.

In vivo human ^{31}P spectra have been obtained using a 1.5T MR imaging and spectroscopy system (Philips Gyroscan). A closely fitting phosphorus head coil is placed round the subject's head and both are positioned within the proton imaging head coil. Images are obtained to identify the volume to be studied. The magnet is shimmed to 0.25ppm on the volume of interest using SPARS (spatially resolved spectroscopy). The phosphorus spectrum is then acquired using ISIS (image selective in-vivo spectroscopy). Methods of spectral processing have been investigated to give a reliable estimation of peak area ratios.

Localised brain spectra have been obtained from 16 normal subjects of which 10 have been repeated after a delay of at least 1 month. The mean pH was 7.00 with a standard deviation of 0.07; the percentage difference between repeated measurements was 0.6%. Results will be presented on twenty patients with brain tumours, in some cases both before and after therapy.

MP22.3

An Adiabatic Half-Passage Pulse in Human Forearm ^{31}P NMR Spectroscopy. S. A. Altobelli*, M. V. Icenoglet, and E. Fukushima, Lovelace Medical Foundation, and VA Hospital Ambulatory Care Unit, Albuquerque, NM, USA

This study evaluated an amplitude and phase modulated pulse¹ in forearm ^{31}P surface coil spectroscopy at 1.9 T. This pulse performs an adiabatic rapid half passage to reduce the adverse effects of RF magnetic field inhomogeneity. Spectra generated using the pulse have 15% or more S/N than spectra obtained using a single hard pulse which was chosen empirically to produce maximal signal and which is approximately a π pulse at the surface. Increased S/N will improve the time resolution of ^{31}P spectroscopy during studies of forearm exercise. The imager/spectrometer (NALORAC Cryogenics) allows specification of shaped RF excitation in terms of a text file table of RF relative amplitude and phase. The actual amplitude, pulse duration (t_p), transmit phase and offset frequency (f_s) can then be specified at run time. In these experiments, N-point RF shape tables of the form: amplitude = $\sin(m\omega)$, phase = $K \cdot \sin(m\omega)$, with $m = 0, 1, \dots, N-1$ were used. N was either 256 or 512, ω was $\pi/(2(N-1))$, and K was constant. The amplitude of the pulse follows one-quarter cycle of sine and the phase variation causes a frequency sweep which follows one-quarter cycle of cosine. The sweep ends at $f_0 + f_s$ and begins at $f_0 + f_s + NK\omega/(360 \cdot t_p)$, where f_0 is the NMR frequency.

¹ MR Bendall and DT Pegg, J. Magn. Res., 67, 376 (1986).

MP22.4

The DISC Pulse Sequence: Depth and Inversion with Surface Coils, G.D. Clarke* and R.B. Rehr, Medical College of Virginia, Richmond, Virginia, 23298

Inversion of nuclear magnetization is difficult when attempting selective excitation with surface coils because the inhomogeneous magnetic fields produced by these probes will rotate the magnetization through a large range of angles. We have developed and tested a pulse sequence which can invert magnetization at a selected chemical shift while also allowing a degree of spatial localization for *in vivo* spectroscopy.

A shaped, complex sech pulse is used for the inversion of selected peaks within the entire sensitive volume of the sample. A two cycle, 90 msec sech pulse will produce nearly uniform inversion of a 100 Hz region in a spectrum. After a variable delay, four consecutive pulses are cycled through 16 phases which produces a "depth pulse". An FID from a volume undergoing a rotation close to 90° is observed. The T_1 's of various metabolites can be measured using the inversion recovery experiment. The DISC sequence can also produce reliable values for the flux through the creatine kinase reaction as demonstrated by both *in vitro* and *in vivo* inversion transfer measurements.

MP22.6

A NOVEL PROBE FOR A 7.6 CM WIDE BORE NUCLEAR MAGNETIC RESONANCE SPECTROMETER D.R. Harrison, S.A. O'Connor*, D. Reid, P.J. England & P.G. Morris¹ Smith Kline & French Research Ltd, The Frythe, Welwyn, Hertfordshire, AL6 9AR U.K. and Biochemistry Dept., University of Cambridge¹

Critical data on how medicinal compounds affect the function of whole animal organs can be obtained by means of a wide bore 7.6 cm nuclear magnetic resonance (NMR) spectrometer, operating at a frequency for protons of 360 MHz and phosphorus of 145 MHz, which can perform detailed biochemical analyses of the whole working organ. To maximise the data which may be obtained we have designed, developed and tested, with a variety of organs, a novel reproducible probe for the NMR spectrometer, which allows: the temperature in the region of the coil to be monitored and kept constant; the temperature of the perfusate to be kept at 37°C; the organ to be stimulated electrically if necessary; the capacitors on the RF coil to be fine tuned whilst the probe is within the spectrometer. The probe is versatile in that different sizes of coil for different whole organs may be accommodated up to the maximum size of the probe. The excellent signal to noise characteristics of the probe have enabled us thus far to study rapid changes (10-20s) in the concentration of high-energy phosphate compounds in perfused rodent hearts induced by established as well as novel cardiotoxic agents.

MP22.5

Design of Notch Band Magnetic Resonance Pulse Sequences Using Optimal Control Techniques, V. Smith*. Department of Radiation Oncology, University of California, San Francisco, CA 94143.

Optimal control theory has recently been used to design selective pulses, both for magnetization inversion and for time reversal. This approach has been extended to design pulse sequences providing uniform excitation over a specified frequency range except for a narrow band having essentially zero excitation. Such sequences can be used, for example, for water-suppressed proton spectroscopy by centering the notch of zero excitation at the water resonant frequency. The Polak-Ribiere conjugate gradient method was used to minimize an objective function based on the product of the actual and desired magnetization vectors. This product was calculated, typically, over a pulse sequence of 128 points for each of 21 frequencies covering the range of interest. The excitation profiles produced closely matched the ideal and did not exhibit the errors seen when the inverse Fourier transform small-angle approximation is used.

MP22.7

HYDRATION OF NITROGENOUS COMPOUNDS IN THE URINE MEASURED BY H-NMR SPECTROSCOPY, S.Nakaya*, Y.Tanaka, Y.Yoshioka, and N.Yasuda, Dept. of Physiol. 2., Sch. of Med., Iwate Medical University, Morioka, Japan.

High resolution H-NMR spectroscope (80MHz, 1.9T.) has been used to analyze human urine. The peaks of many components, especially nitrogenous compounds such as creatinine, free amino acids, etc. have been identified in the FT-spectra of normal urine. In the present study, we examined the interaction between several such compounds and water by comparing T_1 and T_2 of water protons (NMR relaxation times) at several different concentrations (0.1 - 10 M for urea, 0.01 - 0.8 M for creatinine, 1 - 10 mM for uric acid, 0.01 - 3 M for glycine). With the increase of the concentration, T_1 decreased linearly (2 - 3 sec) and T_2 decreased exponentially (0.1 - 2 sec) with all compounds examined. The hydration number (mol H₂O/mol) calculated based on the T_1/T_2 ratio (Kumosinski and Pessen) was 8 for glycine, 4 for urea, and 0.5 for creatinine. For uric acid, the degree of hydration seemed to be smaller in acidic than in alkaline solutions which suggested that the urate crystals might be formed more easily in aciduria.

MP22.8

PMR SPECTROSCOPIC ANALYSIS OF BLOOD PLASMA FROM HEALTHY AND CANCEROUS PATIENTS, D.A. Wilkinson*, H.R. Giles, H.F. Acevedo, P.N. Shrivastava, B. Jammillo, Allegheny-Singer Research Institute, Pittsburgh, PA 15212 and J. Dadok, A.A. Bothner-By, P. Mishra, Carnegie-Mellon University, Pittsburgh, PA 15213.

Blood plasma from fasted cancerous patients was compared with plasma from fasted healthy males and females using 620 MHz PMR spectroscopy with various degrees of resolution enhancement. Significant variations in the methylene and methyl resonances, arising mainly from the lipoproteins (VLDL, LDL, HDL) were observed along with changes in the levels of β -hydroxybutyrate. These changes are accentuated by using difference spectroscopy, a technique which may provide more and better information about blood plasma than other techniques currently employed (e.g. line-width measurements). Our data also show that factors such as sex and age are important in assessing the spectra.

MP23.1

Measurement of Three Dimensional Bone Architecture by Micro-computed Tomography. L. A. Feldkamp, S. A. Goldstein, M. J. Flynn*, Ford Motor Co., Univ. of Michigan, and Henry Ford Hospital, Detroit, Michigan.

A system for high-resolution, three-dimensional, x-ray computed tomography has been constructed and is being applied to studies of the architecture of *in vitro* specimens of trabecular and cortical bone. The system is comprised of a microfocus x-ray source, rotational and translational stages, x-ray image intensifier, vidicon camera, video digitizer, and computer with array processor. Images obtained at a sequence of rotational positions are converted to maps of 2D projection integrals and processed with a cone-beam reconstruction algorithm (1). Typical reconstruction sets for specimens in the 1 cm³ range consist of 200³ density values. Resolution for this sample size is roughly isotropic with FWHM of 50 micrometers. Better resolution can be achieved over a smaller volume by increasing the geometric magnification. In applications to bone architecture, reconstructions are subjected to morphological analysis.

1. Feldkamp, Davies, Kress, J. Opt. Soc. AM A2, 612 (1984)

work supported in part by NIH-SIO-RR03348, AR34399, and AR31793.

MP22.9

Limits for Fast Exchange: Practical Considerations for NMR Relaxation Measurements. L. John Schreiner, McGill University, Department of Radiation Oncology, Montreal, Canada.

The apparent nuclear magnetic relaxation rates measured for heterogeneous systems containing protons in a number of different environments, or spin groups, are functions of exchange rates between the spin groups and of the true inherent relaxation rates and spin densities of each group. If the exchange is 'slow', the apparent relaxation rates are the inherent rates; if exchange is sufficiently 'fast', the whole system is observed to relax with a single rate. The exchange rate conditions for the slow and fast regimes are determined with respect to the inherent relaxation rates of the spin groups. Therefore, for example, the apparent proton T₁'s of tissue are well explained by the fast exchange two-state model, while the apparent T_{1ρ}'s and T₂'s of tissue are not. The details of the two-site exchange model will be reviewed to clarify the behaviour of the apparent relaxation in the transition from the slow to fast exchange regimes. It will be shown that throughout the transition the spin relaxation is characterized by two magnetization components. As the fast exchange regime is approached, the magnetization fraction of the high relaxation rate component becomes vanishingly small. A practical limit for the onset of fast exchange, in terms of the inherent relaxation rates and the spin densities of the spin groups, will be presented. This limit for apparent fast exchange is dependent on the ability of the spin relaxation measurement to resolve the small fast relaxation component. The errors associated with the failure to resolve this component will be discussed.

MP23.2

A QCT Method for Analyzing the Spatial Distribution of the Bone Mineral within the Femur, M.M. Goodstitt^{1*}, D.C. Kushner², S.C. Orphanoudakis³, R.F. Kilcoyne¹, M.L. Richardson¹, S.M. Ott¹, W.P. Shuman¹, ¹University of Washington, Seattle, WA, ²Massachusetts General Hospital, Boston, MA, ³Yale University, New Haven, CT

Presently, nearly all QCT bone mineral analysis techniques determine the mean mineral content within the trabecular region. This mean value, however, may not be very representative of the distribution of bone mineral content, and it does not yield specific information about where the bone is being resorbed and remodeled. We have developed a new method which automatically outlines the borders of the cortical and trabecular regions in cross-sectional CT images of bones, and determines the bone mineral content (BMC) within multiple concentric zones in each region. The BMC is referenced to that in a set of 6 calibration rods (97 - 1460 mg/cc CaCO₃) which is scanned separately from the patient. Histograms of the BMC within the cortical and trabecular regions are generated as are tables of the BMC within each zone. The technique has initially been applied to CT images of the midshaft of the femur, and will in the future be applied to other bones.

*Work supported by NIH BRS grant RR05432

MP23.3

CT Brain Volumetrics for Alzheimer's Disease, Nai-Chuen Yang*, Peter K. Leichner, Godfrey D. Pearlson, Jose A. Mendizabal, Joseph B. Bryer, Upma Dhingra, Alan Tien and William G. Hawkins, Department of Radiation Oncology and Department of Psychiatry, The Johns Hopkins Hospital, Baltimore, Maryland.

A new algorithm is developed to calculate the cerebrospinal fluid (CSF) and brain volumes from CT scans of the brain. Computer software is used to contour the brain automatically and strip off the skull. The CT number distribution for each slice is generated and saved in a histogram. Beam-hardening effects are corrected in two steps. First, a linear regression analysis is carried out for mean CT numbers versus brain sizes for the brain slices. The mean CT numbers for all slices are then shifted to a standard value to take care of the "apical" artifact. "Shifted" histograms are then generated for all slices and summed together to get a global histogram. A global CT number threshold is then calculated with a two-gaussian model and it is accurate enough to separate and highlight the CSF's and the brain tissues in the central regions of all the "shifted" images. The "cupping" artifact causes the peripheral CSF's too high in CT numbers and an empirical formula is then used to correct for it. Preliminary studies show that the CSF versus brain ratios range from 12-22% in Alzheimer's Disease and 3-7% in normal controls.

MP23.5

Locally Optimal Run-Length Compression on CT Images without Restriction to Pixel Value, J. Liu* and M.W. Engelhorn, Zhejiang University, P.R. China

Locally optimal run-length compression on CT images reported by other contributor is only applicable to CT images whose pixel value is 12-bit. However, pixel values of CT images may be variable from 8-bit to 16-bit. Single byte coding (SBC) has been put forward to solve this problem. No matter how many word-length of pixel value is, the single byte coding based on byte has no trouble with it always. But one of most important problem in SBC is how a run-length size of noncompressible pixels would be decided. So called "noncompressible pixels" are not certainly in fact noncompressible, only a gain from compression of these pixels is too small, so they are regarded as noncompressible. In order to search out a length of noncompressible pixels a search method and a discriminator are defined. Then run-length of noncompressible pixels can be determined reasonably with the strategy, and experiments have shown SEC are successful.

MP23.4

Improvements on Locally Optimal Run-Length Compression on CT Images, J. Liu* and M.W. Engelhorn, Zhejiang University, P.R. China

In locally optimal run-length compression on CT images differential entropy is selected as a criterion for compression. The reported compressed results for 12-bit CT images are 8-9 bits/pixel which are far from the criterion of these images which are from 5.5 to 6 bits/pixel.

Analysed result has given one of reason why the compression can not reach the upper limit is that the strategy is not perfect, option of a optimal compression format in every run is not always ensured with that method. The compressed results after the improvements are generally closed to the differential entropy, about 5.5 bits/pixel for 12-bit CT images. Thus the results have challenged to that the differential entropy is selected as a upper limit for compression.

MP23.6

Practical applications of the use of re-constructed CT images in radiotherapy planning, C. Sims*, I. H. Manifold and J. Conway, Weston Park Hospital, Sheffield, S10 2SJ, England.

Some tumours, notably those of the head and neck and the oesophagus, require to be treated in a non-transverse plane. They may be displaced horizontally or vertically or both. Conventional planning of such tumours is difficult due to the difficulty in interpreting simulator films in such planes. CT gives improvements in the localisation of the tumour and possibly, more importantly, critical structures such as the spinal chord and the brain stem. We have developed a method of reconstructing transverse CT images into the appropriate oblique plane. Software has been written on the Picker Independent Treatment Planning System (ITPS) to allow planning to take place utilising central axis and off-axis oblique CT images

The results of phantom studies will be presented to show the accuracy of the method in addition to detailed examples for patients with tumours of the parotid, middle ear and oesophagus. Finally, the problems of verification will be addressed, together with a general discussion on the problems and pitfalls of planning in oblique planes.

MP23.7

Errors in CBF Determinations by Xenon-Enhanced CT. WF Good, D Gur*, H Yonas, JM Herron. University of Pittsburgh, Pittsburgh, PA, 15261, USA

The contribution of errors in arterial xenon concentration estimations, CT noise and xenon arrival time to errors in the determination of regional cerebral blood flow by the xenon-enhanced CT technique was evaluated by computer simulation and confirmed through a series of *in vivo* and phantom experiments. The results of this study indicate that approximating the arterial data by a single exponential build-up introduces relatively small errors. On the other hand, significant sources of error were found to be caused by CT noise and inaccuracies in estimating the xenon starting time in relationship to sequential scanning times. The overall system's errors in estimating CBF using this method depend on many factors and can be significant. Using current technology, it is not uncommon that estimated flow value in a single pixel have errors associated with it which exceed 100%.

MP23.8

Ionization Chamber Imaging of Megavoltage X-ray Treatment Portals, G. Luxton^{*1}, R. Gomez², M.A. Astrahan and T.T. Pham¹, ¹University of Southern California School of Medicine, Los Angeles CA 90033, and ²California Institute of Technology, Pasadena CA 91109.

Imaging of megavoltage x-ray beams was investigated using a 1 atm. gas ionization chamber, filled either with air or fluorinated hydrocarbon (freon), used for its higher density. The prototype detector consisted of a parallel array of 64 linear anodes separated 1 mm center to center. Anode to cathode gap was 4 mm. Images were formed by computer reconstruction from multiple projections, using the technique of filtered back projection, as in computerized tomography (CT). Reconstruction time on an IBMTM AT-compatible computer was 2 min. A 10 mm diameter cavity of 25 mm depth in a 50 mm thick acrylic phantom was imaged with an air filled chamber at 4 MV. With freon fill, the one-dimensional full width half maximum (FWHM) was 2.0 mm for a slit in a 4 MV x-ray beam, almost independent of thickness of lead screen used to enhance contrast. Chamber resolution for a slit in a 21 MV beam decreased from 2.0 mm FWHM for no screen to 3.2 mm FWHM with a 1.5 mm thick lead screen.

MP23.9

A portal verification system for external beam radiotherapy using a two-dimensional array of silicon transit dose detectors, I.Uchida† Y.Ornai, T.Tomaru, T.Yamashita**† M.Nakazawa** and K.Kaneta**† Cancer Institute, Tokyo,**Cancer Institute Hospital, Tokyo, Japan.

A portal verification system using a two-dimensional array of 289 silicon diodes has been developed to verify patient setup and the correct delivery of dose to the patient. Using this device, instantaneous information about the actual treatment beam passing through the patient can be collected simultaneously with the commencement of irradiation. The collected data are stored on a floppy disk for analysis at a later time. By doing quantitative dosimetric analysis, size and shape of each treatment field and water-equivalent thickness map within a treatment portal are displayed on a CRT and printed out. By the comparison of the data obtained during different treatment sessions, field placement errors and changes of the patient thickness can be estimated and also from instant data obtained during a treatment, patient movement and motion of internal anatomy can be detected.

MP23.10

Solid-view 3D-imaging for Brain Implants, K. Ayyangar*, N. Suntharalingam and Leslie Tupchong, Department of Radiation Therapy and Nuclear Medicine, Thomas Jefferson University Hospital, Philadelphia, PA 19107 and K.T. Daniel Yeung, Keh-Shih Chuang, Medical Image Processing Group, Dept. of Radiology, University of Pennsylvania, Philadelphia, PA 19026

Improved visualization of brain implants and the associated dose distributions, through either solid-view modelling or wire frame display has recently been incorporated into the planning procedure at TJUH. This was accomplished by adapting Movie-BYU software along with our Vax 8300 and Lexidata Image processor hardware. It is now possible to display tumor volumes, radioactive segments of catheters and isodoses all as a 3D volume display. The resultant 3D object is interactively rotated to visually analyze the adequacy of the proposed implant. The display time for each solid view is in the range of 1-2 min per image. Wire frame data can be rotated much faster at 20 sec per image. Currently, the display time is a limitation. Work is progressing however, to improve interactive time using hardware capabilities of the Lexidata. The clinical usefulness of this new feature will be discussed with representative implant cases.

MP23.11

Computer Modeling of Fast Heavy Ion Radiography

Julius J. Almasi*[§] and Cornelius A. Tobias
Lawrence Berkeley Laboratory
University of California, Berkeley, CA 94720

Heavy ion radiography (HIR) images are usually reconstructed from the residual range distributions of the primary heavy ion beam behind the object. In the past plastic detector stacks were used to determine the location and residual range of the primary heavy ions. We amend the possibility of using a single plastic detector sheet. The location and residual range of the primary heavy ions behind the object can be determined from the coordinates and the parameters of the etched tracks on a single detector sheet. A series of calculations have been carried out to determine the possible resolution and contrast of the (HIR) images using different heavy ions with different energies. We have calculated the absorbed dose in the patient as well as other benefits and limitations of this new method. Results of this calculation will be presented. We found that the new technique of analysis is faster than analyzing whole stacks of plastic and it can also give higher density resolution.

§ NIH postdoctoral fellow, Present address
Siemens Medical Labs., 2404 N. Main Street
Walnut Creek, CA 94596

MP23.13

On-line portal verification,
S. Shalev*, K. Leszczynsky, T. Lee,
Manitoba Cancer Treatment and Research
Foundation, Winnipeg, Canada R3E 0V9,
and L. Reinstein, A. Meek, Stony Brook
University Hospital, NY 11794.

A digital imaging system has been constructed for the acquisition of on-line portal images and the verification of beam locations during treatment. The detector consists of a metal/phosphor screen combination which is viewed by a high sensitivity video camera via an angled mirror. The video images are processed by an IT-151 digital processing system with a host IBM PC-AT. Software has been written to permit real-time frame summation and non-uniformity corrections, and contrast enhancement is attained by thresholding, filtration, real-time convolution and histogram modification techniques. Spatial resolution is better than 1 lp/mm, and contrast resolution is greatly superior to film. Examples of on-line portal images are shown for the head and pelvis, using a cobalt therapy unit and a 4 MV linac. A "movie mode" permits the visualization of patient movement during treatment. Portal images are compared with the prescribed portal boundaries from simulator films, and any significant discrepancies are displayed for immediate operator intervention.

MP23.12

Reduction of scatter in portal imaging.
S. Shalev*, T. Lee and L. Reinstein,
Manitoba Cancer Treatment and Research
Foundation, Winnipeg, Canada R3E 0V9,
and Stony Brook University Hospital, NY
11794.

Portal films and on-line portal verification images obtained with high energy radiation exhibit poor contrast resolution and are notoriously difficult to use. Image quality can be improved with the use of a thick metal plate to preferentially absorb incident electrons which have been scattered in the patient. We have examined the scatter to primary ratio for films exposed under copper plates of different thicknesses, using radiation from linacs with 6, 15 and 25 MV maximum photon energy. A 20 cm thick tissue equivalent phantom simulated patient scatter. It was found that the scattered radiation can be reduced to about 10% of the primary beam for small fields and sufficiently thick plates. The experimental technique is described, and the implications in terms of improved portal image quality are discussed. The thickness of front screens in most commercial portal film cassettes is shown to be inadequate for optimal contrast resolution.

MP23.14

Patient Dose Estimation Using
Measured Portal Dose Distribution,
X. Ying* and J.W. Wong, Washington
University School of Medicine, St.
Louis, MO, USA.

Treatment planning calculations are only nominal representations of the dose delivered due to many treatment uncertainties. Portal dose distribution, or image, include the treatment uncertainty information. With accurate dose calculations; CT data that adequately described the patient; an approximate model of the CT "error", the measured entrance and portal dose images can be used as constraints to adaptively improve the estimation of the actual dose delivered. The CT data are first used to predict a portal image. The ratios of the measured and predicted portal doses are used for CT corrections. The corrections can be made in terms of thickness and/or density and are confined to the region based on the "error" model. A recalculated image is then compared with measurement to begin another iteration until the images agree to satisfaction. In cobalt-60 simulations, excellent corrections were made for both density and/or thickness changes. (Supported by NCI grant CA-41574).

107

MP23.15

Accuracy in matching of portal and simulator images for patient set-up verification. H. Meertens*, J. Bijhold and M. van Herk, The Netherlands Cancer Institute, Amsterdam, The Netherlands

In order to determine discrepancies between intended fieldedges as documented on the simulator image and actual fieldedges as determined from portal images, corresponding anatomical structures in both images have to be matched. We developed a method for this purpose. After matching the digital images, field rotations and translations can be determined. The effect of the accuracy in the delineation of anatomical landmarks used for matching on the accuracy of the measurement of displacements of fieldedges was studied. Results showed that precise matching is extremely important if fieldedge discrepancies less than a few millimeters have to be determined. The influence of the choice of anatomical structures on the measurement will be shown for various tumor sites.

MP23.17

Methodology and Computer Program for Transposition of Image-defined Trajectories into Arch-Quadrant Stereotactic Devices - Henry Ford Hospital, Det., MI Zamorano L,* Dujovny M, Martinez-Coll A, Malin G.

Arch-quadrant stereotactic frames work based on the principle of aiming a target point from any entry of a formed sphere of known radius. Advances in Image-technology (CT, MRI, PET) intracranial lesions can be geometrically characterized with 3D or multi planar software and the best trajectories to aim these lesions can be selected and plotted on the image. The transposition of these trajectories (angular setting) into stereotactic systems is mandatory in many stereotactic procedure like multi-trajectory serial biopsy and to correlate Image-data with histology, interstitial intracavitary radiotherapy and image-guided laser resection. We developed a methodology and computer program (Fortran, Basic) to calculate angular setting of arch-quadrant frames. Frames need to be adapted isocentrically to the CT (MRI) and parallel to the plane of scanning. A trajectory will be defined by two points coordinates that are measured directly from an axial, a reformatted or scoutview images or the 3D display. The mathematical fundamentals to calculate Angle A in the coronal plane and angle B in the sagittal plane will be represented. Experimental and clinical examples assessing the accuracy of the methodology and program are presented.

MP23.16

The precision of determining compliance with prescribed fields from conventional portal films, P.B. Dunscombe* and K. Fox, Manitoba Cancer Foundation, Winnipeg, Manitoba, Canada R3E 0V9.

Increasing emphasis is being placed on ensuring that the treated portal in radiotherapy is identical to that prescribed by the physician. With a variety of portal imaging techniques either in use or under development it is timely to consider the precision with which Field Placement Errors may be quantified and the factors which influence this precision. 370 measurements of Field Placement Errors (FPEs) have been made by 16 observers on 20 prescription-treatment film pairs taken during routine radiotherapy for Ca prostate. Analysis of the distribution of FPEs measured under several different conditions has shed light on the significance, for the precision of the measurement, of the following factors: (a) relative magnification of prescription-treatment films; (b) the experience of the observer; (c) the contrast on the treatment film and (d) a double exposure technique.

MP23.18

EVALUATION OF A COMMERCIAL MAMMOGRAPHY IMAGE ENHANCEMENT SYSTEM, R.H. Behrman*, P.G. Zrmenhof, and M.J. Homer, Tufts-New England Medical Center, Boston, MA 02111

A commercial mammographic image enhancement system which implements a real-time local adaptive video processing algorithm based on the Wallis equation (1) is evaluated. Measurements of the conspicuity of microcalcifications in mammograms made with a mammographic phantom will be presented. These measurements were made with and without the enhancement system for contact as well as magnification mammograms, under and over exposed films, and "realistic" mammograms from actual breasts superimposed on the phantom. Distortion, high and low contrast spatial resolution, and variations of the conspicuity across the field of view are also characterized.

(1) Wallis, R.H., "An approach to space variant restoration and enhancement of images," Proc. Symp. on Current Math. Problems in Image Science, Naval Postgraduate School, Monterey, CA, Nov. 1976.

MP23.19

3-D Reconstruction of Left Ventricle(LV) applied to Coronary Artery Disease(CAD), LU PING and MA KONG FU, MAIL BOX 163, Zhejiang University, Hangzhou, PRC

A microcomputerized image processing system for 3-D reconstruction of LV has been developed and applied clinically for diagnosis of CAD. Using image sequence analysis technique, it will be fast to detect automatically endocardial and epicardial boundary of echocardiograms and reconstruct 3-D LV. LV will be divided into 20 3-D regional walls and 3-D images can be displayed dynamically in CRT with 4 windows which individually and rotatably display 3-D shortening of wall motion, 3-D wall thickening, 3-D wall thickness and normal relation of coronary artery perfusion to 20 regional walls in pseudo color quantitatively. The location of coronary artery obstructions can be predicted by observing the abnormality of wall motion, thickening and thickness. The location, sizes and extent of myocardial infarct and ischemic can be detected. A group of patients have been examined with this technique. Contrasting with coronary angiography, the result has made good coincidence.

MP23.21

A Critical Look At Video-Based Imaging Workstations. V. V. Velocci, W. M. Gentles, W. Ho, R. Reed, Sunnybrook Medical Centre, University of Toronto, Toronto, Ontario, M4N 3M5, Canada.

The application of video-based image processing workstations to medical and other imaging disciplines is becoming commonplace. Most of these systems incorporate commercially available hardware with custom software to perform the fundamental functions of image acquisition and processing. The power available in today's personal computers allows rapid analysis and processing of images but the performance of components responsible for display and especially image acquisition is far from optimal (even with high-priced components). The inherent image quality of the original films can be significantly degraded as a result of the non-linear combination of effects at every stage of quantization and display.

Four categories of effects may be demonstrated: 1) variations in transillumination intensity, and video camera response, 2) geometric distortion introduced by the video camera, the frame acquisition board and the final display monitor, 3) noise from the camera and acquisition electronics and, 4) a compromised dynamic range in the overall system due to signal amplitude mismatching and quantization limits.

All these factors, when not corrected, combine to compromise system spatial resolution, dynamic range and geometric representation of the image. This study will detail these effects and show that even when reasonable corrective measures are taken satisfactory image quality is achievable only under some conditions.

MP23.20

Noise Properties of Cineradiographic Films. M. Kiguchi, Y. Fujimura, T. Furukawa, R. Masuya, H. Yuasa, S. Nakagaki, Y. Ishimi and Y. Kodera*, Hiroshima University, 1-2-3 Kasumi, Minami-ku, Hiroshima, Japan

Noise properties of two cineradiographic films (Kodak CFT and Fuji MI-CF) were evaluated by Wiener spectral method. Films were processed by two different chemicals with several temperatures of developer (20-26°C) and different processing speeds (12-20 feet/min). At 24°C and 14 feet/min with Fuji chemical, relative speed and average gradient were 100 and 1.67 for CFT film, and 174 and 1.35 for MI-CF film, respectively. Three noise samples for each film which had the same gradients and sensitivities were prepared with different processing conditions.

For all processing conditions, both quantum mottle and film graininess were higher in MI-CF film than CFT film. Although MI-CF film showed no evident differences among Wiener spectral values at any temperatures of developer, CFT film showed temperature of about 25-40% of Wiener spectral values at the low temperature.

MP23.22

Three Parameter Equivalent Spectra as a Measure of Beam Quality, John M. Boone, Ph.D., Thomas Jefferson University Hospital, Philadelphia, PA 19107

Radiological imaging equipment has undergone considerable technological improvements in recent years, and as a result there is an increased need to precisely monitor the quality of x-rays for specific examinations. This is especially true in low dose, quantitative imaging and dual energy subtraction applications. In diagnostic radiology, the half value layer remains the "gold standard" index of beam quality. A technique is presented which, based on theoretical and empirical models, is capable of accurately describing the x-ray energy spectrum using three parameters; the equivalent kilovoltage (kVeq), equivalent aluminum filtration (Al_{eq}), and the anode angle. Aluminum attenuation data are used to determine the values of kVeq and Al_{eq}, while the anode angle is generally known a priori. The concept of the equivalent spectra is easily understandable, and provides an accurate yet concise way of reporting x-ray beam properties. The 3 parameter equivalent spectra model includes tungsten target attenuation and characteristic x-ray production. The equivalent spectrum may be preferred over the HVL for applications where spectral quality is important.

MP23.23

Variances in Exposures Due to Energy and Intensity Responses of Contemporary Diagnostic Exposure Meters, Louis K. Wagner*, University of Texas Medical School, Houston, Texas, Frank Cerra, Thomas R. Fewell, Thomas R. Ohlhaber, and Burton Conway, Food and Drug Administration, Rockville, Maryland.

Variances in exposure measurements using a variety of contemporary diagnostic exposure meters may result from systematic errors due to calibration, energy-dependence and intensity-dependence. The majority of general purpose diagnostic exposure meters tested agreed to within 10% of each other if exposure rates were below 5 R per second and beam-qualities were typical for general purpose radiology, excluding mammography. Variances up to 40% were observed for general purpose exposure meters at mammographic beam qualities. In the mammographic range, mammographic exposure meters varied less than 3%. For exposure rates comparable to those in barium enema radiography the variances ranges up to 25%.

MP23.25

Effects of X-ray Tube Voltage Waveforms on Image Quality and Patient Dose, M. Matsumoto*, H. Kubota and H. Kanamori, Osaka Prefectural College of Technology, Osaka 572, Japan

The measurement of photon spectra has been carried out for various tube-voltage ripple-rates at 70 kV using objects of various thicknesses made of aluminium and acrylic resin. Photon spectra were transformed to energy spectra and exposure spectra, and then exposure attenuation curves were obtained. By using the radiographic sensitivity spectra of five screen-film systems and x-ray energy spectra, their radiographic sensitivity attenuation relations were introduced. From these radiographic sensitivity attenuation and exposure attenuation relations, mAs values and patient doses for obtaining the same radiographic density levels were compared for various tube-voltage ripple-rates. The blurring sizes in the radiographs due to object velocities were discussed. The results show quantitatively that the smaller ripple-rate yields less mAs values, hence there is less blurring in size due to object motion, as well as being able to use a lower patient dose. The advantages of three-phase units compared with single-phase units were quantitatively demonstrated.

MP23.24

Patient Dose Monitoring in Diagnostic Radiology using Therapy Verification Film, R.A. Geise* and H.J. Ansel, University of Minnesota Hospital and Clinic and V.A. Medical Center, Minneapolis, MN

The measurement of patient skin entrance exposures during fluoroscopic procedures is complicated by the frequent movement of the patient and the use of automatic brightness controls for spot filming, cine and fluoroscopy. Small dosimeters such as TLDs can not be properly placed on the patient beforehand and kVp and mAs data may be inadequate for determining doses due to changing focus-skin distances. Radiotherapy verification film has been found to have a response in the useful exposure range for GI exams and cardiovascular cine. The dependence of sensitivity on kVp and variations in backscatter are small (less than 5%). Skin entrance exposures determined using film agreed with TLD measurements within a maximum range of 21%. Film dosimetry also provides information about the field size which is needed for determining scatter doses.

MP23.26

Mean Organ Radiation Doses in Cardiac and Carotid DSA, A. Mustafa*, and J. Janczek, Faculty of Medicine, Kuwait University.

Patient skin doses as well as radiation sensitive mean organs doses from cardiac and carotid digital subtraction angiography procedures were measured using a RANDO phantom, TLD calibrated dosimeters, and a Digitron 2 system.

In cardiac DSA, a 30 degrees RAO projection was performed using the continuous mode at a rate of 25 frames/second over a period of 10 seconds. In carotid DSA, the high load pulse mode technique was used at the rate of 2 frames/sec. to obtain RAO, LAO, and Towns views. A total of 20 frames/View were acquired. The phantom positioning, preparation, screening and exposure factors were made as close as possible to those done on patients.

In cardiac DSA a mean entrance dose of 121 mGy was measured. The highest mean organ dose was for the lungs with a value of 14.4 mGy, and a range of 1-60 mGy. In carotid DSA, mean entrance doses of 177 mGy (RAO), 142 (mGy) (IAO) and 185 mGy (Towns view) were measured. The highest mean organ dose from the three projections was to the thyroid with a value of 21 mGy followed by the eye lens with a mean dose of 4.7 mGy. All other organs received mean doses below 1 mGy from either procedure.

MP23.27

Non-Invasive kVp Measurement on High Frequency Generators, M. High*, N.Y. Medical College, Valhalla, NY 10595, A. Olson, SUNY Medical Center, Brooklyn, NY, and J. Eisenbarth, Beth Israel Med. Center, NY, NY

Seven different commercial non-invasive kVp measuring devices have been evaluated on several high frequency x-ray generators, both fixed and variable frequency types. The kVp monitors were all calibrated against the same invasive voltage divider on the same three phase generator to assure they worked properly with generators they were designed for.

The accuracy and usefulness of these kVp monitors was then determined when used on several of the newly popular high frequency generators. There was quite wide disagreement among the non-invasive kVp monitors, implying that the user of a non-invasive kVp meter should be aware of just how suitable his individual device is for use with a particular high-frequency generator.

MP23.29

Problems and Solutions in Planning the Acceptance Testing of the Radiodiagnostic Equipment of a New University Hospital, N. Pállikarakis*, Z. Kolitsi, G. Panayiotakis and B. Proimos, Medical Physics Dpt, Univ. of Patras, 260 01 Patras, Greece.

The new University Hospital of Patras with a capacity of 730 beds has recently been completed. It is the first of three hospitals to be handed over to medical service fully furnished and equipped by the contracting enterprise. X-ray diagnostic units include radiography, fluoroscopy, angiography, conventional and computed tomography, mobile units and peripheral accessories. The acceptance testing procedure is designed to: (a) ensure that the performance meets the contract specifications, (b) establish a reference performance level and (c) comprise a pilot guide for the acceptance testing of the two other hospitals.

A work plan and protocols have been developed to cover the required tests. The main checks apply to mechanical and electrical safety, beam geometry, beam quality and intensity and radiation safety features. Specific tests apply to biplane angiography, fluoroscopy, tomography and the peripheral accessories, i.e. grids, cassettes and processors. The above tests will be carried out with the aid of commercially available as well as "home made" equipment. The experience gained during this procedure will be discussed.

MP23.28

A Prototype of Multiple-slit X-ray Beam Imaging System for Clinical Applications. Y. Kume*, K. Doi, X.-W. Xu, P. S. Prieto, R. A. Schmidt, L. B. Dixon, Dept. of Radiology, The Univ. of Chicago, Chicago, IL 60637

Multiple-slit beam imaging technique has been proposed to obtain high quality radiologic images with I.I.-TV digital system. This imaging technique can provide high signal-to-noise ratio and low patient dose by removal of scatter and veiling glare, if the physical parameters involved with this technique are properly selected.

Based on our previous studies, we have designed a prototype of multiple slit beam imaging system for clinical applications. We employ a linear stepping motor for accurate control of driving a multiple-slit assembly (MSA) and a high frame rate for image acquisition (60 frames/sec) in order to achieve short exposure time (less than 0.3 sec). We shall also present methods of reducing line artifacts which may be caused by the inaccuracies in the slit width and slit separation of the MSA, and by the variation in x-ray exposures among different original frames. Preliminary results on clinical cases will be presented.

Supported by USPHS Grant CA24806.

MP23.30

Anthropomorphic Phantoms for X-Ray Imaging System Evaluation, C. B. Caldwell* and M. J. Yaffe, University of Toronto, Toronto, Canada M4X 1K9

Conventional methods of evaluating x-ray imaging systems generally involve assessment of the detectability of simple objects against uniform backgrounds. It is not clear how well results of these tests relate to clinical radiography where radiologists search for specific anatomic details against highly complex backgrounds. We have been developing anthropomorphic phantoms, radiographs of which present realistic images, similar to those of patients, to the observer. By providing more realistic detection tasks, such phantoms may be more appropriate than conventional phantoms for assessing and optimizing imaging systems.

We describe the development of anthropomorphic phantoms using data derived from actual patient images. Phantoms are designed in layers, which are fabricated by a combination of numerically-controlled milling and photochemical techniques. Methods of designing both high spatial resolution phantoms and tissue-equivalent phantoms from dual energy radiographs will be presented. Finally, a study will be described which seeks to assess our phantoms' ability to evaluate imaging systems by correlating radiologists' ratings of image quality of patient and phantom radiographs.

111

MP23.31

Morphological Reference system of Human Structure using Computer Graphics, Naoki Suzuki^{1*}, Mikio Itou², Tetsuo Okamura¹
ME Research unit Jikei Univ. School of Med. ¹Nihon Kogaku K.K. ²
105 Minato-ku Tokyo, Japan

We have developed a system of the morphological database of the human body structure using a computer graphics technique. We designed this system as a general purpose reference system of body structure by reviewing the three dimensional image of bodies according one's purpose. This system is able to use with an ordinaly 16 bit personal computer and possible to carry the system only by diskets that install the program.

The system has 6 subprograms. They are male wholebody, female wholebody, cranial part, thoracic part, heart and abdominal part. Users are possible to rotate or enlarge the three dimensional image on CRT and also possible to eliminate a disused part to clear the aimed organs. Dissection technique is available to dissect the body surface or the organ to observe the inner structure of the model.

This system is supposed to be useful as a diagnosis support system for various medical imagings and as a tool for the education of medical students.

MP24.1

A Treatment Planning Technique for 3-D Dynamic Stereotactic Radiosurgery, D. Lefkopoulos*, P. Nouet, M. Rouzaud, J.N. Foulquier, M. Schlienger, A. Laugier. Services de Radiothérapie, Hôpital Tenon, 4 rue de la Chine, 75020 Paris, FRANCE.

The goal of stereotactic radiosurgery (SR) is to deliver a large radiation single dose with a high degree of spatial accuracy into a small target volume (1 to 3 cm), within the brain.

We propose a treatment planning technique for calculation of 3-D dose distribution with a 15 MV Linac (Saturne 43 CGR MeV). We use eight additional cylindrical collimators (6 to 20 mm diameter). For target localization and patient immobilisation during treatment, the Talairach Stereotactic frame is used. Anatomical data (3F) are obtained from stereotactic arteriography, CT-scan and multiple stereotactic biopsies (if indicated). Calculation algorithms are based on coordinate transformations and use the measured elementary beam central axis percentage depth doses, dose profiles and TMR data to compute the 3-D dose distribution. The computing system is a microVAX-II computer and an FPS 120B array processor. We already have performed 56 SR (50 MAV - 6 tumors).

Optimization is mandatory in SR because of the high dose level. We have developed such a method imposing a 3-D provisional dose matrix. A "best possible" plan of irradiation can be found.

MP24.2

Dose Distributions in Dynamic Stereotactic Radiosurgery, B. Pike*, E.B. Podgorsak, T. Peters, C. Pla, and A. Olivier, McGill University, Departments of Neurosurgery and Radiation Oncology, Montréal, Canada

A treatment planning technique for calculation of dose distributions in dynamic stereotactic radiosurgery with a 10 MV isocentric linear accelerator will be presented. The treatment planning for dynamic radiosurgery is a three dimensional problem, since during treatment both the gantry and the couch rotate simultaneously, the gantry from 30° to 330° and the couch from 75° to -75°. The dose calculation accounts for the three dimensional nature of the problem and is based on the two dimensional Milan and Bentley algorithm for the calculation of tissue-maximum-ratio distributions. The patient surface and anatomical information is obtained from a family of CT or MR scans, and a stereotactic frame is used for target localization, treatment set-up, and patient immobilization during the treatment. The dose calculational algorithm follows the gantry and couch rotation in an incremental fashion, and relies on measured stationary beam central axis percentage depth doses and dose profiles to calculate the normalized tissue-maximum-ratio distributions over a matrix of points defined on one of three orthogonal planes (transverse, sagittal, or coronal). The algorithm has been implemented within a general purpose stereotactic image analysis software system, allowing the user to analyze stereotactic CT or MR images, localize target points, as well as to calculate and superimpose the dose distributions directly onto any CT or MR image. The dose calculation algorithm will be discussed in detail and the calculated dose distributions for the dynamic radiosurgery compared with measured data.

MP24.3

A Computer-Controlled Radiotherapy Technique for Carcinoma of the Esophagus, C.W. Cheng*, R.L. Siddon, B.E. Bjarngard, Joint Center for Radiation Therapy, 50 Binney street, Boston MA 02115, U.S.A.

The curvature of the esophagus and its close proximity to the spinal cord render major difficulties in the treatment planning for esophageal cancer. A dose inhomogeneity of 125% and a cord dose at the tolerance limit are considered acceptable. We have studied a computer controlled radiotherapy technique using irradiation at a number of fixed gantry angles. At each gantry angle, a number of static fields are applied. Along the gantry rotational axis, they abut to cover the desired volume, while each field is adjusted to conform to the target in the relevant transverse plane. This is made possible by independent collimator jaws. With dose rate control, the technique produces the same effect as if tissue compensators were used for each gantry angle. Dose distributions are compared with a four-field technique and conformation rotation without the subdivision into fields along the rotational axis. The proposed technique gives a dose inhomogeneity of 107% throughout the entire volume and a cord dose well below tolerance. The beam-on time is 1.7 times that of the four-field technique.

MP24.4

EVALUATION OF CORRECTION FACTOR DISTRIBUTIONS IN THORACIC TREATMENT PLANNING

Katherine Mah* and Jake Van Dyk

Ontario Cancer Institute, Toronto, CANADA M4X 1K9

Dose computational algorithms which account for the effects of inhomogeneities are becoming increasingly sophisticated. However, the implementation of inhomogeneity corrections in routine treatment planning remains controversial. Certainly in radiotherapy of the thorax, differential transmission through lung tissues can lead to errors in both target and lung doses. Consequently, this results in inaccurate radiotherapy, major inconsistencies in dose data collected from multicenter clinical trials, and inaccurate dose-response data.

To assess the impact of tissue inhomogeneities on routine treatments, the equivalent tissue-air ratio method was used to derive correction factors. CT-based distributions consisting of inhomogeneity correction factors were generated for 100 patients who were entered into a prospective, clinical study on lung damage. The correction factors were analyzed within the target volume, at the point of target absorbed dose, within the irradiated lung volume and at the spinal cord. Results will be presented according to photon energy and treatment technique. The effects of ignoring inhomogeneities on our dose response data for lung damage will be discussed.

MP24.6

Accuracy of Beam's-Eye View Localization. Robert Smith*, James Galvin. Hospital of the University of Pennsylvania. 3400 Spruce Street. Philadelphia, PA.

Beam's-Eye View (BEV) treatment planning has been routinely employed in our clinic over the last two years using a G.E. 9800 CT scanner and G.E. Target planning system. This study examines the accuracy obtainable from BEV planning when the patients are scanned in the treatment position by personnel trained as both CT Technologists and Simulation Technologists. In order to test the accuracy of BEV planning, simulator films were obtained by setting up to the marks placed as part of the CT procedure and used as reference for the BEV procedure. Transparent hardcopy overlays of the BEV output which includes the target volume, treatment field and block placement were used to test the agreement of the two procedures. In order to facilitate the comparison, the BEV images were presented as "shadow" images instead of the more typical "wire frame" approach. The comparison included an examination of the position of the reference marks on the simulation film and measured differences in the position of reference structures drawn on the simulator film and also identified on the BEV image. In general, the two procedures were found to agree to within 5 mm for a wide range of treatment sites. Possible explanation of the differences is the effect of volume averaging of the reference structures when thick CT cuts (0.5 or 1.0 cm) are used. The magnitude of this difference is important if the BEV is to be used to generate shielding blocks for those cases where it is difficult to determine block placement using a simulator radiograph. This situation occurs, for example, when overlying structures hide information on the simulator film. Problems associated with this treatment planning technique will also be discussed.

MP24.5

TREATMENT PLAN OPTIMIZATION FROM QUANTITATIVE BEAM'S EYE VIEW VOLUMETRIC CONSIDERATIONS, L.C. Myriantopoulos*, G.T.Y. Chen and D.R. Speilbring, University of Chicago, Chicago, IL, USA

The Beam's Eye View (BEV) method has many clinical applications. We have expanded BEV's potential by calculating the volume of structures intersected by a beam which is blocked so as to encompass the target, viewed from an arbitrary angle. Plots of such volumes, as a function of gantry angle, show distinct minima and maxima. In the case of a target in the right lung, occupying approximately 20% of its volume, the fraction of the left lung volume irradiated was minimum (4%) at 30° , reached 32% at 105° , became 5% at 200° and 40% at 275° . (AP= 180° , left = 90°). The minima for the cord were centered at 135° and 315° and were separated by two broad maxima. Treatment plans are best compared dosimetrically using dose volume histograms (DVH). However, current computational power renders the calculation of DVH too time consuming for clinical use. This work introduces the extended BEV technique, which relies on geometry, as a much faster alternative to comparing treatment plans. Results for single beams are correlated with the corresponding DVH. The technique is then extended to multiple fields by keeping track of the number of beams through a given pixel. The volumetric results of the combinations chosen by BEV are compared with the corresponding dosimetric ones, as well as with the results for the actual treatment.

MP24.7

3-D Non-Coplanar Treatment Planning, G.J. Kutcher*, and C. Burman, Memorial Sloan-Kettering Cancer Center, New York, NY, USA

In conventional treatment planning the central axis' of the treatment fields are usually parallel to axial planes of the patient. With the availability of the new 3-D dose planning systems it is possible to design, calculate, and display treatment plans with non-coplanar fields. Strictly, these would be plans in which the central axis' of three or more radiation fields do not form a plane. However, plans in which the radiation fields are coplanar, but are in a plane inclined with respect to an axial patient plane comprise an important class of treatment plans that also can be designed with 3-D dose planning systems.

Data will be presented on target and normal tissue dose distributions for elliptically shaped tumors that are irradiated with non-coplanar fields. The use of planar compensators to produce homogeneous dose distributions will also be discussed. The use of non-coplanar fields to reduce doses to normal critical structures will be illustrated with treatment plans for patients with para-nasal and pelvic tumors.

MP24.8

An Interactive Method for Optimization of Electron and Photon Beam Mixing Through the Use of a Feasibility Search Algorithm, G. Starkschall¹, and G.A. Henkelmann², Dept. of Radiation Physics¹ and Dept. of Clinical Radiotherapy², Univ. of Texas M.D. Anderson Hospital and Tumor Institute, Houston, TX 77030.

When combining electron and photon beams for radiation therapy treatment planning, the provisional determination of optimal beam weights can be achieved by specifying dose constraints at various points and selecting any combination of beam weights that yields a dose distribution satisfying these constraints. This procedure differs from the more conventional optimization schemes in which dose values are specified and the optimization algorithm calculates that beam weight distribution that yields a dose distribution that comes closest to the optimal distribution. In the event that there is no combination of beam weights that satisfies the choice of treatment modalities and dose constraints, this method allows for interactive user modification of treatment modalities and dose constraints.

MP25.1

MRI-PET CORRELATION USING A COMPUTERIZED REGION-OF-INTEREST ATLAS A C Evans*, C Beil, S Marrett, C J Thompson, A M Hakim. McConnell Brain Imaging Unit, Montreal Neurological Institute, Montréal, Québec.

A procedure is described for combining anatomical information from MRI (or CT) and functional information from PET in a rapid fashion. MRI data is combined with a procedure for the definition, storage and recall of anatomically-based regions-of-interest (ROIs). An atlas of standard ROIs, defined for a set of 18 parallel planes spaced at 6mm intervals, provides a starting ROI template for each patient slice. Global adjustments to scale, orientation and position are applied to obtain an initial match. Individual ROIs may then be moved, deleted or re-drawn as needed to refine the match.

The ability to store the ROI templates ensures reproducibility of analysis over long periods and introduces a standardization of analysis technique. In 25 brain structures, the mean coefficient of variation in glucose utilization measurements obtained by 5 neuroanatomically-trained observers was reduced from 8.1% for manual ROI definition to 4.0% using the template approach with MRI.

Template analysis for space-occupying lesions such as tumors or infarcts is illustrated with PET data from a stroke study emphasizing the facility for rapid, reproducible analysis of multi-functional studies. MRI/PET matching for a structurally intact caudate nucleus having reduced glucose utilization in Huntington's disease emphasizes the accuracy of anatomical localization required to quantify small structures.

MP24.9

Auto-Contouring of Risk-Organs in Radiotherapy Treatment Planning, J. N. Roy*, P. Steiger and C. C. Ling, Department of Radiation Oncology, University of California, San Francisco, CA 94143.

It is desirable to automatically locate and contour risk-organs such as kidney, liver and spinal canals on CT images for radiotherapy planning. This is often difficult with simple techniques based on threshold criterion because of overlap in CT numbers with the surrounding tissues. Thus, contouring techniques require substantial operator intervention. Our aim in this work was to minimize operator dependence and optimize the efficiency of the contour tracking process for these organs. We have adopted the quantitative image evaluation technique (QUIET) which takes into account a prior knowledge of the organ anatomy and offers among many options, contour tracking, contour smoothing and contour shape analyses. Our contour tracking algorithm allows defining a contour in extremely noisy and low contrast environments and contour smoothing technique provides selective elimination of convex and concave contour segments. Further details about this technique will be discussed.

MP25.2

Minimizing Brain Motion Contribution in MR Diffusion Imaging
K K Kwong*, D Chien, R B Buxton, T J Brady, B R Rosen. Massachusetts General Hospital, Boston.

In magnetic resonance imaging of diffusion, the diffusion weighted image can have significant signal changes when the diffusion encoding gradient is in one direction but not when the gradient is rotated by 90 degrees. Our interpretation for this is that signal attenuation is produced only when the applied gradient is along the motion direction, therefore areas of anisotropic brain motion will or will not have signal attenuation, depending on the direction of the diffusion encoding gradient. We observe a shift in position of signal attenuation in the image when the diffusion encoding gradient is rotated by 90 degrees.

A subtraction of the two images with diffusion sensitization in orthogonal directions gives a map of 'flow' or 'motion' signals. Adding the absolute value of this difference image to the original image enables the calculation of the diffusion coefficient minimizing brain motion or flow contribution.

MP25.3

Comparison of Presaturation and Selective Excitation for Slab Definition in 3D FLASH MRI, M.L. Wood* & V.R. Runge, Tufts University and New England Medical Center, Boston, MA 02111

Selective excitation and presaturation have been evaluated as two techniques for defining a slab from a more extensive volume in three-dimensional (3D) FLASH magnetic resonance imaging (MRI). Selective excitation was achieved using a 2.6 millisecond radio-frequency (rf) pulse. The presaturation technique used a 2.6 ms selective rf pulse to excite tissue on both sides of a volume of interest. A non-selective rf pulse for imaging followed 10 ms later and it excited the slab more uniformly so that typically the slices deviated in intensity only one-half as much as with selective excitation. The reduced image intensity within presaturated regions minimized the consequences of aliasing. The presaturation technique also allowed a 3 ms shorter TE and avoided incomplete rephasing in the slice selection direction.

MP25.5

Magnetic Resonance Imaging Studies of Fluid Velocity Profiles

Kenneth A. Kraft, Panos P. Fatouros and Ding-Yu Fei, Medical College of Virginia, Richmond, VA 23298

Velocity profiles in flow models simulating a variety of normal and pathologic vascular conditions have been investigated using magnetic resonance imaging (MRI). Validation experiments under identical conditions were carried out using laser Doppler velocimetry (LDV). Fluid having a T_1 relaxation time and viscosity similar to that of blood was circulated at a constant rate through the imager's 2.35 T magnet. From MR images of flow profiles, quantitative velocity information, as well as estimates of wall shear forces can be extracted. Images of flow through axisymmetric constrictions clearly reveal jet phenomena, flow separation, and regions of turbulence. Likewise, flow profiles through symmetric bulbs demonstrate flow reversals in separation zones, consistent with vortical secondary motion. The correlation of MRI-derived velocities over a wide range (5 - 180 cm/s) with identical LDV measurements was excellent.

MP25.4

Surface Coil Excitation with Different Transmit Pulses for High-Quality MR

Imaging, R. Bader*, J. Gehrig, H.-J. Zabel, and W.J. Lorenz, German Cancer Research Center, D-6900 Heidelberg, West Germany.

High-quality MR imaging is performed by using surface coils as RF antenna systems. However, the inhomogeneous RF transmitting field of surface coils reduces the quality of MR images in cases where no homogeneous excitation with body or head resonators is possible. A method leading to areas of nearly homogeneous sensitivity or constant signal intensities for uniform phantom materials is described. The new technique bases on a surface coil excitation with different transmit pulses and the superposition of the resultant image matrices to an averaged image. The RF pulse intensities are determined by computer simulations of the signal yield shapes versus the axial distance to the center of a flat coil or loop. The signal intensity at a distance of half the coil diameter exceeds that obtained with a single surface coil excitation by a factor of 4 and is even 1.5 times that with a homogeneous body or head resonator excitation, if the signal intensities are normalized to the respective maximum signal intensities at the center. The evidence in image quality improvement will be demonstrated.

MP25.6

Two-Dimensional MR Flow Imaging. R.R. Price*, D.R. Pickens, T. Conturo, G. Smith, W. Riddle, C.L. Partain and A.E. James, Jr., Vanderbilt University, Nashville, Tennessee

Constant flow along a linear magnetic field gradient produces a shift in the phase angle of the transverse magnetization in direct proportion to the velocity component along the gradient direction. Several investigators have utilized "balanced gradients" and paired RF pulses to compensate for phase shifts resulting from flowing spins to produce MR angiograms. MR angiograms derived from one-dimensional flow compensation sequences often suffer from artifactual flow voids when the flow direction deviates from the flow-encoding direction. We have developed imaging sequences which in essence interleave two imaging sequences within a single acquisition in which flow-encoding is achieved for both orthogonal (x and y) directions. Following acquisition, special reconstruction software derives the component velocity images as well as the direction-insensitive magnitude image. Measurements have been carried out in flow phantoms, prepared animal models and volunteers. Flow images illustrating reduced direction-sensitivity achieved by two-dimensional flow encoding as compared to one-dimensional encoding sequences are presented.

MP25.7

Optimizing of Exciting and Saturating Selective Pulses for MR Imaging

U. Klose, Radiologische Klinik, D-7400 Tübingen, FRG

MR imaging requires a excitation with frequency-selective pulses to achieve an image of a well defined slice. To realize thin slices, the use of small frequency band widths is necessary, requiring greater pulse lengths in the time domain. As signal intensity decreases exponentially with time, it is desired to shorten echo time as much as possible. Therefore the choice of RF pulse length has to be a compromise between accurate slice profiles realized by long RF pulses and short echo time.

For a selective pulse several pulse forms and filter functions can be used. To adjust the pulse form to the demand of a choosen sequence, the profile of the excited slice can be measured by a special sequence. In a similar way the optimal pulses for the saturation of well defined slices can be determined, which is desirable for some applications in MR imaging like zooming free of fold-over effects.

For the design of selective pulses for excitation and saturation a computer programme has been developed to generate arbitrary pulse forms, choose the needed frequency band width and shift the central frequency of the RF-pulse. The properties of a variety of pulse forms has been determined experimently and will be demonstrated. For example it can be shown, that the slice profile after a excitation with a half sinc pulse is sufficient for imaging, leading to a skorter time for refocusing the slice selection gradient and a shorter echo time.

MP25.9

APPLICATIONS OF IMAGE REFORMATTING FOR MAGNETIC RESONANCE IMAGING, M.E. Brummer, MSc*; R.L. Eisner, PhD; W.A. Fajman, MD; M.C. Brunner, MD; D.G. Schwartzberg, MD; Emory University Dept. of Radiology, Atlanta, GA 30322.

Multi-Planar Reformatting (MPR) is the generation of planar images in any orientation from a three dimensional (3D) data set. We have developed a dedicated MPR software package for use with magnetic resonance (MR) images acquired with three dimensionally symmetric resolution using 3D Fourier acquisitions. Bi-linear interpolation is used to generate single-oblique reformats, and tri-linear interpolation for double oblique cuts. Typical data set sizes vary from 256*128*12 to 256*256*64 pixels with approximately 1 mm resolution in all directions.

3D MR knee images required interactive MPR, allowing multiple oblique views for optimal visualization of meniscus, cruciate ligaments and other irregularly shaped structures. Also, using a 3D acquisition followed by MPR, the scan protocol for knee imaging is substantially simplified, compared to conventional multi-slice techniques. MPR of 3D acquisitions of the pituitary gland provided excellent visualization of small lesions. The extremely large datasets (typically 3-10 MBytes per scan) will make specific demands on hardware architecture and software for future MR image processing stations.

MP25.8

Slice Separation in Simultaneous Multislice MRI by J.B. Weaver*, P. K. Spiegel and T.R. DeRoo, Dartmouth-Hitchcock Medical Center, Hanover, New Hampshire, USA.

Simultaneous multislice MRI acquires images of multiple parallel body sections with the same number of echoes that a conventional sequence requires for a single slice. The technique requires the select gradient to be on during the echo to separate the sections in the bandwidth sampled by the system. As many as sixteen sections have been imaged simultaneously. While there is potential to increase the number of sections imaged per unit time by a factor of sixteen or more, a factor of two to four is more reasonable for routine imaging with the present hardware.

The limitation on the number of sections obtainable with the simultaneous multislice technique is that the images become more blurred as the parallel sections are brought closer together and as the field of view is made larger. We identified an index of blurring.

We will describe the simultaneous multislice technique and two ways of limiting the field of view. The first method of limiting the field of view involves limiting the extent of the 180 pulse in the read direction. The second method uses presaturation pulses. We will compare the methods, describe the effects on image quality and show images obtained using both methods.

MP26.1

Response characteristics of plane-parallel ionization chambers for obliquely incident photon beams

B.J. Gerbi* and F.M. Khan, University of Minnesota, Dept. of Therapeutic Radiology, Minneapolis, MN 55455.

It has previously been shown that fixed-separation plane-parallel ionization chambers overestimate the dose in the buildup region of normally incident high-energy photon beams [1]. These chambers also tend to overestimate the dose in the buildup region of obliquely incident photon beams. This overresponse at oblique incidence is greater than that observed for normally incident beams and is a function of chamber design, angle of beam incidence, and energy of the beam. Data will be presented that illustrates this overresponse of fixed-separation plane parallel chambers versus results obtained using both an extrapolation chamber and thin layers of LiF thermoluminescent powder. A method to correct for this overresponse will also be presented.

1. D. E. Velkley et al., Med. Phys. 2, 14 (1975).

116

MP26.2

THE EFFECT OF THE BUILD UP CAP MATERIAL IN THE IONIZATION CHAMBER RESPONSE FOR Co-60 GAMMA RAYS. M.P.O. Rocha, Dep. de Protecção e Segurança Radiológica/LNETI, Lisboa, Portugal, L.N. Rodrigues, E.R. Cecatti, and C.E. de Almeida*, Instituto de Radioproteção e Dosimetria/CNEN, Rio de Janeiro, Brazil.

In order to determine the absorbed dose in a medium through the calibration factor based on exposure or kerma in air, the knowledge of the influence of the wall and build up cap materials on the ionization chamber response is required. The effect of the attenuation and scattering of ⁶⁰Co gamma rays in the wall and build up cap of the ionization chamber as well as their no-air equivalence were studied for TK01 ionization chamber (Delrin wall). For that, build up caps with different thicknesses were constructed from Delrin, Lucite, graphite, C-552, A-150, and aluminum. It was performed three series of 25 measurements each for each cap which were individually corrected for pressure and temperature. The experimental set-up was thermally insulated therefore variations less than 0.1°C have been observed during each serie of measurements. The original chamber cap were measured through out the experiment and it was observed an agreement better than 0.1%. The response results for a special material were plotted as a function of the wall and cap total thickness and extrapolated to the thickness corresponding to the mean center of electron production. The correction factors for a specific thickness were analysed in relation to the cap material and the relative responses compared to the values calculated by the Spencer-Attix formalism for the cavity theory.

MP26.4

COMPARATION STUDY OF TWO PLANE PARALLEL IONIZATION CHAMBERS.

C. Cinos and M.C. Lizuain*, Hospital de Bellvitge. Barcelona (Spain).

The use of plane parallel ionization chambers is recommended for accuracy dosimetry of the high energy electron beams and they must be used in electron beams of energies below $E_0 = 15$ MeV (Spanish Protocol of Radiotherapy Dosimetry).

A study of two plane parallel chambers has been made for obtaining the correction factors. The polarity effect, the recombination correction and the absorbed dose to air calibration factors have been measured. The stability of both chambers and the leakage current have also been determined.

Ionization chambers: PTW 0.4 cm³, M 23343 and NACP - graphite
Electrometer: N.E. 2500/3 - Ionex

Irradiation equipment: Linac Therac 20-Saturno.

MP26.3

VALIDITY OF DOSE MEASUREMENTS AT HIGH ATOMIC NUMBER INTERFACES IN MEGAVOLTAGE PHOTON BEAM; Indra J. Das*, Kenneth R. Kase, and Faiz M. Khan[†], Dept. of Radiation Oncology, Univ. of Mass. Med. Center, Worcester, MA 01605, and [†]Dept. of Therapeutic Radiology, Univ. of Minnesota Hospital, Minneapolis, MN 55455, USA.

Measurement of dose or dose perturbation factors at high Z interfaces are usually performed with a thin window parallel plate ion chamber. In the past, the use of ion chamber readings for the dose measurements has been questioned. This presentation describes the various measurement problems and studies in detail the associated problem of the validity of dose calculation. Out of three factors (stopping power ratio, charge collection at the interface and W/e) needed for the determination of dose, stopping power ratio and charge collection were critically investigated. Using several types of commercially available parallel plate chambers, extrapolation chamber and TLD powder, the validity of dose measurement was studied for photon beams in the range of Co-60 gamma rays to 24 MV X-rays. It was observed that at high Z interfaces, most parallel plate ion chambers accurately measure dose for higher energy beams (> 10 MV), but for lower energies, there is a significant difference between measured doses with different detectors. It is suggested that at high Z interfaces and lower energies, dose measurements should be performed with either an extrapolation chamber or with a very thin window parallel plate chamber.

MP26.5

DOSIMETRY WITH IN AIR CALIBRATED IONIZATION CHAMBERS FOR MEDIUM ENERGY X-RAYS.

J. Seuntjens, H. Thierens*, A. Van der Plaetsen and O. Segaert, Standard Dosimetry Laboratory, Rijksuniversiteit Gent, Ghent, Belgium.

According to current codes of practice the absorbed dose to water, D_w , for medium energy X-ray qualities is determined by in phantom measurements with ionization chambers calibrated in air under reference conditions. The absorbed dose to water D_w , is found using the equation

$$D_w = M_u N_k (\bar{\mu}_{en}/\rho)_{w,air} p_u k_u$$

In present work the $(\bar{\mu}_{en}/\rho)_{w,air}$ conversion factors, averaged over the energy fluence spectra at the measuring point inside the phantom, are determined for X-ray qualities specified by kV_p and HVL of the primary beam. These spectra are calculated from measured primary spectra by the Monte Carlo method. Perturbation factors p_u for a 0,6 cm³ graphite cylindrical chamber are determined following the same procedure. Quality correction factors k_u are deduced from an experimental determination of the energy response. For X-ray qualities with 2 mm Al < HVL < 5 mm Cu the p_u and k_u corrections are respectively smaller than 2 % and 1 %. The results show also that accurate determination of the air kerma-dose to water conversion factors require beam specification by kV_p and HVL.

1 1 7

MF26.6

Application of ^7LiF thermoluminescent dosimeters in clinical neutron beams with energies ranging from d(14)+Be to p(65)+Be.

S. Vynckier^{*}, B. Hocini and A. Wambersie, UCL-Cliniques Universitaires St-Luc, 1200 Bruxelles, Belgium.

Application of thermoluminescent dosimeters for fast neutron dosimetry is restricted due to their low neutron sensitivity. In this paper we report the variation of the relative sensitivity k_{ij} (neutrons compared to ^{60}Co photons) of Lithium-7 Fluoride (TLD700) as a function of different neutron energies. The neutron irradiations were performed at the neutrontherapy facility of Louvain-la-Neuve using a d(20)+Be, a d(50)+Be, a p(34)+Be, a p(45)+Be, a p(65)+Be and a p(75)+Be neutron beam, and at the Gent facility using a d(14.5)+Be neutron beam.

The k_{ij} -value increases with energy. For example, 10.5% and 57% was found at the maximum dose depth for the d(14.5)+Be and the p(65)+Be neutrons respectively. The low k_{ij} -value at low neutron energies restricts their applicability to the determination of the γ -component, as reported in the literature. The increase at high neutron energies allows the measurement of the neutron dose, since the γ -component for these neutron beams is small. The influence of total dose (supralinearity), depth in phantom and field size will also be reported.

MP26.8

THE ENERGY RESPONSE OF LiF TLD-100 to Low and High Energy Photons and to High Energy Electrons for Varying Dosimeter Thickness. C. Reft, Michael Reese/University of Chicago Center for Radiation Therapy, Chicago, IL, 60637

A number of papers have reported differences in sensitivity of LiF TLD-100 to x-rays and high energy electrons in comparison to that for ^{60}Co gamma rays in water and polystyrene media. Cavity theories and atomic number differences between the dosimeter and media have been used in attempts to explain these variations. In view of the difficulties of calculating the relative responses of TLD's over a range of energies, it is recommended to calibrate them using radiation of the same energy as that to be measured. This is not always practical or convenient. In this work the energy response of pre-selected LiF TLD-100 chips was measured in water for photon energies of 0.010, 0.024, 0.045, 0.25, 4, 6, 10, 18, and 24 MV as well as ^{60}Co , and in polystyrene for electron energies of 6, 9, 12, 15, 18 and 22 MeV. The results for three different TLD thicknesses (0.25, 0.4 and 0.9 mm) were compared with the theoretically calculated energy response from Burlin cavity theory which is a function of cavity thickness. A discussion of the experimental and theoretical results will be presented.

¹A. Mc Kinley, 1981 Thermoluminescence (Bristol, U.K.: Adam Higler) 66.

MP26.7

The orientation of TLD's - effects on dose assessment. T.M. Kehoe and D.I. Thwaites^{*}, Western General Hospital, Edinburgh, Scotland.

The main advantage of TLD materials is their capability of dose estimates at isolated sites without the necessity of direct connection to cumbersome ancillary equipment. Their size permits many TLD's to be positioned in close proximity, giving good spatial resolution. Although some methods have been devised to introduce TLD's into internal cavities, most are placed on the patients skin.

At sites deep within the body which are inside the primary beam and well away from the penumbra region, the scattered radiation is reasonably uniform. Under these conditions we would not expect the orientation of the TLD to be important. In areas of non-uniform scatter such as outside the primary beam and at the surface, orientation is important.

The orientation effects on LiF chips, discs and rods placed on the surface of a phantom have been investigated for both photon and electron beams. In addition the orientation effects for scatter photon fields outside the primary beam have been investigated. The results are presented with emphasis on radiotherapy applications.

MP26.9

Experience with a computerized TLD Reader, H. Gfirtner^{*}, T. Gerster and H. Kett, Staedt. Krankenhaus, Med. Physik, D-839 Passau, FRG.

We work on TL dosimetry since many years and reached two years ago a reproducibility of better than 2% (single standard deviation). In order to ameliorate precision further and perhaps facilitate the sample handling we interfaced last year our Harshaw model 2000 TLD analyzer to a PDP 11/35 minicomputer.

TL signal, temperature signal and clock are acquired during each readout and stored on floppy disk. The terminal's bell is used to inform the operator about the readout status. (e. g. announces that the next TLD has to be put on the planchet)

The evaluation of the glow curves, which is performed after the readout, runs either interactively or automatically.

Using this computerized TLD reading we achieved a reproducibility of better than 1%.

MP26.10

Measurement of Planar Dose Distributions Using Film in Therapeutic Electron Beams, A.S. Shiu, V.A. Otte and K.R. Hogstrom, Dept. of Radiation Physics, University of Texas M.D. Anderson Hospital and Tumor Institute, Houston, TX 77030.

In this paper, two techniques were used to obtain the isodose distributions in a plane containing the beam axis. The first technique reconstructs isodose distributions from the central-axis percentage depth dose (CAX %DD) and the off-axis profiles. These profiles were determined from the film optical density profiles corrected for film non-linearity. The fluence factor and scaling factor were applied to the CAX %DD measured in the solid film phantom to convert to CAX %DD in water. The second technique combines the ion-chamber CAX %DD measured by an ion chamber in water with the off-axis profiles measured using film in the solid phantom to construct the isodose distributions. Comparison of the resulting isodose distributions from both techniques with ion-chamber measurements for 7, 12, 15 and 18 MeV electrons will be presented. The agreement between the results of the second technique and the ion-chamber measurement is within 1% from 95% to 10% isodose lines.

These investigations were supported in part by NCI grant CA-06294.

MP26.12

STUDY OF THE CHARACTERISTICS OF SEMICONDUCTORS FOR IN VIVO DOSIMETRY DURING TOTAL BODY IRRADIATION AT LOW DOSE RATE, J. Van Dam* and A. Rijnders, University Hospital St. Rafaël, Dept. of Radiotherapy, 3000 Leuven (Belgium).

The characteristics of Therados EDE semiconductors have been studied in view of their use for in vivo dosimetry during TBI with 18 MV X-rays at low dose rate.

Six semiconductors have been exposed simultaneously with a Nuclear Enterprises 0.6cc thimble ionization chamber at depths of 3, 19 and 34.5cm in Perspex, corresponding to dose rates of 0.07, 0.05 and 0.03 Gy.min.⁻¹ respectively. The mean ratio of the semiconductor over the chamber signal increases from 1.009 to 1.015 at 19 and 34.5cm depth respectively, with reference to the value observed at 3cm depth. The influence of dose, dose rate and degradation of photon energy with depth will be analysed selectively. This study in TBI conditions will be extended to higher dose rates of max. about 4 Gy.min.⁻¹. Moreover the influence of temperature increase from room - to skin temperature has been studied. The dosimeters were applied on the outer surface of a Perspex water tank with heating element. The surface temperature was measured by a thermistor. Marked differences were observed between the six dosimeters: when increasing surface temperature from 22°C to 31°C (average skin temperature) the increase in responses varied between 0.5 and 3.5%.

MP26.11

A Pit Fall of Film Dosimetry for Combined Modalities of Treatment Beams, M. Kao* and W.L. Hsu, Rush-Presbyterian-St. Luke's Medical Center, Chicago, IL, and Tri-Service General Hospital, Taipei, Taiwan.

Since the constant sensitivity of film to higher energies photon beams and the constant mass stopping power in the medium of the therapeutic energy range electron beams, the film has been used for megavoltage photon beam and electron beam dosimetry studies in medical physics. The data obtained from a single exposed film is equivalent to hours machine time with ionization chamber and phantom measurements. Film has been used for routine clinical dosimetry evaluation in the area such as the scattering from foreign bodies in a homogeneous phantom, the beam penumbra and uniformity studies, and at the junction of more than one beam of a patient set-up, etc. This film dosimetry has been used for combined modalities of beams and energies together. In the study we find a pit fall of dose interpretation of film dosimetry in applying to the junction of electron beam with photon beam. Some reasons are due to the film response difference to the incident direction of the electron and the photon beams, and the dose calibration to the media with respect to the phantom used. Without proper precaution, this film dosimetry leads to more than 7% deviation and even more from the actual dose expected. In some cases, it underestimates the hot spot at the junction considered.

MP26.13

Dose estimates with a water calorimeter. T.M. Kehoe, G. Galloway, J.R. Greening and D.I. Thwaites*, Western General Hospital, Edinburgh, Scotland.

A water calorimeter is an absolute instrument for direct measurement of absorbed dose in the medium of clinical interest. Recent and on-going work is establishing the technique as a practical method of obtaining absorbed dose. The water calorimeter built at Edinburgh has been used in both high and low LET therapy radiation beams. Dose estimates have been compared to ionisation chamber measurements converted to dose for the low LET radiation using the latest IAEA protocols (1983, 1985). The calorimeter over-estimates by ~5.5% for 10MeV electrons and ~4% for 4 and 9MV photons. Results are presented for a wider range of energies over a range of dose rates and field sizes and different water conditions.

The over-response of the water calorimeter has been attributed to the heat defect in water i.e. the disparity between the absorbed energy from the radiation field and that appearing as heat via the observed temperature rise. An independent method of measuring the heat defect by a comparative absorption technique is described.

MP26.14

Telescopic Method to Measure Backscattered Radiation from Collimator to Beam Monitor Chamber, Hideo Kubo, University of Rochester Cancer, Rochester, New York 14642

Charge collected by the monitor chamber is produced primarily by the primary photon beam. The controversy is whether or not an additional charge is created by the back scattered radiation (BSR) from the secondary collimator jaws. A pair of 10cm thick cerrobend blocks with a 6.3mm hole in the middle was used to measure BSR. One block was placed against the secondary collimator and the other 200cm from the source. A Farmer chamber with proper build-up was positioned behind the second hole to measure charge as a function of the collimator opening. Because the two holes were aligned to see a fixed area of the source and flattening filter, but not the secondary collimator jaws, the chamber reading should neither be influenced by flattening filter scattering nor collimator scattering and should reflect the correct amount of BSR. Results for 18 MV x-rays from a Therac-20 and a Clinac-1800 indicate that approximately 8% and 1%, respectively, of field size dependent output is attributed to BSR when the field size was changed from 2cm x 2cm to 40cm x 40cm. The Therac-20 result is in agreement with that by Patterson and Schragge (Med. Phys. 8, 312, 1981).

MP26.16

Clinical Experiences of Patient Dosimetry. G. Rikner* and S. Hallén, Department of Hospital Physics, University Hospital S-751 85 Uppsala, Sweden

There are several dosimetric calculations which have to be performed before the prescribed dose can be delivered to the patient in external radiation therapy. To ensure correct calculations, direct patient dose measurements have been performed for many years with semiconductor detectors connected to DPD 5 electrometers. To achieve field size independent readings build up caps have covered the detectors. However, this at the expense of perturbation of the radiation field, which is depending on the radiation quality. A maximum perturbation of about 5% has been noticed.

In a retrospective study which contains more than 500 measurements the agreement between prescribed and measured doses have been investigated. It was found that 95% of all measurements showed agreement within 5% for the SSD and isocentric treatments. This figure increased to about 8% when wedged fields were used. No reasons for these deviations could be noticed. For larger deviations these could, however, be explained by 1) not correct dose per monitor unit setting, especially in complicated irregular fields, where it is difficult to estimate an equivalent field size, 2) not stable dose monitor of the accelerator and 3) other systematic errors.

MP26.15

A METHOD OF INCREASING SENSITIVITY OF PIEZOELECTRIC QUARTZ DOSEMETERS, A Ghosh, Royal Armed Forces Hospital, Riyadh, Saudi Arabia and K V Ettinger* II University of Rome, Italy.

Piezoelectric quartz dosimetry is based on changes in the resonant frequency of resonators following an irradiation. The frequency changes are caused by alteration in the elastic constants of quartz caused by changes in the charge state of impurities, which act as electron traps. The radiation response of quartz resonators was modified by drifting alkali metal ions into the bulk of the resonator, using Doherty method. It was also possible to introduce very small amounts of Al by means of drifting from Al-Hg amalgam applied to the surface. The resonators were fabricated from originally pure material, of so called 'sweet' variety. After the impurities were introduced into 0.3 mm thick resonator, the continuous application of an electric field redistributed these impurities throughout the material. The measured sensitivity to gamma radiation has increased by a factor of 3 - 25, bringing the useful range of quartz dosimetry very close to the radiotherapy dose range. For mass use the doping may be provided at the stage of crystal growing from the hot solution.

MP26.17

ESR READ-OUT OF INORGANIC SOLID STATE DOSEMETERS, K V Ettinger, II University of Rome, Italy.

Many of the solid state radiation dosimeters depend in their action on formation of paramagnetic species, like free radicals, colour centres, electron and hole traps. ESR read-out is very accurate and non-destructive. In pure alkali halides colour centres formed on irradiation give rise to an ESR signal, with amplitude depending parabolically on the absorbed dose. Zero-dose signal depends on the degree of purity and concentration of point defects. Introduction of impurities may result in appearance of paramagnetic centres, even without irradiation, depending upon the value of ground state spin of incorporated ions. Material known as TLD-100, which is essentially LiF with a few controlled impurities gives a strong ESR zero-dose signal, owing to the presence of transition metal impurities, but LiF:Mg, LiF:Ca, LiF:Ba, NaCl:Mg and KCl:Mg, all prepared by interdiffusion and coprecipitation give only a weak zero-dose signal, while preserving strong response to radiation, almost linear with dose. Some of the paramagnetic centres in bivalently doped alkali halides have been identified and are described in more detail.

MP26.18

Environmental Effects of CR-39 Track Detectors

Julius J. Almasi*, Siemens Medical Labs.
2404 N. Main Street, Walnut Creek, CA 94576

CR-39 detectors are more frequently used in various fields of Medical Physics and Health Physics. CR-39s have many advantages over other low cost passive detectors. However, in experiments someone must be very careful with the application of these detectors because of the environmental effect of CR-39s. We are reporting about an environmental effect of CR-39s which can cause orders of magnitudes of errors in dose measurements. A mathematical model will be presented to describe the geometry of etched tracks on detectors which suffered from this environmental effect. This model can also be used to estimate the errors of a measurement caused by this effect. We will present several different methods to avoid this environmental effect. We will present a computer program which we developed to estimate the sensitivity and the resolution of CR-39s at a particular measurement. This program takes into account not only the environmental effects but also the errors introduced by the etching procedure and the image analysis system used to count and measure the etched tracks.

MP26.20

THE COMMISSIONING OF AUTOMATED SCANNING DOSIMETRY SYSTEMS, C. R. Blackwell, R. A. Dahl, D. E. Mellenberg*, Mayo Clinic and Mayo Foundation, Rochester, Minnesota.

The complexity of modern commercial scanning dosimetry systems requires a systematic approach to assuring their proper operation. A protocol for testing these systems was developed to assess correct performance. The following areas were included: 1) Accuracy and reproducibility of detector positioning; 2) Precision and stability of system detectors and electronics; 3) Method of data acquisition; 4) Data processing and 5) Data output consistency. This protocol was applied to two commercially available systems, including the PS/2 Model 60 controlled Wellhofer WP600C. Results of the protocol measurements will be presented. This protocol represents an important component of an overall radiotherapy equipment quality assurance program.

MP26.19

Postal Dosimetry Comparisons with Alanine Dosimeters, K.J. Olsen¹ and J.W. Hansen², ¹ Dept. Rad. Phys. Herlev Hosp., 2730 Herlev, Denmark. ² Acc. Dept. Risøe Nat. Lab. DK 4000 Roskilde, Denmark.

When alanine is exposed to radiation stable free radicals are produced which may be measured by Electron Spin Resonance (ESR). Our dosimeters consist of alanine mixed with 5% polyvidone in the shape of 2 mm thick cylinders of 4.5 mm diameter. Alanine dosimeters have been exposed to various beam qualities in the dose range 10-100 Gy at radiation therapy centers in USA, Finland, Poland and Denmark and measured at Risøe Nat. Lab. Doses were determined by comparison with alanine dosimeters exposed to a ⁶⁰Co beam calibrated with Fricke Dosimetry. At doses above 10 Gy the standard deviation for dose measurement was 1.1%. Dosimetry comparisons better than 2% at the 95% confidence level are possible. The dosimeters are easy to handle, robust and cheap and may be read repeatedly. Fading after 100 Gy of ⁶⁰Co gamma-rays is less than 2% in 4 years. Alanine dosimeters are useful for dosimetry comparisons both for photons and electrons and the negligible fading make them ideal for documentation of patient doses in radiation therapy.

MP27.1

Large Field K-edge Subtraction System for Coronary Angiography using Synchrotron Radiation, I. K-edge Subtraction System in JAPAN, M. Akisada*, S. Watanabe, I. Anno, T. Takeda, M. Kakihana, K. Nishimura, S. Hasegawa, K. Konisi, K. Hyodo, M. Ando, Univ. of Tsukuba, Saitama Medical School, Univ. of Electro-comm., Univ. of Kyushu, Photon Factory KEK

The K-edge subtraction method is suitable for the reduction of the misregistration in the subtracted image of the intravenous coronary angiography. Synchrotron Radiation (SR) available at the Photon Factory, National Laboratory for High Energy Physics, provides a new X-ray source which is highly suitable for K-edge subtraction. This is due to its high intensity, its parallelism and its monochromaticity available in a monochromator system. Since the SR beam size is relatively small for in-vivo imaging, a special diagnostic system; two dimensional imaging system, were constructed. The potential use and value of energy subtraction were successfully demonstrated.

And also an attempt at enhancing the boundary obtained from IVDSA coronary angiography was performed using "Minimum Difference of Density Method", because the boundary of the opacified coronary artery was difficult to be differentiated from the overlapping opacified ventricles.

MP27.2

Expanded visualization capacity
in the display of medical images.

Paul R. Moran, PhD
Wake Forest University, The Bowman Gray School
of Medicine, Department of Radiology
Winston-Salem, NC 27103

Human visualization of medical image display is severely limited, because eye-brain physiology restricts to contrasts of 1%, and less in non-ideal viewing conditions. The visual dynamic range, therefore, is something less than 7-bits of gray-scale. Over the FOV in medical images, however, the originally acquired image-array pixel values can easily span dynamic ranges of 13 to 15 bits. Thus the intensity-scale of image information is often 50 to 250 times greater than what the human observer can visualize in a single conventional image rendition. Steven Pizer and colleagues at UNC showed that image-array values may be mapped, in principle, so that the essential detail information can be well-displayed and visualized in 7-8-bits of displayable data. The methods for that scientific demonstration, adaptive histogram equalization (AHE), can be vastly improved through a recently discovered alternative adaptive image-intensity mapping, dynamic adaptive contrast-windowing methodologies.

MP27.4

Reconstruction of Dynamic Left Ventricular Cavity Shape from Bi-directional Projection Images. H.Matsuo*, I.Horiba, A.Iwata, N.Suzunura, Y.Takao and K.Hayasaki, Nagoya Inst. of Tech. Nagoya, 466, Japan

3-dimensional imaging of left ventricle is required to improve diagnostic evaluation of cardiac wall motion and cardiac function. We propose an algorithm to reconstruct dynamic 3-D shape of left ventricle from bi-directional DF(digital fluorographical system) images. It utilizes contrast density information and the conic beam co-ordinate. The evaluation of the algorithm has been performed by the experiments using plastic phantom modeled on a real left ventricle of a hog. Fairly good reconstructing results have been achieved. We have applied the method to reconstruct a human left ventricular cavity shape using sequential images of left ventricle taken from RAO30 and LAO60 by conventional DF system. The resulting reconstructed images are displayed on TV-monitor as a movie of heart-beating image, which can clearly express local wall motion disorder.

MP27.3

Evaluation of a Slot Scanned X-ray Imaging System incorporating a TDI CCD. D.W. Holdsworth* and R.K. Gerson, University of Toronto, Toronto, CANADA, M4X 1K9 and A. Fenster, John P. Robarts Research Institute, London, CANADA, N6A 5K8.

Radiographic image quality is degraded by noise due to scattered photons. Scanned projection radiography with a 1 to 2 cm wide slit beam of radiation will remove most of this unwanted scatter without introducing excessive x-ray tube heat loading. We have developed such a slot scanned system in which a charge-coupled device operating in the time-delay-integration mode is used to detect the optical output from an x-ray image intensifier. 56 image lines are collected simultaneously to reduce image acquisition time. The system has been designed to improve lesion detectability in digital angiography and digital mammography.

We have constructed a prototype imaging system which acquires 512 X 256 images in about 2 s. The limiting spatial resolution of the system is determined primarily by the x-ray image intensifier MTF. Measurements of the CCD dark noise (270 noise equivalent electrons) and full well capacity (580,000 electrons) indicate a camera dynamic range of 2150 when cooled to 5° C.

MP27.5

QUANTIFICATION AND VISUALIZATION OF 3D CARDIAC IMAGERY. N.F. Ezquerra*, E.V. Garcia, J.W. Peifer, C.D. Cooke, J.L. Klein, J.P. Skelton, and W.S. Briggs, Georgia Tech and Emory University

In order to aid physicians in the visualization and determination of the extent and severity of coronary artery disease, a technique has been developed to unify the physiological information obtained from thallium-201 (Tl-201) perfusion distribution, and the anatomical information obtained from coronary arteriography. The perfusion information is obtained from tomograms of the myocardium after patient injection of Tl-201 at peak exercise, and the information is then quantified to obtain maximal count profiles that are mapped onto a 3D ellipsoid that approximates the myocardium. The patient-specific arterial tree, which is superimposed on this ellipsoid, is obtained from a 3D geometric reconstruction performed on simultaneous biplane angiographic images. The reconstructed arterial structure is approximated by successive segments of generalized elliptical cone frusta, and along with the color-coded myocardium are modeled using a software package that we developed. The methodology has the capability of displaying models that can be viewed and illuminated from any orientation in space. This methodology has been tested with a phantom and is currently being tested with patient studies.

MP27.6

A New Approach to Light Imaging of the Breast

Abund O. Wist*, Panos P. Fatouros and P.R.S.
Kishore, Medical College of Virginia,
Richmond, Virginia 23298

New, non-invasive imaging techniques utilizing non-ionizing radiation for detecting malignancies of the breast are continually being sought as an alternative to mammography. We have designed, constructed and currently are testing a light imaging system which includes a pencil light beam, a scanning mechanism, provision for significant scatter reduction, a variable wavelength light source, and a low-noise sensitive detector. This system configuration was used to quantify scatter reduction and produce images of breast phantoms having low, medium and high scattering properties. The use of a tightly collimated beam improves dramatically contrast and resolution at the expense of detected signal strength. Similar measurements with a conventional wide-angle configuration illustrate a severe loss of image quality especially in high-scatter phantoms. Work in progress includes the development and use of more realistic breast-like phantoms, more powerful light sources, and faster and more sensitive detection systems.

MP27.8

Information Spectra of Radiographs Including Effects of Scatter and Object Velocity,
H. Kanamori*, M. Matsumoto and H. Kubota,
Kyoto Institute of Technology, Kyoto 606,
Japan

The information spectrum is offered as an overall expression of image quality and system performance. Its formula is

$$I(\nu) = \log_2 \sqrt{1 + p(\nu)/n(\nu)} \text{ bits}$$

where ν , $p(\nu)$ and $n(\nu)$ are spatial frequency, signal Wiener spectrum and noise Wiener spectrum, respectively. The information spectrum combines synthetically the contrast, the latitude, the sharpness by $p(\nu)$ and the granularity by $n(\nu)$, and is expressed as a function of spatial frequency. The information spectrum can be readily calculated by using the dynamic range, and the MTF and noise Wiener spectrum at medium dynamic range. The detectability of a low-contrast object and the resolution of an object can be explained by information spectral values in low- and high-frequency ranges respectively.

The contrast degradation effect of scatter, the blur due to object velocity, and the detectability-enhancement effect of poor MTF are demonstrated by the information spectra.

MP27.7

Evaluation of Radiographic film MTF by means of a Linear array of Photodiodes

A. Castellano⁺, G. Borasi^o, E.M. Staderini[#], G.E. Gigante^{#,*}, + Dip. Fisica Universita' di Lecce, ^o Ospedale Civile di Reggio E., [#] Centro per l'Ingegneria Biomedica dell'Universita' di Roma "La Sapienza", Corso Vittorio E. 244, 00186 Roma, ITALY.

The method to evaluate the performances of radiographic systems is actually that to determine the MTF of a film, or film-screen combinations. To do this is necessary to measure the ISF using test samples and a microdensitometer (m.d.), the procedure is quite long, because of the reading of the film pattern with the m.d.. For many radiographic examinations the spatial frequency upper limit is below that of the m.d. The availability of linear array of photodiodes and CCD has opened an attractive way to perform densitometric measurements. The spatial resolution of these detectors, i.e. the distance of two neighbor sensitive elements, are in the range 7-25 microns. Therefore, the Nyquist frequency of these detectors are in the range 70-20 lp/mm, without any optical magnification of the pattern. These performances are lower than that attainable with a m.d., but are enough to measure the ISF of a radiographic film, used for typical clinical examinations. We have tested this using a linear array of photodiodes (Reticon) to measure the MTF of radiographic films, a comparison with a traditional procedure has been done. The results obtained by means of the prototype system are satisfactory. Now we will develop a dedicated densitometric system, to be used in the evaluation of MFT.

MP27.9

Specifications and Acceptance Testing of Diagnostic X-ray Equipment for a Developing Country, M.R. Tecson*, I. Talusan and E. Estoesta, Radiation Health Service, Department of Health, Manila 1003, Philippines.

The Radiation Health Service of the Department of Health is the regulatory agency for the control of electronically produced radiation in the Republic of the Philippines. Oftentimes it is consulted for purchase specifications and acceptance testing of diagnostic x-ray equipment.

The report discusses the difficulties encountered in preparing purchase specifications and in doing acceptance testing for newly installed 100-mA, 125 kVp x-ray units for primary care hospitals. Several factors normally taken for granted for developed countries are of major significance in the Philippines. Examples are problems in the availability, quality and stability of power supply. Once equipment has been delivered and installed, a medical physics team from our office has to travel to remote places to do the acceptance testing. Factors like difficulties in travel, security risks and the lack of suitable instruments for rugged travel have to be taken into account. Other administrative factors must also be considered.

MP28.1

A Review of Futuristic Detector Design Concepts for Achieving Ultra High Resolution in PET Cameras. Wai-Hoi Wong, University of Texas Graduate School of Biomedical Sciences, Houston, Texas, USA.

The resolution of PET cameras has been improved steadily in the last 10 years. Current commercial cameras have 'intrinsic' detection resolutions in the 5-6mm range which is still two times worse than the theoretical limit. Current efforts are in improving the intrinsic resolution to the 2-3mm range and simultaneously decreasing the expense of using thousands of photomultipliers with their affiliated gamma-ray counting electronics. Decreasing the hardware complexity is desirable from the inventory, production, reliability and service considerations. Interesting concepts with various degrees of compromises between resolution and complexity have been proposed recently. These compromises also have significant impacts on the usable dynamic ranges in the count-rates of the cameras. Furthermore, some designs focus at improving the central resolution while others stress resolutions in a larger area. Esoteric scintillation light sensors from silicon avalanche photodiodes to specially designed multi-anode (or cross-wire-read-out) proximity imaging photomultipliers have been employed. Various interesting 1 and 2 dimensional analog decoding schemes using common photomultipliers have also been proposed. This paper reviews these interesting design concepts and compromises.

MP28.3

Evaluation of a Masked Orbiting Transmission Source (MOTS) for PET Attenuation Correction.

N. T. Ranger* and C. J. Thompson
McConnell Brain Imaging Centre,
Montreal Neurological Institute; and
Medical Physics Unit, McGill University

Transmission scans are routinely performed to correct for gamma ray attenuation in positron emission tomography (PET). The transmission scan must be done before administration of the positron labeled compound. A new technique is proposed and evaluated in phantoms and human subjects which allows the transmission scan to be done after, and in some cases simultaneously with the emission scan. The transmission source, which orbits around the inside of the patient aperture, consists of a 3 mm disk of Ge^{68} enclosed in a lead collimator.

Only events from detector pairs which are collinear with this source are selected for the transmission scan, significantly improving contrast. Most remaining coincident events can be used to reconstruct an emission scan with reduced efficiency. The lead surrounding the source prevents contamination of the transmission scan by the emission scan. An attenuation coefficient of $.096\text{ cm}^{-1}$ for both water and a Ge^{68} solution with specific activity of over 5 kBq/cc, demonstrated excellent rejection of scattered radiation and radiation from the object being scanned.

MP28.2

Correction for the Effects of Spatial Resolution in Emission Tomography, R.W. Rowe, University of Texas Health Science Center, Houston, TX 77030.

The quantitative accuracy of emission tomographic images (PET and SPECT) is limited by the spatial resolution of current camera systems. Activity and size measurements in small objects are subject to severe errors because part of the activity at any point is detected at neighboring locations. This so-called spillover causes blurring of edges, cross-contamination of adjacent activity spaces and inability to recover true activity (so-called partial volume loss). Based on computer simulations, we have developed a pixel image correction procedure for cardiac PET which removes spillover from the myocardium into the ventricular bloodpool, liver, stomach and lungs, and removes spillover from the high activity myocardium into the bloodpool and low activity regions of the myocardium. As a result, normal myocardial activity is restored to within a few percent of its true value and the accuracy of defect activity measurement is improved. Size restoration also results. The same principles can be applied to other imaging applications in both PET and SPECT and promise to enhance the clinical utility of emission tomography.

MP28.4

Effects of Axial Resolution and Sampling on Image Contrast for Multiplanar Emission Tomographic Systems, E.M. Kluksdahl* and K.J. Kearfott, Electrical and Computer Engineering Department, Arizona State University, Tempe, AZ 85287-5706.

Because of partial volume effects, axial spatial resolution may greatly affect object visibility and data integrity for multiplanar emission tomographic imaging systems. Simulations have determined the relative importance of axial resolution and sampling on object contrast. Gaussian curves represent the point spread function of a multiplanar emission tomographic system. Ring-to-ring separation and axial full-width-at-half-maximum (FWHM) are varied to determine the contrast of objects at differing axial positions. When the FWHM is increased from 6 mm to 12 mm, the wider FWHM has a 50% decrease in contrast compared to the narrower FWHM. For a 3 mm object centered in a detector ring, 25% of the true contrast is obtained for a FWHM of 6 mm, in comparison to 13% with a FWHM of 12 mm. When the object is positioned at the axial midpoint of the detector ring and cross plane for a ring separation of 13 mm, 21% of the true contrast is obtained for a FWHM of 6 mm compared to 12% with a FWHM of 12 mm. The decreased object contrast of wider FWHM point spreads, in the absence of specialized 3D reconstructive algorithms, could thus produce data losses or misleading artifacts more serious than those due to small inter-ring gaps.

124

MP28.5

Relative Performance of Simulated Annealing and Traditional Iterative Method for a Miniaturized SPECT, S.E. Hill*, K.J. Kearfott, Arizona State University, Tempe, Arizona.

An image simulation and reconstruction system for a novel miniaturized multi-detector SPECT design has been used to compare the relative performance of simulated annealing and a traditional iterative reconstruction technique. A variety of simulated phantoms were used with a range of photon counts between 50,000 and 700,000. The SPECT design had 128 detectors arranged in groups of 16 surrounding each of 8 pinholes. The 5 cm. radius sample was divided into 1961 2 mm. square reconstruction bins. Results show comparable reconstruction quality between the two methods for all noise levels. Acceptable reconstructions were obtained for about 100,000 counts and up on the basis of a picture distance measure of 0.55 using a normalized root mean squared distance measure. The simulated annealing method is also shown to be consistent in reconstruction quality and time, although its reconstruction time is yet excessive for a microcomputer.

MP28.7

The Hartley Transform: A High Speed, Real Domain Fourier Transform Substitute, M. Steckner, D. Drost, F. Prato, St. Joseph's Health Centre of London and University of Western Ontario, London, Canada.

The Hartley Transform (HT), a real domain Fourier Transform (FT), was applied to Nuclear Medicine image processing. The HT is 40% faster and requires 50% less memory than an FT.

The discrete representation of the HT is:

$$N \cdot H(f) = \sum_{t=0}^{N-1} h(t) \cdot \text{cas}(2\pi f t / N) \quad h(t) = \sum_{f=0}^{N-1} H(f) \cdot \text{cas}(2\pi f t / N)$$

where $\text{cas}(2\pi f t) = \cos(2\pi f t) + \sin(2\pi f t)$ and N is the number of data points. The HT is equivalent to the FT if and only if the input data is real.

The Fast FT algorithm was modified for the HT*. Since no complex operations are required, computation time was reduced by 40% and memory requirements were halved. Clinical and bar phantom Nuclear Medicine images were filtered (Hanning filter) by both FT and HT and the output images compared. Total counts (3×10^6) differed by less than .001% and no one pixel (mean 500 counts) differed by more than one count. A difference map did not suggest any systematic pattern. The HT can replace the FT in all signal processing applications where the input data is real, e.g. SPECT imaging where filtered back projection image reconstruction requires extensive filtering.

* Cooley JW, Tukey JW: An algorithm for the machine calculation of complex Fourier series. Math Computation APR/65, v19, p297-301

+ Bracewell RN: The Hartley Transform. New York: Oxford, 1986.

MP28.6

Ectomography using a Rotating Slant Hole Collimator, S. Dale* and P. Edholm, Karolinska Institute, S-10401 Stockholm, Linköping University, S-58185 Linköping, Sweden.

Ectomography is an alternative tomographic method in gamma camera imaging. With a rotating slant hole collimator 64 projections are registered and the desired sections are reconstructed by a two-dimensional filtered back projection technique. When imaging sections that are parallel and close to the body surface ectomography is advantageous to SPECT: the distance from the camera to the patient will be shorter and constant during the whole registration. This results in a high and uniform resolution and a low and uniform attenuation. So far we have studied 1) coronar 99m-Tc sections of healthy and fractured hip joints for prediction of the healing course, 2) short axis 201-Tl sections of the heart for detection of coronary heart disease or infarction and 3) coronar 99m-Tc sections of the thyreoidea. The hip joint and the heart were imaged with both SPECT and ectomography.

MP28.6

Left Ventricular Mass Estimation from SPECT Tl-201 Myocardial Perfusion Short Axis Slices Using Bullseye Analysis and Edge Detection in Dogs. MJ Tamas*, RL Eisner, JC Cedarholm, AS Boyers, D Dunn, SE Martin, R Greene, MT Jones, A Gober, RE Patterson. Carle Fraser Heart Ctr/Crawford Long Hosp of Emory University, Dpts of Medicine (Cardiology) & Radiology-EUSM; Georgia Inst of Technology, Atlanta, GA

The bullseye protocol (BP) synthesizes SPECT Tl-201 myocardial perfusion three dimensional (3D) data into a 2D display. When this data is compared against a normal (nl) reference file it accurately detects coronary artery disease. We have used BP and an edge detection algorithm (EDA) to measure total left ventricular (LV) mass and the %LV that is underperfused. Twenty anesthetized dogs were injected with isoproterenol as a stress agent and imaged: 9 were nl references, 7 others were also nl, and 4 had partial coronary stenosis. The %LV supplied by the stenosed artery was measured by post-mortem stains. SPECT images were reconstructed, and BP was performed on the stress images. The EDA extracts endocardial and epicardial boundary points on each short axis slice through a radial search for the zero crossing of the 2nd derivative of the count intensity profile. Ischemic areas on each slice were determined by BP. Estimated LV mass vs. measured LV mass correlated reliably ($r=0.88$). Preliminary data suggest that BP can predict the %LV that is ischemic during stress ($r=0.90$, $SEE=3\%$, $n=4$).

MP28.9

A Probabilistic Analysis of Thallium Myocardial SPECT Images²

M. Jamzad*, A. Uchiyama¹, H. Toyama², and H. Murata³
 *1 Dept. of Elec. & Comm. Sch. of Sci. & Eng. Waseda U. Tokyo. 2) Inst. of Clin. Med. Tsukuba U. Tsukuba. 3) Div. of Nucl. Med. Toranomon Hospital, Tokyo.

A probabilistic method is developed for analyzing the extend and severity of ischemia by comparing the early and delayed SPECT images of Thallium after the physical exercise. For both, early and delayed stages, 10 short axial images (slices) are extracted from apex to base. For each image the center of left ventricular cavity, the inner and outer edges of myocardium are automatically detected. Each slice is divided into 8 equi-angle sectors. Also the heart is divided into 8 equi-angle vertical sectors from apex to base. For each slice of early and delayed, a defect probability matrix P is created such that $0 \leq P(i,j) \leq 1$ shows the severity of ischemia of pixel (i,j) of myocardium of that slice.

Using these matrices, the defect probability for each slice, for each sector of each slice and for each vertical sector are calculated and displayed on CRT by means of images, curves and histograms. They show what percentage of the area of each slice and that of lateral, anterior, septum and inferior has how much defect. These curves, histograms and images give a comprehensive and easily understood information about the condition of the heart in early and delayed stages.

MP28.2

A Method for Multi-element Imaging in X-ray CT.

J. Fryar* and K.J. McCarthy
 National Institute for Higher Education, Dublin, Ireland

When analytes are already present within an object (matrix) they can be imaged in a single X-ray CT scan by passing a continuum of X-rays through the object and measuring transmitted fluxes within narrow energy bands on either side of the absorption edges of the analytes. It is shown that by extrapolation of results to the absorption edges, matrix effects are eliminated. In the process, dead time effects are minimized. The projection data is analyte equivalent thickness along the beam direction. A reconstructed image shows analyte concentration. A small apparatus was built to test the theory. In previous work the analytes were discretely located within the matrix. In the present experimental results the analytes are intermixed within the matrix. When reconstructing an image for any one analyte, the other analytes are treated as part of the matrix. The reconstructed images are compared with images produced by raster scanning a thin slice of the object taken from the CT image plane. In a water like matrix a few centimeters in diameter the sensitivity is of the order of 10^{-3} - 10^{-5} g/cc for 10^7 incident photons.

MP29.1

A Modified Anger Camera System for Coherent Scatter Tomography

J. Kosanetzky*, G. Harding
 Philips GmbH Forschungslaboratorium Hamburg, Vogt-Koelln-Str. 30, D-2000 Hamburg 54, FRG

When x-rays impinge on an object, part of the quanta will be scattered elastically into a small cone of about 10 deg. aperture. Due to interference effects the spatial distribution of the scattered radiation for a certain material is characterized by an individual scatter-pattern. One can use these pattern to differentiate between materials. Use of a conventional x-ray tube allows a CT-like imaging of a slice through an extended object within a short measuring time. Image contrast reduced by the polychromatic nature of the incident radiation can be enhanced by use of a modified 'Anger Camera' system as a detection unit. A short overview of the physical background will be presented together with our new detection system. Results will be given which demonstrate the improvements in image contrast and the feasibility of our method for material characterization.

MP29.3

Synchrotron Radiation Computed Tomography with large area monochromated beams, F. Toyofuku*, K. Konishi, K. Nishimura, K. Hyodo, M. Ando, M. Akisada, A. Maruhashi, A. Suwa, S. Hasegawa, and E. Takenaka, Kyushu University, Maidashi 3-1-1, Higashi-ku, Fukuoka 812, Japan.

Synchrotron radiation has a lot of advantages as a source of X-rays for computed tomography. Several systems have already been developed using a slit beam geometry, aiming to achieve the highest spatial resolution of 10 μ m or less. We have developed a synchrotron radiation CT system with an area beam geometry using an image intensifier and a high S/N TV camera as a two-dimensional detector. Large area monochromatic X-rays were obtained from a wiggler beam using a silicon crystal with [311] asymmetric reflection. A rat phantom injected with iodine on a rotating table was projected onto the image intensifier. A total of 100 projection video images covering 180 degrees were acquired in a single scan. Axial sections were obtained by using the filtered backprojection method. By taking two images above and below an iodine K-absorption edge (33.17keV), it was possible to obtain an iodine image. Three dimensional images were also obtained from all of the reconstructed cross sections. It was suggested that this system has the possibility of rapid three-dimensional volume imaging of a specific element in a human body.

MP29.4

Potential medical applications of differential tomography, R. Cesareo, Centro per l'Ingegneria Biomedica, Università di Roma, Italy, S.Q.G. Mahabally, Dept. of Physics, University of Rajshahi, Bangladesh, L.J. Pedraza, Centro de Estudios Nucleares, Universidad N.A. de Mexico.

Attenuation coefficient of each element exhibits sharp discontinuities (K,L,...) in correspondence with the minimum energy values for the ejection of an electron from its different shells. These discontinuities can be employed for detecting and isolating the presence of an element in any matrix when a pair of monoenergetic radiations are used which closely bracket the energy of discontinuity of the element. The difference between two tomographies carried out with a selected pair of radiations is only sensitive to the presence of a given element. By employing an X-ray tube with external interchangeable secondary targets, quasi monoenergetic X-rays can be produced. A mini CAT-scanner has been employed, using NaI(Tl)/HPGe detectors connected to a multichannel analyzer and a PC-Apple II E for obtaining differential tomographs. The presence of Ag, Pb and I in different samples have been studied by using secondary targets of Sn/Sb (Ag-isolation), Y/Zr (Pb-isolation) and LaI/LaII (I-isolation). This method may be used for studying the I-flow in blood vessels and to enhance the presence of a given tracer element used in medical diagnostic applications.

* Intern. Centre for theoretical Physics (Trieste-Italy) for Training and Research in Italian Laboratories.

MP29.6

Precise Delineation of Radiotherapy Targets by Quantitative Computed Tomography, T. Lei and W. Sewchand *, Dept. of Rad. Oncology, Univ. of Maryland Hosp., Baltimore, MD 21201

A major disadvantage of current CT-based techniques for delineating radiotherapy targets is their reliance on visual perception and subjective selection of CT-value thresholds. A new quantitative automatic method has been developed which accurately identifies and precisely quantifies a target-of-interest (TOI) on the CT image. The basis of this approach is that the pixel CT image of normal tissues has an asymptotic Gaussian distribution and is ergodic in mean and variance. Thus, estimates (m, v^2) of the mean and variance are obtained by spatial sampling and spatial averaging. A CT-value filter with pass-band ($m-kv, m+kv$) is designed to create an accurate isolated image of a specific normal tissue. When multiple normal tissues are enclosed in a region-of-interest (ROI), unique boundaries between images of these tissues are obtained by a suitable choice of k-values that ensures no overlap between tissue-specific filter passbands. When a TOI (e.g. tumor) is included in the ROI, specific normal tissues are subtracted from the ROI to yield an isolated true image of this TOI.

This approach provides an accurate 2D/3D display of TOI's and generates significant necessary data (area/volume, density distribution, relative location, etc.) for quantitative evaluation of response to treatment. Examples of this application will be presented.

MP29.5

An Isotope Computed Tomography Scanner for the Precise Measurement of Bone. T. N. Hangartner, Wright State University, Dayton, Ohio, U.S.A.

A special computed tomography (CT) scanner has been developed for the precise measurement of bone. The scanner, which employs an ^{125}I source and counting electronics, is a translate-rotate system and allows the measurement of cross-sections up to 200 mm diameter. The machine is optimized for the quantitative evaluation of trabecular bone at the distal end of arms and legs. These measurement sites are particularly important because fractures of these bones represent good indicators for osteoporosis.

The precision of the measurement of trabecular bone density is about 0.5%. This is an improvement of close to an order of magnitude compared with commercial scanners in average clinical settings. Responsible for this high precision are the mechanical design of the scanner; the choice of an optimal energy for the photon source; the stability and efficiency of the detection system; the various corrections for deadtime, background, beam-hardening and scattering; the system of evaluating the images. This scanner will be used primarily in a research setting. The high precision of the measurements allows the evaluation of changes in bone density through disease or treatment over weeks and months rather than years. Smaller patient groups will suffice for obtaining significant data as the measured changes can be evaluated for each individual patient, and no need for averaging over large groups is necessary to reduce the noise of the measurement method.

MP29.7

Geometrical Aspects of Computed Tomography: Sensitivity Profile and Exposure Profile, R.M.Gagne, Ph.D., Office of Science and Technology, CDRH, FDA, Rockville, Maryland

A simple model has been developed for the generation of theoretical sensitivity and exposure profiles perpendicular to the tomographic plane in computed x-ray tomography. The model incorporates the functional dependence on scanner geometry, focal spot size and shape, and detector sensitivity. The sensitivity and exposure profiles are best depicted as the convolution of functions, when appropriately scaled, describing the focal spot distribution and the transmittance of the pre- and post-patient collimators. Predictions of the model agree well with experimental results on both sensitivity and exposure profiles for small and large nominal slice thicknesses from five different CT x-ray systems. The CT x-ray systems selected represent both state of the art and older scanner models. Comparisons are also made on the degree of matching of the sensitivity and exposure profiles for each scanner which can be used as a measure of geometrical efficiency in the direction perpendicular to the tomographic plane.

MP29.8

Observer Efficiency in Size-Discrimination on CT Images, A.R. Bleier, P.F. Judy*, R.G. Swensson, and I. Kazda, Harvard Medical School and Brigham and Women's Hospital, Boston, Massachusetts, 02115

This experiment compared the efficiency of observers relative to physical image calculations, in size-discrimination tasks of single features or feature pairs on CT images. The stimuli were images of two disks added to CT scans of water. Eight sets of images were studied at two levels of disk contrast. Observers performed three rating tasks with each set of images: 1) the sizes of single features (smaller vs larger), 2) the size-differences of feature-pairs and 3) the average sizes of pairs.

Within each specified task and disk contrast, the mean d_a (an index of observer performance, derived from the rating ROC curve) was proportional to Task SNR (a cross-correlation calculation that measures how accurately the physical image information could be used), with a slope (observer efficiency) less than unity. For low-contrast disks these slopes were similar in all three tasks (0.386 ± 0.011). For high-contrast disks these slopes were lower, only slightly in the size-difference task (0.352 ± 0.004) but considerably so in the single-feature task (0.267 ± 0.006) and the average-size task (0.260 ± 0.014).

The higher level of observer efficiency in the size-difference rating task suggests that it is a more "natural" task for observers to judge differences in the size than the sizes of single features or the average size of feature-pairs.

MP30.1

On a numerical calculation of energy deposition by broad high energy electron beams, H. Huizenga * and P.R.M. Storchi, Rotterdam Radiotherapeutic Institute, 3075 EA Rotterdam, The Netherlands.

Dose deposition by broad high energy electron beams as calculated by Monte Carlo codes have been reported by several authors. These calculations take a lot of computer time and the results feature statistical uncertainty. Up to now Monte Carlo calculations are not suited for radiation therapy planning. Therefore, the feasibility of a numerical calculation method has been investigated. The method is based only on the basic physical interaction processes of high energy electrons and matter. The method is a drastically improved version of the phase space time evolution method as described by Cardoro and Zucker (Nucl.Sc.Eng 45,107,1971). The calculated depth dose curves, energy spectra and angular distributions agree very well with the Monte Carlo results of Andreo and Brahme (Rad.Res. 100,19,1984). For the general case of radiation therapy planning, combination of this method with the "redefinition pencil beam method" of Storchi and Huizenga (PMB,30,467,1985) and Shiu and Hogstrom (9th ICCR,1987) seems promising.

MP29.9

Geometrical, Sampling, and Algorithmic Aspects of Computed Tomography R.M. Gagne, Ph.D., Mary Pastel Anderson, M.S. Office of Science and Technology, CDHR, FDA, Rockville, Maryland

A complete, self consistent, analytic model has been used to generate the theoretical point spread function (PSF) and the associated modulation transfer function (MTF) for computed tomography (CT) using filtered back-projection. The model incorporates the functional dependence of the reconstructed PSF on scanner geometry, focal spot size and shape, and detector sensitivity. The model explicitly includes aliasing effects due not only to sampling within the projections and angular sampling but also to the two-dimensional sampling inherent in the reconstructed image. Unlike previously reported models, special emphasis is placed on the impact of offsetting the detector sampling points in opposing views for scanners with detectors rotating through 360 degrees. In addition, the effects of interpolation between sampling points and of the reconstruction algorithm are also considered in the development. Predictions of the model for the PSF and MTF using the known geometrical characteristics of the scanner and estimates on the reconstruction algorithm from empirical noise power spectra agree well with experimental results for the PSF and MTF from four different CT x-ray systems. For these comparisons, the significance of the aliasing errors is enumerated in the final results.

MP30.2

A Monte Carlo Method for Electron Beam Dose Calculations, H. Neuenschwander, E.J. Born* Dept. of Medical Radiation Physics, Inselspital, University of Berne, CH-3010 Berne, Switzerland

A macroscopic Monte Carlo (MMC) method based on traditional Monte Carlo precalculations as suggested by Mackie and Battista (1) has been developed. Precalculations were done using the EGS4 code system to simulate the transport of perpendicularly incident electrons through macroscopic (typ. 0.5 g cm^{-2}) spheres. The symmetry of this geometry minimizes storage requirements for the resulting probability distributions of emerging electrons at the cost of a rotational transformation that has to be performed after each electron step during the MMC calculation. In order to get physically reasonable results, several essential modifications to the original concept (1) are necessary and will be discussed. MMC results for calculations in water are in good agreement with full EGS4 simulations and were obtained 1 to 2 orders of magnitude faster (depending on parameter values) than EGS4 results for slab geometries. This time gain is expected to be significantly higher for simulations for heavier elements and for dose calculations in close-meshed scoring grids. Current work concerns the generalization of the MMC code to accept measured energy spectra as input data and to consider inhomogeneities by taking into account pixel based density information.

(1) Mackie, Battista; Proc. 8th Int. Conf. on the Use of Computers in Rad. Therapy, 123, 1984

MP30.3

A Model of Fast Electron Penetration

D.J. Perry*, S.K. Rasis, F.C. Deibel, and F.M. Khan. Univ. of MN., Dept. of Therapeutic Rad., Minneapolis, MN. 55455

We introduce a multiple scattering model of charged particle penetration based on previous analysis of Yang and Perry. Our development removes the main limitations of the closely related Fermi-Eyges picture but retains its considerable potential for successful therapeutic applications.

In the time dependent picture discussed first, particles penetrating a material are found on thin curved surfaces which expand and deform as they move away from their point of origin. These surfaces are an exact feature of the multiple scattering transport equation and are defined by three moments of the particle density: the average depth of penetration and the lateral and longitudinal widths. The model is indifferent to the use of small or large angles.

We use this approach to construct spatial distributions under time independent conditions, giving results of practical interest. We compute the energy absorbed in thin planes located at various distances from the source and the lateral extent of these distributions. Results are compared against a previous Monte Carlo computation for 5, 10, 20 MeV electrons incident on water.

MP30.5

Monte Carlo evaluation of methods for deriving electron pencil beam spread. G.A. Sandison*¹, W. Hudai, J. Battista² and D. Savoie¹.

¹Manitoba Cancer Foundation, 100 Olivia Street, Winnipeg, Canada, R3E 0V9.

²Cross Cancer Institute, 11560 University Ave., Edmonton, AB, T6G 1Z2.

The EGS4 Monte Carlo code has been used to generate "benchmark" dose distributions resulting from electron pencil beams of 16 and 22 MeV energy incident upon homogeneous muscle, bone and lung equivalent media. A repeat set of Monte Carlo data was also generated in which bremsstrahlung is ignored. These data are compared to three methods of deriving pencil beam dose distributions from therapeutic electron beams. The results indicate that systematic errors associated with each experimental method can lead to substantial errors toward the end of the electron range. The largest contribution to these systematic errors is the bremsstrahlung background present in collimated broad beams. A new empirical formula based on the Monte Carlo data to modify the pencil beam spread parameter at depth in tissue predicted using Fermi-Eyges theory is suggested.

MP30.4

LOW ENERGY ELECTRON DIFFUSION IN TISSUE LIKE MEDIA

C. Malanaut*, Int.Rad.Dos./BRAZIL

P.J.Paes-Leme and A.S.Paschoa, Pont.Univ.Cat./RJ., BRAZIL

The spatial - energetic distribution of low(E<50 keV) electrons was studied for a source located in a medium simulating biological tissue. The time independent Boltzmann equation was used to model mathematically this distribution. Ionization was assumed to be a perturbation to a quasi - elastic collision process between the electron and the medium. A diffusion limit was obtained, by using a scale parameter, leading to a sequence of recursive partial differential equations, whose solutions were obtained by numerical approximations. Electron ranges were estimated based on this solutions and then compared with values reported in the open literature based on experimental and Monte Carlo methods. Local dosimetry of low energy electrons from internal emitters can benefit by the knowledge of these estimated ranges in biological tissue. Auger electron emitters, for example, have been object of a number of investigations, not only due to their toxicity in general, but also due to their potential application in the selective irradiation of neoplastic cells.

MP30.6

ELECTRON TRANSPORT IN NON-HOMOGENEOUS MEDIA
Rosana C. Falcao*, C. Malanaut*, P. J. Paes-Leme*
*Inst.Fisica-UFRJ, *Inst.Rad.Dos.-CNEH, Dept. Matem. PUC/RJ

Due to the importance of obtaining, with high degree of accuracy, the dose variation at the vicinity of the interface between two media, we propose a mathematically rigorous method to calculate it. The Singular Eigenfunction Method is used to solve a one speed one dimensional Boltzmann transport equation

$$\mu \frac{\partial \phi(x, \mu)}{\partial x} + \phi(x, \mu) = \frac{c}{2} \int_{-1}^1 \phi(x, \mu) d\mu \quad (1)$$

$\phi(x, \mu)$ is the particle flux at point x , with direction μ (μ is the cosine between the x axes and the particle's velocity).

For an infinite medium eq.(1) has the general solution

$$\phi(x, \mu) = a_+ \psi_+ e^{+x/v} + a_- \psi_- e^{-x/v} + \int_{-1}^1 A(\nu) \psi_\nu e^{-x/\nu} d\nu \quad (2)$$

where

$$\psi_{\pm}(\mu) = \frac{v c}{2(v \mp \mu)} \quad \text{and} \quad \psi_\nu(\mu) = \frac{c v}{2(v \mp \mu)} + A(\nu) \delta(v - \mu)$$

The coefficients a_+ , a_- and $A(\nu)$ are to be determined by the boundary conditions and orthogonality relations among the ψ_s .

Suppose we have two adjacent media, a source at $x = -\infty$ and that $\lim_{x \rightarrow \infty} \phi(x, \mu) = 0$. Assuming that the flux might be continuous at the interface, we can obtain the fluxes at medium 1 and at medium 2

$$\phi_1(x, \mu) = a_{0-}^{(1)} \psi_{0-} e^{+x/v} + \psi_0 e^{-x/v} + \int_{-1}^1 A_1(\nu) \psi_\nu e^{-x/\nu} d\nu$$

$$\phi_2(x, \mu) = a_{0+}^{(2)} \psi_{0+} e^{-x/v} + \int_{-1}^1 A_2(\nu) \psi_\nu e^{-x/\nu} d\nu$$

Presently we are calculating $a_{0-}^{(1)}$, $a_{0+}^{(2)}$, $A_1(\nu)$ and $A_2(\nu)$ through numerical methods since the expressions which give these coefficients cannot be integrated analytically.

MP30.7

Effect of Dimensionality of Heterogeneity Corrections on Three Dimensional Electron Pencil Beam Calculations, G. Starkschall; K.R. Hogstrom, S.W. Bujnowski, L. Wang, and A.S. Shiu, Dept. of Radiation Physics, Univ. of Texas M.D. Anderson Hospital and Tumor Institute, Houston, TX 77030.

Electron beam dose distributions have been calculated on a three dimensional grid using a pencil beam algorithm taking into account effects of heterogeneities in either one, two, or three dimensions. Execution times for each of the algorithms on a VAX-based treatment planning system are compared. Execution times are comparable for both the one and two dimensional heterogeneity corrections, in spite of the fact that the two dimensional heterogeneity correction requires an additional calculational loop over fan lines. Execution times for the three dimensional heterogeneity correction are approximately a factor of ten longer than that for the two dimensional correction. The logic and approximations employed to optimize the algorithms for speed will be presented. Finally, the potential applications of these algorithms in electron beam treatment planning are discussed.

This work supported in part by NCI grant CA06294, NCI contract CM67914, and a research contract with International General Electric of New York, Medical Systems Division.

MP30.9

Application of Measured Electron Beam Bremsstrahlung Distributions to a Pencil Beam Algorithm, J.E. Rodgers*, G. F. Popescu and S.N. Rustgi, Georgetown University Hospital, Department of Radiation Medicine, Washington, D.C. 20007

Accurate assessment of pencil beam algorithms requires a proper representation of the bremsstrahlung component, especially at high energies. Previous measurements (1) of bremsstrahlung distributions in 6-18 MeV electron beams from a Varian Clinac-18, which demonstrated that bremsstrahlung is produced primarily in the accelerator head, have been parametrized by the product of the reciprocal of a cubic function (beam envelope) and a Cauchy function near and beyond the cone edge. This model was incorporated into the MDAH(Hogstrom) computer code and compared to measured ionization distributions. Pencil beam parameters yielding best agreement will be presented along with effects these improvements have on ability to account for simple slab inhomogeneities and air gaps.

(1) Rustgi, S.N. and Rodgers, J.E. Med. Phys. 14(5), 884 (1987).

MP30.8

3-D Dose Calculations for Total Skin Electron Therapy, L.D. Simpson*, Washington University School of Medicine, St. Louis, MO, USA.

Total skin electron beam (TSEB) therapy for mycosis fungoides may require the use of 6-8 different patient positions at 3-5m SSD. Each position may require 2-3 low energy electron fields at split gantry positions. A 3-D dose computational model will be presented which permits analysis of alternative TSEB treatment plans. Single-field, experimental input data are required: off-axis profiles for normal incidence; depth dose as a function of incident angle; and the dependence of the dose at d_{max} on distance from the source. The patient surface (or a segment of the patient's surface) is represented as points on ellipsoidal surface segments. The total dose, at each surface point, at depths normal to the surface is given as the sum over all clinical positions for all physical fields. The model produces results consistent with the phenomena experimentally and clinically observed in these treatments. Several examples will be discussed.

MP31.1

An Instrument for Producing Constant Laminar Flow in an MR Imaging Phantom, R. J. Kriz*, R. Stortzum, G. Dobben and A. Horowitz

An imaging phantom has been designed that will produce constant laminar flow at various average velocities through rigid tubes of various diameters.

The phantom consists of six circular tubes 20 cm in length, having diameters of 0.102 cm, 0.207 cm, 0.318 cm, 0.397 cm, 0.476 cm and 0.794 cm. A large reservoir supplies the tubes. Constant flow of 0 to 10 cc/s is provided by a separate reservoir specifically designed to maintain a constant head pressure. The difference between the fluid level in the reservoir and exit overflow is adjustable from 0 to 15.3 cm and kept constant to within 1 mm. The pressure produced by the differential fluid level is reduced by the fluid passing through an orifice in the exit tubing from the phantom. Thus the pressure drop across the phantom is controlled and constant.

MP31.2

3D Magnetic Field Mapping and Confirmation of Hazard Zones for Clinical MRI, Suresh M. Brahmavar, Susan Majka, Martha LaFrance* and J. Robert Kirkwood, BayState Medical Center, Inc., Springfield, MA 01199

The 3D magnetic field mapping of a clinical MRI (1.0 Tesla) facility was done to meet compliance requirements of DPH and DON. The customary extensive planning support provided by the manufacturer was augmented by our own efforts to confirm regulatory magnetic hazard zones of 15, 5, 3 and 1 gauss lines. Such confirmation was of utmost importance because of unique location of MRI facility at BayState Medical Center. The third floor MRI facility is surrounded by other areas such as pathology offices, clinical laboratories, lab computers, electronic cables directly below and adjacent patient rooms, gift shop, etc. The 3D magnetic field measurements were carried out by two gauss meters and axial probes calibrated using 100G, 200G, 1000G standard magnets. Several measurements were taken at different locations on long axis as well as on the short axis of 1.0 Tesla MRI magnet. The ten (10) magnetic field zones ranging from 500G to 1G were established. The results were utilized to implement radiation safety and quality control (RS/QC) program for MRI facility. The working guidelines include safety precautions for magnetic field lines less than the FDA caution zone of 5G.

MP31.4

Utilization of Inversion Recovery Pulse Sequences with Short TI at High Field, S. Albert* and N.E. Leeds, Department of Radiology, Beth Israel Medical Center, New York, N.Y.

Inversion recovery (IR) pulse sequences with short inversion time (TI) were developed and applied chiefly at low (0.15T) and medium (0.5T) magnetic field strengths. The objective of the study was to develop useful IR pulse sequences with short TI times for high field imaging and to discuss and demonstrate the analytical and practical considerations involved. Our studies have been carried out at a field of 1.5T with a whole body superconducting imager (GE SIGNA). Spin-echo data collection is used in our experiments and proper interleaving is required in the multi slice sequences to optimize acquisition time. An additive contribution to contrast from both T_1 and T_2 and fat suppression were obtained with a short TI time of 100ms. Signal suppression of any tissue can be achieved by appropriate selection of TI value. Comparison of the IR images with spin echo (SE) T_2 -weighted images demonstrate in most cases a better contrast to noise ratio, a shorter acquisition time and reduced chemical shift artifacts of the IR images.

MP31.3

A Chronicle Of Philips Gyroscan S5 MRI System: The Evaluation Results Of Image Quality Parameters For The Past 3 Years, Pei-Jan Paul Lin, Northwestern University Medical School, Chicago, Illinois 60611 U.S.A.

Various MRI image quality parameters and descriptors have been evaluated and recorded based on a set of measurement protocols for a Philips Gyroscan S5 MRI system. The performance of the MRI unit has been recorded starting from the prestage/acceptance at the factory [Time: 0], at the initial acceptance testing conducted at the time of "turn-over" to the Hospital [4th Month], at the time of system re-tuning [14th Month], at the time of system up-grading [26th Month], and at the end of two and a half year of clinical services [34th Month]. The results, the improvements and/or the lack of improvements over the 2-1/2 year time span after being placed for clinical imaging can be employed to establish a basic quality assurance [QA] program and to optimize the QA procedure. A brief discussion on a few specific problems encountered such as low "signal-to-noise", RF shielding, and shimming of magnet will be included.

MP31.5

A Quantitative Study of Magnetic Resonance Imaging, W.K. Chu, University of Nebraska Medical Center, Omaha, Nebraska, USA

The objective of our study was to investigate, through quantitative analyses under the framework of pattern recognition, the possibility of enhancing detectability and/or specificity of lesions shown in Magnetic Resonance Imaging (MRI). Sixty sets of MRI liver images were studied. Thirty were obtained from patients with hemangioma, a common benign liver tumor, and thirty were from patients with other types of localized lesions. A 1.5 Tesla MRI scanner was used for data collection. Quantitative features measured included grey scale intensity values and variations of normal liver tissues, intensity values and variations within lesions, calculated T2 relaxation and backgrounds. More features were developed based upon these measured values. After feature selection process, it was found that a normalized intensity ratio between the lesion and its surrounding normal liver tissues provides the highest separation between hemangioma and all other localized liver lesions. With a threshold ratio of 16.8 an accuracy of 95 percent was achieved.

MP31.6

Dispelling Some Doubts About Back Projection Reconstruction in MR Imaging,

A. V. Lakshminarayanan*, Dept. of Radiology,
University of Alabama at Birmingham, 619 South
19th Street, Birmingham, AL 35233

It is widely believed that the (back) projection reconstruction technique of acquiring MR images is more susceptible to magnetic field non-uniformities than 2DFT methods and results in images with poorer signal-to-noise characteristics. This belief is due to misimplementation of the projection reconstruction scheme and a failure to compare equivalent scan strategies.

Images are presented that demonstrate the robustness of the back projection method in the presence of inhomogeneities and the relative advantages and disadvantages of the two approaches. Compared are signal-to-noise ratios, field and RF uniformity requirements, gradient requirements, the ability to obtain high-resolution images, effect of motion, and computational complexity.

MP31.8

PROTOCOL-DEPENDENT CALCULATED VOLUMES FOR MAGNETIC RESONANCE IMAGES IN CANINE GLIOMA. Robert L. Galloway, Jr., Robert J. Maciunas, Anne L. Faillinger. Vanderbilt University, Nashville, TN.

Primary CNS tumors have a structure which includes a solid tumor core surrounded by a zone of infiltrating tumor cells. The planning of safe resections and efficacious therapies depends on a clear understanding of the tumor margins and volume. In the presented study, cloned gliosarcoma cells were implanted in adult, mongrel dogs and grown for two weeks. Each animal was imaged using four common magnetic resonance (MR) timing sequences and protocols: T_1 -weighted, T_2 -weighted, proton density and gadolinium-enhanced T_1 -weighted images. The volumes were determined by marking tumor margins on spatially-sequential, parallel, slice images. The images were then computationally stacked and the volume was calculated based on the image pixel spacing and the slice thickness. Each sequence provided a different, distinct volume. The possible sources for these differences and their relationship to the underlying physiology and "true" tumor margins are discussed. This work was supported in part by a grant from Sun Microsystems, Inc., Mountain View, California.

MP31.7

A System for Tissue Characterization Studies by NMR, K. Homma* and E. Takenaka¹, Mechanical Engineering Laboratory, MITI and National Defence Medical College¹, 1-2, Namiki, Tsukuba Science City, Ibaraki 305 JAPAN

A system for tissue characterization studies in Medicine and Biology is proposed. The system is constructed by a NMR (Nuclear Magnetic Resonance) and two subsystems - an image processing system and an expert system. The image processing system installed in a computer extracts features from three dimensional NMR images reconstructed in accordance with imaging methods (MRI). Tissue functions are also analyzed by the chemical shift analysis (MRS). On the other hand, the expert system evaluates and characterizes biological tissues based on the extracted features (spin density, relaxation times and three dimensional structures). The system is equipped with a knowledge base concerning these features in normal and pathological human, rat and rabbit tissues. The LISP language is used for the tissue characterization. The system communicates directly with a PACS (Picture Archiving and Communication System).

MP31.9

Biexponential transverse relaxation accuracy of an 0.5 T MR imaging unit.
A Fransson*, Karolinska Institute, S-10401
Stockholm, A. Ericsson, B. Jung, University
Hospital, S-75185 Uppsala, Sweden.

In magnetic resonance imaging biexponential transverse relaxation processes in biological tissues have been reported. To investigate the capabilities of biexponential resolution of our imaging unit, measurements were performed using a binary phantom as a model. Mono- and biexponential relaxations were assessed with software developed for discrete multiexponential functions. Only transverse relaxation was investigated by applying a spin-echo-sequence with 32 echoes.

The results indicate a relatively accurate and stable resolution of the slow component in different environments. The ratio of relaxation rates between the two components demands a factor of two for a satisfactory resolution probability.

A system specific component systematically added to the signal in one direction has been found, resulting in biexponential relaxation from monoexponential signal-input.

MP31.10

Development of a proton NMR imaging system based on industrial standard VME-bus for Bio-Medical and Bio-technical applications, L. Malmgren, B.R.R. Persson, B. Blad, T. Pola, M. Frank, Lund University, Dept of Radiation Physics, S-221 85 LUND, Sweden.

The aim of the present project is to develop a semiportable general NMR imaging research system for both *in vitro* measurements and *in vivo* imaging. This system will fill the great need for low-field NMR-equipment to be used for measurements of tissue samples and imaging of experimental animals in parallel with the use of costly high-field clinical NMR-systems. Thus a proton NMR imaging system for experimental research have been developed based on a broad band spectrometer, two high resolution (16 bit) ADC's, and a four channel programmable gradient generator all compatible to a VME-bus. We have an air-winded whole body Oxford magnet shimmed at 0.07 tesla (possible to rise 0.15 tesla) which is specially dedicated to research and technological development. The NMR imaging system is built as a stand alone system which can be used with various types of magnets. The very flexible gradient controller and pulse programmer will select all desired pulse sequences required for different applications.

MP31.12

A Coil Desensitizing Technique to Suppress Respiratory Artifacts in MR Imaging of the Spine, A. V. Lakshminarayanan*, Dept. of Radiology, University of Alabama at Birmingham, 619 19th Street South, Birmingham, AL 35233

Motion of the abdomen (in particular, the subcutaneous fat) introduces artifacts in 2DFT MR imaging which seriously interferes with the diagnostic utility and quality of lumbar spine examinations. Flat (License Plate) surface coils tend to reduce these artifacts in spine images but result in non-uniform signal brightness in the PA direction. Described is a receive-only "surface coil" based on the well-known Helmholtz type of design. The geometry of the coil is such that its response is uniform. In addition a mechanism has been added to desensitize the imaging system to signals from moving structures both during RF transmission and reception. Images are presented that demonstrate a high degree of uniformity and the suppression of motion artifacts. Also presented are images that demonstrate that the same techniques can be used to eliminate fold-over artifacts.

MP31.11

A Complex Phantom for a Fast and Complete Image Quality Evaluation in MRI B. Aubert* N. Aubert and F. Aubry, Institut Gustave-Roussy, 94805 Villejuif Cedex, France.

In order to perform a fast, easy but complete image quality evaluation in MRI, a complex phantom has been designed. It consists of a perspex cylinder (20 cm diameter, 30 cm length) containing five identical modules surrounded by a copper sulfate solution. Three of these modules are located at the isocenter of the phantom in order to study the axial, coronal and sagittal planes, the two others at a distance of ± 11 cm (away from the isocenter) to study the multi-slice mode in the axial direction. Moreover, oblique planes crossing the cylinder axis can also be analysed. Each module allows to evaluate fourteen parameters including uniformity parameters, slice parameters, spatial resolution, geometric distortion, T_1 and T_2 measurement, ghosting, ... This phantom is very useful for daily quality control (10 minutes acquisition time) or for a more complete quantitative analysis after preventive or curative maintenance, or modification of the machine. It has been used with various MR imaging machines. A special software giving an automatic image analysis has been developed on a Signa System⁽¹⁾ (General Electric).

(1) CIERM - Hôpital de Bicêtre - 94270 le Kremlin -Bicêtre, France.

MP31.13

QA/QC Phantom for NMR Imagers. MS Rosenthal*, University of Pittsburgh, Pittsburgh, PA, 15261, USA

We have developed a QA/QC phantom for NMR imagers. This phantom, constructed out of acrylic, provides the ability to measure slice thickness, slice spacing, SNR, CNR, linearity, and intrinsic sensitivity. The phantom consists of a cylindrical tube with two inserts. The first one is another smaller cylindrical tube with an acrylic rod at an angle for slice measurement. The second insert consists of a 'plus' sign arrangement of acrylic with holes for 13 tubes containing H₂O and D₂O. For each tube the concentration of water varies from approximately 1 mmol/mL to 55 mmol/mL. The rest of the phantom is filled with a copper sulfate solution and propanol which is used to inhibit growth in the solution. We have used this phantom to test an NMR system as well as compare the characteristics of different pulse sequences. This phantom provides an easy method to test the intrinsic sensitivity of the NMR system which will indicate changes in machine function.

MP31.14

NMR Local Imaging by the Fresnel Transform Technique using a Nonlinear Field Gradient, Y. Yamada*, S. Ito, K. Tanaka and Z. Abe, Utsunomiya Univ., Utsunomiya 320, Japan.

NMR Fresnel transform imaging technique proposed by authors uses a nonlinear field gradient with a quadratic field intensity profile. The center position of the nonlinear field gradient, where the differential gradient is zero, is moved at a fixed amount in each successive imaging pulse sequence to produce nonlinear phase encoding in that moving direction. A spin density image is reconstructed from collected signals by the computer processing. The imaging region in this technique is limited to the moving range of the nonlinear field gradient. When suitable conditions are selected, the aliasing artifact is not produced in the reconstructed image. The conditions for producing local image with no artifacts are discussed and experimental results are presented. Unlike the case of conventional Fourier transform technique, no selective excitation procedure or no use of surface coil is needed to obtain a local image. A spatial resolution better than 1 mm can be easily obtained. Moreover, the imaging time in this technique is comparable to that of the conventional Fourier transform technique.

MP31.16

141 Cases of Brain SPECT Imaging with $^{99m}\text{Tc}-(\text{d,l})\text{HM-PAO}$ and Quantitative Analysis, Yuan Aina and Zhao Huiyang*, Zhong Shan Hospital, Shanghai Medical University, Shanghai, China.

This paper describes a recent study of 141 cases with SPECT of the brain using $^{99m}\text{Tc}-(\text{d,l})\text{HM-PAO}$. Among 141 cases, 93 cases were examined by CT and 6 confirmed by surgical operation. The method used in this study allows the proper and quantitative diagnosis of the region and the degree of regional ischemic. Comparisons with CT were performed. Results show that for stroke and tumor, the ischemic regions obtained are consistent with those obtained using CT, while the method used is much better than CT for the diagnosis of transient ischemic attack, migraine, epilepsy, dementia and slight trauma. In addition, this method is used to indicate the degree of these brain diseases and it can also be used to detect the location of the epilepsy focus, to predict the stroke and to measure the blood flow of tumor.

MP31.15

Reconstruction of intracranial vascular system using 3-planes magnetic resonance tomograms, Naoki Suzuki^{1*}, Kouji Simizu², Tetsuo Oamura¹ ME Research Unit Jikei Univ. School of Med.¹ Shimazu K.K.²

It is very difficult to reconstruct the three dimensional (3D) image of intracranial vascular system with only a set of transverse CT image of the cranium. Because the intracranial vascular system shows frequently circling and meandering. We tried to reconstruct the 3D image of whole intracranial vascular system using 3-planes tomograms. The CT examination was performed by a super conductive MRI scanner (SNT-50, Shimadzu) and transverse, sagittal and coronal images are utilized as 3-planes tomograms. Only transverse sectioned vascular images in each tomogram are picked up and processed for the 3D image. Vertically running vessels along Z axis are reconstructed by a set of transverse tomograms. In the same way, vessels running along X and Y axis are reconstructed by a set of sagittal and coronal tomograms, respectively. These three images are combined in 3D coordinates to a whole vascular system in the cranium including carotid arteries and jugular veins. Anterior, middle and posterior cerebral arteries and basilar artery were also able to display on the 3D image. In this method, it was possible to display not only arteries but also veins such as superior sagittal, transverse and sigmoid sinus in one image.

MP31.17

Quality Control Studies in Estimation of Lesion Size in SPECT, M.M. Rehani* Department of Medical Physics and Bio-Engg., Sher-I-Kashmir Institute of Medical Sciences, Srinagar-190011, INDIA.

The accurate estimation of lesion size in SPECT requires stringent quality control work up and evaluation. Besides flood acquisition and off-set correction, a number of parameters like matrix size, count rate, choice of filter, attenuation etc. affect the results. For our study we used ZLC 3700 gamma camera with Array Processor and Data Spectrum Phantom with six plexiglass cold spheres of dia 31.8, 25.4, 19.1, 15.9, 12.7 and 9.5 mm. Tc-^{99m} activity in injection vial was used for simulating a hot source in cold surrounding. The number of pixels along the diameter and voxel estimation in different silices was resorted to for estimating the size. The results show that, for the count rates normally encountered in clinical practice, the choice of 64x64 matrix, use of Shepp-Logan-hanning reconstruction filter, appropriate off-set correction and attenuation correction result in estimation of lesion size within $\pm 7.5\%$ between 16 mm to 32mm. This study has great utility in quantitative imaging.

MP31.18

ASSESSMENT OF MYOCARDIAL SPECT RECONSTRUCTIONS USING A HEART PHANTOM UNDER CLINICAL CONDITIONSC.C. Robilotta^{*1}, M.F.S. Rebelo^{§1}, R. Abe²

1-Instituto de Física, Universidade de São Paulo
 2-Instituto do Coração, Hospital das Clínicas
 São Paulo, S.P., Brasil

In order to assess the effects of 360° and 180° samplings and those from 3 different reconstruction methods, cardiac phantom studies had been developed. The plastic heart phantom, containing 2 small infarcted regions, is placed in an elliptical phantom, simulating the human chest. Both 360° and 180° data had been collected with the whole phantom, with and without scatter medium, positioned under typical clinical conditions, using a single-head rotating camera. A second positioning with the heart centralized along the rotation axis has also been used.

Backprojection reconstructions using the ramp, Hann and Parzen filters had been applied to produce the tomographic images. Visual inspections, contrast-ratios and count profiles analyses had been carried out and provide means for evaluating the 2 controversial sampling modes as well as to identify the scatter/attenuation effects and the reconstruction artifacts.

§ Financial supports from FAPESP and FINEP.

MP31.20

Evaluation of Parallel Hole Collimators Used for SPECT Imaging. E.A. Silverstein* and S.M. Spies, Northwestern Memorial Hospital, Chicago, Illinois.

Consistency of septal angulation of a parallel hole collimator is more important for SPECT than for planar imaging. In this work two types of measurements, one local and one global, are developed for evaluating this consistency. The local measurement involves placing a point source of radioactivity (Tc-99m) about 15 cm from the collimator under test. A gamma camera faces the other side of the collimator at a distance of 50 cm. The source is fixed with respect to the camera. Thus, the same portion of the camera field is used for all measurements. Suitable setups permit the collimator to be moved sideways, or the camera-source system can be moved. Variations in septal angulation cause the image of the point source to move. The long 50 cm lever arm amplifies the angular variations. A precision of 0.5 mm in measuring the image position gives a sensitivity of 1 milliradian, with greater sensitivity realizable. The variation in septal angulation can thus be assessed. The global measurement uses images of point sources placed at a large distance from the camera-collimator system being tested. Visual and computer analysis of these large point source images reveal defects in septal angulation not apparent in the flood performed with a sheet source.

MP31.19

Synthesis of Stereo Pairs From Reconstructed SPECT Data for 3-D Viewing, E.A. Silverstein*, S.M. Spies, A.M. Zimmer and W.G. Spies. Northwestern Memorial Hospital, Chicago, Illinois.

In this work, an attempt is made to utilize the human stereopsis capability to obtain a more effective presentation of SPECT data. Planar parallel projected views were synthesized from 64x64 reconstructed SPECT data and viewed as stereo pairs. Rather than displaying opaque surface contours, our displays have the form of a translucent image. We believe that this style makes better use of the available data, since the whole data set is always in view. Viewing was done by various means: Pairs were shown side by side on a CRT or 8x10 film and fused with a stereo viewer. Alternating blue left and red right images in the same location on the CRT were viewed with blue left and red right eye filters. A commercial liquid crystal polarizing display was also tried. The kinds of images viewed included Tc-99m PYP cardiac images, Tl-201 myocardial images, Tc-99m PYP bone images, and labeled monoclonal antibody images with both I-131 and In-111. Far less smoothing than usual was needed to make the images acceptable. Synthesized single views suggest the possibility of eliminating planar imaging in some situations. Projected enhancements include the use of motion by panning, tilting and rotation, the use of real perspective, and increase of resolution to 128x128.

MP31.21

The Effect of Different Flood Field Correction Methods on SPECT Images. A van Aswegen, PH Pretorius, CP Herbst, MG Lötter and PC Minnaar, University of the Orange Free State, Bloemfontein, South Africa.

Effective quality control is of utmost importance in performing reliable single photon emission computed tomography (SPECT) studies. SPECT images have to be corrected for flood field (FF) non-uniformities prior to reconstruction in order to eliminate ring artifacts. Three types of FF images were evaluated i.e. (i) a Tc-99m filled sheet source (TSS), (ii) a Co-57 sheet source (CSS) (both acquired with a low energy high resolution collimator) and (iii) a Tc-99m point source (TPS) imaged without collimation. Integral uniformity (IU) measurements were done on all FF. The effect of the FF on tomographic resolution and uniformity was evaluated. IU of TPS was superior to CSS and TSS for central field of view. No significant difference could be found for either resolution or tomographic uniformity for the different FF. TPS is therefore recommended for non-uniformity correction provided collimators used for SPECT acquisition are intact.

MP31.22

A Comparison of Radiation Dose from External Sources of Gd-153 and Eu-155,
G.D. Frey*, C. Starr, C. Lam and
K.M. Spicer, Medical University of
South Carolina, 171 Ashley Avenue,
Charleston, South Carolina 29425.

When single photon emission computed tomography (SPECT) is done simultaneously with transmission computed tomography (TCT) done with a radionuclide source; the TCT data is used to produce attenuation measurements and scatter corrections used to improve the fidelity of the SPECT images. This study calculated the radiation doses from transmission sources of Gd-153 and Eu-155. Doses were calculated for slabs of tissue from 5 cm to 20 cm thick. The results are presented in the form of curves that show the average dose to the tissue per primary transmitted photon. This data can be used to select appropriate nuclide sources for TCT.

MP31.24

SPECT Imaging by Using a Multislice Fan Beam Collimator, Y. Akiyama*
S. Sakata and N. Yui, Chiba Cancer
Center Hospital, 666-2, Nitona-cho,
Chiba-shi 280, Japan.

A multislice fan beam type casting collimator for SPECT was introduced in our institute. (hole size: 1.8mm, septum: 0.3cm, hole length: 40mm, energy: 160KeV, focus: 750mm, F.O.V.: 350mm). An interpolation method developed for a fan beam type X-ray CT was modified and utilized to reconstruct the SPECT images. This algorithm was confirmed by means of computer simulation. Primary photopeak data were obtained using a 20% energy window centered at 140KeV for Tc-99m and 159KeV for I-123. Beforehand we studied various problems concerning the fan beam collimator by computer simulation method and by the use of a DIV/CON collimator, whose converging side produces similar data to a fan beam collimator. We compared the fan beam collimator and a low energy high resolution parallel hole collimator. Concerning the resolution and sensitivity the fan beam collimator is superior to the parallel hole collimator. This was confirmed by various phantom studies and clinical examinations.

The authors thank F. Kinoshita for expert technical assistance. This work was supported in part by a Grant-in-Aid for Cancer Research (60-39) from the Ministry of Health and Welfare, Japan.

MP31.23

A Quantitative Theory for the Measurement of Cerebral Blood Flow with ^{99m}Tc -HMPAO and SPECT
T.Y. Lee* and I.W.T. Yeung, Radiology, St. Joseph's Hospital and Medical Biophysics,
University of Western Ontario, London,
Ontario, Canada N6A 4V2

The radiopharmaceutical, ^{99m}Tc -HMPAO, has been developed with the expectation that it can be used to measure cerebral blood flow (CBF) with SPECT. However, because of its limited extraction efficiency (EE) and unstable binding to the brain parenchyma, the quantification of CBF with it has proved difficult using simple models. We have developed a theory in which the transport, transcappillary exchange and reversible binding of ^{99m}Tc -HMPAO are modelled. It is shown that the total tissue concentration of the material, A_t , is related to the arterial concentration, CBF and EE. A_t can be measured in-vivo noninvasively with SPECT, and the arterial concentration of the lipophilic form of HMPAO is measured by octanol extraction such that CBF can be estimated by non-linear curve fitting using the operating equation of our proposed model.

MP31.25

QUALITY CONTROL OF SPECT SYSTEMS : EFFECTS FROM SOME BASIC MISADJUSTMENTS

C.C. Robilotta*¹, M.A. Oliveira^{§1}, M.F.S. Rebelo^{§1},
R. Abe². 1-Instituto de Física, Universidade de São Paulo, 2-Instituto do Coração, Hospital das Clínicas, São Paulo, S.P., Brasil.

It is widely known that quality control of equipment conditions, data acquisition and reconstruction methods are extremely critical in order to produce reliable SPECT images. Effects due to: a) detector gantry misalignment, b) unsatisfactory detector tuning, c) wrong computer centre of rotation, d) inhomogeneity of collimator septa/holes and others are often mentioned but seldom shown in the literature.

Point- and line-sources, cold- and hot-rods phantoms studies had been developed for a wide field of view rotating camera coupled to a low energy high resolution collimator. Reconstructions were accomplished using ramp, Hann and Parzen filters. The aim of this contribution is to show the effects due to the factors a), c), d) as well as source-detector distance, scatter medium and counting statistics on the sinograms and the reconstructed images.

§ Financial supports from FAPESP and FINEP.

MP31.26

Analysis of reconstruction filters on tomographic noise in SPECT imaging, R. Moretti, A. De Agostini, S. Belletti*
L. Mascaro, Health Physics Dept., Spedali Civili, 25100 - Brescia, Italy

Noise level of a reconstructed image modifies lesion detection capabilities of a tomographic system. Selection of the appropriated back-projection filter function is of greatest importance in optimizing image characteristics.

We have analyzed the influence of various window functions (Bt, Hm, Pz, Wn, Mz) on the noise level of images obtained with a rotating SPECT gamma-camera system.

Computer simulation of cold lesions (diameters ranging from 10 mm to 35 mm) embedded in a uniform background activity with a Gaussian noise function distribution was compared with theoretical and experimental data.

Analysis covered useful matrix size, angular step and was extended to low, medium and high image count densities.

Results were used for obtaining practical indications to clinical implementation of automatic filter selection.

MP31.28

SPECT Reconstruction of Symmetric Radioisotope Distributions From a Very Limited Number of Views. T. Lowinger*, D.S. Marsden, Department of Radiology, St. Luke's/Roosevelt Hospital Center, New York, N.Y. 10025

Objects with symmetry properties may be reconstructed in a tomographic study from a limited number of views. We studied a number of reconstruction algorithms that have previously been developed for astronomy and electron microscopy and used them to reconstruct 3-dimensional isotope distributions from a single projection. An algorithm invented by astronomers to determine mass distribution in globular clusters has been applied to tumors. Often a tumor will exhibit radial symmetry in its uptake of isotope thus, 3-D isotope distribution may be calculated from a single view. In bone scanning, cylindrical symmetry is exhibited by parts of the humerus and other bones. Such structures can be reconstructed from a single planar view. We have obtained tomographic reconstructions from a single view and from 2, 3, 4 views of phantom and patient data. The 3-D isotope distributions obtained compared well with theoretical predictions and actual SPECT studies. This method of tomography is available for any scintillation camera interfaced with a computer.

MP31.27

Effects of collimators design on image characteristics in tomographic gamma-camera system, A. De Agostini, R. Moretti, S. Belletti*, L. Mascaro, Health Physics Dept., Spedali Civili, 25100 - Brescia, Italy.

Selection of corrected collimator system for qualitative and quantitative gamma-camera SPECT imaging is of the utmost importance in optimizing Nuclear Medicine tomographic procedures. Collimator design (number, diameters and length of holes) modifies the physical parameters of reconstructed images, such as spatial resolution, contrast, noise level, lesion detection and so on.

Three types of parallel holes low and medium energy collimators were used for quantifying image parameters.

Results show the importance of collimator choice in modifying image physical characteristics, and were used for optimizing acquisition parameters of clinical emission tomography.

MP31.29

Image Properties of Digitized Radiographs, Y.Kodera*, M.Ogawa, M.Fujita and T.Wada, Hiroshima University, 1-2-3 Kasumi, Minami-ku, Hiroshima, Japan

A digital image processing system for a medical x-ray image was developed. The system is made up of a minicomputer, a high resolution laser scanner and a laser printer. A digital image was obtained from a film radiograph by the laser scanner. The pixel size was variable from 56.6 to 198.1 μm with a pitch of 28.3 μm and the density resolution was 10 bit. An output image of the laser printer was produced with a pixel size of 85 μm at a 8 bit density level.

As sigmoidal relationship was found between input and output densities, linear transformation was then made by use of a look-up table. Resolution of this system was mainly determined by the pixel sizes of the laser scanner and depended on the scanning directions. In a digitized image of screen film systems the radiographic mottle was reduced in high spatial frequency range, but a little increase in low frequency range. Some clinical radiographs were processed and would be presented.

MP31.30

Quantitative Uniformity Analysis in Radiological Image Intensifier-TV Systems Using a Digital Image Processor. P. Cooney, K.P. Maher and J F Malone, F.D.V.H., Meath Hospital, Dublin 8.

Uniformity is a well defined term used to describe the response of gamma cameras to a "uniform" radiation input. It is not routinely included in the performance specification of x-ray image intensifier-TV (XII-TV) systems, where it can influence such applications as vascular, cardiac and quantitative digital studies. Its specification poses a number of problems such as the absence of any agreed measurement methods and tolerances, and the compound effect of the individual component uniformities.

A quantitative study of XII-TV system uniformity was performed, based on a refined version of the NEMA Definition for gamma cameras, with the use of a real-time digital image processor (Quantel, I-100). Uniformities of $\pm 50\%$ and higher, were observed. The influence of image noise and matrix size has been investigated. Measurements and definitions were also developed for the individual system component uniformities and applied to a number of systems in routine hospital use. A considerable variation between systems was evident. A detailed analysis of the results will be presented.

MP31.32

The Use of Rare Earth Filtration in Digitally Enhanced High Milleamperage Fluoroscopy, G.D. Frey*, R.A. Miller and R.C. Holgate, Medical University of South Carolina, 171 Ashley Avenue, Charleston, South Carolina 29425.

The use of high ma digitally enhanced fluoroscopy has made it possible to do operative angiography with mobile C-arm devices. However the conventional aluminum filtration (1 mm AL) is used the skin entrance exposures can be very high. Exposures greater than 30 R/min occur at 120 kV and 20 mA. The use of a rare earth filter(*) reduces the skin entrance exposure by a factor of a 2 at 120 kV and a factor of 4 at 60 kV. However image quality deteriorates if the rare earth filter is used without adjusting the kV to lower values. If the kV is reduced image quality is maintained. This study determined the appropriate kV's to use with the rare earth filter. Image quality studies with phantoms and patient studies show that substantial exposure reductions are possible without loss of image quality.

*R-filter RSP Inc., San Carlos, CA

MP31.31

Computerized Analysis of the Heart in Digital Chest Radiographs. N. Nakamori*, K. Doi, V. Sabeti, H.-P. Chan, S. Katsuragawa, H. MacMahon. Kurt Rossmann Lab. for Rad. Image Res., Univ. of Chicago, Chicago, IL 60637

Some of the most useful diagnostic information in chest radiographs is related to the size and shape of the heart. We are developing an automated method to determine the contour of the projected cardiac image in PA chest radiographs and to obtain a number of measures related to the size and shape of the heart including the long and transverse dimensions, the projected heart area and the cardiothoracic ratio. In order to obtain "gold standards", four radiologists traced their best estimates of the entire contour of the heart on 12 radiographs, including the largely invisible inferior margin. These contours expressed in terms of radial distances from the center of the heart were analyzed by using Fourier analysis. Results of Fourier coefficients were used as a guide to obtain an approximate pattern of the heart image by fitting a shift-variant sinusoidal function to detected edges of the heart. The heart and diaphragm boundaries were determined from the detected edges in horizontal and vertical profiles, respectively. We found that the contours of heart images obtained with our automated method agreed well with those obtained by radiologists. We shall present preliminary results on clinical usefulness of our method.

Supported by USPHS Grants CA24806, HL36238, and The Whitaker Foundation.

MP31.33

Image Formats: Five Years After the AAPM Standard Format for Digital Image Interchange, G.Q. Maguire Jr.* and M.E. Noz+, Department of Computer Science, Columbia University, New York, NY 10027 *Department of Radiology, New York University, New York, NY 10016

The publication of AAPM Report No. 10 was the first attempt to standardize image formats in the medical imaging community. Since then, two other groups have formed (CART - the Scandinavian collaboration for Computer Assisted Radiation Therapy treatment planning, and ACR-NEMA, a collaboration whose purpose is to formulate a standard digital interface to medical imaging equipment). The AAPM format uses key-value pairs in plain text to keep track of all information associated with a particular image. The radiation oncology community in the U.S. has been defining key-value pairs for use with CT, nuclear medicine and NMRI images. Additionally, both ACR-NEMA and CART have been defining fields for use with the same types of images. The time has come to unify the naming of these fields. The CART collaboration has introduced a data base which is available electronically, but is maintained by a group of individuals. ACR-NEMA operates through committee meetings. To insure a consistent set of field names in such a rapidly developing arena requires the use of a server rather than a committee. Via a server a person would inquire if a particular field had been defined. If so, the defined name would be returned. If not, the person would be given the opportunity to define the field. The next inquiry would return the previously defined field. A number of computerized services already operate in this manner. As new modalities are added to the imaging repertoire, it would be easier and faster to ensure the consistency and adequacy of the data base; e.g., in the present version of its standard, the ACR-NEMA fields are adequate for CT but there are almost no fields suitable for describing the parameters associated with nuclear medicine and NMRI images.

MP31.34

A CCD Photoreceptor System for Measurement of Image Quality Descriptors, F.J. McCraw*, J.A. Bencomo, and L.M. Marsh, University of Texas System Cancer Center, 1515 Holcombe Blvd, Houston, TX. 77030

A 256 pixel CCD line detector designed for optical character recognition has been adapted for capture of its video output signal. This signal was conditioned and synchronized for digitization by an IBM Data Acquisition and Control Adaptor in an IBM XT computer. A lens and mirror system is used to both focus an image on the receptor and to remove the sensitive CCD device from the direct x-ray beam. Software has been developed to provide for acquisition control, storage and processing of the data. An initial evaluation of the device sensitivity, dynamic range and accuracy has been performed. It is expected that this device can be used to facilitate measurement of image quality descriptors necessary to optimize clinical image techniques.

MP31.36

Image PC-Study of the architecture of a workstation for image processing in a medical environment E.M. Staderini and G.E. Gigante*, Centro Ingegneria Biomedica dell'Universita' di Roma, Corso Vittorio E. 244 00178 ROMA

The personal processing of images is going to be a primary need in such fields of medical research in which images are a medium to get transfer and deliver diagnostic knowledge. The architecture of an image processing system is now well established, consisting of an image capturing block, a processing unit and an output display. The availability of fast arithmetic processors allowed us to develop a versatile system with an hardware convolver capable of doing convolutions with programmable size and shape kernels. The system is completed with high capacity storage units (hard disk, optical disk) configuring a complete personal workstation. The system is controlled by an IBM-PC and uses a high resolution CCD camera to acquire images. The first results obtained with such system, regarding its performances and limitations, are discussed. The workstation is going to be used in a digital radiographic system whose preliminary results are shown.

MP31.35

Performance of Antiscatter Grid in Digital Radiography: Effect on Signal-to-Noise Ratio. H.-P. Chan*, K. L. Lam, Y. Wu, H. Fujita, K. Doi, Kurt Rossmann Lab. for Radiologic Image Research, Dept. of Radiology, Univ. of Chicago, Chicago, IL 60637

We have studied the effect of antiscatter grid on the signal-to-noise ratio (SNR) of low-contrast, quantum-noise-limited objects in digital radiography. In a theoretical analysis of the SNR, we found that the effectiveness of a grid is determined by a performance index, which is proportional to the contrast improvement factor and inversely proportional to the square root of the Bucky factor of the grid. Results of Monte Carlo simulation studies and experimental measurements with an I.I.-TV digital system indicate that, for a given patient exposure, the improvement in SNR achieved by the use of a conventional grid is limited. The reduction of scattered radiation, however, reduces the relative effect of system noise on the SNR of a low-contrast object, thereby extending the useful dynamic range of the imaging system.

Supported by USPHS Grant (NIRA) HL36238, The Whitaker Foundation, and USPHS Grant CA 24806.

MP31.37

Use of the effective dose equivalent, H_E , in PET studies. W. Huda* and G.A. Sandison, Manitoba Cancer Foundation, 100 Olivia Street, Winnipeg, Canada, R3E 0V9.

The effective dose equivalent, H_E , can be used as standard radiation dose parameter in all imaging modalities which utilize ionizing radiations including Positron Emission Tomography (PET). A simplified method for evaluating H_E values for the positron emitters ^{11}C , ^{13}N , ^{15}O and ^{18}F is presented. H_E values for a range of PET studies have been computed based on biodistribution data available in the scientific literature. Low dose PET studies include a bolus administration of 28 mCi ^{15}O ($H_E = 100$ mrem) and 2 mCi ^{18}F L dopa ($H_E = 130$ mrem). High dose PET studies include 20 mCi ^{11}C DMO ($H_E = 560$ mrem) and a 1 hour (steady state) inhalation of a total 250 mCi ^{15}O ($H_E = 890$ mrem). The mean H_E value of 13 diverse PET studies was computed to be 390 mrem.

139

MP32.1

Radiotherapy Dosimetry Intercomparison in the U.K.
D.I. Thwaites* and J.R. Williams†, * Medical
Physics, Western General Hospital, Edinburgh,
Scotland; † Medical Physics, Belvidere Hospital
Glasgow, Scotland.

The IPSM (HPA) Radiotherapy Topic Group has initiated a study, involving all UK radiotherapy centres, aiming to establish the degree of variation between measured and stated dose for all MV photon beams under reference conditions and to compare measured doses in three-field treatments to those calculated by the local planning procedures. A phantom has been designed and constructed, having relatively simple geometry, but enabling a range of factors to be tested. Doses measured in this, using an ionisation chamber, are compared to those stated or calculated from clinical data in each centre. About half the centres have now been included.

A preliminary analysis of the earlier results shows a mean discrepancy under reference conditions of 0.1% (standard deviation 1.7%, maximum discrepancy 4%). Consistency with field size variation was generally within 1% and always within 2%. For planned three-field dose distributions, the average dose ratio (measured to calculated) was 1.020 with no inhomogeneity present (s.d. 1.2%, range 1.007 to 1.033). With a lung-equivalent insert present, these results changed only marginally.

An extended updated analysis is presented. As sufficient data is obtained analysis will consider the effect of different variables, such as beam energy, treatment planning system factors, etc.

Sponsors of the project include NE Technology, Negretti Aviation, IGE Medical Systems.

MP32.3

ESTIMATION OF OUTPUT OF 12 MeV LINEAR
ACCELERATOR (MEVATRON-74) FROM G1T-PUT
FACTORS, Surinder K. Kaul‡, Wajahat H.
Andrabi, Rakesh K. Kaul

Department of Medical Physics and
Bio-engineering, S.K. Institute of Med.
Sciences, Soura, Srinagar, Kashmir-India.

A simple empirical method has been suggested for the output measurements of the arbitrary fields from known output factors for 10 MV Photons from Mevatron-74 Linear Accelerator
OF (X,Y)=OF (X,10) OF (10,Y) - (1)
OF (X,Y)=OF (X,10) OF (10,Y) and (2)
for rectangular and square fields respectively. Where 'OF' stands for output factor and 'X,Y' denote the field axis. The results obtained have been compared with experimental measurements of 10 MV photons. The percentage variation in individual cases is less than 1%. It has been noticed that the output of fields $X \times Y \neq Y \times X$. A possible explanation for this discrepancy has been given.

MP32.2

Comparison of protocols for photon dosimetry,
B.J. Mijnheer*, The Netherlands Cancer Institute,
Amsterdam, The Netherlands, F.W. Wittkämper and
A.H.L. Aalbers, National Institute of Public
Health and Environmental Hygiene, Bilthoven, The
Netherlands, and L.M. Chin, Harvard Medical School,
Boston, USA

Recently a number of national and international organizations revised their protocols for megavoltage x-ray and γ -ray beam dosimetry, to incorporate new concepts and refined data. The differences in recommendations in these reports with respect to type of reference instrument, calibration, measurement procedure and reference data for physical parameters, will be reviewed. Despite these differences, it will be shown that the agreement in absorbed dose determinations is very good. In addition, the values for absorbed dose derived according to one of these new protocols showed agreement within 1.0% with values obtained with a graphite calorimeter.

The absorbed dose to a medium irradiated by orthovoltage x-ray beams is usually determined according to the formalism recommended by the ICRU. Experiments using different types of ionization chambers and analysed according to the ICRU and a new formalism, will be described. Results will be compared with those obtained recently by other groups using different calibration or measurement procedures.

MP32.4

Dosimetry of the Photon Beam of
the CGR Orion 5MV Linear
Accelerator, C.W. Coffey*, R.E.
George†, B. Stokes, B. Berner
and M. Sanders, Radiation
Medicine Department, University
of Kentucky Medical Center,
Lexington, Kentucky, 40536.
†Radiation Oncology Department,
School of Medicine, Indiana
University, Indianapolis, IN,
46223.

Beam characteristics and dosimetry of the CGR Orion 5MV, 100-cm SAD isocentric, linear accelerator are presented. The relevant physics parameters of central axis depth dose, tissue-maximum ratios, surface dose, and relative field size correction factors are presented for two independent Orion 5MV accelerator installations. Additionally, the percentage depth dose data is compared with data from other commercial low-energy accelerator photon beams. Other clinical beam parameters investigated and reported include: field flatness, symmetry, isodose curves, and wedge attenuation. An assessment of dosimetry for the independent-jaw collimator assembly also is presented.

MP32.5

The Characteristics of Small X-ray Beams from Linear Accelerators, J-S Tsai*, GK Svensson and BE Bjarngard, Joint Center for Radiation Therapy, Harvard Medical School, Boston, MA 02115, U.S.A.

We use 6 MV X-ray beams of diameter ≥ 12.5 mm for stereotaxic intracranial irradiations. Smaller fields are of interest for treatment of AVMs and functional disorders. This study aims to characterize such beams ≤ 12.5 mm. Most measurements have been made with radiographic film. When the beam size is reduced, the dose at a given depth goes down and is about 50% at 2 mm of that at 8 mm diameter. The TMR is not affected, indicating that the dose/kerma ratio changes with beam size but not with depth. Geometric unsharpness dominates the penumbra. The influence of electron spread is limited to 2 mm laterally. Results with a beam-spot camera show that an accelerator with a 90° bent beam has a larger and more elongated beam-spot than one with a straight beam. In the latter machine, the source position was found to be more stable for different gantry angles. The isocentric accuracy of our straight-beam linear accelerator is better than ± 1 mm, as is the mechanical accuracy of the stereotaxic positioning aids. It is concluded that for 6 MV x-rays fields down to 8 mm diameter can be utilized. For smaller fields, penumbra effects gradually contribute to the spread of dose outside the target.

MP32.7

THE EFFECTS OF SECONDARY BLOCKING ON OUTPUT FACTORS FOR 4, 6 AND 24 MV PHOTON BEAMS. C. Reft, Michael Reese/University of Chicago Center for Radiation Therapy, Chicago, IL 60637

Most dose calculation systems account for the change in machine output as a function of rectangular collimator field sizes through the use of output factors. However, most treatment fields are irregularly shaped due to secondary blocks, intended to shield vital organs or normal tissue. In some clinical situations, such as extended mantle and half-field head and neck treatments, more than half of the area defined by the machine collimators may be blocked by secondary blocks. The effects of secondary blocking can be significant as shown by Meli¹ for a 6 MV photon beam. This work assesses the effects of secondary blocking as a function of collimator opening, SSD, blocked field area and arrangement for 4, 6, and 24 MV photon beams. A simple but accurate method is described for calculating output factors for blocked fields from a limited number of in-air and in-phantom dose measurements as a function of collimator setting. Comparisons of calculations with measurements for some typical patient treatment fields will be presented.

¹J. Meli, Med. Phys. 13:405, 1986.

MP32.6

Explanation for the Degree of Back Scattered Radiation from Collimator into Monitor Chamber, Hideo Kubo* and Pocheng Cheng, Department of Radiation Oncology, University of Rochester Cancer Center, 601 Elmwood Avenue, Rochester, New York 14642, Department of Radiation Oncology, Albany Medical College and VA Hospital, New Scotland Avenue, Albany, New York 12208

By simulating a flattening filter, beam monitor chamber and collimator jaws of a linear accelerator, we have measured the relative amount of back scattered radiation (BSR) from the collimator jaws into the monitor chamber. BSR was found to exist in photon beams of all three linear accelerators we studied, i.e., a Clinac-6, Clinac-20 and Therac-20. The Clinac-6 6MV photon beam showed little BSR dependence on collimator jaw opening. This was attributed to the presence of a fixed mirror in a beam path which absorbed most of the BSR. The Clinac-20 18 MV photon beam showed a smaller BSR dependence than the Therac-20 18 MV photon beam due primarily to 1) a larger chamber-to-collimator distance, and 2) a thick exit window on a monitor chamber. The Therac-20 18 MV photon beam showed the strongest BSR dependence on collimator opening due to 1) a small chamber-to-collimator distance, and 2) a thin exit window on a monitor chamber.

MP32.8

Dosimetric Evaluation of a D-shaped Field Used for Treating Retinoblastoma With 4MV X rays.

Shirish K. Jani*, Edward C. Pennington, and David H. Hussey, University of Iowa Hospitals & Clinics, Iowa City, Iowa

Retinoblastoma is a common intraocular childhood disease treatable with radiation. The most widely used treatment technique includes a small single D-shaped lateral field using megavoltage x rays. The aim is to treat the entire retinal surface and spare the lens. In spite of its widespread use, only a limited amount of dosimetric evaluation of this field is reported in the literature. Here, we report on the dosimetric aspects of a 2.5 cm x 2.5 cm D-shaped field with 4 MV x rays from a Varian Clinac 4/80. A 12.5 cm thick lead block was used to obtain sharp beam edges. Surface dose and buildup regions were measured with a parallel plate ionization chamber. The output, percent depth dose, beam flatness and the penumbra were obtained. Results showed that the beam output was approximately 7% higher than an equivalent open field. Dose to the temporal retina at a depth of 0.5 gm/cm² was 97% of the maximum dose requiring no added beam spoiler. It is concluded that special dosimetric evaluation of this D-shaped field is needed for clinical use.

MP32.9

Dosimetry of Photon Beams From A Philips SL25 Dual Energy Linear Accelerator, G. Mitev*, S. Rajaratnam, M.K. Islam, U.F. Rosenow, Albert Einstein College of Medicine and Montefiore Medical Center, Bronx, NY 10467

Characteristics of 6 MV and 25 MV photon beams from a Philips SL25 Linear Accelerator are described and compared to published data. Included are measurements of percentage depth dose, output factors, crossbeam profiles, and the resulting isodose distributions. Special attention is given to the following SL25 capabilities: Dose distributions for effective photon energies resulting from mixed 6 MV and 25 MV beams; effective wedge angles from 0° to 60°, generated with the motorized 60° wedge, by mixing wedged and open beams; off-centered fields as defined by the independently movable collimators. The feasibility of generating effective photon energies in between 6 and 25 MV with the SL25 mixed beam mode is investigated, and an example of matching a 15 MV photon beam from the Siemens Mevatron 20 is presented. The usefulness of a continuously variable versus a discrete set of effective wedge angles is discussed. Characteristics of asymmetric beams are demonstrated. The consequences of these special features for treatment planning are briefly outlined.

MP32.11

Dosimetric Measurements of Superficial X-ray Therapy Machine, F.J.Lin*, C.S.Chen, C.P.Tu, N.M.Tsang, Department of Radiation Oncology, Chang Gung Memorial Hospital, 199, Tung Hwa North Road, Taipei, Taiwan, R.O.C.

Superficial x-ray treatment facility has been used for many decades. It is still used in some hospitals for the treatment of localized superficial lesions such as skin cancer. Dose and relative dose measurements were made with cylindrical chamber and normalized at phantom surface in many institutes. The measurement results of relative dose for cylindrical chamber and parallel plate chamber varied about 30% at the surface but agree within 0.5% at 0.5 cm depth when data were normalized at 1 cm depth. The surface dose is dependent on the chamber wall thickness. Measurements of percentage depth dose were performed with parallel plate chamber in water and polystyrene. The difference of the values in water and polystyrene was about 10% from a depth of 1 cm to 3 cm for data normalized at 1 mm depth. We also studied the output, relative output factor, field flatness, uniformity index with calibration depth at 1 cm depth to minimize the uncertainty of surface dose.

MP32.10

Characteristics of photon beams from Philips SL-25, Jatinder R. Palta*, K. Ayyangar, Inder Daftari and N. Suntharalingam, Department of Radiation Therapy and Nuclear Medicine, Thomas Jefferson University Hospital, Philadelphia, PA 19107

Philips SL-25 is a multimodality linear accelerator with new type of beam transport system and independent collimator jaws. A comprehensive dosimetric study of 6MV and 25V x-ray beams produced by this machine are presented. This includes: (1) the beam flatness changes with depth, field size and energy, (2) surface and depth dose characteristics of individual beams (3) mixed beams of different fractions, (4) output factors for open and wedged fields, (5) isodose distributions for open and wedged fields, and (6) lead and cerrobend transmission for field shaping. The beam characteristics at off-axis points for open and wedged fields are also described to evaluate its impact on the asymmetrically placed fields.

MP32.12

Analysis of the penumbra components in high energy photon beams, M. Simonian and J.C. Rosenwald*, Institut Curie, 26, rue d'Ulm 75005 Paris, France.

At the edge of higher energy photon beams, several factors contribute to the penumbra:

- The finite size of the source (geometrical penumbra)
- The leakage through the collimator (transmission penumbra)
- The radiation scattered from the head
- The photons scattered from the medium
- The finite range of the secondary electrons spread out laterally.

These components are analysed using on one hand a theoretical approach based on the 3D superposition of point-spread functions, and on the other hand experimental results obtained in conditions where it is possible to quantify each of these components.

It is shown how the penumbra slope and shape are modified as a function of the energy, field size and depth for each component.

We thank R. Mackie for providing us with software and data used for theoretical calculations.

MP32.13

DOSE PERTURBATIONS AT HIGH ATOMIC NUMBER INTERFACES IN PARALLEL OPPOSED MEGAVOLTAGE PHOTON BEAM IRRADIATION, Indra J. Das*, Faiz M. Khan†, and Kenneth R. Kase, Dept. of Radiation Oncology, Univ. of Mass. Med. Center, Worcester, MA 01605, and †Dept. of Therapeutic Radiology, Univ. of Minnesota Hospital Minneapolis, MN 55455, USA.

Uniform dose distribution is required in a target volume for curative radiation therapy. The dose uniformity depends on photon energy, thickness of irradiating volume and presence of inhomogeneity. Dose perturbations in the vicinity of high Z interfaces cause dose non-uniformity due to the loss of electronic equilibrium. In a single photon beam, there is a dose enhancement on the backscattered side of the inhomogeneity for all photon energies, but on the transmission side dose enhancement occurs for the energies greater than 10 MV and a dose reduction occurs for the energies lower than 10 MV. For parallel opposed beam, the dose enhancement is always observed on either side of the inhomogeneity. Dose perturbation is seen up to the range of secondary electrons generated by the photon beams. Dose enhancement was studied for the commonly used inhomogeneities such as bone, steel (in the form of prosthesis), and lead, as a function of photon energy, thickness, width and depth of inhomogeneity, and radiation field size. These data will be valuable in predicting dose at high Z interfaces in parallel opposed beams used clinically.

MP32.15

Direct Measurement and Use of Tissue-air Ratios for Megavoltage Radiotherapy Beams, B. Thomadsen*, T.R. Mackie, S. Shahabi, B. Paliwal, University of Wisconsin, Madison, Wisconsin, United States of America.

Uncoupling the z-drive on a commercial scanning water phantom, fastening the z-position read-out to a float, and fixing an ionization chamber in the water tank, modifies the system to directly measure tissue-air ratios (TAR). As per Suntharalingam, Shalek, and Lanzl (1972), by calculating the dose in-air as the dose in-phantom divided by the TAR (as the ratio of readings, not doses), in use, inappropriate factors cancel. For high energy beams (e.g., 24 MV) graphite yields more compact build-up caps than lucite, but without the pair-production problems of aluminum.

The use of in-air measurements with a build-up cap to characterize the intensity of the radiation incident on the phantom simplifies the separation of collimator-dependent from patient-geometry-dependent variables, as compared to methods often used with tissue-phantom or tissue-maximum ratio systems.

Sample tables will be presented.

Suntharalingam, N., Shalek, R.J., Lanzl, L., AAPM Quarterly Bulletin, June 1972, 61-62

MP32.14

Comparison of Air Gap Buildup Factors for 18 MV, 6 MV, and Cobalt 60 Photons. D.L. Wilson, Dept. of Radiation Oncology, University of Louisville Brown Cancer Center, Louisville, KY 40292

A thin window ion chamber (Markus) placed inside a polystyrene phantom was used to measure dose buildup factors behind various air spaces for 18 MV, 6 MV, and Cobalt 60 photon beams. A large dose buildup effect is observed for smaller field sizes. This effect becomes more pronounced at the higher energies, and may have clinical significance when treating small fields with 18 MV photons. The dose buildup effect is of much less importance at larger field sizes. There is no significant reduction of dose behind air cavities when very large fields are used such as in whole body or hemibody treatments, even at 18 MV. When high energy photons are used for whole body treatment, superficial doses can be effectively increased by adding a thin plastic sheet well in front of the patient. Buildup data for various field sizes and air cavity dimensions are presented from measurements made on the Therac 20, Therac 6, and Theratron 780 therapy machines.

MP32.16

On the Necessity of Scatter-air Ratios, B. Thomadsen*, L. Asp**, T.R. Mackie, S. Shahabi, B. Paliwal, University of Wisconsin, Madison, Wisconsin, United States of America.

The usual practice for calculating dose rates in irregularly-shaped radiotherapeutic photon beams entails the summation of scatter-air ratio (SAR) contributions from partitioned sectors of the field (referred to as a Clarkson procedure) (1,2). This procedure yields an effective SAR which, when added to the tissue-air ratio (TAR) for a "zero area field" (TAR₀), gives the TAR for the point of calculation. Shrivastava (3) has pointed out the insensitivity of the resultant TAR to the accuracy of the TAR₀, because the SAR table comes from subtracting the same value of TAR₀ from TARs that is added again in the Clarkson procedure.

In fact, the Clarkson procedure requires neither the TAR₀ nor SAR, as shown below:

$$\begin{aligned} \text{TAR(irg)} &= \text{TAR}_0 + (1/n) \sum \text{SAR(radius)} \\ &= (1/n) \sum [\text{TAR}_0 + \text{SAR(radius)}] \\ &= (1/n) \sum \text{TAR(radius)} \end{aligned}$$

Thus, only the TAR values need be summated.

**Current affiliation Bowling Green Medical Center, Bowling Green, KY, USA.

1. Clarkson, J.R. Brit. J. Radiol. 14 (1941) 265.
2. Cunningham, J. Shrivastava, P. Wilkinson, J. Computer Programs in Biomedicine 2 (1972) 192.
3. Shrivastava, P., Summers, R., Samulski, T., Baird, L., Phys. Med. Biol. 24 (1979) 818.

MP32.17

Dosimetry Measurements in Presence of Dental Materials for Therapeutic Radiation Beams, Subhash C. Sharma*, Ph.D., Maritza O. Jenkins**, D.D.S., Niranjan Bhandare and Allan G. Farman**, Ph.D., Dept. of Radiation Oncology, School of Medicine and School of Dentistry, University of Louisville, Louisville, Kentucky 40292.

Metals (13 x 16 x 1.5 mm approximately) of Stern hard type II gold, medium type III gold, Amalgam, Tirconium, and Lead placed in a polystyrene phantom, forming a symmetric field of 5.0 x 5.0 cm were exposed to different therapeutic beams of radiation (Cobalt-60 photons, 6 MeV, 9 MeV, 13 MeV, 17 MeV, and 20 MeV electrons). A thin-window parallel plate small volume ionization chamber was used to measure transmission and backscatter radiation. As expected, the results showed dose enhancement at the entrance side of the metals. In addition, we will report results of using film and thermoluminescent dosimetry thin chips to measure dose distribution around the metals. We intend to use this experimental data to evaluate the computer algorithms used in the computerized treatment planning, specifically for head and neck cancer patients containing the dental restorative materials and treated with radiation beams.

MP32.19

Loss of Beam Edge Sharpness for High Energy Photons in Low Density Materials, Kenneth E. Ekstrand*, Bowman Gray School of Medicine, Winston-Salem, NC 27103 and Walter H. Barnes, Moses H. Cone Memorial Hospital, Greensboro, NC 27401.

The problem of central axis dose reduction for high energy photon beams traversing normal lung tissue is well known. An additional problem, which may be not as well appreciated, is the loss of electronic equilibrium on the periphery of high energy photon beams, resulting in an increase in the penumbra occurring in lung. We have compared profiles of x-ray beams ranging in energy from 4 MV to 18 MV. The profiles were measured at 10 cm depth in unit density and lung density (.26) phantoms. At the highest energy the 20% to 80% penumbra width was measured to be 7.5 mm in the unit density material, whereas in the lung phantom the width was 18 mm. At 4 MV the situation was reversed, that is, the penumbra was slightly smaller in the lung phantom.

Most radiation therapy treatment planning computer programs do not take into account this change in beam profile when calculating dose in the lung. This can result in an unanticipated underdosing when high energy x-rays are used. We recommend that lung treatments be carried out at x-ray energies of 6 MV or less.

MP32.18

Dose Perturbations Around Stainless Steel Implants, E.C. Scarbrough*, N.C. Ikoro, P.P. Antich, U.T Southwestern Medical Center at Dallas, Dept. of Radiology, 5323 Harry Hines Blvd., Dallas, TX 75235-9071

Interfaces are created in tissues and bones by implantable stainless steel trays used in the surgical management of oropharyngeal cancer; dose perturbations around such interfaces are measured with ultrathin (nominally 50 microns) TL dosimeters. The ultrathin dosimeters are of dimension and sensitivity appropriate for precise and accurate measurement of dose perturbations at these sites. Results are consistent with previous work on Cobalt-60 gamma beams. New data on 6 MV photon beams is presented. Implications for therapy and techniques to reduce the dose enhancement due to backscattered electrons are discussed.

MP32.20

Influence of Aluminum and Bone on Dose Distributions for Photon Beams

E.E. Klein*¹, R.K. Rice, B.J. Mijnheer, L.M. Chin, Joint Center for Radiation Therapy, Harvard Medical School, Boston, MA 02115

The influence of bone and aluminum simulating bone on dose distributions for 4 and 15 MV photon beams has been studied in detail. The data is being used to evaluate existing heterogeneity correction algorithms and to guide in the development of new ones. Various phantom geometries, including bilateral femur geometries were studied. Measurements were made with a thin window parallel-plate chamber, a small diode, and film. The vertical (both proximal and distal) and lateral interfaces were studied for various field sizes and bone sizes. Significant underdosing was observed for the 4 MV photons distal to the bone and aluminum. This is followed by a second buildup region. Overdoses were observed both proximal and lateral to both bone and aluminum of about 15%. The bone and aluminum have similar influences on photon dose distributions.

¹Present address: Cleveland Clinic Found. Cleveland, Ohio 44106

MP32.21

INFLUENCE OF HIP PROSTHESIS IN HIGH ENERGY PHOTON DOSE DISTRIBUTIONS

C.H. Sibata, J. Mastandrea, H.C. Mota* and P.D. Higgins. Cleveland Clinic Foundation. 9500 Euclid Ave, Cleveland, OH, 44106, USA.

Radiotherapy treatment of patients having hip prostheses are a common problem facing dosimetrists and physicists when a treatment plan is being done which requires irradiation of the pelvic area. Normally this problem is avoided by changing the 4-field "box" technique to one which does not irradiate the prosthesis. To quantify the perturbation of these devices, studies of attenuation and transmission were made on 6 and 18 MV photon beams using two different hip prosthesis compositions. These studies have shown that an attenuation of as much as 40 % can be found in a single beam profile under the prosthesis. In principle, the perturbation caused by these devices could be calculated and accounted for by using compensators. We have attempted to study the capability of a dose planning system to predict the attenuation and transmission of these devices as compared with measurements.

MP32.23

Radiation Dose Non-Uniformity Caused by Permanent Vascular-Access Injection Ports. F.R. Bayne*, H.W. Merrick, N. Samsami, R.R. Dobelbower, Jr. Medical College of Ohio, Toledo, Ohio.

Injection ports are frequently used to maintain permanent vascular access in patients with malignant disease. The injection ports allow blood sampling as well as infusion or injection of chemotherapeutic agents directly into the circulation. The access catheters are usually placed in the subclavian vein with the injection port being implanted in the infraclavicular area. These injection ports are entirely self-contained underneath the skin and may have been placed in an area which subsequently requires radiation treatment. A comprehensive study of the perturbation effects of the injection ports when placed in the path of the beam was carried out. All dose measurements were performed either in water or polystyrene using stainless steel and titanium injection ports manufactured by Davol. The radiation beams were 6 MV and 10 MV X-rays and 6, 9, 12, 15, and 18 MeV electrons. The data indicate that the presence of injection ports significantly alters the radiation dose and dose uniformity. For example, the dose underlying a stainless steel port is reduced by 47% when 18 MeV electrons are used. This paper presents the dosimetric data, discusses the clinical significance of the results, and provides recommendations for design modification of the ports.

MP32.22

Modification of the Dose in Radiation Fields Due to the Presence of a Mandibular Prosthetic Implant, K.P. Doppke, S. Sailer, Massachusetts General Hospital, Ms, USA*

Patients with head and neck cancers are often treated after major reconstructive surgery and they occasionally have had replacement of their mandible with a stainless steel prosthesis. This prosthesis is 8mm wide, 3mm thick and with holes spaced every 8mm center to center. The resulting modification of the dose distribution was evaluated for low and medium energy x-rays and 6, 9, and 12 MeV electron beams normally used in the treatment of these patients. Dosimetry measurements were performed using film to evaluate the dose distribution and a parallel plate chamber was used to study the local changes due to the backscattered radiation. The results demonstrate that the dose beyond the stainless steel is significantly modified in the electron fields, with a maximum increase in dose of 17% due to backscattered electrons. There are areas in depth where the dose increase was 24% higher than the open field for the 12 MeV beam and somewhat less for the lower energy beams. A dose reduction of greater than 50% is seen behind the stainless steel. The modification of dose in depth for the photon beams was less, but a dose increase of 26% was measured due to backscattered radiation in the cobalt-60 beam.

MP32.24

DOSE PERTURBATIONS ASSOCIATED WITH RETRACTED MISSING TISSUE COMPENSATORS, D. Robinson*, J.W. Scrimger, Department of Medical Physics, Cross Cancer Institute, Edmonton, Alberta, Canada

We have studied experimentally the degree to which retracted missing tissue compensators in the presence of irregular surfaces are able to restore the dose distribution obtained with a normally irradiated regular surface. Initial results were obtained for a flat slab geometry¹, and recent investigations have concentrated on conical geometries which are amenable to mathematical analysis. The experimental arrangement involves a hollow cone immersed in water, with the associated water deficiency compensated by a geometrically reduced retracted unit density cone. Results of measurements made in ⁶⁰Co, 6MV and 15MV photon beams will be presented, and the extent to which a simple analytical approach is able to explain the data will be discussed.

¹Megavoltage photon beam dose reduction with retracted tissue compensators. DM Robinson, JW Scrimger. Phys Med Biol 1987; Vol. 32, No. 8: 1031-1037.

MP32.25

Comparative Analysis of Dosimetry Protocols for Electron Beams - some Physical and Clinical Implications, D.I. Thwaites* and A.E. Nahum†, * Medical Physics, Western General Hospital, Edinburgh, Scotland; † Medical Physics, The Royal Marsden Hospital, Sutton, England.

Various national and international dosimetry protocols have appeared between 1980 and 87. Different approaches have been followed and different values used for various parameters, due to advancing knowledge during this period. Thus international consistency has been lost. National consistency is also reduced, as inevitably all centres do not adopt new recommendations uniformly at the same time.

The various electron protocols are compared to each other and to older recommendations and the inconsistencies discussed. The clinical implications of the changes in dose (up to ~5%) from older to more recent schemes are considered. In particular, the influence of using different phantom materials under older and recent protocols is detailed. The non-recognition of fluence ratios in pre-1980 protocols and their general recommendation of polystyrene or water as interchangeable phantoms has significant implications for consistency then, but also for the present situation on changing to newer protocols. Finally, an analysis of the revised HPA Code of electron dosimetry is presented. An expression is derived for C_e as used in that Code and this is evaluated for the NE 2571 cylindrical chamber, using the most recent physical data. ICRU 37 stopping powers are used consistently throughout. HPA C_e increase too slowly with depth at all energies, but there is good agreement with the present work at depths close to D_{max} .

MP32.27

Depth Dose Flattening of Low Energy (≈ 10 MeV) Electron Beams, H. Alasti*, D.M. Galbraith, Princess Margaret Hospital, Toronto, Ontario, Canada

Low energy electron beams commonly have large dose gradients on both sides of d_{max} , limiting the depth of tumor which can safely be contained within a $\pm 5\%$ dose specification. Clinically it is preferable to minimize the dose gradient while maintaining the sharp gradient beyond d_{max} . Several methods are described which satisfactorily flatten the depth dose in this manner for cone and trimmer collimated beams at small and large field sizes.

MP32.26

Dosimetry Of Open And Shaped Electron Beams From A Philips SL25 Accelerator, S. Rajaratnam*, G. Mitev, M.K. Islam, and U.F. Rosenow, Albert Einstein College of Medicine and Montefiore Medical Center, Bronx, NY 10467

Output factors, depth dose curves and isodose distributions for electron beams from a Philips SL25 will be presented. A systematic investigation was also carried out on the effect of using cutouts. Centrally and asymmetrically placed cutouts of differing field sizes, were used on each of the cones. Attempts were made to determine a functional relationship between output or dose distribution and cutout/cone combination. The possibility of using equivalent fields for electrons was also investigated. In addition, a strong dependence of virtual source position on beam energy, and collimator size was observed. The implications of these results for treatment planning will also be discussed.

MP32.28

The Distance Dependence of Electron Dose from a Varian Clinac 2500 Linear Accelerator, P.H. Huang* and R. Hagg, Division of Radiation Oncology, Scripps Clinic & Research Foundation, La Jolla, CA 92037, U.S.A.

Dose variation with distance was measured at d_{max} in a polystyrene phantom with a parallel-plate ion chamber furnished with appropriate buildup for six electron energies of 6-22 MeV from a Varian Clinac 2500 linear accelerator. Relative dose normalized to 100 cm source (assumed to be at 100 cm from the isocenter) to detector distance (SDD) was determined from 100 130 cm SDD for five cone sizes ranging from 6x6 to 25x25 cm². Significant deviation from inverse-square divergence with respect to the assumed source position was noted for most of the electron energies and cone sizes. Relative dose versus SDD was plotted in log-log scale to calculate the slope of the curve. The slope varied from 3.17 for 12 MeV electron energy and 6x6 cm² cone to 1.9 for 22 MeV electron energy and 20x20 cm² cone, resulting in a virtual source at 60.5 and 106 cm to the isocenter, respectively. For the same cone, the variation of the slope was relatively insensitive to different electron energies except for 6 MeV. However, the slope changed drastically with cone size for each electron energy. These indicate that dose measurement in a phantom should be made for treatment distances other than calibration distance for electron irradiation.

MP32.29

Fluence Ratios for Electron Beams for Various Plastics compared to Water, D.I. Thwaites, Medical Physics, Western General Hospital, Edinburgh, Scotland.

There is a gradual move away from plastic phantoms for electron beam dosimetry, due to charge storage effects and uncertainties in fluence ratios to water. However most protocols still recommend plastics and many centres world-wide still employ them. Previous work on fluence ratios, comparing clear polystyrene and water, has been extended in energy. This shows a linear variation in M_w/M_p from ~ 1.025 at effective energy of 3 MeV to ~ 1.005 at 15 MeV, using a graphite-walled Farmer chamber. Thus differences are observed of up to 1% to the values used in the AAPM dosimetry protocol, but there is reasonable agreement with values extracted from the ICRU Code. Results are presented and compared to other published values. Discrepancies reflect differences in polystyrene samples, in the characteristics of the chambers used and in angular and energy spread of the electron beams. Some of these factors are investigated.

In addition fluence ratios have been measured for other plastics, including some commercial solid-water equivalent phantom materials. For PMMA, values are unity for effective energies above 10 MeV, falling to ~ 0.99 at 3 MeV (M_w/M_{PMMA}). RMI solid-water (older formulation) shows differences to actual water of around half those observed for polystyrene and is thus a better water substitute than polystyrene for electrons. More importantly, it shows negligible charge storage effects. Results for other materials are presented and discussed.

MP33.2

Dose-volume Study for Combined External and Selectron Intracavitary Irradiation, T. Ganesh*, N.R. Datta, R.C. Joshi, S.Narayanan, Rajendrakumar and G.K.Rath, IRCH, AIIMS, New Delhi, INDIA.

The ICRU brought out its report # 38 on 'Dose and Volume Specification for Reporting Intracavitary Therapy in Gynecology' in 1985. Since then its theoretical and practical advantages have been largely acknowledged by many radiotherapy centers around the world. Based on these ICRU guidelines, a dose-volume study has been performed on patients treated by combined external (15MV X-rays) and intracavitary radiation (Selectron). The total reference air kerma (TRAK), reference volume, doses at reference points in organs at risk and those related to bony structures for a typical Selectron application have been calculated. The relationship between TRAK and reference volume for different doses of external radiation has also been studied. The reference volume has been calculated by constructing voxels around the applicator instead of taking the product of its three dimensions. This dose-volume study was done using the Nucletron Treatment Planning System.

MP33.1

Uncertainty in Point A Definition: A Comparison of Different Methods, T. Ganesh*, N.R. Datta, R.C. Joshi, S.Narayanan, Rajendrakumar and G.K.Rath, IRCH, AIIMS, New Delhi, INDIA.

Despite the fact that point A has been extensively used for dosimetry in the intracavitary irradiation of carcinoma uterine cervix, there is still considerable uncertainty in its exact definition. According to the Manchester system, in which point A nomenclature was first introduced, it was defined as a point situated 2cm laterally from the uterine canal and 2cm up from the level of the mucous membrane of the lateral fornices. In clinical practice, however, point A is often taken 2cm up from the flange of the intrauterine catheter or from the last active source in it and 2cm lateral from the central canal. Since point A plays a crucial role in the treatment of cervix carcinoma, a study has been carried out on patients treated with Selectron to assess how these different practical definitions produced variations in point A dose rate, ICRU reference volume and doses at other reference points. Computerised dosimetry has been done for different point A definitions and the variations have been analyzed.

MP33.3

Choice of LDR vs HDR for Ca-cervix Treatment: Radiobiological considerations. U. Madhvanath, DRP, Bhabha Atomic Research Centre, Bombay-400 085, India.

Shouldered survival curve of HDR (1.5-2.5 Gy/min.) changes to exponential at LDR of 1.5-2.3Gy/h. This implies change in the repair capacity of irradiated cells whether that of cervix carcinoma (tumour) or normal tissue (of rectum, bladder or colon). Both these dose rates either at Point 'A' or at critical normal tissues have relevance because of the differences in the T_c between carcinoma and normal tissue cells. Because of shorter T_c of Carcinoma cells, 15h as against 45h of colon cells, a differential cancer cell killing advantage is obtained in the case of LDR technique. Further, resistant S phase is overcome as irradiation times are always more than 15h and perhaps the anoxic cells as well. In the HDR technique as both the tumour and normal critical structures are in identical high fields, no repair differential is available and as irradiation times are only a few minutes per session, multiple treatments (at least 5 or 6) are required that too at weekly intervals to overcome the stage resistance. Thus, radiobiological considerations advocate LDR with better cure rate whereas administrative patient load considerations led oncology centres to go for HDR technique.

MP33.4

Use of Scout Views for Source Localization in Gynecological Implants E. Yorke*, George Washington University, Washington, D.C. 20037 & C. Clifton Ling, University of California, San Francisco, San Francisco, CA 94143

When CT scans are used for evaluation of dose distributions in gynecological implants the source positions are determined from orthogonal films. It would be desirable to use AP and lateral scout views taken concurrently with the scans for source localization. The distortion which is known to exist in the scout views has prevented such use. Much of the distortion is caused by the marked beam divergence due to the short FAD of CT scanners. It can be corrected by geometrical transformations provided that the patient position relative to the scanner axis is not changed between scout views and the axis position is marked on both scouts. A phantom with wires approximating gynecological implant sources was used to compare endpoint localization accuracy from orthogonal scout views and from simulator films. Simulator films are most accurate (end-points localized with standard deviation of ± 0.7 mm). Scout views corrected by simple magnification are least accurate (± 3.1 mm with some endpoints in error by more than 5 mm). Correction for beam divergence improves localization to ± 1.3 mm with all endpoints localized to better than 4 mm.

MP33.5

CT Compatible Version of the Fletcher System for Intracavitary Treatment, K. J. Weeks* and S. L. Schoepfels, University of Michigan Medical Center, Ann Arbor, MI 48109.

The use of CT scans to delineate the anatomic relationships of intracavitary cervix applicators, tumor, rectum and bladder has been limited by streak artifacts produced by the metal applicator and/or tungsten shields. To eliminate this artifact, a new variation of the Fletcher system for treatment of cervix cancer has been developed. The applicator has been constructed of acrylic. The tandem and colpostats have been designed along the lines of the Fletcher-Suit-Delcos applicator used previously in our department. The principal design modification has been to afterload both sources and tungsten shields. The choice of shield position is flexible and is chosen to conform to Fletcher's original applicator. This lightweight system enables the radioactive source positions to be clearly defined in relationship to the tumor as well as critical structure volumes, such as rectum and bladder, through the use of a routine CT scan after placement. This work presents the rationale, design and procedural aspects of the new system as well as examples of simulator and CT imaging of the system after placement. Volume dose calculations, shielding design, and future development work will be discussed.

MP33.6

Dosimetric Evaluation of a New Gynecological Brachytherapy Device, E.D. Slessinger*, P.W. Grigsby and C.A. Perez, Washington University School of Medicine, St. Louis, MO, USA.

A new device for gynecological brachytherapy application has recently been developed. It is called MIRALVA, an acronym for the Mallinckrodt Institute of Radiology Afterloadable Vaginal Applicator. The development of MIRALVA was prompted by the need to treat the wide range of vaginal and cervical cancer target volumes with an optimal dose distribution, in a single application, utilizing either manual or remote afterloading technique. The plexiglass device is comprised of a cylindrical portion that enlarges at the vaginal apex. It contains three channels for the placement of Cesium-137 tubes or spheres. The central channel allows for a tandem that extends either to the vaginal apex or higher as an intrauterine device. The remaining two channels allow source placement laterally in the right and left aspects of the vaginal apex. The outer dimensions can be varied to provide an optimal fit while the surface contours are designed to provide a relatively uniform dose distribution to the vaginal mucosa. Thermoluminescent and film dosimetry studies in a special solid polystyrene phantom provided the necessary data to evaluate the resultant dose distributions.

MP33.7

Recovery of Arbitrary 3-D Radiograph Geometry in Brachytherapy from a Minimal Set of Reference Markers, Bruce A. Lulu, Radiation Oncology, University of Arizona, Tucson, AZ 85724, USA.

In radiation therapy, verification of brachytherapy plans ideally involves the calculation of true source positions relative to some fiducial landmarks. This method permits the use of arbitrary unknown film geometry, as might occur in surgery with a portable X-ray unit, as well as display of source positions (and therefore isodose lines) relative to patient anatomy seen on CT. This technique is also used to locate arteriovenous malformations relative to a stereotaxic frame.

With two radiographs, one can reconstruct source positions in 3-D by finding the intersection of the two lines passing through the same arbitrary source. We consider the situation where the fiducial markers are coplanar but not collinear, and that the 3-D coordinates of these markers are known in some arbitrary coordinate system. Absolutely no other knowledge of the geometry is given. We then derive the coordinates of a line passing through the target and the brachytherapy source, as well as the target coordinates relative to the previously mentioned arbitrary coordinate system. We show that for coplanar, non-collinear points, four points are necessary and sufficient for this reconstruction.

148

MP33.8

Use of a Pass-through Ionization Chamber for Brachytherapy Quality Assurance. M.A. Earle*, K.M. Hutchins and R.K. Ten Haken, University of Michigan, Ann Arbor, MI 48109.

An integral part of brachytherapy quality assurance programs should be confirmation of source strengths stated by manufacturers prior to use in patients, as pointed out in recent reports by AAPM Task Groups 24 and 32. Even if pending national regulations make these checks mandatory, they will only be consistent with existing ALARA programs if they can be accomplished quickly, easily and with minimum exposure to staff. To that end, we have developed an in-house assay program based around a pass-through, re-entrant well air ionization chamber enclosed in a lead brick cave. Different inserts have been designed and fabricated for use with individual I-125 seeds, strings of Ir-192 seeds, Cs-137 tubes and P-32 suspensions. For example, a thin glass tube suspended by low mass supports along the central axis of the chamber is used for assaying strings of Ir-192 seeds. With this arrangement, strings are threaded from their lead shipping container, through the calibrator, and into another lead container for transfer to the patient. Using the response function for a single seed vs. position, appropriate conversion factors have been derived for any arbitrary number of seeds per string.

MP33.10

Multiphase-CT Interactive Treatment Planning and Stereotactic I-125 Brachytherapy Zamorano L,* Dujovny M, Yakar D, Malik G, Sheehan M. Henry Ford Hosp. Det. MI

Computer dose calculations for interstitial implants of radioactive seeds within intracranial tumors requires a knowledge of the spatial coordinates of each seed. A method is presented by which Multiphase-CT under stereotactic conditions is used for computer dose calculations. Multiphase-CT is used to determine size, shape and main axis of tumors; this information is integrated with a computerized planning system. The aim is to achieve a distribution of a selected isodose curve adjusted to the defined tumoral borders. After preplanning selection, CT scan with the fixed stereotactic frame is performed. Multiphase CT images and scoutviews (AP and lateral) are used to plot the trajectory of selected planes of treatment and coordinates are calculated. Catheters are placed stereotactically loaded with codified dummy seeds. Postoperative CT with stereotactic frame is performed; Multiphase and scoutviews images are used to determine the location of dummy seeds and the relationship of catheters to tumor borders. Measurements are compared with preplanned and minor discrepancies can be corrected by altering distance, number, activity of seeds or dose/rate. Simulation with conventional orthogonal film technique and final isodose distribution curves in all 3 planes are generated and superimposed.

MP33.9

Dosimetry of Large Interstitial Templates J. M. Paul*, R. F. Koch, P.C. Philip and F. R. Khan, NWCH, Arlington Heights, IL, 60005

Although the Paris system has been used in interstitial brachytherapy using single or two plane implants, no attempts have been made so far to use this system for large multiplanar implants, as encountered in the Syed-Neblett type of interstitial gynecological templates. We have investigated this possibility in order to quantify the dose delivered with such templates, involving many hundreds of seeds with as many as 44 needles, instead of arbitrarily quantifying the dose delivered on the basis of isodose curves generated with treatment planning computers. Based on our analysis, using three-plane Paris implants, we find that the overall quality of these implants could be improved in most cases while using only one-half or less as many needles; which considerably simplifies implant procedures and subsequent localization and dosimetry. These results are presented in this paper using integral volume vs. dose rate curves, and tabulated values such as: integral dose, variation of the basal dose rate, volume irradiated to dose rate greater than twice the stated rate and an objective parameter called uniformity index.

MP33.11

I-125 Dose Distributions In Various Tissues, D. Huang*, M. Schell, K. Weaver, C. Ling. Department of Radiation Oncology, University of California, San Francisco, CA 94143.

The low energy photons of I-125 interact with tissues primarily via the photoelectric effect which is strongly Z dependent. Thus, the dose distributions of I-125 sources in media of different effective Z may not be the same. We used LiF and CaF₂ thermoluminescent rods to measure dose distribution in tissue equivalent materials corresponding to muscle, adipose, and bone. The measured data were parameterized as polynomials and compared to Monte Carlo calculations and to the findings of Dale*. The calculated and measured results, for distances between 0.5 and 7 cm., were in good agreement. These data provide basic data for dose distribution calculations when I-125 seeds are implanted in or near inhomogeneous tissues, e.g. breast or bone.

* Medical Physics 10(2) 1983, p. 176-183, and 13(6) 1986, p. 963-964.

MP33.12

TLD Dosimetry for I-125 Eye Plaque
S.T. Chiu-Taao*, I.L. Anderson, L. Stabile
Memorial Hospital, New York, NY 10021

Extensive measurements using LiF TLDs were made for COMS⁺ 20 mm eye plaque both containing a single 6711 seed at the center and containing a complete loading of twenty-one seeds. TLD cubes of 1 mm on an edge were used in a solid water eye phantom. Measurements were performed at 2 mm or closer intervals up to 14 mm from the "sclera" throughout a central plane within the eye. The single-seed measurements were made with and without the gold backing. The results for single seed configuration were compared with the dose distribution in a homogeneous solid water phantom. We found that the presence of silastic (Zeff=11.2) between the seed and the measurement points introduced dose reduction in the eye by about 10% (central axis) to 15% (off-axis). Adding the gold backing over the silastic did not appear to modify the dose significantly. These data with silastic and gold agree well with our Monte Carlo results. The TLD results for the multi-seed configuration were found to agree with calculations which treats the seeds as isotropic point sources with dose as a function of distance derived from the transverse-axis data in homogeneous phantom and incorporating a correction factor for filtration by silastic.

*Collaborative Ocular Melanoma Study
Work supported in part by NCI contract NO1CMS7776

MP33.14

Substitution of Pd-103 for I-125 in the Treatment of Choroidal Melanomas,
E.G. Scarbrough*, N.C. Ikoro, P.P. Amich, U.T. Southwestern Medical Center at Dallas, Dept. of Radiology, 5323 Harry Hines Blvd., Dallas, TX 75235-9071

Pd-103 has recently become commercially available for use in brachytherapy as a potential substitute for I-125. A computer program has been written to compare the treatment of choroidal melanomas with eyeplaques containing each of the two isotopes. The program takes into account the increased tissue absorption of Pd-103 gammas, anisotropies of the radiation field, reduced coherent scatter due to the presence of the gold eyeplaque, and the cut-off of the treatment volume due to the gold plaque. Results of this study indicate that the anisotropies and increased tissue absorption do not place serious limitations on the use of Pd-103 for this purpose. In addition, the increased tissue absorption reduces the radiological hazard to personnel in the vicinity of a patient with such an implant.

MP33.13

Dosimetry Considerations for I-125 Seeds Implanted on a Curved Surface, S.C. Prasad*, D.A. Bassano, P.I. Fear, G.A. King and J.A. Winfield, SUNY, Health Science Center, Syracuse, N.Y., U.S.A.

I-125 seeds are commonly used as permanent interstitial implants for various malignant tumors. For volume and planar implants, currently available tables can be used to determine the number of seeds needed, the activity of the seeds and the seed separation. In our institution, a new implant technique is being used to treat highly malignant brain tumors using I-125 seeds. Tumors of the brain, with a histology of high grade astrocytoma or glioma, are first surgically removed. I-125 seeds are next implanted, as a permanent implant, along the wall of the cavity formed by the removal of the tumor. No simple nomogram exists to preplan an implant in which the seeds are distributed on the surface of a hollow cavity. We have developed a computational model to determine the number of seeds needed and the activity of seeds once the size of the cavity and the dose are specified. The model is based on spherical geometry and has been implemented on an LSI-11/23 computer. The details of our technique and results will be presented.

MP33.15

Angular Dependence of the Dose Rate for High Activity Ir-192 Sources Used in Remote Afterloaders, G. A. Ezzell*, Gershenson Radiation Oncology Center, Harper-Grace Hospitals/Wayne State University, Detroit, MI 48201

High activity (typically 370 MBq) Ir-192 sources are frequently used in high dose rate remote afterloading applications. These sources are usually calibrated by measuring the exposure or air kerma at a reference distance on the perpendicular bisector of the source axis. Patient dose calculations usually assume an isotropic point source model. The dose rate anisotropy was measured in water for distances representative of patient treatments. Doses at 1 cm from an endobronchial treatment catheter were also measured using TLD and a 0.03 cc ion chamber. The results show that the simple point source model underestimates the dose by 2-6% depending on the active length of the source train, and that this underdosage can be explained by applying the anisotropy data. Appropriate parameters of a line source model are presented.

150

MP33.16

INTRABRONCHIAL IRRADIATION WITH MODERATE DOSE RATE USING A SIMPLE ECONOMICAL AFTER LOADING DEVICE TO HANDLE THE HIGH ACTIVITY Ir-192 SEEDS, WILLIAM C. KAN*, STEVEN H. STOKES, RADIATION ONCOLOGY CENTER, SOUTHEAST ALABAMA MEDICAL CENTER, DOTHAN, ALABAMA 36302-6987

An inexpensive manual after-loading device used for intrabronchial irradiation with high activity Ir-192 seeds was constructed. Twenty patients have been treated with one to four sessions receiving 600-700 cGy at 1 centimeter radius per treatment. Ninety percent of patients experienced relief of symptoms associated with an obstructing intrabronchial carcinoma. Review of the film and ring badge reports on both the Radiation Therapist and the Radiation Physicist performing these procedures did not show an excessive radiation exposure. Our after loading device and method of treatment has been proven to be simple, economical and safe for the treatment of intrabronchial carcinoma. Construction of our device and method of treatment will be discussed.

MP33.18

Evaluation of activity of Cs-137 seed sources used in a remote after loading system (Selectron LDR)
V.K. Sharma*, V. Poopathi, L. Aggarwal
MDOCT&RF, LUDHIANA (INDIA)

In intracavitary treatments the radiation dose delivered to tumour & its surrounding normal tissues is proportional to the activity and specific gamma ray constant of the sources used. Hence it is important to ensure that there exists a good uniformity in the activity of the sources when used in large number. The mean apparent activity of all the sources should be determined before actual use.

A perspex calibration phantom was fabricated at our place to hold the ionisation chamber and the plastic catheters with sources and dummy pellets parallel to long axis of the chamber in a cylindrical geometry at 120°. The measurements were taken in water and the values were used to derive mean apparent activity and correction factors for attenuation in water and steel. This procedure was carried out as a part of the quality assurance programme in LDR Brachytherapy Dosimetry.

MP33-17

Dose Correction Factors for Ir-192 in the Presence of Inhomogeneities, S.N. Rustgi*, G. Popescu and J. Rodgers, Department of Radiation Medicine, Georgetown University Hospital, Washington, D.C. 20007

The influence of inhomogeneities on dose in water around a 10 Ci Ir-192 source has been assessed. The inhomogeneities studied include aluminum, cork, and styrofoam which simulate bone, lung, and a low density medium, respectively. The measurements were made possible by the high activity of the Ir-192 source and were performed with a 0.1cc PTW ionization chamber which has good spatial resolution. Since dose in the vicinity of small sources has steep gradients, positional accuracy is extremely important. The measurements were made in a Therados RFA3 phantom which has a positional accuracy of $\pm .5$ mm and a positional reproducibility of $\pm .2$ mm. Dose correction factors, which are ratios of ionization in the presence of inhomogeneity to ionization at the same point in a homogeneous water phantom, were measured for distances up to 20 cm from the inhomogeneity. A 0.7 cm aluminum slab reduces the dose beyond inhomogeneity by 5% at distances from 3 to 20 cm. For a 2.5 cm thick cork inhomogeneity the correction factor increases from 1.04 at 1 cm to 1.12 at 20 cm. The dose correction factor for a 6 cm slab of styrofoam increases from 1.12 at 1 cm to 1.39 at 19 cm.

MP33.19

Cs-137 Dosimetry Table for Asymmetric Source, R. Waggener*, J. Lange, J. Feldmeir, P. Eagan and S. Martin, The Univ. of Texas Hlth Sci. Cent., San Ant., USA

A common Cs-137 brachytherapy source has a 2 cm length with 1.38 cm active length, AL. The AL is not symmetric with respect to the source center because of an eyelet in one end of the source. Current dose tables assume symmetric source loading. A computer program was written to calculate a asymmetric distribution using the manufacturers source specifications. Corrections were made for attenuation and obliquity through the source material, walls and ends. Table values have been confirmed by ferrous sulfate measurements using small volumes. Table values agree with published values at points greater than a few cm from the source center. A knowledge of the asymmetric dose distribution should be useful for some therapy situations.

MP33.20

Dosimetric Evaluation of Endobronchial Iridium-192 Implants Using Computerized Tomography. S. Shahabi, Ph.D., M. P. Mehta, M.D., B. R. Thomadsen, M.S., T.R. Mackie, Ph.D., University of Wisconsin Medical School, Madison, WI 53792

Conventional dosimetric evaluation of endobronchial implants has relied upon orthogonal radiographs.

We present herein the application of computerized tomography in determining the dose distribution around endobronchial implants and its advantages over conventional dosimetry. The availability of serial transverse slices enables possible three-dimensional dosimetry. Better delineation of critical structures, especially the cord and esophagus allows better evaluation of the doses delivered to these structures. Better definition of the precise location of the endobronchial implant and, therefore, a more accurate assessment of the volume of lung and surrounding mediastinum irradiated is also possible. The CT cuts also enable generation of dose-volume histograms and 3-dimensional dose-volume complication probability curves.

In conclusion, we feel that computerized tomography may enable us to supersede conventional radiographic techniques for dosimetric evaluation, and allow a more precise definition of doses delivered to a volume of interest as well as to critical structures.

MP33.22

Interstitial Brachytherapy Pre-planning According To Paterson-Parker Rules Facilitated by Microcomputer, R.E. Drzymala, Washington University School of Medicine, St. Louis, MO, USA.

A program, written in FORTRAN for use on a IBM compatible microcomputer, prompts the user for the input parameters necessary to pre-plan interstitial implants according to Paterson-Parker Rules. Allowing differential loading of sources to achieve a homogeneous dose distribution within the treatment volume, the code accommodates point sources (seeds) as well as linear sources. The logical flow of the program encourages the user to think about and enter the margin around the gross disease to arrive at a tumor volume, to decide on the shape of the volume to be implanted, to specify the spacing between sources and to estimate the dimensions of the implant for appropriate coverage. Violations of the Paterson-Parker Rules are checked in the flow of the program, thereby providing a learning tool for new residents or junior physicists. The violation warnings are noted but can be overridden to permit minor deviations from the rules to accommodate unusual circumstances. Additionally, one can allow the program to choose the spacing and loading of sources for a quick treatment pre-plan.

MP33.21

Routine Calibration of Brachytherapy Sources with a Well-Type Dose Calibrator using Standard Calibrated Sources. Azam Niroomand-Rad*, Michael T. Gillin. Department of Radiation Oncology, Medical College of Wisconsin. 8700 W. Wisconsin Ave. Milwaukee, WI 53226, U.S.A.

Brachytherapy, which refers to short-distance treatment, requires an accurate knowledge of the dose distribution in the implanted volume. A critical step in the determination of the dose distribution involves an accurate calibration of brachytherapy source strength. Following the guidelines recommended by AAPM Task Group No. 22(1), a routine calibration procedure for brachytherapy sources Cs-137, Ir-192, and I-125 has been developed. Using a single potentiometer setting, the calibration method for these sources is described. Some of the problems associated with the calibration of sources are discussed. The calibration of sources are performed with a well-type dose calibrator using standard calibrated sources obtained from The United States (NBS), British (NPL), and French (LMRT) national laboratories. Selected characteristics of dose calibrator are reported. By considering the NBS calibrated source as a reference source, the calibration correction factors for Ir-192 and I-125 are described. The result of intercomparison of the calibrated sources by national laboratories indicates some discrepancies between the calibrated sources. These discrepancies which are within the stated uncertainties are sometimes larger than expected. (1) AAPM Report No. 13 (1984).

MP33.23

SET OF PROGRAMMES FOR RADIOTHERAPY TREATMENT PLANNING.
PART II - BRACHYTHERAPY TREATMENT.
M.C. Lizuain*, C. Pino and C. Cinos.
Hospital de Bellvitge. Barcelona (Spain).

Brachytherapy programmes calculate the distribution of dose produced by implants of linear radioactive sources of any form. The capsule filtration effect and the gamma ray attenuation in tissue are taken into account. Two orthogonal radiographs are used to localize the sources. In the case of the curved sources, the two projections of the source are fitted to cubic spline functions from which, the spatial coordinate of a set of source points are obtained. In this way the curved source is considered as a set of small right sources. The dose distribution is represented by means of isodose curves on any plane. The computer is a PC (Vectra H.P.) with 640 K-bytes RAM Memory, 80286 Intel microprocessor and 80287 co-processor, 40 M-bytes hard disc driver. A digitizer as input device and one plotter and one printer as output.

1. 2

MP33.24

- Detailed Calculation of Radiation Energy Spectrum and Spatial Dose Distribution in Water for ^{137}Cs and ^{192}Ir Point Sources, Y. Takaku*, K. Takeuchi**, *Fukushima medical College, **Ship Research Institute, Japan.

Radiation transport calculation is made with a PALLAS discrete ordinates code, designated to solve a numerical solution of the Boltzmann transport equation. The calculation of primary γ -ray transport is carried out for point sources of ^{137}Cs and ^{192}Ir placed at the center of a 10cm radius water sphere, resulting in γ -ray angular fluxes at each radial mesh at each energy mesh. The γ -ray angular fluxes generate secondary electrons arising from interactions of photoelectric effect, Compton scattering and pair production. Furthermore, these electrons generate Bremsstrahlung radiations. All the processes are traced with the PALLAS code to obtain γ -ray energy spectra, dose rate distributions, secondary electron energy spectra, X-ray energy spectra and X-ray dose rate distributions within the water phantom.

MP34.2

Determination of differential w-values for proton, deuteron, 3-He and 60-Co gamma-ray beams in several gases, T. Hiraoka*, K. Kawashima and K. Hoshino, 9-1, Anagawa-4-chome, Chiba-shi, 260 Japan

The differential values, w, the mean energy necessary to produce an ion pair have been determined for several gases in atmospheric pressure. The gases investigated were air, argon, nitrogen, carbon dioxide, methane, and methane based tissue-equivalent. The tank gases were used of pure grade. Six different ionization chambers in six different sizes were used in this study. The measurements were carried out in the irradiation of 70 MeV proton, 43 MeV deuteron, 99 MeV 3-He ion and 60-Co gamma-ray beams. In each chamber, collected charge was measured for several applied voltages and averaged for both polarities. By dividing the energy loss (stopping power) by the number of ion pairs produced (ionization measured), relative values of w were presented for the gases and the radiation qualities under investigation. The use of these w-values for the evaluation of absorbed dose with ionization chambers for proton beams gave good agreement with a TE calorimeter. Therefore, it is estimated that these w-values are accurate to within about 2 %.

MP34.1

Comparison of Variable and Fixed Modulation Proton Beam Dose Distributions in the Cranium, M. Urie*, Massachusetts General Hospital, Boston, MA 02155, USA.

The dose to normal tissues in the entrance region of a proton beam can be reduced if the Bragg peak is spread out (modulated) to a different width at each point in the field to precisely encompass a complex target shape, rather than being modulated to a uniform width determined by the greatest breadth of the target. Dose distributions calculated with fixed and with variable modulation proton beams were compared on patients with chordomas in the base of skull. 3D treatment planning allowed quantification of the dose differences throughout the head; dose-volume histograms of critical normal tissues were calculated and compared. With target doses of 66-72 Gy, variable modulation was found to reduce the dose to some brain tissue by 15-20 Gy. Correlation of the magnitude of the dose reductions with size, shape and location of the tumor will be presented. These data may aid in judging whether or not the dose differences are of great enough significance clinically to justify the greater complexity of variably modulated proton beams.

MP34.3

Proton Radiation Therapy. Where will it be in the year 2000? J.M. Sisterson*, K.N. Johnson, A.M. Koehler, Harvard Cyclotron Laboratory (HCL), J.E. Munzenrider, Massachusetts General Hospital (MGH) and M.S.Z. Rabin, University of Massachusetts, Amherst.

By the end of 1987 more than 8000 patients in the world had been treated with proton beams using facilities originally designed for nuclear physics. The successes that have been achieved will be illustrated by using the HCL/MGH experience where 4139 patients had been treated. The long term results from HCL/MGH show that proton radiation therapy is indeed a viable modality. The superior dose distributions possible with proton therapy make this the treatment of choice for selected sites. By the year 2000, there may be as many as 20 proton therapy centers in the world, ranging from large facilities routinely using protons to treat all sites, to small units dedicated to the treatment of a single site. Treatment philosophy as well as cost and real estate constraints dictate the final design of any facility, the mix of facilities is determined by patient populations. Plans, cost estimates (ranging from \$1-50 million) and possible marketing mix will be presented.

153

MP34.4

Fast Neutron Dosimetry Using Digital Autoradiography, J. Kleck*, J. Smathers, L. Myers and B. Stewart, University of California, Los Angeles U.S.A.

Many conventional techniques using film have been developed for beam characterization and dosimetry in photon and electron therapy. Film is of less value in either quantitative or qualitative dosimetry in fast neutron therapy beams. This is primarily due to the relatively high film sensitivity to small amounts of photon and electron contamination in the neutron beam.

A technique has been developed at the UCLA Neutron Therapy Facility whereby thin (3.18 mm) sheets of acrylic plastic may be positioned in a water phantom and activated in the p(46)Be neutron beam. The resulting activation distributions in the acrylic characterize the high energy component of the neutron kerma. The principal reactions contributing to the activation are C-12(n,2n)C-11 and O-16(n,2n)O-15, both with activation thresholds close to 20 MeV. The activated acrylic plate is used to expose a Europium doped Barium Fluorohalide plate, which is subsequently digitized by a Computed Radiography system using a 15 mWatt HeNe laser. The spatial resolution of the resulting image is 2.5 lp/mm with 8 bits of contrast resolution. This research is supported by NCI contract CM 97315.

MP34.6

Evaluation of the Gamma Component in a Neutron Therapy Beam. M. Yudelev and D.T.L. Jones*, National Accelerator Centre, 7131 Faure, South Africa

Neutron beams are always accompanied by gamma rays and for therapeutic applications the gamma dose component has to be determined because of its different biological effect. In this work a tissue equivalent (TE) ionization chamber, which is equally sensitive to neutrons and gamma rays and a Geiger-Müller (GM) counter, which is relatively insensitive to neutrons, have been used in a p(66 MeV)/Be neutron therapy beam to determine the gamma dose. Using the "lead attenuation method" the neutron sensitivity (k_U) of the GM counter is estimated to be 0.06 from preliminary data. From measurements made in a water phantom for various field sizes with both the TE chamber and the GM counter the gamma dose component can be evaluated. The gamma dose was found to be 3.8% of the total dose at dose maximum for a 10 x 10 cm² field. At a depth of 10 cm in water gamma rays constitute 5.3% of the total dose for a 5 x 5 cm² field increasing to 10.1% for a 30 x 30 cm² field. For a 10 x 10 cm² field at a depth of 10 cm in water the gamma component at 10 cm from the central axis it is 30%. Measurements of the effects of different beam filters will also be presented.

MP34.5

KCCH-Cyclotron and Demonstration of Neutron Dosimetry, Hyun-Woo Chung*, Kyoung-Hwan Son, Chul-Koo Cho, and Seong-Yul Yoo, Korea Advanced Energy Res Institute, Seoul, Korea

The purpose of this presentation is to outline the measurement made at Korea Cancer Center Hospital, KAERI, and to present the result obtained.

These measurements were designed to demonstrate the compliance of the isocentric fast neutron facility.

- a) Neutron production and delivery
- b) Physical parameters of the neutron beam.
- c) Neutron Beam Calibration including n ratio and detector design
- d) Treatment planning
- e) Health physics considerations, etc.

Will be covered the above topics.

MP34.7

Dosimetric Intercomparisons of p(>60 MeV)/Be Neutron Therapy Beams. D.T.L. Jones*, National Accelerator Centre, 7131 Faure, South Africa, S. Vynckier, Université Catholique de Louvain, Belgium and S.W. Blake, Clatterbridge Hospital, U.K.

In order to compare clinical and other data from neutron therapy centres it is essential for dosimetry intercomparisons to be undertaken. The centres involved in the present study were the National Accelerator Centre (NAC), South Africa [p(66 MeV)/Be], The Université Catholique de Louvain (UCL), Belgium [p(65 MeV)/Be] and the MRC Cyclotron Unit, Clatterbridge Hospital (MRC), U.K. [p(62 MeV)/Be]. In the first phase of the study measurements were made with a NAC TE ionization chamber at UCL and MRC and compared with measurements made using local equipment. The ⁶⁰Co calibrations of the ionization chamber at UCL and MRC agreed within 0.1% of that at NAC. In the UCL neutron beam the response of the NAC chamber differed by a maximum of 0.2% for all conditions from the mean of the responses of all the chambers used. Measurements made with the NAC ionization chamber in the MRC neutron beam were between 0.6% and 1.0% higher than those made with the MRC chamber. The results are highly satisfactory as agreement of ±2% is more typical for such studies. Phase two measurements (at NAC) will also be described.

154

MP34.8

The Effects of Various Filters on a p(66 MeV)/Be Neutron Therapy Beam.
D.T.L. Jones* and M. Yudelev, National Accelerator Centre, 7131 Faure, South Africa

Several different types of beam filters may be required for the clinical use of a neutron source. These include shaped metal filters which flatten or rotate the beam profiles, hydrogenous filters which harden the beam and reduce the RBE differential between surface and depth and metal filters which absorb charged particles. The effects of such filters on dose rate and dose distribution have been investigated on the National Accelerator Centre's p(66 MeV)/Be (40 MeV) isocentric neutron therapy beam. Iron filters flatten the beam to within $\pm 3\%$ at 10 cm depth in water for all field sizes while the maximum off-axis dose enhancement at the surface is +7%. Tungsten wedge filters rotate the beam profile at 10 cm depth by 30°, 45° and 60°. For a 10 x 10 cm² field the addition of 1, 3 and 5 cm thick polyethylene filters reduces the dose rate to 93%, 80% and 70% and increases the 50% depth dose from 16.2 cm to 16.5, 16.9 and 17.2 cm respectively. A few millimetres of lead or steel has only a marginal effect on the build-up characteristics of an uncompensated beam. Adequate restoration of skin sparing is achieved if bolus material is lined with 2 mm of lead.

MP 34.10

Calculated microdosimetry of primary and scatter neutron fluence components in a muscle equivalent phantom for En < 20 MeV., R.E. Wallace* and P. Bloch, Univ of Penna, Dept of Radiation Oncology, Phila., Pa.

The calculation of effective neutron dose requires knowledge of (1) the KERMA, (2) the microdosimetry of charged particles delivering the dose, and (3) the biological response as a function of charged particle lineal energy (ie: LET). The microdosimetry of charged particles associated with primary and scatter neutrons were calculated as a function of depth in a muscle equivalent phantom. The microdosimetric spectrum for primary neutrons (P) is spatially invariant. The microdosimetric spectrum for scattered neutrons (S) was found to be nearly independent of depth. The dose average lineal energy, $\langle y \rangle_d$, for primary and scatter components are different, and for the total (P+S) neutron dose, $\langle y \rangle_d$ varies significantly with depth. This behaviour will be discussed with regard to the variation of $\langle y \rangle_d$ with neutron energy. A strategy will be presented to compute a dose response factor using constant values for primary and scattered neutron components.

MP34.9

Fast Neutron Sources for Therapy-Current Problems and Need for Basic Data, M.A. Chaudhri*, Austin Hospital and University of Melbourne, Melbourne, Australia.

In this paper a brief review of the historical development of the production of therapy neutron beams is presented, with special reference to the author's contribution, using the available nuclear data. Different nuclear reactions and target systems have been critically examined regarding their suitability for cyclotrons of different sizes. A few current problems in this field, especially relating to the non-availability of appropriate nuclear data, where the nuclear and radiation physics communities can greatly contribute, are highlighted. Specific recommendations are made as to what sort of nuclear data need to be acquired/compiled that would be most useful in the neutron therapy programme.

MP34.11

Calculating Radiation Dose in Heterogeneous Media With Different Atomic Numbers, T.R. Mackie, B. Thomadsen*, S. Shahabi, B. Paliwal, Department of Medical Physics and Human Oncology, University of Wisconsin, Madison, Wisconsin 53706

The use of the convolution/superposition method for photon beam cavity calculations was explored. The dose per unit fluence near slab and three-dimensional phantoms, that contain heterogeneities with differences in atomic number, were computed using convolution kernels generated in a water phantom. The energy released at the interaction sites was scaled with respect to the ratio of the mass energy absorption coefficient of the medium to that of water. The dose deposited at the dose deposition sites was scaled to the ratio of mass collision stopping powers (Bragg-Gray) between the medium and water. The results were compared to Monte Carlo calculations and measurements. Very good agreement was obtained for air and aluminum slabs located in the build-up region in a water phantom at photon energies of 1.25, 10 and 20 MeV between the convolution/superposition method and Monte Carlo benchmarks of Bielajew and Rogers (2). Reasonable agreement was obtained with the measurements of Ogunleye et al. (3) obtained in LiF TL dosimeters in aluminum, copper and lead phantoms irradiated by Co-60 photons.

1) Bielajew, A.F. and Rogers, D.W.O., Presented at the Workshop on the Convolution Method for Calculating Radiation Dose, Regina, Canada (1986).

2) Ogunleye, O.T., Attix, F.H., and Paliwal, B.R., *Phys. Med. Biol.* **25**, 203-213.

MP34.12

Separation of Primary and Scatter Doses in a Co-60 Photon Beam, P. Nizin*, K. Kase and B. Bjarngard, Joint Center for Radiation Therapy, Harvard Medical School, Boston, MA 02115, USA, and University of Massachusetts Medical Center, Department of Radiation Oncology, Worcester, MA 10605, USA.

Results of theoretical considerations and experimental measurements are presented, which allow the separation of primary and scatter doses in Co-60 photon beams. If a small attenuator is placed in the beam, the dose from primary radiation will be altered but the dose from scattered radiation will not change significantly. The ratio of the primary doses C can be determined by relative attenuation measurements. It can be shown that the dose from primary radiation in the water is

$$P = (1 - I/C)(D - D_i),$$

where D and D_i are measured total doses without and with the attenuator in the beam. Measurements were made with aluminum and graphite attenuators. It was found that the results do not depend upon the material used. The data for primary and scatter doses are in good agreement with recently published values. A correction factor for possible perturbation of phantom-generated scatter is established, and application of the method to megavoltage x-ray beams is discussed.

MP34.14

Monte Carlo Studies of Small Inhomogeneity Dose Perturbations in Photon Beams, S.S. Hancock*, W.S. Ge, C.X. Yu and J.W. Wong, Washington University School of Medicine, St. Louis, MO, USA.

Photon dose is enhanced locally near bone-like material. We have studied the relative contribution of the various charged particle transport components for 6 MV and 18 MV x-rays. The EGS4 code was used to calculate the angular distribution and energy spectra of the charged particles emerging from spherical inhomogeneities in water. Compton and pair-production interactions in the sphere and water are scored separately. The results are then used in a simpler CSDA model to delineate the characteristic of the various dose perturbation components. There is a net reduction of charged particle fluence emitted at small angles and a net increase at larger angles. Contributions due to the charged particles originating from the sphere and the water medium peaked at different directions. The total charged particle flux per unit area emerging from the sphere is independent of its size. (Supported by NCI grant CA-41574).

MP34.13

On Methods of Photon Dose Calculations, J.W. Wong* and J.A. Purdy, Washington University School of Medicine, St. Louis, MO, USA.

We have examined eight approximate methods for photon dose calculations: Ratio of TAR (RTAR), modified Batho power law, and Differential SAR (DSAR) method, all developed prior to CT; Equivalent TAR (ETAR) method, developed to make use of CT data but needing increased computer power; FFT convolution, scatter ray-tracing Delta Volume (DV), Dose Spread Array (DSA), and Differential Pencil Beam (DPB) methods, developed more recently, using theoretically generated input data, but having limited practical applications because of inadequate computer power. Horizontal slab phantom measurements were used to study photon transport corrections. RTAR overestimated lung corrections by about 10%. Not all scatter ray-trace approaches were better as DSAR was inferior to Batho. FFT approximation omitted ray-tracing and led to large artifacts at depth. Ray-tracing DV, DPB and DSA methods agreed with cobalt 60 measurements mostly to within 2%. Non ray-tracing ETAR was only slightly inferior for these geometries. (Supported by NCI CA-41574 and CM-47696).

MP34.15

A 3D Implementation of the ETAR Method Using FFT Convolution, C.X. Yu*, P.Y. Yan and J.W. Wong, Washington University School of Medicine, St. Louis, MO, USA.

The equivalent tissue-air-ratio (ETAR) method, despite known weaknesses, provides results that rival scatter ray-trace methods for photon dose calculations when electronic equilibrium exists. Although fully 3D in formulation, an empirical CT slice coalescing approach is used to reduce the calculations to a more manageable 2D form. As a result, the method is not suitable for irregular beam shaping. We have noted that the ETAR calculations represent a density convolution which can make use of the FFT technique. 3D ETAR FFT calculations, more versatile than the 2D version, have been implemented on our VAX 8600. The FFT approach compares favorably with results using the earlier version and measurements. Calculations for 32^3 volume elements took less than 2 min., while the direct convolution took about 1 hr. The approach offers a much improved option over current 1D methods for practical 3D RTP until more advanced methods become practical. (Supported by NCI grant CA-41574).

MP34.16

Installation of the EGS4 Monte Carlo Code on a Microcomputer System, S. Walker and D. Jette*, Institute of Applied Physiology and Medicine, 701 16th Avenue, Seattle, WA 98122.

We have installed the EGS4 Monte Carlo code¹ on the new Compaq 386/20 microcomputer system. This microcomputer, with its 32-bit wordlength, 20 MHz clock speed, and Weitek mathematics coprocessor, promises to rival a mainframe system in its Monte Carlo run speed, and at very much less cost. The installation is by no means trivial, with an appropriate operating system and Fortran compiler required, and conversion of the EGS4 files from mainframe to microcomputer format is fairly involved. However, this work should help other researchers to install EGS4 on their own microcomputer systems. We present benchmark tests of running EGS4 on our system, vs. a VAX mainframe system.

These investigations have been supported by a grant (#7 R01 CA41490) from the National Cancer Institute.

1. W.R. Nelson, H. Hirayama, and D.W.O. Rogers, "The EGS4 Code System", Stanford Linear Accelerator Report 265 (Stanford University, Stanford, CA, 1985).

MP34.18

Corrections to Scatter Dose in Heterogeneous Media for Photon Beams,

R.K. Rice*, B. E. Bjarngard, and L. M. Chin, Joint Center for Radiation Therapy, Department of Radiation Therapy, Harvard Medical School, Boston, MA 02115

To calculate photon dose distributions in heterogeneous media accurately it is necessary to consider changes to the primary and scatter components of the dose separately. Existing algorithms using this procedure usually involve an integration over the irradiated volume. For a 3-dimensional integration the time required is prohibitive for routine treatment planning. We have developed an algorithm to correct the scatter component of the dose in layered media by calculating the effective scatter-to-primary ratio (SPR) along the central ray. The SPR is determined based on the radiologic depth and density-scaled field size at each interface. By combining this effective SPR with a 2-dimensional scatter integration and primary dose correction accurate results (<5% error in total dose) are achieved for a variety of geometries and beam energies including a mediastinum geometry for 4 and 15 MV photon beams. Measured results are compared with the new algorithm and Monte Carlo simulations.

MP34.17

Optimization of CBEAM model parameters for linac photon beams, K. Ayyangar, I. Daftari*, J.R. Palta, and N. Suntharalingam, Department of Radiation Therapy and Nuclear Medicine, Thomas Jefferson Univ. Hospital, Philadelphia, PA 19107

Measured beam profiles and central axis depth dose data for photon beams from our linear accelerator are used to generate a dose matrix representing the full beam. Using the modified CBEAM model, a corresponding dose matrix is also calculated. The calculational model requires a set of 3 parameters to define the beam intensity at beam edges and 3 for the primary profile factor expressed as a function of distance from the central axis. An additional parameter to account for the transmission of the beam through the collimator is also included. An optimization program has been adapted to automatically adjust the parameters used in the CBEAM model to minimize the chi-square between the measured and calculated data. The process of optimization is repeated for different field sizes. Typically the average values of the parameters for small (6x6 cm²), medium (10x10 cm²) and large (20x20 cm²) field sizes are found to represent the beam adequately for all field sizes. The calculated and the measured doses at any point agree to within 2% for any field size in the range 4x4 cm² to 40x40 cm². The method of optimization and the agreement of the data with measurements will be discussed.

MP34.19

Applications of a Laplace Transform Pair Model to Deconvolve the High Energy Photon Spectra from Transmissions Measurements. J.S. Ramaswamy*, W.F. Hanson, B.R. Archer, and A.L. Boyer, Department of Radiation Physics, University of Texas System Cancer Center, Houston, TX.

No direct method currently exists to measure the energy spectra of megavoltage photon beams. Monte Carlo simulation and several indirect experimental methods have been suggested to quantify high energy photon spectra. We are exploring the Laplace transform pair method as a practical method of determining high energy photon spectra. By modeling the transmission curve and the spectrum with analytical functions, one can use a Laplace transform to deduce one from the other. Spectra reconstructed from transmission data measured using different materials are intercompared to verify the uniqueness of the Laplace transform pair model. Spectra on and off the central axis of 6 and 18 MV photon beam thus determined are compared with the spectra generated by Monte Carlo simulation. The selection of attenuators, measurement of maximum energy of the photon spectra, and conversion of chamber response to fluence are discussed.

This work supported in part by P.H.S. Grants CA 43840 and CA 10953 awarded by the National Cancer Institute, DHHS.

137

MP34.20

A Geometric Parameter for Representation of Scatter in Photon Beams, C.H. Obcemea*, H. Rashid and B.E. Bjarngard, Joint Center for Radiation Therapy, Boston, MA 02115 USA.

Before measured dose data for photon beams are used for dose calculations based on scatter integration, primary and scatter dose components must be separated and the data edited. We have examined how this may be aided by a simple geometric expression for the scatter-to-primary ratio: $SPR = A_1 r d / (A_2 r + d)$. This is a qualitative description of first-order scatter as a function of depth d and average field radius r . The data used were tissue-phantom ratios (TPR) for 8 MV X-rays ($d=2-30$ cm, square fields $s=4-35$ cm) and TAR data for Co-60 ($d=0.5-30$ cm, $s=4-75$ cm). The primary and scatter components were separated by three different approaches, one based on the formula above, with $\pm 1\%$ agreement. The resulting TPR or TAR values were then fitted to the expression with a least-squares procedure. The accuracy was in general within $\pm 2\%$ for Co-60, somewhat less at $d=30$ cm. For 8 MV X-rays, only occasional points at shallow depths gave discrepancies greater than 1% .

MP34.22

An Algorithm for Design of Beam Compensators, M.D. Renner, T.P. O'Connor, H.M. Bermudez, Dept. Radiation Therapy, Community Hospital, 1500 N. Ritter Ave., Indianapolis, IN 46217, USA.

A three dimensional computer program was written for the VAX computer that can produce isodose curves in any plane of the patient's body for virtually any beam setup that can be achieved on the treatment machine, including any combination of blocks, wedges, and beam compensators, provided the patient can be scanned on a CT scanner in the treatment position. Computed doses are accurate to within 3% at one standard deviation on comparison with measured values in an anthropomorphic phantom. Beam compensators are optimally designed to give a uniform dose to any plane or midsurface that intersects a single beam, or to give a uniform dose to the volume defined by the intersection of two or more beams. The primary and scatter components are taken into account separately, as well as the patient's shape and internal heterogeneities. The design of the beam compensators is formulated as a linear programming problem and solved with a variation of the Simplex Method. Beam weighting factors are also obtained as part of the solution.

MP34.21

A High-Precision Method for Computing the Missing-Tissue, N. Samsami*, F.R. Bagna and S. Hoke, Medical College of Ohio, Toledo, Ohio

High Precision radiation therapy requires that a uniform dose be delivered across the entire treatment volume. To accurately compensate for the effects of the missing tissue, it is imperative that all the necessary parameters which can affect dose in the treatment volume be determined. We have developed a precise, yet practical technique for computing the thickness of missing-tissue along the ray-lines. The technique takes into account the phantom scattering effects, the missing-tissue scatter reduction and the scattering due to the collimator jaws. To assess the most suitable tissue-compensator material, a series of measurements were done using polystyrene, lead, Cerrobend and polyethylene-lead. All dose measurements were made in tissue-equivalent phantom using 6MV (Clinac 6/100) and 10MV (Clinac-18) photons. Our data indicate that tissue-equivalent materials provide more accuracy than high-atomic number materials. Additionally, using the described method, dose uniformity can be achieved with less than a few percent error over the entire clinically-used range of depths, missing-tissue thicknesses and field sizes. This method is particularly suitable for generating cross-sectional layers of missing tissue using computer software.

MP34.23

SET OF PROGRAMMES FOR RADIOTHERAPY TREATMENT PLANNING. PART I - EXTERNAL HIGH ENERGY PHOTON BEAMS. M.C. Lizuain*, C. Pino and C. Cinos. Hospital de Bellvitge. Barcelona (Spain).

A set of Fortran-77 programmes for Radiotherapy treatment planning have been developed in a PC. The Cunningham and Wilkinson method was used for calculating the dose distribution in high energy radiation beams. The values of Co-60 SAR and TAR were taken from the literature and RX-18 MV were calculated from measures made with ionization chambers.

The programmes consist of three parts:
 1: Generation of tables of numbers giving the radiation distributions for beams of rectangular cross-section with or without wedge filters.
 2: Calculation of absorbed dose at points of one volume irradiated with one or two irregular section beams.
 3: Calculation of dose distribution in a plane of a volume irradiated by several regular beams. (Six fixed or isocentric beams or two rotational beams).

MP34.24

Computing dose distribution for electron beams with rotated collimator using Generalized Gaussian pencil beam algorithm, S. Hyödynmaa*, Technical Research Centre of Finland, Medical Engineering Laboratory, Box 316, SF-33101 Tampere, FINLAND

Generalized Gaussian pencil beam algorithm has been used for computing the absorbed dose for electron beams. In this work the algorithm was applied for computing the dose distributions for fields with rotated collimator. The computation is based on calculating the integration limits along the height of the field to the field edges at the position of each pencil beam. The computation was tested for a rotated 10x10 cm field for $\bar{E}_0 = 11.4$ MeV electrons (Microtron 14) in a water phantom. With collimator rotations up to 30° the agreement with measured values inside the field was good. Outside the field the computation overestimates the dose (isodose curve shift < 5 mm). With collimator rotations higher than 30° the computation started to underestimate the dose inside the field (isodose curve shift < 5 mm up to 60° rotation). Outside the field the overestimation went up to 8 mm isodose curve shift for 60° rotation. The computation gives fairly good results inside the field for quite large collimator rotations. The approach can also be used for computing dose from irregularly shaped fields, and computation in slices outside the fields is possible.

MP34.26

Multiple-Scattering Angular Distributions in Electron Dose Calculation, D. Jette*, Institute of Applied Physiology and Medicine, 701 16th Avenue, Seattle, WA 98122.

A problem with using Fermi-Eyges multiple-scattering theory in electron dose calculation is that that theory predicts a Gaussian distribution in particle direction, at any particular depth in a broad electron beam. Such a Gaussian distribution ignores the single-scattering tail of the real angular distribution, leading to inaccurate dose calculation. On the other hand, Molière multiple-scattering theory includes single large-angle scattering, but is valid only for constant energy, and hence only near the surface of the irradiated material. Our second-order multiple-scattering theory¹ does modify the Gaussian distribution so as to predict increased scattering at large angles, but like the Fermi-Eyges theory it does not include the process of single large-angle scattering. We compare the predictions of these multiple-scattering theories with EGS4 Monte Carlo calculations, and discuss how to append a single-scattering theory to achieve accurate electron dose calculation.

These investigations have been supported by a grant (#7 R01 CA41490) from the National Cancer Institute.

1. D. Jette, Med. Phys. 12, 178 (1985).

MP34.25

The Effect of Oblique Incidence upon Electron-Beam Dose Distributions, D. Jette*, Institute of Applied Physiology and Medicine, 701 16th Avenue, Seattle, WA 98122.

Surface curvature of the patient can significantly influence the dose distribution in electron-beam teletherapy. In this study we systematically examine the effect of oblique incidence upon electron-beam dose distributions, comparing the predictions of Fermi-Eyges multiple-scattering theory and of second-order multiple-scattering theory¹, with EGS4 Monte Carlo calculations. In particular, we evaluate the finding of Ekstrand and Dixon², that the effect of oblique incidence is to increase the dose at small depths and to decrease it at large depths.

These investigations have been supported by a grant (#7 R01 CA41490) from the National Cancer Institute.

1. D. Jette, Med. Phys. 12, 178 (1985).
2. K.E. Ekstrand and R.I. Dixon, Med. Phys. 9, 276 (1982).

MP34.27

A real time CT-linked 3-D treatment planning system, T.Nishidai*, Y.Nagata, M.Takahashi and M.Abe, Kyoto Univ., Kyoto 606, Japan

A real time CT-linked treatment planning system, called a CT simulator, has been developed. The basic system consists of a CT scanner, a multi-image display component, a treatment planning device with real time visual optimization and a laser beam projecting component. All the components are combined on line and work simultaneously. With the treatment planning device, visual optimization and fast reconstruction of dose distributions, oblique slices and simulation images are available. Accurate 3-D dose distribution is calculated with heterogeneity correction by the new equivalent TPR method on any interested slice. On two large multi-image monitors, the CT images and scannograms involving the target outline, ROI, field size, block localization and dose distribution can be observed and an optimal planning is searched. The laser beam projector locates the planning result, e.g. beam center, field size. This new CT simulator can be used for 3-D planning and simulation for radiotherapy within a reasonable short time. The research was done in collaboration with Shimazu Co. and NEC Co..

MP34.28

Implementation of a Three-Dimensional Planning System Using the GKS Graphics, D. L. McShan*, University of Michigan Medical Center, Ann Arbor, MI 48109.

The Graphics Kernel System (GKS), an ISO/ANSI graphics standard, has been used to implement a full function three-dimensional radiation therapy planning system. The standard provides a uniform interface between the treatment planning software and a variety of graphical display devices. While GKS is presently only a 2-D graphics standard, our implementation provides for device handler extension (via GKS escape functions) to support overlay graphics, gray scale image displays, and other image processing functions. For 3-D graphics, a software layer written in FORTRAN has been interfaced to GKS calls and provides the necessary tools to handle multi-format windows, 3-D coordinate transformations (including perspective for beam's eye view displays), clipping planes, axonometric displays and surface rendering. An overview of the functionality of this implementation will be presented along with a discussion of its performance in routine clinical operation.

MP34.29

Further Exploitation on Using Wedge Filters in Radiation Therapy Planning, Yi-min Hu,* Ning Lin, Chun-li Zhang and Hong-zhi Zhang Radiation Oncology Dept., Cancer Institute (Hospital), Chinese Academy of Medical Sciences, Beijing, China.

On summarizing the experience of using wedge filters in radiation therapy planning, authors derived theoretically a formulae which can in practice guide the planners who use Treatment Planning System or help the radiotherapists who haven't got Treatment Planning System at present to choose independently the optimum wedge angles and dose weightings of the beams to be used to achieve a very uniform dose distribution in target volume while sparing effectively the normal tissues around and the critical organs nearby. The dose distributions deduced from the formulae are confirmed by RTPLAN and Film dosimetry in Anderson Phantom.

MP34.30

Comparison of Theraplan Electron Dose Calculations with Measurements in an Anthropomorphic Phantom, J. Cygler* and J. Ross, Ontario Cancer Foundation, Ottawa Regional Cancer Centre, 190 Melrose Ave., Ottawa, Ontario K1Y 4K7

Electron dose distributions in an anthropomorphic (Rando) phantom were measured using TLD-100 rods. CT scans of the head and chest wall sections of the phantom were done using a GE 9800 scanner. The measured doses for 6, 9, 13, 17, 20 MeV beams were compared with isodose distributions calculated with Theraplan Version 04 software [A.E.C.L.]. This program performs inhomogeneity corrections based on pixel by pixel data. Discrepancies between measured and calculated doses for the head are of the order of 10-14%. For the lungs Theraplan greatly overestimates the dose. The differences between measured and calculated data are larger for the larger electron energies (up to 40% for 20 MeV). The reasons for such big discrepancies are discussed in terms of the assumptions inherent in the algorithm employed by Theraplan.

MP34.31

Verification of External Beam Teletherapy Plans Produced by CT-Based Planning Computer, Lilian V. Rodriguez,* Jose R. Reyes Memorial Medical Center, Department of Health, Manila 1003, and Agnett P. Peralta, Radiation Health Service, Department of Health, Manila 1003, Phillipines.

The first CT-based treatment planning computer in the Phillipines has been installed at the Radiotherapy Department of the Jose R. Reyes Memorial Medical Center. This development provides a new level of accuracy and precision in the field of radiation therapy in the country. The present work describes the procedure performed to investigate the accuracy of treatment plans made for external photon beam teletherapy. The study consists of two parts. The first part is designed to detect any programming error. The second part involves verification of dose calculations by actual measurement in a phantom.

MP34.32

QUANTITATIVE EVALUATION OF ALTERNATIVE PLANS DURING COMPUTERISED RADIOTHERAPY TREATMENT PLANNING PROCEDURE

S L Kapoor, TSG Integrations
202 Ashok Bhawan, 93 Nehru Place
New Delhi

The role of treatment planning in the radiotherapy procedure is to assist the doctor in arriving at a prescription in order to give better quality of treatment to the patient. The prescription is a treatment scheme based on the clinical information about the patient, therapeutic objectives and the physical treatment plan. Alternative treatment plans are normally visualised by the doctor with the help of treatment planning systems to arrive at a plan which best meets the overall objectives. This paper suggests an easy-to-use scheme for quantitative evaluation of treatment plans.

The scheme is based on comparing the desired dose to the various parts of the body (treatment objective) with the calculated dose for a given treatment plan. A direct comparison of the objective with the actual dose values at the points of interest yields valuable quantitative data for evaluating the effectiveness of alternate plans.

MP34.34

Objective Measures of Radiation Therapy Treatment Plan Quality, Bruce A. Lulu, Radiation Oncology, University of Arizona, Tucson, AZ 85724, USA.

When comparing competing radiotherapy treatment plans, it is useful to abstract from the plans objective measures of quality (MOQ) more compact than the usual multiplanar isodose distributions. Traditionally, concepts such as minimum target dose, percent dose inhomogeneity throughout the target volume, and more recently the dose-volume histogram, have been used. We present four measures of plan quality that can be derived from a dose-volume histogram by inspection. These dimensionless measures contain two physician-adjustable parameters that have clear clinical meanings. The MOQ are applicable to teletherapy plans and as well as brachytherapy plans. The MOQ require the concept of target volume, which could in fact be an isodose surface, as well as no other clinically significant structures other than "target" and "non-target". We show that all four MOQ are necessary in the sense that a plan with three good MOQ can be constructed that is clearly clinically unacceptable. Conversely, the four MOQ are sufficient to characterize all the essential features of an ideal plan.

MP34.33

Irregular Portal Planning in Radiation Therapy - Use of CT Images for Target Volume Delineation, Preparation of Shields and Templates, Anil Kumar Sharma* and R. Ravichandran, Kidwai Memorial Institute of Oncology, Bangalore - 560 029, India.

The aim of radiatic therapy planning is to find an optimal way to deliver radical radiation dose to the specified target volume while sparing the surrounding healthy tissue as much as possible. A method is described to utilise Computed Tomography data to provide accurate information for delineating the target volume and to ensure reduction in the volume of healthy tissue in the radiation field. Tumour bearing areas are marked on the individual scans of the exposure series and projected onto the lateral and AP topograms to get the irregular portals. The resultant irregular portal is additionally superimposed with the superior, middle and inferior cutlines which help in positioning the patient and decide the collimator, couch and gantry angles. By employing suitable magnification factor, individual shields are prepared from the topogram films carrying projected ROI's defined in the sequential tomograms. These topograms are also used as templates for adjusting the shielding blocks.

MP34.35

Development of a dose calculation workstation, J Viitanen*, J Heinilä, S Hyödynmaa and H Puurunen, Technical Research Centre of Finland, Medical Engineering Laboratory, P.O. Box 316, SF-33101 Tampere, Finland and Dosetek Oy, P.O. Box 2, 02131 Espoo, Finland

In connection with the Nordic Research Program CART (Computer Aided Radio Therapy) we developed a new comprehensive and flexible concept for the dose calculation workstation for radiation therapy. The CT-based system, CADPLAN, has been implemented on a modern workstation, Hewlett Packard 9000/350, although the development work has been done on a VAX-11/750.

The menu and mouse driven system includes vast image processing facilities like beam's eye view presentation, multislice display, image reconstructions and 3D surface models. The photon dose calculation algorithms use pixel-by-pixel based generalized power law or equivalent TAR method for inhomogeneity corrections. For compensating filter calculations an iterative method is used. The electron distributions are calculated using the generalized Gaussian pencil beam algorithm. Boluses can be inserted on the patient and included in the calculation and dose histograms in the given ROI's can be generated.

Software for intracavitary calculations is available in the system. The intracavitary distributions can be combined with external distributions and superpositioned on CT-slices

MP34.36

3D Computerized Treatment Design Using Modern Workstations, George W. Sherouse*, Radiation Oncology, University of North Carolina, Chapel Hill, NC 27514

In recent years the rapid evolution of high-performance workstations has given rise to new models in the computer industry for the deployment of computing resources. For departments where a great deal of computing power is required, a network of single-user workstations with shared access to files and unique peripherals has become a cost-effective alternative to more conventional centralized computing. Moreover, even for sites where one or few workstations are needed, the ability to place very capable computers with high-resolution graphic displays on users' desktops opens new possibilities for the design of highly interactive software tools. A prototypical workstation network configured to support three-dimensional radiotherapy planning will be presented. The richness of this approach will be illustrated by description of some 3D radiotherapy software tools, designed and built using the UNIX[†] operating system and the X Window System available on most modern workstations.

[†]UNIX is a trademark of Bell Laboratories

MP34.38

A PROJECT FOR AN EXPERT SYSTEM IN RADIOTHERAPY

L. Azario, A. Piermattei, G. Arcovito, Physics Inst., Univ. Catt. S. C., ROMA L. Andreucci*, A. Schenone, National Cancer Institute, GENOVA C. Bacci Phys. Dep., "La Sapienza" Univ., ROMA R. Bernabei, S. D'Angelo, M.P. De Pascale Physics Dep., "Tor Vergata" Univ., ROMA

Data coming from CT, NMR and PET images are well treated by means of optimized software. A typical use of the computer for this kind of research is to store a great deal of clinical data to optimize the treatment planning. The aim of our project is to make an expert system to contribute to clinical treatments of different pathologies, especially related to increasing quantity of the radiological informations. The realization will be completed in this subsequent steps. In a first time we will develop the software for the tridimensional reconstruction of images coming from a CT system. In the second step, we will realize a software to estimate the dose distribution and the isoeffect to optimize the radiotherapeutic treatment. The aim of this poster is to show with some detail the purposes of this project and the status of the our tridimensional imaging software.

MP34.37

Some Experiences on Radiation Therapy PACS E. Takenaka, Y. Wada, R. Hosaka and T. Fukui. National Defense Medical College

Fifty national university hospitals have been year by year annoyed by piling up of X-ray films due to the development of many imaging modalities. Study group of radiology department of national university hospitals has been discussed PACS to be made in their hospitals. As a member of group, we have checked and studied the function and performance of radiation therapy PACS. Radiation therapy PACS treats all kinds of medical images in addition to radiographs. This PACS are the most suitable to determine TNM and target volume, to detect early recurrence and metastasis and to teach radiation oncology to medical students and post graduate students. A PACS module with a laser scanning digitizer, two high resolution CRTs, light discs etc was set in radiotherapy section. Information contents of medical images, function and performance of this PACS module and experiences on module will be reported.

MP34.39

A PC BASED WORKSTATION FOR THE PLANNING OF STEREOTACTIC NEUROSURGERY

T M Peters*, J A Clark, G B Pike, A Olivier. McConnell Brain Imaging Unit, Montreal Neurological Institute, Montréal, Québec.

Stereotactic surgery requires knowledge of cerebral structures derived from more than one image source. We have developed a PC-AT based workstation which accepts patient images, made with the stereotactic frame in place, from CT, MRI and DSA modalities. Reference markers on the frame may be identified in the images to establish the coordinate geometry for each modality.

Target points may be identified on each image type and trajectories of probe paths to these points defined. Targets identified on one set of images may be transferred automatically to other images of the same patient, in order for example to guarantee a vascular free path of approach to a target point deep within the brain.

To date several hundred patients have had stereotactic surgery performed on the basis of plans using this system. Procedures included biopsy and aspiration of lesions, implantation of electrodes for the recording of deep EEG signals, and radio-surgical techniques based on the use of a high energy linear accelerator.

MP34.40

Maximum Utilization of Radiation Oncology Computer System

Simon C.P. Lam, Steven H. Mahood, Larry L. Windedahl, Michael L. Matheny, Morristown Memorial Hospital, Morristown, NJ 07960

Contemporary high speed, high capacity, multi-tasking systems can adequately perform routine clinical treatment planning, and other ancillary functions.

We put together a local computer network, centered around a parallel link of two PDP 11/73 computers. It is capable of simultaneously performing active treatment planning in 2 stations. It is capable of performing a multitude of tasks simultaneously in 10 stations. Its digital image processing ability enables optimal combination of images from different modalities for treatment planning. Video linkage between simulator and physician's offices help streamline the patient throughput. Direct data link between treatment units and main frames facilitate the accuracy of treatment plan implementation. It also provides recording and verification of actual treatments given.

Ancillary tasks handled by this network include patient and staff scheduling, fiscal planning, project integration and analysis and remote communications to both the Hospital Information System and Radiology Information System. A direct link to the Nuclear Medicine MicroVAX computer is also provided.

MP35.2

A direct comparison of water calorimetry and Fricke dosimetry

Ken R. Shortt*, C.K.Ross, N.K.Klassen and G.D.Smith, Division of Physics—NRCC, Ottawa, Canada K1A 0R6

We have completed a direct comparison of water calorimetry and Fricke dosimetry for 20 MV x-rays. The calorimeter consisted of a small sealed vessel containing 100 ml of stirred water saturated with a 50/50 mixture of H₂ and O₂ gases. Based on calculations and previous experiments involving different gases, we estimate that the heat defect for this system is -2.1%. The calorimeter was filled with 100 ml of air-saturated Fricke solution and irradiated under identical conditions. Our Fricke system uses the Svensson and Brahme value for ϵG of $3.515 \times 10^{-3} \text{ l cm}^{-1} \text{ J}^{-1}$ and gives agreement to within 0.2% with the dose to water for ⁶⁰Co γ -rays obtained via graphite calorimetry. After correcting the calorimetric measurements for the effects of the foreign mass (mostly glass), we find the dose to water determined by water calorimetry is 1.006 ± 0.004 times the dose determined by Fricke dosimetry. We plan to make the same comparison for ⁶⁰Co γ -rays and a range of electron energies. Eventually, we hope to establish a calibration service at high energy based on this water calorimeter as a primary standard and Fricke dosimetry as a transfer standard.

MP35.1

Synthetic diamond crystals as "state of the art" dosimeters
R.J. Keddy* and T.L. Nam
Schonland Research Centre, University of the Witwatersrand
PO Wits, Johannesburg, 2050 South Africa

The main attraction of using diamond as an in-vivo or as an environmental dosimeter is that it is "tissue equivalent" to a high degree. It is however also non-toxic, robust and stable and can repeatedly be used. Only a rare group of natural diamonds act as efficient detectors of ionizing radiations however but diamonds with optimum quantities of selected impurities can be synthesized to act as radiation detectors with performance responses that are superior to other tissue equivalent materials. The diamonds can be synthesized to act as thermoluminescent dosimeters or as ionization chambers. Therapy doses can easily be recorded and radiation levels approaching natural background values can be detected. Depending upon the application, the linearity of response extends over five orders of magnitude of dose within a useful range that extends to nine orders. The physical forms of the synthetic material can be crystals, grits or powders. All types of ionizing radiations can be detected, particulate as well as electro-magnetic. Because of the tissue equivalence and stability of these specially synthesized stones they could very appropriately be used as the detecting component in instruments calibrated in "absorbed" rather than "exposure" dose, also because of their small volumes ($\approx 1 \text{ mm}^3$), they would lend themselves well to the miniaturization of such instruments.

MP35.3

Feasibility of Non-Equilibrium Dosimetry with a Fricke Ferrous Sulfate System, L.D. Simpson, Washington University School of Medicine, St. Louis, MO, USA.

Physicists' ability to measure dose under clinical, non-electronic equilibrium conditions is weak. Models to predict dose for external and internal sources thus remain incomplete and unverified. The most sophisticated models affected by this weakness are the Monte Carlo codes which have not been verified in some regions of non-electronic equilibrium. Limitations of existing experimental techniques will be reviewed: to include ionization chambers, TLD, and the Fricke ferrous sulfate dosimeter. Alternative methods for overcoming these limitations will be discussed. Emphasis will be placed on my development of a new Fricke ferrous sulfate dosimetry system. The water-equivalent detector volume is $< 0.001 \text{ cc}$, configurable as a $< 4\mu$ thick disk or as a cylinder 1 mm diameter by 1 mm length. The detection limit is $< 0.1 \text{ Gy}$. Two important system components will be discussed: 1) a transition metal analyzer based on high performance ion chromatography and 2) the modified Fricke detectors.

163

MP35.4

The point of measurement for thick-walled ion chambers in γ -beams

Alex F. Bielajew* & D.W.O.Rogers, Division of Physics—NRCC, Ottawa, Canada K1A 0R6

When ion chambers are used for determining exposure in point source ^{60}Co fields, there is an uncertainty on the point of measurement owing to the finite size of the chamber and the spatially varying photon fluence. In this paper we present a theory for the point of measurement building upon an "exact" theory of ion chamber response in uniform fields¹. The theory is general enough to allow for fields of arbitrary spatial configuration but for this paper we consider point sources only (i.e. $1/r^2$ dependence). We demonstrate that for practical distances (SSD's $\geq 50\text{cm}$ or so), there is a negligibly small correction ($<0.03\%$) relative to the geometric center of the air cavity. This is demonstrated by Monte Carlo simulations for all standard ion chamber geometries, plane-parallel, thimble-type, and spherical. This is at variance with the ^{60}Co exposure standards at the PT⁷ and BIPM² where point-of-measurement corrections of the order of 0.5% are used. Neither the NBS nor the NRC(Canada) apply such a correction although uncertainties of 0.1% and 0.2%, respectively, are associated with this correction. We recommend that point-of-measurement corrections not be applied for thick-walled ion chambers in ^{60}Co beams and that no error be associated with this correction.

- 1) Bielajew A.F., Phys. Med. Biol. 30(1985)419-427.
- 2) Niatel M.-T. et al, Metrologia 11(1975)17-23.

MP35.6

Stopping power ratios in electron beams.
P.Andreo*, A.Brahme and A.E.Nahum,
Karolinska Institute, S-10401 Stockholm,
Sweden. and Royal Marsden Hospital, Surrey
SM2 5PT, England.

Most of the existing dosimetry protocols agree in the recommended values for the water/air stopping power ratios in electron beams, i.e., the values from Berger as given in the AAPM protocol. Experimental results have shown that the use of s -ratios derived for mono-energetic and mono-directional beams is adequate for beams with certain energy and angular spread, but not for "clean" beams.

Calculations have been performed using the Monte Carlo method. Computed $s_{\text{water,air}}$ for beams without energy and angular spread do not show significant differences from the Berger values, especially for the electron beam energies more commonly used in Radiotherapy ($E_0 < 20\text{ MeV}$). The inclusion of energy and angular spread in the calculations has shown a variation of $s_{\text{water,air}}$ at the depth of the maximum absorbed dose.

MP35.5

Radiation dose distribution in Agar gels imaged by MR, L.Ciraolo*, M.Bucciolini, F.Milano, R.Renzi, Fisica Medica, Università di Firenze, Italy.

Radiation dose can be measured through the changes induced in the ferric ion concentration of a Fricke solution. The conversion of ferrous to ferric ions affects the NMR relaxation times of protons in water, too.

Some authors (Gore et al., Phys.Med Biol., 1984, 29, 1189) have already found the increase of longitudinal and transversal relaxation rates to be linear respect to the absorbed dose.

In this work, a solution of ferrous ions in Agar gel (Appleby et al., Med Phys., 1987, 14, 382) has been irradiated with a X-ray beam (25 MV) from a Linac. T1 and T2 values have been evaluated by an imaging MR machine.

This approach is aimed to employ the spatial resolution offered by the MRI technique in the dosimetry of complex radiation treatments.

MP35.7

Dose Distributions of the First Clinical Stereotactic Radiosurgical Unit (Gamma Knife) in the United States, G. Lindner*, N. Smarra, University of Pittsburgh, Pittsburgh, PA

On August 14, 1987 the first stereotactic radiosurgical procedure was performed in the United States using the Leksell Gamma Knife at Presbyterian University Hospital in Pittsburgh, Pennsylvania. Gamma Knife radiosurgery refers to stereotactic localization and subsequent single treatment, closed skull irradiation of a brain lesion with 201 highly focused beams of cobalt 60 radiation. Treatment planning is done on a Digital MicroVAX II computer running software developed at the University of Uppsala, Uppsala, Sweden specifically for the Gamma Knife. The hemispherical array of sources, the large number of small diameter beams and the steep dose gradients surrounding a target lesion make physical characterization of the radiation field complex. In phantom film and LiF thermoluminescent dosimetry (TLD) measurements were performed. Our studies have shown good agreement between measured and computer generated field profiles and isodose distributions for 4, 8, 14 and 18 mm diameter fields.

164

MP35.8

Measurement of Charged Particle Contamination in a Megavoltage Beam,
N.C. Ikoro*, E.C. Scarbrough, P.P. Antich, U.T. Southwestern Medical Center at Dallas, Dept. of Radiology, 5323 Harry Hines Blvd., Dallas, TX 75235-9071

The magnitude and penetration of electron contamination in 6 MV X-ray beam is investigated using a specially built Charged particle detector. The charge detector, with an aluminium electrode, is used in the direct measurement of contaminant electron fluence. The fluence is converted to dose by comparison with the fluence and dose measured from a modified 6 MeV electron beam. Further analysis of the electrons is carried out using the detector in conjunction with a permanent magnet.

Present data suggest that contamination electrons can be explicitly characterized; the observed changes in the build-up region, with collimator opening, are due to electrons; backscattered electrons from the medium are responsible for as much as 35% of the observed surface dose at maximum collimator setting, at standard treatment distance.

MP36.1

The Light Propagation Physics of Breast Transillumination Imaging, D.Wyman*, M.Patterson, V.Hansen, V.Peters, The Ontario Cancer Treatment and Research Foundation, 711 Concession Street, Hamilton, Ontario, Canada, L8V 1C3

Breast transillumination imaging is a method of detecting abnormalities based on the differential transmission through the breast of red and infrared light. We quantitatively assess the propagation of light through various tissues in an attempt to determine both the optimization and limitations of the method.

This assessment is based on determining the fundamental optical properties of regular, fibrous and malignant breast tissue by first measuring, for tissue samples, the reflected and transmitted light using an integrating sphere. These measurements are inverted to yield optical properties through iterative Monte Carlo simulation. Phantom models have been constructed for a range of optical properties. Both Monte Carlo simulation and diffusion theory are used as mathematical models.

Presented results of imaging simulations using both models quantify the sensitivity of breast transillumination imaging to geometry and nature of the abnormality within the breast, wavelength of light, extent of scatter rejection and method of detection.

MP35.9

Angular Emission of Secondary Charged Particles from Small Cylindrical Volume for 6 MV and 18 MV X-Rays, S.S. Hancock*, C.X. Yu and J.W. Wong, Washington University School of Medicine, St. Louis, MO, USA.

An understanding of charged particle productions and transport in finite size volume element is important for accurate dose calculations. We have measured the angular emission of the charged particles from small acrylic, aluminum and copper cylinders in 6 MV and 18 MV x-ray beams to study the effects of size and composition of irradiated volume. Electron contaminations, primary and scattered photon contributions were minimized. Charged particle emission due to pair-productions increased with atomic number. Coulomb scattering shifted the emission to larger angles. The charged particle flux at each angle became proportional to surface area when the cylinder diameter approached the charged particle range. The measurements agreed with Monte Carlo simulations. The effects of multiple coulomb scattering play a major role in the angular distribution of the charged particles.

(Supported by NCI grant CA-41574).

MP36.2

Analysis of trace elements in seminal fluid by X-ray fluorescence, R.CESAREO*, Centro Ingegneria Biomedica - Università La Sapienza, A. MAGRINI & G. IZZO, Fisica Medica - Università Tor Vergata, G. D'OTTAVIO & A. LAGANA', Ospedale S. Carlo di Nancy - Rome - Italy, L.J. PEDRAZA, Centro de Estudios Nucleares - Universidad Nacional Autónoma de México, S.Q.B. MAHTABOALLY, Physics Department - Rajshahi University - Bangladesh

Energy dispersive X-ray fluorescence induced by monoenergetic photons was used in the analysis of trace elements in seminal fluid. Monoenergetic radiation of various energies was obtained by using an X-ray tube with secondary external targets (Sr and Zn). Fluorescence radiation from each secondary target was collimated and sequentially used to irradiate fluid samples deposited on thin filters. A linear relationship between X-ray counts and content of each element was found. 44 samples of seminal fluid from 22 infertile males were analyzed. Potassium, calcium, iron, copper, and zinc were detected and quantitatively assessed, minimum detectable limits being 1 ppm (Fe, Cu and Zn) and 50 ppm (K and Ca). A close linear correlation between Zn, K and Ca levels was found, regardless of the pathological condition.

MP36.3

Light Scattering and Propagation in Tissue, H Key*, P C Jackson and P N T Wells, University of Bristol, Bristol BS1 6SY, UK

The development of improved light transmission imaging requires more information on the scattering and propagation characteristics of tissues at visible and near infra-red wavelengths. We are especially keen to exploit the full potential of transillumination imaging for the detection and diagnosis of breast cancer.

Volume scattering functions of normal and pathological tissues have been measured at several wavelength bands that correspond to high tissue transmittance. Experimental data have been incorporated into a Monte Carlo model for simulating the propagation of light in three-dimensional tissue geometries. The model is being used to predict transmitted intensity distributions for different geometries and tissue albedos and to study the efficiency of spatial and temporal image filtering techniques.

MP36.5

Influence of EEG by Static Magnetic Fields, L. von Klitzing*, G. Tessmann, Med. Univers. Lübeck, D- 2400 Lübeck, W. Germany

Recently we reported about changes of somatosensory evoked potentials (SEP) by static magnetic fields used in clinical n.m.r.-equipments (von Klitzing et al., 1987). By further experiments we found increased power spectral intensity values in the discrete EEG-frequency bands, but only at the right hemisphere not at the left. The relative energy changes are different in the frequency bands. Obviously, there is a memory effect after a longer stay in a static magnetic field (>20 min, 0.2 T s-l), because the energy values are not decreasing immediately.

MP36.4

Elastic Characteristics of the Self-Expanding Metallic Stents,

B.G. Fallone, Diagnostic Physics
University of Texas, M.D. Anderson
Hospital & Tumor Institute
Houston, TX 77030

Elastic properties of the self-expanding metallic (Gianturco) stent were measured. Hooke's law was used to characterize the stent with respect to its caliber, length and radius by a coefficient of stiffness. Although this coefficient was independent of the radius of the stent, we found that it was directly dependent on its caliber. For a stent of a particular caliber and length, the fractional change in radius determined the force exerted by the stent. For small radial displacements of the stent, the force required to compress it was directly proportional to the radial displacements; for large displacements, the force depended upon a power series of the fractional radial displacement. A hyperbolic function was empirically introduced to approximate this type of relationship between force and radial displacement. Tension and pressure exerted by the stent were calculated and the use of such results with normal vessels was suggested.

MP36.6

The propagation of light through biological tissue, J. Bews*, S. Shalev, Manitoba Cancer Treatment and Research Foundation, Winnipeg, Canada R3E 0V9

A detailed study of light propagation through biological tissue has been carried out under tightly controlled experimental conditions using TEM, a synthetic homogeneous material which simulates the optical properties of glandular breast tissue over the range 550 to 900 nm. Experimental light distributions were measured in TEM for two irradiation geometries (isotropic point source and isotropic planar source in an infinite medium), and shown to be well predicted by Linear Transport and Diffusion theories in regions distant from the source. The parameters required to generate the theoretical distributions are the mean free path (MFP) and the scatter/attenuation coefficient (c) for the medium. We found that MFP for TEM varies from 0.206 to 0.495 mm over the spectral range 550 to 900 nm, and that c is close to unity. Linear Transport theory was used to demonstrate how light propagation through the medium depends on spectral variations in these parameters, and in particular the very critical dependence on the value of c . The results are interpreted in terms of the transport of light through tissue at different wavelengths, and the effect of hemoglobin on the process.

MP36.7

Microcomputer Approach to Biomorphometry,
F.Bersani, M.Nichelatti*, C.Pallotti, G.Pallotti,
P.Pettazzoni,
Department of Physics, 40126 Bologna, Italy.

Stereology offers the microscopist a practical methodology by which parameters of structures can be inferred, by calculations, from measurements performed on section. In the first part a system of data acquisition based on conventional stereological method (Point-Counting) is discussed. The morphometry program collects data from digitizer and calculates area, perimeter, volume and statistics.

In the second part the image processing by a Real-Time Video Digitizer Module for the IBM PC AT is discussed. The digitized image is processed using a computer program that traces, by algorithms of various kind, the contour of the object and extracts various features from the image. The advantage of this device is that it measures the micrograph features with greater precision than the manual point counting procedures and that one tracing operation yields several pieces of information. The disadvantage is that profile or features with density near to the background may be missed, so that the information retrieved is not representative.

MP36.9

Comparative study of the effects of different insulines administered by iontophoresis techniques. J.Bustelo*, M.J.Medialdea and F.Vilaplana
Avd. dela Marina, 3-5.11007 CADIZ/1:SPANA.

The present paper treats of comparative study in rabbits, of the effects of different insulins administered by iontophoresis techniques. The objectives of this investigation try to evaluate which type of insulin is the best capable for this percutaneous application. Specifically were developed the following experiments:

1. Archive that the insulin pass through the skin "in Vivo" without it losing its biological activity, using an electrical field.
2. To extend its activity.
3. To rationalise the time of insulin administration.

A study was carried out on a group of 125 rabbits "in vivo". Were determined the values of glycemia after the insulin application by means of iontophoresis during 30 minutes.

MP36.8

THE GENERATION OF ULTRASONIC WAVES BY IONIZING RADIATIONS, N.A. Baily*, University of California, San Diego, La Jolla, California 92093, USA

Theories of radiation damage based on the assumption that high temperature thermal spikes were produced in irradiated materials date back to the work of Dessauer in 1923. Numerous investigations followed, most of which showed indirect evidence for the presence of localized regions of high temperature.

Recent physical investigations involving the detection and measurement of ultrasonic waves associated with the irradiation of both liquids and solids have shown conclusively that these result from high temperatures produced in small regions ($1 \mu\text{m}^3$ or less).

Calculations of temperatures and acoustic wave pressures for various energy depositions in different size volumes will be presented. It will be shown that utilization of the characteristics of this acoustic field (amplitude, spatial and time distributions, frequency characteristics, etc.) will yield the ionization energy deposited, the direction of its development, track width (for charged particles), and spatial distribution of delta rays.

MP36.10

Clinical Measurements of Trabecular Bone Mineral Density in a Normal Population, and in a group of Osteoporotics, using the Ratio of coherent to Compton Scattered Photons in the calcaneus; M.A. Greenfield, J.D. Craven* and S. Shukla, University of California, Los Angeles, California, USA.

Trabecular bone mineral density (TBMD) is obtained in the calcaneus by measuring the ratio of coherent to Compton scattered photons produced by a collimated beam of 60KeV photons from an Am-241 source (44.4-GBq) with a scattering angle of 71° and a highly collimated solid state Ge detector. Calibration standards are comprised of varying amounts of ground bone mixed homogeneously in a volume of petrolatum. The method has an absolute accuracy of 5%, and has a reproducibility of 3.4%. To date measurements have been made on 87 normal males (ages 22-77) with a mean TBMD = 274 mg/cc (SD=46), and on 240 normal females (ages 18-85) with a mean TBMD = 250 mg/cc (SD=40). In striking contrast the TBMD of 20 male and 9 female paraplegics are 162 mg/cc (SD=56) and 138 mg/cc (SD=30) respectively. The TBMD of a group of 25 osteoporotic females is 189 mg/cc (SD=33). Comparisons of these findings will be made with conventional Quantitative Computed Tomography (QCT) and Dual Photon Absorptiometry (DPA).

167

MP36.11

Is Passive Microwave Radiometry (PMR)
a Medically Useful Diagnostic Tool?
R.H. Behrman*, and E.S. Sternick,
Tufts-New England Medical Center,
Boston, MA 02111

Biological systems emit thermally generated electromagnetic energy at all frequencies. In the microwave region, the intensity of this radiation is directly proportional to the absolute temperature of the emitting tissue. Since inflamed tissue, some malignant tumors, and organs with high metabolic rates have slightly higher temperatures than surrounding tissue, external measurements of microwave emissions could indicate the presence of underlying disease. Whether this technique will prove useful, depends upon a variety of parameters which include the temperature discrimination and spatial resolution of the microwave radiometer, tissue thicknesses, and the frequency of the microwaves being detected. Using two independent theoretical approaches we have carried out detailed calculations of microwave emissions from several types of layered biological tissue interfaced with direct and remote sensing radiometers to investigate these factors. Our results indicate that PMR is a promising diagnostic tool for a number of medical applications.

MP36.13

A Method for Removing Prolongation of
Mean Transit Time due to Response Time,
M. Arakawa*, K. Kambara, T. Segawa,
H. Miyazaki, F. Ando and S. Hirakawa, Gifu
University School of Medicine, 40, Tsukasa-
machi, Gifu 500, Japan.

The response time of the indicator detecting system distorts dilution curve and prolongs mean transit time (MTT). In the thermal-dye technique for measuring lung water, correcting method for apparent prolongation of MTT associated with response time is unsettled. We obtained step function response curves of 5 different thermodilution systems and measured mean response times (MRT). Using model with flow loop system filled with warmed 0.9% saline solution that is circulated at 6 different flow rates, we simultaneously obtained a pair of thermodilution curves from a pair of thermodilution systems both positioned at the same place. Multiple combinations of thermodilution systems and flow rates are made. Differences of MTTs ($\Delta MTT, y$) yielded a close approximation of differences of MRTs ($\Delta MRT, x$), $y = 1.77x - 0.04$ ($r = 0.95$, $n = 72$). Therefore, we can remove apparent prolongation of MTT by subtracting MRT from MTT.

MP36.12

Computed Microtomography with Synchrotron Radiation from the X-26C Beam Line at the National Synchrotron Light Source.
P. Spanne* and M.L. Rivers+, *Radiation Physics Dep., Linköping University, S-58185 Linköping, Sweden, +Dep. Applied Science, Brookhaven National Laboratory, Upton, N.Y. 11973, USA

The very high X-ray photon fluence rates available at synchrotron radiation sources now makes computed microtomography with spatial resolution in the μm -range possible. Experiments at the X-26C microprobe beam line at the National Synchrotron Light source at Brookhaven National laboratory have yielded images with spatial resolution down to about 20 μm and show the potential to improve the resolution down to at least 1 μm in imaging small dead objects. This creates a new microscopy method for imaging microstructures in tissue samples. Since no chemical preparation is required such a development will for the first time make possible non-destructive studies of tissues. Calculations show that CT imaging of small laboratory animals can be done without inducing radiation injury at 50 μm spatial resolution. By use of a line-shaped radiation beam, a photodiode array detector, and CAMAC acquisition modules, an image can be obtained in about a minute.

Research supported by NIH USPHS Fellowship FO-TW03735, RR01838, DOE DE-AC02-76CH00016, MFR 7557

MP36.14

Fluid Therapy Consultation System (FLUIDEX)

Shoichiro Hara* and Toshiyuki Furukawa

Institute of Medical Electronics,
Faculty of Medicine, University of Tokyo,
7-3-1 Hongo, Bunkyo-ku, Tokyo 113

FLUIDEX is an expert system which can help in the diagnosis of fluid imbalance of the patient as well as recommend the optimal prescription for the infusion therapy. The characteristics of the system are: (1) a hierarchical inference engine which acts like a filter to select the most appropriate hypotheses from those initially generated; (2) a knowledge base which can convert qualitative characteristics of the patient into quantitative ones or compensate deficit data; and (3) a simulation model of the electrolytes and water metabolism. FLUIDEX's evaluation using actual patients has demonstrated its usefulness in the medical environment.

FLUIDEX can not only propose the diagnosis and prescription, but also offer simulation facilities which are able to trace its diagnostic process using its input data and give computer-aided instruction of fluid therapy.

108

MP36.15

Biological Soft X-ray Contact Microscopy: A New Look at the Living Cell, G. D. Guttman, Center for X-ray Optics, Lawrence Berkeley Laboratory, Berkeley, CA 94720, U.S.A.

Within the past decade, several technological advances have contributed to the increased success of imaging living cells by soft x-ray microscopy. The easiest approach to this technique is the contact method, which is analogous to x-ray lithography. The contrast mechanism is due to absorption at the carbon and nitrogen K edges. The region of interest, also known as the "water window", is 23.6 Å λ <math>< 44.8</math> Å. Advances in materials have brought the Si₃N₄ vacuum window and x-ray sensitive polymers into use in soft x-ray microscopy. The Si₃N₄ vacuum windows used in the sample chamber isolate the cells from the vacuum but still allow x-rays to pass. X-ray sensitive polymers, such as polymethylmethacrylate (PMMA), have a resolution of ~50 Å when exposed to x-rays with a wavelength of 25 Å. This is a considerable improvement in resolution over films that were used more than 20 years ago. New x-ray sources, such as high intensity synchrotrons and plasma sources, have opened the possibility of imaging the living cell "instantaneously". These improvements have made soft x-ray contact microscopy a viable technique for imaging living cells. Sample images will be shown. This research is supported by the U. S. Department of Energy under Contract No. DE-AC03-76-SF00098.

MP36.17

Concepts of viscoelasticity and thixotropy of blood.

J.C. LELIEVRE* and C. LACOMBE.

Unité de Biorhéologie, CHU Pitié-Salpêtrière, 91 Bd de l'Hôpital, 75013 Paris, France.

At a normal hematocrit, blood is a thixotropic gel. At rest, this gel exhibits viscoelastic and plastic behaviors.

First, one indicates the principles which underlie the general formulation of the constitutive law of thixotropic fluids.

Then, one precises the experimental methods which are most suitable for characterizing this law (hysteresis loops method, step method). Different examples of thixotropic behavior are presented (blood, fuel oil, N-bentonit, etc). Theoretical methods are briefly discussed. These methods lead one to consider elasto-thixotropy as non-linear viscoelasticity.

Finally, examples of experimental set-up are given and related difficulties are discussed. Applications to blood and to red cell suspensions are indicated and discussed in terms of RBC aggregation.

MP36.16

Triple-Pulsed X-ray Generator Having Variable Spectra, E. Sato*, H. Isobe and T. Yanagisawa, Department of Physics, Iwate Medical University, 3-16-1 Honcho-dori, Morioka 020, Japan

The construction and the fundamental studies for the triple-pulsed x-ray generator having variable spectra for biomedical radiography are described. This generator consisted of the following components: a high-voltage generating unit, a voltage divider unit, three high-voltage pulsers, a triple-parallel impulse switching system, a high-power gas diode having three terminals, a turbo molecular pump, and three x-ray tubes having cold cathodes. The x-ray tubes were of the demountable diode type and were connected to a turbo molecular pump which allows operation at pressures of less than 1×10^{-3} Pa. For the single-tube generator, the pulsers were charged to the same or different voltages of less than 100kV by using a voltage divider unit and were connected to the x-ray tube through a high-power gas diode using SF₆. For the triple-tube generator, since three pulsers were connected directly to the tubes without a diode, three x-ray outputs could be obtained simultaneously. The minimum time interval for the single-tube type was about 100ps, and the pulse width ranged from 100 to 300ns. The x-ray quality (average spectrum distribution) became hard according to increases in the charging voltage and the thickness of metal filters outside of the x-ray window.

MP36.18

A Study of Photo-Nuclear Reactions in Tissue, P.D. Allen, M.A. Chaudhri*, Australian Radiation Laboratory and Austin Hospital, Melbourne, Australia.

The total yield of photoneutrons from soft-tissue equivalent material, irradiated with bremsstrahlung of end point energy from 6 MeV to 28 MeV, has been measured using the 35 MeV University of Melbourne Betatron and a 4π Halpern-type neutron detector. The results are compared with calculations based on the cross-sections for neutron production of constituent elements of tissue (H, C, N and O). It is shown that the less common isotopes of the constituent elements (H-2, C-13, N-15, O-17, O-18) must be included to obtain agreement with the measured yields. The dose equivalent imparted to tissue by the photoneutrons is estimated for the energy range from 6 MeV to 30 MeV and compared to other measurements/estimation (where available). Furthermore, the dose equivalent due to all photonuclear reactions is estimated for energies of 24 MeV and 30 MeV.

169

MP36.19

Fluoride Determination in Bones and Teeth of Experimental Animals, M.A. Chaudhri*, Austin Hospital and University of Melbourne, Melbourne, Australia.

In a programme to study the effect of water fluoridation on calcified tissues, the F concentrations of the bones and teeth of experimental animals, which were kept on fluoridated water were determined by prompt activation analysis.

Powdered bone samples were pressed into the grooves of the aluminium target holder, while whole teeth were used as such, for irradiation purposes. The samples and the standard were covered with a thin aluminium foil and irradiated, in turn, with 2 MeV protons at 20 nA intensity. The 6-7 MeV gammas from the $F(p, \alpha \gamma)O$ reaction were counted with a 5 x 6 inch NaI(Tl) detector, placed at 135 degrees to the beam direction.

The bones of the animals who were given fluoridated water (250 ppm of F) for 15 and 45 days, were found to contain about 5 and 10 times more F than the bones of control animals respectively. Similarly, the teeth of the animal on fluoridated water (2 pp of F) contained twice as much F as those of the control animals.

MP36.20

Radiographic Characteristics of a Single-Shot Flash X-ray Generator Having Three Types of Tubes, H. Isobe*, E. Sato and T. Yanagisawa, Department of Physics, Iwate Medical University, 3-16-1 Honcho-dori, Morioka 020, Japan

The construction and the radiographic characteristics for a single-shot type of high intensity flash x-ray (FX) generator is described. This generator consisted of the following components: a control board, two high-voltage power supplies for positive and negative voltages, a high-voltage coaxial oil condenser of 120kV-0.2 μ F, a gas gap switch with a high current capacity of about 100kA, a low impedance coaxial transmission line, and three types of FX tubes, each of a different type. The electric charge stored by the condenser was discharged to the FX tube when the gap switch was closed. For the Type A tube, a conical anode and cathode electrode were employed in order to obtain a smaller focus of less than 0.5mm in diameter and to change the beam quality according to changes in the anode-cathode space. The Type B tube utilized a conical anode and a ring cathode for obtaining a higher intensity and a wider energy spectrum distribution. The Type C tube could produce slightly hard FX by permeating this radiation through various kinds of foil anodes. The cathode electrode was changed to either a conical or a pipe shape according to the radiographic objectives.

MP36.21

A High-Speed Radiographic System Utilizing A New-Low Impedance Flash X-ray Generator, S. Kawasaki*, E. Sato, H. Isobe and T. Yanagisawa, Department of Physics, Iwate Medical University, 3-16-1 Honcho-dori, Morioka 020, Japan

A high-speed radiographic system utilizing a new type of single-shot flash x-ray generator with exposure times of about μ s is described. This system was constructed in order to analyze the high-speed motion of biomedical objects and consisted of the following components: two types of delay switches, a delayed pulse generator, a digital radiography (CR), and a flash x-ray generator developed by the authors. The flash x-ray generator consisted of the following components: a high-voltage generator, a high-voltage pulser, a vacuum pump, and a combined remote x-ray tube with two sets of anode and cathode electrodes. When the radiographic object triggered the delay switch, a short electric pulse was produced and transmitted to the delayed pulse generator. An accurate delayed flash x-ray was produced when the delayed pulse was transmitted to the high-speed impulse switching system inside of the high-voltage pulser. Next, when the radiographic object was exposed to the controlled x-ray under the optimum radiographic conditions, the permeating x-rays produced the digital image.

MP36.22

A High-Frequency Field-Emission X-ray Source for Soft Radiography, E. Sato*, S. Kawasaki, H. Isobe, J. Takahashi, Y. Yasuda, H. Arima, T. Akitsu, S. Oikawa and T. Yanagisawa, Department of Physics, Iwate Medical University, 3-16-1 Honcho-dori, Morioka 020, Japan

A field-emission x-ray source for soft biomedical radiography is described. This x-ray source was constructed in order to obtain a higher dose rate using a cold cathode x-ray tube without a tungsten filament. This x-ray source consisted of the following essential components: a DC-AC converter with an output voltage of 1 to 10kV and a rectangular AC frequency of 2-20kHz, a Cockcroft circuit, a field emission x-ray tube with a rod anode and a ring cathode, and a vacuum pump. The tube voltage and the current were determined by the output voltage of the Cockcroft circuit and the circuit resistance of the discharge line. The spectrum distribution primarily varied according to the tube voltage and the anode material. The effective focal spot size was determined by the diameter of the anode rod and ranged from 0.5 to 3.0mm in diameter. The electric wave form of the tube voltage, the tube current, and the x-ray output displayed a high frequency ripple corresponding to the A-C frequency, but the deviation of the x-ray intensity was only a few percent. Various kinds of soft radiographs were obtained by controlling the radiographic conditions.

MP36.23

Investigations on Developing Mouse Testis after an intrauterine Low-Level Tritiated Water (HTO) Exposure. Sangeeta Pareek* and A.L. Bhatia, Department of Zoology, University of Rajasthan, Jaipur - 302 004, India

Tritium, a radionuclide of hydrogen, may emerge as a major radiopollutant of prime concern from the view point of health hazards. It is also used in tracer study for the determination of total body water. The incorporation of tritium in the genetic constituents (DNA) is of prime concern since its turnover is expected only in the event of cell death. An attempt has been made in the present study to evaluate the changes in total cholesterol, protein and DNA content in the postnatally developing mouse (at 4 and 6 weeks) testis under a continuous tritiated exposure at the dose level of 0.3 μCi (11.1 kBq) and 3.0 μCi (111 kBq)/ml of drinking water from gestation day 18. Cholesterol content increased significantly at both the dose levels. Protein concentration, however, decreased after irradiation. DNA content increased at 4 weeks, but did not show any significant change at 6 weeks after the exposure at both the doses. Besides this, the behaviour of spermatogenic cell populations viz. Spermatogonia A, I, B; Spermato-cytes R, L, Z, P and Spermatis have also been evaluated. Results will be discussed in the light of metabolism of tritium with special reference to testis.

MP36.24

Neurochemical Studies on Developing Mouse Brain under continuous tritiated (HTO) exposure from 17th day in utero. A.L. Bhatia* and Sangeeta Pareek, Department of Zoology, University of Rajasthan, Jaipur - 302 004, India.

The effects of low doses of tritiated water on the neurobiological system have not been sufficiently explored, though it has been demonstrated that after a protracted HTO-exposure, tritium (^3H) is retained in larger amounts for longer duration in mouse brain. Present study is an attempt to evaluate the total cholesterol, glycogen and phospholipid of the brain during postnatal development under a continuous tritiated exposure at the dose level 0.3 μCi (11.1 kBq)/ml of drinking water from gestation day 17. Cholesterol level showed a deficit by 20.92% at 1 week which gradually increased and reached at peak level by 3rd week of age. Thereafter it decreased and achieved a steady state after 4 weeks approximately 27.0% below the control value. An elevated level of glycogen content was marked till 5th week p.p. which decreased at 6th week of age. Phospholipid level was found decreased in all the studied age groups which was pronounced at the early intervals (1-3 weeks). The results will be discussed in the light of tritium incorporation and metabolism of various neurochemical constituents.

MP37.1

HOSPECTRAL IMAGING IN NUCLEAR MEDICINE. D. Gagnon* Montreal Heart Institute, Montreal, QC, Canada.

Holospectral Imaging (HI) is a novel approach to digital image processing in nuclear medicine to eliminate contamination resulting from Compton scattering. The method requires that the energy information is made available for all photons, irrespective to their primary or scatter characteristics. From the HI data, a set of frames representing images at different energies is created which allows for a multidimensional description of the imaging processes. In fact, by multivariate analysis, the original data can be transformed into a series of eigenimages and eigenvalues that made possible the distinction of the specific contribution to the image of both unscattered and scattered photons, and noise. The first eigenimage corresponding to the unscattered image, and the second the image of what cannot be explained by the first namely, the scattered image. The image of the Poisson noise, unstructured by definition, is represented by smaller eigenimage. A filtering process can be performed then to reduce the scattered contribution. Some holospectral images, from computer simulation, phantom and from patient, will be presented and interpreted with the multidimensional language. Preliminary results of the Compton removal capabilities will also be shown.

MP37.2

Chest-Imaging Using Self-Scanning Linear Diode Arrays. D Sashin*, BS Slasky. University of Pittsburgh, Pittsburgh, PA, 15261, USA

A high detail diode array digital chest unit has been developed which produces digital images having a matrix of 2356 x 2000 pixels with a 14 x 16" field of view. This technique achieves high detail through the use of self-scanning linear diode arrays (1024/inch) that have a wide dynamic range and high spatial resolution, which separates this method from other digital radiographic techniques. A very significant feature of our system is the rejection of scattered radiation because of the fan geometry, resulting in increased contrast sensitivity at a lower radiation dose (5 and 10 mR for PA and lateral views, respectively) than that obtained by area imaging techniques. The entire image of the chest is recorded in less than 2 seconds with an exposure time of less than 3 ms. The present machine upgrades our previous model: a) the x-ray tube and detector assembly is moved; b) erect imaging can be taken; c) the field of view has been increased; d) the matrix size has been greatly expanded; and e) a higher resolution rare earth phosphor screen. After reconstruction, the images are digitally processed to improve image quality.

1 7 1

MP37.3

Optical Image Processing with Liquid-Crystal Display for Image Intensifier/Television (II/TV) Systems: Dynamic Range Compression and Signal-to-Noise Ratio Improvement. K. L. Lam*, H.-P. Chan, K. Doi, Kurt Rossmann Lab. for Radiol. Image Research, Dept. of Radiology, Univ. of Chicago, Chicago, IL 60637

We are developing an optical image processing (OIP) device using a liquid-crystal display (LCD) to modify the transfer characteristic of an II/TV imaging system and to perform unsharp masking on the output image from the II. The LCD which is driven at TV frame rate is placed in the optical path between the II and the TV camera, and is displaced from the focal plane of the optical system in order to blur the displayed mask image. By controlling the transmittance of the LCD according to the output image from the II, we can compress the dynamic range of the image detected by the TV camera. Our experimental results demonstrated that compressing the dynamic range of low-quantum-noise image with the OIP device improves the signal-to-noise ratio of the detected image. Furthermore, by an appropriate modification of the transfer characteristic, the detective quantum efficiency over the entire image can be maintained at the level of the high-exposure area of the image.

Supported by USPHS Grant (NIRA) HL 36238, The Whitaker Foundation, and USPHS Grant CA 24806.

MP37.4

On the automatic assessment of Image Quality in Digital Subtraction Angiography
C.H. Slump, Philips and Picker Medical Systems, Eindhoven, the Netherlands.

The important image quality parameters in DSA are: spatial, (low-) contrast and temporal resolution. Furthermore contrast and spatial uniformity, contrast linearity, subtraction artefacts, radiation exposure levels and noise.

The image quality performance is usually evaluated non-invasively by means of appropriate phantoms. The pertinent images are then visually inspected. Resolution test pattern images (line-pairs per millimeter) and contrast-detail (C-d) images are famous for their inter- and intra-observer fluctuations in measured values.

The automatic i.e. the observer independent assessment of the image quality parameters from the phantom images has great advantages for quality assurance programs. The ease of such a procedure for routine checks, and the possibilities for additional computer aided tests (expert system search trees) in case of malfunctioning may also have its impact on remote serviceability.

As example of the above approach the presentation will focus on the automatic evaluation of the DSA system's low-contrast resolution. The procedure is based on signal-detection theory and image processing. A test-statistic is calculated which indicates the likelihood of the presence of a certain contrast at specified false alarm and "miss" probabilities.

MP37.6

FAST AUTOMATIC VESSEL TRACING AND STENOSIS EVALUATION IN DIGITAL SUBTRACTION ANGIOGRAPHY USING SPECIAL PROCESSORS AND PARALLEL ALGORITHMS.

K. Barth*, U. Bittner, B. Eicker, P. Marhoff, SIEMENS AKTIENGESELLSCHAFT, Med. Engineering Group, Henkestr. 127, D-8520 ERLANGEN, West Germany

In the last years fully digital angiographic imaging systems at high resolution have been introduced to clinical application. Matrix sizes of upto 1024 pixels squared and amplitude discrimination with 8 to 10 Bits are available as a standard now. This opens a new perspective for quantitative assessment of fine image structures like stenotic lesions of the coronary arteries. However, the algorithms known from previous systems with cine-film quantitation or with lower resolution have to be basically revised and improved with respect to accuracy and speed of computation. Research on the best way for automatic tracing of vessel center-lines and subsequent border calculation has been carried out in this laboratory investigation. This has lead to refined kernel design for the tasks of vessel detection and geometric or densitometric measurement. Globally correct performance is achieved with dynamic programming on the basis of a minimal cost algorithm. Filtering including median filtering and kernel convolution has been implemented on special hardware, mostly with parallel algorithms, providing fast computation even at the largest matrix size.

MP37.5

Large Field K-edge Subtraction System for Coronary Angiography using Synchrotron Radiation III: High Speed Acquisition of Video Images for the Energies above and below K-edge
K. Nishimura*, K. Hyodo, R. Hosaka, M. Ando, F. Toyofuku, M. Akisada, G. Hasegawa, E. Takenaka, Saitama Medical School, Moroyama, Iruma, Saitama, Japan

We are developing a image acquisition system for K-edge subtraction coronary angiography using I.I. and video cameras. To obtain a K-edge subtraction image of moving coronary vessels as a quasi still image, the energy must be changed rapidly in the order of a few msec. Because the two images appear in the output screen of I.I. subsequently within a few msec, the images cannot be stored in different TV fields but in a same TV field by a conventional method. To solve this difficulties we designed the system consisting of a half mirror, a couple of video camera with optical shutters which were made from PLZT. The optical output of I.I. was divided into two directions by the half mirror. The shutters can be made open and close by applying a voltage to them. With proper timing signals, a video camera can see only the image above the K-edge and the other can see only the image below the K-edge. Blanking technique was used to avoid the adverse effect caused by simultaneous writing and reading of video signal on a video camera. The shutter were found suitable for our purpose with respect to response time and dynamic range.

MP37.7

Topological Image Compression, H. Riml*
McGill University, Montreal H3A 2B4, Canada

Digital images typically contain one megabyte of data. The storage and transmission of such large data sets strain the capacity of current technology. Thus there is need to exploit structural properties of these data sets in any attempt to compress them. We present:

- 1) A FRAMEWORK which allows a classification of traditional approaches to image compression, and arising from this framework
- 2) A new technique called TOPOLOGICAL IMAGE COMPRESSION. It uses homeomorphisms ("rubber-sheeting" transformations) on both geometrical and brightness information of a "reference image" so that it becomes identical to the "target image".
- 3) An ALGORITHM which implements topological image compression
- 4) preliminary analysis of the EFFECTIVENESS of the algorithm for radiological images, which shows that for this very specific application the algorithm outperforms all others by at least an order of magnitude
- 5) A demonstration that a failure of the algorithm to work for "reasonable" distortion coefficients is a strong indicator of potential medical lesions. In this "MASKLESS SUBTRACTION RADIOLOGY" the distorted reference image becomes the mask image for the target image, and the difference between them the potential lesion.

MP37.9

Digital Subtraction Angiography Using an Efficient Method for Scatter Rejection,
D. Plenkovich*, Department of Radiology,
Tulane Medical Center, New Orleans, LA

Scattered x-ray radiation and veiling glare reduce contrast and signal-to-noise ratio in digital subtraction angiography. The use of grids is trade-off between lesser amount of scatter and reduction in the percentage of detected primary radiation, thereby increasing patient exposure. Grids, air gaps, and paired scanning slits are not effective against veiling glare because veiling glare occurs after radiation has passed through any of this antiscatter devices. Highly efficient rejection of both x-ray scatter and veiling glare is achieved using multiple scanning fore slits and computer algorithm which keeps only portion of each digitized image in the projection of the slits. The resultant image is obtained adding a series of slit images together. Digital subtraction angiography of a dog was performed using 8:1 grid and combination of same grid and scanning-slit method. Visualization of small blood vessels is better in the slit-plus-grid image due to superior rejection of scatter and veiling glare. The digital scanning-slit technique increases the signal-to-noise ratio in subtracted image of a 20-cm-thick polystyrene phantom by 50%.

MP37.8

Minimizing Artifacts In Eigenimage Filtering (1)
J.P. Windham*, D.A. Reimann and D.O. Hearshen,
Henry Ford Hospital, Detroit, Michigan 48202.

Eigenimage filtering is a linear filter which produces a composite image from a sequence of images in which a desired feature is suppressed. A potential source of error in the interpretation of filtered images are projection artifacts. Projection artifacts are the result that any pixel vector may be represented as a linear combination of the desired and interfering signature vectors, and a specific vector which is orthogonal to the subspace, $R(d,u)$ containing the desired and interfering signature vectors. That component of the pixel vector parallel to the desired signature vector will be projected into the filtered image, and represents real information or is an artifact. A method which minimizes artifacts has been developed. This method determines a vector which is orthogonal to the subspace, $R(d,u)$. This vector is used to form a filtered image that contains only those pixels whose pixel vectors have a component orthogonal to the subspace, $R(d,u)$. This image is used to form a mask image. Any pixels contained in the mask image are not retained in the filtered image since they may represent an artifact. The technique is demonstrated for simulated and Magnetic Resonance Image sequences.

(1) J. P. Windham, et al, "Eigenimage Filtering in MR Imaging", JCAT 12 (1): 1-9, Jan./Feb., 1988

MP38.1

ISODOSE AND ISOEFFECT DISTRIBUTION FOR BRACHYTHERAPEUTIC TREATMENT PLANNING OPTIMIZATION, A. M. Di Nallo*, L. Begnozzi, L. D'Angelo and M. Benassi, Regina Elena National Cancer Institute, Rome, Italy.

To improve the therapeutic ratio and to reduce late effects in critical organs a treatment planning optimization is needed. Tumor control probability and complications depend on radiobiological and physical factors. An attempt to represent the effect due to these factors has been done; since simple dose computations (Gy) are not suitable, particularly for combined modality treatments, where intracavitary irradiation is used with external beams, an optimized treatment is possible only calculating the "biological effect". A computerized program which works on a PDP11/34 and on an IBM compatible PC has been created. It determines isodose and isoeffect distributions for high dose rate brachytherapeutic sources. Treatment parameters are of maximal importance because of possible complications in critical organs observed with high dose rate irradiation technique.

MP38.2

A Critical Comparison of High and Low Dose Rate Remote Afterloading, Colin G. Orton*, Gershenson Radiation Oncology Center, Harper-Grace Hospitals/Wayne State University, Detroit, MI 48201

The recent surge in interest in high dose rate (HDR) remote afterloading and the availability of HDR equipment make it important to critically compare HDR techniques with the low dose rate (LDR) treatments they are replacing. Even though the HDR modality has been used for many years to treat a variety of diseases, little experience has been gained with these techniques compared with conventional LDR brachytherapy. Hence there is a reluctance on the part of many radiotherapists to even consider adoption of this new technology unless convincing evidence can be given to show that it represents an improvement.

In this paper a critical comparison has been made between these two modalities of radiotherapy, taking into account both physical and biological considerations and, if available, clinical results. In order to quantitate any potential benefits derived by conversion to the HDR technique, a term therapeutic advantage is proposed. Values of the therapeutic advantage have been calculated using various bio-effect dose models and these show that significant advantages can be achieved if the HDR treatments are sufficiently fractionated.

MP38.4

Continuous Vs. Discrete Sources in the Paris System of Implants, J. M. Paul*, R. F. Koch, P. C. Philip and F. R. Khan. NWCH, 800 W Central Road, Arlington Heights, IL 60005

Since the Paris system of interstitial brachytherapy is based on iridium wires, the consequences resulting from the substitution of discrete point sources in afterloading ribbons have been analysed by the authors for single ribbons, and single and biplanar implants. The results of this analysis show that the homogeneity parameters, such as: total activity, treatment volume, total volume that receives over twice the stated dose (rate), average dose rate, etc., for seeds with customary spacing of about 1 cm are comparable to those using wires. It is also found that 1 cm seed spacing often improves the quality of the implants, as measured by an objective parameter called uniformity index, which takes into account both the dose homogeneity and total treatment volume within an implant. This paper is intended to dispel any belief, based on visual effect of isodose curves around discrete sources, that implants with line sources (wires) produce better dose homogeneity.

MP38.3

REPLACEMENT CORRECTION FACTOR IN BRACHYTHERAPY PHOTON DOSIMETRY BY IONIZATION CHAMBERS. G. Arcovito*, A. Piermattei, F. Andreasi-Bassi - Medical School, Catholic University, Rome, Italy

A correction factor for absorbed dose measurements by means of ion chambers at distances-to-source of the same order of chambers' dimensions, as in phantom dosimetry of brachytherapy sources, must be determined to account for effects due both to the replacement of phantom material by cavity air and to finite size of ion chambers. We report measurements by four commercially available ion chambers made in phantom, at distances ranging between 1cm and 10cm from a 192Ir point source of 2mm in diameter and 1mm in height. Absorbed dose values were obtained from ion chamber readings using the Spencer-Attix formulation without introducing correction factors as mentioned above. Deviations from expected dose values up to 20% were found. We present a formulation and a calculation model of a correction factor of chamber readings which resulted dependant, at the shortest distances-to-source, also on these distances, while at the farrest ones it is dependent only on the chamber's diameter and photon energy. A good agreement between our data and results reported in the literature for longest distances-to-source was found.

MP38.5

Planning and Evaluation of Stereotaxic Brain-Tumor Implants of I-125 Seeds, L.L. Anderson*, A.D. Osian and P.B. Sher, Memorial Sloan-Kettering Cancer Center, New York, NY 10021.

An approach to planning stereotaxic I-125 brachytherapy of brain tumors has been developed which involves least-squares optimization of single-seed tube positions within the target contour, followed by a combining of seeds from neighboring tubes in order to reduce the total number of tubes. Seed orientation, which must be specified to include dose anisotropy, is controlled by having all tubes emanate from an extra-cranial virtual entry point. Typically, a standard deviation of 12-15% achieved among target-contour (CT enhancement margin) points for single-seed optimization is increased to 15-20% in the final multi-seed tube configuration. Dose evaluation from post-implant CT images makes use of tube-air as well as seed image data and may involve transformation of achieved seed locations back to pre-implant scans on the basis of specified anatomical points within the head.

MP38.6

Theoretical Evaluation of Dose Distributions in Water about models 6711 and 6702 ¹²⁵I Seeds.
J.F. Williamson* and F.J. Quintero, Dept. of Rad. Oncology, Univ. of Arizona, Tucson, AZ 85724.

We have used the Monte Carlo method to calculate the two-dimensional dose distributions about the models 6711 and 6702 seeds from first principles. Our code models the detailed internal structure of the sources as well as photon absorption and multiple scattering in the medium. At distances of 2 cm to 5 cm, our calculated data are in excellent agreement with the measurements of Ling¹ and Schell². In contrast to their results, which were limited to distances greater than 5 mm, we report artifact-free dose estimates for distances ranging from 0.1 cm to 7.5. A truncated Fourier series is used to describe the Monte Carlo data in terms of a small number of measured coefficients allowing our data to be accurately reproduced for treatment planning purposes. A limited set of experimental data was found to be very useful in optimizing and validating the geometric model assumed by our calculations in the absence of a sufficiently precise description of the seed structure. These validated geometric models can be used with confidence to investigate more complex phenomena such as the dosimetry of eye plaques or of tissue heterogeneities.

¹Med Phys 12: 652-655. ²Int J Radiat Oncol Biol Phys 13: 795-799.

MP38.8

Evaluation of Planar Ir-192 Implants (Using the Three Volumetric Irradiation Indices, C. B. Saw* and N. Suntharalingam, Department of Radiation Therapy and Nuclear Medicine, Thomas Jefferson University Hospital, Philadelphia, PA 19107

The clinical approach for interstitial implants usually is an attempt to deliver a specified dose rate, typically 1000 cGy/day, and also achieve an acceptable dose homogeneity in the treatment plane located at the periphery of the target volume. In this study, planar Ir-192 implants configured to meet the desired clinical goals are quantitatively evaluated in terms of the three volumetric irradiation indices.¹ The planar implants are constructed with ribbons arranged in parallel, comprising of either single or double planes. Each ribbon is made up of uniform activity seeds spaced 1.0 cm apart. These implants are used to treat 1.0, 2.0 and 2.5 cm thick target volumes. The irradiation indices measure the effective coverage of the target volume, the relative dose homogeneity within the target volume, and the volume of normal surrounding tissues being irradiated above the prescribed dose. The optimal ribbon spacing for different size implants are derived from such an analysis.

¹C. B. Saw et al., Med Phys 13, 580, 1986.

MP38.7

Interseed Effects on Dose for I-125 and Ir-192 Implants, Ali Meigooni*, Jerome Meli and Ravinder Nath, Yale University School of Medicine, Dept. of Therapeutic Radiology, 333 Cedar St., New Haven, CT, 06510, U.S.A.

In brachytherapy treatment planning, dose at a point is calculated as the sum of the dose contributed by each individual source in a uniform medium. However, a typical implant has many sources close to each other, so that primary and scattered radiation from one source reaching a point could be affected by the presence of the other sources. Importance of this interseed effect was evaluated for two different multiseed configurations in a solid water phantom: a) for 3 I-125 (Model 6702) seeds, aligned with their longitudinal axes coincident, it was found that the dose along the axis of the seeds equals the sum of the doses from the individual seeds. However, for the 3 seeds aligned with their transverse axes coincident, the dose along the transverse axes of the seeds is about 8% lower than the sum of the doses from the individual seeds; b) for a 2-plane implant, each plane containing a 3 x 3 array of sources in a 1 cm square grid, the results show no interseed effect for Ir-192 sources and a 10% and 20% effect for I-125 Models 6702 and 6711 sources, respectively.

MP38.9

Dosimetric Parameters for I-125 and Ir-192 Sources, K. Weaver*, C. Barnett, D. Huang, C. Ling, M. Schell, V. Smith, Radiation Oncology Department, University of California, San Francisco, 94143.

One task required by an NCI Brachytherapy Contract was to evaluate published dosimetric parameters for commonly used brachytherapy sources. To fulfill this requirement we investigated Ir-192 seeds and two models of I-125 seeds. Measurements were with LiF powder in water-equivalent phantoms. Data were corrected for background, sample mass, and finite detector volume. Results will be discussed in terms of a particular dose parametrization, and will be compared to Monte Carlo calculations as well as published data. Our results agreed well with published data for relative quantities such as radial and angular dose dependence. Our measured value for the Ir-192 dose rate constant was 4.55 cGy cm² mCi⁻¹ hr⁻¹, which also was as expected. However the measured dose rate constants for I-125 seed models 6702 and 6711 were 1.16 and 1.05 cGy cm² mCi⁻¹ hr⁻¹, values well below those in general use.

This work supported by NCI Contract CM-57708.

Section III

Biomedical Engineering Scientific Papers

BE1-A.1

Channels as Enzymes. R.S. Eisenberg, Department of Physiology, Rush Medical College, 1750 W. Harrison, Chicago IL 60612, USA.

Ionic channels are proteins embedded in biological membranes containing an aqueous tunnel that allows ions to pierce the energy barrier of the low dielectric lipid of the membrane. Ionic motion is driven by the gradient of electrochemical potential across the membrane and modulated by the potential of interaction between the ion and the channel protein.

It is useful to think of channels as catalysts for diffusion, as enzymes specialized for passive transport, as molecules which pose many of the same barriers to understanding as enzymes. Topics in enzymology have analogs in membrane biology, e.g. an enzyme's active site \leftrightarrow the channel's pore; enzyme isolation \leftrightarrow separation of conductances or channels; enzyme classification \leftrightarrow channel nomenclature; enzyme specificity \leftrightarrow channel selectivity; enzyme activation \leftrightarrow channel modulation.

The fundamental mechanism of channels—diffusion through a potential field—is more amenable to physical analysis than the fundamental mechanism of enzymes. A random walk in a potential is described by a Fokker-Planck equation that can be solved to give the rate constant of traditional state diagrams of channels. The predictions of these diffusion models can then be compared with experimental measurements of open channel current under a variety of conditions.

BE1-A.3

Sodium-Calcium Exchange in Heart: Regulation by $[Ca^{2+}]_i$. W. Gil Wier, University of Maryland at Baltimore, Baltimore, MD, U.S.A.

Sodium-calcium (Na/Ca) exchange is a process believed to be important in control of contractility and in normal and abnormal electrogenesis in the mammalian heart. Recently, changes in $[Ca^{2+}]_i$ have been recorded that can be attributed to the operation of an electrogenic, voltage-dependent sodium-calcium exchanger in mammalian heart cells. Single voltage-clamped guinea-pig ventricular myocytes were perfused internally with the fluorescent Ca^{2+} -indicator, fura-2, and changes in $[Ca^{2+}]_i$ and membrane current that resulted from Na/Ca exchange were isolated through the use of various organic channel-blockers and impermeant ions. Information on subcellular localization of $[Ca^{2+}]_i$ was obtained by imaging the changes in fura-2 fluorescence with the use of a fiber-optically coupled CCD camera and digital image processing. Depolarization of cells elicited slow, spatially uniform increases in $[Ca^{2+}]_i$, with the maximum increase depending on internal sodium ion concentration, external calcium ion concentration and membrane voltage. Repolarization was associated with the extrusion of Ca^{2+} and an inward current. A mathematical model of Na/Ca exchange has been formulated that can describe these results.

BE1-A.2

STRUCTURE AND FUNCTION OF MEMBRANE CHANNELS. CHEMISTRY AT THE SINGLE MOLECULE LEVEL. Olaf S. Andersen* and Roger E. Koeppe II, Dept. Physiol. Biophys., Cornell Univ. Med. Coll., New York, NY 10021, and Dept. Chem. Biochem., Univ. Arkansas, Fayetteville, AR 72701.

The function of transmembrane channels is determined by the amino acid sequence of the channel-forming proteins and by the three-dimensional folding of the sequence in the membrane. But it is not obvious how functional properties of membrane channels should be predicted from chemical and structural data. To obtain information on this problem, we have used channels formed by the linear gramicidins to examine how the function of a channel is affected by alterations in the channel-forming peptide sequences. The gramicidins are suitable for such studies because the structure of the transmembrane channel is known. This is important for two reasons: one can establish functional criteria for structural invariance among channels; and one can use constraints imposed by knowledge of the channel structure to guide the interpretation of functional results. Channels formed by gramicidin analogues illustrate how single side chain substitutions can result in ten-fold conductance changes without affecting the channel structure. The side chains do not contact the permeating ions, emphasizing that there need not be close proximity between the region where a chemical alteration is produced and the region where the functional perturbation is induced.

BE1-A.4

Enzyme-mediated Ion Transport
J. Mailen Kootsey,
Duke University Medical Center,
Durham, North Carolina 27710, USA

Several ion transport mechanisms known to contribute to ion regulation and electrophysiology in nerve and muscle cells involve the binding of ions to a large protein molecule, followed by a conformational change in the enzyme molecule. Examples of such transport mechanisms include the Na^+ , K^+ ATPase, the Ca^{++} ATPase, Na^+ , Ca^{++} exchange, and Na^+ , H^+ exchange. Both biochemical and electrophysiological measurements have been made on many enzyme transport systems. This paper reviews the theoretical methods used to describe ion transport by enzyme molecules. State diagrams are used to describe the transport process with rate coefficients derived from experimental data and thermodynamic constraints. Net rates are calculated for physiological processes and unidirectional flux rates are calculated for tracer experiments. Classical enzyme calculations were based on analytical solutions of simplified reaction schemes, but numeric solutions by digital computer now make it possible to study the behavior of more complex and realistic reactions.

BE1-B.1

SIMULATION OF MOTOR UNIT ACTION POTENTIALS :
COMPARISON WITH CLINICAL RECORDINGS

Sanjeev D. Nandedkar*, Ph.D.

Duke University Medical Center, Durham, NC 27710

A motor unit action potential (MUAP) is the spatial and temporal summation of action potentials of all fibers belonging to one motor unit (MU). The MUAP waveform depends on the MU architecture, i.e. the number and size of muscle fibers in the MU, the distribution of muscle fibers in the MU territory, etc. The relationship between the MU architecture and the MUAP waveform also depends on the type of the recording electrode. We simulated normal MUs and then altered their architecture to simulate various pathologic processes such as loss of muscle fibers, regeneration of fibers, reinnervation, increased variability of fiber diameter, etc, that are known to occur in nerve and muscle diseases. Single fiber EMG, concentric needle EMG and Macro EMG MUAPs were simulated from simulated normal and pathologic MUs. Although the numerical values of the features of the simulated MUAPs differed from the clinical recordings, simulations demonstrated many patterns of abnormalities seen in nerve and muscle diseases.

BE1-B.3

Phase Locked Loop Method to Process Surface EMG, M.Cesarelli*, R.Castaldo, F.Clemente, M.Bracale, Cattedra di Elettronica Biomedica Nucleo di Ricerca di Ingegneria Medica e della Riabilitazione C.N.R., Faculty of Engineering, University of Naples, Via Claudio 21, 80125 Napoli, Italy.

A new method for evaluating EMG spectral parameters based on the analogue locked loop technique has been proposed.

As P.L.L. technique can be applied to follow the instantaneous frequency of a narrow band signal, the EMG is SSB modulated to obtain instantaneous frequency waveform. The average of the instantaneous frequency of the signal is an unbiased estimator of mean frequency, i.e. muscle fatigue indicator, and the average of its absolute value is the variance of spectrum.

A prototype based on this method has been developed. This application offers the possibility of a real time measurement of surface EMG spectral changes during isometric and isokinetic sustained tasks and is particularly important in applications for studying the muscle fatigue.

BE1-B.4

Principal Component Analysis in Electromyography, N.B. Jones*, P.J. Lago and A. Parekh, University of Leicester, LE1 7RH, U.K., University of Porto, 4000 Porto, Portugal.

Much of the progress in diagnostic medicine depends on the harnessing of computer power. It is now sensible to use extensive data reduction techniques for extracting the essential features from images or signals. Principal component analysis (PCA) is recognised as a potent method of multivariate analysis which dramatically reduces dimensionality and is an efficient aid to classification. The application of this technique to electromyography is particularly attractive because signals arise in this area of clinical practice which contain an extensive amount of information. Not only can PCA be applied directly to the classification of motor unit action potentials but it can also be used for the classification of interference patterns by the prior use of a spectral analysis technique. The progress of neuropathic and myopathic disorders have been followed in simulation using these methods via two and three dimensional displays. Experience with a limited set of real data shows that good separation of cases may be achievable in clinical applications.

BE1-B.5

Magnetomyography: non invasive recording of intracellular currents in skeletal muscle, W.L.C. Rutten *, and J.H.M. Put, University of Twente, 7500 AE Enschede, The Netherlands.

Magnetomyography is a non-invasive technique for the in vivo detection of very weak magnetic fields of active skeletal muscle. In a configuration in which the detection coil has a toroidal shape and in which the muscle is lead through the centre of the toroid, magnetic responses can be measured which correspond to the intracellular longitudinal currents in active muscle fibers. For this the muscle must be enclosed by the toroid as closely as possible and both must be immersed in a well conducting fluid. The system has an average equivalent noise limit of 1 nA/Hz over a bandwidth of 10 kHz. This value is sufficient to measure fields in the order of picoTeslas produced by single motor units in EDL and Tibial muscle of rat and mouse. Responses have a biphasic shape which strongly indicates that the disturbing (triphasic) contributions of fields due to currents in the volume conductor inside the muscle, but outside the active unit, are very small. The method offered us the possibility to make fiber distribution profiles along the muscle, to determine conduction velocities and to measure current-to-force relationships in a way much easier (and non-invasively) than by electrical methods. Combined with EMG measurements and model simulations the method leads to parameter reduction in the models.

BE1-C.2

A Distributed - Parameter Model of the Myelinated Nerve Fiber, J.A. Halter and J.W. Clark Jr., Department of Electrical and Computer Engineering, Rice University, Houston TX 77251-1892

Recent electrophysiological studies on both mammalian and amphibian myelinated nerve fiber have produced new information about the distribution of ionic channels in the fiber, the dynamics of the ionic channels as well as the electrical properties of the myelin sheath and the underlying axolemmal membrane. These studies allow for the formulation of new more explicit models of the nerve fiber, particularly for the internodal and paranodal regions where the passive electrical properties and the function of ionic channels are under debate. For example, the mechanism for the depolarizing afterpotential has been proposed to be storage of charge on the internodal axolemma requiring either a higher conductivity for the myelin sheath than traditionally thought, or a significant conductive path through the periaxonal space. New models can address these issues. In this study, a new distributed-parameter model is developed allowing for representation of both the amphibian and mammalian nerve fiber. The model describes the myelin sheath separately from the axolemma, includes a periaxonal conductance pathway, uses new ionic channel descriptions for the node and internode and incorporates a more explicit description of the nodal and paranodal region than in previous models. The relative influence of these parameters on the behavior of the myelinated nerve fiber will be discussed.

This work supported in part by NSF Grant EC8405435.

BE1-C.1

Leakage Conductances in Axons and their Myelin Sheaths, A. R. Blight*, Purdue University, West Lafayette, IN 47907.

Microelectrode recordings from mammalian axons and their myelin sheaths indicate that there is a descending order of myelin leakage conductance and a balanced ascending order of nodal leakage conductance in the series: central spinal axons, peroneal nerve sensory fibers, peroneal nerve motor fibers. From the aspect of conduction velocity and energetics, the relative distribution of conductances between node and myelin appears to be of little consequence over a wide range, as long as the combined input impedance of the fiber is optimal. Relative variations in myelin sheath nodal conductance appear to be significant for other aspects of axon function, among which threshold modulation and accommodation are the most obvious possibilities, though the broader functional significance of differences in these properties is not yet well understood.

BE1-C.3

Magnetic Measurements of Action Currents in Bundled Nerves, J.P. Wikswo, Jr.* and R.S. Wijesinghe, Vanderbilt University, Nashville, TN 37235 USA
We are using toroidal pickup coils and a low-noise current-to-voltage converter to record the magnetic field produced by the compound action current (CAC) propagating along isolated nerve bundles from the earthworm and frog. By assuming the shape of the transmembrane potential, we can use our volume conductor model for an axon off-center in a sheathed, anisotropic bundle to compute the single-fiber action current (SFAC) and potential (SFAP). By coupling this model with a non-negative least-squares algorithm, we can deconvolute both the CAC and the conventionally-recorded compound action potential (CAP). The resulting conduction velocity distributions (CVDs) are compared to the fiber diameter histogram (FDH) obtained histologically. In this inverse calculation, the intracellular and extracellular conductivities, temperature, and the distance between stimulus and recording sites are the most important parameters; the extracellular conductivity and the thickness and conductivity of the myelin sheath affect the CVD from the CAP more than the CVD from the CAC. The slower conduction velocity classes of both CVDs are affected by noise more than the faster classes. The volume conductor model, the CVDs, and the FDH are used to reconstruct the CAC and CAP. Because the SFAC is biphasic while the SFAP is triphasic, the CAC has less cancellation than the CAP, suggesting that CAC deconvolution may be more accurate than CAP deconvolution.

BE1-C.4

A Double-SFAP model for the Nerve Compound Action Potential, G. Contento*, M.R. Malisan and R. Budai, Depts of Medical Physics and Neurophysiopathology, Ospedale S. Maria della Misericordia, Udine, Italy.

The conduction properties of peripheral nerves can be characterized by the distribution of conduction velocities (DCV) of the constituent fibres. Methods for the estimation of DCV rely on a linear model of the Compound Action Potential (CAP) which can be easily measured in vivo. A basic assumption of the model requires that a unique waveform of the Single Fibre Action Potential (SFAP) is representative of the whole class of fibres conducting at a given range of velocities. Failure of this assumption may concern initial neuropathies where normal and pathological fibres co-exist in the same nerve and conduct at the same velocity but with different SFAP waveforms. The present model of the CAP allows a weakened assumption on fibre grouping and describes the conduction of both kinds of fibres. Due to the invariance of the model to a set of linear transformations, an external input other than the measured CAPS is necessary in order to resolve the DCV of both fibre groups and their relative contribution.

BE1-D.2

A Model of Reentry Based on Anisotropic Discontinuous Propagation, M.S. Spach*, P.C. Dolber, J.F. Heidlage, Duke University, Durham, NC, USA

Available models of cardiac reentry depend solely on the active membrane conductances to alter propagation. The purpose of this paper is to show that different anisotropic passive properties produce different propagation responses to the same change in the sodium conductance. In uniform anisotropic bundles, premature action potentials propagated as a smooth process until propagation ceased simultaneously in all directions. In nonuniform anisotropic bundles, however, early premature action potentials produced either unidirectional longitudinal conduction block or a dissociated zigzag type of longitudinal conduction (a safer type of propagation similar to transverse propagation). Directional differences in velocity demonstrated that anisotropic propagation was necessary for reentry to occur within an area less than 50 mm². Sodium channel blocking drugs also produced dissociated zigzag longitudinal conduction in nonuniform anisotropic bundles, but not in uniform anisotropic bundles. These results show that obliteration of side-to-side electrical coupling between fibers provides a primary mechanism for reentry to occur within very small areas (1-2 mm) due to propagation phenomena that do not occur in tissues with tight electrical coupling in all directions.

BE1-D.1

Effects of Tissue Geometry on the Initiation of a Cardiac Action Potential, R.W. Joyner*, Departments of Pediatrics and Physiology, Emory University, Atlanta, GA 30322

We used rabbit papillary muscles (PM) and isolated ventricular muscle cells to compare the effects of Lidocaine on decreasing cardiac excitability. For the PM we defined tissue excitability as the inverse of the current required to initiate a propagated action potential from a local stimulus. For the isolated cells we defined cellular excitability as the inverse of the current required to initiate a membrane action potential. For PM, Lidocaine with elevated $[K^+]_o$ decreased \dot{V}_{max} , decreased conduction velocity, and strongly decreased tissue excitability. For the isolated cells, Lidocaine with elevated $[K^+]_o$ decreased \dot{V}_{max} but had little effect on cellular excitability. We interpret our results on the differences of effect on tissue excitability versus cellular excitability as a consequence of the syncytial nature of the PM. The electrical load of the surrounding cells makes the tissue excitability dependent upon the amount of inward current that the locally excited cells and the surrounding cells can generate. We successfully simulated these phenomena with numerical solutions of action potential initiation in an isopotential cell as compared to a two dimensional disk of excitable tissue.

BE1-D.3

EXCITABILITY, SAFETY FACTOR OF PROPAGATION AND PREFERENTIAL BLOCK IN ANISOTROPIC TISSUE

Bruce M. Steinhaus*, Ph.D., Carmen Delgado**, Ph.D. and Jose Jalife**, M.D., *Univ. of Utah, Salt Lake City, UT, **SUNY/Upstate Medical Center, Syracuse, NY

The success or failure of propagation in anisotropic myocardium was studied using simulations of action potential propagation and isolated tissue experiments. Longitudinal (L), uniform transverse (UT) and nonuniform transverse (NT) tissue directions were modeled in a Beeler-Reuter based one dimensional cable. Stimulation threshold was smallest in the NT direction. The safety factor during propagation was determined as the total axial current during depolarization divided by the current just necessary for continued propagation and was largest in the L direction. The strength-interval plot for the junction between L and NT directions identified a range of stimulus strengths which resulted in NT but not L propagation at the basic cycle length while higher stimulus strengths resulted in L but not NT propagation. Experimental strength interval plots from 10 L shaped preparations of isolated sheep epicardial muscles had similar characteristics. Results show directional differences in excitability and safety factor of propagation in anisotropic tissue. These properties can be a major factor in the genesis of reentrant arrhythmias.

BE D.4

Contribution of active Na-K transport to membrane repolarization, F.A. Roberge and R. Lemieux, University of Montreal, Montreal, Canada.*

The small size of cardiac cells, the restricted myocardial interstitial space, and the relatively important Na^+ influx and K^+ efflux create conditions leading to substantial changes in $[\text{Na}]_i$ and $[\text{K}]_e$ during the action potential. An efficient Na-K pump, sensitive to both $[\text{Na}]_i$ and $[\text{K}]_e$, is then necessary to restore as much as possible of the original Na^+ and K^+ gradients at each cardiac cycle. These variations in $[\text{Na}]_i$ and $[\text{K}]_e$ induce important changes in the passive membrane currents via the corresponding changes in equilibrium potentials. These factors, together with the Na-K pump current, determine the shape of the action potential. A model of the cardiac cell membrane incorporating active Na-K transport was used to study the ionic current changes occurring during the action potential, following repetitive stimulation at rates between 0.2 and 3.3/s. The diastolic levels of $[\text{Na}]_i$ and $[\text{K}]_e$ increase at higher frequencies since the pump cannot maintain the concentration values absolutely constant. It is observed that the contribution of active Na-K transport to membrane repolarization becomes increasingly important as the rate of activity increases.

BE1-E.2

FUNCTIONAL ELECTRICAL STIMULATION OF THE PARALYZED LARYNX, I. Sanders* MD, Mount Sinai Medical Center, New York, NY 10029

In laryngeal paralysis the vocal cords come together in the midline of the larynx and cause a life threatening airway obstruction. To rehabilitate this condition function must be restored to the muscle which controls vocal cord opening, the posterior cricoarytenoid (PCA) muscle. The unique challenge is that the PCA muscle is in a denervated condition and to date there has been little research performed on the stimulation of denervated muscle.

Initially 12 dogs were studied under varying conditions of electrode placement, electrode polarity, electrode orientation to muscle fibers, and over a wide range of pulse width and pulse amperages. From this original study an electrode array was adopted for chronic experimentation. Four dogs were allowed to atrophy for six months and at the end of that period two of the dogs underwent three months of electrical stimulation by implanted electrodes.

Results indicated that a variety of stimulation parameters and electrode arrays are capable of causing clinically useful vocal cord opening. In addition prolonged stimulation can restore function to severely atrophied PCA muscle. Further research is required into an electrode array which localizes current to the PCA so that current does not spread to surrounding structures.

BE1-E.1

UPPER EXTREMITY ASSIST DEVICES, P.H. Peckham*, M.W. Keith, G.B. Thrope, and K. Stroh, Case Western Reserve University, and the Veterans Administration Medical Center Cleveland, Ohio 44109

Functional neuromuscular stimulation (FNS) has been developed to provide control of the paralyzed extremity of the cervical level spinal injury patient. Subjects are implanted with either percutaneous electrodes or an implanted stimulator to provide activation of the muscles. The electrodes are implanted in the major finger and thumb flexor and extensor muscles, and coordinated movement patterns are controlled by a portable external control module. Movement of the shoulder regulates hand opening and grasp in two grasping configurations.

Subjects with FNS systems demonstrate the ability to perform activities of daily living such as eating, writing, and grooming that they are unable to achieve without the assistive system. Such systems have been in outpatient use for over five years. Recent developments, including combining surgical reconstruction and the implantable stimulator, have further improved function and reduced the user's care and maintenance of the system.

Supported by the National Institute on Disability and Rehab. Research and the Veterans Administration Rehab. Research and Development Service.

BE1-E.3

Cardiac Assist Device: Larry W. Stephenson, M.D.,* Dept. of Surgery, University of Pennsylvania, Philadelphia, PA 19104, U.S.A.

Skeletal muscle can respond adaptively to increased functional demands. This adaptive capacity is commonly observed during the training of athletes, but to a greater extent when skeletal muscle is subjected to chronic electrical stimulation. Muscle conditioned in this way shows a greatly increased resistance to fatigue. During the stimulation process, the muscle is transformed from a muscle of mixed fiber type to one of a uniform population of type I fatigue-resistant fibers. The changes are documented by immunohistochemical criteria. Myosin isozymes change. There is an enzymatic shift toward aerobic metabolism. The bioenergetics of electrically conditioned muscle are similar to those of heart muscle. We have exploited this transformation phenomenon to develop skeletal muscle ventricles capable of performing the continuous work required to assist the failing heart. These ventricles generate greater stroke work than the right ventricle, and can pump blood in the circulation effectively for weeks. This research indicates that a chronic non-fatiguing biologic pump motor constructed from skeletal muscle appears to be achievable. This concept holds promise for long-term augmentation or replacement of the failing cardiac ventricles.

BE1-E.4

Collision Block of Motor Activity in Peripheral Nerve. James D. Sweeney, J. Thomas Mortimer, Donald R. Bodner and A. Stewart Ferguson, Applied Neural Control Laboratory, Dept. Biomedical Engineering, and Division of Urology, Dept. of Surgery, Case Western Reserve University, Cleveland, Ohio 44106.

Collision block of efferent motor activity may offer a clinically viable alternative to other techniques for electrically blocking peripheral nerve transmission. A collision block will result when artificially produced Antidromic Unidirectionally Propagating Action Potentials (AUPAPs) annihilate orthodromic action potentials. We are developing implantable "spiral" nerve cuff electrodes that can reliably produce such AUPAPs.

These Asymmetric Two Electrode Cuffs (ATECs) are specifically designed to produce a collision block of pudendal nerve motor activity. Pudendal nerve mediated spasticity of the perivestibular striated sphincter has hindered attempts by others to develop a bladder neuroprosthesis for spinal cord injured patients. In acute animal experiments we have studied the effectiveness of the ATEC design in producing trains of pudendal nerve motor AUPAPs between 1 and 50 Hz. Both monophasic and balanced-charge biphasic quasitrapezoidal stimuli have been used. In chronic animal experiments the long-term effectiveness and safety of pudendal nerve collision block is currently being studied. A finite-difference model of the electric field generated by an ATEC is also being developed as an aid for electrode design.

BE1-F.2

A Task Analysis Strategy for Modeling and Assessment of Human Locomotion. James J. Carollo*, Human Performance Institute, University of Texas at Arlington, Arlington, TX 76019

The problems associated with gait assessment are due in part to the absence of global models of human locomotion, incorporating both biomechanical and neurophysiological information. Task analysis has been employed to simplify model development, and coupled with resource based performance theory, provide a framework for assessment.

Walking is described as a repetitive sequence of tasks where each task in the sequence has specific objectives which must be accomplished within the time period allotted. The CNS is modeled as a controller which translates these objectives into descending neural commands (resources), targeted for the functional units (muscles) associated with the current task. A biomechanical model of the trunk and lower extremities is used to determine the resultant joint angles and torques associated with the neural input, with these values used to simulate afferent feedback.

* Supported by Dallas Rehab Foundation

BE1-F.1

Theoretical Basis for Brain Motor Control Assessment. G.V. Kondraske*, Human Performance Institute, University of Texas at Arlington, Arlington, TX, USA. (17-273-2335)

Sound conceptual bases which lead to testable hypotheses are essential for assessment of complex systems, such as in brain motor control. Generalizable performance theory concepts are presented as a basis for defining basic elements of performance and for structuring a quantitative approach to assessment in this area.

An elemental resource modeling approach is used to define structures functionally and dimensionalized performance measurands. Maximal stresses along isolated dimensions of performance are used to determine resources available. Task analysis is used to define a series of worst-cases unidimensional stresses on system resources. Resource economic principles are applied to a multi-dimensional and multi-unit system model to define simple criteria oriented rules for assessment. Combinatorial optimization to minimize stress across performance resources is considered as a control strategy and discussed in the context of assessment. Supportive experimental data are presented. Experimental approaches are discussed.

BE1-F.3

Assessment of Healthy and Disordered Neurocontrol of Gait. M. Malezic*, M. Gregoric and J. Krajnik, J. Stefan Institute, and University Rehabilitation Institute, Jamova 39, 61001 Ljubljana, Yugoslavia

Central nervous system control of muscles during gait can be seriously altered in patients with the upper motoneurone dysfunctions. In incomplete spinal cord lesions, the impaired supraspinal control results in diminished centrally programmed and suprasegmental reflex activity with increased segmental reflexes. EMG recordings of muscle activity during walking combined with measurements of forces and phases of gait may so help in understanding the pathophysiology of abnormal locomotor patterns, as well as in evaluating the restorative procedures. Centrally programmed control is assessed in the tibialis anterior muscle, normally active when unloaded, while soleus, the antigravity muscle, is a monitor for suprasegmental and segmental stretch reflexes. Changes in the averaged rectified and filtered EMG signals are studied before the foot contact, within the latency ranges of segmental and suprasegmental reflexes after it and before the push-off.

BE1-F.4

Polyelectromyography (PEMG) as a Tool to Evaluate the Efficacy of Therapeutic Manoeuvres in Motor Disorders, B. Cioni*, M. Meglio, Facolta' di Medicina e Chirurgia, Largo Agostino Gemelli, 8, 00168 Roma, Italy

Surface PEMG was used to assess modifications of motor control following therapeutic manoeuvres in 40 patients. A percutaneous test trial of spinal cord stimulation was performed in 33 of them. 13 with spastic hemiparesis due to ischemia of the middle cerebral artery, 13 with spastic paraparesis from a spinal lesion and 7 with multiple sclerosis. 5 patients with spinal cord lesions received intrathecal injection of anti-spastic drugs and 2 patients underwent surgical removal of a spinal compression. Surface EMG of the upper and/or lower extremity muscles was recorded (t.c. 0.03 msec, 15 mm/sec, 100 uv/cm) during spontaneous relaxation, voluntary and passive movements, provoked clonus, phasic and tonic stretch reflexes, Babinski's response and gait. The evaluation included neurological examination and the use of semi-quantitative scales to score motor activity. The protocol was done before and after the therapeutic manoeuvres. The results were consistent with the clinical outcome in all patients. Analysis of the EMG recordings allowed speculation on the mechanisms involved in the therapeutic procedure and the neurophysiological criteria for the selection of patients.

BE1-G.1

Cardiac Potential Mapping in the United States. R. Lux*, Cardiovascular Research and Training Institute, University of Utah, Salt Lake City, Utah

Electrocardiographic potential mapping in the U.S. has expanded from the body surface mapping studies of two decades ago to include cardiac surface and transmural measurements of the present. Research is progressing along theoretical, experimental and clinical lines. Major emphasis of body surface mapping is application to noninvasive detection and assessment of cardiac diseases missed by conventional electrocardiography, e.g., coronary disease without infarction, cardiomyopathies, and arrhythmia vulnerable states. Availability of high resolution torso and heart images and cardiac surface potential information has renewed interest in forward and inverse models for purposes of characterizing normal and abnormal cardiac electrophysiology. Intramural and cardiac surface potential mapping has rapidly evolved for use as a tool for intraoperative mapping to assess ventricular arrhythmias and to understand the 3D spread of excitation and recovery. The latter is of particular interest for improving understanding of the effects of anisotropy on cardiac conduction.

BE1-F.5

Comprehensive Assessment of Control of Motor Activity: Brain Motor Control Assessment (BMCA), A.M. Sherwood*, M.R. Dimitrijevic, Division of Restorative Neurology and Human Neurobiology, Baylor College of Medicine, 7000 Fannin Suite 2140, Houston TX 77030

The objective of this project is to develop a clinical system for the automated assessment of the control of movement in humans when that control is impaired by severe trauma or disease. Surface EMG signals offer an available method for understanding motor activity related to movement. Computerized methods for assessment of neurocontrol of motor activity based on EMG recordings from multiple muscle groups are being developed. Along with 12-16 channels of surface EMG, the BMCA protocol utilizes event markers and position transducers to record voluntary automatic and reflex maneuvers. The BMCA system is based on an Apollo 4000 workstation with a SignifiCAT ADC board and software. Features of neurocontrol in individual patients are documented for studies of underlying motor control mechanisms in humans. BMCA is also used in single or longitudinal studies of the properties of malfunctioning nervous systems. Specific goals include: protocol assistance, comprehensive data logging, quantitative results, and classification of the type and severity of the functional disorder.

BE1-G.2

User-friendly body surface potential mapping in myocardial infarction. Fred Kornreich* and Mikhail Kavadias. Free University Brussels (VUB), Belgium.

Body surface potential maps (BSPM) provide more information on the electrical activity of the heart than can be obtained from the standard 12-lead ECG or the VCG. Moreover, sequential instant-by-instant maps allow direct association of surface potentials with major wavefronts within the heart and have advanced the electrophysiologic bases of diagnostic ECG criteria. Despite these advantages, widespread use of maps as a diagnostic tool is still lacking; the non-traditional data display and the insufficient accumulation of clinical-pathologic correlations are at present, the main factors hampering acceptability by the clinical community. Using 120-lead data from 236 normal individuals and 258 patients with documented first Q-wave myocardial infarction (MI), qualitative and quantitative interpretation criteria are determined and presented in a format that can be easily viewed and interpreted by the cardiologist. The method rests on the development of *discriminant maps*, obtained by subtracting at each instant group-mean normal maps from respectively anterior and inferior MI group-mean maps and dividing the resulting values at each electrode site by the corresponding pooled standard deviation. Similarly, discriminant maps are produced for each single individual and indicate the presence, location and timing of significant abnormalities. By quantitatively extracting and displaying abnormal features in individual patients and in particular, significant losses of potentials in early and mid QRS, MIs could be identified and located at first glance by the cardiologist, however little familiar he may be with BSPMs. The developed criteria can easily be implemented in knowledge-based systems for computerized analysis of maps.

BE1-G.3

Recent Japanese Contribution to Cardiac Potential Mapping, K.Harumi*, H.Stunakawa, G.Nishiyama, S.Kanesaka, Y.Okamoto* and T.Musha*, Showa Univ. Fujigaoka Hosp. Tokyo Inst. Technol*, Yokohama, Japan

Since the body surface mapping systems was introduced by Yamada to Japan, many research works were contributed to the field of the body surface map(BSM) in our country, the detection of breakthrough of right ventricular excitation, the localization and size of myocardial infarction, the location of preexcitation, the site of conduction block in RBBB, exercise BSM, and so on. Recently a standardization to enable the exchange of mutual BSM data from different institutions was proposed by Japanese group. As one of application of BSM to clinical use, we developed with Musha's group the method to evaluate the nondipolar contents(the residue) on the BSM. The following results have been obtained; two peaks of the residue during QRS and single dipolarity during T in the normals, the higher residue in the early part of QRS in anterior infarction and also in inferior infarction, which has the higher residue in later part of QRS, the inverse relation of the residue at middle of QRS and the size of anterior infarction, the higher residue in early QRS as the evidence of infarction with CLBBB and others.

BE1-H.1

Simulation of Normal and Epileptiform EEGs with Chaotic Solutions of Static Nonlinear Coupled Ordinary Differential Equations. Walter J. Freeman*, University of California, Berkeley California 94720

Measurements of the fractal dimensions of normal and epileptiform EEGs recorded from the olfactory bulb and prepyriform cortex of waking rats and rabbits indicate that the aperiodic and unpredictable activity, previously thought to be "noisy", has low dimensionality consistent with deterministic chaos. Sets of differential equations are constructed in accordance with the known physiological and anatomical properties of the bulb and prepyriform and their neurons. The solutions contain domains of chaotic behavior closely resembling "spontaneous" EEG activities in a variety of normal and pathological states, including basal chaotic background activity, bursts with inhalation, and repetitive spikes and waves that accompany complex partial seizures known also as petit mal epilepsy.

BE1-G.4

Substantiation of a Practical Lead System for Electrocardiotopography, P. Kneppo* and L.I. Titomir, Institute of Measurement and Measuring Technique of the Slovak Academy of Sciences, 842 19 Bratislava, Czechoslovakia

Three rows of eight electrodes symmetrically distributed in horizontal planes and electrodes on the head and left leg are used. The instantaneous potential distribution all over the chest surface can be reconstructed by means of expansion of this distribution in the series of spherical functions up to the 3-rd order terms. The expansion is calculated with respect to variables expressing the lengths of mutually orthogonal arcs along the chest surface. Then the coefficients of the expansion are determined as linear functions of the potentials measured by the unipolar leads of Nelson's system. Applying a similar expansion also to the cartesian coordinates of the chest surface, it is possible to obtain rather simple expressions for low order multipole components of the cardioelectric generator. Simultaneous use of Nelson's lead system and the techniques of spherical functions expansion significantly simplifies topographical measurement and multipole analysis of the cardioelectric field.

BE1-H.2

Spontaneous Cellular Population Oscillations in Hippocampal Slices. R.D. Traub*, R. Miles and R.K.S. Wong, IBM Watson Research Cir., Yorktown Heights, NY 10598 and Dept. of Neurology, Columbia University, New York, NY 10032.

Oscillations in large neuronal populations (thousands of cells) occur in *in vitro* hippocampal slices, especially when synaptic inhibition is partially suppressed. Periods range from a few hundred ms to several seconds. Treatments such as further blockade of inhibition that increase the amplitude of such oscillations also diminish the frequency. These activities are detected by dendritic field potentials or by dual intracellular recordings. They also occur in a randomly connected network model with a random distribution of spontaneous bursting rates, provided that intrinsic cellular properties and synaptic actions and connectivities are based on physiological data. In the model, the period and amplitude are influenced by the time course of the long intrinsic afterhyperpolarization, the strength of recurrent excitatory synapses, and the time course of slow IPSPs. While the population as a whole oscillates (every few hundred ms, a cluster of about 1% of the cells fires a burst, generating synaptic potentials in most of the rest of the cells), the cellular composition of the clusters has no apparent periodicity. Globally coherent oscillations also occur in a model with 9000 pyramidal cells wherein the synaptic connections are spatially restricted (as suggested by recent data). In such distributed models, the frequency of the oscillation does not depend on the total number of cells, but only on the local network properties. *In vitro* oscillations may provide insight into general rhythmic possibilities of isolated cortex.

1.04

BE1-H.3

Dynamics of the EEGs as Signals of Neuronal Populations (Alpha Rhythms): Linear and Non-linear Properties, F.H. Lopes da Silva*, Biological Center, Universiteit van Amsterdam, 1098 SM Amsterdam, The Netherlands

Models of neuronal populations can be useful to understand how EEG signals are generated and propagated in the brain. To simulate alpha activity as function of both space and time a model of a simplified cortical network was constructed. The time-dependent behavior of the neuronal membrane potentials was described by linear transfer functions. Static nonlinearities relate membrane potentials to impulse densities. The spatial-dependent behavior was described by exponentially decaying functions of the type $C(x) = C_1 \exp(-c|x|)$ where $1/C$ is the characteristic length. The model generates alpha activity with characteristics in agreement with experimental data. From the phase shift at the alpha frequency as function of space the characteristic lengths of the neuronal network were computed. These were found to be of the same order of magnitude as the basic cortical module estimated from histology. Linear and non-linear properties of this type of models including the transition between linear and nonlinear dynamic behavior, as seen during epileptic seizures, are analysed.

BE1-I.2

Current Distributions in Bisyncytial Tissue, J.P. Wikswo, Jr.*, B.J. Roth and N.G. Sepulveda, Vanderbilt University, Nashville, TN 37235 USA
The electrical behavior of cardiac tissue has been studied using an idealized 2-dimensional, finite-element model that accounts for the bisyncytial nature of the tissue and the anisotropy of both the intracellular (IC) and extracellular (EC) spaces. Previously we examined current, voltage, and magnetic field distributions from a circular activation wavefront for various anisotropies. We have now determined the IC, EC, and transmembrane (TM) potentials resulting from injecting current (1) into the EC space, and (2) into both the IC and EC spaces. In (1) the isopotential distribution (ID) is elliptical for both the EC and IC spaces. The TM ID is elliptical only for equal anisotropy ratios (EAR), and complicated for other anisotropies. In some cases depolarized and hyperpolarized regions are adjacent, which may have implications for reentry, fibrillation and defibrillation. In (2) the ID for the IC and EC spaces is not elliptical; the TM ID has an unexpected pattern and both depolarized and hyperpolarized regions are present. These results are compared to *n vivo* measurements of virtual cathode sizes. We conclude that in 2-D anisotropic tissue, current injection results in spatially intricate potential and current distributions that depend strongly upon tissue anisotropy. Some of these effects were not previously recognized because other models used only equal anisotropy ratios.

BE1-I.1

Biphasic Waveforms for Defibrillation, J. Jones* and R. Jones, Georgetown University and V.A. Medical Center, Washington, D.C., U.S.A.

Automatic internal defibrillators have been developed for implantation in high-risk patients whose arrhythmias are refractory to drug treatment. However, due to the high defibrillation threshold for the existing monophasic truncated exponential waveform, these defibrillators are heavy and bulky, and the high currents required can induce ventricular dysfunction. Since defibrillation results from excitation of ventricular cells, we studied relative excitation and dysfunction thresholds for biphasic waveforms in the cultured cell model and possible mechanisms for threshold alteration with computer simulations of stimulated cardiac action potentials. Shaped biphasic waveforms produced a significantly larger decrease in excitation threshold under "fibrillation conditions" (high K_0 and short cycle length) than under normal conditions in the cultured cell model. Computer simulations suggest that the decreased threshold is due, in part, to improved fast excitation channel activation with biphasic waveforms. Similar biphasic waveforms decreased defibrillation threshold in the dog, calf, and perfused rabbit heart models. These results suggest that biphasic waveforms decrease defibrillation threshold by improving excitation of ventricular cells in the fibrillating heart.

BE1-I.3

Simultaneous Potential Field and Cardiac Recordings from the Heart During Ventricular Defibrillation.

F.X. Witkowski* and P.A. Penkoske, University of Alberta, Edmonton, Canada.

Electrical defibrillation (DF) is the only known generic form of therapy for ventricular defibrillation. We have developed a three-dimensional electrophysiological mapping system capable of simultaneously recording both the actual high voltage field created by a DF shock and the immediate post-shock activation. Using transmural directly-coupled (DC) electrodes 120 left and right ventricular sites were examined with a newly developed DC mapping system. Each electrode was coupled to 2 amplifiers (DC-500 Hz) one with a dynamic range of $\pm 130\text{mV}$ (electrogram) and the other $\pm 500\text{V}$ (DF field).

Successful DF required 100% of the sites examined to be depolarized, with the first beat post-DF originating in the area of minimum DF potential. Unsuccessful defibrillation demonstrated at least one site of ineffective DF that correspond to the area of minimum DF potential.

BE1-I.4

3D FINITE ELEMENT ANALYSIS OF INTERNAL DEFIBRILLATION - N. Thakor, K. Kothiyal, B. Shankar, L. Fogelson, Biomedical Eng., Johns Hopkins University, Baltimore, USA

In internal defibrillation high energy shocks are delivered by epicardial patch electrodes or endocardial catheters. A finite element method (FEM) is used to numerically solve Laplace's equation for the heart modelled as a volume conductor. A computer model is constructed from 1473 elements and 2063 nodes. FEM solves current density (CD) and energy (EN) distribution in the heart for three electrode configurations- patch-patch (PP), catheter-patch (CP) and catheter-catheter (CC) - and various geometries and placements.

The simulations indicate that: 1) PP and CP more effectively deliver EN to myocardium (82% and 80%) as compared with CC (68%). 2) Specific electrode placements do not significantly affect EN delivery to myocardium. 3) Electrode size significantly affects EN distribution, especially in the vicinity of electrodes. 4) Only a small fraction of the myocardium receives high CD (50% at 0.1 A/cm² and 4.3% at 0.5 A/cm²). 5) Very high CD (1.67 A/cm² in CC and 1.14 A/cm² in PP) are observed at the edges of electrodes. These results suggest effective electrode designs and the role of EN and CD in internal defibrillation.

BE1-J.2

Quantitative Analysis of EEG Activity: Is There Chaos In The Future? Ben H. Jansen*, University of Houston, Dept. of Electrical Engineering, Houston, TX 77004, USA.

The quantitative analysis of the 'spontaneous' electrical activity of the brain (EEG) is aimed at providing the electroencephalographer (EEG'er) with 1) an objective tool to analyze EEGs, and/or 2) with a sensitive tool to extract information from the EEG not obtainable otherwise. Early techniques were either heuristic or based on adaptations of methods originally designed for other applications. More recently, methods have been developed that take the specific characteristics of the EEG into account. For example, syntactic methods and (adaptive) segmentation techniques were developed to deal with the nonstationary nature of EEGs; the importance of contextual information was acknowledged through the use of expert systems to allow for reasoning involving complex spatial and temporal relationships utilized in the visual EEG analysis. Even more recent are methods based on a *model* of the neural masses, involving non-linear differential equations that exhibit a 'chaotic' (as opposed to a random) behavior with a striking similarity to the actually recorded EEG. This paper will present a critical review of these state-of-the-art techniques.

BE1-J.1

EEG Evoked Response
Quantification and Detection
Jorge I. Aunon*
Colorado State University
Ft. Collins, CO 80523

Evoked brain potentials have been used for many years to evaluate the activity of selected sensory systems. Traditionally, averaging has been used as the tool of choice in order to extract the average evoked brain potential from the on-going EEG. During the last 15 years a diversity of new techniques have been developed in order to quantify the single evoked potential. Some of these techniques will be described and compared. Ultimately, the question must be asked as to whether these techniques have really made an impact on the knowledge of evoked potentials.

BE1-J.3

SPATIAL DISPLAY AND ANALYSIS OF EEG/EP DATA.
D. Lehmann*, Dept. of Neurology, University Hospital, CH-8091 Zurich, Switzerland.

Prerequisite for correct spatial display ("mapping") of EEG/EP data is adequate spatial sampling. Treatments (means, differences, correlations) over maps require locally unique values, obtained by spatial offset removal (av. ref.) or high pass filtering (gradient, CSD). Data reduction of map series should be space-oriented. Spatial analysis aims at the recognition of the "electric landscapes" for which e.g., the locations of the positive and negative extreme potential might be used. Adaptive segmentation of EEG/EP map series into epochs of stable map landscapes identifies brain functional microstates. Different microstates might manifest different steps or modes of brain information processing, e.g., different states at stimulus arrival are associated with different behavioral outcome of processing (reaction time), and attending vs ignoring incoming information produces landscape differences in a given segment of the event-related map series.

BE1-K.2

The Design of Multiple Electrode Mapping Instrumentation.

F.X. Witkowski* and P.A. Penkoske
University of Alberta, Edmonton, Canada.

Improved methods for assessing three-dimensional distributions and rapid temporal changes of activation, repolarization, systolic and diastolic potentials in extracellular unipolar electrogram recordings would enhance studies of arrhythmogenesis. To assess all these parameters requires directly coupled (DC) mapping techniques.

Mapping systems to date have been limited by physical constraints of electrode design, number of channels simultaneously sampled, duration of continuous data storage and three dimensional representation of the data. Approaches to each of these problems will be discussed. A new system that has recently been developed will be presented capable of DC transmural myocardial interrogation from 384 channels simultaneously, each channel sampled at 2KHz, capable of continuous storage of 3,500 MBytes (60 minutes), with fully automated data analysis and three dimensional data presentation.

BE1-K.3

Mapping Electrical Impulse Propagation in the Heart for the Study of Cardiac Arrhythmia Mechanisms, Andrew L. Wit*, Columbia University, New York, New York.

Myocardial infarction in humans results from obstruction of a coronary artery that results in death of cardiac muscle. Infarction is accompanied by disturbances in the rhythm of the heart beat. Eventually ventricular fibrillation may occur that results in the absence of cardiac output and sudden death. We have been studying the cardiac electrophysiological effects of coronary obstruction in the dog to determine how these rhythm disturbances occur. To do this we have designed a data acquisition system that enables us to record electrical activity at 192 sites in the heart, digitize the signals and analyze activation times with a computer. We have shown, using this system, that coronary occlusion changes the conductile properties of cardiac tissues which have a diminished blood supply. This in turn results in a phenomenon known as re-entrant excitation; the conducting impulse does not die out after activating the heart once as it does normally, but rather continues to propagate in a circular pattern throughout the ventricles activating them over and over again. This causes a rapid heart beat and eventually ventricular fibrillation.

BE1-K.4

Recording and Imaging Cardiac Electrical Activation Using Voltage Sensitive Dyes, Stephen Dillon*, Columbia University, New York, New York.

Voltage sensitive dyes (VSDs) are a class of molecular probes which can linearly transduce variations in membrane potential into changes in their absorption and/or fluorescence. VSDs bind to the outer membrane leaflet of cells so that voltage is detected as a component of the electrical field. With appropriate instrumentation it is possible to record "optical action potentials", i.e. the signal developed by the variations in cellular voltage generated during cardiac activation. This approach, therefore, allows one to study the details of impulse propagation at a large number of sites, far more than is possible using microelectrode techniques. While high density electrographic mapping can also provide such information, VSD recording can provide data about the impulse itself (ex. upstroke velocity, refractory period). Further by using laser scanning or CCD cameras one can develop high resolution images of impulse propagation. This kind of data could be used to understand the mechanisms of arrhythmogenesis and their pharmacological treatment.

BE1-L.1

Long-term Monitoring in Epilepsy,
J. Gotman*, Montreal Neurological
Institute, McGill University,
Montreal, Quebec, Canada

The electroencephalographic (EEG) correlates of epilepsy are sometimes rare and unpredictable, as are the seizures themselves. It is therefore necessary to perform long-term monitoring of the EEG and of the patient's behavior to obtain a full documentation of the disorder. Monitoring sessions may last from 24 hours to several days. Behavior is monitored by video.

Long-term EEG recordings can be performed on analog tapes; video tapes are most commonly used at present. Since it can be very tedious and expensive for somebody to review a 16-channel EEG recorded during several days, two strategies have been developed to facilitate the process. Fast review systems allow displaying the EEG on a monitor at 10 to 60 times the recording speed; this can be a very efficient process, particularly with 8 or fewer channels and when only major events are to be captured. Automatic detection methods, usually running on-line, allow processing 16 and sometimes more channels and detecting specific epileptiform activity such as interictal spikes, spike-and-wave bursts and seizure patterns; these methods are far from perfect but can be used effectively if biased towards minimizing false negatives. Possible avenues to improve the performance of existing methods will be discussed.

BE1-L.3

EEG Monitoring in Surgery

R.A.F. Pronk*, A.J.R. Simons, E.H.J.F. Boezeman
Nicolet Biomedical Instruments, Madison, WI, USA

Continuous monitoring of the functioning of the brain by means of the recording and processing of the electroencephalogram (EEG) can be clinically useful during surgical procedures where the cerebral perfusion and metabolism are at risk, for example, during neurosurgery, carotid endarterectomy or cardiac surgery. The main objective of EEG monitoring during surgery is to prevent irreversible brain damage resulting in postoperative neurologic complications. For example, in carotid endarterectomy, there is a risk of cerebral ischemia when the carotid artery is clamped and the collateral blood supply is inadequate. Then, a decision to use a temporary bypass shunt is often based on significant ipsilateral slowing or voltage attenuation of the EEG data recorded during test clamping of the carotid artery. Temporary bypass shunt used or not, in both cases, it is strongly recommended to continue the EEG monitoring in order to detect aberrant EEG activity caused by cerebral ischemia. For the continuous intraoperative EEG monitoring, it is almost a practical requirement to use a computerized system which provides the recording of the EEG of both hemispheres, EEG data processing, feature extraction and display, and the automatic generation of warnings at the occurrence of aberrant EEG activity. Experiences with such a computer-assisted monitoring system will be discussed.

BE1-L.2

Sleep Analysis as a Data Reduction Program

Jack R. Smith
Electrical Engineering Department
University of Florida
Gainesville, FL 32611

Sleep analysis can be interpreted as a data reduction problem. Sleep staging, for example, consists of reducing 30 seconds of data to one byte and of reducing an eight hour record to less than 1000 bytes of information. Sleep staging provides an incomplete and inadequate description of a night's sleep. A subject reports that one night's sleep is much better than the next, yet sleep staging does not discriminate between them. There are methods for extracting additional information from the polysomnography data which more completely describe a night's sleep. The data reduction (sampling rates, number of channels, bits/sample and feature extraction) depend on the amount of information required by the clinician, and the method plays an important part in the system design and system cost. This paper provides system requirements for a variety of sleep data reduction methods.

BE1-L.4

Objective Assessment of Anticonvulsant Efficacy by Analysis of Interictal EEG Activity, J.D. Frost, Jr.*, R.A. Hrachovy, D.G. Glaze, and P. Kellaway, Baylor College of Medicine, One Baylor Plaza, Houston, Texas.

Although routine electroencephalography (EEG) provides definitive information essential to the diagnosis and classification of seizure disorders, it is not useful for assessing the effectiveness of drug treatment in individuals with partial (i.e., focal) seizures. We have demonstrated that seizure hazard can, however, be determined in a quantitative manner through computer analysis of interictal EEG spike waveforms. Children with discrete spike foci and simple or complex partial seizures have been studied before and during treatment with several anticonvulsant medications. Average spike parameters were determined during 5- to 45-minute EEG samples obtained during NREM sleep. Measurements included spike amplitude (A), normalized sharpness (S), duration (D), and a mathematical derivation, the composite spike parameter (CSP), defined as $CSP = A \times D/S$. In patients whose seizures were controlled by the drug treatment but whose EEGs continued to show interictal spikes, there was a decrease in the average spike amplitude, duration, and CSP, and an increase in normalized sharpness, compared with the pretreatment baseline values. These findings indicate that computer-based EEG analysis of interictal activity may provide an objective means for monitoring anticonvulsant drug efficacy.

BE1-M.1

Inverse Solutions in 2D Using Propagation Models

Tadashi Ihara and Roger C. Barr*

Duke University, Durham, NC 27706 USA.

If excitation proceeds away from a site of origin located somewhere within a two-dimensional sheet of excitable tissue, can the site of origin be determined by examining the waveshapes on a few extracellular electrodes? We examined this question in a number of specific examples, with computer simulations. The calculations assumed a stylized action potential shape. Propagation velocity was assumed constant but anisotropic (usually $x:y$ was $3:1$), although results for isotropic propagation were compared. Waveforms arising from the "true site of origin" were compared to the waveforms arising at the same electrode sites when other "trial sites of origin" were used. Most often the RMS error between trial and true waveforms, averaged over the electrode sites, was used to characterize the difference between sets of trial and true waveforms. For the examples we evaluated, the error surfaces giving the RMS error as a function of trial site looked complex and were not simply extensions from known 1D cases. How many extracellular waveforms were required to find the origin, if everything else was known? Surprisingly, with anisotropic propagation and low noise, the site of origin could be found unambiguously with only two extracellular electrodes (waveforms), except for symmetric examples, where three extracellular electrodes were required. Having more electrodes allowed recognition of the site despite higher (simulated) noise levels.

BE1-M.3

RECOVERY OF EPICARDIAL POTENTIALS FROM BODY SURFACE DATA IN A REALISTIC GEOMETRY TORSO, BJ Messinger-Rapport and Y Rudy, Case Western Reserve University, Cleveland, Ohio, U.S.A.

Inverse electrocardiography has as its goal the reconstruction of cardiac electrical events from information obtained non-invasively at the torso surface. The epicardial potential distribution, as a solution to the inverse problem, mirrors the electrical events within the underlying myocardium in more detail than is possible from the body surface potential map alone. Although in principle the epicardial potential solution can be recovered from the complete set of body surface potentials, the ill-posed nature of the inverse problem makes it necessary to apply regularization techniques to stabilize the inversion.

The inverse solution was tested on measured data on a realistic geometry, electrolytic tank with a beating dog's heart placed in the anatomically appropriate position. The effect of error in estimating the placement of the heart within the torso tank was examined, it was found that Tikhonov regularization would permit a 1 cm error in estimation, but a 2 cm error could result in significant loss of resolution. Additional results are presented from a pilot study of the effect of the number and position of leads on the inversion. Results of these studies suggest that a stylized torso, based on a limited number of measurements, could replace the set of measured electrode locations. An example of a stylized torso with inverse epicardial solutions is presented.

BE1-M.2

Localization of pre-excitation and arrhythmogenic sites by a single moving dipole, P. Savard*, M. Shenasa, R. Nadeau, P. Page Hôpital Sacré-Coeur, Montréal, Canada.

Epicardial mapping was used to evaluate the accuracy of a single moving dipole (SMD) for the localization of ventricular activation in patients subjected to anti-arrhythmia surgery. Body surface potential maps (BSPM) and epicardial electrograms were recorded with 63 leads in 12 Wolff-Parkinson-White (WPW) patients and in 8 patients with ventricular tachycardia (VT) during 14 induced VT episodes. The SMD parameters were computed from the BSPM using the same torso model which included lungs. In WPW patients, the SMD trajectory during the delta wave accurately depicted the progression of pre-excitation away from the location of the accessory pathway found during surgery, and towards the rest of the heart. In VT patients, during the first 40 ms of the QRS the SMD moved erratically whereas the SMD orientation was grossly correlated with the location of initial activation: upwards from the apex, left-wards from the right ventricle and right-wards from the left ventricle. In conclusion, the SMD seemed to depict pre-excitation better than VT, because: 1) ECG baseline is difficult to identify in rapid VT, 2) cardiac activity is more complex during VT because of multiple wavefronts and myocardial infarction.

BE1-M.4

Inverse ECG Model based on Minimum Relative Entropy Reconstruction Principle, C. L. Nikias*, D. H. Brooks, and J. H. Siegel, Northeastern University, Boston, MA and MIEMSS, University of Maryland, Baltimore, MD.

In response to the shortcomings of time-domain least-squares (LS) based methods, we introduce to the inverse problem of Electrocardiography an established frequency domain method, the minimum relative entropy (MRE) reconstruction principle, derived from an information-theoretic criterion. The MRE method reconstructs the power spectrum of each epicardial signal, starting from torso ECG measurements and incorporating the actual torso geometry of a single patient. Although this method does not have the advantage of being able to estimate the time domain signals, it can estimate frequency domain parameters which have been shown in our studies to be potentially useful in the detection and quantification of important cardiac dysfunctions. We compare results obtained with the MRE and LS methods as a function of both measurement noise and the size and shape of subarrays of torso sensors. Our results show that the MRE method appears to be more robust and in addition shows improved performance even with a small, compact subarray of sensors.

Work supported by Whitaker Foundation

189

BE1-0.1

Tissue Stimulation Using Magnetic Fields: Current Technology - Uses and Problems W.A. Tacker, Jr., and J.D. Bourland Purdue University, West Lafayette, Indiana, 47907

Magnetic field stimulation is used experimentally in place of electrical field stimulation because it is less painful, and may be safer. Present design of the magnetic coils produce large fields with diverse, and as yet poorly understood neurophysiological effects on tissue, especially in the CNS. Sites of stimulation, and pathways which mediate the responses have been proposed, but to date are unproven.

Stimulus duration, intensity and shape have not been optimized. The stimulus intensity is proportional to the rate of change of the magnetic field and stimulus duration is equal to the period during which the field is changing. The interaction of magnetic fields with tissue is weak, so very strong pulsed magnetic fields are required. Consequently, due to coil heating, repetition rates must be low and averaging techniques to analyze the neural responses are impractical.

Magnetic stimulators designed for high intensity, concentrated fields at repetition rates of several Hz are needed to exploit this exciting new technique.

BE1-0.3

Theory and Solutions for Magnetic Stimulation of Tissues, John Nyenhuis and J.D. Bourland, Purdue University, School of Electrical Engineering, West Lafayette, IN 47907

In magnetic stimulation of tissue, current pulses are applied to a coil near excitable tissue. The current in the coil generates a time-varying magnetic field which induces a stimulating electric field in the tissue. Except for the simplest conditions, analytical solution is intractable. Our approach is to calculate approximate solutions by digital techniques, and to verify them by measurement of the voltage between two probe tips in a tank of saline solution placed above the coil.

Model results can be used to guide the design of magnetic stimulators. For example, our model shows that efficient energy coupling requires a coil radius greater than the coil-to-tissue separation. A second result from the model reveals a complication for the user of a magnetic stimulator of conventional design. The peak intensity of the electric field is located near the radius of the coil, when the coil is near the target tissue. However, the peak intensity occurs further outside the radius of the coil as the distance between the tissue and coil increases. Use of multiple coils can obviate this potentially confounding effect.

BE1-0.2

An Introduction to Magnetic Stimulation of the Brain and Neuromuscular Tissue, A.T. Barker, I.L. Freeston, and R. Jalinous, Department of Medical Physics and Clinical Engineering, Royal Hallamshire Hospital, Glossop Road, Sheffield, UNITED KINGDOM.

The technique of magnetic stimulation of neuromuscular tissue, developed at the University of Sheffield, England, is becoming widely used for the clinical assessment of both central and peripheral nerve pathways. This paper will trace the historical development of the technique and describe the basic theory behind magnetic stimulation. Its advantages and disadvantages, compared to conventional electrical stimulation, will be considered and the safety of magnetic stimulation of the brain will be discussed in terms of such parameters as induced electric field, current density, charge and power deposition.

BE1-0.4

Experience with Intraoperative Transcranial Magnetic Motor Evoked Potential (MEP) Monitoring, C.B. Shields, H.L. Edmonds, M.P.J. Paloheimo, J.R. Johnson, and R.T. Holt, Division of Neurosurgery, University of Louisville, Louisville, Kentucky.

Intraoperative spinal cord monitoring with somatosensory evoked potentials (SSEP's) does not monitor motor pathways, is very sensitive to anesthetics and requires time-consuming averaging techniques. With IRB approved informed consent, in 35 patients having major spinal surgery, lower limb potentials were obtained on a Cadwell MES 10 with transcranial motor cortex magnetic stimulation. EMG leg responses were obtained with a neurometrics analyzer (Cadwell). Respiratory gas concentration (O₂, CO₂, N₂), blood pressure, heart rate, EEG and upper facial muscle EMG's were continuously monitored, and 90% neuromuscular blockade was estimated with electrically evoked peripheral motor responses. Painless magnetic stimulation produced motor responses in all awake patients preoperatively without spinal cord pathology. Intraoperative responses were obtained in 71% of cases. MEP amplitude varied from 5-5,000 Mcv, and latency duration was 35±3 ms. Low dose volatile anesthetics reduced MEP size. We can monitor both sensory (SSEP) and motor (MEP) functions of the spinal cord in awake and anesthetized patients. No untoward effects of magnetic stimulation were noted, but ongoing studies are assessing effects on the brain.

BE1-P.1

New methods to investigate the electrogenetic mechanisms of atrial arrhythmias in the clinical setting.

M. Alessie (*), R. Antolini (+,§), R. Bonamini (&), M. Disertori (°), W. Lammers (*), L. Mangiardi (&), F. Ravelli (§)

(§) I.R.S.T., (+) Dept. Physics, Univ. Trento, (°) Dept. Cardiol., Trento, Italy, (&) Ist. Cardiol. Univ. Torino, Italy, (*) Dept. Physiol., Univ. Limburg, Maastricht, NL

In modern cardiological practice, many patients suffer from disabling cardiac arrhythmias, such as atrial flutter or fibrillation. These patients are studied during catheterization of the heart and the therapeutical decisions are based on a trial-and-error criteria due to the lack of information concerning the underlying electrogenetic mechanisms. We developed new methods of data analysis based on the study of the atrial cycle length variations. We demonstrated that during atrial flutter these variations are due to mechano-electrical effects related to the influence of the ventricular contraction on the atrial walls. This physiological mechanism allows to find out the mechanism of the arrhythmia (circus movement) as well as some electrophysiological parameters of clinical interest. During atrial fibrillation the analysis of the atrial cycle length fluctuations allows the evaluation of the refractory period of the atrial tissue. The spatial dispersion of this parameter is an important factor in the induction of this arrhythmia. All results obtained with the clinical data are compared with computer simulations.

BE1-P.3

Computer-Assisted Cardiac Electrophysiology During Cardiothoracic Surgery, D. S. Buckles, M. E. Harold and P. C. Gillette, Pediatric Cardiology, Medical University of South Carolina*

Conduction system aberrations, accessory pathways, ectopic foci and other electrical disorders of the myocardium are frequently amenable to surgical intervention. Effective surgery requires specific knowledge of the locations and types of disorders. This information is often obtained during electrophysiology studies in the cardiac catheterization laboratory, but must be verified in the operating room. Also, electrophysiology mapping must be accomplished immediately following the surgical procedure to ensure good results. A microcomputer-based system for mapping and graphic display of data has been developed for use during pediatric open heart surgery. Signals are acquired from reference and mapping leads with a modified PPG VR-16 recorder, and are then processed by an IBM PC/AT with a Data Translations DT-2801A A/D board. The computer analyzes the relative timing of as many as eight reference and mapping signals, then displays the results in any of several color-coded cardiac surface maps. As well as being rapid and reliable this method provides an easily comprehended display of the information required for effective surgical intervention.

BE1-P.2

Improved Diagnostic Performance of Computerized Multivariate ST/HR-analysis in Myocardial Ischemia, H. Sievänen, L. Karhumäki†, I. Vuori†, J. Malmivuo, Biomedical Engineering Laboratory, Tampere University of Technology, SF-33101, Tampere, Finland, †Kanta-Häme Central Hospital, Hämeenlinna, Finland, ‡UKK Institute for Health Promotion Research, Tampere, Finland.*

Regardless of its high sensitivity to detect myocardial ischemia the ST/HR-analysis is not applicable as a clinical diagnostic test due to its relatively low specificity. The clinical performance of the test is improved significantly by taking into account the properties of the ST/HR-slope, the ST-segment value and shape, maximum heart rate and the ECG lead. By means of the specific multivariate approach the normal exercise ECG response is accurately distinguished from the ischemic response.

The computerized multivariate ST/HR-analysis has no expectations about the patient material without any loss in the diagnostic performance. Disregarding the manifestation of the underlying ischemic disease the sensitivity and the specificity of our method were 100% and 87%, respectively. The corresponding clinical performance was 93.5%, which implies the superiority of the multivariate ST/HR-analysis in respect to other noninvasive ECG based diagnostic tests.

BE1-P.4

Knowledge Representation of Cardiac Electrophysiological Phenomena in a Real-Time Measurement Environment

W.J. Inler (§), R. Antolini (+,§), M. Kirchner (§), F. Ravelli (§)

(§) I.R.S.T., I-38050 Trento - Povo, Italy

(+) Department of Physics, University of Trento

In automatic interpretation of on line measurements in clinical electrophysiological tests, the knowledge representation of electric phenomena of the heart includes numerical and symbolical issues: sequences of time-intervals, phase-cycle relations and stimulation response patterns from different protocols. We integrated a knowledge-based test support system into a real time waveform recognition and measurement device. It delivers descriptions of the beat-to-beat data plots and interpretation hints. The inferences about electrogenetic mechanisms of the arrhythmias and their pharmacological control are obtained in real time by means of heuristics that need only a couple of points rather than complete a posteriori statistics. Clinical examples concentrating on the atrial activity (atrial flutter and fibrillation) elucidate our "smart instrument" approach.

BE1-P.5

A portable system for digital recording of electrocardiogram, G. Baudoin and M. Chauouche*ESIEE, BP 99, Noisy le Grand(France)

"Holter" systems are portable tape recorders which record 24 hours of electrocardiographic signals (ECG). Replacing them by digital recorders presents several advantages: a) elimination of mechanical problems, b) possibility of simultaneous data processing, c) a better quality of recorded signals. But the digital recording of 24 hours of ECG signals with a 200Hz sampling rate and 8bits by sample requires a 14Mbytes memory area. The development and testing of several data compression methods applied to ecg have revealed that the Karhunen Loeve expansion with a learning phase is very efficient. This technique, used in conjunction with preprocessing and segmentation of signals leads to a data rate reduction by a factor of about 10 (the relative mean square error is less than 2% for a digital rate of 200bs⁻¹). A new robust QRS detection algorithm has been developed which is particularly efficient of noisy signals ("sportif"). This algorithm is based on mathematical morphology. The on line processing can be implemented on digital signal processors, and the new 1Mbits RAM makes it possible to develop a digital holter system.

BE1-P.6

ANALYSIS OF MULTI-LEAD EXERCISE ELECTROCARDIOGRAPHY, USING SINGULAR VALUE DECOMPOSITION(SVD), U. Tachinardi* and S.S. Furue, Heart Institute of São Paulo, C.P. 8091, S.P.-BRAZIL.

Although multi-lead ECGs (mLECG) proved to be useful tool to enhance Exercise ECG (EE) accuracy, they greatly enlarge the amount of data to be stored and analysed, with a great level of redundancy. The other problem in mLECG is to choose the proper leads to make measurements (like ST segment shift). We propose the use of SVD to analyze mLECG of EEs. This method calculates the principal signals (PS) that can substitute the measured signals. For this purpose we used an orthogonal array of EE signals (X, Y, Z) of normal and ischemic patients, and calculated their PS in which several EE parameters were extracted, i.g. the ST segment area measured in the first two PS suggests a good agreement with invasive angiographic findings even better than traditional EE analysis methods. The PS signals can be analysed alone or plotting the loops of a pair of them. As the first two PS represent more than 95% of the total information, the use of both together is a good way to represent the electrocardiographic phenomena, allowing the display of the biggest part of the energy in only one plane. An interesting feature is to lower the noise level in the first two PS. When applying SVD, the EE values are normalized, it means that the PS are less affected by anatomical discrepancies between the patients and by the different technical protocols used.

BE1-Q.1

Underdamped Multiphasic Sinusoids in the Defibrillation of 100 kg Calves, J. Schuder, W. McDaniel*, H. Stoeckle, University of Missouri, Columbia, Missouri, U.S.A.

Experimental studies indicate that asymmetrical biphasic rectangular waveforms are far superior to critically (or near-critically) damped sinusoids and to uniphasic trapezoidal waveforms. Nevertheless, perceived problems in creating such biphasic shocks in clinical apparatus have resulted in the latter two waveforms continuing to dominate the clinical defibrillation field. In the present study, 120 fibrillation-defibrillation episodes in which transthoracic defibrillation was attempted in six 92-109 kg calves with a very much underdamped sinusoid in which zero crossings were separated by 4.05 ms and the successive peaks were +58, -16.5, +4.7...A were interlaced with 120 episodes involving a rectangular waveform having a leading half-cycle of +38 A, 4 ms and a lagging half-cycle of -18.5 A, 4 ms. The underdamped sinusoids, with resistance of 21.0±2.6 Ω and a mean delivered energy of 148 J were successful in 88 (73%) of the episodes. Values for the rectangular waveforms were 21.1±2.5 Ω, 151 J, and 91 (76%). Since the success rate for the two waveforms are not significantly different, the results suggest that the effectiveness of the underdamped multiphasic sinusoidal waveform is comparable with the biphasic rectangular waveform and, hence, also appreciably superior to the shocks used clinically.

BE1-Q.2

Detrimental Effects of an Epicardial Patch on Transthoracic Defibrillation, J.P. Wikswo, Jr.*, N.G. Sepulveda and D.S. Echt, Vanderbilt University, Nashville, TN, USA

Implantable defibrillator systems use one or two epicardial patch electrodes insulated on one side to minimize energy loss in the lungs and thorax. However, there is a clinical concern that the presence of internal patch electrode(s) may increase the energy required for transthoracic (external) defibrillation due to the patch insulation. Ironically, this problem would be greatest in patients whose high internal energy requirements mandate two large patches for successful internal defibrillation. We have therefore studied the effects of insulated internal patches on the external defibrillation threshold using a 2-dimensional mathematical model of the canine thorax with the predictions that defibrillation requires ≥ 80 % of the heart to be rendered inexcitable by a current density ≥ 35 mA/cm². Without a patch electrode, 106 Joules were needed to defibrillate the model transthoracically. The addition of a single 16 cm² insulated patch to the LV apex increased the required energy to 184 J. Larger patches and the use of two patches further increased the transthoracic energy requirements. While our 2-D model can only approximate the transthoracic current distributions in a 3-D thorax, we conclude that large epicardial patch electrodes can significantly increase transthoracic defibrillation needs.

1988

BE1-8.3

FIBRILLATION THRESHOLD AND VENTRICULAR WEIGHT. E Ruiz, J Rodríguez, I Medina and ME Valentinuzzi. Bioingeniería, Universidad Nacional de Tucumán, cc 28 suc 2, 4000 Tucumán, Argentina.

The objective was to search for a possible relationship between ventricular weight (VW) and fibrillation threshold (FT). We used 14 small cats (average VW 2.5 g, SD 0.4), triggering fibrillation with single 5 ms rectangular pulses synchronized with the ECG and adequately delayed. Bipolar hook electrodes were placed on the basal region of the heart. FT was scaled to VW obtaining an overall average of 7.9 mA/g (SD 3.7) for 52 measurements. Average results from three other groups of larger animals were: 5.9 mA/g (SD 1.4) in 4 dog puppies of 5 g VW (SD 0.9), 1.0 mA/g (SD 0.6) in another 4 puppies of 20 g VW (SD 3.8) and 0.24 mA/g (SD 0.08) in 11 adult dogs 64 g VW (SD 14.8). We did not run any statistical comparison between groups, but these results show a tendency, i.e., as ventricular weight increases, fibrillation threshold decreases. Thus, hypertrophied hearts would fibrillate more easily than normal size ones. CONICET and CIUNT grants.

BE1-8.5

A SEQUENTIAL ALGORITHM FOR DETECTION OF VENTRICULAR FIBRILLATION - N. Thakor and Z. Yi-Sheng, Biomedical Engineering, Johns Hopkins University, Baltimore, MD, USA.

Ventricular fibrillation (VF) is a life-threatening arrhythmia that must be immediately and accurately detected. An automatic implantable defibrillator delivers a lifesaving high-energy shock to the heart when VF is detected. An algorithm is presented that reliably discriminates VF from other ventricular arrhythmias.

VF signal is first compared with a threshold (20% of peak) to obtain a binary signal. The mean value of time interval between threshold crossing is smaller in tachycardia and VF than in normal rhythm. The variance of these intervals is smaller in tachycardia than in VF. A test is constructed that discriminates between mean and variance of threshold crossing intervals of different arrhythmias. A sequential algorithm, based on Wald's hypothesis technique, is constructed. The decision to detect VF is made for successive, 1 second segments of sampled data. The detection thresholds are established so as to obtain desired false positive and negative rates.

In a study of 170 episodes, VF detection accuracy was 95% after 3 segments, 97.6% after 5 segments and 100% after 7 segments.

BE1-8.4

A Preliminary Study on the Index for the Excitability of Myocardium, Xin-yin Xu, Ye-cho Huang*, Xian Medical University, Xian, China.

Geddes reported that the membrane time constant T of myocardial cell derived from the experimental data of pacing and defibrillation are reasonably similar, and T equals chronaxie c approximately. Huo Zong Lian advanced that the standard electrical quantity a he named was an actual index for the excitability of tissue or cells. The experiments about excitability of myocardium (EM) have been done on 5 patients and 7 dogs with the pacing system analyzer we developed. EM was changed by drugs and strength-duration curves were measured by stimulation threshold, varying rectangular current pulse durations (0.01-2.5ms). Then the constants b and a in WEISS formula were calculated, and c was derived from a/b . Results: (1) a decreases or increases as EM rises or reduces respectively, but b and c do not. (2) The average T of patients and dogs are 1.311 ± 0.406 (SD) and 1.069 ± 0.322 (SD) respectively. Considering strength-duration curve for energy and the function of energy compensation in pacemaker, the pulse duration of pacemaker had better be designed about $T/2$.

BE1-R.1

Time Frequency Distribution Mappings of Event-Related Potentials in Kornhuber Experiments.

F. Babiloni*, S. Salinaro†, A. Urbano
Ist. di Fisiologia Umana-Università di Roma "La Sapienza"-Piazz.le A.Moro 5-00100 ROMA

†Dip. di Informatica e Sistemistica-Università di Roma "La Sapienza"-Via Eudossiana 18-00184 ROMA

Spectral analysis is one of the most used tools in signal processing, however the underlying hypothesis, for its use is the steady state behaviour of data to be processed. In many cases, the biological signals are deeply non stationary. This motivates the need for the data description in a time frequency joint domains. We attempt this non stationary spectral analysis to the signals recorded during a Kornhuber experiment, we want to study changes in the amplitude of Fourier coefficients at different frequencies, and their temporal relationships. At this purpose we recorded Kornhuber potentials in normal and parkinsonian subjects from 30 channels placed on the scalp. We computed the time frequency distribution of the signals by different algorithms. Data windowing is performed by Hanning or split-cosine functions. A PDP11/23 plus computer was used for data processing.

3D graphics shows the time frequency distribution for every signal recorded. Amplitude and power color mappings were also performed, at frequency of interest, in order to follow the temporal evolution of Fourier components over the whole scalp.

BE1-R.2

Estimation of ERP Parameters based on the Time-sequenced Adaptive Filter, N. Takano* and K. Yana, Hosei University, Koganei City, Tokyo Japan.

Accurate estimations of latency, amplitude and waveform of ERPs (Event Related Potentials) are difficult because of their low signal (ERP)-to-noise (background EEG) ratio. Averaging method and the adaptive correlation filter have been utilized for these estimations. As an improved method, we would like to propose the following procedure. Step1: Average original EEG data to make a reference waveform for adaptive filtering. step2: Compute time dependent filter coefficients on and around the peak point of the reference waveform. step3: Obtain the amount of time-shift for each original data which gives the best match between the reference waveform and filter output. step4: Average time-shifted original data according to the amount given by step3 to make an improved reference waveform for adaptive filtering. Repeat steps 2-4 until the convergence condition based on the amount of time-shift in the step3 will be met. step5: Perform the ERP signal emphasis for each time-shifted data to obtain the estimate of single ERP waveform and its amplitude, by the time-sequenced adaptive filtering technique. The preliminary experiment showed the improvement in the estimations of ERP latency and amplitude. This method may also give us the estimate of single ERP waveform in each original data.

BE1-R.4

A Two Dimensional Approach on the Problem of Filtering Evoked Potentials, O. Svensson, Telecommunication Theory, University of Lund, Box 118, S-221 00 Lund, Sweden.

When it is of interest to follow changes of an evoked response it is necessary to achieve an interpretable response with few trials. Filtering methods can be used both along the traces and cross the traces. The LMS adaptive filter algorithm is used for filtering along the traces. The bias as well as the sensitivity to changes in the response for the LMS adaptive filter are analysed. Evoked responses often contain higher frequencies at the beginning of the response than towards the end. The response is therefore divided into different time slices where different adaptive filters operate in the different slices.

Averaging is the common method for filtering cross the traces. This method can be viewed as a FIR-filter having a uniform impulse response. By using an IIR-filter with an exponential impulse response instead, higher weight can be given to the latest trial and hence changes in the response are easier to follow. The time constant of this cross trace filter can easily be tuned to obtain an optimal trade off between time constant and signal to noise ratio in the response. Results based on simulated data are presented where both white and EEG-like background noises are used.

BE1-R.3

ADAPTIVE FILTERING OF TRANSIENT EVOKED POTENTIALS - N. Thakor* and C. Vaz, Biomedical Engineering, The Johns Hopkins University, Baltimore, MD 21205, USA.

Evoked potential (EP) monitoring may be an important technique in monitoring the status of the brain in neurological surgery and intensive care. This requires that transient and time-varying events be captured. An adaptive filtering (AF) technique is presented that rapidly improves signal-to-noise ratio (SNR).

EP signals are modelled by a Fourier linear combiner (FLC). Fourier coefficients for a truncated series are estimated. A least-mean-square (LMS) algorithm is employed to recursively minimize the mean-squared error (MSE) between successive ensembles and the FLC model of EP. The LMS algorithm permits improvement in MSE, as well as adaptation to time-varying events. Comparison with ensemble averaging reveals that AF improves SNR more rapidly and tracks transient changes in EP amplitudes.

This research deals with two theoretical issues: 1) optimal selection of model order, and 2) selection of fast convergence rates while maintaining stability.

AF technique is currently being tested in two protocols: neurologic response to 1) induced hypoxia in dogs, and 2) induced hypotension in human volunteers.

BE1-R.5

Methods for single sweep processing of evoked and event-related potentials

D. Liberati, S. Cerutti, G. Pavesi
CNR-CTS, Dipartimento di Elettronica,
Politecnico, Milano, Italy

The variability occurring in successive evoked (EP) or event-related (ERP) potentials obtained with the same protocol from the same patient becomes more and more evident with the increasing of the complexity of the involved neurophysiological or psychological task. Moreover, in monitoring during neurosurgery, a variety of sweep-by-sweep changes in the main parameters of the evoked potentials can provide important feedback information about the correctness of the surgery itself. In such cases, a method developed for detecting the sweep-by-sweep variability becomes an important tool.

The proposed techniques are based on the additive superposition of signal and noise (background EEG), and on a model of the EEG itself as an Autoregressive process.

On the basis of this model, a few parameters are sweep-by-sweep extracted which try to describe the dynamics of the neural response.

Results obtained on both simulated and real signals confirm the capability of the model for single sweep classification, besides showing improvement in the S/N ratio in respect to the traditional filtering.

BE1-R.6

A Linear System's Approach to the Relationship between Visual Evoked Potentials and the Prestimulus EEG.

Michael E. Brandt* and Ben H. Jansen, University of Houston, Dept. of Electrical Engineering, Houston, TX 77004, USA.

Various signal theoretic procedures (e.g., averaging, adaptive filtering) can be used to improve the signal-to-noise ratio of evoked potential (EP) measurements. It is conceivable that methods based on a model of EP generation could lead to a dramatic increase in performance. Specifically, knowledge of the relationship between the EEG immediately preceding the EP and the shape of the EP could be of major importance. This relationship is largely unknown. Previous work in this area has generated some support for the hypothesis that the EP is essentially a modified version of the EEG present at the time of the stimulation.

In the present study, healthy volunteers were subjected to a long series of randomly presented, identical flash stimuli over a one hour period. Clustering was done on the 1 sec prestimulus intervals and the poststimulus epochs corresponding to a given prestimulus cluster were used to compute an average EP (AEP). The relationships between prestimulus EEG and VEP shape thus discovered will be discussed.

BE2-A.2

Modeling and Simulation of the Effects of Antiarrhythmic Agents, T. C. Jannett, L. C. Sheppard, and G. N. Kay, The University of Alabama at Birmingham, University Station, Birmingham, AL 35294

Pharmacologic control of a physiological variable requires knowledge of the dynamics of the response to drug infusion. Mathematical modeling and simulation were employed in the development of an automated system for lidocaine administration. A model of the rate of premature ventricular contractions (PVC rate) and its response to lidocaine infusion was developed in system identification experiments. The model was used to design a closed-loop control system for the regulation of the PVC rate at a desired set point. Infusion rate constraints were developed based on the analysis of a pharmacokinetic model to limit the predicted lidocaine serum concentration to a safe level during operation of the closed-loop system. Operation of the system was validated in computer simulations of the PVC rate and the lidocaine serum concentration during closed-loop drug infusion.

BE2-A.1

AUTOMATED DELIVERY OF I.V. ANESTHETIC AGENTS: MODELING CONSIDERATIONS, James R. Jacobs* and Peter S. A. Glass, Department of Anesthesiology, Duke University Medical Center, Durham, NC 27710 USA

Until the pharmacodynamics of general anesthesia have been better quantified, reliable and versatile closed-loop administration of intravenous anesthetic agents will not be possible. Alternatively, we feel that open-loop delivery of these drugs is optimally realized with a pharmacokinetic model-driven system, where the physician titrates the theoretical drug plasma concentration to achieve the desired clinical effect. This approach requires techniques for modeling both the pharmacokinetics of the drug(s) being infused and the plasma concentration-effect relationship. With regard to the former, discrete and analytical approaches to the real-time simulation of compartmental pharmacokinetic models have been developed and are readily implemented in software; real-time sensors of actual drug plasma concentration are not available and, in our opinion, are not necessary. Although elegant concentration-effect models have been suggested for some drugs, for i.v. anesthetic agents, the determination of Cp50's (analogous to M.A.C. for inhalational anesthetic agents) by logistic regression modeling has proven to be the most useful in clinical practice.

BE2-A.3

Hydrogels for Controlled Delivery of Drugs
T. J. Laughlin, Schering-Plough Corporation, Memphis, TN, and R. L. Dunn*, Vipont Laboratories, Inc., Ft. Collins, CO.

Hydrogel alloys can be prepared by blending select hydrophobic and hydrophilic polymers. The integrity of the alloy is determined by the noncovalent bonds (ionic, dipole-dipole, and hydrogen bonds) and hydrophobic interactions formed between polymers.

We have been investigating the controlled-release and swelling properties of blends of polystyrene maleic anhydride and poly(vinyl acetate). The water sorption rate, water sorption capacity, and thermoplasticity can be controlled by selecting the proper composition and processing procedure. We have observed sorption capacities for up to 30 times the weight of the alloy. We have also observed an apparent zero-order release of tetracycline and insulin from tablets made from these alloys. The release appeared to be controlled by an erosional mechanism.

BE2-A.4

Automatic Computer Control of Neuromuscular Blockade, T.J. Quill*, P.S. Glass, J.R. Jacobs, and J.G. Reves, Duke University Medical Center, Durham, N.C., 27710

The design and development of an automatic computer controlled infusion system for the administration of either vecuronium bromide or atracurium besylate for human surgical relaxation is described in detail.

The system utilizes a Puritan-Bennett evoked EMG unit and an Intel 8088 microprocessor based modified adaptive PID controller driving an IVAC medical precision infusion pump, and successfully maintains the evoked EMG consistently within narrow tolerances. The controller utilizes an internal pharmacokinetic model based upon measured drug characteristics in order to provide noise detection and elimination. Results of system performance upon 40 human subjects are presented. The principles described could be easily utilized in the development of other automated drug delivery systems based upon closed loop pharmacodynamic feedback.

BE2-B.2

Polymeric Implants for Delivery of Anticancer Agents, J. D. Strobel*, T. J. Laughlin, F. Ostroy+, M. B. Lilly+, B. H. Perkins, and R. L. Dunn, Southern Research Institute and University of Alabama at Birmingham+, Birmingham, AL.

We have prepared prototype implants for the controlled release of three anticancer agents: misondazole (MSND), adriamycin (ADM), and cytosine arabinoside. The studies were undertaken to determine the feasibility of delivering the drug directly to malignant tissue to increase efficacy and reduce toxicity. It was anticipated that the drug-releasing implants would be used in combination with radiation or hyperthermia treatments. Therefore, for implants that contained MSND or ADM, orthodontic wire was coated with the drug and a polymeric excipient. Drug and polymer were matched to achieve the targeted rate and duration of release. A variety of polymers were examined for permeability characteristics, including a polypropylene, a polyethylene, an ethylene vinyl acetate copolymer, a polyether polyurethane, polycaprolactone, a hydroxyethyl methacrylate/methacrylate copolymer, and a DL-lactide/glycolide copolymer. Fabrication processes included melt spinning and dip coating.

BE2-B.1

Prostacyclin - Releasing Sutures for the Prevention of Venous Thrombosis R. L. Dunn, C. A. Eddy, and L. E. Laufe Ft. Collins, CO and San Antonio, TX

The prostacyclin analogue Iloprost from Schering AG, Berlin, West Germany was incorporated into polycaprolactone, a biodegradable polymer. The blend of drug and polymer was extruded as a monofilament on a melt indexer and drawn to a size 9-0 suture. The fiber containing 0.25 ug of drug per centimeter of fiber was armed with a 100-um 3/8 circle taper-point needle. Control sutures were prepared using polycaprolactone and no drug. Bilateral transection and anastomosis of the common femoral vein was conducted in thirteen rats with the drug prostacyclin-releasing sutures on one vessel and the control sutures on the contralateral vessel. An examination 24 hours post-operatively showed the prostacyclin-sutured anastomoses were patent with a uniform absence of thrombosis. The control anastomoses gave five patent and eight occluded vessels with a dense, well-organized fibrinous clot that filled the entire lumen. These results demonstrate the effectiveness of the local delivery of prostacyclin from the suture in inhibiting thrombus formation.

BE2-B.3

Fuzzy Control of Arterial Pressure by Drug Infusion Using a Fuzzy Expert System FLOPS

H. Ying, L.C. Sheppard, and D.M. Tucker

- 1) Department of Biomedical Engineering University of Alabama at Birmingham Birmingham, AL, 35294, USA.
- 2) Kemp-Carraway Heart Institute Birmingham, AL, 35234, USA.

Fuzzy controllers are conceptually rule-based and have the ability to control processes without explicit mathematical models. In this paper we propose a new type of fuzzy controller which is not based on the existing fuzzy control theory. Instead, this fuzzy controller is based on general-purpose Fuzzy Logic Production System FLOPS. Human mean arterial pressure was regulated by this fuzzy controller, in digital computer simulation, by controlling the infusion rate of the drug, sodium nitroprusside. In the presence of non-stationary background arterial pressure variation, mean arterial pressures of different patients with different sensitivities to sodium nitroprusside were controlled satisfactorily. Furthermore, the simulated results using a first-order linear model demonstrated that the performance of the proposed fuzzy controller was superior to that of a fine-tuned Proportional-Integral (PI) controller.

BE2-B.4

Automatic control of halothane anesthesia, F.J. Sasse *, G.F. Schils and V.C. Rideout, University of Wisconsin, Madison, WI 53792, USA.

The design and laboratory implementation of a controller for halothane anesthesia in dogs is described. Difficulties with the control of mean arterial pressure (MAP) during linear (PI) control prompted the design of an ON/OFF controller. The ON/OFF controller provided fewer tradeoffs between stability and speed of response.

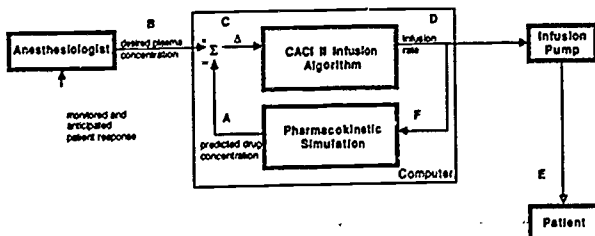
Recognizing that the desired and undesired effects of an anesthetic span several physiological systems, a method was devised to coordinate the control of two physiological variables (MAP and an EEG measure) with the single anesthetic agent.

The design criteria of a controller for inhalation anesthetics are discussed in detail. Clinical issues considered are the possible clinical utility of an automatic controller, the clinical timeframe, and the general characteristics of the clinical control of the depth of anesthesia. Related control issues considered are the choice of a control method, the desirability and limitations of adaptation, the choice of output signals, and the user interaction.

BE2-C.2

CACI II: PHARMACOKINETIC MODEL-DRIVEN DRUG DELIVERY, James R. Jacobs,* Peter S.A. Glass, Eric D. Hawkins, J.G. Reves, Department of Anesthesiology, Duke University Medical Center, Durham, NC 27710 USA

CACI II (figure) is a pharmacokinetic model-driven drug delivery system for intravenous anesthetic agents. The output (A) of a 3-compartment pharmacokinetic simulation is compared with the setpoint plasma concentration (B). A simple infusion algorithm acts on the error signal (C) to generate an optimal drug infusion rate (D) to [theoretically] maintain the setpoint plasma concentration during a specified period of time. Drug is delivered to the patient (E) and the model is updated (F). The physician may adjust the setpoint as often as required to titrate a stable anesthetic. CACI II has been used to deliver fentanyl, sufentanil, alfentanil, propofol, sufentanil/midazolam, or fentanyl/midazolam as the primary or adjuvant anesthetic to more than 100 patients. The clinical utility of CACI II has been excellent, and we believe that devices of this nature will play a major role in the future of intravenous drug therapy in a variety of clinical settings.



BE2-C.1

Spermicide-Releasing Vaginal Diaphragm, Benjamin S. Kelley*, Richard L. Dunn, Amelia G. Potter, Southern Research Institute, 2000 9th Avenue S., Birmingham, AL.

Vaginal barrier diaphragms are a viable and convenient means of reversible contraception, but acceptance is limited because of the messy creams or jellies and maintenance. We have studied the release kinetics of the spermicide nonoxonyl-9 (NN9) from biocompatible thermoplastic elastomers. This has included examining manufacturing processes that can be used to economically manufacture the elastomer-spermicide-lubricant/rate modifier blend. The goal has been to develop a convenient barrier contraceptive that is inexpensive, effective, and requires a lower degree of user motivation. Animal studies using either diaphragms or medicated rods have also been conducted in baboons or rabbits to screen for efficacy and safety. We have found that effective doses of NN9 can be delivered from several different biocompatible elastomers over a 24-hr period without greatly compromising the physical properties of the elastomers. Our goals have been to release about 30 mg of NN9 from the diaphragm in 1 hr and about 150 to 180 mg over a 24-hr period. We hope to soon begin Phase I human clinical trials. (Sponsored by the National Institute of Child Health and Human Development.)

BE2-C.3

Open and Closed-Loop Control of Premature Ventricular Contractions, T. C. Jannett, G. N. Kay, and L. C. Sheppard, The University of Alabama at Birmingham, University Station, Birmingham, AL 35294

An automated drug delivery system which incorporates open-loop and closed-loop lidocaine infusion for the suppression of premature ventricular contractions (PVCs) was tested in clinical trials. On the first day of the study, an open-loop infusion regimen based on a pharmacokinetic model was used to quickly achieve and maintain a therapeutic lidocaine serum level. On the second day of the study, closed-loop control was used to regulate the PVC rate at a set point level after a therapeutic serum concentration was achieved by open-loop infusion. The drug infusion rate was constrained during closed-loop control to keep the predicted serum concentration between upper and lower limits. Measured concentrations were compared to predicted values. During closed-loop drug infusion, satisfactory regulation of the PVC rate was achieved with predictable serum concentrations.

BE2-C.4

Insulin Administration with Implantable Pumps by Various Routes, W. Zingg* and M.V. Sefton, Research Institute, The Hospital for Sick Children, Institute of Biomedical Engineering and Department of Chemical Engineering, University of Toronto.

Parenteral administration of insulin is mandatory. Traditionally it is given subcutaneously once a day. To cope with individual metabolic requirements, multiple injections and continuous infusion by wearable or implantable pumps have been used; the infusion can be subcutaneous, intravenous or intraperitoneal. We have assessed these routes in a homogenous population of rats, and found a wide variability. The route is not important because of the presence of normal compensatory factors. In diabetics however, there is a deficit of these factors and as a result the metabolic control is defective because of a lack of counterregulatory action. Both constant infusion rate and programmable - telemetry commanded implantable pumps are useful in selected patients, but without a continuous glucose sensor to create a closed-loop system the application is limited. Other major problems are power consumption and the biological reaction to the presence of the implant.

BE3-A.1

The Distributed Transmural Parameters of LV Function, Metabolism and Perfusion, R. Beyar* and S. Sideman, Biomedical Engineering, Technion-IIT, Haifa, Israel.

A model approach to the inter-relationship between left ventricular (LV) mechanics, perfusion and energetics in a symmetrical ellipsoidal shape is presented. The complex model is composed of a hierarchical set of tightly linked models which combine the geometry of the LV, its fibrous structure, radial electrical activation, and properties of the muscle fibers to yield the stress and pressure distribution within the LV wall, which in turn affect the perfusion and energetic models. The energetic model links the mechanical parameters of an individual fiber contraction via its length and force to yield the local and global oxygen consumption. The perfusion model utilizes the pressure distribution from the mechanical model, combined with the oxygen demand as specified by the energetic model, and uses basic laws of microcirculation dynamics, in order to simulate the distribution of myocardial perfusion across the LV wall. Combining these three models yields the temperature distribution across the LV wall. This model approach provides a tool to study the complex interrelationships between the different aspects of cardiac contraction.

BE2-C.5

Automatic Control of Anesthetic Delivery and Ventilation During Surgery, R. G. Ritchie*, E. A. Ernst, B. L. Pate, J. D. Pearson, L. C. Sheppard, University of Alabama at Birmingham, Birmingham, AL 35294

Use of a closed rebreathing circuit for anesthesia delivery offers several advantages: conservation of anesthetic agent, natural heating and humidification of inspired gases, less pollution, and improved monitoring. However, the technique requires careful control of the fresh gas and anesthetic delivery. An anesthesia delivery system has been developed which automatically controls fresh gas delivery, anesthetic delivery, and ventilation in order to regulate circuit volume, oxygen concentration, end-tidal anesthetic concentration and end-tidal PCO₂ in a closed breathing circuit. The system makes available the advantages of the closed-circuit technique without encumbering the anesthesiologist with its more demanding control tasks.

During animal testing, the system's response to step changes in end-tidal PCO₂ setpoint, end-tidal anesthetic setpoint, and oxygen uptake were recorded. All controllers were stable and exhibited clinically acceptable response times. End-tidal anesthetic concentration could be quickly increased without opening the breathing circuit. During circuit volume regulation, oxygen delivery tracked sudden changes in oxygen uptake, making the system a good monitor of changes in oxygen uptake.

Funding: Ohmeda Grant #RMR080283

BE3-A.2

Integrity of myocardial fiber structure maintained by fiber load induced local growth. T. Arts*, P. Bovendeerd, F. Prinzen, R.S. Reneman, University of Limburg, 6200 MD MAASTRICHT, The Netherlands.

A change in hemodynamic load induces adaptations of the heart within a few weeks. Despite this flexibility in local growth, integrity of global myocardial fiber structure is maintained. In a computer simulation two hypothesis on the underlying growth control mechanism were investigated, both having in common that muscle fiber growth/degradation is induced by maximum muscle fiber stress. When controlling end-diastolic sarcomere length (SL), on the long term the structure appears to be unstable. However, when controlling the number of sarcomeres along a myocardial fiber by the amount of sarcomere shortening during systole (positive feedback), the transmural course of muscle fiber orientation is found to be very stable selfcorrecting and close to anatomical findings. Thus, the global, complicated cardiac structure can be maintained by the control signals fiber stress and sarcomere length, which are locally available at the cellular level.

BE3-A.3

Accurate Prediction of Stroke Work from Systolic and Diastolic Pressure-Volume Relations in the Isolated Canine Heart, W.L. Maughan*, D. Kass, K. Sagawa, Johns Hopkins Medical Institutions, Baltimore, MD 21205.

It would be valuable if cardiac performance assessed under one set of conditions could be applied to predict performance under other conditions. If end-systolic pressure-volume relationship is modelled by a linear function ($P_{es} = E_{es}(V_{es} - V_0)$) and end-diastolic pressure-volume relationship by an exponential function ($P_{ed} = A e^{B(V_{ed} - V_0)}$), stroke work can be predicted (SWp) under various filling pressures (Ped), afterloads (Ea) and contractile states (E_{es}, V_0). To test the model predictions, we compared SWp with measured stroke work (SWm) in 12 isolated canine hearts ejecting against a computer controlled loading system. For Ped from -5 to 31 mmHg (mean 6.8 ± 8), Ea from 2 to 32 mmHg/ml (mean 9.4 ± 4.8), and E_{es} from 2.6 to 11 mmHg/ml (mean 5.4 ± 1.3), $SWm = 1.09SWp + 20.7$ mmHg-ml ($r^2 = .964$, $n = 213$, $SEE = 126$). Multiple regression showed small independent influences of Ea, Ped, and dog on the residuals, probably related to slight changes in the shape of the pressure-volume loop with each variable.

Thus the systolic and diastolic pressure volume relations can be modelled and used to accurately predict cardiac performance over a wide range of different preloads, afterloads and contractilities for a given isolated heart.

BE3-B.1

ESOPHAGEAL CARDIAC PACING IN MYOCARDIAL ISCHEMIA: EFFECTS ON LEFT VENTRICULAR AND ARTERIAL SYSTEM FUNCTION. J. K-J. Li*, Dept. of Biomedical Engineering, Rutgers University, Piscataway, N.J. 08855-0909 USA.

Different modes of cardiac pacing and pacing sites have been shown to alter the performance of the left ventricle. This paper reports the effects of transesophageal cardiac pacing during myocardial ischemia.

Experiments were performed on open chest anesthetized dogs. Bipolar pacing catheter was utilized after establishing the strength-duration curve for threshold pacing. Pacing was initiated after one hour occlusion of the left anterior descending coronary artery. Left ventricular and aortic pressures, aortic flow, segment length and the electrocardiogram were recorded.

Results show that a higher heart rate during pacing was accompanied by a slight decrease in mean arterial pressure, flow, and segment shortening. Arterial pulse transmission characterized by forward and reflected travelling waves also showed a small change. Thus, esophageal cardiac pacing alters regional myocardial and arterial system dynamics only to a limited extent.

BE3-A.4

ASSESSMENT OF LOCAL MYOCARDIAL FUNCTION IN VIVO - R.S. Reneman*, F.W. Prinzen, C. Augustijn and T. Arts, Departments of Physiology and Biophysics, University of Limburg, Maastricht, The Netherlands

In vivo global left ventricular (LV) function can be determined relatively easily, but reliable assessment of local myocardial performance is still problematic, mainly because the devices used interfere with myocardial fiber function. Local fiber stress is generally estimated using mathematical models of LV wall mechanics. The values of intramyocardial pressure (IMP), a variable of importance in studying the relation between myocardial contraction and perfusion, are still under debate. There is agreement about the positive gradient of IMP from endo to epicardium. However, it is still unknown whether IMP in the endocardial layers is about equal to or significantly higher than LV cavity pressure, although recent micropressure measurements and model predictions support the former idea. In vivo epicardial fiber shortening can be assessed relatively accurately from the deformation parameters, as determined locally with x-ray or video techniques. With the latter, epicardial fiber shortening can be assessed simultaneously in 35 areas of the LV free wall, allowing investigation of, for example, the interaction between ischemic and non-ischemic areas. From the epicardial deformation parameters, endocardial fiber shortening can be estimated during normoxia and ischemia.

BE3-B.2

Fluid-Fiber-Collagen Description of the Myocardium Applied to Different Left Ventricular Geometries, J. Ohayon, M. Lewkowicz, and R.S. Chadwick*, Theoretical Biomechanics Group, Biomedical Engineering and Instrumentation Branch, Division of Research Services, National Institutes of Health, Bethesda, MD 20892.

The microstructure of the collagen sheath or weave surrounding a myocyte and the collagen struts interconnecting neighboring myocytes is incorporated into a fluid-fiber-collagen continuum description of the myocardium. The sheaths contribute to anisotropic elasticity, while the struts contribute to an isotropic component. Elastic moduli of the composite myocyte-sheath complex and the strut matrix are estimated from existing passive biaxial loading data from sheets of canine myocardium. The contribution of the sheath to the elasticity of the myocyte-sheath complex is critically dependent on the helical pitch angle.

Calculations are presented for different geometrical configurations: a thick-walled finite cylinder; a thick-walled sphere; and any thick-walled truncated body of revolution close to a cylinder, to show both the effects of collagen and assumed geometry on ventricular function. We found that the collagen strut matrix tends to: increase myocardial tissue pressure during systole, with endocardial tissue pressure exceeding left ventricular pressure; decrease tissue pressure during diastole, and thus facilitate myocardial blood flow, and; aid filling during ventricular relaxation by providing a suction effect relying on a release of stored elastic energy from the previous contraction.

BE3-B.3

Analysis of the Left Ventricle Mechanics.
A. MOUTAHAR, and C. ODDOU.
L.M.P, Université Paris 12, Créteil, France.

An analytical model was developed considering the left ventricular wall as an axisymmetric and pressurized thick ellipsoid shell in mechanical equilibrium. The myocardium is supposed to behave like a continuous medium essentially made up of contractile fibers embedded in a fluid matrix. The pitch-angle of the fibers, viewed as geodesic lines on the wall surfaces, is varying with the localisation within the wall. A linear rheological behavior for the fiber at their different stages of excitation was assumed.

Drawing from canine experimental data the geometrical and rheological model input parameters, this analysis helps determine the local stresses and strains within the wall. In particular, it was shown that the fiber length varies during the cardiac cycle in the range between -10% to 20%, relatively to the rest reference state. Moreover, an increase in the shell longitudinal curvature induces a uniform fiber strain distribution within the wall. The systolic torsional motion and structure eccentricity were found to be greater than the diastolic ones. In agreement with ultrasound measurements, the model predicted that the relative variations during the overall cycle of the internal minor diameter, internal major axis and equatorial wall thickness are respectively 33%, 14% and 30%.

BE3-C.1

Forces determining transmural distribution of myocardial blood flow, J.I.E. Hoffman*, A. Flynn, G. Aldea, D. Coggins, W. Hussein, R. Austin, University of California, San Francisco, California, U.S.A.

Left ventricular systolic intramyocardial tissue pressures equal cavity pressure below the endocardial (deep) surface and are near atmospheric below the epicardial surface. This implies that in the superficial left ventricular muscle, there should be a large pressure gradient from extramural coronary arteries to tissue, and therefore that there should be significant systolic perfusion of the superficial muscle from the extramural arteries. However, studies of the capacitance of these extramural arteries indicate that little of the blood that enters the arteries in systole actually perfuses the myocardium. The discrepancy can be explained by postulating that in systole, the increase in deep intramyocardial pressure raises intravascular pressures in the deep microvessels above pressure in the extramural arteries, whereas in the superficial muscle, intravascular microvessel pressures are below extramural arterial pressures. These pressure differences cause blood to move retrograde from deep microvessels to superficial intramyocardial arteries, thereby competing with systolic inflow from the extramural arteries. Experimental observations support this hypothesis.

BE3-B.4

Delayed end-ejection as a determinant of enhanced relaxation rate during an increase in stroke volume Masatsugu Hori, Masafumi Kitakaze, Yoshio Ishida, Hideo Kusuoka, Akira Kitabatake, Michitoshi Inoue⁺, Takenobu Kamada, Hiroshi Abe⁺⁺

The 1st Dept. of Med. and Dept. of Medical Information Science⁺, Osaka Univ. School of Medicine, Osaka National Hospital⁺⁺

Ventricular relaxation rate is enhanced when stroke volume is increased. To test the hypothesis that enhanced ventricular relaxation in this condition is due to delayed end-ejection associated with an increase in stroke volume, the left ventricular volume and ejection of the perfused isolated canine hearts (cross-circulation) were controlled by a servo-pump, and ventricular relaxation rate was assessed by the time constant (T) of isovolumic left ventricular pressure decay in various conditions. As stroke volume was increased, T was decreased (relaxation was accelerated) only when end-systolic volume was concomitantly decreased. When ejection velocity was increased, the relaxation rate was increased in almost all experiments. However, when the timing of end-ejection was clamped, T was not significantly altered even with a large change in ejection velocity. These results indicate that neither the extent nor velocity of ejection affects the ventricular relaxation rate but the delay of end-ejection enhances the relaxation rate when the stroke volume is increased.

BE3-C.2

Coronary Pressure-Inflow Relationships, R. E. Mates, SUNY at Buffalo, Buffalo, NY 14260, USA.

The mechanisms responsible for observed coronary pressure-inflow behavior remain controversial, particularly the observation that diastolic inflow ceases at pressures above right atrial pressure. Because of blood vessel compliance, phasic inflow differs from flow in the microcirculation. Since the latter is difficult to measure, models have been proposed to relate inflow to microcirculatory flow. We have utilized the flow response to coronary pressure perturbations to characterize pressure-inflow relationships. A lumped model consisting of a viscoelastic compliance, a resistor and a back pressure has been found sufficient to describe sinusoidal and ramp perturbations in prolonged diastoles. Rapid ramp perturbations analyzed with a nonlinear optimization technique have been used to evaluate model parameters during normal diastoles, with similar results. As in the prolonged diastoles, parameters differed significantly from control when the circulation was dilated with adenosine. Resistance was lower and capacitance higher in the vasodilated bed. Back pressure was lower in the dilated bed, although still significantly above right atrial pressure. We conclude that pressure-inflow relations do not vary significantly during diastole and that results obtained in prolonged diastoles can be applied to diastoles in normal cycles.

BE3-C.3

Quasi linear input behavior of non-linear model of intramyocardial perfusion, J.A.E. Spaan, University of Amsterdam, Department of Medical Physics, The Netherlands.

Compression of intramyocardial vessels is apparent from the increased venous and decreased arterial coronary flows in systole. Moreover, time averaged intramyocardial blood volume depends on the magnitude of left ventricular cavity pressure. Hence, it is plausible that flow patterns in all types of vessels but dependent on the depth in the myocardium are influenced by changes of volume either directly (capacitive flow) or indirectly because of a change in resistance.

The relative contribution of the different effects were assessed in a multi layer model of the ventricular wall in which arterial, capillary and venous compartments are put in series for each layer. Based on a pressure volume relation for each compartment reflecting stiffening of vessels at higher pressures and a relation between resistance and the inverse of volume squared the volume displacements and resistance variation were predicted.

The input effects of the non-linear model resemble the input of a constant RC network with small time constants (< 0.2 s) while the other system variables vary slowly (characteristic times > 1 s).

BE3-D.1

Myocardial Regional Flows and Metabolism: PET Studies, J. B. Bassingthwaite, M. M. Graham, and R. B. King, University of Washington, Seattle, WA 98195.

Because first order compartmental models are applicable to the parameterization of myocardial blood-tissue exchange processes from indicator dilution or PET or SPECT data only under severely limiting circumstances, we are using axially distributed models. These account for axial gradients within the capillary-tissue units and for the effects of axial diffusion. Heterogeneity of regional flows is accounted for on the basis of fractal distribution. The rates of transmembrane transport (across 2 endothelial surfaces and the myocyte surface) and intracellular reactions forming metabolites can be estimated only from the kinetics since external detection does not distinguish either localization or molecular form of the radioactive tracer. Glucose models of this form give quite different estimates of substrate metabolism than do compartmental models. An argument for preferring the estimates from distributed models is that they fit high resolution time-course data well, whereas compartmental models do not. Other arguments regarding the preference are inferred from the anatomy and from observations of spatial gradients in concentrations of other solutes. Conflicts in estimates of metabolic rates from different experiments are probably resolvable by making use of the most realistic models. (Supported by NIH grants CA42045 and HL38736.)

BE3-C.4

The Presence and Significance of Venous Level Coronary Collaterals, J.M. Downey and M.V. Cohen, University South Alabama, Mobile AL 36688

To measure venous level collateral connections, the great cardiac vein (GCV) and the anterior descending coronary artery (LAD) were cannulated in an open chest dog. Dye studies indicated that under baseline conditions the GCV drained exclusively from the LAD (10/11 dogs) and LAD and GCV flows were equal. Perturbations in the LAD flow were not reflected in the GCV, however. LAD occlusion caused only a 56% decrease in GCV flow, while peak GCV flow during reactive hypoxemia consistently underestimated peak LAD flow by nearly 40%. Simultaneous LAD and GCV occlusions resulted in near equilibration of arterial (13.6 ± 1.3 mmHg) and venous (12.4 ± 1.2 mmHg) pressures. The data closely fit a model which assumed the presence of a low resistance venous anastomosis. The resistance of the segment distal to the venous anastomosis was $10.0 \pm 1.5\%$ of the LAD resistance, while the resistance of the venous collateral averaged $9.9 \pm 3.0\%$ of the LAD resistance. Following LAD occlusion, ^{133}Xe washout decreased from 0.86 ± 0.16 to 0.13 ± 0.02 ml/min/g. Retroperfusion of the GCV with arterial blood during occlusion significantly enhanced the washout by 85% to 0.23 ± 0.03 ml/min/g ($p < 0.005$) showing that venous level collateral flow is somewhat nutritional. (supported by NIH grant HL 20648)

BE3-D.2

CARDIAC CONTRACTION AND CORONARY FLOW

Katsuhiko Tsujioka* and Fumihiko Kajiya
Department of Medical Engineering, Kawasaki
Medical School, Kurashiki, JAPAN

We recently reported that the intramyocardial capacitance vessels are composed of two functional components: usual capacitance and unstressed volume. Thus, the phasic coronary flow may be caused by the mechanism that the blood entered into the intramyocardial vessels during diastole would be squeezed out into the coronary vein by cardiac contraction during systole. To clarify this squeezing out dynamics, we analyzed the response of great cardiac vein flow (GCVF) after sudden cessation of coronary inflow by laser Doppler velocimeter in open-chest anesthetized dogs. GCVF decreased mono-exponentially after the cessation of coronary inflow. Thus, the time constant of GCVF decay was calculated and the blood within intramyocardial vessels during steady state (V_0) was obtained as time-integral of GCVF after cessation of inflow. When GCVF during steady state (F_0) was changed by altering coronary tonus, perfusion pressure, heart rate and contractility, the unique linear F_0 - V_0 relation determined F_0 , but there was no significant relation between F_0 and T . We conclude that the coronary vein flow is caused by squeezing out of blood within intramyocardial vessels and is regulated mainly by V_0 , not by T .

BES-D.3

Assessment of Myocardial Perfusion and Myocardial Blood Volume Using Ultrafast-CT, J. A. Rumberger*, M. L. Marcus, Mayo Clinic, Rochester, Minnesota, and University of Iowa, Iowa City, Iowa.

Ultrafast computed tomography (CT) uses a unique electron beam technology to allow for videodensitometric analysis of indicator clearance data from the great vessels and the myocardium. Following intravascular injection of iodinated contrast, 50 msec, high resolution images are acquired at up to 2/cardiac cycle from multiple cardiac levels. Selection of regions over the left ventricle, aorta, and myocardium allow characterization of contrast clearance from each vascular site using a gamma variate curve. Application of classic theory to these data have shown promise for intravenous injection techniques with regard to quantitation of regional flow per unit volume and the ratio of myocardial blood volume to central blood volume when compared to simultaneous assessment using radiolabeled microspheres ($r = .85$, $SEE = 50$ cc/100 g/min, $r = .84$, $SEE = 5$ percent, respectively). This approach may have broad application to the evaluation of patients with a variety of cardiac diseases.

BES-E.2

Cardiac Structure and Function Quantitated with Multislice Computed Tomography (CT), N. Chung and E. L. Ritman*, Mayo Medical School, Rochester, MN.

The fast, high repetition rate, volume scanning computed tomography Dynamic Spatial Reconstructor was used to quantitate cardiac structure and function in intact experimental animals. From the scans performed during a right atrial injection of contrast agent, Iwasaki et al demonstrated 95% accuracy of estimates of myocardial muscle mass (Am J Physiol 246: H138-42, 1984) and Hoffman et al obtained the same accuracy for volumes of all cardiac chambers (Radiol 155:739-44, 1985). Myocardial perfusion estimated from opacification of the myocardium during an aortic root injection of contrast agent was shown by Wang et al (Clinical Res 34:947A, 1986) to match values estimated by microspheres over a wide range of values. Chung et al (Physiol 30(4):54, 1987) demonstrated a good correlation between myocardial oxygen consumption and ventricular pressure volume loop area.

We conclude that quantitation of multiple aspects of cardiac structure and function can be obtained simultaneously from a single volumetric CT scan during a contrast medium injection.

BES-E.1

Magnetic Resonance Imaging Assessment of Regional Ventricular Function, James T. Willerson,* University of Texas Southwestern Medical Center at Dallas, Texas

A quantitative nuclear magnetic resonance imaging method has been developed for evaluating regional left ventricular function. Short-axis images of the heart were obtained at end-diastole and at 100 msec intervals thereafter. Regional diastolic left ventricular wall thickness and maximal percent systolic wall thickening were measured at the level of the papillary muscles in each of 6 segments. In 6 normal dogs, the mean end-diastolic wall thickness was 9 ± 1.6 mm and the mean maximal percent thickening was $61 \pm 11\%$. In 6 dogs with 4 day old infarcts, maximal percent thickening was $5 \pm 8\%$ ($p < 0.001$) in the infarcted segments. In 10 normal human volunteers, the mean end diastolic wall thickness was 10.1 ± 1 mm and the mean maximal percent systolic wall thickening was $60 \pm 18\%$. Using the mean value obtained in normal volunteers, reduced maximal percent systolic wall thickening was defined as a value 2 SD or more below the normal values. Seven patients with regional wall motion abnormalities were independently assessed by nuclear magnetic resonance imaging and biplane ventriculography. Compared to regions identified as akinetic or dyskinetic by biplane ventriculography, nuclear magnetic resonance imaging demonstrated reduced maximal percent systolic wall thickening in the same segments with a sensitivity of 94% and specificity of 80%. Abnormalities of regional systolic wall thickening are accurately identified using this quantitative nuclear magnetic resonance imaging technique.

BES-E.3

Measurements of Left Ventricular Shape and Function, S. Sideman*, H. Azhari, U. Dinnar and R. Beyar, Biomedical Engineering, Technion-IIT, Haifa, Israel.

A new method of detecting regional left ventricular (LV) dysfunction by 3-D reconstruction of the LV is presented. In general, the 3-D shape of the heart at end diastole and end systole is transformed to a helical coordinate system. By that the 3-D information is transformed into a continuous one-dimensional signal. Input data were obtained by various measurement techniques including echocardiography, Cine CT and MRI. Three levels of analysis were performed: a) Shape analysis and a shape distortion analysis assisted by the Karhunen-Loeve transform, b) analysis of endocardial motion from end diastole to end systole as a measure of regional dysfunction, and c) analysis of wall thickness and thickening as a measure of LV regional dysfunction. The combined technique of assessing pathological LV shape and function represents a powerful tool which, together with the fast developments of a new generation of 3-D imaging methods, will greatly enhance non invasive cardiac diagnostics.

BE3-F.1

Assessment of Left Ventricular Systolic and Diastolic Mechanics Using Ultrafast-CT, J. A. Rumberger*, M. L. Marcus, Mayo Clinic, Rochester, Minnesota, and University of Iowa, Iowa City, Iowa.

Ultrafast computed tomography (CT) uses a unique electron beam technology to allow for evaluation of left ventricular (LV) function at multiple levels. Cine framing rates of 17/second allow stop action images of the heart using intravenous contrast injection techniques. Quantitative analysis of LV mass (SEE = 5 g) and LV stroke volume (SEE = 1.5 cc) are possible. Time-dependent ventricular volume information can be analyzed per tomographic level as well as for global analysis; curve fitting techniques allow for characterization of maximum emptying and filling rates. These CT techniques have broad applications towards the noninvasive diagnosis of coronary artery disease and quantitative investigations regarding LV response to surgical and pharmacologic therapy.

BE3-F.3

The Use of Diastolic Sounds to Characterize Cardiac Performance: Theoretical Studies

W. Welkowitz,* J. Wang, B. Tie, S. Lewkowitz, J. Semmlow, Department of Biomedical Engineering, Rutgers University.

It has been proposed that diastolic sounds can be used to suggest potential problems of cardiac performance. In particular, such sounds can indicate the presence of partial blockage in the coronary tree and perhaps quantitate the blockage.

In order to carry out theoretical studies pertaining to this problem it is necessary to first produce an acceptable model of the coronary artery tree which can be used to predict flow throughout the cardiac cycle for any blockage location. Once the flow through the blockage is calculated, then it is necessary to construct a model of the sound generation mechanism. Finally, the propagation of this sound to the outside of the body must be analyzed.

A model of the arterial tree which includes area variations during systole (including occlusion) and peripheral regulation has been analyzed and coronary flows in all parts of the system have been calculated for normal and constricted cases. These agree well with measurements. Finally, using these flows, sounds generated by turbulence at these constrictions have also been calculated.

BE3-F.2

Dynamic Transverse Stiffness Can Estimate Myocardial Wall Stress during Single Contractions, H. Halperin*, J. Humphrey, P. Chew, K. Sagawa, J. Tsitlik, F. Yin, Johns Hopkins Hospital, Baltimore, MD 21205

We have shown that transverse stiffness (TS) [the ratio of indentation stress to strain during transverse indentations] is related to in-plane wall stress at the peak of contraction. Those studies required 20-40 beats for one determination of TS. We developed a new servo system that can indent muscle cyclically at frequencies up to 100 Hz, while maintaining the contact stress constant throughout a contraction. In-plane wall stress was measured directly in five isolated ventricular septa while TS was determined during each contraction. For values of in-plane stress from 0.05 to 2.0 g/mm², TS varied from 2.1 to 25.7 g/mm² and was linearly related to the in-plane wall stresses in each septum ($p < 0.001$, ANOVA). The slopes of the individual relationships between TS and wall stress from systole were similar to those from diastole [mean \pm SEM] (9.1 ± 1.6 vs 10 ± 3.1 , $p = \text{NS}$), but the intercepts with the TS axis were greater than those from diastole (11.8 ± 1.6 vs 4.2 ± 0.6 g/mm², $p < .016$). Thus, dynamically determined TS is linearly related to in-plane stresses and can be used for quantitative estimation of in-plane stresses throughout a contraction cycle.

CET-A.2

Management and Maintenance of Health Care Equipment - WHO's Global Effort. A. Issakov, World Health Organization, Geneva, Switzerland.

Most developing countries are facing tremendous wastage of resources and severe limitations of all aspects of health care delivery due to the ineffective management and maintenance of health care equipment. The reason for this is the lack of awareness, policy commitment, effective infrastructure of health care technical service, manpower development programmes and a comprehensive approach at a country level. The results of international action undertaken by various organizations and agencies were far from anticipated due to lack of coordination and duplication of efforts in some areas with others being neglected.

Responding to the growing concern over the existing situation WHO has initiated a global programme directed towards strengthening of national capabilities for the development of comprehensive systems for effective management of health care equipment.

The programme aims to meet its objectives by building up common coordinated action, by facilitating collaboration between all agencies concerned and by mobilizing resources for comprehensive, integral and coherent action as part of strategies developed with the aim of achieving the goal of Health for All.

CET-C.1

A PROFILE OF CERTIFIED CLINICAL ENGINEERS, L. Fennigkoh, St. Luke's Medical Center, Milwaukee, WI, USA.

In an attempt to obtain a profile of Certified Clinical Engineers (CCE's) and their thoughts on the profession, a questionnaire was sent to 346 CCE's worldwide. A remarkable 72% return revealed, in part, the following:

- 57% of the CCE's are employed by hospitals, 15% by manufacturers, 12% by academia, and 13% are consultants in private practice;
- 50% of CCE's have been with their current employer for 6-9 years;
- 48% of the hospital-based CCE's previously worked in hospitals, while 36% of non hospital-based CCE's left hospitals for their present jobs;
- the CCE's average age is 44 years;
- 37% of the CCE's are also registered Professional Engineers;
- median salary range for hospital-based CCE's is \$40-45,000/yr, while that of their non hospital-based counterparts is \$50-55,000/yr (on average, hospital CCE's are also 5 years younger than non hospital CCE's).

Although the general conclusions suggest that the certification process in particular and the profession in general is in distress, CCE's believe the profession has made significant contributions to health care and continues to remain a viable career choice.

CET-C.3

Preliminary Results of an International Survey of Clinical Engineering Departments. M. Frize, Regional Clinical Engineering Service, 330 Archibald Street, Moncton (New Brunswick) E1C 2Z3, Canada.

In a survey of clinical engineering departments in several countries, with 80 respondents, 14% indicate that they do not have an engineer on their staff; 49% of departments report to administration; 30% to plant/maintenance; 6.5% to the medical director and 11% to others. However, only 62% of departments reporting to plant find this satisfactory, whereas 100% of those reporting to administration indicate satisfaction. The proportion of departments performing 90% of more in-house repairs were: 68% for medical equipment; 19% for medical imaging; 13% for the laboratory; 44% for anesthetic equipment; 6% for non-medical devices. The proportion of departments being "always" consulted prior to equipment acquisition is higher where there are engineers on staff and also higher in University versus non-University hospitals. Several other variables will be discussed and variances between countries will be shown. These preliminary results indicate the presence of great disparities between clinical engineering departments in the same country and from one country to another.

CET-C.2

Clinical Engineering in the U.S.:
The Administrator's Viewpoint, M.J. Shaffer, D.Sc. and M.D. Shaffer, M.S., George Washington University Medical Center, Washington, D.C. U.S.A.

In a survey of 250 hospitals with 89 respondents, it was found that administrators running clinical engineering departments received in their college courses an average of 0.6 hours of training in clinical engineering matters, while they considered 4.1 hours are needed. They had an on-job experience of 6.5 years, while recommending 4 years as an appropriate minimum. As to reporting hierarchy, 42% recommended both Clinical Engineering and Plant Operations should report to the same administrator, 22% recommended they should report to separate administrators, and 31% recommended that Clinical Engineering should report as a division of Plant Operations. Concerning their attitudes, on a scale of 0-5 with 5 highest, the administrators rated their clinical engineering responsibilities with little power (2.0) and chance to make their name (2.3), with moderate prestige (3.65), and with high acceptance of their authority (4.01) and pride of achievement (4.4).

BE4-A.1

Clinical Engineering: A Focused Biomedical Engineering and Career Program

Barry Feinkert, Ph.D., P.E., C.C.E
Center For Engineering Analysis
Northbrook, Illinois 60062 USA

A clinical engineer is an engineer who applies the science of engineering to the delivery of health care. He or she is concerned with the application of engineering theory and analysis to diagnostic and therapeutic systems as well as to patient care and life support in general.

Clinical engineering has emerged as the only areas of biomedical engineering that has crystallized into a unified body of knowledge similar to the other classical disciplines of engineering. Clinical engineering will be discussed from the view of career opportunities, both hospital and industrial; educational preparation required of the clinical engineer—courses; laboratories and internships, and certification in clinical engineering.

The emerging areas of medical radiation engineering and clinical engineers as part of an artificial heart transplant team and other advanced areas of health care delivery as new paths in the career development of the clinical engineer will be discussed.

BE4-A.2

State Orders to Clinical Engineering in the GDR

D.Kraft*, Zentralklinik, DDR - 5303 Bad Berka, GDR

The ministry of health in the GDR have devoted attention for many years the specialized field of biomedical engineering in medical institutions.

1. On April 1st 1981 the decree on the postgraduate study biomedical engineering for scientific and technological university graduates, which work in medical institutions, came into force. This study is an integral part in systematically organized development training - analogously to the continuation training to become a medical specialist. (Requirements for attendance, setup and course, study material, attendance of other medical institutions as guest, final examination, professional bye-identification).

2. On January 24st 1982, the decree on the structure and organization of biomedical engineering by medical institutions came into force.

The basic unit of clinical engineering has the following duties: Responsibilities for guaranteeing readiness for use, efficiency and safety of medico-technical equipment, assignments in the care for patients as direct partner and under the physicians responsibility; assignments within the plan component of science and technology at the institution, assignments in the field of educational development, assignments in the field of planning and economy.

BE4-A.3

Biomedical Engineering in an electronic engineering curriculum: a ten years experience in Spain, R. Pallas-Areny*, Division de Instrumentacion y Bioingenieria, ETS Ing Telecom, Box 30002, 08080 Barcelona, Spain.

Biomedical Engineering is not recognized as a profession in Spain, nor are there university or school qualifications in this subject. But the medical equipment industry, hospitals and even distributors need engineers with a certain knowledge of medical instrumentation.

In engineering curricula in Spain there are no elective courses and any change in them must be introduced under the umbrella of an existing course. Taking advantage of our responsibility for already existing Instrumentation and Transducers courses and their laboratory practicals we changed our program 10 years ago and 50% of it now consists of Medical Instrumentation. In it, biomedical topics are considered not as an end in themselves but as a mean of introducing, for example, low level signal amplification, interferences, pressure and flow measurements, electrical safety, imaging, and energy interactions with living beings. A parallel compulsory laboratory course concentrates on analog signal processing.

BE4-A.4

EDUCATION AND TRAINING FOR CLINICAL ENGINEERING IN THE U.K.

V C Roberts*

Department of Medical Engineering,
King's College School of Medicine, LONDON

No formal course of instruction exists within the UK which leads towards an undergraduate or postgraduate degree (or certification) in clinical engineering. The presently preferred route is via one of several MSc courses in bioengineering (including medical electronics and biomechanics). These degrees are then followed by suitable periods of on-job training in the clinical environment.

Postgraduate training programmes are available for those in health care who seek professional registration as a Chartered Engineer. However, their pursuit is dependent on the sympathy of the head of each department of Medical Engineering or Medical Physics. A number of part time post-qualification courses are either planned or being run and these will need to address aspects of business management as well as scientific updating. There is evidence that the UK's Hospital Engineering Service is increasing its involvement in clinical engineering, particularly in the area of equipment management.

BE4-A.5

BIOMEDICAL ENGINEERING EDUCATION IN THIRD WORLD NATIONS - T. Krishna Murthy* and M. Dhananjaya, Dept. of Biomedical Engineering, India Institute of Technology, Bangalore, India.

Compared to developed nations, the disease pattern and socioeconomic conditions among the majority of people warrants a modified approach regarding planning and utilisation of trained manpower, even use of automation and semiautomation though inevitable and desirable may have to be restricted to certain centres of excellence having the necessary back-up facilities. There can be no doubt that biomedical engineers, clinical engineers, rehabilitation engineers and medical equipment technologists are needed for the major hospitals, medical colleges and other specialised medical research centres. Courses have to be planned depending on the utilisation of such trained manpower. Besides regular courses, short and long term refresher courses, workshops and symposia form a major part of Biomedical Engineering education and training. So, a cautious need based approach with necessary modification and adaptation in consultation with the state medical and health care authorities may lead to optimum utilisation of such manpower.

BE4-A.6

SUPPLEMENTAL TRAINING FOR CLINICAL ENGINEERS AND TECHNICIANS: INTERNSHIPS, G.I. Johnston* and R.L. Morris, Oregon Health Sciences Univ.

Engineers and technicians graduate from four-year and two-year programs with little or no practical experience. This is understandable and not necessarily undesirable. An electrical engineer or electronics technician has an enormous variety of career choices upon graduation, all of which cannot and should not be addressed in the academic curricula. They should first of all be competent in the fundamentals of their engineering or technical discipline. It should then be, and historically has been, the responsibility of the hiring organization to provide training specific to the company's product or service. For bachelors level biomedical and clinical engineers and for many biomedical equipment technicians this process has been subverted in favor of providing life science education at considerable cost to the engineering curricula. That subversion has been aided and abetted by hiring organizations failing to provide apprentice or internship training programs necessary for the completion of the education process. Several solutions to this problem will be presented and discussed.

BE4-A.8

Expanding Horizons of the Clinical Engineer: The Artificial Heart, Michael S. Bernstein*, M.S.E., P.E., C.C.E. Methodist Hospital of Indiana, Indianapolis, IN 46202

The Clinical Engineer's Horizon of responsibility has been expanded to include the Total Artificial Heart. The patient is totally dependent on an electromechanical device therefore changing clinical engineering's responsibility from indirect to direct patient care. Before, during, and after the implant surgery the clinical engineer has crucial responsibilities. The Clinical Engineer is responsible for the constant state of readiness of the support equipment and the nursing staff. Immediately before and during implant, the clinical engineer must set up the equipment systems for their specific use. Because the artificial heart does not provide ECG signals, the operating room/intensive care monitoring systems cannot be used in the conventional way. Support must be provided on a 24 hour a day basis during the implant period. During the explant/transplant, the clinical engineer is responsible for the supervision of the artificial heart console and shutdown assisting the surgeon in proper transfer from artificial heart to heart-lung bypass to transplant.

BE4-A.7

Estimating the Number of Clinical Engineers in the United States, M. Baretich*, University of Colorado Health Sciences Center, Denver, Colorado, USA.

Estimates of the number of clinical engineers practicing in the United States range from a few hundred to several thousand. At least two methodological factors contribute to this wide variance: (1) Different definitions of the term *clinical engineer*. (2) Different statistical estimation techniques.

The definition of a clinical engineer should be as broad as possible yet exclude personnel not holding appropriate professional credentials (education, licensure, certification, experience, etc.). Statistical estimation techniques should be carefully chosen and correctly applied. This paper addresses these issues and offers recommendations for future estimates.

The author estimates that there are 500 to 1000 practicing clinical engineers in the United States. However, a definitive survey should be undertaken to determine the number more precisely. Without such basic information regarding the profession, preparation for the 21st century will be difficult.

BE4-B.1

Standards: An Overview, A. Wald*, Department of Anesthesiology, Columbia-Presbyterian Medical Center, New York, NY 10032

In the most general terms, there are four types of standards. First, there are standards that relate to measurements. These standards permit the conduct of science and technology and also foster trade and commerce. A second type of standard would more appropriately be referred to as a uniformity document. Thus, there are standard screw threads, kitchen counter heights, and transistor characteristics.

Then there is a more intangible type of standard. A standard that does not necessarily refer to any physical product, but rather to some type of human behavior or activity. This type of standard is often only written down in the broadest terms. It is often based on some consensus of what society as a whole expects, either for the ideal condition or for what can be expected practically. Finally, we have what would best be called, product standards, that is standards that relate directly to a particular product. Such standards can include criteria such as materials, construction, operation, performance, labeling, safety, and efficacy.

Standards must be addressed in their own right, in terms of legal, economic, and technical considerations. Some aspects of standards on an international basis will be presented.

BE4-B.2

Multiple Roles of International Standardization in Medical Engineering, S. E. Lindell, University of Lund S-2041 Malmö, Sweden; and R. J. Plaszczyński* SEE/CFTBM, F-75724 Paris, France

The first author is chairman of Technical Committee TC62 "Electrical Equipment in Medical Practice" of the International Electrotechnical Commission (IEC) and the second one has been involved for the last 18 years in the creation of international standards within numerous IEC working groups. Their experience enables them to emphasize the role of standardization not only for the optimization of the characteristics and cost of equipment but also for promoting a better mutual understanding between the people concerned. Since 1906 the IEC continues to develop an international collaboration between manufacturers and users of electrical equipment. Experts from 42 countries participate through their National Committees in the activities of about 200 Technical Committees & the Sub-Committees of the IEC. Its Central Office is situated in Geneva, Switzerland. The TC62 was established in 1966 and now comprises 4 Sub-Committees with 30 working Groups. World-wide voluntary standardization facilitates a closer cooperation between physicians and engineers involved in the establishment of safety rules concerning patient, operator and surroundings and furthermore contributes to the transfer of the know-how and technology from developed to developing countries.

BE4-B.4

Safety regulations for medical equipment in Germany
U. Boenick*, P.M.Schroeder, A.Miksicek

On the 1st of January 1986 the German "Medizingeräteverordnung" (regulation upon safety of medical appliances) has obtained legal validity. This regulation divides technical equipment used in the medical environment into four groups according to their function and purpose.

To be allowed to sell equipment subjected to group 1 (life preserving device) or group 2 (implantable energized parts) a type examination and an official approval by the Industrial Inspection Board is necessary.

For devices conforming to group 3 and 4 (energy-driven and non-energized equipment) a voluntary type examination can be conducted, permitting the manufacturer to hold the GS-label (Geprüfte Sicherheit = proved safety).

The responsibility of manufacturers, distributors and customers, maintenance of the equipment and other details are regulated by law.

BE4-B.3

The Impact of International Standard Development on Medical Devices
Mort Levin*

Easy global communication is tending to blur distinctions between U.S. and other standards. What are the forces shaping this phenomenon? How do these forces influence medical devices?

Marketing across international boundaries requires that manufacturers design to standards acceptable to the importing user. Economic forces encourage producers to participate in worldwide standard development in order to learn about events taking place and to share in the decision process.

Safety of medical devices is a concern of users, producers and regulators. Since users and regulators are also impacted by finances, economics and safety tend to bring all parties together for the benefit of the patient. The impact of easy communication on international standard activity and the resulting influence on medical devices will be discussed in greater detail.

BE4-B.5

U.S. Electrical Safety Standards. Focus on Leakage Current and Oxygen Enrichment
A. Lipschultz* PE CCE, Waterbury Hospital, Waterbury, Connecticut 06721

There are two major U.S. Standards dealing with hospital electrical safety: AAMI Safe Current Limits Standard; and NFPA 99, Health Care Facilities. The chassis leakage current value in these standards of 100 microamperes is substantially lower than the IEC value of 500 microamperes. The reason for this appears to be historical as well as a different assignment of risk values. Some of the difference also is a result of the lower U.S. line voltage. The rationale for the AAMI value is well documented. The values chosen by the other standards is not well documented. One aspect of the NFPA 99 standard that I am very familiar with is the use of electricity in oxygen enriched atmospheres. I will use this example to illustrate the process by which this standard was significantly modified to reflect the data I had accumulated. The original philosophy in this matter was that all electrical equipment should be kept away from any portion of the oxygen delivery system. The new philosophy looks at the place where the oxygen enriched mixture is actually expelled to the atmosphere, and at the temperature and/or energy that the electrical device is capable of generating.

BE4-B.6

PROPOSAL TO IMPROVE THE ELECTRICAL SAFETY SITUATION IN PUBLIC HOSPITALS (TUCUMÁN).
CJ Felice, CP Breitman, OJ Barrionuevo, OR Batallán, HD Gramajo, VI Rotger and MI Vercellone. Bioingeniería, Universidad Nacional de Tucumán, cc 28 suc 2, 4000 Tucumán, Argentina. ME Valentinuzzi*

Without considering more or less incidental short courses, in Argentina there are: A) Bioengineering (undergrad level), six-year well-structured program, Universidad Nacional Entre Ríos. First graduates by 1991. B) Residence in Hospital Engineering (grad level), at several hospitals, Buenos Aires City, three years. C) A few universities (Tucumán, Buenos Aires, Technological) offer courses at the undergrad level. However, although a good introduction, they are not enough for the full training of Clinical Engineers. We propose: 1) Talks about the subject. 2) Courses for hospital technicians. 3) Courses for hospital directors, medical and paramedical personnel. 4) To prepare a roster of professionals with some kind of training in CE to be presented to hospital authorities for possible hiring. 5) Field visits and detailed analysis of the situation at all public hospitals to obtain a complete overview.

BE4-C.2

Electrophysiological Studies of Laser and Suture Anastomoses in Rat Sciatic Nerves,

T.A. Benke*, J.W. Clark, and P.J. Wisoff,
Department of Electrical & Computer Engineering,
Rice University, Houston, TX 77251-1892;
S.A. Shehab, Texas Heart Institute, Houston, TX 77225;
S. Schneider and J. Laurent, Texas Children's Hospital,
Houston, TX 77030

Conventional suture repair of peripheral nerves results in fibrotic reaction which is detrimental to nerve regeneration. As an alternative procedure, a laser can be used to reanastomose severed peripheral nerves. This study presents electrophysical measurements of the right sciatic nerve of Wistar rats which has been surgically cut and reanastomosed either by means of sutures or a laser weld. The left sciatic nerve is left untouched and serves as a control for that animal. Each nerve was placed in a lucite bath containing a linear array of electrodes and filled with Krebs's solution. The nerve was then stimulated with a pulse of .01 msec duration, and the response measured. Computer simulations of short lengths of nerve are compared with the measurements to account for the progressive diminishment in amplitude of the action potential with increasing distance from the stimulation site and to understand the nature of the injury potential at the distal end of the nerve fiber.

BE4-C.1

STIMULATING EFFECT OF LASER AND NONCOHERENT RED LIGHT ON REGENERATION OF RAT SCIATIC NERVES - Tan Runchu*, Qiu Yiguang, Tan Yankong, and Ma Guo-guang, Sun Yat-Sen University of Medical Sciences, Guangzhou, P.R.C.

This is an important basal study of laser medicine on the biological function with laser. The target might come from the energy, the wavelength, the coherency and the polarization. So far as present time is concerned, there were the differential opinions, as some authors considered the biological effect relate to coherency, wavelength, energy, etc. So we took to coherency and wavelength. The following results:

1. The 633nm red light and laser of other wavelengths could stimulate the regeneration of nerves.
2. No significant difference was found between the effects of coherent and noncoherent lasers on sciatic nerve regeneration.
3. The difference of wavelength had no influence on the stimulating effect of laser upon sciatic nerve regeneration.

BE4-C.3

Biomedical Engineering Approach, Theory and Biomechanic Basis of AIDS Laser Therapy and Curative Computed Tomography for Combined Diagnostic and Treatment. V. Vasilionkaitis*, Lithuanian Cancer Research Institute, Vilnius, Lithuania, USSR

According to mechanism of human immunodeficiency virus (HIV) persistence the system of anti-HIV laser traps together with electrochemical devices against AIDS is proposed. Laser traps from I to 10 classes depending selectivity installed with blood or lymph separators (e.g. types of Aminco, IBM, Hamonetic, Fenwall, Ito-Flow-Through) together with original chamber with mobile walls in turn for external exposure at curative screen (contact therapy, sterilization, photoradiation, immunostimulation, killing, elimination) and return of blood elements to natural flow. Also a curative computed (CCT) tomography (x-CT, SPECT/PET, ultrasound, MRI) was substantiated with collection of CCT devices for immediately treatment after precise diagnostic: mobile CT-microscalpel with correcting tracers, CT-selective drug delivery system in scanning layers, CCT devices for remote ligation, clip or cutting, canals performing, angioplasty, dilatation, cytotherapy. Number of CCT programmes are unlimited at all organs or tissue for different CT or magnetic resonance imaging therapy, surgery or microsurgery.

BE4-C.4

Laser Coronary Angioplasty Using CO Laser under Visualization by Coronary Angioscope, T. Arai, M. Nakagawa, M. Kikuchi*, K. Mizuno, K. Arakawa, T. Shibuya, K. Satomura, A. Miyamoto, Y. Okamoto, K. Horiuchi, K. Isojima, A. Kurita, H. Nakamura, A. Utsumi¹, and K. Takeuchi², National Defense Medical College, Saitama, Japan. ¹Mitsubishi Cable, Indus. Ltd., Hyogo, Japan. ²Fukuda Denshi Co. Ltd., Tokyo, Japan.

A fundamental investigation of laser coronary angioplasty using CO laser under visualization of intra-lumina lesion by coronary angioscope is described in this paper. In vitro experiment of CO laser irradiation to human atheroma indicates strong ablation effect with tissue selectivity without any thermal damage to vascular wall. CO laser light, 5 μ m of its wavelength, can be delivered by flexible infrared glass fibers. The authors have been successfully reported flexible energy delivery of CO laser by As-S chalcogenide glass fiber. According to an estimation using experimental results of the energy delivery, 3.3W CO laser power may be available in human left coronary artery. By every 3.5s irradiation of this power can vaporize 7mg atheroma. To targetting and positioning of the laser irradiation, we develop thin coronary angioscope catheter of which outer diameter less than 5F(1.66mm). A top small round balloon can occlude blood flow to reduce blood flushing fluid.

BE4-C.6

Laser Surgery and Medicine in Japan.
T. Atsumi, University of Tokyo, 7-3-1 Hongo, Bunkyo-ku, Tokyo, 113, JAPAN

The research and development on laser surgery and medicine was started by using ruby laser to study the irradiation effects on tissues of mice in the University of Tokyo in 1965.

The first clinical trial of ruby laser therapy for a skin cancer patient was experienced in 1967.

In Japan, surgical laser units such as CO₂, Nd-YAG, argon were developed and widely used in clinical cases, argon dye laser was used for PDT, He-Ne and diode lasers are applied for low power therapy and CO, Nd-YAG and excimer lasers have been started to use for angioplasty.

At the present state, 230 Nd-YAG, 170 CO₂, and 30 argon lasers have been installed in the Japanese hospitals and medical institutes.

The Japanese Society of Laser Surgery and Medicine was organized in 1979 and the 1,012 members including the 800 medical doctors and the 150 engineers and the others were registered at the date of March 1988.

According to the wide spread of the laser units for medical use, the education of clinical engineers for laser surgery and medicine and their qualification become the important problems.

The safety guideline was also made by the safety committee of the Japanese Society of Laser Surgery and Medicine.

BE4-C.5

Laser Induced Autofluorescence Analysis of Arteriosclerotic Arteries,
G. Pettit*, S. Kubodera, F.K. Tittel, M. Sartori, P. Henry, and R. Sauerbrey, Department of Electrical and Computer Engineering, Rice University, Houston, TX 77251-1892 U.S.A.

Laser angioplasty has the potential to be a treatment for coronary artery disease. Currently, one of the main problems with this approach is uncontrolled damage to the vessel wall, including perforation. Therefore, real time diagnostic techniques, such as tissue autofluorescence analysis which could indicate when laser application should be terminated, are highly desirable.

Argon ion laser radiation at 457.9 nm has been shown to elicit characteristic spectra which allow discrimination between normal arterial wall and arteriosclerotic regions. In addition, this spectral analysis has been used to determine when a diseased region has been penetrated and normal tissue reached by excimer laser ablation. Since ideally a single laser system would be used for both analysis and ablation, 351 nm excimer laser radiation delivered via optical fiber has been tested as a means of eliciting autofluorescence signatures.

BE4-C.7

ADVENTITIAL TEMPERATURES AND EXTENT OF DAMAGE DURING *IN VITRO* APPLICATION OF A LASER THERMAL PROBE TO CANINE ARTERIES

J.H. TORRES*, A.J. WELCH and J. GHIDONI
THE UNIVERSITY OF TEXAS AT AUSTIN
THE UNIVERSITY OF TEXAS HEALTH SCIENCE CENTER AT SAN ANTONIO

A laser thermal probe with a 2mm diameter was heated by an argon laser at powers of 1 to 4 watts and applied to femoral, renal and carotid canine arteries *in vitro* in 5 to 10 second pulses. The probe was placed inside the arteries and its temperature was measured by a thermocouple welded to it (the probe). A 3-5 μ m thermal camera was used to measure the temperature rise at the adventitial side of the vessels. Three cases were considered: 1) no liquid in the vessel, 2) the artery filled with saline, and 3) the artery filled with blood. The extent of damaged was determined by histology and correlated with the temperatures achieved by the probe and the temperatures measured at the back surface of the vessel. The temperatures obtained were also correlated with the applied laser energy.

This work was supported by the Free Electron Laser Biomedical/Material Science Program : ONR contract number N00014-86-K-0875.

BE4-C.8

Laser Speckle Displacement Cardiography, G. Ramachandran*, Megha Singh, Biomedical Engineering Division, Indian Institute of Technology, Madras - 600 036, India.

A new non-contact and non-invasive technique to monitor cardiac functional disorders has been developed. It is based on laser speckle interferometry in which speckles, produced by the interference of laser light, scattered due to the roughness of a surface are utilized for measuring the displacement of the surface. An electronic shutter has been developed for controlling and synchronizing the laser exposure with the electrocardiography (ecg) of the subject. Recording is performed on a holographic plate and the developed plate is analyzed by point-wise filtering technique. The displacements are interpolated statistically and are plotted to contain a perspective mapping of the activity as seen on the chest wall. By this method, the cardiac displacement activity during various phases of the cardiac cycle has been obtained and compared for healthy male subjects. Its application to the patients suffering from cardiac functional abnormalities provides details of the malfunctioning region of the heart and shows excellent to good agreement with that of 2D - echocardiography.

BE4-D.2

Automation in the Pediatric Exercise Laboratory, Frank M. Galisto, Jr., M.D., Children's Hospital National Medical Center, Washington, D.C.

Increasing complexity in the pediatric exercise physiology laboratory has lent itself to automation. Measurements that are becoming increasingly important to fully assess the exercise performance in children include: electrocardiogram, blood pressure, respiratory gas exchange in the form of oxygen consumption, carbon dioxide production and minute ventilation and cardiac output typically in the form of acetylene re-breathing. These parameters cannot be measured simultaneously without computer-controlled data acquisition and online analysis. The computer serves to interface input devices such as the respiratory mass spectrometer and pneumotachograph, acquires data and performs online computation of the various parameters. The computer prepares the final report in a timely fashion so that data is available for analysis by the physician at the completion of the exercise test without delay.

This paper will emphasize the studies undertaken with discussion of the complex methodology required and the usefulness of automation in the pediatric exercise physiology laboratory.

FE4-D.1

ADVANCES IN MEASUREMENT OF RESPIRATORY GAS EXCHANGE IN CRITICALLY ILL PATIENTS, Edward J. Truemper*, Larry S. Jefferson, Yadin B. David, David L. Walding, Baylor College of Medicine, Houston, Texas

The use of oxygen consumption, carbon dioxide production, and respiratory quotient determinations in critically ill patients are assuming increasing importance in guiding therapeutic interventions for cardiopulmonary, nutritional, and metabolic support. Despite the wide variety of commercial and custom designed instruments available, serious limitations exist which restrict their application and interpretation when used on certain patients. Potential factors that must be considered include: use of endotracheal tubes, high fraction of inspired oxygen, certain mechanical ventilatory modes (continuous flow, high peak flow rates) and water vapor. In critically ill children, the fast respiratory rates and small lung volumes often further limit the technical capabilities of most instruments. An outline of these various factors limiting instrument application is presented. Methods for reducing equipment error and improving instrument performance will be discussed.

BE4-D.3

Application of the equation of motion to mechanical ventilation. P. Richardson* and T. Hansen, 1 Baylor Plaza, Houston, TX. Passive exhalation lung mechanics (compliance C, resistance R and time constant TC) are used to characterize the pulmonary pathophysiology of infants with lung disease in newborn intensive care units. We use the equation of motion ($P = V/C + \dot{v}$) to describe lung volume (V) and gas flow (\dot{v}) during passive exhalation when pressure P for the respiratory system equals 0. TC is calculated from the slope of flow-volume curve, C is determined either as quasi-static C or dynamic C, then R is calculated from TC/C. Two different techniques are used in determining lung mechanics and the results are usually different. For mapping severity or stage of disease, we clamp the infant's endotracheal near end-inhalation and allow pressures in the lung to reach equilibrium then release the clamp for passive exhalation to the atmosphere; therefore, the ventilator is momentarily removed from the system for quasi-static measures. For determining the effects of ventilator settings on dynamic lung mechanics, measurements are made during mechanical ventilation. An IBM-XT computer is used to sample flow and airway pressure then calculate C, R and TC. Tidal volume, respiratory rate and airway pressures are also calculated. Computer math modeling is applied to flow-volume curves that are not linear and a distribution of time constants is calculated.

BE4-D.4

The Use of Magnetic Resonance Spectroscopy in Hypoxia. G. Gutierrez*, Pulmonary Division, Univ Texas Health Science Center, Houston, TX.

Magnetic resonance spectroscopy (MRS) is a new technique with great potential in the non-invasive diagnosis and treatment of tissue hypoxia. MRS works by directing high frequency radio pulses into tissue samples placed within a strong and homogeneous magnetic field. The radio energy absorbed by certain nuclei in tissue produce a spectrum where different peaks correspond to various important biologically active molecules. The area under the peaks provide a relative measure of the tissue concentration of these molecules. Two important, naturally occurring, isotopes are 1-H (proton) and 31-phosphorus. Proton MRS is widely used to create tomographic images, but it also provides information on the tissue concentration of numerous compounds, such as free fatty acids and lactate. 31-phosphorus MRS can be used to follow changes in the energy state of the cell as it measures ATP, phosphocreatine, inorganic phosphate and intracellular pH. The possible role of this technique in characterizing cellular events in hypoxic tissues, as well as the relative advantages and disadvantages of proton and 31-phosphorus MRS, will be discussed.

BE4-D.6

Clinical Use of Continuous Cardiac Output Measurement System with the Modified Thermo-dilution Catheter, T. Kano, S. Sekii*, M. Katayama**, K. Miyasaka**. Dept. of ME-Service, Mitsui Memorial Hosp, Terumo Corp*, National Children's Med. Res. Center**, 1, Kanda Izumi-cho, Chiyoda-ku, Tokyo 101, Japan

Recently thermodilution (TD) cardiac output (CO) measurements are widely used in many clinical cases. However, it is impossible to get CO values continuously in such a conventional TD method requiring frequent intermittent cold injection which may affect patients.

We've developed Continuous Cardiac Output Measurement (CCOM) system to solve the above problems. In this system, the Modified TD catheter (KATS/catheter) is used. This catheter has two thermistors; one is for the conventional TD method, the other is for detecting heat loss dependent upon blood flow velocity (BFV). So, once CO is measured by the conventional TD method during the continuous measurement of BFV, the relation between CO and BFV is decided ($CO/BFV=S$ corresponding to the sectional area of pulmonary artery). After this, CO can be measured continuously by measuring BFV. The correlation coefficients between CCOM values and electromagnetic flow meter values were 0.966 (n=18) in hemodynamic model, and 0.944 (n=29) in animal experiment. CCOM system is now clinically tested and good results are being obtained.

BE4-D.5

Portable device for continuous monitoring of oxygen uptake. K.Sato*, T.Tamura, and T.Togawa, *Univ. of California, San Diego, La Jolla, CA 92093, U.S.A., Tokyo Med. & Dent. Univ., Tokyo, Japan

An apparatus for continuous monitoring of oxygen uptake without discomfort was developed. The subject wore a hood through which air was drawn by an exhaust blower. The oxygen concentration in the hood was maintained constant by a servo-controlled blower, so that the flow rate was essentially proportional to the oxygen uptake. The flow rate of the main stream was measured by a time-of-flight flowmeter located in the exhaust hose. Flow rate and oxygen concentration signals were digitized and stored on a memory chip. The entire device, composed of these several parts, was assembled in a small package (wt=3kg) which the subject carried on his back. Upon removal of the memory chip after each experiment, data were transferred into a microcomputer where trends of oxygen uptake were calculated. The measurements made with this instrument are comparable to those made with a Douglas bag collection and gas analysis.

BE4-E.1

Ethical Codes in Biomedical and Clinical Engineering - An International Comparison, Jan Persson*, Dept. of Biomed. Eng. and Center for Medical Technology Assessment, Linköping University, S-581 83 Linköping, Sweden.

In 1987 the International Federation for Medical and Biological Engineering (IFMBE) started a project aiming at an international comparison of the ethical standards under which biomedical and clinical engineers work. An inquiry on these matters was sent to the affiliated organizations of the IFMBE.

Issues considered were existence and applicability of ethical codes or guidelines for professional engineers, clinical and biomedical engineers and physicians. Comments on the need for ethical guidelines were also demanded.

In February 1988 one third of the member countries of the Federation have responded to the inquiry. Few have a code at present, but several countries consider devising a code or feel the matter of high importance. Pros and cons will be discussed.

BE4-E.2

Biomedical Innovations: The Role of Ethics, M. N. Maxey*, Biomedical Engineering, The University of Texas at Austin, Austin, Texas.

Professionals responsible for innovations in biomedical technology are increasingly vulnerable to accusations by critics who claim that ethical considerations are rarely a factor in determining the merits of a particular innovation. As a consequence critics have captured the "moral high ground," and the images of Faust and Frankenstein tend to dominate public perceptions of technology-out-of-control.

Biomedical technologists must take a more active role in restoring public confidence on at least two fronts: (1) shaping the public debate by demonstrations of concern for ethical principles in anticipation of social implications of innovations; (2) preparing students to deal more effectively with emerging ethical issues.

BE4-E.4

Should Bioethics Training Be A Part of Clinical Engineering Curriculum?, S. Saha*, P. Saha, Louisiana State University Medical Center, Department of Orthopaedic Surgery, Shreveport, Louisiana 71130.

The fact that we need to provide an education that can prepare doctors and other medical personnel to face ethical problems is becoming more recognized. Yet, a similar need remains unrecognized for the bioengineer. The evergrowing dependence of health care on technology is creating the need to instill an ethical consciousness and a strong understanding of personal responsibility in those Clinical Engineers who provide that technology in the hospital. As members of the health care team, Clinical Engineers must be prepared to face ethical issues arising from defective or inadequate equipment, scarcity of resources, conflict of interest, confidentiality, clinical research, "truth-telling," and care of the terminally ill. Thus it is important that clinical engineers, during their undergraduate and graduate training, should be exposed to the problems of biomedical ethics and to the principles which should guide them to deal with these difficult issues. With the rapid development of medical technology, new ethical questions are bound to evolve and thus clinical and biomedical engineers should also take part in continuing education on such topics so that they will be well prepared to face these issues so that we can assist in the progress of modern medicine. Examples of some of these issues will be discussed.

BE4-E.3

Ethics in Clinical Medicine
C. William Hall, Southwest Research Institute
San Antonio, Texas, U.S.A.

Over the past two decades, life support systems have been developed which allow maintaining life during a difficult period and give the patient an opportunity to return to a productive life of respectable quality. However, these same life support systems bestow upon the physician and family a difficult decision. Once it is obvious that the patient will be unable to return to a quality of life that contains joy or productivity, should the life supports continue to be used or discontinued. Probably, the most famous clinical case which focused public attention to this problem was that of Karen Ann Quinlan. Because of its wide news media coverage, the Quinlan case requires no discussion here. Because of the United States' cultural background, euthanasia or "mercy killing" is not practiced in this country. However, the rising costs of hospitalization and medical bills are creating debates on this issue. Currently, the U.S. government only allows the support systems to be disconnected but demands that the individual be kept comfortable. In many cases, the patient is allowed to make a decision about the use of life support systems by initiating the "living will". Whether the decision is made by the patient or family, most persons agree that an individual should be allowed the opportunity to die with dignity.

BE4-E.5

Protecting the Rights of Human Research Subjects, H. Wigodsky*, University of Texas Health Science Center, San Antonio, Texas 78284-7750

There are ethical and practical reasons for protecting the rights of human research subjects. Appropriate laws have been enacted and regulations have been published. A regulatory organization has been established in government, research institutions, and elsewhere to assure protection of the rights of human research subjects particularly in government sponsored research including research with drugs and devices. Research investigators are well advised to familiarize themselves with these processes to make the proper responses.

212

BE4-E.6

Professional Society Impact on the Status of Clinical Engineering as a Profession, Gerald R. Goodman*, University of Texas System Cancer Center, Houston, Texas.

In the United States at present, there are three professional societies working to represent the interests of clinical engineers, and an international certification commission for clinical engineering.

A reasonable question to ask is if these societies work to the best interest of clinical engineering, and are the best use of the financial resources available to promote the clinical engineering profession?

An answer to these questions can be found through a review of the sociology literature in the area of role theory, where professional societies are identified as only one element in a natural developmental history of successful professions.

Clinical engineering would be better served through an examination of the professionalization process, and the development of a single society that best meets the exclusive interests of clinical engineering.

BE4-F.2

A Public Database on Medical Devices
Chr. van Nimwegen* and J. Boter,
Medical Technology Unit TNO, P.O.Box
188, 2300 AD Leiden, The Netherlands.

During the last decennia the growth in use of medical devices in health care has been tremendous. Industry offers a wide variety of makes and types to the consumer. Health care institutions need assistance in purchasing suitable devices and solving problems concerning reliable and safe functioning of devices in critical areas. Therefore, there is a growing need for objective information on commercially available medical devices.

We developed a database, which contains:

- an inventory of diagnostic and therapeutic equipment offered to the Dutch market-place;
- information on publications like evaluation reports, hazard reports, market surveys, review articles etc.;
- important specifications of a number of types of medical devices;
- information on national and international standards concerning medical devices.

Since the beginning of 1988 the database is directly accessible for health care institutions. The database presented has a relational file structure while the data are presented in a videotex environment.

BE4-F.1

PATIENT-CARE TECHNOLOGY EVALUATION, Y. David*, Biomedical Engineering, Texas Children's Hospital, Houston, Texas 77030 U.S.A.

The delivery of Health-Care Services are becoming more technology intense than ever before. In addition the rate of the introduction of new technologies into the health care environment is accelerating. Thus, hospitals are facing pressures to allocate their limited resources to the acquisitions and operation of these newer technologies.

Biomedical Technology assessment is being debated at various decision making levels. Government, Health Care insurers, and professional societies are participating in the search for the optimal methodology for assessing Biomedical technology. At the hospital level, however, limited support is available to guide the selection. The fitting of new devices into the unique practice of an individual hospital seems to be a suboptimal process. Hospitals using decisions based on evaluations by an interdisciplinary team of experts can improve operations and thus patient-care.

BE4-F.3

Clinical Engineering in Primary Care, Jan Persson*, Lars Borgquist and Claes Debourg, Dept. of Biomed. Eng. and Center for Medical Technology Assessment, Linköping University, S-581 82 Linköping, Sweden.

Primary care is in many countries expanding with regard to extent and content. Technologies originally intended for the hospital are transferred to primary health care centers, often without analyses of effects. In this study an inventory of medical devices, their use and need for maintenance and training, was made comprising the health care centers in Sweden. Measures of standard level with regard to medical devices and chemical laboratory tests were found to differ significantly between the counties. The standard measures increase with size of the care center as measured by number of district physicians, and to extent of specialities available. The standard level of medical devices also increases with distance to the hospital. Policy decisions within the county councils and the physicians background in hospital care seem to be important to the choice of technologies.

A number of devices are pointed out where there is a need for increased efforts by clinical engineers concerning training for correct use and maintenance.

A model for the diffusion of technologies to primary care is proposed.

BE4-F.4

Modeling the Impact of Technology
in Neonatal Intensive Care, R.T.
Almeida, M. de Carvalho, J.M.A.
Lopes, and R.B. Panerai*, COPPE/
FIOCRUZ, Rio de Janeiro, Brazil.

The relationship between multiple technologies routinely used in neonatal intensive care units (NICU) and outcome variables such as length of stay and weight gain was assessed by considering the utilization of 53 technologies in 82 patients with birthweight in the range 1000-1999g. The technologies studied correspond to 22 diagnostic/monitoring technologies, 29 methods of treatment, and 2 techniques of psychological support.

The total number of technologies utilized per case (TU) can be explained by the 5 min Apgar score and the index of severity of illness with a coefficient of multiple determination (R^2) of 0.86. The length of stay (LS) is explained by TU and birthweight (BW) with $R^2=0.70$, and the percent weight gain by LS, BW, and gestational age with $R^2=0.49$. The three models are significant at the $p<0.001$ level. These results can be applied to technology assessment and the evaluation of relative performance of different NICU.

BE4-F.6

Assessment of Medical Devices
J.F. Dyro, State University
of New York, Stony Brook,
New York 11794.

Through assessment of medical devices, biomedical engineers in health care facilities circumvent the familiar problems of frequent failures, high cost of operation, incompatibility with other devices and user misuse and misapplication. Softgoods and disposable products are assessed by University Hospital's Standards & Evaluation (S&E) Committee which includes members from most hospital departments. Patient care equipment acquisitions are reviewed by biomedical engineering (PME). In-house assessments supplement information available from sources such as governmental agencies, independent research laboratories, shared service organizations, journals, professional organizations and the old boys' network (OBM). Disposable blood pressure transducers, physiological monitors, defibrillators, infusion pumps, continuous noninvasive blood pressure monitors, data management systems and apnea monitors have been evaluated by biomedical engineering.

BE4-F.5

A Programme for the Assessment of Health-Care Technologies in Japan, Makoto Kikuchi, Dept. of Med. Eng., National Defense Med. Col., 3-2, Namiki, Tokorozawa, Saitama, 359, Japan.

Since 1975, high-level medical technologies have begun to be widely used in hospitals and clinics in Japan. At the same time, national health-care expenditure has increased from 240 billion yen or 2.7 per cent of the gross national product (GNP) in 1955, to 18 trillion yen or 5.1 per cent of the expected GNP in 1987. Since the burden of these expenditures has increasingly shifted from individual patients to society, the Government has attempted to stop or at least slow down the rapid escalation of health-care costs. In this paper, the author introduces the unique situation and tendency of high-level health-care technologies in Japan compared with western countries, and also discusses the role which medical technology has played in this transition of the health-care system. He also draws attention to the urgent need to establish the actual programme for assessment of health-care technologies appropriate for the national health-care system, and then discusses the new methods used in developing the fundamental criteria and the effective programme for the assessment of health-care technologies, which has been under study for the past year in Japan.

BE4-F.7

Health Equipment Planning and Procurement: Experience from a Developing Country, B. Wang*, ASEQ/Secretaria da Saúde, São Paulo SP, Brasil 05403.

Within the State of São Paulo a new health system is being formed by uniting federal, state, city, and philanthropic health services. This new system is composed of approximately 544 hospitals (with a total of about 84,500 beds), 1000 clinics, and 10 research centers. This system serves, together with private institutions, a population of about 30 million. For this system, a special advisory office, directly subordinated to the Health Secretary, was created to establish and implement a policy on health equipment, including all stages of its life cycle, i.e., planning, procurement, installation, utilization, maintenance, refitting, and eventually, obsolescence. Particular emphasis was given to the development of a methodology and supporting databases for planning and procurement, because of the large amount of capital investment needed for new facilities and for improving the existing ones.

BE4-F.8

International Medical Device Hazard Reporting Network, Elliot B. Sloane*, MSEE, ECRI, 5200 Butler Pike, Plymouth Meeting, PA 19422 USA

ECRI, a nonprofit medical technology assessment agency since 1965, has been designated by the World Health Organization (WHO) as the Collaborating Center for Information Transfer on Medical Devices. Its fundamental task is extending and maintaining the multilingual International Medical Device Nomenclature (IMDN) system. Secondly, ECRI is collecting worldwide medical device problem reports and organizing them with the IMDN for rapid analysis. Finally, ECRI will disseminate reported risks and hazards of commonly used medical devices to the WHO member nations. The global economy of the 1990's and beyond will cause significant changes in the distribution, use, and safety of medical technology. In over 20 years, ECRI's experience is that virtually all medical products, whether diagnostic or therapeutic, have some level of risk. No country is able to test and certify all of the medical devices used within its borders. Also, it is unethical, uneconomic, and unnecessary for each country to learn on its own, building on its own tragic experiences. Growing international trade and interdependence makes the IMDN-based comprehensive ECRI/WHO International Medical Device Hazard Reporting Network essential for all countries and patients.

BE4-F.10

Technology Assessment: Small Volume Infusion Pumps, Barbara Ann Bukowski*, 10103 Prospect Hill, Houston, Texas 77064

This research explored a methodology for technology assessment within the health industry. Phase I reports the development and testing of the Candidate Adoption-Use diffusion paradigm and the time series analysis of external SVIP diffusion. Compared to the classic diffusion model, CA-U more accurately explained the empiric diffusion trends. CA-U favors utilization as opposed to adoption behavior. SVIP chemotherapy is a technology applied, monitored and maintained by nurses. Phase II reports on the prospective survey of 117 random patients who adopted and used SVIP. Their functional ability in self care, social role and interaction, employment and activities of daily living was analyzed. There was sufficient evidence that the alternative inpatient technology restricted activity whereas SVIP outpatient therapy permitted patients to function more independently and in a social lifestyle, thus adding quality to life.

BE4-F.9

Comparative Evaluation of Medical Equipment, B. van Eijnsbergen*, TNO-Corporate Planning Department, P.O. Box 297, 2501 BD The Hague.

Within the European Community a project on Comparative Evaluation of Medical Equipment is going on. The aim of the project is a) co-ordination on the activities in the field of evaluation of medical equipment of the Member Countries, b) to collect, store and distribute publications on evaluations of medical equipment and c) to draft protocols for comparative evaluations of medical equipment.

In the known literature-data-bases reports of evaluations are mostly not present (grey literature), so that a special data-base has to be set-up for this aim. In the Netherlands such a data-base is already functioning for some years. Since in different other countries similar data-bases are in preparation, a network-system of them can provide (on line) information.

Protocols on evaluation of infusion-systems and ultra sound diagnostic equipment has been drafted. The use of a same protocol in an evaluation has the advantage of possibility of comparison of the results.

BE4-F.11

A.H.C.T. - RELEVANCE TO THIRD WORLD NATIONS
T.G. Krishna Murthy*, Bangalore, India

The realistic assessment of Health Care Technology appropriate and relevant to these nations involves a scientific and planned need based approach. Majority of people (about 80 percent) in these nations which are highly populated are. So technology and trained manpower utilisation implies setting up both centres of clinical excellence where the required back-up facilities are ensured and also at the majority of other centres where the essential diagnostic, therapeutic and bioanalytical instruments which are low to moderate cost and are simple and rugged. Clinical experience in the last decade indicates the application of integrated therapy utilising both modern and locally prevalent systems of medicine. Such a step ensures carrying medical care to the doorsteps of remote rural areas. The GRAHCT of WHO located in Copenhagen in consultation with clinical engineers in these nations can enlighten and educate the medical and health care experts which can go a long way in attempting to achieve the really formidable challenging goal of HEALTH FOR ALL BY 2000 A.D.

BE4-G.1

**CURRENT STATUS AND FUTURE CHALLENGES FOR
CLINICAL ENGINEERING IN THE U.K.**
V C Roberts*

Department of Medical Engineering,
King's College School of Medicine, LONDON

Clinical engineering has only recently become "officially" recognised in the United Kingdom following the establishment, by the Biological Engineering Society, of a Scheme of Certification. This applies to those practising professionally as clinical engineers within the UK's National Health Service, and fully accords with the IFMBE guidelines for registration.

Many health care scientists work on clinical engineering activities, but so far only a small number have sought certification, a situation which should change as the certification scheme achieves credibility. The main challenges for the future, dictated by a diminishing national health care resource, will involve the clinical engineer taking a full role as a business manager and not merely a scientist. The educational and training implications of this have yet to be properly addressed.

BE4-G.3

Clinical Engineering in Brazil, B. Wang*, Assoc. Bras. de Engenharia e Manutenção Hospitalar, c/o CEB/ UNICAMP, Cx Postal 6040, Campinas SP, Brasil 13081.

For many years, medical equipment was purchased in Brazil without regard to its maintenance needs and costs. Preventive maintenance was almost inexistent and services were provided solely by manufacturers' representatives at high cost and with low efficacy. Often it was easier to buy a new equipment instead of repairing the old one. Thus a critical situation was generated: about 20-40% of all existing equipment (i.e., about US\$ 2-3 billion worth) is out of order.

In the last 5-10 years, a few hospitals established their own clinical engineering teams to take care of technology planning, selection, acquisition, maintenance and operators' training. The good results obtained by them are spurring others to follow the same approach, and even the government to modify its health policy.

Last year, a Brazilian Association of Hospital Engineering and Maintenance was created to promote further advancement of this area.

BE4-G.2

PRESENT AND FUTURE OF CLINICAL ENGINEERING DEPARTMENTS IN JAPANESE HOSPITALS, N. Ono*, Dept of Med. Eng. Service, Mitsui Memorial Hospital, 1, Kanda-Izumi-cho, Chiyoda-ku, Tokyo, Japan 101

The national certification law of clinical engineering (CE) technicians was recognized in the Di * in May '87. However, there are a few established CE-departments in Japanese hospitals. Although there are about 7000 CE-technicians, most of them engage in hemodialysis treatment in small clinics. There are only about 20 all-round CE-departments in Japan. They engage in the engineering service similar to those in U.S. and other countries except for repairs. At the same time they engage in the clinical service, which means operation of many kinds of medical engineering equipment, such as extracorporeal machines, hemodialysis machines, respiratory assist devices and other life supporting equipment. In the very near future, we must establish the organization and re-education system of CE-technicians, and also the relationships between in-house CE-departments and the manufactures. I would like to report on these future programs.

BE4-G.4

CLINICAL ENGINEERING IN ITALY

R. Merletti*, Politecnico di Torino, Torino, ITALY
D. Bravar, Rip. App. San., USL 1 triestina, Trieste, ITALY

A five year research project in Clinical Engineering (CE) has been completed by the Italian National Research Council in 1988. Purpose of the project was to survey, coordinate and link in a national program the existing local CE activities and to provide guidelines to the National Health Service (350642 beds) for establishing CE Departments and recognized CE positions at least in the major hospitals. The results indicate that 16 clinical engineers and 70 BHET are actually operating in Italian hospitals (most of them affiliated to the Trieste Local Health Unit), while 350 engineers and 1750 BHET would be needed in the country to meet the minimum requirement of 1 eng./1000 hosp.beds and 1 tech./200 hosp.beds). On the basis of a survey on 12 hospitals the value of biomedical equipment in Italian hospitals has been estimated as 18,000 \$/hosp.bed while the annual maintenance cost is 1,120 \$/hosp.bed (national average) with minimal values at 770 \$/hosp.bed in hospitals with CE activities.

Among the research products, described in over 2000 pages, are: a software package for equipment management (a possible national standard), a set of manuals about purchase criteria, operating principles, standards and safety problems, maintenance requirements of OR, ICU, radiological, clinical chemistry and physical therapy equipment. Pilot evaluations of cost/effectiveness of some radiological and clinical chemistry services are also described. As experienced in other countries, the establishment of CE Departments appeared to be the only way to control the inflation of modern health technology while increasing hospital safety and effectiveness. No training programs are offered by universities for clinical engineers. Experimental training of BHET has started in two cities with funds provided by the EEC and by regional administrations. However the lack of official positions and career prospects and the low hospital salaries make industry offers more attractive to the newly graduates. Two national programs are expected to be approved in the next few years for training clinical engineers and BHETs. This first coordinated national effort provides health authorities with very clear directions about the appropriate approach to the issue of health care technology management.

BE4-G.5

Biomedical Engineering Challenges for Southern Africa, MA Poluta*, GG Jaros, Department of Biomedical Engineering, Groote Schuur Hospital and UCT Medical School, Cape Town, RSA.

Southern Africa is a developing region facing both first and third world problems in health care. In the context of health care technology a need-driven rather than a technology-driven approach is desired. "High-tech" solutions are often prohibitively expensive from both capital and maintenance cost considerations and are not always the best or most appropriate engineering solutions to meet given needs. It is also pertinent to ask whether a developing region can justify a local equipment industry. We propose that such an industry is both desirable and viable. In particular, biomedical engineers together with clinical engineers, clinical technologists and other health care workers, have a key role in such an environment. Only through their continued involvement will an appropriate and cost-effective transfer of technology be accomplished. This presentation will examine some identified needs as well as examples of solutions proposed and implemented by our department.

BE4-G.7

EVALUATION OF PROVINCIAL PUBLIC HOSPITALS IN TUCUMAN FROM A CLINICAL ENGINEERING VIEWPOINT. CJ Felice, CP Breitman, OJ Barrionuevo, OR Batallón, HD Gramajo, VI Rotger and MI Vercellone. Bioingeniería, Universidad Nacional de Tucumán (UNT), cc 28 suc 2, (4000) Tucumán, Argentina. Max E. Valentinuzzi*

Objective: To evaluate electrical safety in the five main public hospitals (about 1400 beds) of the Tucumán Province (1,000,000 people) of Argentina. Field visits were performed and a detailed questionnaire was given to one of the hospitals (321 beds). For the latter: (a) No intramural maintenance is performed to medical equipments. (b) Electrical safety standards are not applied. (c) There is no adequate consulting mechanisms for the acquisition of new equipments. (d) No training is offered to the personnel. For all hospitals: (1) Even knowledge of electric safety standards is essentially non-existent. (2) There is no Clinical Engineering Department. Maintenance personnel takes over a few CE tasks. Repairs are sent outside. (3) Within hospitals, the available maintenance personnel does not have enough skill. At a national level, there is a hospital standard (IRAM 4220) which considers only general aspects of medical equipments.

BE4-G.6

Clinical Engineering in Hungary, M. Susánszky, National Institute for Hospital and Medical Engineering /ORKI/, P.O.F. 32, H-1525 Budapest 114 Hungary, N. Richter⁺, MEDICOR, P.O.B. 150, H-1389 Budapest 62, Hungary

Being aware of the present situation of clinical engineering in Europe it seems to be worth giving an account of the Hungarian achievements which could be a model of an effective system in a small country. In Hungary there are about 100,000 hospital beds and the health care is entirely organised and financed by the state. Within the health service there are about 220 qualified engineers working in jobs that are connected with clinical engineering. It is a local peculiarity that only a smaller number of them works for the maintenance, unlike in other European countries. At the same time they have larger responsibility for preparing of decisions concerning the purchase of medical equipment and for maintenance management.

The technical staff of the hospital, under leadership of clinical engineers, does only the less difficult maintenance work.

BE4-H.1

The Relationship Between Clinical Engineering Activity and Financial Support - Report from an Investigation by Clinical Engineers, Bengt Lindberg* and Bengt-Olov Wieck, Clinical Eng. Dept., East Hospital, S-416 85 Gothenburg, Sweden.

The increased use of medical technical equipment in hospitals has been more rapid than the follow-up by administrative personnel involved in the financial support to this activity. An investigation was carried out to highlight the problem. The value of the medical technical equipment in our hospitals was estimated and the cost for service and maintenance to keep this equipment work safely was calculated. We compared this cost with the grant that is spent on such activities by the hospitals.

A comparison was made between the cost and time to repair equipment from either an external company or by the biomedical engineering department of the hospital.

The investigation showed a large imbalance between the use of biomedical equipment and the financial support for its use.

With the results we hope to increase the awareness of the hospital management of the consequences there are in introducing new equipment into hospitals.

BE4-H.2

Profit from Organized Medical Engineering Center at Kitasato University Hospital
Satoshi Watanabe, M.D.*
Medical Engineering Center & Department of Anesthesia, Kitasato University Hospital, Sagami-hara, Kanagawa, Japan.

Medical Engineering center at Kitasato University Hospital was established in 1981 to organize all medical equipments excepting for those instruments which belong to clinical laboratory and X-ray department. This center provides not only engineering service as maintenance and repair of equipments, but also extends to promotion and education activity, and examination and development of new devices.

We have studied the amount of financial resources which contributes to profit of hospital in the past one year. The accumulative cost of repairs was calculated with labor, managing and time share. This amount was compared with those expenses which we ought to pay if they are repaired by manufacturers. The total expense was cut down to one eighth of the amount of requisition by the manufacturer.

BE4-H.4

Clinical Engineering Productivity Management: A Case Study,
A. Mahachek; The Johns Hopkins Hospital, Baltimore, Maryland, 21205

Described in chronological order are the steps taken to install productivity measurements and controls within the Clinical Engineering Department of a large teaching hospital. Motivation for this project involves both preparation for going "for profit" and the need to resolve an over-budget condition of labor cost. The project steps include current hospital management reports, database adequacy, supervisors' time logs, computerized budget spread sheets, testing changes on a financial simulation model, developing labor task standards, and departmental labor performance reporting. The project yields significant positive results for the department's performance versus budget and also leads to growth in supervisory and management skills.

BE4-H.3

A Program to Increase Equipment Durability in Brazil, Magalhães R.A*., Panerai R.B., Nobre F.F., Wiederbecker N.G., Machado J.C., Vieira C.R.S., INAMPS+ and COPPE/UFRJ, Rio de Janeiro-BRAZIL.

The transfer of medical technology to developing countries has been characterized by the early deterioration of costly equipment resulting from inadequate planning, installation, and maintenance. Attempting to change this pattern, and to increase the medical benefits resulting from deployment of 48 modern imaging devices in several regions of Brazil, a special program has been set up to prevent the classical factors which have been responsible for the reduced useful life of similar technologies. Before delivery, a detailed contract was established with the manufacturer regarding shipment, insurance, guarantee, and maintenance. Following the installation of each device, a clinical engineering team inspects several aspects of the physical installation, environmental conditions, and operator training. The protocol also includes basic electrical measurements and tests of image quality. All abnormalities detected were immediately reported for correction. This program can be regarded as a conceptual model which can be useful for other countries facing the problems surrounding technology transfer.

BE4-H.5

A KNOWLEDGE BASED MIXED ARCHITECTURE FOR ELECTROMEDICAL EQUIPMENT MANAGEMENT
P.F. Branca, P. Cuppa*, A. Mura, F. Vinelli, Lab Artificial Intelligence, Rome, Italy

Since 1983 the Chemical Engineering Service of the Children Hospital "Bambino Gesù" of Rome, established in 1981, utilizes a traditional data base system the management of 2350 electro-medical equipments (global value 21 MS). From the acquired experience the necessity of this traditional data base was confirmed, and the growth of new problems that can not be solved by means of these systems appeared.

In particular the usefulness of Artificial Intelligence Techniques in the equipment management appeared. In this paper a model based on mixed architecture is proposed.

This model is capable to identify dynamically the significant parameters for life cycle strategy of each equipment.

The architecture is based on: traditional data base (inventory data, maintenance data, costs), algorithmic model (costs and productivities prevision); and, finally, knowledge associated to an expert system.

BE4-H.6

The equipment control system, MEDEQ, as a tool in the reinvestment process, L. Löfstedt*, C. Nerhed and B. Eklund, Medical eng. dpt, University Hospital, Uppsala, Sweden.

The University Hospital in Uppsala has medical equipment for 80 million dollars value, calculated 1987. All equipment, and day to day information about it is continuously registered in our equipment control system MEDEQ.

The hospital has need for 20 MUSD as capital money 1988. But we have only 5.5 MUSD available, for both reinvestment and investment in new technology. If all money is used for medical equipment it gives a reinvestment period of 15 years in our hospital. The lifetime of medical equipment normally ranges between 5 and 15 years.

The reinvestment process must therefore be carefully done, and the need for adequate information is obvious. One important information source is our equipment control system, MEDEQ, which we have been using for more than 10 years. We have found it to be a very useful tool in the reinvestment process.

BE4-H.7

Funding strategies for clinical engineering in the Maritimes, *M. Frize, A.L. Nickerson, Reg. Clin. Eng. Service, 330 Archibald St, Moncton NB/NSAHO, 5614 Fenwick St, Halifax NS.

Two methods of comparing workload and funding requirements of clinical engineering services are considered.

A first method is the traditional managerial approach of assessing workloads, in total hours, and dividing by the number of hours representing a full time equivalent (1100 hours). The total workload includes repair hours, scheduled periodic maintenance and incoming inspections. The base of 1100 hours takes into consideration that 30% of the total activities are not accountable and belong to the "other" activities category.

A second method is to assess the replacement value of the equipment supported. The budget is expected to be in the 5 to 7% range, including overhead. The budget value would be lower when applied to radiology, typically 3-5%.

The value of using both methods in parallel is to develop experience which could lead to more effective resource management. One or both these methods may enable a valid comparison of in-house, shared, and manufacturers' services. Actual results and experience will be discussed.

BE4-I.2

Choosing The Optimum Network For Real-Time Information Distribution
K. H. Okumura*, Hewlett-Packard
Waltham, Massachusetts 02254

When choosing a network architecture and protocol, one must consider the nature of the information which is being transported by the network. Physiologic waveforms, parameters, and alarms require different considerations than journal articles and electronic mail. The equipment-hostile nature of the hospital environment relative to the office environment must be considered when designing devices for use in the hospital. And in the event of failure, it must be easy to replace instruments without disrupting function of the network.

The CareNet utilizes a highly reliable central controller with a 32-msec polling cycle in a star topology to provide real-time transmission of data fail-safe and reliable operation, environmental integrity, and flexible configuration. Devices may be interfaced to CareNet to provide gateways to other networks in the hospital.

BE4-I.3

Data management in the ICU by automatic means- SPEEDSCAN(c).

R.Inglis*,A.Pannike,J.Rueger, Unfallchirurg. Klinik,J.W.Goethe Universitaet Frankfurt(Germany/West)

A system for parameter-evaluation, -edition and -documentation with a scanner has been developed as a new and error-free tool for data processing in the Intensive Care Unit. Specifications: Using a scanner for data-entry there are no more keyboard entries to be made. Data are processed after fixing the values on data sheets that are configured like multiple choice data sheets using pencil-marked items as regions of interest. There is no more time (and money) lost waiting for altered and reprinted data sheets any more, the main factor in losing lots of time at the beginning of almost every study as the sheets are printed on the user's impact printer by himself. There is no limitation applying the system to logical, numerical and character-type data, therefore there also is no limitation combining the data acquired by SPEEDSCAN with those resulting from other automatic tools as laboratory computers and systems for patient-monitoring.

BE4-I.5

A New Method of Handling Medical Records with Laser Technology. J.H.U. Brown, Ph.D. and Carlos Vallbona, M.D. University of Houston and Baylor College of Medicine, Houston, Texas

Working with Sumitomo/CSK of Japan we have been able to place 2 million bytes(700 pages)of information on a plastic credit card by a laser imprinting method. The method is cheap(cards are about \$2) and rapid. The information can be read into the card at 64kb/sec and read out at the same speed with an error rate of about 10-11. Any piece of information can be located within one second. We have developed software to place a complete medical record on the card formatted so that any portion(demographics, procedures, treatment, drugs, etc) can be located and accessed. The card can be read and updated at will with a simple reader which attaches to a p.c. so no main frame computer is needed. The card can be copied or tape backup can be provided. Summaries of all data can be easily produced on the computer and printed out if desired and X-rays and ecgs as well as identification photos can be placed on the card. The system is under test in the Harris County Hospital District and at NASA and results will be presented. The concept being tested is that the patient can carry his own medical record with him at all times and it can be accessed and updated at any contact with the health care system. Records are instantly available in emergencies, in out patient clinics or the hospital. Needed administrative information such as ICD codes and occupational codes are built into the program to be accessed automatically. Billing can be added as desired.

BE4-I.4

Development of a totally integrated hospital information system: HUMANE Michitoshi Inoue and Hiroshi Takeda* Department of Medical Information Science, Osaka University Medical School Fukushima-ku, Osaka 553, Japan

Owing to the chance of the hospital reconstruction by 1992, the concept of the "intelligent hospital" is introduced to Osaka University Hospital. HUMANE (Human-oriented Universal Medical Assessment system by Network Environment) is named for the totally integrated hospital information system to be the core of the intelligent hospital plan. The infrastructure of the HUMANE will be consisted of the optic fiber loop LAN (100 and 400Mbps) for digital data and digital image communication and star-type LAN (10Mbps) for voice and analog image. In developing the system configuration, the micro-medium-main frame link (MML) is considered to handle the centralization/decentralization problem. The order entry system will be the major part for the integration of the patient-oriented administrative and clinical data into a common file and to reduce the clerical errors and total work load. As doctors and staffs must access the database directly from the computer terminals, human-oriented man-machine interface should be installed. Picture Archiving and Communication System (PACS) will be one of goals of HUMANE. As many problems must be solved for the total image information system, mini PACS will be the choice at the initial stage.

BE4-I.6

Problems of Medical Record Storage by a Laser Disk System, Kazunobu Yamauchi,* Takayuki Miura, Nagoya University Hospital, 65 Tsurumai-cho, Showa-ku, Nagoya, Japan.

An optical disc filing system is one of the new methods to memorize the contents of medical records. This system can not only store large amount of medical records, but also send information to several areas in the hospital. However, there are some problems of image quality and durability of the disc. The present study investigated the problems with image quality as to the content of medical records. An Hitachi Optical Disc Filing system was used, which is a stand-alone type with memories of 2.6 GB. Various contents of medical records such as discharge summary, present illness, progress notes, ECGs and polaroid pictures were put through the image scanner, and were compared with output images. Image data such as discharge summary and present illness were clearly reproduced by a resolution of 200 dots per inch (dpi). However, polaroid pictures of UCGs or sketches by doctors needed a resolution of 400 dpi with 32-64 gradation. ECGs needed a resolution of 400 dpi with 2 gradation. Records in more than 2 colours of ink such as renograms, nurses' notes and doctors' sketches were reproduced in monochrome images, so the colour signals could not be distinguished. In conclusion, the optical disc filing system is useful to store medical records, but it must be improved so as to distinguish colour information.

BE4-I.7

Use of Microcomputers in Medical Informatics - Experience in Belgrade Health Care System, Z. Božović*, V. Brusić, D. Djaković, V. Srdanović, Z. Stojiljković and M. Trajković, Center for Multidisciplinary Studies, Belgrade University, Slobodana Penezića-Krcuna 35, 11000 Belgrade, Yugoslavia.

During the last three years the Group for Medical Informatics at the Center for Multidisciplinary Studies of the Belgrade University has been developing a system approach suitable for the needs of the Belgrade health care organizations.

Using modern analyzing tools and new software concepts as well as having studied features of the local health care system, various applications have been developed. These applications include:

- primary health care information systems;
- hospital information systems;
- decision support systems.

The paper also discusses some problems arising from specific features of the regional health care system, development tendencies and the possibilities of implementing them in the Belgrade health region.

BE4-I.9

Kyoto University Hospital Information Network System on Ethernet, T. Takahashi, A. Hirakawa, Y. Okada*, Department of Biomedical Informatics, Kyoto University Hospital, Shogoin, Sakyo-ku, Kyoto, JAPAN.

Network and database are the key points of Hospital Information System in the near future. 9 CPU's and more than 300 terminals are connected on Ethernet in Kyoto University Hospital. MUMPS manages the distributed database on this network system.

In former system, there were 10 dedicated lines to connect 8 CPU's and more than 180 terminals are connected individually to their CPU's. So it was difficult to expand the system without explosion of complexity. Ethernet and MUMPS brought us the flexibility to connect new CPU's or new terminals anywhere on line.

PACS and PBX networks will join this network to realize the distributed multimedial hospital information environment.

BE4-J.1

Holter Monitor in Coronary Angiography, G.R. Yu*, Zhen D.S., Y. Zhen and S.H. Bao. Ren Ji Hosp., Shanghai Second Medical University.

50 cases, 41 male and 9 female, aged 47-63, were monitored by Holter during coronary angiography. 46 with EF over 0.6 and 4 less than 0.4. Of 35 with fixed stenosis, 32 had a stenosis over 50%; 7 had 1 VD, 21 had 2 VD and 4 3 VD. Of 15 without pacemaker, all had a HR over 60 during left ventriculogram, 2 sinus bradycardia during left coronary angiography and 7 below 50/min during right coronary angiography, followed by 1 VF, 2 VT and 1 sinus arrest lasting for 4.2 sec. No serious arrhythmia was observed in 35 cases with pacemaker. There was less change of QRS voltage, duration, ST-T and less ventricular premature beat in cases with than without pacemaker. Of 4 with EF less than 0.4, all had significant STT changes during angiography. Of 5 with marked sinus bradycardia, persistent VT and transient Q wave, 2 showed spasm and 3 2VD. It was concluded that pacemaker might prevent serious complication during coronary angiography.

BE4-J.2

Source of False Deviation of S-T Segment in Ambulatory Electrocardiogram and its Elimination by a Compensation Circuit
K. Iwao*, A. Yokoi, S. Suzuki, T. Goto, K. Doniwa, K. Kamiya & M. Okajima
Fujita-Gakuen Health University, Toyoake, Nagoya Area, 470-11, Japan

In commonly used ambulatory electrocardiogram through a DR magnetic tape recorder, false deviation of S-T segment is frequently observed. Frequency responses of the system were checked with commercial ambulatory ECG systems. The phase shift was assessed by Wagner's method. The characteristics of the systems were found much worse than that of ordinary ECG equipments both in gain and phase responses. The decay of -3 dB in gain was observed in 0.2 Hz and the lead of 45 deg in phase was observed in 0.6 Hz. In order to investigate which of these 2 responses play major role in generating false S-T deviation, a computer program was run with 2 frequency responses models i.e. i) real gain responses obtained in the above test plus fictitious phase responses with no shift, ii) fictitious gain responses with no cut-off plus the real phase responses. The actual ECGs were fed into the mathematical filters. The false S-T deviation were found to be caused mostly by enormous lead in phase. Intending to diminish the lead in phase to the point of ordinary ECG recorder, a compensation circuit was designed and inserted in the commercial ambulatory ECG system. In the trial by 20 ECGs, the compensated system showed no false deviation in S-T segment.

BE4-J.4

A WORK STATION TO STUDY AMBULATORY BLOOD PRESSURE, F. del-Pozo*, F. Halberg(£), E. Gómez-Aguilera and J.L. Zoreda, Dpt. Bioingeniería, E.T.S.I. Telecomunicación, Madrid, Spain; (£) Chronobiology Labs. Univ. of Minnesota. USA

Based on the Blood Pressure (BP) ambulatory system we published recently, it has been developed a BP Work Station, supported on a PC-compatible system, to identify the new information content in the ambulatory blood pressure recordings, in comparison with conventional casual BP determinations; that could be pertinent in prevention, screening, diagnosis, prognosis and treatment.

The BP profile data manipulation procedures is a menu driven collection of software packages oriented to: 1) the assessment of BP reference limits, homogenized according to different factors; 2) the statistical modelling and parametrization of the systematic temporal variations, to account for a large part of the BP variability; 3) the estimation of BP excess indexes.

Acknowledgments.-CICIT. Grant No. 2911-83

BE4-J.3

Microprocessor-Based System for Measuring Lung Water, Bing-Nan Hung*, Yun-Bin Lin, Chih-Ming Shen† and Kang Hsu††, Department of Biomedical Engineering, Chung Yuan Univ., Chungli, Taiwan (32023), Republic of China

+ Biomedical Engineering Department
Tri-Service General Hospital
Taipei, Taiwan, Republic of China

†† Chest Medicine Department
Tri-service General Hospital
Taipei, Taiwan, Republic of China

In this study, the IBM PC/XT was used as the mainframe and was connected with two thermal dilution cardiac output computers and one dye dilution cardiac output system. By applying the method of thermal dilution and dye dilution to heart-lung circulation system, three cardiac output curves were recorded. After analyzing the dilution curves, the extravascular lung water (EVLW) were calculated according to the principle of thermal-dye and single thermal indicator method respectively. The system has been tested in-vitro and in-vivo to calculate the lung water. The results were as reliable as the gravimetric methods.

BE4-J.5

Frequency Characteristics of Volume Elastic Modulus in Finger Arteries
H. Shimazu, H. Ito, A. Kawarada (Dept Physiol, Kyorin Univ, Mitaka-shi, Tokyo, Japan) & K. Yamakoshi (The Res Inst, Appl Electr, Sapporo shi, Hokkaido, Japan)

Frequency characteristics of viscoelastic properties expressed by an index, volume elastic modulus (Ev), were indirectly evaluated in human finger arteries. Ev was defined as $\Delta P / (\Delta V / V_a)$; where ΔP is pressure change and $\Delta V / V_a$ volume change ratio. A volume compensation sphygmomanometer was used to determine beat-to-beat arterial pressure in an index finger, and transmitted infrared photoelectric plethysmograph to detect $\Delta V / V_a$ in a ring finger, simultaneously. During the measurement of arterial volume change in the ring finger, transmural pressure (Pt) was varied with applied cuff pressure which was controlled by sinusoidal variations (0 - 30 Hz) superimposed on the same pressure detected in the index finger so as to cancel the pulsatile volume change in the artery. Thus, Pt in the ring finger varied only by the sinusoidal pressure variation (ΔP). Therefore, frequency characteristics of Ev were determined by this method among subjects with different ages and sexes during stress loadings.

BE4-J.6

Non-invasive Measurement of Instantaneous Blood Pressure in Superficial Temporal and Radial Artery by the Volume-Compensation Method. K. Yamakoshi*, S. Tanaka, H. Ohnuma, A. Kamiya¹⁾, H. Shimazu, A. Kawarada, H. Ito²⁾ & P. Rolfe³⁾, 1)Hokkaido Univ., Japan, 2)Kyorin Univ. School Med., Japan, 3)Keele Univ., U.K.

We have previously devised an ingenious technique called volume-compensation method, based on the vascular unloading principle, which allows the beat-by-beat measurement of systolic and diastolic pressure and the recording of the pressure waveform in the human finger continuously and non-invasively. This employs a transmittance-type photoelectric plethysmography for the local detection of arterial volume changes in the finger. The present study concerns the blood pressure measurement in the superficial temporal and radial artery based on this method. Accordingly, we have designed a volume-servo system which comprises (i) locally pressurized pneumatic cuff, (ii) reflectance-type photoelectric transducer fixed just under the cuff, (iii) electro-pneumatic converter for controlling the cuff pressure pneumatically and (iv) volume-servo control circuit. Using this system we have successfully measured the indirect instantaneous blood pressure both in the temporal and the radial artery, comparing with the finger blood pressure obtained simultaneously by our previous instrument. Due to local arterial pressurization this system seems to allow more stable measurements of longer period of time.

BE4-J.8

A TECHNIQUE FOR NONINVASIVE DIAGNOSIS OF DYSPHAGIA. N.P. Reddy, E.P. Canilang, M.B. Rane, and J. Casterline, Univ. of Akron, Akron, OH 44325 and Edwin Shaw Hosp., Akron, OH 44312

Dysphagia, a disorder of the swallowing mechanism, is a common problem encountered in the rehabilitation of stroke and head injured patients. We have recently identified and developed techniques to quantify several biomechanical parameters that characterize oral musculature in dysphagic patients (Reddy et al 1985). In the present investigation, we have developed techniques, to noninvasively measure the paryngeal phase and coordination. Acceleration was measured at the throat by placing two ultra miniature accelerometers on the skin over the throat, and swallow suction pressure was simultaneously monitored. In normal individuals swallowing gave rise to typical acceleration pattern and there was no time lag between the pressure and acceleration waves. In dysphagic patients, the acceleration pattern was either absent or was delayed, and was significantly different. This technique can aid the clinician in diagnosis of dysphagia.

BE4-J.7

Detection of Fetal Atrial Activities without Signal Averaging. M. Ishijima*, Y. Takeda, Y. Sakurai, Tokyo Women's Medical College, Tokyo, Japan

Ensemble averaging is a common approach to investigate fine structures of fetal ecgs. The fundamental drawback of the ensemble averaging is the impossibility of single beat observation which may exhibit its maximum power under arrhythmias. We developed a new system to overcome the situation and to observe single beat fetal ecgs including its atrial activities without averaging. The method involved multiple body surface electrode and a brief estimation of electrical axis of the fetal atria by a ultrasound image scanner. The electrodes were placed on the abdomen of expectant mother in such a manner that the electrical axis was a center of the spread electrodes in circle. The fetal ecg was calculated with the multiple signals by finite element method taking into account of distances among electrodes. The method was applied on the third trimester mothers in an electrically shielded room. The calculated results showed distinctive P waves of the fetal heart in consecutive beats. The waveforms were, however, contaminated by emg of the fetus when it was awake, and diminished according to the rotation of the fetus. Otherwise, it was a possible method to observe single beat fetal ecgs from the body surface.

BE4-K.1

Future Technologies, Y. Sakurai, Tokyo Women's Medical College, 8-1 Kawada-cho, Shinjuku-ku, Tokyo, Japan

Medical technologies are advancing so rapidly that medical system might change revolutionarily in the near future. When new information media system will diffuse widely in the society, medical system will develop from hospital into "Hospitale", where medical facilities, social institutions and homes will be closely connected each other with information network on the basis of person to person relationship. In this system, a mobile medical facility is important to deliver a medical practice to the spot. The development of superconducting element might give a strong impact to medical technologies. The operating theater is too big to accommodate only one patient who should be surrounded with strictly aseptic atmosphere. So the new concept of "operating capsule" might be developed which will be made of transparent wall and a patient will float in the air inside the capsule with a magnetic power coming from superconducting materials. In this paper, several kinds of future dream in clinical engineering will be mentioned in SF way.

BE4-K.2

In vivo Cerebral Metabolic Monitoring with Near Infra-Red Spectroscopy (NIRS).

P. Rolfe, Maureen Thorniley, YABD Wickramasinghe. University of Keele, Stoke-on-Trent ST4 7QB, U.K.

In vivo near infra-red spectroscopy (NIRS) has emerged over recent years as a method with the potential for continuous monitoring of important biochemical phenomena. Characterisation of the absorption spectra of all absorbing species is essential if quantitative measurements are to be made. The relevant absorbers in the range 750 to 910 nm are oxy and deoxy haemoglobin, oxidised and reduced cytochrome oxidase, and a generalised 'tissue' component.

Instrumentation for neonatal cerebral monitoring comprises laser diode sources at 4 or more wavelengths, optical fibres to convey the radiation to and from the head, optical detectors, and processing facilities. Our studies have been carried out on purified enzyme, cell suspensions, perfused organs, intact rat brain with both blood and fluorocarbon perfusion, human adult and neonatal limbs, and neonatal heads. The feasibility of continuous in vivo monitoring has been demonstrated.

BE4-K.4

Advances in instrumentation for flow cytometric measurements, J. Eichmeier and V. Kachel, Technical University Munich, D-8000 Munich, FRG

A new flow cytometer has been developed which combines electrical cell volume measurements with simultaneous multiparameter fluorescence detection. The flow chamber is suitable particularly for fast sample exchange and kinetic measurements. A mercury high pressure lamp with broad light spectrum allows the excitation of a large number of fluorescent dyes. The data are evaluated by an IBM-AT-Personal Computer, stored in list mode and presented on a color display in the form of one-, two- or three-parameter histograms. Areas of application of such devices are tumor diagnosis, immunology and basic medical and biological research.

BE4-K.3

Future Perspectives in Cardiac Assist: Totally-Implantable Permanent Artificial Heart M. McGee*, R. Kung, S. Parnis, O.H. Frazier Texas Heart Institute, Houston, Texas and Abiomed, Inc., Boston, MA.

The scarcity of donor hearts limit the benefits of heart transplantation to 2000-2500 of the estimated 17,000-35,000 patients needing cardiac replacement. Mechanical devices to support or replace temporarily the failing heart are currently being used with encouraging results. However, these systems require large power/control consoles which limit patients' mobility and are therefore not suitable for long-term support. We are involved with the design, development and testing of a permanent, electromechanically-actuated total artificial heart, under a program supported by NHLBI. The design criteria for this system are: 5 years of tether-free operation; flow rates of 8 L/min at < 120 B/min into a mean aortic pressure of 110 mmHg and mean pulmonary artery pressure of 25 mmHg; autoregulated control responsive to varying circulatory demands; non-thrombogenic, non-hemolytic blood-contacting materials which minimize or eliminate the need for anticoagulation; anatomic and physiologic compatibility; rechargeable external battery power for >10 hours; and rechargeable implantable battery power for >45 minutes.

These efforts will result in a mechanical system which will provide permanent circulatory support with the patient quality of life required.

BE4-K.5

Analysis of Sound at Urethral Flow, H. Teriö*, P. Ask, Department of Biomedical Engineering, University of Linköping, 581 85 Linköping, Sweden

The idea behind this project is to try to find a noninvasive method to detect obstruction of urinary flow by sound measurements at the body surface. In the vascular system it is known, that turbulent flow through obstructions produces sound, the spectrum of which can be used to assess the obstruction. Low frequency peaks in the sound spectrum are related to the elasticity of the artery whereas the changes at the higher frequencies are related to the degree of the obstruction and the flow velocity.

We have measured generated sound at various degree of obstruction in an urethral flow model. In these experiments we have used latex and silicon tubes with different wall thickness and diameter. The obstructions have been produced by squeezing the tube with a rod connected to a micrometer screw and the sound was recorded with a condenser microphone.

The sound spectrum shows clear intensity increase with increasing obstruction. Some changes in the frequency spectrum characteristics could also be observed.

BE5-A.1

Effect of Spaceflight on the Rat Skeleton, David J. Simmons*,
University of Texas Medical Branch,
Galveston, TX 77550

In young growing rats, spaceflights of 7-18.5 days retard the rate of bone formation without affecting bone resorption. Total bone mass is reduced, particularly in the trabecular regions of the skeleton. The vertebrae are weaker than normal when tested in compression, but the torsional strength of the long bones are not compromised. The ratio of mineral to matrix is not abnormal (calvaria, ribs, jaw, femur, incisor dentin). Gradient density analyses demonstrate that the global decrease in bone formation in microgravity is associated with qualitative changes in bone composition, and that these disturb the maturation of the (slowly) forming matrix and mineral moieties. Spaceflight compromises the formation of collagen intramolecular links and the growth of apatite crystals. Fourier analysis of dentin electron microprobe scans indicate that these maturational deficits do not reflect an abnormal phasing of the circadian and ultradian Ca-P biorhythms. Rather, they point to the influence of persistently high matrix sulfur concentrations (proteoglycans) on bone biomineralization. We conclude that microgravity affects the maturity of the growing skeleton and, thereby, its mechanical strength.

BE5-A.3

A Cellular Based Computational Model for the Deposition and Resorption of Bone Tissue, S. C. Cowin, Tulane University, New Orleans, LA 70118. USA.

The transduction of mechanical information to chemical information, the mechanism underlying the functional adaptation of bone tissue (Wolff's Law) has not been established. Furthermore, the means by which cell populations are subsequently controlled has not been identified. In this contribution the evidence concerning the biological strain transduction mechanism is briefly reviewed. A model for the surface deposition and resorption of bone tissue based on the cellular level concept of a cell activity function is reviewed. The applications of this model to the prediction of bone modeling and remodeling are briefly summarized.

BE5-A.2

Mechanical vs. Metabolic Factors in the Development of Osteoporosis, Manmohan Singh*, Michael Reese Medical Center, Chicago, IL 60616

In the postmenopausal female patient osteoporosis results from two basic etiological factors: (i) the bone may resorb in response to a metabolic need for calcium, or (ii) the bone may adjust to lowered mechanical stresses as activity level and muscle mass decline with age. It is possible to separate two types of bone loss by measuring the bone density of radius at two sites in the forearm. Distal bone density (DBD) is measured at the "5 mm site" which contains about 50% trabecular bone. Middle bone density (MBD) is measured at the "2/3 site" which contains 98% cortical bone. The two readings are expressed as percentages of adult mean values and compared. Two types of bone loss are seen: Type A: if MBD is greater than DBD by 10% or more. It indicates an accelerated loss of trabecular bone probably due to bone resorption for metabolic needs. Type B: if MBD equal DBD to within $\pm 9\%$. It indicates a balanced loss of trabecular and cortical bone probably due to adjustment of bone to lowered mechanical stresses.

BE5-A.4

Skeletal Biomechanics and Aging, Subrata Saha*, Dept. of Orthopaedic Surgery, Louisiana State University Medical Center, P.O. Box 33932, Shreveport, Louisiana 71130.

Although many investigators have tested the load-carrying capacities of whole bones and the mechanical properties of bone tissue, only few have focussed their attention on how these properties change with age. Similarly, only a few authors have attempted to quantify the relationship between the changes in the microstructure and chemical composition of bone tissue and its mechanical properties. Also, little is known about how changes in the shape of a whole bone (either in diameter or cortical thickness) affect its load-carrying capacity. A complete picture of the simultaneous changes in the biomechanical, structural, and microstructural variables is almost never available because authors who test whole bones often do not examine the microstructural or chemical changes in the bone tissue. Similarly, investigators who test small, machined bone specimens often do not consider the overall size or shape of the whole bone. Available data on the changes in the mechanical properties of whole bones and bone tissue will be presented. How the load-carrying capacity of whole bones changes with decreased cortical thickness (with aging) will also be discussed.

BE5-B.1

In-Vivo Mechanical Response of the Human Growth Plate Close to skeletal Maturity, J Kenwright, A J Spriggins and J L Cunningham*, Oxford Orthopaedic Engineering Centre and Nuffield Orthopaedic Centre, Oxford OX3 7LD, U.K.

Recent studies on leg lengthening using epiphyseal distraction have suggested that lengthening of the growth plate without fracture is possible in immature subjects using low rates of distraction. If this process were possible in patients close to skeletal maturity it could be advantageous since most lengthenings are performed at this stage when an accurate assessment of leg length inequality is possible. In this study the distraction forces have been measured and are related to in-vivo biological events.

Axial force during distraction was monitored daily using a purpose built loadcell attached to the external fixator. Slow distraction rates of 0.5mm/day were applied as were constant distraction loads well below those found in-vitro, from an amputation specimen, as leading to fracture. For all the distraction regimes applied it has not been possible to lengthen the limb without there being evidence of fracture, as assessed both radiographically and by a sudden decrease in the peak distraction force. With both constant distraction rates and loads growth plate failure occurred between 600-800N, considerably below that seen in-vitro of 1700N. It would appear therefore, that fracture must always occur in this age group.

BE5-B.3

REGIONAL BONE DENSITY IN THE PROXIMAL FEMUR AND ITS CORRELATION TO BIOMECHANICAL PROPERTIES MD Smith, DL Dickie*, A Cooperman, SA Goldstein, MJ Flynn, University of Michigan, Ann Arbor, and Henry Ford Hospital, Detroit, MI.

The cost of hip fractures is enormous, in both human suffering and financial respects. In order to assess the significance of regional bone mineral density in the proximal femur, twenty-two cadaver specimens were scanned using a density specific computed tomography protocol. They were then embedded into steel collars and loaded anatomically until fracture occurred. Subsequent hip screw pull out tests were performed, which measures the ability of the bone to be successfully repaired using this fixation device.

Five regions in the femoral head and neck area were measured using interactively positioned regions of interest on a coronal plane (parallel to the neck and shaft surfaces). Traditional Singh values from standard radiographs were also determined for each femur by an orthopaedic resident, an experienced orthopaedic surgeon, and a radiologist.

The correlation of resident's Singh index to fracture load was $r=.593$, the orthopaedic surgeon's and radiologist's were $r=.463$ and $r=.333$, respectively. The regional densities near the superior and medial surfaces of the femoral head correlated to fracture load with $r=.798$ and $r=.719$, respectively. The screw pull out resistance and lateral surface regional density were correlated with $r=.837$.

BE5-B.2

Micromechanics Modeling of Compact Bone Tissue, H. A. Hogan*, Mech. Engr. Dept., Texas A&M University, College Station, Texas 77843-3123.

Compact bone tissue can be treated as a fiber reinforced composite material with at least three phases. Osteons form the main fiber component and are surrounded by a concentric layer of cement line material. These structures are assumed to be arranged in a close packed hexagonal array embedded in a matrix of interstitial lamellar bone. A micromechanics analysis of this system has been studied using a finite element model of a representative volume element of material. A two-dimensional mesh with linear elastic constituent material properties has been considered initially. The micromechanics approach allows study of the relationship between constituent properties and overall macroscopic material response. Also, "micro-level" stress distributions are examined. For a given macroscopic, or average, stress or strain level, the finite element model gives the detailed stress and strain distributions amongst the separate model constituents. Refinements to include more realistic constitutive relations for the discrete components are also considered.

BE5-B.4

Stress Relaxation Behavior of Three Human Bones, A.H. Uçışık* and C. Bindal, Boğaziçi University and Istanbul Technical University, Istanbul, Turkey

Three human bones, tibia, femur, fibula, which were amputated from same person, were isolated from soft tissues and kept in deep freeze until experiments run. Samples taken were close to the knee joint. Loads were applied with constant crosshead speed on the several different parts of single crosssection of each bone by a diamond indenter specially attached to the Instron Universal Testing Machine. After reaching to the previously decided value of load, by keeping crosshead level constant, stress relaxation started. Comparisons in terms of stress relaxation as well as elastic properties were made for each single bone depending on test test location and among three bones. Due to strong anisotropy, microstructural differences, relaxation time and the amount of load relaxed were not same everywhere on a single crosssection of each bone. Differences among tibia, fibula and femur were stronger. Thus, mathematical modelling of bone with available data is almost impossible.

BE5-B.5

Anisotropic Viscoelastic Constitutive Equation of Trabecular Bone of Human Spine, Cheng Peilai*, Dept. of Mechanical Engn, Tianjin Institute of Technology, and Chen Hongxing, Tianjin University, Tianjin, P.R.C.

The anisotropic viscoelastic constitutive equation has been established by uniaxial constant loading creep experiments on 37 cm^3 cubic specimen cut from human spine. The trabecular bone has been assumed as a transversely isotropic body. Two kinds of cm^3 cubic specimen were cut from L_1-L_5 : one along the vertical and transverse direction and another one along 45° and -45° direction to vertical axis. Altogether 37 cubes were cut. The load was applied on vertical, transverse and 45° directions of trabecular respectively. The displacements along the loading and lateral directions were measured simultaneously. The experimental results showed that trabecular bone behaves as anisotropic viscoelastic material and the creep rate varies with its direction. The two-, three-, and four-parameter Kelvin models were used to model the experimental results and the three-parameter Kelvin model was shown to be excellent with average errors of 1.26%. The time-dependent anisotropic viscoelastic constitutive equation of trabecular bone of human spine was established and all parameters in constitutive equation were obtained.

BE5-C.1

Quantitative Evaluation of Bone Mineral Density. C.C. Gluer*, J.E. Block, P. Steiger, H.K. Genant, University of California, San Francisco, CA 94143.

A variety of techniques for non-invasive quantitative evaluation of bone mineral density are available for assessing metabolic bone diseases. Quantitative Computed Tomography (QCT) has the capability for precise three-dimensional anatomic localization, providing a selective measurement of highly responsive trabecular bone. Mainly applied to the assessment of the spine, techniques for hip mineral quantification are also being developed. Results obtained on 538 healthy women illustrate the use of QCT spinal measurements in the delineation of normal age-related bone loss. For peri-menopausal women accelerated bone loss of -4.4 mg/ml/year ($p < 0.0001$) was found as compared to a non-significant decrease of -0.45 mg/ml/year for pre-menopausal women and an average rate of change of -1.9 mg/ml/year ($p < 0.0001$) for post-menopausal women. Other studies comprise the evaluation of estrogen effects on bone, the assessment of fracture threshold and risk, and the study of the association of various exercise regimens to bone mineral density. QCT will be put in perspective to other quantitative techniques such as Dual Photon Absorptiometry and Quantitative Digital Radiography.

BE5-B.6

A Simple Constitutive Equation for a Cortical Human Bone, Jia-Ju Sun* and Jie Geng, NW. Inst. Archit. Engng., Xian, Shaanxi, P.R.China.

This short study presents a simple viscoelastic constitutive equation for the cortical human bone with haversian systems. The equation is obtained. The mechanical model is considered in accordance with the testings.

BE5-C.2

Redistribution of Bone Tissue in the Humeral Cross-Section of Growing Rats Following Swimming Training, A. Simkin, I. Leichter* and A. Swissa. The Jerusalem Osteoporosis Center, Dept of Orthopaedics, Hadassah University Hospital, Racah Institute of Physics and Cosell Center, Hebrew University, Jerusalem, Israel.

The effect of non-habitual physical activity on bone remodelling at two sites along the rat humeral shaft was examined in this study. Two groups of rats were trained to swim for one hour a day, for 20 weeks at two training levels. The control group consisted of sedentary rats. Parameters of cross-sectional bone morphology were used to evaluate the response of bone architecture to mechanical loading. The strength of bone was assessed by measuring the ultimate compressive force and stress. The cortical cross section area and principal area moments of inertia were found to be significantly higher, by up to 13% and 57%, respectively, in the swimming groups than in the controls. Examination of the ratio between the major and minor area moments of inertia revealed that the bone became more eurycnemic. The ultimate compressive force was significantly higher, by up to 14%, in the swimming rats, while the changes in ultimate stress were not significant. Our results indicate a gain of bone strength due to increased periosteal apposition and modified bone tissue distribution. The marked changes in bone morphology are attributed to the different nature of the forces and moments exerted on the humerus during swimming, compared to locomotion.

BE5-C.3

CARBON ARTIFICIAL BONE REPLACEMENT FOR BONE TUMOUR TREATMENT (7 CASES REPORT); - Chen Lantian* and Jian Kunyuan, Central Hospital of Jilin City, Jilin Province, P.R.C.

With the development of bi-medical engineering, people paid more attention to Artificial bone, through the further study to carbon material, we started making Artificial bone with Low Temperature Isotropic carbon in 1979, we had done the treatment of bone tumour with replacement of Artificial bone for seven cases until 1984, two cases of 2-3 degree giant cell tumour of lower end Radius, three cases of 2-3 degree giant cell tumour of upper Humerus (one case relapse), these five cases were seriously eroded and damaged by swelling giant cell tumour, they could not be treated with excision and bone graft or bone cementing because the soft tissue was eroded by tumour. One case of Fibrohaemangioma of upper right Ulna with pathological fracture. One case of fibrous dysplasia of right upper Ulna with pathological fracture.

Follow-up - the longest for these cases was eight years, the shortest was two years and two months, the average was five years and ten months (three cases follow-up time more than six years). In all cases, no loosening, no relapsing of the tumour, and no metastasis would occur.

Follow-up examinations revealed that the results were satisfactory.

BE5-D.1

A Review of Total Hip Prostheses, J.A. Albright*, LSUMC, P.O. Box 33932, Shreveport, LA 71130

The use of implants in the human hip joint has increased dramatically over the past 75 years. The record includes: experience with numerous materials at the turn of the century; the Smith-Peterson cup arthroplasty; the Austin Moore prosthesis; the Judet prosthesis; the Charnley THP, together with innumerable second generation modifications by others. Cemented hip prostheses were universally accepted in the United States without a serious evaluation of efficacy. Now there is a growing disaffection with cement and a current shift toward porous surfaces, but limited information on results.

Upon review, several points emerge: 1) The body isolates most foreign materials and does not act as if they were an integral part of a functional unit. Those materials which have been utilized to date appear inadequate. 2) Technical design, material properties, and surgical skill determine short-term success. 3) Physiological response determines long-term success. 4) The response of bone cannot be determined with certainty for an extended period of time. The number of years needed is dependent on the magnitude of the response. 5) The acceptance of new devices and procedure by orthopaedic surgeons is very responsive to marketing strategies.

BE5-C.4

MECHANICAL PROPERTIES OF THE TRABECULAR BONE OF THE VERTEBRAL BODY, ZHU DEJING*, CUI JIAN, SUN CHANGZHU, XU YANGHE, SU YONGJUN, BIAA, PRC.

An experiment on the mechanical properties of the vertebral cancellous bone has been performed. About 314 cancellous specimens from the human vertebrae and 139 specimens selected from pig's vertebrae were compressed to break along the vertical axis, the transverse axis and the sagittal axis respectively. 8 intact vertebrae were compressed, too. The strength, the elastic modulus, the Poisson's ratio and the apparent density of the cancellous bone of human vertebrae and the pig's vertebrae were determined. The pattern and the feature of the trabecular bone were observed and the mechanical properties of the cancellous bone affected by its trabecular structure were discussed. The results show there is no significant difference in the mechanical properties between the parameters in the direction perpendicular to the vertical axis. However, the strength and the elastic modulus in the axial direction are significantly greater than those in their perpendicular directions. Both the apparent density and the trabecular structure are two important factors affecting the mechanical properties of the cancellous bone.

BE5-D.2

Material and Engineering Technology in Orthopedic Implant; Yesterday, Today and Tomorrow. Dane A. Miller*, Ph.D. Biomet, Inc., P.O. Box 587, Warsaw, Indiana, 46580 USA.

Archaeological evidence from prehistoric times suggests that for many centuries, attempts have been made to treat orthopedic injuries and diseases with implanted foreign materials. With centuries of historic experience, it has been only in the past two decades that the successful total joint and trauma products of today have evolved. Of special note are the total hip and total knee prosthesis which have revolutionized the treatment and prognosis of today's arthritis patient. Until the advent of contemporary total joint replacement, the arthritic patient was subjected to a series of pharmacological and surgical treatments of limited success which ultimately resulted in the disability of the patient. Today's success rates, often reported above 95% good or excellent, are a result of a combination of new materials, new design information and improved surgical techniques facilitated by improved instrumentation for the surgeon. The arthritis patient of today can, almost without reservation, look toward a return to full activity following total joint replacement. As we look ahead to the next decade, similar "improvements" in both evolutionary and revolutionary technology can be anticipated. Several examples of this wave of future technology will be presented.

BES-D.3

"The Orthopaedic Implant Manufacturer: Challenges for the Year 2000," Richard W. Treharne, Richards Medical Company, Memphis, Tennessee

All US-based orthopaedic implant manufacturers will have many challenges to face by the year 2000. The first of these challenges will be an increase in demand for products. The aging of the "baby boomers," the gradual increase in life expectancy, and the advances being made in all other non-orthopaedic areas of medicine means that the year 2000 will have an increased usage of orthopaedic products. A second challenge will be regulatory. The power and authority by the FDA over the orthopaedic implant manufacturer continues to increase and will pose a severe challenge by the year 2000. A third challenge will be financial. Third-party reimbursement will always be a critical issue and even more challenging in the future. A fourth challenge will be legal. Product liability issues will be a challenge for all companies in the future. A fifth challenge is technology. What will be the new technical horizons in the future? Where will the advances in ligaments, composites, external fixators, and other biomedical devices come from? These challenges and questions of the future will be addressed.

BE5-D.5

A Biodegradable IM Nail with Interlocking Crosspins: Initial Computational and Experimental Results, H. A. Hogan* and D. A. Hulse, Texas A&M University, College Station, Texas 77843-3123.

A biodegradable IM nail with interlocking crosspins is under consideration. Because the stiffness of such materials is much lower than that of steel, a series of interlocking crosspins are needed for sufficient stability. Understanding the mechanics of the deformation and load transmission behavior of the device is an essential element in its ultimate development. A simplified finite element model of the system has been developed and studied. Initial trends in the variation of overall implant stiffness with various system parameters have been established. A wooden model of the system has been tested experimentally and reveals highly nonlinear behavior due to local material failure near component interfaces. The current model, therefore, only models the initial response of the system at very low loads. Modification of the model to include these effects has been initiated and is continuing. Developing an adequate, yet computationally cost-effective, model is the overriding goal of these efforts.

BE5-D.4

COMPOSITE MATERIALS FOR TOTAL JOINT REPLACEMENT
Michael T. Manley*, Osteonics, Allendale, NJ

Composite biomaterials are the next major step in total joint replacement technology. At present, orthopaedic composites fall into the categories of coated metals (particularly ceramic coated titanium), polymers reinforced with chopped fibers, design specific composites and laminated composite structures. Clinical experience has been gained from the first two materials while the latter two have been used only in animal studies.

The major advantages for composites in orthopaedic applications is the new possibilities available to implant designers. Material anisotropy and the tailoring of material properties are now a realistic possibility. Biologically active components can be deliberately incorporated into the material design. Ion release to tissue present in all metal systems can be obviated and the radiolucent character of composites will allow more careful monitoring of bony interfaces. Composite materials have the potential for long term joint replacement rather than limited term joint substitutes. This presentation will highlight the use of composites in orthopaedic applications with illustrative clinical and animal studies.

BE5-D.6

The Design and Testing of External Fixator Bone Screws. J L Cunningham*, M Evans and J D Harris, Oxford Orthopaedic Engineering Centre, Nuffield Orthopaedic Centre, Oxford OX3 7LD, U.K.

In external fixation bone screw loosening is still a major problem. In this study the design factors affecting the mechanical strength at the bone screw interface were assessed, and experimental screws designed and tested which are intended to maximise the holding power of the screw and minimise screw loosening. Push-in, pull-out and bending tests on various commercially available 6mm screws and the experimental screws were carried out both on a synthetic material and in bone. Fatigue tests were also carried out on all of the screws to determine susceptibility to loosening. Photo-elastic tests on different screw threadforms were also performed. The results of the push-in and pull-out tests indicate that the cutting head and threadform of the screw have a marked effect on the holding strength. The bending stiffness of a screw can be increased by 33% by a small (10%) increase in core diameter. The number of fatigue cycles to loosen a screw can be influenced by both the threadform and by an increased core diameter. The photoelastic tests show that most of the applied load is distributed over the first few threads closest to the applied load, and that the area between the thread crests is subjected to high shear stresses.

BE5-D.7

Carbon-Titanium-Combine Femoral Head Prosthesis (A Clinical Report 100 Cases), Chen Lantian*, Jian Kunyuan and Wang Shiqing, Central Hospital of Jilian City, Jilian Province, China.

Since January 1980 through November 1986, replacement arthroplasty with Carbon-Titanium-Combine femoral head prosthesis was done in 100 cases; there were 64 fresh (subhead femoral neck fracture), 20 old, 3 pathologic (Aneurysmal bone cyst) femoral neck fracture, 13 Avascular necrosis of femoral head.

The longest follow-up was 7 years and 8 months and the shortest was 1 year and 11 months. The average was 3 years and 10 months.

Follow-up examinations revealed that the results were satisfactory (only 2 cases occur sinking of the prosthesis, 1 case periarticular Calcification, 2 cases suffered traumatic femoral shaft fracture).

BE5-E.1

A Biomechanical Analysis of the Steffee Plated Thoracolumbar Spine, Stephen P. Courtney*, John M. Lipka, Subrata Saha, and James A. Albright
Orthopaedic Surgery, LSU Medical Center
P.O. Box 33932, Shreveport, LA 71130-3932

Patients with unstable thoracolumbar spine fractures benefit from surgical reduction and rigid internal fixation. The Steffee spinal plates represent one type of transpedicular screw fixation device currently utilized for stabilization.

The torsional, flexural, and lateral bending stiffness of 2 embalmed and 2 fresh thoracolumbar spines were measured before and after a simulated fracture of the 12th vertebra fixed with Steffee spinal plates. The Steffee plated thoracolumbar spines did not differ significantly in behavior from the normal thoracolumbar spines in torsion. In flexion the plated thoracolumbar spines were significantly less stiff ($p < 0.05$) than the normal thoracolumbar spines. In lateral bending, the Steffee plated spines were less stiff than the normal thoracolumbar spines, but the deviation from normal was not significant. Removal of the anterior plated nuts had no significant effect in the biomechanical performance of the Steffee plated spines. In summary, the Steffee plated thoracolumbar spines behaved very similar to normal in torsion.

BE5-E.2

The Biomechanics of L-Rod Interlock to Prevent Sidesway of the Scoliotic Spine, G. McNeice*, and B. Allen Jr., Division of Orthopaedics, University of Texas Medical Branch, Galveston, Texas, 77550.

This study was prompted by clinical evidence of post-surgery progressive sidesway of some pediatric spines during the fusion period. A spine model was constructed to provide simulation of the ligamentous spine. A test table was designed to allow incremental apical rotation with lateral load application. Standard 3/16" diameter L-Rods were wired over the thoracolumbar spine and then loaded laterally to demonstrate the kinematics of wire-rod interplay and subsequent slippage. An interlock device was designed and component tested to provide inter-rod locking. The device was constructed using MP35N metal for use of either 316L Stainless Steel or MP35N spinal rods. Additional instrumentation including a torque device and operating room calibration was designed. The interlock device was designed to resist a 2000 N shear slip force in order to resist a lateral load of 500 N placed at the top of the spine. This was estimated to provide a safety factor range of 2 to 4 times the expected lateral loading.

BE5-E.3

The Biomechanics of Neck Trauma-Injury Envelopes and Applications to Gymnastics, G. McNeice*, T. Oxland and P. Scott, Civil Engineering, University of Waterloo, Waterloo, Ontario, N2L 3G1, Canada.

Catastrophic cervical spine injury amounts to approximately 10,000 new cases each year in the U.S.A. Estimates indicate each of these cost society about \$400,000 and that about one-third is due to falls. The present paper summarizes the injury tolerance data and proposes injury envelopes which can be used to predict injury severity following accidental human impact. Application is made to the study of safety matting as used in the sport of gymnastics. Only vertical head-first impacts were simulated experimentally. The test facility comprised a drop impact mechanism with variable mass and impact velocity. A combination of impact force, moments, acceleration and displacement were measured simultaneously to allow full assessment of impulse, energies and deformation. Additional tests were conducted using a Hybrid III anthropomorphic test dummy for impacts on mats currently on the market. Impulse values remained insensitive to impact severity, suggesting that it is not a good parameter for injury assessment. Protective matting has a limiting percentage of energy absorbency and appears to remain constant for any one mat construction.

BE5-E.4

Space Truss - A Systems Approach To Cervical Spine Mechanics, S.M. Levin, Potomac Back Center, 5021 Seminary Road, Alexandria, VA 22311

A space truss system is proposed as a structural model for the cervical spine to replace the present post and lintel or lever model. Lever models are reductionistic and present apparent solutions to local problems but fail to give a comprehensive understanding of biomechanical design. Systems theory modeling is used to develop a rational basis for the use of a space truss with an internally vectored icosahedron as the finite element of a hierarchical truss system. Some advantages of a truss system are omni-directional stability and within the same instant, flexibility, local load distribution and low energy requirements. Physical properties of biological material and icosahedral truss systems coincide and allow for unique biologic characteristics such as non-linear stress-strain curves and Poisson's ratio approaching unity. One basic model is applicable to all cervical spines of any species under any condition of loading.

BE5-E.6

The Biophysics of the Spine in the Evolution of Man on the Earth, M. Pevano, "Functional Education and Rehabilitation", La Sapienza University, 00185, Rome, Italy

The A. shows a "human model" selected from some case studies which consider subjects in a state of insufficient redressment in the sagittal plane (hypercyphotic with involvement of the non-rigid cervico-thoracic spine) which react favorably to a vertical compression applied by the operator's hand on the neck/trapezius angle. Reaction means "functional verticality" which according to the biomechanical law invariability may also have evoked a dynamic erect posture as it should have been experienced by the evolutionary families between Genus a Hominoid and Homo. The above functional adjustments should have been compulsorily assumed while the evolutionary families carried huge quantities of heavy materials towards the open plains to defend themselves against aggressors through the construction of rudimentary but effective walls. The A. studying the "human model" defines the weight (about 12,5 Kg) and location (neck/trapezius angle) of these materials which a transitional being between genera Hominoid and Homo should have favorably carried. In this paper the A. analyzes the compressive/tensile forces which from the necessity to maintain the erect posture may have guided towards the structural changes observable in fossil remains.

BE5-E.5

RESEARCH ON MECHANICS OF THE SPINE, Zhu Dongming*, Sun Changzhu, Xu Yanghe, Zhang Hua, Sheng Jinfang, Beijing Languages Institute, Beijing, P.R.C.

The study on the mechanical properties of each section of the vertebral column is the foundation of biomechanics of the spine. Research has been conducted on the mechanical properties of the intervertebral disc and the cancellous bone of vertebrae. The anisotropy of the vertebrae and the intervertebral disc was calculated, analyzed and given explanations. The method of finite element and its application in biomechanics was discussed. Three models of the motion segment were introduced: Sailer's axially symmetric model, Shiraziadi's model of the 2-3 vertebrae of lumbar spine and its intervertebral disc from a 29-year old female body and Simon's model of porous materials.

Also, the biomechanical model of the spine has been discussed.

BE5-E.7

Biomechanic Research of Treating in the Thoracic and Lumbar Vertebrae Compressed Fracture Gu Yun-wu, Wang Xiao-tong*, Han Hui Tianjin Hospital Orthopaedic Institute Tianjin, P.R.C.

Functional exercises with a pillow under the part of lumbar compressed fracture, mean while a spinal rack is putted on the part of thoracic and lumbar fracture, are a good method of treating in thoracic and lumbar compressed fracture.

According to the animal experiments, fresh spinal specimen experiments and clinical test, it is evident that the more serious compressed fracture is, the smaller reduction force is needed.

Although using the method of function exercises with a pillow, the function of the spinal would still recover slowly due to staying on bed so long time. For solving this problem the spinal rack was used to keep a fixed force so that the patients could do functional exercises on the ground.

BES-E.8

Experimental Study on Effect of Spine Transmitting Vibration, Liu Zhen-tian, and Liu Run-nan, Nanjing Institute of Technology, P. R. China

In this paper, the caused vibration in the roads of different flatness were chosen to be as the exciting source of vibration situation. The Vibration information of the vehical and human buttock and human head was collected. Using signal digital process technique to analyse the power srectrum, in the viewpoint of energy, we discussed the transmitting effect of the vibrated human body, and studied the transmitting situation among the car's chassis, the chair and the head. Vibration strength transmitting through the spine, frequency beyond 6Hz is absorbed by the spine and other physiological parts of the body. Absorbed energy protects the head, but this part of energy is dissipated in some physiological parts (like heart, lung, stomach, liver and four limbsect.), excessive energy will injure these parts.

BES-F.2

Measuring System for Contact Pressure Distribution in Artificial Knee Joint, H. Kurosawa*, K. Yamakoshi, T. Yamanoi and A. Kamiya, Research Institute of Applied Electricity, Hokkaido University, Sapporo, Japan.

Although a number of biomechanical studies of the human knee joint have been carried out, the kinematics of the knee joint is not fully understood. The artificial knee joint replacement surgery is usually indicated for the severely damaged knee. To date, many kinds of artificial knee joints have been designed. In some cases reoperation is needed to treat complications such as loosening of prosthesis. We have developed a microcomputed-based system which allows the measurement of contact pressure distribution in artificial knee joint during operation in order to prevent complication due to malalignment of the joint. The system is composed of (i) measuring apparatus where twelve pressure sensors are buried in the trial of tibial component and (ii) graphic display to visualize the changes in pressure distribution. In vitro experiments shows that only a limited area of the joint was subject to the loading in the malaligned knee. When the quadriceps force was applied, the pressure force of the femoro-tibial joint varied according to the magnitude of the force as well as the flexion angle.

BES-F.1

A Theoretical Analysis for the Characteristics of Articular Joints, M. Zaki, Lept. of Industrial Prod., Mar. Sira University, Mansoura, Egypt.

A simple model of two porous parallel plates with reference to the human articular joints was suggested and studied in the presence of synovial fluid. Variation of pressure, load capacity, time of approach, concentration of lubricant, minimum film thickness and the effect of cartilage porosity upon lubrication, have been investigated. The mathematical analysis was based on the continuity of pressure and velocities at the interface of the synovial fluid film and the three cartilage layers possessing different porosities. The study brings out many valuable and important results which are in good agreement with earlier experimental observations.

BES-F.3

The Biomechanical Analysis of Removal of the Meniscus, Wang Yi-jing, Shanghai University of Science and Technology, China.

Meniscectomy is one of the most frequently performed orthopaedic operations. In this thesis, removal of the meniscus is analysed biomechanically with Finite Element Method (FEM). A two dimensional plane stresses FEM has been developed by author, using the method of combining FEM with strain gauge measurement with the model, FEM analyses are carried out under several pathological condition. The results are compared with that in normal knee. The results are compared with that in pathological knee. The results of computing show that it is influential on stress field in the knee after meniscectomy.

BE5-F.4

The Biomechanics of the Intracranial Pressure Response to Closed Dynamic Impact Injury to the Spinal Cord, Maurice S. Albin*, Leon Bunegin, University of Texas Health Science Center, San Antonio, Texas 78284

In severe trauma, combined spinal cord and craniocerebral injury is not unusual. Previous studies on evaluation of force propagation from site of spine/cord injury to brain via/cerebrospinal fluid pressure waves has been intrinsically limited because impact injury was accomplished directly on the exposed spinal cord. Thus, such energy attenuating structures such as skin, muscle, bone, and ligaments were removed due to the laminectomy itself. This problem was obviated using a dynamic, closed, impact injury instrument delivering 1.0×10^7 dynes/kg force to the T₁₀ vertebral interspace in the cat. A fast rise time semiconductor transducer was connected to an intracranial subarachnoid bolt and impact force calculated using an optical-electronic detector. CSF waves were digitized and averaged after subtraction of impact artifact. After impact, the CSF pressure wave in the cranium reached an amplitude of 30 mmHg over a period of 8.0 msec with the pressure peaking 3.8 msec after impact.

BE5-F.6

Biomechanical Research of Function Shelves in Treatment of Articular Fracture Wan Xiao-tong*, Gu Yun-wu, Han Hui, Tianjin Hospital Orthopaedic Inst.

Articular fracture is common in patient with fracture and difficult in treating. These external fixations have been applied to clinic and biomechanic characteristics have been concluded. The external fixations were made of small bulk, less weight and small structure. After reduction, the fixations were fixed on part of fractures and acted on a reduction force. The strain forces for reduction, which were used to treat humeral transcondy and Bennett's fracture, were about 4-10kg. The compressed forces, which used to treat olecranal, patellar and calcaneal fractures, were about 4-27kg. The static moment was about 9.5kg-cm for treating olecranal fracture, about 3kg-cm for treating Bennett's fracture, about 18kg-cm on calcaneal fracture, about 7.4kg-cm on humeral transcondy fracture, about 13.1 kg-cm on patellar fracture when the patient standing. These external fixations were made of the good elastic materials, so the elastic recovering forces were very well. During patient's exercise, the strain and compressed forces float up and down about 1-3kg. the moments float between 21-20kg-cm. The early function exercises were good for heal of fracture and could prevent stiff joint. During exercising, the static strain force float between ± 0.43 kg, and static compressed force between ± 1.3 kg. After 3-4 days, the static strain and compressed forces went down to 50-70% but the float forces went up one to three times as much as float forces of beginning.

BE5-F.5

Transient Pressure Changes in the Spinal Canal under Rapid Headmovements. M Svensson*, B Aldman, P Lövsund, T Seeman, T Örtengren. Chalmers Univ of Techn. S-412 96 Göteborg Sweden

After whiplash injuries in rear end car collisions at low impact velocities, car occupants often suffer from pain in the neck and pricking fingers. They also often lose consciousness immediately after the impact. Mostly neither injuries to the tissues nor signs of impact to the head can be diagnosed. The injury mechanism has not yet been given a satisfactory explanation. The spinal canal changes its length when the head is pivoted in the sagittal plane. Assuming the cross-sectional area of the canal constant, an exchange of fluid between the spinal canal and the ambient tissues must take place by an alteration of either volume of cerebro spinal fluid in the meningeal tubes or blood volume in the veinplexa of the epidural space or both. Measurements of fluid pressure in the spinal canal in both anesthetized pigs and in a mechanical model show marked differential pressure gradients in the canal under simulated whiplash. This is probably a result of the expedited fluid flow. We are now studying the detailed effects of these pressure-flow phenomena to be able to understand the injury mechanisms.

BE6-A.1

Ventilatory fluctuations and dynamics of the respiratory chemical control system, A. M. ElHefnawy*, Ph.D, Biomedical Engineering Dept, Cairo University, Giza, Egypt.

Ventilatory fluctuations are studied by incorporating noise into a mathematical model of the human respiratory chemical control system. Uncorrelated Noise is imposed on various system parameters including metabolic rates, receptors, and blood flows. The resulting fluctuations show the differential sensitivity of ventilation to the studied parameters. In addition, the central component of ventilation is negatively correlated with the peripheral component, resulting in a total ventilation which is less variable than the algebraic sum of its components. Spectral analysis of the fluctuating ventilation shows a peak around 0.025 Hz, mainly due to the peripheral component of ventilation. This is the same frequency encountered by increasing controller gain to destabilize ventilation. The spectral peak is diminished in both cases by increasing the level of inspired CO₂. The results support that respiratory oscillations might be due the system dynamics.

BE6-A.2

DEPENDENCE OF UPPER AIRWAY CALIBER ON INSPIRATORY MUSCLE ACTIVITY DURING SLEEP, D.W. Hudgel*, Case Western Reserve University, Cleveland Metropolitan General Hospital, Cleveland, Ohio, U.S.A.

It is hypothesized that chest wall muscle contraction during inspiration, by producing an intraluminal subatmospheric pressure, has a collapsing effect on the compliant segments of the upper airway in man during sleep. This collapsing effect is counterbalanced by a dilating force generated by contraction of muscles surrounding the upper airway. To examine this hypothesis, we recorded upper airway and chest wall muscle inspiratory tonic and phasic electrical activity and upper airway resistance during periodic breathing in healthy subjects and obstructive sleep apnea patients in NREM sleep. A disproportionate decrease in upper airway relative to chest wall muscle inspiratory activity resulted in an increase in upper airway resistance or occlusion. In contrast, an increase in upper airway muscle inspiratory activity out of proportion to chest wall muscle activity caused a decrease in upper airway resistance, or resulted in airway opening from an apnea. These findings demonstrate the importance of the relative inspiratory activities of upper airway and chest wall muscle contraction during inspiration in setting upper airway caliber during sleep.

BE6-A.4

Periodic Breathing: A Model with Experimental Observations, D.C. Shannon*, D.W. Carley and Ch. Maayan, Massachusetts General Hospital, Boston Massachusetts 02114

A minimal model of periodic breathing was developed. It defines the conditions for PB in terms of: 1) CO_2 sensitivity, 2) cardiac output, 3) mixed venous CO_2 , 4) circulation time, and 5) mean lung volume for CO_2 . In each of 38 healthy subjects, awake (15), asleep (23), 8 with familial dysautonomia and 2 lacking CO_2 sensitivity, we studied the relationship between relative stability (R) and loop gain (LG) of the CO_2 control system. LG was estimated using measured values of the 5 model parameters. We tested the hypothesis that LG determined R. We found a positive correlation between R and LG ($r = 0.74$, $p < .01$, $N = 85$) and between measured R and predicted R; ($r = 0.09$, $p = > .1$ serial correlation of residuals); the mean residual was not different from zero ($p > .1$). Sustained PB occurred at $LG > 1$ and never at $LG < 0.7$. The average duration of a PB cycle was 29.0 sec; predicted = 36.2s ($r = 0.57$, $p > 0.5$ comparison of slope with unity). Results were similar awake and asleep. Given the above 5 parameters LG was estimated and this model predicted relative stability and, cycle duration of PB in healthy subjects awake and asleep, in Familial dysautonomia and in congenital central hypoventilation.

BE6-A.3

Sleep-Induced Effects on Chemoreceptor Responsiveness and Its Implications, J.A. Dempsey*, University of Wisconsin Medical School, Madison, 53705.

During NREM sleep the ventilatory response to hypercapnia or hypoxia remains substantial, while small reductions in arterial P_{CO_2} strongly inhibit breathing, so that at $P_{aCO_2} = 40$ mmHg expiratory time increases 2-3 X and at $P_{aCO_2} = 35$ mmHg T_E increases 10-15 X. This combination of sleep effects on chemo responsiveness has the following effects: a) causes periodic breathing in hypoxia; b) causes augmentation of diaphragm and accessory muscles of respiration--including abdominal expiratory muscles--when airway resistance is high during eupneic breathing; c) permits complete "resting" of inspiratory and expiratory respiratory muscle activity when P_{aCO_2} is reduced 2-3 mmHg, (via nasal mechanical ventilation); d) increases upper airway resistance--in "susceptible" subjects--when P_{aCO_2} is low (such as during unstable hyperpnea) and decreases upper airway resistance when P_{aCO_2} is high and P_{O_2} low (such as at end-apnea during periodic breathing). The site of transient hypocapnic inhibition and hypercapnic excitation resides primarily at the carotid chemoreceptors. (Supported by NHLBI).

BE6-A.5

Spectral and Coherence Analysis Applied to Sleep Apnea, D.A. Silage* and A.I. Pack, Department of Electrical Engineering, Temple University and the Department of Medicine, University of Pennsylvania, Philadelphia, PA, USA.

Spectral analysis by digital comb filtering of ventilation and the coherence between ventilation and the frequency content of the electroencephalogram (EEG) are used to describe the hypothesis that there are temporal relationships between the periodicities in ventilation and oscillations in state affecting the "wakefulness: input to the ventilatory control systems. The analysis indicates that there is no appreciable lag between the oscillations and a significant ($p < .05$) coherence (0.8) at a frequency of approximately 0.012 Hz or a period of 83 seconds. This result is similar to the observed cycle time of ventilatory periodicities during Stage 1-2 sleep in our elderly subjects. The long cycle time suggests that they are not produced by the carotid body and in our studies the oscillations in ventilation persisted during oxygen breathing, although apnea was abolished.

BE6-B.1

ANALYSIS OF THE RESPONSES TO ABRUPT SPONTANEOUS VENTILATORY DISTURBANCES, M.C.K. Khoo*, Univ. of Southern California, Los Angeles, CA 90089.

Deep breaths that abruptly raise ventilation (hyperventilatory sighs) or spontaneous pauses of a few seconds duration represent approximate impulse disturbances to the respiratory control system. By analyzing the ensuing changes in ventilation and alveolar PCO₂, the dynamic properties of the peripheral chemoreflex loop may be inferred. Denoting the changes in ventilation or alveolar PCO₂ as $x(t)$, a large class of responses may be characterized as $x(t) = A \exp(-bt) \cos(\omega t)$ or $x(t) = A \exp(-bt) (1 + bt)$. In this study, we propose the simplest physiologically plausible model that can yield the above types of responses. We derive analytical expressions that relate the best-fit coefficients (A, b and ω) to the parameters of the closed-loop control system, which include loop gain and the time delay inherent in the loop. This computational procedure represents a simple method for assessing the degree of stability of the respiratory control system without the need for external interventions, such as inspired gas mixtures or forced ventilatory maneuvers.

Supported in part by the Whitaker Foundation and NIH Grant RR-01861.

BE6-B.3

VARIATIONS IN THE SIGNAL STRENGTH AND CONSISTENCY OF RESPIRATORY NEURONAL ACTIVITY AND THEIR PHYSIOLOGICAL SIGNIFICANCE, John Orem*, Department of Physiology, Texas Tech University Health Sciences Center, Lubbock, TX 79430.

Respiratory neurons are, by definition, active during a particular phase of the respiratory cycle. However, the relationship between the activity of a neuron and some phase of the respiratory cycle is not always obvious, and some quantitative technique is necessary to detect the relationship and to define the strength and consistency of it. This presentation will show 1) that the analysis of variance is a powerful tool for detecting respiratory activity; 2) that an effect size statistic can be used to quantify the respiratory signal strength and consistency of that activity; and 3) that classification of neuronal activity according to its signal strength and consistency is important to an understanding of the effects of sleep on the respiratory system and of the mechanisms for behavioral control of that system.

BE6-B.2

Quantitative Analysis of Upper Airway and Respiratory Muscle Electromyograms and Electroencephalogram during Sleep, E. Onal*, D. Carley, R.M. Aronson and M. Lopata, University of Illinois at Chicago, USA

In studying the effects of sleep on respiration and the sleep-induced disorders of respiration, quantification of upper airway and respiratory muscle activity provides important information for the interpretation of sleep-induced changes in minute ventilation and respiratory system mechanics. We record genioglossus muscle activity by a bipolar needle electrode inserted perorally and diaphragmatic activity by a gastroesophageal catheter, while the sleep stages are monitored by electroencephalogram (EEG). The electrical activity of both muscles (EMG) is amplified, band-passed between 30 and 600 Hz, rectified and averaged over consecutive 200 ms intervals, providing a "moving time average" measurement of activity. Similarly, to derive a continuous "state index" (SI), a 5 s time window is moved through each EEG waveform in 1.25 s increments and the power spectrum is computed for each increment. The total power between .5 and 10 c/s is derived from each spectrum to provide the individual points of the SI function. Studies in normal subjects with sleep-induced periodic breathing and patients with occlusive sleep apnea reveal a close association between SI and EMG. However, the assumption that state changes are the sole determinant of periodicity, apnea onset and resolution cannot be confirmed.

BE6-B.4

UPPER AIRWAY PRESSURE-FLOW RELATIONSHIPS DURING SLEEP: EFFECTS OF CHEMICAL AND MECHANICAL STIMULATION. R.A. Parisi*, N. Krawciw, D.A. Hutt, N.H. Edelman and T.V. Santiago. Department of Medicine, UMDNJ-Robert Wood Johnson Medical School, New Brunswick, N.J.

Upper airway (ua) narrowing results in activation of pharyngeal and laryngeal dilator muscles via mechano- and chemoreflexes. However, the extent to which these reflexes may modify airway resistance to overcome obstruction, especially during sleep, is unclear. We measured inspiratory airflow (\dot{V}) and pressure differences (mask to hypopharynx to trachea) to assess supraglottic (sg), laryngeal (lx) and total ua resistance (R) in 4 goats during wakefulness (W), slow wave (SWS) and REM sleep. Changes were measured during single-breath flow-resistive loading (FRL; 18 cm H₂O/1/s) and during asphyxic chemical stimulation (CS) produced by rebreathing 10% O₂ in N₂. Rsg and Rlx both increased from W to SWS to REM ($p < 0.05$). During CS in each state, Rsg and Rlx decreased at comparable \dot{V} . FRL resulted in a large increase in Rsg over the range of \dot{V} achieved, while Rlx did not change. For all states at any level of CS, loaded Rsg was a function of unloaded Rsg ($r = 0.86$). We conclude that partial collapse of the pharynx occurs during FRL. Thus, defense of the upper airway by dilator muscles is not sufficient to overcome pharyngeal narrowing. This is more critical during sleep due to the greater baseline Rsg. (Support: HL16022, HL07467, HL01549, UMDNJ #20-87)

BE6-B.5

Acoustic and Magnetic Resonance Imaging of Extrathoracic Airways, Kingman P. Strohl*, Peter L. Hoekje, E. Mark Haacke, and Lee J. Brooks, Case Western Reserve University, Cleveland, OH 44106

We compared two noninvasive methods for measurement of extrathoracic airway size and response to positive transmural pressure. By acoustic imaging (AI) with airborne sound introduced through the mouth, a one-dimensional measure of airway cross-section over the travel path of the sound is obtained 5 times per second, tracking dynamic changes in area. Magnetic resonance imaging (MRI) provides information in two and three dimensions about the composition and configuration of the tissues surrounding the airway, but at the present time requires imaging times longer by 2 to 4 orders of magnitude than does AI. Images were obtained by both methods in six supine normal subjects breathing through a mouthpiece, with and without administration of continuous positive airway pressure (5-10 cmH₂O). Both methods provided similar values for airway size along the extrathoracic airway, and identified similar regional variations in static airway size in response to an increase in airway pressure. With AI, changes in airway size were observed to correlate with inspiration and expiration, while MRI revealed specific anatomic details about the yielding and unfolding of the airway wall in response to static pressure changes.

BE6-B.6

Mathematical Analysis of Periodic Breathing in NREM Sleep, N.S. Cherniack* and G.S. Longobardo, Case Western Reserve University, Cleveland, Ohio

We used a mathematical model of the respiratory control system to systematically investigate the effect of severity of disturbances to breathing and system parameters on periodic breathing during sleep. The model consisted of multi-compartment representation of O₂ and CO₂ stores, a peripheral controller sensitive to O₂ and CO₂, and a central controller sensitive to CO₂. The effects of hypoxia and hypercapnia on the upper airway muscles were not considered. An episode of hyperventilation or asphyxia was used to disturb the control system. Simulations with the model produced the following findings: the number of apneas associated with periodic breathing were greater as circulation time increased; controller gain increases also made the number of apneas greater, but at each level of circulation time there was a range of controller gain changes which caused little change in apnea number; there were more apneas with hypoxia; the number of apneas increased with sleep associated reductions in metabolic rate and the more rapidly resting pCO₂ rose at sleep onset; and the more intense the disturbance, the more apneas there were. It is known that hypoxia and hypercapnia have multiplicative effects on controlling gains. The precise form of these multiplicative interactions had important effects on the occurrence of periodic breathing. The results suggest that the occurrence of periodic breathing depends on a number of different factors including system parameters and disturbance intensity.

BE6-C.1

FLUID BALANCE AND MACROMOLECULAR TRANSPORT IN THE LUNG. Robert J. Roselli*. Department of Biomedical Engineering, Vanderbilt University. Nashville, TN 37235.

A multiple pore model of steady-state fluid and macromolecular transport has been applied to measurements of vascular pressures, lymph flow, lymph and plasma concentrations of several proteins, and the permeability surface area for urea in sheep lungs. Two pore sizes (approximately 5nm and 26nm, in proportion 10,000:1) are sufficient to describe lymph data collected during baseline conditions and following microvascular pressure elevations, saline infusion, and plasma infusion. A two compartment plasma-interstitial model which uses the above pore structure has also been developed to describe unsteady-state fluid and macromolecular exchange in the lung. Additional model parameters, such as interstitial compliance and filtration coefficient of the lymphatic barrier, are estimated using lymph data collected after a step increase in vascular pressure. Model predictions indicate that only a small fraction of the interstitium is accessible to exchanging protein - a phenomenon verified by experiment. This model is currently being used to interpret vascular permeability from tracer experiments where radioactive macromolecules are injected intravascularly and transvascular exchange measured with external detectors. (Supported by NHLBI 19153, NIH BRSG S07-RR07201)

BE6-C.2

Transcapillary Transport Pathways in Skeletal Muscle, P.D. Watson* and M.B. Wolf, Dept. of Physiology, University of South Carolina, Columbia, SC 29208, USA.

In the conventional view of transcapillary movement, water and solute cross by the extracellular route. Both pore and fiber matrix models of pathways assume this. Using osmotic pressure of small molecules (urea, NaCl, sucrose, and raffinose) to drive water across the microvessels of the isolated cat hindlimb perfused at high flows (>100 ml.min⁻¹.100g muscle⁻¹), water flow rates (>0.005 ml.min⁻¹.mmHg⁻¹.100g muscle⁻¹) were obtained which were comparable to flows driven by hydrostatic pressure or large molecule osmotic pressure (0.01). Using these data to calculate reflection coefficients for these molecules gave values >0.5, close to that for serum albumin, 0.8. These data cannot be easily fitted by models where water and solute use the same path, and are best explained if most of the water flow passed through the endothelial cells rather than around them. Supported by USPHS Grant HL 24314 and the South Carolina Heart Assoc.

BE6-C.3
 PHYSIOLOGICAL REGULATION OF CAPILLARY PERMEABILITY, V.H. Huxley*, Dept. Physiology, Univ. Missouri Medical School, Columbia, MO, USA

The study of transcapillary water and solute has concentrated on factors influencing hydrostatic and osmotic forces at the capillary wall. For the most part the exchange vessel wall is viewed as a passive barrier which may be disrupted under pathological states. Recent studies of water and solute flux in individually perfused microvessels suggest a role for active modulation of the capillary barrier. Specific examples, from this laboratory, include conditions of hypoxia and anoxia or infusion of atrial peptide or sodium nitroprusside. In these cases we observe changes in hydraulic conductance and/or permeability of the capillary wall to solute. The responses are specific to the treatment, dose and duration. They can be modified or inhibited by a variety of agents. The mechanisms whereby the exchange barrier properties are altered appear to be regulated by the endothelial cells in consort with at least one other cell type (pericyte, nerve or mast cell?) under normal conditions.

VHH is an AHA Established Investigator

BE6-C.4
 KINETICS OF CAPILLARY CO₂ EXCHANGE AND pH EQUILIBRATION, Akhil Bidani*, Department of Medicine, University of Texas Medical Branch, Galveston, TX. 77550, USA

In vivo kinetics of capillary CO₂ exchange and intravascular pH equilibration are determined by the complex interaction of multiple factors. The most important of these are (a) the rate of CO₂ hydration-dehydration reactions within plasma and in red cells, and (b) the kinetics of red cell anion exchange. The role and influence of these factors has been examined using a detailed mathematical model of the reaction and transport processes that occur in blood during and after capillary gas exchange. Furthermore, this model has been used to analyze and explain experimental data obtained by us in intact animals and in isolated perfused animal lungs. These studies indicate that blood might not reach electrochemical equilibrium during capillary transit. Additionally, several commonly used drugs adversely affect the rate of capillary CO₂ exchange and intravascular pH equilibration, by modifying the kinetics of specific reactions and/or transport processes involved in gas exchange. Such detrimental effects on gas exchange and acid-base homeostasis might be particularly important in patients with limited cardiopulmonary reserve.

BE6-D.1
 INCLUSION OF AIRWAY WALLS IN LUMPED ELEMENT MODELS OF THE RESPIRATORY SYSTEM. A. C. Jackson* Dept. Biomed. Eng., Boston Univ., Boston, MA.

A 6-element model consisting of a central branch (with a resistance and inertance) separated from a peripheral branch (with a resistance, inertance, and compliance) by a shunt compliance (C_s), thought to represent alveolar gas compression, has been used for respiratory system impedances (Z_{rs}). This model was fit to Z_{rs} in nine dogs (2-96 Hz) but C_s estimated using the model was not correlated with C_s computed from independent measurements of thoracic gas volume. One reason for this may be because of the distorting effects of airway wall shunt impedance, Z_{wall} . To test this, two methods of compensating Z_{rs} for the effects of Z_{wall} of the upper airways were investigated. Both methods rely on a measure of impedance with the airway occluded at some point. This provides a separate measure of Z_{wall} which is assumed to be a shunt impedance in parallel with the impedance peripheral to the closure, Z_{per} . In each of the dogs, Z_{rs} was measured (2-96 Hz), the tracheas were occluded just above the carina and Z_{wall} was then measured. Z_{per} computed by both techniques were physically unrealistic in that the real part became negative above 56 Hz. It is concluded that neither of these techniques can be used to account for the shunt impedance of the tracheal wall.

Supported by NIH grant HL-31248.

BE6-D.2
Modeling the Low-Frequency Mechanical Behaviour of the Respiratory System, J.H.T. Bates*, McGill University, Montreal, Quebec, Canada.

The mechanical properties of the respiratory system are conveniently assessed in terms of the relationships between three easily measured quantities - pressure and flow at the airway opening, and pressure in the esophagus. However, the relationships between these quantities are dependent on the frequency of ventilation. It is clearly important to understand the mechanical behaviour of the respiratory system at naturally occurring frequencies, which are virtually always less than two Hertz. We consider data from the following three types of experiments on anesthetized paralyzed dogs, all yielding low-frequency (0-2 Hertz) information: a) passive expiration, b) the cyclical ventilation of the lungs, and c) the sudden interruption of flow at the airway opening during passive expiration. It is apparent that both the lungs and the chest wall of a normal animal are well modeled as systems with two mechanical degrees of freedom. Further experiments in which alveolar pressures are measured directly in open-chested dogs during flow interruption demonstrate that one of these degrees of freedom in the lungs is the inflation of the lungs as a unit, while the other is accounted for by the viscoelastic properties of the lung tissues. A similar model structure is invoked for the tissues of the chest wall.

BE6-D.3

WHAT MEANING CAN BE GIVEN TO RESPIRATORY MECHANICS PARAMETERS WHEN ESTIMATED THROUGH CURRENTLY USED MODELS?

P. Barbini*, G. Cevenini, University of Siena, Italy
G. Avanzolini, A. Cappello, University of Bologna, Italy

A nine-element RLC model of the respiratory system, which takes into account both low and high frequency behavior, is used as a quantitative tool for investigating the meaning of parameters identified in artificial ventilation and forced pressure oscillations. This model, characterized by a series airway and two parallel tissue compartments, enables us to generate realistic transpulmonary pressures by using mouth flow signals typical of these two respiratory conditions and parameter values representative of dogs.

Two and four lumped parameter models are used for estimation from low frequency signals, while a six-element model is applied in high frequency conditions. Parameter estimation procedure is performed in the time-domain and the Powell algorithm is used to minimize the root-mean-square error between simulated and model-predicted pressure.

At very low frequencies (less than 1.5 Hz) the two-element model is preferred and its compliance reproduces the total one, while the resistance assumes an intermediate value between the two tissue resistances. When the input signal spectrum reaches 3 Hz, the four-element model is preferred. All parameters are satisfactorily estimated even if the resistance in series with the lower lung compliance is overestimated. At high frequencies (4-200Hz) the six-element model allows a good estimation of airway parameters. The tissue resistance and inertance are the parallel of the respective elements in the two tissue compartments, while the tissue compliance assumes an intermediate value. In conclusion, different signals require different models which provide complementary information on respiratory mechanics.

BE6-E.1

One and Two Dimensional Wave Mechanics Models for Oscillating Flows in Respiration, M.A.F. Epstein*, F. Moslehi, M.A. Pisani and J.R. Ligas, University of Connecticut Medical School, Farmington, Connecticut, U.S.A.

Recent interest in the physical phenomena underlying inhomogeneities in gas distribution within the lung has identified the need to predict pressure and velocity distributions throughout the airways. Wave mechanics provides a potent analytical tool for characterizing such oscillatory flows. The equations of motion for a gas undergoing small amplitude sinusoidal oscillations with negligible viscous effects were expressed as a one dimensional wave equation. This model is capable of describing the velocity and pressure fields (transient and steady state) in a number of geometries including slightly compliant ducts and horns. A two dimensional model which includes viscous dissipation has been solved analytically to predict the time dependent radial and axial velocity and pressure distributions. This approach has great promise for understanding airway flow fields.

BE6-D.4

ISSUES WHEN FITTING LUMPED MODELS TO RESPIRATORY IMPEDANCE DATA. K.R. Lutchen*, Boston University, Boston, MA 02215.

Many studies have tried to estimate respiratory system properties by fitting lumped models to impedance data. Here we review the consequences and issues with this approach. The overall theme is the trade-off between model identifiability and being able to maintain a model structure with physiologically relevant parameters. We examine how, for a given clinical condition, data from a specific frequency range limits the complexity of proposed models. These models, in turn, inherently limit the ability to resolve specific system properties or features. To demonstrate this we use "forward-inverse" modeling. Several kinds of detailed forward models (FMs) are used to generate data from 0-4 Hz, 4-128 Hz, 0-128 Hz, and 0-200 Hz. The FMs can have a structure to purposely distinguish anatomic regions (eg., a common airway leading to parallel pulmonary pathways then a common pleural node and then parallel chest wall pathways). For other FMs, the elements can be systematically altered to indicate specific types and amounts of disease (eg. inhomogenous airway disease only). Then, the limitations of simpler inverse models required for uniquely fitting these data in the presence of measurement noise are explored. We also examine constraining some parameters based on independent measurements. Supported by NIH Grant 31248 and The Whitaker Foundation.

BE6-E.2

Anesthesia Ventilator

T. Cadena and F. Prieto*

Instituto Nacional de la Nutricion
Universidad Autonoma Metropolitana
Mexico

A practical, low-cost anesthesia ventilator is one of the notable medical equipment needs in Mexico and probably in other developing countries.

We propose a pneumatic-power, electronic control, constant flow ventilator, built with low cost, locally available industrial pneumatic, measuring and electronic parts. Flow rate, respiratory rate, relative inspiratory and pause periods and end expiratory pressure are set by the user. The pneumatic circuit provides the pressure to drive an anesthesia bellows.

The ventilator has been put to test during animal experimental surgery and has proved safe and effective in a variety of surgical procedures.

BE6-E.3

Microcontroller for a Volumetric Respirator
A. Martínez M., C. López A., J. Jiménez A.
Universidad Autónoma Metropolitana - Izt.
Departamento de Ingeniería Eléctrica
Av. Purísima Y Michoacán. México, 09340 DF

We have designed a microcontroller-based system for the display and control of all the functions involved in a volumetric ventilator designed by Instituto Nacional de la Nutrición in collaboration with UAM-Iztapalapa. It was designed around the 8031 microcontroller, and auxiliary chips such as the 8254 programmable timer and the ADC0809 8 channel, 8 bit A/D converter.

The system is divided into three parts: display, monitoring and control, and alarms. The monitoring and display subsystems are based upon the coupling of flow and pressure transducers to the A/D converter, and the measuring of O₂ concentration. Different parameters such as respiratory frequency, tidal volume and inspiration/expiration ratio can be displayed and controlled. Several alarms are included, such as apnea, airway pressure, minute volume, absence of electrical energy and absence of gases; default volumes for operation are included to enable the system to assure positive safety under all normal and failure conditions.

BE6-F.1

Propagation and Damping of Flow Disturbances in the Bronchial Tree in High-Frequency Ventilation. P.Niederer, E.Bush, Inst. of Biomedical Eng. and Med.Informatics, University of Zurich and Swiss Federal Inst. of Technology, Switzerland; D.Spahn, E.Schmid, Inst. of Anesthesiology, University Hospital, Zurich, Switzerland; P.P. Lunkenheimer, Dept.of Exp.Surgery, University of Munster, FRG.

Unstable flow processes such as turbulence production or eddy-shedding caused by turbulent flow conditions, bifurcations, abrupt diameter changes, and entrance effects in general have been suggested to be mechanisms for gas exchange enhancement in High-Frequency Ventilation. The question arises whether such flow disturbances actually reach the periphery of the lung in spite of the damping provided by the viscosity of the air and the viscoelasticity of the lung tissue.

Propagation and damping of flow disturbances were modelled mathematically on the basis of a one-dimensional flow approximation taking into account the above mentioned damping mechanism. The results were compared to measurements made on tubes of various lengths, diameter and quality, as well as on dried pig lungs. The dependence of the damping is demonstrated as function of frequency and tube diameter, and the ratio of viscous to viscoelastic damping is discussed. It is found that high-frequency flow disturbances are strongly damped out in the small terminal airways, in spite of the short propagation distances associated with the peripheral lung structures.

BE6-E.4

Respiratory Drive Monitor Integrated in a Ventilator,
L. G. Hellström*, B. Hallén,
and D. Linnarsson,
Karolinska Institute, Box
60400, 104 01 Stockholm,
Sweden

A critical problem in intensive care and anesthesia is to decide when the patient can take over his own breathing from a ventilator. For clinical application, we have integrated a system for non-invasive determination of respiratory drive into a Siemens-Eléma Servo Ventilator 900C. The system determines the respiratory drive by evaluating the pressure drop during the first 0.1 sec of an occluded inspiration (P_{O.1}). This can be monitored, together with other relevant respiratory parameters, on a breath by breath basis. No additional valves or sensors are required. A small personal computer connected to a Servo Computer Module controls the measuring process, presents the result and stores it on file. Respiratory occlusion pressures agree well with simultaneous values obtained with a standard method.

BE6-F.2

Axial Flow Development during High Frequency Sinusoidal Oscillations in Airways. D. Isabey, Unité de Physiologie Respiratoire INSERM U 296, Hôpital Henri Mondor, Créteil, France.

From detailed measurements of sinusoidal flow resistance in a cast of central human airways, we partitioned frequency (f) -- tidal volume (V_T) diagrams for peak flow and flow reversal into separate regions in which the levels of unsteadiness are predictable (JAP 61 (1): 113-126, 1986). The dependence of resistance on f and V_T in each region was characterized by non-dimensional parameters describing the relative effect of the forces governing the flow motion in each. One of them is an alternative Strouhal number $\epsilon = (4L/d) \cdot (\alpha^2/Re) \cdot \cos\omega t$, varying throughout the flow cycle which seems to be the key to understanding flow resistance in a range of f and V_T commonly used during high frequency ventilation. We propose extending the Blasius solution for flow development along a flat plate to the boundary layer equation with a non-steady term. This showed that ϵ always remains proportional to the instantaneous and local ratio of the unsteady term over the convective term confirming the pertinence of this parameter for oscillatory flow. When this parameter is applied to axial velocity profiles previously measured during sinusoidal flow in a 3:1 model of the human central airways, the velocity profile dependence on the different levels of unsteadiness is confirmed.

BE6-F.3

A REVIEW OF GAS TRANSPORT PROCESSES IN HIGH FREQUENCY VENTILATION R.D. Kamm[†], Department of Mechanical Engineering, Massachusetts Institute of Technology, Cambridge, Massachusetts 02139, USA.

An overview of the different physical mechanisms responsible for gas transport during high frequency ventilation will be presented and cast in a unified and simplified form that more clearly identifies those factors that limit the rate of gas transport. One simplification introduced simulates the enhancement of molecular diffusion due to the movement of gas back-and-forth through regions of varying cross-sectional area. Predictions are made of the local resistance to gas transport associated with different pulmonary airways. Two resistive zones are identified; one in the vicinity of the trachea and another more peripherally in airways having diameters in the range of 1.0 to 2.5 mm. This suggests that new efforts should be devoted to better understanding the nature of transport in these zones and to the development of variations in the method of ventilation that have the greatest influence there.

Supported by the NHLBI, grant HL 33009.

BE6-G.1

Connection between Microscopic Structure and Macroscopic Mechanical Properties of the Lung, Y. C. Fung[†], University of California, San Diego, La Jolla, CA 92093, U.S.A.

To derive the constitutive equations and material constants of the lung tissue from the microstructure, the widths and curvatures of the collagen and elastin fibers in the pulmonary alveolar walls and alveolar mouths are measured. Together with rheological data of these materials, the morphometric data are used to compute the stress-strain relations of the alveoli. The geometry of the alveolar ducts is analyzed and compared with known data. The validated duct model is used to compute the macroscopic stress-strain relationship of the lung tissue. In the calculation, the micro-strain of the duct is allowed to be different from the macroscopic strain. Among other things, it is shown that a usual hypothesis about soft tissue mechanics: that the elastin fibers are straight and take up load at low stress level, whereas collagen fibers are curved initially and takes on an increasing share of load only when an increasing portion of them are straightened, is wrong, at least for the lung. (Research supported by NIE NHLBI HL 26647.)

BE6-F.4

Computer Simulation of CO₂ Gas Exchange During Mechanical Ventilation
P.W. Scherer[†], G.N. Neufeld,
J.D. Schwarz[†], S.J. Aukburg
Department of Bioengineering[†] and Department of Anesthesia,
University of Pennsylvania
Philadelphia, Pennsylvania 19104
USA

Conventional mechanical ventilation differs from spontaneous breathing mainly in the flow waveform produced by the ventilator and the manner in which the lung is expanded by positive pressure. We have developed a computer model of steady state CO₂ gas exchange based on the solution of the one dimensional convective diffusion equation in the Weibel symmetric trumpet bell model of the human bronchial tree. The computer model allows us to determine the position of the tidal volume (V_T)-FRC interface as it moves during inspiration and expiration and to determine the amount of CO₂ which has been transferred into the VT from the FRC by molecular diffusion. By using the computer model, we can investigate the effect of many system variables including: acinar airway structure, anatomic dead space, breath flow waveform, breathing frequency, tidal volume, breath hold duration, and acinar blood flow distribution on the amount of CO₂ expired per breath and the form of the CO₂ washout curve seen at the mouth on expiration. The model predicts that in the absence of breath holding, frequency and tidal volume are much more important than breath waveform shape in determining the efficiency of CO₂ gas exchange during mechanical ventilation.

BE6-G.2

Finite Element Model of Alveoli and Ducts
R. Lowe^{†1}, D. Hitchings², F.L. Matthews²
and R.C. Schroter¹. Physiological Flow
Studies Unit¹ and Aeronautics Dept²
Imperial College London SW7 2AZ

Knowledge of the mechanical behaviour of the lung is important for understanding its function and monitoring abnormalities. Recent work by Lowe et al (J. Biomechanics 19,541-549,1986) on effects of the constituent tissue and surface lining of the alveolar structures has shown that a mathematical model of a single alveolus of prescribed geometry and assumed material and surface tension properties can be used to generate pressure-volume cycles for whole lungs *in vitro*. Finite element methods were used to determine the distribution of stress for a system of forces due to the applied pressure on the structure. In an extension of this model we aim to reproduce the network of alveoli surrounding the duct. The chosen shape of the alveolus lends itself ideally for this purpose, enabling simplification of the model due to symmetry. By producing an accurate functional representation of the duct we hope to examine the role of interdependence of alveoli and the effect of non-homogenous alveolar units.

BE6-G.3

Mechanical Properties of the Lung Parenchyma Determined from 3-D Reconstructions. R.R. Mercer* and J.D. Crapo, Duke University, Durham, N.C.

The surface tension on the thin walled alveolar septa and the collagen-elastin connective tissue network within the septa are major factors in parenchymal micro-mechanics. 3-D reconstructions from serial sections have been used to study the mechanics of alveoli and alveolar ducts in lung parenchyma. The results indicate that connective tissue elements act to enhance lung stability at volumes greater than end-expiratory volume by distributing stress between adjacent regions. Reconstructions demonstrate fine collagen fibers (5-30 fibrils/fiber) interconnecting the collagen rich alveolar entrance rings (80-300 fibrils/fiber) of adjacent alveolar ducts. Elastin fibers are predominantly located on the edge of alveolar entrance rings and interconnect adjacent rings. This indicates that stress distribution in the lungs is due to the elastin interconnected system of alveolar entrance rings and the fine collagen fibers interconnecting the alveolar entrance rings of adjacent alveolar ducts. The elastin interconnected alveolar entrance rings are under tension at all levels of lung inflation while the fine collagen fibers in the alveolar septa are under tension and distributing stress when the alveoli through which they pass are near full inflation.

BE6-H.1

Conceptual Problems in Rib Cage Kinematics.
R.C. Saumarez, Dept. Cardiological Sciences,
St George's Hospital Medical School, London
SW17 0RE, United Kingdom.

The kinematics of the rib cage have proved hard to analyse. These difficulties stem from:

- Unrecognised functional differences between the human and quadruped rib cages and the functional and morphological differences between the human upper and lower ribs.
- The transformation of a rib between two points may be expressed as a rotation and a translation. The trajectory of the rib cannot be deduced from this transformation yet ribs are often assumed to rotate about a single axis.
- The rib cage probably moves with its components fitting together. With monoaxial rotation there are small misfits at the four joint surfaces on the rib. While these are "negligible" compared to the dimensions of the rib, very large forces would have to be created to overcome these misfits. Also, with monoaxial movements, variations in rib cage motion cannot be accounted for except by rib deformation which would require very large forces. These problems are resolved if the rib cage is treated as a multi-element mechanism which can move within the constraints imposed by the geometry of its joint surfaces.

BE6-G.4

Surface Tension Driven Flows in Thin Liquid Linings D.P. Gaver, III and J.B. Grotberg,
Northwestern Univ. Evanston, IL.

We study the events following the impaction of an aerosol droplet containing an immiscible surfactant on the lung's liquid lining. Surface tension gradients drive a "Marangoni" flow within the film, spreading the aerosol, and providing a larger area for the transport of substances carried by the aerosol. We used lubrication theory to derive non-linear partial differential equations describing the evolution of the surfactant concentration and the film thickness, and found their solution by numerical integration. The driving mechanisms in this problem are surface tension gradients, surface diffusivity of the surfactant, and gravity. Several dimensionless parameters, which mainly depend upon the thickness and viscosity of the film and the composition of the aerosol, influence the behavior of the solutions.

Our results show the possibility of a wide range of behaviors depending upon the magnitudes of the parameters. However, for all cases in which the gravitational parameter was non-zero, we observed an initial spreading of the aerosol accompanied by a localized thinning of the film. A recirculation region in the form of a ring vortex develops and the film finally relaxes to a flat interface.

BE6-H.2

Intrathoracic Pressure Dynamics with Forcing at the Airway Opening and Chest Wall
S.A. Ben-Haim* and G.M. Sidel
Technion, Haifa, Israel and Case Western Reserve
University, Cleveland, Ohio 44106

We have developed a mechanistic model of ventilatory dynamics which accounts for movements of the lung, rib cage, abdominal wall, and diaphragm. The applications of the model include the analysis of positive-pressure ventilation (PPV) and cardiopulmonary resuscitation (CPR). To determine optimal strategies for these therapies, we have simulated the dynamics of the ventilatory system with various forcing functions. With respect to PPV, we addressed the question "For a given tidal volume and breathing frequency, is there a pressure or flow input waveform that produces minimal airway and pleural pressures?" The intent is to deliver sufficient ventilation, but with minimal pulmonary and cardiovascular side effects. With a variety of waveforms we found that none could minimize airway and pleural pressures at the same time. With respect to CPR, we addressed the question "Can occlusion of the airway opening during chest-wall compression provide a positive effect on cardiac output by increasing intrathoracic pressure?" Both model simulations and animal experiments showed that airway occlusion during CPR could provide significant improvements.

BE6-H.3

STRUCTURAL MODEL OF THORAX AND ABDOMEN FOR RESPIRATORY MECHANICS, S.H. Loring, Department of Environmental Science and Physiology, Harvard School of Public Health, Boston, MA 02115.

Respiratory mechanics includes both pulmonary mechanics and mechanics of the "chest wall", by which we mean the mechanics of the thorax, the abdomen and the diaphragm. The geometrical complexity of the chest wall and its associated muscles of respiration makes rigorous analysis of the mechanics of the respiratory system difficult. We have used a structural model of the human rib cage and abdomen that incorporates many geometrical and functional features important to the understanding of respiratory mechanics. This structural model of the respiratory system with two degrees of freedom of motion incorporates realistic geometries and mechanical properties of intercostal and abdominal musculature and can predict the actions of respiratory muscles. The rib cage, diaphragm, abdominal wall and lungs are characterized by nonlinear stress-strain characteristics that depend on muscle activity. The positions, volumes, forces and pressures for each set of initial conditions are found by determining mechanical equilibrium by an energy equation. Many such determinations allow predictions for large displacements. The model predicts passive respiratory system behavior and the action of individual respiratory muscles that are qualitatively consistent with physiological data. (Supported by HL33909 and HL19170).

BE6-H.5

Influence of Body Position on Ribcage and Diaphragm Shapes. S. Margulies*, J. Rodarte, P. Bergsland, E. Hoffman. Mayo Foundation, Rochester, MN, 55905.

We evaluated the effect of lung (L) volume (V) and dorsoventral pleural pressure gradient ($dPpl/dx$) on the shape of the ribcage (R) and diaphragm (D). Six anesthetized dogs were scanned in a 3-D CT imaging system at TLC and FRC while prone and supine. After pneumothorax (PN) was introduced, 5 were studied supine and 1 was also studied prone. Cross-sectional areas of L, mediastinum (M), and subdiaphragmatic contents (SD) were determined from 1.6 mm transverse slices. The shapes of D and R ($R=L+SD+M$) were evaluated from the cephalo-caudal distribution of cross-sectional area ($A(z)$). In both positions, $A(z)$ of R at FRC could be modelled as

$$AFRC(z) = K[A_{TLC}(z)]$$

where $K = (V_{FRC}/V_{TLC} \text{ of } R)$. PN reduced $dPpl/dx$ to zero and thus increased the transdiaphragmatic pressure (P_{di}) gradient. At FRC PN had no effect on D shape while at TLC, the dependent portion of the D moved cephalad and the independent region moved caudal. These results are consistent with the presence of a $dPpl/dx$ in the intact dog which influences the shape of the diaphragm at TLC when the average P_{di} is small, and has little effect at FRC when average P_{di} is comparably large.

BE6-H.4

Mechanics of Compartmental Models of the Chest Wall, Theodore A. Wilson, Department of Aerospace Engineering and Mechanics, University of Minnesota, Minneapolis, Minnesota 55455 U.S.A.

The methods of mechanics require that a linear elastic system with two degrees of freedom be described by three compliances. In most of the literature, the compliance that describes the coupling between rib cage and abdomen is implicitly assumed to be zero. Deschamps et al. find that in seated subjects, the coupling compliance is small, but consistently positive, contrary to current models.

The methods also provide definitions of the effective forces exerted by respiratory muscles. These forces are proportional to the rate of change of muscle length with compartmental volume. A simple model of the geometry of the diaphragm yields predictions that are consistent with Hubmayr's data on the changes in pleural pressure and chest wall shape caused by diaphragm twitch.

Supported by National Heart, Lung, and Blood Institute Grant HL-21584.

BE6-H.6

Rib Cage Modeling from X-Ray Measurements, C.M. Kenyon*, T. Pedley, and T. Higgenbottom, Dept. of Applied Mathematics and Theoretical Physics, Cambridge University, Cambridge CB3 9EW, England.

A continuing problem in respiratory physiology is in relating measurements of the chest wall to the underlying anatomical structures. We present here an adaptive kinematic rib cage model which takes as input the positions of a small number (≈ 10) of points on the thorax measured on lateral and posterior-anterior x-rays, and then adapts mathematical representations of the bones and joints to fit. In this way the positions and shapes of the manubrium, sternum, vertebrae C7-L1, and the position of the sixth rib on each side are determined from measurements and mathematical models.

This technique relies on two hypotheses. 1) that the constraints of a functional rib cage are such that the variation in rib cage shape between individuals can be described by a small number of variables. 2) that the bones of the rib cage fit together such that they can move with only a small number of degrees of freedom.

The model has been validated using x-ray data from 12 patients before and after median sternotomy required for coronary artery bypass surgery. Errors were found to be $\pm 5\text{mm}$ and $\pm 3^\circ$ for dimensions and orientations respectively. Full size computer plots of the rib cage were compared with actual x-rays to measure the error, and also where there were discrepancies the shapes were altered interactively to examine the effect on the numerical predictions. In addition the technique showed itself to be able to detect the small change in rib cage configuration which occurs after the operation in conjunction with a decrease in the total lung capacity and residual volume (1/ and 0.5/ respectively).

BE6-I.1

Energy Dissipation in an Airway Bifurcation
A. Tsuda, B. Sivilonis, R. Kamm, and J. Fredberg,
The Biomech. Inst., Worc. Polytech. Inst., Univ.
Mass. Med. Sch., Mass. Inst. Tech., Harvard Univ.,
Massachusetts, U.S.A.

We measured energy dissipation associated with large amplitude periodic flow through airway bifurcation models. Each model consisted of a single asymmetrical bifurcation with each branch terminated into identical elastic loads. Sinusoidal oscillations were applied at the parent duct such that the upstream Reynolds number (Re) varied from 30 to 5000 and the Womersley parameter (α) from 2 to 30. Pressures were measured continuously at the parent duct and at both terminals, and instantaneous branch flow rates were calculated.

Time-averaged energy dissipation, E_v , in the bifurcation was computed from an energy budget over a control volume integrated over a cycle. We found that when flow amplitude was small (tidal volume to dead space ratio, $V_t/V_d \ll 1$), E_v could be regarded as quasi-linear and α alone was sufficient to describe the effects of unsteadiness. When flow amplitude was large ($V_t/V_d \gg 1$), the influence of free stream convection was significant and E_v became quasi-steady as α increased. The behavior of E_v suggested an analogy to steady curved tube flow. This study demonstrates that only two nondimensional parameters, α and V_t/V_d , are necessary and sufficient to describe E_v in a given geometry during sinusoidal flow. Supported by HL33009 and HL34616.

BE6-I.3

*The Expiratory Pressure-Flow
Character of the Lung*

J.M. Collins*, R.D. Kamm and A.H. Shapiro
Massachusetts Institute of Technology
Cambridge, Massachusetts

Experiments were conducted to study the pressure-flow relationship during steady expiration in a multi-generation human lung model (J. Hammersley and D. Olson). A subtraction technique was developed to allow measurement of the pressure drop across a single generation within the network. Experiments, first conducted in a planar idealized airway, covered the Reynolds numbers from 50 to 8000. Sensitivity studies were then performed to determine the influence of variations in geometry and flow distribution.

The results for a single bifurcation were then used to synthesize the pressure-flow character of a complete airway network. The numerical predictions are in close agreement with published data, and demonstrate that branching asymmetries enhance the contribution of the lower airways to the total flow resistance, particularly at low flow rates and with more viscous gases.

Supported by HL-33009

BE6-I.2

Mechanical Effects Induced by Jets in Airways. D. Isabey, Unité de Physiologie Respiratoire INSERM (U 296), Hôpital Henri Mondor, Créteil, France.

Tracheal jets have recently been shown to contribute to airway gas transport and are frequently used in different types of mechanical pulmonary ventilation such as High Frequency, Jet Ventilation or Constant Flow Ventilation (CFV). The behavior of such jets in the airway resembles that of confined jets in a tube. The latter have strong mechanical effects which have never been deeply investigated nor quantified for the respiratory system. We thus studied the mechanical effects of using a new endotracheal tube that allows gas injection in the lower trachea. Fresh gas, which flows through several thin capillaries molded into the tube wall, is injected at high velocity near the distal end of the tube, producing local air entrainment. We applied the momentum flux theorem including wall friction to this system and performed measurements in a tracheal tube. Both show that this local air entrainment mechanism created either a positive pressure gradient (as occurs during CFV) and/or an overall entrained flow through the core tube, with a predictable quadratic relationship between airway pressure and injected flow rate. Lastly we present the mechanical and physiological results obtained with this system in patients ventilated with CFV or assisted by pressure support.

BE6-I.4

Effect of Oscillatory Frequency and Inspiratory:Expiratory Ratio on Tracheal and Alveolar Pressures in a Rabbit Model, D. Winter,* SwRI, San Antonio, Texas, D. Gerstmann, A.F. Taylor, K. Nose, J.M. Fouke, R.A. deLemos, SFBR, San Antonio, Texas.

During high frequency oscillatory ventilation (HFOV) in an intubated, open-chest rabbit model, we measured pressures in the trachea and alveoli using a stainless steel tracheal monitoring tube and a low-mass pleural capsule. Ventilator pressures were also measured proximal to the 2.5 mm ET tube. Oscillatory pressure amplitude (P_{amp}) and mean airway pressure (P_{aw}) were recorded for the 3 airway locations in each animal for each of 6 randomly chosen inspiratory:expiratory (I:E) ratio (1:2, 1:1) and frequency (10, 15, 20 Hz) combinations. Nine animals were studied using a right thoracotomy to place upper lobe capsules on 4 and middle lobe capsules on 5 animals. Analysis of variance tests showed no change in tracheal or alveolar (in both lobes) P_{amp} that was related to changes in ventilator frequency or I:E ratio. There was, however, a marked increase in tracheal P_{aw} as I:E ratio was lengthened from 1:2 to 1:1. Tracheal to ventilator P_{aw} ratios increased from 0.795 ± 0.132 to 1.163 ± 0.133 (mean \pm SD) ($p=0.0001$, t-test) in the middle lobe capsule group when I:E was increased. Similarly, in the upper lobe group, tracheal to ventilator P_{aw} ratios increased from 0.731 ± 0.111 to 1.158 ± 0.265 ($p=0.0004$) as I:E increased. We speculate that higher tracheal P_{aw} at I:E 1:1 could result from unequal proximal/distal airway inspiratory-expiratory impedances, resulting in volume redistribution to the large airways. Casts of the large airways showed that the upper lobe airway branch had a much smaller radius of curvature than the middle lobe branch (approximately 3 mm vs 15 mm) and a much larger turning angle (approximately 150° vs 50°). The increased pressure drop in the upper versus the middle lobe may be a result of this geometry.

245

BE6-I.5

Theoretical Considerations of Nasal Airflow Mechanics, G.O'Neill and N.S.Tolley, University Hospital of Wales, Cardiff, U.K.

A mathematical model relating nasal airflow and pressure, using Bernoulli's equation applied to flow through the nasal valve region, has been shown to give values of nasal resistance which correlate well with those measured experimentally. It is concluded that the nasal valve is the primary location for nasal resistance and that the nasal vault contributes a negligible amount to the total trans-nasal pressure drop. Flow limitation is predicted in the model by incorporation of a term describing nasal valve stiffness. The interrelationship of the alar wing and nasal valve are demonstrated and the model is discussed in terms of aiding the understanding of normal airflow physiology and what implications this may have to nasal surgery.

BE6-I.6

AIRFLOW DYNAMICS IN THE CONDUCTING AIRWAYS OF THE LUNG: S.K. KESAVAN, AND N.P. REDDY* BIOMED. ENGR. DEPT., UNIV. OF AKRON AKRON, OHIO 44325

Three-dimensional air velocity patterns were measured in a 2:1 plexiglas model of the conducting airways of the human lung using a hot-film anemometer. A polyisobutylene solution in decalin was used as a viscoelastic simulant of tracheal mucus. Both steady and oscillatory flows were studied. Air flow rates were varied to simulate conditions varying from normal to heavy breathing. The experimental results show the skewed and complex nature of the velocity profiles as air cascades through the branches. Model geometry was found to exert a greater influence than flow Reynolds number on the velocity profiles. Results of flow visualization experiments conducted to study the interaction of a turbulent air flow with a lining of polymer mucus analog illustrate the formation of interfacial waves, and the alteration of the turbulent boundary layer. (Supported by Univ. of Akron Faculty Research Grant).

BE6-J.1

Hemodynamic Modelling of Rapid Vascular Occlusions in the Lung, J.H. Linehan*, T.A. Bromikowski, and C.A. Dawson; Marquette University, Medical College of Wisconsin, Zablocki VA Medical Center; Milwaukee, Wisconsin

Hemodynamic analyses of the information contained in the transient arterial and venous pressure curves following vascular occlusion has proved useful in attempting to understand the relationship between the structure and function of the pulmonary vascular bed. In an experimental setting wherein the lung flow is constant, rapid occlusion of the pulmonary vein for a short time or simultaneous occlusion of both the artery and vein provides quantifiable pressure data which can be interpreted using models which consider the distribution of vascular resistance versus vascular compliance. In particular, the locus of vasomotion with respect to the site of major vascular compliance, the microvasculature, is detectable. We have further shown that the pressure of the microvasculature can be readily determined from the simultaneous occlusion experiment. Recently we have explored the impact of fluid inertance on the interpretation of the arterial pressure decay curve following arterial occlusion. Since the arterial occlusion maneuver can be done in vivo by inflation of the balloon of a Swan-Ganz catheter, we have extended our models to interpret the information content of the resulting arterial pressure decay curve to provide an upper bound of the microvascular pressure.

Supported by Grant HL-19293 and the Veterans Administration.

BE6-J.2

On the Use of Arterial Density Fluctuation to Assess the Variation in the Blood Volume of the Pulmonary Capillaries, J. S. Lee* and L. P. Lee, University of Virginia, Charlottesville, Virginia, U.S.A.

When the rabbit or dog is ventilated by a respirator, we find that the gravimetric density of arterial blood has a component which fluctuates at the same frequency as the ventilation. We have hypothesized that this fluctuation is due to the presence of the Fahraeus effect in the capillary blood flow and the ventilatory induced deformation of the pulmonary capillaries.

The density fluctuation due to the ventilation and the density dilution due to the injection of a low density saline bolus into the vena cava are measured by a Density Meter. Regarding the dilution curve as the transfer function of indicator dilution in the central circulation, we use the Fourier transform of this transfer function to assess the attenuation and time delay in the transport of sinusoidal concentration through the central circulation. With this assessment and the Fahraeus effect, we determine the density fluctuation in blood leaving the pulmonary capillaries to quantify the volumetric change of the capillaries induced by the ventilation. (Supported in part by HL 36285)

BE6-J.3

Modeling the Pulmonary Input Impedance Spectrum, C. Lucas*, B. Ha, G. W. Henry, J. Ferriero and B. Wilcox, The UNC School of Medicine, Chapel Hill, North Carolina, USA.

The simple shape of the pulmonary input impedance spectrum has led to the development of models of varying complexity which mimic its salient features, including the frequency and amplitude of the first modulus minimum, characteristic impedance, and fluctuations indicative of a bed with reflections. Models are used 1) to produce realistic afterloads for the right ventricle and 2) to interpret vascular responses to system perturbations or alterations, e.g., drug infusions, structural abnormalities, or surgical interventions. Interpretation is often difficult; success depends not only on the validity of the model, but also on 1) the quality of underlying pressure and flow signals--which are difficult to obtain *in vivo* in the cardiorespiratory cycle-sensitive pulmonary artery, 2) the technique used to calculate the spectrum of a system which may be quasi-linear at best, and 3) the technique used to estimate model parameters given the calculated spectrum. The pressing need for improved methods for diagnosing pulmonary vascular impairment, particularly in infants and children, emphasizes the importance of continued development of special models which are age appropriate and which have parameters sensitive to physiological changes associated with pulmonary vascular disease. (Supported by HL35389.)

BE6-J.4

Modeling the Structure and Blood Circulation in the Lung, M. R. T. Yen and Y. C. Fung, Memphis State University, and University of California, San Diego, La Jolla, California, 92093. U.S.A.

To model blood flow one has to model the structure first. Thus one has to validate both the geometric and rheological models of arterial and venous trees, the microvasculature, and the alveoli, alveolar ducts, and airways. New data have been obtained on the collagen and elastin bundles in these structures; and used to derive theoretical values of the distensibility of capillary sheets. The theoretical values are compared with experimental values. Further, new data on the coupling between the arterioles and venules with the alveoli and ducts are obtained. These improvements are incorporated into a theory of pulmonary circulation. The validated theory is used to probe the effect of a variety of parameters on pulmonary pathophysiology. (Supported by NIH NHLBI grants HL-26647, HL-34440, and HL-07089.)

BE6-K.1

Clinical and experimental measurements of the pulmonary clearance of inhaled Tc-99m-DTPA, P Wollmer*, E Evander, B Schmekel and B Jonson, University of Lund and AB Draco, Lund, Sweden.

The transfer of water soluble substances across the alveolocapillary barrier can be studied by means of a radiolabelled tracer substance in the form of an aerosol and measurement of the pulmonary clearance of the tracer by external detection. Measurement of the pulmonary clearance of inhaled Tc-99m-DTPA is a simple and non-invasive procedure, which can be performed with standard nuclear medicine equipment. In animal experiments, we have shown that the rate of pulmonary clearance is related to the functional integrity of the surfactant system. There are probably also other rate limiting factors, e.g. the permeability of the alveolar epithelium.

In normal man, the pulmonary clearance of inhaled Tc-99m-DTPA follows a monoexponential course with a half-time of approximately 70 minutes. In smokers, the clearance curve follows a biexponential course and the abnormality is related to the smoking habits. In patients with interstitial lung disease, the pulmonary clearance of inhaled Tc-99m-DTPA also follows a biexponential course and is related to other indicators of disease activity.

This simple technique promises new insight into the pathogenesis of lung diseases and may be useful for diagnosing and monitoring lung diseases.

BE6-K.2

VENTILATION STUDIES WITH RADIO-AEROSOLS
G. Coates, M.D., McMaster University
Hamilton, Ontario, Canada, L8N 3Z5

The perfusion lung scan performed with a gamma camera and ^{99m}Tc -macro aggregated albumin (MAA) produces an image of the regional distribution of lung blood flow. The scan is sensitive to changes in regional blood flow but is not specific since both primary defects in perfusion such as pulmonary embolism and defects secondary to a regional decrease in ventilation such as asthma or chronic obstructive lung disease all can produce similar scan pattern. The ventilation scan produced with inhaled radio-gas such as ^{133}Xe was introduced to increase the specificity of the perfusion lung scan for pulmonary embolism. There are inherent difficulties in the routine use of radio-gas, many of which are overcome by using radio-aerosols. The ones most commonly used are submicronic aerosols of technetium-99m (^{99m}Tc) labelled DTPA or sulfide colloid. This paper will discuss the use of submicronic aerosols in patients with suspected pulmonary embolism and in children with a variety of conditions including asthma, inhaled foreign body and congenital lung defects.

BE6-K.3

Aerosol Dispersion Used as a Test of
Pulmonary Function,

M. McCawley, NIOSH, Morgantown, WV and
H. Abronst, West Va. Univ., Morgantown, WV, USA

The dispersion of an aerosol bolus was found to be an effective means of differentiating groups of smoking (average exposure of 20 pack-years) and non-smoking subjects ($p < 0.0001$). Their mean differences for standard respiratory function indices obtained from spirometry (FVC, FEV₁, and FEF_{25-75%}) were smaller and non-significant. These tests were also done before and after bronchodilation on subjects with a history of reactive airways. The changes detected were consistent with caliber changes in the small airways. A gamma distribution model, simulating a single mixing chamber (with incomplete mixing) in parallel with a variable by-pass fraction, was used to account for the differences seen in the various groups that were tested. This model allows a parameter to be derived for both series and parallel ventilation. Measurement of the Peclet number for the alveoli obtained in this fashion agrees with the value previously estimated by other researchers.

BE7-A.1

Qualitative Reasoning With Incomplete Knowledge in Medicine, B. J. Kuipers*, University of Texas at Austin, Austin, Texas 78712 USA.

Incomplete knowledge is a fact of life in medicine: the detailed structure of physiological mechanisms involved in a patient's disorder may be only partially understood, and many parameters of the patient state are unknown or even unmeasurable in a clinical setting. Model-based reasoning methods such as numerical simulation require specific numerical values for each model variable, and specific curves to be assumed for each functional relation, even where this level of precision is not justified by available knowledge.

Qualitative simulation allows qualitative descriptions of the possible behaviors of a mechanism to be derived from incomplete, qualitative descriptions of its structure and initial state. Where the information provided is insufficient to specify a unique behavior, the prediction is a branching tree of possible behaviors. We have recently developed several new methods to improve our QSIM algorithm: (1) application of higher-order derivatives; (2) use of a global phase-space perspective; (3) abstraction by time-scale to decompose complex mechanisms into a hierarchy of simple mechanisms; and (4) techniques for incrementally incorporating quantitative constraints into the qualitative model. The goal of this work is to permit model-based diagnostic and therapy-selection reasoning in the face of incomplete knowledge.

BE6-K.4

Imaging of Radioaerosols to Measure Mucus Flow within Lung Airways.

W. Michael Foster, VAMC-Northport & SUNY-Stony Brook, NY USA 11794.

Lung airways of humans have mucus lining that is continuously transported to the larynx from lung periphery by ciliary activity of epithelial cells of the mucosal surfaces. Mucus is replenished primarily by secretory products of cells interspersed among mucosal cells or located within submucosal glands. Mucus prevents desiccation and buffers underlying tissue from inhaled irritants; convergence of mucus to the larynx not only maintains luminal airway patency for convective flow of gases but provides deliverance from the continued presence of inhalational hazards which have deposited onto airway surfaces.

Noninvasive methodology is utilized to study mucus transport in man. Radioaerosol (Fe₂O₃ spheres labeled with ^{99m}technetium) are inhaled into the lung and subsequent clearance of insoluble spheres is measured by Anger camera as index of mucus flow. In addition to recording the collective function of all airways, this technic provides a measure of the velocity of mucus flow within central airways. Kinetics of mucus clearance can be assessed under controlled conditions and compared to experimental perturbations in healthy and diseased airways. Effects on mucus flow are described for therapeutic agents which improve conductance of lung gases, and for noxious gas, ozone, present in pollutant smog.

BE7-A.2

Simulation Methodology in the DEVS-Scheme Environment

Bernard P. Zeigler* and Tag Gon Kim*

Dept. of Electrical and
Computer Engineering

University of Arizona
Tucson, AZ., 85721

We review the concepts of knowledge representation and modelling and simulation methodology which facilitate computer exploration of alternative artificial worlds, such as self-sufficient bio-regenerative human habitats.

An object-oriented computer environment which supports such simulation studies is briefly described. A simplified example is given to demonstrate the power of the approach.

246

BE7-A.3

An AI Approach to Modeling in Biology

Alain Pavé* Laboratoire de Biométrie
Université Cl. Bernard, Lyon 1, 69622 Villeurbanne Cedex

François Rechenmann - Laboratoire ARTEMIS/INRIA
Université J. Fourier (Grenoble) - 38402 St Martin d'Hères

To construct or to choose and finally use mathematical models in Biology requires many different skills which make this approach complex. The french Group EDORA, concerned by modeling problems in biology, works in the conception and the development of new softwares to aid such modeling approaches. An AI solution was chosen, based on an Object Centered representation of knowledge. In this framework declarative and procedural knowledge can be represented and handled by an inference engine called SHIRKA. The representation, the actual structure of the knowledge base and the basic inference processes will be presented and discussed. EDORA approach illustrates the interest of AI in the software design, for the utilization by non specialists of complex tools at different levels, and also as formalization tool of knowledge. This last remark, i.e. AI as modeling framework itself, suggests that it will be complementary or even alternative to mathematical modeling when it presents drastic limitations which is often the case in biological sciences.

BE7-A.4

Qualitative Nets as Components of Brain Models, A. de Callatay, IBM A.K. Watson IEC, La Hulpe, B-1310 Belgium*

The studied qualitative nets have one-way connections with all-or-none irreversible synapses (latches). Each group of cells works as a recording content addressable memory (RCAM) storing simple production rules. RCAMs are nodes of a well-formed directed circular network system (DNPS) solving problems as a logic program interpreter. In the simulated robots, the feature extractors are sampled to produce the symbols processed in DNPS. The output symbols are the set-points of servo-mechanisms. Timing is provided by internal clocks. The invariant repetitive rules learned by experience are: *Action C changes the state from A to B*. The processing phases are: 1) the intention B is chosen, e.g. by a perceptron; 2) the DNPS finds which C can change A in B; 3) the set C of muscular commands is executed; 4) the evoked salient events enable a well-connected lattice of RCAMs; 5) the rules describing the actual episode are added into these RCAMs. Simulations have shown that learning is fast. The general system permits chunking, subgoaling, reasoning by analogy, adaptation, habituation, and parsing. DNPSs are mapped to mammalian brains, predicting how biological circuits may work, e.g. latch closure is mapped to dendritic spine resorption.

BE7-B.1

Fast Computation of Convection-Diffusion-Permeation-Consumption Algorithms for Blood-Tissue Exchanges, J. B. Bassingthwaite, J. I. S. Chan, and C. Y. Wang, Univ. Washington, Seattle, and Michigan State Univ., East Lansing*

The complexity of solving partial differential equations for capillary-tissue exchanges in multicellular organ models is ordinarily sufficiently handicapping to obviate the use of such models for standard approaches to analysis. Yet the demands for accurate parameterization are such that the simplest adequate models are of this form. The use of a Lagrangian sliding fluid element approach allows the coupling of diffusion and convection with permeation and transformation, giving computational efficiency without sacrifice of accuracy. Linear models gain further efficiency by computing eigenvalues during the initial condition segment of the program. Diffusion is handled by computing axial diffusion terms after solving for radial exchanges, in effect using local expressions rather than global matrix inversions. The results for a capillary-endothelial cell interstitium-parenchymal cell model is an approximate speed up of about 10^7 compared to the analytic solution, an expression requiring solving roots, calculating Bessel functions and double and triple convolution integrations. Speed is essential to the optimizing of the fits of such models to data for outflow dilution or for residue function data acquired by external isotope detection, as with positron tomography or emission computed tomography or reconstructive tomography in general. (Supported by NIH grant HL38736.)

BE7-B.2

*Edora Methodology for Biological Systems Modeling
Alain Pavé* Biometrics Lab. UCBL
F - 69622 Villeurbanne Cedex*

The main goal of the french EDORA project is the design of a software to aid mathematical modeling in Biology, based on AI concepts and on high level graphic capabilities. It led to the development of AI tools, particularly an inference engine SHIRKA, working on an Object-Centered representation of knowledge. A first prototype of the software enables to choose a model in a model base following different criteria, to estimate parameters from experimental data and to recognize the mathematical structure of a model (i.e. is it known in the base ?) ... A short description the software architecture and of the structure of the knowledge base give ideas for the future computer aided modeling systems. We note that the necessity of the formalization of knowledge has a positive feed-back effect on the domain of expertise itself, e.g. mathematical modeling in biology, which is at least so interesting than the software itself. Finally, we also note that formalisms and adapted reasoning processes developed on AI concepts are themselves good tools for modeling. As mathematical models, particularly in biological sciences, present important limitations, AI formalizations could be a new approach. The extension of modelling is one of the new center of interest of the EDORA group.

247

BE7-B.3

Complex Models Development
Methodology in Biomedicine,
Dietmar P. F. Möller*, Drägerwerk AG,
Medical Technology, D-2400 Lübeck, W.-Germany

Modeling, simulation and parameter estimation are of growing importance for the determination of non-measurable parameters and state variables of dynamic biomedical systems. The common problems arising from modeling and simulation in engineering and in biomedical science, especially the possibility of solving them by applying the same methods to a wide range of systems research, have improved the cooperation between these different areas. It is of importance to note that in biomedicine in general modelbuilding is an essential approach to estimate clinically important but not directly measurable system parameters and internal system states where even an essential excitation of the system, as required for efficient parameter estimation, is normally not allowed for medical reasons.

Model development is generally based on the

- a-priori knowledge of the system being modeled (system must be observable)
- experimental data consisting of measurements available from patients or from literature.

From the methodological point of view there are three types of concepts which depend on the a-priori knowledge based on the knowledge of the inputs or the knowledge of the outputs or the knowledge of the system state for the decision of the unknowns, which will be discussed in detail.

BE7-B.5

Qualitative Simulation of Biomedical Processes - An Aid in Decision Making, F.E.Cellier*, University of Arizona, Tucson, AZ 85721, U.S.A.

Biomedical and clinical processes are frequently characterized by relatively large numbers of different variables interacting with each other in a poorly understood fashion. Eg. in open heart surgery, the surgeon measures a number of body functions of his patient that he believes to be related to the current status of the patient. He would like to simulate the interactions between these variables on line to be able to forecast potential problems early on in the game. However, the equations governing these interactions are largely unknown, and there can be noticed a tremendous variability in the behavioral patterns exhibited by different patients.

This paper describes a methodology that lends itself to the modeling and simulation of such types of processes. One of the major characteristics of this methodology is the fact that the model building and model validation activities are not separated from each other, and that the obtained models are optimized for maximum forecasting power.

BE7-B.4

Simulation of Catheter-Manometer Dynamic Response

R.P. van Wijk van Brievingh⁺ and F. Pasveer,
Delft University of Technology, NL-2600 GA Delft
The Netherlands.

Blood-pressure signals from Catheter-Manometer systems are distorted by the system response. Simulation as a transmission-line in the time domain includes the non-characteristic termination by the transducer and by air-bubbles as causes of wave reflection. System parameters are: catheter compliance, fluid column inertance and flow resistance per unit of length, determining the characteristic impedance Z and the transmission factor γ which are complex functions of frequency. The discontinuities are accounted for by compliances, determining complex reflection coefficients. This model is mathematically described by two hyperbolic partial differential equations with time and position as independent variables, and appropriate initial and boundary conditions.

The equations are solved by the method of characteristics, leading to two ordinary differential equations describing the forward and backward travelling waves. Excitation with signals obtained from catheter-tip measurements shows good agreement between model and reality. The simulation may also be used for signal distortion compensation purposes.

BE7-B.6

Bond Graph based Physiological Models.

J. Lefèvre*, D. Roucou, B. Debande,
G. Ellinghaus and S. Huberty,
Louvain University, Brussels, Belgium.

Physiological models use various formalisms: energetical (electric analogs, mechanical and hydraulical networks, thermal and chemical systems) others are more simple: compartments, biochemical maps, block diagrams. We present a unified Bond Graphs approach to design separate and/or coupled models using any of these formalisms. Physical parts are thermodynamically based and phenomenological parts use a kinetic approach. Biological structures are clearly displayed and submodel compatibility is evaluated by algorithmic causality checking. A package will be presented which implements modular modeling and automatic coding of model specifications into routines suitable for simulation. Coupling of Bond graphs and AI tools for model analysis (causal qualitative analysis) will be discussed using muscle models as examples.

BE7-C.1

FRACTALS IN PHYSICAL SCIENCES,
S. H. Liu*, Oak Ridge National
Laboratory, P.O. Box X, Oak Ridge,
TN, 37831-6032

Most natural objects do not conform to Euclidean geometry, which is the backbone of modern science. As a result the study of irregular objects has eluded physical scientists until recently. The turning point occurred a decade ago when Mandelbrot published an impressive collection of evidence that nature often prefers fractal geometry instead. As new examples of fractals are being found in almost every branch of science, we are confronted with two tasks: (1) to understand the natural processes by which fractals are formed, and (2) to uncover the new physical properties resulting from fractal geometry. This lecture consists of an introduction to the basic concepts of fractal geometry, a brief discussion of modern theories of fractal growth, and examples of how well-known physical processes are modified, often beyond recognition, by the new geometry.

Research was sponsored by the Division of Material Sciences, U.S. Department of Energy under contract DE-AC05-84OR21400 with Martin Marietta Energy Systems, Inc.

BE7-C.3

BIFURCATIONS IN A MODEL OF THE PROPAGATING CARDIAC ACTION POTENTIAL. M.R. Guevara,
Department of Physiology, McGill University,
Montreal, Quebec, Canada H3G 1Y6

An ionic model of a strand of cardiac muscle is investigated. The strand is assumed to obey the one-dimensional cable equation, which is numerically integrated. The proximal end of the cable is stimulated with a periodic train of current pulses. For sufficiently high rates of stimulation, block of propagation occurs; i.e. not every stimulus produces an action potential that traverses the entire length of the cable. Various rhythms of block such as Wenchebach, reverse Wenchebach, alternating Wenchebach, Mobitz II, and alterans are seen as the stimulation frequency or some other parameter is changed. We associate the appearance of a new rhythm as a parameter is changed with a bifurcation. Each rhythm in time is associated with a specific structure in space, leading to the concept of a spatiotemporal pattern.

Supported by grants from the MRC and NSERC.

BE7-C.2

Fractal Kinetics of Ion Channels
L. S. Liebovitch, Columbia Univ. NY, 10032

Currents through individual cell membrane ion channels can be resolved by the patch clamp technique. The observed sequence of open and closed states provides information on the kinetics of the changes in conformation occurring in a single molecule. We found that the statistics of this open \rightleftharpoons closed switching is self-similar when viewed at different time scales. That is, the effective kinetic rate constant k_{eff} measured at time scale t_{eff} has the form $k_{\text{eff}} = A t_{\text{eff}}^{1-D}$ where A is the kinetic setpoint and D the fractal dimension. Such kinetics are predicted by a model where there are many conformational states of the channel with approximately the same energy minimum and where the activation energy barriers between these substates are characteristic of a slightly non-linear oscillator. Processes at different time scales are linked because the same underlying physical mechanism produces both the small energy barriers (of the fast processes) and the large energy barriers (of the slow processes).

Supported by NIH grant EY6234 and the Whitaker Foundation.

BE7-D.1

Nonlinear Dynamics and Percolation Processes in Cardiac Arrhythmias, Bo E.H. Saxberg, Daniel T. Kaplan, Joseph M. Smith, and Richard J. Cohen*, Harvard-MIT Division of Health Sciences and Technology, Cambridge, MA.

We have shown that finite element models of cardiac conduction processes can account for a wide range of disturbances of cardiac conduction processes including reentrant tachycardia and fibrillation.

We have found that spatial inhomogeneity in local electrical properties of the myocardium as well as the nature of the dynamical behavior of the local elements can play important roles in determining the electrical stability of the system. We have applied concepts from percolation theory and nonlinear dynamics to characterize the behavior of this system and to develop new techniques of identifying latent electrical instability of the heart. Some of these techniques have been successfully applied experimentally and clinically. For example, we have identified subtle *electrical alternans*, an ABAB type pattern of variation in QRS and T wave morphology of the surface ECG, to be a quantitative indicator of enhanced susceptibility to fibrillation in simulations, animal studies and human studies. *Electrical alternans* represents a period doubling behavior in this system. We are addressing the question of whether higher order periodicities regularly occur and whether fibrillation can be characterized as a 'chaotic behavior' in the framework of the theory of nonlinear dynamics.

BE7-D.2
**FRACTAL NETWORKS AS THE BASIS FOR
 HETEROGENEITY OF MYOCARDIAL BLOOD FLOW**
 J.B. Bassingthwaite*, J.H.G.M. van Beek, and R.B. King,
 University of Washington, Seattle, WA, 98195,
 and Vrije Universiteit, The Netherlands,

Local myocardial blood flows range over six-fold in the normally functioning heart in anesthetized sheep and rabbits and in awake baboons. Flow distributions have relative dispersions ($RD = SD/mean$) that closely follow a fractal relationship with respect to voxel size, the mass, m , of the pieces into which the heart is divided:

$$RD(m) = RD(m_0) \cdot (m/m_0)^{1-D}$$

where the fractal dimension D is about 1.14, and m_0 is a chosen reference voxel mass. The regression coefficients were 0.99 in sheep and baboons, and 0.98 in rabbits. The values of $RD(m_0)$ varied considerably from animal to animal; in the awake baboons the range was 0.15 to 0.30. The shapes of the distributions were relatively stable over time. A useful explanation is provided by a fractal recursive branching of the arterial tree. Purely deterministic dichotomous branching with specific asymmetry at the branch points can fit the data. So does symmetrical branching with Gaussian variation in daughter radii. Neither recursion reduces to the equation above. Two dimensional fractals appear the most suitable.

Supported by NIH grants HL19139 and HL38736.

BE7-D.3
**Fractal models of vascular beds with
 and without anastomoses.** J. Lefèvre*
 Louvain University, Brussels, Belgium.

Fractal models may be used to study blood flow in vascular beds with a functionally required uniform perfusion. Three steps are necessary: to find an approximate topology, to model spatial constraints and dimensions of vessels, to choose flow equations and implement computations. We introduce here topological approximations of large beds based on minimum square error between Horsfield countings in the model and in real samples. The method, based on an angiogenetic simple model, reproduces structural aspects (proximal topology, number of terminals, distribution of average lengths) and results in very simple computation for blood flows. Anastomoses may be introduced and their effect evaluated on very large scale models. The quality of the approximation is assessed by Monte Carlo simulations and may be increased by constructing higher order approximating beds. Examples discussed are pial and pulmonary beds.

BE7-E.1
**Parameter Estimation in a Model of the Electrical
 Activity of a Single A-V Nodal Pacemaker Cell,**
 C.R. Murphey*, J.W. Clark Jr., W.R. Giles† and
 G.V. Naccarelli‡, Rice Univ., Houston TX
 77251-1892 †Univ. of Calgary Medical School,
 Calgary, Alberta, Canada T2N 4N1, ‡Univ. of
 Texas Medical Center, Houston, TX 77225

In the past decade suction-pipette whole cell voltage clamp techniques have been used quite successfully to obtain electrophysiological data from single, isolated cardiac cells of practically any type in the mammalian heart. In this study we successfully apply a nonlinear least-squares parameter estimation technique to a model of the A-V nodal pacemaker cell and action potential data from single, isolated A-V nodal myocytes. The model is based on voltage clamp data reported from a variety of sources in the literature. It characterizes the transmembrane ionic currents, the membrane Na^+/K^+ pump, the Na^+-Ca^{2+} exchanger, changes in compartmental concentrations of Na^+ , K^+ , and Ca^{2+} , intracellular buffering of Ca^{2+} , and uptake and release of intracellular Ca^{2+} by the sarcoplasmic reticulum. The estimation technique has been used to determine a number of key physiologic parameters associated with this mathematical model, and is capable of providing a close model-generated fit to action potential data. In addition, parameter sensitivity analysis is used to determine the influence of changes in important model parameters on the action potential waveform.

BE7-E.2
CHAOTIC BEHAVIOR IN TOAD VENTRICLE. GV
 Savino, DL González and L Romanelli,
 Bioingeniería, Universidad Nacional de
 Tucumán and Centro Arg Estud Radiocom
 Compatib Electromagnética (CAERCE), cc 28
 suc 2, 4000 Tucumán, Argentina.
 Max E. Valentinuzzi*

We recorded monophasic action potentials with small suction electrodes from toad ventricles (*Bufo arenarum*) which were paced by pulses of slowly increasing frequency. Resulting time series, attractor reconstruction and spectral analysis gave a transition to disordered behavior which is compatible with Feigenbaum scenario (Physics Today, Dec 83, p 46). Subharmonic components ($f/2$, $f/4$) was systematically detected in the power spectra. The disordered solutions yielded a continuous spectrum which allowed their characterization. It has been conjectured that Feigenbaum's route can be a precursor of fibrillation in the mammalian heart. In such case, generalized ischemia due to fall in blood pressure appears as an additional complication. *Bufo arenarum* does not have a coronary system; thus, this complication is minimized. Conclusion: Cardiac syncytium presents a chaotic behavior when driven at increasing rates. CONICET and CIUNT grants.

250

BE7-E.3

3-D Simulation Model for the Electrical Activity Characteristics in the Ischemic Heart, E. Barta and S. Sideman*, Technion- Israel Institute of Technology, Haifa, 32000, Israel.

A macro-global level approach is utilized to simulate the electrical activation process in the ischemic left ventricle (LV). The propagation pathway is chosen so as to minimize the time of activation, subject to the following simplifying constraints: 1) Only 3 orthogonal directions of propagation are permitted, 2) the geometry is an ellipsoidal one, and 3) the activation potential signal is a rectangle function with 2 possible on and off values. The proposed model results in instantaneous activation maps throughout the myocardium in sequential heart beat cycles. The relatively short computing time, typical to this model, enables to investigate the formation and development of electro-pathological phenomena, the dependence of the activation characteristics on the geometry of the ischemic region, the effect characteristic signal propagation speeds, the refractory periods, the rate of "shooting" of the pacing cells and the rate of "shooting" and the location of the ectopic points. Thus, once the proper physiological conditions are defined, this model may eventually serve to evaluate the effects of various drugs on specific parameters involved in cardiac performance.

BE7-E.5

Forward problem simulation of Electrocardiographic body surface potential map using individualized torso-heart models, K.Kamiya*, K.Sakakura, A.Iwata, N.Suzumura, K.Ohta, T.Goto, K.Douniwa, K.Iwao and M.Okajima, Nagoya Inst. of Tech., Nagoya, 466, Japan

In order to interpret the variation of body surface potential map depending upon configuration of the torso and heart, a forward calculation system by the finite element method using the torso-heart model so built as to fit to each individual was developed. Electromotive force moments of the ventricles were expressed by multiple dipoles. The torso was divided into about 5,000 tetrahedron elements with intention to give smaller element size to the regions with higher current density. Such heart-torso models were built for five individuals with different body figures in height and weight. Body surface potentials were calculated using these models, bringing about body surface maps which were different from each other but matched fairly well to the actual map obtained with respective individual.

BE7-E.4

The Simulation of the Cardiac Excitation Propagation for the Analysis of Arrhythmias K.Mitsui*, N.Shibata, Y.Fukui, System Engineering, Tokyo Denki University, Saitama, 350-03 Japan

A new simulation model of the ventricular excitation propagation was established, which enables the analysis of the mechanism of the cardiac arrhythmias. The ventricular model consists of 361 cell units, formed as two dimensional 19 x 19 cells. Each cell unit has three phases of the activation cycles represented by depolarized, refractory, and non-refractory periods. The simulation analysis is for the case that the strong electrical energy is introduced for the induction of arrhythmias.

As a simulation results, re-entrant pattern of the cardiac conduction propagation was observed, when refractoriness was prolonged in a specific area of the model, and the specific timing of the coupling interval of the shock was used. This results was compatible with the experimental results previously.

BE7-E.6

On the Resolution Power of the Inverse ECG Solution Method, T. Furukawa*, T. Aoki and S. Hara, Institute of Medical Electronics, Faculty of Medicine, University of Tokyo, 7-3-1 Hongo, Bunkyo-ku, Tokyo 113, Japan.

As an easily understandable example of the application of inverse solution in clinical diagnosis, a method to estimate the epicardial potential distribution through an inverse solution process using the source data obtained from body surface potential measurements is presented. The inverse solution is based on the boundary element method.

The resolution power of this method was carefully investigated with animal experiments in which two foci of myocardial injury were made on the ventricular anterior wall using a specially designed freezing device, and the results of the inverse solution were compared to those actually measured. The resolution power was estimated to be 3.5 in the animal experiments; however, it was higher in the computer simulations (2 cm).

In another experiment, the freezing injury was made on the endocardial myocardium. In this experiment, the resolution power was much lower due to the masking effect of the myocardium. However, in all cases, the centers of the foci were exactly estimated.

BE7-F.1

Measurement and Modeling of Virtual Cathode Effects in Cardiac Muscle, J.P. Wikswo, Jr.*, J.P. Barach, W.A. Altemeier, and D.M. Roden, Vanderbilt University, Nashville, TN 37235 USA

When cardiac tissue is stimulated with a small cathodal electrode, an activation wavefront propagates away from the stimulus site. At threshold, the size of the region initially depolarized by the stimulus is a minimum and is known as the liminal length. As the stimulus strength is increased, the initially-depolarized region enlarges. Since propagation begins at the edge of this region, rather than at the electrode, this region is termed the virtual cathode (VC). Measurements of the arrival time of the wavefront at multiple electrodes can be used both to determine the conduction velocity and to estimate the size of the VC. A 10 mA, 0.5 ms stimulus pulse applied to a 250 μ m epicardial electrode will produce a VC ranging from 2 to 4 mm, depending upon fiber direction and tissue excitability. We have used a two-dimensional electrode array on the *in vivo* canine heart to study the virtual cathode effect and to determine how activation propagates away from the virtual cathode. Certain features of the data can be explained using a one-dimensional, non-linear, core conductor model for cardiac propagation, while other features appear to require a two- or three-dimensional anisotropic bidomain model. The existence of the virtual cathode effect may have significance in cardiac pacing, cardiac defibrillation, and the stability of reentrant arrhythmias.

BE7-F.3

STATISTICAL DERIVATION OF AIMED ELECTROCARDIOGRAPHIC LEADS, Gy. Kozmann, R.L. Lux and L.S. Green, Cardiovascular Research and Training Institute, University of Utah, Salt Lake City, UT 84112

A statistical method is suggested to derive "aimed leads" (AL) -linear combinations of unipolar leads-which respond to cardiac sources in localized regions of the heart, while suppressing the contributions of other regions. Body surface potential distributions (BSPD) of a representative group of normal (NOR) subjects and that of the patients with localized myocardial infarction (MI) were used. The AL derivation is based on the determination of that linear combination of the BSPDs which maximize the separation between the NOR and the MI group considered according to a mean square criterion. By systematically comparing the NOR group with MI groups of different location, ALs can be derived for anatomical regions of the myocardium. The same learning sets allow the estimation of Bayes-type decision schemes to give regional information about the strength of electric sources. The examples presented were computed by the use of 40 each NOR and anterior and inferior MI patients. The computations were carried out in the Karhunen-Loeve domain representation of BSPDs and the results were transformed back into the measurement domain.

BE7-F.2

Simulation of the effects of myocardial anisotropy on electrocardiographic potentials, R.M. Gulrajani* and M. Lorange, Institute of Biomedical Engineering, University of Montreal, Montreal, Canada.

A heart model that incorporates myocardial anisotropy with a reduced conductivity in the endocardium-to-epicardium direction is described. The effects of this anisotropy on the resultant dipoles of the model, and on the subsequently-computed vectorcardiogram, electrocardiogram and body surface potential map are considered. The heart dipoles are oriented oblique to the outwardly-propagating excitation fronts, with a consequent narrowing of the simulated vectorcardiographic loops. During late depolarization, when the excitation fronts are partially tangential to the intraventricular blood masses, the oblique dipoles are even more so. Introduction of these high-conductivity blood masses results in Brody-effect decreases in the second peak of the scalar vectorcardiogram, and in diminished S waves in the electrocardiogram, as has been experimentally observed. Finally, the simulated body surface potential maps support, on a qualitative basis, the hypothesis of a partial cancellation of myocardial anisotropy and intraventricular blood mass effects on surface potentials.

BE7-F.4

Reliable Detection of Myocardial Ischemia by Modified ST/HR-analysis, H. Sievänen*, L. Karhumäki†, I. Vuori‡, J. Malmivuo, Biomedical Engineering Laboratory, Tampere University of Technology, SF-33101, Tampere, Finland, †Kanta-Häme Central Hospital, Hämeenlinna, Finland, ‡UKK Institute for Health Promotion Research, Tampere, Finland.

The maximum ST/HR-slope analysis has been shown to improve the reliability of the exercise ECG in detection of the coronary artery disease (CAD). However the statistically significant slope is not always calculable, which limits the clinical applicability of the test. A supplementary slope based on the two last measured ST-segment levels is comparable to the statistically significant slope as an accurate indicator of CAD. As for the ECG leads required for optimal ST/HR-analysis chest leads V_4 and V_5 are the most sensitive to detect the ischemic response regardless of the site of the perfusion defect. Furthermore, to provide an all-inclusive detection of CAD leads II and aVL are incorporated to the analysis. This lead system guarantees the appearance of the indicative slope ($>1.3\mu\text{V}/\text{bpm}$) practically in all ischemic cases. The performance of our method in detecting the underlying ischemia was 97.5% within our patient material (40 patients with various MIs).

BE7-F.5

Simulation of electrocardiogram (EKG) by a finite state automat. F. Prieto. Universidad Autonoma Metropolitana Iztapalapa. 09340, Mexico, D.F.

A computer program is used to simulate the genesis of the EKG by means of an array of cells each of which can be in one or three possible electrical states, i.e. resting, active or refractory, and change state according to certain rules (order of change, conduction of action potential) and parameters (duration of each state). The shape of the array and the number of cells in it can be designed by the user, arrays may be stored in or read from disk. Most parameters are assigned according to cell location but may be changed if the user so wishes. Three frontal plane EKG leads may be chosen for display. A dipole is formed wherever a cell in the "active" state is an immediate neighbour of a cell in some other state. Each individual dipole contributes to the potential at each "electrode" according to the "square of the distance" rule and simple addition of effects. Interesting experiments and demonstrations are made possible by run time parameter changes.

BE7-G.1

Identification of Multiparametric Signals in Time Domain, C. Druzgalski*, California State University, Long Beach, Ca..90840, USA

Characteristic patterns of respiratory airflow and corresponding respiratory sounds with their peculiar spectral composition reflect conditions of pulmonary ventilation. These combined signals are used to develop partly linear regression models. Specifically, synthesized models, ACF and PACF patterns and their relations with frequency analysis as well as dynamic interrelationships between time series provide improved analysis of acoustical signals and their correlation with underlying patterns of respiratory airflow. In particular, the implementation of these concepts of computerized rather than visual model determination on a PC based system enhances on-line analysis of these signals.

In order to accomplish this time domain characterization of signals, an analysis based upon the classification of the ARIMA (p,d,q) models which specify autoregressive and moving average factors with a corresponding degree of stationarity is conducted. Obtained patterns of autocorrelation functions (ACF), and partial autocorrelation functions (PACF) are automatically compared with the theoretical patterns of these functions. Spectral signatures and corresponding ARIMA models provide supplementary characterization of various conditions of ventilation.

BE7-F.6

Enhanced Methods for ECG Signal Averaging Applied to Detection of Ventricular Late Potentials. R. Jané, P. Caminal**, J.M. Domínguez**. *Institut de Cibernetica, Diagonal 647, 08028 Barcelona, Spain. **Hospital Sta. Creu i S. Pau.

The purpose of this study is to obtain the ventricular late activity from the surface ECG. Signal averaging of the High Amplification ECG is the technique used to recover these micropotentials. In this work, the signal is measured by means of a two-channel electrocardiographic system: a low-gain amplifier for the reference ECG acquisition and an isolated low-noise high-gain amplifier for the late potentials obtention. The selected leads are a standard bipolar limb lead for reference and a special bipolar precordial lead for a high amplification. The detection of the small high-frequency potentials after the QRS complex is limited by inaccuracy in the beat synchronization. Recently, some papers have been published about the incidence of the alignment errors in signal averaging. Probably, the low prognostic accuracy reported is due to these technical problems. In order to obtain useful results several synchronism methods have been used in the present work, including double level estimation and matched filter estimation. Results obtained by signal averaging of the ECG from patients with distinct cardiac disease (myocardial infarction, ventricular tachycardia) are presented. A comparative analysis of the different temporal alignment methods has been performed. The incidence of the bipolar precordial lead position and the selected bandwidth has also been evaluated.

BE7-G.2

A Parametric Approach for the Analysis of Membrane Current Fluctuations, K. Yana*, Hosei University, Koganei City, Tokyo 184 Japan, H. Mino, Juntendo University, Hongo, Tokyo 113 Japan.

Membrane current fluctuations have been analyzed to reveal the kinetic properties of single ion channels at biological membranes. The power spectrum pattern is associated with kinetic properties of the single ion channel. Therefore, the accurate estimation of the power spectrum has been a crucial task in the analysis. Discrete Fourier Transform (DFT) method has been conventionally used for the estimation. However, the parametric method would be more efficient when parametric autoregressive (AR) or autoregressive moving average (ARMA) models are to be held for the phenomena. We would like to note that the membrane current fluctuations could be modeled as (n-1,n-2) ARMA model, where 'n' is the number of kinetic states of the single ion channel. Since ARMA parameters are explicitly associated with kinetic properties, we could estimate them by the ARMA parameters. Computer simulation revealed the parametric method requires less than 25% record length to achieve the same estimation accuracy with the conventional DFT method. The proposed method would be an alternative method for the analysis of membrane current fluctuations.

BE7-G.3

An Adaptive Mechanism for the Regulation of Blood Glucose, E.A. Woodruff* and R.B. Northrop, University of Connecticut, Storrs, Connecticut.

The purpose of this research is the closed-loop regulation of the blood glucose concentration (BGC) in a Type-1 diabetic when sparse measurements of the BGC are available. A model reference technique is implemented to provide an estimate of the BGC. Whenever a BGC measurement is not available the BGC estimate is used in the controller realization.

After developing the model reference off-line, a computer simulation is realized for the closed-loop regulation of the BGC in a Type-1 diabetic. An on-line parameter estimation scheme is implemented to update the parameters of the model reference during the closed-loop simulation. These parameter estimates can be used to adjust some of the controller parameters to enhance the robustness of the controller.

Since a linear model reference was evolved off-line from a complex, nonlinear glucose-insulin plant, a Kalman filter is utilized as the on-line parameter estimation scheme to update the parameters of the model reference. The Kalman filter is used, since this method is excellent in dealing with the transient properties of the parameters when there is a short data record. In addition, UD factorization algorithms are implemented to ensure that the covariance matrix remains positive semi-definite during closed-loop operation.

BE7-G.5

COMPARTMENT MODEL ANALYSIS OF CREATINE KINETICS IN MAN.

H. Thierens(1)*, J. Delanghe(2), J. Seuntjens(1), M. De Buyzere(2) and O. Segaert(1), Phys. Lab. (1) Clin. Chem. Lab. (2), Faculty of Medicine, Rijksuniversiteit Gent, Ghent, Belgium.

Important transient rises in serum and urine creatine concentrations are observed after myocardial infarction and damage to skeletal muscle. As creatine is released by the damaged cells within a few hours following injury, enhanced levels in serum and urine are indications for an early diagnosis of a myocardial infarction in patients.

A compartment model is developed to describe the creatine concentration in serum and urine as a function of time following an infarction or muscle injury. In the model the damaged tissue, the plasma pool, the skeletal muscle tissue and the liver are considered as different compartments. The values of the parameters describing the kinetics between these compartments are derived from basic data on the creatine metabolism. The creatine concentrations in serum and urine are obtained by numerical integration of the differential equations resulting from the model using the Runge-Kutta approximation method.

Effects of variation in total amount liberated by the injury, sex, age (renal clearance size) and body weight are investigated. The results of the simulation are compared with clinical data.

BE7-G.4

Fast Algorithm of Prony's Method and Application to Physiological System Analysis, L. Wang, N. Xu, F.S. Yang*, Tsinghua University, Beijing, P.R.C.

From physiological point of view, it is often an adequate assumption that many biomedical signals are composed of complex exponentials with various time delay. Prony's method can be used for the decomposition. The problem is that the conventional algorithms are noise sensitive and time consuming. A method based on an extension of DFT is proposed. It operates much faster than the conventional methods and performs fairly well with respect to noise. Applications to compartment analysis and to evoked potential and Doppler blood flow signal analysis will be presented.

BE7-G.6

The Analysis Of Multiexponential Curves By Padé Approximants And Size Identifiability Of Compartmental Models Z. Bajzer*, A. Myers and F.G. Prendergast, Dept. of Biochemistry and Molecular Biology, Mayo Foundation, Rochester, Minnesota 55905

A common problem in mathematical modeling of dynamical biological systems is the analysis of curves described by multiexponential functions. The method based on Laplace transform and Padé approximants [Nature, 326(1987)169] offers the possibility to detect the number of components in multiexponential curves, as well as their parameters. We present two generalizations of this method: i) when the curve is the convolution of multiexponential function and experimentally known instrumental impulse response function; ii) when the signal is not time dependent but is given as Fourier transform in the frequency domain. Examples are provided by the analysis of tryptophan fluorescence in proteins. The Padé-Laplace method is discussed as a tool for determining the number of compartments in compartmental models. In addition to formal developments, we perform simulation studies, especially with respect to the efficiency of the method when the noise level in output functions is varied.

BE7-H.1

Vowel Recognition using an Auditory Model,
T.S.Yoon*, J.H.Lee, S.H.Park, Yonsei Univ.,
S.H.Beack, Myongji Univ., Seoul, Korea.

The characteristics of human peripheral auditory system are applied to Korean vowel recognition. The model of auditory system consists of three parts ; the band pass filter bank with delay tabs, which represents the resonance of basilar membrane, the interaction part between filter bank and the cochlear fluid, and mechanical-neural transduction of haircell part. The output of this model takes the shape of auditory nerve firing probability as a function of time. The firing pattern of each nerve is synchronized to the input signal and only the frequency components corresponding to CF are intensified. Consequently, the amplitudes of formant frequencies are manifested in running spectra, which arrange nerve firing pattern as their CF's. In addition, pitch of the vowel can be estimated from the maxima of low CF's firing patterns. Therefore, the output of the model represents the major feature of the vowel. Speaker-independent recognition test using these features shows the accuracy of 96 % for closed, and 96.47 % for open test.

BE7-H.3

Analysis of Feedback Systems in the Body
With Use of Autoregressive Modelling.
Takao Wada*, Kidney Center, School of
Medicine, Keio University, Tokyo, Japan

Autoregressive modelling has been applied for feedback regulation of various mechanical systems. Recently, we demonstrated the usefulness of Akaike's approach of autoregressive modelling for analyzing immunologic systems in the body. In the present study, I tried to confirm its usefulness for analyzing other systems, such as endocrinologic and metabolic systems.

Time series studies were done on 6 albino rabbits with or without administration of angiotensin converting enzyme inhibitors. Although the raw blood chemistry data showed seemingly bizarre fluctuations, the analysis with Akaike's method enabled to describe the impulse response curve proper to each system under study. Also, Akaike's relative power contribution, which was calculated from the matrix of autoregressive coefficients and the covariance matrix of the white noise term, was found helpful to disclose the cause-and-effect relationship between the variables composing the system. Thus the analytical results clearly demonstrated that the well known discrepancy between the in vivo effects and in vitro effects of angiotensin converting enzyme inhibitors is due to the existence of multiple feedback pathways in the body.

BE7-H.2

Beat-by-Beat Analysis of Cardiovascular Control with Multivariate Autoregressive Modeling, S.Kalli, V.Turjanmaa, S.Majahalme, M.Sydänmaa, V.-M. Häggman. Technical Research Centre of Finland and Tampere University Central Hospital. Tampere, Finland

Spontaneous oscillations and fluctuations occur in blood pressure and heart rate are related to the cardiovascular control. This paper proposes to study them with multivariate autoregressive modeling technique, which describes each signal as a linear combination of the past values of its own and the other signals. The model is used to determine the interaction between the variables. The method was applied to the analysis of blood pressure and heart rate interactions in normotensive and borderline hypertensive subjects in supine and standing positions. The interaction increased significantly in standing position in both subject groups, but no significant difference could be found between the groups.

The method proved to be a feasible way in studying complicated interactions between heart rate and blood pressure.

BE7-H.4

Simulation using SPICE2 of an Enzyme System which captures Energy from an Oscillating Electric Field. D. C. Mikulecky, Department of Physiology and Biomedical Engineering Program, Medical College of Virginia Commonwealth University, Richmond, VA 23298-0551.

Austumian et al. (P.N.A.S. 84:434-438, 1987) have introduced a model for an enzyme system which captures energy from an oscillating electric field. The energy from the field drives the reaction in the direction of ATP synthesis. Using the circuit simulation program SPICE2 as a general-purpose simulator, the system is easily simulated. Furthermore, a D.C. transfer curve can be generated by SPICE2 which clearly demonstrates that all the steady states available to the system result in ATP breakdown. ATP synthesis occurs only when the system is forced to oscillate. SPICE2 is also used to generate the frequency dependence of certain aspects of the system. The use of SPICE2 as a general-purpose simulator will be discussed. Also, the modeling of chemical reactions in membranes which depend on electric-fields across the membranes will be explained. (Invited presentation).

BE7-H.5

Characterization of Nonlinear Biological Systems by Wiener and Volterra Kernels, Naohiro Ishii*, Katsumi Yoshine, Haiwen Chen, Nagoya Institute of Technology, Showa-ku, Nagoya 466, Japan.

Many nonlinear characteristics are found in the biological systems. More often, nonlinear biological systems are available only as "black boxes". Then we can only obtain information about systems inner structure by the relation between systems input and output. By using the input and output, we characterize the nonlinear structure of the biological systems by applying the Wiener's G-functional expansion and Volterra series. In biological systems, the linear and nonlinear subsystems are interconnected in cascade or with feedback. Then, conditions of the nonlinear biological systems are derived, particularly the linear and nonlinear subsystems in cascade and with feedback loops, by using the Wiener's and Volterra's kernels words. These conditions are constructed as algorithms of characterization of black boxes. Then we applied these algorithms to the computer simulated black boxes and retinal neurons in the visual system, by using input and output measurements.

BE8-A.2

Blood Purification for Chronic Renal Failure, Prakash R. Keshaviah*, Ph.D., Regional Kidney Disease Program, Minneapolis, Minnesota

Significant developments have taken place in blood purification techniques for end state renal failure over the last three decades. The population on chronic dialysis has grown enormously with over 90,000 patients currently on dialysis. In addition to hemodialysis and peritoneal dialysis, therapies such as hemofiltration, hemodiafiltration and high flux dialysis have been developed. These therapies have become much more efficient and treatment times have decreased from 36 hrs/wk to between 6 and 9 hrs/wk. Equipment used for blood purification in renal failure has become much more sophisticated with incorporation of microprocessor technology and other innovations. Quantitative modeling approaches such as urea kinetics, heparin kinetics and kinetics of vascular refilling are being used more extensively. In spite of the population on dialysis being older and having more co-morbid conditions, significant improvements in morbidity and mortality have occurred. The correction of the anemia of renal failure by human erythropoietin along with reductions in treatment time and symptoms during dialysis are expected to contribute to the improved well-being and rehabilitation of the patient with chronic renal failure.

BE8-A.1

DEVELOPMENTS IN BLOOD OXYGENATION
Peter D. Richardson*
Division of Engineering and Biology and Medicine
Brown University, Providence, RI 02912

Blood oxygenation science, technology and application have passed through several stages. The science has focussed on understanding the principles of transport in the convective flow setting of many different geometrics, and on the avoidance of excessive protein deposition and thrombus formation on surfaces. Flow in curved channels has attracted much attention because of increases in transport that are possible. The effects of blood pulsation superimposed on a steady mean flow over membranes have been investigated in many flow passage shapes. Passages which are not flat or straight, and which have ridges or curvature instead, give improved transport rates. The ideal situation where anticoagulation begins at entry into an extracorporeal circuit and ends when blood emerges from it has not yet been attained. Technology has concentrated on materials, especially membranes, and construction methods, and much attention has been given to detail in circuits and monitoring capabilities. The failure to demonstrate significant clinical benefits in the extracorporeal membrane oxygenation trials (ECMO) has been followed by questioning of the benefit of vigorous respiratory therapy being applied simultaneously. Application developments have been centered especially on seeking improved concurrent treatment modalities for the natural lungs when support during acute respiratory distress (ARDS) is provided. There is encouraging progress.

BE8-A.3

Augmentation of Detoxification by Hemoperfusion, B. Brian*, W. Dorson, V. Pizziconi, Arizona State University, Tempe, AZ 85287.

Hemoperfusion is an effective therapy for the removal of soluble toxins up to the column breakthrough limit. Many of the most dangerous substances are protein bound and the removal using adsorption media, such as coated activated carbon (CAC), is limited by the inability of the bound toxin to diffuse and adsorb within the adsorbent matrix. However, the removal can be significantly augmented by the addition of a biocompatible unbinding agent (solutizer) proximal to the column entrance. The action of the solutizer is to increase the unbound fraction of toxin available for intraparticle diffusion and subsequent adsorption. This concept has been proven for numerous drugs of abuse, cholesterol, and bilirubin. A unique combination of a pore diffusion adsorption model and a simplified protein binding model is used to predict the solutizer and toxin dynamics within a CAC column, a priori, with parameter estimation from simplified experiments.

BE8-A.4

Solute Transport in a Hybrid Bio-Artificial Pancreas,
M.R. Pillarella *, A.L. Zydney, Department of Chemical
Engineering, University of Delaware, Newark, Delaware

Many of the long-term complications associated with the current treatment of diabetes by insulin injections have been linked to the lack of physiologic glucose and insulin control. Recent studies have demonstrated the potential of the hybrid bio-artificial pancreas in controlling blood glucose concentration, but the insulin response to a glucose stimulation remains unacceptably slow.

We have developed a detailed theoretical model for solute (glucose and insulin) transport in a hollow fiber membrane bio-artificial pancreas. The model explicitly accounts for convective transport arising from Starling flow in the device, including the effects of protein and red cell polarization on the flow patterns. Also included is the reduction in solute diffusivity in the porous membrane as well as the enhancement of solute transport in the lumen arising from shear-induced red cell migrations.

Model predictions agree well with *in vitro* data taken in Amicon hollow fiber cartridges (30,000 MW cutoff). Results indicate that increasing convective transport significantly improves the insulin response. The model provides a fundamental understanding of the important phenomena governing solute transport and can thus be used in the design of improved clinical devices.

BE8-B.2

Membranes for Plasma Fractionation,
P.S. Malchesky, M. Zborowski, and Y. Nosè,
Department of Artificial Organs, Cleveland
Clinic Foundation, Cleveland, Ohio

Advances in the extracorporeal on-line treatment of blood for therapeutics have made it an effective technique in clinical applications. Further development to increase its cost effectiveness and simplicity of operation is required. Membrane separation technology is ideally suited to meet these needs. Membrane fractionation of plasma has been studied for the selective removal of macromolecules from plasma. Solute selectivity and removal amounts have been shown to be strongly related to the choice of the membrane and the temperature of operation. Operation in the cold (cryofiltration) is particularly effective in the removal of solutes forming microaggregates at below physiologic temperature such as cryoaggregatable proteins (as cryoglobulins and immune complexes) and very large macromolecules. Operation at above physiologic temperature (thermofiltration) is more effective in lipoprotein fractionation of the low and very low density lipoproteins from the high density lipoproteins. Clinical studies have shown that these techniques are easy to perform and safe to use. In addition, expensive plasma replacement products are not required making membrane plasma fractionation a preferred alternative to plasma exchange.

BE8-B.1

Renal epithelial cells grown on permeable membranes as a potential ultrafiltration processor, P. Aebischer,* T.K. Ip, Brown University, Providence, RI 02912, USA

Dialysis has dramatically changed the prognosis of renal failure, yet it remains burdened by considerable morbidity because of the non-physiologic manner in which it performs some of the most critical renal functions. The combination of an ultrafiltration device with exchangers that actively transport solutes may lead to a device that could purify blood in a more physiologic manner. We are presently studying the transport capacity of the exchangers. Our approach consists of growing functional kidney epithelial cells in a tight monolayer on permeable membranes. The cell lines LLC-PK1, a proximal tubule-like cell and MDCK, a distal tubule-like cell, can be grown to confluence on nitrocellulose, cellulose, polyacrylonitrile and polysulfone either in hollow fibers or on flat sheet permeable membranes. Attachment factors must be used in order to obtain this coverage. Dual label tracer studies reveal that inulin and glucose move across all unseeded membranes with similar rates in either direction. LLC-PK1 cell seeded membranes are impermeable to inulin but demonstrate a net apical to basolateral glucose flux. Depending on the membrane used this glucose flux varies significantly. The effects of attachment factors, substrate and cell types on the mass transport capacity of the seeded membrane are under study. We conclude that renal epithelial cells can control the permeability of a membrane to various solutes, thus opening the way to the development of a biologically controlled ultrafiltration processor.

BE8-B.3

EXTRACORPOREAL IMMUNOADSORPTION

George Buffaloe*, Ph.D, COBE Laboratories, Inc.
1201 Oak St.
Lakewood, Colorado 80215-4407

Extracorporeal immunoadsorption (EI) is defined as the use of immobilized immunologic reagents for the treatment of blood outside of the body, for therapeutic purposes. After many years of laboratory and clinical studies, EI is emerging as a therapeutic modality that today can be applied to a number of disorders.

Recent advances in fabrication engineering and biotechnology are being applied to create new systems. There are certain core criteria that must be met in the development of EI systems which include materials biocompatibility, flow/pressure/volume parameters, and circuit design. Systems can be designed to treat whole blood, plasma, or cellular fractions. Because of the highly selective nature of EI, a major impediment to the application of this technology to treat current medical problems, is lack of definition of the etiology of a significant number of disorders to which EI might be applied. Thus, in the near term, EI will likely play a role in the elucidation of disease mechanisms, and in the future, EI has the potential of becoming an effective form of therapy.

BE8-B.4

Critical Look at Controlled Studies in Plasma Exchange, U. R. Shettigar,*
Department of Surgery, Building 535,
University of Utah, Salt Lake City, 84112,
USA.

This study makes an attempt to explain poor results of controlled trials in plasma exchange (PE) and better results of uncontrolled trials reported in the literature. This is done by looking at different treatment variables, namely: frequency and length of treatment, volume and type of plasma exchanged, early or late institution of PE and suppression of protein rebound phenomena. Controlled trials of PE have been reported in Chronic Progressive Multiple Sclerosis (MS), Rheumatoid Arthritis (RA) and Acute Vascular Rejection (AVR).

Outcome of PE appears to be influenced by the above treatment variables. Regarding MS and RA, the controlled studies, except one, performed only a few PE treatments as compared to the longer and more frequent uncontrolled studies. Such short studies may give erroneous conclusions.

BE8-C.2

Effects of Flow on White Blood Cell Adhesion, Aggregation and Arachidonic Acid Metabolism, L. V. McIntire*, M. B. Lawrence, Biomedical Engineering Laboratory, Rice University, Houston, Texas, 77251, USA.

The effects of flow on the adhesion of leukocytes to endothelial monolayers and biomaterial surfaces was investigated using a parallel plate flow chamber. In the wall shear stress range seen in venules, the dependence of adhesion on flow is extremely strong, leading to little adhesion at wall stresses above 4 dynes/cm², even on IL-1 activated endothelium. In addition, using concentric cylinder viscometer, the effect of stress on leukocyte arachidonic acid metabolism and aggregation was determined. There is an important role of platelets in determining the metabolites formed by stressed leukocytes and the aggregation kinetics. PMN leukocytes produce mainly 5-HETE when stressed in purified suspensions, but produce leukotriene B₄ when stressed in the presence of platelets.

BE8-C.1

COMPLEMENT ACTIVATION BY BIOMATERIALS,
Richard Johnson and Kenneth Burhop.

Since the pioneering work of Craddock et al (New Eng. J. Med. 296, 769 (1977) implicated complement activation as the probable cause of granulocytopenia during hemodialysis, there has been a growing awareness of the role of complement in the analysis of device performance. This presentation will review studies of complement activation by various materials employed in clinical settings, in animal model studies and in *in vitro* experiments. Based on these studies several approaches have been identified to fabricate materials that display a diminished capacity to activate complement. Factors believed to be important in this regard include surface nucleophilicity and the presence of negatively charged groups that influence the binding of C3a and C5a anaphylatoxins. In addition, surface chemistries that influence the involvement of control proteins (Factors H and I) have been found to affect the complement activating potential of a biomaterial. Analysis of materials currently employed in hemodialysis illustrates the importance of Factor H in limiting the extent of activation and suggests that materials which facilitate involvement of this protein will display improved biocompatibility.

BE8-C.3

CONTINUOUS MONITORING OF PLATELET ACTIVATION REACTIONS IN A CONTROLLED SHEAR FIELD. T. D. Giorgio and J. D. Hellums; Biomedical Engineering Laboratory, Rice University, Houston, TX 77251, USA.

A rotational viscometer has been fitted to permit monitoring of: (1) light transmission as an indicator of platelet aggregation, (2) light emission as an indicator of release, and (3) fluorescence to indicate intracellular calcium ion concentration.

Results show that the shear stress intensity influences both the extent of platelet aggregation and the size distribution of the formed aggregates.

Intracellular calcium ion concentration increases only at moderate and high shear stresses. Platelet aggregation which occurs in response to low dosages of added ADP and/or low intensity shear stress is reversible and is not accompanied by a rise in intracellular calcium ion concentration.

Platelet release increases with shear stress. Addition of ADP accelerates the release in a concentration-dependent way which is also potentiated by increased shear stress intensity. Continuous monitoring of release makes it possible to estimate platelet surface concentrations of released chemicals. The platelet surface concentrations correlate well with expected rates and extents of aggregation.

BE8-C.4

Influence of Surface Chemistry on Biological Interactions at Polymeric Interfaces,

A.S. Hoffman, Center for Bioengineering, FL-20,
University of Washington, Seattle, WA 98195

When polymeric biomaterials are exposed to a biologic environment, it is generally agreed that events begin with adsorption of a layer of proteins. The proteins in this layer can be displaced and/or biologically, chemically or physio-chemically modified during the proceeding seconds to minutes. Thus, the adsorbed proteins can change in relative abundance, organization and antigenicity. Enzymatic reactions can also occur at the interface. It is this protein layer which mediates subsequent cellular interactions, such as the inflammatory response or thrombosis, as well as embolization. The surface composition of the polymer substrate has a significant influence on this sequence of events. There have been many different approaches taken to modify the surface composition to make it more or less responsive to the biologic environment. For example, surfaces have been modified by radiation grafting or plasma gas discharge treatments to deposit new surface compositions, which are sometimes later modified by attachment of biologically active agents such as anti-thrombogenic agents. Surfaces have also been modified by adding surface active agents to the polymer, which accumulate at the surface during the formation process. Surfaces have also been modified by direct chemical modification of the original material.

In this paper, I will briefly review the influence of such treatments on biologic interactions, and then I will present our own recent results on a rather surprising and exciting effect of surface treatment on such interactions.

BE8-D.2

Color Doppler Studies of Normal Mitral Valves
M. Jones*, E.E. Eidbo and R.E. Clark, National Heart, Lung and Blood Institute, Bethesda, MD

Transthoracic color-encoded Doppler (Aloka SSD-880 system) studies were performed upon the native mitral valves (MV) of 20 sheep. Heart rates were varied between 60-120 and cardiac outputs between 60-120 ml/min/kg. Studies were performed in real time and with electrocardiographic gating at 10 ms intervals. During early diastole, aortic closing volumes and forward displacement fronts of blood at 20-40cm/s, lasted 10-40 ms prior to MV opening. At the onset of passive left ventricular (LV) filling, the MV began to open, blood flow accelerated, becoming mildly turbulent with regions of vortex shedding behind the MV leaflets. By mid diastole, the leaflets were widely open and broad, laminar profiles (velocities < 60 cm/s) extended to the LV apex; flow occupied 100% of the MV orifice. Thereafter, blood displaced from the LV apex appeared as regions of flow reversal along the LV free wall and septum producing partial closure of the MV. After atrial systole, LV inflow again accelerated (often > 60 cm/s) and the MV again opened. In late diastole, flow reversals produced by displacement caused near closure of the MV prior to the onset of LV systole; thus the MV had a minimum closing volume, lasting only 10-20 ms. During isovolumic systole, the MV leaflets shuddered with turbulent velocities adjacent to them. These observations may be compared to flow disturbances caused by prosthetic cardiac valves and do have implications regarding future valve designs.

BE8-D.1

DYNAMIC VISUALIZATION OF VELOCITY PROFILES IN THE ASCENDING AORTA IN HUMANS.
P.K. Paulsen*, J.M. Hasenkam, O. Albrechtsen, Department T, Aarhus University Hospital, 8200 Aarhus N, Denmark.

As late valve related complications such as thromboembolism and hemolysis are thought to be caused by hemodynamic disturbances, the present paper focused on the study of these downstream of normal aortic valves (n=8, prior to coronary bypass surgery) and St. Jude Medical (n=4) and Starr-Edwards Silastic ball valves (n=3) in humans.

A hot-film anemometer system with a 1 mm conical L-shaped needle probe was used to register blood velocities at 41 almost evenly distributed measuring points in the cross sectional area of the ascending aorta. Later data analysis using a computerized drawing technique enabled us to make three-dimensional plots of the velocity profile at 100 time intervals during one mean heart cycle. By successive photography of each plot animated films were made. In patients with normal aortic valves flat but skew profiles were seen with a counterclockwise rotation of the skewness during systole. After insertion of the artificial heart valves, their design was reflected in the velocity profiles.

BE8-D.3

In Vivo Measurement of Turbulence downstream of Aortic Valves.

J.M. Hasenkam*, H. Nygaard, J.H. Østergaard, E.M. Pedersen, P.K. Paulsen and B.A. Schurizek. Dept. Thorac. Cardiovasc. Surg. Skejby Sygehus. Aarhus Univ. hosp. and Instit. Experim. Clin. Res. Aarhus University. 8000 Aarhus, DENMARK.

Turbulent shear stresses are considered to cause hemolysis, thrombo-embolism and endothelial damage downstream of artificial valves. Quantitative turbulence studies in vivo have been made only scarcely. Therefore, the numerous in vitro fluid dynamic studies are difficult to compare with the clinical situation. We made 33 aortic valve replacements in pigs and used a 1 mm hot-film anemometer probe, inserted 1 diameter downstream of the valve ring in the ascending aorta, for blood velocity measurements in the entire cross sectional area. Twenty heart cycles were recorded succeedingly in each of 41 measuring points. The ensemble averaged velocity energies were subtracted from the instantaneous velocity energies in frequency domain for extraction of mean systolic turbulence energies, and 3-dimensional visualization of turbulence profiles were made. Maximum Reynolds Normal Stress (RNS) was approximately 500 Nm^{-2} downstream of artificial porcine valves. Mean spatial mean systolic RNS ranged from 20 to 70 Nm^{-2} . Difficulties in comparing experimental data from different centers and the need for international standardization will be discussed.

BE8-D.4

Flow Mapping of Bioprosthetic and Tilting Disc Heart Valves in the Mitral Position: In Vivo and In Vitro Studies, A.P. Yoganathan*, M. Jones, H-W. Sung, E.E. Elabo, S.T. McMillan and R.E. Clark, Georgia Institute of Technology, Atlanta, GA 30332-0100.

2-D imaging and color-encoded Doppler studies were performed on 9 types of clinical and preclinical bioprosthetic valves and 5 types of tilting disc (TD) mechanical valves in the mitral position in sheep. The TD valves were oriented with the major orifice to the left ventricular (LV) free wall (FW) or to the LV septum (S). Porcine valves had high velocity (150-200 cm/s), turbulent, non-central, eccentric jets during diastole. Areas of flow separation and vortex formation were observed beneath the leaflets. Pericardial valves had broad central, but often asymmetric, velocity jets with in-orifice turbulence which decayed about 2 cm downstream. The observations in vivo were comparable to those obtained in vitro by laser Doppler. TD valves had two high velocity jets (max velocities 1-2 cm/s in both orifices). In FW & S orientation, vortex shedding and entrainment of adjacent blood produced eddies of velocity reversal measuring 20-30 cm/s just distal to the disc. Greater intraventricular turbulence occurred with S than with FW orientation. In S orientation, large areas of reverse velocities (25-50 cm/s) directed against the minor orifice inflow occurred along the LV FW in mid and late diastole. In contrast, valves in FW orientation had velocity profiles which became laminar and directed to the LV apex 1-2 cm distal to the disc, measuring 50-90 cm/s in mid and late diastole.

BE8-E.1

Comparative Study of St. Jude and Edwards-Duromedics Bileaflet Valves Using Laser Anemometry. R. Fatemi* and K.B. Chandran, University of Iowa, Iowa City, IA, 52240.

An *in vitro* comparative study of St. Jude (SJ) and Edwards Duromedics (DM) Bileaflet valves of size 27mm was performed under steady (18 lpm; approximate peak systolic flow rate) and physiological pulsatile flow (time averaged flow rate of 6 lpm) conditions in an axi-symmetric chamber using Laser Doppler Anemometry (LDA). LDA measurements were obtained in two different orientations; one perpendicular to the leaflet tilt axis (O1) and one parallel to the tilt axis (O2). The axial and transverse velocities as well as turbulent shear stress were measured in both orientations at two different locations distal to the valves. The velocity profiles at peak systole show presence of stronger vortex in O1 orientation in the sinus region for flow past SJ valve compared to the DM valve. Velocity profile distal to the SJ valve in orientation O2 was relatively flat whereas for the DM valve, a jet-like flow was present. This may be due to the curved geometry of the leaflets of the DM valve. We measured higher magnitudes of maximum turbulent shear stress for the DM valve (765 dynes/cm²) compared to the SJ valve (675 dynes/cm²). The higher turbulent shear stress of the DM valve can be attributed to its thicker leaflet, smaller angle of leaflets opening and the presence of the leaflet curvature.

BE8-D.5

EFFECT OF PROSTHETIC HEART VALVE ORIENTATION; IN VITRO STUDIES
J.D. Walker, W.M. Phillips*, W.G. Tiederman
Purdue University, W. Lafayette, IN 47907

Influence of tilting disc heart valve orientation on flow through a curved-tube aortic model was studied. The primary criterion for evaluating performance was turbulent shear stress levels. Simultaneous, 2-component laser velocimeter measurements were made using a mock circulation loop to simulate physiological pulsatile flow. A 22 mm diameter glass tube with a 41 mm radius of curvature modeled the average dimensions of the adult aorta. Results at mid-arch showed low turbulence levels in early systole and no influence of valve orientation. Fluid from the ventricle reached mid-arch at mid-systole showing strong valve orientation influence and increased turbulence levels. With the major orifice of the valve adjacent to the inner curved wall, the peak turbulent shear stress was 307 dynes/cm². Rotating the valve 180 degrees, the peak turbulent shear stress was a reduced value of 91 dynes/cm². At the exit of the curved section, the flow was independent of valve orientation and the turbulent shear stress levels were an order of magnitude lower. These studies show that the major orifice of tilting disc valves should be adjacent to the outer curved wall to minimize turbulent shear stress levels.

BE8-E.2

FLUIDDYNAMICS AND FUNCTIONAL PERFORMANCE OF BIOPROSTHESES H. Reul*, E. Knott, M. Giersiepen, U. Steinseifer, Helmholtz-Institute for Biomedical Engineering, Aachen, West Germany

Since the number of different types of Bioprostheses is continuously increasing it becomes more and more difficult for the implanting surgeon to differentiate the advantages and disadvantages of specific valve types. Therefore, it may be of great help for the surgeon to have comparative independent test results which are obtained under carefully controlled conditions and are relevant to the clinical situation.

This paper covers laboratory testing methods such as pressure drops in steady and pulsatile flow, closure and leakage volumes, energy losses and velocity field evaluation by means of Laser-Doppler-Anemometry. Pressure drop measurements under various steady and pulsatile flow conditions serve as a reference for similar clinical situations. Energy losses and regurgitant volumes also have an immediate clinical impact since they are a measure for the additional work load of the heart. The detailed analysis of the downstream velocity fields allows a localization of high shear-stress regions, wakes, flow separation and wash-out of the valves in context with blood damage, platelet activation and potential thrombus deposition. Comparative test results for about 15 different valve makes will be presented and relative valve performance will be discussed.

BE8-E.3

NOVEL FLOW VISUALIZATION TO DETECT SITES OF THROMBUS GENERATION AT ARTIFICIAL HEART VALVES
K. Affeld*, P. Walker, K. Schichl, Universitätsklinikum Rudolf Virchow, Berlin, F.R.G.

The flow through artificial heart valves has been studied at great length using various methods. LDA has especially rendered many results. Unfortunately, we still do not have a detailed picture of how the overall instantaneous flow looks. Although the flow has been visualized and photographed, the pictures show little details, mainly because of the small size of valve and the high velocity of the flow. To overcome these obstacles a mock circulation has been developed, which generates a flow for a 10 to 1 enlarged model of a heart valve (Bjork Shiley). This large size and the use of water reduces the velocity to 1/35 of a real one. Together with the enlarged scale this improves the lighting condition by the factor of 350. The flow is kept similar by ensuring that the Reynolds-number, the Strouhal-number and a third describing the buoyancy of the occluder are the same. The flow is made visible with suspended particles, injected dye, hydrogen bubbles and particles generated directly in the boundary layer. The interest is concentrated on flow separation - "stagnant flow" - known to be the preferred sites for thrombus generation. These sites are found in the wake of the ring and behind the struts. In the real valve they are of minute size - about 1×2 mm - and hardly detectable. In the enlarged model they are clearly visible. Their location coincides with the sites of observed thrombi reported by others.

BE8-E.5

The Interaction of Wall Shear Stress and Prosthetic Valvular Cusp, S. Einav*, D. Stoler, J.M. Avidor, D. Elad, and L. Talbot, Tel Aviv University, Tel Aviv 69978, ISRAEL, and University of California, Berkeley, CA 94720, U.S.A.

High levels of wall shear stress on the surface of valvular cusps can cause mechanical damages to the blood cells and the cusps' surfaces. The shear stresses are also responsible for mechanical failure of prosthetic heart valves. Quantitative measurements of wall shear stress in the vicinity of the leaflets is thus essential for diagnosis of suspected complications and an important information for design and fabrication of bioprosthetic heart valves. For this purpose we measured the velocity distribution along the inside wall of the cusps of a tri-leaflet heart valve with a two color laser Doppler anemometer system. The wall shear stresses on the cusp surface were computed and found to range from 80 to 120 N/m^2 during the ejection phase. Wall shear stresses of up to 180 N/m^2 were measured in loci of cusp flexure and the boundary layer accelerated. The results of this study show a correlation between the high shear stress loci and the clinically (animal) observed regions of cusp calcification.

BE8-E.4

Effects of End Diastolic Ventricular Volume on the Dynamic Performance of Prosthetic Heart Valves, M.C.S. Shu and N.H.C. Hwang*, Cardiovascular Flow Dynamics Lab, University of Houston, Houston, TX 77004

The dynamic performances of eight clinical prosthetic heart valves (PHV) in both mitral and aortic positions are studied by using three fixed left ventricular end-diastolic volume models (FVM), and a supplemental varied left ventricular end-diastolic volume model (VVM). The experiment is carried out to observe a relationship between the PHV performance and the three fixed left ventricular end-diastolic volumes, under otherwise identical conditions. The results are compared to those obtained from the VVM. Systematic analysis of the in vitro data indicates that changing ventricular end-diastolic volumes does exhibit significant increase of pressure drops across the valves, alteration of regurgitation patterns and decrease of "the effective valve area" (EVA).

BE8-E.6

Studies of the Flow Field of Bi-leaflet Mechanical Valves with Cambered Profile, Zhenhuang Kang*, Bioengineering Institute, Chengdu University of Science & Technology, Chengdu, Sichuan, China

Bi-leaflet mechanical valve with cambered profile was designed as a new valve type based on thin airfoil theory. It is the purpose of this design to improve the closing behavior of mechanical cardiac prostheses so that the impact and regurgitation can be reduced. In addition to the design of above-mentioned valve, in order to get some features of the flow field and situations of thrombus formation, we have conducted experimental studies about the wall shear stress and the flow field of the valve by using electrochemical technique and hydrogen bubble technique respectively. Moreover, a numerical study by means of FEM was also done. Finally, a quantitative concept about the flow field was obtained, and some useful data for the valve design were provided through comparative studies for different leaflet cambers and opening angles.

BE8-F.1

HEART VALVE ENGINEERING: STEPS OF QUALITY ASSURANCE - J. Köhler, Aerodynamisches Institut, Aachen, West Germany.

Steps of the development of test standards for artificial heart valves (AHV) within a project sponsored by the German Government are described. Provided are acceptance tests for new types of valves on the one hand, and random tests for already approved valve types on the other.

The following test steps are under work: Development and definition of the medical and technical basis for the quality assurance of AHV; development and definition of test devices and test procedures; comparative assessment of already marketed valve types by present day and new test methods.

A list of test parameters and test steps has been defined in the project with regard to test devices urgently needed (geometrical parameters, flow parameters, deformation- and force-parameters). A number of corresponding test devices is under work or available as prototypes.

It can be summarized that quality assurance of prosthetic heart valves - new and current types - has not yet been sufficiently developed. Not only the qualities to be measured but also the procedures and the test devices have to be defined for rational valve testing. The volume loss, the deformability of the valve rim and the safety of the valve structure have to be taken into account more deeply in quality assurance of AHV.

BE8-F.3

Quantification of Mitral Regurgitation from Turbulent Jet Theory

E.G. Cape*, A.P. Yoganathan, E.G. Skoufis, and R.A. Levine, Georgia Institute of Technology, Atlanta, GA 30332-0100

Due to well-recognized disadvantages of invasive diagnostic techniques, there is great need for a method to assess mitral valve incompetence noninvasively. Using currently available technology such as ultrasound Doppler velocity measurement and Color Doppler flow mapping, attempts have been made to correlate regurgitant volume with color jet area, etc. We have taken a more fundamental approach and derived a theoretical model for the flow rate through a regurgitant lesion, based on turbulent jet theory. The equation expresses the flow rate through the lesion as a function of ultrasound Doppler measurable parameters.

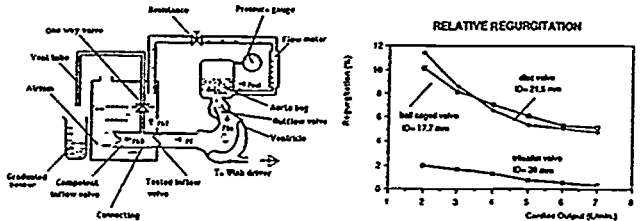
In order to test the validity of the equation, we constructed a cylindrical flow chamber with small circular orifices of varying sizes. A 2 MHz transducer (continuous and pulsed wave) interfaced to a Vingmed SD-100 ultrasound Doppler system was placed distal to and parallel to the regurgitant jet and the appropriate velocities measured at varying flow rates.

Thirty-six combinations of volumetric flow rate and orifice size were tested and the calculated flow rate compared to the actual. An average deviation of only 6.0% was found. The model shows high potential as a noninvasive method and has the additional advantage of being theoretically grounded.

BE8-F.2

Simple Device For The In Vitro Measurement Of Regurgitation Of Prosthetic Heart Valve In Mitral Position, Long-Sheng Yu, Willem J. Kolff, Division of Artificial Organs, Dumke Building, Univ. of Utah, Salt Lake City, Utah 84112

Measurement of regurgitation of prosthetic heart valve is important in evaluating the performances of artificial valves. The electromagnetic (E-M) flowmeters are most commonly used, but with certain disadvantages. Our recently developed device, called Bi-Inflow Valve Regurgitation Tester (BIVRT) is simple, cheap and easy to operate with low error in backflow measurement as compared to that of E-M flowmeter and without the disadvantages of phase-line shift, and axial asymmetry, disturbance of flowpath, and the necessity of computer data processing. The variation in measured results by the BIVRT is about 2.5%, which is more accurate than that by the E-M flowmeter. By the use of BIVRT, comparison of backflows of disc valve, ball caged valve and tri-leaflet valve were found to be that the latter is about 1/5 of that of the former two. Further experiments showed that the backflow measurements of a disc valve by the BIVRT and the E-M flowmeter versus filling volume under the same condition were found to be that the readings by the former method is 20% lower than those by E-M flowmeter. For the comparison of "the one-inflow valve mode testing" with a single disc valve and "the bi-inflow valve mode testing" with one disc valve and one tricuspid valve, the E-M flowmeter was used for good correlation. The results of these two modes were found to be quite close to each other. Reasons for the lower backflow measurements in the BIVRT method as compared with those by the E-M flowmeter are due to: 1) the resistance of the vent tube and its one-way valve; 2) the leakage of the additional competent valve; 3) the reverse suction of the vent tube during diastole for the BIVRT set-up; and 4) measurement error by the E-M flowmeter.



BE8-F.4

Flutter in Bileaflet Cardiac Valve Prostheses, T. H. Reif* and Ned H. C. Hwang, Republic Medical Products, Inc., Dayton, OH, and Cardiovascular Fluid Dynamics Laboratory, Houston, TX

The rotational form of Newton's second law of motion is solved based on the dimensions of a size 27 mm Carbomedics Prosthetic Heart Valve (pm). The lift force and pitching moment are estimated from potential flow theory, while the drag force is estimated from the lift force and a blunt body empiricism. Buoyancy and gravitational effects are based on the assumption of homogeneous leaflets. Other assumptions include uniform flow, negligible friction at the pivot axis, and a symmetry condition. Oscillations are observed in the opening dynamics of the order of 1-10 Hz. The frequency of the observed oscillations is dependent upon the orientation of the gravitational field and the flow rate. These results suggest that the natural frequency of the rotational second order system may significantly affect the flutter of bileaflet cardiac valve prostheses.

BE8-F.5

Effect of Flow Rate on the Prediction of Effective Valve Orifice Area from Hemodynamic Measurements, R. Scnoephoerster* and K.B. Chandran, University of Iowa, Iowa City, Iowa.

A study was performed to test the prediction capabilities of the clinically used Gorlin formula as well as the Aaslid and Gabbay formulas for the effective orifice area (EOA) of prosthetic heart valves. Pressure gradient, flow, and valve opening area measurements were performed on four 27mm valve prostheses (Edwards-Duromedics, St. Jude, Edwards-pericardial, and a trileaflet polyurethane valve) each mounted in the aortic position of an *in vitro* pulse duplicator. With the known valve orifice area, a discharge coefficient (Cd) was computed for each of the four valves and three EOA formulas. All Cd's were observed to increase with increasing systolic flow rate (SFR). An empirical relationship of Cd as a linear function of SFR was determined through a regression analysis for each of the valve geometries which improved the accuracy of the prediction of the EOA. Further work is needed to test for the effects of valve size on the Cd, as well as determining Cd's for prosthetic heart valves of other geometries.

BE8-G.2

Fluid Mechanical and Transport Factors in Slow Continuous Renal Replacement Therapies. Thomas L. Pallone*, Division Nephrology, Univ. Rochester, Roch., NY

Continuous arteriovenous (AV) hemofiltration (CAVH) and hemodialysis (CAVHD) are important modalities for treatment of hemodynamically unstable patients with renal failure. Blood flow rate in these circuits is governed by the AV pressure gradient, total circuit resistance and blood viscosity. Distribution of hydraulic pressure is governed by the relative location of circuit component resistances. Filtration rate by the hemofilter/dialyzer is governed by transmembrane hydraulic and plasma oncotic pressures and membrane hydraulic permeability. The many variables involved make circuit optimization difficult.

To aid proper circuit construction, mathematical models have been developed which, given patient and circuit characteristics as inputs, predict system performance. Assumptions include the modelling of components as Poiseuille resistors and neglect of concentration polarization of plasma proteins. Spatial variation of blood viscosity is considered. Predictions of performance agree with results of *in vitro* perfusion experiments.

BE8-G.1

MASS TRANSPORT IN PERITONEAL DIALYSIS
J. M. Woll*, M. J. Lysaght, and J. W. Garber,
Baxter Healthcare Corporation, Round Lake, IL

Peritoneal dialysis is a blood-cleansing process widely applied for the treatment of patients with end stage renal disease. Hypertonic dialysate is periodically infused into the peritoneal cavity by gravity through an indwelling catheter. Plasma water and solutes which would normally be cleared by the kidney are transported from blood to dialysis solution through a rather complex series of resistances including capillary endothelium, interstitial tissue, peritoneal membrane and fluid boundary layers. Fluids traverse this "membrane" in response to osmotic pressure differences; solutes are removed by diffusion; both may be returned to the bloodstream via the lymphatic circulation.

Despite its complexity, the process may be adequately described by the analogy to a simple planar membrane separating two well mixed pools. This allows the calculation of equivalent transport parameters which characterize the system including: hydraulic permeability, sieving coefficient and mass transfer coefficients. These transport parameters may be readily extrapolated and interpolated so that the behavior of a wide variety of solutes may be predicted from a relatively small number of experimental measurements.

BE8-G.3

THE EFFECT OF MASS TRANSFER LIMITATIONS ON INSULIN SECRETION IN HYBRID ARTIFICIAL PANCREAS

Clark K. Colton*, Keith E. Dionne, and Martin L. Yarmush, Department of Chemical Engineering, Massachusetts Institute of Technology, Cambridge, MA 02139.

One approach to diabetes therapy is implantation of xenogeneic islets immunosolated by interposition of a semipermeable membrane between the islets and the bloodstream or tissue. Internal vascularization normally present is lost after isolation, forcing the islet to depend instead on external and internal diffusion to provide an environment wherein the beta cells survive and secrete insulin. Two problems are described. (1) The effect of glucose and insulin diffusional limitations on observed insulin secretory dynamics. Results from mathematical models define design conditions required to preserve intrinsic insulin secretion kinetics. (2) The effect of pO_2 on intrinsic insulin secretion. Measurements in perfusion and static culture demonstrate markedly reduced second phase secretion under reduced pO_2 conditions. These results correlate with a lower islet core pO_2 , as predicted by a mathematical model, for glucose-stimulated as compared to basal conditions.

BE8-G.4

GLUCOSE AND INSULIN KINETICS IN A BIOARTIFICIAL PANCREAS

M.Y. JAFFE N^o; UTC, UA CNRS 858
Dpt de Génie Biologique, BP 649,
60206 COMPIEGNE CEDEX, France

A bioartificial pancreas is an implantable device connected to the diabetic host as an arteriovenous shunt. It contains insulin secreting cells (Langerhans islets), separated from the circulating blood by a semi-permeable membrane to avoid immuno rejection. We present here a model which describes the operation of such a device from a fluid mechanical point of view and evaluate the respective contributions of diffusion and ultrafiltration to the glucose and insulin mass transfer. It is shown that the pressure drop along the blood channel produces across the first half of the channel an ultrafiltration flux towards the islet compartment followed in the second half by an equal flux in reverse direction from islets to blood. The mass transfer analysis is carried out for an optimal geometry in which a U-shaped blood channel surrounds closely a very thin islet compartment formed by a folded flat membrane. A complete model of insulin release by this device is developed and is compared with in vitro data obtained with rats islets.

Satisfactory kinetics is achieved with a polyacrylonitrile membrane used in hemodialysis. But the model shows that the membrane hydraulic permeability should be increased by a factor of 10 to significantly improve the performance.

BE8-H.2

The Medical Device Regulation in the Federal Republic of Germany, H. Hutten, Institute of Physiology, Johannes Gutenberg-University, D-6500 Mainz, FRG

The Medizingeräteverordnung (MedGV) has been enacted on Jan. 1st, 1986. Its objection is the protection of users, patients and third persons against any avoidable risks that might be related with medical devices (m.ds). In separate paragraphs, the MedGV specifies the regulations both for market admission and employment of m.ds. The m.ds are classified in one of four classes. The 1.class consists of a list with 25 high-risk devices. The 2.class comprises all energy-powered implants. The remaining energy-powered m.ds belong to the 3.class and all other m.ds to the 4.class. The most relevant regulations of the MedGV are: (1) m.ds of class 1 and 2 need a type-related market admission in which further particulars are specified. (2) m.ds of class 1 and 3 have to be listed in an inventory. (3) Only specifically trained users are allowed to employ m.ds of class 1 and 3. (4) m.ds of class 1 are only free for the first operation after a complete functional check and operating instruction have been made by the producer or supplier. (5) A detailed book must be kept for each class 1 m.d. (6) Accidents with personal injuries must be reported to the authorities. (7) m.ds supplied before Jan. 1st, 1986 had to undergo a safety check by authorized experts within two years if proper maintenance in the past could not be proved by the owner.

BE8-H.1

Current Issues of Medical Device Policies in Japan, M.Saito* and M.Kikuchi, Inst. Medical Electronics, Fac. Med., Univ. Tokyo, Tokyo 113, Japan

The advent of complex systems, costly devices and technologies requiring extremely high reliability, is not making the role of policy-making agencies difficult and complex. The task should not simply be considered as a regulating mechanism. Pre-assessment of coming technology, guidance of industry and medical professionals, education and standardization are some of the important items to be added to regulatory functions. The reliability of technology should be secured from a large-scale standardized production as well as from flexible small-scale production. In international cooperation, the diversity of requirements from different countries should be considered. A simple-minded uniform guide or regulatory mechanism will not work. A quality assurance program may work for a certain level of technology but may be hazardous to others. Sometimes, technology is too advanced and standard quality assurance does not pay for the danger. Some of the topics that require urgent study are: internationally translatable but flexible nomenclature, pre-assessment of technology, man-machine safety standard, testing method and devices, etc. Some of the recent effort in Japan will be described.

BE8-I.1

Current Status of Biomedical Engineering in the Research and Development on Artificial Heart. K. ATSUMI, University of Tokyo, 7-3-1 Hongo, Bunkyo-ku, Tokyo, 113, JAPAN

Artificial heart is aiming to construct the simulation model which substitutes cardiac functions of biological heart. It is divided into two modes - ventricular assist device (VAD) and total artificial heart (TAH) - by replacing the cardiac functions partially or totally.

At the present state, 300 clinical cases of VAD and 7 cases of TAH were experienced in the world and artificial heart is highly evaluated as the essential therapeutic method to cure the deteriorated patients with severe heart ailure.

In the symposium, the R & D on TAH is mainly discussed.

TAH is constituted from three parts - blood pump, driving unit and energy source - . Until now, air driven type of TAH were studied in the animal experiments and clinical applications, however, in future, implantable TAH will be implanted in human of which project has recently been started in the several eminent facilities.

The problems and solutions of biomedical engineering on TAH will be discussed in the symposium which is formed from the two sessions, one is material, blood pump, monitoring and control and another is energy conversion and energy source. The topics of the discussions will be concentrated to the R & D on implantable TAH.

BE8-I.3

EFFECTS OF HEAT DISSIPATION FROM MECHANICAL DRIVEN ARTIFICIAL HEARTS ON BLOOD AND TISSUE COMPONENTS. A SYSTEMATIC IN VITRO STUDY, H. Harasaki*, and Y. Nosé, Cleveland Clinic Fdn., Cleveland OH 44106

Management of waste heat imposes a new problem inherent to currently developed implantable energy converters for artificial hearts. Effects of predicted surface temperatures in coagulation, (APTT, PTT, TT) platelet % max., aggregation (AGR) retention (RET), and BTG and PF4 release and viability of various tissue cells were studied in vitro. The results are summarized in the Table below.

	Epos. Time	37°C	42	47°C	
APTT	15 min	41.0 ± 7.7	49.8 ± 2.2*	69.5 ± 12.8*	sec
PT	15 min	19.4 ± 0.6	20.8 ± 1.8	27.7 ± 2.1	sec
TT	15 min	16.1 ± 1.9	19.8 ± 0.9*	30.6 ± 5.2 *	sec
AGR	1 hr	77.8 ± 8.6	37.2 ± 6.6*	0 *	%
RET	1 hr	83.7 ± 0.9	80.1 ± 6.7	32.4 ± 12.0	%
BTG	15 min + ADP	272 ± 31	294 ± 56	195 ± 52*	ng/ml
PF-4	15 min + ADP	113 ± 22	120 ± 19	73 ± 15*	ng/ml

*statistically significant as compared to 37°C

This data indicates that blood becomes less thrombogenic on the heated surface, and explains out previous in vivo observation that neointima formed on the heated surfaces is thinner than that on a un-heated surface of the blood pump. Fibroblasts were more heat resistant than endothelial and smooth muscle cells and 91% viable even after 2 hr. exposure to 47°C.

BE8-I.2

Segmented Polyurethanes as Basic Material for Cardiovascular Artificial Organs T. Matsuda, Res. Inst., Nat'l Cardiovasc. Ctr., Fujishiro-dai, Suita, Osaka, Japan

One of the crucial tasks for guarantee of the reliability of blood pump is to ensure its system's antithrombogenicity. This paper assesses to define determinant factors and mechanistic aspects of short-term and long-term antithrombogenicity of segmented polyurethanes used for blood pumps. The short-term antithrombogenicity was found to be markedly influenced by species of adsorbed plasma proteins. The adsorption of cell-adhesion promoting proteins such as fibrinogen and fibronectin greatly enhanced platelet adhesion and aggregation. Both coagulation and complement systems were activated directly on polymer surfaces. Segmented polyurethanes were found to be relatively inert toward these biological responses.

On the other hand, longer-implantation resulted in the formation of proteinaceous multilayer, which proceeds as a time-lapse process. The stability of multilayering was found to be the determinant for long-term antithrombogenicity. Besides these, blood flow rate and implantation period were also major determinants. Thus, time-variant multi-factorial interactions determine system's antithrombogenicity.

BE8-I.4

Development of A Multi-Function Control System for Artificial Hearts

T.Yamaguchi*, T.Shimooka, Y.Mitamura

Section of Medical Electronics, Res. Inst. of Appl. Elect., Hokkaido Univ. Sapporo 060 Japan

We have developed a portable control system for pneumatic artificial hearts. This control system enables automatic blood pressure control without invasive blood pressure measurements as well as conventional pumping methods.

Blood pressures are measured indirectly in the control system. When driving pressure is changed gradually, the pressure when a diaphragm in the pump begins to move equals to arterial or atrial pressure. Waveform of drive pressure is regulated by electronic air pressure regulator and diaphragm movement is detected by optical sensor.

Based on the indirectly measured values, blood pressures are controlled. The microcomputer based control system maintains the blood pressures constant regardless of changes in peripheral resistance or circulatory blood volume by changing drive rate, %systole, positive pressure and negative pressure.

In vitro experiments disclosed accurate beat-by-beat estimation of arterial and atrial pressure and precise regulation of blood pressures. The control system is useful for driving artificial hearts optimally without the troubles of infection and thrombus formation.

BES-I.5

New Control Method of Artificial Heart
K. Imachi, I. Fujimasa, and K. Atsumi
Inst. of Med. Electr., Faculty of Med.,
Univ. of Tokyo, Hongo, Bunkyo-ku,
Tokyo, Japan

Total artificial heart(TAH) control method is too primitive stage for the patient to enjoy a high quality of life like a healthy person. One of the difficulty to establish an ideal TAH control method, is that there is no adequate detecting method of the cardiac output(CO) demand of the living body. As a step to the ideal TAH control method, a new control method of TAH during the exercise was developed in our laboratory. CO change curves for various grades of treadmill exercise(TE) are obtained from control goat as a time function(objective function curve:OFC). The correlation between treadmill speed and physical activity rate(PAR) which is defined as the time average of upward acceleration of the body, is obtained as a linear function. These functions are memorized in a microcomputer. The TAH control procedure is as follows. 1)When the TE start, its speed is detected as PAR by an acceleration sensor. 2)The microcomputer choose an OFC according to the PAR. 3)TAH driving parameters of both blood pumps are controlled predictively for the pump output to fit with the OFC under a control algorithm installed into the microcomputer. The system worked well in the animal experiments, and its effects on metabolism was also proven.

BES-J.2

*Solenoid Energy Converter of the Novacor
Clinical Left Ventricular Assist System*
P. Miller*, J. Jassawalla, H. Chen,
D. LaForge, P. Portner. Novacor Medical
Corporation, Oakland, California, USA

The Novacor Left Ventricular Assist System (LVAS) uses a balanced pulsed solenoid electromechanical energy converter for blood pump actuation. Under development since 1970, the current version of this simple lightweight driver has essentially only two moving parts -- the identical armature/spring assemblies -- coupling directly to the blood pump pusher plates. When energized, the two solenoid armatures close rapidly, efficiently converting electrical input power into mechanical energy stored in the "decoupling" springs. The springs then deliver their stored energy to the pump at a rate governed by the physiologic load. The balanced solenoid closure results in no reaction torques, gyroscopic effects, or momentum transfer to the body. Because the entire LVAS is symmetrical, there are no unbalanced loads on the energy converter frame or blood pump housing.

The system has been extensively tested *in vitro* and *in vivo*, in multiyear endurance tests and animal experiments as long as nine months. A multicenter clinical trial of the Novacor LVAS has been ongoing since 1984. System efficacy has been demonstrated in successful bridge-to-transplant applications of up to 90 days.

BES-J.1

DEVELOPMENT OF AN ELECTRIC MOTOR
DRIVEN TOTAL ARTIFICIAL HEART,
W. Weiss, M.S.*, G. Rosenberg, Ph.D.,
A. Snyder, Ph.D., W.S. Pierce, M.D.
Pennsylvania State University, Hershey
Medical Center, Hershey, Pennsylvania

An electric motor-driven total artificial heart utilizing a roller screw drive is being developed. A 3-phase brushless DC motor produces bidirectional rotary motion which is translated to the rectilinear motion of the roller screw shaft. Pusher plates at either end of the shaft alternately compress left and right blood sacs contained in pump cases located at either end of the motor housing. Bjork-Shiley convexo concave tilting disc valves are used. A compliance chamber permits left-right stroke volume differences, which are utilized by the motor controller to balance left-right pump outputs.

Electrical power is delivered to the implanted motor controller via a pair of coils, one subcutaneous and one external. An external battery pack will operate up to 10 hours, while an implanted backup battery will operate up to 45 minutes.

BES-J.3

Energy Source and Energy Transmission for Artificial Hearts, V. Poirier*, C. Sherman, K. Dasse, Thermedics Inc., Woburn MA 01801

Artificial hearts and heart assist systems require significant power levels which cannot be met with implantable power sources. The two most widely used energy sources are air and electricity. The air systems, generally used for short term, require an external air compressor while the electric systems require chemical storage batteries. Transmission of energy from the external sources can be accomplished by two means. For electrical energy transfer, transcutaneous energy transfer systems which utilize two coils of wire to inductively couple the energy into the body are used. In this form, energy is transferred without penetration of the integument. For transfer of air or electrical energy, percutaneous energy transfer systems are utilized, which can become an integral part of the body.

BE8-K.1

Fluid Mechanical Analysis of Blood Flows with an Intra-Aortic Balloon Pumping
T.K. Hung and H.S. Borovetz, University of Pittsburgh, T.E. Natan, Jr., Carnegie-Mellon University, Pittsburgh, PA 15261

For three-dimensional blood flow in the descending aorta with an intra-aortic balloon counter pulsation, the radial axis, r , for the Navier-Stokes equations in the cylindrical coordinates, (r, θ, z) , is transformed to a dimensionless axis:

$$R = \frac{r - b(\theta, z, t)}{a(\theta, z, t) - b(\theta, z, t)} + 1$$

where the radii of the balloon (b) and aorta (a) and their motions are the prescribed boundary conditions for the computational flow simulation. Local acceleration components were employed in the determination of the transient pressure field from the divergence of the Navier-Stokes equations. The pulsating spiral flow processes were analyzed by correlating the longitudinal velocity profiles, the secondary flows, and the pressure and shear fields with the deflation and inflation of the balloon during a cardiac cycle. The study was supported by an NIH Grant HL33934 from the National Heart, Lung, and Blood Institute. The Cray X-MP supercomputer at the Pittsburgh Supercomputing Center was used for this investigation.

BE8-K.3

Development of Nutating Centrifugal Blood Pump, T.Akamatsu, Kyoto University, Kyoto 606, Japan

Conventional centrifugal blood pumps have weaknesses of infection through shaft seal for direct motor drive and blood degeneration in journal bearing for closed magnetic coupling drive. A centrifugal pump with a nutating (not rotating) impeller, so called Tea Spoon Pump, can overcome these weaknesses. This pump is allowed to have only one impeller for its mechanism. Therefore its pump efficiency was not so high. But by our following inventions it is much improved; (1) annular pump room surrounded with inner guide wall and outer casing wall, (2) spiral inlet passage, (3) well-contoured outlet passage and diffuser. Rectified flow is obtained as if a piston (impeller) pushes blood in an endless cylinder (annular pump room), and the pressure difference between outlet and inlet is sustained by centrifugal force of rotating blood flow.

At present, the pump efficiency is raised up to 45% compared with the previous 32%. Undesirable hemolysis in the previous pump was larger than that in the roller pump. But in the present improved pump, we can expect the lower hemolysis. Pulsatile flow can be obtained by the on-off run of the motor and the addition of a check valve at the outlet of the pump.

BE8-K.2

Optimum Design of a Compact Centrifugal Blood Pump: Casing Configuration and Pump Performance, S. Tanaka^{*}, K. Ito, K. Yamakoshi, A. Kamiya, K. Horiuchi^Δ & M. Kusakabe^Δ, Res. Inst. Appl. Electr., Hokkaido Univ., Sapporo, & ^ΔTerumo Inc., Tokyo, Japan.

For the use of extracorporeal circulation, we have previously developed a compact centrifugal blood pump driven directly by a miniature DC servomotor. Through in vitro tests, it was found that the configuration of the impeller having the blade angles at the inlet of 20 deg and at the outlet of 50 deg was the most appropriate for this pump with respect to the pumping capacity and the decrease in hemolysis.¹⁾ In this study, the effect of the volute casing on the pump performances was evaluated to determine an optimum configuration of the pump casing. It was demonstrated that the pumping capacity and the degree of hemolysis produced by the pump with volute casing were significantly improved at high flow rate region compared with those by the pump without volute casing. It was suggested through this study that the optimum design of the casing configuration should be made according to the range of flow rate required.

Reference: 1) S. Tanaka et al, Trans. ASME, J. Biomech. Eng., 109(3), 272 (1987)

BE8-K.4

Optimization of Pulsatile Pump Flow Parameters, R.Fumero, F.M.Montevecchi, S.Scuri^o, Politecnico di Milano, Italy.

The differentiation between effective and ineffective forms of pulsatile flow during cardiopulmonary bypass has been often stressed. Factors such as ejection phase duration, peak flow, etc, must be chosen in order to achieve the energy content of flow wave which maintains capillary patency and, on the other hand, to avoid excessive mechanical trauma on blood cells. The influence of arterial line and aortic cannula, which modify considerably the pulse, must be considered too. A pneumatically driven and microprocessor controlled pulsatile pump for pediatric extracorporeal circulation has been developed. In order to optimize flow parameters, both energy loss in the aortic cannula, which is a reliable index of blood damage, and output energy past the cannula must be evaluated. For this purpose, a finite difference program has been used to calculate transient flow and local pressure drops in the arterial line. The program has been also validated by comparing numerical results to experimental measurements assessed in a simple mock circulation. Numerical simulations have been performed under the same conditions of mean flow rate for different pulse rate (60,70,80 b/min) and ejection phase duration (40,50,60% of pulse period). The results have provided useful directions for optimum choice of systolic to diastolic time ratio.

267

BE8-K.5

STUDIES ON ELECTRONIC CONTROL PNEUMATIC DRIVING SYSTEM FOR ARTIFICIAL HEART

Yang Zi-bin, Zhu An-ping, Lu song-fang,
Han yan, Huang Wen-mei, Wang Xiao-roig,
Shan Hui-min

DePart. of Biomedical Engineering
Institute of Basic Medical Sciences
Chinese Academy of Medical Sciences

Beijing China

Highly reliable electronic control and pneumatic driving system for artificial heart has been developed. It was consisted of two subsystems which are electronic control subsystem and pneumatic power supply. The compressed air adjusted from 0~400 mmHg was supplied by compressor or by compressed air station. The vacuum pressure adjusted from 0~200 mmHg was supplied by a vacuum pump.

In the electronic controller, the driving signal is received from either ECG for synchronous drive with the heart beats or signal generator for asynchronous. The controller monitors ECG signal level and also the driving pressure to check the function of pressure regulator, vacuum regulator and magnetic valves.

After a series in vitro tests, the AH driving system has been used in animal experiments. During the period of animal experiment, the AH driving system has worked all together for more than 500 hours and continuously worked for 267 hours. The functions of the AH driving system was shown to be normal and stable, so it is suggested to be used in AH experimental study.

BE9-A.1

PLASMA MACROMOLECULES IN HUMAN AORTIC INTIMA

Elsbeth B. Smith*, Dept. of Chemical Pathology,
Foresterhill, ABERDEEN, AB9 2ZD Scotland.

Endothelium transports macromolecules into the intima. In normal adult intima the concentration of low density lipoprotein (LDL-Mr 2×10^6) is twice the plasma concentration and for most macromolecules relative concentration is directly related to Mr. High concentrations are not necessarily pathogenic; pathogenicity probably results from processing within the intima, and this may be influenced by haemodynamic factors. LDL may be internalized by macrophages, subjected to extracellular proteolysis, or tightly bound. Fibrinogen is accompanied by degradation products (FDP) that appear to be derived from fibrin. This implies continuous conversion of fibrinogen to fibrin, and continuous fibrinolysis. Release of tightly bound LDL by incubation with plasmin is correlated with the amount of cross-linked fibrin degraded ($r=0.688$, $p<0.01$). These complex interactions must be dependent on factors such as residence time and mixing which will, in turn, be influenced by haemodynamic forces. Some proliferative lesions accumulate a core of extracellular LDL-derived lipid, whereas others in the same artery do not. Could haemodynamic factors influence oxygen and lactic acid concentrations deep in the lesion, and hence the release of lysosomal proteases?

BE8-K.6

Mechanical Studies on the Left Ventricular Recovery Process from Induced Heart Failure by Cardiac Assist. T.Nakamura*, K.Hayashi, J.Seki^o, H.Noda^o, T.Nakatani^o, H.Takano^o and T.Akutsu^o. Hokkaido University, Sapporo, and ^oNational Cardiovascular Center, Osaka, JAPAN.

Pneumatically driven, diaphragm-type left ventricular assist devices (LVADs) were chronically implanted between the left atria and the descending aortas of goats. Myocardial infarction was induced in the anterior myocardial area by the multiple ligations of coronary arteries. Left ventricular diameter, segment length and wall thickness were measured with sonomicrometers implanted in the ventricle. Bulk and regional mechanical work of the left ventricle were calculated from these dimensions and the left ventricular pressure. LVAD pumps were removed when the cardiac function seemed to be recovered. Cardiac and hemodynamic data were obtained until around 1 month after the pump removal.

The LVAD reduced the bulk and regional mechanical work. In cases that the hearts were recovered successfully, the difference between the bulk work done during pumping-on and -off decreased gradually, concomitantly with recovery, and the LVAD pumps could be weaned off within 1/2 month. In some of these cases, the ischemic regions were healed by the LVAD pumping and became to be able to do mechanical work.

BE9-A.2

Paracellular Pathways for Transport of Low Density Lipoprotein, J. Rutledge*, F. Curry, P. Davis and J. Lenz, University of California, Davis, CA

Low density lipoprotein (LDL) is transported across endothelium by receptor-mediated and vesicular pathways. We have evaluated paracellular pathways of transport of LDL in high permeability states in isolated perfused frog mesenteric microvessels. LDL was fluorescently labeled with DiI and 20,000 MW dextran, a molecule which lacks receptor-mediated transport, was labeled with FITC. By alternating sets of light filters, we were able to image these fluorescent molecules almost simultaneously. Fluorescence intensity of the microvessel and surrounding tissue was measured by photometer. The endothelium was perturbed with the calcium ionophore, A23187, which effects a transient increase in permeability.

Our studies have shown that permeability of LDL and dextran have similar magnitude and time course after the infusion of A23187 which suggests similar pathways for these molecules. In addition, LDL transport has been shown to increase with increased capillary pressure. Because water flow increases as capillary pressure increases, this coupling of LDL transport to water flow suggests a paracellular pathway for LDL transport.

BE9-A.3

Optimal Design of Experiments to Quantify Transport and Degradation in the Arterial Wall, E.D. Morris, G.M. Saidel, and G.M. Chisolm*, Cleveland Clinic Foundation and Case Western Reserve University, Cleveland, Ohio 44106, USA.

A dynamic, one-dimensional model is used to depict the transport and metabolism of low density lipoprotein (LDL) in arterial tissue. The model includes decreasing concentration of tracer in plasma, permeabilities at both luminal and media-adventitial boundaries; diffusion and convection through interstitial space and degradation by smooth muscle cells of the media. Model parameters representing these processes can be estimated from transmural concentration profiles of labeled LDL generated in vivo across the arterial wall. The sensitivity of the model output to changes in parameter values was examined. An optimal experiment design was defined to be one that maximized precision of the estimates. Three designs were considered: 1, a single bolus injection of *I-LDL, 2) sequential injections of *I-LDL and **I-LDL (*I and **I are distinguishable isotopes of iodine), and 3) a simultaneous injection of *I-LDL and **I-TC-LDL; TC is an iodinated tyramine cellobiose adduct that accumulates in cells after LDL degradation and is not removed. The optimization procedure compared the three designs for a wide range of circulation times. Our results prescribe a simultaneous injection of *I-LDL and **I-TC-LDL and a circulation time of 18 hours. Funded by NIH (HL29582)

BE9-A.5

Chronic hypertension decreases the in vivo albumin uptake by the rat aorta, A. Tedgui*, J. Belmin, J.B. Michel and L. Juan, INSERM Unité 141, Hôpital Lariboisière, 75010 Paris, France.

Changes of protein transport across the arterial wall may facilitate atherogenesis. We have studied the effects of chronic hypertension and its therapy by a converting enzyme inhibitor (CEI), on the in vivo albumin uptake by the aortic media of hypertensive rats (2 K-1 C) (HR), 8 weeks after application of the clip. Blood pressure of some HR was lowered to a normal level by injection of nicardipine prior to the albumin uptake measurement, in order to separate the effects due to hyperpressure from those due to structural changes.

The transmural distribution of the relative albumin concentration across the wall was obtained using a frozen serial sectioning technique (10 μ m), 90 mn after injection of 125 I-albumin.

Hypertension decreased the mean medial relative concentration (MRC): $1.53 \pm .38\%$ (n=8) in HR and $2.02 \pm .65\%$ (n=10) in control (p < 0.01). This decrease was even larger in HR with acutely lowered blood pressure: $1.16 \pm .32\%$ (n=7) (p < 0.01). In the CEI treated animals, MRC ($1.56 \pm .41\%$, n=10) remained lower than in control (p < 0.01). The medial thickness was increased in HR ($120 \pm 14.1 \mu$ m, n=8) as compared to control ($92 \pm 6.5 \mu$ m, n=10, p < 0.01), and was normalized by CEI ($95 \pm 8.9 \mu$ m, n=10). The collagen density, measured by histomorphometry, was increased in HR: $11.5 \pm .8\%$, n=15 vs $8.2 \pm .7\%$, n=10 in control (p < 0.01), but remained increased after CEI ($11.9 \pm .9\%$, n=10).

Structural changes of the aortic wall induced by chronic hypertension seem to be responsible for the important decrease of the medial permeability to albumin in HR. The increase in the collagen density of the media observed in HR was not reversed by a 4 weeks CEI treatment. This accounts for the maintained decrease of the albumin uptake in CEI treated animals with a normal pressure and thickness.

BE9-A.4

Effect of Hemodynamics on the Rate of LDL Transport in Lesioned and Nonlesioned Aorta, S.A. Berceci*, S.J. Durham, D.P. Showalter, V.S. Warty, S.K. Tanksale, H.S. Borovetz

LDL transport and catabolism were studied in lesioned and uninvolved abdominal aortae of 10 WHHL rabbits and in abdominal aortae of 10 NZW rabbits perfused *in vitro* for 20 hours under "normotensive" (P = 70/40 mm Hg, Q = 50 ml/min) or "hypertensive" conditions (P = 100/70 mm Hg, Q = 100 ml/min). Freshly excised arteries were perfused with normothermic rabbit serum to which was added LDL doubly labelled with I^{131} and I^{125} tyramine cellobiose (I^{125} -TC). Post-perfusion tissue biopsies were analyzed for intact I^{131} -LDL and accumulated I^{125} -TC-labelled degradation products.

Under normotensive conditions, the plasma LDL flux in WHHL lesioned aorta was 4.28 nl/mg/hr, 1.5 times larger than in uninvolved WHHL aorta (p < 0.001) and 2.9 times above that in NZW aorta (p < 0.001). Under hypertensive conditions, the plasma flux in WHHL lesioned aorta was 7.54 nl/mg/hr, 1.7 times larger than in uninvolved WHHL aorta (p < 0.001) and 2.5 times above that in NZW aorta (p < 0.001). The study suggests that hypertensive hemodynamic conditions exacerbates the already elevated flux of LDL into atherosclerotic tissue.

BE9-B.1

Cultured Endothelial Monolayers: A Model for Transport Studies, R. Bizios*, R.S. Cargill, R.D. Iveson, and L.A. Holleran, Department of Biomedical Engineering, Rensselaer Polytechnic Institute, Troy, New York, 12180-3590, U.S.A.

Cultured endothelial monolayers provide a model for investigating the transport properties of endothelium under experimental simulation of various conditions (such as hyperoxia and anoxia) which induce and/or contribute to cell injury. Measurements of mass flux across the monolayers *in vitro* provide a quantitative index of the time course of cell injury.

Bovine pulmonary artery endothelial monolayers were grown to confluence on polycarbonate (0.8 μ m pore diameter) membranes. Transport of albumin was studied under a 4 gm percent concentration gradient at 37°C and over a 2 hour period. Abluminal albumin concentrations were determined by the Lowry assay.

Permeability coefficients of the endothelium were calculated from the mass flux data and were in the order of 10^{-5} cm/sec. The results indicate that in addition to endothelium other subendothelial tissues and/or cells contribute significantly to the resistance to transport across the blood vessel wall. (Supported by the Whitaker Foundation).

BE9-B.2

Mass transport properties of different blood vessels. M. J. Lever* and M.T. Jay. Physiological Flow Studies Unit, Imperial College, London, SW7 2AZ

We have re-examined the nature of the variation of the transport of materials between the blood and vessel walls at different sites in the circulation. This subject has been examined in many previous studies and differences found in the rates and extent of tracer uptake at different sites have been attributed to many factors, including differences in the shape or turnover of endothelial cells, in the properties of the glycocalyx, in the number of plasmalemmal vesicles and in local blood pressure and flow.

Our studies have included measurements of both the short-term and steady-state uptake of tracers by different vessels in vivo and also of the equilibrium uptake of tracers by those vessels and their hydraulic conductivities in vitro. Steady-state tracer levels in different vessels in vivo appear to be related in part to the distribution volumes of the tracers in the wall tissue and in part to the permeabilities of the different layers of the vessel wall.

BE9-B.4

Microarchitectural Changes of Human Aortic Bifurcations with Reference to Atherogenesis, Y. Yoshida*, T. Oyama, T. Yamane, M. Mitsuata, T. Yamaguchi, and G. Ooneda², Yamanashi Medical College, 409-38, Yamanashi, 1 National Cardiac Vascular Center Research Institute, 565 Osaka, 2 Geriatrics Research Institute and Hospital, Maebashi 371, Japan

Apical and outer wall intimas at branchings of inferior mesenteric arteries from aortas of human autopsy cases were investigated. The outer wall intima, a low shear stress region, was thicker than the apical intima, a high shear stress region, except in cases younger than one month. Deposit of β -lipoproteins in the outer wall intima increased with age, but not that in the apical intima. Electron microscopic studies revealed that collagen fibers increased markedly in the apical intima in the third decade. Among the dense collagen fibers, intimal smooth muscle cells (SMC) exhibited contractile phenotype. The outer wall possessed mucinous intima accompanied with synthetic SMC. Atherosclerotic rabbit intimal SMC cultivated on type I collagen gel increased cAMP production to change phenotype from synthetic to contractile and to suppress DNA synthesis. As a result, blood flow dynamics may induce cellular and microarchitectural changes in vessel walls which are favorable or resistant to atherogenesis.

BE9-B.3

Time dependent filtration in a porous elastic cylinder-Application to Water transport in the artery wall, Girija Jayaraman, Centre for Atmospheric Sciences, I.I.T., Hauz Khas, New Delhi-16.

The time dependent filtration of water through the wall of a soft porous elastic cylinder is studied theoretically. The artery wall is modelled as a mixture of an incompressible liquid and porous elastic solid whose permeability is a function of the applied pressure. The luminal pressure is considered to be harmonic in time and the matrix is assumed to be elastically and hydraulically isotropic. Analytic solutions are presented for some simple relations between pressure and permeability but numerical results are found for more general relations. Special features of the pressure distribution across the wall are discussed for the important particular case when the characteristic consolidation time is large compared to the characteristic load time.

BE9-B.5

The study on the role of hemodynamic forces in the development of atherosclerotic lesions, N. Sakata, K. Kawamura and S. Takebayashi, Fukuoka University, Fukuoka, Japan

At the present time, there are conflicting hypotheses concerning the hemodynamic mechanisms of the atherogenesis. One is Fry's "shear stress hypothesis"; the other Caro's "boundary layer diffusion hypothesis". In order to clarify the role of hemodynamic forces in the development of human atherosclerotic lesions, we have studied the localization of atherosclerotic lesions and morphological changes of endothelial cells over the atheromatous plaques. Early atherosclerotic lesions occurred predominantly at the outer walls of bifurcations and distal to the center of the inner curvature at curves, where wall shear stress is considered to be low. In contrast, the flow divider of bifurcations and the outer curvature of the bends, presumably high shear regions, were free of the lesions. Endothelial cells over the atherosclerotic lesions were significantly less elongated and had more prominent microvillous projections as compared with those in lesion-free areas. These results suggest that focal hemodynamic forces, presumably low shear stress, are implicated in the development of the atherosclerotic lesions as related to morphological changes of endothelia.

**BE9-C.1
LOCALIZATION AND SIZE OF EARLY SUDANOPHILIC
LESIONS IN CHOLESTEROL-FED RABBITS**

Margot R. Roach*, Christine Zeindler, and Ralph Kratky
The University of Western Ontario
London, Ontario, Canada. N6A 5C1

We have developed a method to cast aortas of rabbits with Batson's methyl methacrylate. Casts made at 100 mm Hg shrink to a size equivalent to that at 78 mm Hg (diastolic pressure). The tissue is digested off with 0.1 N KOH, and then analyzed with the scanning electron microscope. Segments of cast are mounted on a spit so all sides can be viewed. Composite photographs are analyzed to show the location and size of the plaque which is identified by: i) small fragments of material, probably elastin, ii) cells, and iii) a rough surface. The length of the plaques is measured at 10° intervals on a polar grid.

The earliest lesions, after one week on a 2% cholesterol diet, were lateral. By two weeks they were spreading more distally. The area of the lesion was related to the area of the branch in any one rabbit. Since the size of the branch is roughly related to the flow, this suggests that branch flow determines the size of the lesions.

Supported by the Heart and Stroke Foundation of Ontario.

**BE9-C.3
Localization of Human Atherosclerotic Lesions**
J. Fredrick Cornhill*, Edward E. Herderick
The Ohio State University, Columbus, Ohio

The topographic distribution of atherosclerotic lesions has been a prime factor in suggesting a role for hemodynamic forces in atherogenesis. Probability-of-occurrence maps of the human aorta for sudanophilia and raised lesions and average thickness maps were created using image processing (n=237; B & W; 15-34 years). In the thoracic aorta, high probabilities of sudanophilia were associated with the dorsal surface (from 30% to > 50%) while the ventral surface was virtually spared (< 10%). The regions of the highest probability of sudanophilia (> 50%) were located midway between the origins of successful pairs of intercostals. The intercostal flow dividers were spared. In the abdominal aorta, the dorsal distribution of sudanophilic lesions observed in the thoracic aorta continued with regions of high probability being located midway between the lumbar ostia (> 30%). Regions of high probability were associated with the inflow tracts of the celiac, superior and inferior mesenteric (IM), and right and left renal ostia (> 50%). Regions distal to all ostia and the apex of the aortiliac bifurcation were spared (< 10%). A region of high probability was also observed along the ventral aortic surface extending from the level of the renal ostia to the origin of the IM. The association of the disease with specific geometric entities suggests that hemodynamic forces probably play a role in the localization of some of these lesions; however, this role is probably played in concert with many other important localizing biochemical, cellular, mass transport, and structural factors.

**BE9-C.2
Flow Patterns and Distribution of Atherosclerotic
Lesions in Human Coronary and Cerebral Arteries,**
T. Karino*, S. Mabuchi and T. Asakura, Montreal
General Hospital, Montreal, Quebec, Canada.

To investigate the potential role of fluid mechanical factors in the localized genesis and development of atherosclerotic lesions in man, the exact anatomical locations and the flow patterns at such sites in the human coronary and cerebral arteries were studied in detail by means of flow visualization and high speed cinemicrographic techniques using isolated transparent coronary and cerebral arteries prepared from humans postmortem. It was found that in both coronary and cerebral arteries, atherosclerotic lesions were localized exclusively at the outer walls (hips) of major bifurcations and T-junctions, and at the inner wall of curved segments where flow was either slow or disturbed with the formation of slow recirculation and secondary flows and where wall shear stress was low. In no instance, were atherosclerotic lesions found at and around the flow divider where fluid velocity and wall shear stress were high and where the formation of early atherosclerotic lesions have been observed in experimental animals fed high-cholesterol diets. The results indicate that there is a strong correlation between the sites of low flow velocity (low wall shear stress) and the preferred sites for the genesis and development of atherosclerosis in man.

**BE9-C.4
Atherogenesis as an adaptive process gone
wrong? The roles of hemodynamics and arterial
geometry, M. H. Friedman*, The Johns Hopkins
University Applied Physics Laboratory,
Laurel, Maryland 20707 USA**

Hemodynamic measurements made in our laboratory and others' show that the fluid dynamic shear stress at the vascular wall is remarkably similar in different segments of the human arterial tree. The possibility that this similarity could reflect adaptive processes in the wall is consistent with a model of intimal thickening recently developed to explain the complex dependence of intimal thickness on mural shear seen in a collection of human arterial bifurcations. According to this model, the intima eventually becomes thickest at sites exposed to relatively low or oscillatory shear stresses. If the thickening process is mediated by sensed shear and the regional vascular geometry is such that the shear is locally reduced, then inappropriate focal thickening could result. Thickening would be further enhanced if, in contrast to the situation in straight segments, intrusion into the lumen results in a further reduction of wall shear. This situation would be exacerbated in vascular segments whose specific geometric parameters are such that wall shear is inordinately reduced at susceptible foci.

271

BE9-C.5

WALL STRESS AS A MAJOR CONTRIBUTOR TO ATHEROSCLEROSIS. M. Thubrikar*, R. Eppink, S. Nolan, University of Virginia, Charlottesville, Va.

Atherosclerotic lesions generally occur at arterial branch sites, which are also the sites of stress concentration produced by intra-arterial pressure. Wall stresses were determined at the bovine circumflex coronary arterial branch using finite element analysis. The arterial branch was modeled as intersecting cylindrical shells incorporating variations in the branch geometry, thickness, and material properties. In rabbits fed a high cholesterol diet, we explored whether atherosclerotic lesions could be inhibited by reducing wall stress. To reduce the wall stress, peri-arterial casts were placed at lowered arterial pressure at the left renal arterial branch and at the aortic bifurcation. The results indicate that in the bovine coronary artery the wall stress was 3-4 times greater at the branch than in straight segments. In rabbits, atherosclerotic lesions were inhibited at selected sites only when the wall stress was reduced by cast placement. Hence, wall stress appears to be a major contributor to atherosclerosis.

BE9-D.2

Enhanced Low Density Lipoprotein (LDL) Receptor Expression in Cultured Bovine Arterial Endothelial Cells (BAEC) Exposed to Elevated Fluid-Imposed Laminar Wall Shear Stress. EA Sprague, SA Logan, EH Edwards, CJ Schwartz and RM Nerem. University of Texas Health Science Center, San Antonio, Texas and Georgia Institute of Technology, Atlanta, Georgia

Our previous studies have demonstrated that cultured BAEC exposed to a high laminar wall shear stress (HS, 30 dyne/cm²) exhibit an enhanced receptor-mediated endocytosis of LDL relative to either low (LS, <1 dyne/cm²) or no shear (NS) stress. The objective of this study was to determine whether this enhanced LDL endocytosis was due to a change in LDL receptor affinity and/or number. Using new large capacity parallel plate viscometers connected in series, confluent BAEC on polyester sheets are exposed to HS, LS, or NS in the presence of circulating lipoprotein deficient medium to maximize LDL receptor expression. After 24 hr, the sheets (98 cm²) are removed and subdivided for 4°C binding studies using increasing concentrations of ¹²⁵I-LDL. BAEC exposed to HS exhibited an increase in LDL receptor number without a change in affinity relative to cells exposed to LS or NS. These data were confirmed in similar binding studies using a radiolabeled monoclonal antibody (IgG-C7) specific for the LDL receptor. Our results indicate that shear stress signals are recognized and transduced to influence important cellular functions including LDL receptor expression.

BE9-D.1

Platelet Adhesion to Endothelial Monolayer in vitro, T. Takano*, C. Mineo and R. Hashida, Department of Microbiology and Molecular Pathology, Faculty of Pharmaceutical Sciences, Teikyo University, Sagamiko, Kanagawa 199-01, Japan.

Platelet adherence and subsequent aggregate formation on damaged vessel walls may be fundamental events in the initiation of an atherosclerosis.

To study the mechanisms of platelet adhesion to endothelial injury, we developed a novel model in tissue culture system. The porcine aortic endothelial cells cultured on gelayed type I collagen supported by a dacron sheet were injured according to a removal of teflon rings. Rabbit platelets labelled with ⁵¹Cr were counted to measure the amount of platelet adhered to injured part of the cell monolayer quantitatively. In this system it was found that both fibronectin and fibrinogen were essential to platelet adhesion in addition to collagen. This in vitro model should be useful to elucidate the mechanisms of platelet adhesion, which may be connected with atherogenesis induced by blood flow related stresses.

BE9-D.3

EFFECTS OF SHEAR STRESS ON ENDOTHELIAL CELL PROTEIN SYNTHESIS, S. G. Eskin*, K. J. Angelides, B. Wible, L. T. Navarro, L. V. McIntire; Depts. of Surgery and Physiology and Molecular Biophysics, Baylor College of Medicine, Dept. of Chemical Engineering, Rice University; Houston, Texas, U.S.A.

Cultured bovine aortic endothelial cells were subjected to steady shear stress (25 dynes/cm²) in an in vitro flow system, to investigate biochemical changes resulting from hemodynamic forces. After shear stress periods from 6 to 24 hrs., the cells were labeled with 0.25 mCi/ml ³⁵S-methionine for 30 min. followed by a cold chase with complete medium for 30 min. Radiolabeled synthetic proteins were separated by 2 dimensional gel electrophoresis. Isoelectric focusing gels were run in the first dimension under nonequilibrium conditions. SDS polyacrylamide slab gels with a 4-15% linear gradient were run in the second dimension. Autoradiograms of gels from shear stressed cells show differences in location and intensity of proteins synthesized. Differences to be analyzed are proteins from shear stressed cells which are not present in controls, indicating the synthesis of new proteins, and clear changes in spot intensity between experimental and control cells which we have observed.

BE9-D.4

Effect of Hydrodynamic Stress on Intracellular Metabolism of Human Umbilical Vein Endothelial Cells, L. V. McIntire[†], M. U. Nollert, S. Diamond and S. G. Eskin^ψ, Biomedical Engineering Laboratory, Rice University, Houston, Texas, USA, 77251 and Department of Surgery, Baylor College of Medicine^ψ, Houston, Texas, USA.

The role of steady and pulsatile shear stress on human umbilical vein endothelial cells (HUVEC) intracellular metabolism was investigated using a parallel plate flow chamber. HUVECs were cultured as monolayers which formed one side of the chamber. Cells were incubated with ¹⁴C-labeled arachidonic acid prior to flow exposure. HPLC coupled with scintillation counting was employed to quantitate the kinetics of metabolite formation. In some cases, specific metabolites were confirmed using radioimmunoassay. Stresses in the physiological range (0-30 dynes/cm²) have dramatic effects on HUVEC arachidonic acid metabolism. Both the magnitude and rate of change of stress appear to be important. Possible biochemical mechanisms of stress signal transduction and implications for protein synthesis regulation are presented.

BE9-E.1

Cytoplasmic Calcium Response to Fluid Shear Stress in Vascular Endothelial Cells. J. Ando and A. Kamiya. Research Institute of Applied Electricity, Hokkaido University, Sapporo 060 Japan

Vascular endothelial cells modulate their structure and functions in response to changes in hemodynamic forces such as fluid shear stress. We have studied how endothelial cells perceive the shearing force generated by blood flow and the substances(s) that may mediate such a response. We identify cytoplasmic free calcium ion (Ca⁺⁺), a major component of an internal signalling system, as a mediator of the cellular response to fluid shear stress.

Cultured monolayers of bovine aortic endothelial cells loaded with the highly fluorescent Ca⁺⁺-sensitive dye Fura 2 were exposed to different levels of fluid shear stress in a specially designed flow chamber, and simultaneous changes in fluorescence intensity, reflecting the intracellular free calcium concentration ([Ca⁺⁺]) were monitored by photometric fluorescence microscopy. Application of shear stress to cells by fluid perfusion led to an immediate several-fold increase in [Ca⁺⁺] within 1 minute, followed by a rapid decline and finally a plateau somewhat higher than control levels during the entire period of the stress application. Repeated application of the stress induced similar peak and plateau levels of [Ca⁺⁺] but at reduced magnitudes of response.

BE9-D.5

MECHANISM OF HEMODYNAMIC SHEAR STRESS STIMULATION OF ENDOTHELIAL CELLS

J.A. Frangos* and A. Bhargyalakshmi
The Pennsylvania State University, Department of Chemical Engineering, University Park, PA

Blood rheology is a major modulator and effector of vascular cell response. One of the aspects of blood rheology that appears to be important is fluid shear stress on the endothelium. Changes in cell morphology, cytoskeleton, pinocytosis and metabolism are well documented. Using prostacyclin production as a sensitive marker of the endothelial cell response, we investigated the mechanism of shear stress stimulation of endothelial cells. The onset of shear stress leads to a transient burst in prostacyclin production which plateaus to an elevated steady state level. Increasing levels of shear lead to increased long-term production rates. Chelation of extracellular calcium by 2mM EGTA inhibited the steady state phase, while chelation of intracellular calcium by 30 μM quin-2 inhibited both initial and steady state phases. Inhibition of intracellular calcium mobilization by TM-8 inhibited only the initial phase. The calcium channel blocker nifedipine had no effect. These results suggest that the onset of shear leads to intracellular calcium mobilization, while extracellular calcium influx occurs in the long-term, but not via voltage sensitive channels.

This work was supported in part by NSF-EET 8708692 and PHS/Biomedical Research Support Grant.

BE9-E.2

RESPONSES TO SHEAR STRESS OF A CULTURED VASCULAR ENDOTHELIUM

L. Tamisier, A. Caprani, P. Péronneau*.
INSERM U. 256, Hôpital Broussais, Paris, France.

Endothelial cells from human umbilical vein, cultured under hydrodynamic stress are investigated in order to specify the role played by the flow. The stress conditions are applied as soon as the beginning of the culture in order to be in steady state when the cell layer is confluent. Electrical impedance measurements of the layer are performed to characterize the different structures of the layer and to detect their modifications. Thus we obtain a value of the junction resistance and of the membrane capacitance, and an electrical characterization of the extracellular matrix and of the macromolecular layer adsorbed on the cells. We follow the time variation of these parameters during a shear stress step and after comeback to the initial value. We show that all these parameters are modified by the shear stress variation with high time constant values (several hours). In particular, we show at the junction level an increase of the permeability that leads to an obstruction by the macromolecules of the medium.

BE9-E.3

Relation between Wall Shear Stress and Micro-filament Bundles in Endothelial Cells in Canine Coronary Artery *in vivo*, A.Kitabatake*, J.Tanouchi, M.Uematsu, K.Ishihara, K.Fujii, Y.Yoshida, H.Ito, M.Hori, M.Inoue, T.Kamada, The First Dept. of Medicine, Osaka University School of Medicine, Osaka 553, Japan.

To elucidate the mechanism of atherogenesis with respect to local flow dynamics in the coronary artery, we investigated the relation between shear stress (SS) *in vivo* and the amount of microfilament bundles (MF) in the endothelial cells (EC) in the left anterior descending coronary artery (LAD) of 5 mongrel dogs. We obtained phasic flow velocity profiles using a 20 MHz multigate pulsed Doppler flowmeter. SS was determined as the velocity gradient at each wall multiplied by the blood viscosity. The velocity profile at its peak velocity in LAD skewed toward the outer side. Thus the peak SS at the outer side was greater than that at the cardiac side (44.8 ± 5.5 vs 21.2 ± 4.3 dyne/cm², $p < 0.01$). The amount of MF in EC was evaluated by transmission electron microscopy as the ratio of the area filled with MF to the total area of EC (F/C). F/C at the outer side was greater than that at the cardiac side (18.9 ± 9.8 % vs 14.4 ± 7.1 %, $p < 0.05$). These results suggest that in the canine coronary artery, MF in EC increases under the condition of high shear stress *in vivo* as an adaptation to its mechanical stress environment.

BE9-E.5

Pulsatile Shear Stress Effects on Cultured Vascular Endothelial Cells. M.J. Levesque* and R.M. Nerem, Georgia Institute of Technology, Atlanta, Georgia 30332, U.S.A.

The influence of pulsatile shear stress on vascular endothelial monolayers has been studied using cultured bovine aortic endothelial cells on a Thermanox plastic cover slip positioned in a parallel plate, laminar flow chamber. Both steady and pulsatile shear stresses were employed, with peak values ranging as high as approximately 100 dynes/cm² and with exposure times up to 24 hours. The pulsatile flow environment consisted of a mean shear stress upon which a 1 Hz, sinusoidal, non-reversing component was superimposed. Measurements included both cell shape and cell mechanical properties for confluent monolayers and cell proliferation for subconfluent monolayers. The results indicate that pulsatile shear stress produces significantly enhanced responses compared to that due to a steady shear stress. The results also suggest that vascular endothelial cells cannot only recognize a fluid mechanic signal but can differentiate between steady and pulsatile flow. This ability to recognize differences in hemodynamic environment may be an important factor in the determination of the focal pattern of atherosclerosis.

BE9-E.4

Viscoelastic Property of Cultured Porcine Aortic Endothelial Cells measured by the Micropipette Technique, M. Sato*, N. Ohshima and R. M. Nerem, Univ. of Tsukuba, Ibaraki 305, Japan and Georgia Inst. of Tech., Georgia 30332, U.S.A.

Viscoelastic properties of cultured porcine aortic endothelial cells were measured using the micropipette technique for normal cells (mechanically or trypsin detached from the substrate) and the cells of which cytoskeletal elements were disrupted by cytochalasin B or colchicine. In the micropipette technique, a part of the cell was aspirated into the tip of the micropipette under a microscope by applying stepwise an aspiration pressure, ΔP . The time course of the aspirated length, L , into the pipette was measured from a TV monitor screen by replaying the recorded video tape. The data was analyzed in the form of the time course changes in the stiffness parameter of the cell, $K = R \times \Delta P / (L/R)$, where R is the pipette radius. It was found that the creep deformation process of the cells was composed of two different phases. The stiffness parameter was expressed as an exponential function of time in each phase.

BE9-F.1

Flow Induced Proliferation of Endothelial Cells H. Masuda*, K. Tohda, K. Kawamura, T. Shozawa, & A. Kamiya, 2nd Department of Pathology, Akita University School of Medicine, Akita, Japan, and Research Institute of Applied Electricity, Hokkaido University, Sapporo, Japan

It is known that vascular diameter is dependent on blood flow, although its mechanism has not been fully understood. We observed the morphological change of the endothelial cells which are loaded by high blood flow. Arterio-venous anastomosis between the common carotid artery and ipsilateral external jugular vein was constructed in dogs and rats. Endothelial cells in the shunted common carotid artery proximal to anastomosis where blood flow increased were observed histologically and ultrastructurally. After 4 weeks, they increased from about 3,000/mm² to 6,000/mm² either in dogs or rats. A tracer study using Bromodeoxyuridine (BrdU) indicated that they proliferated with cell division. Relative artery stenosis, about 2/3 of internal lumen, was constructed to the common carotid artery of dogs. After 4 weeks, in the stenotic portion where blood flowed in high velocity, endothelial cells were also much increased. We think elevated blood flow induces endothelial cell proliferation, which should be important to understand the role of blood flow in atherogenesis.

BE9-F.2

The Evidence of a New Method for Screening of the Atherosclerosis Based upon the Pulse Wave Velocity

Tan Qing, Dazong Jiang*, Institute of Biomedical Engineering, Xi'an Jiaotong University, Xi'an, China

According to Moens-Korteweg equation, pulse wave velocity (PWV) will rise with the increasing of Young's modulus and thickness of blood vessel wall and decreasing of the vessel radius. It suggests that PWV will rise in patients with atherosclerosis and can be used to diagnose such disease. It is preferable that the vessel between aorta valve and carotid artery is chosen for measurement for many reasons. We define a new parameter as pulse wave transmission time (PWTT) in this vessel segment and it can be measured on phonocardiogram (PCG) and CPT simply. Because the true length of the vessel is very hard to measure noninvasively but it is closely related with subject's height, we prefer PWTT as an indicator rather than PWV where height is considered. Also several other factors are thought to have influence to PWTT in normal subject, such as blood pressure, body weight, sex, age, and mass index which should be considered. By a large amount of measurements on healthy volunteers (more than 200), 5 nonlinear multivariate statistical models were given and one of them is thought to be practical in diagnosis where PWTT is non-linearly related with height and age only. The difference between PWTT measured and the expect healthy PWTT given by our model is considered to be the diagnosis criterion. It is proved that can distinguish the man healthy or ill by many measurements with patients who were diagnosed with atherosclerosis. This result shows the new noninvasive diagnosis method for atherosclerosis disease is feasible, especially for mass screening.

BE9-F.4

Atherosclerosis Research Using MRI with Three-dimensional Vessel Reconstruction, J. Hale*, J. Rapp, X-M. Pan and L. Kaufman, UCSF-RIL, 400 Grandview Drive, South San Francisco, CA 94080 USA

MRI is known to be effective in showing vascular pathology. However, it has not been used extensively in clinical situations. One reason is the difficulty for those unfamiliar with tomographic images to understand them as they are most commonly displayed. We have developed software that converts cross-sectional images into the angiographic formats surgeons are more accustomed to analyzing. The software also reveals information not shown in the standard magnitude displays and films. Using three-dimensional reconstruction we have demonstrated a method of characterizing lesions that is potentially more accurate than angiography, at least for large vessels. Our most recent work has been to explore the ability of MRI to detect the presence of thrombus. Early results are encouraging, and we are incorporating this new data into the three-dimensional display software.

BE9-F.3

Multi-channel Doppler ultrasound studies of arterial blood flow in human subjects: effects of interventions, including vasoactive agents. C. G. Caro*, N. Watkins, K.H. Parker, M. J. Lever, C. J. H. Jones, Physiological Flow Studies Unit, Imperial College, London, SW7 2AZ

The occurrence of atheroma in arteries appears to be correlated with the blood flow pattern. In adult human subjects the disease occurs preferentially at sites where the time-average wall shear is low. It has been found that these are also sites where the shear undergoes small pulsatile excursions and large variations in direction during the cardiac cycle. It is possible to alter the arterial blood flow pattern by means of pharmacological agents and cigarette smoking. We are now extending our studies on blood flow in the superficial femoral artery of healthy subjects using a multi-channel Doppler ultrasound device. The device provides velocity profiles during the cardiac cycle as well as spatially averaged values. We are attempting to examine the effects of various interventions.

BE10-A.1

Heart Rate Variability in Adults and Infants - An Overview R I Kitney*, Department of Electrical Engineering, Imperial College, London SW7 2BT, UK.

The field of heart rate variability (HRV) analysis in adults and infants has expanded rapidly over the last few years. The paper will review these developments both in terms of signal processing and modelling and will provide an introduction to the HRV workshop. Key areas to be covered are normal and abnormal HRV patterns in adults, and the use of HRV analysis in the study of autonomic neuropathy. HRV development in babies will also be discussed and the differing patterns of activity during the first year of life described. The final section of the paper will consider the role of HRV analysis in the study of SIDS.

BE10-A.2

Spectral analysis of variability in neuro-vegetative control systems: why and when?
John M. Karemaker,* Dept. of Physiology, AMC
Meibergdreef 15, 1105 AZ Amsterdam, NL

Recent literature has shown a revival of interest in the analysis of biological oscillators.

Especially the quantification of variability in an easily measurable parameter such as heart rate has found many supporters. Parameters extracted from such spectra have been used to quantify alertness, psychological stress or cardiac health. However, the widespread application of this technique seems more likely linked to the distribution of computing power than to our increased knowledge of the underlying physiology. Basic issues still are: is an observed periodicity due to

- a. a central nervous system instability in the 'circuitry' that controls the observed phenomenon (temperature, respiration, blood pressure, heart rate), or
- b. the fortuitous outcome of a set of coupled oscillators, both in the CNS and periphery, or
- c. the 'tuned filter' behavior of a control loop, set in motion by noise-like perturbations?

As long as these questions are not settled we should refrain from too much interpretation of too scanty data on too complex a system as is an 'unsedated subject, sitting quietly in a chair'.

BE10-A.4

A model of short-term blood pressure and heart rate variability.
J.J. Settels*, K.H. Wesseling, BMI-TNO, Academic Medical Center, Amsterdam, the Netherlands.

A continuous blood pressure recording shows surprising variability. Short term variability includes components with periods of a few seconds to several hours. The most powerful short term blood pressure stabilizing mechanism is the baroreflex, and the question is raised whether blood pressure variability exists in spite of the baroreflex or is mediated by the baroreflex. Blood pressure and heart rate variability were studied using noninvasive and invasive registrations on patients and healthy subjects in conjunction with a model of a baroreflex and cardiopulmonary reflex controlled circulation. In the time domain, the significant level shifts in mean pressure sometimes observed in the 24 hour day are difficult to reconcile with a properly functioning baroreflex, but can be reproduced by baromodulation i.e. modulation of baroreflex loop gain only, in terms of inhibition or facilitation of nervous activity. Since the baroreflex is fast acting changes in blood pressure can be fast also. In the frequency domain, proper random baromodulation together with statistically independent random modulation of the vagal reflex gain on heart rate explains the pressure and rate power density spectral components around 0.1 Hz and below 0.05 Hz taken in resting subjects. Periodic baromodulation explains spectral phenomena of respiration.

BE10-A.3

24-HOUR ANALYSIS OF HEART RATE AND ARTERIAL BLOOD PRESSURE VARIABILITY SIGNALS
S.Cerutti*, G.Baselli, M.Bertocchi, S.Civardi, A.Guzzetti, L.Furlan, A.Pagani, M.Pagani
Department of Electronic Engineering, Politecnico and Medical Pathology, University of Milano, Italy

A procedure for the analysis of 24-hour ECG and arterial blood pressure variability signals is presented. These signals are processed through spectral analysis carried out via parametric techniques. Power density spectra are obtained on 512 consecutive cardiac cycles for the whole 24-hour period and a few parameters are extracted in each spectrum (normalized power in low frequency and high frequency bands and their ratio together with the classical mean and variance values).

The plotting of such parameters provides quantitative indexes for the evaluation of the sympatho-vagal balance in the control of heart rate and arterial blood pressure.

In particular, during the nocturnal hours there is a marked increase of high frequency components and a correspondent decrease of low frequency components. This fact may be explained by the predominant role elicited by the parasympathetic system during the night.

This procedure of signal processing is actually routinely applied in a medical pathology department of a major university hospital in Milano for clinical purposes.

BE10-A.5

ASSESSMENT OF AUTONOMIC NERVOUS RESPONSES DURING AUTONOMIC STRESS TESTS BY POWER SPECTRAL ANALYSIS OF HEART RATE FLUCTUATIONS IN PATIENTS WITH IMPAIRED LEFT VENTRICULAR FUNCTION
A.Tani*, Y.Ishida, Y.Yoshida, H.Kusuoka, M.Hori, A.Kitabatake, M.Inoue, T.Kamada, K.Kimura, T.Kozuka, The 1st Dept. of Med., Dept. of Radiol., Osaka Univ. Osaka 553 Japan

To noninvasively assess the autonomic nervous activities, we developed a computer assisted method determining the autoregressive power spectral density (PSD) of ECG R-R interval fluctuations. Using this method, we studied the autonomic responses to orthostatic stress (OS) and cold pressor stress (CP) in 6 normals (NL) and 5 patients with prior myocardial infarction (MI). Mean LV ejection fraction (EF) was $62 \pm 5\%$ (mean \pm SE) in NL and $48 \pm 8\%$ in MI. PSD contained two major components in power at low (0.1Hz :LF) and high (0.25Hz :HF) frequency which have been assumed to reflect sympathetic and parasympathetic activities, respectively. With OS, LF:HF ratio as a marker of sympatho-vagal balance increased from 1.7 ± 0.6 to 9.6 ± 4.8 in NL but remained almost the same in MI. With CP, the ratio increased in both groups, 1.7 ± 0.6 to 4.5 ± 2.5 in NL and 1.1 ± 0.5 to 6.5 ± 2.0 in MI. Thus in MI patients with decreased LVEF, the autonomic response to OS is blunted indicating decreased baroreflex responsiveness, although the response to CP is preserved.

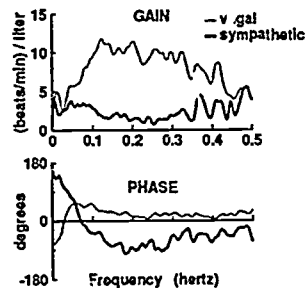
276

BE10-B.1

RESPIRATORY SINUS ARRHYTHMIA: A PROBE OF AUTONOMIC CONTROL OF THE HEART

J. Philip Saul*, Ronald D. Berger, Richard J. Cohen
Harvard Medical School and MIT, Boston, MA

Modulation of both cardiac sympathetic and parasympathetic efferent activity occurs with respiration. We developed and tested an efficient new technique to noninvasively investigate autonomic cardiac control by using respiration as a frequency probe of the autonomic nervous response. The heart rate response to respiratory activity was determined in 14 normal adults during 6 minute periods in which the respiratory rate was voluntarily controlled in a predetermined but erratic fashion. Selective autonomic blockade, with either atropine (0.03 mg/kg) or propranolol (0.2 mg/kg), and changes in posture were used to dissect the sympathetic and parasympathetic contributions. The gain and phase of the frequency response functions describe how the autonomic nervous system responds to a stimulus, in this case respiration, as a function of frequency. We found that the sympathetic (standing + atropine) response is characterized by markedly reduced gain above 0.1 Hz and a phase delay, while pure vagal (supine + propranolol) modulation of heart rate is characterized by higher gain at all frequencies and no phase delay (figure). The data provide the basis for noninvasively quantifying the sympathetic and vagal components of cardiac control in an individual, and the technique should be useful in the diagnosis and management of autonomic dysfunction.



BE10-B.3

A study of the human Baroreflex System by Heart Rate Variability spectral analysis during anaesthesia

B.J.ten Voorde*, G.J.Scheffer, Th.Faes, O.Rompelman
Medical Physics Group, Vrije Universiteit Amsterdam
POB 7161, 1007 MC Amsterdam, The Netherlands

Short term regulation of arterial blood pressure is largely a function of the autonomic system through baroreceptor reflexes. Two effecter mechanisms are heart rate, mediated para- and sympathetically and vasomotor control, mediated only sympathetically. Heart Rate Variability (HRV) spectra reflect these autonomic functions in low frequency (LF) power, related to blood pressure variations and high frequency (HF) activity, respiratory sinus arrhythmia.

We developed a bedside HRV data-acquisition/processing system to perform clinical HRV studies. We studied HRV spectra during selective blockades of autonomic efferent pathways: - Blockade of vagal baroreflex control of heart rate caused a dramatic decrease of both LF and HF HRV power; - Blockade of the sympathetic baroreflex control loop of vasomotor activity through epidural analgesia did not alter HF nor LF power in HRV significantly for the group of patients studied.

The strong vagal influence on heart rate control is a well known phenomenon. The latter result though raises new questions around the origin of LF HRV, which is believed to be inherent to the vasomotor baroreflex loop. Possible explanations will be discussed.

BE10-B.2

On respiratory variations in blood pressure non-related to sinus arrhythmia, P. Riu*, J. Colominas, J. Rosell, and R. Pallas-Areny, Div. Instrumentacion y Bioingenieria, ETSI Telecom, Box 30002, 08080 Barcelona, Spain.

Blood pressure is subject to the simultaneous influence of several actions, including respiration. This produces a sinus arrhythmia (RSA) which is the main factor considered when analyzing respiratory variations in blood pressure. There is a frequency modulation of the arterial pulse wave which is apparent also in the ECG signal.

Our results in normal subjects indicate that there is a considerable difference in the cardiac frequency measured beat to beat depending on whether it is calculated from the ECG or the external pulse wave. This difference persists independently of the algorithms applied for the measurement. By subtracting both frequencies, and interpreting the result as a time signal sampled at non-regular intervals corresponding to the instantaneous cardiac period, this shows a good correlation with the respiratory signal (nasal thermistor). This indicates that, aside from the RSA, there are other respiratory influences on blood pressure, perhaps through the variation of the pulse wave velocity as pointed out by several authors.

BE10-B.4

SOME RECENT RESULTS IN THE ANALYSIS OF HEART RATE VARIABILITY IN DIABETIC NEUROPATHY

Th.J.C.Faes*, P.Lanting, B.ten Voorde, O.Rompelman, J.J.Heimans, Medical Physics Group, Free University.
POB 7161, 1007 MC Amsterdam, The Netherlands

Diabetes Mellitus may affect the autonomic nervous system. An observable effect is the change in heart rate variability (HRV), caused by the reduced innervation of the SA-node. Different techniques of HRV analysis are used to diagnose diabetic neuropathy. Spectral analyses of HRV offers an useful tool for analysing both sympathetic and parasympathetic influences on HRV.

Instrumentation has been developed that allow for on-line bedside analysis of HRV different statistical HRV-parameters as well as spectra are estimated; the results are available immediately after finishing the measurement. So far we measured HRV in 74 healthy adults and in 44 adults suffering from diabetic neuropathy. We found e.g. that in adults with diabetic neuropathy the energies in frequency bands round the respiratory frequency and the Baroreflex Oscillation Frequency (BOF) are reduced. The observation that the BOF is shifted to lower frequencies and that the BOF and the IE-value are correlated ($R=0.8$, $p 0.02$) suggests that the BOF is also under parasympathetic influence. Spectral analysis of HRV has proven to be possible in clinical practice and provides a method to analyse the sympathetic and parasympathetic influence on HRV separately.

27 17

BE10-B.5

Neonatal Vagal Tone:
Diagnostic and Prognostic Implications
Stephen W. Porges, Ph.D.
Human Development and Psychology
University of Maryland

Heart rate patterns have long been used in neonatal assessment. Underlying this research is the assumption that heart rate variability is a manifestation of central mechanisms mediated primarily via the vagus nerve. Our laboratory has conducted a number of studies demonstrating that accurate quantification of respiratory sinus arrhythmia provides a sensitive measure of cardiac vagal tone. This presentation will focus on our application of the vagal tone measure with normal and high risk neonates. Studies will be presented describing: the relationship between neonatal vagal tone and clinical outcome; the development of vagal tone in the pre-term infant; the influence of sleep state on vagal tone; the relationship between vagal tone and duration of hospitalization; the relationship between vagal tone and autonomic reactivity to medical procedures such as circumcision, lumbar punctures, and gavage feeding.

BE10-C.1

"HRV in Healthy, Fullterm Neonates",
K. Baldzer, F. Dykes, S. Jones, D. Davet and
D. Giddens; Emory University School of Medicine
Georgia Institute of Technology
Atlanta, Georgia 30332

We have studied Heart Rate Variability (HRV) in 20 normal fullterm infants during quiet sleep, between 30-60 hrs. postnatally. Using spectral analysis, we examined the following: low frequency power (.04-.20Hz), respiratory sinus arrhythmia (RSA) power (i.e., power at peak respiratory frequency +/- .2Hz), total power, and respiratory rate. For data obtained from stable 100 second records our infants fell into two groups. Group A infants exhibited a greater RSA power and lower respiratory frequencies (.5-.7Hz), whereas Group B infants had very little RSA power and frequencies of .7Hz or above. Slopes of low frequency (LF) and RSA powers vs. total power were significantly different for the two groups: Gr A: LF vs. total .32 ($r=.89$); RSA vs. total .41 ($r=.93$). Gr B: LF vs. total .73 ($r=.99$); RSA vs. total .04 ($r=.72$).

Our experience with HRV in healthy adults and in preterm infants suggests that the Group A fullterm neonates have spectral characteristics similar to adults while the Group B neonates tend toward preterm behavior. The quantitative indices derived from HRV spectral analysis in this investigation may thus be of value in the study of maturation of CR control.

BE10-C.2

A STUDY OF CARDIOVASCULAR REGULATION USING HARMONIC ANALYSIS David Gordon*, Div Cardiology, Children's Hospital of Philadelphia, Philadelphia, PA

A retrospective clinical study of 44 infants and children that had serious heart disease conducted June 1983 to July 1985 at The Children's Hospital in Boston, and The Children's Hospital of Philadelphia using a bedside monitor that performed heart rate and respiratory activity spectral analysis revealed that specific spectral patterns of 18 patients who sustained a cardiac rest differed significantly from others in the study group ($p<0.0001$). We report here the results of a double blinded clinical study from December 1986 until January 1988 on 404 patients which constituted approximately 90% of the postoperative cardiac surgical patients. The patients were monitored for approximately 24 consecutive hours after surgery. The fundamental premise of these investigations is rooted in the conjecture that quantifying fluctuations in heart rate and respiratory activity are sufficient to provide sensitive and specific indicators of impending and in process cardiorespiratory life threatening events. Implicit in this investigation is the impact that evolving patterns of surgical and intensive care management will have on the indicators discovered in the previous study. This conjecture will be tested, and the evolutionary changes in patient management will be correlated with the dynamical process studied using methods which have their origins in the harmonic analysis of multiple time series.

BE10-C.3

DETERMINATION OF SLEEP STATE USING RESPIRATORY VARIABILITY Gabriel G. Haddad*, and Tze L. Lai, Dept Pediatrics, Columbia Univ, Coll of Physicians and Surgeons, New York, NY

It is known that cardiorespiratory variables in rapid eye movement (REM) sleep are different from those in quiet sleep (QS). We thus asked whether such variables can be used for the determination of sleep state. We studied nine normal full term infants at 1 and 4 months of life. EEG, EOG, and postural muscle EMB were recorded. Means of RR interval, respiratory cycle time (Ttot) and tidal volume, and coefficients of variation (CV) of the same variables, were obtained for 30-s intervals throughout each sleep study. We developed a statistical decision rule using CV of Ttot for the classification of REM and QS in blocks of 5-min periods. Of 85 epochs staged as QS by neurophysiologic and behavioral criteria, 79 epochs (or 93%) were classified correctly as QS using our decision rule. Of 85 epochs staged as REM sleep, 84 were classified as REM sleep and only 1 misclassified as QS. We conclude that in young infants 1) the variability of cardiorespiratory parameters can separate quiet from nonquiet sleep better than the mean values and 2) sleep staging using a decision rule based on CV of respiratory cycle time can be performed with high degree of accuracy.

BE10-C.4

RESPIRATION AND R-R INTERVAL TIME SERIES IN SLEEP APNEA - Toshi-Hiro Nishimura*, Dept. of Elec. Eng., Oita Univ., Oita, JAPAN

This study describes a method of evaluation about the information of respiration and heart beat obtained from the newborn. It is possible to estimate sudden infant death syndrome in advance by investigating cross correlation between respiration and R-R interval in stationary state and sleep apnea.

The alternation of interval on wave form is calculated by the information of ECG which is detected from the newborn. The envelope on respiration waveform is calculated by the information of respiration which is detected from the foregoing newborn. This envelope is sampled every R-R interval on the information of ECG. Cross correlation between the alternation of interval on waveform from the foregoing information of ECG and the envelope on respiration which is sampled are calculated. This method is constructed so that the relation between advance and delay of respiration and R-R interval in which the value of cross correlation is large is evaluated.

By foregoing results of cross correlation, it is shown that cross correlation between respiration and R-R interval is changed from stationary state within a few minutes before nerve center type sleep apnea. By calculating automatically cross correlation between respiration and R-R interval, for example, it is possible to find just a few minutes before sleep apnea state of newborn and to inform the state.

BE11-A.1

Control-Space Diagrams for Flow Through Collapsed Tubes, C.D. Bertram*

University of New South Wales, Australia 2033

The operating points for a Starling resistor can be described on axes of pressure drop along the tube, flow-rate, and transmural pressure at the downstream end (p_{e2}), as a curved surface which is independent of external conditions, i.e. parameters up- and downstream of the tube. The stability of an operating point depends on both internal and external conditions, and so at each parameter combination the surface is partitioned differently into regions of distinct behaviour. No special advantage is then possessed by this presentation. Position on a given surface is determined by two control variables, here upstream pressure p_u and external pressure p_e . The surface can be mapped onto a plane with these axes. However, for a given p_u , the interesting behaviour regions are traversed in a relatively small p_e range about a p_e increasing linearly with p_u . The resulting control-space diagrams contain zones which cannot be attained experimentally by setting p_u then altering p_e , because \bar{p}_2 changes discontinuously as the tube collapses or changes oscillation mode. Other regions of behaviour show three distinct frequency ranges plus, at unexpectedly moderate p_u and p_{e2} , yet-higher-frequency oscillations which may be modulated by the low-frequency modes.

BE10-C.5

The Transmission of Circulatory Disturbances to the Neonatal Brain.

S Bignall,* R I Kitney and R P A Rivers
Dept of Paediatrics, St. Mary's Hospital Medical School, * Department of Electrical Engineering, Imperial College. London, UK.

Abnormal patterns of cerebral blood flow velocity (CBFV) have been shown to be associated with brain damage in the preterm infant. We have previously demonstrated that signal processing techniques applied to blood pressure and CBFV waveforms can reveal details of the regulation of brain blood flow in infants undergoing intensive care. The CBFV disturbances arise from modulation phenomena produced by respiration and spontaneous motor activity.

Hitherto these events have been considered to be stationary phenomena. However, more detailed analysis has revealed complex interactions between blood pressure and CBFV. The elucidation of these interactions requires the use of signal processing techniques which are capable of tracking non-stationary events on a short time basis. The methods which will be described are also capable of investigating the degree of chaos in the system under study.

BE11-A.2

Effect of Entrance and Outlet Rigid Pipes on Flow in Collapsible Tubes, Y. Matsuzaki* and T. Matsumoto, Nagoya University, Dept. Aeronaut. Engng., Chikusa, Nagoya, Japan 464

In order to study self-excited oscillations of a finite-length collapsible tube, a simple two-dimensional flow channel is used together with Cancelli and Pedley's one-dimensional flow theory which may account for the pressure loss due to flow separation. A flexible part of the flow channel consists of two elastic membranes, and entrance and outlet rigid parts are made of pairs of parallel rigid walls. The analysis includes the effect of longitudinal membrane tension caused by an initial strain and membrane deflection. For the entrance and outlet rigid channels, the inertia of fluid mass and viscous resistance due to the walls are also taken into account. Numerical results show that the entrance and outlet rigid channels have a great influence on the flow characteristics. For initially unstrained membranes, the amplitudes of membrane and flow oscillations are small. On the other hand, when the membranes are less flexible because of the initial strain applied, the oscillations become large and chaotic.

BE11-A.3

Characteristics of Shock-Wave propagating through a partially collapsed Rubber Tube, M. Snimizu*, Tokyo Institute of Technology, 2-12-1 Ookayama Meguroku Tokyo, Japan.

As observed in Korotokoff sound generation, a steep ascending limb (shock-wave) is formed when a compression wave is traversing down a partially collapsed blood vessel or rubber tube. Behavior of the tube in the shock-wave region has not been known well and many hypotheses are proposed. To make clear the relation between the vessel cross-sectional area and the transmural pressure (tube law) in the shock-wave region, an experimental study using a thin walled silicone rubber tube has been conducted, in which rubber tube diameter and internal pressure are measured at the same location and simultaneously. From the experiment, it has been known that, when the degree of collapse is low, the tube law obtained with the assumption of no energy loss at the shock region agrees well with the real one.

BE11-A.5

Stability of the flow through a collapsible tube mounted in a rigid hydraulic circuit, J.W. Reyn*, Delft University of Technology, Department of Mathematics, P.O.Box 356, 2600 AJ Delft, The Netherlands.

There is investigated how wave propagation in the flow through a nearly cylindrical collapsible tube filled with an incompressible, inviscid fluid interacts with the flow in the upstream and downstream rigid segments of the hydraulic circuit in which the collapsible tube is mounted. This leads to the study of eigenmodes of the classical wave equation satisfying somewhat unusual boundary conditions dictated by the matching of rigid and flexible parts of the circuit. The characteristic equation, determining the frequencies of the eigenmodes, is of a transcendental quasi-polynomial type and the location of its roots is analysed. It appears that for subcritical flow ($S < 1$) all eigenmodes are damped, whereas for supercritical flow ($S > 1$) also growing eigenmodes exist. Here S is the index being the ratio V/C , where V is the fluid speed in the collapsible tube and C the speed of wave propagation.

BE11-A.4

Flow Limitation and Flutter Phenomena in Collapsible Tubes J.B. Grotberg, N. Gavriely, T.R. Shee and D.W. Cugell, Northwestern University, Evanston, Illinois

We studied flutter in collapsible tubes as a possible mechanism for the generation of respiratory wheezes. The pressure-flow relationships and the wall oscillations of thick-walled, self-supporting latex and Silastic tubes mounted between rigid pipes were measured. We found loud hunking sounds and tube wall oscillations that occurred only when the tubes were buckled and flow-limiting, i.e. when the flow became constant and independent of downstream driving pressure. The overall range of oscillatory frequencies was 260 to 750 Hz for air flow, presenting as sharp peaks of power on the frequency spectrum. The oscillatory frequencies were higher at higher fluid velocities and with narrower distance between opposing flattened walls. The experimental data were compared with predictions of our fluid dynamic flutter theory and the vortex-induced wall vibrations mechanism. The results of the tube experiments and the theory predictions are consistent with measurements of flow limitation and wheezing breath sounds made by our group on excised dog lungs and in normal human subjects.

BE11-B.1

Flow Induced Instability of Collapsible Tubes P.M. Webster*, and C. Walsh Univ. of Toronto Inst. for Aerospace Studies, and Faculty of Medicine, Toronto, Canada.

Problems in physiologic fluid flow have stimulated the development of continuum mechanics from its infancy. Euler described the governing equations for one dimensional flow in collapsible tubes. Their solution models flow limitation in the caval and cerebral veins, the membranous urethra, the airways and elsewhere. The dynamic instabilities accompanying flow limitation, most obvious as the wheeze of forced expiration, are not modeled by these equations. Two dimensional linear models of uniform channels do yield dynamic instabilities but not flow limitation. Other approaches include relaxation oscillations, vortex shedding, and one dimensional models with longitudinal tension. Experiments with a latex membrane stretched over a rigid channel with a local minimum depth show a pressure profile similar to open channel flow limitation and aerodynamic chokes. Dramatic, growing, waves move downstream from the constriction suggesting aeroelastic flutter in the region of supercritical flow. We will present high speed photography (5000 frames/s) and preliminary numerical solutions in the context of a general review of the medical implications of such phenomena.

BE11-B.2

Simulation of Flow Pattern During Forced Expiration, D. Elad*, R.D. Kamm, and A.H. Shapiro, Tel Aviv University, Tel Aviv 69978, ISRAEL, and Massachusetts Institute of Technology, Cambridge, MA 02139, U.S.A.

Flow limitation during forced expiration is simulated by a mathematical model which is based on methods of analysis for one-dimensional flow in collapsible tubes. Airway compliance is modeled using a semi-empirical, lung-volume dependent tube law with the tethering effects of the parenchyma lumped into the wall properties of the airway. This mimics the parenchymal-bronchial interdependence for collapsed airways, and provides a more realistic representation of airway collapse. The maximal flow-volume curves generated by the model compare well with physiological data. For the first time, the pattern of steady flow downstream of the flow limiting site (choke point) is computed, including regions of supercritical flow and elastic jumps. The model examines the effects of effort in excess of that required to limit flow. In addition, the effects of airway closure and fluid compressibility are incorporated into the model and their contribution to the flow-volume curve is analyzed.

(Supported by HL-33009 and Bat-Sheva de Rothschild Foundation)

BE11-B.4

Transitions Between States of Subcritical Flow in Tubes That Do Not Close at Negative Transmural Pressure, Theodore A. Wilson*, Department of Aerospace Engineering and Mechanics, University of Minnesota, Minneapolis, Minnesota 55455 U.S.A.

Certain features of maximum expiratory flow curves of some canine lungs suggest that limiting flow through the airways is not unique. There is a maximum flow that can pass through a collapsible tube if the tube is sufficiently compliant. A lower flow is allowed at either of two values of lateral pressure and tube area. At the higher pressure, flow is subcritical; and at the lower pressure, flow is supercritical. Transitions from supercritical to subcritical flows are allowed; reverse transitions are not. If the tube does not close at large negative transmural pressures, a given flow can pass through the tube at three values of lateral pressure. It appears that transitions between the subcritical flow states, the states with the lowest and highest values of lateral pressure may be allowed. If these transitions occur, the flow through a collapsible tube with axially varying properties is not unique and flow-limitation-at-wave-speed could occur for different flows.

Supported by National Heart, Lung, and Blood Institute Grant HL-21584.

BE11-B.3

Urine flow through the ureter, D.Griffiths*, Erasmus University Rotterdam, Netherlands

The ureter is a collapsible, muscular tube that conveys urine from the kidney to the bladder. Peristaltic contractions move successively along it towards the bladder. A fundamental property of a collapsible tube is the "tube pressure" at which it collapses. At a "compressive zone" (a region of elevated tube pressure) the velocity of a flowing fluid may reach a critical value and in this case the compressive zone controls the flow pattern. A peristaltic contraction represents a moving compressive zone. Lubrication-theory analysis shows that it is potentially able to pump urine through the ureter at flow rates up to a maximum "carrying capacity". The reality is more complicated: (a) at low peristaltic frequencies sometimes no contraction is present in the ureter and uninterrupted discharge from kidney to bladder may occur; (b) urine is discharged into the bladder against an outlet resistance, including the bladder pressure itself. Many different flow patterns are possible, in most of which peristalsis acts as an inefficient pump, allowing bladder pressure changes to be transmitted to the kidney, or even hindering the urine flow. Experiments in pigs illustrate these conclusions.

BE11-B.5

A Non-Homogeneous Model for Human Expiratory Flow, R.K. Lambert*, Massey University, New Zealand.

The merging of two dissimilar flows in a tube junction is underspecified by the conservation laws of mass and energy. One more relationship is needed. The empirical equation of Wilson et al (*JAP* 59:1924-1928,1985) has been used in conjunction with the computational model of Lambert et al (*JAP* 52: 44-56,1982) to develop two-lobe models for expiratory flow from non-homogeneous human lungs. Cases investigated include both maximal and partial forced expirations as well as steady sub-maximal flows. The investigations were carried out with asymmetric peripheral and middle airways constrictions with both central and more peripheral mixing of the flows and with and without central flow limitation. The effects of variations in regional lung compliance were also studied. Supported in part by grant HL 21584.

BE12-A.1

The existence of steady flow in a collapsed tube
O.E. Jensen* and T.J. Pedley, Department of Applied
Mathematics and Theoretical Physics, Silver Street,
Cambridge CB3 9EW, England.

Self-excited oscillations arise during flow through a pressurised segment of collapsible tube, for a range of values of the time-independent controlling pressures (upstream, downstream and external). They come about either because there is a steady flow corresponding to these pressures, but it is unstable, or because no steady flow exists. We investigate the existence of steady flow in a one-dimensional collapsible-tube model, which takes account of both longitudinal tension T and jet energy loss E downstream of the narrowest point. For a given tube, the governing parameters are T , flow-rate Q , and transmural pressure P at the downstream end of the collapsible segment. For any fixed P and T there are two critical flow rates Q_1 and Q_2 . For $Q < Q_1$, two collapsed solutions exist when $E = 0$ but only one when $E \neq 0$; for $Q_1 < Q < Q_2$ there are no solutions when $E = 0$, but one solution (with the upstream part of the tube distended and the downstream part collapsed) when $E \neq 0$; for $Q > Q_2$ there exists only a solution with the tube everywhere distended and $E = 0$. The results are compared with those of Reyn (theoretical) and Bertram (experimental).

BE12-A.3

Expiratory Flow in a Collapsible Bifurcation,
D. Katz*, D. Elad, and S. Einav, Tel Aviv University
Tel Aviv 69978, ISRAEL.

The bronchial tree is a complex system of branching compliant tubes. During expiration, air is flowing from the peripheral daughter tubes into the parent tubes, until it converges to a single stream in the trachea and expelled from the mouth. The airways are flexible tubes which undergo major geometrical changes, especially during forced expiration. In this study we present a one-dimensional simulation of air flow through a simplified model of a single Y-bifurcation. The bifurcation is assumed elastic and its mechanical properties are defined by a modified tube law. The model is numerically analyzed by the two steps MacCormack method which was found suitable for such type of fluid-structure problems. Numerical calculations were performed for two different streams that enter the bifurcation with either subcritical or supercritical flows. Preliminary results show that the interaction between the daughter streams, while merging in the parent tube, ~~affect~~ affect the final flow pattern. It is also observed that the angle between the daughter tubes has a significant effect on the degree of merging of the flows. The results indicate that flow limitation (choked flow) as well as elastic jumps may occur in the parent tube due to the initial conditions at the entrance.

BE12-A.2

Dynamic Measurement of the Geometry of Fluid Filled Collapsible Tubes, D. Elad*, M. Sahar, S. Einav, J.M. Avidor, R. Zeltser, and N. Rosenberg, Tel Aviv University, Tel Aviv 69978, ISRAEL.

Physiological flows such as blood flow in veins or air flow in the lungs can be simulated by flow through collapsible tubes. When the external pressure exceeds the internal pressure, the tube is partially collapsed and attains a multitude of complex cross sections. The contour of the tube is determined by the local dynamic equilibrium between the moving fluid and the properties of the tube wall. Since any physical contact with the tube alters the dynamic equilibrium, existing techniques are capable of measuring cross-sectional areas only. The cross sectional contours have not yet been experimentally determined. Experimental data of the tube geometry is particularly important for better understanding of large amplitude wave propagation and the overall fluid dynamic behavior across an elastic jump. This work presents experimental results of fluid flow through a collapsible tube (latex tube), including the measurement of the tube geometry by a novel non-contact technique, based on the Rasterstereography method. The three-dimensional geometry of the tube is reconstructed from the images of the tube by advanced techniques of image processing. Here we report on representative results of steady flows at different combinations of flow rates and chamber pressure. However, the technique can successfully measure dynamic changes of the geometry of a fluid-filled elastic tube and provide new experimental data which is useful for analytical predictions.

BE12-A.4

Oscillations in a Collapsed-Tube Analog of the brachial artery under a Sphygmomanometer Cuff,
C.D. Bertram* and C.J. Raymond, University of
New South Wales, Australia 2033.

because the dynamics of a Starling resistor (SR) are strongly influenced by the diverging flow at the downstream end, where the most collapsed cross-section rapidly changes to the (usually) circular attachment, it has been suggested that SR oscillations have little application to physiological vessels. To demonstrate that the oscillations do not depend on the presence of an unphysiologically abrupt change from compliant to rigid tubing, a silicone rubber tube of length 30.7 inside diameters and wall thickness-to-radius ratio 0.3 was set up passing through a larger-diameter compliant tube stretched between the rigid pipes of a short SR pressure chamber, so that under external pressure the outer tube pressed on the tube and the two collapsed together. The outer tube stretch ensured that the compressive force applied to the inner tube over its central 10.3 diameters was reduced to zero smoothly at the ends of the central section. The inside diameter of the SR chamber pipes was sufficient that the inner tube passing through did not contact opposite sides even if collapsed. Operating points have been mapped as for a SR. Oscillations at frequencies from 3.2 to 320 Hz have been observed.

BE12-A.5

Numerical Simulation of Flow in the Trachea, Incorporating a Membrane Wall Model, C. Walsh*, P. A. Sullivan and J. S. Hansen, UTIAS, 4925 Dufferin St., Downsview, Ont., Canada, M3H 5T6

Flow limitation and wheezing occur during forced expiration and the quantitative observations of flow rate, pressure and frequency have been matched by previously published experimental results from a mechanical model of the human trachea. This presentation deals with a nonlinear, one-dimensional, numerical simulation of the mechanical model. In contrast to past analyses using tube law plus constant axial tension models, the present analysis leads to a natural dependence of axial tension on transverse displacement. Further, the axial tethering constraint implicit in the tube law approach can be dropped, allowing membrane inertia to enter through the wall axial equation of motion. We have examined axisymmetric flow through an annular duct with an axially tethered membranous inner wall and the dependence of axial tension on radial displacement causes only minor modifications to the predicted behaviour. It is anticipated that dropping the tethering constraint will have more dramatic consequences.

BE12-B.2

Characterization of Hemorheology in Total Artificial Heart (TAH) Implantation, T. Hung*, D. Butter, C. Yie, R. Kormos, H. Borovetz, B. Griffith and R. Hardesty, University of Pittsburgh, Pittsburgh, Pa., USA

Blood rheology was examined in 14 patients who underwent from 2 to 35 days of Jarvik-7 TAH support as a bridge to cardiac transplantation. Rheological abnormalities observed included increased RBC rigidity, increased blood viscosity and elevated fibrinogen concentration. Using the non-Newtonian Casson fluid model, blood viscosity was expressed in terms of ultimate Newtonian viscosity (UNV), yield shear stress (YSS) and shear rate. Experimental results showed that UNV for our TAH patients was within normal range, however, YSS was from 13 to 38% above normal. These results indicate that increased RBC rigidity and fibrinogen concentration are major causes of increased blood viscosity, specifically high YSS, in these patients.

BE12-B.1

The Effect of Respiratory Static Volumes on Heart Valve Sounds, C.S. Lessard, J.J. Im*, and J. Lay, Texas A&M University, College Station, TX 77843

The effect of respiratory static volumes on heart valve sounds as obtained from a tracheal microphone may provide an insight into the relationship between respiratory static volumes and heart sounds. Spectral analyses of the first heart valve sounds (HVS1), the second heart valve sounds (HVS2), and the combination of the first and second heart valve sounds (HVS3) were obtained at the four different respiratory static volume conditions, i.e., breath held following normal tidal volume inspiration, normal tidal volume expiration, functional inspiratory capacity, functional expiratory capacity. The Cooley-Tukey FFT algorithm was applied to the HVS data to obtain an estimate of HVS spectra. Descriptive statistics, i.e., peak frequency (FPK), mean power frequency (MPF), bandwidth (BW) were calculated from the frequency spectra of HVS at the four conditions. Finally, the respiratory effect on heart valve sounds was obtained by the analysis of variance procedure for a two-way classification resulting from a factorial experimental design. The results indicate that the HVS2 spectra are affected by the respiratory static volume conditions. The HVS1 spectra and the HVS3 spectra are unaffected by the respiratory static volume conditions.

BE12-B.3

Non-invasive study of hemodynamic effects of respiration on baroreflexes, M. GUERRISI* & A. MAGRINI, Fisica Medica, Università Tor Vergata-Rome-Italy, J.J. SETTELS & K.H. WESSELING, BMI-TNO Academic Medical Centre - Amsterdam - The Netherlands

Beat-to-beat variations in heart rate and arterial blood pressure during controlled respiratory maneuvers performed by 13 healthy subjects at rest were analyzed using a model of the short-term controlled cardiovascular system, including nervous reflexes from both high and low pressure receptors. Arterial blood pressure was measured non-invasively in a finger by a calibrated servo-plethysmo-manometer (FINAPRES). Mechanical effects of the respiratory maneuvers were simulated on a computer by varying the value of intrathoracic pressure in the circulatory model.

Model analysis of experimental results shows that most of the complex hemodynamic and heart rate effects due to inspiration can be explained by making a single hypothesis of temporary baroinhibition. Effects of expiration on heart rate appear to be weaker and mediated by baroreflexes via a different mechanism which remains to be further investigated.

BE12-B.4

Theoretical approach to the analysis of passive mechanical interactions between heart chambers, M. GUERRISI & A. MAGRINI*, Fisica Medica - Università Tor Vergata -- Rome - Italy

The concept of compliance of an "open elastic wall" ("wall compliance") is introduced in order to establish a theoretical basis for the analysis of global mechanical properties of adjacent elastic chambers sharing a common wall. It is shown that the proposed definition of "wall compliance" includes, as a limit case, the classical definition of compliance of a "closed elastic cavity". Theory was applied to the analysis of passive ventricular interaction on the basis of a model formulated in terms of "wall compliances". In order to test the applicability of the method proposed, reported data on excised and in situ canine hearts without pericardium were fitted with the model assuming non-linear wall compliances. Thus, the mechanical properties of the ventricular free walls and septum were separately assessed. It is concluded that the reported need to define a single "effective external pressure" for one of the ventricles, besides not being theoretically justified in the beating heart, would be overcome with the proposed approach.

BE12-B.6

A CONTRIBUTION IN ULTRASOUND PULSED DOPPLER HUMAN ARTERIAL BLOOD FLOW MEASUREMENTS DURING VASCULAR SURGERIES.

V. PUGLIESI*, P. GARCIA, N. BOCCI, R. RIEU, R. PELISSIER
Institut de Mécanique de Fluides - UM 34 du CNRS
1, rue Honorat 13003 Marseille, France
P. BERGERON, M. REGGI, R. COURBIER
Hôpital St Joseph. Service de chirurgie vasculaire. Marseille

To evaluate some criterion of quality and optimum state in arterial bypass grafting, despite routine arteriography, we have developed a perioperative methodology to measure spatio temporal blood flow velocity profile, and thus calculating the volume flow rate, assuming that the vessel is circular and velocity profile is quasi axisymmetric with respect to the measuring plane. This technique involves an easy to use elastic probe support set up close to the artery in a very good way positioning, and a low cost velocimeter which processes the crystal signals.

Emission frequency is 8 Mhz or 15 Mhz, pulse repetitive frequency is selected from 50 khz to 70 khz, doppler shift frequency to velocity signal conversion is obtained by a zero crossing method which is adequate since the sample volume is small, maximum measured velocity is about ± 1.2 m/s. A data acquisition and processing system computes in 11 to 15 channels all the numeric and graphical results in order to view them in quasi real time. The system take into account a cardiac pulses synchronization and breathing effects during measurements; so we had to integrate the velocity profiles for 30 s when processing is in progress to achieve a minimal dispersion value (<5%).

In vivo measurements have been made on 30 patients (>100 data flow measurements) before and after grafting principally at the level of carotid and femoral arteries.

BE12-B.5

Artificial Heart Geometry Determined by NMR Imaging for a Patient, C.Uyama*, S.Takatani, Y.Taenaka, H.Takano and T.Akutsu, National Cardiovascular Center Research Institute, Fujishirodai 5, Suita, Osaka, 565 Japan

When transplanting a total artificial heart to a subject, it should be connected without pulling or pushing the tissue of the remaining heart and thorax wall. In order to do so, a heart geometry, especially, geometry of the tricuspid and mitral valves, aorta and pulmonary artery should be estimated to obtain a good connection of the artificial heart. We took 12 transverse thoracic NMR images triggered by ECG. Each NMR image was taken 1cm apart, perpendicular to the longitudinal axis. Contours of pericardial heart, ventricles, atria and inner wall of thorax were entered by a digitizer into a computer. We calculated, by interpolation method, contour of each part of the heart on a plane of every 2mm apart longitudinally. Three-dimensional heart and thorax model were made by accumulating 2mm thick plastic plate whose shapes were determined by the contours. Furthermore, a remaining heart model which was made in the same way gives us sizes of the tricuspid and mitral valves and directions of these two valves and so on. These geometry thus obtained will be useful to produce the total heart suitable to a patient.

BE12-B.7

On the Transport of Sinusoidal Density Fluctuation in Catheter Flows, Q. Ye, J. S. Lee*, L. P. Lee, and M. Hunter, University of Virginia, Charlottesville, Virginia, 22908 U.S.A.

When a sinusoidal concentration is the input to the dispersive flow in a catheter, we show mathematically that the output is the input attenuated by A and shifted by t_d . This function $A \exp(-i\omega t_d)$ is the Fourier transform of the transfer function characterizing the dispersion of indicator through the catheter flow.

To verify this analysis, we imposed a unit step input to the catheter and measured the density change to establish the transfer function of the catheter. Using the same catheter, we sampled the rabbit's aortic blood and monitored its density fluctuation. In this experiment, the sampling flow rate and the ventilation frequency were varied to change the product ωt_m of which ω is the frequency and t_m the mean transit time of the catheter. The attenuation and time delay of the density fluctuation was determined in reference to the ventilation pressure. We found that the dependence of the attenuation and the time delay on ωt_m agrees with the prediction from the Fourier transform. This agreement supports the use of the transform analysis to determine the transport of density fluctuation occurring in the vascular system of the lung. (Supported in part by HL 36285).

BE12-B.8

Investigation of the Controller Models of the Human Cardiovascular System

R I Kitney,* M A Chabbani, Biomedical Systems Group, Dept of Electrical Engineering, Imperial College, London SW7 2BT, UK

Keywords: Modelling, Simulation, Cardiovascular System, Control of Central Nervous System.

Because of its complexity, describing the human cardiovascular system in quantitative terms is particularly difficult. As a result, there have been a number of attempts to produce computer models of various degree of complexity over the last twenty years. These models have varied from simple teaching simulation with only few segments to very complex models which not only model the systemic circulation in terms of large number of elements, but include cardiovascular dynamics and physiological control. It is in the area of control where significant disagreement still exists. What is required is a model which is capable of simulating physiological responses in both normal subjects and patients suffering from cardiovascular diseases, which includes an accurate model of the control function.

This paper investigates some of the key controller models available and their integration into human cardiovascular models of varying complexity. The controller models which will be discussed are capable of producing accurate simulation of cardiovascular control for a range of physiological situations including various standard validity tests.

BE12-B.10

Inner Wall Extraction of a Blood Vessel on a Coronary Cineangiogram for a Vessel Diameter Estimation, Y. Yanagihara*, T. Sugahara, N. Sugimoto, C. Uyama, National Cardiovascular Center Research Institute, Suita, Osaka, 565 Japan.

Measurement of a coronary vessel diameter is utilized to estimation of artery stenosis. Cineangiography is the best way to show us coronary arteries in a living body. As X-ray scattering makes cinepictures noisy, an accurate measuring method is required. At the first step, in order to determine which filter is the most accurate to measure blood vessel diameter on the coronary cineangiogram, several sizes of vessel phantoms on cine film taken under different energy and contrast substance densities were calculated by using several edge detection filters. The entropy and the Gaussian filters were found to be twice as accurate as the derivative filters. At the next step, in order to extract blood vessel area on a coronary cineangiogram, locations of vessels on the periphery of image is first extracted. Then, a vessel area over the image is selected. The entropy filter is applied to this area. The detected vessel edges were as accurate as that determined by a radiologist. This method can be applied to coronary cineangiograms, including stenosed sites.

BE12-B.9

The Properties of Frequency Selection of Some Arterial Beds, S.T. Young* and W.K. Wang, Yang-Ming Medical College, Taipei, Taiwan, R.O.C.

The deformation of the pressure wave as they travel through the circulation provides a way of measuring the characteristics of arterial tree. Tube model still is a generally accepted explanation of the deformation of the pulsatile pressure waves, and it can easily explain a lot of phenomena of circulation system. However, the property of the frequency selection of arteries suggested by this present supplies more reasonable explanation, especially the impedance patterns of arteries and the change ratios of each harmonic of waves when they traveling through the aorta. This study would like to emphasize a observed phenomena that each artery have different preferred frequency band, and work as filters of electrical circuit. Highpass in superior mesenteric artery, bandpass in renal artery, and complex filter in gastric artery were observed in this study. We expected there would be more filtering types identified. The experimental data supported our suggestion, and to offer a acceptable explanation for some debated issues of the circulation system.

BE12-B.11

Computer Simulation of the Human Cardiovascular System under Lower Body Negative Pressure V. K. Sud*, All-India Institute of Medical Sciences, New Delhi, India, M. W. Bungo, J. B. Charles, NASA Johnson Space Center, Houston, Texas, and R. Srinivasan, KRUG International, Houston, Texas.

The present work simulates the distribution of blood pressures and flow velocities in the entire cardiovascular system of a normal human. The cardiovascular system is modeled as an arrangement of interconnected elastic vessels. The pumping action of the heart is represented by time-varying elastance characteristics of the ventricles. The finite element model is direct and versatile in its applicability.

Solution of the model equations is obtained from a knowledge of the dimensions of the vessels, peripheral resistances of the arteriole-capillary-venule junctions, and the rheological properties of blood. The results include changes in steady and pulsatile flows due to transition from normal to stressed conditions. Of particular interest is the percentage redistribution of pressures and flow velocities in the various regions of the cardiovascular system due to lower body negative pressure stress with both normal and reduced amounts of circulating blood volume, the latter representing the effects of weightlessness encountered during space flight.

Work supported by National Research Council, USA.

285

BE12-B.12

Measurements of SVC and IVC Vascular Resistance and Compliance During Cardiopulmonary Bypass in Open Heart Surgery T.Tsuji*, K.Suma and T.Togawa, Inst.for Med. & Den. Nngng., Tokyo Med. & Den. Univ., 2-3-1, Kanda Surugadai Chiyodaku Tokyo 101, Japan

Vascular resistance and compliance during cardiopulmonary bypass(CPB) was studied in 21 cases of open heart surgery.

The venous return (Fsvc, Fivc) from the superior and inferior caval veins (SVC, IVC) were measured by an electromagnetic flowmeter. The aortic, SVC and IVC pressures (AP, Psvc, Pivc) were measured by pressure transducers.

The vascular resistance in the SVC area (Rsvc) was obtained from $(AP-P_{svc})/F_{svc}$, and that of the IVC area (Rivc) from $(AP-P_{ivc})/F_{ivc}$. The systemic resistance (Rsys) was calculated from $1/R_{sys} = 1/R_{svc} + 1/R_{ivc}$. The SVC and the IVC drainage tubes were clamped alternatively for about 6 seconds. The compliance of SVC area (Csvc) was obtained from V_{svc}/dP_{svc} (V_{svc} : accumulated volume in SVC, dP_{svc} : increased SVC pressure). The Civc was obtained in the same way as the Csvc. The systemic compliance (Csys) was calculated from $C_{sys} = C_{svc} + C_{ivc}$.

Resistance and compliance changed depending upon the time course of the CPB.

BE12-B.14

Increased right atrial contraction in patients with myocardial infarction, T. Noda*, M. Arakawa, T. Takaya, T. Nagano, K. Kagawa, S. Kojima, H. Miwa, and S. Hirakawa, Second Department of Internal Medicine, Gifu University School of Medicine, 40, Tsukasa-machi, Gifu 500, Japan

In the infarcted heart, right ventricular function is varyingly impaired, but right atrial function has never been studied. First, we made 6 casts of the cadaver right atrium(RA) and measured their volumes with Simpson's rule, filming them by biplane cineatriography. The true volumes (x) agreed with measured volumes(y), $(y=0.94x+2.1 \text{ (} r=0.99))$. Second, in 9 patients with normal heart(C-group) and 9 patients with myocardial infarction (MI-group), we constructed pressure-volume loop of the RA. The volume expelled by atrial contraction (ejection volume of the RA, RAEV, y) correlated positively with volume at the beginning of atrial contraction(preload of the RA, RAVd, x) $(y=0.42x+2.8 \text{ (} r=0.54))$. The RAEV for the comparable levels of RAVd was significantly higher in MI-group than in C-group. We conclude that the right atrial contraction is augmented homeometrically and heterometrically in the infarcted heart.

BE12-B.13

Diastolic compliance of the left atrium and the left ventricle in man, T. Nagano*, M. Arakawa, T. Tanaka, M. Yamaguchi, T. Takaya, K. Kagawa, T. Noda, H. Miwa and S. Hirakawa, Second Department of Internal Medicine, Gifu University School of Medicine, 40, Tsukasa-machi, Gifu 500, Japan

During slow filling period, 1) the left atrium (LA) and the left ventricle (LV) become a common chamber, and the internal pressure equals, and 2) blood flowing from the pulmonary vein will be distributed according to the magnitude of each chamber compliance. We studied normal relationship of chamber compliance between the LA and LV in 8 patients with coronary artery disease. We performed biplane cineatriography coupled with direct recording of LA pressure, and single plane cineventriculography. Calculating volumes of the LA and LV with area-length method, and constructing the pressure-volume relations of the LA and LV, we fitted data to the exponential function and determined diastolic compliance of the LA and LV at the end of diastasis (CL_{LA} , CL_{LV}). The CL_{LA} and CL_{LV} were 1.64 ± 0.41 (mean \pm SD) ml/mmHg/m² and 4.21 ± 1.13 , respectively. We conclude that compliance of the LV is two to three times larger than that of the LA.

BE12-B.15

Simulation Studies on the Myocardial Oxygen Supply-Demand Relation During the Valsalva Maneuver. P. Caminal*, M. Vallverdú*, R. Jane*, J.M. Augé*, C. Creixells*. Institut de Cibèrètica, Diagonal 647, 08028 Barcelona, Spain. Hospital Sta. Creu i S. Pau.

Intrathoracic and abdominal pressures are severely increased as a result of the performance of straining activities. Such activities may predispose to potentially lethal arrhythmias in patients with coronary artery disease. In order to analyse the effects of intrathoracic and abdominal pressure patterns on coronary flow, a cardiovascular system model has been developed. The model includes CNS controls of heart rate, peripheral resistance, coronary resistance, myocardial contractility and venous tone. A simulation program has been written and the model has been validated by means of in vivo data under two experimental conditions: Equilibrium conditions (Pre-Valsalva maneuver) and Valsalva maneuver (VM) phases (I to IV). In the parameter estimation stage an optimization module has been developed. It is a collection of subprograms tailored for use with the digital simulation language. The effects of higher intrathoracic pressures, longer duration of the VM and two consecutive maneuvers have been investigated using the model. Results show that the evolutions of myocardial oxygen supply-demand relation during different VM patterns are not the same for all patients. The estimated parameters of the neural control are different in each patient, with a high variability. This is the reason why a VM may be convenient for some coronary artery disease patients but very dangerous in other patients with the same pathology.

BE12-B.16

The Effect of Intra-aortic Balloon Pumping on the Myocardial Ischemia in Goats, Z.N.Xue*, H.O.Chen, L.Li and L.R.Zhang, West China University of Medical Science, Chengdu, Sichuan, China

Intra-aortic balloon pumping (IABP) can improve the balance of oxygen demand and supply for injured heart. After ligation of a coronary branch, the serious problem is genesis of cardiac arrhythmia. As arrhythmia occurred, lidocaine was used. The total dose of lidocaine given was used as estimation for arrhythmic incidence. The incidence of arrhythmia was influenced by dosage of amobarbital. IABP was started 0.5hrs after coronary ligation and maintained for 3hrs. Under similar dosage range of this anesthetics, the incidence of arrhythmia during 24 hrs after coronary ligation was much lower in IABP group than in the untreated group. Average necrotic weights of myocardium, hemodynamic parameters and ECG changes were no significant difference between these two groups. These results suggest the IABP could reduce the incidence of ischemic arrhythmia.

BE12-B.18

Three dimensional reconstruction of the human carotid bifurcation, Naoki Suzuki^{1*}, Kouji Hori², Souichiro Mochio², Yukihide Isogai², Mikio Itou³, Sachio Miyamoto³, Sinpei Tada³, Fumio Tsujimoto³, Sinpei Tada³, Tetsuo Okamura¹, Mt. Research Unit¹ Dept. of 3rd. Internal Med.² Dept. of Radiology³ Jikei Univ. School of Med., Nihon Kogaku K.K.⁴ 105 Minato-ku Tokyo, Japan

A noninvasive measurement technique producing three dimensional (3D) images of the carotid artery bifurcation has developed. Series of transverse images of the carotid arteries with 2D echography are digitalized and translated to values in 3D coordinates with distance data among each images.

Processed data are able to display on CRT as a wireframe model or a surface model. By this method we constructed 3D images of the common carotid artery (CCA), internal carotid artery (ICA), external carotid artery (ECA) and skin surface. After some clinical measurement, we confirmed following properties of this technique. Rotation and movement technique were useful to recognize the shape of bifurcation and the relative location with skin surface and helpful for the vascular operation. Dissection technique was suited for the observation of the inner shape of vessels and the structure of plaques in it. We also add the information about the distribution of blood velocities on 3D image obtained by a pulse Doppler technique. These images help us to recognize the relation with the morphological irregularity and the rheological changes in the vessel.

BE12-B.17

Frequency Domain Analysis of the Radial Artery Pulse: Age Related Changes. D. Winter, B. Mather*, Southwest Research Institute, San Antonio, Texas, M. O'Rourke, R. Kelly, St. Vincent's Hospital, Sydney, Australia.

We have monitored the radial artery pulse pressure waveform non-invasively using a high fidelity pressure transducer applied to the skin directly over the radial artery. The transducer has a small pressure sensitive area (5 mm²) with a frequency response from 0 to 2 KHz. Applanation of the artery allows the direct recording of the arterial pressure waveform. In a series of animal tests, the waveforms recorded non-invasively showed no significant difference in amplitude or phase when compared to direct intraarterial recordings.

Radial artery pulse waveforms were recorded non-invasively in 1005 subjects aged 2 to 91. Pulse waveforms for each subject were ensemble averaged and grouped by age decade. The waveforms in each decade were truncated to the shortest heart cycle in the decade and an average waveform for each decade was computed. Normalized power spectral densities were estimated using fast Fourier transform techniques. Power spectral densities showed significant differences between the first and second decade, the fourth and fifth decade and the fifth and sixth decade. The amplitude of the fundamental harmonic between each of the age groups increased and the energy in the higher harmonics decreased with age. In the first decade, energy in the third harmonic was significantly higher than in the second. By the second decade, the harmonic amplitudes decreased monotonically. The establishment of normal aging patterns allows the identification of abnormal pulses which may be related to cardiac or vascular diseases.

BE12-B.19

Volume change of the coronary circulation on a heart rate step, J. Dankelman*, I. Vergroesen* and J.A.E. Spaan**.

* Department of Mechanical Engineering, Delft University of Technology, Delft.

** Department of Medical Physics, Academic Medical Centre, University of Amsterdam, the Netherlands.

Intramyocardial blood volume depends on the compression by heart contraction. The volume change of the coronary circulation on a heart rate step has been investigated in seven anesthetized goats. Heart rate step of 30 beats/min were performed between 60 and 150 beats/min under constant pressure and under constant flow perfusion conditions. Arterial (CAF) and venous flow (CVF) were measured. The intramyocardial volume change was determined from the digitized flow signals by $(CAF - \alpha * CVF)dt$, with α the ratio between arterial and venous flow in the steady state. Blood volume decreased with an increasing heart rate.

Volume change with constant pressure perfusion conditions was 0.31 ± 0.03 ml/100g (mean \pm S.E.) and with constant flow perfusion was 0.13 ± 0.02 ml/100g.

Model simulations, in which the venous resistance is dependent on transmural pressure, could explain the difference in volume change between constant pressure and constant flow perfusion.

BE12-B.20

Optimal Design of Vascular Grafts
A. I. Rachev; Institute of Mechanics
and Biomechanics, 1113 Sofia, Bulgaria.

There exists an increasing interest in fabricating synthetic grafts with compliance similar to that of the natural arteries. The purpose of this paper is to propose a method for optimal, from mechanical view point, design of grafts made of synthetic material whose elastic properties can be controlled. It is supposed that the initial dimensions and the mechanical behaviour of the artery to which the graft is anastomosed are given. The internal diameter and the wall thickness of the graft as well as the values of the constants in the constitutive equations for its material are to be determined by means of multiobjective optimization. Two partial criteria of optimization are defined - the distance between the functions representing the internal diameters of the artery and the graft over the physiological pressure range and the distance between the characteristic impedances. A global criterion for selection of the preferable solution is proposed. Examples of grafts made of composite material are considered.

BE12-B.21

Densitometric Method for Derivation of Left Ventricular Ejection Fraction from Cineangiographic Films. M. Niczan*, D. Sapoznikov, M. Mossery, Y. Mahler and M. Gotsman, Jerusalem College of Technology, Jerusalem 91160, Israel

Left ventricular (LV) volume and ejection fraction (EF) are routinely derived from cineangiographic films obtained during catheterization. By injecting contrast medium LV volumes can be calculated from LV silhouettes, using various assumptions regarding LV geometry. However, for patients having abnormal ventricular function, these assumptions are not always justified.

In cineangiographic films, the grey level of each pixel in the LV region is proportional to the depth of the LV cavity at the corresponding point. EF can be derived from the values of the integral grey level all over the LV region, obtained at two successive diastoles, assuming that: 1. The contrast medium is distributed homogeneously all over the ventricle. 2. The amount of contrast medium at the second diastole is the same as that at the previous systole.

EF was calculated by the two methods: densitometry and the area-length method. Good agreement was obtained, indicating that the assumptions which the two methods are based upon are generally justified.

BE12-B.22

RECENT PROGRESS IN CORONARY FLOW MONITORING. G. Tomonaga, K. Hori, Y. Ogasawara*, K. Tsujioka*, F. Kajiya* Tenri Hospital, Tenri, Nara *Dept. of Medical Engineering and Systems Cardiology, Kawasaki Medical School, Kurashiki, Okayama Japan

Great advance in medical engineering has made it easy to get real-time data about cardiac patients. But measurement of coronary blood flow has been very difficult in clinical fields, although it is essential to monitor the condition of the patient with coronary artery disease. In this paper, several recent progresses of clinical monitoring of coronary blood flow will be discussed, especially the development in our country. We will talk about the results of our recent research: 1) 20 MHz 80 channel dual mode (zero-cross and Fourier transform) ultrasound Doppler method and its application to evaluation of the coronary artery flow velocity during cardiac surgery and 2) laser Doppler catheter and its clinical applicability. In addition, we will touch upon some results of other Japanese research groups, e.g., the transesophageal Doppler method to quantitate coronary blood flow and the combined two dimensional and Doppler echocardiography to detect coronary arterial flow non-invasively.

BE12-C.1

One-Compartmental Model and Evaluation of A Hybrid Artificial Kidney (HD/HP System), Y.L. Chang* and C.J. Lee, Dept. of Chemical Engineering, National Tsing Hua University, Hsinchu, Taiwan, R.O.C.

A mass transfer model with recycle flow is proposed for evaluating the performance characteristics of a system composed of a hemodialyzer (HD), and a hemoperfusion cartridge (HP). Solutions for the recycled systems of two different sequences of arrangement, i.e., HD-HP and HP-HD are obtained and discussed in terms of their performance efficacies.

Theoretical computations reveal that the concentration oscillation phenomenon may be observed with recycled flow system under certain conditions. This oscillatory behavior is related to the competitive adsorption/desorption characteristics in a fixed bed with recycled flow but has nothing to do with the dialysis operation. The results of mathematical analysis conclude that during early stage of operation, the HD-HP arrangement has higher efficiency for favorable adsorbing solutes, and that the HD-HD has higher efficiency for unfavorable adsorbing solutes.

BE12-C.2

ANALYSIS BY DIGITAL SIMULATION
OF THE ANTIDIURETIC HORMONE (ADH)
IN BURN PATIENTS
Laura Roa, Gomez-Cia T., Cantero A.
E.T.S.I.I., 41012-Sevilla, Spain.

Burn injury provoke a protein and liquid shifts from plasma to interstitial compartment, so plasma volume decreases. ADH increments water reabsorption at renal collecting ducts and diuresis decreases. ADH control mechanism has been incorporated to a mathematical model for digital simulation of burn injury. ADH secretion as a function of nervous stimulus, extracellular osmolality and circulatory mean pressure has been quantified. The simulation results have been tested against experimental and clinical data, showing a reliable model behavior. Diuresis analysis has importance in burn patients by its facility as clinical monitoring parameter of patient response to reanimation treatment.

BE12-C.4

HAEMODYNAMIC MODELLING OF
THE RENAL CIRCULATION
IN THE MANAGEMENT OF TRANSPLANTATION
C R Deane*, D Taube, D Goss, V C Roberts
Department of Medical Engineering,
King's College School of Medicine, LONDON

Experience with the measurement of vascular hydraulic impedance in the reconstruction of the peripheral vasculature, and the use of these measures in conjunction with lumped parameter models of the arterial circulation, has now been applied to the problem of monitoring renal transplantation.

Measurements have been made, using an Acuson Colour Duplex system, of blood flow velocity in the renal artery, immediately following transplantation, and every two days thereafter for a maximum period of 10 days. In cases of rejection and nephrotoxicity, these flows have been correlated with the results of biopsy. This data has been used to establish a tentative model of the renal circulation which we believe would be of value in predicting impending rejection without the need for more invasive measures.

BE12-C.3

A Model for Renal Control of Long Term Blood Pressure; Richard B. Davis*, Paul A. Taiganides*, Herman R. Weed

A model has been introduced which simulates the response of the renal system to changes in salt intake. It is based on the renal function curve which describes the relationship between salt intake and blood pressure.

It is proposed that the renal system is the sole control of blood pressure in the long term. The model also offers an explanation for salt sensitive and insensitive hypertension by analyzing two types of pathologies: reduced renal function and reduced renal pressure. The normal model limits the blood pressure to a 40% increase despite a 2400% increase in salt intake. Inducing a 70% failure of the kidneys, the model becomes salt sensitive, allowing the blood pressure to vary 90% for the same change in intake. With a 50 mmHg drop in renal pressure, simulating stenosis, the model increases the blood pressure but maintains its salt insensitivity, limiting the blood pressure to a 25% change due to salt loading.

BE12-C.5

Intracellular pH in Regulation of Gap Junctional Conductance in Frog Proximal Renal Tubules.
W. Rehwald*, C. Hallbrucker, and F. Lang
Dpts. of Medical Physics & Physiology, University
of Innsbruck, A-6020 Innsbruck, Austria

To test for the influence of intracellular pH (pH_i) on gap junctional conductance in proximal renal tubules, three conventional microelectrodes were impaled into different cells of the same tubule and potential difference across the peritubular cell membrane (PD) continuously recorded. Current was injected into one cell and PD deflections determined at the other two. The results allowed calculation of the lumped resistance of luminal and peritubular cell membrane ($R_m = 53 \pm 7 \text{ k}\Omega \text{ cm}$) as well as the resistance of the cellular core ($R_c = 164 \pm 14 \text{ M}\Omega \text{ cm}$). pH_i was recorded with pH sensitive microelectrodes. When extracellular pH is reduced from 7.8 to 7.4 by increasing CO_2 from 1 to 2.5%, pH_i decreases from 7.74 ± 0.04 to 7.45 ± 0.04 , PD decreases from -62 ± 2 to -44 ± 3 mV, R_m increases by $31 \pm 6\%$ and R_c by $31 \pm 11\%$. Inhibition of Na/K-ATPase by 0.1 mmol/l ouabain reduces PD, alkalizes the cell, increases R_m but does not significantly increase R_c . 1 mmol/l cyanide depolarizes the cell and increases both, R_m and R_c . Potassium free extracellular perfusates hyperpolarize the cells and increase both, R_m and R_c . 100 $\mu\text{mol/l}$ mepacrine depolarize and alkalize the cell but increase both R_m and R_c . In conclusion, R_c is sensitive to alterations of pH_i . However, R_c and pH_i can be dissociated pointing to additional determinants of gap junctional resistance.

BE12-C.6

INLET OXYGEN-SUPPLY HEMODIALYSIS (80 CASES-TIME REPORT)
P. WANG DA-YONG, et al FIRST HOSPITAL OF HUBEI MEDICAL
COLLEGE, WUHAN, HUBEI, CHINA.

Some having chronic renal failure patients have been proceeded in 80 cases-time by treatment of hemodialysis with H_2O_2 in dialysate. The hydro-dioxide can supply oxygen to the blood directly through the dialyse membrane, it called inlet oxygen-supply hemodialysis. The biological reaction is a catalysis owing to the hydro-dioxide enzyme in the blood to work, the hydro-dioxide decomposed into water, oxygen and thermal energy quickly ($2H_2O_2 \rightarrow 2H_2O + O_2 + 474 \text{ cal}$). The most of these oxygen integrates hemoglobin to form oxygenated-hemoglobin, that improves PaO_2 and SaO_2 concentration and provide the tissues to use, the few of other dissolves in the plasma and passes the pulmonary circulation through the blood-oxygen defence regurgitating diffusible to breath out.

According to the experiment, when inlet oxygen-supply hemodialysis, the safe amount of H_2O_2 using is VH_2O_2 ($0.2\% H_2O_2 \text{ ml} = Hb \times W \times 0.98$). This numerical value (5-10% of all blood capacity) is in the scope of the body's capacious vessel that can be regulate, so it is proper.

The inlet oxygen-supply hemodialysis makes PaO_2 and SaO_2 remarkable rising, so the complicate rate of the dysequilibrium syndrom in the dialysis is low. In addition, this therapy can provides an effective way that it surmount the lung to supply the oxygen directly to the blood, it can be improve the hypoxemia promptly, to relax the cardia failure and pulmonary edema, and to remove the poverty-stricken symptom of the respiration, so it has the fine effect of the cure for the uremia that worth to promote.

BE12-D.1

Downsizing and Clinical Engineering Strategies in the United States

M.J. Shaffer, D.Sc.* and M.D. Shaffer, M.S., The George Washington University Medical Center, Washington, D.C.

U.S. hospitals are facing cost-cutting pressures due to new reimbursement practices, increased reliance on out-patient clinics and pre-paid systems, and increased competition from other hospitals. Occupancy data shows in-patient care is on the decline. Hospitals are thus looking to reduce costs and develop new lines of business.

In these changing conditions clinical engineering strategies include

- a) maintaining the integrity of the service through professional associations and standards, performance measurements, and comparison of departmental values with those of other providers, and
- b) contributing to new business opportunities such as shared services, technology assessment, microcomputer applications, and training.

BE12-C.7

THE EXTRACORPOREAL CIRCULATION AND ULTRAFILTRATION OF ASCITIC FLUID - INTRODUCE A NEW TECHNIQUE OF THE TREATMENT FOR OBSTINATE ASCITIC
P. WANG DA YONG, et al FIRST HOSPITAL OF HUBEI MEDICAL COLLEGE, WUHAN, HUBEI, CHINA

(ABSTRACT)

According to the principle of ultrafiltration, authors designed a new technique of ascitic extracorporeal circulation and ultrafiltration.

The medical engineering principle of the extracorporeal ultrafiltration of ascitic is an extracorporeal material transfer. The ascitic through the fiber line of dialyzer and cleaning partly. As the condition of dialysis is stable state, the cleaning quantity of ascitic is directly proportional to the pressure of ultrafiltration (TMP) and the time of ultrafiltration.

$$\frac{C_b - C_e}{C_b} = QW$$

(annotation): C_b : The urea concentration of the ascitic in front of begining ultrafiltration(mg%).
 C_e : The urea concentration of the ascitic after the end of ultrafiltration (mg%).
 QW : The average discharge of the ascitic at the course of the ultrafiltration.

Not only this method can relieve the suffering by eliminated the ascitic largely and promptly, patients had not the evil of aggravating failure owing to the protein discharge, but also the doctor had not the worry that have to frequent ultrafiltration, because the output quantity of the ultrafiltration is more than the increasable quantity of the pausal period of the ultrafiltration.

BE12-D.2

ADMINISTRATIVE COMMITMENTS FOR CLINICAL ENGINEERING DEVELOPMENT,

Michael J. Shaffer, D.Sc., The George Washington University, Washington, D.C., U.S.A.

High technology and managed health care in the United States is challenging clinical engineers to expand and develop new opportunities. As a prerequisite, clinical engineers need determine the extent of hospital administration commitment to their support of:

- a. personal computer consultation, programming and maintenance services at the clinical department level,
- b. maintenance integration, with automatic funding of expensive spare parts kits and adjustment of maintenance operating budget with the purchase of capital equipment, with service manual needs included in purchase orders, and with service contracts regularly reviewed,
- c. in-service technical training prioritized and scheduled by management,
- d. staffing adjustments for specialized technology assignments, and
- e. unrelated business income including telecommunications voice/data, switching and cabling issues, shared service maintenance, etcetera.

BE12-D.3

TECHNIQUES FOR ACHIEVING CREDIBILITY WITH HOSPITAL ADMINISTRATORS, G.I. Johnston and R.L. Morris*, Oregon Health Sciences Univ.

Hospital administrators have difficulty assessing the impact of the enormous potential of a discipline, clinical engineering, for which there are few management models. Furthermore those which have been developed are written in "engineeringese" and reported in the clinical engineering literature rather than the hospital administration literature. They have even more difficulty allocating adequate resources which would enhance the value of the department to their organization. Any department not census driven is automatically suspect! Since it is unlikely administrators will have, or take the time to, learn more about this strange new department, it behooves the clinical engineer to seek methods for achieving the support and respect of hospital administrators. Clinical engineers can (must) work both inside and outside their hospitals to improve their credibility and status with hospital administrators. They must begin publishing their management articles and models in journals which hospital administrators read. And they must develop internal reporting and budgeting systems which hospital administrators can relate to. Some suggestions will be presented and discussed.

BE12-D.5

Development of "wide use" PHD(Personal Health Data) management system. K. Ishikawa*, H. Takeda, H. Inada, M. Inoue, and S. Sakai, Kagawa Med. School, 1750 I Kito Miki Cho, Kagawa, 761 07, Japan

We are developing a PHD(personal health data) management system which will monitor the individual's health throughout his life.

The basic system configuration is organized around the personal computer with a new audio visual telephone. IC memory card system link up. The health information is qualified into three levels, which are "personal ID informations", "basic physical informations" (i.e. blood pressure, pulse rate, body temperature etc.), and "technical informations" (i.e. medication, surgical specific medical histories etc.). The IC memory card will be used as the major information transport media. The development of a PHD system is not only concerned the new health information management system, but also contributes the formation of the regional synthetic medical service system.

BE12-D.4

A Financial Simulation Model for Clinical Engineering, A. Mahachek*, The Johns Hopkins Hospital, Baltimore, Maryland 21205

Budgetary performance is becoming as important as technical performance for many clinical engineering departments. Building a financial model using a personal computer spreadsheet software package is an ideal way to prepare a budget, track actual performance, and test policy or personnel changes. The clinical engineering manager gains new insight and understanding of the department's operations while building and manipulating the model. The existence of a financial simulation model instills confidence and projects competence when communicating with hospital senior administration. This customized financial model is in actual budget use (for 3 years) at a major teaching hospital. Also described are the simulated changes in policy and/or personnel that resulted in actual management changes in the clinical engineering department.

BE12-D.6

ASSESSMENT OF BIOMEDICAL TECHNOLOGY IN A UNIVERSITY HOSPITAL IN NICARAGUA, Robert P. Patterson*, UMHC Box 297, Univ. of Minn. Hospital, Minneapolis, MN 55455, USA

In Nov. of 1987, a medical team consisting of physicians, nurses, a respiratory therapist, a biomedical engineer, and a rehabilitation engineer visited the University Hospital and medical school in Leon, Nicaragua to assess needs and provide assistance. The hospital had 360 beds and the medical school graduated 250 students annually. Some of the obvious deficiencies were no working ventilators, no working ECG or blood pressure monitors, and no blood gas measurement capability. The repair technicians faced a lack of parts and Spanish manuals for U.S. made equipment, lack of a medical understanding of the function and use of the equipment, and high ambient temperatures. Three different brands of U.S. made ECG monitors failed apparently due to the high temperatures in the non-air conditioned hospital. Two of the monitors were restored to use by installing fans. In one of the top hospitals in Nicaragua, the level of technology available was low.

BE12-D.7

HEALTH CARE TECHNOLOGY - RELEVANCE TO THIRD WORLD NATIONS - T. G. Krishna Murthy* and D. V. S. Raju, Bangalore, INDIA.

The impact of advancements of technology particularly in the last decade has been phenomenal. Instruments utilising mini and micro computers have led to optimum utilisation of the very limited resources available for health care delivering programmes in the highly populated and poverty ridden third world nations. Planning and Co-ordinating of such programmes have to be based mainly on the disease pattern prevalent and actual needs. So a need based approach for the appropriate utilisation of technology is inevitable. The WHO group on GPHACT located in Copenhagen has initiated steps in this regard and are building up their database at the university of Linchoping. The target of HEALTH FOR ALL BY 2000 A.D., is a really formidable challenge. Besides modern medicine, local systems of medicine whose clinical therapeutic potential has to be evaluated in a planned and scientific manner along with YOGA therapy can be gainfully utilised to provide medicare at very moderate costs to the millions even in the remote rural areas in the third world nations.

BE12-D.9

Audiovisual Material aimed at the Prevention of Clinical Accidents, R.P. van Wijk van Brievingh and F. Koornneef, Delft University of Technology, NL-2600 GA Delft, the Netherlands.

Accidents in hospitals have to be analyzed in a system-analysis approach. The subsystem "Humanware" is the most difficult to describe. Human error, however, is governed by internal processes which can be mastered by awareness of critical situations and by organizational measures. Before this is possible, a positive attitude towards the discussion of accidents and incidents has to be bred. The use of audiovisual aids is of value here, as by the repeated discussion of situations shown, objectivation as well as reference to own experiences is induced. After an introduction of a general system model with indication of the entities and relations, the background of the "attention problem" is elucidated with reference to every-day hospital situations. For example, in the operation theatre the team has to rely on their own resources as well as on what the "outside world" has prepared. Awareness of the limited attention capacity has to determine task-division and protocol. Attitude changes have to be supported by quality-assurance measures by the management. Part of these will be registration and proper discussion of accidents and incidents in a "guilt-free" situation.

BE12-D.8

MAINTENANCE OF BIOMEDICAL EQUIPMENT - T.G. Krishna Murthy* and N. Krishna Swamy, Bangalore, INDIA

Maintenance and utilization of equipment used in medical institutions and hospitals have been a major problem in all third world nations. Various factors have led to the under utilization and non-utilization of equipment. The major factor has been the total lack of essential back-up facilities in the form of trained manpower and availability of spares, majority of equipment are imported and due to a very rapid rate of obsolescence in developed nations, the suppliers in majority of instances regret to provide the badly needed spares. Health care is the responsibility of the states and there appears to be total ignorance about the need of trained manpower to ensure optimum utilization of equipment. However, in the last decade, a number of service and maintenance centers have been set up. In India, plans are under way to set up the medical instruments maintenance corporations on a national level to apply necessary correctives.

BE12-D.10

Protocol for Maintenance and Repair to Suction Apparatus potentially exposed to High Risk Infections. D. Naughton, B. Murphy, L. English, J. Mahady and J F Malone*, F.D.V.H., St. James's Hosp. & Trinity College, Dublin 8, Ireland.

Suction apparatus is commonly repaired or subject to schedule maintenance in hospital Clinical Engineering Units. It is possible for body fluids to be drawn directly into the machine, including the pump, thereby contaminating it. Under normal circumstances the associated maintenance problem is unpleasant and time consuming, as the unit must be dismantled, cleaned and reassembled. However it is no longer merely unpleasant, it may be potentially lethal, given the associated increased risk of exposure to a Category III Virus such as Hepatitis B or HIV. To cope with the above we have established a protocol to protect Biomedical Engineering Staff who must perform repairs/preventive maintenance on suction units. The protocol is both Preventive and Procedural in that it (a) aims to prevent faults/behaviour that will result in the ingress of fluids; and (b) sets out a formal procedure to be followed during transport and repair of the unit that address the infection risks if the unit (i) need not be opened, and (ii) if it must be opened.

BE12-D.11

MEDEQ - A Medical Equipment Information System. C. Nerhed*, L. Löfstedt and B. Eklund, Dept of Medical Engineering, University Hospital, S-751 85 Uppsala, Sweden.

MEDEQ is an information system for medical equipment and it has been used at the University Hospital in Uppsala for almost ten years. More than ten thousand equipments are stored in the database and it is used by over 30 persons on a daily basis. MEDEQ is also used by six other hospitals in Sweden. MEDEQ has been developed in a VAX/VMS environment using the relational database MIMER. A fourth generation programming tool has been used to implement the system. Great emphasis has been made to make the system versatile and easy to use. MEDEQ consists of functions for inventory, maintenance and cost analysis. The data stored are used for a variety of purposes e.g. inventory, investment plans, and to find weaknesses and security risks in the equipment.

BE12-D.13

EMC Measurement and Evaluation in HE Equipment. Z.Ohta*, NEC San-ei Instruments, Ltd., Tokyo, Japan.

As a result of recent increase in the use of HE equipment, the consideration of EMC (Electromagnetic Compatibility) in hospitals has become very important for the safety of patients. EMC is classified roughly into EMI (Electro-magnetic Interference) and Immunity. In Japan, we organized a committee for study of EMC in HE equipment under the Technological Committee of Medical Electronics (Chairman: Z. Ohta), EIAJ (Electronics Industry association in Japan), with the assistance of the Ministry of International Trade and Industry. EMI was measured in 9 kinds of equipment in accordance with CISPR/B(S)42. Some equipment exceeded the limit for the radiated field strength. Immunity was measured in 5 kinds of equipment in accordance with some standards published in Japan and abroad, because no international standard is available for Immunity now. The ability of rejection differed from equipment to equipment, showing the property of each engineering technique.

To satisfy the standards, it is necessary to improve the environment such as the shield of equipment especially for the therapeutic equipment, as well as the technical design of each equipment.

BE12-D.12

Performance Indicators for Equipment Servicing Teams. D Whelpton*, King's Mill Hospital, Sutton-in-Ashfield, Nottinghamshire, UK.

All departments of the British National Health Service are required to show efficiency. Accordingly, maintenance departments are increasingly required to measure performance. It is difficult to make valid cost comparisons. In any case, it may be that financial cost is only one of several parameters to be considered. Whilst in-house servicing must be competitive, other criteria, such as rapid response, availability of staff education and advice on when and how to replacement equipment are also important. Experience gained in operating an equipment management system will be discussed.

BE12-D.14

The Norwegian Inspectorate for Biomedical Equipment and the National System for Accident Report and Investigation. Johansen A.*, F. Nilsson, E. Fønstelien, STEM, 1320, Stabekk.

Norway (4.0 mill inhabitants - approx 100 different hospitals of a high medical and technical standard) has had compulsory governmental inspection and control of electrical medical equipment in health institutions since 1980. The inspection has been carried out by 8-12 highly skilled engineers on the basis of a combination of a total and a random selection of patient rooms and/or equipment categories.

Since 1980 there also has been an enforced obligation to immediately report, day and night, any incidents or near-accidents where electrical medical equipment may be involved. The Inspectorate investigates accidents in the actual hospital if necessary.

A steady decrease (around 40% to 10% of the equipment installed) of the faults and the defects found and a parallel increase in the number of accidents and near-accidents reported is elucidated and theoretical and practical explanations are proposed.

The administration of the inspection and the reporting system will be thoroughly explained.

BE12-E.1

A Computerized Strength Evaluation System for Children using the Cybex-II Isokinetic Dynamometer. C.A. Rodriguez*, D.S. Glass†, *Texas A&M University, †Texas Scottish Rice Hospital.

A PC-based control system for the Cybex-II Isokinetic Dynamometer is being developed to assist in the evaluation of strength and endurance of knee extensor and flexor muscles. The system will be used to observe the course of the disease and the effects of surgery, drug therapy and physical therapy in children with neurologic and orthopaedic disabilities. Several computer-controlled isokinetic evaluation systems have been developed in the past, but primarily for adults in sports medicine and rehabilitation. The computer system controls the speed of the exercise, and collects torque and position data. The data is plotted in real time and biomechanical parameters of patient performance (e.g., torque-to-body weight ratio, work, time to fatigue, maximum torque, position at maximum torque) are determined.

BE12-E.3

A COMPUTER AIDED PROCEDURE FOR THE MANAGEMENT OF DIABETIC PATIENTS, E. Gómez-Aguilera* and F. del-Pozo, Dpt de Bioingeniería, E.T.S.I. Telecomunicación, Madrid, Spain.

A new procedure, running on a PC-compatible, has been designed to help the diabetological training of patients and physicians; and facilitate the precise, and error free, therapy selection procedures. To allow a parsimonious approach to the task of defining the optimum treatment for each patient.

This therapy selection tools and the patient follow-up graphic-analytical aids, are supported on a minimum metabolic model for the estimation of blood glucose, that works on the information provided on diet, insulin sequence, and exercise regime. Thus, this procedure, during training sessions or, in real follow-up situation, can be used for the detection and identification of the causes (including behavioural sequences) of any metabolic accident or the evaluation of therapies; which will finally provide to the patient a progressive knowledge of her/his own illness, and a treatment individualized and adaptable to daily circumstances.

Acknowledgments. -CICIT. Grant No.2911-83.

BE12-E.2

A Computerized ERG Monitor
Shiro Usui, Ei-ichiro Nagasaka*
Manabu Sakakibara and Yozo Miyake†
Toyohashi Univ. of Tech., Toyohashi 440
and †Nagoya Univ., Nagoya 464 Japan

A computerized portable ERG monitor was developed for a clinical use with the aid of modern digital signal processing technology.

It is known that the ERG is a summative potential composed of a-, b-wave and oscillatory potential, which are sensitive to various types of eye disease and thus the amplitude, latency and inter-peak interval of each component provide a good cue for a diagnosis. However, each component is being mixed together both in time and frequency domain and thus it is impossible to isolate the components by the conventional methods such as an adjusting time constant of amplifier or a so-called manual method.

Here we developed a totally computerized portable ERG monitoring system which is able to isolate oscillatory potentials and detect each parameters automatically with utilizing digital filtering techniques such as moving average and digital differentiation. This computerized electroretinometer was tested in daily clinic and found enough beneficial to ophthalmologists with easy use and high precisions.

BE12-E.4

Measurement of spontaneous anaesthetic parameters by a microcomputer system, M.A.Tooley, S.A.O'Connor* and D.J.Wilkinson, St. Bartholomew's Hospital, London, England.

A microcomputer system for the measurement of parameters of ventilation and blood pressure in the spontaneously breathing anaesthetised patient is described. The system continuously calculates minute volume, respiratory frequency and mean end-tidal carbon dioxide concentration averaged over a minute. Also four cardiovascular parameters are measured which are updated every 60 seconds. The inputs are obtained from a wet-wedge spirometer, a capnograph and a blood pressure monitor. The methods of computer calculation are described in detail. The computer results are compared with those obtained by manual calculation and are all in agreement to within 3%. The system described has the capacity to record and display a wide variety of further measurements made during anaesthesia. This system provides invaluable information for research and teaching but may also be useful during routine anaesthesia.

204

BE12-E.5

Intelligent Computer Control of Blood Pressure on Induced Hypertensive Chemotherapy for the Cancer Treatment
Y. Fukui*, M. Suzuki
*Tokyo Denki Univ., Saitama, Japan
Tohoku Univ., Sendai, Japan

Chemotherapy with Angiotensin II (AII) induced hypertension has been expected as a powerful cancer treatment in recent Japan. The idea of the therapeutic strategy is based on the experimental findings of the micro-circulation: "AII infusion causes the vaso-constrictive effects on the normal blood vessel, but not the tumor. As a result, for AII induced hypertension (150 mmHg mean arterial pressure), most of the blood flow to the tissues pass through the tumor, which enables the effective delivery of the anti-cancer drug to the tumor selectively."

The current problem of the clinical hypertensive chemotherapy is how to perform the safe and smooth elevation as well as the steady regulation of the blood pressure by the proper AII infusion. To overcome this, intelligent closed-loop control system of hypertension has been developed. Intelligent means in a sense that the computer behaves like the expert physician's treatment way, where optimal control and sensitivity adaptation algorithms are used to infuse the AII automatically. Satisfactory blood pressure control were realized on the animal (100 rats) experiments, which may be applicable to the clinical cases.

BE12-E.7

A Systems Approach to Microsurgery
Steve Charles, M.D., 6401 Poplar
Avenue, #190, Memphis, TN 38119

Ophthalmic microsurgery has progressed from hand-positioned and hand-actuated to hand-positioned and remotely-actuated ocular instruments. The next revolution will produce remotely-positioned and remotely-actuated instrumentation, i.e., microrobotics, for dexterity augmentation. A parallel revolution in the downsizing of tools is occurring, resulting in the need for MEMS technology. Ophthalmology is a machine-dependent specialty embracing both the patient-machine interface and the surgeon-machine interface. A multidisciplinary approach to systems integration has been developed for the ophthalmic microsurgery operating room and the office, utilizing technology transferred from military applications. These include expert systems, speech recognition and synthesis, programmable pump and valve arrays, and virtual control and display. The computational aspects of the operating room system developed, referred to as the Ocular Connection Machine, consist of machine management functions and information management functions.

BF12-E.6

Measurement and Analysis: Mechanics of Body Sway, Din Jianxin, Wen Xiaoyang* Huazhong University of Science and Technology, Wuhan, P.R.China

Reported a new method to research balance mechanics of human. A monitoring system of body sway was developed. Body sway information was obtained from the crystal rate gyroscope and the data were processed by TP-801 single board computer. The characters of body sway in normal state and ataxic patients were given.

A series of new results on body balance mechanics based on PDS (power density spectrum) technique to analysis Romberg posture (orthostatic reflex) were found.

BE12-E.8

The Vision-Aided Speech Training System Based on the Microcomputer for the Deaf. J. Yao, Z.H. Gao and R.C. Chen, Shanghai Jiao Tong University, Shanghai, P.R.China.

The speech training system can be used to help the people who can not speak because of congenital loss of hearing to train pronunciation themselves.

The speech training system proposed in this paper is a new type of visible speech training device which is based on the technique of isolated word speech recognition. The system can compare the pronunciation produced by the deaf with the standard pronunciation to decide if the input pronunciation is correct and how its quality is. And then the system can convert these information into the visible signals to instruct the deaf to do training. The major difference between this visible speech training system and the other now available ones is that the system we developed does not use the features extracted from the speech waveform, but directly uses the results of speech recognition as the visible signals. Thus, this system is more convenient to use and provides an environment of self-tutor for the deaf who have some knowledge in pronunciation. The simulated system of this kind of speech training device has been accomplished on the IBM-PC/XT microcomputer.

BE12-E.9

The Engineering on Computer Diagnosis and Adjustment of Color Perception Abnormality
Chen Xiaoguang*, Wei Jizhou, Liu Hongjian,
and Jiang Chunxiao, Bethune Medical Uni-
versity, Xin Min Avenue 6, Changchun, Jilin
P.R. CHINA

Based on a vast amount of experiments, the topological model for human color perception is developed. It is discovered that its process is surprisingly similar to that of the signal processing in color TV systems, hence it is possible of the adjustment of its perversion. We have developed micro-computerized device which output data such as the classisification of the abnormality and its level, and the optimum adjustment curve. By Auto CAD operation system we developed a software including 35 sepectrum carts for perversion checking. The charts can be used by will and displayed in high resolution. In the process of man-machine dialogue, the oplimum effect achieved, then the device will display the diagnosis and the adjustment curve in print form. Finally, and appropriate adjustment glasses will be made for each client.

BE12-E.11

3D/Multiplanar CT-Guided Stereotaxis: An
Adaptation System - Henry Ford Hospital -MI.
Zamorano L*, Dujovny M, Flynn M, Block R.

3D/Multiplanar data obtained from CT interfaced with stereotaxis is becoming an indispensable tool in the diagnosis and treatment of brain lesions. Size, volume, shape, axis of lesions, definition of coordinates, angles, and areas can be obtained and corrected with the aid of multiplanar or 3D images. A major goal is the transposition of these imaging generated data into the stereotactic space. An adaptation of the CT compatible frame "Komai" is presented which allows transfer of 3D/Multiplanar CT generated data with high grade accuracy ($\pm 1\text{mm}$). An adapter to the scanning room table was designed allowing isocentric relationships to the gantry and parallel to the scanning plane. The design was made of fiberglass avoiding CT artifact and allowing a complete range of scanning so that with inverted positioning of the frame it is possible to aim targets near the skull base or posterior fossa. An angular localization system attached to the Xscale allows translation of plotted trajectories of re-formatted or scoutviews into the Y-Z plane. A computer program allows considerable accuracy in the translation of CT data into stereotactic space with special reference to preselected plotted trajectories. These modifications and adaptations enable performance of diagnostic and treatment of brain lesions.

BE12-E.10

IDENTIFICATION OF THERMAL MODEL FOR HUMAN TISSUE DURING ULTRASONIC HEATING & ITS MICROCOMPUTER-CONTROLLED MEASUREMENT DEVICE MIN-HE CHENG* AND HONG-ZHANG WANG, Precision Instrument Dept, Shanghai Jiao Tong Univ, Shanghai, P.R. China

Hyperthermia by ultrasonic, as a method for cancer treatment, has been applied to clinic trial for many years. Its effect has been confirmed. But a non-invasive method of monitoring temperature distribution during heating still remains unsolved so far. Present method of temperature estimation depends on skin temperature and doctor's experience. In this paper, a simple model structure of temperature distribution in human tissue, which is based on one-dimension bio-heat equation, is developed. The model parameters for real tissue are estimated from patient treatment through the use of a system identification technique. The temperature distribution during hyperthermia can be predicted by this model, and non-invasive temperature measurement can be realized. To verify the feasibility of this method, the simulation temperature field is made by computer. The result is more satisfactory and indicates that the simple control model structure is adequate through identification of phantom model parameter. An identification-prediction measurement device is made by microcomputer TP-801 and better results are obtained by experiment heating fresh excised pig tissue. It's possible to apply this method for clinic non-invasive temperature measurement during hypothermia. But there are still a lot of work to do.

BE12-E.12

Computerized rhinomanometry: equipment
and models

Filip Versnick (*), Marc Nyssen, Peter Clement

ENT dept. Academic Hospital Jette and
Medical Informatics Dept. Vrije Universiteit Brussel
B-1090 Jette, Belgium

Rhinomanometry is a technique to obtain an objective and quantitative value of the functioning and/or the obstruction of the nose.

During the experiments, the transnasal pressure difference is measured simultaneously with the corresponding transnasal airflow, for each side of the nose.

We designed a system by which the analogue pressure and corresponding flow signals, generated by the rhinomanometer are sampled at a definite frequency and digitized by a real-time computer system, connected to the local UNIX workstation. The workstation handles the mathematical processing but also provides a lot of graphic possibilities, to visualize the results.

In this paper, we present the methodology that allows investigation of rhinomanometric characteristics in depth, such as frequency content, determination of the optimal sample frequency.

The long term goal is the development and testing of mathematical models that describe transnasal pressure/flow curves and parameter analysis, to understand and determine the characteristics of transnasal breathing in view of future clinical applications.

The first results are presented.

BE12-E.13

Mathematical Signal Analysis and Acquisition System
V. Madina B.A., J. Azpiroz L.
Universidad Autonoma Metropolitana-Izt.
Av. Parisina Y Michoacán México 09340 D.F.
MEXICO

We have designed a system for the acquisition and analysis of biomedical signals, based on an IBM-PC (XT or AT) compatible computer. It consists of a 16 channel, 12 bit A/D converter card, designed and built at our laboratory, and a digital signal processing package which contains such functions as signal acquisition, digital filtering, fast Fourier transform, spectral density, and convolution, together with several modes of displaying the signals.

The menu-driven, modular design of the system permits the easy addition of other signal and analysis routines, as well as the easy transference of some functions to other software packages. The software was written in Pascal, with several routines in 8088 assembly language.

Applications of this system now include the spectral density analysis of electroencephalographic signals for brain mapping and the acquisition and filtering of transthoracic impedance signals for the determination of cardiac output.

BE12-E.15

PC-based equipment for the assessment of strength during various hand grips.
O. Lindahl*, T. Bäcklund, S. Karlsson, T. Söderberg, University Hospital, S-901 85 Umeå, Sweden.

Endurance and motor skills of the hand grip are important parameters in the pre and post operative investigation of patients with injured hands. We have constructed an equipment based on a PC to which we have interfaced specially designed strain gauge sensors for hand grip, pinch grip, twist grip, wrench grip and push. During the Motor skill test, the patient is instructed to adjust the grip force, displayed as the height of a moving bar on the PC screen, to keep the force within 45% to 55% of maximal power. Failures during 30 sek of test are registered. In the Endurance test, the patient is instructed to grip with maximal power and keep this grip as long time as possible. Maximal force, fatigue, area and raise (force/sek) are calculated and displayed together with the force curve on the computer screen. All results are documented on a plotter.

The preliminary results shows that this method gives high reproducibility and is a first step towards a standardized method for evaluation of grip strength in injured hands.

BE12-E.14

A DISTRIBUTED MONITORING SYSTEM FOR ARRHYTHMIA AND ISCHEMIA MONITORING
G. Passariello*, F. Mora, J. L. Coatrieux⁽¹⁾ and D. Almeida⁽²⁾, Universidad Simón Bolívar, Grupo de Bioingeniería y Biofísica Aplicada, Apartado 89000, Caracas, Venezuela 1080

Recent development and demonstration of efficacy of antiarrhythmic drugs and other cardiac agent, have suggested the need for more quantitative, individualized diagnosis and treatment, increasing the complexity of instrumentation systems. Current advances in microinformatics, hardware and software, digital signal processing, pattern recognition and artificial intelligence, have resulted in the possibility of developing more sophisticated cardiac monitoring systems, without necessarily involving a large centralized computer by distribution of the intelligence from the bedside unit to the central station. A general philosophy of a distributed intelligent system for a Coronary Care Unit (CCU) is described. This includes: ECG analysis for arrhythmia detection and ST segment quantification, event counting, trend plotting and patient supervision during drug therapy. The tasks mentioned are integrated within an expert system. Also the development of an intelligent bedside unit for two beds based on a personal computer as a preliminary step toward the complete system is presented.

- (1) Université de Rennes I, Groupe de Signaux et Images en Médecine, Rennes-Francia.
- (2) Hospital Universitario de Caracas, Unidad de Cuidados Coronarios, Caracas-Venezuela.

BE12-F.1

Estimation of turbulent shear stresses in pulsatile flow downstream of aortic valves.
H. Nygaard*, M. Giersiepen, J.M. Hasenkam, D. Westphal, P.K. Paulsen, H. Reul, Engineering College, Århus, Denmark. Dept. of Thorac. & Cardiovasc. Surg., Skejby Sygehus, Aarhus University Hospital, Denmark. Helmholtz-Institute for Biomed. Eng., Aachen, FRG.

Measuring turbulent shear stresses is of major importance in artificial heart valve evaluation. Bi- and unidirectional fluid velocity measurements enable calculation of Reynold's Shear Stress ($\tau = -\rho \cdot \bar{u}_i \bar{u}_j$) and Normal Stress ($\sigma = \rho \cdot \bar{u}_n^2$). τ is important due to the relation to hemolysis and thrombus formation, but σ is the only obtainable parameter in vivo. Therefore, determination of a correlation factor between τ and σ is pertinent. In a pulsatile flow model, Laser Doppler (LDA) and Hot-Film (HFA) anemometry were used for simultaneous bi- and unidirectional fluid velocity measurements downstream of a Metronic Hall and a Hancock Porcine aortic valve. Velocities were registered in two flow field locations and at four cardiac outputs. The velocity signals were subjected to analog signal processing prior to digital turbulence analysis, as a basis for calculation of τ and σ .

A correlation factor of 0,48 with a correlation coefficient of 0,98 was found. Implying $\tau = 0,48 \cdot \rho \cdot \bar{u}_n^2$. Estimation of turbulent Shear Stresses in the region of aortic valves, based on the axial velocity component alone, seems possible.

BE12-F.2

Some Mechanical Methods for Design and Improvement of Cardiac Valve Prostheses, Diao Yingmin, Qian Zhongfan, Xia Zhigao, and Shi Defang, Tongji University, Shanghai, China.

This paper proposed some mechanical criteria for design and improvement of cardiac valve prostheses: reasonable stress distribution both in the stent and on the leaflets, because the stress concentration may cause deformation and rupture of the stent, and it can also make the leaflets calcified and torn.

For this reason we applied appropriate mechanical methods to a unileaflet valve as an example. The photo-elasticity stress analysis is used in the stent to find the location of stress concentration. By improving the design the maximum stress decreased to $1/2-1/3$ of the original design. For the leaflets, in view of the definite relationship between the stress distribution and design parameters (D, H, a, b, c), calculating the stress distribution by finite element analysis, we determined that the object of optimization should be $\min(\max \sigma_i(H, a, b, c))$ (D was given). So a group of optimized parameters was obtained. These methods can accelerate the ripe of a new type of valves.

BE12-F.4

High Strain Rate Viscoelastic Behavior of Bovine Pericardial Xenograft Materials: Effect of Alternative Crosslinking Methods, Sean A. Haberer*, J. Michael Lee, and Christopher A. Pereira, Centre for Biomaterials, University of Toronto, Toronto CANADA

Clinical failure of bioprosthetic heart valves has been linked to fatigue of leaflet materials in regions of high stress. While the high strain rate mechanical properties of the leaflet material are required for stress analysis and valve design, these have not been measured. Bovine pericardial xenograft samples were prepared by: (1) chemical treatment in glutaraldehyde (GA) or carbodiimide (CD); (2) physical treatment: freeze-drying or heat/vacuum drying; or (3) a combination of the above. The resulting materials were tested using a computer-interfaced tensile testing apparatus, piggy-backed onto an Instron servo-hydraulic testing machine. Measurements included cyclic loading, stress relaxation, and forced vibration. Loads of 20, 40, and 80 g were applied under loading frequencies of 0.01, 0.1, 1, and 10 Hz. The stress-strain curves for fresh pericardium (10% strain at 80 g) and GA or CD crosslinked materials (20% strain at 80 g) were both nearly independent of strain rate; however, in either case, the hysteresis loop at 10 Hz was markedly enlarged. Stress relaxation depended strongly on loading rate - reaching 40% stress loss at 100 s (10 Hz). Previous low strain rate studies have underestimated the viscoelastic response of these materials.

BE12-F.3

Three-dimensional flow mapping down stream mechanical mitral and aortic valve prostheses using ultrasonic velocimetry, F. Cassot*, D. Morvan, G. Tonietto, R. Pélissier, C.N.R.S.-L.M.A and I.M.F.M., Marseille, France.

A thorough hemodynamic characterization of artificial heart valves involves a detailed study of the tridimensional and unsteady post valvular velocity field. Cardiovascular simulators now exist which enable to duplicate *in vitro* the physiological conditions of transvalvular flow (LV and aortic shapes, elasticity, pressure and flow waveforms). Instantaneous velocity maps were set behind disk and ball valves in mitral (anatomically shaped LV) and aortic position, from ultrasonic Doppler measurements. Among the considerable amount of information gathered, the more striking features concern, as yet : the LV vortex flow pattern formation (related to the rolling up of the shear layers at the valve level) in mitral position; damping of the post-valvular disturbances (aortic wall elasticity effect), skewness of velocity profiles in the near wake of disk and ball valves, in aortic position; reverse flow and vortex structures much more important for disk valves than for the ball ones are strongly dependent upon disk orientation. These data may also serve as a background knowledge in the interpretation of blood flow velocity observations (comparisons with color Doppler will be presented).

BE12-F.5

Scanning Electron Microscopic (SEM) Examinations of a Ceramic Prosthetic Heart Valve for Use as a Cardiac Prosthesis, Y. Mitamura*, K. Otaki, K. Hosooka, T. Yuta, and T. Mikami, Hokkaido Univ., Sapporo 060, Japan

Fractures and thrombus generation of prosthetic valves have led to a development of a more durable and thrombo-resistant heart valve comprising a single crystal alumina disk and titanium nitride valve ring. Blood compatibility was examined by SEM examinations of the valves implanted in sheep for 35(#1), 26(#2), 20(#3), and 23(#4) days. The ceramic valves were incorporated into a pneumatic assist pump. The pump was paracorporeally implanted between the left atrium and the descending aorta in a sheep.

There was little fibrin and few platelet colonies on the alumina disks (#1, 2, 3, 4), except for a small amount of deposition of fibrin and platelets on the outflow alumina disk (#1). There was no gross platelet deposition on the TiN rings, except for some deposition of fibrin and platelets on limited regions (#1, 2, 3, 4).

The adhered platelet number was few and the shape change was mild on both the single crystal alumina disk and the TiN valve cage. The ceramic valve is a promising heart valve for cardiac prostheses.

BE12-F.6

The Role of Chordal Geometry in the Development of Systolic Anterior Mitral Motion

E.G. Cape*, E. Gieseking, D. Simons, A. Jimoh, A.E. Weyman, R.A. Levine, and A.P. Yoganathan, Georgia Institute of Technology, Atlanta, GA 30332-0100

In patients with hypertrophic cardiomyopathy, the mitral valve moves anteriorly, assuming a unique shape with mitral-septal contact centrally and preserved orifice area laterally. The purpose of this *in vitro* study was to test the hypothesis that anterior motion of a membrane in a flow field can be generated by altering the distribution or effectiveness of chordal tension tethering the membrane. Accordingly, a horizontal leaflet mounted in a flow chamber was attached by cords at its distal end to a series of upstream screws. Chordal tension was varied by turning the screws or shifting them anteriorly within the model. Leaflet motion was recorded photographically and echocardiographically.

Anterior motion with the same unusual configuration seen in patients was reproduced by decreasing central chordal restraint while tension on the leaflet edges was maintained. Directing chordal tension anteriorly caused greater degrees of anterior motion at earlier stages in the release of chordal restraint; increased flow rate had a similar but less marked effect. These studies suggest that primary geometry alterations in the papillary muscle-mitral valve apparatus are capable of playing an important role in determining the presence and geometry of systolic anterior mitral leaflet motion.

BE12-F.8

Amorphous Coating Materials for Heart Valves, A. Bolz* and M. Schaldach, Zentralinstitut für Biomedizinische Technik, Universität Erlangen, D-8520 Erlangen, FR of Germany

Pyrolytic carbon coating represents today's state of the art in the manufacture of cardiovascular implants such as artificial heart valves. However, comparative studies with other materials have demonstrated the possibility of improving haemocompatibility. Based on an electrochemical model considering the activation of fibrinogen as an redox process in the solid-blood interface, new materials such as semiconducting Ta doped rutile ceramics have been experimentally evaluated. An electron concentration of approximately 10^{20} cm^{-3} with a band gap of 3.2 eV have met antithrombogenic requirements. Technological problems related to the ceramic structure resulted in the evaluation of coating processes such as reactive sputtering and chemical vapor deposition (CV) of TaN, SiN and SiC. These materials are deposited as amorphous doped semiconducting layers using processes proven in the manufacture of amorphous photovoltaic cells. Preliminary results have demonstrated the feasibility of producing a variety of electronic structures to meet blood compatibility requirements. The technology of plasma activated chemical vapor deposition offers advantages which match electrochemical, solid state and tribological requirements in the design of artificial heart valves.

BE12-F.7

HYDRODYNAMIC PERFORMANCE OF BEIJING BOVINE PERICARDIAL VALVE (BN2) AND STEADY FLOW TESTER USED IN CLINICAL Liu Yinglong*, Zhu Xiaodong and Xi Baoshu, Cardiovascular Inst and Fuwai Hosp, Chinese Academy of Medical Science, Beijing, China

Beijing bovine pericardial valve (BN2) was compared *in vitro* with CE, HK, LK, BS s 60, HC and GZ. The open pressure drop of BN2 is lower than that of porcine valve, the ΔP is lowest among the valves tested and the EOA of BN2 23, 2.7 CM^2 is the largest at 12 L/M in steady flow, also at 2-6 L/M in pulsatile flow. The CD of BN2 is about 70-85% and PI 50-65%. The backflow are 7.7% in LK, 5.6% in BN2, 4.4% in GZ, 3.3% in CE, 2.9% in HC. After replacement, the mean mitral EOA of 14 pts increased from 0.97 to 3.45 CM^2 , MVR from 139 to 243 ML/S. CO doubled while mean LAF decreased from 21.1 to 14 mmHg and ΔP cross mitral valve from 14.7 to 3.5 mmHg. All of the CO, CI, SI, PA, PCWP, SR, PR, PAR, LVSWI and rvswi recovered to normal levels 91 hrs after operation. The steady flow tester used is small, nonpoisonous, easy cleaning and sterilisation. Vanes turning is driven by electrical machine pump with which the flow rate can be over 30 L/M. Our experiment also showed a good correlation between ROA and EOA in 134 samples and fairly good correlation of EOA between *in vitro* and *in vivo*.

BE12-F.9

Pulsatile Turbulent Formation in the Human Aortic Arch in Response to Valve Orientation of Prosthetic Heart Valves - In-vitro Model Assessment -, H.Minamitani*, E.Okada, T.Miyazawa and A.Shinoda, Hiyoshi 3-14-1, Yokohama, Japan

Pulsatile turbulent formation in the human aortic arch was investigated in response to valve orientation of prosthetic heart valves by using laser Doppler visualization technique and pulsatile mock system. The used system mimics human aorta including three major branches and left heart. Turbulent intensity, turbulent energy density, power spectra of the turbulent flow components as well as shear stress were measured for three different valves. Turbulent formation was greatly dependent on the vessel geometry and the valve orientation, advanced as far as top of the aortic arch and affected the flow in the major branches such as brachiocephalic, and common carotid arteries. Total hydrodynamic assessment regarding the turbulence and systolic energy dissipation suggested that major orifice of Bjork-Shiley disc valve should be oriented to the aortic outer curvature, and that commissure of SJM valve setting in parallel to the curvature gave the best performance. As for Bioprosthetic valve, placing one of the three leaflets on the inner curvature site was found advisable. These orientations provided less obstructive effect on the outflow tract, smoother flow formation, and less turbulent energy density in the aortic arch.

BE12-F.10

A NEW MOCK CIRCULATION FOR ARTIFICIAL HEART VALVES
K. Affeld*, K. Schichl, A. Mohnhaupt, A. Spiegelberg
Universitätsklinikum Rudolf Virchow, Berlin, F.R.G.

In a mock circulation designed for the testing of artificial heart valves one has to imitate the flow through the valve and the aorta. The first task can be achieved without great difficulty, while the second is quite complicated. The generation of the pressure pulse in the real aorta is very complex. As a result mock circulations vary from lab to lab and consequently the test results. In the new mock circulation the artificial aorta is avoided altogether. It is instead simulated by the movement of a piston, which combines two elements in one - the heart wall and the aorta. During systole, the piston moves according to a physiological flow curve and forces the fluid through the valve. Then it stops and begins to retract. When the valve is closed, a differential pressure across the valve is generated, which causes the piston to go to a different control mode - it now is retracted with a certain elasticity following the diastolic pressure curve. The imitation of the aortic elasticity is thus transferred from hardware to software which means that the model aorta now is well defined. The movement of the piston also serves as a very precise flowmeter. In the new mock circulation valves can be tested with more precision and greater speed. Unlike the traditional mock circulations it is a system open at one end so a valve can be changed with a twist of the hand. It therefore may be useful for the production control of valves.

BE12-F.12

A mathematical model for the study of flow through stenosed valve

Chang-song Geng*, Wen-Yu Kong, Tianjin University

Stenosed valve or artificial valve produces very different flow behaviour from normal in both the valve and the ascending area. Some of characteristic features are jet flow, stagnation zone, large pressure drop across the valve. These characters have much to do with clinical detected problems, such as thrombus formation, endothelial damage, tissue over-growth.

Stenosis (natural valve with stenosed disease or bioprosthetic) and clog (mechanical prosthetic) is the main cause of producing these flow characteristic features. For this reason, we use definite element numerical method to study the flow through a stenosed valve and a mechanical prosthetic. Unsteady flow model experiments are conducted for three types valve (one bioprosthetic and two mechanical prosthetic) to measure pressure drop under varying flow.

The result can help us to understand why and where problems such as thrombus formation occur. So we can improve the valve design. This study is also lay a foundation for computer aided valve design.

BE12-F.11

MECHANICAL BEHAVIOUR OF THE OMNIGRAPH HEART VALVE PROSTHESIS
Josef Köhler*, Peter Guntermann, Paul Holtmann, Aerody amisches Institut, Aachen, West Germany

The study is focussed on the development of standardized test methods for artificial heart valves. Three series of seven original packed OC-valves of size 19 up to 31 could be tested (21 valves). Mechanical and fluidmechanical test parameters: Geometry, deformability, pressure- and volume-loss. Results/Geometrical parameters: The smaller valves show a bigger textile ring diameter and the bigger ones a smaller one than indicated by the manufacturer. The differences are mostly smaller than 1 mm. The valves of size 27 and 29 show the same disc diameter. Deformability and disc gap: The deformation results due to a radial force acting on the valve rim show a good compromise for the width of the bearing gap with relatively small variations. The sensitivity of the valve against these forces (sticking) is a lot smaller than that of the St. Jude valve. Pressure losses and effective valve area: The eff. valve area A_e is approximately independent of the volume flow. The relative ostium crosssection A_e/A_T (A_T = ostium crosssection) amounts 35% to 44%. It increases slightly with increasing valve size. Volume loss: The total volume loss per beat $V_R = V_C + V_L$ (closing volume + leakage volume) increases with valve size. It has - as average for all pumping conditions and sizes - with 3.4 cm^3 about that value, which was obtained for other technical valves, except bileaflet valves.

BE12-G.1

THE PLATELET THROMBUS FORMATION IN A MOVING STREAM FOR EVALUATING HEMOCOMPATIBILITY OF BIOMATERIALS
Xi Tingfei*, Tian Wenhua, Wang Chunren, Lei Xuehui
NICBP, Temple of Heaven, Beijing, China

We study the process of thrombus in normal fresh rabbit platelet rich plasma (PRP) on revolving polymeric loop and discover that this process is divided in five steps, first particles, snow storm, aggregation, plug, thrombus. The time formed snow storm is called Characteristic Thrombus Formation Time (CTFT) and is a parameter of evaluating hemocompatibility of polymers. We study 8 different time of PVC exposed PRP (0, 10, 20, 30, 40, 60, 80, 120 min) in order to ensure that testing are actually measuring activation due to the test materials, results of CTFT (sec) are 0', 144(+109); 10', 194(+50); 20', 204(+62); 30', 192(+22); 40', 97(+22); 60', 79(+30); 80', 129(+58); 120', 109(+47). The best activable contact time is 60 min. The CTFT of five polymers are measured with fresh rabbit PRP at 17 rpm for 60 min. Results of CTFT (sec, \pm s.d., n=5) are PVO, 79(+30); Silicone (Dow Corning Co. USA), 205(+31); Biomer, 212(+42); Pell-ethane 2363- 80 A, 231(+31); Cardiothane, 277(+83). Therefore, the blood materials interactions and mechanism of thrombus formation will investigated with the method developed in this paper.

BE12-G.2

AN INSTRUMENT TO ASSESS VASCULAR CONDUCTANCE IN VIVO. C.P. Burns, S.A. O'Connor, S. Frampton and L.M. Wood, Smith Kline & French Research Ltd, The Frythe, Welwyn Hertfordshire, AL6 9AR, U.K.

Many disease states of the cardiovascular system can be attributed to the inability of blood to perfuse regions of the circulation, e.g. the heart, exercising skeletal muscle or mesentery. By simultaneous measurement of blood flow to the region, and arterial blood pressure, the effectiveness of a drug to increase the vascular conductance of the region can be measured.

We have designed, developed and tested, in vivo in a variety of animals, an instrument which continuously and accurately divides flow and pressure signals to give a signal proportional to conductance. Pulsatile input signals of flow, from an electromagnetic blood flow meter, and pressure, from a blood pressure transducer, are smoothed by a low pass filter prior to passing into a variable gain stage which allows optimal signal inputs to be set for the divider stage. The divider used is an Analog Devices AD535 which accepts signals inputs in the range of 0.2-10V. The instrument can accommodate flow and pressure signals from a variety of species. The instrument is cheap, reliable and easy to use. Vascular resistance may also be simply obtained.

BE12-G.4

On-line Measurement of Red Cell Velocity in Microvessels With an Auto-tracking Window on Television, Wang ZhongRui, Dept. of Scientific Instrumentation, Zhejiang University, Hangzhou, China.

In order to measure the red cell velocity (Vrbc) in microvessels of vital subjects, an auto-tracking window on TV screen has been designed to track the crooked microvessels wobbling caused by heart beating and respiration. The Vrbc is measured on-line by sampling optical density line by line from a microvessel image in the window and calculating AMDF (Average Magnitude Difference Function) of two optical density waveforms sampled from successive frames in a microcomputer. Pulsed Vrbc in mesentery capillaries of frogs have been recorded. The range of Vrbc and calculating rate available in our system are ± 4.5 mm/s and 7-9 times/s respectively. A formula is derived to modify the calculated velocity of vertical movement on TV screen.

BE12-G.3

THEORY OF PULSE PHOTOMETRY OF HEMOGLOBIN AND DYE IN BLOOD

T. AOYAGI, M. FUSE, M. KANEMOTO, Y. SUGIYAMA, K. MIYASAKA*, M. SAITO**
NIHON KOHDEN CORP, *NATIONAL CHILDREN'S HOSPITAL, ** TOKYO UNIVERSITY; TOKYO, JAPAN.

The pulse oximeter measures the photoplethysmogram in two optical wavelengths and calculates $\frac{dA}{dt}$ (ratio of the change rates of absorbances) to find the arterial oxygen saturation. This principle can be applied to measure the concentrations of other dyes in plasma.

As there are red blood cells in blood, the reflection on the surface of the cells and the flattening effect caused by limited distribution of hemoglobin and dye makes the relation between $\frac{dA}{dt}$ and absorption coefficients or dye densities different from that of usual solutions.

We found theoretically and experimentally that the $\frac{dA}{dt}$ of blood is approximately equal to $\frac{dA}{dt}$ of solution even in blood with dye in plasma, when optical scattering is high enough and absorption by the cell is low enough. This will give the base for non-invasive photometry of blood contents for many purposes.

BE12-G.5

Power Spectral Analysis of Vasoactivity in Cutaneous Microcirculation following Thermal injury, R. da Costa*, S.J. Aggarwal, and K.R. Diller, University of Texas, Austin, Texas 78712.

The response of microvasculature to thermal trauma has been studied in dorsal skin-flap chambers of hamsters. Following recovery and normalization of tissue post surgery, fluctuations in the diameter of selected arteriole-venule pairs ranging in size from 10 μ m to 50 μ m and at different branching order sites were measured several times prior to burn and at the same sites post mild contact burn. The experimental vasomotion data was characterized in terms of mean, standard deviation and by the Prony method of spectral power analysis. The A1 (37-50 μ m), A2 (30-50 μ m) and A3 (25-41 μ m) arterioles dilated an average of 58%, 20% and 13% respectively. The fundamental frequency components of most vessels were shifted toward lower values, with some of the higher frequency components disappearing. Supported by a grant from the Whitaker Foundation.

201

BE12-G.6

Measurement of Platelet and Leukocyte Distribution at Branches, J. Perkkiö*, L.J. Wurzinger and H. Schmid-Schönbein, Dept. of Medical Physics, University of Helsinki, SF-00170 Helsinki, Finland

As blood flows through microvessels, erythrocytes and plasma are partly separated from each other. This phase separation gives rise to non-uniform distribution of cells in blood vessels. We have studied the concentration of platelet and leukocytes in blood flow through T-junctions cast in polyester blocks. The main branch diameter was 200 or 100 μm and the side branch diameter 100 or 80 μm , respectively. Human blood samples with different levels of fibrinogen were used. Human fibrinogen (Sigma, U.S.A.) was used for preparation of fibrinogen solutions. Either fibrinogen solution or isotonic buffered saline were added to platelet rich plasma. Concentrated erythrocytes were mixed with these solutions to yield four different samples: hematocrit 0.35 or 0.55 and high or low fibrinogen concentration.

The results showed that the concentration of platelets in the blood from the side branch was about 1.2 - 1.5 times higher than in the reservoir. The concentration of leukocytes in the blood from the side branch was about 0.9 - 1.4 times the value of the blood from the reservoir. The ratios were found to depend on the feed hematocrit and fibrinogen concentration.

BE12-G.8

Fundamental Light-Scattering Characteristics of Red Blood Cells, A. P. Shepherd* and J. M. Steinke, Department of Physiology, University of Texas Health Science Center, San Antonio, Texas, 78284, U.S.A.

Two important optical properties of red blood cells (RBCs), their microscopic scattering cross-sections (σ_s) and the mean cosine of their scattering angles (μ), contribute to the optical behavior of whole blood. Therefore, the adequacy of Mie theory in predicting values of σ_s and μ was tested by experiment. In addition, the effect of red blood cell size on σ_s and μ was investigated in two ways: 1) by studying erythrocytes from the dog, goat and human, three species known to have different RBC sizes and 2) by allowing the RBCs from each species to shrink or swell osmotically. Values of σ_s obtained by measuring the collimated transmittance of dilute RBC suspensions illuminated with a He-Ne laser agreed with those predicted by Mie theory. Moreover, measured σ_s values were directly proportional to RBC volume. By contrast, values of μ from Mie theory were consistently greater than those obtained experimentally by making angular scattering measurements in a goniometer. Thus, Mie theory appears to yield adequate values for the RBC's microscopic scattering cross-section, but by treating the RBC as a sphere with an equal volume, Mie theory fails to take the RBC's anisotropy into account and thus yields spuriously high values for μ . (Supported by HL 36080)

BE12-G.7

Measurement of Non-symmetric Velocity Profiles in Microscopic Blood Vessels: Formation of Compaction Stasis, W. Göbel, J. Perkkiö* and H. Schmid-Schönbein, Abt. Physiologie der RWTH Aachen, D-5100 Aachen, FRG

Blood samples with strongly aggregating erythrocytes have a reduced suspension stability and to sediment under the influence of gravity. We report about the phenomenon of intravascular erythrocyte aggregate sedimentation of human blood samples during maintained flow perfusing micro-channels cast in polyester blocks. Blood flow was examined from a lateral position recording the flow on video tape. Erythrocytes were suspended in isotonic buffered saline containing bovine fibrinogen (7 g/l), albumin (1 g/l) and heparin (2000 IE/l). The velocity profiles were measured by using a dual slit system adapted to the video record. Non-symmetric velocity profiles and pronounced phase separation between erythrocytes and perfusion media were observed at perfusion speeds of 0.5 mm/s, the place of maximum velocity moving progressively out of the center towards the top of the channel. Along the length of the channel the speed of the lower erythrocyte layers progressively slows down and the non-symmetry grows. The results suggest that the enhanced erythrocyte aggregatability may affect the stasis formation via gravitationally induced phase separation leading to non-symmetric velocity profiles.

BE12-G.9

Photon Diffusion Model of the Optical Absorbance of Whole Blood, J. M. Steinke* and A. P. Shepherd, Department of Physiology, University of Texas Health Science Center, San Antonio, Texas, 78284, U.S.A.

Photon diffusion theory has had limited success in modelling the optical transmittance of whole blood. Therefore, we have developed a new photon diffusion model of the optical absorbance of blood. The model, which was derived from the diffusion equation under appropriate boundary conditions, has benefited from experiments to test its fundamental assumptions. Predictions of the model have been compared extensively with transmittance data from whole blood, and the model is consistent with experimental findings. Furthermore, when all parameters associated with a given optical geometry are known, the model needs no variational parameters to predict the *absolute* transmittance of whole blood. However, even if the exact value of the incident light intensity is unknown (which is the case in many situations), only a single additive constant is required to scale experiment to theory. Finally, the model is shown to be useful for simulating scattering effects and for delineating the relative contributions of the diffuse transmittance and the collimated transmittance to the total optical density of whole blood. Applications of the model include oximetry and measurements of the arteriovenous oxygen difference in whole, undiluted blood. (Supported by HL 36080)

BE12-G.10

Erythrocyte Deformability, Total White Blood Cell Count, Platelet Count, and Transcutaneous Tissue Oxygenation as Predictors of Survival in a Canine Septic Shock Model

TW Chung[†], MA Smith^{*†‡}, TL Whitsett[†], EA O'Rear[†], LB Hinshaw[§]. [†]Dept. of Chemical Engineering, Univ. of Oklahoma, Norman, OK, [§]Depts. of Physiology and Biophysics, [‡]Dept. of Cardiovascular Diseases, Univ. of Oklahoma Health Sciences Center, P.O. Box 26901, Oklahoma City, OK 73190, USA.

The effect of shock developing subsequent to gram-negative septicemia on the milieu of hematologic and rheologic factors which govern microvascular tissue perfusion may provide utility in predicting survival in a canine shock model. Hemorheologic parameters measured at 6 hours after the infusion of live *Escherichia coli* which exhibited predictive value of survivability of greater than 24 hours included a 1) less decreased deformability of canine erythrocytes, 2) decreased total peripheral white blood cell count, 3) decreased peripheral platelet count, and 4) increased transcutaneous tissue oxygenation. Differences in mean systemic arterial pressure, heart rate, core temperature, respirations, hematocrit, serum glucose, pH, arterial oxygenation, erythrocyte sedimentation rate, fibrinogen concentration, and plasma viscosity were not discernible between both survivors of greater than 24 hours and non-survivors. Pretreatment of dogs with pentoxifylline did improve erythrocyte deformability but did not improve survival at an LD₁₀₀ challenge. Greater erythrocyte deformability, leukopenia, and thrombocytopenia are associated with greater transcutaneous tissue oxygenation and improved survival likely indicative of a less altered state of systemic microvasculature perfusion.

BE12-G.12

The Determination of Hematocrit (Hct) and of Total Protein Concentration (TPC) in Flowing Blood from the Measurement of the Acoustic Wave Velocity (v),
D. Schneditz*, M. Moser and T. Kenner, Department of Physiology, University of Graz, A-8010 Graz, Austria

The dependence of v on density ρ and on adiabatic compressibility χ_{ad} is given by $v = \rho \chi_{ad}^{0.5}$. In blood, both ρ and χ_{ad} mainly depend on TPC. v is determined by the measurement of the acoustic wave travel time (the resolution is better than 50 ppm). χ_{ad} , which is calculated from ρ and v values, is determined at different TPC, at different Hct and at different temperatures. For porcine blood the coefficient of correlation is > 0.99 and the relation between χ_{ad} , v , TPC (in the range from 90 to 340 g/l) and Hct (in vol%) at 20.0°C is:

$$\begin{aligned} \chi_{ad} &= 4,586.10^{-10} - 3,226.10^{-13} \text{ TPC} & [\text{Pa}^{-1}] \\ v &= 1483,07 + 0,273 \text{ TPC} + 0,000346 \text{ TPC}^2 & [\text{m/s}] \\ \chi_{ad} &= 4,218.10^{-10} - 6,994.10^{-13} \text{ Hct} & [\text{Pa}^{-1}] \\ v &= 1517,31 + 0,8996 \text{ Hct} & [\text{m/s}] \end{aligned}$$

The relation between v , Hct and TPC may therefore be used to continuously monitor blood cell concentrations in circulatory systems.

BE12-G.11

EFFECTS OF HEMATOCRIT ON RHEO-OPTICAL ERYTHROCYTE AGGREGATION KINETICS,

Abel Gaspar-Rosas* and George B. Thurston, Bio-Medical Engineering Program, Department of Mechanical Engineering, The University of Texas, Austin, TX 78712 U. S. A.

Accurate characterization of the aggregation properties of erythrocytes is of great importance in the clinical evaluation of blood. While erythrocyte sedimentation rate is strongly dependent on these properties, more precise quantitative measurement is provided by analysis of the rheo-optical transient following cessation of a flow induced state of cell disaggregation. Conventional clinical rheo-optical methods give a single characteristic aggregation time, while more precise analysis shows the need for two or more aggregation times to fit the exponential optical transients.

The aggregation kinetics are strongly dependent on the hematocrit and this dependence must be accounted for before clinical observations can be standardized. The effect of variations in the hematocrit on aggregation times and weighting factors is presented for both reflected and transmitted light, using a physiological range of hematocrit values of .30 to .60.

The kinetics of erythrocyte aggregation in a thin layer of blood (approx. 0.50 mm) during the first 40 seconds of the transient is analyzed using two aggregation times. The transients of both the light transmitted through the layer and reflected from the surface of the layer are monitored immediately following cessation of an oscillatory flow that produces the initial high degree of disaggregation of erythrocytes. As hematocrit is increased the first (shorter) aggregation time decreases more rapidly than the second (longer) time, with the second time approaching a constant value as the hematocrit exceeds 0.40.

BE12-G.13

TUMOR CELL DAMAGE BY SHEAR STRESS

Wang Junjian*, Liu Yongge, He Xi, Bioeng. Dept., Huazhong Univ of Science & Technology, Wuhan, Hubei, P.R. China

Experiments testing the ability of tumor cells to withstand shear stresses in Couette rheometer are carried out. Above a threshold stress level, EAT (Ehrlich ascites tumor) cells are extensively damaged due to shear stresses. We find that tumor cells are killed 30% to 60% of the population at shear stresses of 25 dynes/cm for one to two hours, which shows fluid shear stress in the physiological range can be the major source of damage to tumor cells in the circulation. At stress below 10 dynes/cm, there is little direct damage because of shear stress. Based upon the assumption that all viable cells have the same specific death rate in shear field, it is easy to induce the function between viability of tumor cells and shearing time. Viability is decreased exponentially with the duration of shearing time, which would be described as $V = e^{-kt}$ (V stands for Viability, t means time and k is characteristic of shear stresses and properties of tumor cells). Also, the threshold stress can be determined by extrapolation. All these derivations are consistent with the results of our experiments.

BE12-G.14

Effects of Hematocrit on Visco-Elasticity of Human Blood, H.Q.Chen, G.H.Zhong, L.Li, Z.N.Xue, West China University of Medical Sciences, Chengdu, Sichuan, China

Human blood exhibits the visco-elastic behavior at low shear rate. The viscoelasticity of human blood can be measured with sinusoidal oscillatory shear flow. Using the Low Shear-30 Sinus Rheometer, we studied the effects of hematocrit (HCT) on apparent viscosity of blood at low (0.512 sec^{-1}), moderate (5.96 sec^{-1}) and high (51.2 sec^{-1}) shear rate, and on viscoelasticity of blood. The results demonstrated that with increasing of HCT, the apparent viscosities at three different shear rates increased exponentially. The fitted curve between HCT and the apparent viscosity at low shear rate was steeper than the others. We found that viscous component (η') and elastic component (η'') also increased exponentially when HCT was increasing and HCT affected the η'' values more obviously than the η' values. This study developed the empirical equations to express the relationship between HCT and η' , η'' and discussed the physical meaning of the elastic component. We suggested that both η'' and the aggregation index (AI) of RBC are objective quantitative indices of aggregation of RBC, but the η'' value is more accurate than the other one.

BE12-G.16

Study of red cell deformability with electrical conductivity method, Wen Zongyao*, Wang Hongru, Chen Sheng Zhao Yuheng and Shen Qiang, Beijing Medical University, Beijing China.

A new type of instrument has been designed by the authors. Though the principle of this instrument is based on electrical conductivity method, the instrument differs from traditional resistive pulse spectroscopy which can also measure red cell deformability by measuring its electrical impedance change. The blood sample is put into the gap between a stationary inner cylinder and a rotating concentric outer cylinder, therefore the red cells are subjected to different shear stress. The change of electrical conductivity which results from red cell deformation can be measured through two poles on inner cylinder, namely, red cell deformability can be measured.

This instrument may measure static and dynamic results for red cell deformation with advantages of satisfactory reproducibility, time-saving performance and economic in cost. All results can be given by a microcomputer.

A series of red cell suspension were tested. The obtained results were analysed and demonstrated that the instrument can indeed measure red cell deformability. Furthermore, a formula of exponential relation between electrical conductivity and red cell deformability has been found.

BE12-G.15

Pulsating flows of inelastic fluids in slowly varying porous tubes - Modelisation of the blood microcirculation - G. Zeggwagh*, D. Bellet, Groupe de Rhéologie I.M.F.T Avenue du Professeur Camille Soula, 31400 Toulouse France

The main purpose of this paper is to present a theoretical and experimental study concerning the pulsating flow of inelastic fluids through porous conical ducts. The model corresponds to blood flow through porous conical vessels.

The theoretical approach is based on an implicit difference method, with Crank-Nicholson scheme. The experimental method based on laser-doppler anemometry is applied to pseudo-plastic solutions.

Same as many authors, we consider fluid flow in tubes, representing blood flow as fluids of one homogeneous phase in porous tubes. We assume that fluid is described by either Newtonian or power law model.

The influence of geometrical, hydrodynamical and structural parameters is systematically examined and related to velocity profiles, flow rate filtration and hydrostatic pressure.

BE12-G.17

Viscoelasticities of Normal Human Blood in Rotational Rheometer, F.Liao*, W.Li, Z. Ding and X.Zhou, China Academy of Traditional Chinese Medicine, Beijing 100700, China

To imitate blood flow in arteries, viscoelasticities of normal human blood were investigated by an oscillation at a frequency of 1.3 Hz and amplitude of 4° superimposed to a constant shear rate of 201 s^{-1} in HAAKE Rotovisco RV100/CV100. For comparison, viscoelasticities of the same samples were determined by pure oscillation as mentioned above. The results showed that the complex module G^* , storage module G' , loss module G'' and complex viscosity η^* at rotation were all significantly higher than that at pure oscillation ($P < 0.001$). The other parameters at rotation, loss factor $\tan \delta$ and relaxation time λ , were significantly smaller than those at pure oscillation ($P < 0.001$). The analysis showed that the average elastic increment was 35.1 compared with the viscous increment of 23.5 when flow condition shifted from pure oscillation to rotation plus oscillation.

BE12-G.18

Permeability of Cultured Endothelial Cell Monolayers: Mediating Role of cAMP, S. A. Casnocha*, L. V. McIntire, and S. G. Eskin, Biomedical Engineering Laboratory, Rice University, Houston, Texas, 77251 and Department of Surgery, Baylor College of Medicine, Houston, Texas 77030, USA.

Endothelial cells (EC), which line blood vessels in a monolayer, function as a permeability barrier between blood and the vessel wall. Monolayers of human umbilical vein EC cultured on a permeable polycarbonate substrate were used to study the effect of intracellular cAMP on permeability. Agonists studied were iloprost, thrombin and bradykinin. Iloprost is a stable analog of prostacyclin, which stimulates EC intracellular adenylyl cyclase activity by binding to an external receptor. Iloprost decreased permeability to 24% of baseline. A similar decrease in permeability was observed in monolayers treated with dibutyryl cAMP and IBMX (which act together to increase intracellular cAMP), suggesting that iloprost's effect on permeability is mediated by cAMP. Thrombin treatment of monolayers resulted in an 11-fold increase in permeability, which was nearly completely inhibited by first treating the cells with dibutyryl cAMP and IBMX. Bradykinin had no significant effect on EC monolayer permeability.

BE12-H.1

Ambiguity of Determining Elasticity of Blood Vessel According to Transit Time of Pulse Wave, Ye GuoFan*, Qin Jie and Chai Ming, Dept. Electronic Engineering, Fudan University, Shanghai, P.R. China.

The means of estimating the elasticity of a blood vessel segment by measuring the transit time (TT) of the pulse wave is widely adopted in diagnoses of arteriosclerosis. Based on Moens-Korteweg's formula, the faster the pulse wave speed C is, the larger the Young's modulus E is. However, the formula is derived from the nonviscous case different from the practical viscous situation, so the phase speed measured C_f is dependent on the Womersley number. For a definite harmonic the C_f/C -curves keep closely constant when 2 . At the early-sclerosis with no significant stenosis and for a vessel like the femoral artery, 3 is true, so M-K formula is applicable. When stenosis degree of vessel radius S begins to 40% with E rising, 2 becomes true, which implies that C_f may be no difference from the normal. In the case of severe case with S 70% (1), C_f can be slower than the normal instead. Our experiment in vivo on a dog's common iliac artery with artificial sclerosis and stenosis verified the above-mentioned law and proved the ambiguity of TT method. (Supported by the National Science Fund of PRC)

BE12-G.19

Angular Distributions of Forward and Backward Light Scattering from Flowing Blood, Munehiro Niwa*, Hiroshi Kanai, Jikei Univ. Sch. of Med. 8-3-1 Kokuryo, Chofu, Tokyo, Japan.

The scattering and absorption characteristics of blood is very important for the application of light to medical and biological engineering. Light irradiate the blood is chiefly scattered by the red blood cells. When the blood flow, the intensity of scattered light from the blood changes from that of blood at rest. It is related to scattering angle, shear rate of the flow and other blood parameters. In the red-nearinfrared region, the intensity of backward scattering increases greatly with the increase of shear rate, and it becomes about double the intensity for blood at rest when the shear rate is 50 l/sec. Then the angular distribution curve changes from circular to asymmetrical flattened ellipsoid. The forward scattering intensity decreases with the increase of shear rate, and it also becomes double when the shear rate is 65 l/sec. Then the angular distribution curve does not change very much.

BE12-H.2

Poststenotic Shear Layer Instabilities, Arterial Wall Vibrations and Coupled Nonlinear Oscillators

J Treiber*, R I Kitney, Biomedical Systems Group, Dept of Electrical Engineering, Imperial College, London SW7 2BT, UK

Detailed analysis of *in vivo* flow velocity measurements downstream of an induced stenosis has identified the existence of oscillatory flow disturbances, thought to arise from vortex shedding and arterial wall vibrations.

As the evolution of shear layers is highly susceptible to low-amplitude disturbances, wall vibrations can greatly affect the vortex shedding process.

In this study the sensitivity of poststenotic flow instabilities is studied experimentally. Forced flow measurements with an LDV downstream of modelled stenoses show that complete flow synchronisation may be achieved at very low forcing levels in steady flow, whereas pulsatile flow is considerably less susceptible. This explains the separability of the two oscillatory flow components observed *in vivo*.

Finally, a mathematical model is described comprising a chain of mutually coupled nonlinear oscillators, that explains flow synchronisation and the differences in susceptibility for steady and pulsatile flow. Interestingly, this model also describes vortex pairing and exhibits a form of turbulence based on the concept of diffusion-induced chaos.

BE12-H.3

Two- and three-dimensional visualization of velocity profiles measured in vivo in the aortic trifurcation in pigs.
EM Pedersen^S, JH Østergaard & VE Knudsen
Dept. Thorac. and Cardiov. Surg., Skejby Univ. Hosp. and Instit. of Experim. Clin. Research, Århus University, 8000 Århus C, Denmark

Atherosclerosis is often located at arterial branches, probably due to local hemodynamic factors. We have studied the velocity distribution in the aortic trifurcation in six pigs (90 kg). Point velocities were successively measured in the distal aorta and in the aortic trifurcation in 21 measuring points distributed across the vessel area using a 1 mm hot-film anemometer probe. Using ECG-triggered ensemble averaging and computerized plotting, 2- and 3-dimensional visualization of laminar velocity profiles were made. The velocity profiles proximally in the iliac artery were asymmetric with very low velocities near the lateral wall including signs of retrograde flow during diastole. Velocity profiles distally in the iliac artery were less asymmetric. Small variations (10%) in heart frequency during the measurement series produced significant artefacts in the profiles. To avoid this in the future it seems pertinent either to: 1) keep a constant heart rate using cardiac pacing 2) to measure velocities in different points simultaneously.

BE12-H.5

The pressure-volume diagram of human aortas is unaffected by sclerosis.
G. Langewouters*, K. Wesseling and W. Goedhard, BMI-TNO, Academic Medical Center, 1105 AZ Amsterdam, The Netherlands.

Segments of 45 human thoracic aortas, aged 30-88 yrs at autopsy, were perfused with 37 °C Tyrode at in-situ length. Two degrees of sclerosis were classified, according to the WHO definition: 26 aortas were normal or only intima affected (atherosclerotic), 19 aortas were also media affected (arteriosclerotic). Pressure-volume (p-V) relations were computed from measured diameter changes due to 20 mmHg pressure steps between 20 and 180 mmHg. A three-parameter mathematical model for the p-V relationship explained over 99% of the variance in volume with pressure for each aorta. Interindividual differences in the model parameters could for the greater part (>60%) be explained by the factor age alone. Arteriosclerotic aortas had a slightly larger volume than atherosclerotic aortas, over the entire pressure range studied. However, at physiological pressures, no differences between the compliances (dV/dp) of the two groups of aortas could be demonstrated (analysis of covariance, p>0.05).

BE12-H.4

The mathematical distributed parameter model for arterial system with wall viscosity and tethering, H. Hirayama* and H. Yasuda, Hokkaido University, N 15, W 7, Sapporo, Japan

To analyze the selective independent effects of the components of the arterial system including the surrounding interstitial tissue, we have constructed a mathematical distributed parameter model for a segmental artery such as the femoral artery or coronary artery. By inputting the biological data into this model, the flow wave transmission was reconstructed. The computed values of the several kinds of the impedances were almost coincided with the experimental data. The fluid dynamical viscous resistance, inertial resistance and the longitudinal impedance decreased with the radius of the artery. The transverse impedance increased with the elastic modulus of the arterial wall E. The characteristic impedance decreased with the radius but its frequency dependence was small. The complex impedance (local impedance) increased with the E and the distance from the entry zone of the arterial tube x. The reflection coefficient was also changed with the E and x. However the effects of the wall viscosity and the tethering of the surrounding tissue was not so marked comparing with the effects of the radius and wall elasticity.

BE12-H.6

Numerical Simulation of Coronary Circulation During Coronary Sinus Occlusion.
W. Schreiner*, F. Neumann, W. Mohl, E. Wolner. 2nd Surgical Dept. University of Vienna, A-1090 Wien, Austria.

In order to study the effect of coronary venous interventions on coronary circulation, a model of coupled differential equations is set up and solved numerically. Aortic pressure and myocardial contraction, obtained by Fourier synthesis, enter as driving forces. Coronary arteries, capillaries and coronary veins are given resistances and compliances dependent on flow and volume, respectively. Integration yields pressures, flows and volumes within the coronary circulation as functions of time. Simulations are carried out for normal perfusion conditions and intermittent coronary sinus occlusion. The venous compliance is modelled as a function of increasing coronary venous volume during coronary sinus occlusion so as to reproduce experimental data obtained from dogs and humans. Results are obtained for changes in phase of coronary flow and the amount of redistribution of blood as a consequence of coronary sinus occlusion.

BE12-H.7

Pressure Variation on the Walls of a Model Arterial Branch During Pulsatile Flow, by

J. M. Khodadadi*, Auburn Univ., Auburn, AL 36849-5341 and N. S. Vlachos, Univ. of Illinois, Urbana, IL 61801

Numerical predictions of pulsatile laminar flow in a plane 90-degree bifurcation have been carried out. The cases of Reynolds numbers of 38 and 102 with the corresponding Stokes numbers of 4.1 and 4.9 were investigated. The results show that one separation zone is established on the bottom wall of the main duct and another on the upstream wall of the branch. The numerical results were also compared to the LDV velocity measurements of the pulsatile flow field, showing excellent agreement in regions outside the separated zones

The pressure field was also obtained during the course of the present study. The detailed variations of the pressure along the walls of the arterial branch model were determined. It is clearly evident that the presence of adverse pressure gradients in the vicinity of the two recirculation zones lead to local flow separation.

BE12-H.9

Numerical Analysis of Fluid-Particle Dynamics in Artery Bifurcations with Stenosis and Surgical Reconstruction, C. Kleinstreiner, M. Nazemi* and J. P. Archie, Jr., NC State University, Raleigh, NC, USA

One of several hypotheses for the progression of atherosclerosis involve hemodynamics and mass transfer where fatty deposits represent tissue and wall shear stress responses. It is of interest to find out if atherosclerotic lesions occur at arterial sites because of locally low or high wall shear stress, laminar/turbulent or recirculating flow or because of a combination of several momentum and mass transfer processes.

As a first step in the analysis of the localization, development and physical effects of atherosclerosis, we solved the Navier-Stokes equations for steady laminar/turbulent flow in a two-dimensional axisymmetrically branching channel representing an aortic bifurcation. A parametric sensitivity analysis concentrated on the stenosis severity (ie, 0%, 35% and 65% lumen reduction), the bifurcation angle (ie, 7.5° and 22.5°), the Reynolds number (ie, 250 and 500), and the widened lumen geometry due to surgical reconstruction. In adding deposits in local areas of low and high wall shear stress, pseudo-transient, localized developments of stenosis were achieved in the parent/daughter tube near the bifurcation. Interestingly enough, these sites coincide with actual fatty plaque locations found in humans.

BE12-H.8

Viscoelastic Properties of Arteries in Human Forearms in Vivo, P. Gizdulich*, Fisica Medica Universita I-50134 Firenze

The viscoelastic pattern of the arterial pressure-volume diagrams was recorded in a forearm segment of 8 healthy subjects. Arterial pressure was noninvasively measured by using a special waveform pressure recording system. Blood pressure was recorded simultaneously in the medium finger of the left and right hand. Arterial volume was measured by using impedance plethysmography. Transmural pressure and arterial blood volume in a segment of the forearm were controlled by using the unloading technique. Shifted loops in repeated subsequent cuff inflation-deflation phases were obtained. In the past, the importance to select very slow cuff deflation rate has been discussed in order to analyze the whole forearm segment. In that protocol a venous increased stasis was induced in one arm. As an immediate consequence, pressure waveform distortion was documented. Our aim here has been to evaluate the influence of the increased venous pressure on local arterial blood pressure. A blood pressure variation between the two hands, related to cuff pressure trend, is occasionally observed. No trend of the differences of the mean pressure in the 8 subject group is documented. Assumptions on linearity of the hand's impedance are discussed.

BE12-H.10

An Experimental and Theoretical Simulation Study of Blood Flow in Arteries, Y. Haggag*, King Saud University, Biomedical Technology Department, P.O.Box 10219 - Riyadh 11433, Kingdom of Saudi Arabia.

The flow of blood through human arteries is simulated by the flow of an analog solution circulating through an elastic rubber tube, under steady state flow conditions. The pressure drop/flow rate relationship is presented from theoretical point of view and compared with the experimental findings obtained from a closed flow circuit. Two theoretical approach are introduced a) tube wall material obeys Hooke's law, b) tube wall material do not obey Hooke's law. Two specimen of elastic rubber tube, smooth and soft, were used to conduct experiments. The first specimen resembles the thoracic aorta or the abdominal aorta dimensions. The second specimen simulates the femoral artery dimensions. The experimental and theoretical results of the pressure drop/flow rate relationship are in good agreement, particularly when the tube wall material is considered not to obey Hook's law. In conclusion, the elastic rubber soft tube may be used to simulate the blood flow in arteries, especially for the relatively large diameter and short length vessels such as the thoracic aorta.

307

BE12-H.11

Wall Shear Stress Calculations in Constricted Ducts
J.A. Ekaterinaris, D.P. Giddens, A.K. MazHer*
Ga Tech, Mechanical Engineering, Atlanta GA 30332

Theoretical and experimental studies on hemodynamics consider blood as an incompressible Newtonian fluid. In the present work the applicability of a low Mach number compressible approach is investigated in order to circumvent the difficulties associated with the numerical solution of the elliptic incompressible Navier-Stokes equations which describe blood flow.

The full compressible flow equations were employed, and the solution was obtained for low Mach numbers so that the incompressible flow limit could be satisfactorily approximated. Solutions were obtained for steady flows in axisymmetric constricted ducts modeling conditions relevant to atherosclerosis studies. The numerical solution was performed with a finite difference implicit scheme using approximate factorization and Alternate Direction Implicit techniques. The wall shear stress of the low Mach number calculations was in good agreement with both, numerical solutions and the experimental LDV measurements for incompressible flows. The present approach is therefore useful for the investigation of near wall phenomena in certain situations which are important in atherosclerosis studies, and it can be extended to treat unsteady and three dimensional flows.

BE12-H.13

Ambulatory Measurement of Beat-to-beat Indirect Arterial Pressure in Human Fingers
A.Kawarada*, H.Shimazu, H.Ito, H.Kobayashi, J.Masuda & K.Yamakoshi, Dept Physiol, Kyorin Univ, Mitaka-shi, Tokyo; K.Yamakoshi is in Res Inst, Appl Electr, Sapporo-shi, Hokkaido, Japan

We had designed volume compensation technique to indirectly determine beat-to-beat arterial pressure and its waveforms in human fingers. It comprises a compression fluid-cuff and its pressure controller and a photo-plethysmograph to detect arterial volume change. Applied cuff pressure onto the finger can be controlled by a servosystem connected to the cuff around the basal phalanx of a finger so as to keep the arterial volume constant at the reference level which correspond to the arterial volume in an unloaded state. In this study, we have developed an ambulatory system to determine arterial pressure using this technique. Pneumatic pressure control system is adopted in it: The frequency response is flat up to 60 Hz. The weight of the cuff and actuator is 180 g, and the total weight including a recorder and power supply 2 Kg. Using this system, arterial pressure in ambulatory condition were successfully recorded during various exercises and stress tests.

BE12-H.12

NUMERICAL SIMULATION OF NONNEWTONIAN BLOODFLOW IN VESSELS
P. STEFFAN*, G. BACHLER, R. PUCHER
AVL LIST GmbH.,
Kleiststraße 48
A - 8020 Graz

For the numerical simulation of blood flow in vessels the consideration of Non-newtonian Flow-Effects influences the flow field. We used the method of finite differences to solve the equations of continuity and momentum for three dimensions. As we were looking at vessels with "large diameter" the mayor nonnewtonian influence is coming from the Rouleaux-effect, which can be described mainly in a connection of viscosity and shearrate. For this link we used the equation of Cross. Using an interactive solution-algorithm we solved these equations for some typical stenotic narrowings. A comparison of newtonian and nonnewtonian flow field shows considerable differences.

BE12-H.14

AN EXPERIMENTAL INVESTIGATION OF PHYSIOLOGICAL TYPE FLOWS IN LEFT VENTRICULAR AND AORTIC ARCH MODELS
R. RIEU*, F. CASSOT**, D. MORVAN*, R. PELISSIER*

(*) I.M.F., 1, rue Honnorat, 13003 Marseille, France

(**) L.M.A., 31, Chemin Joseph Aiguier, 13009 Marseille, France

Using a cardiovascular simulator allowing the production of physiological flow conditions, ultrasonic velocity measurements were made in various elastic singularity models of the cardiovascular system such as aortic arch or ventricular cavities. Two velocity components were recorded in a sample volume of about 1 mm^3 ; then the corresponding velocity vector was obtained at each instant of the simulated cardiac cycle. Using this no classical method, it was possible to obtain new important original results on the main features of the flow. In the aortic arch, skewing effects of the velocity profile toward the inner wall of the bend and rotational creation near this wall illustrate unsteadiness, entrance conditions and curvature effects. Flow characteristics in the anatomically shaped ventricle are associated with an important intraventricular vortex. The analysis of the instantaneous velocity field allows, during the cardiac cycle, the follow up of this structure whose intensity and position are highly depending of the mitral and aortic valve specifications and in particular of vorticity creation on the mitral valve leaflets.

308

BE12-H.15

Mass Transfer to and from the Vessel Wall distal to a Sudden Tubular Expansion, X. Deng*, and T. Karino, Montreal General Hospital, Montreal, Quebec, Canada.

To elucidate the possible role of fluid mechanical factors in the localization of atherosclerotic lesions in man, the effects of disturbed flows or mass transfer to and from the vessel wall distal to a sudden tubular expansion (where an annular ring vortex was formed), were studied both theoretically using computational methods and experimentally by measuring the dissolution rate of donut-shaped benzoic acid pellets which formed the wall of the tubular expansion. It was found both theoretically and experimentally that mass transfer from the vessel wall to the flowing fluid is much higher within the vortex near the reattachment point than anywhere else. Theoretical analyses on mass transfer from the blood to a permeable vessel wall showed that for macromolecules such as lipoproteins, having small diffusin coefficients, a species concentration polarization occurs at the surface of the permeable vessel wall. The accumulation of species was predicted to be the lowest at the separation point and the highest at the reattachment point where the molecules are carried towards the vessel wall by the radially directed curved streamlines of the vortex existing in the vicinity of the reattachment (stagnation) point.

BE12-H.17

ANALYSIS OF HUMAN CEREBRAL ARTERIAL CASTS
RK Pucher, F Anderhuber⁺, St Schuy,
LM Auer, University Graz, A-8036 Graz,
Austria

Compared to other vascular beds the cerebral circulation shows differences in the geometrical structure. Large cerebral arteries themselves and also their bifurcations are exclusively situated on the surface of the brain. Therefore, these arteries are rather long to be able to reach all points of the cortex. 27 arterial casts of human cerebral arteries, containing 1307 single arterial branches, in the diameter range from 3mm to 250um were investigated. The relation of arterial diameter to arterial length was found to be similar in the vascular beds of the anterior (ACA), middle (MCA) and posterior (PCA) cerebral artery. The data is used to develop a mathematical model of the cerebral circulation. The relation of mean intravascular pressure to arterial diameter was calculated for all three vascular beds. It is shown that the pressure head loss in the large arteries of the MCA territory is higher than in the territories of the ACA and PCA. This result shows that additional pressure drops (vasospasm, stenosis) are more likely to cause hypoperfusion in the MCA.

BE12-H.16

CONSTANT SHEER RATE IN HUMAN CEREBRAL ARTERIES, A BASIS FOR A MODEL OF THE CEREBRAL CIRCULATION, R.K.Pucher⁺, F. Anderhuber, St.Schuy, L.M. Auer
University Graz, A-8036 Graz, Austria

Exact knowledge of the structure of human cerebral arteries is necessary for the evaluation of a mathematical model of this complex vascular bed. 725 bifurcations in arterial casts of human cerebral arteries were investigated. Results show that the 3rd power of the diameters of the parent vessels equals the sum of the 3rd powers of the diameters of the daughter-vessels. Sheer rate is therefore only changed minimally. Based on constant sheer rate in cerebral arteries, a model of the human cerebral circulation was developed. The model includes some 30 million arteries, arterioles and capillaries. Non-Newtonian behaviour of blood viscosity is taken into account. Cerebral autoregulation is simulated by means of diameter variation. After numerical solution of the flow equations, pressure gradient, flow velocity, Reynolds numbers and volume flow can be seen in all vessels. Theoretical limits of cerebral autoregulation are calculated and compared with measured data.

BE12-H.18

Pulsatile Flow of Blood Through an Arteriosclerotic Vessel, T.Usha and R.Ponnalagar Samy⁺, Centre for Mathematical Sciences, Vazhuthacad, Trivandrum- 695014, India,⁺ Department of Civil Engineering, Chuo University, Kasuga 1-13-27, Tokyo.

The effects of rheological behaviour of blood and pulsatility on flow through stenosed arteries have been investigated. The rheological behaviour of blood is described as non-Newtonian fluids obeying Casson models. The perturbation technique has been adopted to investigate the flow. The most notable result of pulsatility is the phase lag between the pressure gradient and flow rate, which is further influenced by the non-Newtonian nature of blood and the height of the arteriosclerotic plaque. It is found for the first time that the phase lag between the pressure gradient and flow rate, flow resistance, radius of plug core region and velocity changes along the axial (flow) direction in the stenosed region. It is of importance to know the correlation between the change in the phase lag and the growth or alteration of arteriosclerotic plaque on the arterial wall but it is not still clear what the role this phase lag can play in the growth of stenosis or the development of cardiovascular diseases. It is therefore suggested that a series of experiments is to be conducted to identify the role of the phase lag concerning cardiovascular diseases.

BE12-H.19

An Experimental Study on the flow characteristics in a Sequential Bypass Grafts. S.Kanazawa, T.Fujiwara, H.Inaba, S.Matsuoka, H.Yoshida, T.Katsumura, Dept. of Thoracic and Cardiovascular Surgery, Kawasaki Medical School, Kurashiki, Japan

The sequential bypass surgery is performed frequently for the coronary revascularization to multiple coronary vessel diseases. To investigate hemodynamics in a sequential bypass graft, we provided a sequential bypass graft model between the left and right external iliac arteries using autologous external carotid vein in the dogs. We measured the blood flow rate and velocity profile across the graft using electromagnetic flowmeter and 20MHz 80 channel pulsed Doppler velocimeter, respectively. The flow rate into the side-side anastomosis is always higher than that into the end-side anastomosis. However, enough blood flow was supplied through each anastomosis, indicating the usefulness of the sequential bypass graft for the blood supply to ischemic heart disease with multiple vessel diseases. Regarding the velocity profile, directional skewing of the velocity profile was recognized in the region just proximal to the side-side anastomosis. The reverse flow near the wall opposite to side-side anastomosis suggests the existence of flow separation and recirculation zone in the region. Thus, we considered that the flow condition of the side-side anastomosis is better than that of end-side anastomosis from the view point of fluid dynamics.

BE12-H.21

Hemodynamic disturbances at arterial stenoses in vivo J.H. Østergaard*, E. Morre Pedersen, V.E. Knudsen, J.M. Hasenkam, H. Nygaard & P.K. Paulsen. Dept. Thorac. Cardiovasc. Surg., Skejby Univ. Hosp. & Instit. Experi. Clin. Res., Aarhus University, Denmark

As the progression of arterial stenoses is considered caused by induced local hemodynamic disturbances, we have attempted to characterize the velocity field downstream mild arterial stenoses.

Fifty and 85% area-reducing stenoses were constructed successively by external banding of the abdominal aorta of 6 pigs. Using hot-film anemometry and analog filtering technique, laminar and turbulent blood velocity parameters were measured and computed for 21 points distributed in the vessel cross-sectional area at 3 axial positions.

While the peak systolic velocity was highest 1 diameter downstream 85% stenoses, the absolute and relative turbulence intensities were most prominent 2 diameters downstream. Velocity profiles revealed a typical post-stenotic jet, whereas just downstream the stenoses the relative turbulence intensity demonstrated an "M"-shaped radial distribution. Furthermore, the analyses indicated that the turbulence became more low-frequency further downstream the stenoses.

This study shows, that the peak systolic velocity, the absolute and relative turbulence intensity and the frequency content of turbulence in the post-stenotic velocity field strongly depends of degree of stenosis and radial and axial position of measurement.

BE12-H.20

Evaluation of velocity waveform in intramyocardial artery and vein by laser Doppler method K. Mito*, Y.Ogasawara, O.Hiramatsu, Y. Wada, M. Goto, S. Tadaoka, K. Tsujioka, F. Kajiya, Kawasaki Medical School, Kurashiki, 701-01, Japan.

To evaluate the intramyocardial blood flow pattern, we employed the laser Doppler velocimeter with an optical fiber (0.062mm). The optical fiber was inserted into the intramyocardial artery and vein of five anesthetized dogs, and the blood flow velocity near the rounding fiber tip was measured. The blood flow pattern of the deep septal artery (10-20mm depth) was exclusively diastolic, accompanied by a sharp reverse flow during isovolumic contraction. Following administration of nitroglycerin, it increased the both forward and reverse flows, and the second peak of the reverse flow appeared during mid systole. The blood flow pattern of the intramyocardial vein (depth: 1.0-3.0mm) which empties into anterior interventricular vein increased rapidly during the isovolumic contraction phase. It decreased with the beginning of diastole and a transient reverse flow was observed frequently during early (or mid) diastole. Administration of nitroglycerin resulted in the increase in the systolic flow which showed a double peaked pattern. It also increased the reverse flow. The systolic forward flow in the vein showed a reciprocal relation with that of the reverse flow in the artery. It was indicated that the phasic blood flow patterns in the intramyocardial artery and vein are more reflective to the effect of myocardial contraction and relaxation on the intramyocardial vascular beds.

BE12-H.22

BUCKLING OF A THIN CYLINDRICAL SHELL SURROUNDED BY AN INFINITE MEDIUM: APPLICATION TO CORONARY MICROVESSELS G. SAMAKE, D. GEIGER, C. ODDOU Laboratoire de Mécanique Physique, Université Paris XII - 94010 Créteil, FRANCE.

A theoretical model was developed in order to assess the changes in the lumen area of coronary microvessels during a cardiac cycle. A segment of small blood vessel is assumed to be embedded in an isotropic and infinite medium which is subjected to a time and space varying tissue pressure, as calculated from a left ventricle mechanical model. It was emphasized that, close to the endocardium where the tissue pressure is high and for a sufficiently thin wall vessel, a buckling phenomenon can occur in the occlusion mechanism.

Such an instability process was analyzed under the hypothesis of a linear, isotropic, and elastic behaviour of the medium assumed to be strained in the plane perpendicular to the vessel axis. For a given pressure, our theoretical analysis gives a formula for the critical pressure at which an elastic instability appears, depending on the rheological parameters of the medium.

The results were validated by comparison with those of experiments where a PVC tube was either inserted or tethered within a large piece of latex foam, itself submitted to a controlled pressure.

210

BE12-H.23

A NUMERICAL APPROACH TO PROPAGATIONS OF NONLINEAR PULSE WAVES IN ARTERIES S.G. Wu*, Beijing Polytechnic Univ, Beijing, P.R.China, G.C. Lee, and X.S. Ma*, State University of New York, Buffalo, NY

The present paper mainly deals with methods of numerical solutions for the problems of propagations of nonlinear arterial pulse waves. The artery is assumed to be a thin-walled vessel with the small tissue thickness, and its wall is locally orthognal, anisotropic, elastic and incompressible. In addition, the blood is modeled to be an incompressible Newtonian fluid with the axisymmetrical flow. In this numerical experimentation, the problem of propagations of nonlinear pulse waves in the aorta of a dog is studied, and the calculation is being performed in IBM-4381 computer. The complete numerical results are obtained, they involve solutions of propagations of the following nonlinear pulse waves: pressure, velocities and flowrate of the blood, as well displacements, velocities and stresses of the vessel wall. These results obtained are very useful to explain the mechanism of propagations of pulse waves in arteries.

BE12-I.2

The Acoustic Radiometer Measured Ultrasonic Therapeutic Instrument
Jin Shuwu, Zhejiang University
Hangzhou, China

According to acoustic radiated force theory and Shotton's method, a new type of acoustic radiometer with float tethered chains for measuring output mean sound power from the ultrasonic therapeutic instrumentations and others ultrasonic equipments is developed. The basic principle, construction design, sensitivity calibrated and measured method are described and remarkable advantage of the radiometer is introduced, too. The reflected target with air backing in diameter 6.1cm has the reflected coefficient 99.9%. The vernier gauge and the optical readout system used for measuring displacements by acoustic radiated force. Nine errors of the radiometer is analysed. The measured repeatability error for confidence level 99.7% is better than 2.3%. The sensitivity constant in 0.5-10watts measured range is 10.90mm/w.

BE12-I.1

Ultrasono-Tomography Using FM Chirp Pulse Compression Technique,
T.Moriya*, S.Kiryu, H.Matsukawa, T.Fuse,
Y.Tanahashi+, Tokyo Metropol. Univ.,
1-1, Fukazawa 2-Chome, Setagaya-ku,
Tokyo, 158, Japan, +Tohoku Univ.

To improve resolution of ultrasono-tomography and to remove bioeffects due to the peak intensity of the ultrasonic pulse, we devised a scanning system incorporating FM chirp pulse compression technique.

The B-mode images for tissue mimicking phantoms and abdominal B-mode images are obtained using the system and compared with those obtained using the conventional pulse method.

We have found that (1) the images obtained by this method are similar to those obtained by the conventional pulse method, when the center frequency of the chirp signal from the region of interest is the same with the center frequency of the pulse signal from the same region, (2) without changing the transducer, we obtain the B-mode images with higher lateral resolution only by shifting the center frequency of the chirp signal to the higher frequency.

BE12-I.3

Experiments for a new quantitative reflection imaging, Jian-Yu Lu and Yu Wei*,
Dept. of Biomedical Engineering, Nanjing
Institute of Technology, Nanjing, China

A new quantitative reflection imaging method which reconstructs the sound speed distributions of biological soft-tissues using the outline information and the phases of rf echo signals on these outlines provided by commercial B-scanner has been developed by the authors recently*. This paper reports the experiment studies for image reconstructions using the method introduced above. The rf echo signals are acquired from the commercial Japanese B-scanner SSD-256 using the waveform-storage oscilloscope HP-1780B with a sampling rate as high as 30 MHz. An interface between the B-scanner and the oscilloscope was specially designed to eliminate a random waveform shock caused by big time-delay of the waveform from trigger. The signals sampled are transferred to IBM-PC computer using IEEE-488 parallel interface for image reconstructions. Several agar phantoms were prepared and were put into an echoless tanker for experiments. Compared to the images displayed on the screen of the B-scanner, the images reconstructed are more helpful in the understanding of the structures of the test objects.

BE12-J.1

Early and late microvolt potentials / μV / in patients with ventricular tachycardia/fibrillation. F.Walczak*, R.Kępski, W.Rużyłło, W.Popławska, M.Hoffman. National Institute of Cardiology 04-628 Warsaw, Poland

In patients after myocardial infarction and ventricular tachycardia/fibrillation /VT/VF/ existence of late potentials /LP/ may be often found. Ventricular μV could be also observed in some pts, within /as "notches"/ and even before /as "early potentials" - EP/ of the QRS complex.

In this study relationship between degree and quality of myocardial damage and occurrence of μV , in the low noise eeg recording was evaluated. In 14 pts with primary VT/VF, LP occurred in 71%, EP in 1 pt, the total ventricular activity time /TVAT/ was $\bar{x}=121$ ms and the ejection fraction /EF/ was $\bar{x}=49\%$. In 62 pts with secondary VT/VF, LP had 89%, EP - 32%, TVAT $\bar{x}=134$ ms and EF $\bar{x}=44\%$. The longest TVAT $\bar{x}=147$ ms and the lowest EF - 33% had pts with secondary VT/VF and with EP.

Conclusion: Appearance of early potentials within pts having late potentials indicates higher degree of myocardial injury.

BE12-J.2

Measurement of ventricular activity in multi-directional high resolution e.c.g. R.Kępski*, F.Walczak, M.Hoffman National Institute of Cardiology 04-628 Warsaw, Poland.

Thanks to the spatial electrode location developed in our laboratory, multi-directional low noise / $0.5\mu\text{Vp-p}$ / recording with analog averaging was applied to the μV signal detection. In this way the ventricular activity detection due to 4 different measurement directions was achieved. Advantage of this method: 1.Improvement in small signals detection /like late potentials, QRS-notches, pre-QRS waves etc./, 2.Estimation of the onset and termination points of the QRS "viewed" from different directions, 3.Indication of vectorial orientation of μV signals on the basis of their magnitudes in subsequent traces, 4.Possibility of a single-beat recording or registration with limited number of averaging cycles. Clinical experience: method applied as a routine test for pts with different stages of the coronary heart disease, dilated and hypertropic cardiomyopathy, arrhythmogenic right ventricular dysplasia, mitral prolapse and with ventricular arrhythmias of unknown origin.

BE12-J.3

THE COMPUTER SIMULATION OF THE PASSIVE PROPERTIES IN THE CULTURED MYOCARDIAL CELLS

Qin Chengde*, Hu Yang, Wang Junjian, Dept Bioeng, Huazhong Univ of Science & Technology, and Li Li Xiaoguang, Dept of Medical Elec Eng, Xi'an Medical College, Wuhan, Hubei, P.R. China

Using glass-electrodes (tip $<0.5 \mu\text{m}$) intracellular recording technique, we measured the parameters of the passive properties in cultured Myocardial cells from neonatal rats as follows: membrane capacitance: C_m , $1.6 \mu\text{F}/\text{cm}^2$, membrane resistance: R_m $8.9 \text{K}\Omega\text{cm}^2$, membrane time constant: T_m , 14.2ms .

The R_m and T_m of the cultured myocardial cells were decreased by adding sodium fluoride (NaF , 5ppm) to the perfusing eagle's fluid.

The effects of fluoride on the passive properties in the cultured myocardial cells were simulated by means of Apple-II microcomputer system, according to BR (Beeler and Reuter) model. BASIC language, Euler's method and a self-adaptive procedure were used.

Simulation results suggest that the effects of fluoride on T_m and R_m of myocardial cells were realized through increasing the potassium conductance (G_K) of heart cell membrane.

BE12-J.4

A Method For Noninvasive Determining The Cardiac Electrophysiological Parameters
Fang Zuxian*, Fudan University
Jiang Wenping, Suzhou No.1 Hosp.
CHINA

Measuring of cardiac electro-physiological parameters is a primal thing for study arrhythmia and is an important evidence to make a exact diagnosis and decision how to use anti-arrhythmia drugs.

Usually, 2-4 Catheters were inserted transvenously into heart for stimulating. Now we instead it of using a single quadripolar catheter -electrode transesophageally put a pair of electrodes near the ventricle, so as to stimulate heart effectively to detect the electrical acting of heart.

The instrument for this purpose was designed which is a multi-function programmable stimulator. It can deliver four kind of premature stimuli, S1, S2, S3, S4. Each one may be programmed independently and synchronized with P or R wave picked up from esophagus by the same electrode. The stimulator is also able to determine re-entry tachycardia both by automatic and manipulation.

More than 50,000 cases have been examined in this way in the past 3 years in China.

BE12-J.5

Studies on High Frequency Electrocardiogram in the Early Diagnosis of Coronary Heart Disease, Zhu Wei-ping, Zhang Yun-feng, Zhang Chun-hua, Tang Lin, Wang Shu-chun, and Gao De-en, Shandong Teachers' University, Jinan, China

We conducted the comparative studies between applied high Frequency ECG and selective coronary arteriography to the clinical diagnosis of CHD in three groups of 43 patients with angina pectoris, myocardial infarction and cardiomyopathies. Our data showed that high frequency notches could separate patients in CHD group from patients in cardiomyopathies group and that significant differences were observed between groups ($p < 0.05$). By counting notches in the 6 leads, it would be expected that patients who had more than 6 notches would be associated with 50% or greater obstruction of single or multiple-vessel, demonstrated on coronary cineangiogram. Based on the criterion, the correspondence rate between applied HFECG and coronary arteriography to the diagnosis in CHD was 74%.

Using the high frequency technique, we have studied: 82 new subjects in the middle aged and the aged, results showed that a total of more than 3 high frequency notches in the 6 leads suggested a high probability of CHD.

BE12-J.7

Effect of blood-flow-induced electromotive force on heart in a high magnetic field, U. Ozai* and K. Nakano, Kyorin University School of Health Sciences, Miyasaka 476, Hachioji, Tokyo 192.

There are many conflicting papers about the magnetic field effect. In this study we discussed one of these problems. When a conductive fluid moves across a magnetic field, electromotive force (EMF) is induced perpendicular both to the moving direction of the conductive fluid and the magnetic field. A study was made to investigate the effect of the electrical potential generated by blood flow in the heart in a high magnetic field on the sinus node which provides a rhythm of the heart.

In the first place an experiment was made on rabbits. Two electrodes were placed for the ECG or heart rate monitoring. A magnet energized by an electrical current generated a magnetic field intensity of 4000 gauss at the center between the poles. We investigated the changes in heart rate in response to a magnetic field at various angles (θ) between the dorsofrontal direction of the chest and the north-to-south direction of the field. After a rabbit was placed in the high magnetic field, we determined heart rate under various conditions; when $\theta = 0$ degree, heart rate was fewer than control; when $\theta = 180$ degrees, heart rate was more than control; when θ was 90 and 270 degrees, heart rate was almost of the same as control. From these results it was found that the reciprocal potentials of these blood-flow-induced EMF acted on the sinus node to elicit an increase or a decrease in heart rate. The same results was yielded in the experiment on man.

BE12-J.6

The direction and distribution of His Bundle potential on the body surface, J. Jin*, Xian Medical University, P.R.China; G.Schoffa, University Karlsruhe D-7500 Karlsruhe, F.R.G.

The purpose of this work is to search the optimal lead positions and reasonable space-average methods for non-invasive beat to beat His Bundle potential recording (HBPR). A new IBM-PC XT (or AT)-controlled multichannel ECG system with very high resolution has been developed for this research. The measurement was carried out by 10 health men in normal environment. The direction and the distribution of His Bundle potential on the body surface were investigated with PQ-Segment map and PQ-segment vectorgram, from which the suitable lead positions and the reasonable space-averaging method for non-invasive beat to beat HBPR could be concluded. These new leading methods were then examined by the beat to beat measurement in normal environment by 10 people. The result of this work is a recommendation of the reasonable leading system for beat to beat HBPR.

BE12-J.8

A Low-Cost Real-Time System for Detection of Late Ventricular Potentials, MA Poluta*, IWP Obel, Johannesburg Hospital and University of the Witwatersrand, Johannesburg, South Africa

Non-invasive detection of late ventricular potentials (LVPs) is being used as a screening test for cardiac patients at risk to recurrent sustained ventricular tachycardia, a life-threatening arrhythmia. An LVP measurement system comprising the following modules has been used on over 200 patients :

- A high-frequency ECG module with a gain of up to 500,000 and a bandwidth of 30-2000 Hz. (The upper frequency limit is effectively reduced by trigger time-jitter)
- A conventional ECG monitor module for processing of the reference ECG signal
- A trigger module for generation of the fiducial point, with adjustable refractory period for rejection of extrasystoles
- A Gould 1425 digital storage oscilloscope with waveform processor option for display, averaging and manipulation of the reference and high frequency ECG waveforms.

A 200-millisecond time window is used to display the QRS-complex and ST-segment. The test procedure includes 4 bipolar lead configurations and typically lasts less than 15 minutes. All patient connections are isolated.

BE12-J.9

Recognition and Termination of Paroxysmal Tachycardia, Jiang Ding* and Zu-Xiang Fang Fudan University, Shanghai, P.R. China

Paroxysmal tachycardia (PT) is an abnormal rhythm which can be treated by electric therapy. After analyzing the mechanism of PT, we set up a new threshold for automatic recognition. That is: $TC=1/2(\text{cardiac period})+\text{constant}$. Practical application shows that this threshold is much simpler, more practicable and effective than those currently used in Holters or monitors. It can distinguish with high accuracy between PT and sinus tachycardia. Premature Extra-Stimulation (PES) is a safer method to terminate PT. In order to quickly find the "Terminating Window (TW)", we develop a new searching algorithm named "Half Division". It can adaptively modify the searching direction by detecting the different response to stimulation in different sides of the TW and that reduce the intervals of successive stimuli. Thus it is probably far more efficient than the traditional Linear Scanning algorithm where the searching direction and stimuli intervals are both fixed. Suppose M and N are the equivalent stimuli number of Half Division and Linear Scanning algorithm. theoretical calculation shows that they have the following relation: $M=1.06N$.

BE12-J.11

Performance of a sintered titanium electrode, R. Thull* and M. Schaldach, Zentralinstitut für Biomedizinische Technik, Universität Erlangen, G-8520 Erlangen, FR of Germany

Due to electrochemical properties, the stimulation electrode material does not influence normal thresholds as long as pulse duration is short compared with the time constants of any electrochemical processes, and the electrode surface layer is either electron conducting comparable to the bulk, or the dielectric is suitable thin and of large area.

Contrary to the threshold performance of the material, its structure has a significant influence on the detection capability of small intracardiac signals. In continuation of earlier development studies, an electrode was made of sintered $TiAl_5Fe_{2.5}$. In vitro test results show a very low cutoff frequency and a short recovery time after pulse delivery. Characterization shows both a small deflection from the equilibrium state of the surface structure and ion distribution, which are prerequisites for low energy losses in the electrode tissue interface. Optimal sensing and stimulation properties have been confirmed by a multicentric clinical study.

BE12-J.10

Surface-activated LTI Carbon Endocardial Pacing Electrode, Ye-cho Huang*, Jie Jin, Wei-xing Sun, Chang-zong Cui, Wen Fu, Xian Medical University, Xian, China

A new endocardial pacing electrode material-surface activated lower temperature pyrolytic isotropic (LTIA) carbon has been studied. Its electrical properties were measured in vitro, compared with Pt-Ir, Elgiloy, Ag-AgCl. It possesses very good electrical properties and biological compatibility. The experiments of LTIA carbon endocardial pacing electrode were carried out in two groups - LTIA and Elgiloy. Two electrodes were implanted in each dog's right ventricle and the difference between electrical parameters of these paired electrodes were analysed. Statistical analysis of stimulation threshold, attenuation rate of QRS wave, endocardial ECG and cardiac function after electrode implantation showed that LTIA carbon electrode had a better sensing character and lower chronic stimulation threshold. A reduction in local tissue reaction has been verified by in-vivo tests. This new developed pacing electrodes has been used in clinic since 1985.

BE12-J.12

A Monitor to detect His- and Early Atrial Potentials from the Surface of a Langendorff Perfused Heart, E.Hofer*, G.Stark, H.A.Tritthart, Karl-Franzens-Universität Graz, A8010 Graz, Austria.

Detection of His-Bundle- and early atrial potentials requires intracardiac measurements. We developed a method to measure continuously those signals by a single bipolar epicardiac lead in Langendorff perfused hearts. Simultaneous intracardiac (HBE) and epicardiac (SECG) electrograms were recorded and compared in the time and frequency domain. The power spectra were evaluated to design a monitor, consisting of a preamplifier and a main amplifier with appropriate filters and offset adjustments (overall gain 10^5 , cutoff frequencies of 30,80 and 900,3000 Hz). The trigger input for the oscilloscope is switched to the R-wave of the SECG or to the stimulus signal. With this monitor, the regular SECG and the windowed His- or early atrial potentials can be recorded in a beat to beat manner on t' - screen of a simple digital oscilloscope to evaluate impulse generation and conduction in the intact heart.

BE12-K.1

Cardiac output measurement: Accuracy and precision of thermal dilution and ultrasound techniques measured against a calibrated standard and guidelines for clinical use. G Hutchinson* and L Stratton, ECRI, Plymouth Meeting, PA.

The thermal dilution and ultrasound techniques for measuring cardiac output have comparable accuracy and precision but the specific application may dictate the use of one or the other because of the characteristics and limitations of each. Under our controlled conditions, we found both techniques had errors of 5% or less and had precision of about 2.5% or less; the thermal dilution was technique slightly superior. We tested over a range of 1 to 10 L/m and heart rates of 40 to 180 bpm. For this study, we developed a pulsatile flow, left heart and circulatory system simulator on which we can calibrate the flow. Several flow studies verified that the flow profile within the simulated aorta was realistic. Calibration was accomplished by having the fluid collect in a reservoir and measuring the time to collect a known volume.

In practical usage, errors arising from user technique are more controllable with thermal dilution. In choosing to use one method over another, it is necessary to consider whether absolute accuracy or simple trending is required, if continuous measurement is advantageous, whether simultaneous wedge pressure measurements will be needed, if infection risk must be minimized and the skill of the personnel available.

BE12-K.3

Cardiac Output Assessment by the Single-Breath Method: An Evaluation

R. Srinivasan*, KRUG International, Houston, Texas.

The single-breath method of determining cardiac output is a simple noninvasive procedure requiring measurements of only O_2 and CO_2 concentrations at the mouth during an expiration. However, the method is highly sensitive to measurement errors. Also, any lung tissue absorption of CO_2 that may be present can introduce significant errors in the estimated cardiac output, if not taken into account in the calculations. Recent analysis based on computer simulation has demonstrated the feasibility of obtaining acceptable estimates of cardiac output by the single-breath technique in the presence of both normal measurement errors and lung tissue exchange of CO_2 .

This work extends the above analysis to evaluate the effects of the underlying assumptions of the single-breath method on the estimation of cardiac output. The assumptions include linear CO_2 dissociation, constant O_2 consumption, and homogeneity of the lung. The likely errors from these assumptions were assessed using a gas exchange model with a multi-compartment representation of the lung. The results indicate ways to minimize the errors through appropriate selection of data segments from the expiratory interval.

Work supported under NASA contract NAS9-17720.

BE12-K.2

ALGORITHM FOR CALCULATION OF INFARCTION SIZE AFTER THROMBOLYTIC THERAPY, J. Delanghe, L. Cluyse, H. Thierens*, I. De Scheerder, M. De Buyzere and R. Wieme, Dept. Clin. Chemistry, Medical Physics, State University Gent, Belgium.

Recent advances in myocardial infarction therapy resulted in an early reperfusion of the infarcted zone. As a consequence release of enzyme occurs earlier than in untreated infarctions resulting in different release patterns. As released enzymes show differences in catalytic properties upon aging, classical algorithms for size estimation cannot be used as they overestimate infarction size (up to 30%). Taking into account changes in activation energy of the catalyzed reaction, serum activity of cardiac enzymes (CK, CK-MB) were corrected for loss of specific activity in function of time. A computer algorithm was designed in which time needed to reach peak activity was used as a corrective parameter. Elimination constant of disappearance of CK from serum was calculated from each patient's individual data. Distribution volumes of enzymes were corrected for age. Using these corrections, clinically useful and reliable estimations of infarction size are possible and efficiency of reperfusion can be calculated.

BE12-K.4

Estimation of Mixing Volumes from Bolus Indicator Dilution Curves, E. Fønstelien*, STEM, 1320 Stabekk, Norway.

It can be demonstrated that a bolus indicator response after n mixing compartments may be expressed as

$$c(t) = A([\Gamma(n)]^{-1}(kt)^{n-1} \exp(-kt)) \quad (1)$$

where k is the rate constant flow/volume, $[\Gamma(n)]$ is the Gamma function of n , and t is time. A is a constant governed by the injectate volume, contrast, and injection time. Vascular flow is calculated according to

$$F = c_0 V_i / \int_0^{\infty} c(t) dt = A^{-1} k c_0 V_i \quad (c_0, V_i \text{ are injectate properties}). \quad (1)$$

may be transformed: $\ln(c(t)) = \ln(A/[\Gamma(n)]) + (n-1)\ln k + (n-1)\ln t - kt$ and with $\ln t$ and t as independent variables in a bivariate regression model, it is possible to calculate k , n , and A . The total mixing volume V_t , i. e. the vascular space between the injectate inlet and the concentration reading device can be found as $V_t = nF/k$. A series of thermal dilution measurements on humans at right heart catheterization to find V_t and n is reported. The results are believed to carry diagnostic information. Normally the right heart cavities are $V=210\text{ml}$ and $n=2,5$.

BE12-K.5

Personal Computer Based Cardiac Output Impedance Cardiographer. S.Charleston*,T.Aljama,M.Cadena. Universidad Autonoma Metropolitana -Iztapalapa,E.E Department,09340 Mexico,D.F.,Mexico.

In this work we present design criteria to obtain a cost-effective single card,bus "pc" compatible, impedance cardiographer for measurement of cardiac output in patients at rest and in exercise.

This cardiographer in addition to detect thoracic impedance changes less than 0.1 ohm,using 350 microampers at 50 kilohertz,is able to correct artifacts induced by respiratory and electrode movements.

The system is designed to take advantage of the digital signal processing support found in a personal computer,in order to perform filtering and averaging algorithms correlated with ECG and phono signals.

The performance of this system has been tested on twenty subjects during upright cycle exercise at 0,50,100,150 and 200 watts,using a CO₂ rebreathing method and the Kubicek model to compute the cardiac output.Evaluation of the first results shows good agreement between both methods.

BE12-K.7

Automated Evoked Potentials Analysis for Cardiac Surgery Monitoring, M.A. Gutierrez*, S.S.Furuie, U.Tachinardi and C.P.Melo, Heart Institute of São Paulo University Medical School, C.P. 11.450, São Paulo - BRAZIL.

The response of the Central Nervous System (CNS) to external stimuli, Evoked Potentials (EP), is an important parameter for neurological diagnostic aid. The analysis of some characteristics of the EP allows the clinicians to evaluate possible CNS damages during cardiac surgery. The calculation of the mean EP (MEP) using averaging techniques, enhances the low level of the S/N ratio of EP. The EP monitoring system available, area usually dedicated equipments composed of one stimulator and averaging module, that do not permit software changes.

It is introduced in this paper a microcomputer-based system for EP analysis in cardiac surgery monitoring. The software was developed in PASCAL and ASSEMBLY Languages and consist of the following modules: Acquisition and Display, Disk-Storage and Analysis. The former uses the stimulator synchronism pulse as a trigger to the EP signals and thus MEP calculation, the MEPS area then stored for further analysis. The analysis include response-latency and amplitude estimation as a function of the surgical (from pre-to-post-operative) procedures. Although the aim of this system is to attend cardiac surgery acts, it can also be used in other experimental and clinical studies.

BE12-K.6

A PORTABLE SYSTEM FOR BEDSIDE COMPUTERIZED ANALYSIS OF CARDIAC CYCLE IN CRITICAL PATIENTS, S.G.Lage, M.A.Gu - tierrez, J.L.Santello and S.S.Furuie, Heart Institute-Faculty Medicine-São Paulo University, C.P. 11.450, São Paulo - BRAZIL.

The paper describes the application of a portable system developed in a microcomputer IBM-PC compatible to perform a complete analysis of cardiac cycle events. The simultaneous and continuous computerized evaluation of the ECG and the first derivative curve of thoracic electrical bioimpedance (dz/dt) allows determination of: pre-ejection period, ventricular ejection time, isovolumetric relaxation time and ventricular filling period in critical heart failure during rhythmic and arrhythmic conditions. The software was implemented in Pascal and Assembly languages and consists of the following modules: configuration, acquisition and analysis. The first module permits to set up a sample rate and the number of the signals. The acquisition routines perform the process involved in signal conversion, display and storage during 30 seconds per minute for a total 15 minutes of monitoring. These parameters can be changed according to the different clinical demands. The analysis module correlates the signals using cross-markers to measure the time of systolic and diastolic events. In the Critical Care Unit the system permitted a bedside quantification of normal and abnormal rhythms.

BE12-K.8

A Portable Arrhythmia Monitoring System, Fan Xiaodong, Pang Tianci and Huang Yecho, Xian Medical University, Xian, P.R. China

A long-term arrhythmia monitoring system for ambulatory patients, composed of a microcomputer and a tape recorder, has been developed. Derivation-Sum method is used to recognize QRS complex and measure its width. Arrhythmia is discriminated according to heart rate and QRS width. CMOS NSC800 microcomputer family (including CPU and RAM-I/O-Timer), other CMOS chips (including 6K memory, ADC, LCD) and micro-keyboard are employed to reduce the power consumption, weight and size of the system so that it is suitable for battery-powered and portable. Micro-tape recorder replaces fashionable telephone to establish relation between monitor and central station. Therefore, replay system is simple and low costs. The evaluation is performed according to recorded ECG including various arrhythmia, noise and 256 PVCs. Detection rate of R wave is 96.89%. Negative false detection of PVC is 22, and positive false is 54.

316

BE12-K.9

Battery-type Sequential Pulse Defibrillator by using A Single Capacitor Bank, H. Makino*, Y. Saitoh, Y. Mitamura, and T. Mikami, Niigata Univ., Niigata and Hokkaido Univ., Sapporo, Japan

A battery powered sequential pulse defibrillator was designed and tested for the development of implantable sequential pulse defibrillators by modifying the output circuit. Two GTO thyristors were used as the switching device in the output circuit, and charged energy in a capacitor bank was divided into the first and second pulses sequentially. An electrode catheter which has two glassy carbon electrode elements was introduced through the right jugular vein. The distal electrode(+) was located in the right ventricular apex, and the proximal electrode(-) was located in the superior vena cava. A plate electrode was used as a subcutaneous electrode(-) under the left chest.

In animal experiments, two mongrel dogs (10.4 & 11kg) were anesthetized and mechanically ventilated. The threshold of simultaneous-pulse(5ms) and sequential-pulse(5-1-5ms) defibrillation were 400V(1.44J) and 260V (0.69J) respectively. In our system, the defibrillation energy was 50% less than simultaneous defibrillation. Furthermore, the electrode systems do not require thoracic implantation surgery.

BE12-K.11

A SAMPLED HOLTER ECG TAPE RECORDING SYSTEM FOR MONITORING ARRHYTHMIA, Li Ming Liang*, Tian Anmin, Ministry of Electronic Industry, Shannxi, Baoji, China; Zhang Yiming, Physiology Teaching & Research Office of Fourth Military Medical Inst, Shannxi, China

This paper describes a Holter ECG tape recording system which can record the amplified cardiogram signal obtained from the second electrode on the surface of the body through the (a) low noise amplifier and by the frequency modulation and photoelectricity coupling methods. By adopting the amplifier with a high-resistance and high-common-suppression data as well as the photoelectricity coupling technique, the electric network interference and other environmental interference have been eliminated, thus making the recorded cardiogram signal fidelity and reliable. The adopted Holter technique has also eliminated the error caused by unstable tape speed and the flutter of the recorder. With many advantages such as its multifunction, low consumption, small size and low price, the system is really an applicable medium for widely expanding the Holter dynamic electrocardiogram.

BE12-K.10

Continuous Blood Mass Densitometry in awake humans, M. Moser* , D. Schneditz, F. Jüttner and T. Kenner , Physiolog. Inst., A-8010 Graz, Austria

A method is presented for the continuous arterial blood density measurement in awake subjects. The resonance frequency of a tiny U-shaped glass tube (ID 0.8 mm, sample volume 0.03 ml) perfused with blood is measured continuously. From the oscillation frequency the mass density of the blood (ρ_{b1}) can be calculated very precisely (10^{-2} g/l). We applied this technique in healthy volunteers to observe arterial blood density variations due to breathing and saline injections. Normal ρ_{b1} is around 1049 g/l and ρ_{plasma} around 1019 g/l at 37°C. Inspiration is followed by an increase of ρ_{b1} , expiration leads to a decrease of ρ_{b1} . Depending on breathing volume and frequency, blood density oscillations up to 1.5 g/l were observed. Injections of isotonic saline solution produce dilution curves suitable for calculation of blood volume and blood flow. Theoretical considerations to understand the observed results are presented.

BE12-K.12

Determination of Cardiac Output by Fick's Indirect Method. Using a Modular Micro-Computer System Yañez S.O.*, Medina B.V., Carrasco S.S. JAM-Iztapalapa Av. Purisima Y Michoacán, Mexico. 09340, D.F. MEXICO

One of the clinical indexes most frequently used to evaluate the performance of the cardiovascular system is the cardiac output, where invasive techniques are usually employed for its determination. However, non-invasive methods are preferred if the determination is to be made during exercise.

In this work a system for the automatic determination of the cardiac output during exercise, based on CO₂ rebreathing method, is presented. This system consists of a modular microcomputer, based on a Z-80 microprocessor, with acquisition, processing and liquid crystal display capabilities, connected to a fast CO₂ analyzer and to a flow transducer. The microcomputer automatically performs four stages required to obtain the parameters needed for the evaluation of the cardiac output. These steps include the acquisition and presentation of the following variables: expired minute volume, CO₂ elimination, end tidal PCO₂ and PCO₂ equilibrium in rebreathing maneuver. Based on these parameters, the resulting cardiac output is computed and presented on the liquid crystal display.

317

BE12-K.13

Development of Portable 12-lead ECG Simulator using 3-Wave-Data Synthesis.

H. Makino*, Y. Saitoh, I. Ishii, and J. Yamato, Niigata Univ. Niigata 950-21, Japan

For the development of a 12-lead ECG simulator, a new method for restoring waveforms in less data memory was proposed. From the geometrical relationship of electrode arrangement for the detection of ECG, we selected three basic waveforms (II,VI,V3) which can be used to estimate other waveforms by linear combinations. The basic waveforms were decided from the results of calculating the method of least squares, and the calculated weight coefficients were used for restoration of other waveforms.

In the system, the basic waveform data and the coefficients were stored in a ROM. A 8-bit microcomputer, and two D/A converters (quad type) were used to synthesize the eight channel waveforms. Four other waveforms (III,aVR,aVL,aVF) were combined with the two waveforms(II,III) by using an analogue circuit. Original ECG waveforms were obtained from the ECG tape recording or from the ECG chart using an optical scanner. The sampling frequency was 2.5kHz to input pacemaker spike.

Finally, the data memory became 7Kbytes, including three basic waveforms and coefficients, and it was 62% less than memories from the original eight-wave data recording.

BE12-K.15

Microcomputer Assisted
Cardiokymography, D.X.Guan*,
L.Huang, J.W.Huo, and J.Z.Yan,
China Medical University,
Shenyang, P.R.China.

Cardiokymography (CKG) is a contactless method of recording chest wall movement related to displacements of myocardium. To overcome its technical difficulties in the diagnosis of coronary artery disease, we have developed a suitable CKG transducer and a microcomputer-based multiple CKG system. The CKG transducer which weighs 20g is supported on the chest by a two-layer belt without limiting the chest wall movement. The CKG signal is demodulated through a phase-locked loop. Differentiated CKG signals from two sites on the chest, together with a ECG signal and a respiration signals, are processed in real time by the system. To eliminate breath interference two digital processing methods are adopted: multipoint averaging and adaptive filtering. Recordings during treadmill exercise show both of the methods are efficient and that it is preferable to use the differentiated CKG signal in the clinical diagnosis.

BE12-K.14

Timing Module for a COPAL UA-751 B.P. Recorder, D.J.Stewart, M.A.Chaudhri*, Austin Hospital, Melbourne, Australia

The Copal UA751 is a low cost, digital blood pressure recorder. The user initiates a recording by pressing the start button. The unit inflates the cuff and measures systolic, diastolic and heart rate via the oscillometric method. The readings are displayed on an LCD display and the user then has the option of printing these results on a small thermal printer, or storing up to 14 recordings in memory and printing them out at a later date.

This is OK for "one off" recordings, but in many diagnostic or research applications (such as evaluation of the effects of drugs on a patient's blood pressure) periodic recordings are needed. Traditionally, this has been the realm of machines such as the Johnson & Johnson Dinamap, worth in the vicinity of A\$5,000. To achieve this we have designed and constructed a low cost (ca.A\$50) and simple "Timing Module", with which automatic periodic measurements can be made using the Copal recorder. The design and functioning of this module are described.

BE12-K.16

Signal Processing Techniques and Detecting-Recognizing Algorithms of the characteristic points for ECG, PCG and CPT, Zhou Guang-Hu*, Yu Jia-Xian, Chengdu Inst of Radio Engineering, Chengdu, PR China.

One of the significant means for examining the left ventricle functions is to measure the heart Systolic Time Intervals (STI) of ECG, PCG and CPT. The signal digital processing technique of these three physiological signals and the algorithms of detecting and recognizing their characteristic points are discussed. A twice-filtering algorithm for ECG, a reckoning algorithm with adaptive dual-thresholds for QRS wave and a sample-by-sample base line correction algorithm with piecewise linearization for CPT were proposed to eliminate the main interferences.

This attractive engineering method requires much less computation work using a microcomputer system than the ordinary.

BE12-K.17

Non-invasive Cardiac Output Estimation
by using Inert Gas Inhalation
*Kimura Yuichi, Hayashi Koji,
*Uchiyama Akihiko, Suma Kozo,
*Sch. of Sci. & Eng. WASEDA Univ. **Tokyo
Women's Medical Col., Tokyo, JAPAN

Our method is to measure cardiac output (CO) in non-invasive way. To use this method, we can easily obtain information on pump function of the heart. In our method, the inert gas of only 5% N₂O is used as a tracer. If the concentration of N₂O in the air inhaled by the subject changes stepwise, the ratio of the concentration of the N₂O in inspiration and in expiration is formed by the sum of two exponential curves because of the system function of cardiovascular system. CO can be estimated from the amplitudes and time constants of these curves.

Our system is designed to change the gas concentration stepwise between 0% and 5%. and can calculate CO in a few minutes. All of these processes are done automatically. We measured the CO of 15 dogs to compare with our method and electromagnetic blood flow meter. There was coincidence between these two methods (r=0.8). We can conclude that our method is effective as a non-invasive CO measurement.

BE12-L.2

Mechanical Measurements of the stability of Reduction Fixator for Treating Tibio-Fibular Fracture, Gao Ruiting*, Dept. of Mechanics, Tianjin University, Meng He, and Jin Yang. Institute of orthopaedics and Traumatology, China Academy of Traditional Chinese Medicine

After fixation with the reduction and fixation device, the fractured tibia and fibula can form a new mechanical system with the device. This system should have a certain ability of resisting external disturbance. From the standpoint of clinical practice, there are four types of manifestation of the forces subjected to the wounded leg, namely, the antero-posterior bending, lateral bending, axial compression and torsion. In order to understand the stability of the system, the effect of the reduction and fixation device for fixing the fractured tibia and fibula was simulated with two specimens of cadaver bones and tested mechanically in this experiment. By means of the transducers mounted on the two supporting rods and under the lateral pads, the forces provided by the rods of the reduction device were measured when the oblique or transverse fracture was compressed axially. Meanwhile, the force variations of the pads induced by applying bending or torsion were also measured. The stiffness of the device is compared with same multipin-type fixation devices used abroad.

BE12-L.1

Some Analyses on the Mechanical Behaviour of Elastic Splint for Pelvis Reduction (ESPR), Gao Ruiting*, Xian Re kai, Shen Jifen, Dept. of Mechanics, Tianjin University, Shang Tianyu, and Zhao Wenkuen, Tianjin orthopaedic Institute

Presented in this paper are some biomechanical analyses and measurements of the mechanical behaviour of (ESPR) which has been used with satisfactory results by the orthopaedic Dept. of Tianjin Hospital in curing fracture of pelvis. The tensile force exerted by the elastic band of ESPR was measured with a specially designed transducer. In order to understand the mechanical behaviour of the elastic band, tension, Creep and relaxation tests were conducted; relevant curves with the relationship of tension VS. elongation were obtained and the decrease of reducing force with time caused by the stress relaxation under constant elongation was determined. Static imitations were made on 10 normal adults, clinical monitoring on male patient with pelvis fracture was carried out for 30 hours. dynamic measurements were made on a normal and a invalid respectively when they walked and did exercises; and finally, the reducing forces provided by the splint were analysed.

BE12-L.3

Fracture Toughness of Human Enamel and its Measurements, Y.Zhang*, M.He and C Kan, Institute of Mechanics Chinese Academy of Sciences Beijing

The indentation technique was employed to determine the fracture toughness K_{IC} of human enamel. Four teeth were selected for testing: a maxillary incisor, a mandibular incisor, a maxillary canine, and a mandibular molar. In order to verify the results, the calculation of K_{IC} was performed with two different formulas, in one of which a parameter was modified so that the formula used for ceramics would be more reasonable for enamel. The results obtained from this study indicate that there exists a slight difference in K_{IC} between four different teeth, and for natural tooth the K_{IC} of enamel is about 1.0 MN/M-1.2 MN/M. An error analysis of this method was given in this paper.

BE12-L.4

Three-dimensional Analysis of Stress Distribution in Periodonal Ligament of Human Tooth by Finite Element Method, Y.Zhang*, M.He and S.Zhou, Institute of Mechanics, Chinese Academy of Sciences

In order to determine the physiological stress values in the periodonal ligament (PDL) effectively, a new calculate model and method were established. With this model. the tooth and the alveolar bone were considered to be rigid, and the stress distribution in PDL were analysed by three-dimensional finite element method. In the calculator, the basic solutions of stress distribution in PDL were obtained at first. Based on them the stress distribution in PDL under arbitrary load can be obtained readily with the principle of superimposition. Three typical load cases were selected in this study. And the results of stress distribution under these loads were discussed.

BE12-L.5

A Study on Finite Element Stress Analysis of Endodontically Restored Tooth, W.H.Chang*, Y.S.Ueng, and J.S.S.Wu, Dept. of Biomedical Engineering, Chung Yuan Christian University, Chung Li, Taiwan, 32023, R.O.C.

We use finite element method to analysis the stress magnitude and distribution when several types of loading are applied on endodontically restored tooth. A two-dimensional plane strain finite element model is constructed and applied to evaluate the stress magnitude of different length of post and different material of crown for a given load. In order to get a reasonable accuracy, 190 plane strain quadrangle elements and 216 nodes are used. We get the following results: (1)The dentine is more highly stressed in restoration with both longer posts and shorter posts. (2) The crown is more highly stressed in restoration with resin crown than porcelain crown. (3) The dentine is not influenced in restoration with either resin crown or porcelain crown. (4) Both dentine and crown are more highly stressed in restoration when a horizontal loading is applied at the top of tooth.

BE12-L.6

A new device for the in vivo monitoring of fracture healing by vibration analysis. G. Nikiforidis*, A. Bezerianos, S.Roudis, B Proimos Medical Physics Dept. University of Patras, 26001, Patra, Greece

Uncertainty in the diagnosis of the healing progress of fractured bones renders the development of a quantitative method for such diagnosis useful. In recent years the authors conducted analytical and experimental studies regarding the bending vibration of fractured bones in vitro. On the basis of the aforementioned investigation, a new device was constructed for monitoring the fracture healing in vivo. In the present work a schematic description of the device and its possibilities are given. Specifically: 1) The functional criteria, the components of the apparatus and the experimental conditions of its optimal response are analyzed. Special emphasis is given to the influence of the changing in the supporting conditions of the bone under examination. 2) The repeatability of the measurements is tested and a comparative evaluation between the vibrational spectra of the intact right and left tibiae of the same subject was performed. 3) Finally the differences in the vibrational spectrum of an intact left to that of a healing right tibiae, of the same subject are discussed.

BE12-L.7

Three Dimensional Finite Element Stress Analysis of the SAD Implant Coated with Bioactive Ceramics. Wang Shaoan*, Chen Anyu, and Huang Suhua, College of Stomatology, West China University of Medical Sciences Chengdu, Sichuan, China

The design optimization of dental implant is one of the critical elements for success. The objective of this study was to examine the stress distributions around the dental implants with or without the intramobile shock absorbing device (SAD). The characteristics of this new implant system are: (1) the metal core coated with bioceramics (Hydroxyapatite or Bioactive Glass Ceramics); (2) a shock absorbing device within the implant; and (3) two-phase dental implant. The model was constructed based on our previous studies. Vertical, horizontal, and inclined loads were applied on the occlusal surfaces of the implants, respectively. The results indicated that the implant with the SAD had a better stress distribution around the interface than that of the implant without the SAD. The authors suggest that more implants with the design of the SAD will be used in clinic in the future.

BE12-L.8

Comparison of X-Ray and Isotope-Based Dual-Energy Bone Densitometers. C.C. Glüer*, P. Steiger, R. Selvidge, H.K. Genant, University of California, San Francisco, CA 94143.

Traditional Dual Photon Absorptiometry (DPA) bone densitometers use an isotope radiation sources whereas the newly introduced Quantitative Digital Radiography (QDR) device uses an incorporated X-ray generator. We compared these technologies via phantom and patient studies performed on a Norland 2600 DPA scanner and a Hologic QDR-1000 QDR device. Reproducibility errors obtained on an anthropomorphic spine phantom over a period of 2 months were 1.9% (DPA) and 0.44% (QDR) at skin dose levels of 1.5 mrem (DPA) and 2.6 mrem (QDR). For QDR the error rose by about 50% when increasing the lucite thickness of the phantom from 7 to 8.5 inch. For DPA this was avoided by the adjustable scan speed option. The fat sensitivity was identical for DPA and QDR (1.2% reduction of bone mineral density per 10% by volume fat content). Cross-calibration results of the first 16 patients yielded a coefficient of correlation of $r=0.98$ ($p<0.0001$), a standard error of the estimate of $SEE=0.043$ g/cm² ($CV=4.9\%$) and QDR results lower than DPA by an average of 0.019 ± 0.045 g/cm². The improved resolution of QDR facilitated the identification of bone edges of osteoporotic patients.

BE12-L.10

THE SPINOSCOPE: TECHNOLOGY FOR OBJECTIVE EVALUATION OF SPINAL CAPACITY, S. Gracovetsky*, S. Levy, V. Zeman, R. Ben Said, I. C. Pitchen, J. Hélie, M. Kary, J. Lewis, Concordia University and Diagnospine Research Inc., Montreal, Canada.

A new device, the Spinoscope (Spinex Medical Technologies, Inc. Montreal) has been developed for the objective evaluation of spinal capacity. The Spinoscope collects and processes two basic types of data as the patient performs simple activities, such as lateral bending, flexion, extension, lifting of weights, etc. First, spinal motion and geometry are monitored using an advanced infrared three-dimensional motion analysis system. This system is capable of tracking the position of 24 LED skin-surface markers with an accuracy of 1 part in 500, at a data acquisition rate of 180Hz. This large dynamic range allows the effects of the time-dependent, viscoelastic response of the soft tissues of the spine to be observed. Second, and performed concurrently with the above, the activity of eight muscle groups is monitored bilaterally via skin-surface electromyography. Subjective information (in the form of the patient's responses to a pain questionnaire) is also collected, and processed using artificial intelligence techniques. By this combination of subjective and objective information, the Spinoscope can greatly assist the physician in the diagnosis and follow-up evaluation of spinal injuries. Sensitivity is great enough to allow patient progress to be monitored on a weekly basis.

BE12-L.9

Site-Specific Assessment of Bone Mineral Density at the Proximal Femur by Quantitative Computed Tomography. C.C. Glüer*, P. Steiger, S. Steiger, J.E. Block, H.K. Genant, University of California, San Francisco, CA 94143.

Quantitative computed tomography (QCT) provides for selective measurement of trabecular and cortical bone, and various shapes, sizes and contours of regions of interest (ROI) can be chosen with flexibility. Drawing upon these features to assess bone mineral density (BMD) at the proximal femur, we explored an approach that uses an AP CT scout view to determine the region for axial scanning. Contiguous 3mm slices are obtained encompassing the femoral head, neck and trochanters. Because of the inhomogeneous distribution of BMD at this site, a technique that allows for reproducible placement of the ROI is mandatory. Using contour tracking algorithms to assess trabecular BMD of an anthropomorphic hip torso phantom yielded a reproducibility of 1.3% for a volume of 1.25 ml of trabecular tissue at Ward's triangle (dose about 300 mrem). Corresponding in-vivo results were 1.9-2.5% for volumes of about 10ml (at the neck) and 0.23-0.7% for volumes of 40-45ml (whole proximal femur). Techniques for comparing corresponding ROIs of serial measurements will be presented.

BE12-L.11

Anisotropic Viscoelastic Finite Element Analysis of Vertebral Body, Cheng Peilai*, Dept. of Mechanical Engr. Tianjin Institute of Technology, and Chen Hongxing, Tianjin University, Tianjin, China

An axisymmetric finite element model is employed for the study of the creep behavior of an vertebral body under axial compressive loading. The trabecular bone of vertebral body is considered as a transversely isotropic viscoelastic material and cortical bone and endplate as a isotropic viscoelastic material. A three parameter Kelvin solid model is employed in the finite element model. The material parameters of the anisotropic viscoelastic constitutive relation for trabecular bone was obtained from experimental data. The material parameters of cortical bone is from Yang.

The stress distribution and the deformation of vertebral body under axial compressive loading were obtained. The results indicate that the magnitude of stress in trabecular bone is smaller than that of the cortical bone and the cortical bone carries a major percentage of the compressive loading. The results also show that the stress in vertebral body will redistribute with the increase of time. The vertical deformation have a significant changes during the creep time while the radial deformation have a little.

321

BE12-L.12

Joint Stiffness Following Physiotherapy, J. Bromley, A. Unsworth* and I. Haslock, University of Durham, DH1 3LE, England.

We have designed and built a microcomputer controlled arthrograph to measure stiffness in the mp joint. The joint is oscillated about its equilibrium position and the arthrograph measures the elastic resistance and the energy dissipated during flexion/extension. This is used to assess the effectiveness of treatment.

Stiffness was assessed in rheumatoid patients, to see the effect of physiotherapy. Four modes of physiotherapy were investigated over 6 weeks of treatment. These were wax baths, pulsed ultra sound, exercise and a combination of wax together with ultra sound. Short term changes in stiffness were investigated (after one single application of the mode of physiotherapy), as well as long term effects (repeated applications over 6 weeks).

Wax plus ultra sound produced significant short term reductions in stiffness (torque $p < 0.001$, energy $p < 0.05$). However over the 6 week period of treatment, no significant change was seen in the stiffness before and after the course. In other words each application of wax plus ultra sound reduced stiffness but this increased again by the following application. Pulsed ultra sound alone was similar but wax alone increased the stiffness in the short and long term. Exercise produced no change at all.

BE12-L.14

Reference Material for CT- Measurements on Bones

Faust, U., Institut für Biomedizinische Technik der Universität Stuttgart, Seidenstr. 36, D-7000 Stuttgart 1.

For the quantification of bone mineral a nontoxic, solid water-equivalent reference system with long term stability has been developed.

The reference systems consists of polyethylene, magnesium oxide and calcium carbonate. The produced material has a water-equivalent x-ray attenuation at voltages of 96 and 125 kV and can be used for automatic recalibration of CT-machines. To determine mineral content of bone, a reference material, which is equivalent to bones, was produced by mixing the water reference with apatite. The linearity between CT-numbers and apatite concentration was nearly ideal.

The mineral content of cattle bones (femur) has been determined with quantitative CT and the water- and bone- references. To study the error of varying fat/water ratio in marrow, they have been examined in the native state and after substituting the marrow by water and paraffine. The mineral content first has been calculated from the CT-numbers of bone and reference-material without a correction for this error.

Finally the mineral content was determined with single- and dual- energy-methods with a correction for this error.

BE12-L.13

The influence of low molecular weight components on the viscoelasticity of synovial fluids. G. Ribitsch, V. Ribitsch and D. Schneditz, Dept. of Physical Chemistry Univ. Graz - Austria

Healthy human synovial fluids SF exhibit high viscosity and elasticity due to a component of high molecular weight hyaluronic acid (HA). In the case of rheumatic diseases both viscosity and elasticity decrease remarkable. M_w and the molecular weight distribution (MWD) of HA isolated from those SF does not show significant alterations compared to HA from healthy SF.

Investigations of model substances (Guar, HA from umbilical cord) indicated that the viscoelastic properties of solutions are changed remarkable if polymers with a molecular weight smaller than 10^5 are present. Nevertheless M_w and the MWD were only slightly shifted toward lower values. The same findings were observed with human SF containing small amounts of low molecular weight HA. 5% of low molecular HA added to an healthy SF decreases the viscous component about 30% and the elastic component about 60%. The presence of low molecular components may inhibit the formation of entanglements and weaken the network.

BE12-M.1

RESPIRATORY EFFECT ON THE BLOOD VOLUME OF PULMONARY CAPILLARIES, M. Hunter*, Jen-shih Lee, Timothy Fallon, Lian-pin Lee, University of Virginia, Charlottesville, Virginia 22908

We measured the density variations of aortic blood from the rabbits ventilated by a positive end inspiratory pressure of 6 mmHg or a negative box pressure of the same magnitude. For both ventilation methods, the fluctuation in aortic blood density decreased from .5 g/l at a ventilation frequency of 20 cycles per minute to .2 g/l at a frequency of 35 cycles per minute. Calculated from the density variations, the fluctuations in blood volume of the pulmonary capillaries within one cycle as induced by an intermittent positive pressure ventilation were found to be similar to the ones induced by an intermittent negative pressure ventilation. The corresponding percent change in capillary blood volume decreased from 6.5% at 20 cycles per minute to 4% at a ventilation frequency of 35 cycles per minute. Since the transpulmonary pressure and the transmural pressure across the pulmonary capillaries are the pressures deforming the capillaries, our result suggests that the changes in these two pressures are similar for the two ventilation methods. (Supported in part by HL 36285).

322

BE12-M.2

Axial and Secondary Flow Velocity Patterns in a Human Pulmonary Artery Model
Hsing-Wen Sung* and Ajit P. Yoganathan, Georgia Institute of Technology, Atlanta, GA 30332-0100

The purpose of this study was to characterize the pulsatile flow velocity patterns in an *in vitro* model of a "normal" human adult pulmonary artery. A two-dimensional laser Doppler anemometer system was used to map the axial and secondary velocity fields in the main (MPA), left (LPA) and right (RPA) branches of the pulmonary artery model in both the bifurcation plane and the perpendicular plane.

In the MPA, a broad central flow field was observed. In the LPA, the axial velocity profiles in the bifurcation plane were slightly skewed toward the inner wall. In the perpendicular plane, the axial velocities were relatively evenly distributed. In the RPA, the axial velocities in the bifurcation plane were very unevenly distributed. Higher velocities were observed near the inner wall, while lower velocities were observed near the outer wall and in the center. In the perpendicular plane, very marked M-shaped velocity profiles were observed due to secondary flows. A pair of helical vortices were observed in both the LPA and RPA in which the fluid moved outwardly along the side walls and then circled back inwardly towards the center of the vessel. A simplified one-dimensional axial flow model is used to interpret the observed axial flow distributions. Also, a three-dimensional flow model is used to explain how the secondary flows occur and how they affect the flow velocity patterns in the two daughter branches.

BE12-M.4

DETECTION OF LARYNGEAL PATHOLOGIES THROUGH CEPSTRAL/SPECTRAL ANALYSIS

Can C. Akkoc*(1), Robert L. Norton(1), and William G. Lavelle(2)

(1) Worcester Polytechnic Institute

(2) University of Massachusetts Medical School
Worcester, Massachusetts, USA

Voice samples from normal volunteers and patients with laryngeal pathologies were analyzed using modern signal analysis techniques. Contributions from the larynx (signal source) and the vocal tract (resonator) were deconvolved using long/short liftering in the cepstral domain to detect various pathologies of the larynx. Long liftered autospectra provided information on the acoustic characteristics of the sound signal generated at the larynx, while short liftered spectra displayed the formants in the vocal tract. Analysis of the cepstrum in combination with long/short liftered autospectra provided significant clues to distinguish between the two populations as well as among pathologies. Laryngeal disorders displayed themselves in the long liftered autospectra, while the formants for pathological cases were not significantly different from normals.

BE12-M.3

ANALYSIS OF THE CHANGE OF RIGHT VENTRICULAR EJECTION FLOW PATTERN IN PULMONARY HYPERTENSION BY LUMPED PARAMETER MODEL

Y. Yoshida*, A. Kitabatake, J. Tanouchi, K. Ishihara, K. Fujii, M. Uematsu, H. Kusuoka, M. Hori, M. Inoue, T. Kamada, M. Fukushima†, H. Abe†
The 1st Dept. of Med. Osaka Univ. School of Med., Osaka National Hospital†, Osaka, Japan

To elucidate the mechanism of the change of right ventricular ejection flow (RVEF) pattern and shortening of the time to peak flow (Act) of RVEF in chronic pulmonary hypertension (CPH), we analysed RVEF pattern by a lumped parameter circuit model. The model was composed of four elements, characteristic impedance (R1), inertance of blood mass (L), pulmonary artery compliance (C) and pulmonary peripheral artery resistance (R2). These parameters were determined from cardiac catheterization and Doppler data. RVEF pattern (dome-like, triangular and double peaked pattern) was well simulated by the lumped parameter model as the response to right ventricular pressure input. Step response of this circuit model revealed oscillation pattern. Eigenfrequency [$\omega \approx 1/\sqrt{LC}$] was increased and Act [$\approx (\pi/2) \cdot \sqrt{LC}$] was shortened with the decrease in C in the patients with CPH. These findings indicate that the decrease in pulmonary artery compliance brings about the increase in ω , resulting in the shortened Act and double peaked pattern in RVEF in CPH.

BE12-M.5

Asthmatic Response to Sulfur Dioxide

A. D. Wolint, K. A. Lenner, I. A. Gilbert, E. R. McFadden, Jr., and J. M. Fouke
Case Western Reserve University, Cleveland, Ohio

Cold-air hyperventilation challenges cause a decrease in FEV₁ in asthmatics and direct measures of intrathoracic airway temperatures indicate that the airways cool appreciably during these challenges. Similar challenges with warm-air do not decrease FEV₁, and the airways do not cool as much. Cromolyn sodium, an anti-asthma drug, also limits bronchoconstriction during a cold air challenge and causes the airway to stay warmer. These studies demonstrate that a change in FEV₁ can be correlated to a change in temperature in the airways. Hyperventilation and air temperature have also been explored as parameters which might aggravate the effects of SO₂ on FEV₁ in asthmatics.

We challenged asthmatics with cold air and 0.4 ppm SO₂ in cold air and measured FEV₁. Each mixture was pulled through a heat exchanger, where it was cooled to -10 °C. The subjects expired into a reservoir balloon from which air was being drawn at a constant rate and were coached to breathe at a rate sufficient to keep the balloon filled. In this manner, V_E could be controlled throughout each trial. Subjects were asked to breathe on this apparatus for four minutes and FEV₁ was measured five minutes later. This protocol was repeated at increasing levels of V_E until a 20% decrease in FEV₁ was produced.

Our results demonstrate that in both challenges FEV₁ dropped with increasing levels of V_E, but that the decrement was significantly less when the challenge was performed with SO₂. We hypothesize, therefore, that the challenge induced intra-airway temperature decrease was less with SO₂. This could occur through either of two mechanisms. Since the conversion of sulfur dioxide to sulfuric acid is an exothermic reaction, a warming of the airways could occur. Alternatively, the generation of sulfuric acid could cause an increase in pH. Such changes in pH are known to be associated with increases in blood flow, which could also increase the temperature of the airways.

BE12-M.6

Magnetopneumographic Evaluation of Effects of Silica on Behavior of Magnetic Particles in Rabbit Lungs, Y. Aizawa*, T. Takata, K. Hashimoto, M. Tominaga, M. Kotani†, K. Chiyotani††, Kitasato University, Kitasato, Sagami-hara, Kanaga, †Tokyo Denki University, ††Rosai Hospital for Silicosis, Japan

Silica is known to give a damage to pulmonary tissue and give rise to silicosis. This study was carried out to evaluate the effects of silica on the clearance of iron particles from the rabbit lungs and on the relaxation.

Male rabbits were intratracheally instilled with 20 mg of magnetite (Fe_3O_4) in 1 ml of sterile saline with 30 or 300 mg of silica (SiO_2) in 2 ml of sterile saline. An anesthetized rabbit was magnetized with 0.5mT of magnetic field for 15 seconds and the remanent magnetic field was measured with a fluxgate magnetometer.

Intratracheal instillations of both high and low doses of silica caused delayed clearance of iron particles from the rabbit lungs after 7 days of exposure. The initial relaxation of rabbits exposed to high dose of silica was disturbed for the first one week after instillation.

BE12-M.8

Lung blood flow and lung gas volume determination during open-circuit breathing, H. Larsson* and D. Linnarsson, Dept of Medical Engineering, and Dept of Baromedicine, Karolinska Institute, S-10401 Stockholm, Sweden

The pulmonary blood flow and the functional residual capacity of the lungs can be determined concomitantly by the rebreathing of a gas mixture containing one blood soluble and one blood insoluble indicator gas. We have revised this classical method so that tracer amounts of two gases are dispensed into the inspired gas stream during open circuit breathing. The tracer gases are dispensed at a rate proportional to the flow, thereby providing a constant inspired percentage, equal for the two gases. The gas uptakes of the two tracers are measured breath by breath by means of a flowmeter-gas analyzer assembly. We have used SF_6 as insoluble gas and Freon 22 as soluble gas. Both gases can be analyzed in tracer concentrations by a simple IR technique. The difference in uptake between the two tracers during wash-in is proportional to pulmonary blood flow. The lung gas volume at the end of an expiration (FRC) is determined from the ratio between the amount of SF_6 washed out from the lung and the initial SF_6 concentration before wash-out. Our preliminary results show that both pulmonary blood flow and FRC can be determined during rest and exercise during open-circuit breathing.

BE12-M.7

Applications of wave Spectrum Computer Analysis and Laryngostroboscope observing in studying Laryngeal Function. Shao Qingyu, Zhong Ziliang, Pan Jian, Huang Xiaoyan, Qi Yan

Laryngologic diseases affect laryngeal function therefore vibration of vocal cords and sound waves are changed. Acoustic waves and spectra of 31 normal subjects and 31 patients were plotted by a IBM microcomputer system with 12 bit A/D converter, analysed and compared with results of observing with DDJ-2 laryngostroboscope developed by ourselves. Features of 7 kinds of diseases (including cancer) of vocal cords were studied. Further problems and methods were put forward.

To ensure higher precision of analysis of spectra the FFF with Hanning window technique was used. To get suitable signals every examinee voice his highest "i:" then "a:". The sampling frequency is 13,000HZ. After data processing the number of resonant peaks, noise level (in db) and other parameters can be gotten.

BE12-M.9

Mathematical modeling of measurement errors in gas analyzers during exercise, V. M. Carbajal*, E. G. Urbina-Medal and S. Carrasco-Sosa, Departamento de Ingenieria Eléctrica, UAM-Iztapalapa, Apartado Postal 55-534, 09340 México D. F.

In studying cardiorespiratory physiology and evaluating patients, it has been found very helpful to analyze breath-by-breath patterns of ventilation and ventilatory gas exchange responses to exercise and other physiological stresses. Most of the available techniques that are using gas analyzers to evaluate gas exchange measurements have underestimated the transport delay and the dynamic response, which in turn introduce a significant departure from the real gas behavior for further analysis. We have developed a mathematical model for compensating the on-line calculation of oxygen consumption [$\dot{V}O_2$] and carbon dioxide production [$\dot{V}CO_2$] for both the transport delay and dynamic response of the respective gas analyzers used during exercise. The implementation of the model was carried out in a computer PC compatible system attached to our cardiopulmonary laboratory. We conclude that the model compensation should be performed for the accurate measurement of breath-by-breath gas exchange in order to avoid losing significant information.

324

BE12-M.10

Volume-Pressure "Curve" of Human Pulmonary "Venous" System —Response to Nitroglycerin and Mental Arithmetic Stress Testing— K.Gotoh, Y.Ohsumi, Y.Yagi, H.Takatsu, T.Tsukamoto, Y.Terasima, K.Nagashima and S.Hirakawa*, Gifu University, 40 Tsukasa-machi, Gifu, Japan.

Pulmonary blood volume was estimated with RN-angiocardiology, and mean pulmonary artery wedge pressure (PAW) was measured by Swan-Ganz catheter. When ordinate represented volume (V) and abscissa pressure (P), a short segment of volume-pressure (V-P) curve of human pulmonary "venous" system could be drawn by performing passive leg elevation (LE). The following results were obtained: (1) Nitroglycerin caused the V-P curve of human pulmonary "venous" system to shift toward the left and become steeper, suggesting pulmonary venodilation (n=50). (2) Mental arithmetic stress test (MA) caused the V-P curve of human pulmonary "venous" system to shift toward the right and become near horizontal, suggesting pulmonary venoconstriction (n=23).

BE12-M.12

Reconstruction of the Alveolar Ridges with Bioactive Glass Ceramics. Wang Shaoan*, Yu Zineng, and Chen Anyu College of Stomatology, West China University of Medical Sciences, Chengdu, Sichuan, China

The purposes of this research were to investigate the biomedical fundamentals and the clinical results of the alveolar ridge reconstructions with particulate Bioactive Glass Ceramics. Four beagle dogs were used in animal studies. Three months after extractions of the mandibular posterior teeth of the animals, the materials were placed into the formed subperiosteal tunnels in the ridges. The animals were sacrificed at different time intervals. The specimens were examined by light microscope, SEM, and EDAX, respectively. The histological studies showed that the particulate materials were connected with the tissues firmly. EDAX results indicated that the compositions both calcium and phosphate of the new bone at the interfaces between the materials and the alveolar bone were equivalent to those of the original bone. The clinical results demonstrated that the bioactive glass ceramics material is good for reconstruction of the atrophic alveolar ridges.

BE12-M.11

Human Pulmonary Venous Return Curve —Effect of Nitroglycerin— K.Gotoh*, Y.Yagi, H.Takatsu, T.Tsukamoto, Y.Terasima, K.Nagashima, S.Hirakawa, Gifu University, Tsukasa-machi 40, Gifu, Japan

Cardiac output of left ventricle means an equilibrium point determined by cardiac output curve of left ventricle and pulmonary venous return curve (PVRC). We calculated the compliance of human pulmonary "venous" system (C_{pv}) and that of human pulmonary arterial system (C_{pa}) by our method using RN-angiocardiology and Swan-Ganz catheter. Using these parameters, mean pulmonary filling pressure (P_{mp}) was calculated from the equation: $P_{mp} = (E_{va} + E_{vv}) / (C_{pa} + C_{pv})$ where E_{va} = Extra volume of pulmonary arterial system, E_{vv} = Extra volume of pulmonary "venous" system, in 29 patients with various cardiac diseases. Next, drawing a part of PVRC from P_{mp} on abscissa and the equilibrium point, we examined the response of P_{mp} and PVRC to sublingual administration of nitroglycerin. The following results were obtained: (1) P_{mp} was significantly decreased with NTG (11.7±6.2 → 8.5±5.5 mmHg) (2) PVRC was shifted horizontally to the left with NTG.

BE12-N.1

Numerical mass transfer model in a bioartificial pancreas. D. MORVAN and M. Y. JAFFRIN*. UTC, UA CNRS 858, Dep. Genie Biologique, B.P. 649, 60206 Compiègne FRANCE

Implantation of microencapsulated islets of Langerhans in peritoneal cavity has been proposed as a bioartificial endocrine pancreas. This numerical study investigates the kinetic of glucose and insulin mass transfer between a microencapsulated islet and an arteriole.

The mathematical problem is the evaluation of the glucose and insulin concentration fields inside and outside the microcapsule during the time following an augmentation of the glycemia in the arteriole.

Therefore these concentrations must verify a boundary value problem composed by a set of transient diffusion equations coupled with boundary conditions. The insulin secretion in the islet is represented as the liberation of insulin granules stored in two compartments. The rate of insulin production is controlled by the local value of glycemia in the islet. The numerical resolution is performed using the boundary integrale equation (BIE) method.

The results show that the insulin secretion is amplified when the diameter capsule decreases. In all cases the time lag between the rises of glucose and insulin levels in the blood does not exceed 10 minutes which is enough to normalize the glycemia in diabetics.

BE12-N.2

Technical Determination of Permeation Resistance in Blood Treatment by Membrane Distillation, T. Koyano*, M. Tamura and K. Sakai, Waseda University, Ohkubo Shinjuku-ku Tokyo 160 JAPAN.

Two fluids of different temperatures are caused to flow on either side of a microporous hydrophobic membrane in membrane distillation, and water vapor is transported from the warm to the cool side of the membrane. In this work, effects of polarization layers formed on either side of the membrane on separation of solution components from bovine blood were clarified.

Distilled water, bovine plasma and bovine blood were pumped into a module (surface area: 0.3m^2) composed of polypropylene hollow fibers. Water vapor permeability was measured at warm temperatures at inlet ranging from 307 to 316K, cool temperatures at inlet from 288 to 293K and flow rates from 1.67 to $3.33 \times 10^{-6} \text{m}^3 \text{s}^{-1}$.

Values for permeation resistance of the membrane were 1.6×10^{10} , 1.3×10^{11} and $2.1 \times 10^{11} \text{m}^2 \text{sPam}^{-3}$ for distilled water, bovine plasma and bovine blood, respectively. Higher values were obtained for bovine plasma and bovine blood because of a lowering of vapor pressure and adhesion of serum proteins on the membrane. Values for permeation resistance of warm-side polarization layer were 1.4×10^{10} , 4.0×10^{11} , $8.9 \times 10^{11} \text{m}^2 \text{sPam}^{-3}$ for distilled water, bovine plasma and bovine blood at a flow rate of $5 \times 10^{-6} \text{m}^3 \text{s}^{-1}$, respectively, and increased with the viscosity of test solution.

BE12-N.4

STUDY OF THE INFLUENCE OF THE SHEAR STRESS ON THE ADSORPTION KINETICS OF ALBUMIN ON A PLATINUM ROTATING DISK ELECTRODE.

P. Bernabeu, A. Caprani, P. Péronneau*
INSERM U. 256, Hôpital Broussais, Paris, France.

In order to better understand the interactions of proteins with artificial materials in shear stress conditions, the adsorption of albumin on a platinum rotating disk electrode has been studied. Using electrical impedance measurements, it has been possible to record the kinetics of the adsorption through the changes of the electrochemical double layer capacitance, within the range $0-1700 \text{ s}^{-1}$. This kinetics could be modeled in two consecutive reactions taking place at the interface, this providing 5 parameters: two time constants, τ_1 and τ_2 , and three capacitances, C_d , C_{d1} , C_{d2} , of the surface naked, covered with the reversibly adsorbed protein and covered with the irreversibly adsorbed proteins, respectively. The influence of the shear rate on each of these parameters has then been studied. It has revealed that, although the shear rate variation has no significant effect on the three capacitances, it does influence the two time constants, even after correction for the mass transfer contribution. Thus, τ_1 monotonously decreases as the shear rate increases. Concerning τ_2 , the variations versus the shear rate are more complex and are calling for additional experiments.

BE12-N.3

Oxygen Transfer of Liquid-Liquid Oxygenator
H. Suzuki*, T. Tsuji, K. Tanishita, T. Tamura and T. Togawa, Fac. of Sci. & Tech., KEIO Univ. Kanagawa, JAPAN, Tokyo Med. & Dent. Univ., Tokyo, JAPAN

The use of hemofiltration module as a liquid-liquid oxygenator applied for the long term perfusion is promising because of its excellent and reliable blood compatible features. In the present study the oxygen transfer performance of hemofiltration module was evaluated by *in vitro* water and blood test in order to reveal the feasibility of liquid-liquid oxygenator. The hemofiltration membrane tested was hollow fiber of microporous copolymer of ethylene vinyl alcohol (I.D.=0.2mm, EVAL, KURARAY Co. Ltd.). Both studies showed that the oxygen transfer occurred simply in proportion to the concentration gradient of oxygen across the membrane and oxygen uptake by the bulk flow across the membrane was negligibly small. This signified that the oxygen transfer performance in hemofiltration module could be evaluated similarly with that of gas-liquid membrane oxygenator. The oxygen transfer rate of the hemofiltration module turned out to be quite small ($<15 \text{ ml/m}^2 \cdot \text{min}$) due to the extremely large membrane resistance.

BE12-N.5

Hemoperfusion Treatment in Pigs Experimentally Intoxicated by Paraquat, T.S. Yang (Dept. Genetics and Physiology, Pig Research Institute), Y.L. Chang and C.J. Lee* Dept. of Chemical Engineering, National Tsing Hua University, Hsinchu, Taiwan, R.O.C.

Crossbred gilts (Landrace x Yorkshire), weighing around 70 kg were experimentally poisoned with the herbicide paraquat. When animals were intoxicated by intramuscular injection of the herbicide at levels of 74 mg/kg, 17 mg/kg and 6 mg/kg, the paraquat content in the serum, in all three cases, rose sharply, reaching a peak around 1.5 h after injection and then declining. Hemoperfusion was conducted for 2 h on 6 gilts beginning 2 h after gastric loading of 70 mg/kg paraquat. The mean turnover rate of circulating paraquat was 28.1%. Hemoperfusion treatment for 2 h could remove about 5% of the toxin loaded into the stomach. Prolonged treatment for 6 h did not enhance the turnover rate of circulating paraquat. Fuller's Earth and Na_2SO_4 were given to another 2 orally poisoned gilts 30 min prior to 6 hr hemoperfusion and they survived. Pathological examination revealed capillary congestion in lung, heart, liver and infectious mucosa. Use of hemoperfusion in treating paraquat poisoning might offer protection to lungs from excessive accumulation of the toxin.

326

BE12-N.6

Effect of control parameters on exchanged substances during hemodialysis - A simulation analysis, O. Thews* and H. Hutter, Johannes Gutenberg Universität Mainz, D-6500 Mainz, West-Germany.

A mathematical model is presented that describes the exchange kinetics of urea, creatinine, vitamin B₁₂, sodium, potassium, acetate, oxygen, carbon dioxide, bicarbonate, hydrogen ions and water between the dialysate and different body compartments during hemodialysis. The model has been employed for simulating the effect of control parameters (a) transmembrane pressure, (b) bloodflow through the dialyzer, and (c) the dialysate sodium concentration.

Results: (a) The transmembrane pressure controls the amount of total body water as well as the water distribution between plasma and interstitial space, furthermore the sodium kinetics, however not the potassium kinetics. (b) Blood flow through the dialyzer influences the acid-base-state, but not the water distribution. (c) The dialysate sodium concentration effects mainly the water distribution between extra- and intracellular space, the potassium kinetics and the acid-base state. The oxygen pressure is independent of all three control parameters, whereas oxygen saturation of arterial blood is controlled by all three parameters.

BE12-N.8

Rheological Properties of Gallbladder Bile
A Challenging Problem in Pathophysiology
R. F. Yang, X. Y. Wei, Y. P. Wu
Institute of Bioengineering
Chongqing University, P.R. China

The rheological properties of gallbladder bile are closely related to the biliary secretion, flow, and etiology of gallstone and other diseases in the biliary system. The relationship between the rheological properties and the chemical components of gallbladder bile is very important also. However, those subjects have not been investigated so far. In present paper, behaviour of gallbladder bile is discussed. Various pathological specimens of gallbladder bile, included 1) acute, chronic cholecystitis and cholelithiasis, are collected and measured by using Low Shear 30 rheometer under the shear rate range of 0.01607 - 118.2 s⁻¹. The experimental results have showed that their rheological behaviour is like non newtonian fluids when shear rate is less than 15 s⁻¹, and like newtonian fluids when shear rate is more than 15 20 s⁻¹. Their viscosities are remarkably different among different pathological specimens.

By measuring the viscoelasticity of gallbladder bile, its storage modulus simply increases, its loss modulus first increases and then decreases, with the angle frequency ω increasing. Besides, the positive correlation exists between the apparent viscosity at same shear rate in high shear rate range and the contents of cholesterol C₁ and mucin C₂. Regression equations are respectively $\eta = 4.359 + 0.0268C_1$, regression coefficient $r_1 = 0.9304$, and $\eta = 2.5048 + 0.0078C_2$, regression coefficient $r_2 = 0.9304$. According to those results, we can quantitatively investigate pathophysiology in the biliary system.

BE12-N.7

Applications of a Physicochemical Model of the Fixed Carrier. Hugo A. Massaldi, Instituto de Investigaciones Cardiológicas, Universidad de Buenos Aires, Argentina.

Different variants of the mobile and fixed carrier hypothesis are traditionally used in the biological literature to explain the facilitated transport of substances across cell membranes. Of these, the fixed carrier is getting generalized acceptance as a more feasible transport device. A recently developed physicochemical model (J. theor. Biol. 106:537; 110:35, 1984) of mediated transport provides a contemporary view of the fixed-carrier mechanism. The model, which postulates migration of polar solutes through interstitial channels of intrinsic proteins, is shown to lead to the classical equation of Wilbrandt and Rosenberg for the transport of hexoses as a particular case. Derivation of other expressions, such as that for saturable transport with interactive sites for ion exchange, is also possible through this model.

A distinct feature of the present approach is that it provides the *spatial* character and *displacement* properties of the species, which are not present in the purely enzymatic treatment of the problem. Thus, the conventional parameters T_{MAX} and K_T for hexose transport are defined in terms of a multicomponent permeability coefficient, the effective cross area of protein channels and the sorption constants of the solute onto the protein. By correctly accounting for the initial conditions, the model is capable of describing the active transport of ions as well.

BE12-O.1

Detection of Breast Cancer by Measuring Areolar Blood Flow. M. Nitzan, Y. Mahler and Z. Gimmon, Jerusalem College of Technology, Jerusalem 91160, Israel

The higher metabolism of a malignant tumor demands, generally, higher blood supply, which in the particular case of breast cancer, can often be detected by skin temperature measurements, using thermography. However, the small pathological temperature differences are not clearly distinct from normal temperature fluctuations resulting from various physical and physiological reasons. The non-invasive transient thermal clearance method was used for the detection of breast cancer. It differs from thermography since it measures directly skin blood flow instead of measuring its temperature. As breast carcinoma develops in the milk ducts, which are directed towards the nipple, the blood flow measurements were performed in the areola.

The measurements have shown clear correlation between breast cancer and increase in areolar blood flow, especially in the left breast. The areolar blood flow in a cancerous breast was higher than that in the contralateral breast, as well as higher than the average blood flow in normal breasts.

BE12-0.2

Permeability Measurements of Mouse Embryo Membranes at Temperatures Above and Below Freezing, Douglas B. Walcerz*, Shanti J. Aggarwal, and Kenneth R. Diller, University of Texas at Austin, Austin, Texas, 78752.

The ability to preserve mammalian cells by freezing depends greatly on knowledge of the flows of water and cryoprotectant into and out of the cells. For this reason, measuring the permeability of cell membranes, especially at temperatures below freezing, has become an important matter of investigation. A cryostage has been designed to measure the permeability of cells to water and cryoprotectant at temperatures both above and below freezing. In addition, the stage allows an entire cryopreservation procedure to be performed while continuously observing the cells under the microscope.

The permeability of mouse embryo cell membranes to water and glycerol has been measured at temperatures from -30C to 35C. The survival of cryopreserved mouse embryos at freezing rates from .1C/min to 5C/min has also been measured. Graphs showing membrane permeability vs. temperature, embryo survival vs. freezing rate, and embryo volume vs. time during cryopreservation will be presented. The design of the cryostage will also be presented.

BE12-0.4

HEATING TUMORS WITH EXTERNAL MICROWAVES: 1D SIMULATION, Thomas R. Canfield, Ph.D.*, Loyola University of Chicago, Stritch School of Medicine, Maywood, IL.

A simple finite element model using the transient one-dimensional bio-heat transfer equation was developed to investigate heating tumors with an external waveguide applicators. It has been used to model heating of the canine larynx with external waveguide applicators. In these calculations the applicator was modelled by assuming amplitude of an incoming 915 Mhz plane wave which was attenuated exponentially by the tissue. The applicator was controlled by a temperature at one of the nodes within the tissue. Temperature distributions were computed at every time step to simulate an actual treatment. The results indicate that power deposition does not translate directly into heating. Other important factors are power deposition rate, blood flow, surface boundary conditions, variation of tissue properties with depth, the presence of air cavities.

BE12-0.3

Temperature prediction during hyperthermia, Min-he Cheng & Hong-Zhang Wang*, Precision Instrument Dept. Shanghai Jiao Tong Univ. Shanghai P.R.China

Hyperthermia by ultrasonic, as a method for cancer treatment, has been applied to clinic trial for many years. But a non-invasive method of monitoring temperature distribution during heating still remains unsolved so far.

In this paper, a simple model structure of temperature distribution in human tissue, which is based on one-dimension bio-heat equation, is developed. The model parameters for real tissue are estimated from patient treatment through the use of a system identification technique. The temperature distribution during hyperthermia can be predicted by this model, and non-invasive temperature measurement can be realized.

Identification of phantom model parameter indicates that the simple control model structure is adequate. An identification measurement device is made by micro-computer TP-801 and better results are obtained by experiment heating fresh excised pig tissue.

BE12-0.5

THE ANALYSIS OF RISING TEMPERATURE CURVE MEASURED BY A DEEP BODY THERMOMETER, F.L. Lan* and J.W. Huo, China Medical University, Shenyang, P.R.C.

The Deep Body Thermometer (DBT) based on zero heat-flow principle was first developed by R.H. Fox, 1970. Now, the DBT can measure the temperature 1 cm deep under body skin with an error of 0.1-0.2 c. Nevertheless, a much longer period is needed for a complete measuring (usually 20 minutes or more), and until now, all the data measured were abandoned except the steady value. Actually, the shape of rising temperature curve is related with the temperature distribution under body skin. In this paper, an integral equation was found from a simplified model that relates the rising temperature curve and the initial temperature distribution under the skin. If the initial temperature is linearly distributed, it was proved that the rising temperature curve could be expressed as an infinite series of exponential functions. On this basis, an approximate solution method was obtained that can estimate the steady value in advance. Experiment shows that the method can estimate the steady value with an error less than 0.2 c by using the data measured in 4 minutes and 0.1 c by using the data measured in 6 minutes. By prolonging the measuring period, the estimated value is monotonously increased, and tends to the actual steady value. Moreover, the inverse problem (find the initial temperature distribution from the data measured) is under study.

328

BE12-0.6

Unconstrained Measurement of Temperature and Its Distribution of Decubitus Ulcer Patients
T. Nakano*(1), T. Tamura, T. Fujimoto, T. Tsuji, T. Togawa(2),
(1)South Japan Health Science Center, (2)Inst. for Med. & Den. Engng., Tokyo Med. & Den. Univ., 2-3-10, kandasurugadai, Chiyodaku, Tokyo, Japan 101

Decubitus ulcer is the ulceration of the skin caused by a circulatory disturbance during long confinement to bed. Using sheet containing IC matrix sensors, the surface temperature in 15 areas of the decubitus ulcer patient were measured without pasting sensors directly upon the skin. This data was continuously recorded in EPROM every 5 minutes for 10 hours. After data processing of the signal, the temperature and its distribution were illustrated automatically through graphs. The recorded distribution of the temperatures showed rare posture changes in the patients as compared to those of the normal control. It was observed that the temperatures of the area of the decubitus ulcer were mean 35.5°C and 3°C higher than those of the normal area. There was no difference in the ulcer temperature during sleep and non-sleep periods. This device is useful for prediction and prevention of the decubitus ulcer.

BE12-0.8

Experimental Study of Power Deposition and Power Reflection for Microwave Hyperthermia Antennas, Matthew Pressly* and Dr. J.A. Pearce, The University of Texas at Austin, Austin, Texas

In microwave tumor hyperthermia, the heating is induced by an antenna which radiates microwave energy into the tissue. The pattern of heating induced by different applicators has been studied on a tissue phantom in order to predict applicator performance on human tissue. Minimization of power reflection has also been studied.

The phantom material has electrical properties similar to muscle tissue. Heating patterns are analyzed using thermographic imaging. The frequency-dependent reflection coefficient has been determined for loaded antennas using a Hewlett-Packard 8510B Network Analyzer. Antennas studied include: Spirals, slots, bowties, resonant ring, and parasitic ring.

BE12-0.7

Modeling the Thermoregulatory System Using Thermal Entrainment Technique and a Kernel Method. Dr. Ahmed K. Ahmed*
Faculty of Technological Studies, Kuwait

The system considered here is the process relating the thermal stimulus (input) to heart rate (output) of a man. This paper describes Electronic Equipment developed to control air blower which produces thermal stimulus of hot and cold air at different frequencies to serve for the input to the thermoregulatory system. It also describes experimental procedure and identification procedure of the system model using an algorithm of Kernel identification of voltterra series which greatly reduces the computational burden and eliminates the restriction of using white Gaussian input of a test signal. The calculation, estimation of voltterra Kernels and formulation of the model are presented.

A second order model is the most appropriate for a good estimate of the system dynamics. The model contains the linear part (first order Kernels) and Quadratic part (second order Kernels) in parallel.

Other results and discussion will be presented. It seems that the model may give physiological interpretation of the dynamics of the thermoregulatory system.

BE12-P.1

A Liposome-Based Immunosensor: Detection of Tumor Markers, M. Aizawa*, S. Shimizu, H. Matsumura, H. Yokoyama and H. Kamei, Electrotechnical Laboratory, 1-1-4, Umezono, Tsukuba 305, Japan.

We have developed a new type of biosensing systems where the dynamic light scattering technique is applied to observe agglutination of liposomes caused by an antigen-antibody reaction on their membranes. The liposome is a small spherical body ($d=20-100$ nm) composed of phospholipid bilayers which construct a basic structure in biomembranes. By the use of our system, we tried to detect one of tumor markers, pancreatic oncofetal antigen (POA), in human sera. We prepared a suspension of liposomes having polyclonal anti-POA molecules on their membranes. When a test solution with POA molecules was added into the suspension, agglutination of the liposomes occurred through the POA antigen-antibody reaction. From the dynamic light scattering measurement, we found that there is a linear relation between the size of agglutination products and the POA concentration. On the basis of the relationship, we could estimate the POA concentration in sera with a small sample volume (1 μ l) and in a short period (20 s). The minimum detectable concentration in this sensing system is ca. 200 nanomol/ml under our ordinary experimental conditions.

BE12-P.2

Nonparametric Testing of Plasma Insulin Characteristics as Potential Markers of Breast Cancer Risk (BCR), R.C. Hermida* and C. Hernandez, University of Santiago, Spain.

Among 12 plasma hormones from healthy adult women sampled around the clock and the year, pattern discrimination methods single out plasma insulin as a primary classifier for a high (H) vs. low (L) BCR. The relation between plasma insulin and BCR is an indirect one in all 4 seasons. These data were re-analyzed by bootstrapping (BS) of circadian characteristics, assuming that deviations of each sample from 2 means, those of the BCR-group and the individual, are correlated along the 24-hr scale in keeping with a first order auto-regressive model. Results from BS validate differences in circadian rhythm-adjusted mean for insulin in spring and summer between the L & H BCR groups. Circadian BS is a resampling procedure here suggested to introduce inferential considerations into discriminant analysis and recommended for broad routine use in nonparametric estimation, hypothesis testing and biomedical signal simulation.

BE12-P.4

Thrombolysis in Membrane-Bound Thrombi Using Liposomal-Encapsulated Streptokinase, PD Nguyen[†], EA O'Rear[‡], BM Fung[‡], R Lu[‡], AE Johnson[‡]. [†]Dept. of Chemical Engineering, [‡]Dept. of Chemistry, University of Oklahoma, Norman, OK 73019, USA.

Application of streptokinase (SK) in thrombolytic treatment has been hampered by the uncertainty of optimal dose, arising from immuno-inactivation, complications resulting from underuse of SK, and above all, fear of bleeding. As a result, patients with history of severe hypertension, recent strokes, cerebral hemorrhage, and cerebrovascular diseases are excluded from this kind of treatment. We are currently investigating a new delivery system for the transport of SK to target area by the use of liposomes.

The ability of liposomes to encapsulate drugs, proteins, and nucleic acids have stimulated interest in their use as drug carriers. In our study, high concentrations of SK (10,000 IU/mL) were used for encapsulation in large unilamellar vesicles of phosphatidylcholine. These vesicles have a homogeneous size of less than 0.2 μ m in diameter. During slow flow through membrane-bound thrombi, liposomal encapsulated SK retained the ability to activate the fibrinolytic system, presumably by lysing of vesicles from shear forces. By monitoring the pressure drops across the Nuclepore membranes and clot-dissolving time, the preliminary results show that the capability of SK-encapsulated liposomes to dissolve clots are comparable to that of an equivalent amount of unencapsulated SK in platelet-poor plasma. We believe that the therapeutic efficacy would be improved if SK or other plasminogen activators were encapsulated in a medium such as liposomes and only released when it has reached the blood clots, and that hemorrhagic phenomena might be greatly alleviated by the relative dampening of diffusive to convective transport.

BE12-P.3

Reference Region for Rhythm Parameters of Plasma Cortisol in Children of Short Stature, R.C. Hermida*, L. Garcia and F. Halberg, Universities of Santiago, Spain & Minnesota, USA.

21 plasma cortisol profiles, sampled from Bavarian children every 4 hrs for 24 hrs across all seasons, served for the computation of a so-called paradism, a 90% prediction region for the amplitude(A)-acrophase(θ) pair. Cortisol data from 32 Spanish children (20 boys and 12 girls) aged 6-14 yrs, of short stature, sampled at about 3-hr intervals for 24 hrs across all seasons, were also analyzed by linear harmonic analysis. The best fitting period is 24 hrs for either sex and all subjects. The circadian parameters were interpreted by reference to the Bavarian paradism. Despite differences in age, ethnicity, climate, diet, health and sampling conditions between both populations, individual estimates of the circadian A and θ were inside the Bavarian paradism for 19 boys and 9 girls. Cortisol marker rhythmometry based on relatively few samples constitutes a practical approach for parameter estimation of the adrenal cortisol cycle.

BE12-P.5

The Relationship Between Composition of Tumor Cells and Its Damaged: Liu Yongge, Wang Junjian*, Quan Lin, Dept. of Bioengineering, Huazhong Univ. of Sci. and Tech., Wuhan, Hubei, P.R.C.

Experiments are designed to determine how the cell structure is damaged by shear stresses in Couette rheometer. We find that viability of EAT (Ehrlich ascites tumor) cells at about 41°C and S180 (sarcoma 180) at about 43°C abruptly decreased by shear stresses 25 dynes/cm, compared with the slow and linear loss of viability with the rise of temperature from 30°C to 40°C. This abrupt change is consistent with marked change of cell membrane microviscosity which is caused by bilayer systems of membrane undergoing a thermotropic phase change (phase transition) from the liquid-crystalline to the liquid with the rise of temperature.

So the sharp change of viability is due to phase transition of cell membrane. This indicates that the cell membrane fluidity is vulnerable to shear stresses. The larger the membrane fluidity of, the easier damaged the cell is. The viability of tumor cell treated with colchicine is raised, which suggests that the deformability is limited by cell microtubules. On account of the high nuclear/cytoplasmic ration in many cancer cells, mechanical stresses at the cell surface are transmitted to the nuclear membrane and contents and even nuclear membranes are damaged while surface membranes are not in some cells. Not like the special structure tumor cell cannot protect from shear kill.

BE12-P.6

THE BIORHEOLOGICAL PROPERTIES OF HUMAN NORMAL AND PATHOLOGICAL GALLBLADDERS - G.H. Zhong*, Y.P. Wu, G.R. Wong, West China University of Medical Sciences, Chengdu, Sichuan, P.R.C.

According to the "thin shell theory" and some suppositions, a two-dimensional quasi-elastic strain energy function of gallbladders based on the biliary histology was established. The relationships between the stress and strain of the gallbladders were obtained. A new non-contact system which was composed of VDA (Video-Dimension-Analyzer), Pressure transducer and other transmissions was used to measure the two-dimensional deformation of gallbladders. A non-linear multi-dimensional curve fitting method was applied to fit the measured results. We found that the biorheological properties of gallbladders were related to their histology structures. Furthermore, we found that the strain energy function and its parameters can be used to evaluate some biliary diseases such as cholecystopathy clinically.

BE12-P.7

Iontophoresis with insulin in dogs. J. Bustelo*, F. del Pozo, M.J. Medialdea and F. Vilaplana. Fundacion C.G.M. Instituto de Bioingenieria. Avd. de la Marina, 3-5. 11007 CADIZ ESPAÑA.

The objective of this investigation is the - insulin administration using traditional - techniques of iontophoresis as an alternative to the traditional treatments of Diabetes Mellitus.

The different experiments were: the possibility of introduce insulin through the intact skin without it losing its biological and to determine the best parameters that permit the elaboration of the principles of a non-invasive insulin pump.

A study was carried out on a 50 dogs were - made "in vivo", divided into four groups. - Were determined the values of insulinemia and glycemia after the insulin application by means of iontophoresis during thirty minutes.

BE12-P.8

A Study on A New Adsorptive Antidote for Artificial Liver. Xu, Guo-Fang; Wu, Yang; Peng, Wei-Chao; Zhou, Han; He, Shu-Chu; etc., Research Institute of Biomedical Engineering, Jinan University, Guangzhou, People's Republic of China

This text reports a result of a staged study on a new adsorptive antidote for artificial liver. This adsorptive antidote was prepared from a natural chitin raw material by simple chemical and physical treatment. It has a good biological compatibility and a relatively strong adsorbability to bilirubin, endotoxin, heteroaromatic amino acids.

A static test showed that 1 g of this antidote could decrease the bilirubin in a 10 ml plasma with a concentration of 50 units to 20-25 units within 2 hours and the amount adsorbed was 0.25-0.30 mg/g. As for endotoxin, it was decreased from 54 FC/ml to 4-5 FC/ml and the amount adsorbed was 500-510 FC/g. The amount adsorbed of some heteroaromatic amino acids in complex amino acids were as follows: Phenylalanine 1.52 mg/g; Tyrosine 1.20 mg/g; Histidine 1.31 mg/g. Filling 70 g of this adsorbent into an artificial liver device, we performed a blood perfusion for 2 hours to experimental dogs of icterus model weighing 11-14 Kg. The contents of bilirubin and glutamic pyruvic transaminase in the blood before and after perfusion were decreased respectively by 53-63 % and 42-48 %. The experimental dogs recovered normal activities and appetite soon and survived after perfusion. An experimental female dog even mated and got pregnant after perfusion. Nevertheless, experimental dogs of the same model without perfusion treatment would die within several days.

BE12-P.9

An Experimental Approach to the Hemocompatibility and Permeability of Activated Charcoal Coated with Silastic and Its Copolymers, Liu You-chu, Dong Guang-jiao, and Wang Xiu-yu, Dept. of Chemistry, The Fourth Military Medical College, Xian, Shaanxi, P.R.C.

The methyl vinyl silastic (PVMS) and its copolymers, PVMS-MA and PVMS-AM coated activated charcoal (AC) that prepared by ^{60}Co radiation methods. Studies on hemocompatibility of these coated materials have been carried out by SEM and pseudocoloring of a grating encoded phase-picture method. The results of our in vitro studies show that the permeability of silastic and its copolymer-coated charcoal for librium is very high. The detoxication efficacy of the coating appeared PVMS-MA-AC > PVMS-AM-AC > PVMS-AC. The platelets on PVMS-MA copolymer were slightly deformed. The number of adhered platelets to the copolymer coating was 28% of the platelets adhered to PVMS and was only 8% of the platelets adhered to AC. The results suggest that the hemocompatibility of the PVMS-MA copolymer induced by radiation is better than silastic and that the copolymer coatings are likely to be used hopefully for detoxication of artificial kidney or artificial liver. Abbreviation AM acrylamide; MA methacrylic acid.

BE12-P.10

Low intensity constant direct current effect on wound healing, N. Atalay,* G. Aydın, B. Işık, S. Toktaş, Medical Fac. of Dicle Univ. Biophysics Dept. Diyarbakır, TURKEY

The effect of low intensity constant direct current on soft tissue wound healing in rabbits was studied and the healing rate of electrically stimulated wounds were compared with the controls. Secondly Hydroxyproline content of granulating wound was analyzed in electrically stimulated and control groups.

Current was obtained from a specially designed low intensity direct current generator which keeps current constant by regulating the voltage. 100mA- 150mA direct current was applied to the wounds and max. output voltage was limited to 6V. Electrodes used were stainless-steel mesh ones and control wounds were covered by dummy pads with no electrode in it. One day of negative current was applied and process continued with positive current until the healing process was completed. Current application procedure was 8-10 hours/day and 6 days/week. Hydroxyproline content of both of the groups were determined at 7th and 12nd days by Woessner's method.

It was found that the healing was accelerated with constant direct current application and hydroxyproline content of electrically stimulated wounds were higher than the control ones.

BE12-P.12

Analysis of Circadian Rhythmicity of Fasting Insulin in Children of Short Stature, L. García*, R.C. Hermida, T. Iglesias and C. Ludeña, Hosp. Materno-Infantil, La Coruña & University of Santiago, Santiago (Spain)

Insulin concentrations (in $\mu\text{IU/ml}$) were determined by radioimmunoassay in plasma obtained at ~3-hr intervals for 24 hours from 11 boys and 7 girls of short stature, aged 6-14 yrs. Circadian rhythm parameters were computed by the single and population mean cosinor fits of a 24-hr cosine curve

Gender	P	MESOR ¹ ±se	Amplitude±se	Acrophase ² ±se
Boys	.005	30.8±3.0	12.7±2.5	-299°±9°
Girls	.052	34.1±4.0	17.0±5.0	-251°±13°
All	<.001	32.1±2.2	13.1±2.0	-277°±10°

1 Midline estimating statistic of rhythm.

2 From midnight, with 360°=24 hours.

Evaluation of risk by appropriately designed questionnaires should next complement blood sampling for hormonal determination and proper signal processing and parameter estimation in groups of children differing in gender, age or ethnicity, among other factors.

BE12-P.11

An experimental system for quantitative determination of mechanical parameters of human hair. G. Nikiforidis*, D. Tsambaos, A. Bezerianos, P. Prokopiou University of Patras, 26001, Patra, Greece.

A quantitative indicator of the general status of the human hair can be given by the exact determination of the principal parameters characterizing its mechanical behavior. In the present study an experimental procedure, which determines the stress-strain curve of human hair under different strain rates is analyzed. In this paper the following is described: 1) The mechanical components and the system of transducers 2) The electronic circuits by which the strain is applied and the stress as a function of time is measured 3) The mathematical algorithm and the program of calculus for the determination of Young modulus, yield strain, ultimate strain and relaxation modulus of human hair. In this framework following a standardized protocol the statistical correlation of the mechanical behavior of human hair to the findings of morphological and biochemical analyses as well as the clinical examinations, is possible. Consequently quantitative determinations of the influence of different factors such as U-V radiation and pharmaceutical treatment, on the condition of human hair can be performed.

BE12-P.13

AN APPROACH FOR SHORTENING MEASURING TIME OF HUMAN BODY TEMPERATURE, X.L. Zheng, C.L. Peng and E.X. Zheng*, Chongqing University, Si Chuan, P.R.C.

The rapid measurement of human body temperature is necessary for the clinic and daily life. This paper submits the electrical model of body temperature measuring system.

Under certain conditions, the model can be simplified as an R-C circuit of second order. The process of body temperature measurement is determined by the thermal resistance and capacitance of human body and also of the sensor. According to the model, discussions have been had for the shortening of measuring time of body temperature. We considered here how to decrease the effect of initial temperature of the sensor. We present the preheating method to avoid the influence of environmental temperature.

On the basis of preheating method, a prototype of the fast-response electronic clinical thermometer has been constructed. The measuring time is less than 30 seconds and the accuracy is better than $\pm 0.1^\circ\text{C}$ for oral and rectal temperature measurements. This shows potential advantages in clinical uses.

2 2 2

BE12-P.14

AN AMBULATORY SCREENING DEVICE FOR THE DETECTION OF SLEEP RELATED BREATHING DISORDERS

T. Penzel, G. Amend, K. Meinzer, J.H. Peter
Med. Poliklinik of Philipps-Universität Marburg

Sleep-related breathing disorders (SRBD) are of high prevalence (10%) in a male population with an age between 40 and 60 years. To diagnose these disorders extensive investigations in a sleep laboratory are necessary. Therefore the need for an easy to handle screening device is growing.

Different studies in our sleep laboratories showed that the time course of heart rate and a frequency analysis of nocturnal breathing sounds reflect the structure of sleep very well. Physiological and pathological patterns can be differentiated.

In collaboration with a medical electronics firm we succeeded in the development of a small portable device based on the analysis of heart rate and nocturnal breathing sounds. The device records the heart rate beat-to-beat with a resolution of 1 s and 6 bit in a solid state memory. Two further bit/s record loudness of breathing sounds and the normalized power in the frequency range between 50 cps and 800 cps which is typical for snoring. A recording up to 18 h permits a comparison of night-time and day-time pattern. Data are read out via a serial interface and can be analyzed in a PC.

Pattern analysis on heart rate and time intervall analysis on breathing sounds allow efficiently to differentiate normal sleep, sleep apnea and other indications for further sleep lab examinations.

BE12-P.16

The Computer Simulation for Ultrasonic Point Objective Image, Zhou Guang-Lu*, Yi Ji-Ping, Chengdu Inst. of Radio Eng., Chengdu, PR China.

To simulate a B-mode ultrasonic image on computer has been considered of great significance for the obtainment of accuracy and optimization in a practical design work for B-mode ultrasonic system. However, the reliability of simulation results depends on the analysis of a sound field. The sound field distribution is used to simulate the practical image in a linear array B-mode ultrasonic field.

The image function and the point response function have been successfully derived and they are all dealt with in the frequency domain.

BE12-P.15

Automated Plastic Forming System for Artificial Organ Components with a Robot, H. MATSUDAIRA*, T. TOGAWA & K. TSUCHIYA, Dept. of Mech. Engng., Sch. of Sci. & Engng., Waseda Univ. Tokyo Med. & Dent. Univ., Tokyo, JAPAN.

A new plastic forming system was developed. The principle of this system is piling up cross-sectional layers to form the entire figure. Each layer was fabricated by extruding forming material intermittently in a series of locations using a plastic dispenser attached to a robot which was controlled by a computer. As the material, a room-temperature curing and an ultra-violet curing silicone rubber which viscosities are roughly 800-1,000 Pa were used.

In the preliminary experiment, simple shapes such as straight tubes, bifurcating tubes, tubes having leaflets in the inside and spiral tubes were formed. Errors in forming process remained within 0.5 mm. The result suggests a possibility of applying this method to form plastic models which are difficult to be formed by the casting or machining.

BE12-P.17

Mapping of Pain by Electrical Impedance Measurements, Couros Ghaznavi*, Roman Chucky, University of Bridgeport, Bridgeport, CT 06601

Our study attempts to objectively map by means of dermic impedance measurements, the painful site. The hypothesis on which our study rests is that in a healthy individual, dermic impedance measurements would reveal a symmetry of electrical patterns. Pain alters this symmetry. Changes in circulation take place in the painful site and this leads to a change in impedance values. The study undertaken here is to probe the reasons and to find an effective method of localizing painful areas. An instrument at a frequency of 200 KHz has been designed to locate the low impedance points on the skin.

The impedance between two specific points of the body is a function of the frequency of the applied voltage. At high frequencies, electrical current effectively short circuits the entire cell by penetrating the high capacitive cell wall. Thus, the impedance of a cell shows only incremental changes beyond a critical frequency. This frequency is approximately 200 KHz for the skin. Consequently it's assumed that the disymetry of the dermic impedance noticed is due to changes in circulation.

BE12-P.18

An Algorithm for Detecting Parameters of Abnormal Nystagmus Beats
L San*, Institute of Aviation Medicine, Beijing, China

The key point in ENG data processing is identification of ENG waves and extraction of abnormal nystagmus beats. A new algorithm has been developed in our Lab and was called 'Moving Mean Threshold.' Interference, such as oculomotor waves or blink waves, added to nystagmus beats, and became abnormal beats. Based on the fact of that the interference became very narrow pulses relative to time domain of slow phase when the ENG waves were differentiated, we used the mean ranging from -S.D. to +S.D. as estimation of the slow phase velocity. Thus the interference can be cancelled notably. The characteristics of the algorithm are: 1) Parameters of normal ENG waves can be calculated correctly. 2) Interference added to ENG can be cancelled. 3) Because of its smoothing effect, high frequency interference, such as EMG, can be filtered. More than 3500 of ENG records of all kinds of abnormal beats have been processed with this algorithm, and the correct rate of identification of ENG parameters with this algorithm is 98.4%. The algorithm is very suitable for processing ENG records of patients.

BE12-P.20

The Identification of Parameters in Heterometric Autoregulation of Cardiac Contractility, Han Yan-an*, Li Shao-xiong, Zhao Xue-wei, Kong Su-ming, Shandong Medical University, Jinan, P.R. of China

The system identification technique was applied to study the dynamic process of the heterometric autoregulation in ventricular contraction. The experiments were carried out in two groups of adult Wistar rats. The process can be described by a second order differential equation. Using Gauss-Newton method the parameters a, b, c and d were obtained. The ventricular contractility is regulated by parameters a, b, c and d. Among the parameters c is the most important one which reflects the relationship between arterial pressure deviation and the derivative of end diastolic pressure $d(EDP)/dt$, determining the stability of the system and assessing the contractility of the ventricular myocardium. If the value of c is less than $-ad/b$, the system is unstable. The blood pressure tends to drop down indicating the contractility of the myocardium is impaired.

BE12-P.19

Myoelectric Control of Practical Artificial Limbs, LUO Yong-zhao*, Shanghai Institute of Physiology, Chinese Academy of Sciences, 320 Yue Yang Road, Shanghai, China

The loss of muscles, atrophy and dysfunction of the muscles in the amputees' stumps result in a shortage of the sources of EMG control signals. In order to solve this problem, less EMG signal patterns are used to control more actions of artificial limbs and from less muscles more EMG control patterns are produced. One kind of our artificial hands only need one EMG pattern. It is used to control the opening of the fingers. The closing is automatic. For the arm prostheses with three degrees of freedom only three EMG signal patterns from two muscles are used. Whole arm prostheses can be controlled by EMG signal from three muscles around the stump. To meet the needs of different kinds of amputees, a series of upper limb prostheses has been developed and used by many amputees.

BE12-P.21

Long-Term Continuous Monitoring of 'Activities of Daily Living' with Particular Reference to Solitary Senile People, K. Ikeda*, A. Watanabe and M. Saito, Institute of Medical Electronics, University of Tokyo, Bunkyo, Tokyo 113, Japan

A long-term ADL monitoring system, especially for solitary senile people, which consists of a number of transmitters with vibrosensors and a common receiver with data-processing and data-memory units, is designed for trial. The transmitters are small enough to be stuck on utensils or furnishings, such as toilet door, refrigerator door, or kitchen drawers.

When one of the vibrosensors detects any activity of the subject, it transmits its own code signal for several times running, otherwise it remains quiescent. All the transmitters for one particular subject use same radio frequency. When the receiver detects the radio signal and succeeds in identifying a particular code at least three times in succession, the code is to be stored as an event in its memory unit together with its occurrence time.

The contents of the memory is automatically read out at a fixed period, and sent to the institution concerned, through the telephone line, in order to be analyzed. The capability and usability of this system are discussed to some extent, especially from the view point of health care for the aged.

BE12-P.22

Test for Ergodicity of Normal Human Blood Pressures, F.E. Yates*, L.A. Benton, S.J. Berry and M.J. Korenberg, Crump Inst. for Medical Eng., UCLA, Los Angeles, CA; Dept. of Elect. Eng., Queen's University, Kingston, Ontario, Canada.

We hypothesized that repeated measures of 24 h ambulatory blood pressure in single normal individuals might recapitulate the statistics of similar single records of a cross section of normal subjects, with respect to ultradian (< 24 h) periodic dynamics. Systolic and diastolic blood pressures (SBP, DBP) were measured every 7.5 min for 24 h. We obtained 13 records on each of 2 subjects (L - 35 y woman, F - 59 y man), and single records (group R) on 13 men and 6 women (24-65 y). All subjects had 24 h rhythms in both blood pressures. We examined variances of each record for ultradian periodic structure using the fast orthogonal search method of Korenberg, which models data as a (not necessarily harmonic) series of sine/cos pairs as features. We windowed the features into 3 domains: ~9 h, 6 h, 3 h. *Results:* % occurrence rates of significant features for SBP (9, 6, 3 h) and DBP (9, 6, 3 h) were: F (38, 31, 15) (46, 46, 23)/L (38, 38, 31) (54, 23, 15)/R (16, 26, 10) (47, 21, 16). No group had an ultradian feature prevalence (fp) > 55%, but all 3 groups had a 9 h DBP fp > 45%. R had no other fp > 25%, whereas F and L had SBP 9 h fp = 40%. L also had SBP 6 h and F DBP 6 h fp = 40%. *Conclusions.* (1) ultradian rhythmic structure of normal human BP is inconstant, (2) near-periodic features are not rare (fp = 30% overall), (3) a 9 h DBP feature is most common, (4) individuals have distinguishing "dynamic signatures" seen in the distribution and occurrence rates of their ultradian rhythms. (Supported by the Hartford Foundation.)

EE12-P.24

Digital recovery of respiratory rhythm from the ECG and the pulse wave, J. Colominas*, J. Rosell, P. Riu and R. Pallas-Areny, Div. Instrumentacion y Bioingenieria, ETSI Telecom, Box 30002, 08080 Barcelona, Spain

The physical proximity of organs of respiratory and cardiovascular systems results in a mechanical interaction between them and the corresponding presence of interferences in the signals retrieved from one, which may be attributed to the other. Neural control mechanisms are also responsible for another kind of interaction in the form of a respiratory-induced cardiac rhythm variability (respiratory sinus arrhythmia, RSA). By modelling the way in which the interaction modifies signals associated with one system, we can consider the result of the interaction as a means of inducing information from one system into the signals associated with the other, and then try to recover it. Our experimentally assessed models indicate that, aside from the RSA, there is an amplitude modulation and a base band component associated with the respiration, both in the ECG and in the external pulse wave. By digitally processing these signals, we recover the respiratory rhythm from them without any hardware modifications for existing equipment, thus increasing the amount of information obtained for the same cost.

BE12-P.23

Circadian Rhythms in Systolic and Diastolic Blood Pressures (SBP, DBP) in Normotensive Humans, L. A. Benton*, M. J. Korenberg, S. J. Berry and F. E. Yates, Crump Institute for Medical Engineering, UCLA, Los Angeles, CA; Dept. of Elect. Eng., Queen's University, Kingston, Ontario, Canada.

Ambulatory SBP, DBP and heart rate (HR) were measured every 7.5 min for 24 h in two groups of normal subjects: younger (Y, 14 men and 7 women, 24-65 y) and older (O, 7 men and 10 women, 66-95 y). Variance structure of the ~192 measurements per subject was examined by the Fast Orthogonal Search method of Korenberg, modeling data as a series of sine/cos "features", which, unlike the standard Fourier series, is not necessarily harmonic (comensurate). Any feature reducing variance $\geq 5\%$ was considered significant. (Shuffling a data set eliminated all features.) We could detect features between 0.5-24 h. *Results:* All subjects had strong ~24 h ("circadian") rhythms in SBP, DBP, and HR. In Y there was also a 9 h feature in DBP ($p < 0.01$), but no other ultradian (< 24 h) periodicity in any variable. In contrast, O showed prominent 9 h and 3 h features in both SBP and DBP, as well as a 6 h feature in DBP. HR had no ultradian features in any group. There was no sex difference in these findings. *Conclusion:* Cardiovascular pressure dynamics change with age in normotensive subjects such that ultradian rhythms become prominent in both SBP and DBP after age 65. (Supported by USPHS Grant GM 23732 and the Hartford Foundation.)

BE12-P.25

The Electro Optical Modulation of Cytochrome C, Yu Wei*, Yong-Qing Hwang & Ci Lin, Nanjing Institute of Technology, Nanjing, China

Recently it is an interesting research topic in bioelectronics to find some certain molecules and biomolecules which can be used in electronic devices. Two structure frames of cytochrome C are made in our Lab. One is a thin membrane of cyt-C immobilized in gel of PPA, the other is the Langmuir Blodgett film of lipid absorbing cyt-C molecules. A measurement system with microcomputer has been developed in order to obtain the electro-optical modulation character of cyt-C. The samples of cyt-C are inserted into two electrodes which are light transparent and applied with alternative voltage. The photo transmission in cases of different electrodes, applied voltage, irradiation frequencies and immobilizing method etc, has been recorded. The photo transmission is changed according to the redox of cyt-C. Finally, it is tried to explain the mechanism of the electro-optical character of cyt-C.

BE12-P.26

ENZYME CATALYZED ETHANOL DETOXIFICATION OF THE DOG David Whitmire*, Dept Chemical Engineering, Auburn Univ, Alabama

An ethanol detoxification formulation using a three enzyme system with substrate pumped cofactor recycling (SPCR) was used successfully in dogs. When administered intraduodenally to anesthetized dogs the formulation caused a 35 to 45 percent reduction in intravenously administered blood ethanol over that of the control. When administered intragastrically prior to the intragastric administration of ethanol, the formulation prevented greater than 96 percent of the expected amount of ethanol from appearing in the vascular space.

BE12-P.28

A data acquisition system for electrical impedance imaging, J. Rosell*, R. Pallas, P. Riu and P. Rolfe+, Div. Instrumentacion y Bioingenieria, ETSI Telecom, Box 30002, 08080 Barcelona, Spain, and Dep. of Biomed. Eng. and Med. Phys., Univ. of Keele, United Kingdom(+).

In an impedance measurement system using N accessible points, the number of independent measurements for image reconstruction is $N(N-1)/2$. We have developed a system that increases the speed of data presentation by carrying out $N-1$ simultaneous measurements. It consists of analog measurement circuitry controlled by a microprocessor card communicated to a personal computer via an IEEE-488 bus. The PC is in charge of data processing and image presentation. The driving signal is generated from an EPROM, which feeds a D/A convertor and is successively applied to different electrode pairs using a commutation stage. 15 voltages are simultaneously measured by amplification and coherent demodulation and then digitized by a single A/D convertor. Digital signals are then optically coupled to the following stages.

BE12-P.27

Sensors and systems for the measurement of energy flux through skin, L. Yu*, D.Y. Liu Oceanic University of Qingdao; H.Zong, Qingdao Electronic Co. Qingdao, P.R.China.

The energy or heat flux through body skin is different in concept from skin temperature. People who have the same skin temperature may have unequal energy flux. Energy flux may be used to probe the temperature within the body and has some relations with the conditions of inner organisms. So that it may become a useful parameter for clinical diagnosis. Descriptions of the sensors and systems that used are given, their functions and measurements are presented.

BE12-Q.1

APPLICATION OF BIOMEDICAL ENGINEERING TO SKIN MANAGEMENT, E. Flam, Ph.D.*, NTL Associates, Inc., 29 Ainsworth Avenue, East Brunswick, NJ 08816

In an earlier study the importance of aeration to the proper management of the skin in prevention of decubitus ulcers was discussed. This current paper presents further research into the factors that contribute to the health of the skin. When skin is subjected to adverse environmental conditions, it experiences changes in its physical properties. Exposure to mechanical aggravations compounds the problem, and when internal factors, such as disease states are added, the combined result is significant downgrading of the skin's integrity and ability to protect. These contributing factors have been analyzed. A technique for developing a weighted equation of their effects is presented to help the biomedical engineer select the most suitable ranking and arrangement of conditions for a particular patient.

BE12-a.2

A pocket-sized computer as electronic memo-book for patients. H. Hutten* and J. Bergeler, Johannes Gutenberg-Universität, D-6500 Mainz (FRG)

Many patients have to keep memo-books in order to supply the doctor with diagnostically and therapeutically relevant data. Typical examples are diabetics (blood glucose, insulin injection, food, hypoglycemia, other events) and pain patients (center of pain, extent of pain region, degree of pain, pain expression, applied drug etc.). A special pocket-sized computer was developed that meets all requirements for an electronic memo-book. It contains a 8-bit CPU, a 64-kByte EPROM (program), a 32-kByte RAM (system software), a 32-kByte EEPROM (data), a quartz-controlled clock, and a V24-interface. The system is battery powered (6 months with usual employment) and an additional buffer battery for the protection of program and data. It is operated by 14 keys (0-9, Y/N, decimal point, ON). The user program is arranged as sequential menu with branches. The user is asked by the system via a display (2 lines, 20 characters each). All answers are displayed and can be outputted via the interface on a monitor or printer.

BE12-a.4

Instruments for a New Direction in Surgery. J. Wickham, R. Miller, M. Coptcoat, K. Ison*, T. Mills and P. Swain, Department of Minimally Invasive Surgery, Institute of Urology, London WC2H 8JE, England.

The future of surgery is clear. Patients want treatments to be less painful and mutilating, while administrators want patients to recover more quickly and cost less to service. Surgical procedures are under pressure to become less invasive. Less cutting means faster healing and opens up the prospect of using more local or minimal anaesthetic regimes. The challenge to scientists and engineers is to develop instruments which promote minimally invasive surgery.

Endoscopic techniques are employed for diagnosis and intervention in an increasing number of medical specialities. We review these areas of application, with particular emphasis on surgical techniques and associated instrumentation. We describe novel endoscopic sewing, stapling and cutting machines developed locally. We also comment on additional devices which will foster the applications of endoscopic surgery and pave the way for the formation of a new surgical grouping.

BE12-a.3

INNOVATIONS FOR IMPROVED HEALTH CARE
T.G. Krishna Murthy* and Swamy Lakshminarayan
Bangalore, India

Recent advancements in Science, Technology, engineering and medicine coupled with the emergence of interdisciplinary fields and closer interaction and Co-ordination have led to the development and clinical utilisation of a number of battery operated therapeutic appliances and devices. An integrated therapeutic approach which has the final target of providing patient relief at moderate costs provides a challenging opportunity to the present decade of engineers, scientists and technologists to evolve new techniques in close interaction with medical specialists. Nearly 10 per cent of the population of most nations are handicapped due to one reason or the other. Rehabilitation engineers have a really important and vital technosocial role to play. Greater challenge lies in innovating adaptive techniques depending on the socioeconomic conditions and the actual needs. The coming decade may witness the attainments of targets which can lead to the goal of HEALTH FOR ALL BY 2000 A.D.

BE12-a.5

Endoscopic Liquidiser and Surgical Aspirator. K. Ison*, M. Coptcoat and J. Wickham, Institute of Urology, London WC2H 8JE, England.

Surgical techniques are becoming less invasive and new instruments are being developed to support this trend. A need is emerging for a device which can remove appreciable quantities of tissue quickly through a small diameter, for example in endoscopic prostatectomy. We report the development of a machine to do this.

The device cuts and liquidises tissue for removal by suction through an endoscope or laparoscope. Its detailed design will be described. An experimental system has been constructed to look at the effects of cutter design on the mechanisms controlling the removal rates of different tissues. These rates are comparable with those achieved using diathermy during in vitro and in vivo trans-urethral prostatectomy (>10 g/min), but are faster in model laparoscopic procedures (>30 g/min).

When used on soft tissue in patients, aspirated particles vary from micrometres to millimetres in size. Size distributions depend on cutter and tissue type. The device has also been used to fragment calculi. Progress with the device will be reviewed and its applications discussed. The feasibility of using the machine under robotic control is being studied and results from this assessment will be presented.

337

BE12-a.6

Evaluation of Portable Insulin Infusion Pumps,
U. Boström*, B. Bouligand and I. Ström,
Clinical Engineering Department, University
Hospital of Linköping, S-581 85 Linköping,
Sweden.

Portable insulin infusion pumps have been used in Sweden since 1981. They are now used by about 300 patients. A prognosis has shown that in 1988 there should be about 30 000 portable insulin infusion pumps in use all over the world. Several designs are represented on the market. More and more sophisticated programmable pumps are introduced. There is a need for technical assessment of safety and reliability before the hospital decision of purchase.

The basic technical principles of portable insulin infusion pumps have been studied and the technical safety problems have been analyzed. Advantages, disadvantages and maintenance problems for five different types of pumps have been analyzed through testing, interviews with physicians and studies of literature. A test method suitable for clinical engineering departments will be presented. The possibilities to make safety controls and to maintain the pumps will be discussed.

BE12-a.7

Image Processing of Foot Pressures for Assessment of Leprosy, I. Sailaja, K. M. Patil*, C. Eswaran and K. S. Rao, Biomedical Engineering Division, I. I. T, Madras -600036, India

The application of digital image processing in the assessment of leprosy is described. A monochrome analog image of the feet is obtained by breakdown of total internal reflection of light on a device called barograph. The intensities in the image are related to the pressures under the feet of a subject standing on the barograph. The scheme of image processing adopted after digitizing the image, for noise suppression and edge detection is highly computationally effective to be useful in processing vast amount of data. Segmentation aids in edge detection obviating the necessity of using complex thinning and connectivity algorithms. The processed image gives (i) centres of pressures of both feet, together and individually, useful in the determination of the side to which the subject is leaning, (ii) isopressure contours giving a picture of the distribution of pressures under the feet and (iii) pressure under specific areas of interest. Analysis of the above parameters shows that the leprosy subjects develop high peak and average pressures in specific areas on the deformed and insensitive foot.

BE12-a.8

Study of Body Movements of Alzheimer Disease and Schizophrenic Patients Using Unconstrained Measurement.
T. Fujimoto*, T. Toyosima, T. Tsuji and T. Tozawa, Inst. for Med. & Den. Engng., Tokyo Med. & Den. Univ., 2-3-10, Kandasurugadai Chiyodaku Tokyo, Japan 101

The close relationship between body movements and mental state is well known especially in mental disorder where the characteristic abnormalities of movement are observed. We measured these body movements using an acceleration sensor without constraints. The continuous accelerations of waist, right wrist and ankle along with an electrocardiogram were simultaneously measured and recorded by a cassette data recorder. After processing the signals, the amplitude and frequency of the accelerations were plotted on the graph, and quantitative changes, coherent relations and wave pattern were studied. The changes in the quantities of movement well reflected the mental state of the patient. The graphs for Alzheimer disease showed simple and sporadic changes in the movements. Those of the schizophrenic showed sporadic, repetitive and stereotypic patterns. This device is useful in measuring the movement of the patient which helps to analyze the differing mental states of the psychiatric patient.

BE12-a.9

Model DTZ-1 Medical Electronic Syringes, Li Ming Liang* He Yi Xia and Tian Anmin* No.409 Hospital, the Ministry of Electronic Industry, Shaanxi, Boaji, China

The Medical Electronic Syringes resolve the problem of manually delivering drugs in intravenous injection for the nursing staff and make the intravenous injection into the process of the electronic instrument, dosage and meanwhile, make the speed of the intravenous injection adjustable, in addition, reduce the nurses' labour intensity. The syringes have widely range preset timer so that the cardiotonic glucoside, calcium and other injection, etc. which need to be injected in vein slowly in clinical treatment, can be injected even more scientifically. The medical electronic syringes are also able to be used for delivering drugs quickly, transfusing blood and keeping the infusion pipe a long time for the patients who are all seriously. The widely ranged preset timer for the intravenous injection has great autonomy in hospital or at home and makes the intravenous injection more adaptable specifications.

1. Suitable range for injection: for various drugs by syringes in 50mL and 100mL maximum pushing force 500g.

BE12-Q.10

Model Zj-1 Steam Curing Device,
Li Ming Liang* and Tian Anming, No.
409 Hospital, the Ministry of Elec-
tronic Industry, Shaanxi, Boaji,
China

This device is used for curing common cold, influenza as well as allergic rhinitis. The cure efficiency comes up to 88.9%. This device is superior to the other similar device in heating without two times. The temperature of the outlet is controlled between 40°C—60°C. The device is possessed of the simple structure, low cost, low power consumption and perfect functions, so it is very economical, practical and convenient. The curative effect for curing common cold is quick and no side effects. Specifications

1. Temperature measuring accuracy
(35°C—55°C) $\pm 1^\circ\text{C}$.
2. Temperature controlling accuracy
(35°C—55°C) $\pm 1^\circ\text{C}$.
3. Cover insulation resistance 1000M
4. Power consumption
heating condition 300W.
heat preservation condition 170W
5. Power voltage 220V $\pm 10\%$.

BE12-Q.12

Technical study on the Efficiency of Heat and Moisture Exchangers (HME).

P.M. Schroeder, U. Frucht, C. Ullrich,
U.Boenick* and W.König

In order to humidify inhaled gases in anaesthesia and intensive care disposable Heat and Moisture Exchangers (HME) have been introduced.

A new experimental set up was developed to investigate the efficiency of HME's. Nine commercially available HME's were measured. To prevent harm to the patient, the relative humidity of inhaled air should be at least 70%. Only 4 of the 9 HME's tested fulfilled this condition. With respect to the requirements for minimal dead space and an optimal moistening effect, only one of the HME's met the goals. HME's might be an alternative to traditional ways of humidifying inhaled gases.

BE12-Q.11

BEATE - A new System for Testing the Function of Hospital Ventilators

U.Boenick*

Up until now, no integrated measuring system has been available for determining the ventilation parameters volume, volume-flow and ventilation pressure, as also the gas-specific variables oxygen content, temperature and humidity. In order to overcome this deficiency, the Institute for Biomedical Engineering at the Technical University, Berlin has developed a portable lung simulator with an integrated tester, known by the name of BEATE. Now, for the first time, a test system that permits the rapid and simple determination of all the ventilation parameters relevant to safety, can now take its place alongside the systems already long available for the testing of electrical safety in accordance with VDE 0750.

BE12-Q.13

OUTPUT PRESSURE WAVEFORM EVALUATION OF IV INFUSION PUMPS

E. Amori*, Servizio Fisica Sanitaria e Bioeng, Parma, Italy

The high degree of accuracy and safety reached by the recent intra-venous infusion pumps, has led to a widespread adoption of these systems in almost every field of medicine, especially where long term and precise pharmacological treatments are needed. Different techniques in delivering the fluid into the venous system are currently available (revolving roller, linear peristaltic, volumetric).

The aim of this investigation is to calculate and measure the transient component of the output pressure waveform exerted in the different types of pumps tested. Furthermore, the influence of the stroke volume infused in each pumping cycle on the hydraulic venous impedance, i.e. resistance and compliance, is demonstrated. Results show that pressure transient component differ significantly from the volumetric or roller system to the linear peristaltic in which the infusion seems to be much smoother. This fact reflected at the input site of the venous system implies a different stress and hence a minor possibility of inflammations or thrombosis.

BE12-8.14

A Simple Exerciser for Nickel Cadmium Batteries in Medical Equipment, K.O'Brien, M.A. Chaudhri*, Austin Hospital, Melbourne, Australia

The inability of medical equipment to exercise NiCd batteries to maintain peak performance and good service life, has meant costly replacement of the batteries. In order to lower the wastage and avoid the tying up of a large amount of laboratory equipment to cater for the different capacity batteries, we designed and constructed our own simple exercising system.

It was designed using the standard Eurocard with a DIN 41612 connector, and six exercising modules are housed in a single BOPLA Combicard case. Each module allows selection of any three constant current charge rates to suit the particular battery and the battery is simply connected, the module reset, and automatic cycling will then take place. The "exerciser" will firstly constant-current-discharge the battery to the minimum recommended voltage and then constant-current-charge for the recommended time. It will then repeat the cycle twice.

BE12-8.16

A Patient Monitoring System in the Operating Rooms, Toyoki Kugimiya*, M. Tsuzuki, K. Numata, Surgical Center, The Department of Anesthesiology, University of Tokyo Hospital, 7-3-1, Hongo, Bunkyo-ku, Tokyo, 113, Japan

A sophisticated patient monitoring system during anesthesia is indispensable not only for high risk patients, but for complicated surgical procedures, such as open heart surgery and extensive surgery for malignancies. To build up a system which is suitable for a particular institution requires a careful planning based upon the needs arising from its clinical activities.

In our new operating theater, which started to function at the beginning of this year, a system which was designed to meet most demanding clinical situations was installed. The system includes cardiovascular and respiratory monitoring systems and other parameter monitoring. Close cooperation between clinicians (mainly anesthesiologists) and clinical engineers was found to be essential for the proper and efficient management of the system for the patients' benefit.

BE12-8.15

Reuse of Indeflators, J.Hagekyriakou, M.A. Chaudhri*, Austin Hospital, Melbourne, Australia

During coronary angioplasty, and some other interventional radiological procedures involving the use of a balloon catheter, an instrument is used to both inflate and measure the inflated pressure. Sterilization and re-use of such an "indeflator" had originally proved impossible, due to the fact that the contrast/saline solution used in the indeflator reacts with the brass component of the pressure gauge, resulting in the production of a salt which accumulates within the gauge and syringe. We have devised a method of successfully removing this salt from the indeflator prior to sterilization. The process involves dismantling the gauge/syringe assembly, washing out the gauge several times and then freeze-drying it. This removes the salt and water which is trapped within the gauge. The gauge and syringe are then re-assembled and sent for ethylene-oxide sterilization.

The gauges may be used virtually indefinitely provided they are not damaged whilst in use.

BE12-8.17

Column-Minireactor-Based Enzyme Analyzers of Metabolites, A. Simonian*, Ts. Avakian, Yerevan Physics Institute, Armenia, USSR.

Enzyme analyzers based on column minireactors have some advantages against enzyme electrodes. They allow to solve analytical problems in microbiological industry and medicine on determination of organic substances in multicomponent solutions. The use of such systems allows to control and manipulate biotechnological processes and simplify the analytical procedures in clinics. A wider as compared to enzyme electrodes range of determination of concentrations, a shorter time of contact of reaction products with the enzyme, little influence of processes of the substrate and the reaction product mass transfer are to be referred to the advantages of flow-through systems. We have constructed a flow-through enzyme analyzer providing for a highly specific determination of lysine concentration in the culture fluid, of glucose and uric acid in the blood serum or urine. The range of determination of concentrations for lysine is 5.5-55mM, for glucose - 0.3-16.6mM, for uric acid - 0.06-6mM.

BE12-a.18

HYPERALUMINEMIA OF PATIENTS WITH NEPHROPATHY, Y.F. Chiang*, T.B. Ian, Dept. of Nephrol. Wuhan General Hospital P. R. China

This paper reports the results of measurement of 182 serum samples of 142 patients (pits) with nephropathy, 116 cases of hyperalbuminemia (HA) were found by atomic absorption spectrophotometry (40.14% of pits were ill with glomerular disorders (GD), 41.55% of pits were tubular interstitial disorders (TID)). Of which 32.39% of pits were of normal renal function (NRF), and 49.3%—chronic renal failure (CRF). S_{AL} of normal controls were 0.63 ± 0.09 $\mu\text{mol/L}$, S_{AL} of cases with GD and TID were 4.42 ± 2.16 and 4.48 ± 2.59 $\mu\text{mol/L}$ respectively ($P > 0.05$). Before and after administration of $AL(OH)_3$, S_{AL} of controls showed significant change (0.45 ± 0.613 $P > 0.05$), while the urine AL was very significantly elevated (0.725 ± 1.43 and 2.85 ± 2.04 $\mu\text{mol/L}$ $P < 0.01$). S_{AL} of NRF was 3.475 ± 2.404 and of CRF was 5.442 ± 2.347 $\mu\text{mol/L}$ ($P < 0.01$). After hemodialysis and Continuous Ambulatory Peritoneal Dialysis, the S_{AL} levels were significantly increased, but significantly decreased after Gastrointestinal Dialysis.

Symptoms of HA mainly were: anemia, muscular and bony pains, encephalopathy.

The related factors and mechanisms of HA were briefly discussed.

BE12-a.19

Viewing and Evaluating Device for Stereoradiographs J. Barsai*, B. Heiner, and T. Illes, Medicoor Training Centre, P.O.B. 150, H-1389 Budapest 62, Hungary

The device of our design and manufactured by the Hungarian Optical Works/MOM/ is for the simple and prompt evaluation of stereoradiograph pairs. Our idea in designing the device was to relieve the radiologist from calculations. Our solution by mechanical means actually makes use of a hyperbolic function of four variables. The equation is $t = p \cdot f : b + p$, where t is the distance between the point under examination and the basic plane, p is the stereoscopic parallax, b is the distance between the focal points, f is the SID/source-image distance/. The pair of stereoradiographs viewed in the device through a binocular eyepiece give the viewer a stereoscopic effect. The problem is to determine the distance of the point under examination to the basic plane. The device solves this problem fully. All points can be localized in 2-3 mm accuracy. The device can be handled also by persons having no faculty of stereoscopic vision.

BE12-a.20

Application and Field Trials of Videophone in Health Care, P. Kaitila*, Vistacom Industries Inc., Kipparinkatu 2, SF-02320 Espoo, Finland

Applicability of a videophone with motion picture was studied in different areas of health care. Three field trials were carried out: a communication link between a long term patient in a hospital and her family, a consulting link between a health care station and the emergency clinic of a hospital, and remote assistance of a handicapped person at home. People learned in a short time to operate the equipment. Videophone proved to be practical. X-ray images could be shown to specialists in the hospital. Different moves of arms and legs could also be shown. Teleconsultations mainly succeeded. According to results, the number of patients to be moved from health care station to hospital could be decreased. Videophone seemed to suit well in consulting major fractures of bones. Operational telemedicine service may be arranged, especially for areas with low population densities, when further development of certain technical features of videophone has been realised.

BE12-a.21

New algorithms to detect the anaerobic threshold noninvasively, P. Gizdulich*, P. Panuccio, L. Viroli, F. Cresci, Dept. Fisiopatologia Resp., Universita I-50134 Firenze, ITALY

During increasing muscle efforts, many ventilatory functions show a discontinuity which is related to the anaerobic phase that replaces the aerobic state. The anaerobic threshold is usually evaluated by applying a 2-segment linear model for a clinical and diagnostic purpose. We analyzed the three most commonly used pairs of parameters: \dot{V}_E in function of $\dot{V}O_2$, \dot{V}_E versus $\dot{V}CO_2$, $\dot{V}CO_2$ versus $\dot{V}O_2$. The three functions have been studied during exercise with a cycle-ergometer. In ten healthy subjects data were collected every 15s by using a computerized acquisition system, until the subjects were exhausted. For each function we split the N -data set in two series of data: the initial n and the subsequent $N-n$. Two linear regressions were computed for every possible n . In order to select the best value of n , two new algorithms have been proposed and compared to the least square error method, usually applied. Reliability of the 3 algorithms was tested by the within subjects analysis of variance. $\dot{V}CO_2$ in function of $\dot{V}O_2$ was documented to be unreliable. As for \dot{V}_E vs $\dot{V}O_2$ and \dot{V}_E vs $\dot{V}CO_2$, the new algorithms showed a greater reproducibility than the least square method.

BE12-8.22

Ergonomic Analysis of Japanese PACS, R.HOSAKA* and E.TAKENAKA, Dept. of Radiology, National Defense Medical College, 3-2 Namiki, Tokorozawa-shi, Saitama-ken, 359 JAPAN

PACS (picture archiving and communication system) is a useful equipment in a field of radiology. Japanese industries also develop same types of equipments. But, there are several problems in the Japanese PACS. One of them is a problem about its man-machine interface. Almost of Japanese PACS have a poor man-machine interface. It is constructed by a character key-board as a input device, and one or two high-resolution monochrome CRT as a output device. This type of interface is not useful to control the equipment. In this study, present interface system and new interface system are compared from view point of handling time length. Both systems are constructed on a micro-computer like as a PACS control system. In a case of present type, a key-board and a monochrome CRT are used as interface devices. In the other case, a touch-screen and a RGB-CRT are used as interface devices. The result of experiments seems to indicate that the time length of new type is shorter than present type. The difference of both time length is approx. 10 [%].

BE12-8.24

A New Patient Record System Based on a Laser Card J.H.U. Brown, Ph.D., University of Houston, and Carlos Yallbans, M.D. Baylor College of Medicine, and H. Kitasonono, CSK, Tokyo

A method has been devised of placing 2 million bytes (700 pages of information) on a standard sized credit card so that a medical patient can carry the card with him at all times, update it at each visit, and have it available during emergencies. Dimples are impressed in the card with a milliwatt laser beam which also serves as the reading device. Write speeds are in excess of 20 kb/sec and read speeds are about 65 kb/sec. Any single datum can be located in less than one second, with an error rate of 10^{-11} . The information can be added to as desired and the information can be read with an ordinary IBM® p.c. with no main frame needed. Xrays and ECGs can be placed on the card. The software on a floppy disk is designed to present medical information in conventional format (socioeconomic data, drugs, operations, treatment, prognosis, etc) with the additional ability to add free text as desired.

The system is under test at the Harris County Hospital District Clinics and at NASA. Evaluation of the system under test will be presented.

BE12-8.23

Applied Values of Rheoencephalogram (REG) in Clinical Practice, Tian Anmin, Dept. Pharmacology, Baoji Medical and Nurses' School, Baoji, Shaanxi, P.R. China.

1. The vaso-headache may be classified according to characteristics of REG (from 930 patients), i.e. RWHA (the REG wave of high amplitude); RWLA (the REG wave of low amplitude).
2. The classifications of REG in vaso-headache may guide to use medicines. The effective rate of the vasoconstrictor drug for 250 patients with RWHA was 96.7 % and of the vasodilator drug for 50 patients with RWLA was 39.5 %.
3. The REG may keep watch on the state of cerebral blood and arteriosclerosis. This data (from 498 middle-old aged mental workers) show that the cerebral blood often is insufficient and that the cerebral arteriosclerotic index of REG is gradually increased to follow the increment of age.

BE12-8.25

Experimental Measurements for Assessing the Influence of Static Magnetic Fields on Pacemakers, V. Barbaro, P. Bartolini, M. Donnellini, D. Ialongo, S. Margarita, Istituto Superiore di Sanità - Roma, Italy.

Static magnetic fields can adversely affect the pacemaker (PMK), switching it from the operative status to a predefined test mode. This effect is obtained by means of the excitation of the reed relay built inside the PMK. It has been realized a system to produce a uniform static magnetic field in a volume enough large to contain PMK. The circular coil of the system has been excited by a current generator and the produced magnetic field strength has been continuously and slowly changed. The PMK was put inside the solenoid and its operating mode was monitored. When the test mode appeared the field value was recorded. The measurements were repeated with the PMK positioned along the three orthogonal axes, for each PMK the minimum recorded field value (B_{min}) has been taken in account. 127 PMKs by 12 manufactures were tested. The B_{min} ranged from 7.5 to 54 Gauss with a mean value of 20.3 Gauss. These values can currently occur in some environments.

BE12-Q.26

OXYGEN ADVISOR: A Computer System for Oxygen Therapeutics D. John Doyle MD PhD, University of Toronto, Toronto, CANADA

Interest in quantitatively assessing pulmonary function and predicting blood oxygen tension (PO₂) and saturation following changes in inspired oxygen has existed since the advent of oxygen therapy. Potential advantages of such methods would be to reduce the frequency of arterial punctures and to minimize the incidence of hypoxemia and oxygen toxicity. OXYGEN ADVISOR is a small hand-held computer system which 1) computes a number of indices of pulmonary gas exchange and oxygen transport (eg, shunt fraction, arterial-alveolar oxygen tension ratio), 2) predicts PO₂ changes following oxygen changes and 3) produces patient-specific oxy-hemoglobin dissociation curves from patient temperature and arterial blood gas data. The computer hardware is based on a Sharp 1500 microcomputer with a four color graphics plotter. Its small size and ease of use makes it very practical for use in critical care environments.

BE12-Q.28

Computers and Safety - A Challenge for All

G.R. Symonds*

Bureau of Radiation and Medical Devices
Department of National Health and Welfare
Ottawa, Ontario, Canada K1A 0L2

The integration of digital computers into medical diagnostic and therapy equipment has resulted in major advances in patient care. The pace of this development has been very rapid, with design emphasis placed on innovation and functionality. That this process has not been without problems is evidenced by patient injuries and deaths, with the resulting increase in attention by government regulators, standards organizations, professional organizations and the manufacturers themselves.

The set of issues raised by these problems covers a wide range: the multidisciplinary nature of the design process, user training and qualifications, the man/machine interface, and the applicability of safety engineering and quality assurance to both hardware and software. Even the concept of a "single fault" will require rethinking with regard to what constitutes a "component" in programmed systems using complex microcircuits.

The current trend in government regulation and safety standards writing is one of international consensus. This, taken with the above, promises an interesting challenge for everyone involved.

BE12-Q.27

Linear analysis of dynamic response in heart rate to physical activity in daily life, Takeshi Toyoshima*, Tatuo Togawa and Takayuki Tsuji, Tokyo Medical and Dental University, 2-3-10 Kanda-Surugadai, Chiyoda-ku, Tokyo 101, Japan.

In order to analyze the dynamic response of heart rate to physical activity including posture change under unconstrained daily life, a system for quantitative evaluation and simultaneous recording of these parameters was developed. In this system, the intensity of physical activity was evaluated by measurement of acceleration at the subject's waist and postures were discriminated as standing, sitting, stooping and lying, according to the inclinations of special angular switches attached at the thigh and the sternum of the subject. This recording system was applied to five healthy subjects. Then the dynamic response of heart rate to physical activity was analyzed applying linear system analysis, regarding heart rate as the output, and physical activity and posture change as the input of a linear system.

The results showed that the heart rate did not only simply follow the intensity of the physical activity, but it also responded as a first-order linear system with a time constant of about 70 min, and that the heart rate increased and decreased instantly with posture change by about 11% both from sitting to standing and sitting to lying.

BE12-Q.29

A Digitized Recorder for Ambulatory ECG
S.Hashiguchi*, T.Mitomi, Y.Kondo, Yamanashi University, Kofu, Japan,
K.Tamura, and S.Komori, Yamanashi Medical College, Tamaho, Yamanashi, Japan.

A digitized recorder for ambulatory ECG has been developed. It consists of an AD converter, a buffer memory, a magnetic recorder such as a portable VCR or DAT. 12-channel ECG signals, sampled at the rate of 250Hz, are converted to 12bit data and temporarily stored in the buffer memory. When the buffer memory is fully occupied by the data, the data are read out at the rate of 198kbytes/s and recorded on a 8mm video tape or a digital audio tape as PCM data. ECG waveforms of 12 channels can be recorded for 31 hours in a 120-type magnetic tape.

The reproduced waveforms were not distorted and no significant differences were noticed between the control signal and the reproduced signal. The fidelity of the reproduced waveforms is much better than the conventional (analog recording) ambulatory ECG recorders, and good enough to apply the myocardial ischemia analysis, where the reproducibility of the ST-portion of the waveform is of the most importance.

BE12-a.30

Assessment of vascular reactivity by thermal entrainment of heart rate, A. Lindqvist*, J. Jalonen, P. Parviainen, K. Antila, I. Välimäki and L.A. Laitinen, Research Institute of Military Medicine, Helsinki and Cardiorespiratory Research Unit and Institute of Applied Mathematics, University of Turku, Finland.

Sympathetic nervous system transmits thermoregulatory circulatory oscillations. Oscillations of the blood pressure are controlled by the periodic heart rate variability. We studied the usefulness of thermal entrainment of heart rate variability to measure thermoregulatory nervous function by using a standardized water bath stimulator. Periodic thermal stimulation of legs was performed to 7 healthy control subjects between 0.01 and 0.10 Hz. Fast Fourier-transform power spectra of the systemic skin blood flow and heart rate signal were calculated. In the skin thermally induced response exceeded spontaneous oscillations ($p=0.01$). Periodic heart rate variability could be entrained only occasionally ($p=0.82$). Sympathetic vascular reactivity can be measured from the skin blood flow but not from the heart rate variability.

BE12-a.32

A Study of Representation Method of Intrapartum Fetal ECG, F. Yano, S. P. Ninomija*, Aoyama Gakuin University, Tokyo, K. Idogawa, Seitoku Gakuen College for Women, Chiba, M. Tatsumura, K. Maeda, Tottori University, Tottori, Japan

The condition of a fetal heart can be estimated from a fetal ECG. To diagnose intrapartum fetal distress at childbirth, it is important to make detailed variation records of fetal heart rates with a baseline by fetal ECG R wave. For the sake, it is necessary to detect the exact locations of the peaks of fetal R waves. We have developed a procedure to confirm the location of the peak of fetal ECG R wave from leaded fetal ECGs involving many noises or artifacts.

The method to detect as follows: At first, we use which fetal ECGs digitalized at the rate of 400 samples per second. Second, we compute a moving variance by using 32 points and finding a point that exceeds a criteria. Third, we compute a regression line by some moving interval of the point. Forth, we select the absolute maximum in the positive slope and the negative slope of the regression line. Fifth, we define the peak point of fetal R waves from the point of intersection of these regression lines.

As the result, the location of the fetal R waves can be confirmed. Moreover, we have developed a method of representing the fluctuation of fetal R-R intervals.

BE12-a.31

Biomedical Pattern Discrimination of Circadian Neonatal Cardiovascular Characteristics.
R.C. Hermida* and F. Halberg, Univ. Santiago, Spain & Univ. Minnesota, USA.

In order to distinguish newborns at low or high risk of developing a high blood pressure (BP) later in life, 16 characteristics of time series on systolic, mean arterial and diastolic BP and heart rate (HR) monitored automatically at 5-hr intervals for 48 hours, are here used for classification by a so-called monotest, an all-subsets variable selection technique for biomedical discriminant analysis. When the circadian amplitude of diastolic BP and the 50% range and standard deviation of HR were used concomitantly as classifier for 62 newborns, this procedure yielded a 83.8% classification equivalent to prior criteria, the latter being based on the presence or absence of a family history of high BP, as determined by questionnaire. The monotest complements rhythmometric procedures, used earlier to separate groups of newborns with or without a family history of high BP, and defines a set of individualized criteria for risk assessment.

BE12-a.33

Objective recognition of fetal behavior with computer analysis of fetal actogram. K. Maeda*, N. Nagata, K. Nakajima, M. Tatsumura, Tottori University School of Medicine, Yonago 683 Japan

Fetal behavior including its active state, resting state and fetal breathing movement (FBM) is usually analysed by human observation of real-time, B-mode screen. Further objective technique is fetal actogram, which is the recording of fetal movement (FM) signals obtained by analog processing of ultrasonic Doppler low frequency signals. Visual analysis of the record revealed clear recognition of fetal active and resting states. FBM was also recorded. As the FM is expressed with spike signals, it was introduced into AD converter and the digital data were analysed with PC98XA computer. Simple statistics of spike amplitude and interval, frequency histograms of spike intervals, their 3-D number histograms in 10 rejection levels, and envelopes of spikes were obtained. Noise level was estimated to be the lowest rejection level from amplitude statistics and histogram. Fetal active state showed high amplitude and wide interval distribution, frequent peak signals in 3-D histograms with high amplitude, and frequent envelopes. Fetal resting state showed signal disappearance. FBM showed moderate but characteristic findings. The results showed objective and automatic recognition of fetal behavior.

344

BE12-Q.34

Computer simulation of intrapartum fetal distress diagnosis without uterine contraction, K.Maeda* and A.Makio, Tottori University School of Medicine, Yonago 683 Japan

Conventional diagnosis of fetal distress needed 2 channel records of fetal heart rate (FHR) and uterine contraction (UC). Because UC is maternal signal, the diagnosis only with fetal sign, FHR, is the purpose of this study. Fetal monitor output including FHR and UC signals was analysed by the 2 computer programs including UC parameter and without it in the same 65 patients who completed the vaginal delivery. Quantitative FHR parameters were our FHR score evaluated in 5min and fetal distress index (FDI) obtained in 15min. These were analysed with the programs. The results obtained with and without UC in 30min immediately before childbirth were compared to umbilical arterial blood (UA). FHR score and FDI showed clear correlation between the two analyses. Correlation between FHR parameters and UA pH was better in FDI than FHR score. The cases who had 3 points or more of FDI showed significantly low UA pH. Sensitivity and specificity for the prediction of lower UA pH than 7.25 were 86.4% and 88.6% in the cases who were analysed by the program with UC, and they were 86.4% and 90.7% when UC signal was not used. The possibility of FHR diagnosis without uterine contraction will be expected from these results.

BE12-R.2

A Method for Decreasing Mapping ECG Electrodes via Wigner Distribution, Shiro Usui*, Sozo Iwata, Naohiro Toda, Junji Toyama⁺ and Kazuo Yamada⁺⁺, Toyohashi Univ. of Tech., Toyohashi 440, ⁺Nagoya Univ., and ⁺⁺Meitetsu Hosp., Nagoya 464 Japan.

Body surface ECG mapping is known to be useful for diagnosis of heart diseases. However, it requires so many electrodes that causes problems in setting electrodes and recording the signals. To make it for daily clinical use, it is expected to decrease the number of electrodes. Lux et al. proposed a method for this by using correlation information between the electrodes. However, the number of electrodes must be given beforehand and it requires tremendous computation time to get the transfer matrix.

We propose here a new direct method utilizing the sampling theorem. We first apply the Wigner distribution analysis for a given map to find the local spatial frequency distribution. Then by picking up the highest frequency at each electrode position for each maps in one whole beat, the local maximum-spatial-frequency-band map has been constructed. Applying the sampling theorem to this map, the electrode arrangement can then be given directly. For example, an equally spaced 91 channel map, the number of electrode is enough to be in half. The proposed method requires less calculation than Lux's method and gives a minimum number of electrode and its arrangements.

BE12-R.1

3-D Mapping of the Body Surface and Epicardial Potentials, A. Calderon; T. Aoki, N. Yamanoi and T. Furukawa, Institute of Medical Electronics, Faculty of Medicine, University of Tokyo, 7-3-1 Hongo, Bunkyo-ku, Tokyo 113

A system has been developed in which the human body surface potentials and the epicardial potentials are displayed in a 3-dimensional format using wire-frame models of the human torso and the heart. This work makes use of the tools of computer graphics to help the doctor in his understanding and evaluation of the cardiac potential distributions.

To illustrate the applications of this system, several cases with abnormal ECG - right bundle branch block (RBBB), chronic myocardial infarction (OMI), and left ventricular premature beat (LVPB) - are given as examples of deviations from a normal path; results obtained from the animal experiments are also presented.

The increased realism and spatial resolution capabilities of the system, as compared to ordinary ECG and the 2-dimensional contour map alone, lead to a clear understanding and interpretation of the underlying electrical phenomena of the heart while making a diagnosis or presenting experimental results.

BE12-R.3

INTERPRETATION OF BODY SURFACE POTENTIAL MAPS BY MYOELECTRICAL MODEL SIMULATION RESULTS
Dan Adam* and Samuel Sideman
The Department of Biomedical Engineering,
Technion, Haifa 32000, Israel

A model of the heart and torso is used to generate epicardial and body surface potentials from the myocardial electrical sources. The electrical sources are produced by the activation processes of the left and right ventricles which are simulated by a 3-dimensional finite-elements model. The heart model allows the description of the orientation of the myocardial fibers and their distributed velocities and refractory periods. A Purkinje network is also included. Point sources are defined on the surface which separates the activated areas from the non-activated areas. A human torso model is used for the calculation of the body surface potentials. These potentials are presented as standard E.C.G., or as the more informative potential maps. The simulated maps have been used to aid the interpretation of clinically measured maps. Specifically, simulated activation patterns due to ischemia show an early, low amplitude peak in the maps during the early stages of the QR period. This phenomenon, which has not been found in normal maps, has been located in clinically measured maps. Thus, the simulated maps generated by the anisotropic model are useful in quantifying and extracting clinically important features from measured body surface potential maps. This represents a step towards the quantitative classification of the measured maps.

BE12-R.4

Computer Simulation of Human's Cardiac Activation Sequence, Yang Jihai and Shen Fenglin*, University of Science and Technology of China, Hefei, Anhui, The People's Republic of China

Based on anatomy data and bioelectric character of the human heart, simulation of activation sequence is accomplished on a microcomputer. The heart is composed of 5018 cell units (cuboid 3.12mm*2.26mm*2.22mm). Three different kinds of cells has been considered: cells of atrium, ventricle and conduction system. The conduction speeds are assumed to be 50 cm/s, 100cm/s and 150cm/s accordingly. The excitation start-points in ventricles are chosen at four sites, corresponding to Durrer's experimental observations. The simulation result is qualitatively similar to Durrer's. Program possesses enough flexibility for any necessary changing in the simulation. Some abnormal excitation processes are simulated.

BE12-R.5

Computer Model of an Inhomogeneous Human Torso, Sui Wenquan and Shen Feng-lin*, University of Science and Technology of China, Hefei, Anhui, People's Republic of China

Based on the atlas of sectional human torso anatomy, a three dimensional computer model of human torso including four cavities (LV, RV, LA, RA) of heart, two lobes of lung and body surface and a three dimensional myocardial model are both introduced in this paper. The torso model depicts the structures and appropriate proportion of the relative organs inside human body, especially of the heart, with more than 10,000 surface triangles. The myocardial model, with 4,632 elements including muscle of atria and ventricle will be used in the overall simulation study of human cardiac electrical activities. Algorithms for the model construction, offering the flexibility for any change of the parameters of the models are given in detail. Meanwhile the validity of the models for the purpose of simulation research of electrocardiogram is discussed. Other possible applications of the models are searched either.

BE12-R.6

An Inverse Electrocardiographic Solution by Using Boundary Element Method, You-shan Yang, Wei-xue Lu, Zhejiang University, Hangzhou, P.R. China

Based on the Laplace differential equation and the realistic torso geometric model, the Boundary Element Method (BEM) is programmed to compute the electrical active potentials of the human's heart during the QRS period from potentials measured on the human's body surface. The group of X-CT tomographies containing the whole heart was used to build torso geometric model which is related to BEM algorithm. The effect on the interface of the lung and the thoracic cavity is considered in the algorithm. The body surface potentials are collected by the apparatus called The Body Surface Potential Mapping System. This apparatus is consists of IBM-PC computer, sample & communication controller, multi-analog amplifier and electrode vest. The results support the possibility of using BEM algorithm and realistic torso model to determine the potentials of the heart from the body surface potentials.

BE12-R.7

Recording and Analysis of Ventricular Late Potentials on the Body Surface. Shao Qingyu*, Jiang Ping, Shao Janhua, Zhu Xinglei, Chen Kong.

Ventricular late potentials (LPs) were recorded from the body surface in 105 patients. 50% of those with myocardial infarction and aneurism showed LPs and 15-16% of patients with PVCs or angina showed LPs. Spectrum analysis showed there was a peak between 70 Hz and 140 Hz in frequency spectrum histogram of every patient with LPs. Two different bipolar precordial recordings were made (V4-V6, V4-V9). The ECG signals was amplified, 50Hz trapped and high-pass filtered, 70Hz low-frequency cutoff was chosen. The top of the R wave was used as a time reference. QRS template and QRS area algorithms were made to reject PVCs or false QRSs. Averaging of more than 150 beats LPs could be recorded. To eliminate ring effect bidirectional digital filtering was made. After data processing 12 parameters could be gotten for analysis.

BE12-S.1

The Application of the Kharhunen-Loeve Transform to Temporal Sequences of Spatial EEG Images, M. Lazar, Z. Koles*, Department of Applied Sciences in Medicine, University of Alberta, Edmonton Alberta, Canada, T6G 2G3

The Kharhunen-Loeve transform (KLT) is a useful technique in analyzing the underlying structure in a set of multivariate data. The transform, when applied to image sequences, yields a set of orthonormal basis images and a set of coefficients such that the mean squared error in reconstructing the image sequence with fewer than the optimal number of basis images is a minimum. From the coefficient sequence related to each basis image the normalized power represented by each basis image may be computed. The basis images once created may also be used to examine other image sequences by projecting the new data onto the basis functions and measuring the normalized power values.

The KLT has been applied to sequences of images representing the spatial activity of the EEG from healthy volunteer subjects, where a 31 electrode montage has been used to spatially sample the scalp voltage distribution with a temporal sampling rate of 120cps. Applying the KLT to up to 2400 images (20s of data) indicates that typically 5 (out of 31) basis images and the respective coefficients are required to represent over 90% of the variance in the original images with an average reconstruction correlation between the original and reconstructed images of over 0.85. Moreover, images from the same individual in the same cognitive state not used in creating the basis images could be projected onto the basis functions with similar results, indicating the indeed the basis images represent common scalp voltage distributions.

BE12-S.3

A Quantitative Analysis of the Amplitude Modulation in the Spindle Frequency Band of Sleep EEG in Elderly Subjects.

U. Barcaro, E. Bonanni, F. Denoth, L. Murri, C. Navona, A. Starita* and A. Stefanini, Pisa, Italy

The amplitude modulation of the 12.5-14.5 Hz band activity of sleep EEG was studied by the computation of three parameters: the modulation index (A), the root-mean-square frequency of the modulation (B) and the root-mean-square frequency of the first derivative of the modulation (C). An investigation carried out on 6 elderly subjects showed that: a) for 5 out of them, the mean values of each of the three parameters were able to discriminate between NREM and REM sleep; b) no significant shift was found between the elderly group and a control young group, for both the REM and NREM mean values of each of the parameters.

BE12-S.2

Spectral Analysis of EEG-A Hartley Approach, P.S. Ravindra* and Rajesh Prabhakaran, Regional Engineering College - Trichy, India.

Non-invasive techniques for the recording and analysis of electrical phenomena of the brain using ELECTROENCEPHALOGRAPH have gained large importance. The EEG waves recorded from the scalp vary in frequency and amplitude. Some of the most important inferences from these recordings may be drawn from their spectra. A manual inference is prone to biasing towards most prominent components and being oblivious of other components that may carry substantial information. Spectrum Analyzers using FFT have been developed.

A system that solves the same problem using HARTLEY TRANSFORM may be used to obtain the COMPRESSED SPECTRAL ARRAY of the spectra. The use of this transform decreases the analysis time drastically, compared to conventional spectrum analysers. This feature will expedite the analysis of EEG recordings where amount of data is very large. The mathematical basis to justify the use of this transform is given. A system which incorporates a FAST HARTLEY TRANSFORM PROCESSOR has been designed. It is a real time microprocessor based system.

BE12-S.4

Nonlinear Alpha Wave Response under the Feedback Control of Weak EM Fields, Zhong Jicun*, P.O. Box 422, Zhejiang University, Hangzhou, P.R. China

A general structure of an adaptive control system using MEFP is given. By this control, a synergetic system can evolve into a more highly ordered state. We apply the theory to the induction of high level Alpha waves of human EEG. To this end, a microprocessor based real-time feedback control system was built.

Fifty seven subjects were tested and 86% showed an obvious augment of their Alpha activities during feedback.

Three features of the Alpha wave response have been found: 1) EM feedback will be effective only when the subject is quiescent, relaxing and eye-closed, and the response can be easily inhibited by any arousal. 2) Only when the feedback signal is within a "window" of optimal parameters can the Alpha waves be mostly activated. 3) Unusual subjective feelings of relaxing were found in subjects with good response.

BE12-S.5

40 Hz (36-42 Hz) and Sensory Motor Rhythms (SMR) (11-15 Hz) as EEG State Variables, C.C. Turbes* and G.T. Schneider, Creighton University, Omaha, NE 68178.

There is evidence that certain brain rhythms may signal the occurrence of different brain states. Support for this hypothesis may be provided by evidence that processing of information is changed during different brain states. The prestimulus period preceding the auditory evoked potential (AER) is converted to a power spectral estimate. These power spectra are used to sort for the AER when certain power values for the (36-42 Hz) and the (11-15 Hz) frequencies are reached in the prestimulus period of the sensory motor cortex (11-15 Hz) and the amygdala (36-42 Hz). Attempts are made to measure the performance of the 40 Hz and SMR estimators. This relates to the spread of their probability density functions over a given data sampled. The measure of this spread is the variance of these estimators. These studies are made in the cerebral cortical and subcortical brain regions in cats. Cross correlation, coherence and phase spectral methods are used to examine the interaction of certain brain regions.

BE12-S.7

An Application of Event Related Brain Potentials (ERP) for Testing the Ability to Recognize Dot Patterns, H.Goto* and T.Adachi, Tokyo Metropolitan Police Hospital, Tokyo 102, and T.Utsunomiya, Science University of Tokyo, Noda 278,

ERPs were investigated during judgement of match-mismatch of two successive dot patterns. A given trial comprised, sequentially, a variable number (2 to 4) of random dot displays (RDD), a first 5-dot-pattern (5DP), a variable number (2 to 4) of RDDs, a second 5DP, then two RDDs. Each RDD or 5DP was 20 ms in duration. A RDD or 5DP was presented in a trial at a rate of one every one second. 144 trials were presented in random space and sequence. The 2nd 5DP was identical to, or mirror-image of, or neutral (neither identical nor mirror-image) to the 1st 5DP. 5 normal subjects were told in advance to press the pertinent switch as fast as possible after each trial to signify whether the 2nd 5DP was identical to, or mirror-image of, or neutral to the 1st 5DP. EEGs in parietal and temporal leads were averaged by a microprocessor. In examinations of evoked potentials to the 2nd 5DPs, P650 was observed. The peak latency of P650 to mirror-image was significantly larger than that of P650 to identical and neutral 5DP. These results suggest that it takes a longer time to recognize mirror-image than to judge identical and neutral patterns, and that ERPs can be useful for testing the ability to recognize dot patterns.

BE12-S.6

The State Analysing Method for EEG, Luo Jian*, Zheng Qingliang, Inst. of Elec. Eng., Conqing University, Chongqing, China, District People's Hospital of Shapingha, Congqing, China.

EEG signal directly reflect the varying process of the cerebral mental and physiological state, so the nonstationary character of EEG signal is closely relative to the varying process of the cerebral state. During a relatively stable cerebral state EEG signal displays on approximate stationary signal segment. While the varying of the cerebral state occur EEG signal becomes a nonstationary signal, and the nonstationary degree is closely relative to the varying degree of the cerebral state. By means of the analysis of the adaptive stationary segmentation and further processing in every stationary segment, we obtain a method which can display the varying process of cerebral state, called state analysing method for EEG signal can apply to clinic and neurophysiological research, or to thinking science and psychometry. For example while object's internal factor and external factor is specified, the varying process of his cerebral state will appear with regularity, by which we can distinguish abnormal from normal.

BE12-S.8

Criterion for Using Adaptive Filter to Improve the Signal to Noise Ratio of Averaged Evoked Response

Miriam Furst*, Department of Electronic Systems, Faculty of Engineering, Tel Aviv University, Tel Aviv, Israel

The amplitude of Brain Evoked Responses (BER) varies from tenths of a microvolt to tenth of microvolts and is embedded in the ongoing electroencephalogram (EEG). This response is usually obtained by averaging hundreds to thousands of repeated recordings following an identical stimulus. The average (ABER) is the best estimate for BER when the noise is random of a zero mean. If BER and the noise (EEG) have different spectrums then it is possible to reduce the signal to noise ratio of ABER. Several attempts were done to improve ABER by using a Wiener filter whose parameters were obtained from the averaged response. In many cases this process did not improve the signal to noise ratio. We suggest to apply an optimum adaptive linear time-invariant filter on ABER which yields OBER. The optimal filter impulse response $[h_{-m} \dots h_0 \dots h_m]^T$ is derived while assuming that ABER is the expected BER, and m is the filter's order. Let define the mean square errors of ABER and OBER as σ_a^2 and σ_o^2 respectively, it will be shown that if the noise is stationary and ergodic then $\sigma_o^2 = \sigma_a^2 \sum_{i=-m}^m h_i^2$. It is therefore clear that the signal to noise ratio of ABER can be improved by applying the suggested adaptive filter only if $\sum_{i=-m}^m h_i^2 < 1$.

BE12-S.9

REAL-TIME DETECTION OF EEG ARTIFACTS

C. Muñoz Gamboa* and E. Saldívar
Univ. Autónoma Metropolitana - Iztapalapa
09340 México D.F., MEXICO

A new algorithm for real-time detection of EEG artifacts is presented. The algorithm was developed through a new classification of EEG artifacts in three groups:

1. Frequency distinguishable artifacts, like muscular movements.
2. Artifacts due to the acquisition technique, such as ECG reception.
3. Artifacts having frequency components in the EEG band, and appearing in spatial patterns. In this group are: loose electrodes, false contacts, ocular movements, and blinking.

Artifacts belonging to the third group are the most interesting because they appear in most EEG recordings. The others are rejected by digital filtering or by means of a good acquisition technique.

The algorithm is based upon the processing of three parameters: amplitude and time thresholds, and the spatial patterns of the events. These parameters, obtained and processed in real time, are enough to detect every artifact occurrence from group three. Further processing, also in real time, permits the total recognition of this type of artifacts, with a reliability of 97.6%.

BE12-S.11

SOME PHYSIOLOGICAL CHANGES IN INDUCED MEDITATIVE STATE (a case study),
V. Lepicovska*, J. Mrkvicka, C. Dostalek,
H. Beran, Inst. of Physiol. Regul., C.S.
Acad. of Sci., Prague, Czechoslovakia,
S. Vishnudevananda, Phys. Lab., Sivananda
Yoga Centre, Val Morin, Canada.

Constituents of ancient methods of concentration (used a.o. in rituals) have been included with a desirable effects into modern medicine, especially in functional diseases, enabling thus the patients improve the quality of life without side-effects. In this case study a very marked inhibition of pain was reached at.

Measurements of EEG, ECG, blood pressure and respiration was taken in the course of the shivaistic ceremony called Kaavadi, in which 108 spears were inserted into the tongue, cheeks and chest. The EEG deactivation appeared to be on the background of autonomic activation. Maximal increase of spectral power (300 percent) was measured in the alpha range. Maximal changes in theta and delta range did not reach post hyperventilation increase.

BE12-S.10

A Small Size System of Automatic Detection for Safety Driving Based on Electroencephalogram, F. Yano, H. Kodama, S. P. Ninomija*, Aoyama Gakuin University, Tokyo, K. Idogawa, Seitoku Gakuen College for Women, Chiba, K. Sato, Bioinformation Laboratory, Tokyo, Japan

We developed a practical system to prevent vehicle accidents resulting from driver's dosing. On limited access highways in long distance driving it is difficult for the driver to maintain a watchful driving condition because of the state of monotony resulting from receiving less stimuli. It is recognized that a burst of slow alpha rhythm occurs on the EEG when cerebrum activity goes down because of less tension or the tendency to drowsiness. For safety driving, it is important to detect the drowsy condition. EEG data were collected from driving experiments on the highway. The detection of slow alpha rhythm was analyzed by statistical method as follows:

We compute regression line and moving variance by moving least square method. We defined slow alpha rhythm which satisfied some conditions about slope and variance. This method possesses stability respect artifact, as it were, ECG, EMG, alternating current waves and eye blinking. By this method, we developed online real-time system by 16 bits personal computer.

As the result, accurate detection of slow alpha rhythm on an on-line real-time method has become possible.

BE12-S.12

Estimation Algorithm for Spread Forms of Spindle Waves in Multi-channel EEG,
Yoshikazu Ueda*, Naohiro Ishii,
Nagoya Institute of Technology, Showa-ku,
Nagoya 466, Japan.

Spindle waves are the characteristic signals in electroencephalogram, but have been unknown in their spread form. We present an algorithm for estimating the spread form of spindle waves in multi-channel data. Our algorithm is able to calculate within two phasic dominants and the spread direction of spindles on a head. In our algorithm, the remarkable frequency components are extracted from spindles. Second, the frequency-wavenumber spectral of each component is analyzed in partial field. The last, the spread form of the spindle wave is estimated by studying these partial wavenumbers geometrically and synthetically in whole field. As applying our method to EEG data, we got two results. One is that the phasic dominant of spindle with a low frequency component exists in the central field of the head and with a high component in the parietal one. The other is that the most of spindles spread from rear part to frontal one on the head.

BE12-T.1

ECGxpert, an expert system for EKG analysis, S. Jenichen Gieseler* and N. Wiederhecker, Programa de Eng. Biomédica/COPPE, CP: 68510, Rio de Janeiro, Brasil, CEP 21945

The EKG is a biological signal with a host of information and therefore of complex analysis. ECGxpert is a expert system designed to aid physicians, with few experience in EKG analysis, and students in training programs. Instead of acquiring and interpreting the EKG, the system request from physician those parameters which are used in routine analysis by cardiologists. The system, implemented in PROLOG, provides a menu-driven user interface and an explanation system, allowing to add certainty measures to answers, simulating an inexact reasoning. The knowledge base contains the expert's knowledge about EKG interpretation in form of production rules. As final result the system generates a complete report about analysis including advices on future procedures.

BE12-T.3

An Expert System of Medical Diagnosis of Icteric Patients, J.C. Nievola, W.C. de Lima*, C.I. Zanchin & W. Dantas, Universidade Federal de Santa Catarina, P.O. Box 476, 88.049 Florianópolis, SC, Brazil, Telex 482 240 UFSC BR

The scope of this work is to implement an expert system to aid the gastroenterology experts in the diagnosis of icteric patients. The system is composed of a knowledge base and an inference engine. The knowledge base is based on the major points in which the expert develops his work. Then, this knowledge is used for an inference engine that wants to establish the possibility to each one of the diseases considered. This knowledge base has 74 rules, occupying 17,3 Kbytes. The inference engine, with 103 Kbytes, is implemented in Turbo Prolog's language, in a PC compatible microcomputer. It has two phases: a preliminary diagnostic, and a final response. The system has an initial menu, where the user chooses one of the following aspects: General Information, Load Knowledge Base, Edit Knowledge Base, Consult and Exit. In the consult mode, the user answers questions about the patient history, his physical conditions and laboratorial examinations. After this, a ranking of possible diseases is obtained, based on the idea of fuzzy set theory. The result of the consult is analysed by the expert physician before treatment is initiated.

BE12-T.2

VERTIGO: an expert system for the classification of dizziness A. Buizza, G. Magenes*, M. Manfrin, E. Mira, R. Schmid, P. Zanocco - University of Pavia, Italy

A consultation model for the differential classification of dizziness has been developed by means of the shell EXPERT (Weiss and Kulikowski, 1979). More than 30 types of vestibular disorders characterized by the presence of dizziness as the major symptom are considered. The knowledge base has been synthesized in about 350 production rules. Data have been limited to patient history as the assessment of the diagnostic accuracy that can be reached by careful evaluation of case history is one of the goals of the research.

VERTIGO is able to collect patient data by means of a flexible questionnaire reproducing the strategy followed by a skillfull clinician in history taking.

The diagnostic conclusions are proposed with a certainty factor representing their plausibility. The reasoning followed by the system to reach a certain diagnostic conclusion can be explained to the user in a pseudo-natural language which illustrates the production rules activated for that conclusion. Two versions of Vertigo have been realized, one running on a VAX computer, the other on IBM PC. The model is being validated by human experts belonging to the international community of ORL clinicians, who were not involved in building VERTIGO.

BE12-T.4

Decision support system for treatment selection in oncology. S. Hyödynmaa*, P. Koları, K. Näriäinen, A. Ojala, J. Rantanen and N. Saranummi, Technical Research Centre of Finland, Medical Engineering Laboratory, Box 316, SF-33101 Tampere, FINLAND

Decision support can be utilized at several stages in oncology. We are developing a system for three stages: therapy decision making, design of treatment protocols and analysis of therapy results. A prototype is functioning for the treatment decision making in inoperable lung cancer. The object oriented system has been implemented on a Xerox 1186 workstation with Interlisp-D and LOOPS. The input information required covers patient ID, diagnosis, symptoms, examination and test results, tumor data and staging. During the reasoning the system checks the correctness of the diagnosis, checks if there are indications for immediate treatment and checks if the intention of therapy proposed by the user is relevant. The system has been tested with cases of lung cancer patients and a panel of oncology experts has evaluated the principles of using the system and the human computer interface. The final aim of the work is a decision support system for oncology. The next step will be the building of an oncological clinical register for the system. The integration of the system components as an oncological information network is also essential.

BE12-T.5

A Syntactic Analysis of the Auditory Brain Stem Responses, Hironori Koyama*, Tokyo Denki University, 2-2, Kandanishiki, Chiyoda, Tokyo, Japan 101

A syntactic algorithm has been developed to automatically detect and identify the wave components of the auditory brain stem response (ABR). The algorithm for the wave detection is described using an attribute grammar.

A typical ABR pattern is composed of seven sub-patterns, namely Wave I, Wave II, ... and Wave VII. After normalization and piecewise linear approximation, an ABR is represented in the form of a sequence of triplets. Each triplet consists of a slope segment symbol and two attribute values, the amplitude and latency of the slope. Then a triplet sequence is parsed according to the attribute grammar devised for the wave detection. For the detected waves, a heuristic algorithm based upon a priori knowledge on latencies is applied to assign each wave to one of the seven candidates.

A preliminary test has shown that 90 to 95% of the waves are detected and identified successfully by the algorithms, including the case that some of the wave components are missing in ABR patterns.

BE12-T.6

Disease Classification Model Based on The Hierarchical Evaluation of a Symptom *T. SEKIYA, A. WATANABE, S. KATO, M. ARUGA and M. KIKUTI
3-2 Namiki, Tokorozawa, Saitama 359 JAPAN

It is important for the decision making in medical diagnosis and treatment to classify the diseases. It is not sufficiently carried out by using merely the statistical method. We reviewed what is done by medical doctors in their decision making to find a bearing striking resemblance to their mental model. We propose a new model which has the flexible algorithm for compensating missing symptoms, taking into account the degree of contribution of each symptom to diagnosis.

This model adopts the time series representation of every symptom such as threshold element, integral element, differential element and so on. The concept of the symptom weight evaluations contributes to the compensation of the missing symptom and provides the flexible algorithm for the classification of medical data. Furthermore, this model is able to utilize to deeper reasoning, because it is corresponding in all of a physics model.

BE12-U.1

FIELD THEORY OF ELECTROGLOTTOGRAPHY AND MEASUREMENT FOR PHONATORY BIOMECHANICS
Wan Mingxi* Cheng Jinzhi
Dept of Information and Control Engineering
Xi'an Jiaotong University, Xi'an,
The People's Republic of China

Electroglottography (EGG) is more convenient to be a monitoring method of laryngeal function than high-speed films, photoglottography, ultrasonic glottography and glottography by inverse filtering acoustic or laryngeal air flow signal, due to non-invasion and low cost. However, what does the EGG waveform tell us about phonation is ambiguous. This study was designed to provide the interpretation of the EGG waveform based on electrical field theory and vocal folds activity. This paper also introduces a two channel EGG system with a multiple electrodes array, which makes simultaneous investigation of vertical and horizontal vibration of vocal folds possible, and approaches the origin and sensitivity of EGG signal.

BE12-U.2

A New Method for the Vocal Cord Disease Diagnosis, R.C. Chen, Q. Ling, Y. Z. Jing

The traditional method to diagnose the vocal cords disease of a speaker is through the observation with the laryngoscope or making mediate diagnosis according to the spectrogram of the speaker. But one problem is that it is not easy to observe the vocal cords with the laryngoscope as well as to record the results in a simple and objective way. Another is that the spectrogram is a mediate information about the vocal cords disease and not of much value to diagnosis. In this paper the method of linear prediction analysis on the short-time interval for glottal inverse filtering from the acoustic speech waveform is discussed and a new way approaching to the vocal cords disease diagnosis is presented.

BE12-U.3

A Speech Onset Analyzing System,
B.F. Smith,* R.M. Kroll
Clarke Institute of Psychiatry,
250 College St. Toronto, Ont.,
Canada M5T 1R3

Carefull study indicates that, for the most part, disfluencies in the speech of stutterers are caused by the application of abrupt, excessive tensioning of the vocal folds during the initiation of phonation.

The device described in this paper, a speech onset analyzer (SOA), monitors the harshness of speech onset and provides instantaneous positive feedback when subjects achieve their targets. A built in pair of counters record the number of attempts and the number of correct responses so the unit may be used in the absence of a therapist. The counts cannot be altered by the subject. Voice onsets may be monitored for single syllabic utterances or for continuous speech.

The unit is battery operated, small and light weight. The use of filters gives equal response to both male and female voices.

The SOA eliminates human error in the extremely difficult task of judging the adequacy of responses at several levels because it is reliably calibrated to uniform standards.

BE12-U.4

DEVELOPMENT AND APPLICATION OF PROGRAMMABLE AUDITORY STIMULATOR
Jia Rui Lin* Lie Yi Fang Han Shan Zhu
Bioengineering Department
Huazhong University of Science and Technology
Wuhan, China

The paper introduces a programmable auditory stimulator for human brain stem Auditory Evoked Response (AERP) tests. It can generate 3 modes, about more than 60 kinds of waveform, according to require, they can be transmitted to the ears by earphones separately.

The system was consisted of a small system by Intel 8085A microprocessor, where the data of various waveform are stored 2 chips of EPROM of system. The mode, frequency or period of the signals can be changed with the states of the switch in the front of panel are recognized by the program. A tone burst is produced by a voltage control amplifier (VCA), the envelopes are supplied by the programmable signals. And white noise generator was obtained by a cheap electronic circuit. In addition, a slide switch of the stimulus polarity selection can determine signals of the positive, negative or alternate polarity.

The programmable auditory stimulator has been applied for the research of the human brain stem AERP and has obtained satisfying results. It is also suitable for many other applications.

BE12-U.5

The Frequency Domain Feature Analysis of Brainstem Auditory Evoked Potential,
Ma Xiao-Bo, Gao Shang-Kai, Zhou Li-Gao,
Dept. of E. E., Tsinghua University,
Beijing, China, Pei Hong-En, Jiang Wei,
General Navy Hospital, Beijing, China.

Brainstem Auditory Evoked Potential (BAEP) which has important significance in objective audiometry and diagnosis of acoustic neurinoma has been widely used in clinic. The parameters of BAEP, now mainly the time domain parameters, sometimes are not sufficient to make a diagnosis. And usually wave IV and V in time domain are not easy to be separated. Therefore we hope to extract new parameters of BAEP for clinical use.

This paper developed the features in frequency domain of the BAEP of guinea pigs which underwent the simulated nerve tumor operation by using autoregressive model and spectra estimation, and some results were applied to BAEP diagnosis of human patients. Experiments indicated that the peaks of spectra of BAEP of guinea pigs having lesions will move toward lower frequency interval than that of normal guinea pigs. The sum of phase angle differences of bilateral poles θ and the difference of normalized prediction errors of bilateral AR models are presented as new parameters of BAEP for clinical diagnosis.

BE12-U.6

Coherence Spectral Studies of Averaged Brain Evoked Potentials During the Action of Amphetamine,
C.C. Turbes* and G.T. Schneider, Creighton
University, Omaha, Nebraska 68178.

These studies are made on cats and are concerned with power and coherence estimates of auditory evoked potentials at cerebral, cortical and subcortical regions. Certain chemical agents are used to alter the background EEG activity and auditory evoked potentials. In these studies the d and l isomers of amphetamine are used. The analog data is collected and stored on FM tape for computer processing. The data is processed using power, coherence, partial coherence and phase spectral analyses. Comparisons are made of the pre, during, and post amphetamine data of both EEG and auditory evoked potential activity. There are changes in the autospectral, coherence, and partial coherence spectra that relate to the action of amphetamine. Special consideration is given to these data estimates and then interpreted as it relates to the interaction of brain regions during the various drug induced patterns of behavior.

BE12-U.7

QUANTITATIVE ANALYSIS FOR EXPERIMENTALLY INDUCED PERILYMPHATIC FISTULA BY PRESSURE MONITORING AND CONTROLLING SYSTEM, T.HORIUCHI*, T.DOHI, T.MASUZAWA, T.FUJIKI, I.SAKUMA, T.FUTAKI, M.HARA and Y.NOMURA,
The Univ.of Tokyo, 7-3 Hongo, Tokyo, Japan

The cause of perilymphatic fistula, a subgroup of sudden deafness, has not been clearly understood. To study its etiology quantitatively, the inner ear pressure monitoring system with a computer controlled pressurizing device and three types of low pressure monitoring sensors was constructed and utilized in ex vivo experiments using white guinea pigs. Hypothesizing that cerebrospinal pressure increases cause a rupture of the round window membrane, direct or indirect pressurization to cerebrospinal region and simultaneous measurement of inner ear and cerebrospinal pressure were carried out.

The ruptures of the round window membranes were seen in the experiments with direct saline infusion into the cochlea when the increment of inner ear pressure were above 370 mmH₂O. There was no sign of the ruptures when squeezing abdomen was employed as an indirect pressurization although cerebrospinal pressure increased.

It is conclusive that this system is feasible to analyze pressure changes in the inner ear and cerebrospinal region simultaneously and useful to study on the etiology of perilymphatic fistula.

BE12-V.2

3-dimensional Superimposed Description of Thallium-201 Myocardial Scintigram and Coronary Arteriogram, T.Akatsuka*, T.Takeda#, S.Natsubori, T.Nakajima, Y.Tamura, and M.Akisada#, Yamagata University, Yonezawa 992 and #University of Tsukuba, Japan

To evaluate ischemic heart disease(IHD), thallium-201 myocardial scintigram(TMS) and coronary arteriogram(CAG) are the most important images for the diagnosis. By using the single photon emission CT, 3-D reconstruction of left ventricle can be performed, and CAG can describe the structures of coronary artery clearly. To understand the details of the regional myocardial ischemia and stenotic coronary artery, it must be very useful to display the 3-dimensional of TMS and CAG. At first, the experiment was performed on the arterial model and actual TMS, now actual TMS and CAG are in use. Two images are adjusted as the left descending coronary artery is lying 15 degree right from the center of the anterior wall on TMS. The relation between the degree and extension of myocardial ischemia and the degree and position of stenotic artery might be well assessed by this 3-D superimposed description.

BE12-V.1

Quantative Analysis of Influence of Various Factors on the Detection of Details in Roentgenological Image, A.M.Gurvich, Moscow Research Institute for Roentgenology a. Radiology, 117837, Moscow, GSP-7, Profsoyuznaja, 86

Calculation of details detection on the image can play an important role in turning roentgenology into quantitative science. When calculating it's necessary to take into consideration the fact that the threshold contrast is determined by the cumulative influence of the two main noise components, one of which depends on the instrumental part of the image forming system and the other - on the eye. The possibility of the calculation can be illustrated by means of: 1) determination of the permissible limits in increase of radiation sensitivity of the image transformers; 2) comparative analysis of various methods and technical means of radiodiagnostic investigation; 3) evaluation of the influence of morphological noise; 4) choice of physico-technical conditions and image quality control methods. The sign of optimal alignment of informativity and dose is the balance of all the main components of noise

BE12-V.3

Computed Color Imaging of Gastric Mucosal Hemodynamics. S.kawano, S.Tsuji, N.Sato, T.Kamada. Dept. of Med., Osaka Univ. Med. Sch., Osaka 553, Japan. The microcirculatory disturbance was emphasized to play an important role in the gastric ulceration. In this study, the computer-assisted imaging of gastric mucosal hemodynamics was performed. The reflectance spectrophotometry system was applied to the human gastric mucosa under endoscopy as reported previously(N.Sato, Gastroenterol. 1979). From the data at 20 points in the stomach, the computer-assisted color image of mucosal blood distribution was made. Moreover, to obtain the mucosal blood distribution in real time, the electronic endoscope was directly coupled with the image analyzer and microcomputer. The logarithmic ratio ($\log V_r/V_g$) of the videosignal in R and G images was calculated with image analyzer and computer. The ratio at a region of interest was proven to have a good correlation with Hb concentration of mucosa measured by reflectance spectrophotometry. With the methods, the gastric mucosal hemodynamic changes were investigated in patients with gastric ulcers. By the imaging of gastric mucosal hemodynamic, it was possible to predict the ulcer formation and healing.

BE12-V.4

AUTOMATIC DETECTION OF CORONARY ARTERY WALL CONTOURS IN PATHOLOGIC SLIDES.

L Moura and R Kitney.*

Dept of Electrical Engineering,
Imperial College, London SW7 2BT, UK.

The paper describes an image processing technique for the detection and labelling of arterial wall contours in images obtained from cross-sectional slices. A gradient operator is applied to the image and generates points of interest at likely edges. These points are then used as starting points by a contour follower algorithm leading to the formation of one-pixel-wide lines, called segments. Heuristic search is used to locate closed sets of segments which minimize a cost function based on the ratio between a contour's square perimeter and the enclosed area. This function is minimized by a circle so that the algorithm tends to find circle-like structures. Constraints imposed on segment connection avert the formation of inconsistent shapes and also speed up programme execution. Further processing includes closed curve filtering using least square fitting; and the labelling of contours according to their position in the image and to the gradient direction (inward/outward) along the contours.

Results have shown that the method's strength lies in its ability to correctly find the wall contours even when major gaps are present, provided that some long segments are formed. The method is suitable for locating and labelling round-shaped structures which frequently occur in Biology, such as blood vessel cross-sections and cell outlines.

BE12-V.6

Data Compression for Medical PACS, V.A. Pollak*, D. Meyer-Ebrecht, W. Krybus, Univ. of Saskatchewan*, Saskatoon, Sask, Canada; Technical Univ. of Aachen, Aachen, Germany.

PACS is an acronym standing for "Picture Archiving and Communication Systems." Imaging devices represent a large and increasing proportion of modern medical technology. The pictures acquired by these devices are an essential part of the medical history of the patient and a large proportion of them needs to be preserved, frequently together with verbal comments for future consultation. Traditionally the carrier medium for pictorial information was photographic film. Storage of film especially in large quantities requires space and retrieval is slow and error prone. This is where PACS comes into play. There the pictorial information is stored electronically, preferably in digital form. For retrieval the stored information is accessed electronically and transmitted to the place where it is needed by standard communication facilities. In the majority of cases the distances involved are relatively short, but even very large distances can easily be bridged. The number of pictures annually acquired in a medium size hospital can go into the tens of thousands. Billions of bytes are necessary to store and to transmit this volume of data. Data compression seems to be the most effective way to handle this problem. The features of a data compression system specifically developed for medical images are described in brief.

BE12-V.5

A Digital Processing Method to Obtain Separated Bone and Soft Tissue Pictures by Using of Dual Energy X-ray Projections

Boge Wu , Dazong Jiang *
Institute of Biomedical Engineering
Xi'an Jiaotong University
Xi'an , China

The difference of X-ray attenuation coefficient between bone and soft tissue depends on the X-ray energy being discussed, based on this relationship our method called Gray Level Piece-wise Adjustment Step-wise Subtraction was developed. Perform a specific digital operation on gray level of each pixel of a subject's two X-ray projection pictures of different energy, so that for every corresponding pixel pair, in the total gray level, component contributed by soft tissue can be adjusted to the same, then by subtraction of the two pictures, all soft tissue information is removed and a mask picture that contains the information of bone contents distribution only is obtained. Subtract this mask once by once from the original low energy picture which contains the most soft tissue information until bone image disappeared and the remainder become a soft tissue only picture. Using X-ray films / TV camera, experiment according to this method was completed on a personal computer equipped with special image processing hardware. In X-ray projection we use copper and tin filter to emphasize high and low energy contents respectively. Some successful pictures with soft tissue only for bone-soft tissue phantoms have been obtained through above operations. We hope this method can be implemented in a X-ray, I.I., TV system to construct a new low cost processing system and it will be also useful for angiography with Iodine contrast medium .

BE12-V.7

A Method for Continuous Measurement of Width and Area in Medical Images, Wang ZhongRui*, Dept. of Scientific Instrumentation, Zhejiang University, Hangzhou, China.

A method for continuous measurement of vessels diameter from TV image is presented. It is based on PDM(Pulse-Duration Modulation) and DPDM(Demodulation of PDM) principles. An auto-tracking window is formed on TV screen to cover the segment of vessel to be measured. The window signal is a series of pulses with the duration proportional to the width of the vessel and the period equal to the interval of a line sweeping. We use a low-pass filter to demodulate it. The output width waveform is transferred to a microcomputer through A/D converter frame by frame. Then the width waveform of a vessel in a frame of image or the variant width at a site we interested in may be sent to a chart recorder by D/A conversion. It is demonstrated that the method may be applied to measure the width and area of other medical images of any shape a lightly wobbling.

BE12-W.1

Signal Detecting Technique of Hemodynamics, D.X. Zhang, Nanchang Hemodynamics Institute, Nanchang, Jiangxi, China

To use an information processing system with pressure and volume wave transducers in diagnosis is the technique, a biomedical engineering and combination of traditional chinese & western medicine, Based on linear systematic theory and physio-anatomic state, blood circulation system was divided into several units on each of which, we established relevant mathematic expression which reproduced an in vivo waveform very closely ($r=0.99$). Thus the hemodynamics parameter equations in contrast with invasive technique were derived, the detection of flow volume, pressure, modulus, resistance etc. of circulation system resulting in $r=0.88-0.975$. Widely using the technique in the clinic field, we studied traditional chinese medicine and hemodynamics diagnosis, guard of emergency and predicts of many diseases. For example, when diagnosing coronary disease by the technique and selective coronary arteriography, we got the diagnostic coincidence ratio as 93%.

BE12-W.3

Adaptive Analysis of Harmonic Oscillation for Biological Signals, M.Mita, T.Onoda and M.Hirano, Iwate Medical University, O20 Morioka, Japan.

A mathematical method of discrete signal processing of harmonic oscillation in a finite window has been found. The signal is sampled and analyzed in the finite window which is regarded as the basic period of an oscillation. Each instantaneous value of harmonics is successively given by fixed linear transformation of the arithmetic means of the data from frequency sampling. By using this method, fundamental frequency of an oscillation, its harmonics and their mutual phase relation can be estimated precisely. This method can estimate the most adaptive basic period T of the signal whereafter time window is chosen accordingly. The frequency resolution is determined by the adaptive fundamental frequency and by the highest frequency component involved in the original signal. This method supplies an algorithm for designing electronic circuits and computing programs.

BE12-W.2

Fourier Analysis of Averaged Signals
A. Fadda, M. Neroni, Istituto Superiore di Sanita', Via Regina Elena 299 00161 Roma, Italy.

When harmonic analysis of averaged signals is required the following considerations may be useful. The averaging process can be seen, in the frequency domain, as a comb filter with major lobes at frequencies equals to k/T , where k is an integer and T is the trigger period. As the number of averaged records increases the main lobe becomes narrower and the side lobes become more little and numerous. For large number of records, the averaged signal waveform is substantially reduced to the periodic component. So it is correct and useful to make a Fourier Transform of the signal using a simple rectangular window and an analysis duration as short as the trigger period with no loss in resolution or leakage problems. We applied this technique in the field of pattern electroretinography obtaining a fast calculation of the 2nd harmonic of averaged signals.

BE12-W.4

A Modified Adaptive Filter for Biological Signals. I.B. Stamboliev, M.P. Mintchev, I.B. Ratchev, Higher Institute of Mechanical & Electrical Engineering, Sofia-1156, Bulgaria.

The low frequency biological signals processing to obtain an important diagnostic information is a main problem of electro-gastrography. A filtering of the electro-gastrographic (EGG) signal must be done without affection on its frequency range, phase and amplitude. It is also necessary a strong suppression of the noise components included or nonincluded in the signal frequency range. An optimization of the security and flexibility of well known modified adaptive filters is made and the device is completely computerized. Results of simulated human EGG-signal processing are given. The capabilities of digital modified adaptive filters using Fast Fourier Transform are described. The parameters of the filter provide the electrical activity of the human stomach processing but changing them the device application area may be extended.

BE12-W.5

Data Compression for ECG and a High Speed Circuit of DCT, Sheng-Mei Shen and Wei-Xin Xie, Dept. of Electrical Engineering, Northwest Telecommunications Engineering Institute, Xian, PRC

For the special wave of Electrocardiogram, this paper discusses the data compression performance of three kinds of orthogonal transformations (DFT, DCT and DWT), shows that DCT has the best performance among them. We found some properties of ECG data compression. Based on the properties, we propose a segmental processing method and an adaptive method for ECG data compression. Using our methods, the compression performance can be improved and distortion reduced. We also present a real-time 8-point DCT using the continuous valued logic hardware which are developed recently in China. The DCT is with a high speed satisfying the medicine applications.

BE12-W.7

Spectral Analysis of Vertical Acceleration of the Body during Jumping, S.C. Su*, K. Tsuchiya, T. Tamura, T. Toyoshima and T. Togawa, Sch. of Sci. & Eng., Waseda Univ., and Tokyo Med. & Dent Univ.

The vertical acceleration was analyzed by Fourier transform and power spectrum during jumping was investigated.

Vertical accelerations on the back and the head were measured simultaneously with strain-gauge accelerometers. One accelerometer was placed at the back by elastic belt and the other was firmly hold by teeth. Seven male subjects were performed different jumping cycles (20 to 120 times/min by every 20 times). The wave forms were analyzed with Fourier analyzer.

The results showed the frequency distributions of the back and the head were similar but the magnitude of power spectra at the back was 4 to 6 dB greater than that of the head for all subjects and cycles. In the jumping cycle of 100 to 120, the significant harmonics of the fundamental frequency which corresponded to jumping cycle could be seen up to 25 Hz, and the fundamental frequency revealed the largest magnitude. However, in jumping cycle below 80, the harmonics could be seen only 10 Hz, and the second harmonics revealed the largest magnitude. The difference caused by the difference of jumping modes, i.e., one is intermittent, the other is continuous. Frequency around 12 to 15 Hz revealed the natural frequency of the body.

BE12-W.6

Power-Spectrum Analysis of REG with Prony Method, Liou Xiaoxiang, Zhou Shouchang, and Chu Mingjie, Theoretical Electrical Research Institute, Chongqing University, Sichuan, PRC

Rheoencephalograph (REG) has been widely applied to clinical diagnosis in our country. But up to now, most of the medical units still employ the backward manual method to analyze REG by viewing and measuring with ruler. Since there are many kinds of waves in time domain, there are many kinds of distinguishing methods which are not convenient in clinical diagnosis. So this paper adopts power-spectrum analysis to overcome wave differences that, the ages, sexes, and measurement etc. must result in error of REG of patients which may make some pathology characteristics disappear. Since REG is a kind of the lower frequency signal and FFT has random undulate in 0-12Hz, it is not suitable here. This paper probes a new time-domain-identification method--Prony method and try to use Marple and Covar algorithm in estimation of the order and determination of the parameters. After deriving time-model of REG, it will be transformed with Fourier Transform. The experiments have showed that the new method is significant, and may worth to be further investigated.

BE12-W.8

Accurate Estimation of Parameters of Multiple Damped Sinusoids in Noise & Their Application to The Analysis of Biomedical Signal. TANG YU* ZHEJIANG UNIVERSITY HANGZHOU PRC(CHINA)

We improve the method, which Kumaresan and Tufts (KT) presented, for estimating the damping factor and frequency of multiple exponentially damped sinusoids in additive noise. We use backward predictor to separate the signal zeros from other zeros and compute the backward estimated value of parameters, then use forward predictor to compute the forward estimated value of parameters. At last we use the mean of backward and forward estimated values as the estimate of parameters. This method was demonstrated to have a very good performance by numerical simulation, in comparison to original KT method and Prony method. The estimate of damping factor and frequency is unbiased. The variance of the estimates approaches the Cramer-Rao bounds. We give some examples (VEP & PEG) to demonstrate their application to the analysis of biomedical signal.

BE12-X.1

Accuracy enhancement in stereometric systems based on 1-D optoelectronic transducers.

(°) A. Cappozzo, F. Gazzani, V. Macellari*. Istituto Superiore di Sanità - (°) Università "La Sapienza". Roma, Italy.

The accuracy of the optoelectronic system COSTEL and of the associated stereometric model was assessed. The hardware is based on three 1-D cameras composed of linear image sensors (2048 elements CCDs) and toroidal lenses, and the calibration procedure is totally automatic. The laboratory physical dimensions imposed a small distance among the cameras and therefore small angles (about 23 degrees) between optical axes. A small (1.2 x 0.8 x 0.8 m) and light, easy to manage, calibration object was used, which covered a small portion of the measurement field. These constraints usually entail large errors in the reconstruction of the 3D coordinates of markers. The results we obtained were the following. The s.d. of the error, for markers farther than 1 m from the center of the measurement field, was lower than 3 mm along the axis pointing the cameras, and lower than 1.5 mm along the other axes. This accuracy is to be attributed to an especially devised stereometric model.

BE12-X.3

The summary of Double J-loop Elastic Silicone Posterior Chamber Intraocular lens Implantation. Zhou Kai-Yi* 48 Ying Men Kou Street, Chengdu, Sichuan, China. Shu-Guang Biomedical Engineering Research Institute. It is ten years, since we made the first anterior chamber intraocular lens by using GNY 515 silicone material and implanted it. In Sep, 1981 we continued to design elastic silicone posterior chamber intraocular lens (ESPCIOL). After we tested on animals, we got the suitable implantation method and instruments. In Aug. 1982, the first ESPCIOL was implanted into human eye and its result was extremely successful. In more than five years, we have implanted 100 ESPCIOL among 96 patients. The results are pretty good. 20-30 days after the operation, the mean naked visual acuity of 100 eyes was 0.68 ± 0.32 . Follow-up 5.5 years - 0.5 year (mean 2.5 years), the mean follow-up visual acuity was 0.89 ± 0.23 . For past 10 years we have operated more than 200 eyes (include ACIOL, Iris-Plane IOL), which confirm ESPCIOL being benefits of extremely biocompatibility, softness (reduced in situ trauma) and top security. The main complications caused by implanted ESPCIOL are: the thickening of posterior capsule (23%) and forming posterior synechia (25%, especially for the 2nd-stage implantation). All these problems can be solved easily.

BE12-X.2

Stereotaxic System for Diagnostic and Therapeutic Procedures, T. Ribbe*, M. Bergström, J. Boéthius and T. Greitz. Dept. of Medical Engineering, Karolinska Institutet, S-10401 Stockholm, Sweden.

A head fixation system has been developed enabling exact transfer of positions between neuroradiological and therapeutic procedures. The key item of the system is a base plate that can be rigidly attached to the patient's head, either by a plastic mould helmet or by screws fastened to the calvarium. The base plate may easily and accurately be attached to various diagnostic and therapeutic units. Coordinates of target points (X,Y,Z) in these units are directly related to the base plate. The system has been used for diagnostic procedures such as plain skull radiography, computer tomography, cerebral angiography, positron emission tomography, magnetic resonance tomography and gamma camera examinations as well as for therapeutic procedures such as stereotaxic biopsy, stereotaxic open surgery and radiation treatment. For surgery a new instrument has been developed giving the surgeon opportunities to be able to reach the whole brain (no dead angels) and maintain sterility.

BE12-X.4

Relationship of Intracranial and Anterior Fontanelle Pressure in an Invitro Model, Leon Bunegin*, Maurice S. Albin, University of Texas Health Science Center, San Antonio, Texas 78284

An invitro model of the anterior fontanelle (AF) was developed based on anatomical measurements taken from 17 babies ranging in age from 1 to 42 days. Anterior fontanelle pressure (AFP) and intracranial pressure (ICP) appear to correlate closely when (a) the transducer base plate has sufficient cross-sectional diameter so that it can rest on the scalp overlying the bone adjacent to the fontanelle margin, (b) application pressure on the sensing device is sufficient to keep the transducer base plate in contact with the scalp overlying the bone adjacent to the AF margin, (c) a transducer attachment technique be used that minimizes drift due to adhesive slippage and material relaxation. (d) transducer sensitivity to patient motion was minimal, (e) a means for assessing transducer drift in situ is present.

BE12-X.5

Relationship of Intracranial Pressure and Anterior Fontanelle Membrane Displacement in an In Vitro Model, Leon Bunegin*, Maurice S. Albin, University of Texas Health Science Center, San Antonio, Texas 78284

An invitro model of the anterior fontanelle (AF) was developed based on anatomical measurements taken from 17 babies ranging in age from 1 to 42 days. After repeated pressurization of the model cranium, it was noted that (a) positive simulated intracranial pressure (ICP) always produced an AF bulge; (b) negative simulated ICP always produced a AF depression; (c) zero simulated ICP resulted in the AF membrane lying flat, parallel to the plane described by the edges of the cranial bones that form the AF; (d) the extent of the AF membrane displacement is not linearly proportional to the simulated ICP; (e) the bony area around and adjacent to the AF membrane seems to remain in a stable orientation over a range of simulated ICPs.

BE12-X.7

Theoretical Investigation of Magnetic Field Cautery, Nabil M. Abdul-Kadir* and Manar A. Ezzadeen, Electrical Engineering Department, College of Engineering, Mosul University, Mosul, Iraq.

Magnetic field cautery can be done by inserting a small solid metallic cylinder inside the body to reach and touch the damaged area. Magnetic field can be applied from outside to cause the temperature of the cylinder to increase to the required temperature for cauterization.

This paper presents a mathematical analysis of magnetic field diffusion and eddy current inside a cylindrical metals and the calculation of rise of temperature in these metals due to eddy current loss.

These calculations have been made with the aid of computer for two cylinder positions with respect to the applied field. The first case consists of applying the field in parallel to the axis of the cylinder (axial field), while the second case is by applying the field perpendicularly to the axis of the cylinder (radial field). These two programs compute the increase of the temperature at the surface of the cylinder with time for different metals and frequencies. Low frequency has been used to ensure large skin depth and good penetration in the body.

BE12-X.6

Automatic Power Control for Cutting and Coagulation in High-Frequency Surgery. K. Fastenmeier* and G. Flachenecker, University of the Bundeswehr Munich. D-8014 Neubiberg, Fed. Rep. of Germany.

In the field of high-frequency surgery, all standard high-frequency units use manual power setting. On this account, the average power applied to the patient is always much higher than necessary for the cutting and coagulation effect. This fact increases the well-known electrical hazards for the patient, as deep necrosis, burns, and nerve- and muscle stimulations.

It can be shown that the cutting effect is related to an electric spark between surgical probe and tissue. We use the nonlinear behaviour of this spark as a criterion for the automatic control of the output power. A high-frequency unit with very low internal harmonic distortion has been developed. The harmonics generated by the spark are measured and compared to a preset value. The difference is used as a signal for the automatic output power control. By this means, the extension of the arc is continuously kept to the lowest level sufficient for a proper effect during cutting. In the coagulation mode, the output power is pulsed. Every pulse is terminated as soon as a spark is detected.

Recent measurements show a significant reduction of applied output power during cutting and a very rapid, yet safe coagulation effect.

BE12-X.8

A Method of Creating a New Microwave Field for Intrauterine Treatment. Ji Hongwei*, Wang Liran, Tsao Suyueh*, Wang Xueqing, 202 Hospital, Shenyang, China(P.R.C).

Recently we designed a special form of microwave radiator which is applicable to both treatment of functional uterine bleeding and termination of very early pregnancy. It is so designed as to change the circular or ellipsoid pattern of radiation field on meridian plane to be one of triangular form, so that the radiation energy received by the whole uterine wall tends to be distributed more evenly. Microwave at 2450 MHz is transmitted through a semirigid cable to the radiator. An elongated structure of an elastic butterfly loop was built in the radiator designed according to the rule of $\frac{1}{2}\lambda$ dipole radiation. The energy deposition pattern of this newly-designed radiator conforms well to the triangular shape of the uterine cavity. Correction of position and diameter of the butterfly loop can increase the coupling strength and make the microwave energy to be transmitted directly and evenly to the cornua uteri of both sides. Radiators for different sizes of uterine cavity were made. Manikin tests with egg-white showed a triangular energy deposition pattern on the frontal surface. The longest upper edge of it was 4.5 cm and the shortest, 2cm. Painless operation was assured by overlapping of the two wings of the butterfly to reduce its diameter below 3.8 mm on entering and coming out through the narrow cervical canal. This radiator has already been applied clinically.

BE12-X.9

Surgical Treatment of Acute Inflammatory Diseases of Liver, Bile Ducts, Pancreas with the application of New Physical Methods, V.S.Zemskov*, N.N.Korpan, Ya.I.Khokhlich and V.A.Pavlenko, Kiev Medical Institute, 252004 Kiev Schevchenko Bul. 13, UkSSR.

In surgical treatment of 4392 patients with acute inflammatory processes of liver, bile ducts and pancreas there were applied the methods of external local hypothermia (3919) with the help of apparatus "Cryoelectronica-7" and intraoperational cryosurgical action by means of "Cryoelectronica-4" (334 patients) developed at the clinics. While treating 102 patients with obturating jaundice of non-neoplastic etiology after the operation the intravenous lazer irradiation of blood was being conducted by Helium Neon Lazer, lazer apparatus AFL-1 and monofibrous optical light conductor. 37 patients were treated by lazer therapy, besides electro-magnetic irradiation of low intensity was applied on the points of acupuncture. Clinical experience of application of physical means of treatment by cooling, lazer and electro-magnetic action testifies to their high efficiency in surgical treatment of patients with the given pathology.

BE12-Y.2

Performance of a twelve-electrode intraneural stimulation device in silicon technology, W.L.C. Rutten*, H. van Wier and J.H.M. Put, University of Twente, 7500 AE Enschede, The Netherlands.

A multielectrode array in silicon technology has been developed to investigate one of the present bottlenecks in electrical stimulation: how to interface neurons with electronics in a sensitive stable and selective way. The array consists of twelve platinum surfaces (20x60 μm , at 50 μm from each other) on a 50 μm thick tip shaped silicon substrate. The tip was inserted in the peroneal nerve of the rat to stimulate the EDL muscle during acute experiments. A six channel stimulator delivered independently controlled pulse series to the electrodes to elicit isometric twitch or tetanic muscle contractions. Sensitivity was such that one single motor unit could be selected at most of the electrodes in the array. Stable stimulation was possible over long periods, only limited by the condition of the stimulated nerve bundle, i.e. over a period of about four hours. Recruitment curves of stimulation current versus muscle force at a single electrode had a dynamic current range of about 20 dB. In order to examine selectivity we developed a test using the refractory properties of neurons and simple assumptions for the volume conductor near the electrodes and the distribution of the nodes of Ranvier. Results of the test lead to the optimal choice of electrode configurations and stimulus conditions to maximize selectivity.

BE12-Y.1

Effects of Altering Core Body Temperature on Somatosensory and Motor Evoked Potentials, Siavash S. Haghighi*, John J. Oro, Clark Watts, University of Missouri-Columbia, Columbia, Missouri

The effects of core temperature on the motor evoked potentials (MEPs) were explored in rats. Temperature was gradually increased from 37.5 C to 40.5 C or more, and later decreased from 37.5 C to 28 C or less. MEPs elicited by motor cortex stimulation were recorded over the spine at baseline temperature and after stabilizing the temperature at a given degree.

The D wave latency of the MEP was decreased with hyperthermia ($p=0.008$) and increased with hypothermia ($p=0.009$). The conduction velocity was increased with hyperthermia and decreased with hypothermia. There was no significant change in amplitude with hyperthermia ($p=0.55$) although there was a trend toward reduction with hypothermia ($p=0.09$). The interpeak latencies between the D and I waves were variable but tended to decrease with hyperthermia and increase with hypothermia. The MEP deteriorated above 42°C and below 28°C.

Core body temperature has a significant effect on the MEP and should be considered when interpreting changes in this signal.

BE12-Y.3

Effect of Dispersion on Compound Action Fields of Peripheral Nerves

G. Curio*, S.N. Erne*, L. Trahms
Phys.-Techn. Bundesanstalt- Institut Berlin - FRG
+ Freie Universität Berlin - FRG

Recently, we reported on the first biomagnetic detection of Compound Action Fields (CAF) of peripheral nerves in vivo. Surprisingly, the morphology of the signals was monophasic and not in agreement with the expectation on the basis of a simple couple of current dipoles. We present here a model calculation to show that this morphology is the consequence of the dispersion due to the different propagation velocities of the neuron population.

BE12-Y.4

The Effect of a Refractory Period on IPFM in the Nervous Systems, T.Matsuoka and H.Morita*, Utsunomiya University, 2753 Ishii-machi, Utsunomiya, Japan.

It has been shown that in the nervous systems the method of signal transmission is integral pulse frequency modulation (IPFM) and a refractory period exists after occurrence of pulse. The refractory period consists of absolute refractory period (ARP) and relative refractory period (RRP). In this paper, the effect of the refractory period on IPFM is studied analytically and through computer simulation. It is found that the refractory period gives the following effect to IPFM.

1. In IPFM with ARP, pulse density increases in proportion to the logarithmic value of input signal and is led to saturation. Due to these two characteristics, S/N of IPFM does not decrease for additive Gaussian noise. And ARP causes synchronizing pulse train with input periodic signal. The period of the input signal can be known by use of the synchronization.
2. In IPFM with RRP, the change of pulse density with input signal is smaller than in it without RRP. Consequently, dynamic range of input signal becomes wide.

BE12-Y.6

A Suggestion about the Use of a Single Parametric Criterion to Representing the Excitability

Dazong Jiang†, Shaohua Zhang
Institute of Biomedical Engineering
Xi'an Jiaotong University
Xi'an, China

Excitability is one of the fundamental properties of biological tissue. It is generally recognized that Intensity-Duration Curve can properly represent the excitability. The curve is usually interpreted by Weiss formula $i = a/t + b$, which contains two parameters to determine the shape of the curve. Some scientists use rheobase and chronaxie to describe excitability and some scientists suggest use excitability and another term irritability to represent excitability. All these representations involve two parameters. In practise, if we can describe excitability with a single parametric criterion instead of two, it will be convenient to compare the variation of excitability in different conditions. We consider the minimum distance of $i-t$ curve to origin can briefly represent the main characteristics of $i-t$ curve. Based on this idea we suggest the minimum distance (R) as a single parametric criterion of excitability. The validity of the idea is demonstrated by experiments using sciatic-fibular nerve of toad under different conditions.

BE12-Y.5

Chemical Sensing Based on Concentration Effects on Neuron Membrane Properties, R.S. Skeen,*† B.J. Van Wie,† S.J. Fung† and C.D. Barnes,† †Chem. Engr. Dept., †Dept. of Vet. and Comp. Anat., Pharm. and Physiol., Washington State University, Pullman, WA 99164-2710.

The purpose of this work has been to explore the potential of monitoring changes in neuron membrane properties as a means of chemical sensing. To study this, the effects of ethanol between 0.2 M and 1.0 M, and n-butanol between 0.016 M and 0.063 M on the repetitive firing frequency of neurons from the snail *Limnea stagnalis* were measured. Results show that both alcohols induced concentration dependent changes in the firing frequency-stimulating current (F-I) relationship. Normalization of data reduces variations between individual neurons creating a common basis for comparison. This allows the neurons to be classified into groups that show distinct normalized firing frequency response profiles to alcohol concentration. Good reproducibility of response within each group is shown. These findings are discussed in relation to the development of a neuron-based solid-state chemical sensor.

BE12-Y.7

A device for monitoring EMG spontaneous activity during tetany (*)A. Pepino, R. Castaldo, M. Bracale, A. Starica (***) B. Rossi (****). *Univ. of Naples Electr. Dept. Via Claudio 21 Naples (I) **Univ. of Pisa Inform. Dept. C. so Italia 40, Pisa (I) ***Univ. of Pisa Neuro, Clinic Via dei Savi, Pisa (I). The automatic analysis of the EMG spontaneous activity recorded during the activation tests (ischemia, hypernea) supplies quantitative data on the extent of electrolytic changes induced by this syndrome. A specially implemented algorithm applied to the EMG signals makes it possible to quantify the observed amount of the EMG spontaneous specific activity that is correlated to metabolic disorders. A friendly-user device which is based on the previous algorithm has been designed. It performs an automatic recognition of spontaneous EMG activity and provides on-line a graphical representation and three measurement parameters of the biological response to the activation tests.

BE12-Y.8

Evaluation of Thin-Film, Chamber-Type Microelectrodes for Stimulation

M. Hill* and O. Prohaska, Case Western Reserve University, Cleveland, OH 44106.

Safe and effective neural stimulation demands minimal damage to tissue and electrode, while maintaining sufficient current and charge densities to functionally stimulate. With recent advances in solid-state technology, a new chamber-type microelectrode has been fabricated. Based on the geometrical design and a differential current density theory, the design meets these demands.

Evaluation of the chamber-design was made by performing comparative in vitro stimulation experiments between Au thin-film microelectrodes with and without the chamber. The criteria of evaluation were light microscopy observations and potentiographic methods. Increased current passing capabilities of the chambered-electrode was demonstrated; however, due to a non-uniform current distribution within the chamber, some concentrated edge corrosion occurred. Computer modelling aided in optimizing the chamber-geometry to reduce this non-uniformity and corrosion potential.

The realization of an improved microelectrode for stimulation has been shown.

BE12-Z.1

The Theory of 'Channel and Network' and 'Breath' in Traditional Chinese Medical Science and Its Relation with Bioelectricity, Gu Zhimin* and Yu Guorui, Res Ctr. Shanghai

A great deal of experiments on animals and human body has come to the discovery that the characteristics and effects of 'Bioelectricity' are extremely similar to those of 'Breath' recorded in ancient China's medical books. This 'Breath' doesn't mean the air one breathes. Its substantial base is the 'Bioelectricity' through an invisible system of 'Channels and Networks'. In accordance with this doctrine, the Equilibrium Detector for Channels and Breath' and Equilibrator for Channels and Networks' have been developed. Emitting a micro-current pulse, these two instruments may balance the effect of positive and negative bioelectricity, make the blocked 'Channels and Networks' through, and, therefore, give satisfactory cure effectiveness confirmed by clinic applications to about 200,000 patients/times. The figures of entire recovery of some diagnosis as follows:

Cervical vertebra	83.0%	Sciatica	89.4%
Antrum gastritis	87.0%	Chilblain	88.5%
Obliterans arteritis	80.0%		
Facial paralysis	92.4%		

BE12-Z.2

Frequency Selection of Meridians in Chinese Medicine, T. L. Hsu, W. K. Wang¹, Y. Y. Lin Wang² and Y. Chang, Biophysics Lab., Institute of Physics, Academia Sinica, Joint appoint with Institute of Biomedical Engineering, Yang-Ming Medical College, ¹Department of Physics, National Taiwan Normal University, Taipei, Taiwan, R.O.C.

Meridians, the hypothetic lines which connect groups of acupuncture points, play very important roles in both Chinese medicine and Chinese Kung-Fu. The acupuncture points on the same meridian were suspected to be a series of arterial trees connected by same artery and all these arterial trees on the same meridian might resonate with similar frequency or frequencies as the multiple of heart rate.

Theoretical derivation using a homogenous electric circuit analog model suggested two selected resonant frequencies, one came from the artery and the other one came from the arterial trees. It also indicates that if the arterial trees on the same meridian could be modulated to a better resonant condition, the blood pressure wave would propagate with less attenuation and larger speed. Since pressing the acupuncture points could change the vibrational condition so is the resonant frequency. This mechanism also provides explanation of the medication effect of acupuncture. The releasing "Chi" effect in Chinese Kung-Fu might be also due to the modulation of resonant frequencies of the arterial trees by controlling the well trained muscle tone around the arterial trees. Some experimental results will be discussed.

BE12-Z.3

Implemental System for Diagnosis, Treatment, Teaching and Consultation of Chinese Traditional Medicine, Wei Jizhou*, Jiang Chunxiao, Wei Sudan, Chen Ziaoguang, and Liu Hongjian, Bethune Medical University, Xin Min Avenue 6, Changchun, Jilin, P.R. CHINA.

Implemental System is built on the basis of artificial intellectual faculties--Specialist System. Actually, it is a neutral (an empty) program. As long as the data of theoretical designs of medicine are inputted, the electronic computer would automatically produce a specific specialist system. It is constituted from the knowledge stock of intellectual faculties, data stock, inferential machine of an association, renewal of knowledge, explanation etc. 300 different diseases have been tested and verified, all fulfilled the design requirements and achieved good result.

BE12-Z.4

Real time multifunction pulse diagnosis analyser, L.Yu*, D.M.Lu, J.K.Sun. Oceanic U. of Qingdao. Qingdao, P.R.China

Pulse diagnosis is important in Chinese traditional medicine. Doctors test the pulse of the artery of wrist and pick up informations from the feeling of fingers. There are pulse analysers that can measure and record pulse's wave form and amplitude but all can not be used simultaneously with the finger test, so that it is not very useful for clinical diagnosis. We designed a new kind of pulse analyser that get rid of this trouble. Its sensor is a multilayer thin and flexible transducer. It can be used under Doctor's finger and measure and record the wave form, amplitude, static pressure simultaneously with Doctor's finger test. It can measure three positions of the artery at the same time, and also may be used synchronously with CEG, ACG, PCG, etc. So that it has all the functions that demand by finger test. An introduction of this pulse analyser is provided with the records of several kinds of pulses, and also some combined data with other kind measurements.

BE12-Z.6

A Fuzzy Attribute Syntactic Method Classifying and Recognizing APPCM, Zhang wei-lian, Tian Zhi-fen and Wang Ai-min*, Northeast University of Technology, P.R. China

Recently, how to make an objective recognition of the Arterial Pulse wave Pattern according to Chinese Medicine by a computer system instead of by physician's palpation has been interested by many researchers. In the paper a new method of the APPCM recognition is presented, in which 28 kinds of single arterial pulse and 10 kinds of unusual pulse according to APPCM are recognized. The fuzzy feelings of the physicians of Chinese medicine are classified using a fuzzy attribute region and for picking out the main features of different arterial waveforms a series approaches are proposed, e.g., peak-unit expression, period estimation, baseline fluctuation correction and noise filtering. Moreover in the method proposed in the paper arterial pulses are classified into four groups according to the different ways of the pulse distortion, i.e., rate distortion group; period distortion group; form distortion group and position distortion group.

A computer system for APPCM recognition is set up in the hospital, where the data sampled in the General Railway Hospital of Shen Yang are classified and recognized. The simulation results obtained by the system are in keeping with that by the Chinese physicians in clinical practice.

BE12-Z.5

Signal and Information Processing in Biomedical Engineering and Impacts on Traditional Chinese Medicine, Zhao Ping-Ya* and He Zhen-Ya, Digital Signal Processing Research Group, Radio Department, Nanjing Institute of Technology, Nanjing, P.R. China.

Rapidly developing, the signal and information processing has been playing a more and more important role in medical science and biomedical engineering and is beginning a influence on traditional Chinese medicine. Over the last decade, the present authors, in cooperations with their colleagues, have devoted themselves to the studies of new techniques of signal and information processing and their applications in medical sciences, both the Western and Chinese, several dozen research papers have been published in IEEE, IPAC and other international organizations' journals, transactions and other periodicals, read out at their workshops, conferences, symposiums and congresses, and some research achievements were rewarded by Chinese national awards. This paper gives a modern perspective on current status of the area and the authors' works whether they have been published or not. While all aspects of the area are discussed, emphases are given to the following:

- * one-dimensional signal processing applied to ECG, EEG, MEG, EHG and others;
- * medical imaging;
- * the Chinese medical ideas based artificial intelligence for automatic detection and recognition of diseases from the signals and images;
- * medical expert systems, both the Western and Chinese;
- * hospital management automation.

References of the published materials are given.

BE12-ZZ.1

On the Shape of the Relaxation Curve of Remanent Magnetic Field Produced by Magnetic Particles in Cells, I. Nemoto*, K.Ogura and H. Toyotama, Tokyo Denki University, Hatoyama, Saitama, Japan, and Stanley Electric Co., Tsukuba, Japan.

Ferrimagnetic particles ingested by macrophages produce a weak magnetic field around the cells when strongly magnetized by an external field. The field from the cells decays with time (relaxation) due to the movements of the microstructures of the cell. The measurement of relaxation is expected to provide information on the activities of intracellular motility. We previously proposed a model for the phenomenon, employing the rotational Brownian motion in which thermal agitation kT was replaced by some unknown energy E_r . According to this model, relaxation curve should decay as an exponential curve. However, actual curves show a large deviation from a single exponential curve. This does not necessarily mean that the model is inappropriate. The deviation may be explained by distributions of the parameters involved in the model. They are particle size, the size of the phagosome or lysosome containing the particles, the energy E_r and the apparent viscosity. Taking into account the distribution of the parameters would make the curve fitting easier but more arbitrary. The question is not one of how precisely the curves can be fit but which model reflects the actual process better than the others. As yet we can not give a definite answer but, instead, we have several models, the data they would produce, and their interpretations.

BE12-ZZ.2

Magnetophoresis for Separation of Monocytes and Diagnostic Evaluation of the Phagocytic Capacity, H.Minamitani*, T.Shimamura and M.Aiba, Keio Univ., Hiyoshi 3-14-1, Kohoku-ku, Yokohama 223, Japan.

Magnetophoresis is a new method to separate monocytes phagocytizing iron dextran microspheres and to evaluate the phagocytic capacity in patients with liver diseases based upon the separation efficiency of the monocytes from mononuclear cells under magnetic field. Mononuclear cell suspensions were prepared from heparinized peripheral blood in the patients and in healthy volunteers by density centrifugation. The mononuclear cells were incubated with iron dextran microspheres at the ratio of 20 particles to 1 cell at 37°C for 30 min and dropped in a glass chamber filled with RPMI solution. High DC magnetic field of 6 kG was applied to one of the outer wall of the chamber and a cover glass was placed in the corresponding inner wall. Magnetic microsphere phagocytized monocytes migrated towards the glass while the other mononuclear cells such as lymphocytes fell down onto the bottom of the chamber. Both the monocytes and lymphocytes were fixed, stained and observed under vital microscope to count the phagocytized monocytes and the other cells. The monocyte phagocytic capacity was calculated from the ratio of the migrated monocytes to the others. The results showed that the phagocytic capacities of hepatoma and liver cirrhosis became significantly lower than those of healthy volunteers, and that the magnetophoresis was extremely available to evaluate the phagocytosis.

BE12-ZZ.4

Establishment of the method of Hybridoma Cytoelectrophoresis Assay, X.Yan*, J.Wang, S.Zhang and X.Ling, Tianjin Cancer Institute, Tianjin, China (P.R.C.)

A novel serodiagnosis method with monoclonal antibodies, hybridoma cytoelectrophoresis assay, and its application for detecting PA3 antigen in sera of lung cancer patients are described. The method was developed on the basis of the theory that hybridoma cell surface electric charges can be affected by the binding reaction antigen and antibody. Hybridoma cell line PA3 producing monoclonal antibodies to lung cancer was used as the natural "biobeads" carrying the antibodies. Of all 163 cases, PA3 cell slowing rate $\geq 35\%$ was found in 35 of 46 lung cancer patients (positive rate, 76.08%), 8 of 35 patients with other cancers (22.86%), 3/32 for benign diseases of lung (9.38%) and only 3/50 for normal persons (6.00%). The sensitivity, specific, accuracy and repeatability were characterized. The results suggested that this new technique be a potential biomedical and immunological method in serodiagnosis of lung cancer.

BE12-ZZ.3

Feedback Control of a Cobe 2997 Centrifugal Cell Separator, S. Wooten*, J.N.Petersen, B.J. Van Wie, Chemical Engineering Department, Washington State University, Pullman, WA 99164-2710

In order to obtain more efficient operation of a COBE blood cell centrifuge (Model 2997, SS II chamber), modifications were made to allow complete computer control. The clinical cell separator was interfaced to a microcomputer for automatic feedback control of interface position. An optical sensor was used to indicate total cell concentration in the buffy coat product stream. This cell concentration is used as an indicator of the chamber interface position. A feedback control scheme was used to control the interface position by automatically adjusting the red blood cell and plasma product rates. Using this controller, an operator can easily maintain interface position, and thus total cell concentration in the buffy coat product stream. This controller has allowed us to investigate optimal operating regions for the centrifuge.

BE12-ZZ.5

Sequential effects of Bupivacaine Combined with Hyperthermia on Tumor Cell Surface Electricity, J.Wang, X.Yan*, S.Zhang and T.Zhang, Tianjin Cancer Institute, Tianjin, China

Sequential effects of bupivacaine combined with hyperthermia on the membrane electric charges of human cervix carcinoma cell line hela were investigated. The results of cell electrophoresis assay indicated that the slowing rate of cell migration for the treatment sequence of bupivacaine before heat (BH sequence, 79.2%) was significantly higher than that of reverse sequence (HB sequence, 64.0%, $P < 0.01$). Comparing with HB sequence, colony formation rate of Hela cells dropped from 49.33% to 37.33% when cells were treated with BH sequence, showing that BH treatment afforded more pronounced thermosensitizing effect than HB treatment did. The speed of cell migration showed a positive relationship with colony formation rate ($r = 0.876$, $P < 0.05$). The evidence suggested that the difference of thermosensitizing effects between BH and HB sequential treatments be most likely related to the different changes of cell surface electricities inflicted by the two reverse sequences.

BE13-A.1

Structural Modeling of Soft Tissue Mechanics, Y. Lanir, Technion-Israel Institute of Technology, Haifa, 32000, Israel

The mechanisms which give rise to the mechanical response of tissues are intimately associated with their structure and composition. The most important structural elements are networks of long fibers (primarily collagen and elastin) and a fluid-like matrix consisting of water, small solutes and proteoglycan macromolecules. The following features must be considered in developing structural material laws: a. The fibers at rest are generally undulated in a nonuniform manner. b. The fibers' orientation is generally nonuniform as well but often preferred orientations exist. c. The negatively charged groups on the glycosaminoglycans afford them with osmotic properties.

Under tensile deformations the contribution of the matrix is very small. Under compressive loading, on the other hand, the matrix contribution is of essential significance. Stochastic models which relate microstructure to overall mechanical response have been developed for fibrous tissues in general and for specific tissues such as tendon, skin, parenchyma and the myocardium. These models can readily account for the observed complex anisotropic and nonlinear properties of tissues while offering a realistic insight into the internal dynamic structure. In addition they can serve as a useful tool by which specific pathological processes can be diagnosed based on mechanical tests.

BE13-A.3

A New Approach to Vascular Mechanics

J.D. Humphrey*, R.K. Strump† & F.C.P. Yin†
*University of Maryland and †Johns Hopkins Medical Institutions, Baltimore, MD U.S.A.

Despite extensive efforts, there are no uniformly accepted stress-strain relations for blood vessels. Possible reasons for this may be (1) the use of purely phenomenological relations, which cannot directly account for load-induced changes in the structure, and (2) the lack of appropriate experimental data. Thus, we suggest a structurally-motivated approach to formulate pseudostrain-energy functions, W , for various vessels. The analysis includes large deformations, nonlinear material behavior, load-dependent anisotropy, material heterogeneity, incompressibility and residual stresses. Using this approach we identify new experimental protocols necessary to quantify the material symmetries of blood vessels and determine specific functional forms of W directly from data.

BE13-A.2

STRESS-STRAIN RELATIONSHIP OF THE THORACIC AORTA

H W Weizsäcker, J Vossoughi, T D Kampp, Physiologisches Inst Der Karl-Franzens-Universität Graz Austria, Catholic Univ of America, Wash DC, Univ of S California-LA

Cylindrical segments of rat thoracic aortas were subjected to simultaneous axial stretch and internal pressure in the physiological range of deformation. The passive elastic properties of the aortic wall were analyzed in terms of Kirchhoff stresses and Green-St Venant strains by plotting the stress-strain relationship for several constant levels of complementary strains. From curves so obtained, the 1-st partial derivatives of stress with respect to strain were computed and plotted as a function of strain.

The results show that the axial stress-strain curves are roughly similar to the circumferential stress-strain curves in that the slopes of the curves are finite initially, go through an inflection and rise steeply at large strain levels. The S-shape of the stress-strain curves is reflected in the curves of partial derivatives which are concave upward displaying a minimum at strain levels occurring in vivo.

BE13-A.4

A Layered Cylindrical Shell Model for an Artery, Hilmi Demiray*, Research Institute for Basic Sciences, Box 74, Gebze, Kocaeli-TURKEY, and Raymond P.Vito, Georgia Institute of Technology, School of Mechanical Engineering, Atlanta, GA 30332, U.S.A.

Assuming that an artery consists of an orthotropic medial and isotropic adventitial layer, a set of strain energy density functions for each layer is introduced and the values of material coefficients are obtained by comparing the analytical results of a bi-axially stretched specimen with those of experimental measurements. Having determined the material coefficients, a two layered cylindrical shell model is introduced and the distributions of stresses through arterial wall and the inner pressure as a function of deformation are obtained. In this model, although the radial stress is continuous at the interface, the slope of it and other normal stress components become discontinuous. This result is due to assumptions we have made about the layered structure of arteries.

304

BE13-A.5

**RHEOLOGICAL BEHAVIOUR OF
BIOLOGICAL POROUS MATERIALS :
VISCOELASTICITY AND
POROELASTICITY.**

Olivier LE GALLO, Salah NAILI,
Didier GEIGER*;
UNIVERSITE PARIS VAL DE MARNE
Laboratoire de Mécanique Physique
94010 CRETEIL FRANCE

Many composite materials of biological interest are made up by a solid elastic matrix embedded in an interstitial viscous fluid. To study the rheological behaviour of these materials their diphasic character is to be considered. So, if a viscoelastic approach seems adequate to describe their behaviour, only a diphasic model, taking into account the fluid dynamics in the solid matrix, leads to a physical interpretation of the mechanical properties of these materials.

To determine the stress and strain fields in the whole medium (fluid and matrix), as well as the pressure in the interstitial fluid, the poroelasticity theory has been developed (Biot, 1941).

In this study, we point out the fact that an overall description, using the viscoelasticity theory, does not have any intrinsic meaning, and so that this type of model is only suitable to characterise the mechanical properties of the material in a given situation and for a given state of loads.

We suggest also a new method to integrate the poroelasticity equations and compare the theoretical results to experimental measurements.

BE13-B.2

**Indirect Measurement of Elastic Modulus
& Diastolic Pressure in Human Finger
Arteries by Cuff-vibration Technique**

K.Seki*, H.Shimazu, H.Ito, A.Kawarada,
M.Akimoto, & K.Yamakoshi, Dept Physiol,
Kyorin Univ, Mitaka-shi, Tokyo; K.Yamakoshi
is in Res Inst, Appl Electr, Sapporo-shi,
Hokkaido, Japan

Diastolic pressure (P_d) and volume elastic modulus (E_v) defined as $\Delta P / (\Delta V / V_0)$ were indirectly measured by vibrating a finger with a 10 Hz sinusoidal pressure during a gradual decrease in occlusive cuff pressure (P_c). Sinusoidal and pulsatile changes in volume (ΔV) and its ratio against the mean arterial volume ($\Delta V / V$) were detected by an infrared photoelectric plethysmograph. It is known that volume change in an artery shows a maximum amplitude at the transmural pressure (P_t) equal to 0 mmHg due to the nonlinear visco-elastic property of arterial wall. For the same reason, the amplitude of sinusoidal volume variation reaches its maximum at the end-diastolic phase when P_c was controlled to be exactly equal to P_d . The indirect P_d values determined by this method were compared with those simultaneously measured. Using the vibration technique systolic, mean and diastolic pressure can be indirectly determined by means of the volume oscillometric method.

BE13-B.1

**ON VARIATION OF MECHANICAL PROPERTIES OF
AORTIC TISSUE**

J Vossoughi*, School of Engineering and
Architecture, The Catholic University of
America, Washington DC 20064

Several factors such as age, anatomical location, disease type and stage, etc effect the mechanical properties of blood vessels. This paper systematically studies the variation of mechanical properties of thoracic and abdominal bovine aorta along the circumference as well as along the length. Past work indicates that the stiffness of the vascular vessel varies along the aortic tree but not significantly. In this work it is shown that the stiffness along the length of the aorta varies much more than it was recorded before.

Also it is shown that the stiffness of the aorta at any given location along the length varies depending on the location along the circumference of the aorta. It is shown that the aorta is stronger along the dorsal axes and weaker along the ventral axis.

BE13-B.3

**Non-invasive evaluation of venous
compliance and arterial resistance in
the forearm,** P. GIZDULICH*, Fisica
Medica - Università di Firenze, M.
GUERRISI & A. MAGRINI, Fisica Medica -
Università Tor Vergata - Roma, F.
IELLAMO, Fisiopatologia Medica -
Università Tor Vergata - Roma, Italy

Dependency of forearm venous compliance and arterial resistance on increasing venous pressure, due to prolonged venous occlusion, was investigated. Sudden cuff inflations of 30 torr, starting from various cuff pressure values, were carried out. Beat-to-beat arterial pressure in a finger was recorded by a calibrated servo-plethysmo-manometer (FINAPRES). Increases in forearm cross section area were recorded by a strain-gauge plethysmograph. Venous compliance was calculated from the asymptotic value of the plethysmographic signal and the cuff pressure. Blood flow was evaluated from the initial slope of the plethysmographic signal. Results show that blood flow varies significantly with the venous pressure. Arterial resistance and venous compliance did not show any significant dependence on venous pressure in the investigated range of venous pressures (0-60 torr).

BE13-B.4

Effect of exercise training on biochemical and biomechanical properties of rat aorta, T. Nosaka, M. Matsuda, M. Sato, N. Ohshima and H. Fukushima, University of Tsukuba, 1-1-1 Amakubo, Tsukuba, Japan

We studied the effect of prolonged physical exercise on the fibrous proteins of rat aorta, associating with the aortic wall elasticity. Twelve male rats were divided into 6 sedentary control rats (C) and 6 training rats (T) that ran voluntarily in a free wheel from 9 weeks to 25 weeks of age.

The aortic elastin and collagen contents in T were not significantly different from those in C. The content of calcium in elastin was lower in T than in C. Elastin isolated from the training rats showed significant decreases in some of polar amino acids. The incremental elastic modulus values were significantly lower in training rats than in controls, at the extension ratio of 1.5 and 2.0.

We conclude that prolonged voluntary running from an early age provides training rat with a extensible aorta, relating to elastin with fewer calcium deposits and degenerative changes.

BE13-B.5

EFFECT OF ENZYME DEGRADATION ON THE PARAMETERS OF A CONSTITUTIVE MODEL OF THE CANINE CAROTID ARTERY, Thomas R. Canfield, Ph.D., Loyola University of Chicago, Stritch School of Medicine, Maywood, IL.

A constitutive model of canine carotid has been developed. It is based upon a symmetric formulation in the three principle strains. The artery is assumed to be incompressible and behave as a thick walled anisotropic tube. The properties can vary across the wall thickness. The parameters of the model are estimated by minimizing the weighted squared error between estimated and measured values of diameter and longitudinal distending force as a function of pressure and longitudinal extension. The model is currently being used to evaluate material changes induced by selective degradation of the arterial wall with the enzymes collagenase and elastase. The results of these studies will be discussed.

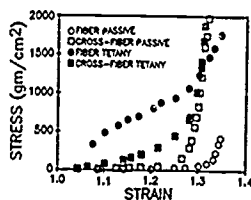
BE13-C.1

Anisotropy of Isolated Perfused Striated Muscle During Passive and Tetanized States.

R. K. Strumpf*, J. D. Humphrey†, F. C. P. Yin*.

*Johns Hopkins Medical Institutions and †University of Maryland

There are no data comparing the stress-strain relations of passive and active striated muscle under simultaneous biaxial loading. We measured the biaxial stress-strain relationship in 10 isolated, perfused canine diaphragms. Specimens of uniform thickness and fiber orientation were simultaneously loaded in the fiber (F) and perpendicular cross-fiber (CF) directions. Deformation was measured in the central region. Equibiaxial stretching over the same strain range was imposed in F and CF directions both in the passive state and during tetanic contraction. Representative stress-strain relations are shown below. These data clearly demonstrate anisotropy and its dependence on muscle activation.



BE13-C.2

ISOTONIC AND ISOMETRIC MEASUREMENTS ON CAROTID ARTERIES, W.W. von Maltzahn, R.W. Calcote, S.M. Jayaraman, University of Texas at Arlington, Box 19138, Arlington, TX 76019

We built an experimental apparatus for measuring the mechanical properties of arterial walls under both isometric and isotonic conditions. A segment from the common carotid artery of a dog was mounted on grooved pin connectors between two stainless steel cantilever arms, and was submerged in physiological salt solution at 37°C. In the isometric mode, both pin connectors were attached tightly to stationary cantilever arms; in the isotonic mode, one pin connector moved freely back and forth, guided by a sleeve bushing. Conversion from the isometric to the isotonic mode was easy. Isometric experiments were carried out at constant axial stretch ratios of 1.3, 1.5 and 1.7; while isotonic experiments took place at constant axial loads of 0.5N, 1.0N and 1.5N. One strain energy density function was used to describe all experimental data. The function was an exponential with a three term quadratic polynomial in the exponent. The independent variables were the tangential and axial Green-St. Venant strains. For most measured arteries a reasonable agreement between measured and modeled data was achieved. The agreement was not as good as one can achieve when modeling isometric or isotonic data only.

366

BE13-C.3

Models of Myocardial Tissue Swelling. D.K. Bogen*, University of Pennsylvania, Philadelphia, PA 19104

Myocardial fluid content, already 80% of the normal myocardial volume, can increase when any of the fluid compartments (intravascular, intracellular, and interstitial) of the tissue is increased. While the diastolic stiffness of the left ventricle generally increases in parallel with an increase in the fluid content of the heart muscle, this phenomenon has yet to be explained. Insight into this problem can be gained by considering several models for nonlinear, biphasic, elastic materials which undergo large scale swelling. These models partition the fluid spaces of the tissue into one or more compartments with rod-like and membranous elastic structural elements. These models can also be conveniently formulated in terms of strain energy density functions which reflect the amount of tissue swelling and the relative partitioning of fluid into the compartments, as well as the anisotropy of the tissue. When this formulation is applied to a simple thick-walled, spherical model of the left ventricle, the swelling behavior of the diastolic ventricle can be predicted. One interesting result of the model is that the effects of swelling are strongly dependent on the anisotropy of the tissue.

BE13-C.5

Collagen Fiber Orientation of the Diaphragmatic Central Tendon Quantified by Small Angle Light Scattering. M.S. Sacks* and C.J. Chuong, University of Texas at Arlington, P.O. BOX 19138, Arlington, TX 76019

We are studying the mechanics of the diaphragm to further our understanding of pulmonary respiration. The diaphragmatic central tendon, a collagenous structure, transmits forces between the costal and crural muscles. Our previous work has shown mechanical anisotropy in its stress-strain curves. To explore the anatomical origins of the mechanical anisotropy, we have used a HeNe laser based small angle light scattering device to quantify collagen fiber orientations, since collagen fibers are the major force transmitting components in tendon. This technique allows precise quantitation of the direction and degree of orientation of the collagen fibers. Results show two distinct fiber layers, which are oriented perpendicular to each other, throughout the tendon. Fibers in the layer at the thoracic side are aligned predominately parallel to the surrounding muscle fibers. (Supported by NSF EET8707665 and NIH HL35914).

BE13-C.4

THE DOUBLE-HEADED CROSSBRIDGE ATTACHMENT IN SKELETAL MUSCLE FIBERS

A Tozeren*, Dept of Mechanical Engineering, Catholic Univ of America, Wash DC 20064

A simple model of a double-headed crossbridge is introduced to explain the retardation of force decay following stretch in skeletal muscle fibers. The critical assumption in the model is that once one of the heads of a crossbridge, say head 1, is attached to one of the actin sites available for attachment, the attachment of the second head will be restricted to a level of strain determined by the attachment of head 1. The unique feature of the model is the prediction that, in the presence of a ligand (PPi, ADP, AMP-PNP) and absence of calcium, the half time of force decay is many times larger than the inverse rate of detachment found in solution. This prediction is in agreement with measured values of half times of force decay in fibers under similar conditions (Schoenberg and Eisenberg, 1985, *Biophys J* 48:863-871). Our computations show that the apparent cooperativity in crossbridge binding experiments (Brenner et al, 1986, *Biophys J* 50:1101-1108) can be partially accounted by the double-headed crossbridge attachment.

BE14-A.1

Oscillatory Flow of Non Newtonian Blood Analog Fluids in a Curved Artery Model. D. Mann and J. M. Tarbell*, Department of Chemical Engineering and the Bioengineering Program, The Pennsylvania State University, University Park, PA 16802.

The influence of non Newtonian rheology on wall shear rate in steady and oscillatory flow through a rigid curved artery model was studied experimentally. Wall shear rate was measured by flush mounted hot film anemometry at 6 locations and the following 4 fluids were investigated under nearly identical flow conditions: (1) aqueous glycerin (Newtonian) (2) aqueous polyacrylamide (shear thinning, elastic) (3) aqueous Xanthan gum (shear thinning, inelastic) (4) bovine blood. For steady flow conditions there was little difference at any of the 6 locations in the wall shear rate levels measured for the 4 fluids. However, dramatic differences were apparent for oscillatory flows, particularly at the inner curvature 180° from the entrance of the curved artery model. For example, at that position the peak shear rate for polyacrylamide was 5-6 times higher than for glycerin and 2-3 times higher than for blood. Aqueous Xanthan gum provided the best model of bovine blood over all positions and flow levels considered.

BE14-A.2

VISCOELASTIC STRESS-STRAIN RELATIONS IN BLOOD: EFFECTS OF HEMATOCRIT, George B. Thurston,*
Department of Mechanical Engineering, The University of Texas, Austin, Texas 78712, U.S.A.

Testing the viscoelasticity of whole blood provides a sensitive indication of the way erythrocytes aggregate and how they deform in flow. These rheological properties are strongly dependent on the hematocrit, and because of variations in both normal and pathological blood, must be accounted for in clinical practice.

A viscoelastic stress-strain profile in which both the viscous and elastic components of the shear stress are plotted vs the amplitude of the oscillatory shear strain (measured at a fixed frequency) shows characteristics of the blood sample which relate directly to the microstructure of the blood. The elastic stress is proportional to the maximum energy per unit volume stored (the maximum elastic energy density developed) during the cycle per unit of strain. The viscous stress is proportional to the energy density lost in each cycle per unit strain. The elastic energy is stored in the process of stretching and orienting the erythrocytes.

In the physiologic range of hematocrits, the viscoelastic stress-strain profile retains its basic characteristic inflections when the hematocrit is changed by adjustment using the blood's autologous plasma. However, changes in hematocrit by hemodilution with Lactated Ringer's solution and Dextran solution produce characteristics which cannot be accounted for on the basis of viscosity of the suspending fluid, and must be attributed to changes in erythrocyte aggregation tendency and deformability.

BE14-A.4

Influence of Physico-chemical factors on the individual white cell transit time.

M. THAO CHAN*, B.B. GUPTA**

* Lab. Hoechst, Tour Roussel Hoechst, F92800

PUTEAUX

** UTC, BP 649, F 60206 COMPIEGNE

Knowledge on the rheological properties of leukocyte are essential for the understanding of their functional behaviour in health and disease, including their release from the bone marrow, motion and deformation during phagocytosis. The Cell Transit Time Analyzer (CTA) detected the transit time of individual cells passing through 5 μm pores of polycarbonate filters (OLIGOPORE) under low hydrostatic pressures (0-10 cm of water).

The histogram and the logarithm curves of frequencies distribution of 2000WBC between 0-1 s. were expressed as well as the number of plugging cells during the transit.

Influence of different physico-chemical factors such as : pressure, temperature, anti-coagulants, and suspending media were analyzed.

The sensibility of the apparatus was demonstrated in the 3 populations : controls, elderly, peripheral vascular disease patients.

BE14-A.3

The Complex Viscosity of Blood in Narrow Capillaries Determined Under Oscillating Flow Conditions, D. Schnedlitz*, V. Ribitsch, and T. Kenner, Department of Physiology and Institute of Physical Chemistry, University of Graz, A-8010 Graz, Austria

The viscoelastic properties of blood and of red blood cell (RBC) suspensions are determined by means of a capillary rheometer, where the fluid in the capillary is set into sinusoidal oscillations. From the detection of the volume flow, the pressure gradient and the phase angle between both, the viscous η' and the elastic η'' component of the complex coefficient of viscosity η^* of the sample is calculated. The frequency of the oscillations is set to the fixed value of 2Hz and the amplitude of the oscillations is increased in discrete steps. The maximum wall shear-rate $|\dot{\gamma}|$ ranges from 0.1s^{-1} to 200s^{-1} (for a 1mm i.d. capillary). Making use of narrow capillaries (i.d. from 0.8mm to 0.2mm) the heterogeneity of the suspension becomes of importance. The reduction of the tube diameter leads to a marked decrease of η' and η'' in aggregating blood samples especially at low $|\dot{\gamma}|$. The extent of viscoelastic shear-thinning is decreased as well. From these results we conclude that RBC-aggregation facilitates oscillating blood flow in narrow tubes.

BE14-A.5

Shear-Induced Platelet Trauma,
B. L. Capes and L. F. Mockros*,
Northwestern University,
Evanston, Illinois 60208, USA

Shear stress is well-known to alter platelet function and morphology. Quantitative relationships are developed to relate various indicators of platelet stimulation/lysis to the level of stress, τ , and duration of that stress, t . Platelet-stimulation/lysis is indicated by availability of PF-3; changes in platelet concentration; release of serotonin, ADP, ATP and β -thromboglobulin; changes in platelet aggregability; and platelet loss of LDH and AP. Available data collected with uniform shear devices are fit to a functional relationship of the form $\tau t^a = 10^b$, with 'a' generally falling between 2 and 4 and 'b' relating to the degree of stimulation/lysis and generally falling between 6 and 16. The data include shear stresses that range from 10^1 to 10^4 dynes/cm² and exposure times that range from 10^{-3} to 10^4 . The developed relationships can be applied to the non-uniform shear fields typical of medical devices. When applied to flows through tubes, these relationships are shown to predict a degree of platelet trauma that is in reasonable agreement with the measured trauma that has been reported in the literature.

368

BE14-B.1

Structure-Function Relationships of the Arteriolar Wall, G.E. Sleek*, Barry University, Department of Biomedical Sciences, Miami, Florida 33161.

Arterioles undergo dramatic structural changes during vasoconstriction. Little is known about how the arteriolar wall directs the rearrangement of its cellular components as it changes diameter. We hypothesize that intercellular junctions between the endothelium and vascular smooth muscle (i.e. myoendothelial junctions - MEJs) direct the restructuring observed during vasoconstriction. An ultrastructural analysis of hamster cheek pouch arterioles constricted to varying degrees was undertaken to test the hypothesis. Our data show that the frequency of MEJs in constricted vessels is almost twice that observed in dilated arterioles ($P < 0.05$). A preferential distribution of MEJs was also observed with respect to the deformations which occur periluminally. The data indicate that MEJs may be labile entities, forming and dissociating as the vessel undergoes changes in diameter. Our data also suggest that MEJs act as foci of force transduction between the two cell types of the arteriolar wall.

BE14-B.3

ACTIVE MECHANICAL PROPERTIES OF SMALL ARTERIES IN SKELETAL MUSCLE. J.H. Lombard*, W.J. Stekllel, E. Monos, and H. Eskinder; Dept. of Physiology; Med. Coll. Wisconsin; Milwaukee, WI 53226, USA.

A significant component of microvascular resistance in skeletal muscle may reside in the small arteries. To assess active responses in these vessels, gracilis arteries ($189 \pm 7 \mu\text{m}$, o.d.) were isolated from anesthetized rats, cannulated with micropipettes, and mounted in an *in vitro* chamber which allowed transmural pressure to be controlled. Active responses to increases in transmural pressure were expressed as: 1) isometric tangential wall tension, 2) isometric tangential wall stress, and 3) isometric tangential wall strain. Active tension and active stress progressively increased in response to 20 mmHg increments in transmural pressure between 0 mmHg and 160 mmHg (myogenic activation). Active strain initially increased (0-40 mmHg), and then remained fairly constant through 160 mmHg. At control pressure (80% of mean arterial pressure), active strain in the gracilis artery ($-27 \pm 2\%$) was significantly higher than that in the larger saphenous artery ($-9 \pm 2\%$). In contrast, intestinal mesenteric arteries did not exhibit active strain or myogenic activation. The presence of active tone and myogenic responses in small arteries supplying skeletal muscle suggests that these vessels may have a significant role in regulating vascular resistance in this tissue. (NIH #HL-37374, NIH #HL-29587, and Established Investigator Award (JEL) from American Heart Association).

BE14-B.2

Mechanics of the Arteriole Wall, R.S. Chadwick*, and J. Ohayon, Theoretical Biomechanics Group, Biomedical Engineering and Instrumentation Branch, Division of Research Services, National Institutes of Health, Bethesda, MD 20892.

We have developed a two-dimensional mathematical model of the arteriole wall to help understand the relationship between mechanical equilibrium geometry, transmural pressure, vasomotor tone, and elastic constants. The model is comprised of three functional regions: an intima represented by a finite number of endothelial cells each having a finite cross sectional area; a media described as a finite layer of a continuum of fluid, collagen, and smooth muscle cells assumed to contract in the circumferential direction, and; an adventitia considered as a finite layer of fluid and collagen. With specified stress-free reference configuration, transmural pressure, elastic moduli, and degree of vasomotor tone, the finite deformation of the model arteriole is determined subject to incompressibility constraints and lateral interactions between adjacent endothelial cells. Because the problem is nonlinear more than one equilibrium solution can be found. We look for the solution with minimal elastic strain energy. Usually this corresponds to a state where the endothelial cell membranes have zero strain energy. Using the model we found that smaller arterioles (having a greater fraction of cross sectional area comprised of cells) are much more efficient at increasing their hydrodynamic resistance than larger arterioles. We found the model is very sensitive to small changes in media thickness in the sense that a relatively large increase in transmural pressure is required to keep the lumen area constant.

BE14-B.4

Wall Anatomy and Mechanical Properties of Microvessels in Skeletal Muscle, G.W. Schmid-Schönbein, T.C. Skalak, F.A. DeLano, S. Chu, Univ. of California, San Diego, La Jolla, CA 92093 and Univ. of Virginia, Charlottesville, VA 22908

The blood vessels in the microcirculation of skeletal muscle are completely surrounded by muscle cells. In that position the different hierarchies of arterioles, capillaries and venules have a distinct wall morphology. It contains endothelium, basement membrane, a tapering elastica intima and smooth muscle along the arterioles, pericytes along a major portion of the collecting venules, collagen, mast cells, and specific structural features in the adventitia, such as nerves and lymphatics. Dynamically the blood vessel walls are distensible and exhibit nonlinear viscoelastic properties. Upon a step transmural pressure the diameter shows an instantaneous elastic expansion which is followed by a slower time dependent expansion. At long times a new steady state diameter is reached. The vessels are relatively stiff, and in contrast to blood vessels in other organs, venules exhibit the stiffest properties of all microvessels. These viscoelastic properties have many implications with respect to blood flow and transport in skeletal muscle.

Supported by NSF Grant DCB 85-16662 and in part by USPHS Grant HL-10881.

BE14-C.1

LENGTH-TENSION RELATIONSHIP OF MAXIMALLY ACTIVATED ARTERIOLES. M.J. Davis^o and R.W. Gore. Dept. of Medical Physiology, Texas A&M Univ., College Station, TX 77843 and Dept. of Physiology, Univ. of Arizona Tucson, AZ 85724.

Segmental differences in the microvascular response to physical and chemical stimuli may possibly be explained in terms of the length-tension relationship of vascular smooth muscle at different points along the vascular tree. To test this hypothesis, we isolated single arterioles for study in vitro so that arteriolar pressure and activation state could be precisely controlled. 1st-, 2nd-, and 3rd-order arterioles (1A, 2A, 3A; i.d. = 20-60 μ m) were dissected from the hamster cheek pouch and cannulated with micropipettes using methods described by Duling and Gore (Am. J. Physiol. 241:H108, 1981). Pressure-diameter curves were recorded for maximally-activated vessels in high K⁺ and norepinephrine solution, and for passive vessels in Ca⁺⁺-free solution over an internal pressure range of 5 to 400 cmH₂O. Maximal active wall tension varied from 600 (3A) to 1600 (1A) dynes/cm, but maximal active wall stress varied only from 4 (1A) to 6 (3A) $\times 10^6$ dynes/cm². The average value for wall stress is very similar to that obtained in hog carotid artery (Dillon et al., Science 211:495, 1981). These results support the concept that smooth muscle from vessels of different size is mechanically similar and that longitudinal differences in arteriolar wall stress in vivo may explain the response gradients observed in the microcirculation. Wall buckling in arterioles at short radii broadens the peak of the active stress-length curve and may extend the pressure range over which arterioles are most sensitive to physical and chemical stimuli. Supported by NIH HL-13437, HL-38104 and Texas AHA #85G-063.

BE14-C.3

Myocardial microvascular properties and the prediction of coronary flow, J.A.E. Spaan^o, University of Amsterdam, Department of Medical Physics, The Netherlands.

One would like to understand the mechanics of flow in coronary arteries and veins from basic properties of the microvessels and their mechanical loading by cardiac contraction. Under normal conditions intramyocardial blood volume is appr. 12% which amount is increased by 25% when the heart is arrested. Assuming that tissue pressure falls from ventricular luminal pressure at the endocardium to zero in the epicardium one calculates an intramyocardial compliance value of 0.1 ml/mm Hg. This is close to the value derived from the product of capillary distensibility and intramyocardial bloodvolume. Compression of this intramyocardial compliance by heart contraction explains well the phasic flows in coronary arteries and veins. The intramyocardial compliance leads to over-estimation of zero flow pressures if venous outflow has not ceased.

A further analysis of coronary dynamics requires more information on myocardial microcirculation especially on the non-linear pressure volume relation of the microvessels and the distribution of pressure and flow velocities in them.

BE14-C.2

Arteriolar vasomotion and changes in perfusion conditions

D.W. Slaaf^o, H.H.E. Oude Vrielink, G.J. Tøngelver and R.S. Reneman. Laboratory for Microcirculation, University of Limburg, Maastricht, The Netherlands

The arteriolar diameter varies rhythmically (vasomotion) even under seemingly stationary conditions. The relation between vasomotion and arterial pressure reduction and vasodilation was studied in the rabbit tenuissimus muscle using intravital microscopy. Vasomotion has a limited effect on the resistance of the transport arterioles (TA), but its considerable effect on the resistance in terminal arterioles dominates the flow pattern in the TA. Reduction of perfusion pressure leads to effective vasodilation and a gradual increase in cycle length (CL) and amplitude (A) of vasomotion. Vasodilation as a result of vascular relaxation (adenosine superfusion) did not result in a change in CL, whereas A decreased. Thus, vasodilation per se does not result in increased CL and A. Arterial pressure and blood cell velocity (normalized to diameter) had the strongest relation with the increase in CL. Increases in CL over more than 40% occurred if arterial pressure was considerably reduced with a concomitant reduction in flow or increase in effective diameter. CL and A do not change as a result of simple scaling. The major change seems to be a delayed onset of the constriction phase, with minor adjustments of the basic vasomotion pattern.

Supported by MEDIGON 900-517-157

BE14-D.1

Leukocyte Behavior at a Bifurcation of Arteriole in the Rat Mesentery, Masaaki Sato^o, Shin-ichi Sakuraba and Norio Ohshima, University of Tsukuba, Tsukuba, Ibaraki 305, Japan

Leukocyte behavior at a bifurcation of arteriole in the rat mesentery was analyzed by introducing a fluorescent dye technique. Diluted acridine orange was intravenously infused to observe the leukocytes in the microvessels under a fluorescence-TV intravital microscope. Blood flow velocities and leukocyte flux were measured at 36 arteriolar bifurcation sites. The experimental results are summarized in the form of a leukocyte distribution function which is defined as the leukocyte flux as a function of the bulk flow into the daughter vessels. The leukocyte distribution function was nonlinear and the partitioning of leukocytes flux between daughter branches was strongly dependent on the eccentric position of the cells at the upstream entrance to the branch. Only the leukocytes flowing at a central region in the upstream parent arteriole were divided between two branches according to a sigmoidal distribution function which generally expresses "preferential distribution" of particles at vessel bifurcations.

BE14-D.2

Wall shear rate and velocity profiles in arterioles. D.W. Slaaf, G.J. Tangelder, T. Arts and F.S. Reneman, Laboratory for Microcirculation, University of Limburg, Maastricht, The Netherlands.

Velocity profiles were determined in vivo in rabbit mesenteric arterioles and used to calculate least estimates of the actual wall shear rate in these microvessels (17-32 μm diameter). Fluorescently labeled platelets, used as natural markers of flow, were visualized by intravital fluorescence video microscopy. Velocity and mean radial position of platelets flowing within a thin optical section around the median plane of the vessel, were determined. Data points could be obtained as close to the wall as 0.5 μm . The velocity profiles were flattened as compared to a parabola. To satisfy the no-slip condition a thin layer of fluid with a steep velocity gradient near the wall has to be assumed. Least estimates of wall shear rate (WSR), as calculated using the mean velocity gradient in this layer of fluid, ranged from 472 to 4712 s^{-1} (median 1700 s^{-1}). These values are at least 1.46-3.94 (median 2.12) times higher than those calculated for a parabolic velocity profile (WSR-P) with the same volume flow. The ratio WSR/WSR-P might also be used as a least estimate of the apparent viscosity of blood in the arterioles relative to the viscosity of plasma. The median value of 2.12 compares well with the value of approximately 2.34 as found in cat mesentery using measurements of pressure gradients.

BE14-D.4

OPTIMUM Capillary Network in the Skeletal Muscles for Oxygen Transport to Tissue, A. Kamiya, A. Oota and M. Shibata, Res. Inst. Appl. Electr. Hokkaido University, 060, Sapporo, Japan

The optimum capillary network for oxygen (O_2) transport to tissue was estimated using Krogh's cylinder model in the skeletal muscle. The tissue mass supplied by a single capillary in the center was estimated as the area of positive O_2 tension under a given condition of capillary flow and tissue O_2 consumption rate. The total mass was determined as the function of the capillary number and total blood flow. The energy cost to maintain the vascular system with n terminals (capillaries) was assessed by the minimum volume model by Kamiya and Togawa (1972). The efficiency of the entire system was evaluated by calculating the ratio of total tissue mass/ energy cost. The results of the calculation using physiological data of muscle blood flow and O_2 consumption rate in man revealed the optimum capillary number of $(5 - 10) \times 10^3$ and the capillary density of 200 - 500/ mm^2 which coincided well with the physiological estimates of these values in the human skeletal muscles. It was concluded that the capillary network system in the skeletal muscle is constructed so as to attain the highest efficiency in O_2 transport to tissue.

BE14-D.3

Estimation and Analysis of Platelet-Analogue Concentration Profiles in Blood Flow, J. Shane Kippenhan*, Joachim H. Nagel, Eugene C. Eckstein, Dept. of Biomedical Engineering, University of Miami, Coral Gables, FL 33124, USA.

Radial concentration profiles of platelet-sized particles in blood flow through small tubes were estimated from groups of observations of particle distances from tube walls. Methods based on the kernel method of probability density estimation allowed easier quantitative characterization of the near-wall peak that often occurs in the distributions; such peaks were difficult to quantify with previous histogram methods. These methods also yielded a higher spatial resolution of the distributions' features.

Additionally, curve fitting of the Fourier transform of the density estimates was used to model the experimental data. This Fourier transform represents the "characteristic function" that describes all moments (mean, variance, etc.) of the data's distribution. Such analytical descriptions of the distributions, based on two or three parameters, enable compact representations of sets of data, thus facilitating the study of the relationship between these parameters and rheological conditions.

The above methods can be applied whenever handling data that consists of lists of numerical observations in one or more dimensions.

BE14-D.5

LIPID SOLUBILITY INCREASES THE SENSITIVITY OF INDICATORS FOR ENDOTHELIAL DAMAGE IN THE LUNG. T. R. Harris*, L. E. Olson, and A. Pou, Vanderbilt University, Nashville, TN 37232.

Tracers such as ^{14}C -urea (U) can be used in indicator-dilution curves to assess diffusivity-surface area product ($D^{1/2}S$) for the lung vascular capillary barrier. A persistent problem is the need to separately assess diffusivity and surface area. We have proposed that tracers which were both lipophilic and hydrophilic might be useful in such separation. Recently, we proposed that ^{14}C -propanediol (P) could be used to eliminate the effects of surface area by observing the ratio of $D^{1/2}S$ for U to that for P (Harris et al. *J. Appl. Physiol.* 62, 1852, 1987). This work showed that the square of the ratio of $D^{1/2}S$ for P and U (R^2) decreases from 1.7 to 1.06 when capillary permeability is increased by infusion of alloxan in isolated perfused dog lung preparations. Theory developed in this paper showed that this implied a 5-fold increase in true capillary permeability. This theory also predicts that R^2 changes from baseline should be even greater if lipid solubility of the diol is higher. Thus, we used ^{14}C -butanediol as a tracer and compared it to U in another group of isolated dog lung studies. Results show that R^2 alters from 3.5 to 1.3 after alloxan indicating again a 5-fold increase in true capillary permeability. These results suggest that partially lipid soluble tracers when used with urea provide sensitive measures of lung vascular damage.

BE14-D.6

Measurements of Single Capillary Permeability of Macromolecules in Skeletal Muscle

M. Shibata* and A. Kamiya,
Research Institute of Applied Electricity,
Hokkaido University, Sapporo 060, JAPAN

Transport mechanism of macromolecules across capillary wall has been debated by several investigators. To clarify this mechanism, we tried to establish a new fluorescent intravital microscopic method for direct measurement of single capillary permeability of macromolecules based on the "double pore theory". The rabbit tenuissimus muscle was used for the measurement of local tissue concentration curve following the intravenous injection of FITC-conjugated Albumin (FA67, M.W. = 67,000) and Dextran (FD155, M.W. = 155,000) from video-image of microcirculation obtained by Argon laser excited fluorescent microscope-TV system. The measured tissue concentration curve was best-fitted with the theoretical curve in the parabolic partial differential equation and the diffusive(D) and convective(V) components of transport across the capillary wall were determined. Capillary permeability coefficient(P) was calculated from D value as $P=D/X$, where X is the diffusion distance (length of pore). P values of FA67 and FD155 obtained tissue concentration curves were 9.5 ± 5.9 and 6.8 ± 3.1 , which values were well consistent with the values obtained whole organ measurements. It was concluded that present method is useful to measure the local capillary permeability of macromolecules.

BE14-E.2

Curvature Elasticity of Mechanically-formed Lipid Membrane Tethers, Richard E. Waugh*, University of Rochester School of Medicine and Dentistry, Rochester, NY 14642.

A tether is a thin cylinder of membrane that can be formed from the surface of a cell or bilayer vesicle by pulling on a small region of the surface (point attachment). Early observations indicated that tethers exhibit elastic character, and that their radius decreases as the axial force on the tether increases. The coefficient that relates the axial force to the tether radius is the membrane bending stiffness. We have developed a new experimental approach to measure the force and radius of tethers formed from vesicular membranes to determine the membrane bending stiffness and test proposed equilibrium relationships between the membrane tension and the tether force. The force is generated by the negative buoyancy of a glass bead that has adhered to the surface of the vesicle. The tether radius is calculated from the displacement of the projection of the vesicle into the pipet. Preliminary measurements of force and tether radius from phospholipid membranes of stearyl-oleoyl-phosphatidylcholine indicate a bending stiffness of these membranes between 1.7×10^{-19} and 3.0×10^{-19} Nm. They also indicate that the relationship between aspiration pressure and tether force predicted on the basis of thin membrane theory is not valid.

BE14-E.1

Cell Pucker Measurements of the Mechanical Properties of Viscoelastic Layers, M. Duszynk, B. Schwab, E. Elson and G. Zahalak*, Washington University, St. Louis, Missouri 63130, USA

We have recently developed a new instrument, the Cell Pucker, for measuring cellular deformability, and applied it to measure the stiffness of many different types of cells including erythrocytes, fibroblasts, lymphocytes, and islet cells. In order to increase confidence in the technique and also to establish a basis for interpreting cell-pucker measurements in terms of fundamental mechanical properties it was deemed desirable to test a material which had been well characterized by other means. Thin (0.1mm) layers of three polydimethylsiloxanes (PDMS) were prepared and tested by indenting their surface with pokers (0.10µm diameter) driven by triangular displacement waveforms. The nominal values of the viscosities of the three PDMS samples were respectively 12.5, 30.0, and 60.0 Ns/m². From measurements of the force and magnitude of indentation at the pucker tip it was possible to determine the relaxation function of the PDMS. This function can be characterized by three parameters: the short- and long-time elastic moduli, G_0 and G_∞ , and viscosity η . Determination of η by two different methods yielded (14.5, 24.8, 65.2) and (15.4, 34.7, 78.4) Ns/m², in reasonably good agreement with the nominal values. The long-time modulus, G_∞ appears to be related to the surface tension at the PDMS-water boundary.

BE14-E.3

Electroporabilization and Fusion of Adherent Lipid Vesicles: David Needham*, Department of Mechanical Engineering and Materials Science, Duke University, Durham, N.C. 27706.

Lipid bilayer membranes in close enough contact will mix and "fuse" under the action of appropriate destabilizing stimuli. In our experiments, close contact is established by attractive forces between membranes (e. g. van der Waals forces, the presence of non-adsorbing polymer and positive dielectrophoresis). Membrane breakdown and destabilization of contact is made to occur via an applied d.c. pulse. We use a technique of micropipet manipulation in order to experiment on single lipid vesicles or single adherent pairs. The lipid composition, mechanical properties and adhesive interactions of these vesicles is well characterized. A double chamber with transfer pipet allows vesicles to be selected from one chamber, transferred into the adjacent chamber, containing the desired solution and placed between parallel Pt electrodes. Electroporabilization and fusion is assayed via direct observation, and geometry and structure of the post-fusion product are determined by micropipet suction. Initial results suggest that internal volume is conserved whilst excess membrane area is taken up as an adherent 'flap' spanning the lumen of the spherical fusion product. This 'flap' can be peeled apart by the application of pipet suction and the membrane is pulled into the surface.

BE14-E.4

ANALYSIS OF THE STRENGTH OF ADHESION BETWEEN A PAIR OF CYTOTOXIC T-CELL AND TARGET CELL

Aydin Tozeren*, o-Li Paul Sung and Shu Chien, Mechanical Engineering Department, The Catholic University of America, Washington DC 20064 and Department of Physiology, College of Physicians and Surgeons, Columbia University, NY NY

A micromanipulation method is used to determine the strength of adhesion between a pair of cells by measuring the energy per unit area that must be supplied to reduce the region of contact between the cell pair. We show that the strength of adhesion is not constant during peeling but increases with decreasing contact area for pairs of cytotoxic T-cell (F1) and target cell (JY). This new finding supports the notion that the crosslinking protein molecules slide towards the leading edge of the separation while remaining attached to both cells. The driving force for this movement is the elastic energy stored in the crosslinks by the membrane tensions. The strength of adhesion of F1-JY pair is found to be three to six times larger than the corresponding strength of F1-F1 pair.

BE14-F.1

Micromechanical Manipulation of Electrically Fused Red Blood Cells. Donna Miles-McCollum*, Dept. of Biomedical Engineering and Robert M. Hochmuth, Dept. of Mechanical Engineering and Materials Science, Duke University, Durham, NC 27706.

A system previously developed for the fusion and micromanipulation of red blood cells has been modified to allow a more "gentle" fusion process and a variation of conditions for cellular manipulation. Cells are suspended in a 200mOsm salt-sucrose solution and flushed into a 250 μ m thick channel lined with Pt electrodes 0.75 mm apart. The cells are aligned in a AC field and fused in large quantities with four DC pulses of 3-5kV/cm height and 20-25 μ s width. Several types of fusion products are obtained depending upon the extent of fusion. The most gently fused cells are attached by a tether while other pairs of fused cells are joined by a larger tunnel-like structure or a fully swelled lumen. These results suggest that the fusion process begins with point lipid attachments and perturbations and then progresses to spectrin involvement. The fused cells are flushed into a larger manipulation chamber with a 295mOsm solution which results in a partial deflation of the cells and allows the connecting structures to be viewed more clearly. Micromanipulation is being used to investigate the extent of communication between the cells of an apparent fused pair and to characterize the mechanical properties of the fusion site.

BE14-E.5

Detachment of Red Blood Cells from Adhesive Contact with Rigid Substrates by Micropipet Suction: Experiment and Analysis, D. Berk* and E. Evans, University of British Columbia, Vancouver, B.C. V6T 1W5.

When cells form adhesive contacts, the chemical affinity that causes the contact to spread is opposed by the work of cell deformation. Likewise, when adhesive contacts are separated by the action of external forces, the mechanical deformability of the cell moderates the action of those forces and affects the application of stresses to the contact region. Thus, the cell acts as a transducer or coupler between the applied force and the adhesive contact. We have recognized this feature in the design and analysis of experiments to measure the physical properties of adhesion. In these experiments, suction pressure from a micropipet is used to detach adherent red cells from rigid surfaces. We employ a finite-difference computational algorithm to solve the equations of mechanics governing red cell deformation and provide a complete description of the detachment process. Consequently, we are able to explicitly measure the energy per unit area required to separate red cells agglutinated by antibodies or lectins.

BE14-F.2

RBC Membrane Shear Modulus of Elasticity Derived from Observations of Steadily Tank-Treading Cells, S. Suter*, P. Pierre and G. Zahalak, Washington University, St. Louis, MO - 63130, USA

An algorithm has been developed for the approximate calculation of the membrane stress distribution and the internal pressure of a steadily tank-treading red cell (Tran-Son-Tay et al, 1987, Biophys. J., 51:915). The algorithm is based on an idealized ellipsoidal model of the tank-treading cell (Keller and Skalak, 1982, J. Fluid Mech., 120:27) joined with experimental observations of cell dimensions (projected length and width) and tank-treading frequency. The resulting expressions for the membrane stress resultants, when applied to the two curvature extrema of the central streamline, reduce to two simultaneous equations which are explicit in μ_m , the membrane shear modulus of elasticity, and implicit in the cytoplasmic pressure, p_c . Solutions of these equations for a series of experimentally observed motions, corresponding to graded levels of applied shear rate, $\dot{\gamma}$, yield values of μ_m and p_c which increase monotonically with the applied shear rate and, thus, the overall cell elongation induced by the shear flow. Over the range of $\dot{\gamma}$ covered, the calculated μ_m varies from 0.5×10^{-3} to about 5×10^{-3} dynes/cm, corresponding to values of the principal extension ratio from about 2 to 3. According to these findings, based on dynamic membrane equilibrium considerations, the red cell membrane exhibits strain-stiffening elastic behavior.

BE14-F.3

Determination of r.b.c. Membrane Elastic Modulus from Viscoelasticity Measurements on a Dilute r.b.c. Suspension

X.Y. Lin & D. Barthes-Biesel,* Université de Compiègne, U.A. CNRS 858, BP 649, 60206 Compiègne France.

The motion and deformation of a r.b.c. suspended in a shear flow may be qualitatively represented by means of a capsule model (i.e. a liquid droplet surrounded by a deformable membrane). There exists presently a complete model of the time dependent behaviour of a spherical capsule suspended in a linear flow, that includes the determination of the bulk rheological properties of a dilute suspension of such particles. In particular, the loss and storage moduli may be expressed exactly in terms of the intrinsic properties of the particles.

The aim of this work is to show how this model may be used to interpret oscillating shear measurements on a dilute (haematocrit between 5% and 10%) suspension of r.b.c.'s in a viscous medium (Dextran, viscosity between 7 and 10 mPas). The frequency range varies from .05 to 1 Hz. The suspensions exhibit a measurable viscoelasticity and a comparison between the experimental and theoretical moduli leads to an evaluation of the membrane surface shear elastic modulus which varies between 10 and $2 \cdot 10^{-6}$ N/m, a value comparable with the results obtained from micropipette experiments.

BE14-F.5

An Adaptive Pulse-editing Technique for Accurate Aperture Impedance Cell Size Analysis and Erythrocyte Deformability Measurement.

T.C.Fisher,* A.C.Fisher.
Bioengineering Unit, University of Strathclyde, Glasgow, G4 0NW, Scotland, U.K.

For most haematological applications, cell volume analysis is performed by the aperture impedance (Coulter) technique. The underlying principle is that the changes in resistance (detected as voltage pulses) as cells are drawn through a minute aperture are directly proportional to the cell size. This is an approximation, and volume distributions obtained in this manner are skewed by the inclusion of anomalous pulses. Various methods have been devised to deal with this problem, but are generally expensive and/or complex and not applicable to standard equipment. This system comprises an interface which digitises the height and duration of pulses output from a cell counter and passes this data to a microcomputer. All subsequent processing is performed in software. The pulse-editing technique is based on the relationship of pulse height and duration and will be discussed in detail. The major advantage is that it is auto-adaptive; i.e. the criteria for artefact rejection are established by statistical analysis of the incoming data, rather than being pre-determined. Used with a basic cell counter, performance compares very favourably with expensive haematology analysers. An exiting spin-off is that this technique also provides a rapid and simple means to measure erythrocyte deformability.

BE14-F.4

Regulation of Red Cell Membrane Deformability and Stability by Skeletal Protein Network, N. Mohandas,*
Department of Laboratory Medicine and Cancer Research Institute, University of California, San Francisco, California, 94143, USA.

Biophysical and biochemical evidence accumulated during the last decade suggests that a membrane skeletal protein network consisting of spectrin, actin, and protein 4.1 linked to band 3 in the fluid lipid bilayer through ankyrin is responsible for various red cell membrane material properties. Recently, a number of investigators have attempted to define the key skeletal protein associations by relating measured changes in membrane deformability and membrane mechanical stability to well-defined skeletal protein abnormalities in red cells from congenital hemolytic anemias with membrane dysfunction. From these studies, the membrane skeleton emerges as a network of folded spectrin molecules held together by protein-protein associations which occur at both ends of the spectrin heterodimer. Disruption of either the spectrin-actin-protein 4.1 complex at one end of the spectrin molecule, or of spectrin self-association at the other end resulted in a marked decrease in membrane mechanical stability. On the other hand, an increase in inter- or intramolecular associations of the skeletal proteins or increased association of integral membrane proteins with the skeletal network resulted in profound decreases in membrane deformability. These data imply that different skeletal protein interactions regulate membrane deformability and mechanical stability.

BE14-G.1

Models of Capillary Blood Flow

R. Skalak*, N. Özkaya, M. Sugihara-Seki
Bioengineering Institute, Department of
Civil Engineering & Engineering Mechanics
Columbia University, New York, NY 10027

Several theoretical models of capillary blood flow have been evaluated by computational investigation of the influence of various factors. The effects of elasticity of the red blood cell membrane are shown to lead to reduced pressure drop at high flow velocities. Computation of the entrance flow into a narrow capillary shows that the deformability of the cell allows smooth entry with little change in mean cell velocity. The stability of multfile (double file) flow of red blood cells (2D model) is investigated numerically. Rigid cells appear to be neutrally stable in double file flow, but deformable cells may have preferred configuration.

304

BE14-G.2

Modelling the Mechanics of White Blood Cells: Elongational Flow and Passage through a Stenosis
X. Z. Li₁, D. Barthes-Biesel_{1*}, C. Thao Chan₂,

1 Université de Compiègne, BP649, F60206 Compiègne,
2 Lab. Hoechst, 3 Tour Roussel, F92800 Puteaux

A white blood cell is modelled as a spherical capsule, i.e. a liquid drop surrounded by a viscoelastic membrane. A numerical technique is used to predict the motion and the deformation of the cell in two situations: *case1*, when it is suspended in an unbounded axisymmetric elongational flow; *case2*, when it is forced to squeeze through a constriction with a smaller diameter. In both cases, the internal viscosity of the cell and that of the suspending liquid are equal.

In *case1*, the cell bursts when the capillary number (ratio of the external viscous forces to the membrane elastic forces) exceeds a critical value. The membrane viscosity only affects the characteristic response time of the cell to a change in flow conditions.

In *case2*, the resulting deformed capsule shapes resemble those of w. b. c. going through Nucleopore filters. Cell break-up may occur, but the higher the membrane viscosity, the higher the critical capillary number. The additional head loss through the stenosis increases sharply with membrane viscosity. This model may be used to gain a qualitative understanding of the dynamics of w.b.c.'s subjected to hydrodynamical forces.

BE14-G.4

Contractile Cortex-Liquid Core Model for Blood Phagocytes: Effect of Augmented Dissipation in Cortex,
E. Evans and A. Yeung, University of British Columbia, Vancouver, B.C. V6T 1W5

Extensive evidence shows that the active contractile apparatus in blood phagocytes is concentrated in a cortical layer adjacent to the outer plasma membrane. We have shown that these cells deform passively as very viscous liquid suspensions of organelles and granules. A significant question is what is the viscous resistance of the cortical layer compared to the interior cytoplasm? We have developed a variational method to predict the entry of a spherical cell into a tube where the cell structure is modelled by a viscous liquid core coupled to a viscous-contractile outer shell. Here, we present results which show that when there is no drag at the tube wall, augmented dissipation in the cortex has little effect on the rate of entry until the viscous properties of the cortex are very large. Therefore, the rate of entry of liquid-like spherical cells into tubes versus suction pressure provides a direct measure of the effective viscosity of the interior suspension of cytoplasm and organelles. Data for flow of single blood granulocytes into suction micropipets yield values on the order of 10^3 poise for the effective viscosity at 25°C.

BE14-G.3

A plate model for determining the elastic modulus of shear-exposed endothelial cells, C. Byrd, R. M. Nerem, and L. T. Wheeler*, U. of Houston, Houston, TX 77004.

Experimental studies have shown that endothelial cells maintain a flattened and elongated shape following exposure to shear stress and subsequent detachment. Their mechanical properties, which are studied using micropipette experiments, are influenced by the level as well as the duration of the shear stress. In a recent study, carried out in collaboration with D. P. Theret, M. J. Levesque, and M. Sato (to appear, J. Biomech. Engrg.), with the aid of an axisymmetric homogeneous halfspace model suggested by the experimental observations, we determine an expression for an effective Young's modulus for such cells. In the present discussion we report on progress toward an axisymmetric plate model. This model uses the solution of the halfspace model as the initial step in an alternating scheme. In the second step, a traction boundary value problem is used to remove the tractions from the plane corresponding to the free surface of the plate and in the third step a mixed halfspace problem is solved to correct for the perturbations to the boundary conditions on the loaded face introduced in step two. This three step process is repeated until the desired level of accuracy is obtained.

BE14-G.5

A New Method to Measure Active Cytoplasmic Strain in Human Neutrophils, S. Simon* and G.W. Schmid-Schönbein, AMES-Bioengineering, University of California San Diego, La Jolla, CA 92093 USA.

A requirement for neutrophil locomotion and phagocytosis is active cytoplasmic deformation. To understand how the nonuniform actin-myosin contractile elements in the cytoplasm effect spontaneous pseudopod formation and locomotion, we developed a new method to measure planar Lagrangian and Eulerian strains from the displacement history of a triad of internalized latex markers. The microsphere displacement histories were recorded on video along with the cell contour. The triad's principle strains, orientation, stretch ratios as well as the overall cell stretch ratios and orientation were computed. The intracellular strains were found to be large relative to the overall cell shape change. Principle stretch ratios ($\lambda=1/1$) were predominantly dilatational in the direction of pseudopod formation ($\lambda=2.6\pm 1.5$) and contractile in the perpendicular direction ($\lambda=.7\pm .4$). Regional strain analysis in the vicinity of the pseudopods revealed moderate contractile strains. The transitional region, between pseudopod and cell body, exhibited large shear strains. It appears that the motive strain field is small in the gelled pseudopod region and large in the cell body.

Supported by USPHS grant HL-10881.

375

BE15-A.1

INTRACARDIAC FLOW VECTOR MAPPING BY 2-D DOPPLER ECHOCARDIOGRAPHY

A.Kitabatake*, J.Tanouchi, K.Ishihara, K.Fujii, M.Uematsu, Y.Yoshida, H.Kusuoka, M.Hori, M.Inoue, T.Kamada The 1st Dept. of Medicine, Osaka Univ. School of Medicine, Osaka, Japan

To investigate the intracardiac flow dynamics in terms of regional flow direction and absolute flow velocity, we have newly developed two-dimensional (2-D) flow vector mapping by 2-D Doppler echocardiography. On the basis of the equation of continuity, we determined orthogonal velocity components to the ultrasound beams from the parallel velocity components to the ultrasound beams measured by 2-D Doppler echocardiography, assuming that there is no perpendicular flow component to the echo plane. We applied this method to left ventricular (LV) flow in normal subjects and patients with LV dysfunction. Results were. In normal subjects, all intraventricular flows converged towards the outflow in midsystole. In patients with LV dysfunction, outflow streams were not so converged, because of remnant of inflow in midsystole, although outflow tract abruptly narrowed morphologically. Absolute velocity and convectional acceleration were significantly lower in patients with LV dysfunction than those in normal subjects. Flow vector mapping is a new technique to provide a quantitative flow mapping in cardiovascular system.

BE15-A.3

A Feasible Method of Measuring the Absolute Flow-rate of a Regurgitation, Shunt, and Stenosed Flow by Color Doppler, M. Sugawara*, Y. Seo† and H. Hongo‡, The Heart Institute of Japan, Tokyo Women's Medical College, Tokyo, 162 Japan, and †Medical Engineering Laboratory, Toshiba Corporation, Otawara, 329-26 Japan.

The issuing flow-rate of a jet, Q , is given by $Q = v_n A$, where v_n is the issuing velocity of the jet and A is the cross-sectional area of the orifice. However, the measurement of A of a jet in the cardiovascular system, such as a regurgitation, shunt, or stenosed flow, is difficult. On the assumption that the jet is "free", the following relations apply between the diameter of the orifice D , the length of the laminar core of the jet L , the centerline velocity of the jet v_x at an arbitrary distance $x (> L)$ from the orifice, and v_n : $L = 6.8D$ and $v_x/v_n = L/x$. From these equations we obtain $Q = 0.017(x v_x^2)/v_n$. Jets into a water bath through orifices with various diameters were studied. The issuing flow-rate was measured with an ultrasonic flowmeter mounted around the tubing connected to the orifice. v_n , x , and v_x were measured by using various functions of a color Doppler flow imaging system. There was a good linear correlation between the Q 's estimated from the above equation (Y) and measured with the flowmeter (X) irrespective of the diameter of orifices: $Y = 1.01X + 0.06$ ($r = 0.96$, $SE = 0.19$).

BE15-A.2

Could color Doppler areas of regurgitant jets have a physical significance?

B. Diebold, A. Delouche, Ph. Delouche, J.P. Guglielmi, Ph. Dumée and P. Péronneau*. INSERM U. 256, Hôpital Broussais, Paris, France.

Color Doppler evaluations of intracardiac regurgitant jets are often used for assessing valvular insufficiencies, but the physical relationship between the velocity fields and the severity of the leaks has never been studied. Our in vitro model was designed to measure the velocity fields in a pulsatile turbulent jet with various peak velocities ($v = 2.5$ to 5.5 m/s), orifice diameters ($d = 5.8$ to 11.3 mm) and receiving tube diameters ($D = 16$ to 30 mm), simulating a large variety of valvular leaks. The results demonstrate, at peak velocity, the presence of a central core within which the velocity is uniform. Below a threshold velocity (V_t), this core is free: its length (l) is independent of v , and proportional to d ($l = 6.2 d \pm 0.4$ (mm), $r = 0.99$). V_t is due to the receiving tube: $V_t = 14.4 d/D + 8.3$ (m/s) ($r = 0.95$). Thus, in the absence of aliasing, color Doppler measurements of the central core of regurgitant free jets would allow an accurate evaluation of the severity of the leaks.

BE15-A.4

Detecting STI from Blood Flow Velocity measured by Doppler Ultrasound and ECG, Wei-qi Wang*, Qi-ming Song and Qian-ming Shao, Dept. of Elec. Engn., Fudan Univ., Shanghai, China

The ratio of Pre-ejection Time (PEP) and Left Ventricular Ejection Time (LVET) is called Systolic Time Interval (STI). We explored a new method for detecting STI only with two biosignals, ECG and blood flow velocity.

The method consists of two parts:

I. Utilize Doppler ultrasound to detect blood flow velocity and detect ECG simultaneously in order to obtain PEP and LVET.

II. The computer control whole system, recognize R wave, initial and end points of blood flow velocity waveform with software. Let R wave as a synchronous point, accumulate the velocity of blood flow. Display the two biosignals. Calculate and print PEP, LVET, STI, HR.

The method has been used in clinic for cardiac function examination at three hospitals in Shanghai.

316

BE15-A.5

The Pre-ejection-period of the Fetal Heart: Noninvasive Detection during Labor with Doppler Ultrasound and Phonocardiogram, B.C. Yu, Yang-ming Medical College, Taipei, Taiwan, R.O.C.

The purpose of this study is to measure the pre-ejection-period (PEP) of the fetal heart during labor. The PEP is defined as the time interval from the onset of ventricular depolarization to the opening of the aortic valve (Q_{AO}). The PEP is of interest because it is related to myocardial contractility. It is measured with the combination use of abdominal ECG and the audio output of ultrasound Doppler cardiogram. Bandpass filter with cutoff frequencies at 750 and 1000 Hz is designed to locate the component wave that correlates the opening movement of the aortic valve (AO). Fifty pregnant women with a gestational age between 36 and 40 weeks are studied. AO is detected in 84 per cent (42 of 50). The average value of PEP is 78±12ms. This value agrees well with the result measured from phonocardiogram. The factors that prolong or shorten PEP, such as hypoxemia or umbilical cord occlusion, are currently under investigation.

BE15-B.1

Evaluation of Pulsed Doppler Measurements of Velocity Profiles, R.S. Rabinovitz*, C.J. Hartley, M. J. Levesque, R. M. Nerem, Baylor College of Medicine, Houston, Texas, and Georgia Institute of Technology, Atlanta, Georgia.

Velocity signals measured by a pulsed ultrasonic Doppler velocimeter (PUDVM) are derived from convolution of a finite-size sample volume with the velocity field. This results in a spatial smoothing and lengthening of the measured velocity profiles. A computerized simulation was developed to evaluate the accuracy of the velocity profile measurements obtained by a 20 MHz PUDVM. The model includes transmit burst length, acoustic attenuation, far-wall reflection, receiver gate width, and a zero-crossing-counter with threshold levels. To examine the performance of the simulation, a Poiseuille velocity profile was used as an input, and the output velocity profile was compared to that measured by the PUDVM for fully developed laminar flow in a straight tube ($20 < Re < 310$). The simulated velocity profiles and the derived wall shear rate (WSR) closely approximate the measured values. Based on the simulation, it was found that the velocity errors were greater near the walls, resulting in an underestimation of the WSR. The relative error in WSR increased with an increase in WSR and with a decrease in vessel diameter. It was also found that due to far-wall reflection, one cannot determine both the position of the far-wall and the shape of the velocity profile unambiguously.

BE15-B.1

An automated computer-run Doppler process for measuring experimental cardiac output. An in-vitro study. D. KALMANSON*, C. VEYRAT, H. VUTHIEN, S. GARCIN, G. PALLOT, Y. LEMERDY. Fondation ROTHSCHILD, Paris - FRANCE. CNAMTS & ARNTIC.

A Doppler velocimeter (ATL851) was fed to a computer (Normrel AT+) and a software devised to automate entirely the recording and calculation of flow rate. The Doppler probe was fixed at a certain distance of a pipe ($\phi=20$ mm), whose pulsatile flow could be set and made variable by an electric pump. The Doppler gate was first positioned at the centre of a cross section of the pipe, and thereafter, all the processing became automatic. 1/A series of points of the elliptical cross-section was determined. 2/An elliptical regression then calculated the centre, diameter and the angle θ between the beam and direction of flow. 3/ About 30 points within the cross-section were explored, and their mean Doppler frequency shift recorded. 4/ These frequency shifts were averaged, with a correction for the angle θ for each point. An orthogonal projection was computerized, and the systolic flow rate in cc/systole was yielded. 40 experiments were performed with various outputs ranging from 45 to 110 cc / systole. Accuracy of the measurements was $\pm 15\%$, for an incident angle ranging between 40 to 55°. Comparison with thermodilution showed a similar accuracy.

BME Ultrasound Symposium.

BE15-B.3

Pulmonary Artery Velocity Profiles, C. Lucas, B. Ha*, G. W. Henry and J. Ferreira, The UNC School of Medicine, Chapel Hill, North Carolina, USA.

Measurement of pulmonary blood velocity noninvasively with Doppler ultrasound has stimulated interest in relationships between velocity patterns and abnormal pulmonary hemodynamics. Using an intraluminal 20 MHz pulsed Doppler needle probe, velocity profiles have been obtained in the main pulmonary artery (MPA) of lambs and dogs during control conditions and while hemodynamics were altered via hypoxia or MPA particle (20-50 μ) embolization. Intraanimal results were consistent with clinical observations, i.e. increased PA pressure and/or resistance corresponded to decreased acceleration time (AT = time from the onset of systole to peak velocity) and increased maximal flow reversal (V_{neg}), though inter-animal variability precluded using either AT or V_{neg} to quantify accurately pressure or resistance. Prominent backflow along the posterior wall of the MPA was often observed during control conditions, while AT appeared to depend largely on vessel compliance and the signal processing technique used. The shape of the profiles obtained suggested that fluid dynamics in the MPA of these animals can be more appropriately modeled as flow in curved rather than straight tubes. Preliminary studies of *in situ* casts of the right ventricle and major PAs of lambs show the importance of the subvalvar infundibular region, supporting this hypothesis. Future work will focus on delineating the importance of geometry in determining MPA velocity patterns. (Supported by HL35389.)

BE15-B.4

Human Regional Blood Flows During Simulated Microgravity: A Noninvasive Doppler Flowmetry Study
ER Greene, KW Tawney,* EC Johnson
Lovelace Medical Foundation, Albuquerque, NM, USA

To determine the effects of simulated microgravity on human regional blood flows, we used previously validated, noninvasive image-guided Doppler flowmetry to measure spectral blood velocity waveforms and systolic lumen diameters in 5 lean and fasting healthy, untrained adults (25-39 years, $\bar{x} = 32$). From these measured variables, regional blood flows (ml/min) from the internal carotid (CO), subclavian (SQ), superior mesenteric (MQ), renal (RQ), and femoral (FQ) arteries were calculated during the supine position (SU) and after 120 minutes of -10° head-down tilt (HD). Simultaneous measurements of heart rates (HR), mean cuff blood pressures (BP), and Doppler cardiac outputs (CO) were also obtained. Results ($\bar{x} \pm SD$) were as follows (* = $p < 0.05$ versus SU):

	CO	SQ	MQ	RQ	FQ
SU	680 ± 175	247 ± 71	559 ± 271	556 ± 168	197 ± 47
HD	636 ± 108	229 ± 57	551 ± 94	382* ± 141	167 ± 37

HR, CO, and BP did not change significantly. In all subjects, RQ and its percentage of CO decreased during HD. These results suggest that in the large conduit arteries (except renals) which supply major organ systems, blood flows remain stable during the cephalad blood volume shifts induced by 120 minutes of -10° head-down tilt in young healthy adults.

BE15-B.6

Application of the Zoom Wigner Transform to Blood Disturbance Velocity Waveforms, H Talhami and R I Kitney*, Dept of Electrical Engineering, Imperial College, London SW7 2BT, UK.

The paper will discuss the application of the Zoom Wigner transform to the analysis of blood disturbance waveforms obtained downstream of a stenosis. As will be shown in the paper the ZWT has certain advantages over both the FFT and modern spectral estimation methods, particularly in relation to the frequency resolution of specific components.

Short records of the disturbance velocity waveform for various levels of occlusion, namely 40 and 74%, were transformed to obtain a Wigner time/frequency distribution which showed the flow field behaviour in the preselected frequency bandwidth. The results were found to be of significantly higher quality than those obtained using other spectral estimators.

BE15-B.5

Rapid stenosis location by Doppler Ultrasound, using a new Video tracking method. D.H.King*, J.Reidy, L.Robinson, P.Nesbit, M.Payne, K.Photiou, S.Kontis, M.G.Taylor and R.G.Gosling. Guy's Hospital, London Bridge, London SE1 9RT, United Kingdom

Theory Arterial cross sectional area is inversely proportional to blood velocity in an unbranching artery. Doppler shift is proportional to blood velocity, therefore by monitoring Doppler shift it is possible to deduce the presence of area changes within the arterial lumen. This principle has been employed in the Quicksan technique which is described below.

Method A 4MHz hand held CW Doppler probe is scanned along the longitudinal axis of the artery. The location of a LED light mounted on the probe tip is continuously monitored by an overhead video camera. A micro computer records the peak Doppler shifted frequency and calculates the probe XY position, and then, using this data, plots out a fixed width line, in red, representing the normal lumen, and then overprints with a yellow line, whose width is related to frequency shift. Diagnosis of complete occlusion is made if the characteristic signs of collateral formation are evident in the Doppler shift Spectra. In this case the yellow line is set to equal the lumen width. Thus Quicksan superimposes a notional map of arterial cross sectional area over a video image of the patient. This image is similar in appearance to the conventional arteriogram. However, it differs in three respects:- (a) It is completely non-invasive (b) It yields data comparable to multi plane views of the arterial system (c) It is not affected by timing and dilution artefacts which can degrade arteriographic image quality.

BE15-C.1

The Transverse Doppler Technique for Blood Flow Measurement, V.L. Newhouse*, Drexel University, Philadelphia, PA 19104, USA.

Existing ultrasonic systems for blood flow measurement which use the well known Doppler equation, only estimate the velocity component in the beam direction, and are restricted to beam to flow angles less than about 60° . A recently discovered technique will be described, using the Doppler spectral bandwidth as well as the center frequency with which it is possible to estimate *the velocity component normal to the beam axis as well as that in the beam direction*, and to measure flow velocities *directed at all angles to the beam axis, including 90°* .

This "transverse Doppler" technique makes use of the fact that any scatterer moving through the focus of a sound beam will have its echo amplitude modulated by the beam side lobes in such a way as to produce a Doppler spectrum whose width is proportional to the velocity component normal to the beam axis.

BE15-C.2

ACCURATE MEASUREMENT OF BLOOD FLOW USING ULTRASOUND AND TIME DOMAIN CORRELATION, I. Hein*, V. Suorsa, J. Zachary, R. Fish and W. D. O'Brien, Jr., University of Illinois, Urbana, IL 61801.

Using time domain correlation, the volume fluid flow in a vessel can be accurately and precisely estimated without any previous knowledge of the vessel size, flow velocity profile, or transducer measurement angle. This technique observes the change in arrival time (instead of frequency) of ultrasonic pulses reflected from moving scatterers. It has been validated in a blood flow phantom system using both a blood mimicking substance and porcine blood. The transducer measurement angle has been determined within 5%, and pulsatile flow has been measured up to 150 beats/min with accuracies better than 18%. Currently, this method is being experimentally investigated under in vivo conditions, with the eventual application being the diagnosis of venous thrombosis in humans. [Work supported by NSF/NHLBI 1 R01 HL 39704.]

BE15-C.4

ADVANTAGES OF SMOOTHED SPECTRUM ESTIMATE FOR ANALYSIS OF DOPPLER SIGNAL SPECTRUM
M. Piechocki, A. Herment, A. Delouche, Ph. Dumée, P. Péronneau*.
IPPT, Polish Academy of Sciences, Warsaw, Poland ;
INSERM U. 256, Paris, France.

The aim of our study was to establish a simple method for the improvement of the instantaneous spectrum estimate definition. An analysis of the statistical properties of FFT spectrum estimate applied to the Doppler signal allowed us to develop a smoothing procedure of this instantaneous estimate. The smoothing of the FFT spectrum estimate is achieved through a low pass filtering in the frequency domain. The performances of smoothed spectrum estimate were theoretically and experimentally studied. The variance of the smoothed spectrum estimate is similar to that of simple FFT estimate averaged over several cardiac cycles. The procedure established improves sensibly the accuracy of the relation between the shape of the spectrum and the flow parameters. In result, more exact determination of flow characteristics like its stability or its maximum velocity even in case of low signal to noise power ratio is possible.

BE15-C.3

Transit-Time Broadening Estimation with Fourier Transform and Autoregressive Techniques
Dominique Davet*, Steven A. Jones, Don Giddens
Georgia Institute of Technology
George W. Woodruff School of
Mechanical Engineering

Spectral broadening due to transit-time ambiguity from a Pulsed Doppler Ultrasound system was examined with Fourier transform and autoregressive methods of spectral estimation. Measurements were obtained from laminar flow at several velocities, and the spectral characteristics were compared with a theoretical model for transit-time broadening (Garbini et al.; JFM, 1982). Data records of 4, 35, 70 ms were processed with FFT and Burg AR (model order 4 and 32) methods, and the spectral width was calculated as a function of the peak frequency, from the basic formula given by Garbini. All the curves fit a good linear regression, as predicted by the Garbini model. The AR model of order 4 yielded the lowest standard deviation for short records, at all velocities. The regression for the FFT technique deviated from the model, in that it did not pass through the origin, whereas the AR method gave good results. It is concluded that the FFT estimation technique itself contributes significantly to spectral broadening for short data records, and the AR technique more accurately predicts transit-time broadening.

BE15-C.5

Pulsed Doppler Velocity Estimation via Autoregression and Fourier Transform
Steven A. Jones* and Don P. Giddens
Georgia Institute of Technology
George W. Woodruff School of
Mechanical Engineering

Doppler Ultrasound data have been collected from a physical flow model and processed via Fourier transform and autoregression techniques to compare the accuracy of these methods.

The measurements were performed with a 10MHz pulsed Doppler probe at the throat of a contoured constriction with 90% area reduction. Various Reynolds numbers were used, and the flow was laminar with a blunt velocity profile. Doppler signals were digitized and records were processed with Fourier transform and Burg Autoregression methods to yield curves of velocity as a function of time. Velocity was estimated from both the peak and the normalized first moment of the spectrum. Standard deviations of the resulting time series data were then examined.

For peak detection, low model order autoregression (e.g., order 4) yielded the lowest variance, approximately half of that for the Fourier transform method. The first moment time series was almost identical for both spectral techniques, but the variances were larger than those derived from peak detection.

BE15-C.6

Phase Locked Loop Method for Doppler US Investigation, F.Clemente*, M.Cesarelli, R.Castaldo, M.Bracale, Cattedra di Elettronica Biomedica-Nucleo di Ricerca di Ingegneria Medica e della Riabilitazione C.N.R.- Faculty of Engineering, Via Claudio 21 80125 Napoli, Italy.

A new method for evaluating single frequency waveforms from Doppler Ultrasound signals based on the analogue locked loop technique has been proposed. P.L.L. technique can be applied to follow the instantaneous frequency of the Doppler signal. The average of the instantaneous frequency of the signal is an unbiased estimator of the mean frequency and the average of its absolute value may be related to the variance of Doppler Spectrum.

Therefore the first parameter shows the shape of the mean blood flow velocity; the latter is an estimator of the spectrum broadening.

A prototype based on this method has been developed. Some interesting clinical results considering young health people and arteriopathic patients show the possibility to evaluate different hemodynamic conditions.

BE15-D.2

In-Vitro Assessment of the 20MHz Intracoronary Ultrasound Doppler Velocity (IDV) Catheter, D Abouelnasr,* D Churchwell, D Giddens, S Jones, Carlyle Fraser Heart Ctr/CWL Hosp of Emory U; EUSM. Dept of ME, GA Inst of Tech, Atlanta, GA

IDV Catheters are currently under investigation as a means of estimating coronary flow by measuring coronary blood flow velocity (CBFV). Before large scale use of the catheter on human subjects, we performed in vitro studies for the assessment of performance under simulated clinical conditions: 1. Sample volume size was measured by moving the catheter about a fixed target and plotting the Doppler-shifted frequency DSF power as determined by autoregression versus distance. The sample volume diameter remained very close to that of the catheter as compared to laser-Doppler anemometer (LDA) measurements made at the same location, and compared very well. The effects of near-wall location were observed by placing the catheter in a 3mm diameter coronary model, and 4mm downstream, the effects of a wake may be seen in low, fluctuating velocities. At ranges of 5 to 10mm, the DSF velocity was higher and more stable. CONCLUSIONS: 1. The sample volume size remains discrete to a range of 10mm, and is small enough to be wholly contained within the coronary artery. 2. Based on LDA measurements, the DSF is accurate. 3. The size and effect of the wake behind the catheter must be determined. 4. Autoregression analysis of the DSF is sensitive enough to measure velocities up to a range of 10mm.

BE15-D.1

Catheter tip imaging with ultrasound, N. Bom*, H. ten Hoff, C.J. Slager, F.C. van Egmond, W.J. Gussenhoven, Thoraxcenter, Rotterdam and Inter-university Cardiology Institute of the Netherlands.

Presently many recanalization methods are being developed to reopen obstructed arteries during catheterization. Such a new obstruction removal technology is the spark erosion method. An evaluation study has been carried out to see if ultrasound imaging on the tip of a catheter could be developed to - eventually - guide selective spark erosion for removal of atherosclerotic plaque and other possibly eccentrically located arterial obstructions. Following early work with 32-element circular phased array technique a less complex mechanical scanning method has been designed. Six designs were studied that fall into two categories. In the first category an internally rotating mirror deflects the ultrasound beam over 360 degrees. No moving parts are present outside the catheter. The second category incorporates an exteriorly rotating tip where the echo imaging and the spark erosion electrode are active in almost the same arterial cross-section. A 40 MHz ultrasound echo tip has been built which rotates at 3000 rpm. With this prototype real-time imaging was studied in animal experiments and human arterial specimen obtained from the pathology laboratory. Results show a clear correlation between the plaque and the echo image.

BE15-D.3

Effect of Aortic Valve Replacement on Coronary Artery Flow Velocity Waveform in Patient with Aortic Valve Disease
S.Matsuoka*, S.Kanazawa, Y.Wada, M.Goto, K.Mito, Y.Ogasawara, O.Hiramatsu, K.Tsujioka, T.Fujiwara, F.Kajiya, Kawasaki Medical School, 577 Matsushima, Kurashiki, 701-01, Japan

Aortic valve disease is frequently accompanied by an abnormal myocardial perfusion. The purpose of this study was to clarify the characteristics of the coronary artery blood flow velocity in patients with aortic valve disease. Five patients with aortic regurgitation(AR), three with aortic stenosis(AS) and four with aortic stenosis and regurgitation(ASR) were studied before and after aortic valve replacement(AVR) by our 20MHz 80 channel pulsed Doppler ultrasound velocimeter. The velocity waveform and the velocity profile across the vessel were measured at the left anterior descending coronary artery(LAD). The velocity waveform in AR showed a large systolic flow and a relatively small diastolic flow with short duration. In AS, the early diastolic acceleration of the velocity was significantly attenuated and a systolic reverse flow was always observed. The velocity waveform in ASR was in between of AR and AS. Immediately after AVR, the velocity waveform returned to normal diastolic predominant pattern.

BE15-D.4

Intraoperative Evaluation of Blood Flow Velocity Waveforms in Different Types of Coronary Artery Bypass Grafts - Sequential Saphenous Vein Graft and Internal Mammary Artery Graft-, S.Kanazawa, T.Fujiwara, S.Matsuoka, T.Katsumura, *Y.Ogasawara, *K.Tsujioka, *F.Kajiya, Depts. of Thoracic and Cardiovascular surgery, and *Medical Engineering, Kawasaki Medical School, Kurashiki, Japan

The patency of the aorta-coronary bypass graft may closely relate to the blood flow waveform and geometrical blood flow disturbance in the graft as well as the volume flow rate. We investigated the blood velocities in two types of coronary artery bypass grafts, the life span of which are known to be different, i.e., the sequential saphenous vein bypass graft (shorter span) and the internal mammary artery graft (longer). The velocity was measured by dual mode (zero-cross and FFT), multichannel, high frequency ultrasound measurements during bypass graft surgery. In the vein graft, the skew of the velocity profile and the flow separation were always recognized at the region just proximal to the side to side anastomosis and the change in the direction of skew was observed along the bridge portion, while a parabolic velocity profile with a narrow spectrum was observed in the internal mammary artery graft. These characteristics of blood velocity may be attributable to the patency of the graft.

BE15-D.6

Pulsed Ultrasound Doppler in Cardiac Output Monitoring, J.B. Ruo*, A.P. Yoganathan, and M.A. Colson, Georgia Institute of Technology, Atlanta, GA 30332-0100

Doppler echocardiography provides a technique to continuously monitor cardiac output (CO), indicating the overall cardiac status of a patient during the immediate post-operative period. To develop a relationship between the actual CO and a Doppler-derived CO, an *in vitro* pulsatile flow study was performed involving the use of a Vingmed SD-100 Doppler ultrasound system and two different 5 MHz implantable Doppler probes. One of the probes emitted a conical beam, while the other produced a wedge-shaped beam. For tilting disc, bileaflet, and porcine heart valve designs, spectra were obtained at 2, 4, and 6 l/min and at 2, 3, and 4 cm distances from the valve ring. Peak velocity was measured as well as CO determined by an electromagnetic flow probe and by mean and maximum Doppler velocity spectra. A profile factor was then calculated as actual CO/Doppler derived CO.

Results show a linear relationship between Doppler CO and actual CO with correlation coefficients ranging from 0.95 to 0.99. For a given valve design using the maximum velocity spectra for Doppler CO evaluation, the profile factor was found to remain relatively constant, independent of actual CO and distance from the valve: approximately 0.37 for the tilting disc, 0.44 for the bileaflet, and 0.29 for the porcine. Therefore, this factor may be used to characterize prosthetic valve types.

BE15-D.5

POSTOPERATIVE MONITORING OF REGIONAL MYOCARDIAL FUNCTION IN MAN. C.J. Hartley*, R.S. Rabinovitz, L.J. Suignard, B.S. Patel, J.E. Chelly, M.O. Jeroudi, G.P. Noon, and R. Bolli, Baylor College of Medicine, Houston, TX 77030.

We have developed an ultrasonic method to measure regional systolic thickening (ST) of the left ventricle (LV). The sensor is a silastic coated 2 mm 10 MHz transducer sutured loosely to the epicardium during surgery with the leads exteriorized near the chest drain. The sensor is extracted 2 to 3 days postoperatively by pulling on the leads. Thickening is measured by sensing the phase of echoes within a range-gated sample volume placed in the wall near the endocardium. Each cycle of phase corresponds to tissue displacement of $\lambda/2$ or 0.075 mm. Thickening fraction (TF), a dimensionless index of function and ischemia, is determined by dividing ST by the range-gate depth.

In 12 coronary bypass patients, TF ranged from 15% to 35% intraoperatively and remained stable or decreased slightly during the early postoperative period. In one patient, however, ST was replaced by thinning (usually a sign of ischemia) during this time. All sensors were removed without incident. This technique provides continuous monitoring of regional LV function and its recovery and modification by drugs during the early postoperative period.

BE15-E.1

A Sonographic Technique for Reducing Beam Distortion by Subcutaneous Tissues. G. Kos*, D.A. Carpenter, D.E. Robinson, Ultrasonics Institute, Sydney, Australia

All sonographic equipment assumes that the speed of propagation of ultrasound in soft tissue is constant whereas in fact it varies by up to 10% from the normally assumed value of 1540 m/sec. This variation is particularly significant in the subcutaneous tissues and can cause deviation and broadening of the beam and an increase in side lobes, resulting in significant degradation in sonographic image quality. These aberrations have been evaluated on a beam generated by a linear array transducer following propagation through layers of various geometry and velocity. A compensating technique has been developed which allows the possibility for correcting for these aberrations based on the control of the timing and the amplitude of the signal of each element both in transmission and reception.

BE15-E.2

Bubble Sizing for Cardiac Applications, P. M. Shankar, Drexel University, Department of Electrical and Computer Engineering, Philadelphia, PA 19104

The noninvasive measurement of pressure in different chambers of the heart is very important in cardiology. Recently it has been proposed that bubbles may be injected into the circulatory system and their size changes can be monitored as they pass through the chambers of the heart. Ultrasound is an excellent tool to track and size the bubbles. The author and his colleagues have proposed a new technique of measuring sizes called the Double Frequency technique. In this technique the bubbles are insonified by two sound fields, a high frequency imaging field and low frequency pumping field. The sum and difference frequency signals generated from the oscillations of the pumped bubbles are used for size measurements. Preliminary in-vitro experiments showed that such technique can be used to measure pressure changes in the ambient atmosphere by measuring their size changes. In this paper a summary of results on sizing microbubbles in circulation using double frequency techniques will be presented.

BE15-E.4

Speckle Reduction in Ultrasonic Imaging using Two-dimensional Phase-insensitive Receiving Arrays,* J.J. Ciesey,* C.R. Meyer, and P.L. Carson, University of Michigan, Dept. of Radiology, Ann Arbor, MI 48105

Specular noise, which is inherent in all coherent energy forms, can limit the quality of ultrasonic images. Speckle can be reduced by adding images formed by transducers with different characteristics. The amount of speckle reduction was found to be a function of the impulse response and the input pressure waveform of the transducer.

A pulse-echo imager which utilizes two-dimensional phase-insensitive receiving arrays has been developed to reduce speckle in ultrasonic images. Four receiving arrays were constructed each containing 64 segmented annulus (SA) or hexagon elements with either spherical or conical focusing. Preliminary results for a conically focused SA array showed using 64 elements independently reduced speckle by a factor of 3.8² over combining all elements into one subaperture. The results agreed with values found from the impulse response of the transducers.

* This work was supported in part by PHS Grant #2-R01-HD17243-05 awarded by the National Institutes of Child Health and Human Development.

BE15-E.3

Ultrasonic Imaging of Blood and Its Potential Applications in Studying Hemodynamics and Rheology, K. K. Shung* and Y. W. Yuan, Bioengineering Program, Pennsylvania State University, University Park, PA 16802

With the advent of technology, blood which used to be considered anechoic in ultrasound imaging can now be visualized when a high frequency scanner is used. Work in our laboratory and elsewhere has shown that blood flow patterns can be readily visualized in vivo or in vitro in a mock flow loop. It has been found that blood echogenicity is critically dependent upon red cell aggregation which is affected by the shear rate produced by the flow and fibrinogen content of the blood. Echo intensity correlates well with viscosity of the blood at low shear rate since viscosity is also shear rate dependent at low shear rates. More recently, a region with complete cell depletion was consistently found to occur in flowing whole blood under certain conditions at low shear rates. This phenomenon has never been reported previously. In this paper recent experimental results and real-time ultrasonic images will be presented to illustrate these observations. Also to be addressed is the relevance of ultrasonic imaging as a tool for studying hemodynamics and blood rheology.

BE15-E.5

Medical Focussing Ultrasonic Transducers with Gaussian Surface Velocity Distribution, Jin Shuwu* Zhejiang University, Hangzhou, China

The theoretic analysis, design of the construction and measurement of the sound field for medical ultrasonic transducer with Gaussian surface velocity distribution are described. The piezocrystal plate of the radius 6mm is made from Nb_2O_5 piezoelectric ceramics. The resonant frequency is 2.5MHz. The acoustic lens of the focal length 59mm is made of epoxy resin. The Gaussian transducers have equivalent radius 3mm.

The focussing Gaussian transducers are measured by the sound field tested instrumentation and imaged by the acousto-light diffraction device, and compared with the usually plane transducers, the focussing plane transducers and the focussing Gaussian transducers of equivalent radius 4.8mm. The developed Gaussian transducers have better near field characterization than others. There appear none of the maxima and minima of acoustic pressure and reduce the minor lobes so as to improve the resolution of A&M mode ultrasonic diagnosis instrumentations.

BE15-E.6

A Novel Method for Pulse-echo Ultrasonic Tomography, W.C.A. Pereira and J.C. Machado*, COPPE/UFRJ-BIOMÉDICA, C.P. 68510, 21944-Rio de Janeiro-RJ, Brazil

A new method to obtain two dimensional map of ultrasonic wave speed is proposed. The method consists of insonifying a medium with an ultrasonic pulse and receiving the scattered wave on the same transducer used as transmitter and in another one placed aside. Each scatterer illuminated by the irradiated wave returns an echo to both transducers. Then by measuring the time of flight for each echo arrived on both transducers the position of each scatterer, related to the transmitting transducer, and the wave speed in the medium existent between consecutive scatterers can be obtained. Computer simulation of this method by transmission of an ultrasonic sine wave burst (pulse width of 5.12 μ secs and wave frequency of 2.5 MHz) through a medium consisting of polystyrene spherical particles (diameter varying from 0.6 mm to 1.0 mm) surrounded by water has provided encouraging results for the proposed method.

BE15-F.2

NON-INVASIVE ASSESSMENT OF VESSEL WALL PROPERTIES. R.S. Reneman*, T. van Merode and A.P.G. Hoeks. Depts. of Physiology and Biophysics, Univ. of Limburg, Maastricht, The Netherlands.

Multigate pulsed Doppler systems (MPDS) allow the on-line recording of velocity profiles in arteries and the relative diameter changes of these vessels during the cardiac cycle ($\Delta d/d$). From the width of the profiles the arterial diameter (d) can be assessed. From $\Delta d/d$, d and brachial artery pulse pressure the distensibility coefficient (DC) and cross-sectional compliance (CC) of the common carotid artery can be estimated (Reneman et al, *Ultrasound Med. Biol.* 12, 465-471, 1986). In 80 volunteers, DC and CC decreased linearly with age from the third age decade. DC and CC were found to be lower in young borderline hypertensives ($n=15$) than in normotensives ($n=13$), although blood pressure differences between these subjects were limited. The detection of local changes in arterial wall displacement in addition to that of flow disturbances improved the accuracy of the diagnosis of minor (<30% diam red) atherosclerotic lesions (diag acc: 95.3%; sens:90%; spec:90%). Since with the MPDS used displacement of the anterior and posterior wall cannot be distinguished, a technique based on phase tracking of the RF-signals, generated by the arterial walls, was developed. This method is simple and allows the separate recording of anterior and posterior wall displacement.

BE15-F.1

Effects of Ultrasound on Mammalian Gonads, F. Dunn*, Bioacoustics Research Lab., University of Illinois, Urbana, IL 61801, USA

There are circumstances in which human gonads have the opportunity to receive significant ultrasound exposures during clinical diagnostic and therapeutic regimes. Thus, studies were conducted to determine whether morphological alterations of male and female gonads can be produced by ultrasound as intensities approach therapeutic levels. Mouse testes and ovaries were exposed *in vivo* to 1 MHz CW ultrasound at spatial peak intensities in the range 2 to 100 W/cm^2 for times ranging from 300 to 1 sec. The gonads were removed surgically at times ranging from immediately following to 63 days post irradiation and prepared histologically for microscopic analysis.

The observed alterations in testis can be classified according to the number and type of affected cell layers in the seminiferous tubule. Leydig cells were unaffected. Spermatocytes are affected before the spermatogonia, contrary to the situation following ionizing radiation.

In the ovary lesions are manifested by pyknosis of the cells, vacuolization of cells and tissue, eosinophilic cytoplasm, and general cellular disruption. Increases in the amount of PAS positive material appeared in the interstitial tissue. Luteinized structures appeared to be preferentially altered.

BE15-F.3

Ultrasonic System for Noninvasive Measurement of Regional Elasticity of the Artery, K. Yamamoto*, T. Imura, T. Mikami and H. Yasuda, Hokkaido University, N13-W8 Sapporo, Japan.

To measure noninvasively the regional elastic properties of the artery, we have developed an ultrasonic system, which comprises an ultrasonic displacement meter, an echographic equipment and a personal computer. The displacement meter is designed to track pulsatile motion of the anterior and posterior walls of the artery at the proximal and distal sites and also designed to enable us to monitor easily a measured site on the display; therefore, even a deep vessel such as the aorta can be measured. From pulsatile diameter change, mean diameter and/or pulse pressure, the personal computer calculates the pressure strain elastic modulus E_p and regional pulse wave velocity PWV. E_p and PWV were measured on healthy subjects along the carotid, iliac and femoral arteries and the abdominal aorta. These measurements showed the progressive increase with distance to peripherals. Age-related increase in E_p of the abdominal aorta was also found in another series of measurement on 61 subjects. The system demonstrates the feasibility of noninvasive detection of atherosclerotic change.

BE15-F.4

Stump Tissue Stiffness Measurements of Above-knee Amputees Using Doppler Ultrasound, T. Krouskop, M. Malinauskas*, D. Winningham, J. Williams, Baylor College of Medicine, Houston, Texas.

Many problems for above-knee amputees stem from poor fit of their prostheses. At present the interaction of the residual limb with the socket is still not well understood. Characterization of live human tissue is difficult but is possible through mathematical models or non-invasive systems.

A Doppler ultrasound system was used to measure the stiffness of stump tissue in twelve above-knee amputees. Measurements were made at three locations on each stump: anterior, posterior, and medial. Both shallow (0 to 1.5 cm) and deep (0 to 3.5 cm) readings were taken. Results indicate that there are significant differences between shallow and deep readings, these differences being especially apparent at the anterior portion of the stump. However, no differences were detected among testing sites on the stump or between shallow and deep readings at posterior and medial areas.

General stiffness values can now be found with this system. Investigation into methods to increase location and depth sensitivity are ongoing.

BE15-F.6

In Vivo Frequency Response Measurements Using Ultrasound, M. C. Hastings, Georgia Institute of Technology, Atlanta, Georgia

A system using low-power ultrasound was developed to measure the in vivo frequency response of internal organs to a mechanical stimulus. The system has two focused ultrasonic transducers, a transmitter and receiver. The organ to be examined is placed within the crossed foci of the transducers and insonified by the transmitter. The phase modulation resulting from the response of the tissue to the external stimulus introduces sidebands about the ultrasonic carrier in the spectrum of the received echo. The localized displacement of the organ is determined from the ratio of the amplitudes of the carrier and the sidebands. The sensitivity and spatial resolution of the measurement primarily depend on the diameter, focus, and frequency of the ultrasonic transducers. Presently, 6.35 mm transducers operating at 20 MHz are being used to investigate the mechanics of auditory organs in fish. This system can detect 12 Angstrom displacements with a spatial resolution of 0.28 mm. Localized density variations within organs can also be determined using this dynamic measurement technique. Applications include distinguishing different types of kidney stones and identifying soft tissue tumors.

BE15-F.5

PRESSURE MEASUREMENT BY ANALYSIS OF RESONANT FREQUENCY OF ELASTIC MICROCAPSULES
K.Ishihara*, A.Kitabatake, J.Tanouchi, K.Fujii, M.Uematsu, Y.Yoshida, T.Nagakura, M.Hori, T.Kamada, M.Inoue, T.Tamura†, K.Chiharat, H.Abe†,
The 1st Dept. of Med. Osaka Univ., Osaka 553
†Fac. of Eng. Sci. Osaka Univ., Osaka 560
†Osaka National Hospital, Osaka 553 Japan

We have developed a pressure measurement system using ultrasound. The principle is that resonant frequency of elastic microcapsules in liquid shifts depending on the surrounding pressure.

Methods Pressure-sensitive microcapsules were made of vinylidenedichloride-acrylonitrile copolymer containing harmless gas. Microcapsules, classified into several classes according to the diameter, were injected into an airtight cistern. Ultrasound was projected from a transmitter driven by function synthesizer. We compared the changes of frequency spectrum of the ultrasound passing through microcapsules with the changes in pressure. Results 1)The frequency spectra showed marked attenuation in specific frequency, indicating resonance of the microcapsules according to the diameter. 2)The resonant amplitude in the frequency spectrum linearly changed with the pressure. 3)The resonant frequency also increased with the pressure.

Conclusion We have confirmed experimentally the potential of this new pressure measurement method using the resonant frequency of microcapsules.

BE16-A.1

Design Considerations for Auditory Prostheses
C. Finley, Research Triangle Institute,
Research Triangle Park, N.C. 27709 USA

In the past development of auditory prosthesis systems has followed largely an empirical path. Electrode designs presently available for human use incorporate features that were dictated by the constraints of mechanical construction and insertion the physical unit into the cochlea. Speech processor development has followed in a similar vein, being largely limited by the range of available technology that would ultimately permit wearable processors. These approaches have proven remarkably successful in some individual patients but have failed miserably in others. This presentation focuses upon the basic mechanisms of neural stimulation with intracochlear electrodes and seeks to explain the basis for dramatic performance differences among individual patients using the same prosthesis system in terms of variations in survival of neural elements within the cochlea. Design principles are discussed that allow a speech processing strategy to be tailored to the specific anatomical and physiological status of an individual patient. In addition, considerations for design of optimal electrode arrays are discussed.

BE16-A.2

A New Model of Extracochlear Prosthesis for the Profoundly Deaf, Y.Hirata*, T.Ifukube, J.Matsushima+ and N.Hoshimiya, Res. Inst. of Appl. Elect., +Medical School, Hokkaido Univ., Japan.

A new model of an extracochlear prosthesis that stimulates via an electrode superficially placed on the round window membrane of cochlea was proposed as a less invasive alternative to insertion in the scala tympani. We have developed a Pt-Ir stimulation electrode coated with polyvinyl alcohol gel that is proved to be biocompatible material. The electrode is suitable for the extracochlear prosthesis because it can tightly contact to the round window membrane without damage it. As for a speech coding method, we have proposed a new idea that the pitch signal and the second formant frequency could be transmitted simultaneously by combining those two signals. In this method, an additional stimulation pulse is inserted among pitch pulses and the time delay of the pulse from the pitch pulse is in proportional to the second formant frequency. Those time sequential stimuli were given to guinea pigs through the round window membrane using the coated electrode and compound action potentials from cochlear nerve bundle were recorded. In this report, the efficacy of the electrode and the speech coding method is evaluated based upon the experimental results.

BE16-A.4

Model Structure and Parameters Estimates for the Source Derivation of Auditory Brainstem Responses, S.Kahtoh*, T.Sekiya, M.Aruga, K.Yamazaki and M.Saito, * Teikyo University of Technology, 2289-23,Otani, Uruido, Ichihara, Chiba, Japan

To obtain significant findings on ABR generators, ABRs to sine wave stimuli, were recorded in 10 normal Ss. The stimuli ranged from 50 to 80 dB HL at between 0.1 and 1.0 KHz for more 512 responses, were given to both ears simultaneously. The responses within 10.24 ms, were recorded between the vertex and earlob with common grand at the frontal, and represented as a continuous curve in the complex plane in which separate plots for phase and vector length as function of frequency were shown. By using this result, we obtained the frequency characteristic of ABRs and used a fortran computer program to fit a linear transfer function to given frequency response magnitude and phase data. A conjugate search was used that minimizes the integral of the absolute value of the error squared between the model and the data. The transfer function model suggested that ABRs have three vectors as model parameters, which are proportional, derivative and second order lag element.

BE16-A.3

A Nonlinear Model for Kemp Echoes R. Newcomb*, P. Gómez and V. Rodellar University of Maryland, College Park, MD 20742 USA and Universidad Politécnica de Madrid, Madrid, Spain

Kemp Echoes are under investigation as a noninvasive means of characterizing and diagnosing damage to inaccessible parts of the ear. For this characterization signal processing techniques are used to set up a lattice digital synthesis filter from the Kemp Echo data. The parameters of the lattice are also determined in terms of the material properties of the ear. By comparing the two determinations of the lattice, structural anomalies of the inner ear can be isolated. Because second order effects are important to the interpretation of Kemp Echoes, nonlinearities become significant to this technique as a diagnostic tool. Nonlinearities due to membrane and fluid interactions within the ear are incorporated in the Kemp Echo lattice model presented.

Supported by NATO Grant 0395/87 and NSF Grant MIP 85-06924.

BE16-A.5

A Neuro-Synaptic Model of Pitch Perception with Auditory Memory, K. Itoh*, Facilt Med, Univ Tokyo, Tokyo 113, Japan.

A model of temporal information processing in the auditory system was presented on the basis of the interaction of fast synaptic potentials as well as slow synaptic potentials in order to analyze the mechanism of pitch perception of complex sounds.

In the model, the pitch was determined through five processes, i.e., the transduction of acoustic signals to cochlear microphonics, to fast synaptic potentials and to nerve discharges in the cochlea, the summation of the discharges in the cochlear nucleus, the extraction of the discharge periodicities in the inferior colliculus, the temporal-to-spatial translation of the periodicities by slow synaptic potentials in the medial geniculate body, and the determination pitches by picking local peaks in the auditory memory space of the integrated slow synaptic potentials in the auditory cortex. The model could explain the extraction and cancellation process of difference tones as well as synchrony suppression.

255

BE16-B.1

Computerised Analysis of Eye Movements,
G.O'Neill, University Hospital of Wales, Cardiff, U.K.

The simplest method of eye movement analysis is by direct visual observation whereby an evaluation can be made of gaze nystagmus, refixation saccades, slow pursuit movements and vestibular nystagmus induced by positioning, thermal and rotational stimuli. The degree of analysis possible however is clearly limited, e.g. thermally or rotationally induced vestibular nystagmus may be quantified by either timing the duration of the response or counting the number of nystagmic beats in a given time interval.

Following some notable publications in the 1950's, clinics became more aware of the advantages of the technique of electro-oculography in the assessment of vestibulo-ocular function with such measures as nystagmus amplitude, frequency and slow-phase velocity being available from the chart recording. The amount of information which may be extracted, even by this method however, is limited by constraints of the speed, accuracy and endurance of the human being. It may be argued that a computerised system of recording and analysis would provide not only a more detailed, but also a more standardised evaluation of eye movements than is possible by conventional means.

Because of the difficulty in programming a computer to deal with the analysis of weak and irregular nystagmic eye movements, most computer systems to-date incorporate a large degree of manual decision making. The ultimate system would be one which could analyse eye movements accurately without human intervention. This paper describes a fully computerised system with examples of analysis of refixation saccades and responses from thermal, optokinetic and rotational stimuli.

BE16-B.2

Smooth Pursuit Eye Movement Characteristics Depending upon Attention to a Moving Target, Y.Ebisawa*, H.Minamitani and M.Takase, Keio University, Hiyoshi 3-14-1, Yokohama, 223 Japan

It is considered that characteristics of human eye tracking movement are changeable by the level of subject's attention to a moving target. 256 pieces of LED were arranged horizontally in a line. The position of the target, only one lighted LED, was moved sinusoidally at 1 Hz, ± 10 degree by a micro-computer. Eye position signal was recorded by electro-oculographic technic. Target Brightness Feedback (TBF) method, which is one type of visual feedback methods, was developed in order to increase the attention. Under the TBF condition, the target comes to be darker when subject cannot correctly track it. He must track the target as accurately as possible so that the target does not turn darker. Under non-feedback condition, the target is always bright and the subject tracks the target as usual.

The characteristics of eye movement under the TBF condition were compared with those of non-feedback condition. Saccadic components were removed from total eye movements by our new algorithm. The gain of smooth pursuit movement to the target movement increased and the phase delayed when the attention increased by the TBF.

BE16-B.3

Electro-oculographic measurement of inter-saccadic latency in congenital nystagmus, G. Bosone, R. Reccia, G. Roberti, P. Russo*, University of Naples, I-80125 Naples, Italy.

We measured the frequency distribution of latencies of the quick phase of nystagmic eye movements in patients with congenital nystagmus (CN), from electro-oculographic (EOG) records of the oscillatory eye movements in eight patients. Since it is commonly accepted that the same non-defective oculomotor system controls the generation of both (normal) saccades and quick phase eye movements in CN, our measurements were considered as giving the distribution of inter-saccadic latencies in the range 0.1-0.6 s. For each patient, we recorded a 3-4 s long EOG, repeating each session 22 times. The average inter-saccadic latency was computed for each record, by evaluating the peak time-frequency of the EOG spectrum with digital power spectral methods. The frequency distribution of these average latencies is peaked at about 220 ± 40 ms, with a gaussian-like shape.

BE16-B.4

Three Dimensional Measurements of the Ocular Fundus and Evaluation of the Papillary Excavation in Glaucomatous Eyes, T.Yoshimura*, H.Nakatani and N.Suzuki, Faculty of Eng., Kobe Univ., Rokko Nada, Kobe 657, Japan

Vertical and equidistant parallel grating lines are projected onto the ocular fundus from right side of pupil and a set of stripes reflected into the normal direction by the fundus is recorded with a TV camera. The deformation of the detected grating images gives the depth of the excavation on the ocular fundus. In order to accurately detect the grating image, we have used a new method, which subtracts two fundus images before and after shifting the projected gratings by a half period. By using this technique, the background noise due to blood vessels on the images is removed and only the grating images have been detected. From the deformation of the each stripe of the accurately detected grating image, we evaluate three dimensional distribution of the ocular fundus, the depth of the optic disc and cup-disc ratio. In glaucomatous eyes with visual field changes, the excavation starts in the retinal area and the corresponding rim is destroyed. We discuss that the glaucomatous visual field changes is dependent on the excavation showed above.

BE16-B.5

Development of a micromachined transensor for monitoring of intraocular pressure

Y Lindén†, B Hök, L Ejdesjö, L Tenerz, Electronics Department, Institute of Technology, University of Uppsala, Box 534, S 751 21 Uppsala, Sweden, B Svedbergh, Institute of Ophthalmology, Academic Hospital, S-750 14 Uppsala 14, Sweden.

Nontraumatic, continuous monitoring of intraocular pressure is an important, as yet unsolved problem, in several states of disease, including glaucoma. We suggest for solving this problem, the utilization of a passive transensor, consisting of a resonant capacitive-inductive network, in which the resonance frequency is a function of pressure. We show that such a passive transensor can be integrated with an artificial lens without impairing normal seeing and be implanted in the eye without trauma. Monitoring of the resonance frequency can be performed by means of microelectronic circuitry encased in eye-glasses. In this paper, the technology of transensor fabrication is presented, using micromachining techniques, like photolithography, deposition, etching and anodic bonding. This results in excellent performance, high reproducibility, and low cost. Data on prototype performance compared with theoretical estimations are given.

BE16-C.1

Dynamic Analysis of Accommodation and Pupil Diameter under the Natural Viewing Condition, F. Okuyama*, T. Tokoro, K. Yana and M. Nagayama, Tokyo Medical and Dental University, Tokyo, Japan.

Accommodation, the the focusing system in the human eye, and changes in pupil size occur together. This is similar to a camera when focusing and diaphragm size change together. It is considered that these two functions in the eye occur together in order to perceive a clear visual image and maintain it. This dynamic relationship has been widely discussed in the literature.

We measured accommodation by infrared optometer and pupil diameter by TV infrared pupilmeter simultaneously under natural binocular viewing conditions while viewing a stationary actual target. Fluctuations of accommodation and pupil diameter were analyzed by cross-correlation function and cross-spectrum using an FFT (Fast Fourier Transform) signal analyzer (SM-2100, IWATU Electric Co.). The results yielded a minus correlation between two fluctuations. This demonstrates that pupillary constriction occurs with a decrease of accommodation resulting in a deeper optical depth in the human eye.

BE16-B.6

An approach of early glaucoma detection
Yin Chang*, Institute of Biomedical Eng.
National Yang Ming Medical College
Yao-An Fu, Chang Gung Memorial Hospital
Taipei, Taiwan, Republic of China

Can glaucoma be early detected? Color sensation test may provide a valuable indication of early glaucoma symptom which the glaucoma suspects are not aware. A 4-channel, 12-bit precision light intensity and computer controlled, anomaloscope employed Moreland's color match equation is built to give the color sensation test at Chang Gung Memorial Hospital in this study. The result shows the glaucoma patients and some glaucoma suspects have "blue shift" of match point and have a wider matching range than the normal observers.

BE16-C.2

Eye Length Measurement by Laser Interferometry

A.F. Fercher*, Universität Wien, A-1090 WIEN

If the pupil of the eye is illuminated by a collimated laser beam the reemitted light exhibits fringes similar to the well-known Newton's interference fringes. Using this phenomenon together with an adequate interferometric technique we have been able to measure the optical length of the eye with a precision of .03 mm. The geometrical eye length was obtained from the interferometrically measured optical length by using an average refractive index according to Gullstrand. A series of in vivo measurements of several human beings shows a good correlation with the acoustically determined eye lengths. This technique is noninvasive and no additional means such as anesthesia are needed. The high transversal resolution of this technique may lead to additional possibilities, e.g. the measurement of the surface profile of the fundus.

387

BE16-C.3

A Finite Element Model of Radial Keratotomy Surgery, R.P. Vito,* J.W. Shin, Georgia Institute of Technology, Atlanta, Georgia; B. McCarey, G. Waring, Emory University, Atlanta, Georgia.

Though radial keratotomy is commonly used by surgeons to correct refractive errors, the mechanical basis for the surgery is not well understood. The immediate surgical outcome is determined only by mechanical factors while, in the long term, other effects, such as wound healing, are important. Accordingly, we have used a finite element based model of the cornea to simulate the effects of various surgical and physiological parameters as well as surgical errors on corneal curvature.

Results indicate that incision length and depth are important determinants of surgical outcome; a fact consistent with clinical observations. The effects of surgical errors, such as incisions of unequal depth or length, were surprisingly small.

BE16-C.5

Use of a Programmable Remapper as a Potential Aid for Patients with Visual Field Defects, David S. Loshin*, University of Houston, College of Optometry and Richard D. Juday, Tracking and Communications Division, NASA Johnson Space Center, Houston, TX

A Programmable Remapper which is a digital image processing machine of unique design and function has been developed at NASA, Johnson Space Center. The Remapper is designed to perform coordinate transformations in real-time on video images. The original intent of the Remapper was to simplify some aspects of pattern recognition in video imagery. NASA's interest arises from problems in automated tracking and docking of spacecraft and in autonomous landings on Mars. The Remapper's potential application to human low vision became apparent early in its development. In cases of ocular pathology that result in retinal field defects such as retinitis pigmentosa and macular degeneration, portions of the visual space are lost. The Remapper can warp displayed images so that they fall onto viable retina and thus provide information that would otherwise not be perceived. We have developed and will report on algorithms for several types visual remappings using an image processor (with static images) to demonstrate the concept.

BE16-C.4

COMPUTER AIDED VISUAL FIELD DIAGNOSIS
G.C.Filligoi*, L.Capitanio, N. Accornero

Visual Field (V.F.) analysis is widely used in clinical practice for the important informations it provides in neurologic and ophthalmic pathology.

In the last years many computerized devices have been set-up in order to achieve better results, but their purpose is mainly concerned on collecting data and presenting a map of the results.

In our project we developed first a system for collecting V.F. data using a standard IEM-XT computer with a black and white monitor for presentation of the light stimuli. For the analysis of the field we developed a dedicated software using techniques of image processing for extraction of scotoma's features (i.e., shape, size, position, etc. of V. F. losses) and recognition of other typical field defects.

Afterwards, a procedure for the analysis of the logical sequence used by the neurologists to set a diagnosis on the basis of the V.F. data have been implemented.

The decision tree which models this strategy parallelly drives the acquisition of the proper features automatically extracted from the data.

Our preliminary results confirm both validity and reliability of the parameters used in V.F. automatic analysis.

BE16-C.6

The Limits of The Man-Machine Interface With Respect to the Visual System.
H. Pichler, F. Pavuza, G. Beszedics, Tu Wien, A-1040 Vienna Austria

In the field of medical instrumentation a state of the art man-machine-interface includes, in most cases, a cathode ray tube (CRT). Alphanumeric displays, combined with picture processing offer a powerful information system to the user and are commonly applied in the field of measurement systems, system operation and state control.

The visual part of the cognitive system offers a measurable overall modulation transfer function. (MTF), which is a combination of both the MTF of the CRT and the human eye. The MTF of the CRT's screen depends on the type of screen (monochrome or color, the latter one characterized by the type of implemented shadow-mask). Both functions must be intelligently combined to obtain an optimized MTF for the overall system, or to adapt the screen parameters to the characteristics of the human eye.

The paper describes the MTF of a typical human eye, its approximation, and the MTF of the different CRTs. In addition, the recommended parameters for displays working with commonly used TV and HDTV-systems are given.

388

BE17.1

Biodynamic Response Determination to Transitory Acceleration, Paul H. Frisch*, Frank Lambert, Applied Physics Inc, 31 Highview Avenue, Nanuet NY 10954

Transitory acceleration profiles experienced by military pilots during air combat maneuvers (ACM), emergency egress, and crash/impact events have demonstrated significant performance limitations, during ACM, and injury potentials ranging from mild trauma to death. Research efforts addressing methods of enhancing pilot physiological acceptability and limiting injury mechanisms, have focused on dynamic simulation of pilot/crew station interaction during transitory and sustained acceleration. Simulation via human analogues, such as anthropomorphic manikins dynamically and mechanically simulate human response, while loading the ejection seat and crew station as would the human counterpart. Dynamic manikin testing provided detailed insight to potential injury mechanisms and provide a criteria for evaluation and comparison of complex aircraft escape systems and crew stations. The ability to measure the three dimensional biodynamic response of a human surrogate, predicts the focus and G-loading the pilot will experience. Detailed knowledge of this environment enables new protective devices (G-suits, reclining seats) and modified crew stations to be developed reducing the physiological stress imposed on a pilot. The presentation will focus on manikin development simulating human biofidelity and response, and instrumentation techniques enabling the measure of the six degree of freedom response of the manikin.

BE17.3

PORTABLE GAIT LABORATORY: PRELIMINARY RESULTS, D. Aronson, H. Kang*, V. Musselman, and A. King, Department of Orthopaedic Surgery, Wayne State Univ. School of Medicine, Detroit, Michigan, U.S.A.

The gait analysis laboratory has evolved from a research tool to a clinically accepted modality for studying children with neuromuscular disorders. Current gait analysis laboratories are expensive and require considerable space. This study was undertaken to compare the early results of our portable gait lab with existing gait analysis laboratories. Five children between 7 and 10 years of age were studied with the portable gait lab. The lab consists of shoe-borne load cells, portable data acquisition system, SP2000 motion analysis system, and a personal computer. The shoe-borne load cells were used to collect three-dimensional ground reaction force data. The SP2000 system was interfaced with a personal computer to record three-dimensional kinematic data from the hip, knee, ankle and foot. The results revealed that cadence, stride length, and walking velocity were slightly less than that previously published by conventional gait laboratories. By contrast, the ground reaction forces, joint range of motion, and EMG's correlated very closely with previously published data. The portable gait lab provides ground reactive data from multiple steps, which is a major advantage over conventional laboratories.

BE17.2

CINEMA-1.C AND DYNAMIC GAIT ANALYSIS

Pelisse F.¹, Geiger D.^{2*}, Marie F.¹
 (1) Centre d'Etudes et de Recherches de l'Appareil Locomoteur - 94460 VALENTON
 (2) Laboratoire de Mécanique Physique, Université Paris XII - 94010 CRETEIL (FRANCE)

Computation of the forces applied to the hip, knee and ankle joints during human locomotion requires the knowledge of ground reaction and kinematics. This study presents a method which provides a graphic representation of the load applied to the lower limb joint during the stance phase of the walk.

The use of a force-plate (0,8 x 0,3 meters), on line with a computer allows the quantification of the resultant force of the pressure exerted between foot and ground. In order to record the spacial-temporel evolution of the geometrical center of the joint, a small incandescent lamp is externally located on the virtual axis of flexion of the joint. The position of the lamp relative to the force plate (external boundaries) is measured by means of two linear C.C.D. cameras (1728 cells - 13x13 µm). Camera lens of 50 mm and 135 mm are used for measurement in sagittal and frontal plane respectively. An additional hemi-cylindrical lens is set inside the body camera in order to magnify the size of the vertical field. The force-plate and kinematic data are recorded every 0,01 second during the stance phase of the gait cycle. During the computation of analysis of the joint force transmission, a parallax correction is performed.

A mathematical model similar to Harrington's one is used for simulation of the biological structure of the knee.

BE17.4

VAT - Vestibular Autorotation Test - in the clinic and in weightlessness. A. Månsson* and S. Vesterhauge University Hospital Copenhagen, Denmark.

Vestibular ocular reflex (VOR) both vertical and horizontal is tested during voluntary head oscillations. Testing the vestibular function in the frequency range 2-6 Hz is possible without the need for expensive turntables. Head movements are recorded via an angular rate sensor. If corresponding compensatory eye movements are coded via superficial electrodes. Anticomensatory eye movements and visual interference are avoided by using stimulus frequencies above 2 Hz. Auto calibration of the eye signal level is performed using 0.5 Hz head rotation with the eyes fixating a distant point. The VOR transfer function is determined using cross power spectral analysis. Head rotations are guided by a frequency modulated sound signal.

The test have been used both in the clinic to evaluate patients and in space research related parabolic flight experiments, latest in NASA's KC-135 aircraft. Transfer function parameters are stable and reproducible and the utilization of the test in otoneurological patients is promising.

359

BE17.5

THE VARIABILITY OF A SIMPLE LEARNED MOVEMENT

R.L.G. Kirsner* & E. Byrne. St. Vincent's Hospital, Fitzroy, Victoria. 3065. Australia.

Learned ballistic movements executed in response to visual cues display considerable variability. Far from being an artifact, the variability is a fundamental part of the response and provides a measure of the central control of muscle activity.

Step shifts in the position of a vertical line on a video monitor were corrected by rotation of a subject's forearm. Rotation, angular acceleration, biceps and triceps emg were recorded on a computer. The acceleration waveform has been found to provide a very sensitive and quantifiable measure of response variability.

Limited patient studies have shown that in cerebellar dysfunction, the acceleration amplitude is considerably decreased while the variability and time course of the movement are much larger than normal.

From a clinical viewpoint, this technique can provide considerable insight into abnormal central integration of ballistic movements. It may also suggest treatment strategies useful in rehabilitation as well as providing an objective assessment of recovery.

BE18-A.1

Fiber-wrapped Chambers for Computation of Three-dimensional Blood Flow in the Heart. D.M. McQueen* & C.S. Peskin, Courant Institute of Mathematical Sciences, New York, USA.

The goal of our project is the computer prediction of three-dimensional flow patterns of blood in the chambers of the heart. Our computational approach is based on the fiber-oriented method which we have employed successfully in two dimensions. Detailed dissections of the paths of muscle fibers in animal hearts (by other researchers) have revealed a complex pattern of trajectories on nested toroidal shells contained in a basket-like sheath. Before attempting to construct a model of the heart, we have computed flows in some simpler three-dimensional structures. We have constructed a torus by means of a network of closed elastic fibers which make several turns about the torus lumen while making one circumferential turn. In this setting we have studied the flow resulting from the passive relaxation of an initial bulge in the torus and the peristaltic flow resulting from a wave of muscular contraction circulating around the torus. The results from this latter study compare well with a simple linear theory.

We are now constructing a whole heart model employing fibers which follow geodesic paths on a number of relatively simple geometric shapes.

BE17.6

Analysis of Self-Induced Hand Oscillation as a Model of Physiological Tremor
A. Watanabe*, K. Goto, and M. Saito, Institute of Medical Electronics, University of Tokyo, Tokyo 113, Japan.

Tremor is expected to provide neurological information if its mechanism is fully understood. The objective of the present study is to establish the mathematical model of physiological tremor based on the oscillation characteristics of the hand.

The two-reflex-loop model is proposed, which is composed of the mechanical system and the spinal and supraspinal reflex loops. The most important parameter in the model is the gain ratio of the two reflex loops. Two types of measurements are performed: slow relaxing movement and posture maintenance. In the former experiment reflex oscillation characterized by the double-line spectrum is induced separately from mechanical oscillation. In the latter the relationship between the acceleration and EMG is investigated by the Fourier analysis. The physiological parameters estimated agree well with those reported in the literature. The diversity of frequency change of physiological tremor can be attributed mainly to the change in the loop gain ratio.

BE18-A.2

Theoretical modeling of the coronary circulation, C. Guiot*, C. Cancelli, T.J. Pedley and P.G. Piantà, Dip. Anatomia e Fisiologia Umana dell'Università di Torino, Corso Raffaello 30, I0125 Torino, Italy.

A model of the left coronary circulation as a network of collapsible vessels mimicking the microvascular compartment can satisfactorily reproduce the coronary flow rate, provided a distributed, one dimensional, separation free, viscous flow theory is assumed for each vessel.

Any simpler representation, amounting to a lumped model of vessel resistance and compliance, as some workers have proposed, cannot reproduce the observed waveforms. The reason is that the scale for time variations of the transmural pressure in early and late systole is too short in comparison with the time scale defined by the system elasticity for wave propagation effects to be ignored. Both a distributed and a lumped model have been worked out in detail, showing that for a given range of physiologically sensible parameter values the first one can realistically simulate the main features of the coronary flow waveform, while the latter exhibits unobserved artifacts and disturbances.

BE18-A.3

Model Prediction for the Interactive Forces Between Contracting Myocardium and Coronary Vessels,
Y. Lanir* and E. Nevo, Technion-Israel Institute
of Technology, Haifa, 32000, Israel

Mechanical interactions between contracting myocardial tissue and intramyocardial vessels has a dominant effect on the coronary flow. Previously proposed models of the coronary circulation have considered the isotropic intramyocardial tissue pressure (IMP) as representing these interaction forces. Morphological studies have shown however, that intramyocardial vessels are attached to neighboring myocytes by a dense network of collagen struts. Hence the force exerted on each vessel is the sum of contributions from the isotropic hydrostatic pressure of the interstitial fluid and from the anisotropic solid stress of the collagen. The latter contribution depends on the specific orientation of each vessel.

Experimental evaluation of intramyocardial solid stress is not possible, but it can be evaluated from theoretical stress analysis. Recently a structurally based myocardial material law has been developed in our laboratory and applied in a model of the left ventricle. Simulation of the whole cardiac cycle resulted in histograms of stress and pressure fields which lead to evaluation of the forces exerted on each vessel as a function of its location in the wall and orientation. These results will be presented and discussed in terms of their relevance to the coronary circulation.

BE18-A.5

A Mathematical Model of Reactive Hyperaemia,
S. W. Smye*, M. I. G. Bloor[†], Medical Physics Dept
St. James Hospital, Leeds LS9 7TF, UK. [†]Applied
Maths Dept. Leeds University, Leeds. UK.

Reactive hyperaemia, the increase in blood flow after a period of circulatory occlusion, involves a variety of vascular control processes including metabolic, myogenic and passive factors.

The role of a pressure-related change in vascular resistance, due to the myogenic response, has been considered in detail using a tube model of the limb arterial system. The equations describing the flow, local pressure p , and cross-sectional area of the tube S , include a relationship between S and p (myogenic response) the form of which is constrained given that p should evolve in a stable manner. Independent experimental justification is available.

The solutions describe flow which rises, within 5s of occlusion release, to a peak of approximately 10 times resting flow, decreasing to normal over the following 30-60s. These results are consistent with venous occlusion plethysmography and isotope clearance methods. The model predicts that the flow variation is principally due to the changing pressure-gradient and not to the relatively small change in S . The model clarifies the role that myogenic responses may play in reactive hyperaemia.

BE18-A.4

Coronary pressure-flow relation after transition from blood to Tyrode perfusion in the maximally dilated diastolic cat heart, L.C. van Dijk, R. Krams, P. Sipkema and N. Westerhof[‡].
Vrije Universiteit Amsterdam, PO Box
7161, 1007 MC Amsterdam, The Netherlands

In 6 isolated, diastolic arrested, maximally vasodilated cat hearts, we studied changes in coronary pressure-flow (P-F) relations (with zero flow pressure intercept, P_{int}) after a change from blood to Tyrode. The pressure-flow relations were fitted with a mathematical model: $P_0(1 - \exp(-F/F_0)) + k \cdot F + P_{int}$; P_0 , F_0 , k and P_{int} are model parameters. P_{int} (in kPa, mean \pm SD) changed from 2.0 \pm 0.94 during blood perfusion, to 2.5 (\pm 0.55), 2.6 (\pm 0.68), 2.5 (\pm 0.94), and 2.7 (\pm 1.34), during Tyrode perfusion for 2:15, 5:30, 10:30, and 25:00 minutes, respectively. Resistance (defined as the ratio of perfusion pressure and flow at 10 kPa perfusion pressure) steadily rose to about 170% of the value during blood perfusion. The observation that the apparent intercept pressure is maintained, when a particle free (Newtonian) perfusate is used, may indicate that this intercept is not a result of blood rheology alone. The increase in resistance with decreased perfusate viscosity, suggests an effect of edema, which increases interstitial volume at the expense of intravascular volume.

BE18-A.6

**TRANSCORONARY DENSITY TRANSPORT
FUNCTIONS OBTAINED BY ITERATING
THE CONVOLUTION INTEGRAL**
E. Gallasch*, T. Kenner, Universität
Graz, A-8010 Graz, Austria

During transition of a bolus of indicator fluid through a network of arteries, capillaries and veins, a series of events influences the variation of the time course of the concentration of the indicator bolus.

A usual descriptor for the transition of an indicator through a vascular bed is the transport function $h(t)$. Because its nearly impossible to produce an ideal impulse injection on the upstream side we have developed a model adjustment technique for the calculation of the transport functions from the up- and downstream curves. The square error (difference between model and measured output) is minimised iterative by the steepest decent technique.

As a result we show that this method exhibits some advantages (stability against observational errors and additional noise) over usual methods via fourier transform or numerical deconvolution.

BE18-B.1

Evaluation of blood velocities in ventricular and atrial coronary circulations by three different means of access using a laser Doppler method, F. Kajiya*, Department of Medical Engineering, Kawasaki Medical School, Kurashiki, Japan

A laser Doppler velocimeter(LDV) with an optical fiber has been demonstrated to be useful for measurements of the coronary circulation. Using LDV, we took three means of access to the vessels according to the difference in measuring objects: (1)Large epicardial coronary artery and vein. We inserted the fiber from the side wall into the vessel with an aid of a cuff. (2)Relatively small artery and vein of which wall is transparent to laser beam:we measured the velocity noninvasively to the vessel by placing the fiber tip on the surface of the vessel. (3)Intramyocardial artery and vein:we inserted the fiber into the vessel from the vascular portion just penetrating into myocardium. The velocity profiles across the vessels as well as the velocity waveforms near the central axial region in the circumflex coronary artery and the great cardiac vein were measured by the first access. The small artery and vein velocities on the left atrium were measured by the second access. The velocity waveforms in the deep septal artery and in a small intramyocardial vein were evaluated by the third access. The characteristic of the velocity in each vessel will be discussed as well as possible causes of the velocity waveform.

BE18-B.3

Fluid Dynamic Differences Between Smooth and Irregular Coronary Stenoses: Their Implications In Lesion Progression, A Churchill*, D Abouelnasr, D Giddens, S Jones, Carlyle Fraser Hrt Ctr/ Crawford Long Hosp of Emory U, EUSH, Dpt of ME, GA Inst of Tech, Atlanta, GA

The pathology of a coronary intimal plaque is causally related to the rate of its progression to total occlusion. Complex plaques are more likely than simple plaques to occlude rapidly. On angiography, complexity corresponds to luminal irregularity (LI). The purpose of this work is to assess fluid dynamic factors of stenoses which might explain these observed differences. Models of 90% cross-sectional area reduction stenoses were constructed based on angiographic measurements of coronary arteries. Four models were made simulating lesions with and without LI. These models were placed in a steady flow circuit. Reynolds numbers (Re) from 25-200 (simulating various points in the cardiac cycle) were utilized. Flow visualization was attained by illumination with laser light. Laser Doppler anemometer (LDA) measurements were made at various locations in each model. Conclusions: Flow through all four models remained laminar through the range of Re tested. There were no major differences in the primary flow features between the models with and without LI. However, in the irregular lesions, small recirculating zones occurred in the concave portions of the lesion downstream of the stenosis throat. This is a common location of platelet deposition in complex intimal plaques.

BE18-B.2

Skewness of Profiles of Velocity in the Coronary Arteries of Dogs, David R. Bell*, Hanl N. Sabbah and Paul D. Stein, Henry Ford Heart and Vascular Inst, 2799 W. Grand Blvd, Detroit, MI

Multiple range gate Doppler velocimetry was used to examine the velocity profile within the lumen of the left circumflex (L. circ) and left anterior descending (LAD) coronary arteries of 10 anesthetized open-chest dogs at rest, after propranolol and after intracoronary adenosine. Profiles of velocity during peak diastolic flow were skewed toward the outer walls of the vessels ($P < 0.007$). The extent of skewness was not affected by propranolol or adenosine. Shear rates were significantly lower along the inner wall in comparison to the outer wall under all conditions, both in the L. circ and LAD coronary arteries ($P < 0.017$)

	SHEAR RATE (sec ⁻¹)			
	L. Circ		LAD	
	Inner Wall	Outer Wall	Inner Wall	Outer Wall
Control	428+70	597-99	354+65	640+61
Propranolol	256+39	596+108	306+59	419+81
Adenosine	1150+330	1990+526	1131+287	1781+318

In conclusion, irrespective of the levels of flow, the velocity profiles were skewed toward the outer walls of the coronary arteries. Consequently, the shear rate was lower along the inner wall.

BE18-B.4

Wall Shear Stress Calculations for Human Coronary Arteries, H.M. Olsmats*, R. Hostenstein, W.A. Seed and R.M. Nerem, Georgia Institute of Technology, Atlanta, GA., 30332-0405, U.S.A.

Estimates of wall shear stress in the human left epicardial coronary arteries have been carried out using a computer model of the coronary circulation. Pressure and flow are calculated by employing the one-dimensional continuity and momentum equations for flow with friction. The geometry of the left main (LM), the left anterior descending (LAD), and the left circumflex (LCFX) coronary arteries was taken from measurements on human post-mortem casts, and the input pressure waveforms were digitized recordings of aortic and left ventricular pressure from humans. Shear stress as a function of time was calculated, using the method of Benson et al. (Cardiovascular Res., 10:568-576, 1980), for the LM, the LAD-LCFX bifurcation, and at various positions along the LAD and the LCFX. Both fully developed flow and entrance effects were taken into account. The general range of wall shear stress was found to be from 0 to 50 dynes/cm², with peak shear stresses occurring in the entrance region of the LM. Negative shear stress values were observed, particularly in the distal portions of the LAD and of the LCFX.

BE18-B.5

Coronary Circulation Under High Sustained Gravity, S. H. Zhou, E. M. Collins and R. Collins*, Technical University of Nova Scotia, P. O. Box 1000, Halifax, Nova Scotia (Canada B3J 2X4).

When pilots of jet combat aircraft execute operational manoeuvres, large angular accelerations are produced which cause blood to drain from the brain and heart toward the feet. We wish to develop a mathematical model for the coronary circulation in such an accelerative environment, with a view to improving our understanding of the cardiac performance of jet pilots. The governing equations of motion will contain not only terms related to these accelerative forces, but also incorporate active neural control of the vascular calibers and heart rate. A quasi one-dimensional unsteady flow model will be presented along with preliminary calculations of the pressure and flow fields under a variety of operating conditions.

BE18-C.1

Quantitative Assessment of Blood Velocity Characteristics with Doppler Ultrasound

D.P. Giddens*, R.I. Kitney & S.A. Jones
Georgia Institute of Technology and
Imperial College of Science
and Technology

Doppler ultrasound measurements of blood velocity must be derived from the frequency content of the Doppler signal. However, several factors contribute to a smearing or broadening of the spectral content, so that velocity estimation can be difficult under certain circumstances. Spatial gradients, temporal changes, turbulence and the method of spectral estimation can all result in uncertainty in velocity estimation. In particular, the requirement of obtaining good frequency response in the measurement of temporal variations in velocity is directly at odds with the requirement of securing velocity resolution. Experimental data will be presented which illustrate these points, and the application of autoregressive/maximum entropy methods to velocity and spectral estimation will be discussed by way of examples taken from both laboratory measurements and human studies.

BE18-B.6

A noninvasive method for the three dimensional image of coronary artery, Tetsuo Okamura^{1*}, Naoki Suzuki¹, Zenji Nakano², Michihiko Matsui³, Tsuneo Suzuki⁴, Sachio Ikawa⁴, ME Research unit¹ Dept. of Pediatrics² Dept. of Cardiosurgery³ Dept. of Laboratory medicine⁴ Jikei Univ. School of Med. 105 Minato-ku Tokyo, Japan

We developed a method for the three dimensional (3D) visualization of coronary arteries using ultrasonic two dimensional (2D) echogram. The system for this method consisted of an ultrasonic 2D echograph to get the images of an aimed vessel and a computer graphics system which reconstructs 3D image of the vessel. In order to collect transversed images of the coronary artery we applied ECG triggering and image processing technique. Because the coronary artery moves with the pulsation of the heart and its location from the surface is too far to get a clear image. A probe was placed in the 2nd or 3rd intercostal space. Successive images are taken by moving the probe to the direction of distal part of coronary artery. In our experiments, we came to the conclusion that the 3D model using coloring and shadowing gave a clear view of the shape and the structure of vessels. Especially in case of aneurysmal dilatation, the change in wall thickness and distribution of plaques in the vessel can be visualize, where the angiographic method can not provide us with these informations.

BE18-C.2

Evaluation of Human Coronary Flow Dynamics in Health and Disease by 80 Channel 20 MHz Ultrasound Pulsed Doppler Velocimeter, Y. Ogasawara*, K. Mito, S. Matsuoka, S. Kanazawa, K. Tsujitoka and F. Kajiya, Kawasaki Medical School, 577 Matsushima, Kurashiki, Japan

Human coronary blood flow velocities (the left anterior descending coronary artery (LAD)) were measured by the 80 channel 20 MHz ultrasound pulsed Doppler velocimeter developed in our laboratory. The depth resolution of our system is 0.2 mm and the sample volume for each sampling point is $\pi \times 0.5^2 \times 0.2 \text{ mm}^3$. Doppler signals from 80 channels are detected by a zero-cross method and a signal from an optional channel is analyzed by a fast-Fourier transform method, both in real time. With this method, we have been able to analyze detailed blood velocity profiles across vessels, as well as velocity distribution (spectrum) in a sample volume. Two type of probe was designed to measure different objects: A cuff type probe was used for velocity measurements of a bypass graft and a plate-type probe holder was used for the measurements of the native LAD. In the post-stenotic region of the LAD, the velocity waveform was systolic predominant and the velocity profile was irregular with wide spectrum, while the velocity patterns became normal, i.e., diastolic predominant immediately after graft operation. The coronary artery velocity also changed significantly after aortic valve replacement in the patient with the valve disease, i.e., from systolic to diastolic predominant.

BE18-C.3

FREQUENCY DOMAIN DECOMPOSITION OF FLOW VARIABLES UNDER PULSATILE FLOW CONDITIONS
Baruch B. Lieber, State University of New York at Buffalo, Department of Mechanical and Aerospace Engineering, Buffalo NY 14260.

Concern over turbulence-induced hemolysis has led numerous hemodynamicists to measure the effects of fluctuating stresses on red blood cells. Although many agree that turbulence may cause hemolysis and reduce durability of red blood cells, there is no agreement upon neither the magnitude of turbulence stress levels nor the duration of their application required for cellular damage. Since pulsatile flows in hemodynamics occur at fairly moderate Reynolds numbers, flow patterns may wax and wane and may include coherent structures and oscillations of distinct frequencies in addition to turbulence, resulting in nonstationary phenomena. The frequency domain approach, based on the transformation of the unsteady Navier-Stokes equations into the frequency spectrum, provides a method to discriminate between small scale (cellular) turbulent stresses and large scale (inertial) stresses induced by coherent fluctuations. Flow variables are separated into a pulsatile trend, coherent fluctuations and random variations. Decomposition of a variable into its constituents is achieved using pattern recognition and frequency domain filtering for the pulsatile trend, matched filtering is then applied to discriminate between turbulence and coherent structures.

BE18-C.5

3D Solid Modelling of Arterial Structures Using Ultrasound.
R I Kitney, Department of Electrical Engineering, Imperial College, London SW7 2BT, UK.

There is now considerable interest in the use of three dimensional modelling techniques for the study of arterial structure. The primary motivation of this work is the development of new diagnostic techniques for arterial disease. The majority of modelling methods developed to date have used a wire modelling approach. The work which will be presented in the paper uses full voxel space to create 3D solid models of high quality.

The paper will also describe the application of these methods to ultrasonic imaging of arteries. The results of clinical trials will be presented in which 3D solid models of arterial structures are compared with pathological slides of the same structures.

BE18-C.4

Measurements of Blood Flow by MRI
John Gore*
Yale University Medical School
New Haven, CT

Developments in Nuclear Magnetic Resonance imaging have provided powerful new methods for probing vascular anatomy and detecting various types of blood flow phenomena. Methods are also under development for quantitation of blood flow in major vessels, in steady as well as pulsatile conditions, and for estimating perfusion at the capillary level. A variety of techniques are being evaluated. Vascular architecture may be studied in cross-sections at various angles using the multiplanar capacity of MRI, while projection images obtained by subtraction techniques give images much like conventional angiograms. Flowing materials give rise to signal alterations in MR images that depend on their velocity, acceleration or higher moments, as well as their precise spatial and temporal patterns. Paramagnetic contrast agents or other blood pool labels can also be used to study perfusion effects. Various methods have associated problems or artifacts that are under active investigation, but the potential nonetheless exists to develop relatively precise flow measurements non-invasively in deep structures using standard conventional MRI equipment.

BE18-D.1

Blood Flow in the Heart and Large Vessels,
M. Sugawara, The Heart Institute of Japan,
Tokyo Women's Medical College, 8-1 Kawada-cho,
Shinjuku-ku, Tokyo, 162 Japan

Various systems for measuring the pressure and velocity of the blood have been developed, and a considerable amount of experimental and clinical data are now available. The introduction of the hot-film anemometer with its high spatial resolution and frequency response has greatly extended our knowledge of the blood flow in the aorta. Here, we describe the development of flow and transition to turbulence in the aorta in dogs. Turbulence in the cardiovascular system can also be detected with clinically used devices, such as the multi-sensor catheter. The so-called "anacrotic notch" is analyzed in relation to transition to turbulence in cases with aortic or pulmonary stenosis. Blood flow in the left ventricle can also be measured with a multi-sensor catheter. The interaction between the swirling motion generated by the inflow from the atrium and an aortic regurgitation during diastole is analyzed. Compared with the diastolic flow-pattern, the systolic flow pattern in the left ventricle is rather simple. However, prior to the major ejection wave of the blood velocity and posterior to the P wave of the ECG, there is a spiky velocity wave. The cause of this spike is analyzed.

BE18-D.2

Analysis of the flow field in a 3D-model of the carotid artery bifurcation, C.C.M.Rindt[†], A.A.v. Steenhoven, A.Segal, R.S.Reneman and J.D.Janssen, Eindhoven University of Technology, Postbus 513, 5600 MB Eindhoven, The Netherlands.

To obtain insight into the complex flow patterns in the human carotid artery bifurcation, steady flow in a rigid 3D-model was analysed by finite element calculations based upon a standard Galerkin-formulation of the complete Navier-Stokes and continuity equation. These calculations were performed at physiological Reynolds numbers and validated with laser-Doppler measurements. In the bulb high axial velocities were found near the divider wall and a region with reversed axial flow occurred opposite to the flow divider which occupied about 25% of the local cross-sectional area. At the end of the carotid sinus an axial velocity plateau was observed near the non-divider wall. Secondary flow at the entrance of the carotid sinus was completely directed towards the divider wall but halfway the bulb it shows a vortex, quite similar to the vortex found in a curved pipe. At the end of the bulb secondary flow was highly influenced by the tapering geometry at this site. From the data obtained it is concluded that secondary flow has a pronounced effect on axial flow. From a numerical 2D-simulation it was found that the main differences between 2D- and 3D-flow are due to the absence of secondary flow in the 2D-situation.

BE18-D.4

A Computational Approach to Biomedical Fluid Dynamics
A. MazHer*, D. Giddens, J. Ekaterinaris
Georgia Institute of Technology
George W. Woodruff School of
Mechanical Engineering

Besides biochemical factors, fluid mechanical factors may play an important role in atherogenesis. The local wall shear stress, and the local velocity distributions are of primary interest in the hemodynamical aspect of atherosclerosis. Detailed information about the flow field can be obtained from mathematical model studies. Hence flow patterns are investigated here in a simplified three-dimensional arterial model. The blood is considered as an incompressible Newtonian fluid obeying the Navier-Stokes equation of the fluid flow and a computational approach is employed to solve these equations. A computer program is written utilizing the space marching method to integrate the Navier-Stokes for steady blood flow for different geometries. The program is used to solve many problems that of interest to hemodynamic studies. Results for slow through curved stenosis and through curved aneurysm are obtained and discussed. These results show the ability of the numerical methods to calculate the velocity fields with separation and secondary flows and wall shear stress for 3D configurations.

BE18-D.3

Numerical Analysis of Pulsatile Wall Shear Stress in an Arterial Bifurcation, K. Perktold* and D. Hilbert, Techn. Univ. Graz, A-8010 Graz, Austria

The study of fluid dynamic phenomena and flow-induced mechanical stresses in human blood vessels is of great interest in order to clarify the contribution of hemodynamic factors on the pathogenic mechanism of atherosclerosis and thrombosis. A hemodynamic factor of considerable physiological importance is the wall shear stress.

Here pulsatile flow through an arterial bifurcation model is analysed numerically. The computer simulation of the time-dependent, three-dimensional Navier-Stokes equations is based on a special finite element method.

The numerical results show the behavior of the time-dependent wall shear stress vector field and identify the zones of high and low wall shear stress values during the cardiac cycle.

BE18-D.5

Electrical model of the circulation without "blood flow through the vessel wall"
J.E. Tsitlik*, H.R. Halperin, and F.C.P. Yin,
The Johns Hopkins Medical Institutions,
Baltimore, MD 21205

In electrical models of the circulation, the compliance of a vessel is represented by a capacitor. Inside a blood vessel, a change in the volume of blood causes an equal magnitude but opposite sign change in the volume outside the vessel. In models, these changes are represented by equal magnitude but opposite sign changes in the charge on the plates of the capacitor. The capacitance is generally connected in parallel with a resistor representing the viscous friction. Therefore, charge can move from one plate of the capacitor to the second via this resistor. Such a current is equivalent to a volume of blood moving from the inside of the vessel to the outside, i.e. "flow through the vessel wall". To prevent such "flow", electrical models of the circulation should have the second plate of the capacitor connected not to the resistor, but to a terminal representing the pressure in the space outside the vessel, e.g. the intrathoracic space. This space, in turn, should be connected to the ambient space via another capacitor representing the compliance of the surrounding structure, e.g. the thoracic cage. Thus, proper connection of these capacitors can prevent erroneous model predictions, and may lead to better understanding of the circulation.

BE18-D.6

Modelling Competitive Interference Between Adjacent Terminal Lymphatics, W.A. Hymar*
Bioengineering Program, Texas A&M Univ.,
College Station, Texas, USA.

A simple model of the fluid dynamics of the terminal lymphatic collection system suggests that increased flow through one vessel in response to micro localized edema, or other tissue pressure elevation in the supplying tissue, will cause a decrease in flow in adjacent lymph vessels which meet at distal branch points. The effect of this decreased flow is to retard fluid collection through these adjacent vessels and therefore to cause the tissue region of their origin to also accumulate fluid and tend to become edematous. The result of this analysis is that edema would appear to propagate at the microcirculatory level. The fluid mechanics of this phenomenon is similar to effects in the arterial system called steal where changes in relative arterial branch resistance can cause, in the presence of significant proximal resistance, a marked decrease in branch flow when the contralateral resistance is reduced.

BE18-E.2

New Laser Doppler Velocimeter with a Dual-Fiber Pickup

M.Goto*, O.Hiramatsu, M.Kagiyama, K.Mito,
Y.Wada, S. Tadaoka, S.Matsuoka, Y.Ogasawara,
D.Kilpatrick, K.Tsujioka, F.Kajiyi
Kawasaki Medical School, Kurashiki, Japan

To measure the blood flow velocity accurately by excluding lower blood velocities stagnated at the vicinity of the fiber tip, we developed a laser Doppler velocimeter (LDV) with a dual fiber pickup. The pickup consists of two thin clad fibers (a graded-index multimode, clad. 62.5 μ m and core. 50 μ m) which are placed side by side. Thus, the measured spot was extended away from the fiber tip. The He-Ne laser beam (632.8nm, 5mW) was focused on the entrance of one fiber and introduced into the blood stream with a spreading angle of 5°. The backscattered light was collected by another fiber with a receiving angle of 17.3°. Doppler signals were analyzed by a spectrum analyzer. The spectrum of the Doppler shift frequency showed a sharp peaked pattern. The frequency corresponding to the peak power showed an excellent linearity with the known blood velocities. In the poststenotic region of the canine coronary artery, broad spectrum was obtained, whereas narrow spectrum was obtained in normal coronary artery. This indicates the utility of our system to the analysis of the disturbed flow region.

BE16-E.1

A method for frequency stabilization of multimode He-Ne lasers in laser-Doppler flowmetry, P.Å. Öberg, Dept of Biomedical Engineering, University of Linköping, S-581 85 Linköping, Sweden.

In most commercial laser-Doppler instruments for blood flow measurements unstabilized He-Ne lasers are used as light source. These low power, low-priced lasers are often impaired by frequency instability to an extent which can be interpreted as blood flow variations. The mechanism behind the frequency variations are changes of length of the laser cavity due to thermal expansion. Such instabilities can be efficiently reduced by means of a feedback temperature control system sensing the intensity of two orthogonally polarized modes. The difference between the two mode intensities is used as an error signal controlling the thermal expansion of the laser cavity. The stabilization device has been evaluated in models and comparative blood flow measurements. Stabilization of this type is recommended to be used in laser-Doppler flowmeters especially in applications where low perfusion levels are of particular interest.

Acknowledgements: Håkan Rohman, Hans Pettersson and Håkan Deblén contributed substantially. National Swedish Board for Technical Development (STU) supported the work with grant 86-4217.

BE18-E.3

Local blood perfusion in human anterior tibial muscle examined using single fiber laser Doppler flowmetry

E. Göran Salerud¹ and Knut Kvernebo²
Dept Biomedical Engineering, University Hospital, Linköping, Sweden¹ and Akers University Hospital, Oslo, Norway².

Laser Doppler-flowmetry has successfully been applied to superficial tissues. Local perfusion deep within tissues has not been studied extensively. Single fiber laser Doppler flowmetry offers a possibility to measure the perfusion continuously within a tissue and with a minimum of trauma.

In twelve healthy volunteers, local perfusion in the anterior tibial skin and muscle tissues was evaluated. Skin perfusion was recorded with a standard probe, while in muscle the single fiber technique was used. Normal resting values and responses to induced occlusive ischemia of 0.5, 1, 3 and 5 minutes were studied.

All recordings were found to be stable and permitted evaluation. At rest, muscle perfusion measurements lacked vasomotion, while it was observed in most skin recordings. The duration and magnitude of the muscle postischemic response increased with occlusion periods that were shorter than 3 minutes. At longer occlusion periods duration alone increased. In skin the increase was seen up to 5 minutes. The onset of the response was instantaneous for both tissues. The single fiber method has proven a great potential in evaluation of deep tissue perfusion. Improved technique and protocols will make possible the investigation of deep tissue perfusion, not only in muscle tissue, but also in tissues like kidney and brain.

BE18-E.4

Development of LDV Equipments for Blood Flow Measurement, K.Homma*, T.Eiju, K.Matsuda, J.Ohtsubo¹ and K.Shimizu, Mechanical Engineering Laboratory, MITI and the Shizuoka University¹, 1-2, Namiki, Tsukuba Science City, Ibaraki 305 JAPAN

The equipments of LDV (Laser Doppler Velocimetry), that is, a LDV microscope and a LDV fundus camera, based on the differential method have been developed. This method has some advantages that blood flow can be measured in a small observing area with high S/N ratio, etc..

The LDV microscope is mainly consisted of the differential LDV system, and of the microscopic observation system for blood flow and tissue structure. Two laser beams are adjusted to produce fringes and focused on a measuring area (minimum value : 15 μ m in diameter) in blood flow. A frequency shifter included in the LDV optical system (shifted frequency : 160Hz to 7kHz) separates signal component from pedestal one, and the flow speed is measured in a range of 0 to 14mm/sec. On the other hand, the LDV fundus camera is used for the measurement of human retinal blood flow in-vivo with the same LDV method. Fourier and Hadamard transforms, and autocorrelation are used for analysis of blood flow from the signals detected by a photon counter.

BE18-E.6

Angioscopic Observation of Blood Flow

Y.Uchida*, T.Tomaru, F.Nakamura, T.Sugimoto, University of Tokyo, Tokyo, Japan

The changes in blood stream in stenotic artery and their relationship to thrombosis were examined by angioscopy in dogs. The left common iliac artery was perfused with K-H solution and backflow of blood from a lumbar artery was drained into the perfusion circuit. Before constriction, the blood streams in the artery were composed of a coaxial main stream and the streams beside the coaxial stream. After more than 50% constriction, the streams beside the coaxial stream were separated, and produced curls around the outlet of the stenotic segment. Also, the outer layer of the coaxial stream was separated and produced longitudinal curls. Thrombi appeared at the center of both types of curls. Similar changes in blood stream and thrombosis were observed in the common carotid artery during vasospasm. The results indicate usefulness of angioscopy in serial observation of blood stream and thrombosis.

BE18-E.5

Pressure Drop and Velocity Measurements in a 90°-T-Junction, D.W. Liepsch*, R. Schwimmbeck and T. Austin, Eisenhower Medical Center, Rancho Mirage, CA, USA.

Hemodynamic atherogenic factors are determined by the interaction between geometry, flow pulsatility, elastic wall motion and the non-Newtonian flow behavior of blood. Flow pulsatility and non-Newtonian effects were studied in 90°-T-junctions simulating the first septal branch of the left descending coronary artery. Different types of fluids were compared: Newtonian, shear thinning, time varying polyacrylamide solutions, and two-phase fluids, e.g. Tri(hydroxymethyl) aminomethane with 40% ghost cells (red cells without hemoglobin). The viscosities of these fluids were measured in a Couette viscometer and compared with human blood. The pressure drops across the bifurcation were measured in the straight tube and in the branch. The loss coefficients were calculated from the measurements. Velocity profiles were measured with a laser-Doppler-anemometer. The non-Newtonian fluids showed additional and different flow separation zones, compared with the Newtonian fluids. Their secondary flows were also different. The pressure drop was smaller than for the Newtonian fluid. It was found that the pressure loss coefficient is a function of the flow rate ratio and of the absolute value of the entry flow rate.

BE18-F.1

Magnitude Magnetic Resonance Imaging of a Stenosis, D.N. Ku*, Y. Elgandy, R.I. Pettigrew, Georgia Institute of Technology, Atlanta, GA and Emory University, Atlanta, GA

Magnetic resonance imaging (MRI) offers the possibility of producing non-invasive angiograms. The goal of this study was to better understand the physical basis of flow patterns seen by MRI and their likely clinical significance. A fast gradient echo was used on a Philips 1.5 Tesla system. The images were gated for the recording of multiple images and combined into a movie to visualize the dynamic blood flow patterns during the cardiac cycle. A non-magnetic system of pulsatile flow through a stenosis was developed.

MRI magnitude imaging provided a high resolution image of the lumen of the stenosis. Flow through the stenosis showed acceleration of velocity in the throat as a brightening of the intensity. Just distal to the throat, black circles are formed. The jet formed by the stenosis appears light with a dark surround giving the impression of a flame thrower. The black areas appear to correspond to regions of steep velocity gradients, vortex shedding, and turbulence. MRI can provide both an anatomic and physiologic evaluation of hemodynamically significant stenoses.

BE18-F.2

VELOCITY PROFILES IN STENOSSED TUBE MODELS USING MAGNETIC RESONANCE IMAGING (MRI), S. Rittgers*, D. Fei, K. Kraft and P. Fatouros, The University of Akron, Akron, Ohio

Only a limited number of techniques exist which can provide direct knowledge about blood velocity and flowrate in the human cardiovascular system with the majority of these requiring invasive procedures. A time-of-flight MRI velocity measurement technique is evaluated in a constricted tube model having stenoses of 0 to 80% at physiologic flowrates. Results from this study show that MR displacement images can: 1) be obtained within both laminar and disturbed jets (maximum stenotic $Re \approx 4,200$), 2) accurately measure mean jet velocity up to 172 cm/s, 3) detect low forward and reverse velocity regions near the tube wall just downstream of the stenosis ($L/D < 2$), and, 4) demonstrate return to laminar profiles well downstream ($L/D = 10$) of the stenosis. Regions between the jet termination point and re-establishment of laminar flow ($Re > 1500$, > 1000 and > 110 downstream of 40%, 60% and 80% stenosis, respectively) can not presently be detected by this technique.

BE18-F.4

Qualitative and quantitative Investigation of Blood Flow Behavior by MRI. M. Bucciolini*, G.C. Casolo, L. Ciruolo and R. Renzi, University of Florence, Italy.

MR Imaging is a flow sensitive technique which has the potential to give qualitative and quantitative information about blood circulation. The possibility of studying the behavior of blood flow by Magnetic Resonance Imaging looks as an attractive goal, but quantification of flow velocity has yet to be fully accomplished. In order to relate the complex MR signal with proton flow velocity, a calibration in phantom has been carried out by means of an artificial flow circuit. In vivo ECG gated images were then acquired by employing both conventional Spin Echo and Multiphase Fast Imaging sequences. Curves of signal from thoracic vessels versus the phase of the cardiac cycle were obtained. Quantitative preliminary results concerning velocity trend over time are deduced and differences between normal subjects and patients with heart failures are pointed out.

BE18-F.3

Blood Flow Images by Magnetic Resonance Imaging S. Watanabe*, H. Imai, Y. Masuda and Y. Inagaki The Third Dept. of Internal Medicine, Chiba Univ. School of Medicine, 1-8-1 Inohana, Chiba, Japan

Slow blood flow images are seen in some kinds of the cardiovascular diseases by MRI. In this study we will present a clinical application of slow blood flow images in the aortic dissection and mitral stenosis. The false lumen is clearly distinguished from the true lumen since the signal intensity of false lumen is higher due to slow blood flow than that of true lumen in MRI. But a location of the entry is not necessarily detected. We obtained the result that the false lumen near by the entry showed very low signal intensity due to the turbulent flow from an experiment of the continuous flow model of aortic dissection. The location of an entry diagnosed on the base of this result was coincident with angiographic findings in the majority of cases (95%).

In mitral stenosis it is well-known that the thrombi often exist in the left atrium which causes general thromboembolism. But in our study about 13 patients with thromboembolism, the thrombi were detected only in seven patients (54%) by x-ray CT, echocardiogram or MRI, although slow blood flow images in the left atrium were seen in 11 patients (85%) by MRI. It is supposed that a detection of slow blood flow images in the left atrium is clinically useful.

BE18-F.5

The Velocity Profile of Blood Flow in the Presence of Intensive Magnetic Fields, I.I.H. Chen* and S. Saha, Departments of Physiology and Biophysics, and Orthopaedic Surgery, Louisiana State University Medical Center, P.O. Box 33932, Shreveport, Louisiana 71130.

Due to the increasing use of large magnetic fields in magnetic resonance imaging (MRI), it is important to investigate the effect of such intensive magnetic fields on the blood flow in our body. In this study, we have analyzed the general case of blood flow for a wide range of Hartmann's numbers (0.1 to 2.5) by solving the magnetohydrodynamic equation for viscous blood flow. The result indicated that the velocity profiles of blood flow were significantly different for Hartmann's number 0.5 and beyond compared with velocity profiles in the absence of a magnetic field. These results will be of interest in the development of future MRI Technology for diagnostic purposes.

BE18-F.6

Quantitative Measurement of Plug Like and Laminar Flow in MRI, R. J. Kriz*, G. Dobben and A. Horowitz

MRI signal intensity has been previously found to vary with flow in various ways depending on the pulse sequence used. We have measured the average signal change for flowing vs static water as a function of velocity for several commonly used pulse sequences in different diameter tubes on axial images. Differences in average intensity and standard deviation in the ROI's are measured for plug like flow vs laminar flow. Plug flow occurs when fluid enters a tube from a static reservoir under steady conditions. The transition to laminar flow causes the average MRI numbers to decrease, thus fluid having the same average flow but different velocity profiles at different locations along the tube, have different signal intensities.

BE18-G.2

STEADY AND PULSATILE FLOW VISUALIZATION
IN THE ABDOMINAL AORTA

Moore, J.E. Jr.,* and Ku, D.N.

Georgia Institute of Technology, Atlanta, Ga

Carotid atherosclerosis develops in regions of low and oscillatory shear stresses. Similar hemodynamic factors may influence plaque formation in the abdominal aorta. Steady and pulsatile flow visualization was performed in a glass tube model of the aorta. Dimensions for the model were taken from bi-planar angiograms and cadaveric aortas.

Under rest conditions, two regions of relative stagnation appeared on the posterior wall of the aorta. Secondary flow patterns appeared in the abdominal aorta, but not in the thoracic aorta. Under exercise conditions, one thin stagnation region appeared and no secondary flow patterns were visible. With pulsatile flow, the stagnation regions exhibited oscillatory motion. The secondary flow patterns became more complicated, but still appeared only in the abdominal aorta. These vortices propagated downstream during systole, with additional vortices forming in early diastole. For pulsatile exercise flow conditions, virtually no secondary flow patterns appeared. Results from this experiment show that complicated flow patterns exist locally in the abdominal aorta which may influence the development of plaque at this site.

BE18-G.1

Limitations and Validation of the Modified Bernoulli Equation for Velocimetric Estimation of Pressure Gradients, S.Hanya*, S.Nishiyama, Y.Kondou, A.Ishihara, and M.Sugawara**, *Kitasato University, Sagamihara, **Tokyo Women's Medical College, Tokyo, Japan

For patients with various types of stenosis, the modified Bernoulli equation has been used to yield an accurate estimate of transstenotic gradients. Theoretically, the equation is only applicable for a stenosis downstream from which the cross-sectional area enlarges suddenly (orifice-shaped stenosis), however no previous study had systematically confirmed this.

We measured, calculated and compared pressure gradients in 40 patients with stenosis (34 pulmonary and 6 aortic) divided into two groups (27 orifice-shaped stenosis and 13 hourglass-shaped stenosis). Peak jet velocity and pressure gradient were measured simultaneously using a multisensor catheter. The correlation of simultaneous velocimetric and manometric pressure gradients for the patients with orifice-shaped stenosis demonstrated a highly significant relationship ($Y=0.83X+2.012$, $r=0.942$, $P<0.001$).

In patients with hourglass-shaped stenosis, there was no significant correlation ($r=0.229$, n.s.). We conclude that the use of the modified Bernoulli equation for estimating pressure gradients should be limited to patients with orifice-shaped stenosis.

BE18-G.3

Pulsatile Flow Through Models of Compliant Stenoses, Donald F. Young* and Nikolaos Stergiopoulos, Department of Engineering Science and Mechanics, Iowa State University, Ames, Iowa 50011, USA

The pressure-flow relationship for a stenosis is of importance since this relationship is required to determine the effect of the stenosis on blood flow. Most past studies have considered stenoses to have rigid, fixed geometries, but stenoses are often eccentric so that a portion of the arterial wall remains compliant.

In the present study the influence of a compliant wall on pulsatile flow through in vitro models of both subcritical and critical stenoses was investigated. For some tests the geometry of the stenosis changed only a small amount during the flow cycle, but for critical stenoses this small change affected the pressure drop across the stenosis. In other tests the vessel containing the stenosis collapsed because of the low distal pressure created by the stenosis. Pressure-flow relationships are described for both the uncollapsed and collapsed modes of behavior.

BE18-G.4

Fluid Dynamics and Mass Transfer to and from the Vessel Wall in Models of Arterial Stenoses, X. Deng and T. Karino*, Montreal General Hospital, Montreal, Quebec, Canada.

To investigate the effects of disturbed flows on the genesis and development of atherosclerotic lesions in man, fluid dynamics and mass transfer to and from the vessel wall at sites of arterial stenoses were studied theoretically using computational methods. Flow patterns and various other fluid mechanical properties for the steady laminar flow of an incompressible fluid through axisymmetric bell-shaped stenoses were obtained for Reynolds numbers up to 100, by numerically solving the Navier-Stokes equation. Mass transfer to and from the permeable vessel wall of the stenoses was also studied theoretically by solving a diffusion equation in combination with a penetration theory. It was found that mass transfer from the vessel wall to the flowing fluid is highest at the throat of the stenosis, lowest at the separation point and moderately elevated within the vortex formed downstream of the stenosis. Analyses of mass transfer from the fluid to the permeable vessel wall showed that an accumulation of species such as lipoproteins on the vessel wall is lowest at the separation point and highest at the reattachment point. There was a minor secondary peak at the leading edge of the stenosis proximal to the point of maximum constriction.

BE18-G.6

Arterial Function in Postural Change, T. Yaginuma*, T. Noda, H. Komatsu, H. Sekiguchi and S. Hosoda, Jichi Medical School, Tochigi, Japan.

The effects of body position on the aortic flow velocity and pressure signals have been studied in adult male subjects by the aid of multisensor catheters. For each patients input impedance was calculated from 10 harmonics of aortic pressure and flow. The time domain wave form of forward and backward flows and pressures was obtained by computing the inverse Fourier-transform.

The ascending aortic pressure wave form revealed a late systolic peak during decelerating flow velocity in supine position. A large change from supine to standing was to have reflections minimal or more diffuse in spite of increasing input impedance. This was observed similar in shape from the position of 60° tilting bed. Wave shapes of pressure from the straight position of a patient supported by his hip on the edge of the bed, revealed a intermediate form between supine and standing. These results suggests that the magnitude and timing of wave reflections from upper and lower body sites are markedly changed not only by the gravitational effect but by physiological modification.

BE18-G.5

The Effect of Minimal Atherosclerotic Plaque on the Spatial Distribution of Wall Shear Stress - A Model Study - T. Yamaguchi* and S. Hanai, Vascular Pathophysiology Lab., National Cardiovascular Center, Suita, Osaka 565, Japan.

Low wall shear stress (WSS) regions are specific arterial locations prone to atherosclerosis. However, it is likely that the WSS distribution pattern changes markedly when atherosclerotic wall irregularities affect arterial geometry. Very few studies on exact shear stress distribution patterns following the appearance of an atherosclerotic lesion have been reported. We measured model WSS distribution pattern using an electrochemical method. There was a striking and complex change in the WSS distribution around the small model plaque, even when the reduction in area produced by the obstacle was only an order of magnitude of several percent. The WSS value increased to twice or greater than twice the Poiseuille flow value. Our results suggest that the changes in WSS induced by the appearance of an early atherosclerotic lesion may markedly alter the course of the disease.

BE19.1

AUXILIARY PROCESSOR
FOR FAST BIOMEDICAL SIGNAL ANALYSIS

J. Azpiroz Lehan*, A. DeLuca Panaccia
Universidad Autónoma Metropolitana-Iztapalapa
Av. Parisíma y Michoacán, México. 09340, D.F.
MEXICO

We have designed an auxiliary processing system capable of providing real-time signal processing within an IBM-PC compatible computer. where the architecture of this coprocessor was developed specifically to accelerate the execution time of characteristic subroutines used for analysis of biomedical signals such as the fast Fourier transform (FFT), convolution and squared magnitude.

For example, during the calculation of the FFT most of the processing time is used for the multiplications in the "butterfly". The coprocessor was designed to execute these operations efficiently, and uses a 16 bit X 16 bit multiplier chip (MPY016H by TRW) capable of executing a multiplication in 100ns, together with other Schottky-TTL elements in order to operate concurrently with the host microcomputer. This system is able to transform a general purpose microcomputer into a powerful real-time biomedical signal analysis system.

400

BE19.2

"A New Phase Linearization Method for the Common Recursive Digital Filters Used in Medical Signal Processing", P. Järvillehto* and K-P. Estola, Technical Research Centre of Finland, POB 316, 33101 Tampere, Finland.

Medical signal processing typically utilizes the sharp edged filter structures to extract frequency bands of interest, e.g. in ECG and EEG signals. In real time systems where common filter blocks are allowed to have only short delay time and the minimal intersample processing time, the recursive filters are exploited and the phase response cannot thus be kept exactly linear. Nonlinearity in the phase response causes signal distortion due to different group velocities of the signal components.

In this paper, we introduce a method for the phase linearization of the common IIR filters. The phase linearization is based on the stable implementation of the maximum phase equivalent of the original filter. The infinite impulse response is truncated to a finite one, the data is reversed in time domain and fed back to similar filter again. This implies a usage of block processing. After another time reversal and a overlap-and-add section linear phase data is achieved. In some cases the time reversal method can be replaced by the maximum phase FIR equivalent of the original filter, thus enabling usage of the stream processing instead.

BE19.4

ADAPTIVE THRESHOLD PREDICTION IN REAL-TIME ECG DETECTION
Zhou Song-kai, Wang Jian-tao, Xu Jun-rong*
Shanghai Jiao Tong University

We compare ECG signal processed with a threshold to decide if any QRS-complex exists. But arrhythmia ECG changes non-regularly and non-stable. So threshold adjustment must be adjusting adaptively to fit the variance of ECG in real-time detection. The paper discusses the properties of thresholds with linear estimation which need 2-order priori statistical knowledge of thresholds. It is not practical although it has good properties in theory, but it gives us some inspirations to lead to adaptive threshold prediction. Then the paper discusses threshold prediction with 1-order predicting filter, forms adaptive threshold prediction formula on principle of minimum square error, and explains frequency responses of adaptive threshold prediction. We realize the real-time program with assembly language in Intel-8085. The paper introduces threshold prediction with 2-order predicting filter, to the application in threshold predictions, explains and simplifies the formula. The much better results can be obtained than others.

To compare a variety of threshold predicting methods quantitatively, the paper compares 4 kinds of threshold prediction methods with mean square-error (SS1) and mean-error (SS2).

BE19.3

ADAPTIVE RECURRENT FILTER FOR ECG SIGNALS
N. V. Thakor*, Z. Yi-Sheng, J. Wang,
Biomedical Engineering, Johns Hopkins
University, Baltimore, MD 21205, USA

In computer-aided analysis of Electrocardiogram (ECG) signals two problems are important: 1) removal of uncorrelated interference, and 2) classification of QRS-complex morphology. An adaptive recurrent filter (ARF) is presented that learns the shape of the QRS complex only at each recurrence. Uncorrelated interference is cancelled from subsequent beats, and abnormal QRS morphology is detected.

The ARF is constructed as a transversal filter with adjustable weights. Adaptation is started at each occurrence of QRS complex only. The filter algorithm minimizes the mean-squared error between the filter weight and the incoming QRS sample with the aid of a least-mean-square (LMS) recursive estimation algorithm. After the filter has converged (convergence rate is determined by the LMS algorithm), the ARF weights have "learned" the shape of the normal QRS complex. Uncorrelated noise or ectopic beats remain as the residue from the filter.

The ARF has applications in ectopic beat detection, pacemaker analysis, P-wave and atrial arrhythmia analysis, and noise removal.

BE19.5

Digital Filters for Tracking Electrophysiological Chaos, Bernard Saltzberg,
University of Texas Medical School,
Houston, Texas 77030

Current investigations of the chaotic features of electrophysiological activity are mainly focused on deriving the Hausdorff dimension of short samples of normal and abnormal EEG patterns. Because of the computational demands for deriving the Hausdorff dimension, as well as the incompatibility of epoch length and stationarity requirements, this approach is severely limited. Filters based on nonlinear models which exhibit chaotic behavior offer an alternative method of chaotic analysis which overcomes the above problems. These digital filters can provide high resolution continuous tracking of a chaotic feature of the electrophysiological activity in essentially real time. In addition these filters can be implemented on a standard laboratory computer, as opposed to the requirement for supercomputer resources to compute the Hausdorff dimension for comparable amounts of data.

BE19-6

Infracardiac spectral components in cardiovascular signals, R. Pallas-Areny*, J. Colominas, J. Rosell, and P. Riu, Div. Instrumentacion y Bioingenieria, ETSI Telecom, Box 30002, Barcelona, Spain

The spectral analysis of ECG and blood pressure signals is a means of studying the intact cardiovascular control system. In this analysis, the presence of infracardiac rhythms is usually associated with respiratory arrhythmia, thermoregulation and spontaneous vasomotor activity. There is no information available about any other mechanisms which result in spectral components in the same bands. But there is, however, experimental evidence of respiratory information in the spectrum of these signals even when respiratory influence on them via neural control has been purposefully suppressed. This fact remains, so far, unexplained. We show that, even in the absence of respiratory sinus arrhythmia, an amplitude modulation of cardiovascular signals by respiratory movements results in a spectrum showing components in the same bands considered when analyzing the intact cardiovascular control system. Experimental results in a paced patient confirm this hypothesis. We show too that if the respiratory rhythm is not constant, some infracardiac spectral components can be attributed to its variability.

BE20-A.2

Development of an Electrical Impedance Tomography System, L. Bertensam, B. Blad, G. Göransson, U. Lindblad and R.B.R. Persson, Radiation Physics Department, Lund University, S-221 85 Lund, Sweden.

It has been shown, both in theory and in practice, that it is possible to obtain information about the distribution of impedance within an object by driving current through it and measure the voltages that arise on the boundary of the object.

We have developed a system for making such measurements in vivo on humans. The system utilizes 16 electrodes, which are used for alternatively driving currents and measure voltages. The equipment is controlled by a PC/AT compatible computer. The computer is also used for data collection and image reconstruction and presentation.

The present algorithm relies on an enhanced back projection technique, using 15 curved fields and 16 projections. The program automatically compensates for offset and gain errors in the hardware. With this system it is possible to acquire data and present a two-dimensional picture of impedance distribution in a 32x32 matrix.

The future reconstruction algorithm will use an iterative forward technique, based on the Finite Element Method (FEM).

BE20-A.1

The use of dual simultaneous excitation currents in Bioelectric Impedance Analysis, D.N. Smith*, Medical Physics and Medical Engineering, Western General Hospital, Edinburgh, EH4 2XU, Scotland.

Tetrapolar impedance measurements have been widely advocated for determining body composition. In this method a single excitation current passes between two extremities, usually right hand and right foot. Body composition values are derived using multiple regression relationships incorporating $\text{Height}^2/\text{Resistance}$ as the principal variable. This is taken to represent the volume of the body but will be incorrect due to variability of cross section and internal resistivity. Greater precision can be achieved by making separate measurements of impedance for the limbs and trunk and combining these with appropriate weighting factors. However, the use of independent serial measurements results in changes of current distribution within the body and will not eliminate the end effects of each section. The use of two currents of equal magnitude, frequency and phase in parallel paths on the right and left sides automatically reduces the effect of the spreading resistances at shoulder and groin producing a more uniform current distribution in the trunk. An appropriately weighted sum of $\text{Height}^2/\text{Resistance}$ for all segments can then be produced which is a more accurate representation of body volume.

BE20-A.3

Study of the New Temperature Change Measurement Method by Impedance CT, K.Sakamoto*, H.Kanai Sophia University, Chiyoda-ku Tokyo, Japan 102

In the hyperthermia therapy, one of the most important problem is how to measure the temperature of cancer tissue located deeply in the body noninvasively. Electrical impedance of living tissue mainly consists of intra- and extra-fluid impedance whose characteristics are almost the same as that of saline solution and cell membrane which is electrical insulator at radio frequency. Therefore, the temperature characteristics of tissue impedance is the same as that of saline solution which is about $-2.5\%/^{\circ}\text{C}$. Cancer tissue is heated up to around 43°C during hyperthermia therapy, so impedance of cancer tissue decreases about 18%. We tried to measure the impedance change by impedance CT and estimated the temperature distribution in the object. And also we discussed the measurement errors caused by the various kind of noises and geometrical problem by computer simulation and phantom experiment. To take an example, the temperature distribution obtained by impedance CT agrees well that measured actually within 0.5°C differences in one of the phantom experiments. The errors in this experiment could be fathomed from computer simulation results. Even though we got good results in the phantom experiment and computer simulation, since geometrical problem still exists, we continue to study the feasibility of the temperature measurement method by impedance CT.

BE20-A.4

Skin Electrical Parameters Obtained from Low-frequency Admittance Locus Plots, Z.-G. Qiao* and L. Mørkrid, Dikemark Hospital, N-1385 Solberg, Norway.

The electrical impedance of biological tissue can be presented by a Cole-Cole locus plot in the complex plane, usually in a circular form with parameter (R_0 , R_∞ , τ and α). For the investigation of human electrodermal activity which vary in time with sympathetic outflow there are difficulties in obtaining these parameters. The theory developed in this paper shows that an admittance locus plot also is a part of a circle and its low-frequency region (<1000 Hz) is to a very good approximation straight line.

Furthermore from simultaneous measurements at two different frequencies with three electrodes, two lock-in amplifiers and a computerised recording system, it is possible to estimate in real time the parameters ($1/R_0$, τ and α). $1/R_0$ corresponding to zero frequency conductance extrapolated from the low-frequency part of the admittance plot. This new method of measuring and characterising electrode-tissue interface has been used to study spontaneous activity during baseline conditions and evoked responses of these parameters in psychophysiological and neuroendocrinological research.

BE20-A.6

Impedance Measurement of Chinese Meridian System. Maw-Chang Lee*, Wen-Chang Lee, Yin Chang and Chieh Chung, National Yang-Ming Medical College, Taipei, Taiwan, R.O.C.

According to the traditional Chinese medicine, the vital energy 'chi' circulates around the body along the channels called 'ching-lo' (meridians). The acupuncture points (acu-points) are located on the meridians. Stimulating acu-points by needles or other means is to restore the normal flow of chi along the specific meridian, and thus has specific therapeutic effects. However, the physical substrate of meridian is yet to be identified.

The purpose of this study is to examine the electrical properties of the meridian. Acupuncture needles were inserted into the acu-points of patients. Sinusoidal currents at various frequencies were passed through a pair of needles and voltage drops were measured. Impedance was calculated from the voltage-current relations. Preliminary results show that the impedance of meridian did not differ significantly from that of nearby tissue. More rigorous studies are currently under way. (Supported by National Science Council of R.O.C.)

BE20-A.5

ELECTRIC IMPEDANCE FOR EARLY DETERMINATION OF BRAIN DEATH AND FOR PROGNOSIS IN COMA. S.A. Radvan-Ziemniewicz*, Cerebral Clinical Center Bethesda, Maryland 20814, U.S.A.

Rheoencephalography (REG) uses noninvasive electric impedance plethysmography for cerebral circulatory studies. It was markedly improved by author's "regional" REG (RREG). In prolonged and intermittent surveys, this method proved to be safe, more sensitive and reliable, than other indicators for brain viability, e.g. EEG and contrast or isotope arterial perfusion. For experimental testing was also used author's "topischemia"-the transient focal cortical hypoxia and asphyctic anoxia.

In clinical tests for coma of various etiology, the flat tracings of RREG have been more dependable, than the isoelectric EEG, absence of clinical signs of cerebral functions, or any of the invasive, expensive and complicated blood flow tests (1980).

Tracings of impedance fluctuations caused by arterial pulsations, are monitored simultaneously from bilateral pairs of scalp electrodes in repeated sequences: frontal, temporal, occipital and occasionally also parietal. Rheograph measures the impedance changes by floating potential i.e. advanced implementation of double wheatstone bridges bipolar circuit. Two signal oscillators have 20-80 kHz and up to 10 mA. Amplification is in the range of EKG, about 50 x lower than for EEG. Computerization of RREG, called now CRREG brings a new modality of neuroimaging for being developed by this author, advanced studies on human cerebral dynamics.

BE20-B.1

Intracardiac Impedance Plethysmography, G. Boehm* and M. Schaldach, Zentralinstitut für Biomedizinische Technik, Universität Erlangen, D-8520 Erlangen, FR of Germany

Intracardiac impedance plethysmography is gaining increasing interest, in both diagnostic and therapeutic fields. As a diagnostic tool, its main application is to record pressure-volume diagrams. Therapeutically, it is used as a means to provide information of the pumping efficiency of the heart. This method of control finds application for implantable pacemakers and defibrillators. Impedance plethysmography has been shown to be an effective physiological parameter for closed loop control of pacing rate in pacemaker applications, based on its direct relationship to stroke volume.

Investigations with respect to the accuracy of this method, or its optimization, have mainly been established either by performing in vivo or in vitro experiments, or using computer simulation to solve underlying differential equations under special conditions. This paper contributes to the volumetric application of impedance measurements in providing solutions of the Laplace equation under simplified geometrical conditions. Theoretical, experimental, and clinical results confirm the electrode arrangement needed to meet the required accuracy for the various applications and summarizes limitations of the method.

BE20-B.2

Right ventricular volume estimation by conductivity dilution, P.H.Rehak*, H.Metzler and W.Stenzl University of Graz, A 3036 GRAZ, Austria

To evaluate the conductivity dilution method in right ventricular volume estimation an experimental study was carried out in 7 pigs. Variations of cardiac output (CO) and ventricular volumes over a wide range were performed by applying combinations of continuous positive pressure ventilation (PEEP), Dopamine infusion and volume overload. Hypertonic saline was injected directly into the right ventricle and indicator concentration was measured in the pulmonary artery by a catheter-mounted 4-wire conductivity cell.

CO, enddiastolic (EDV) and endsystolic volumes (ESV) were calculated from the unprocessed dilution curves, from filtered curves and by exponential curve fitting. These values were compared with the pulmonary artery flow as measured by an electromagnetic flowmeter and with myocardial segment lengths of the right ventricular free wall, respectively.

Both CO and ventricular volumes showed the best correlation with the reference values when they were calculated from the unprocessed curves (CO: $r=0.92$, EDV: $r=0.87$, ESV $r=0.71$).

The accuracy of the volume estimation - referred to the segment lengths - was not affected by PEEP, Dopamine or volume loading, but all of these factors showed a significant higher influence on the estimated CO than on pulmonary flow.

BE20-B.3

Ventricular Volumetry by Electrical Conductance Measurement : the Importance of Catheter Position, C.D. Bertram* and J.C. Woodard, University of New South Wales, and B.S. Gow, University of Sydney, Australia.

We have recorded measurements with an eight-pole catheter in the right ventricle (RV) of anaesthetised greyhounds, and compared them with simultaneous recordings of e.c.g., RV pressure, pulmonary arterial (PA) flow-rate and tracheal air flow. The catheter was introduced in four different ways: tip at apex from PA or jugular vein, and tip near PA from jugular or femoral vein. Position in the ventricle was determined by videofluoroscopy allied to contrast injection and location of the tricuspid valve by pressure-sensing radio-opaque catheter. Our results show that usable volume signals correlating well with integrated ejected flow-rate are obtainable from all four positions if the catheter is maintained away from where the free wall meets the septum. *In vitro* experiments and simulations confirmed that apparent volume is markedly altered when electrodes approach a boundary, owing to reorientation of flux lines. Hence, while isovolumic shape changes causing blood shifts parallel to the catheter are well compensated by a multi-electrode technique, shifts orthogonal to the catheter are transduced as apparent volume changes. The effects on apparent volume of mechanical or natural lung ventilation generally accord with physiological expectation.

BE20-B.4

Electrical Impedance-Cuff Technique:

A New Plethysmography,
H.Ito*, H.Shimazu, A.Kawarada, H.Kobayashi, J.Masuda & K.Yamakoshi, Dept Physiol, Kyorin Univ, Mitaka-shi, Tokyo; K.Yamakoshi is in Res Inst, Appl Electr, Sapporo-shi, Hokkaido, Japan

A new plethysmograph, called the electric impedance-cuff, was designed for the indirect measurement of blood flow, arterial pressure and compliance in human limb arteries. The device comprises a compression chamber filled with electrolyte solution and a tetrapolar electric impedance plethysmograph whose electrodes are placed inside the chamber; the former for controlling transmural arterial pressure (P_t) and the latter for detecting limb volume (V), mean arterial volume (V) and its pulsatile variation (ΔV). Systolic ($P_{s,am}$) and mean (P_{am}) arterial pressure were determined by detecting respectively the appearance and maximum point of the pulsatile impedance variations during the gradual increase in the chamber pressure using the volume oscillometric technique. Diastolic pressure and pulse pressure (ΔP) were calculated from these pressures using conventional equations. Compliance defined as $\Delta V/\Delta P$ was obtained at various P_t levels controlled by compression pressure.

BE20-B.5

Data Reduction and Modeling of Impedance Cardiograms by Linear Prediction.
M.Cadena*, T.Aljama, S.Charleston, S.Carrasco, R.Camarena. Universidad Autonoma Metropolitana-Iztapalapa. E.E Department, 09340, Mexico 13, D.F., Mexico.

Impedance cardiography is a noninvasive technique for estimation of stroke volume and cardiac output in patients and normal subjects at rest and exercise. Controversial results has been reported by several investigators when they have studied cardiac abnormal patients using Kubicek's model correlated against Fick's and dye methods. The purpose of this work is to describe a new approach to characterize impedance cardiography signal by use of an only-pole linear prediction algorithm. The resulting model coefficients are used as a data reduction feature extraction technique. This model has been tested on twenty subjects during upright cycle exercise at 0,50,100,150 and 200 watts estimates of cardiac output by CO₂ re-breathing method. Also, it has been tested in 10 patients with mitral valve insufficiency, determined by B-scan ultrasound images, with estimates of cardiac output by Doppler ultrasound method. First results suggest this approach can be used as a very sensitive statistical technique to process cardiography signals.

BE20-B.6

IMPROVED SIGNAL PROCESSING TECHNIQUES FOR
THE DETERMINATION OF CARDIAC PARAMETERS
USING THORACIC BIOIMPEDANCESridhar P. Reddy, Liang Y. Shyu, Joachim Nagel, Ph.D.,
Neil Schneiderman, Ph.D.

Noninvasive determination of stroke volume, cardiac output and the systolic time intervals though of great interest in both diagnostic and medical research, still lacks the necessary reliability and precision mainly due to severe shortcomings of the commonly used signal processing techniques. Due to the poor results, even the principle of cardiac output determination based on impedance cardiography remains controversial.

High levels of noise and motion artifacts in the signals call for sophisticated signal processing techniques in order to provide beat-to-beat detection of the single cardiac events, especially in case of exercising patients. So far, simple bandpass filters and threshold detectors have been used for event detection at the beginning and end of electric and mechanical systole. Ensemble averaging of cardiac parameters, increases the reliability but only at the expense of information about transient responses, short-time fluctuations and respiratory modulation.

In order to overcome these problems we have used beat-to-beat detection techniques, such as adaptive matched filtering and phase-sensitive event detection. The phase-sensitive method is based on the assumption, that sudden events within a biological signal source, such as the onsets of slowly changing signals or small local extrema (as the opening of the aortic valve), lead to a sharp change of signal spectrum. The analysis of the momentary frequency or phase has resulted in obtaining a reliable marker for each event. As a result of adaptive matched filter and phase-sensitive event detection, both the reliability and precision have been substantially improved. In order to process the data at sufficiently low cost and to gain clinical acceptance without sacrificing precision, we have developed analysis to be run on a personal computer (PC-AT).

BE21-A.2

Stabilization of FES System for Muscle Tension Control, N.Itakura, K.Fujita, K.Kubo, Y.Iguchi and H.Minamitani, Keio University, Hi-yoshi 3-14-1, Yokohama 223, Japan

We have tried to control muscle tension by using functional electrical stimulation (FES) with PID, PI, I, I-PD or I-P controller which was designed by the Kitamori's controller design method. And experiment have been carried out on gastrocnemius of human lower extremities. The system employing PID, PI or I-PD controller showed stable response to the step command generating relatively low tension, but non-linear characteristics of the controlled process might cause unstable response for higher tension. So it should be clarified how the stable control could be attained all over various strengths of the muscle tension.

In this study, we identified transfer function of the muscle tension of gastrocnemius. Using the data, the control system responses to the step command, generating about 1/4, 1/2, 3/4 of the maximum tension, were simulated in order to discuss how the Kitamori's method can be applied to the control system including non-linear process. From the results, it was found that using the largest gain of the transfer functions was the best way to control stably without oscillation all over the strengths. PI or PID controller showed higher robustness against the non linearity than that I-PD or I-P controller did.

BE21-A.1

Alternating Motor Unit Activation in Electrically Stimulated Muscles, Z.-P. Fang* and J.T. Mortimer, Applied Neural Control Lab, Dept. Biomedical Engineering, Case Western Reserve University, Cleveland, Ohio 44106

A new method has been developed to activate alternately two motor unit groups within a muscle by using a nerve electrode. With alternating stimulation, each of the muscle groups should be required to fire at only half of its fusion frequency to generate a fused whole muscle contraction. This stimulation scheme mimics the asynchronous firing pattern of motor units during natural excitation, and should therefore reduce the muscle fatigue associated with conventional high frequency stimulation. A tripolar spiral cuff electrode was placed on the medial gastrocnemius nerve of the cat. A stimulator was designed to generate narrow rectangular pulses (which activate large axons along) and wider quasitrapezoidal pulses (which activate selectively small axons by differential block of the large fibers) alternately at a desired switching rate. Both nerve action potential and muscle twitch recording indicated that two different motor unit groups could be activated alternately by the scheme. A smooth muscle contraction was demonstrated when each muscle group was stimulated at about half of its fusion frequency. Finally, a comparison test showed that muscles exhibited less fatigue when driven by the alternating scheme. This method may have applications in physiological study and neural prosthesis design.

BE21-A.3

Time-variation of Quadriceps Muscle Force And Related EMG During Uniform Electrical Stimulation In Paraplegics. J. Mizrahi*, M. Levy, Y. Steinvil, Z. Susak, P. Solzi. Technion-Israel Institute of Technology, Haifa, and Loewenstein Rehabilitation Hospital, Raanana, Israel.

A dynamic model of the leg, which enables to calculate the force produced in vivo in the stimulated Quadriceps muscles of spastic paraplegics was developed. The measured kinematics and external dynamics of the activated leg were measured in the sitting and the supine lying positions on specially designed apparatus, to serve as input data for this model. External stimulation of the Quadriceps was used for tetanic contraction, with constant stimulus parameters. Simultaneously, surface EMG activity of the stimulated Quadriceps muscles, as well as their antagonist Hamstrings muscles, was recorded. Conduction velocity of the Femoral and Sciatic nerves was measured before and after each experiment, and was found unaffected by fatigue.

An attempt to correlate EMG and mechanical measurements suggests that the decaying measured force in the fatigued Quadriceps muscle is accompanied by a corresponding decrease in EMG amplitudes. The latencies between stimulus artifact and onset of EMG were 1 and 2 ms, for the Quadriceps and Hamstrings muscles, respectively, indicating that stimulation is direct from the electrodes to the muscles. The force induced in the Hamstrings has negligibly low compared to that of the Quadriceps.

BE21-A.4

An Implantable Nerve Stimulation System, Technical Solution and Applications, H.G. Stoehr*, W. Mayr and H. Thoma, 2nd Surgical Clinic, University of Vienna, Austria.

Functional electrostimulation offers a way for rehabilitation after paraplegia and reinnervation of the phrenic in cases of central paralysis of the breath muscles. We developed multichannel implants (up to 40 electrodes) using thin-film and thickfilm hybrid technology and custom designed integrated circuits as well as sophisticated extracorporeal control units. All stimulation parameters can be controlled preceding each stimulation impulse. Approach to the biological system is done via stainless steel electrodes which are sutured to the epineurium of the nerves to be stimulated. In 1984 first clinical applications in 4 paraplegic subjects proved the principle function of the method. They could stand up from the wheelchair and walk short distances on flat ground. Meanwhile the "lung pacemaker" is produced commercially and allows fatigueless stimulation of the phrenic nerve 24 hours a day. Several high tetraplegic patients could be discharged from the ICU and are now living at home for more than two years.

BE21-B.1

Quantification of Wound Healing after Electrical Stimulation, L. Vodovnik*, A. Stefanovska, D. Križaj, H. Benko†, R. Turk‡, M. Maležič‡‡, Faculty of Electrical Engineering, †University Rehabilitation Institute, ‡‡Jožef Stefan Institute, Edvard Kardelj University, Ljubljana, Yugoslavia

The treatment of indolent wounds presents a major medical, social and financial problem. During the past decades several papers have reported about accelerated healing of chronic wounds using various modalities of electrical or electromagnetic stimulation. Due to lack of quantification, ignorance about the healing mechanisms and inadequate controls, stimulation has as yet not been widely accepted in clinical practice. In our study we primarily addressed the quantification problem but also investigated possible mechanisms and controls.

Decubitus ulcers on ten spinal cord injured patients were daily stimulated with tetanizing currents through PALSTM skin electrodes. The wounds were photographed weekly and slides projected on a digitizing tablet. The areas computed by a CAD program were plotted as a function of time. It was found that an exponential decay of the wound surface is a good approximation. The healing time constants were found to be about 2.4 weeks for trochanter wounds and 4.7 weeks for wounds on the sacrum.

BE21-A.5

Development of the Multichannel FES System for the Paralyzed Upper Extremities. N. Hoshimiya* and Y. Handa†, Research Institute of Applied Electricity, Hokkaido University, Japan, †Shinshu University, School of Medicine, Matsumoto, Japan

Multichannel Functional Electrical Stimulation (FES) is very efficient for the restoration of the paralyzed upper extremities. We developed several microcomputer-based FES systems, and applied them to clinical usage. In this paper, recent progress in the development of the multichannel FES systems will be reported. (1) A master-slave type high performance FES system with 48 channel outputs for the restoration of the hand function of the paralyzed upper extremities of the quadriplegic patient is described, which can control the finger, wrist and elbow, and the stimulation patterns of which can be modified by the patient through the interactive capabilities. (2) A portable 16 channel FES system which is suitable for clinical usage, which will be commercially available in the near future. Creation method of the multichannel stimulation waveforms is identical for both systems, and is based on the EMG activities of normal subjects.

BE21-B.2

Electrical Stimulation for Functional and Therapeutic Use in the Disabled Patient Y. Handa* and N. Hoshimiya†, Dept. of Anatomy, Shinshu Univ. School of Medicine, Matsumoto 390, Japan. †Res. Inst. of Applied Electricity, Hokkaido Univ. Sapporo 060, Japan.

Electrical stimulation by using percutaneously indwelling intramuscular electrodes in order to improve motor function of paralyzed and paretic extremities in the spinal cord injury (SCI) and stroke patients is described. Functional electrical stimulation (FES) by using EMG-based stimulation patterns which were obtained from normal subjects easily provided the severely disabled patient reliable and reproducible control of the paralyzed extremities. Not only locomotive function in paraplegics but also upper extremity function in high SCI patients such as C4 quadriplegics could be restored by this method. Therapeutic electrical stimulation (TES) was applied to paretic extremities of SCI and stroke patients for relieving spasticity and restriction of range of motion (ROM) and improving volitional activities of daily living (ADL). Since safe, easy and steady stimulation was achieved by the percutaneous intramuscular electrode, long-term and frequent stimulation could be realized by patients themselves. They stimulated their paretic extremities over 6 times/day where one time was consisted of 30 min of cyclic stimulation. Such intermittent stimulation method in a day provided apparent and sustained reduction of spasticity because of prolongation of the carry over phenomenon after electrical stimulation. Therefore, an increase in active ROM and improvement volitional ADL were observed within a month. Long-term TES over one year acquired permanent improvement of volitional activities of the patient.

BE21-B.3

FES Control of the Paralyzed Extremities by Percutaneous Electrodes.

Y.Handa*, A.Naito and N.Hoshimiya+

Dept. of Anatomy, Shinshu Univ. School of Medicine, Matsumoto 390, Japan

+Res. Inst. of Applied Electricity, Hokkaido Univ., Sapporo 060, Japan

Restoration of motor function in the paralyzed extremities of spinal cord injury (SCI) patients by FES is described. Helicallly-coiled percutaneous electrodes made by Teflon-coated 19 strand stainless steel wires were used for intramuscular nerve stimulation. Multichannel standard stimulation patterns for controlling paralyzed extremities were obtained from trapezoidal approximation of integrated EMG during motion detected from normal subjects. Input of the threshold and maximum stimulating voltages of each muscle of the patient automatically created stimulation data of FES for each patient. This method easily realized versatile control of multi-joint system of the extremities. Therefore, not only locomotive activities of the paralyzed lower extremities in paraplegics but also upper extremity function of high SCI patients such as C4 quadriplegics could be restored by our multi-channel FES system.

BE21-B.5

Magnetic Stimulation of Localized Area in the Human Cortex, S. Ueno*, T. Tashiro, and K. Harada, Department of Electronics, Kyushu University, Fukuoka, 812, Japan

A method of localized stimulation of the human cortex is proposed. The basic idea is to concentrate induced eddy currents locally in the vicinity of a target in the cortex by a pair of coils which are positioned outside the head so that time-varying magnetic fields pass through the head in the opposite directions around a target. The eddy currents induced at the target are expected to flow together, which results in an increased current-flow at the target. Spatial distributions of eddy currents induced in the head are calculated. The current density at the target makes a peak which is higher by 2-3 times than current densities at non-target regions. The validity of the proposed method is demonstrated by experiments using frog nerve-muscle preparations. A U-shaped core is used. The core is driven by discharge of capacitor bank through a thyristor switch. When the nerve is positioned in the area between magnetic poles, the nerve can be stimulated by a capacitor voltage 400 V, and muscle contraction is observed. In contrast, when the nerve bundle is positioned outside the magnetic poles, nerves cannot be stimulated even by the three times of capacitor voltage 1200 V.

BE21-B.4

Suppression of Volitional and Automatic Activity in Humans by Transcranial Cortical Stimulation, M.R. Dimitrijevic*, D. Moffit, C. Van der Linden, Division of Restorative Neurology and Human Neurobiology, Baylor College of Medicine, 7000 Fannin Suite 2140, Houston TX 77030

Transcranial cortical stimulation has been previously shown to elicit motor evoked potentials (MEPs) in intact human subjects. In addition to the excitatory activity, the stimulation can markedly suppress ongoing activity. To demonstrate this, we used two different experimental paradigms in a group of 10 healthy subjects. Anodal cortical stimulation was applied 1), while making the fastest possible contraction in response to a visual cue, recording surface EMG activity from the thenar (contracted) muscle, and 2), while recording EMG activity from the leg muscles during postural disturbances of subjects standing on a moveable platform (rocker). In both conditions, we demonstrated a silent period. These results illustrate that cortical stimulation, in addition to its excitatory influence also has an inhibitory effect on motor activity established through volitional or postural motor tasks.

BE21-C.1

A practical walking system for paraplegics employing the LSU Orthosis and reciprocal electrical stimulation of the thigh muscles. M. Solomonow*, R. Baratta, H. Shoji, R. Douglas, M. Ichie and S. Hwang. Department of Orthopaedics, LSU Medical Center, New Orleans, LA, USA.

The LSU Reciprocal Gait Orthosis (RGO), which allows paraplegics to assume independent upright posture and reciprocal gait with the aid of only a walker or crutches, was successfully fitted and evaluated in over 112 patients in the last 10 years. This report describes further developments centered on the addition of a four-channel electrical stimulation unit which reciprocally and voluntarily contracts the contralateral quadriceps and hamstring to provide effective and cosmetic reciprocal gait which reduces the metabolic energy consumption of the patient by 37% to 52% as compared to reciprocal gait with the RGO but without the benefit of stimulation. Data will be presented to quantify the reversal of muscle atrophy of disuse by FES over six weeks, the increase in muscle bulk, hip flexion-extension torque, heart rate and PO₂ profiles during the therapy and during reciprocal gait with and without stimulation will be compared to highlight the benefit of this portable system as a practical rehabilitation modality.

BE21-C.2

A Biomechanical Study of two Walking Braces for the Paralysed, M W Whittle* and R J Jefferson, Oxford Orthopaedic Engineering Centre, Headington, Oxford OX3 7LD, England.

Two designs of reciprocal walking brace for paralysed people have recently emerged as practical systems - the hip guidance orthosis (HGO) from Oswestry, England, and the reciprocating gait orthosis (RGO) from New Orleans, USA.

A trial has been conducted to compare the two braces. 22 paraplegic subjects in matched pairs were able to try each brace for 4 months, in a crossover study. At the end of the trial, the subject was able to keep whichever brace he or she preferred. The following assessments were performed at appropriate intervals: clinical, psychological, ergonomic, economic and biomechanical.

The biomechanical assessment made use of two types of gait analysis: videotape was used to determine the general gait parameters and the quality of walking, and the Vicon television/force platform/computer system was used to make detailed kinetic and kinematic measurements. The results show that the differences between the subjects are much greater than the differences between the braces. Nonetheless, differences were observed between the braces, particularly in the patterns of movement.

BE21-C.4

Motorized Exoskeleton Orthosis, Y. Sakurai*, H. Miyamoto, K. Tokimura and Y. Shimazaki, Tokyo Women's Medical College, 8-1 Kawada-cho, Shinjuku-ku, Tokyo, Japan

The handicapped persons with paralyzed lower extremities desire strongly to stand and walk on their own feet. In this paper, motorized exoskeleton orthosis system which assists the walking of handicapped persons will be reported. The exoskeleton frame is fitted to the waist and legs. Hip and knee joint of this frame are powered with electro-hydraulic digital actuator controlled with micro-computer. Through potentiometers mounted coaxially on each joint, changes of joints angles are continuously detected. A pair of foot switch sensor made of pressure-sensitive rubber detect the instant of heel-strike and toe-off. Inclination or three dimensional posture of the body is detected by gyroscopes. The communication and interaction between man and machine are carried out with crutches provided with contact sensor and command switch. Patients can walk, stop, turn to left or right and go up and down stairs with this system.

BE21-C.3

Development and Assessment of Neural Orthoses for Paraplegics

A. Cliquet Jr., S. E. Solomonidis, R.H. Baxendale, B. J. Andrews and J. P. Paul
Bioengineering Unit, University of Strathclyde and Institute of Physiology, University of Glasgow, Glasgow, G4 0NW, U.K.

Several types of orthoses have been designed to assist the locomotion of paraplegic subjects. These vary from pure mechanical devices that work through upper limb mediated posture and gravitational action (e.g. hip-knee-ankle-foot orthoses), to surface functional neuromuscular stimulation on its own which, although more cosmetic than the former, may lead to muscle fatigue and consequent loss of function. A hybrid approach can be used in order to obtain the best of both systems and therefore some hybrid systems that use different control strategies have been developed. Since the energy required to rise from the sitting to the standing position as well as to achieve "aided gait" is provided by the patient's own muscles, analyses of upper limb effort and metabolic cost, were carried out. The metabolic assessment used indirect calorimetry and the biomechanical evaluation was done by incorporating force measuring transducers in the walking aid and recording ground reaction forces. Repeated measurements for each subject fitted with different types of orthoses allowed direct comparison of the relative "efficiency" of each system.

BE21-C.5

A portable EMG Training Device for Amputees with Automatic Data Storage.
U. Boenick*, W. Roßdeutscher and V. Matute,
Technische Universität Berlin, D 1000 Berlin 10, Germany

Best orthopedic management of amputees can be achieved by myoelectrically controlled prostheses, which use the EMG signals of the stump musculature as signal sources. However, in many amputees the EMG after amputation and longer inactivity periods is so weak that the necessary level can not be achieved. The major part of these patients can increase their signal level after a systematic training.

Training devices used for this purpose measure and display the muscle potentials after amplification. A documentation of the time dependent training progress is not possible. To overcome this problem a two channel measuring and training device was developed which stores all features and may help the physician to decide more precisely whether or not a successful prosthetic management of the amputee is to be expected. Experiences from practical applications are briefly reviewed.

BE21-D.1

Adaptation of consumer microcomputer-based technology to create affordable environmental control for the profoundly motor-disabled

David A Boonzaier* and Michael Kieviansky, U.Cape Town Medical School & Grootte Schuur Hospital, Observatory 7925, S.Africa

The combination of a variety of inputs, computers, software and outputs against a background of disabled-users' individual needs and capabilities, has created a morass of choices which the average therapist is ill-equipped to handle. This is particularly true of a developing country with a relatively larger number of rural technologically under-prepared people. Though there are special schools for middle-level disability, eg. Cerebral Palsy, there are few facilities for the profoundly disabled, eg. high-level quadriplegics. It therefore became the responsibility of hospital-based therapists, and parents of disabled people to take the initiative.

Four years ago, a country-wide self-help organisation, INTERFACE: Computers for the Disabled, was established to act as an information/expertise broker. A close liaison has developed between Interface and the U.Cape Town Rehabilitation Technology Group, leading to many collaborative projects.

Common consumer products such as TV remote controllers often contain embedded microprocessors. Depending on the manufacturer's openness for technical access, these devices can often be modified to accept alternative inputs for use by disabled people. This is particularly important since so-called "luxury" devices for the general population become necessities if disabled wish to do normal tasks, eg. opening the door to a visitor, or making a phone call. However, several device specific hand-held controllers often need to be manipulated from the user's customised interface such as joystick, sip-puff, eye-position etc. We have developed a "smart" Microprocessor-based infrared link to offer a wireless, 2-way communication path between a disabled user and the "world" at large. For adaptability we chose RS232C protocol so that not only control information but also messages, eg. notification that an instruction "open the door" had been executed. Device drivers, both input- and output- are loaded to EPROM from a master file by the therapist who is setting up the system to match the disabled user's capabilities and needs. To achieve universality each commercial device will need a standard plug to enable it to be attached to the host microcomputer. The prototype system we have built has already given a great deal of independence to a severely disabled client.

BE21-D.3

Using a Microcomputer to Rehabilitate Communication Ability of Disabled Man, Liuda Chu*, Institute of Electronics, Academia Sinica, Beijing, China

A special microcomputer system has been developed for a severe physically disabled man who may move his foot, a joint or head to press two buttons of the system to control the computer to achieve communication ability with community. The author was involved in this project and developed a program to reach the above goal.

The program is a two-button controlled screen editor which has following functions: automatically to access disk file and save file, button controlled text input, text modification, text print, and alarm function available to secure the user out of accident. A simulated auto-scan screen keyboard on display terminal guides the user to choose alphabets or function symbols to write a letter, a note or a file to be saved or printed. Thus, for a disabled, this system will be only a great tool to communicate with others.

This system may be used both in English and Chinese characters.

BE21-D.2

AN INTEGRATED SYSTEM OF RELATION WITH THE ENVIRONMENT FOR DISABLED PEOPLE

L.Gardeazabal, G. Buldain, A.Arruabarrena, E.Gómez, J.González*, Informatika Fakultatea EHU. 649 pk 20080 DONOSTIA (SPAIN).

There are a great variety of diseases that produce deep problems in the movement (cerebral palsy, hemiplegia, etc.). People who suffer from them see greatly affected their independency and their possibility of relationship with other people. We have designed an integrated system to solve this lack, improving autonomy and communication with people.

This system is divided in three blocks:

- * An infrared-based environment controller that allows to switch on and off electrical devices, pick-up the telephone, etc.
- * A communication tool controlled by a switch for non-vocal handicapped people. Messages are built letter by letter using some edition functions and shown in a LC display. All the messages can be sent to a printer via a parallel connexion
- * A keyboard emulator of a computer allowing to access to a P.C. by a switch. Thus, the user can work with most of the programs available in the market. The connexion of the keyboard emulator with the computer is via an infrared emitter, avoiding the use of multiple wires.

This integrated tool is being used by a group of people who suffered from cerebral palsy in a local association of C.P. ASPACE

BE21-D.4

VIRTUAL SOFTWARE INTERFACING IN REHABILITATION ENGINEERING, B. Rowley*, and C. Davis, Dept. Biomedical Engr., O. Amos, Special Ed. Program, Wright State University, Dayton, Ohio 45435 USA

One of the challenges rehabilitation engineers face is interfacing disabled persons to computers so they can communicate and become productive in the work place. The number of options are limited requiring compromises between needs and current technology. We have developed a virtual interface method (VIM) which overcomes many limitations to the use of software such as word processors, spread sheets, data base managers, and programming languages by those with severe neuro-motor handicaps. The VIM is a resident memory program providing a gateway between augmentative communications software which interfaces the disabled with the computer and commercial software. As a result, the disabled person has access to the same software that able-bodied persons use.

When the VIM is invoked, a special window is opened on the monitor. Through this window the user has control over commercial software using augmentative keyboard techniques. An unlimited number of linked customized windows are available for operation of augmentative software or with forty positions for commands and macros.

BE21-D.5

MODIFIED TACTILE VISUAL SUBSTITUTION DEVICE FOR REPRESENTATION OF TWO- AND THREE DIMENSIONAL PATTERNS, T.Dohi*, T.Horiuchi, H.Narahara, I.Sakuma, T.Masuzawa, The Univ. of Tokyo, 7-3 Hongo, Tokyo, Japan

To promote out-door activity for the blind and minimize their overcaution against the subjects in a far distance, an visual substitutional system being able to provide a greater variety of environmental information for the blind is necessary. For this purpose, three dimensional space recognition training system was developed and tested with normal subjects.

The system is consisted of a tactile (tablet with piezo-electric vibratory pin matrix), two- and three-dimensional environmental models and a visual axis detector using position sensitive device(PSD). These environmental models are programmed in a micro processor and geographically represented on the tactile. PSD can detect the orientation of the subject and represent the shape of model from a certain angle on the tactile via micro processor(visual tracking method).

Five different shapes of two dimensional figure were utilized in the tests with nine normal subjects. Over 80% of discrimination ability was observed on the average when visual tracking method was employed.

Preliminary evaluation showed that this system could be utilized for the environmental recognition training on the congenital blind.

BE21-E.2

Airflow Resistance of a New Voice Prosthesis, A. Ben Jebria*, C. Henry, M. Gioux, F. Devars and L. Traissac, Penn State University, University Park, PA 16802 and Université de Bordeaux-II-33076 Bordeaux, France.

Performance of a new voice prosthesis, used to restore speech in patients following total laryngectomy, was evaluated by measuring in-vitro, as well as in-vivo airflow resistances. The prosthesis is made of a relatively soft polyurethane material, unlike other devices reported have been made of silicone. It has the form of biflanged tube of 0.35 cm diameter and variable length that can be adjusted to fit the morphological structure of the part situated between the trachea and the esophagus of each patient. The fixed flange at the esophageal side of the tube is provided with a one-way-valve system that opens during expiration (for voice production) and immediately closes to prevent leakage of liquid and food. Total device resistances were found in the range of 35 to 46 cm H₂O/L/S when the flow rates ranged from 0.05 to 0.35 L/S. Therefore, our voice prosthesis operates in a range of airflow resistance comparable to that of intact human larynx during vowel production. In addition, the aerodynamic performance of this new prosthesis compares favorably with the various devices reviewed, because it offers the least opposition to airflow.

BE21-E.1

The Use of the Eyes by Severely Disabled People for Communication and Control
P A GRIFFITHS*, E A DYMOND, R POTTER

Many severely disabled people are restricted to eye movement as their sole means of communication. This function has been harnessed in different ways e.g. signals arising from the corneo-retinal potential, the differential reflection of infra red light or monitoring of the eye by a television camera.

Work at Lincoln over several years with people having congenital or acquired disorders has allowed eye movement as a control function to be explored in a variety of different circumstances. This has led to the definition of the important design features of an eye movement system.

These will be described and discussed together with the approach which has been taken to use eye movement in a daily living context so that the user may write letters, control domestic equipment, partake in recreation and through synthetic speech even make telephone calls.

BE21-E.3

Computer Aided Rehabilitation of Aphasia, J. Mäkilä*, Technical Research Centre of Finland, Tampere, Finland, L. Salonen, Helsinki University Central Hospital, Helsinki, Finland.

This aphasia rehabilitation system is built upon a rehabilitation method called Language Enrichment Therapy (LET). Based on systems approach, LET is a comprehensive method, the goal of which is to restore all forms of language processing capabilities by including them into an interactive system. Various linguistic subfunctions are treated in a hierarchical manner in reciprocal relations rather than separately. The computer-aided LET rehabilitation system has been produced for the IBM AT personal computer using graphics and digitized speech. Clinical evaluations started in the spring 1987 using a prototype of the therapy system. Even severely aphasic patients learn to use the system and most of them find working with the computer motivating.

BE21-E.4

Design and construction of a valve for endoesophageal tubes. G. Michanetzis and Y. Missirlis*, Laboratory of Biomedical Engineering, University of Patras, Patras, Greece.

In certain cases of cancer of the esophagus, where surgery is not admissible, feeding the patient is done through a permanent endoesophageal tube. Many clinical studies have indicated, however, that regurgitation of stomach contents takes place when the patient is inclined, after being fed, leading to choking and subsequent death.

The purpose of this study was to construct a bio-compatible passive valve to be mounted on a Celestin tube according to the suggestion of Dr. Lekakos. The operation of the valve would be such as to remain open while the patient is being fed and to close and not allow the stomach contents to regurgitate into the esophageal tube when the patient is inclined.

The final design is that of a hinged disc plate of magnetic material (like the "toilet seat" type of an artificial heart valve) covered with polyurethane. At the vertical or semi-inclined position (45° - 90°) the valve remains open due to gravity, while at the horizontal position (0° - 30°) the disc is attracted by a steel ring covered with polyurethane and the valve closes.

In-vitro testing was performed to verify the operation of the valve and results will be shown on the valve's function in dogs.

BE21-E.5

A specialized electronic game for restoration of function after hand surgery, (*)A.Pepino*, (**)M.Iocco, (*)M.Bracale, (**)N.Misasi

* Univ. of Naples, Electr. Dept. Via Claudio 21, Naples (I)

** Univ. of Naples Orthoped. Clin. Via Pansini, 5 Naples (I)

From a general point of view biofeedback is a form of psychophysiological training where sensorial stimuli representing biological functions, are presented to the organism which produces these events. A specialized electronic game can be considered like a sort of biofeedback device to improve motivation and for monitoring the rehabilitation trend. A video-graphic system, together with a special support for the arm, has been designed for rehabilitation after hand surgery. A clinical evaluation has been carried out on ten patients for three months, and we observed an increased motivation and a correlation between the improvement of finger joint movement, and the score obtained in the training.

This work was financially supported by MPI 40% and C.N.R. "Nucleo di Ingegneria Medica e della Riabilitazione"

BE21-E.6

Basic and Clinical Studies on Electronic Walk Helper, Ying-bing Liu*, Lian-sheng Liu, etc., Surgery Institute, Daping, Chongqing, China.

EWH-1 belongs to one of the FES Walking Helpers with the following main features: Simple construction, small and fine dimension, portability and cheapness, application to both walk helping and treatment with satisfactory efficiency. Experiments on animals and healthy people demonstrated that 0.2ms stimulating pulse at 30-40Hz and 20-80V could attain an optimal effect for the contraction of the paralyzed muscles, and no discomfort to the clinical patients.

Clinical analyses on more than 4000 cases indicated that EWH-1 could achieve the pedal dorsal flex just in those who could dorsally flex their ankles regardless of the course, but had no curing effects in the tetanic hoofbound and severe spasm. Earlier applications could more favor the functional restoration of the paralyzed muscles. EWH-1 could be also used in the walk aiding of the incomplete paraplegia, cerebral palsy and sequelae of the myelitis. Out of the clinical limits for EWH-1, the parameters and multichannels for motor dysfunctions at multiple joints over the knee are undertaken in our lab., so as to meet the critical needs of much more paralytics.

BE22-A.1

A FAST CORRELATION TECHNIQUE FOR MULTIMODALITY IMAGE MATCHING

Anthony Apicella*, Joachim Nagel, Ph D.

Advanced nuclear medicine imaging modalities such as single photon emission tomography and positron emission tomography provide valuable functional or physiologic information. As this information is complementary to anatomic images obtained via Nuclear Magnetic Resonance, the diagnostic potential of the Nuclear Medicine images may be augmented by objective, accurate matching of the different data sets.

Different techniques, such as correlation analysis, edge detection, or fiducial landmarks have been proposed for image matching. They all suffer from severe shortcomings with regard to either reliability and precision or mathematical complexity resulting in unreasonable calculation times.

We developed a new correlation analysis to compute the three dimensional translational and rotational shifts of the image planes necessary to combine or overlay the different images. Current correlation analysis approaches are limited, as the coupling of the registration variables requires an iterative, computationally expensive algorithm. The approach described here improves upon past work by first decoupling the translational and rotational components, thus eliminating the iterative part of the algorithm and significantly reducing the computational expense.

The input images are first transformed into images which are translation invariant. These translation invariant images are converted to polar coordinates and the rotation angles calculated. The rotational corrections are applied to the original images, and then the translation distances are calculated. Given the matching differences between the two data sets, the NMR images are transformed so that they are aligned with the PET images.

BE22-A.2

The Characterization and Quantization of Soft Tissue in MR Images by a Multiple Pixel Intensity, Region Growing Algorithm

Jacob M Agris* and Rui J.P. de Figueiredo, Fellow IEEE

*Dept of Electrical and Computer Engineering, Rice University
P.O. Box 1892; Houston, Texas 77251-1892 tel. (713)527-4020

*Dept of Radiology, Baylor College of Medicine

The characterization and quantization of soft tissue in Magnetic Resonance [MR] imaging is complicated by the nonspecific nature of the imaging modality. It is difficult to determine the composition of the tissue volume corresponding to a particular pixel based solely on T1 and T2 ratios since there are significant partial voluming effects and since T1 and T2 ratios may not uniquely characterize a material that is a chemical mixture. Additional information such as the spatial distance in the image plane or T1 and T2 spectra must be considered. Region growing algorithms such as those presented by Gonzalez and Wintz take into account both the image pixel intensity as well as spatial information. The error function that assigns a pixel to the region is based on a single intensity value for each pixel and is defined as

$$\varepsilon = |I(x_0, y_0) - I(x, y)|$$

where $I(x_0, y_0)$ is intensity at pixel x_0, y_0 and ε is error function.

However, there are two intensities for each pixel corresponding to the T1 and T2 ratios.

We have proposed an error function defined as the vector sum of the intensity differences in each image plane. The intensity $I(x_0, y_0)$ used to characterize the region is classically defined as the intensity of a connected pixel known to be in the region. However this can lead to propagation of a region throughout the image planes. We used an intensity value that is a function of all the intensities known to be in the region of interest. Implementation of an algorithm that uses both spatial as well as the above mentioned, multiple intensity criterion has shown to be a robust method in MR.

BE22-A.4

Constant False Alarm Rate Focus Detection by 2-D Noncausal and Nonstationary WDR Modeling, hao Ping-Ya¹ and He Zhen-Ya, Digital Signal Processing Research Group, Radio Department, Nanjing Institute of Technology, Nanjing, P.R. China.

A X-ray photograph or tomogram can be viewed as a sample of a two-dimensional (2-D) random field represented by a white-noise-driven representation (WDR). Previously, only causal and stationary WDRs were fully used for the lack of a efficient parameter estimation technique to estimate the parameters of the general noncausal WDR which represents the gray level at one point as a linear combination of its neighbors in all directions and a white noise, and only unsatisfactory results were observed. In this paper, we study constant false alarm rate (CFAR) focus detection by means of 2-D noncausal WDR modeling based on an asymptotically consistent and computationally efficient modified least-squares (LS) estimation method recently developed by the authors, for identifying parameters of such a noncausal model (cf. Preprints, 8th IPAC symposium on I.S.P.E., to appear). Furthermore, the nonstationarity is also assumed in the modeling as the image statistics of the focuses and the normal parts of organs are different. Because the modified LS method is for stationary case, we first develop, in this paper, an adaptive companion of the method by carefully exploiting the special structures of the normal equation set of that method. The adaptive method using only local pixels in a sliding data window is a finite memory algorithm and is spatially recursive in nature, and it estimates the parameters of the noncausal and nonstationary WDR consistently and computationally efficiently. Both theoretical analyses and computer simulations show that the estimates produced by this method are about 10 times as accurate as those produced by conventional LS, while the computational complexity of the former is only the square root of that of the latter. Developing a probability density function (PDF) for the photograph based on the noncausal and nonstationary WDR modeling, making significance testing under the CFAR constraint, we constructed a CFAR focus detector by programming PC VISION image processing system with FORTRAN77 and 8088 assembly language. The CFAR detector can easily detect calculuses in urinary organs, pulmonary diseases and other diseases from the corresponding X-ray photographs, while detectors based on other modeling techniques can not. The details about the structure of the CFAR detector and of some experiments are given.

BE22-A.3

Enhancement of Radiographic Images by MTF and Fractal Dimension Evaluation, F. Arduini, S. Dellepiane, C. Regazzoni, F. Sturaro, G. Vernazza*, DIBE University of Genoa, Via All'Opera Pia 11/A Genova Italy.

In medical images human operator focuses his attention on some particular regions or structures of interest: purpose of this paper is to describe a new method suggested for local enhancement of textured areas and to present the related preliminary results. After the computation of the MTF (Modulation Transfer Function) of the whole acquisition system by a bar pattern, a "global restoration" of the image is performed by processing the original image with an appropriate linear shift invariant filter (complementary to MTF curve) keeping attention to reduce noise effect at high frequencies. Then, in order to detect areas of specific texture properties, the fractal dimension D has been calculated by a "fractal preserving method", in order to preserve the anatomical structures. In fact according to this approach, some prefixed masks are positioned around each pixel and D is calculated by averaging on the most homogeneously textured mask (i.e. minimum variance). The fractal dimension D has been evaluated by the "blanket approach". Using the "fractal image" it is possible to localize the presence of specific textured areas and to select appropriately local filters, i.e. with specific frequencies behaviour, to be applied to the restored image. In fact, we recall a presence of a direct relation between D values and spatial frequencies behaviour, in particular low D (e.g. around 2.0) denote quite spatial homogeneous region. Consequently frequencies filters poles have been calculated by taking into account D values. This approach has been verified on some chest radiographic images and the obtained results are quite promising.

BE22-A.5

Digital Subtraction Angiography on a Personal Computer, M.Cesarelli¹, M.Bracale, Cattedra di Elettronica Biomedica-Nucleo di Ricerca di Ingegneria Medica e della Riabilitazione C.N.R., Faculty of Engineering-University of Naples, Via Claudio 21, 80123 Naples, Italy.

The acquisition and the elaboration of images are assuming an important role in the evolution of the medical diagnosis. An image elaboration system needs to store a great number of information in a short time.

Up to now, this job is performed by a minicomputer-size system. The technological progress of the fast electronic and the improvement of the operative system allow the use of microcomputers for this aim.

We are developing a DSA (Digital Subtraction Angiography) system based on personal computer PC AT with an image board subsystem. Digitized 512x512x8 bit images from an external source are stored on main memory, at 1 image/sec. rate and a subtraction is obtained in about 30 seconds.

Considering the price and the performance, the system is useful in the routine work of the neuro and angiography lab.

BE22-B.1

3D RECONSTRUCTION OF A WHOLE HEART USING MRI DATA, M. KUWAHARA*, Osaka Sangyo University, 3-1-1, Nakagaito, Daito-shi, Osaka 574, Japan, and S. Eiho, Automation Research Laboratory, Kyoto University

The gated MRI method gives us several sets of cross sectional images on transverse, coronal and sagittal planes of a heart in a cardiac cycle. In this paper, we propose a method of reconstructing 3D shapes of each part of the heart, i.e., left ventricle, left atrium, right ventricle, right atrium, aorta and pulmonary artery, in a voxel space using three pairs of the above cross sectional images taken at the same cardiac phase: two transverse, two coronal and two sagittal images. We also can observe the 3D heart composed putting together these six parts superimposing on the original cross sectional images.

BE22-B.3

Processing of "in-vivo light microscopy" images to model arterial thrombosis.

Marc Nyssen, Erik Blockeel, René Bourgain

Medical Informatics Dept. Vrije Universiteit Brussel
B-1090 Jette, Belgium

To make reproducible and accurate measurements of the formation and evolution of arterial thrombi during in-vivo experiments with small laboratory animals, a measurement and processing chain has been set up. Light transmission is used to observe the small (.3 mm) arteries, without disturbing the processes involved. The transmission microscope images, captured by a chalnicon camera, are digitized in real-time by a special processor, connected to the local UNIX network.

Unfortunately, blood is a highly scattering medium for light in the visible wavelengths used ($\sim 700\text{nm}$), so that the interpretation of the raw images is not straightforward.

A model for the light transmission through flowing blood was realized and tested. This model takes into account multiple scattering and the geometry of all factors involved, except second order effects, due to flow disturbance by the presence of the thrombus itself.

The impressive amount of numeric processing, necessary to apply the model, is handled by the network of UNIX workstations, which also provide all utilities to visualize the results in different formats: as functional images, as graphs or in numeric formats.

BE22-B.2

Three-Dimensional Processing of Microscopic Images, A. Takahashi* and I. Nemoto, Tokyo Denki University, Hatoyama, Saitama, Japan

In the conventional light microscopy, images of out-of focus regions of the object blur the image of the in-focus plane. We have been investigating methods to get higher resolution in the optical axis of the microscope by processing images of an object obtained with various distances between the objective lens and the object. We have employed the assumption of linearity for image formation and used the parameters of the lens to estimate the transfer function of the optical system. Firstly, under the assumption of incoherent illumination, the inverse problem was solved by essentially applying the inverse of the image formation matrix to the observed images of a cell containing magnetic particles. The results show considerable improvement in three-dimensional resolution. The other method used in this study, which is based on the recently proposed model of three-dimensional image formation, does not require the assumption of incoherent illumination. We have been investigating the possibility of utilizing this method to improve the three-dimensional quality of phase-contrast microscopy. We have shown that this three-dimensional theory can be derived from the wellknown two-dimensional image formation. Based on the theoretical work, we are studying the image formation and recovery in the phase-contrast microscopy by simulation and by using a simple sample.

BE22-B.4

Thermal Image Enhancement by Histogram Specification, Dong-Ho Lee* and J. A. Pearce, The University of Texas at Austin, Dept. of Electrical and Computer Engineering, Austin, Texas 78712

Thermal imagery is typically of low contrast since thermal gradients encountered in biological studies are quite subtle. It is difficult to find targets in a thermal image. Contrast enhancement by histogram modification has been studied.

Histogram equalization is commonly used as a method for enhancing images. However, the image resulting from this transformation is frequently so distorted that landmark identification is not made easier. We have investigated more general transformations to obtain specified output histograms.

One-to-one histogram mapping schemes were compared including a single ramp and dual ramps with differing slopes and intercepts. Examples are shown which illustrate what results are obtained from such transformations.

BE22-B.5

Computer-Assisted Delineation of Vascular Patterns in Thermographic Images

E. K. Y. Chan* and J. A. Pearce
Biomedical Engineering Program
The University of Texas at Austin

Abnormal vascular patterns revealed by thermography may be indicative of an underlying pathology. The goal of this study was to identify and delineate vascular patterns in thermograms of human limbs by using various edge detection strategies. This would aid in the non-invasive diagnosis of occlusive diseases such as vasoconstrictive Raynaud's Disease. The same methodology may be used in the delineation of breast vascular patterns for cancer prescreening. In this study, human forearms were precooled by the application of ice. This created a larger temperature gradient between the skin surface and the regions of the skin located over major vessels. Precooling was followed by a period of ten minutes for thermal equilibration before data acquisition. The initial thermal images were prefiltered with a 9 X 9 square median filtering scheme, so as to improve the performance of both thresholding and zero-crossing edge detectors. Various edge detection templates were then convolved with the filtered images. Results indicated a trade-off between noise reduction and the retention of edge information. The boundary detection method by Frei and Chen gave the most reproducible results.

BE23-A.1

Acupuncture Energies: A Somewhat Medical Model; Joseph M. Helms*, M.D., American Academy of Medical Acupuncture.

The presentation of the Classical Acupuncture Conceptualization of Energy Circulation Networks and then to develop a gross anatomical model of electroionic circulation consistent with the classical information. It will illustrate how the different levels of the acupuncture networks are manipulated with needles to treat various disorders, and how one can understand the therapeutic input in light of the anatomical model.

The hybrid paradigm allows an explanation of the impact of the needle-as-electrode on the electrical and electroionic system of the body, and an academically comfortable organization of acupuncture theoretical and clinical information. It will serve well as the classical reference for the more neurophysiological presentations.

BE22-B.6

Microwave Active Imaging for Biomedical Applications, G.GABORIAUD, J.C. ROSENWALD*, J:Ch. BOLOMEY*, P. BERTHAUD**. Institut Curie, 75u05 Paris, *CNRS-ESE, Plateau du Moulon, 91190 GIF-sur-Yvette **SATIMO, Plateau du Moulon, 91190 GIF/sur/Yvette

A planar microwave camera operating at 2.45 GHz has been realized for rapid imaging of biological structures. Images can be formed by analysing the transmitted or the reflected wave. With multiview proceedings, tomographic reconstruction can be achieved. Microwave images are related to the dielectric properties of tissues and, hence, to any physical or physiological factor whose these properties depend (temperature, water content, blood flow,...) Preliminary devoted to non-invasive thermal control during hyperthermia treatments, the use of the camera is now extended to situations exhibiting higher contrasts: water lung content monitoring, oedema diagnostic of excessive irradiated patients, or organs defreezing control, constitute some representative cases whose preliminary results will be presented.

BE23-A.2

Acupuncture Stimulation of Endogenous Opioids and the Effects on the Immune System, C.C. Moss*, M.D., La Jolla CA.

Acupuncture research in the West has focused primarily on pain therapy. The Chinese literature has suggested far reaching effects on the immune system using acupuncture. In a review of the English literature, two studies exist that show enhancement of cell mediated immunity with acupuncture therapy. A large number of studies have shown that acupuncture stimulates endogenous opioid production in the CSF and blood. An equally impressive body of research shows that the opioids have far reaching in-vivo and in-vitro effects on the immune system.

This review is to suggest that the effects of acupuncture on the immune system could be of great clinical benefit through the manipulation of the endorphin system and that further research in this area should be undertaken.

514

BE23-A.3

ELECTRO-ACUPUNCTURE (EA) ANALGESIA: EVIDENCE FOR ENDOGENOUS OPIOID FACILITATORY AND INHIBITORY EFFECTS D.J. Mayer, Dept. of Physiology, Medical College of Virginia Richmond, VA 23298.

EA has been shown to increase pain thresholds in many species including man. Our laboratory has been involved in investigating the role of endogenous opiates in this form of analgesia in man and rats.

In man, we have challenged the analgesia produced by EA with the narcotic antagonist, naloxone. We found that naloxone almost completely antagonizes the increased pain threshold.

Low frequency EA analgesia in rats has been thought to be mediated by endogenous opioids because naloxone antagonized 2 Hz EA analgesia - partially reversed 2-15 Hz EA analgesia (1 and 20 mg/kg respectively, Han *et al.* *Acta Physiol Sinica* 38(5):475 1986). We conducted experiments with members of Han's laboratory in the U.S. and in their laboratory in China using the exact methods of Han *et al.* In no experiment was opiate antagonist reversal or reduction of EA observed. Rather, we found Naloxone potentiated analgesia in most experiments. Additional studies have elucidated the neural circuitry involved in this opiate anti-analgesia system. These results will be compared to the neural circuitry involved in other forms of analgesia. Supported by H.H.S. award DA 00576

BE23-B.1

Acupuncture: A Neuromodulation Technique For Pain Control, Lorenz K.Y. Ng, Washington DC

Multiple analgesic systems, opioid and non-opioid, are known to exist within the brain and spinal cord. The fact that these systems can be activated by sensory afferent stimulation is the basis for various neuromodulation techniques of pain control. Acupuncture merits consideration as a form of neuromodulation since its effects are produced by afferent sensory stimulation. Acupuncture analgesia results from interactions at different levels of the CNS between nerve impulses arising at the origin of pain and afferent impulses from the stimulation site. Evidence will be reviewed to show that acupuncture stimulation activates certain somatosensory pathways, including central neurohumoral and endorphinergic systems which play a role in modulating nociceptive impulses in the CNS.

Neuromodulation techniques play an increasing role in the treatment of chronic pain. As more knowledge is gained about peripheral control of the central nervous processes, it is likely that acupuncture will gain greater acceptance and importance in treating pain of different etiologies.

BE23-B.2

Quantification of Passive Acupuncture Points for the Prognosis in Pain Management, H. C. Dung, Dept. of Cellular & Structural Biology, University of Texas Health Science Center at San Antonio, San Antonio, Texas.

A major impediment in pain management is the availability of a reliable and objective method for an accurate and convenient measurement of pain in our body. Existence of passive acupuncture points has been used as a tool for a routine quantification of pain. A passive acupuncture point (PAP) is clinically defined as a tender area which can be detected relatively easy on the skin surface by finger-tip pressure of less than two kilograms. The appearance of PAP is known to follow a fairly predictable sequence. Thus, it is possible to mathematically quantitate the numbers of PAP in the entire body surface. The number of PAP is then used linearly to express the degree of pain. A higher degree to pain due to more numbers of PAP denotes a bigger quantity of pain, and vice versa. There are various factors that determine the number of PAP in a patient suffering from pain. Two of the most important factors are the type of diseases and duration of injuries. In general, the manageability of a pain condition decreases as the degree of pain increases. Such clinical manifestation provides a useful criterion to predict the outcome in using acupuncture as a therapeutic modality in managing pain conditions.

BE23-B.3

The Effectiveness of Acupuncture in Managing Pain. Joseph M. Helms; American Academy of Medical Acupuncture.

The effectiveness of acupuncture in managing the pain of primary dysmenorrhea was investigated in a randomized and controlled prospective clinical study. Forty-three women were followed for one year in one of four groups; the Real Acupuncture group was given appropriate acupuncture and the Placebo Acupuncture group was given random point acupuncture on a weekly basis for three menstrual cycles; the Standard Control group was followed without medical or acupuncture intervention; the Visitation Control group had monthly nonacupuncture visits with the project physician for three cycles. In the Real Acupuncture group, 10 or 11 (90.9%) women showed improvement; in the Placebo Acupuncture group, 4 of 11 (36.4%); in the Standard Control group, 2 of 11 (18.2%); and in the Visitation Control group 1 of 10 (10%). There was a 41% reduction of analgesic medication used by the women in the Real Acupuncture group after their treatment series, and no change or increased use of medication seen in the other groups.

BE23-B.5

Stress of Electric Stimulation in Veterinary Acupuncture. Y-C Hwang; School of Veterinary Medicine Tuskegee University, Tuskegee, Al 36088, USA.

Veterinary electroacupuncture (EA may be stressful to the animals, because of its manual restraint, needling, and electric stimulation which are well known stressors. To evaluate stress of EA in the animals, the following 2 studies were conducted. Plasma cortisol concentrations (PCC) of 24 Nubian milking goats were measured before, during and after EA, sham EA, or restraint alone. Mean PCC during and just after termination of the treatment was significantly higher in the EA treated goats (53.6+22.0; 31.4+18.1 ng/ml) than in the goats with restraint only (32.6+10.5; 17.4+9.0 ng/ml). Another group of 8 goats were treated with identical EA. Their cardiovascular and nociceptive responses were compared before and during EA. The results showed very little changes in the cardiovascular parameters. Although signs of stress were noticed during handling and at the beginning of electric stimulation. Animals were characterized by drowsiness during EA, and their nociceptive threshold were significantly elevated. The process of EA, therefore, may not be excessive stressor to the animals. The highly elevated PCC of EA treated goats might be due to concomitant release of ACTH and beta-endorphin from the hypophysis.

BE23-B.4

Clinical Observations of Using "Lo-Tzu" in the Treatment of Chronic Tension Headache. Jong-Rern Chen*, Hamm-Ming Sheu**, Chung-Chieng Wu***, and Jia-Show Liu#. Dept. of Internal Medicine*, Dermatology**, Nuclear Medicine***, and Neurology#, Kaohsiung Medical College, Kaohsiung, Taiwan,

Importance of a classic method of acupuncture, "Lo-Tzu" (intermeridian puncture), for the treatment of chronic tension headache has received more attention recently. Patients suffered from such headache have tendency to display so-called "Shuieh Lo" (blood intermeridian). "Lo-Tzu" at "Shuieh Lo" is found to produce substantial benefit in relieving the headache. Skin biopsy showed that "Shuieh-Lo" used for "Lo-Tzu" turns out to be an abnormally enlarged and dilated venule. Venoscintigraphy of lower limbs with "Shuieh Lo" all show functional stenosis or occlusion of deep vein. Chronic tension headache may be considered as a predisposed factor for the formation of "Shuieh Lo" in the lower limb. It is speculated that the formation of "Shuieh Lo" increase muscle spasm in the neck and head regions, and the muscle spasm, in turn, creates more frequent severe headache. It is believed that the autonomic nerve system plays a role in mediating such a mechanism of interaction reflex. By puncturing the "Shuieh Lo" as in the procedure of "Lo Tzu", the vicious cycle of this interaction reflex may be interrupted, and thus the headache suffering will be improved.

BE23-B.6

Laser Acupuncture for the Treatment of Chronic Back Pain in Horses. B.B. Martin*, A.M. Klide University of Pennsylvania, School of Veterinary Medicine, Philadelphia, PA 19104

Fifteen horses with chronic back pain from 4 months to 48 months, who could not perform at an acceptable level, who did not obtain lasting improvement from other treatments were treated by using a low-powered infrared laser (300 microwatts) (904 nm). The laser was used to stimulate 9 acupuncture points. Treatments were performed weekly. The treatments were performed for 2 minutes per point. The pulse frequency used was 360 pulses per second. After completion of a mean of 11.9 treatments, performance was improved in 11 of 14 horses, 4 of 11 won races, 1 was lost to follow-up and there was no improvement in 3 horses.

416

BE23-B.7

Effect of Low and High Frequency TENS on Provoked Hypertension, P.J. Pontinen* and M.A.K. Mattila, Acupuncture Research Project, Kuopio University, SF-70211 Kuopio, Finland

The analgetic effects of both low and high frequency TENS have been well documented. The circulatory effects of TENS have remained in a more controversial stage inspite of some well-conducted studies showing positive responses in peripheral circulatory disturbances as well as in coronary artery disease. We have studied the circulatory effects of TENS during provoked hypertension in normal healthy adults and in potent hypertensives. Hypertension was induced by a simple hand dynamometer (Vigorimeter). The subjects compressed a rubber ball 4 minutes with 1/3 of their maximal crasping force. Systolic and diastolic pressures and pulse rate were taken at one minute intervals from the opposite hand. TENS (Cefar) was then given for 30 minutes either with 2 Hz or 100 Hz frequencies, electrodes placed on both sides of upper thoracic spine and the compression of the rubber ball repeated as above. The results after 2 and 100 Hz TENS were compared with the control values using Student t-test.

BE23-C.2

Analgesia from acupuncture in rats and a new TENS device in humans. B.Pomeranz*, Depts Zoology & Physiology, University of Toronto, Toronto, M5S1A1, Canada.

We studied spinal cord endorphins in electroacupuncture (EA) analgesia in rats, using low frequency/high intensity EA. In addition we developed a transcutaneous electrical nerve stimulation (TENS) device to deliver acupuncture like TENS (AL-TENS) using similar parameters (low frequency/high intensity), with antihabituation features. We tested this AL-TENS device against conventional EA in patients with chronic pain. Rats were anesthetized with continuous infusion of pentobarbital. Low frequency (4 Hz) high intensity (25x threshold) EA was applied for 15 min via needles to LI 4 in order to suppress tail flick reflexes elicited by radiant heat. Naltrexone (endorphin antagonist) applied to spinal cord via an intrathecal cannula, prevented EA analgesia. In the human study, patients with chronic pain (N=171) were randomly assigned to one of 2 groups: one receiving AL-TENS treatments twice a week for 6 wks, the other receiving EA (with needles). In the short term AL-TENS was as good as EA, but in long term followups AL-TENS outperformed EA, AL-TENS produces superior analgesia because it delivers low frequency/high intensity codes and has antihabituation features which overcomes suppression of monotonous stimulation.

BE23-C.1

Electrical and Acupunctural Stimulation Therapies for Pain Control: Past Achievements and New Directions, C. Richard Chapman*, Department of Anesthesiology, University of Washington, Seattle, Washington

Transcutaneous electrical stimulation and acupuncture are counter-irritational therapies for pain control which are thought to involve central nervous system mechanisms. The precise nature of these effects is a hotly debated issue. It is clear, however, that physical stimulation, like pharmacological stimulation, can be used as prophylaxis against pain in certain medical settings, to modulate acute clinical pain, and to help control chronic pain. This presentation will critically review the state of knowledge in this area, consider possible mechanisms of effect, and highlight recent findings. Specific examples involving human laboratory research will be provided. Problems in research strategy in past research will be reviewed and suggested priorities for future research will be offered.

BE23-C.3

Rational Use of Transcutaneous Electrical Stimulation for Pain Control, D. M. Long*, Baltimore, Maryland, USA

Transcutaneous electrical stimulation (TENS) in its modern form was introduced to medicine in 1970. Broadly based Phase II trials suggested efficacy in pain control beyond the placebo response. Controlled studies identified subgroups for which the effect was greater, acute musculoskeletal pain, pain of peripheral nerve injury origin, and post-operative pain were all shown to be benefited in a high percentage. TENS is now standard therapy for many kinds of pain.

Rational use requires 1) a known diagnosis of a problem likely to respond, a complaint of pain means many things and is not an indication for TENS alone; 2) a committed therapist willing to educate the patient; 3) a patient with the capacity and the interest in spending the time to learn the use of the device; 4) a competently made reliable device with all the necessary software and 5) adequate support to maintain the use of the device long-term.

Mechanisms of action are still unknown. Possibilities include blockade of pain through activation of non-pain carrying sensory systems, activation of descending pain suppression systems, production of endogenous pain blocking neurotransmitters, and peripheral blockade of injured nerves. None are proven.

BE23-C.4

Parameter selection in transcutaneous electrical nerve stimulation - experimental and clinical results. Bengt H. Sjölund, The Pain Clinic, Department of Anaesthesiology, University of Lund, Malmö, Sweden.

With transcutaneous electrical nerve stimulation, many different afferent and efferent fibre systems may be activated transcutaneously. In theory, any biological mechanism that is influenced by afferent and/or efferent nervous activity may then be activated or inhibited. This is illustrated by recent reports not only of pain treatment but of the successful treatment of *ulcus cruris* with this technique.

To optimize the pain control from TENS we have systematically studied which stimulation parameters give the most pronounced suppression of C-fibre mediated nociceptive transmission in experimental animals and of clinical pain in man. Our previous results are supported in that several mechanisms seem to operate, each activated by specific afferents at specific stimulation frequencies.

BE23-D.2

Effects of Transcranial Electrical Stimulation Upon Neurochemicals. C. Norman Shealy, Roger K. Cady, Robert G. Wilkie, and Richard Cox, Shealy Institute, 3525 S. National Springfield, MO 65807.

Using a specific type of electrical stimulator, of which the output is approximately 49% below 1,000 Hz and 51% is 10,000 to 20,000 Hz, we have measured a variety of neurochemicals. Significant abnormalities have been found in chronic pain patients in serotonin, norepinephrine, beta endorphins, and cholinesterase. Following transcranial electrical neurostimulation done daily for 40 minutes over a 2 week period, these neurochemicals often are normalized. The data in over 100 patients will be presented. Relationship between chemicals, that is norepinephrine/beta endorphin, etc. may be more important than absolute values.

BE23-D.1

A Review of Transcranial Electrotherapy Stimulation Techniques, Mechanisms and Application, R. Smith, Private Research and FDA Consultant, Washington, D.C.

The two major types of CES stimulators will be discussed, as will the two major modes of entrance into the brain of the electric current, currently postulated by manufacturers and clinicians. Findings from the literature will be cited. The neuronal mechanisms via which CES exerts its influence will be discussed, along with clinical findings which support current neurohormonal theories of action. The routes of application of CES currents will also be given for the various devices currently being utilized or researched. A short history of the use of CES in the world and in America will be described, plus current U.S. Government position on its use, and certain clinical constraints that have limited its popularity among members of the medical profession in the U.S.

BE23-D.3

TRANSCRANIAL ELECTROSTIMULATION (TCET) REDUCES PAIN SENSITIVITY AND OPIATE ABSTINENCE SIGNS. J.R. Lake*, D. Brubaker, J.B. Murray, G.P. Crucian, R.E. Cook, and D.H. Malin. University of Houston - Clear Lake, Houston, TX 77058, USA.

These experiments studied the effects of extremely small pulsed currents applied bilaterally to low impedance points on the ear, through gold-plated stainless steel electrodes in series with 200 k ohm. The optimal amplitude for inducing analgesia was 10 μ A, far below the flinch/startle threshold of 25-30 μ A.

Sixty rats received 30 min. of either sham stimulation or 10 Hz, 10 μ A, 2 msec biphasic charge-balanced rectangular pulses. Rats were injected s.c. with 3 mg/kg naloxone or with saline and were tested "blind" for pain sensitivity (50°C wet tail flick) before and after stimulation. TCET significantly increased tail flick latency, $p < .01$, in saline-injected rats, but not in naloxone-injected rats.

Since TCET appears to have endogenous opioid effects, it might modulate opiate abstinence syndrome. Rats were infused s.c. for 7 days with 0.9 mg/kg/hr morphine sulfate via Alzet osmotic minipump. A day after pump removal, rats received either TCET or sham treatment and were then observed "blind" for 15 min. for abstinence signs. TCET-treated rats showed significantly fewer signs than sham controls, $p < .005$. However, TCET had no effect in rats receiving 3 mg/kg naloxone. Further experiments determined optimal pulse width and optimal stimulus pauses for relieving abstinence. TCET also significantly reduced the milder abstinence syndrome following 0.5 mg/kg/hr morphine infusion.

BE23-D.4

Psychotherapeutic Effect of Electrostimulation to the Cutaneous Branches of the 10th Cranial Nerve: Y.T. Kusumi, M.D. Raleigh, North Carolina, U.S.A.

The author will present the psychotherapeutic effect of microelectric stimulation (MES) of the cutaneous branches of the 10th cranial nerve. Compared to the traditional electroconvulsive therapy (ECT), MES is uncomparably safe and does not produce negative CNS effects, such as amnesia, or other physical complications, such as bone fractures or cardiac arrhythmias. The author will discuss the indications of MES, the technical aspects of MES, and other issues associated with this therapy.

BE23-D.6

TRANSCRANIAL ELECTROSTIMULATION PROMOTES DROWSINESS IN HUMANS. S. Sands, F.C. Schweitzer*, M. Skolnick; Univ. of Texas, Grad. Sch. of Biomed. Scie., Houston, Texas 77030.

During the course of a large clinical trial of low-current transcranial electrostimulation treatment (TCET) in humans, it has been noted that treated subjects appear to be more likely to sleep than their untreated sham counterparts. Consequently, we recorded EEG topographic maps from 17 subjects (14 males and 3 females, mean age 32) during the administration of 3 levels of TCET (0, 20, and 30uA) while they rested comfortably with their eyes closed. Each subject received 44 minutes of TECT applied transcranially through small stainless steel electrodes applied to the earlobes. EEG segments were obtained during a 3-second pause between continuous trains of positive 2 msec biphasic charge-balanced rectangular pulses delivered at 10 Hz. EEG spectra were computed for 30 electrode scalp locations and mean frequency (MF) computed at one-minute intervals spaced across the recording session.

The results confirmed our observations of increased drowsiness with the application of TCET. A current versus MF relationship was observed with the largest response at 20uA. The twenty uA's showed a significant ($p < .01$) decrease in mean frequency when compared to each subject's Sham (0 uA) session.

BE23-D.5

Clinical Tests of Electrostimulation In Relief of Chronic Pain and Smoking Cessation, M. Skolnick*, M. Blacker, L. Skolnick, J. Langone, S. Sands and D. Smith

Transcranial Electrostimulation Therapy (TCET) has been clinically investigated to determine if the stimulus' observed effect on neurotransmitters assisted subjects' nicotine detoxification and withdrawal and provided analgesic relief of chronic pain. Both studies utilized double blind designs and objective end points. Smoking cessation was defined by decreases in subjects' reported cigarette usage, craving, withdrawal symptoms and salivary cotinine (a nicotine metabolite). Analgesic relief of chronic pain was indicated by the increase of pre- to post-treatment subject musculo-skeletal performance measured by a computerized iso-kinetic exercise device (Kin-Com). The ability to conduct double blind trials stems from refinement of the electrical parameters of the TCET waveform to induce significant effects even though current and voltage are below the sensory level. These study results are consistent with clinical EEG findings using the same electrical parameters to induce relaxation responses in subjects.

BE23-E.1

A Legislative And Medical Applicability Review of Acupuncture, Charles R. Neblett, M.D.*, 6560 Fannin, Houston, Texas.

Acupuncture -- how is it viewed by "organized medicine"? Medical doctors possess vastly varying views concerning its applicability for patient care. When biases are placed aside, the medical community must ask whether acupuncture can fairly be critiqued and judged by the usual strict standards of scientific investigation. Is there sufficient data to justify its utilization? Should a different standard be applied to assess the potential of acupuncture?

Organized medicine has established its position in the legislative arena. What acupuncturists desire and what medicine recommends is much less variable. These views will be reviewed.

BE23-E.2

Regulation and Control of Electro-stimulation Devices by the FDA

Michael Cole; J.D., Washington DC

The passage of the Medical Device Amendments of 1976 to the Food, Drug and Cosmetics Act, and changes in the reimbursement formulas applicable to Medicare and Medicaid coverage, have had a profound effect on the development, testing and approval of electronic devices for medical use. The FDA now has substantial authority to regulate choice of materials, design of circuitry, output levels, software programs and any related aspects of safety, efficacy and reliability. The FDA can also dictate the scope and duration of human tests and the quality and quantity of data needed for device approval. The Agency can also closely regulate advertising and label claims, and restrict distribution to classes of physicians and technicians. After approval, FDA regulates all phases of manufacturing and distribution. The Agency has several substantial enforcement mechanisms to ensure compliance, including criminal actions, seizures, injunctions and fines.

The movement to prospective reimbursement can cripple product development if amounts paid for specific procedures are not sufficient to fully cover the costs of using expensive equipment.

Several case studies will be presented to illustrate the discussion of this topic.

BE24-A.1

Microelectronics in Implant Technology,
M. Schaldach; Zentralinstitut für
Biomedizinische Technik, Universität
Erlangen, D-8520 Erlangen, FR of Germany

The application of electronics in implanted therapeutic devices requires small size, high operational lifetime and extremely high reliability. Continued progress in VLSI-technology and new materials for packaging devices have led to the development of a large variety of medical implants such as:

Impulse circuits for cardiac pacemakers, defibrillators and neuro-stimulators;
DC circuits for bonegrowth and nerve re-generation; and,
control circuits for drug pumps and artificial organs.

A survey of the state of the art for implantable microelectronics must include reliability considerations. Custom LSI and hybrids used in implantable medical products are affected by a variety of failure mechanisms. This paper discusses the underlying causes and delineates design guidelines that minimize their occurrence. In addition, quality and reliability considerations are discussed for procurement of components, fabrication, screening, and testing of circuits. The paper is concluded with an example of the design of a sophisticated dual chamber pacemaker to illustrate the steps taken in the development of a high reliability hybrid design.

BE23-E.3

Regulation of Acupuncture Practices in the State of Texas, H. C. Dung; Department of Cellular and Structural Biology, the University of Texas Health Science Center at San Antonio, San Antonio, Texas 78284.

Though the Texas State Board of Medical Examiners assumed responsibility to regulate acupuncture, and promulgated two separate policy statements with certain differences in the version on the practice of acupuncture, there is no law of statutory power that dictates the use of acupuncture in Texas. According to the conclusion given by the federal judge in Harris County of the State, one of the statements promulgated by the Medical Examiners is "unconstitutional and therefore invalid and without force." Such decision by this federal-court judge creates an effect which, stated boldly, "is to allow acupuncture to be practiced in Texas by any person, trained or not, who calls himself or herself an acupuncturist and offers services to the public." The consequence is very unfortunate and the medical establishments in the State should be blamed for parts of the fault and responsibility. Acupuncture can be easily incorporated into established medical practice. However, no established medical community or institute is willing to accept it, even after urging by the Senate Committee on Health and Human Resources, after the conclusion of two public hearings on the matter.

BE24-A.2

Miniaturized Chamber-Type Oxygen Sensors for Brain Research, O.J. Prohaska^{*,*}, F. Kohl[†], F. Olcaytug[†], A. Jachimowicz[†], K. Pirker[†], W. Chu^{*}, M. Patil^{*}, J. LaManna^{*}.
*Case Western Reserve University, Cleveland, Ohio 44106, USA; †Technical University, Vienna, A-1040 Vienna, Austria; Otto Sensors Corporation, A-1030 Vienna, Austria

A multiple site, multiple parameter probe was developed for brain research. Thin-film and solid-state techniques were utilized to design miniaturized chamber-type oxygen sensors and to combine them with temperature and electrical potential sensors on a needle-shaped glass substrate. The sensors are arranged at an interdistance of 300 μm . A thin silicon nitride insulation layer forms a chamber which covers the Au-Ag/AgCl two-electrode electrochemical systems and is filled with extracellular saline solution. Holes in the chambers provide the contact between the brain tissue and the electrodes and define the recording areas. The response time of the oxygen sensor depends strongly on the sensor design and is in the range between 0.3 sec and 7 sec. The chamber dimensions are in the range of 2 μm to 3 μm in height, 20 μm to 40 μm in width and 100 μm to 140 μm in length; the holes have diameters of 10 μm to 20 μm and the working electrode diameters are between 6 μm and 20 μm . Good resolution, low noise, low oxygen consumption and greatly reduced interferences between sensor and tissue are the main advantages of the chamber design.

BE24-A.3

*Biosensors Based on Chemically Sensitive
Field-Effect Transistors*, Gary F. Blackburn*,
IGEN Incorporated, Rockville, MD

Chemically sensitive field effect transistors (Chem-FET) were first reported in the early 1970's and have received considerable attention since that time, both in the popular press and in scientific literature. Biosensors which employ the ChemFET to detect biochemical events on the surface of the transistor were envisioned for the measurement of enzyme substrate concentrations and for the measurement of antigen and antibody concentrations.

While the development of enzyme-based FET's has been relatively successful, the immunochemically-sensitive FET (IMFET) has seen little progress. The theory upon which the IMFET is founded is based on the ability of the FET to measure changes in the net charge at the sensor-solution interface, if that interface is electrochemically ideally polarizable. Experimentally, the theory has proven difficult to verify because no material investigated to date has maintained such an ideal polarizability after more than a few minutes in solution. Electrochemical measurements of the interfacial properties of hydrophobic polymers, inert metals, and metals coated with organic Langmuir-Blodgett films will be discussed.

BE24-A.5

*A Dynamic Model for Transcutaneous Oxygen
Tension Measurement*

A. Talbot-Pedersen*, M. R. Neuman and
G. M. Saidel

A dynamic model of oxygen transport through the outer skin layers and a polarographic sensor was developed to understand the factors that determine the relationship between $tcPO_2$ and arterial oxygen tension. The model includes the electrolyte, contact fluid, membrane, dead and viable epidermis, capillary loop and tissue of the papillary dermis. Simulations show the importance of stratum papillare blood flow, viable epidermis and stratum papillare metabolic oxygen consumption, oxygen permeability of the skin related to that of the sensor membrane and electrolyte, temperature and the oxyhemoglobin dissociation curve in determining the $tcPO_2$. Simulations were found to be consistent with clinical data from ten healthy adults; however, the importance of having an independent and an accurate method for determination of skin perfusion was demonstrated. The model showed that estimation of the metabolic oxygen consumption of the viable superficial skin tissue is only possible if the oxygen permeabilities of the skin and sensor are accurately known.

BE24-A.4

*Drift-free Blood Na^+ Monitoring by
a Semipermeable Membrane and
an ISFET.* T. Tamura*, K.
Suematsu and T. Togawa, Tokyo
Med. & Dent. Univ. Tokyo 101
Japan

An on-line system for continuous monitoring of blood Na^+ based on indirect measurement was developed. An intermediate solution in contact with blood via a semipermeable membrane was used and its Na^+ concentration was adjusted by a servo control system so that it has the same Na^+ concentration as that of blood. The Na^+ concentration of the intermediate solution was measured with a Na -ISFET because of its fast response and small size. The Na^+ concentration obtained with the monitoring system was compared with that obtained by the ion analyzer. The response time to a step change of the system was about 5 min. In long-term monitoring, the error was within 2 mmol/l. The stability of this system does not rely upon that of the sensor. Besides this, due to the use of the semipermeable membrane, it can operate without blood loss and blood contamination.

BE24-B.1

Fiber-Optic Chemical Sensor Development,
John I. Peterson,* Biomedical Engineering
and Instrumentation Branch, Division of
Research Services, National Institutes of
Health, Bethesda MD

A general overview of the principles of fiber optic chemical sensors will be presented, with some historical background. The emphasis of the discussion will be on the current trends in development and the approaches that are being taken for sensor construction.

An attempt will be made to compare the advantages and disadvantages of fiber optic sensors relative to electrodes.

In addition, a brief description of my current oxygen sensor instrumentation and its application will be given.

BE24-B.2

An intravascular oxygen sensor with a biocompatible diffusion membrane, M. Martin*, K. Yamakoshi, A. Luthra, R. Wolton and P. Rolfe, University of Oxford, U.K.

A catheter-type oxygen sensor that can be dip-coated with various polymer based diffusion membranes has been developed. Electrochemical techniques, such as potential step and time response experiments have been utilised to assess diffusion membrane characteristics of a number of membranes, both modified and unmodified by haemocompatible coatings. Scanning Electron Microscopy has been used to assess the morphology of the same membrane electrodes. In vitro and in vivo assessment on subsequent catheter sensors which employ a polyurethane membrane has been carried out. In vivo studies show linear correlation with a commercial blood gas analyser over the physiological range of oxygen tensions. Catheter oxygen sensors so fabricated may be used continuously in vivo over a 24 hour period without any appreciable loss of signal. Response times of 15-20s in vitro and 40-50s in vivo have been obtained.

BE24-B.4

A Transcutaneous Monitoring of Blood Glucose by Suction Effusion Fluid and Ion Sensitive Field Effect Transistor Glucose-Sensors, M. Kikuchi*, T. Arai, S. Kayashima, N. Negishi, O. Takatani, N. Itoh¹, J. Kimura¹, H. Kuriyama¹, and A. Kaneyoshi¹, National Defense Medical College, Saitama, Japan. ¹NEC Corporation, Kanagawa, Japan.

A transcutaneous monitoring of blood glucose without blood sampling is successfully demonstrated. A suction effusion fluid which is obtained transcutaneously from skin surface by suction is employed as a sample material. This fluid contains glucose and non protein nitrogens in same concentration comparing with blood. Since a effusion rate of the suction effusion fluid is only 0.4ul/min/cm²(skin), we use micro ISFET glucose-sensor of which required sample volume is 5-10ul. In animal experiment, adult-white-rabbit skin eliminated stratum corneum is used. By glucose injection via a femoral venus blood glucose concentration is changed as step-wise. The blood glucose change is mesured both by this transcutaneous method and a conventional blood glucose analyser simultaneously. The transcutaneous monitoring by the suction effusion fluid and the ISFET glucose sensor reveal complete detection of blood glucose change within 15min delay. The authors have also been examined this method to clinical oral glucose tolerance test.

BE24-B.3

Development of Fiber Optic Oxygen and Glucose Sensors, R.V. Shah*, S.C. Margerum and M.N. Gold, Crump Institute for Medical Engineering, UCLA, Los Angeles, CA.

The phenomenon of fluorescence quenching was used to design and fabricate fiber optic sensors sensitive to oxygen and glucose concentrations. The prototype oxygen sensor was fabricated by coaxially grafting a hydrogel, poly(2-hydroxyethylmethacrylate) (HEMA), containing a fluorescent dye, 9,10-diphenylanthracene (9,10-D), to fused silica optical fibers. Grafting was done through the use of silane coupling agents. The resulting sensor was sensitive to solution oxygen concentrations due to oxygen quenching of 9,10-D fluorescence. Dye fluorescence was quenched 20% when the sensor went from an oxygen-free to an oxygen-saturated environment. Transient response times of the sensor were reduced when the PHEMA graft thickness was reduced. Modeling of the transient data gave a diffusion coefficient of oxygen in PHEMA of 2.15×10^{-6} cm²/sec. Incorporation of an enzymatic reaction which consumes or produces oxygen through redox catalysis within the oxygen sensing phase makes feasible the development of sensors specific for the enzyme substrate. We incorporated glucose oxidase into the PHEMA/9,10-D matrix in order to develop a sensor for glucose. Glucose oxidase catalyzes the reaction between glucose and oxygen. In the presence of glucose, the matrix oxygen concentration is lowered, resulting in an increased fluorescent signal, the increase being proportional to the concentration of glucose. It was determined that sensors could be made to measure glucose in the physiological range when the Thiele Moduli were between 5 and 25 (under conditions where glucose concentrations >> oxygen concentrations).

BE24-B.5

A Thermoelectric Enzyme Sensor for measuring Glucose in Blood, M. Muenlbauer*, E. Guillebeau and B. Towe, Arizona State University, Department of Chemical, Bio, and Materials Engineering, Tempe, Arizona, 85287.

The thermoelectric enzyme sensor is a novel calorimetric approach to measuring glucose in blood. The sensor consists of a thin film thermopile constructed on a thin insulating support, rolled and mounted at the tip of a 3-mm diameter catheter. It is rendered sensitive to glucose by immobilizing the enzyme glucose oxidase over the active thermoelectric junctions of the thermopile. When exposed to glucose in solution, the enzyme becomes heated by virtue of the enthalpy change of the enzymatic reaction. A temperature difference between the active and reference junctions of the thermopile results and a glucose-proportional Seebeck voltage is induced.

When operated in blood *in vitro*, the sensor responded to the plasma concentration of glucose. No ambient temperature control was necessary. Dependent on the enzyme loading, the sensitivity was between 20 and 60 nV/mg % and the response was linear up to 250 mg %. The response time was typically less than 10 seconds.

When operated *in vivo* in an anesthetized dog, the sensor responded appropriately to changes in glucose induced by injections of insulin. The response matched that found at the same temperature and flow rate *in vitro*.

BE24-C.1

Laser-Doppler Stethoscope for Loadfree Recording of Skin Vibration, B Hök,*
 Electronics Department, Institute of Technology, University of Uppsala, Box 534, S751 21 Uppsala, Sweden, P Å Öberg, Department of Biomedical Engineering, University Hospital of Linköping, S-581 85 Linköping, Sweden.

The widespread use of the conventional stethoscope points at the richness of skin vibrations as a source of clinical information. Attempts in objectifying these signals have, however been quite disappointing. Phonography, including phonocardiography and phonopulmography, is still not a quantitative, or even calibrated method.

We suggest the use of a Laser-Doppler system as a reference method in phonography. It is shown that, by using a system based on a low power helium-neon laser and single-side-band techniques including a Bragg cell, it is possible to record and quantify the vibration of skin, loaded only by a flexible, thin retroreflecting tape.

Possible optical configurations are discussed, together with estimations of accuracy, bandwidth limitations and noise. Experimental recordings will be shown with parallel conventional microphone signals. Also, the loading effect of applied mass on the skin surface is demonstrated.

BE24-C.2

Temperature Sensing with Fiberoptic Probes for Biomedical Applications, D.A.Christensen*, Dept. of Bioengineering, University of Utah, Salt Lake City, Utah 84112 USA

Applications are increasing for fiberoptic temperature sensing in the clinical environment, including tissue monitoring during electromagnetically-induced hyperthermia (for cancer therapy), blood gas monitoring with multi-purpose fiberoptic catheters, and patient monitoring during magnetic resonance imaging (MRI). Due to their use of nonconducting glass or plastic optical transmission fibers, these sensors possess unique advantages over conventional metallic temperature devices, such as electrical insulation, immunity from crosstalk, and nonperturbation in electromagnetic fields.

Fiberoptic temperature sensors may be classified into three general categories: 1) Intensity, 2) Wavelength, and 3) Time-domain. Examples of each of these sensor types will be presented, including the liquid crystal tip (intensity), fluorescence decay (time-domain), Fabry-Perot cavity (wavelength), and the GaAs semiconductor sensor (wavelength).

BE24-C.3

Optical Fiber Sensor For Joint Angle Measurement
 M.M. Patil* and O.J. Prohaska
 Case Western Reserve University, Cleveland.

Optical fibers were used to design a joint angle measurement device with the intention of using it for controlling finger position in the functional neuromuscular stimulation systems. Light transmitted through a joint of two fibers with their polished endfaces normally held perfectly aligned by silastic tubing, undergoes transmission losses when there is an angular tilt between the fibers. These losses modify the intensity of light, which was detected by a photodiode and was related to the angle between the two fibers. The fibers were placed such that they formed a joint beside (laterally) the phalangeal joint and were fixed on either side of the joint. Hence detection of the angle between the fibers leads to the determination of the finger joint angle.

Sensitivity (between 2 mV/° to 12.2 mV/°) and linearity of this device were found to be dependent on the position of the fibers in the silastic tubing, the tubing itself, as well as the different types, diameters and endface angles of the fibers. Investigations so far indicate that neither hysteresis nor temperature changes significantly affect the angle measurements.

BE24-C.4

LASER-BASED FIBER-OPTIC SENSORS, Frank V. Bright*, Thomas A. Betts, Gino C. Catena, Kevin S. Litwiler, and David P. Paterniti, Department of Chemistry, State University of New York at Buffalo, Buffalo, New York 14214 USA.

Over the last decade, there has been a near exponential increase in the number of fluorimetrically-based fiber-optic sensors. During this time, fiber-optic sensors (FOS) have been developed for the determination of everything from biomolecules to metal ions. However, one of the continuing problems with FOS arises from matrix interferences. To help these interference problems our group has been exploiting the inherent multidimensional nature of fluorescence coupled to fiber-optic sensing. Specifically, our efforts are aimed at polarization, lifetime, and rotational dynamics information measured through long lengths of fiber optic. In this presentation, selected results from our laboratory will be presented. In addition, it will be shown that it is now possible to perform all measurements that were once restricted to a cuvette through a simple fiber optic probe.

BE24-C.5

Evaluation of POET: Combined Pulse Oximetry and End-Tidal CO₂ monitor, E.Y. Cheng*, K.A. Stommel, Medical College of Wisconsin, Milwaukee, WI

The POET (Criticare Systems, Inc.) is the first monitor to combine both the pulse oximeter and side-stream infrared end-tidal CO₂ analyzer into a single unit. In this study we tested the accuracy of the POET in 15 healthy nonsmoking adult volunteers. Each patient was subjected to inspired O₂ fractions of 1.0, 0.21, 0.12, 0.10, and 0.08, and then CO₂ concentrations of 0, 3, 6 and 7.5%. Subjects reequilibrated with room air for 5 minutes between each gas mixture. Pulse oximetry sensors were placed on the index finger (SpfO₂) and the forehead (SphO₂). For each O₂ concentration tested, a 30 second steady-state of SpfO₂ and SphO₂ was needed before drawing arterial blood for SaO₂ determination. A sampling line for PetCO₂ was placed just distal to the one-way exhalation valve. ABG were drawn and analyzed for PaCO₂ after PetCO₂ stabilized for 30 seconds for each concentration of CO₂.

Linear regression was used for data analysis. Correlation coefficients of 0.95, 0.98 and 0.95 were found when comparing SphO₂ to SaO₂, SpfO₂ to SaO₂ and PetCO₂ to PaCO₂ respectively. During this study the range of SaO₂ was between 65-100% and PaCO₂ ranged between 35-55 mmHg. We conclude that the POET provides an accurate, and convenient single unit monitor for following SpO₂ and PetCO₂.

BE24-D.2

Guidewire-mounted sensor for biomedical pressure measurements L. Tenerz*, B. Hök, Electronics Department, Institute of Technology, Box 534, S-751 21 Uppsala, Sweden. T. Engström, O. Hammarström, R. Lönner, Radisensor AB, Kungsgatan 70, S-753 21 Uppsala, Sweden.

We have developed an ultraminiature (0.5 mm diameter) pressure sensor and mounted it at the tip of a thin guidewire used for guiding the sensor to the measuring site. The sensor uses a micro-optical pressure sensing element made by silicon micromachining and fiberoptic signal transmission through a single-strained hard-clad optical fiber. The measurement properties of the sensor (sensitivity, resolution, linearity, stability and frequency response) have been found fully adequate for clinical use. In animal experiments, the measurement properties *in vivo*, and the guiding properties of the assembled guidewire sensors have been verified.

Potential applications of the sensor include left ventricular manometry, coronary artery investigations, manometry in small animals, catheter-tip localization, oesophageal motility measurement. Results will be shown from urodynamic measurements, artery pressure recordings with waveform analysis, venous pressure monitoring, pressure measurements in cardiac muscle tissue and in the kidney tissue.

BE24-D.1

Disposable Pressure Transducers for Research and for Clinical use, N.B. Jones*, G.L. Papageorgiou, V.C. Redding, University of Leicester and The Regional Cardio Thoracic Unit, Leicester, U.K.

It is known that the dynamic fluctuations of arterial blood pressure with time are significant diagnostic and prognostic indicators, particularly when related to flow measurements taken at the same point. Work in this area and on many other biological systems is revealing a requirement for pressure transducers which do not produce serious flow disturbances and can be introduced into very small vessels and cavities. It is also required that *in vivo* transducers be robust and safe and have a wide bandwidth and good signal to noise ratio. If procedures developed as a result of research are to be adopted into routine practice transducers should be easy to use. Disposability of the transducers is also of considerable significance particularly where HIV infection is a possible factor. This paper reviews the situation in pressure transducer technology from this viewpoint and shows that opportunities exist in a new class of fibre optic transducer which have already been made down to 400 µm in diameter, having a bandwidth in excess of 1000 hz and a signal to noise ratio of at least 60 dB.

BE24-D.3

Analysis of Pedobarograms Obtained by a Computerized Platform. A.Starita*, P.Dario, M.Bergamasco and A.Fiorillo, Dipartimento di Informatica; Scuola Superiore S. Anna; Centro "E.Piaggio", University of Pisa, Pisa, Italy.

Quantitative measurements of foot-ground pressure distribution are becoming increasingly important in such areas as orthopaedics, rehabilitation, neurology, diabetology, biomechanics and sports medicine.

Using a recently available commercial system (Orthomat, Polysens S.p.A., Florence, Italy) which consists of a platform incorporating 1024 piezoelectric polymer-based sensors, an interface unit and a personal computer, pedobarographic images have been obtained in different experimental conditions (normal and pathological gait, load transfer). The images corresponding to the time evolution of pressure distribution have been processed in order to extract a number of potentially significant parameters (contact area, center of pressure, maximum load points).

BE24-D.4

The Design of an Ambulatory Blood Pressure Monitor, R. Branstetter* and J. Jaeb, Southwest Research Institute, San Antonio, Texas

Daily blood pressure measurements are not adequate for some ambulatory, hypertensive patients. Often, cardiologists would like several measurements a day. Additionally, measurements taken at particular events during the day, such as when the patient has taken medication, eaten a meal, or had an argument with a spouse, might be very useful.

A group of scientists and engineers have developed an ambulatory blood pressure monitor (ABPM). Measuring 3x7x14 cm and weighing only 800 g, this comfortable device has several important features. The results from 800 blood pressure measurements can be stored in a small, removable, solid-state memory cartridge. Programmable keys on the face of the instrument allow the patient to mark special events during the day. A serial communication port provides easy down-loading of stored data to any computer. A rechargeable battery provides 24 hours of operation.

A CO₂ cylinder and specially-designed valving yields a precise, constant cuff inflation or deflation rate. An important benefit of this gas operated, cuff-inflation system is its very quiet operation, as compared to similar electrical pump systems. EEG records show that operation during sleeping hours can be attained without disturbing the patient. This monitor is the forerunner of the Nippon Colin ABPM-630.

BE24-D.6

Apparatus for Measurement of Skin Elasticity in Systemic Sclerosis
M. R. Neuman*, S. P. Ballou, A. Mackiewicz and A. Lysikiewicz

An extensometer for measuring viscoelastic properties of the skin on the left volar forearm has been developed and applied to discriminate between patients with scleroderma and age, sex and race matched controls. The device stretches the skin from 20 to 28.5 mm at a constant rate of 0.4 mm/s while continuously measuring the associated force. The sensor was held in contact with the skin using a strong double sided adhesive tape which could be pulled away if the skin tension became too great. A microcomputer collects the data and determines the elastance from the slope of the force-elongation curve. A measure related to plasticity is an exponential curve fit to the force relaxation at maximum extension. The device was tested on thirteen patients with clinically documented scleroderma and thirteen matched controls. The scleroderma patients had a mean elastance of 7.1 ± 3.3 (SD) N/mm which was significantly different from controls at 3.5 ± 0.63 (SD) N/mm ($p < 0.005$). This instrument may, therefore, be of use in objectively evaluating patients with early stages of scleroderma.

BE24-D.5

USE OF A PIEZOFILM TRANSDUCER TO VERIFY PROSTHETIC LOADING, A. Levi*, J. Stoessel, ANCO Engineers, Inc., and L. Mader, David M. Grant Medical Center.

A need exists for a capability to accurately measure loads applied on prosthetic limbs by patients. This is critical in determining proper loading of prosthetics and in preventing noncompliance due to patient discomfort and tissue damage. Classic transducers have been too bulky to be of clinical utility. A prototype pressure sensor package consisting of a piezoelectric polymer PVDF (tradename KYNAR) has been constructed that is thin and flexible enough to fit between the patient and prosthetic and thus provide the clinician with sufficient information on the loading contour to permit a more comfortable fit between patient and prosthetic. The piezoelectric film is durable, and flexible enough to conform to any required interface between patient and prosthetic. For this effort, instrumentation was installed on an interface cup for below-knee amputations. The cup was then placed between the patient and the prosthetic. Based upon a series of loading situations, a loading contour chart was generated which could be used by the clinician for modifications to the fit.

BE24-E.1

Development of Medical Telemeter using Indirect Light Transmission, K. Shimizu*, N. Kudo^o, H. Murakami, T. Mikami and G. Matsumoto, Hokkaido University, Sapporo Japan, ^oToshiba Corp., Ootawara, Japan

There have been some reports on the optical telemeters using a direct light transmission. Although their advantages over the conventional radio telemetry have been verified, its application in practice has been limited due to the problems in maintaining the propagation path of the light. To solve this problem a technique using an indirect light transmission is proposed. The distribution of the indirect light in a room was calculated, and the feasibility of this technique was examined in various conditions. To verify the possibility shown in the theoretical analysis, an optical telemeter using the indirect light transmission was developed. The signals of 3 ECG's and a body temperature are multiplexed in time domain and modulated into a PIM pulse sequence. With the developed telemeter the optical biotelemetry from a freely moving subject was carried out. A stable data acquisition was demonstrated even from the subject in exercise.

BE24-E.2

Telemetry System for Intraoral Pressure Measurement, Y. Kato*, T. Kuroda and T. Togawa, 2nd Dept. of Orthodontics, and Inst. for Med. and Dent. Eng., Tokyo Medical and Dental University, Tokyo, Japan.

A telemetry system which can monitor the intraoral muscle pressures in subjects under unconstrained conditions was developed. The system consists of an intraoral unit and an extraoral one. The external unit is about 2.6 kg including batteries and can be carried by the subject. Electromagnetic coupling between an intraoral coil and an extraoral one is used to supply the power to the intraoral unit and to receive the signal corresponding to the pressure of the upper central incisor region. The cantilever type pressure sensor, which is 6 mm in diameter and 1 mm in thickness, was placed on a tooth. This system was applied in four adult male subjects. The averaged labial pressure of the upper central incisor was 1.5 g/cm², 10.9 g/cm², and 5.0 g/cm² during rest, swallowing and speech, respectively. The averaged lingual pressure at the same location was 4.0 g/cm², 19.1 g/cm² and 13.9 g/cm² during rest, swallowing and speech, respectively. It was proved that this telemetry system is applicable for unconstrained, long-term monitoring of intraoral pressures.

BE24-E.4

Free-space Optical Data-link for Biomedical Telemetry, H. Odagiri, K. Shimizu*, and G. Matsumoto, Hokkaido Institute of Technology, Sapporo, *Hokkaido University, Sapporo, Japan.

A real-time transmission of biomedical signals has an increasing significance in the field of biotelemetry particularly in telemedicine. With a view toward the multi-variable analysis of biological parameters under various environmental conditions, a system was developed which enables us to obtain the information of a patient from a remote place. The system consists of two stations connected with a free-space optical link. At the data acquisition site, biological signals are obtained, pre-processed by a microcomputer, multiplexed with color images and sounds, and transmitted in a beam of light. At the data-analyzing site, the light is received, and the different kinds of information are retrieved. Using this system, the data obtained at experimental fields or in a remote building can be fed to a large computer in another building which performs the advanced data-processing. The function of an automatic repeat request prevent the data loss in a short time interruption occurred in the data-link.

BE24-E.3

A MICRO TELEMETRY SYSTEM FOR NEONATAL MONITORING, Kenji Ikeda*, Institute of Medical Electronics, University of Tokyo, Bunkyo, Tokyo 113, Japan

Immature babies, who need intensive care and are protected in incubators, are in almost all cases under fluorescent lightning for the treatments of jaundice of the newborn. In such occasion, the light energy can be utilized as the power source of the transmitter for wireless monitoring of respiration or heart rate of the newborn. A very simple, micro transmitter, which contains no battery but operates using the light energy, for measuring small displacement of abdominal skin surface due to the respiration, is developed and made for trial. The size is 12x12x6mm³, and the weight is approx. 1g. The skin surface displacement is measured by the small change of the air-gap capacitance between the skin and the transmitter itself. The transmitter, being entirely solid without lead wires or connectors, is easy to sterilize and handle. VHF (70-80MHz) radio wave is modulated in FM. As the receiving antenna is installed just on the upper cover of the incubator, only very weak radio wave is enough for telemetering. This can avoid jamming when several systems are used simultaneously in the same room. Some results obtained from practical tests at a maternity hospital will be shown for discussions.

BE25.1

Interaction of Weak ELF Magnetic Fields with Hydrated Protein Channels. A.R. Liboff* and M.D. Sevilla, Oakland University, Rochester, Michigan 48063.

Experiments by different groups designed to test for ion cyclotron resonance (ICR) interactions indicate that it does not occur in all tissues. However, the Ca²⁺-dependent motility of diatoms is a sharp function of ICR tuning as is the uptake of ⁴⁵Ca²⁺ in human lymphocytes. Both systems not only undergo resonant changes as a function of magnetic field frequency but also vary according to the ionic charge-to-mass ratio. If the interaction site lies within the ion channel, and the resonant frequency is determined by the dehydrated ionic mass, this may imply that the ICR transport mechanism occurs in a structured aqueous lining within the channel, and further that channels not having such well-ordered hydration structures may not exhibit ICR. We have formulated a helical hydration model that conforms to the interior symmetry and dimensions of the Gram A dimer channel. This model provides for the transmission of ions without loss of hydration shell through a periodic structure that is responsive, in principle, to ICR. Supported by DOE: offices of Energy Storage and Distribution (ARL) and Health and Environmental Research (MDS).

426

BE25.2

Magnetic Field Influence on Living Tissues
M.S. Markov[‡] Department of Biophysics, Sofia
University, Sofia, Bulgaria

The influence of static magnetic fields as well as magnetic fields produced by AC current has been studied. The range of field strength from background to 350 mT has been carefully studied. The reactions of living tissues has been estimated by number of biophysical parameters including electrophoretic mobility of cells, passive electrical properties of membranes, light scattering, oxygen consumption, transmembrane potential, stability of cells and cell membranes to factors provoking cell lysis.

Existence of specific levels of optimal effects at different tissues has been found. The "permitted" levels of reactivity are similar to the "biological windows" supposed by W.R. Adey.

In a series of experiments has been observed that magnetic field may act as a factor of preventing action of other physical and chemical factors, including ionizing radiation.

BE25.4

Mechanism of Microwave Radiation Effect on Biological Objects, S.I. Kirkilevsky, Ya. I Khokhlich, V.A. Pavlenko[‡] N.N. Korpan, Kiev Medical Institute, 252004 Kiev, USSR.

Theoretically grounded model has been worked out, suggesting that enzyme molecules can be the application point for the microwave electromagnetic field of nonthermal intensity. Frequency resonance of electromagnetic field with the inherent oscillation frequency of the enzyme molecule leads to alteration in kinetics and direction of fermentation.

The experimental research has proved the elaborated theoretical pattern, which allowed to apply pathogenetic approach in treatment and prevention of some diseases by using extremely high frequency (microwave) radiation procedures. The research has resulted in a conclusion that full variety of biological and medical effects induced by microwave EMR radiation can be explained by this hypothetical mechanism, which is of great importance for biology in general, and medicine, and social hygiene.

BE25.3

Influence of the Magnetic Field on Ion Movement near Biological Macromolecules:
Theory and Experiments,

A. Chiabrera *, M. Figueiredo, B. Bianco, J.J. Kaufman and A.A. Pilla, Univ. of Genoa, Italy and Mount Sinai School of Medicine, New York, U.S.A.

Most bioelectrochemical processes depend on ion transport or adsorption. The ion velocity change, due to an electric field whose amplitude is proportional to the time variation of a periodic exogenous magnetic induction field, is computed, taking into account both the dc and ac magnetic Lorentz forces. The ac magnetic induction is very effective provided that its amplitude is related to the ion cyclotron frequency, or to its multiple values, and that the local viscosity is low. The phenomenon occurs at intensities of the dc magnetic induction that are also related to multiple values of the ion cyclotron frequency. The predicted maximal effectiveness offers a consistent explanation of some experimental results so far obtained affecting the swimming direction of paramecia under electromagnetic exposure.

BE26-A.1

Measurements of Regional Blood Flow in the Foot by means of Transient Thermal Clearance Method. M. Nitzan*, Y. Mahler and Z. Abramowitz, Jerusalem College of Technology, Jerusalem 91160, Israel

The non-invasive transient thermal clearance method provides a means for the assessment of regional blood flow (RBF), in unit of ml blood per 100g per minute. The ratio of the blood pressure in the artery supplying the tissue and the RBF in it is the specific microvascular resistance (SMR). RBF and arterial blood pressure were measured on the dorsum of the foot, for diabetic and non-diabetic patients. For most of the non-diabetic patients, RBF and arterial blood pressure were mutually proportional, indicating that SMR is approximately constant. Some of the patients, however, showed different values of SMR, either below or above the range of normal SMR. As for the diabetic patients, no correlation between RBF and arterial blood pressure was found. The mean value of SMR for the diabetic patients was significantly lower than that of the non-diabetic patients.

BE26-A.2

**THERMAL CAMERA IMAGING TO MEASURE
PERFUSION FROM THE TISSUE SURFACE**

J.C. Chan*, J.W. Valvano, Ph.D., J.A. Pearce, Ph.D.,
L.J. Hayes, Ph.D., S.A. Prahl
University of Texas, Austin, Texas

A thermal washout technique is being developed which measures perfusion from the tissue surface. This perfusion measurement is similar to other indicator washout techniques. The basic approach is to apply a heat source to the surface of a tissue for exactly 60 seconds. The heat source is then removed and the temperature recovery is monitored with a calibrated thermal camera. Blood flow significantly affects local heat transfer making this technique quite sensitive. Highly perfused tissue will absorb more heat and, hence will have a smaller temperature increase and a faster recovery back to baseline.

The finite element numerical method is used to model the heat transfer problem with realistic geometries and boundary conditions. The relationship between the actual perfusion and the measured temperature response is determined using both analytical and numerical techniques. It is important that the boundary and initial conditions be carefully controlled and monitored during both the warming and cooling phases. *In vivo* experiments with alcohol fixed canine kidneys demonstrate the feasibility of the technique. The disturbing factors include: uncertainty of the temperature measurement, uncertainty of the time measurement, baseline temperature gradients, and perfusion gradients.

BE26-A.4

Thermal Conductance and the Pattern of Distribution of Blood flow. E. Raman*, V. Vanhuysse, M. Maes and J. Janssens. Univ. of Antwerp, R.U.C.A., B-2020 Antwerp, Belgium.

To examine the active elements of the thermal regulation in extremities many researchers measure the physiological thermal conductance of perfused tissue. The results are often in contradiction with the findings from other blood flow methods (e.g. radioactive clearance rate). We studied the rate of blood flow, the distribution of flow and the heat loss by means of an analytical circulation model and compared the results with the thermal conductance parameter. The model is fitted by experimental blood flow (venous occlusion plethysmography) and heat loss (calorimetry) measurements. Results presented show that thermal conductance is a poor parameter to determine rate of blood flow (systemic errors of 50%) specially when the distribution of flow changes.

Our conclusion is that only analytical studies supply the correct characteristics of the active thermal regulation, such as: cutaneous blood flow, pattern of distribution, counter current heat exchange, blood temperature.

BE26-A.3

Computed Thermography System applied to Dynamic Analysis of Skin Surface Temperature. I. Fujimasa*, T. Chinzei, K. Mabuchi, Y. Abe, and K. Atsumi, RCAST and IME, University of Tokyo, 4-6-1 Komaba, Tokyo, 153 Japan

The computed thermography system (CTS) has been applied mainly to temperature abnormality in steady state caused by sympathetic irregular stimuli and peripheral blood flow obstruction. The fundamental analyzing procedures are the asymmetry detection of temperature distribution and image subtraction between two thermograms. Thermatome and blood flow distribution are two main expressions of the analysis. Recently, thermographic instruments can produce dynamic thermal images using the SPRITE detector or CCD elements. In thermographic laboratories, doctors want to analyze dynamic skin temperature change which is caused by thermal or mechanical stress. For the rapid acquisition of dynamic thermal data, we have been developed a high speed I/O interface and a large RAM memory system on personal computers of PC9801 (NEC) and PC/AT (IBM). The algorithms of the software system consist of two parts: transient analysis and spectral analysis. The principle of the transient analysis in thermal phenomena under strong external load is depended upon the detection of the gradient of temperature change. The pattern expression is named secondary differentiated thermograms. As the spectral analysis, cycles of fluctuation of skin surface temperature are calculated by FFT. The expressed pattern is called the thermal rhythm spectrography. These images are possible to explain dynamic sympathetic function activity to skin arterioles and are useful to the pathophysiological analysis of autonomic nerve disorder.

BE26-A.5

Measurements of Tissue Thermal Conductivity and Perfusion using Sinusoidally Self-Heated Thermistors G. Anderson*, J. Valvano, J. Pearce, L. Hayes
University of Texas, Austin, Texas

A microcomputer based instrument is being developed which simultaneously measures intrinsic thermal conductivity and perfusion. In this technique, the combination of a steady state and sinusoidal voltage is applied to heat a miniature thermistor probe inserted invasively into the tissue of interest. A second thermistor is used to measure the baseline tissue temperature. The applied electrical power and the resulting temperature rise are measured by the microcomputer based instrument.

An approximation is used to lump the heat transfer due to perfusion and conduction into an effective conductivity term. Perfusion is then linearly related to the difference between effective and intrinsic conductivity measurements. The probe sensitivity increases with its size. The steady state response is sensitive to both conduction and perfusion. The excitation frequency is chosen such that the sinusoidal response is sensitive to intrinsic thermal conductivity but insensitive to perfusion. This procedure gives a simple but effective method for separating conductive and convective transport without the necessity of interrupting blood flow, as is required in previous techniques.

The accuracy of the thermal conductivity measurement is 2% over the range of 3 to 6 mW/cm²·°C. Measurements in alcohol-fixed canine kidneys demonstrate that the instrument can simultaneously measure intrinsic thermal conductivity and effective thermal conductivity in perfused tissue.

BE26-A.6

Non-contact Skin Emissivity Measurement by Switching Two Shades of Different Temperatures, T. Togawa, Tokyo Medical and Dental University, 2-3-10, Kanda Surugadai, Chiyoda-ku, Tokyo

Although skin emissivity data in far-infrared region is required for accurate thermographic studies, no convenient method to measure skin emissivity has been provided. A difficulty in the conventional methods is to determine actual radiation source temperature at the skin. To overcome this, we employed a simple reflectance measurement, which is essentially an emissivity measurement. Two shades of 10 cm in diameter were used, and one was kept in room temperature, and the other about 20 C above that. The surface inside the shades was coated with black paint. The object skin surface was kept just under a shade, and the radiation from the skin was observed by a radiometer having sensitivity in 8-14 μ m, through a hole of the shade. Then the shade was switched to the other by a slide mechanism, and observe the change in the radiation energy. The reflectance, and thus the emissivity can be calculated only from the radiation energies before and after switching, and temperatures of these shades, which determine the ambient radiation temperatures under the shades. By this method, each measurement can be made within one minute, and because of non-contact feature, this method is safely applicable for measurements in the pathological skin.

BE26-B.2

Whole Body Heat Balance during the Human Thoracic Hyperthermia, Zheng Lou*, Wen-jei Yang, the University of Michigan, Department of Mechanical Engineering and Applied Mechanics, Ann Arbor, MI48109-2125, USA.

To predict the temperature fields or to derive the heating strategy according to the desired temperature range before tumor treatment, most of the investigators use the so-called bio-heat equation. In the perfusion term of the equation, incoming blood temperature is generally considered to be constant. But due to the large intensity of energy influx, especially in the treatment of the human thoracic tumor, the body core temperature may be raised.

A whole body heat balance model during hyperthermia is developed. In the model, local temperature is calculated using a finite element model. The perfusing blood, along with its energy, is circulated to the rest of the body, where the heat dissipation is calculated using lumped models. With this model the effect of the power dosage on the body core temperature and thus on the temperature fields is analyzed for the human thoracic hyperthermia.

BE26-B.1

A Coupled Electrical and Thermal Finite Element Model of Self-Heated Thermistors
J. Valvano*, G. Anderson, J. Pearce, L. Hayes, C. White
University of Texas, Austin, Texas

Thermistors are used as both active and passive transducers in a variety of medical instruments. Previous thermal models treated the thermistor as either a single point or as a lumped sphere of homogeneous properties. When the thermistor is self-heated, these simple models do not accurately predict the relationship between the applied electrical power and the resulting temperature rise.

A closed form analytic temperature distribution can only be found if the self-heated thermistor is spherical and the power is dissipated uniformly in all regions of the bead. Unfortunately, both assumptions are false. A nonuniform power deposition results because the hottest areas within the thermistor also have the greatest electrical conductivity.

Transient 2-D finite element electrical and thermal models are used to examine the complex interaction between applied electrical power and resulting temperature rise. Realistic geometries can be entered into this program. Initially, the electrical properties and temperature are uniform. At each time step, the electric field is calculated from the electrical properties generated in the previous step. Then, the nonuniform applied power is calculated from the electric field. Then, a new temperature distribution is calculated from the applied power, the thermal properties, and the tissue blood flow. Lastly, new electrical properties are calculated based on the temperature field. This process iterates back and forth until steady state is reached and final power and temperature distributions are obtained.

BE26-B.3

ON THE THERMAL CONTACT BETWEEN BONE AND ARTIFICIAL JOINTS

L. S. Fletcher*, and G. P. Peterson
Department of Mechanical Engineering
Texas A&M University
College Station, Texas 77843

Wherever there is an imperfect mechanical contact and a temperature gradient, a temperature discontinuity will occur. This temperature discontinuity is normally described in terms of the thermal contact conductance, defined as the heat flux divided by the apparent interface area. Understanding of this temperature discontinuity along with the associated thermal conductivity of bone and cement materials is important in order to better understand the thermal phenomena that occur as a result of the heat generated during curing of the cement and also the dissipation of localized heating caused by friction.

Presented here are the results of an experimental investigation in which the effective thermal contact conductance occurring at the interface between bone and stainless steel were measured. Joints utilizing four types of Polymethylmethacrylate (PMMA) based bone cements were tested and measurements of the thermal contact conductance were made along with measurements of the thermal conductivity of the bone material for both saturated and dry conditions.

BE26-B.4

Quantitative Analysis of Tissue Coagulation by Electrosurgical Current, *Choh-Fei Yeap** and *John A. Pearce*, Dept. of Electrical & Computer Engineering, UT-Austin, Austin, Texas.

Electrosurgery has been in wide-spread clinical use for over 60 years, yet physical data on the generation of calibrated lesions are not available.

Electrosurgical current (500KHz) has been applied through a circular electrode (5mm diameter) to canine heart muscle *in vitro*. Rms voltage, current and surface temperature, measured by a thermocouple at the electrode center, were recorded. The surface spatial temperature distribution was also determined using a video-scanning thermal camera. Preliminary experimental results suggest that the electrical conductivity of tissue decreases markedly when coagulation initiates at about 65°C.

The thermodynamics of tissue coagulation by electrosurgery is modeled by nonlinearly-coupled Laplace and Bio-Heat equations including the nonlinear temperature dependence of electrical and thermal conductivity. The 2-D Finite Element and Newton-Raphson methods were utilized to predict power density and temperature as a function of both time and position. Arrhenius reaction rate function was used to estimate severity of tissue damage. Good agreement was obtained between computed and experimental temperatures prior to structural and properties changes due to coagulation.

BE26-B.6

CRYOPRESERVATION OF ORGANS USING OPTIMIZATION METHODS, *G.S. Dulikravich**, *J.V. Madison*, PennState Univ., State College, PA 16803, and *L.J. Hayes*, Univ. of Texas, Austin, TX 78712, USA.

The survivability of living tissues and organs is a strong function of the local cooling rates in each part of the organ. When preserving an organ, a maximum survival rate can be achieved by maintaining optimal local cooling rates. The optimal cooling rates for each type of the tissue can be experimentally determined. We will demonstrate that the optimal local cooling rates can be enforced by unsteady temperature variation on the walls of a container in which the cryoprotective fluid and the organ are located. An optimal time-space variation of the container wall temperature can be determined computationally using an inverse formulation. This represents an entirely new scientific approach to living tissue banking that is based on sound physical and mathematical grounds. The concept of optimized distributed cooling has been recently mathematically formulated and computationally proven by the lead authors for the two-dimensional case of pure heat conduction in a kidney and the cryoprotective fluid. The mathematical model included three regions with different heat diffusivities, but did not account for latent heat release during the phase change. The latent heat release and variable diffusivities will be included.

BE26-B.5

Thermal Monitoring with an Ingestible Rechargeable Capsule, *J.C. Lesho**, *A.F. Hogrefe*, *R.C. Eberhart*, *W.E. Radford* and *H.K. Charles*, Johns Hopkins University Applied Physics Laboratory Johns Hopkins Road Laurel, Md. 20707

Rechargeable ingestible thermal monitoring capsules have been designed, fabricated and tested. Two versions have been attempted. The first continuously telemeters data, while the second telemeters data only when commanded. Both versions use an inductive link for data transmission and recharging. The commandable version also uses the inductive link for commands.

A battery powered receiver has also been designed, fabricated and tested. Data may be logged manually or automatically by an IBM PC.

The ingestible capsule is eight millimeters in diameter and 21 millimeters long. The electronics are encapsulated in epoxy then coated in silicone rubber. The capsule is rechargeable without having to take it apart. The system has a resolution of 0.1°C. Readings from the continuous pill can be taken once per second. The commandable pill can be queried four times per minute.

Results of the first tests of the capsule are summarized in the paper. The ongoing program for the development of a four channel system to measure temperature, pH, heart rate and pressure is also described.

The support of the NASA Goddard Space Flight Center is gratefully acknowledged.

430

Author Index

- Aalbers, A.H.L., 118
 Abbot, J., 11
 Abche, A.B., 20
 Abdul-Kadir, N.M., 338
 Abe, H., 180,303,364
 Abe, M., 137
 Abe, R., 113,114
 Abe, Y., 408
 Abe, Z., 112
 Abouelnasr, D.H., 360,372
 Abramowitz, Z., 407
 Abrons, H., 226
 Aubry, F., 111
 Accornero, N., 368
 Acevedo, H.F., 82
 Acharya, B.L., 24,28
 Adachi, A., 33,61
 Adachi, T., 328
 Adam, D., 325
 Adams, R., 19
 Adelstein, S.J., 67
 Aebischer, P., 237
 Affeld, K., 241, 280
 Agarwal, G.R., 24,28
 Agarwal, Y.C., 80
 Agatenzi, L., 66,129
 Aggarwal, S.J., 281,308
 Agris, J.M., 392
 Ahmed, A.K., 309
 Aiba, M., 343
 Aine, C.J., 32
 Aizawa, M., 309
 Aizawa, Y., 304
 Akamatsu, T., 247
 Akatsuka, T., 333
 Akber, S.F., 63
 Akihiko, U., 299
 Akimoto, M., 345
 Akisada, M., 99,104,150,333
 Akitsu, T., 148
 Akiyama, Y., 114
 Akkoc, C.C., 303
 Akutsu, T., 248,264
 Alastie, H., 124
 Albert, S., 109
 Albin, M.S., 213,337,338
 Albrechtsen, O., 239
 Albright, J.A., 208,210
 Aldea, G., 180
 Aldman, B., 213
 Aldrich, J.E., 51
 Aletti, P., 49
 Ali, M., 66
 Aljama, T., 296,384
 Allen, B., Jr., 210
 Allen, P.D., 147
 Alessie, M., 171
 Almasi, J.J., 31,85,99
 Almeida, D., 277
 Almond, P.R., 54
 Alpen, E.L., 29
 Altemeier, W.A., 232
 Altobelli, S.A., 80
 Alves, R.N., 30
 Amend, G., 313
 Amols, H.I., 51
 Amori, E., 319
 Amos, O.E., 389
 Ampil, F., 41
 Anantha, N., 68
 Anderhuber, F., 289
 Andersen, O.S., 157
 Anderson, G., 408,409
 Anderson, L.L., 128,152
 Anderson, M.P., 106
 Ando, F., 146
 Ando, J., 253
 Ando, M., 99,104,150
 Andrabi, W.H., 118
 Andre, L., 43,56
 Andreasi-Bassi, F., 152
 Andreo, P., 142
 Andreoni, A., 17,24
 Andreucci, L., 140
 Andrew, J.W., 51
 Andrews, B.J., 388
 Angelides, K.J., 252
 Annis, M., 35
 Anno, I., 99
 Ansel, H.J., 88
 Antich, P.P., 122,128,143
 Antila, K., 324
 Antolak, J., 44
 Antolini, R., 171
 Antonuk, L., 57
 Aoki, T., 231,325
 Aoyagi, T., 281
 Apicella, A., 391
 Arai, T., 189,402
 Araj, N., 35
 Arakawa, K., 189
 Arakawa, M., 146,266
 Archer, B.R., 135
 Archie, J.P., Jr., 287
 Arcovito, G., 45,140,152
 Arduini, F., 392
 Arima, H., 148
 Arioka, T., 47
 Aronson, D.D., 369
 Aronson, R.M., 215
 Arruabarrena, A., 389
 Arthur, D.L., 32
 Arts, T., 178,179,351
 Aruga, M., 330,365
 Asakura, T., 251
 Ashayeri, E., 32,48
 Ask, P., 204
 Asp, L., 121
 Astrahan, M.A., 84
 Atalay, N., 312
 Atsumi, K., 189,245,246,408
 Aubert, B., 111
 Aubert, N., 111
 Auer, L.M., 289
 Auge, J.H., 266
 Augustijn, C., 179
 Aukburg, S.J., 220
 Auler, J.O.C., Jr., 27
 Aunon, J.I., 166
 Ausman, J.I., 18
 Austin, R., 180
 Austin, T., 377
 Avakian, Ts.M., 320
 Avanzolini, G.O., 218
 Avidor, J.H., 241,262
 Aydin, G., 312
 Ayton, V.T., 15,80
 Ayyangar, K., 57,84,120,135
 Azario, L., 45,140
 Azhari, H., 182
 Azpiroz, J.L., 277
 Babiloni, F., 173
 Bacci, C., 45,140
 Bachler, G., 288
 Backlund, T., 277
 Backonja, M., 60
 Bader, R., 93
 Badiello, R., 72
 Bagne, F.R., 39,42,51,52,123,136
 Baily, N.A., 145
 Bajzer, Z., 234
 Baker, R.S., 58
 Baldwin, B.C., 51
 Baldzer, K., 256
 Ball, M.E., 19
 Ball, W., 14
 Ballou, S.P., 405
 Banci, G., 48
 Banci, M., 66
 Bao, S.H., 201
 Barach, J.P., 232
 Baratta, R., 387
 Barbaro, V., 322
 Barbini, P., 218
 Barcero, U., 327
 Baretich, M., 186
 Barker, A.T., 170
 Barnes, C.D., 340
 Barnes, G.T., 69,70
 Barnes, W.H., 122
 Barnett, C., 153
 Baron, J.J., 40
 Barr, R.C., 169
 Barrionuevo, O.J., 188,197
 Barsai, J., 321
 Barta, E., 231
 Barth, K., 150
 Barth, N.H., 8
 Barthes-Biesel, D., 354,355
 Bartolini, P., 322
 Baselli, G., 256
 Baskaran, S.V., 64
 Basmadjian, G., 68
 Bassano, D.A., 128
 Bassett, L., 34
 Bassingthwaighte, J.B., 181,227,230
 Batallan, O.R., 188,197
 Bates, J.H.T., 217
 Battista, J.J., 21,44,107
 Baudoin, G., 172
 Bautro, N., 38
 Baxendale, R.H., 388
 Beack, S.H., 235
 Beddar, A.S., 56
 Begnozzi, L., 48,151
 Behrman, R.H., 86,146
 Beil, C., 92
 Bell, D.R., 372
 Bellet, D., 284
 Belletti, S., 71,115
 Bellotti, J., 41
 Belmin, J., 249
 Ben Said, R., 301
 Ben-Haim, S.A., 221
 Benassi, M., 45,48,151
 Bencomo, J.A., 70,117
 Benedict, S.H., 75
 Beneventi, S., 38
 Benitez-Read, E., 14
 Benke, T.A., 188
 Benko, H., 386
 Benton, L.A., 315
 Beran, H., 329
 Berceli, S.A., 249
 Bergamasco, M., 404
 Bergeler, J., 317
 Berger, R.D., 257
 Bergeron, P., 264
 Bergsland, P., 222
 Bergstrom, M., 337
 Berk, D., 353
 Bermudez, N.M., 136
 Berna, V., 71
 Bernabei, R., 140
 Bernabeu, P., 306
 Bernardi, T., 72
 Berner, B., 118
 Bernini, U., 17
 Bernstein, M.S., 186
 Berry, J.A., 51
 Berry, S.J., 315
 Bersani, F., 145
 Bertenstam, L., 382
 Berthaud, P., 394
 Bertocchi, M., 256
 Bertram, C.D., 259
 Bertram, C.D., 262
 Bertram, C.D., 384
 Beszedics, G., 368
 Betts, T.A., 403
 Beuchler, D., 79
 Bews, J., 144

Boy, P., 49
 Beyar, R., 178,182
 Bezerianos, A., 300,312
 Bhagyalakshmi, A., 253
 Bhandare, N., 122
 Bhatia, A.L., 148
 Bianciardi, L., 45
 Bianco, B., 407
 Bidani, A., 217
 Bielajew, A.F., 5,22,142
 Biggs, P., 39,52,59
 Bignall, S., 259
 Bijhold, J., 45,86
 Billings, E.M., 78
 Bindal, C., 206
 Binns, W.R., 46
 Bittner, U., 150
 Bivas, A., 76
 Bizios, R., 249
 Bjarngard, B., 90,119,134,135,136
 Bjorkholm, P.J., 35
 Blackburn, G.F., 401
 Blacker, M., 399
 Blackwell, C.R., 99
 Blad, B., 111,382
 Blake, S.W., 132
 Bleier, A.R., 106
 Blight, A.R., 159
 Bloch, P., 45,74,133
 Block, J., 207,301
 Block, R., 16,276
 Blockeel, E., 393
 Bloor, M.I.G., 371
 Bocci, N., 264
 Bodner, D.R., 162
 Boenick, U., 187,319,328
 Boethius, J., 337
 Boezeman, E.H.J.F., 168
 Bogen, D.K., 247
 Boehm, G., 383
 Bollea, H., 23
 Bolli, R., 361
 Bolomey, J.Ch., 394
 Bolz, A., 279
 Bom, N., 360
 Bonamini, R., 171
 Bonanni, E., 327
 Bonincontro, A., 29
 Boone, J.H., 15,63
 Boone, J.M., 36,72,87
 Boonzaier, D.A., 389
 Boote, E., 75
 Borasi, G., 101
 Borgquist, L., 193
 Born, E.J., 55,105
 Borovetz, H., 247,249,263
 Bosone, G., 365
 Bostrom, U., 318
 Boter, J., 193
 Bouligand, B., 318
 Bourgain, R., 393
 Bourland, J.D., 55,79,170
 Boutillon, L., 44
 Bovendeerd, P., 178
 Bowerman, R., 76
 Boyer, A.L., 22,135
 Boyers, A.S., 103
 Bozovic, Z., 201
 Braacale, M., 158,340,360,391,392
 Brady, T.J., 7,92
 Brahmavar, S.M., 17,23,109
 Brahme, A., 73,142
 Branca, F.P., 198
 Brandt, H.E., 175
 Branstetter, R., 40.
 Bravar, D., 196
 Breitman, C.P., 188,197
 Brewster, L., 13
 Brian, B., 236
 Briggs, W.S., 100
 Bright, F.V., 403
 Brinker, R.A., 21
 Bromley, J., 302
 Brondo, J., 20,25
 Bronikowski, T.A., 224
 Bronn, D.G., 42,52
 Brooks, D.H., 169
 Brooks, L.J., 216
 Brown, J.H.U., 200,322
 Brubaker, D., 398
 Brummer, M.E., 94
 Brunia, C., 34
 Brunner, M.C., 94
 Brusic, V., 201
 Bryer, J.B., 83
 Bucciolini, M., 142,378
 Buchanan, D.S., 61
 Buckles, D.S., 171
 Budai, K., 160
 Buffaloe, G., 237
 Buhle, L., 45
 Buist, R., 62
 Buizza, A., 330
 Bujnowski, S.W., 108
 Bukovitz, A.G., 46
 Bukowski, B.A., 195
 Buldain, G., 389
 Bunegin, L., 213,337,338
 Bungo, M.W., 265
 Burhop, K., 238
 Burman, C., 91
 Burns, C.P., 281
 Burns, P., 10
 Bush, E., 219
 Bustelo, J., 145,311
 Butler, K., 62
 Butter, D., 263
 Buxton, R.B., 7,92
 Byrd, C., 355
 Byrne, F., 370
 Cadena, M., 296
 Cadene, T., 218
 Cady, R.K., 384,398
 Calcote, R.W., 346
 Calderon, A., 325
 Caldwell, C.B., 89
 Camarena, R., 384
 Cameron, J., 70
 Cameron, J.R., 60
 Cametti, C., 29
 Caminal, P., 233,266
 Cancelli, C., 370
 Canfield, T.R., 48,308,346
 Canilang, E.P., 203
 Cantero, A., 269
 Cantone, M.C., 25,26
 Capalucci, J., 52
 Cape, E.G., 242,279
 Capello, A., 218
 Capes, B.L., 348
 Capitanio, L., 368
 Cappa, P., 198
 Cappelzo, A., 337
 Caprani, A., 253,306
 Caprihan, A., 14
 Capriotte, C., 25,77
 Carbajal, V.M., 304
 Cargill, R.S., 249
 Carley, D., 215
 Carley, D.W., 214
 Carlile, P.V., Jr., 68
 Caro, C.G., 255
 Carollo, J.J., 162
 Carpenter, D.A., 361
 Carrasco-Sosa, S., 297,304,304
 Carson, P., 11,76
 Carson, P.L., 362
 Casnocha, S.A., 285
 Casolo, G.C., 378
 Cassot, F., 278,289
 Castaldo, R., 158,340,360
 Castellano, A., 100
 Casterline, J., 203
 Catena, G.C., 403
 Cavicchioli, C., 25
 Cecatti, E.R., 95
 Cedarholm, J.C., 103
 Cellier, F.E., 228
 Cerra, F., 88
 Cerutti, S., 174,256
 Cesarelli, M., 158,360,392
 Cesareo, R., 105,143
 Cevenini, G., 218
 Chabbani, M.A., 265
 Chadwick, R.S., 179,349
 Chal, M., 285
 Chakraborty, D.P., 69,70
 Chambers, R.P., 316
 Chan, E.K.Y., 394
 Chan, H., 16,117,150
 Chan, J.I.S., 227
 Chan, J.C., 408
 Chan, M.T., 348
 Chandra, I., 80
 Chandran, K.B., 240,243
 Chaney, E.L., 55,79
 Chang, S.C., 49
 Chang, S.Z., 201
 Chang, W.H., 300
 Chang, Y., 367
 Chang, Y., 383
 Chang, Y.L., 268
 Chang, Y.L., 306
 Chaouche, M., 172
 Chapman, C.R., 397
 Charles, H.K., 410
 Charles, J.B., 265
 Charles, S., 275
 Charleston, S., 296,384
 Chaudhri, M.A., 74,133,147,148,298,320
 Chavantes, C., 18
 Chelly, J.E., 361
 Chen, A., 300,305
 Chen, C., 36
 Chen, C.S., 54,120
 Chen, D., 26
 Chen, G.T.Y., 91
 Chen, H., 207,301
 Chen, H., 236
 Chen, H., 246
 Chen, H.H., 53,54
 Chen, H.Q., 267,284
 Chen, I.I.H., 378
 Chen, J., 396
 Chen, K., 326
 Chen, L., 208,210
 Chen, R.C., 29,275,331
 Chen, S., 284
 Chen, T.C., 53
 Chen, X., 276,341
 Cheng, C.W., 90
 Cheng, E., 12,13
 Cheng, E.Y., 404
 Cheng, J., 331
 Cheng, M., 276,308
 Cheng, P., 119
 Cheng, P., 207
 Cheng, P., 301
 Cheng, Y.A., 46
 Cheong, W.F., 18
 Cherniack, N.S., 216
 Chew, P., 183
 Chiabrera, A., 407
 Chiang, E., 76
 Chiang, Y., 341
 Chiang, Y.F., 321
 Chien, D., 7,92
 Chien, S., 353
 Chihara, K., 364
 Chin, L.M., 8,118,122,135
 Chinzai, T., 408
 Chiou, R.K., 79

Chisolm, G.M., 249
Chiu-Tsao, S.T., 128
Chiyotani, K., 304
Cho, C., 132
Chougule, A.A., 24
Christensen, D.A., 403
Chrucky, R., 313
Chu, J., 13
Chu, J., 39
Chu, L., 27,389
Chu, M., 336
Chu, R.Y.L., 68
Chu, S., 349
Chu, W., 400
Chu, W.K., 109
Chuang, K.S., 84
Chubaci, J.F.D., 69
Chui, C., 21,22
Chung, C., 383
Chung, H., 132
Chung, N., 182
Chung, T.W., 283
Chuong, C.J., 347
Churchwell, D., 372
Churchwell, A.L., 372
Cinòs, C., 95,130,136
Cintron, O., 12
Cioni, B., 163
Ciraolo, L., 142,378
Civardi, S., 256
Clark, J.A., 140
Clark, J.W., Jr., 159,188,230
Clark, R.E., 239,240
Clarke, G.D., 81
Clayton, P.A., 49
Claeland, C., 60
Clement, P., 276
Clemente, F., 158,360
Cliquet, A., Jr., 388
Cluyse, L., 295
Coates, G., 225
Coatrieux, J.L., 277
Coffey, C.W., 118
Coggins, D., 180
Cohen, M.V., 229
Cohen, R.J., 229,257
Colasanti, A., 24
Cole, M., 400
Collier, J.M., 74
Collins, E.M., 373
Collins, J.M., 223
Collins, R., 373
Colominas, J., 257,315,382
Colson, M.A., 361
Colton, C.K., 243
Contento, G., 160
Conturo, T., 93
Conzay, B., 88
Conway, J., 37,83
Cook, L.T., 6
Cook, R.E., 398
Cooke, C.D., 100
Cooks, R., 56
Cooney, P., 116
Cooperman, A., 206
Coptcoat, M., 317
Cornhill, J.F., 251
Coubier, R., 264
Courtney, S.P., 210
Cowin, S.C., 205
Cox, R., 398
Crapo, J.D., 221
Craven, J.D., 145
Creixells, C., 266
Cresci, F., 321
Crespo, G.G., 30
Crosthwaite, M.H., 66
Crucian, G.P., 398
Cugell, D.W., 260
Cui, C., 294
Cui, J., 208

Cunningham, I.A., 16
Cunningham, J.L., 206,209
Curio, G., 339
Curry, F., 248
Cygler, J., 138

D'Amato, A., 63
D'Angelo, L., 151
D'Angelo, S., 140
D'Ermo, G., 48
D'Ottavio, G., 143
da Costa, R., 281
Dadok, J., 82
Daftari, I., 120,132
Dahl, R.A., 50,99
Dale, S., 103
Dankelman, J., 267
Dantas, W., 330
Dario, P., 404
Das, B.S., 68
Das, I.J., 22,95,121
Das, K.C., 69
Dasse, K., 246
Datta, N.R., 125
Datta, R., 24,41
Datta, S., 24,41
Davet, D., 258,359
David, Y.B., 190,193
Davis, C.A., 389
Davis, M.J., 350
Davis, P., 248
Davis, R.B., 269
Dawson, C.A., 224
De Agostini, A., 115
de Almeida, C.E., xx,30,44,95
de Almeida, R.T., 194
De Backer, G., 68
De Buyzere, M., 234,295
de Callatay, A., 227
de Carvalho, M., 194
De, D.K., 64
de Figueiredo, R.J.P., 392
de Lima, W.C., 330
De Scheerder, I., 295
De Vis, L., 68
Deane, C.R., 269
Debande, B., 228
Debourg, C., 193
deGuzman, A.F., 43
Deibel, F.C., 39,107
del Pozo, F., 202,274,311
Delanghe, J., 234,295
Delano, F.A., 349
deLemos, R.A., 223
Delgado, C., 160
Dellepiane, S., 392
Delouche, A., 356,359
Delouche, Ph., 256
Demiray, H., 344
Demoment, G., 76
Dempsey, J.A., 214
Deng, X., 289,380
Dennett, J.C., 57
Denoth, F., 329
DePascale, M.P., 140
DeRoo, T.R., 94
DeSapio, E., 45
Deslauriers, R., 62
Detorie, N.A., 78
Deutsch, M., 46
Devars, F., 390
Devaru, S., 68
Dhananjaya, M.H., 165
Dhingra, U., 83
Di Nallo, A.M., 48,150
Diamond, S., 253
Diao, Y., 278
Dickie, D.L., 206
Diebold, B., 356
Digby, W., 7
Diller, K.R., 281,308

Dillon, A.R., 316
Dillon, S.M., 167
Dimitrijevic, M.R., 163,387
Din, J., 275
Ding, J., 294
Ding, X., 343
Ding, Z., 284
Dinnar, U., 182
Dionne, K.E., 243
Disertori, M., 171
Dixon, L.B., 89
Djakovic, D., 201
Dobben, G., 108,379
Dobelbower, R.R., Jr., 123
Dohi, T., 333,390
Doi, K., 89,116,117,150
Doiron, D.R., 3
Dolber, P.C., 160
Dominguez, J.M., 233
Dong, G., 311
Doniwa, K., 202
Donninelli, M., 322
Doppke, K.P., 13,123
Dorson, W., 236
Dostalek, C., 329
Douglas, R., 387
Douniwa, K., 231
Downey, J.M., 181
Doyle, D.J., 323
Doyle, L., 37
Drexler, G., 21
Drost, D.J., 103
Drzymala, R.E., 13,130
Ducla-Soares, E., 33
Dujovny, M., 18,40,86,127,276
Dulikravich, G.S., 410
Dumee, Ph., 356,359
Dunajski, Z., 34
Dunbar, B.J., xix
Dung, H.C., 395,400
Dunn, D., 103
Dunn, F., 363
Dunn, R.L., 175,176,177
Duncombe, P.B., 40,86
DuPuy, M., 76
Durham, S.J., 249
Duszyk, M., 352
Dvorak, P., 73
Dwyer, S.J., III, 6
Dykes, F., 258
Dymond, E.A., 390
Dyro, J.F., 194

Eagan, P., 129
Earle, M.A., 127
Eberhart, R.C., 410
Ebisawa, Y., 366
Echsel, H., 63
Echt, D.S., 172
Eckstein, E.C., 351
Eddy, C.A., 176
Edelman, N.H., 215
Edholm, P., 103
Edmonds, H.L., 170
Edoliya, T.N., 80
Edwards, E.H., 252
Eichmeier, J., 204
Eicker, B., 150
Eidbo, E.E., 239,240
Eiho, S., 393
Eiju, T., 377
Einav, S., 241,262
Eisenbarth, J., 89
Eisenberg, R.S., 157
Eisner, R.L., 94,103
Ejdesjo, L., 367
Ekaterinaris, J.A., 288,375
Eklund, B., 199
Ekstrand, K.E., 122
El-Khatib, E., 15,37
Elad, D., 241,261,262,273

Elgandy, Y., 377
 ElHefnaway, A.M., 213
 Elias, P., 34
 Ellinghaus, G., 228
 Ellis, K.J., 20,65
 Elson, E., 352
 Elson, M.K., 79
 Enami, B., 13
 Endo, M., 75
 Engelhorn, M.W., 83
 England, P.J., 81
 English, L., 272
 Engstrom, T., 404
 Eppink, R.T., 252
 Epstein, J.W., 46
 Epstein, M.A.F., 218
 Ericsson, A., 110
 Erne, S.N., 33,339
 Ernst, E.A., 178
 Eskin, S.G., 252,253,285
 Eskinder, H., 349
 Estoesta, E., 101
 Estola, K-P., 381
 Eswaran, C., 218
 Ettinger, K.V., 20,26,75,98
 Evander, E., 225
 Evans, A.C., 92
 Evans, E., 353,355
 Evans, M., 209
 Ezquerro, N.F., 100
 Ezzadeen, M.A., 338
 Ezzel, G.A., 128

 Fadda, A., 335
 Fadell, L.A., 51,52
 Faes, Th.J.C., 257
 Failinger, A.L., 110
 Fajman, W.A., 94
 Falcao, R.C., 107
 Fallon, T., 302
 Fallone, B.G., 144
 Fan, X., 296
 Fang, L.Y., 332
 Fang, Z., 292,294
 Fang, Z., 385
 Farison, J.B., 20
 Farman, A.G., 122
 Fastenmeier, K., 338
 Fatemi, P., 240
 Fatouros, P.P., 15,93,101,378
 Faust, U., 302
 Favella, A., 66
 Fear, P.T., 128
 Fei, D., 93
 Fei, D., 378
 Feinberg, B., 184
 Feldkamp, L.A., 82
 Feldmeier, J., 47
 Feldmier, J., 129
 Folice, C.J., 188,197
 Fennigkoh, L., 184
 Fenster, A., 16
 Fenster, A., 45,100
 Fercher, A.F., 367
 Ferguson, A.S., 162
 Ferreiro, J., 225,357
 Fewell, R., 88
 Field, C., 21
 Figueiredo, M., 407
 Filligoi, G.C., 368
 Finley, C., 364
 Fiorillo, A., 404
 Fish, R., 359
 Fisher, A.C., 354
 Fisher, T.C., 354
 Fitzpatriok, J.M., 35
 Fitzpatriok, P.J., 77
 Flaohensoker, G., 338
 Flam, E., 316
 Fleischman, R.C., 31
 Fletcher, L.S., 409

 Flynn, A., 180
 Flynn, E.R., 32
 Flynn, M.J., 16,82,206,276
 Fogelson, L., 166
 Fonsteliien, E., 273,295
 Fontenla, D.P., 43
 Forester, G.V., 62
 Foster, F.S., 6,9
 Foster, W.M., 226
 Fouke, J.M., 223,303
 Foulquier, J.N., 90
 Fowlkes, B., 11
 Fox, K., 86
 Fraass, B.A., 12
 Frampton, S., 281
 Franchi, F., 66
 Francoini, C., 48,75
 Frangos, J.A., 253
 Frank, M., 111
 Fransson, A., 110
 Frazier, O.H., 204
 Fredberg, J., 223
 Freeman, W.J., 164
 Freeston, I.T., 170
 Frey, G.D., 114,116
 Friedman, M.H., 251
 Fringuelli, F., 66
 Frisch, P.H., 369
 Frize, M., 184,199
 Frost, J.D., Jr., 168
 Frucht, U., 319
 Fryar, J., 16,104
 Fu, C., 28
 Fu, M.K., 87
 Fu, W., 294
 Fu, Y., 367
 Fuchs, H., 10
 Fujii, K., 254,303,356,364
 Fujii, M., 49
 Fujiki, T., 333
 Fujimasa, I., 246
 Fujimasa, I., 408
 Fujimoto, T., 309,318
 Fujimura, Y., 87
 Fujita, H., 117
 Fujita, K., 385
 Fujita, M., 115
 Fujiwara, T., 290,360,361
 Fukuda, H., 69
 Fukui, T., 140
 Fukui, Y., 231,275
 Fukushima, E., 14,80
 Fukushima, H., 346
 Fukushima, H., 303
 Fullerton, G.D., xx
 Fumero, R., 247
 Fung, B.M., 310
 Fung, S.J., 340
 Fung, Y.C., 220,225
 Furlan, L., 256
 Furst, M., 328
 Furvie, S.S., 172,296
 Furukawa, T., 87,146,231,325
 Fuse, M., 281
 Fuse, T., 291
 Futaki, T., 333

 Gaboriaud, G., 394
 Gagne, R.M., 105,106
 Gagnon, D., 149
 Galbraith, D.M., 46,124
 Galoto, F.M., Jr., 190
 Gallasch, E., 371
 Gallini, R., 71
 Galloway, G., 97
 Galloway, R.L., Jr., 110
 Galvin, J.H., 43,91
 Gambarini, G., 25,26
 Gamboa, C.M., 329
 Ganesan, S., 18,24,25
 Ganesh, T., 125

 Gao, D., 293
 Gao, R., 299
 Gao, S., 332
 Gao, W., 73
 Gao, Z.H., 275
 Gaona, E., 54
 Garber, J.W., 243
 Garces, R., 53
 Garcia, E.V., 100
 Garcia, L., 310,312
 Garcia, P., 264
 Garcin, S., 357
 Gardezabal, L., 389
 Gardner, M.J., 60
 Garliok, P.B., 80
 Gaspar-Rosas, A., 283
 Gaver, D.P., III, 221
 Gavriely, N., 260
 Gazzani, F., 337
 Ge, W.S., 134
 Gehrig, J., 93
 Geiger, D., 290,345,369
 Geise, R.A., 88
 Gen, H., 14
 Genant, H.K., 207,301
 Geng, C., 280
 Geng, J., 207
 Gentles, W.H., 71,87
 George, J.S., 32
 George, R.E., 118
 Gerbi, B.J., 39,94
 Gerig, L.H., 3
 Gerson, R.K., 100
 Gerster, T., 96
 Gerstmann, D., 223
 Gfirtner, H., 96
 Ghaznavi, C., 313
 Ghidoni, J., 189
 Ghosh, A., 98
 Giacco, G., 45
 Giani, U., 24
 Giddens, D.P., 258,288,359,360,372,373,375
 Giersiepen, M., 240,277
 Gieseking, E., 279
 Gieseler, S.J., 330
 Giesey, J.J., 362
 Gigante, G.E., 101,117
 Gilbert, I.A., 303
 Giles, H.R., 82
 Giles, W.R., 230
 Gillette, P.C., 171
 Gillies, B.A., 55
 Gillin, M.T., 38,130
 Gimmon, Z., 307
 Giorgio, T.D., 238
 Gioux, M., 390
 Giugni, U., 71
 Gizdulich, P., 321,345
 Glasgow, G.P.,
 Glass, D.S., 274
 Glass, P.S.A., 175,176,177
 Glaze, D.G., 168
 Gluer, C., 207,301
 Gobbi, G., 38
 Gobel, W., 282
 Goner, A., 103
 Goodhard, W., 286
 Goitein, M., 44
 Gold, M.H., 402
 Gold, R., 34
 Goldson, A.L., 32,48
 Goldstein, S.A., 82,206
 Gomez, E., 389
 Gomez, P., 365
 Gomez, R., 84
 Gomez-Aguilera, E., 202,274
 Gomez-Cia, T., 269
 Gonzalez, D.L., 230
 Gonzalez, J., 389
 Good, W.F., 84
 Goodman, G.R., 193

Goodsitt, M.M., 82
 Goransson, G., 382
 Gordon, D., 258
 Gore, J., 374
 Gore, J.C., 6
 Gore, R.W., 350
 Gormiey, L., 34
 Gosling, R.G., 15,358
 Goss, D., 269
 Gotman, J., 168
 Goto, H., 328
 Goto, K., 370
 Goto, M., 290,360,376
 Goto, T., 202,231
 Gotoh, K., 305
 Gotsman, M., 268
 Gow, B.S., 384
 Graocovetsky, S., 301.
 Graham, M.M., 181
 Gramajo, H.D., 188,197
 Granda, C.O., 50
 Green, L.S., 232
 Greene, E.R., 358
 Greene, R., 103
 Greenfield, M.A., 145
 Greening, J.R., 97
 Grefenstette, J., 35
 Gregorio, M., 162
 Gregory, R.C., 59
 Greitz, T., 337
 Griffey, B., 63
 Criffey, R., 63
 Griffith, B., 263
 Griffiths, D.J., 231
 Griffiths, P.A., 390
 Grigsby, P.W., 126
 Grotberg, J.B., 221,260
 Grund, F.M., 79
 Grupen, M., 17
 Gu, Y., 211,213
 Guan, D.X., 298
 Gu, Y., 210
 Guerrisi, M., 263,264,345
 Guevara, M.R., 229
 Guglielmi, J.P., 356
 Guilbeau, E., 402
 Guilot, C., 370
 Gulrajani, R.M., 232
 Gunasekar, J.S.B., 41
 Guntermann, P., 280
 Gupta, B.B., 348
 Gupta, M.M., 29
 Gur, D., 46,84
 Gurvich, A.M., 333
 Gussenhoven, W.J., 360
 Gutierrez, G., 191
 Gutierrez, M.A., 296
 Guttman, G.D., 29,147
 Guzzetti, A., 256
 Gvozdanovic, D., 66
 Gysemans, M., 68

 Ha, B., 225,357
 Haaake, E.M., 216
 Haverer, S.A., 278
 Haddad, G.G., 258
 Hagekyriakou, J., 320
 Hagg, R., 124
 Haggag, Y., 287
 Haggman, V.N., 235
 Haghighi, S.S., 339
 Hahn, P., 13
 Hakim, A.M., 92
 Halama, J.R., 67
 Halberg, F., 202,310,324
 Hale, J.D., 255
 Hale, M.E., 51
 Hall, C.W., 192
 Hall, T., 75
 Hallbrucker, C., 269
 Hallen, B., 219

 Hallen, S., 98
 Halperin, H.R., 183,375
 Halter, J.A., 159
 Hammarstrom, O., 404
 Han, H., 211,213
 Han, Y., 248,314
 Hanai, S., 380
 Hanashima, K., 25
 Hancock, S.S., 134,143
 Handa, Y., 386,387
 Hangartner, T.N., 105
 Hanks, G.E., 39
 Hansen, Ch., 25,26
 Hansen, J.S., 263
 Hansen, J.W., 28,99
 Hansen, T., 190
 Hansen, V., 143
 Hansenkama, J.M., 239
 Hanson, G.P., 30
 Hanson, W.F., 135
 Hanya, S., 379
 Hara, M., 333
 Hara, S., 146,231
 Harada, K., 34
 Harada, K., 387
 Harasaki, H., 245
 Hardesty, R., 263
 Harding, G., 104
 Harms, W.B., 13
 Harold, M.E., 171
 Harris, J.D., 209
 Harris, T.R., 351
 Harrison, D.R., 81
 Hartley, C.J., 357,361
 Haruml, K., 164
 Hasegawa, S., 99,104,150
 Hasegawa, T., 33,61
 Hasenkam, J.M., 239,277,290
 Hashida, R., 252
 Hashiguuchi, S., 323
 Hashimoto, K., 304
 Haslock, I., 302
 Hastings, M.C., 364
 Hatazawa, J., 69
 Hausman, R.E., 29
 Hawkins, E.D., 177
 Hawkins, W.G., 83
 Hayama, K., 64
 Hayasaki, K., 100
 Hayashi, K., 248
 Hayashi, R., 76
 Haydock, C., 67
 Hayes, L.J., 408,409,410
 Hazra, D.K., 80
 He, B.Q., 77
 He, M., 299,300
 He, S., 311
 He, X., 283
 He, Y.X., 318
 He, Z., 342,392
 Hearshen, D.O., 151
 Heidlage, J.F., 160
 Heimans, J.J., 257
 Hein, I., 359
 Heiner, B., 321
 Heinila, J., 139
 Helie, J., 301
 Hellstrom, L.G., 219.
 Helms, J.D., 238
 Helms, J.M., 394,396
 Hendee, W.R., xx
 Henderson, S., 74
 Hendrickson, F., 78
 Henkelman, R.M., 4
 Henkelmann, G.A., 92
 Henkin, R.E., 67
 Henry, C., 390
 Henry, G.W., 225,357
 Henry, L.A., 19,65
 Henry, P., 189
 Herbert, D.E., 6,23

 Herbst, C.P., 113
 Herderiok, E.E., 251
 Hering, E., 60
 Hermanne, A., 68
 Herment, A., 76,359
 Hermida, R.C., 310,312,324
 Hernandez, C., 310
 Herron, J.M., 84
 Hesse, B., 78
 Heukelom, S., 44
 Higgenbottam, T., 222
 Higgins, P.D., 56,123
 High, M., 89
 Hilbert, D., 375
 Hill, J., 60
 Hill, M.R.S., 341
 Hill, S.E., 103
 Hinshaw, L.B., 283
 Hirakawa, A., 201
 Hirakawa, S., 146,305
 Hiramatsu, O., 290,360,376
 Hirano, M., 335
 Hirao, Y., 75
 Hiraoka, T., 131
 Hirata, Y., 364
 Hirayama, H., 286
 Hitohings, D., 220
 Ho, W., 71,87
 Hoohmuth, R.M., 353
 Hooini, B., 96
 Hodson, D., 40
 Hoekje, P.L., 216
 Hoeks, A.P.G., 363
 Hofer, E., 294
 Hoffman, A.S., 239
 Hoffman, E., 222
 Hoffman, J.I.E., 180
 Hoffman, M., 292
 Hogan, H.A., 206,209
 Hogrefe, A.F., 410
 Hogstrom, K.R., 54,97,108
 Hok, B., 367,403,404
 Hoke, S., 42,52,136
 Holdsworth, D.W., 100
 Hohenstein, R., 372
 Holgate, R.C., 116
 Holleran, L.A., 249
 Holmes, R.B., 35
 Holowaoz, J., 75
 Holt, R.T., 170
 Holtmann, P., 280
 Homer, M.J., 86
 Homma, K., 110,377
 Hong, J.H., 53
 Hongo, H., 356
 Horaoek, B.M., 60,61
 Hori, K., 14,268
 Hori, M., 180,254,303,356,364,256
 Horiba, I., 34,100
 Horiuchi, K., 189,247
 Horiuchi, T., 333,390
 Horowitz, A., 108,379
 Hosaka, R., 140,150,322
 Hoshimiya, N., 365,386,387
 Hoshino, K., 131
 Hosoda, S., 380
 Hosooka, K., 278
 Hossain, F., 78
 Houl, K., 267
 Hover, K.H., 78
 Howell, R.W., 7,19,67
 Howells, M.R., 29
 Howland, E., 60
 Hraahovy, R.A., 168
 Hsu, K., 202
 Hsu, T.L., 341
 Hsu, W.L., 97
 Hu, J., 26
 Hu, Y., 14,138,292
 Huang, D., 127,153
 Huang, D.J., 201

Huang, L., 298
 Huang, P.H., 124
 Huang, S., 300
 Huang, W., 248
 Huang, X., 304
 Huang, Y., 173,294,296
 Huberty, S., 228
 Huda, W., 31,70,107,117
 Hudgel, D.W., 214
 Hughes, A., 20
 Huizenga, H., 106
 Hulse, D.A., 209
 Humphrey, J.D., 183,344,346
 Hung, B., 202
 Hung, T., 247
 Hung, T., 263
 Hunt, J.W., 9
 Hunt, M., 13
 Hunter, D.H., 35
 Hunter, M., 364
 Hunter, M., 302
 Huntoon, C.L., xix
 Huo, J.W., 298,308
 Hussein, H., 17
 Hussein, W., 180
 Hussey, D.H., 119
 Hutohins, K.H., 127
 Hutohinson, G., 295
 Hutt, D.A., 215
 Hutten, H., 244,307,312
 Huxley, V.H., 217
 Hwang, N.H.C., 241,242
 Hwang, S., 387
 Hwang, Y., 315
 Hwang, Y., 396
 Hyman, W., 376
 Hyodo, K., 99,104,150
 Hyodynmaa, S., 9,137,139,330

Ialongo, D., 322
 Ioengle, M.V., 80
 Ichie, M., 387
 Idogawa, K., 324,329
 Iellamo, F., 345
 Ifukube, T., 365
 Iga, K., 14
 Iglesias, T., 312.
 Iguohi, Y., 385
 Ihara, T., 169
 Ikawa, S., 373
 Ikeda, H., 49
 Ikeda, K., 29,314,406
 Ikoro, N.C., 122,128,143
 Illes, T., 321
 Im, J.J., 263
 Imachi, K., 246
 Imai, H., 378
 Imura, T., 363
 Inada, H., 271,290
 Inagaki, Y., 378
 Indovina, M.A., 29
 Indovina, P.L., 29
 Inglis, R., 200
 Inoue, M., 180,200,254,271,303,356,364,256
 Iocco, M., 391
 Ip, T.K., 237
 Iramina, K., 34
 Irler, W.J., 171
 Isabay, D., 219,223
 Ishida, Y., 180
 Ishida, Y., 256
 Ishihara, A., 379
 Ishihara, K., 254,303,356,364
 Ishii, I., 298
 Ishii, N., 236,329
 Ishijima, M., 203
 Ishikawa, K., 271
 Ishimi, Y., 87
 Isik, B., 312
 Islam, M.K., 12,120,124
 Isobe, H., 147,148

Isogai, Y., 267
 Isojima, K., 189
 Ison, K., 317
 Issakov, A., 183
 Itakura, N., 385
 Ito, H., 202,203,254,345,384,286
 Ito, K., 247
 Ito, M., 69
 Ito, S., 113
 Itoh, K., 365
 Itoh, N., 402
 Itou, M., 90
 Itou, M., 267
 Iveson, R.D., 249
 Iwamoto, K.S., 42
 Iwao, K., 202,231
 Iwata, A., 34,100,231
 Iwata, S., 325
 Izzo, G., 65,66,145

Jachimowicz, A., 400
 Jackson, A.C., 217
 Jackson, P.C., 144
 Jacobs, J.R., 175,176,177
 Jaeb, J., 405
 Jaffrin, M.Y., 244,305
 Jain, V.K., 68
 Jalife, J., 160
 Jalinous, R., 170
 Jalonen, J., 324
 James, A.E., 93
 Janzad, M., 104
 Janozek, J., 88
 Jane, R., 233,266
 Jani, S.K., 119
 Jannett, T.C., 175,177
 Jansen, B.H., 166,175
 Janssen, J.D., 375
 Janssens, J., 408
 Japp, B., 77
 Jaramillo, B., 82
 Jaros, G.G., 197
 Jarvilehto, P., 381
 Jassawalla, J., 246
 Jay, M.T., 250
 Jayapal, V., 25
 Jayaraman, G., 250
 Jayaraman, S.M., 346
 Jebria, A.B., 390
 Jefferson, L.S., 190
 Jefferson, R.J., 388
 Jenkins, D., 78
 Jenkins, M.O., 122
 Jensen, O.E., 262
 Jeroudi, M.O., 361
 Jette, D., 135,137
 Ji, H., 338
 Jian, K., 208,210
 Jiang, C., 276,341
 Jiang, D., 255,334,340
 Jiang, P., 326
 Jiang, W., 332
 Jimenez, J.A., 219
 Jimoh, A., 276
 Jin, J., 293,294
 Jin, S., 291,362
 Jing, Y.Z., 29,331
 Johansen, A., 273
 Johnson, A.E., 310
 Johnson, E.C., 358
 Johnson, J.R., 170
 Johnson, K.N., 131
 Johnson, R.J., 238
 Johnson, T.K., 79
 Johnston, G.I., 186,271
 Jones, C.J.H., 255
 Jones, D.T.L., 132,133
 Jones, J., 165
 Jones, M., 239
 Jones, M., 240
 Jones, M.T., 103

Jones, N.B., 158,404
 Jones, R., 165
 Jones, S., 258,360
 Jones, S.A., 359,372,373
 Jonson, B., 225
 Joseph, J., 60
 Joshi, R.C., 125
 Joyner, R.W., 160
 Juan, L., 249
 Juday, R.D., 368
 Judy, P.F., 106
 Jung, B., 110
 Juttner, F., 297

Kaohel, V., 204
 Kagan, A.R., 41
 Kagawa, K., 266
 Kagiyama, M., 376
 Kahtoh, S., 365
 Kaitila, P., 321
 Kajiya, F., 181,268,290,360,361,372,373,376
 Kakihana, M., 99
 Kalender, W., 35
 Kalli, S., 235
 Kallman, P., 73
 Kalmanson, D., 357
 Kamada, T., 180,254,256,303,333,356,364
 Kambara, K., 146
 Kamei, H., 63,309
 Kamiya, A., 212,245,247,253,351,352
 Kamiya, K., 202,231
 Kamm, R.D., 220,223,261
 Kampp, T.D., 344
 Kan, C., 299
 Kan, W.C., 129
 Kanai, H., 49
 Kanai, H., 285
 Kanai, H., 382
 Kanai, T., 75
 Kanamori, H., 88,101
 Kanazawa, S., 290,360,361,373
 Kanemoto, M., 281
 Kanosaka, S., 164
 Kaneta, K., 84
 Kaneyoshi, A., 402
 Kang, H., 369
 Kang, Z., 241
 Kano, T., 191
 Kao, H., 97
 Kaplan, D.T., 229.
 Kaplan, R., 55
 Kapoor, S.L., 139
 Karemaker, J.H., 256
 Karhumaki, L., 171,232
 Karino, T., 251,289,380
 Karlsson, M., 79
 Karlsson, S., 277
 Kartha, P., 78
 Kary, M., 301
 Kase, K., 134
 Kase, K.R., 95,121
 Kass, D., 179
 Kassis, A.I., 67
 Katanik, D., 40
 Katayama, M., 191
 Katayama, Y., 63
 Katila, T., 32
 Kato, S., 331
 Kato, Y., 406
 Katsumura, T., 290,361
 Katsuragawa, S., 116
 Katz, D., 262
 Kaufman, J.J., 407
 Kaufman, L., 255
 Kaul, S.K., 118
 Kavadias, M., 163
 Kawachi, K., 75
 Kawamura, K., 69
 Kawamura, K., 250
 Kawamura, K., 254
 Kawano, S., 333

Kawarada, A., 202,203,345,384,288
 Kawasaki, S., 148
 Kawashima, K., 131
 Kay, G.N., 175,177
 Kayashima, S., 402
 Kazda, I., 105
 Kearfott, K.J., 17,102,103
 Keddy, R.J., 141
 Keenan, R.L., 15
 Kehoe, T.M., 42,96,97
 Keith, M.W., 161
 Kellaway, P., 168
 Keller, B.M., 73
 Kelley, B.S., 177
 Kelly, R., 267
 Kennedy, A., 64
 Kenner, T., 283,297,348,371
 Kenwright, J., 206
 Kenyon, C.M., 222
 Kepski, R., 292
 Kesavan, S.K., 224
 Keshaviah, P.R., 236
 Kett, H., 96
 Key, H., 144
 Khan, F.H., 39,94,95,105,121
 Khan, F.R., 59,127,152
 Khodadadi, J.M., 287
 Khokhlich, Y.I., 407,339
 Khoo, H.C.K., 215
 Kiguohi, M., 87
 Kikuchi, M., 47,49,189,194,244,402
 Kikuti, H., 331
 Kilcoyne, R.F., 82
 Kilpatrick, D., 376
 Kim, T.G., 226
 Kim, T.H., 39
 Kim, Y.J., 64
 Kimme-Smith, C., 34
 Kimura, J., 402
 Kimura, K., 256
 Kimura, S., 69
 King, A.I., 369
 King, C., 58
 King, D.H., 358
 King, G., 32
 King, G.A., 128
 King, G.C., 48
 King, R.B., 181,2300
 Kippenhan, J.S., 351
 Kirby, T.H., 7
 Kirohner, M., 171
 Kirikilevsky, S.I., 407
 Kirkwood, J.R., 109
 Kirsner, R.L.G., 370
 Kiryu, S., 291
 Kishore, P.R.S., 15,101
 Kisslinger, A., 24
 Kitabatake, A., 180
 Kitabatake, A., 254,256,303,356,364
 Kitakaze, M., 180
 Kitasonono, H., 322
 Kitney, R.I., 255,259,265,285,334,358,373,374
 Klarmann, J., 46
 Klassen, H.K., 141
 Kleck, J., 7,132
 Klein, E.J.E., 122
 Klein, J.L., 100
 Klein, K.E., xix
 Kleinstreuer, C., 287
 Klemic, G., 61
 Kleviansky, H., 389
 Klide, A.M., 396
 Klose, U., 93
 Klotz, L., 18
 Kluksdahl, E.H., 102
 Knoppo, P., 164
 Knoche, J., 70
 Knott, E., 240
 Knudsen, V.E., 286,290
 Kobayashi, H., 288,384
 Kooh, R.F., 59,127,152
 Kodama, H., 329
 Kodama, R., 18
 Kodera, Y., 87
 Koder, Y., 115
 Koehler, A.M., 131
 Koeppe, R.E., III, 157
 Koh, K., 132
 Kohl, F., 400
 Kohler, J., 242,280
 Koji, H., 299
 Kojima, S., 266
 Kolar, P., 9,330
 Koles, Z., 327
 Kolff, W.J., 242
 Kolitsi, Z., 89
 Komatsu, H., 380
 Komori, S., 323
 Kondo, Y., 323
 Kondou, Y., 379
 Kondraske, G.V., 162
 Kong, S., 314
 Kong, W., 280
 Konig, W., 319
 Konisi, K., 99
 Konishi, K., 104
 Kontis, S., 358
 Koornneef, F., 272
 Kootsey, J.M., 157
 Kooy, H.M., 8
 Kopans, D.B., 35
 Korenberg, H.J., 315
 Kormos, R., 263
 Kornreih, F., 163
 Korpan, N.H., 336,407
 Korrubel, J., 60
 Kosanetzky, J., 104
 Kossoff, G., 11,361
 Kotani, M., 33,51,304
 Kothiyal, K.P., 166
 Koul, R.K., 118
 Kowe, R., 220
 Koyama, H., 331
 Koyano, T., 306
 Kozmann, Gy., 232
 Kozo, S., 299
 Kozuka, T., 256
 Kraft, D., 185
 Kraft, K., 378
 Kraft, K.A., 93
 Krajnic, J., 162
 Krams, R., 371
 Krasin, F., 60
 Kratky, R., 250
 Krawiwi, N., 215
 Kremkau, F.W., 77
 Krishna Murthy, T.G., 185,195,272,317
 Krishna Swamy, N., 272
 Kriz, R.J., 108
 Kriz, R.J., 379
 Krizaj, D., 386
 Kroll, R.M., 332
 Krouskop, T., 364
 Krybus, W., 334
 Ku, D.H., 377,379
 Kubo, H., 98,119
 Kubo, K., 385
 Kubodera, S., 189
 Kubota, H., 88,101
 Kubota, I., 26
 Kudo, N., 405
 Kugimiya, T., 320
 Kuipers, B.J., 226
 Kumar, V.D., 41
 Kume, Y., 89
 Kung, R., 205
 Kurita, A., 189
 Kuriyama, H., 402
 Kuroda, T., 406
 Kurosawa, H., 212
 Kurup, R.G., 52
 Kusakabe, H., 247
 Kushner, D.C., 82
 Kuske, R., 13
 Kusumi, Y.T., 399
 Kusuoka, H., 180,256,303,356
 Kutcher, G.J., 91
 Kuwahara, M., 393
 Kvernebo, K., 376
 Kwong, K.K., 7,92
 Lacey, L., 16
 Lacombe, C., 147
 Laoy, J.L., 19
 LaForge, D., 246
 LaFrance, M., 109
 Lagana, A., 143
 Lage, S.G., 296
 Lago, P.J., 158
 Lahtinen, T., 57
 Lai, T.L., 258
 Laitinen, L.A., 324
 Lake, J.R., 398
 Lakshmanan, A.V., 64.
 Lakshminarayan, S., 317
 Lakshminarayanan, A.V., 110,111
 Lam, C., 114
 Lam, K., 117,150
 Lam, S., 141
 LaManna, J., 400
 Lambert, F., 369
 Lambert, R.K., 261
 Lammers, W., 171
 Lan, F.L., 308
 Lan, R.H., 54
 Lan, T.B., 321
 Lancaster, J.L., xx
 Lane, R., 51
 Lang, F., 269
 Lange, J., 124
 Lange, P.H., 79
 Langewouters, G., 286
 Langone, J., 299
 Lanir, Y., 344,371
 Lanson, H., 44
 Lanting, P., 257
 Lanzl, L., 78
 Larsson, B., 5
 Larsson, H., 304
 Latini, P., 38
 Laura, R., 269
 Laufe, L.E., 176
 Laughlin, T.J., 175
 Laughlin, T.J., 176
 Laugier, A., 90
 Laurent, J., 188
 Lavelle, W.G., 303
 Lawrence, H.B., 238
 Laxton, J., 51
 Lay, J., 263
 Layne, W.W., 78
 Lazar, H., 327
 Le Gallo, O., 345
 Leavitt, D.D., 12
 LeCarpentier, G.L., 17
 Lee, C.J., 268,306
 Lee, D., 393
 Lee, G.C., 291
 Lee, J., 302
 Lee, J.H., 235
 Lee, J.H., 278
 Lee, J.S., 224,264
 Lee, L.P., 224,264,302
 Lee, M., 583
 Lee, T.Y., 65,85,114
 Lee, W., 383
 Leeds, N.E., 109
 Leehan, J.A., 380
 Leetz, H.-K., 58
 Lefevre, J., 228,230
 Lefkopoulc, D., 90
 Lehmann, D., 166
 Lehnert, S., 15

Lei, T., 105
 Lei, X., 280
 Leichner, P., 83K.
 Leichter, I., 76,207
 Leightner, D.J., 79
 Lelievre, J.-C., 147
 Lemerdy, Y., 357
 Leslieux, R., 161
 Lenner, K.A., 303
 Lenz, J., 248
 Leogrande, M.P., 38
 Lepioovska, V., 329
 Lesho, J.C., 410
 Lessard, C.S., 263
 Leszozynsky, K., 46,85
 Lever, H.J., 250,255
 Levesque, H.J., 254,357
 Levi, A., 405
 Levin, M., 187
 Levin, S.H., 211
 Levine, R.A., 242,279
 Levy, M., 385
 Levy, S., 301
 Lewis, J., 301
 Lewis, P., 32
 Lewkowicz, M., 179
 Lewkowitz, S., 183
 Li, J.K., 179
 Li, L., 267,284
 Li, H.L., 297,318,319
 Li, S., 314
 Li, W., 284
 Li, X.Z., 355
 Liao, F., 284
 Liberati, D., 174
 Liboff, A.R., 406
 Lichter, A.S., 59
 Lieber, B.B., 374
 Liebovitch, L.S., 229
 Liepsch, D.W., 377
 Ligeas, J.R., 218
 Lilly, H.B., 176
 Lin, C., 315
 Lin, D., 30
 Lin, F.J., 53,54,120
 Lin, J.R., 332
 Lin, N., 138
 Lin, P.P., 109
 Lin, T., 76
 Lin, X.Y., 354
 Lin, Y., 202
 Lind, B.K., 22,73
 Lindahl, O., 277
 Lindberg, B., 197
 Lindblad, U., 382
 Lindell, S.E., 187
 Linden, Y., 367
 Lindner, G., 142
 Lindqvist, A., 324
 Linehan, J.H., 224
 Ling, C.C., 92,126,127,153
 Ling, Q., 331
 Linnarsson, D., 219,304
 Liou, X., 336
 Lipka, J.H., 210
 Lipschultz, A., 187
 Litwiler, K.S., 403
 Liu, D.Y., 316
 Liu, H., 276,341
 Liu, J., 83
 Liu, J., 396
 Liu, L., 391
 Liu, R., 212
 Liu, S.H., 229
 Liu, S.S., 270
 Liu, X., 27
 Liu, Y., 279
 Liu, Y., 283,310
 Liu, Y., 311
 Liu, Y., 391
 Liu, Z., 212
 Lizuain, M.C., 95,130,136
 Lo, W.H., 201
 Lobrigitto, A., 72
 Lookwood, G.R., 9
 Lodeiro, C., 312
 Lofstedt, L., 199,273
 Logan, S.A., 252
 Lombard, J.H., 349
 Lono, R., 404
 Long, D.H., 397
 Long, K., 55
 Longobardo, , 316G.S.
 Lopata, M., 315
 Lopes da Silva., 165 F.H.
 Lopes, J.H.A., 194
 Lopez, A.C., 219
 Lorange, M., 232
 Lorenz, K.Y., 395
 Lorenz, W.J., 78,93
 Loring, S.II., 222
 Loshek, D.D., 23
 Loshin, D.S., 368
 Lotter, H.G., 113
 Lou, Z., 409
 Lovsund, P., 213
 Low, L., 51
 Low, L.R., 20
 Lowinger, T., 115
 Lowry, M., 80
 Loyd, M., 51
 Lu, D.H., 342
 Lu, J., 291
 Lu, R., 310
 Lu, S., 248
 Lu, W., 326
 Luan, Z., 14
 Lucas, C., 225,357
 Lulu, B.A., 126,139
 Lunkenheimer, P., 219
 Luo, J., 328
 Luo, Y., 314
 Lutohen, K.R., 218
 Luthra, A., 402
 Lutz, W., 53
 Lux, R.L., 163,232
 Luxton, G., 84
 Lysaght, H.J., 243
 Lysikiewicz, A., 405
 Ma, G., 188
 Ma, S., 27
 Ma, X., 332
 Ma, X.S., 291
 Maayan, Ch., 214
 Mabuohi, K., 408
 Mabuohi, S., 251
 Macellari, V., 337
 Machado, J.C.198,353
 MacLunas, R.J., 110
 Mackie, T.R., 121,130,133
 Mackiewicz, A., 405
 MacMahon, H., 116
 Mader, L., 405
 Madhvanath, U., 30,125
 Madison, J.V., 410
 Madsen, E., 75
 Madsen, H.T., 19
 Maeda, K., 64,324,325
 Maes, H., 408
 Magalhaes, R.A., 198
 Magenes, G., 330
 Magrini, A., 66,143,263,264,345
 Maguire, G.Q., Jr., 115
 Mah, E., 44
 Mah, K., 91
 Mahachek, A., 198,271
 Mahady, J., 272
 Maher, K.P., 116
 Mahler, Y., 268,307,407
 Mahood, S., 141
 Mahtaboally, S.Q.B., 143
 Mahtaboally, S.Q.G., 105
 Mahyoub, F., 37
 Maisey, M.N., 15,80
 Majahalm, S., 235
 Majka, S., 109
 Makila, J., 390
 Makino, H., 297,298
 Makino, K., 293
 Makio, A., 325
 Malamut, C., 107
 Malchesky, P.S., 237
 Malezic, M., 162,386
 Malik, G., 18
 Malik, G., 40,86,127
 Malin, D.H., 398
 Malinauskas, M., 364
 Malisan, M.R., 160
 Malliarou, S., 33
 Malmgren, L., 111
 Malmivuo, J., 171,232
 Malone, J.F., 116,272
 Mancini, A., 17
 Mancini, A., 24
 Mandava, V., 35
 Mandelkern, M., 7
 Manfrin, M., 330
 Mangiardi, L., 171
 Manifold, I.H., 83
 Manley, M.T., 209
 Mann, D., 247
 Manoharan, S.R., 24
 Manolis, J., 13
 Mansson, A., 369
 Marchal, C., 49
 Marous, H.L., 182,183
 Margarita, S., 322
 Margerum, S.C., 402
 Margulies, S., 222
 Marhoff, P., 150
 Marie, F., 369
 Markov, H.S., 407
 Marrett, S., 92
 Marsden, D.S., 115
 Marsh, L.H., 117
 Martin, B.B., 396
 Martin, L.J., 19
 Martin, M., 12
 Martin, M., 402
 Martin, S., 129
 Martin, S.E., 103
 Martinez, A., 219
 Martinez-Coll, A., 86
 Maruhashi, A., 104
 Masoaro, L., 115
 Masilamani, V., 18,24,25
 Masealdi, H.A., 307
 Mascen, C., 34
 Mastandrea, J., 123
 Mastrooinque, H., 17
 Mastrooinque, M., 24
 Masuda, H., 254
 Masuda, J., 384,288
 Masuda, Y., 378
 Masuya, R., 87
 Masuzawa, T., 333,390
 Mates, R.E., 180
 Matheny, M.L., 141
 Mather, B., 267
 Mathisen, M.L., 79
 Matsuda, K., 377
 Matsuda, H., 345
 Matsuda, T., 47,245
 Matsudaira, H., 313
 Matsui, H., 373
 Matsukawa, H., 291
 Matsumoto, G., 405,406
 Matsumoto, H., 88,101
 Matsumoto, T., 259
 Matsumura, H., 309
 Matsumura, T., 14
 Matsuo, H., 34,100

Matsuoaka, S., 34,290,360,361,373
 Matsuoaka, T., 376
 Matsushima, J., 365
 Matsuzaki, Y., 259
 Matsuzawa, T., 69
 Matthews, F.L., 220
 Matthews, J.W., 13
 Mattila, M.A.K., 397
 Matute, V., 388
 Maughan, W.L., 179
 Maxey, M.N., 192
 Mayer, D.J., 395
 Mayr, W., 386
 Mazal, D.A., 40
 MazHer, A.K., 288,375
 McCall, A., 48
 McCarey, B., 368
 McCarthy, K.J., 16,104
 McCawley, M., 226
 McCormick, B., 13
 McCraw, F.J., 117
 McCullough, E.C., 50
 McDaniel, W., 172
 McFadden, E.R., Jr., 303
 McGee, H., 204
 McGinley, P., 55
 McGowan, H.D., 77
 McIntire, L.V., 238,252,253,285
 McKetty, M.H., 72
 McMillan, S.T., 240
 McMurry, H.L., 55,79
 McNeice, G., 210
 McParland, B.J., 57
 McQueen, D.M., 370
 McShan, D.L., 12,59,138
 McVittie, R., 55
 Medialdea, M.J., 145,311
 Medina, B.V., 277,297
 Medina, I., 173
 Medvick, P.A., 32
 Meek, A., 85,
 Meertens, H., 45,86
 Meglio, M., 163
 Mehta, B., 40
 Mehta, M.P., 130
 Meigooni, A., 153
 Meinzer, K., 313
 Mell, J., 153
 Mellenberg, D.E., 50,99
 Melo, C.P., 27,296
 Men'izabal, J.A., 83
 Meguetti, J.C., 27
 Mercer, R.R., 221
 Merletti, R., 196
 Merrick, H.W., 123
 Merritt, R., 60
 Messinger-Rapport, B.J., 169
 Metzler, H., 384
 Meyer, C.R., 33,76,362
 Meyer-Ebrecht, D., 334
 Michanetzis, G., 391
 Michel, J.B., 249
 Mijneer, B.J., 44,118,122
 Mikami, T., 278,297,363,405
 Miklos, G., 22
 Miksicek, A., 187
 Mikulecky, D.C., 235
 Milano, F., 142
 Miles, R., 164
 Miles-MoCollum, D., 353
 Miller, C., 17
 Miller, C., 23
 Miller, D.A., 208
 Miller, P., 246
 Miller, R., 319
 Miller, R.A., 116
 Mills, T., 317
 Minamitani, H., 279,343,366,386
 Mineo, C., 252
 Mini, R., 71
 Minnaar, P.C., 113
 Hino, H., 233
 Mintchev, M.P., 335
 Miola, U.J., 26
 Mira, E., 330
 Misasi, N., 391
 Mishra, P., 92
 Missirlis, Y., 391
 Mita, M., 335
 Mitamura, Y., 245,278,297
 Mitchell, T.P., 79
 Mitev, G., 12,120,124
 Mito, K., 290,360,373,376
 Mitomi, T., 323
 Mitsui, K., 231
 Mitsumata, M., 250
 Mittelman, A., 76
 Mittelstadt, S.E., 76
 Miura, T., 200
 Miwa, H., 266
 Miyake, Y., 274
 Miyamoto, A., 189
 Miyamoto, H., 388
 Miyamoto, S., 267
 Miyasaka, K., 191,281
 Miyazaki, H., 146
 Miyazawa, T., 279
 Mizicko, M.K., 47
 Mizrahi, J., 385
 Mizuno, K., 189
 Mochio, S., 267
 Mockros, L.F., 348
 Moeller, J.H., 12
 Moeller, R., 43
 Moffit, D., 387
 Mohan, R., 21
 Mohan, R., 22
 Mohandas, N., 354
 Mohl, W., 286
 Mohnhaupt, A., 280
 Mok, E., 46
 Molho, N., 25,26
 Moller, D.P.F., 228
 Monos, E., 249
 Montague, T.J., 61
 Montevecchi, F.M., 247
 Moore, J.E., Jr., 379
 Mora, F., 277
 Mora, P., 70
 Moran, P.R., 64,100
 Moreuti, R., 115
 Mori, M., 69
 Morita, H., 340
 Moriya, T., 291
 Morkrid, L., 383
 Morris, E.D., 249
 Morris, P.G., 81
 Morris, R.L., 186,281
 Mortimer, J.T., 162,385
 Morvan, D., 278,305,289
 Moser, E., 63
 Moser, M., 283,297
 Moslehi, F., 218
 Moss, C.A., 394
 Mossery, M., 268
 Mota, H.C., 123
 Moura, L., 334
 Mouttahaar, A., 180
 Mrkvicka, J., 329
 Muehlbauer, M., 402
 Mukai, C., xix
 Muller, R.G., 37
 Munro, P., 45
 Munzenrider, J.E., 13,131
 Mura, A., 198
 Murakami, H., 405
 Murata, H., 104
 Murphey, C.R., 230
 Murphy, B., 272
 Murray, J.B., 398
 Murri, L., 327
 Musha, T., 164
 Musselman, V.H., 369.
 Mustafa, A.A., 88
 Myers, A., 234
 Myers, L.T., 7,75,132
 Myriantopoulos, L.C., 91
 Naccarelli, G.V., 230
 Nadeau, R., 169
 Nagakura, T., 364
 Nagano, T., 266
 Nagasaka, E., 274
 Nagashima, K., 305
 Nagata, N., 324
 Nagata, Y., 137
 Nagayama, M., 367
 Nagel, J., 385,391
 Nagel, J.H., 351
 Nahum, A.E., 124,142
 Nalli, S., 345
 Naito, A., 387
 Nakagaki, S., 87
 Nakagawa, M., 189
 Nakajima, K., 324
 Nakajima, T., 333
 Nakamori, N., 116
 Nakamura, F., 377
 Nakamura, H., 189
 Nakamura, K., 26
 Nakamura, T., 248
 Nakano, T., 309
 Nakano, Z., 373
 Nakatani, H., 266
 Nakatani, T., 248
 Nakaya, S., 81
 Nakazawa, M., 84
 Nam, T.L., 141
 Nandedkar, S.D., 158.
 Narahara, H., 390
 Narayanan, S., 125
 Nariainen, K., 330
 Natan, T.E., Jr., 247
 Nath, R., 153
 Nath, R., 58
 Natsubori, S., 333
 Naughton, D., 272
 Navarro, L.T., 252
 Navona, C., 327
 Nayak, C., 9
 Nazemi, M., 287
 Neblett, C.R., 399
 Needham, D., 352
 Negishi, N., 49,402
 Nelson, C.E., 56
 Nemoto, I., 342
 Nemoto, I., 393
 Nerem, R.H., 252,254,355,357
 Nerem, R.N., 372
 Nerhed, C., 199,273
 Neroni, M., 335
 Nesbit, P., 358
 Neuenschwander, H., 43,56,106
 Neufeld, G.N., 220
 Neuman, M.R., 401,405
 Neumann, F., 286
 Nevo, E., 371
 Newcomb, C.H., 8
 Newcomb, R., 365
 Newhouse, V.L., 358
 Nguyen, P.D., 310
 Nibhanupudy, J.R., 32
 Nibhanupudy, R., 48
 Nichelatti, M., 145
 Nickerson, A.L., 199
 Niederer, P., 219
 Niemierko, A., 44
 Nievola, J.C., 330
 Nikawa, Y., 47,49
 Nikias, C.L., 169
 Nikiforidis, G., 300,312
 Nilsson, F., 273
 Ninomija, S.P., 324,329

Ninomiya, S., 69
 Niroomand-Rad, A., 38,130
 Nishidai, T., 137
 Nishimura, K., 99,104,150
 Nishimura, T., 258
 Nishiyama, G., 164
 Nishiyama, S., 379
 Nishizawa, K., 31
 Nitzan, H., 268,307,407
 Niwa, M., 285
 Nizin, P., 134
 Nobre, F.F., 198
 Noda, H., 248
 Noda, T., 266,380
 Nolan, S.P., 252
 Nollert, M.U., 253
 Nomura, Y., 333
 Noon, G.P., 361
 Norman, A., 41
 Northrop, R.B., 234
 Norton, R.L., 303
 Nosaka, T., 346
 Nose, K., 223
 Nose, Y., 237,245
 Nouet, P., 90
 Noz, M.E., 116
 Numata, K., 320
 Nyenhuis, J., 170
 Nygaard, H., 239,277,290
 Nyssen, M., 276,393
 Nystrom, H., 79

 O'Brien, K., 320
 O'Brien, P., 55
 O'Brien, W.D., Jr., 359
 O'Connor, S.A.O., 81,274,281
 O'Connor, T.P., 136
 O'Neill, G., 224,366
 O'Rear, E.A., 283,310
 O'Rourke, M., 267
 Oamura, T., 112
 Obcemea, C.H., 136
 Obel, I.W.P., 293
 Oberg, P.A., 375,403
 Odagiri, H., 406
 Oddou, C., 180,290
 Ogasawara, Y., 268,290,360,361,373,376
 Ogawa, H., 75
 Ogawa, M., 115
 Ogura, K., 342
 Ohayon, J., 179,349
 Ohlhaber, T.R., 88
 Ohnuma, H., 203
 Ohshima, N., 254,346,350
 Ohsumi, Y., 305
 Ohta, K., 231
 Ohta, Z., 273
 Ohtsubo, J., 377
 Oikawa, S., 148
 Ojala, A., 9,330
 Okada, E., 279
 Okada, F., 49
 Okada, Y., 201
 Okai, O., 293
 Okajima, M., 202,231
 Okamoto, Y., 164,189
 Okamura, T., 90,267,373
 Okumura, K.H., 199
 Okuyama, F., 367
 Okuyama, N., 61
 Olcaytug, F., 400
 Olch, A., 41
 Oliveira, M., 114A.
 Olivier, A., 90,140
 Olsen, K.J., 28,99
 Olsmats, H.M., 372
 Olson, A., 89
 Olson, L.E., 351
 Onai, Y., 84
 Onal, E., 215
 Ono, N., 196

 Onoda, T., 335
 Oneda, G., 250
 Oota, A., 351
 Ophir, J., 76
 Orem, J., 215
 Oro, J.J., 339
 Orphanoudakis, S.C., 82
 Ortengren, T., 213
 Orton, C.G., 6,152
 Oshima, N., 346
 Osian, A.D., 152
 Ostergaard, J.H., 239,286,290
 Ostroy, F., 176
 Ota, Y., 69
 Otaki, K., 278
 Ott, S.M., 82
 Otte, V.A., 97
 Oude Vrielink H.H.E., 350
 Overton, W., 32
 Oxland, T., 210
 Oyama, T., 250
 Ozkaya, N., 354

 Pack, A.I., 214
 Paes-Leme, P.J., 107
 Pagani, A., 256
 Pagani, M., 256
 Page, P., 169
 Paliwal, B., 79,121,133
 Pallas-Areny, R., 185,257,315,316,382
 Pallikarakis, N., 21,89
 Pallone, T.L., 243
 Pallot, G., 357
 Pallotti, C., 145
 Pallotti, G., 145
 Paloheimo, M.P.J., 170
 Palta, J.R., 50,57,120,135
 Pan, X., 255
 Pan, Y., 304
 Panaccia, A.D., 380
 Panayiotakis, G., 89
 Panerai, R.B., 194,198
 Pang, T., 296
 Pannike, A., 200
 Panuccio, P., 321
 Papageorgiou, G.L., 404.
 Pareek, S., 149
 Parekh, A., 158
 Parisi, R.A., 215
 Park, C.H., 58
 Park, S.H., 235
 Parker, D.L., 27
 Parker, K.H., 255
 Parnis, S., 204
 Partain, C.L., 93
 Parthasaradhi, K., 53
 Parviainen, P., 324
 Pascal, F., 22
 Paschoa, A.S., 107
 Pascual, J.M.S., 27
 Passariello, G., 277
 Passerini, G., 72
 Pasveer, F., 228
 Pate, B.L., 178
 Patel, B.S., 361
 Paterniti, D.P., 403
 Pathak, C.M., 69
 Patil, K.M., 318
 Patil, M.M., 400,403
 Patterson, M.S., 5,143
 Patterson, R.E., 103
 Patterson, R.P., 271
 Paul, J.M., 59,127,152
 Paul, J.P., 388
 Paulsen, P.K., 239,277,290
 Paulson, D., 61
 Pave, A., 227
 Pavesi, G., 174
 Pavlenko, V.A., 339,407
 Pavlin, C.J., 77
 Pavuza, F., 368

 Payne, D.G., 77
 Payson, M., 358
 Pearce, J.A., 309,393,394,408,409,410
 Pearson, G.D., 83
 Pearson, J.D., 178
 Peckham, P.H., 161
 Pedersen, E.M., 239,286,290
 Pedley, T.J., 222,262,370
 Pedraza, L.J., 105,143
 Peifer, J.W., 100
 Pei, H., 332
 Pelisse, F., 369
 Pelissier, R., 264,278,289
 Peng, C.L., 312
 Peng, W., 311
 Penkoske, P.A., 165,167
 Pennington, E.C., 119
 Penzel, T., 313
 Pepino, A., 340,391
 Pepsiller, P.L., 8
 Peralta, A.P., 138
 Pereira, C.A., 278
 Pereira, W.C.A., 363
 Perez, C.A., 126
 Perkins, B.H., 176
 Perkkio, J., 282
 Perktold, K., 375
 Peronneau, P., 76,253,306,356,359
 Perroche Roux, A.M., 44
 Perry, D.J., 107
 Persson, B.R.R., 111
 Persson, J., 191,193
 Persson, R.B.R., 382
 Peskin, C.S., 370
 Peter, J.H., 313
 Peters, T., 90
 Peters, T.M., 140
 Peters, V., 143
 Peterson, G.P., 409
 Peterson, J.I., 401
 Peterson, J.N., 343
 Pettazoni, P., 145
 Petti, P.L., 74
 Pettigrew, R.I., 377
 Pettit, G., 189
 Pfaff, J.M., 71
 Pham, T.T., 84
 Philip, P.C., 59,127,152
 Phillips, W., 67
 Phillips, W.M., 240
 Photiou, K., 358
 Pianta, P.G., 370
 Pichler, H., 368
 Pickens, D.R., 35,93
 Piechocki, M., 359
 Pierce, W.S., 246
 Piermattei, A., 45,140,152
 Pierrakeas, Ch., 21
 Pierre, P., 353
 Pike, B., 90
 Pike, G.B., 140
 Pilla, A.A., 407
 Pillarella, M.R., 237
 Ping, L., 87
 Pino, C., 130,136
 Pirker, K., 400
 Pirola, L., 25,26
 Pisani, M.A., 218
 Pitchen, I.C., 301
 Pitluck, S., 74
 Piva, R.M.V., 27
 Pizziconi, V., 236
 Pla, C., 90,56
 Pla, M., 56
 Plaszczyński, R.J., 187
 Plazas, M.C., 42
 Pleet, D., 17
 Plenkovich, D., 9,151
 Podgorsak, E.B., 56,90
 Poirier, V., 246
 Pola, T., 111

Pollak, V.A., 334
 Poluta, H.A., 197,293
 Pomeranz, B., 397
 Ponnalagarsamy, R., 289
 Pontinen, P.J., 197
 Poopathi, V., 129
 Popescu, G.F., 36,108,129
 Poplawska, W., 292
 Porges, S.W., 258
 Porter, D., 80
 Portner, P., 246
 Potter, A.G., 177
 Potter, G., 76
 Potter, R., 390
 Potvin, W.J., 20,21
 Pou, A., 351
 Powlis, W., 45
 Pozniak, M., 75
 Prabhakaran, R., 327
 Pahl, S.A., 17,408
 Prasad, G.N.S., 18,24,25,28,64
 Prasad, S.C., 128
 Prasad, S.G., 53
 Prato, F.S., 103
 Predergast, F.G., 234
 Pressly, M., 309
 Pretorius, P.H., 113
 Price, R.R., 93
 Prieto, F., 218,233
 Prieto, P.S., 89
 Prinzen, F.W., 178,179
 Prohaska, O.J., 341,400,403
 Proimos, B., 89,300
 Prokoplou, P., 312
 Pronk, R.A.F., 168
 Pucher, R.K., 288,285
 Pugliesi, V., 264
 Purcell, C., 61
 Purdy, J.R., 4,13,50,134
 Put, J.H.M., 159,339
 Paurunen, H., 50,57,139

 Qi, Y., 304
 Qian, Z., 278
 Qiao, Z., 383
 Qin, C., 292
 Qin, J., 285
 Qiu, Y., 188
 Quan, L., 310
 Quarto, E., 17
 Quill, T.J., 175
 Qing, T., 255
 Quintero, F.J., 153
 Rabin, H.S.Z., 131
 Rabinovitz, R.S., 357,361
 Rachev, A.I., 268
 Radford, W.E., 410
 Radvan-Zienowicz, S.A., 383
 Ragan, D.P., 5
 Raganella, L., 48
 Raisia, S.K., 107
 Rajaratnam, S., 12,120,124
 Raju, D.V.S., 272
 Rakfal, S.H., 56
 Ramachandran, G., 190
 Raman, E., 408
 Ramaswamy, J.S., 135
 Rane, M.B., 203
 Ranger, N.T., 102
 Rantanen, J., 9,330
 Rao, D.V., 7,19,67
 Rao, K.S., 318
 Rapp, J., 255
 Rashid, H., 8,136
 Rastegar, S., 17
 Ratchev, I.B., 335
 Rath, G.K., 125
 Rath, R., 125
 Ravelli, F., 171
 Ravichandran, R., 68,139
 Ravindra, P.S., 327

 Rawlinson, J.A., 45
 Raymond, C.J., 262
 Raymond, C., 38
 Rebelo, M.F.S., 113,114
 Reccia, R., 366
 Rechenmann, F., 227
 Redding, V.C., 404
 Reddy, N.P., 203,224
 Reddy, S., 78
 Reddy, S.P., 385
 Redpath, A.T., 13
 Reed, R., 71,87
 Reft, C.S., 96,119
 Regazzoni, C., 392
 Reggi, M., 264
 Rehak, P.H., 384
 Rehani, M.M., 112
 Rehr, R.B., 81
 Rehwald, W., 259
 Reid, D., 81
 Reidy, J., 358
 Reif, T.H., 242
 Reimann, D.A., 8,151
 Reinstein, L.E., 51,85
 Reneman, R.S., 178,179,350,351,363,375
 Renner, T., 74
 Renner, W.D., 136
 Renzi, R., 142,378
 Reul, H., 240,277
 Reves, J.G., 176,177
 Reyn, J.W., 260
 Reynolds, K.L., 79
 Ribbe, T., 337
 Ribitsch, G., 302
 Ribitsch, V., 302,348
 Ricci, S., 38
 Rice, R.K., 8,122,135
 Richardson, P., 190
 Richards, M.A., 80
 Richardson, M.L., 82
 Richardson, P.D., 236
 Richter, N., 197
 Riddle, M., 17
 Riddle, M., 23
 Riddle, W., 93
 Rideout, V.C., 177
 Rieu, R., 264,289
 Rijnders, A., 97
 Rilmer, G., 98
 Riml, H., 151
 Rindt, C.C.M., 375
 Ritchie, R.G., 178
 Pitman, E.L., 182
 Rittgers, S., 378
 Riu, P., 257,315,316,382
 Rivers, M.L., 146
 Rivers, R.P.A., 259
 Roach, M.R., 250
 Robdeutscher, W., 388
 Roberge, F.A., 161
 Roberti, G., 24,368
 Roberts, V.C., 185,196,269
 Roberts, W.A., 12
 Robertson, G.R.J., 73
 Robilotta, C.C., 27,113,114
 Robinson, D., 123
 Robinson, D.E., 361
 Robinson, L., 358
 Robinson, R.C., 7
 Rocha, M.P.O., 95
 Rodarte, J., 222
 Rodellar, V., 365
 Roden, D.M., 232
 Rodgers, J.E., 36,108,129
 Rodrigues, L.N., 95
 Rodriguez, C.A., 274
 Rodriguez, J., 173
 Rodriguez, L.V., 138
 Roebuck, J., 16
 Rogers, D.W.O., 5,142

 Rolfe, P., 203,204,316,402
 Romanelli, L., 230
 Romani, G.L., 4
 Romano, M., 211
 Rompelman, O., 257
 Rose, D.F., 33
 Rosell, J., 257,315,316,382
 Roselli, R.J., 216
 Rosen, B.R., 7,92
 Rosenberg, G., 246
 Rosenberg, N., 262
 Rosenman, J.G., 79
 Rosenow, U.F., 12,42,120,124
 Rosenthal, M.S., 19,25,46,65,77,111
 Rosenwald, J.C., 40,120,394
 Ross, C.K., 141
 Ross, J., 138
 Rossi, B., 340
 Rotger, V.I., 188,197
 Roth, B.J., 62,165
 Rothenberg, L.H., 31
 Roucou, D., 228
 Roudis, S., 300
 Rouzard, M., 90
 Rowe, R.W., 102
 Rowlands, J.A., 35
 Rowley, B.A., 389
 Roy, J.N., 92
 Roy, O.Z., 62
 Rozenthal, J.J., 30
 Rudy, Y., 169
 Rueger, J., 200
 Ruiz, E., 173
 Rumberger, J.A., 182,183
 Runge, V.R., 93
 Ruo, J.B., 361
 Ruperal, R., 53
 Russell, M., 52
 Russo, P., 17
 Russo, S., 24,366
 Rustgi, S.N., 36,108,129
 Rutledge, J., 248
 Rutten, W.L.C., 159,339
 Ruzyllo, W., 292
 Rylander, H.G., III, 16
 Rymel, J., 37

 Sabbah, H.N., 372
 Sabeti, V., 116
 Sachan, V.K., 80
 Sacks, M.S., 347
 Sagawa, K., 179,183
 Saha, P., 192
 Saha, S., 192,205,210,378
 Sahar, M., 262
 Saidel, G.M., 221,249,401
 Sallaja, I., 318
 Sailer, S., 123
 Saito, M., 73,244,281,314,365,370
 Saitoh, Y., 297,298
 Sakai, K., 306
 Sakai, S., 271
 Sakakibara, M., 274
 Sakakura, K., 231
 Sakamoto, K., 49,382
 Sakata, N., 250
 Sakata, S., 114
 Sakhival, S., 28
 Sakuma, I., 333,390
 Sakuraba, S., 350
 Sakurai, Y., 203,388
 Sala, P., 26
 Saldivar, E., 329
 Salerud, E.G., 376
 Salinari, S., 173
 Salonen, L., 390
 Saltzberg, B., 381
 Samake, G., 290
 Samaratinga, R.C., 14
 Samsani, N., 39,52,123,136
 San, L., 314

Sanders, I., 161
 Sanders, M., 118
 Sandison, G.A., 31,70,107,117
 Sands, S., 399
 Sanford, M.K., 54
 Santello, J.L., 296
 Santiago, T.V., 215
 Santini, M.T., 28
 Sapoznikov, D., 268
 Saranummi, N., 9,330
 Sarfaraz, M., 38
 Sartori, M., 189
 Sasane, J.B., 41
 Sashin, D., 149
 Sasse, F.J., 177
 Sastry, K.S.R., 7,19,67
 Sato, E., 147,148
 Sato, K., 191,329
 Sato, M., 254,346,350
 Sato, N., 333
 Sato, S., 33
 Satouura, K., 189
 Sauerbrey, R., 189
 Saul, J.P., 257
 Saumarez, R.C., 221
 Savard, P., 169
 Saviolis, B., 223
 Savino, G.V., 230
 Savoie, D., 107
 Saw, C.B., 153
 Sawada, T., 34
 Saxberg, B.E.H., 229
 Sayeg, J.A., 59
 Saylor, T.K., 47,79
 Scarborough, E.C., 122,128,143
 Schaldach, M., 279,294,383,400
 Scheffer, G.J., 257
 Schell, M., 127,153
 Schenone, A., 140
 Scherer, P.W., 220
 Schickl, K., 241,280
 Schils, G.F., 177
 Schlienger, M., 90
 Schmekel, B., 225
 Schmid, E., 219
 Schmid, R., 330
 Schmid-Schonbein, G.W., 349,355
 Schmid-Schonbein, H., 282
 Schmidt, R.A., 89
 Schneditz, D., 283,297,302,348
 Schneider, G.T., 328,332
 Schneider, S., 188
 Schneideman, N., 385
 Schoephoerster, R., 243
 Schoepfels, S.L., 126
 Schoffa, G., 293
 Schreiner, L.J., 82
 Schreiner, W., 286
 Schroeder, P.M., 187,319
 Schroter, R.C., 220
 Schuder, J., 172
 Schueler, P., 33
 Schulz, R.J., 43
 Schurizek, B.A., 239
 Schuster, J., 63
 Schuy, St., 289
 Schwab, B., 352
 Schwardt, J.D., 220
 Schwartz, C.J., 252
 Schwartzberg, D.G., 94
 Schweitzer, F.C., 399
 Schwimbeck, R., 377
 Scott, P., 210
 Scringier, J.W., 44,123
 Sour, S., 247
 Sealy, R., 60
 Seed, W.A., 372
 Seeman, T., 213
 Sefton, M.V., 178
 Segart, O., 95,234
 Segal, A., 375
 Segawa, T., 146
 Seibert, J.A., 15,36,72
 Seino, H., 69
 Seki, K., 345
 Seki, J., 248
 Sekiguchi, H., 380
 Sekii, S., 191
 Sekiya, T., 331,365
 Selvidge, R., 301
 Semmlow, J., 183
 Seo, Y., 356
 Sepulveda, N.G., 165,172
 Settels, J.J., 256,263
 Seuntjens, J., 95,234
 Sevilla, M.D., 406
 Sewchand, W., 38,105
 Shaber, G.S., 15
 Shackleton, D., 60
 Shackleton, M.O., 67
 Shaffer, M.D., 184,270
 Shaffer, M.J., 184,270
 Shah, R.V., 402
 Shahabi, S., 121,130,133
 Shalev, S., 13,46,85,144
 Shan, H., 248
 Shang, T., 299
 Shankar, B., 166
 Shankar, P.M., 362
 Shannon, D.C., 214
 Shao, J., 326
 Shao, Q., 304,326
 Shao, Q., 356
 Shapiro, A.H., 223,261
 Sharma, A.K., 139
 Sharma, R.R., 69
 Sharma, S.C., 122
 Sharma, V.K., 129
 Sharp, P.F., 20
 Shealy, C.N., 398
 Shee, T.R., 260
 Sheehan, H., 127
 Shehab, S.A., 188
 Shen, C., 202
 Shen, F., 326
 Shen, Q., 284
 Shen, S., 336
 Shenasa, M., 169
 Sheng, J., 211
 Sheng, Z., 381
 Shepherd, A.P., 282
 Sheppard, L.C., 175,176,177,178
 Sher, P.B., 152
 Sherman, C., 246
 Sherouse, G.W., 55,79,140
 Sherwood, A.M., 163
 Shettigar, U.R., 238
 Sheu, H., 396
 Shi, D., 278
 Shibata, M., 351,352
 Shibata, N., 231
 Shibuya, T., 189
 Shields, C.B., 170
 Shimazaki, Y., 388
 Shimazu, H., 202,203,288,345,384
 Shimizu, K., 377,405,406
 Shimizu, M., 260
 Shimizu, S., 309
 Shimomura, T., 343
 Shimooka, T., 245
 Shin, J.W., 368
 Shinoda, A., 279
 Shipley, W., 39
 Shiu, A.S., 97,108
 Shoji, H., 387
 Shortt, K.R., 141
 Showalter, D.P., 249
 Shozawa, T., 254
 Shrivastava, P.N., 47,79,86
 Shu, M.C.S., 241
 Shukla, A.K., 80
 Shukla, S., 145
 Shuman, W.P., 82
 Shung, K.K., 362
 Shypailo, R., 65
 Shyu, L.Y., 385
 Sibata, C.H., 56,123
 Siddon, R.L., 8,90
 Sideman, S., 178,182,231,325
 Siegel, J.A., 3
 Siegel, J.H., 169
 Sievanen, H., 171,232
 Silage, D.A., 214
 Silverstein, E.A., 65,113
 Simizu, K., 1123
 Simkin, A., 207
 Simmons, D.J., 205
 Simon, S., 355
 Simonian, A.L., 320
 Simonian, M., 120
 Simons, A.J.R., 168
 Simons, D., 279
 Simpson, E.R., 77
 Sirson, L.D., 108,141
 Simms, C., 37
 Sims, C., 83
 Singh, M., 190
 Singh, M., 205
 Sipkema, P., 371
 Sisterson, J.H., 131
 Siwek, R.A., 18
 Sjolund, B.H., 398
 Skalak, R., 354
 Skalak, T.C., 349
 Skeen, R.S., 340
 Skelton, J.P., 100
 Skolnick, L., 399
 Skolnick, M., 399
 Skouffis, E.G., 242
 Slaaf, D.W., 350,351
 Slager, C.J., 360
 Slasky, B.S., 149
 Slater, C.S., 67
 Sleek, G.E., 349
 Slessinger, E.D., 126
 Sloane, E.B., 195
 Slump, C.H., 150
 Snarra, N., 142
 Snathers, J., 7,132
 Snathers, J.B., 75
 Smith, A., 43
 Smith, B.F., 332
 Smith, D., 399
 Smith, D.H., 382
 Smith, E.B., 248
 Smith, G., 93
 Smith, G.D., 141
 Smith, I., 62
 Smith, J.M., 229
 Smith, J.R., 168
 Smith, M.A., 15,80,283
 Smith, M.D., 206
 Smith, R., 398
 Smith, R.B., 91
 Smith, V., 81,153
 Saye, S.W., 371
 Sayles, J., 48
 Snyder, A.J., 246
 Soderberg, T., 277
 Solin, L., 13
 Solomonidis, S.E., 388
 Solomonow, M., 387
 Solzi, P., 385
 Sones, R.A., 36
 Song, Q., 356
 Sontag, M., 12,13
 Soubra, M., 40
 Spaan, J.A.E., 181,267,350
 Spach, M.S., 160
 Spahn, D., 219
 Spanne, P., 146
 Spelbring, D.R., 91
 Spicer, K.M., 114

Spiegel, P.K., 93
 Spiegelberg, A., 280
 Spies, S.H., 65,113
 Spies, W.G., 113
 Sposito, S., 66
 Sprague, E.A., 252
 Spriggins, A.J., 206
 Srdanovic, V., 201
 Srigley, J., 18
 Srinivasan, R., 265,295
 Stabile, L., 128
 Staderini, E.M., 101,117
 Stafford, P.M., 39
 Stamboliev, I.B., 335
 Stancil, P.E., 55
 Stanley, L.D., 55
 Stannard, C., 60
 Starita, A., 327,340,404
 Stark, G., 294
 Starkschall, G., 92,108
 Starr, C., 114
 Steckner, M., 103
 Steenhoven, A.A.V., 375
 Steeves, R., 79
 Stefanini, A., 327
 Stefanovska, A., 386
 Steffan, H., 288
 Steiger, P., 92,207,301
 Steiger, S., 301
 Stein, P.D., 372
 Steinhaus, B.M., 160
 Steinke, J.M., 282
 Steinseifer, U., 240
 Steinvil, Y., 385
 Stekiel, W.J., 349
 Stenberg, J., 79
 Stenzl, W., 384
 Stephenson, L., 161
 Stergiopoulos, N., 379
 Sternick, E.S., 57
 Sternick, E.S., 146
 Stewart, B., 132
 Stewart, D.J., 298
 Stoeckle, H., 172
 Stoehr, H.G., 386
 Stoessel, J., 405
 Stojiljkovic, Z., 201
 Stokes, B., 118
 Stokes, S.H., 129
 Stolerio, D., 241
 Stommel, K.A., 404
 Storch, P.R.H., 106
 Stortzum, R., 108
 Strand, S.-E., 4
 Straton, L., 295
 Strobel, J.D., 176
 Stroh, K., 161
 Strohl, K.P., 216
 Stroink, G., 60,61
 Strom, I., 318
 Strumpf, R.K., 344,346
 Sturaro, F., 392
 Su, S.C., 336
 Su, W.W., 201
 Su, Y., 208
 Subramaniam, S., 25
 Sud, V.K., 265
 Suematsu, K., 401
 Sugahara, T., 265
 Sugawara, M., 356,374,379
 Sugihara-Seki, M., 354
 Sugimoto, N., 265
 Sugimoto, T., 377
 Sugiyama, Y., 281
 Sui, W., 326
 Suignard, L.J., 361
 Sullivan, G.S., 32
 Sullivan, P.A., 263
 Suma, K., 266
 Sum, C., 208
 Sun, J., 207
 Sun, J.K., 342
 Sun, W., 294
 Sun, Y., 188
 Sung, H., 240,303
 Sung, K.P., 353
 Suntharalingam, N., 50,57,84,120,135,153
 Suorsa, V., 259
 Supe, S.J., 41
 Suresh, I., 28
 Suresh, S., 28
 Susak, Z., 385
 Susanszky, M., 197
 Sutura, S., 353
 Suwa, A., 104
 Suzuki, H., 306
 Suzuki, M., 275
 Suzuki, N., 90,113,267,366,373
 Suzuki, S., 202
 Suzuki, T., 373
 Suzumura, N., 34,100,231
 Svedbergh, B., 367
 Svensson, G.K., 119
 Svensson, H., 79
 Svensson, M., 213
 Svensson, O., 174
 Swain, P., 317
 Swanson, R., 18
 Sweeney, J.D., 152
 Swensson, R.G., 105
 Swett, H.A., 10
 Swissa, A., 207
 Sydanmaa, M., 235
 Syed, I.B., 66
 Symonds, G.R., 73,323
 Szabo, J.J., 54
 Tachinardi, U., 172,296
 Tacker, W.A., 170
 Tada, S., 267
 Tadaoka, S., 290,376
 Taenaka, Y., 264
 Taiganides, P.A., 269
 Takahashi, A., 393
 Takahashi, J., 148
 Takahashi, M., 137
 Takahashi, T., 201
 Takaku, Y., 131
 Takano, H., 248,264
 Takano, N., 174
 Takano, T., 252
 Takao, Y., 100
 Takase, M., 366
 Takata, T., 304
 Takatani, O., 402
 Takatani, S., 264
 Takatsu, H., 305
 Takaya, T., 266
 Takebayashi, S., 250
 Takeda, H., 200,271
 Takeda, T., 99,333
 Takeda, Y., 203
 Takenaka, E., 104,110,140,150,322
 Takeuchi, K., 131,189
 Talbot, L., 241
 Talbot-Pedersen, A., 401
 Tahami, H., 358
 Talusan, I., 101
 Tamamura, T., 14
 Tamas, M.J., 103
 Tamegai, T., 69
 Tamisier, L., 253
 Tamura, K., 69,323
 Tamura, M., 306
 Tamura, T., 191,306,309,336,364,401
 Tamura, Y., 333
 Tan, R., 188
 Tan, S., 62
 Tan, Y., 188
 Tanabe, T., 34
 Tanaha3hi, Y., 291
 Tanaka, K., 112
 Tanaka, S., 203,247
 Tanaka, T., 266
 Tanaka, Y., 81
 Tang, J., 28
 Tang, L., 293
 Tang, Y.Z., 336
 Tangelder, G.J., 350,351
 Tani, A., 256
 Tanishita, K., 306
 Tanksale, S.K., 249
 Tanouchi, J., 254,303,356,364
 Tarbell, J.M., 347
 Tarnawski, M., 15
 Tashiro, T., 387
 Tatsumura, M., 324
 Taube, D., 269
 Taveras, J.M., 35
 Tawney, K.W., 358
 Taylor, A.F., 223
 Taylor, G.H., 15
 Taylor, M.G., 358
 Tecson, M.R., 101
 Tedgui, A., 249
 Ten Haken, R.K., 57,59,127
 ten Hoff, H., 360
 ten Voorde, B.J., 257
 Tengerz, L., 367
 Tengerz, L., 404
 Tepper, J.E., 55
 Terakawa, T., 47
 Terashima, Y., 305
 Terio, H., 204
 Tessmann, G., 144
 Thakor, N.V., 166,173,174,381
 Thao-Chan, C., 355
 Thatcher, M., 41
 Therrien, P., 13
 Thews, O., 307
 Thiagarajan, S., 25.P.
 Thierens, H., 95,234,295
 Thoma, H., 386
 Thomadsen, B.R., 121,130,133
 Thomas, S.K., 3,14
 Thompson, C.J., 92,102
 Thomsen, S., 18
 Thorniley, M.S., 204
 Thrope, G.B., 151
 Thubrikar, M.J., 252
 Thull, R., 294
 Thurston, G.B., 283,348
 Thwaites, D.I., 13,38,42,96,97,118,124,125
 Tian, A., 297,318,319,322
 Tian, W., 280
 Tian, Z., 342
 Tiberio, C.A., 48
 Tie, B., 183
 Tiederman, W.G., 240
 Tien, A., 83
 Titomir, L.I., 164
 Tittel, F.K., 189
 Tkacik, M., 78
 Tobias, C.A., 31,85
 Toda, N., 325
 Togawa, T., 191,266,305,309,313,318,323,
 336,401,406,409
 Tohda, K., 254
 Tokimura, K., 388
 Tokoro, T., 367
 Toktas, S., 312
 Tolley, N.S., 224
 Tomaru, T., 84
 Tomaru, T., 377
 Tominaga, M., 304
 Tomita, Y., 49
 Tomonaga, G., 14,268
 Tonietto, G., 278
 Tooley, M.A., 274
 Torres, J.H., 18,189
 Torrisi, J., 36
 Tortal, P., 32
 Tovar, V.M., 54

Towe, B., 402
 Toyama, H., 104
 Toyama, J., 325
 Toyofuku, F., 104,150
 Toyoshima, T., 316,323,336
 Toyotama, H., 342
 Tozeren, A., 347,353
 Trahas, L., 33,339
 Traissac, L., 390
 Trajkovic, M., 201
 Traub, R.D., 164
 Treharne, R.W., 209
 Treiber, J., 285
 Tritthart, H.A., 294
 Trontelj, Z., 33
 Truemper, E.J., 190
 Tsai, J., 119
 Tsambaos, D., 312
 Tsang, N.H., 120
 Tsao, S., 338
 Tsitlik, J.E., 183,375
 Tsuchiya, K., 313,336
 Tsuda, A., 223
 Tsuji, S., 333
 Tsuji, T., 266,306,309,318,323
 Tsujimoto, F., 267
 Tsujioka, K., 181,268,290,360,361,373,37
 Tsukamoto, T., 305
 Tsuzuki, M., 320
 Tu, C.P., 54,120
 Tucker, D.M., 170,176
 Tupchong, L., 84
 Turbes, C.C., 328,332
 Turjanmaa, V., 235
 Turk, R., 386
 Twelves, C.J., 80
 Tyagi, M., 28

 Uchida, I., 84
 Uchida, Y., 377
 Uchikawa, Y., 33,61
 Uchiyama, A., 04
 Ucisik, A.H., 206
 Ueda, Y., 329
 Uematsu, M., 254,303,356,364
 Uerg, Y.S., 390
 Ueno, S., 34
 Ueno, S., 387
 Ulin, K., 57
 Ullrich, C., 319
 Ulmer, W., 80
 Unsworth, A., 302
 Urbano, A., 173
 Urbina-Medal, E.G., 304
 Urie, M., 131
 Urrutia, T., 12
 Usha, T., 289
 Usui, S., 274,325
 Utsumi, A., 189
 Utsunomiya, T., 328
 Uyama, C., 264,265

 v.d.Voorden, E., 34
 v.Harsdorf, S., 33
 Vaananen, A., 50,57
 Valdezco, E., 72
 Valentinuzzi, M.E., xx,173,188,197
 Valeri, L., 66
 Valimaki, I., 324
 Vallbona, C., 200,322
 Vallverdu, M., 266
 Valvano, J.W., 408,409
 van Aswegen, A., 113
 van Beek, J.H.G.H., 230
 Van Dam, J., 97
 Van den Winkel, P., 68
 Van Der Linden, C., 387
 Van der Plaetsen, A., 95
 van Dijk, L.C., 371
 Van Dyk, J., 8,91
 van Egmond, F.C., 360

 van Eljnsbergen, B., 195
 van Herk, M., 45,86
 van Hulsteyn, D., 32
 van Merode, T., 363
 van Nimwegen, Chr., 193
 Van Wie, B.J., 340,343
 van Wier, H., 339
 van Wijk van Brievingh, R.P., 228,272
 Vanhuysse, V., 408
 Vanryckeghem, W., 68
 Varia, M.A., 55
 Vartiainen, E., 57
 Vasilionkaitis, V.V., 188
 Vassilakos, P.J., 21
 Vaz, C., 174
 Velmurugan, V., 18
 Velocci, V.V., 71,87
 Vercellone, M.I., 188,197
 Vergroesen, I., 267
 Verhey, L.J., 73
 Vernazza, G., 392
 Versnick, F., 276
 Vessella, R.L., 79
 Vesterhauge, S., 369
 Veyrat, C., 357
 Vieira, C.R.S., 198
 Vieth, J., 33
 Viggars, D., 13
 Viitanen, J., 139
 Vilaplana, F., 145,311
 Vine, A.K., 59
 Vinelli, F., 198
 Vinitski, S., 63
 Virolli, L., 321
 Vishnudevananda, S., 329
 Vito, R.P., 344,368
 Vlachos, N.S., 287
 Vodovnik, L., 386
 von Eschenbach, A.C., 18
 von Klitzing, L., 144
 von Maltzahn, W., 346
 Vossoughi, J., 344,345
 Vuori, I., 171,232
 Vuthien, H., 357
 Vynckier, S., 96,132

 Wada, S., 34,64
 Wada, T., 115
 Wada, T., 235
 Wada, Y., 140,290,360,376
 Waggener, R., 129
 Wagner, L.K., 88
 Wakai, R.T., 60
 Walcerz, D.B., 308
 Walczak, F., 292
 Wald, A., 186
 Walding, D.L., 190
 Walker, J.D., 240
 Walker, P., 241
 Walker, S., 135
 Wallace, R.E., 74,133
 Wallace, R.E., 75
 Walravens, N., 68
 Walsh, C., 260,263
 Wambersie, A., 96
 Wan, X., 213
 Wang, A., 342
 Wang, B., 194,196
 Wang, C., 280
 Wang, C.Y., 227
 Wang, H., 77
 Wang, H., 276
 Wang, H., 284,308
 Wang, J., 183
 Wang, J., 283,292,310,343
 Wang, J., 381
 Wang, L., 22,108
 Wang, L., 234
 Wang, L., 338
 Wang, M., 26
 Wang, M., 331

 Wang, M.T., 49
 Wang, P.D., 270
 Wang, S., 52
 Wang, S., 210
 Wang, S., 293
 Wang, S., 300,305
 Wang, W., 356
 Wang, W.K., 265,341
 Wang, X., 211
 Wang, X., 248
 Wang, X., 311
 Wang, X., 338
 Wang, Y., 212
 Wang, Y.Y.L., 341
 Wang, Z., 281
 Wang, Z., 334
 Waring, G., 368
 Warty, V.S., 249
 Watanabe, A., 314,370
 Watanabe, S., 69,99,198,331,378
 Watkins, N., 255
 Watson, J.T., xxi
 Watson, P.D., 216
 Watts, C., 339
 Waugh, R.E., 352
 Weaver, J.B., 93
 Weaver, K., 127,153
 Webster, P.H., 260
 Weed, H.R., 269
 Weeks, K.J., 126
 Wei, H., 34
 Wei, J., 276
 Wei, J., 341
 Wei, S., 341
 Wei, X.Y., 307
 Wei, Y., 291,315
 Weinberg, W.S., 16
 Weinhaus, H.S., 47,50
 Weinreb, A., 76
 Weiser, J.C., 46
 Weiss, H., 43
 Weiss, W., 246
 Weizsacher, H.W., 344
 Welch, A.J., 16,17,18,189
 Welkowitz, W., 183
 Wells, P.N.T., 144
 Wen, X., 275
 Wen, Z., 284
 Werner, B.L., 22
 Werner, E., 25,26
 Werner, I.D., 67
 Wesseling, K.H., 256,263,286
 Wessels, B.W., 79
 West, D.J., 15
 Westerhof, N., 371
 Westphal, D., 277
 Weyman, A.E., 279
 Whelpton, D., 273
 Wheeler, L., 355
 Whiting, J.S., 71
 Whitmire, D.R., 316
 Whitsett, T.L., 283
 Whittington, R., 12
 Whittle, H.W., 388
 Wible, B., 252
 Wickham, J., 317
 Wickramasinghe, Y.A.B.D., 204
 Wieck, B.-O., 197
 Wiederhecker, N.G., 198,330
 Wieme, R., 295
 Wier, W.G., 157
 Wiesen, G., 58
 Wigodsky, H., 192
 Wijesinghe, R.S., 159
 Wiksw, J.P., Jr., 61,62,159,165,172,232
 Wilcox, B., 225
 Wilkie, R.G., 398
 Wilkinson, D.A., 47,79,82
 Wilkinson, D.J., 274
 Willerson, J.T., 182
 Willett, C., 39

Williams, G., 21
 Williams, J., 363
 Williams, J.R., 118
 Williamson, J.F., 53,58,153
 Williamson, S.J., 61
 Willis, C., 70
 Wilson, D.L., 37,121
 Wilson, T.A., 222
 Wilson, T.A., 261
 Windedahl, L., 141
 Windham, J.P., 8
 Windham, J.P., 20
 Windham, J.P., 151
 Winfield, J.A., 128
 Winningham, D., 364
 Winter, D., 223,267
 Wisoff, P.J., 188
 Wist, A.O., 15,100
 Wit, A.L., 167
 Wittkowski, F.X., 165,167
 Wittkamper, F.W., 118
 Wolf, M.B., 216
 Wolin, A.D., 303
 Woll, J.M., 243
 Wollin, M., 41
 Wollmer, P., 225
 Wolner, E., 286
 Wolton, R., 402
 Wong, G., 40
 Wong, G.R., 311
 Wong, J.W., 13,23,46,65,134,143
 Wong, R.K.S., 164
 Wong, W., 102
 Wood, L.M., 281
 Wood, M.L., 93
 Woodard, J.C., 384
 Woodruff, E.A., 234
 Wooten, S., 343
 Wright, A.E., 62
 Wu, A., 60
 Wu, B., 334
 Wu, C., 396
 Wu, J., 27
 Wu, J.S.S., 300
 Wu, S.G., 291
 Wu, Y., 117
 Wu, Y., 311
 Wu, Y.P., 307,311
 Wurzinger, L.J., 282
 Wyman, D., 143

 Xi, B., 279
 Xi, T., 280
 Xia, Z., 278
 Xian, R., 299
 Xie, J., 27
 Xie, W., 336
 Xiong, M., 27
 Xu, G., 311
 Xu, J., 381
 Xu, N., 234
 Xu, X., 173
 Xu, X., 89
 Xu, Y., 208,210
 Xue, Z.N., 267,284

 Yaffe, M.J., 89
 Yagi, Y., 305
 Yaginuma, T., 330
 Yakar, D., 40,127
 Yamada, K., 325
 Yamada, Y., 112
 Yamaguchi, M., 266
 Yamaguchi, T., 245
 Yamaguchi, T., 250,380
 Yamaki, M., 26
 Yamakoshi, K., 202,203,212,247,345,384,402,288
 Yamamoto, K., 363
 Yamane, T., 250
 Yamanoi, N., 325
 Yamanoi, T., 212

 Yamashita, T., 81
 Yamato, J., 298
 Yamauchi, K., 200
 Yamazaki, K., 365
 Yan, J.Z., 298
 Yan, P.Y., 134
 Yan, X., 343
 Yana, K., 174,233,367
 Yanagihara, Y., 265
 Yanagisawa, T., 147,148
 Yanez, S.O., 297
 Yang, F.S., 234
 Yang, J., 299,326
 Yang, N., 83
 Yang, R.F., 307
 Yang, S., 391
 Yang, T.S., 306
 Yang, W., 409
 Yang, Y., 16
 Yang, Y., 77
 Yang, Y., 326
 Yang, Z., 26
 Yang, Z., 248
 Yano, F., 324,329
 Yao, J., 275
 Yarmush, M.L., 243
 Yasuda, H., 286,363
 Yasuda, N., 81
 Yasuda, Y., 148
 Yasui, S., 26
 Yates, F.E., 315
 Ye, G., 285
 Ye, Q., 264
 Yeap, C., 410
 Yen, M.R.T., 225
 Yester, M.V., 69
 Yeung, A., 355
 Yeung, I.W.T., 65,114
 Yeung, K.T.D., 84
 Yi, J., 313
 Yie, C., 263
 Yin, F.C.P., 183,344,346,375
 Ying, H., 176
 Ying, X., 85
 Yip, J.W., 25,77
 Yip, Y.P.L., 25,77
 Yoganathan, A.P., 240,242,276,303,361
 Yokoi, A., 202
 Yokoyama, H., 63,309
 Yonas, H., 84
 Yoo, S., 132
 Yoon, T.S., 235
 Yorke, E., 126
 Yoshida, H., 290
 Yoshida, T., 47
 Yoshida, Y., 256
 Yoshida, Y., 250,254,303,356,364
 Yoshimura, T., 366
 Yoshine, K., 236
 Yoshioka, Y., 81
 Young, D.F., 379
 Young, S.T., 265
 YoungLee, 53
 Yu, B.C., 357
 Yu, C.X., 23,134,143
 Yu, G., 341
 Yu, G.R., 201
 Yu, J., 298
 Yu, L., 242
 Yu, L., 316
 Yu, L., 342
 Yu, T., 339
 Yu, Z., 305
 Yuan, A., 112
 Yuan, Y.W., 362
 Yuasa, H., 87
 Yudelev, M., 132,133
 Yui, N., 114
 Yuichi, K., 299
 Yuta, T., 278

 Zabel, H.-J., 93
 Zachary, J., 359
 Zagzebski, J., 10,75
 Zahalak, G., 352,353
 Zaki, M., 212
 Zamenhof, R.G., 86.
 Zamorano, L., 18,40,86,127,276
 Zanchin, C.I., 330
 Zanoeco, P., 330
 Zborowski, M., 237
 Zeggwagh, G., 384
 Zeigler, B.P., 226
 Zeindler, C., 250
 Zeltser, R., 262
 Zeman, V., 301
 Zemskov, V.S., 339
 Zhang, C., 14,138
 Zhang, C., 293
 Zhang, D., 335
 Zhang, H., 138
 Zhang, H., 210
 Zhang, L.R., 267
 Zhang, S., 14
 Zhang, S., 340,343
 Zhang, T., 343
 Zhang, W., 342
 Zhang, Y., 293
 Zhang, Y., 297,299,300
 Zhao, H., 68,112
 Zhao, P., 342,392
 Zhao, W., 299
 Zhao, X., 314
 Zhao, Y., 284
 Zhen, D.S., 201
 Zhen, Y., 201
 Zheng, E.X., 312
 Zheng, Q., 328
 Zheng, X.L., 312
 Zhong, G.H., 284,311
 Zhong, J., 327
 Zhong, Z., 304
 Zhou, G., 298,313
 Zhou, H., 311
 Zhou, K., 337
 Zhou, L., 332
 Zhou, S., 300
 Zhou, S., 336
 Zhou, S.H., 373
 Zhou, X., 284
 Zhu, A., 248
 Zhu, D., 208,210
 Zhu, H.S., 332
 Zhu, J., 68
 Zhu, M., 336
 Zhu, W., 293
 Zhu, X., 279
 Zhu, X., 326
 Zhu, Y., 173
 Zhu, Y.P., 22
 Zimmer, A.M., 65,113
 Zingg, W., 178
 Zong, H., 316
 Zoreda, J.L., 202
 Zue, L.W.,
 Zydney, A.L., 237